SPONSORED BY THE
OPTICAL SOCIETY OF AMERICA

HANDBOOK OF OPTICS

FIBER OPTICS & NONLINEAR OPTICS

• SECOND EDITION •

VOLUME

IV

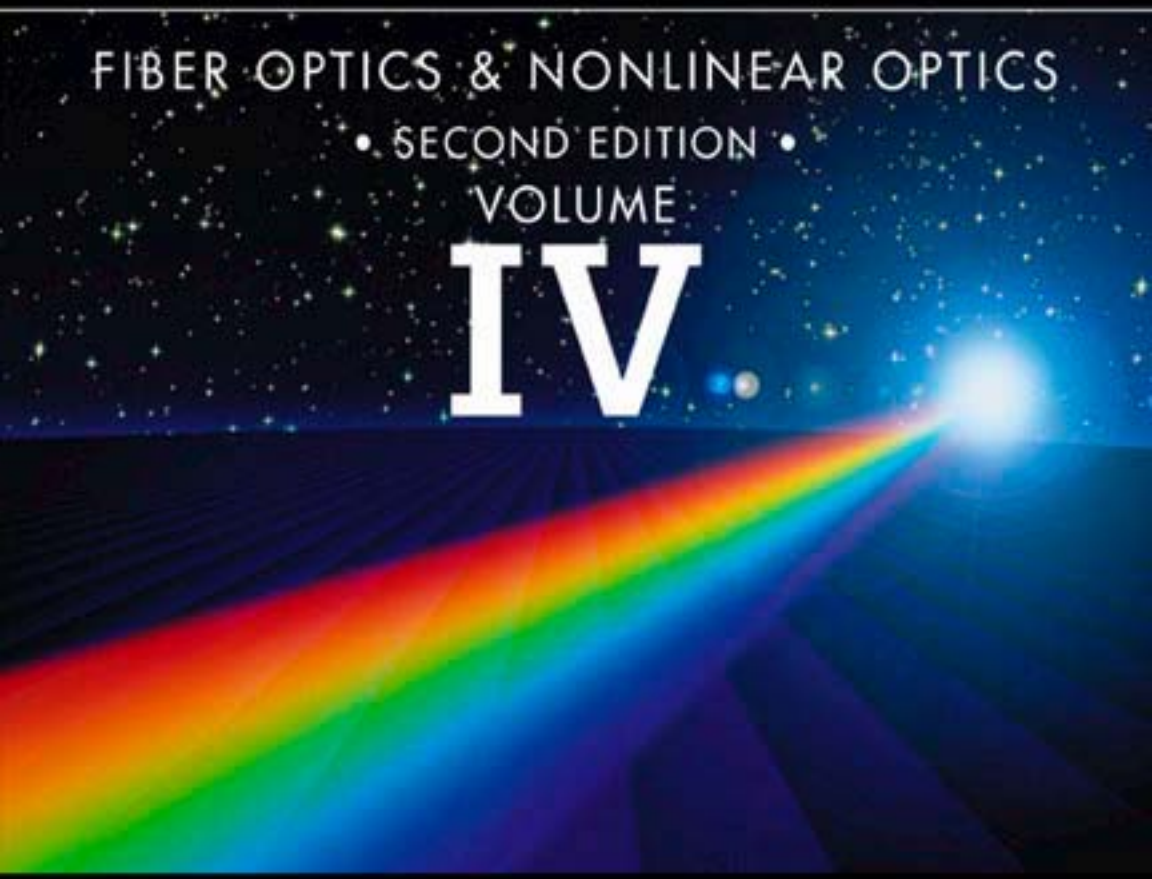

MICHAEL BASS, EDITOR IN CHIEF
JAY M. ENOCH • ERIC W. VAN STRYLAND • WILLIAM L. WOLFE, ASSOCIATE EDITORS

HANDBOOK OF OPTICS

Volume IV
Fiber Optics and Nonlinear Optics

Second Edition

Sponsored by the OPTICAL SOCIETY OF AMERICA

Michael Bass **Editor in Chief**

School of Optics / The Center for Research and Education in Optics and Lasers (CREOL)
University of Central Florida
Orlando, Florida

Jay M. Enoch **Associate Editor**

School of Optometry, University of California at Berkeley
Berkeley, California
and
Department of Ophthalmology
University of California at San Francisco
San Francisco, California

Eric W. Van Stryland **Associate Editor**

School of Optics / The Center for Research and Education in Optics and Lasers (CREOL)
University of Central Florida
Orlando, Florida

William L. Wolfe **Associate Editor**

Optical Sciences Center, University of Arizona
Tucson, Arizona

McGRAW-HILL

New York San Francisco Washington, D.C. Auckland Bogotá
Caracas Lisbon London Madrid Mexico City Milan
Montreal New Delhi San Juan Singapore
Sydney Tokyo Toronto

McGraw-Hill
A Division of The McGraw-Hill Companies

Copyright © 2001 by The McGraw-HIll Companies, Inc. All rights reserved. Manufactured in the United States of America. Except as permitted under the United States Copyright Act of 1976, no part of this publication may be reproduced or distributed in any form or by any means, or stored in a database or retrieval system, without the prior written permission of the publisher.

0-07-141479-7

The material in this eBook also appears in the print version of this title: 0-07-136456-0.

All trademarks are trademarks of their respective owners. Rather than put a trademark symbol after every occurrence of a trademarked name, we use names in an editorial fashion only, and to the benefit of the trademark owner, with no intention of infringement of the trademark. Where such designations appear in this book, they have been printed with initial caps.

McGraw-Hill eBooks are available at special quantity discounts to use as premiums and sales promotions, or for use in corporate training programs. For more information, please contact George Hoare, Special Sales, at george_hoare@mcgraw-hill.com or (212) 904-4069.

TERMS OF USE

This is a copyrighted work and The McGraw-Hill Companies, Inc. ("McGraw-Hill") and its licensors reserve all rights in and to the work. Use of this work is subject to these terms. Except as permitted under the Copyright Act of 1976 and the right to store and retrieve one copy of the work, you may not decompile, disassemble, reverse engineer, reproduce, modify, create derivative works based upon, transmit, distribute, disseminate, sell, publish or sublicense the work or any part of it without McGraw-Hill's prior consent. You may use the work for your own noncommercial and personal use; any other use of the work is strictly prohibited. Your right to use the work may be terminated if you fail to comply with these terms.

THE WORK IS PROVIDED "AS IS". McGRAW-HILL AND ITS LICENSORS MAKE NO GUARANTEES OR WARRANTIES AS TO THE ACCURACY, ADEQUACY OR COMPLETENESS OF OR RESULTS TO BE OBTAINED FROM USING THE WORK, INCLUDING ANY INFORMATION THAT CAN BE ACCESSED THROUGH THE WORK VIA HYPERLINK OR OTHERWISE, AND EXPRESSLY DISCLAIM ANY WARRANTY, EXPRESS OR IMPLIED, INCLUDING BUT NOT LIMITED TO IMPLIED WARRANTIES OF MERCHANTABILITY OR FITNESS FOR A PARTICULAR PURPOSE. McGraw-Hill and its licensors do not warrant or guarantee that the functions contained in the work will meet your requirements or that its operation will be uninterrupted or error free. Neither McGraw-Hill nor its licensors shall be liable to you or anyone else for any inaccuracy, error or omission, regardless of cause, in the work or for any damages resulting therefrom. McGraw-Hill has no responsibility for the content of any information accessed through the work. Under no circumstances shall McGraw-Hill and/or its licensors be liable for any indirect, incidental, special, punitive, consequential or similar damages that result from the use of or inability to use the work, even if any of them has been advised of the possibility of such damages. This limitation of liability shall apply to any claim or cause whatsoever whether such claim or cause arises in contract, tort or otherwise.

DOI: 10.1036/0071414797

Professional

Want to learn more?

We hope you enjoy this McGraw-Hill eBook! If you d like more information about this book, its author, or related books and websites, please **click here.**

For more information about this title, click here.

CONTENTS

Contributors xi
Preface xiii

Part 1. Fiber Optics

Chapter 1. Optical Fibers and Fiber-Optic Communications *Tom G. Brown* **1.3**

1.1 Glossary / *1.3*
1.2 Introduction / *1.5*
1.3 Principles of Operation / *1.6*
1.4 Fiber Dispersion and Attenuation / *1.10*
1.5 Polarization Characteristics of Fibers / *1.13*
1.6 Optical and Mechanical Properties of Fibers / *1.14*
1.7 Optical Fiber Communications / *1.21*
1.8 Nonlinear Optical Properties of Fibers / *1.39*
1.9 Optical Fiber Materials: Chemistry and Fabrication / *1.44*
1.10 References / *1.48*
1.11 Further Reading / *1.51*

Chapter 2. Optical Fiber Communication Technology and System Overview *Ira Jacobs* **2.1**

2.1 Introduction / *2.1*
2.2 Basic Technology / *2.2*
2.3 Receiver Sensitivity / *2.7*
2.4 Bit Rate and Distance Limits / *2.10*
2.5 Optical Amplifiers / *2.12*
2.6 Fiber-Optic Networks / *2.13*
2.7 Analog Transmission on Fiber / *2.14*
2.8 Technology and Applications Directions / *2.16*
2.9 References / *2.16*

Chapter 3. Nonlinear Effects in Optical Fibers *John A. Buck* **3.1**

3.1 Key Issues in Nonlinear Optics in Fibers / *3.1*
3.2 Self- and Cross-Phase Modulation / *3.3*
3.3 Stimulated Raman Scattering / *3.4*
3.4 Stimulated Brillouin Scattering / *3.7*
3.5 Four-Wave Mixing / *3.9*
3.6 Conclusion / *3.12*
3.7 References / *3.12*

Copyright 2001 by The McGraw-Hill Companies, Inc. Click Here for Terms of Use.

Chapter 4. Sources, Modulators, and Detectors for Fiber-Optic Communication Systems ***Elsa Garmire*** **4.1**

4.1 Introduction / *4.1*
4.2 Double Heterostructure Laser Diodes / *4.3*
4.3 Operating Characteristics of Laser Diodes / *4.9*
4.4 Transient Response of Laser Diodes / *4.15*
4.5 Noise Characteristics of Laser Diodes / *4.22*
4.6 Quantum Well and Strained Lasers / *4.28*
4.7 Distributed Feedback (DFB) and Distributed Bragg Reflector (DBR) Lasers / *4.34*
4.8 Light-Emitting Diodes (LEDs) / *4.39*
4.9 Vertical Cavity Surface-Emitting Lasers (VCSELS) / *4.45*
4.10 Lithium Niobate Modulators / *4.50*
4.11 Electroabsorption Modulators for Fiber-Optic Systems / *4.57*
4.12 Electro-Optic and Electrorefractive Semiconductor Modulators / *4.64*
4.13 PIN Diodes / *4.66*
4.14 Avalanche Photodiodes, MSM Detectors, and Schottky Diodes / *4.76*
4.15 References / *4.78*

Chapter 5. Optical Fiber Amplifiers ***John A. Buck*** **5.1**

5.1 Introduction / *5.1*
5.2 Rare-Earth-Doped Amplifier Configuration and Operation / *5.2*
5.3 EDFA Physical Structure and Light Interactions / *5.3*
5.4 Gain Formation in Other Rare-Earth Systems / *5.6*
5.5 References / *5.7*

Chapter 6. Fiber-Optic Communication Links (Telecom, Datacom, and Analog) ***Casimer DeCusatis and Guifang Li*** **6.1**

6.1 Introduction / *6.1*
6.2 Figures of Merit: SNR, BER, MER, and SFDR / *6.2*
6.3 Link Budget Analysis: Installation Loss / *6.7*
6.4 Link Budget Analysis: Optical Power Penalties / *6.9*
6.5 References / *6.18*

Chapter 7. Solitons in Optical Fiber Communication Systems ***P. V. Mamyshev*** **7.1**

7.1 Introduction / *7.1*
7.2 Nature of the Classical Soliton / *7.2*
7.3 Properties of Solitons / *7.4*
7.4 Classical Soliton Transmission Systems / *7.5*
7.5 Frequency-Guiding Filters / *7.7*
7.6 Sliding Frequency-Guiding Filters / *7.8*
7.7 Wavelength Division Multiplexing / *7.9*
7.8 Dispersion-Managed Solitons / *7.12*
7.9 Wavelength-Division Multiplexed Dispersion-Managed Soliton Transmission / *7.15*
7.10 Conclusion / *7.17*
7.11 References / *7.18*

Chapter 8. Tapered-Fiber Couplers, MUX and deMUX ***Daniel Nolan*** **8.1**

8.1 Introduction / *8.1*
8.2 Achromaticity / *8.3*

8.3 Wavelength Division Multiplexing / *8.4*
8.4 $1 \times N$ Power Splitters / *8.4*
8.5 Switches and Attenuators / *8.5*
8.6 Mach-Zehnder Devices / *8.6*
8.7 Polarization Devices / *8.6*
8.8 Summary / *8.8*
8.9 References / *8.8*

Chapter 9. Fiber Bragg Gratings ***Kenneth O. Hill*** **9.1**

9.1 Glossary / *9.1*
9.2 Introduction / *9.1*
9.3 Photosensitivity / *9.2*
9.4 Properties of Bragg Gratings / *9.3*
9.5 Fabrication of Fiber Gratings / *9.5*
9.6 The Application of Fiber Gratings / *9.8*
9.7 References / *9.9*

Chapter 10. Micro-Optics-Based Components for Networking ***Joseph C. Palais*** **10.1**

10.1 Introduction / *10.1*
10.2 Generalized Components / *10.1*
10.3 Network Functions / *10.2*
10.4 Subcomponents / *10.5*
10.5 Components / *10.8*
10.6 References / *10.11*

Chapter 11. Semiconductor Optical Amplifiers and Wavelength Conversion ***Ulf Österberg*** **11.1**

11.1 Glossary / *11.1*
11.2 Why Optical Amplification? / *11.2*
11.3 Why Optical Wavelength Conversion? / *11.7*
11.4 References / *11.9*

Chapter 12. Optical Time-Division Multiplexed Communication Networks ***Peter J. Delfyett*** **12.1**

12.1 Glossary / *12.1*
12.2 Introduction / *12.3*
12.3 Time-Division Multiplexing and Time-Division Multiple Access / *12.16*
12.4 Introduction to Device Technology / *12.24*
12.5 Summary and Future Outlook / *12.42*
12.6 Further Reading / *12.42*

Chapter 13. Wavelength Domain Multiplexed (WDM) Fiber-Optic Communication Networks ***Alan E. Willner and Yong Xie*** **13.1**

13.1 Introduction / *13.1*
13.2 Fiber Impairments / *13.3*
13.3 Basic Architecture of WDM Networks / *13.12*
13.4 Erbium-Doped Fiber Amplifiers in WDM Networks / *13.17*

13.5 Dynamic Channel Power Equalization / *13.21*
13.6 Crosstalk in WDM Networks / *13.24*
13.7 Summary / *13.26*
13.8 Acknowledgments / *13.27*
13.9 References / *13.27*

Chapter 14. Infrared Fibers ***James A. Harrington*** **14.1**

14.1 Introduction / *14.1*
14.2 Nonoxide and Heavy-Metal Oxide Glass IR Fibers / *14.4*
14.3 Crystalline Fibers / *14.8*
14.4 Hollow Waveguides / *14.11*
14.5 Summary and Conclusions / *14.13*
14.6 References / *14.14*

Chapter 15. Optical Fiber Sensors ***Richard O. Claus, Ignacio Matias, and Francisco Arregui*** **15.1**

15.1 Introduction / *15.1*
15.2 Extrinsic Fabry-Perot Interferometric Sensors / *15.2*
15.3 Intrinsic Fabry-Perot Interferometric Sensors / *15.4*
15.4 Fiber Bragg Grating Sensors / *15.5*
15.5 Long-Period Grating Sensors / *15.9*
15.6 Comparison of Sensing Schemes / *15.14*
15.7 Conclusion / *15.14*
15.8 References / *15.14*
15.9 Further Reading / *15.15*

Chapter 16. Fiber-Optic Communication Standards ***Casimer DeCusatis*** **16.1**

16.1 Introduction / *16.1*
16.2 ESCON / *16.1*
16.3 FDDI / *16.2*
16.4 Fibre Channel Standard / *16.4*
16.5 ATM/SONET / *16.6*
16.6 Gigabit Ethernet / *16.7*
16.7 References / *16.7*

Part 2. Nonlinear and Quantum Optics

Chapter 17. Third-Order Optical Nonlinearities ***Mansoor Sheik-Bahae and Michael P. Hasselbeck*** **17.3**

17.1 Introduction / *17.3*
17.2 Quantum Mechanical Picture / *17.6*
17.3 Nonlinear Absorption (NLA) and Nonlinear Refraction (NLR) / *17.9*
17.4 Kramers-Kronig Dispersion Relations / *17.11*
17.5 Optical Kerr Effect / *17.13*
17.6 Third-Harmonic Generation / *17.16*
17.7 Stimulated Scattering / *17.16*
17.8 Two-Photon Absorption / *17.21*
17.9 Effective Third-Order Nonlinearities; Cascaded $\chi^{(1)}$:$\chi^{(1)}$ Processes / *17.22*

17.10 Effective Third-Order Nonlinearities; Cascaded $\chi^{(2)}$:$\chi^{(2)}$ Processes / *17.24*
17.11 Propagation Effects / *17.26*
17.12 Common Experimental Techniques and Applications / *17.28*
17.13 References / *17.34*

Chapter 18. Stimulated Raman and Brillouin Scattering ***J. Reintjes and M. Bashkansky*** **18.1**

18.1 Introduction / *18.1*
18.2 Raman Scattering / *18.1*
18.3 Stimulated Brillouin Scattering / *18.44*
18.4 References / *18.55*
18.5 Further Reading / *18.61*

Chapter 19. Optical Limiting ***David J. Hagan*** **19.1**

19.1 Introduction / *19.1*
19.2 Basic Principles of Passive Optical Limiting / *19.4*
19.3 Examples of Passive Optical Limiting in Specific Materials / *19.9*
19.4 References / *19.13*

Chapter 20. Photonic Bandgap Materials ***Pierre R. Villeneuve*** **20.1**

20.1 Glossary / *20.1*
20.2 Introduction / *20.2*
20.3 Maxwell's Equations / *20.3*
20.4 Three-Dimensional Photonic Crystals / *20.4*
20.5 Microcavities in Three-Dimensional Photonic Crystals / *20.6*
20.6 Microcavities in Photonic Crystals with Two-Dimensional Periodicity / *20.9*
20.7 Waveguides / *20.13*
20.8 Conclusion / *20.18*
20.9 References / *20.18*

Chapter 21. All-Optical Switching ***George I. Stegeman*** **21.1**

21.1 Introduction / *21.1*
21.2 How Do You Switch? / *21.2*
21.3 Real Materials / *21.2*
21.4 How Material Properties Affect Switching in Communications / *21.3*
21.5 Other Device Geometries / *21.5*
21.6 Examples of Operation of All-Optical Devices / *21.6*
21.7 Summary / *21.7*
21.8 References / *21.7*

Chapter 22. Optical Parametric Oscillators ***M. Ebrahimzadeh and M. H. Dunn*** **22.1**

22.1 Introduction / *22.1*
22.2 Basic Principles / *22.2*
22.3 Optical Parametric Generation and Amplification / *22.8*
22.4 Optical Parametric Devices / *22.12*
22.5 Optical Parametric Oscillators / *22.13*
22.6 Continuous-Wave Optical Parametric Oscillators / *22.15*

22.7 Pulsed Parametric Oscillators / *22.50*
22.8 Synchronously-Pumped Parametric Oscillators / *22.54*
22.9 Parametric Oscillator Design Issues / *22.61*
22.10 Conclusions / *22.65*
22.11 References / *22.65*

Chapter 23. Electromagnetically Induced Transparency ***J. P. Marangos*** **23.1**

23.1 Glossary / *23.1*
23.2 Introduction / *23.2*
23.3 Coherence in Two- and Three-Level Atomic Systems / *23.4*
23.4 The Physical Basis of Electromagnetically Induced Transparency / *23.5*
23.5 Electromagnetically Induced Transparency Phenomena / *23.9*
23.6 Electromagnetically Induced Transparency with Laser Pulses / *23.14*
23.7 Steady-State Electromagnetically Induced Transparency with CW Lasers / *23.15*
23.8 Gain and Lasing without Inversion / *23.17*
23.9 Refractive Index Modifications for Dressed Atoms / *23.18*
23.10 Pulse Propagation Effects / *23.19*
23.11 Ultraslow Light Pulses / *23.21*
23.12 Electromagnetically Induced Transparency in Nonlinear Frequency Mixing / *23.22*
23.13 Nonlinear Optics at Maximal Atomic Coherence / *23.26*
23.14 Nonlinear Optics at the Few Photon Level / *23.27*
23.15 Further Reading / *23.28*
23.16 References / *23.28*

Chapter 24. Coherent Optical Transients ***P. R. Berman and D. G. Steel*** **24.1**

24.1 Glossary / *24.1*
24.2 Introduction / *24.2*
24.3 Optical Bloch Equations / *24.3*
24.4 Maxwell-Bloch Equations / *24.5*
24.5 Free Polarization Decay / *24.7*
24.6 Photon Echo / *24.11*
24.7 Stimulated Photon Echo / *24.15*
24.8 Phase Conjugate Geometry and Optical Ramsey Fringes / *24.18*
24.9 Two-Photon Transitions and Atom Interferometry / *24.21*
24.10 Chirped Pulse Excitation / *24.24*
24.11 Experimental Considerations / *24.25*
24.12 Conclusion / *24.27*
24.13 Acknowledgments / *24.27*
24.14 References / *24.27*

Chapter 25. Nonlinear Optical Processes for Ultrashort Pulse Generation
U. Siegner and U. Keller **25.1**

25.1 Glossary / *25.1*
25.2 Abbreviations / *25.3*
25.3 Introduction / *25.3*
25.4 Saturable Absorbers: Macroscopic Description / *25.6*
25.5 Kerr Effect / *25.11*
25.6 Semiconductor Ultrafast Nonlinearities: Microscopic Processes / *25.15*
25.7 References / *25.24*

Chapter 26. Quantum Theory of the Laser ***János A. Bergou, Berthold-Georg Englert, Melvin Lax, Marlan O. Scully, Herbert Walther, and M. Suhail Zubairy*** **26.1**

26.1 Glossary / *26.2*
26.2 Introduction / *26.6*
26.3 Some History of the Photon Concept / *26.7*
26.4 Quantum Theory of the Laser / *26.15*
26.5 The Laser Phase-Transition Analogy / *26.37*
26.6 Exotic Masers and Lasers / *26.42*
26.7 Acknowledgments / *26.46*
26.8 References / *26.47*

Chapter 27. Laser Stabilization ***John L. Hall, Matthew S. Taubman, and Jun Ye*** **27.1**

27.1 Introduction and Overview / *27.1*
27.2 Servo Principles and Issues / *27.5*
27.3 Practical Issues / *27.12*
27.4 Summary and Outlook / *27.22*
27.5 Conclusions and Recommendations / *27.22*
27.6 Acknowleldgments / *27.23*
27.7 References / *27.23*

Chapter 28. Laser Cooling and Trapping of Atoms ***H. J. Metcalf and P. van der Straten*** **28.1**

28.1 Introduction / *28.1*
28.2 General Properties Concerning Laser Cooling / *28.2*
28.3 Theoretical Description / *28.4*
28.4 Slowing Atomic Beams / *28.9*
28.5 Optical Molasses / *28.11*
28.6 Cooling Below the Doppler Limit / *28.15*
28.7 Trapping of Neutral Atoms / *28.19*
28.8 Applications / *28.24*
28.9 References / *28.38*

Index follows Chapter 28

CONTRIBUTORS

Francisco Arregui *Public University Navarra, Pamplona, Spain* (CHAP. 15)

M. Bashkansky *Optical Sciences Division, Naval Research Laboratory, Washington, DC* (CHAP. 18)

János A. Bergou *Institute for Quantum Studies and Department of Physics, Texas A&M University, College Station, Texas; and Department of Physics and Astronomy, Hunter College of the City University of New York, New York, New York* (CHAP. 26)

P. R. Berman *Physics Department, University of Michigan, Ann Arbor, Michigan* (CHAP. 24)

Tom G. Brown *The Institute of Optics, University of Rochester, Rochester, New York* (CHAP. 1)

John A. Buck *School of Electrical and Computer Engineering, Georgia Institute of Technology, Atlanta, Georgia* (CHAPS. 3 AND 5)

Richard O. Claus *Virginia Tech, Blacksburg, Virginia* (CHAP. 15)

Casimer DeCusatis *IBM Corporation, Poughkeepsie, New York* (CHAPS. 6 AND 16)

Peter J. Delfyett *School of Optics/The Center for Research and Education in Optics and Lasers (CREOL), University of Central Florida, Orlando, Florida* (CHAP. 12)

M. H. Dunn *School of Physics and Astronomy, University of St. Andrews, Fife, United Kingdom* (CHAP. 22)

M. Ebrahimzadeh *School of Physics and Astronomy, University of St. Andrews, Fife, United Kingdom* (CHAP. 22)

Berthold-Georg Englert *Institute for Quantum Studies and Department of Physics, Texas A&M University, College Station, Texas; Max-Planck-Institute für Quantenoptik Garching bei München, Germany; and Abteilung Quantenphysic der Universität Ulm, Ulm, Germany* (CHAP. 26)

Elsa Garmire *Dartmouth College, Hanover, New Hampshire* (CHAP. 4)

David Hagan *School of Optics/The Center for Research and Education in Optics and Lasers (CREOL), University of Central Florida, Orlando, Florida* (CHAP. 19)

John L. Hall *JILA, University of Colorado and National Institute of Standards and Technology, Boulder, Colorado* (CHAP. 27)

James A. Harrington *Rutgers University, Piscataway, New Jersey* (CHAP. 14)

Michael P. Hasselbeck *Department of Physics and Astronomy, University of New Mexico, Albuquerque, New Mexico* (CHAP. 17)

Kenneth O. Hill *New Wave Photonics, Ottawa, Ontario, Canada* (CHAP. 9)

Ira Jacobs *Fiber and Electro-Optics Research Center, Virginia Polytechnic Institute and State University, Blacksburg, Virginia* (CHAP. 2)

U. Keller *Institute of Quantum Electronics, Physics Department, Swiss Federal Institute of Technology (ETH), Zürich, Switzerland* (CHAP. 25)

Melvin Lax *Department of Physics, City College of the City University of New York, New York, New York* (CHAP. 26)

Guifang Li *School of Optics/The Center for Research and Education in Optics and Lasers (CREOL), University of Central Florida, Orlando, Florida* (CHAP. 6)

P. V. Mamyshev *Bell Laboratories—Lucent Technologies, Holmdel, New Jersey* (CHAP. 7)

Copyright 2001 by The McGraw-Hill Companies, Inc. Click Here for Terms of Use.

J. P. Marangos *Laser Optics and Spectroscopy Group, Blackett Laboratory, Imperial College, London, United Kingdom* (CHAP. 23)

Ignacio Matias *Public University Navarra Pamplona, Spain* (CHAP. 15)

H. J. Metcalf *Department of Physics, State University of New York, Stony Brook, New York* (CHAP. 28)

Daniel Nolan *Corning Inc., Corning, New York* (CHAP. 8)

Ulf Österberg *Thayer School of Engineering, Dartmouth College, Hanover, New Hampshire* (CHAP. 11)

Joseph C. Palais *Department of Electrical Engineering, College of Engineering and Applied Sciences, Arizona State University, Tempe, Arizona* (CHAP. 10)

J. Reintjes *Optical Sciences Division, Naval Research Laboratory, Washington, DC* (CHAP. 18)

Marlan O. Scully *Institute for Quantum Studies and Department of Physics, Texas A&M University, College Station, Texas; and Max-Planck-Institut für Quantenoptik Garching bei München, Germany* (CHAP. 26)

Mansoor Sheik-Bahae *Department of Physics and Astronomy, University of New Mexico, Albuquerque, New Mexico* (CHAP. 17)

U. Siegner *Institute of Quantum Electronics, Physics Department, Swiss Federal Institute of Technology (ETH), Zürich, Switzerland* (CHAP. 25)

D. G. Steel *Physics Department, University of Michigan, Ann Arbor, Michigan* (CHAP. 24)

George I. Stegeman *School of Optics/The Center for Research and Education in Optics and Lasers (CREOL), University of Central Florida, Orlando, Florida* (CHAP. 21)

Matthew S. Taubman *JILA, University of Colorado and National Institute of Standards and Technology, Boulder, Colorado* (CHAP. 27)

P. van der Straten *Debye Institute, Department of Atomic and Interface Physics, Utrecht University, Utrecht, The Netherlands* (CHAP. 28)

Pierre R. Villeneuve *Department of Physics, Massachusetts Institute of Technology, Cambridge, Massachusetts* (CHAP. 20)

Herbert Walther *Max-Planck-Institut für Quantenoptik, Garching bei München, Germany; and Sektion Physik der Universität München, Garching bei München, Germany* (CHAP. 26)

Alan E. Willner *Department of EE Systems, University of Southern California, Los Angeles, California* (CHAP. 13)

Yong Xie *Department of EE Systems, University of Southern California, Los Angeles, California* (CHAP. 13)

Jun Ye *JILA, University of Colorado and National Institute of Standards and Technology, Boulder, Colorado* (CHAP. 27)

M. Suhail Zubairy *Institute for Quantum Studies and Department of Physics, Texas A&M University, College Station, Texas; and Department of Electronics, Quaid-I-Azam University, Islamabad, Pakistan* (CHAP. 26)

PREFACE

In the preface to Vols. I and II of the *Handbook of Optics,* Second Edition, we indicated that the limitations of keeping within the confines of two books caused us to restrict the contents to optics that was clearly archival. There was much more that could have been included. We hope to have remedied some of that in this volume with expanded coverage on fiber optics and nonlinear and quantum optics. References are provided to chapters in Vols. I, II, and III, as well as to other chapters in Vol. IV.

Optics has been developing so rapidly during the past 20 years that some of the material that has been included, while clearly of archival value, has not yet had the benefit of developed secondary references such as texts and long review articles. Thus, in the tutorial chapters presented in Vol. IV, some of the references are made to primary publications.

The chapters on fiber optics cover both fiber optics themselves and devices and systems for fiber optics communications. We thank Professor Guifang Li of the School of Optics/CREOL and Dr. Casimer DeCusatis of IBM for organizing this section and recruiting the authors. The result is a coherent and thorough presentation of the issues in fiber optics and in fiber optics communication systems. Some subjects covered in fiber optics overlap with the next section on nonlinear and quantum optics. This is natural since the confinement of light in fibers produces high optical fields and long interaction lengths leading to important nonlinear effects.

In the coverage on nonlinear and quantum optics there is a wide range of chapters dealing with established devices such as optical parametric oscillators, newer devices such as optical limiters and all-optical switches, as well as such fundamental issues as electromagnetically induced transparency, coherent optical transients, and laser cooling. To expand on the Handbook's treatment of optical properties of materials, chapters are included on third-order nonlinearities, stimulated Raman and Brillouin scattering, and photonic bandgap materials. A chapter on frequency standards is also included.

The *Handbook of Optics,* Second Edition is only possible through the support of the staff of the Optical Society of America, and, in particular, Alan N. Tourtlotte, Kimberly Street, and Laura Lee. We also thank Steve Chapman of McGraw-Hill Publishing for his leadership in the production of this volume.

Michael Bass, Editor in Chief
Jay M. Enoch, Associate Editor
Eric W. Van Stryland, Associate Editor
William L. Wolfe, Associate Editor

Copyright 2001 by The McGraw-Hill Companies, Inc. Click Here for Terms of Use.

PREFACE

In the preface to Vols. I and II of the *Handbook of Optics,* Second Edition, we indicated that the limitations of keeping within the confines of two books caused us to restrict the contents to optics that was clearly archival. There was much more that could have been included. We hope to have remedied some of that in this volume with expanded coverage on fiber optics and nonlinear and quantum optics. References are provided to chapters in Vols. I, II, and III, as well as to other chapters in Vol. IV.

Optics has been developing so rapidly during the past 20 years that some of the material that has been included, while clearly of archival value, has not yet had the benefit of developed secondary references such as texts and long review articles. Thus, in the tutorial chapters presented in Vol. IV, some of the references are made to primary publications.

The chapters on fiber optics cover both fiber optics themselves and devices and systems for fiber optics communications. We thank Professor Guifang Li of the School of Optics/CREOL and Dr. Casimer DeCusatis of IBM for organizing this section and recruiting the authors. The result is a coherent and thorough presentation of the issues in fiber optics and in fiber optics communication systems. Some subjects covered in fiber optics overlap with the next section on nonlinear and quantum optics. This is natural since the confinement of light in fibers produces high optical fields and long interaction lengths leading to important nonlinear effects.

In the coverage on nonlinear and quantum optics there is a wide range of chapters dealing with established devices such as optical parametric oscillators, newer devices such as optical limiters and all-optical switches, as well as such fundamental issues as electromagnetically induced transparency, coherent optical transients, and laser cooling. To expand on the Handbook's treatment of optical properties of materials, chapters are included on third-order nonlinearities, stimulated Raman and Brillouin scattering, and photonic bandgap materials. A chapter on frequency standards is also included.

The *Handbook of Optics,* Second Edition is only possible through the support of the staff of the Optical Society of America, and, in particular, Alan N. Tourtlotte, Kimberly Street, and Laura Lee. We also thank Steve Chapman of McGraw-Hill Publishing for his leadership in the production of this volume.

Michael Bass, Editor in Chief
Jay M. Enoch, Associate Editor
Eric W. Van Stryland, Associate Editor
William L. Wolfe, Associate Editor

Copyright 2001 by The McGraw-Hill Companies, Inc. Click Here for Terms of Use.

P · A · R · T · 1

FIBER OPTICS

Casimer DeCusatis **Part Editor**

IBM Corporation
Poughkeepsie, New York

Guifang Li **Part Editor**

School of Optics/The Center for Research and Education
in Optics and Lasers (CREOL), University of Central Florida
Orlando, Florida

Copyright 2001 by The McGraw-Hill Companies, Inc. Click Here for Terms of Use.

CHAPTER 1
OPTICAL FIBERS AND FIBER-OPTIC COMMUNICATIONS

Tom G. Brown
The Institute of Optics
University of Rochester
Rochester, New York

1.1 GLOSSARY

A	open loop gain of receiver amplifier
A	pulse amplitude
a	core radius
a_P	effective pump area
A_{eff}	effective (modal) area of fiber
A_i	cross-sectional area of ith layer
B	data rate
B_n	noise bandwidth of amplifier
c	vacuum velocity of light
D	fiber dispersion (total)
E_i	Young's modulus
e_{LO}, e_S	polarization unit vectors for signal and local oscillator fields
F	tensile loading
F_e	excess noise factor (for APD)
g_B	Brillouin gain
g_R	Raman gain
i_d	leakage current (dark)
I_m	current modulation
$I(r)$	power per unit area guided in single mode fiber
k	Boltzmann's constant
J_m	Bessel function of order m
K_m	modified Bessel function of order m

Copyright 2001 by The McGraw-Hill Companies, Inc. Click Here for Terms of Use.

k_0	vacuum wave vector
l	fiber length
l_0	length normalization factor
L_D	dispersion length
m	Weibull exponent
M	modulation depth
N	order of soliton
n	actual number of detected photons
N_{eff}	effective refractive index
N_P	average number of detected photons per pulse
n_0	core index
n_1	cladding index
$n(r)$	radial dependence of the core refractive index for a gradient-index fiber
P	optical power guided by fiber
P_E	error probability
P_f	probability of fiber failure
P_s	received signal power
P_s	signal power
P_R	power in Raman-shifted mode
P_0	peak power
P_0	peak power of soliton
R	detector responsivity (A/W)
RIN	relative intensity noise
R_L	load resistor
$R(r)$	radial dependence of the electric field
S	failure stress
SNR	signal-to-noise ratio measured in a bandwidth B_n
S_0	location parameter
T	temperature (Kelvin)
t	time
T_0	pulse width
U	normalized pulse amplitude
z	longitudinal coordinate
$Z(z)$	longitudinal dependence of the electric field
α	profile exponent
α_f	frequency chirp
α_R	attenuation of Raman-shifted mode
$\tilde{\beta}$	complex propagation constant
β_1	propagation constant
β_2	dispersion (2d order)
Δ	peak index difference between core and cladding

Δf	frequency deviation
ΔL	change in length of fiber under load
$\Delta\phi$	phase difference between signal and local oscillator
$\Delta\nu$	source spectral width
$\Delta\tau$	time delay induced by strain
ε	strain
η_{HET}	heterodyne efficiency
θ_c	critical angle
$\Theta(\theta)$	azimuthal dependence of the electric field
λ	vacuum wavelength
λ_c	cut-off wavelength
ξ	normalized distance
$\Psi(r, \theta, z)$	scalar component of the electric field
Ψ_S, Ψ_{LO}	normalized amplitude distributions for signal and LO
σ_A^2	amplifier noise
$\sigma_d^2 = 2ei_dB_n$	shot noise due to leakage current
$\sigma_J^2 = \dfrac{4kT}{R_L} B_n$	Johnson noise power
$\sigma_R^2 = R^2P_s^2B_n \times 10^{-(\text{RIN}/10)}$	receiver noise due to source RIN
$\sigma_s^2 = 2eRP_sB_nFe$	signal shot noise
τ	time normalized to moving frame
r, θ, z	cylindrical coordinates in the fiber

1.2 INTRODUCTION

Optical fibers were first envisioned as optical elements in the early 1960s. It was perhaps those scientists well-acquainted with the microscopic structure of the insect eye who realized that an appropriate bundle of optical waveguides could be made to transfer an image and the first application of optical fibers to imaging was conceived. It was Charles Kao[1] who first suggested the possibility that low-loss optical fibers could be competitive with coaxial cable and metal waveguides for telecommunications applications. It was not, however, until 1970 when Corning Glass Works announced an optical fiber loss less than the benchmark level of 10 dB/km[2,3] that commercial applications began to be realized. The revolutionary concept which Corning incorporated and which eventually drove the rapid development of optical fiber communications was primarily a materials one—it was the realization that low doping levels and very small index changes could successfully guide light for tens of kilometers before reaching the detection limit. The ensuing demand for optical fibers in engineering and research applications spurred further applications. Today we see a tremendous variety of commercial and laboratory applications of optical fiber technology. This chapter will discuss important fiber properties, describe fiber fabrication and chemistry, and discuss materials trends and a few commercial applications of optical fiber.

While it is important, for completeness, to include a treatment of optical fibers in any handbook of modern optics, an exhaustive treatment would fill up many volumes all by itself. Indeed, the topics covered in this chapter have been the subject of monographs, reference books, and textbooks; there is hardly a scientific publisher that has not published several

books on fiber optics. The interested reader is referred to the "Further Reading" section at the end of this chapter for additional reference material.

Optical fiber science and technology relies heavily on both geometrical and physical optics, materials science, integrated and guided-wave optics, quantum optics and optical physics, communications engineering, and other disciplines. Interested readers are referred to other chapters within this collection for additional information on many of these topics.

The applications which are discussed in detail in this chapter are limited to information technology and telecommunications. Readers should, however, be aware of the tremendous activity and range of applications for optical fibers in metrology and medicine. The latter, which includes surgery, endoscopy, and sensing, is an area of tremendous technological importance and great recent interest. While the fiber design may be quite different when optimized for these applications, the general principles of operation remain much the same. A list of references which are entirely devoted to optical fibers in medicine is listed in "Further Reading."

1.3 PRINCIPLES OF OPERATION

The optical fiber falls into a subset (albeit the most commercially significant subset) of structures known as dielectric optical waveguides. The general principles of optical waveguides are discussed elsewhere in Chap. 6 of Vol. II, "Integrated Optics"; the optical fiber works on principles similar to other waveguides, with the important inclusion of a cylindrical axis of symmetry. For some specific applications, the fiber may deviate slightly from this symmetry; it is nevertheless fundamental to fiber design and fabrication. Figure 1 shows the generic optical fiber design, with a core of high refractive index surrounded by a low-index cladding. This index difference requires that light from inside the fiber which is incident at an angle greater than the critical angle

$$\theta_c = \sin^{-1}\left(\frac{n_1}{n_0}\right) \tag{1}$$

be totally internally reflected at the interface. A simple geometrical picture appears to allow a continuous range of internally reflected rays inside the structure; in fact, the light (being a wave) must satisfy a self-interference condition in order to be trapped in the waveguide. There are only a finite number of paths which satisfy this condition; these are analogous to the propagating electromagnetic modes of the structure. Fibers which support a large number of modes (these are fibers of large core and large numerical aperture) can be adequately analyzed by the tools of geometrical optics; fibers which support a small number of modes must be characterized by solving Maxwell's equations with the appropriate boundary conditions for the structure.

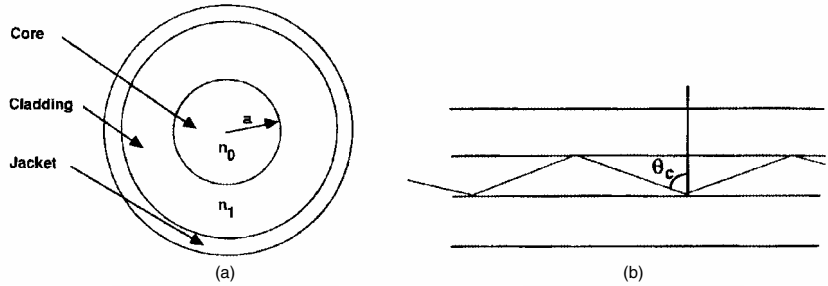

FIGURE 1 (a) Generic optical fiber design, (b) path of a ray propagating at the geometric angle for total internal reflection.

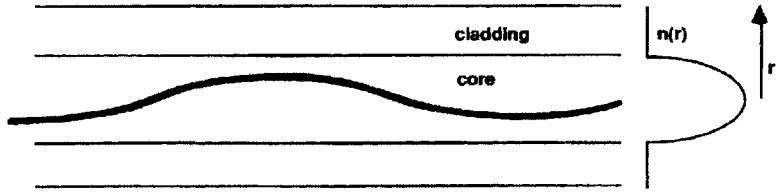

FIGURE 2 Ray path in a gradient-index fiber.

Fibers which exhibit a discontinuity in the index of refraction at the boundary between the core and cladding are termed *step-index fibers.* Those designs which incorporate a continuously changing index of refraction from the core to the cladding are termed *gradient-index fibers.* The geometrical ray path in such fibers does not follow a straight line—rather it curves with the index gradient as would a particle in a curved potential (Fig. 2). Such fibers will also exhibit a characteristic angle beyond which light will not internally propagate. A ray at this angle, when traced through the fiber endface, emerges at an angle in air which represents the maximum geometrical acceptance angle for rays *entering* the fiber; this angle is the numerical aperture of the fiber (Fig. 3). Both the core size and numerical aperture are very important when considering problems of fiber-fiber or laser-fiber coupling. A larger core and larger

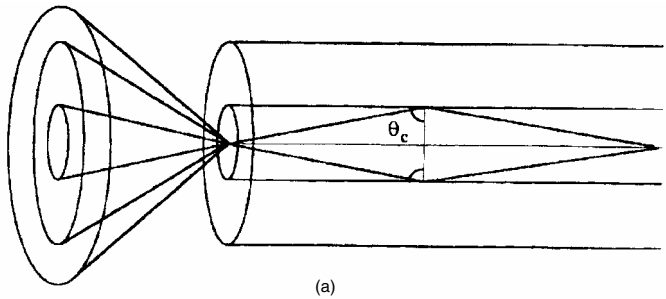

(a)

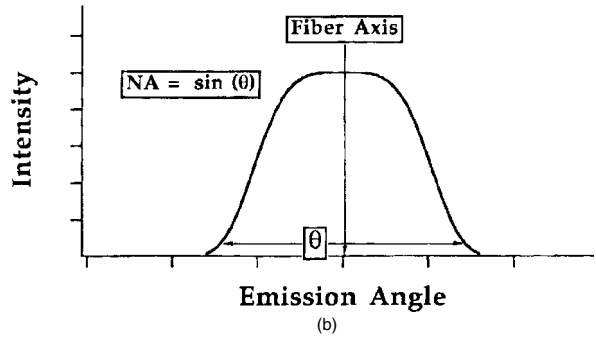

(b)

FIGURE 3 The numerical aperture of the fiber defines the range of external acceptance angles.

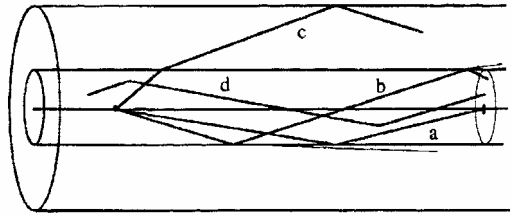

FIGURE 4 Classification of geometrical ray paths in an optical fiber. (*a*) Meridional ray; (*b*) leaky ray; (*c*) ray corresponding to a cladding mode; (*d*) skew ray.

numerical aperture will, in general, yield a higher coupling efficiency. Coupling between fibers which are mismatched either in core or numerical aperture is difficult and generally results in excess loss.

The final concept for which a geometrical construction is helpful is ray classification. Those geometrical paths which pass through the axis of symmetry and obey the self-interference condition are known as *meridional rays.* There are classes of rays which are nearly totally internally reflected and may still propagate some distance down the fiber. These are known as *leaky rays* (or modes). Other geometrical paths are not at all confined in the core, but internally reflect off of the cladding-air (or jacket) interface. These are known as *cladding modes.* Finally, there exists a class of geometrical paths which are bound, can be introduced outside of the normal numerical aperture of the fiber, and do not pass through the axis of symmetry. These are often called *skew rays.* Figure 4 illustrates the classification of geometrical paths.

Geometrical optics has a limited function in the description of optical fibers, and the actual propagation characteristics must be understood in the context of guided-wave optics. For waveguides such as optical fibers which exhibit a small change in refractive index at the boundaries, the electric field can be well described by a scalar wave equation,

$$\nabla^2\Psi(r, \theta, z) + k_0^2 r^2(r)\Psi(r, \theta, z) = 0 \tag{2}$$

the solutions of which are the modes of the fiber. $\Psi(r, \theta, z)$ is generally assumed to be separable in the variables of the cylindrical coordinate system of the fiber:

$$\Psi(r, \theta, z) = R(r)\Theta(\theta)Z(z) \tag{3}$$

This separation results in the following eigenvalue equation for the radial part of the scalar field:

$$\frac{d^2R}{dr^2} + \frac{1}{r}\frac{dR}{dr} + \left(k_0^2 n^2(r) - \beta^2 - \frac{m^2}{r^2}\right)R = 0 \tag{4}$$

in which m denotes the azimuthal mode number, and β is the propagation constant. The solutions must obey the necessary continuity conditions at the core-cladding boundary. In addition, guided modes must decay to zero outside the core region. These solutions are readily found for fibers having uniform, cylindrically symmetric regions but require numerical methods for fibers lacking cylindrical symmetry or having an arbitrary index gradient. A common form of the latter is the so-called α-*profile* in which the refractive index exhibits the radial gradient.[4]

$$m(r) = \begin{cases} n_1\left[1 - \Delta\left(\dfrac{r}{a}\right)^{\alpha}\right] & r < a \\ n_1[1 - \Delta] = n_2 & r \geq a \end{cases} \tag{5}$$

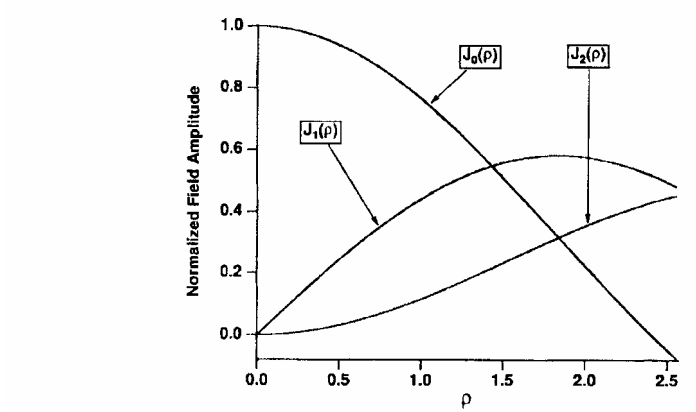

FIGURE 5 Bessel functions $J_m(\rho)$ for $m = 0$, 1, and 2.

The step-index fiber of circular symmetry is a particularly important case, because analytic field solutions are possible and the concept of the "order" of a mode can be illustrated. For this case, the radial dependence of the refractive index is the step function

$$n(r) = \begin{cases} n_1 \; r < a \\ n_2 \; r \geq a \end{cases} \tag{6}$$

The solutions to this are Bessel functions[5] and are illustrated in Fig. 5. It can be seen that only the lowest-order mode ($m = 0$) has an amplitude maximum at the center. Its solution in the (core) propagating region ($r < a$) is

$$R(r) = \frac{J_0\left((n_1^2 k_0^2 - \beta^2)^{1/2}\left(\frac{r}{a}\right)\right)}{J_0((n_1^2 k_0^2 - \beta^2)^{1/2})} \tag{7}$$

while the solution in the cladding ($r > a$) is the modified Bessel function

$$R(r) = \frac{K_0\left((\beta^2 - n_2^2 k_0^2)^{1/2}\left(\frac{r}{a}\right)\right)}{K_0((\beta^2 - n_2^2 k_0^2)^{1/2})} \tag{8}$$

Higher-order modes will have an increasing number of zero crossings in the cross section of the field distribution.

Fibers which allow more than one bound solution for each polarization are termed *multimode* fibers. Each mode will propagate with its own velocity and have a unique field distribution. Fibers with large cores and high numerical apertures will typically allow many modes to propagate. This often allows a larger amount of light to be transmitted from incoherent sources such as light-emitting diodes (LEDs). It typically results in higher attenuation and dispersion, as discussed in the following section.

By far the most popular fibers for long distance telecommunications applications allow only a single mode of each polarization to propagate. Records for low dispersion and attenuation have been set using single-mode fibers, resulting in length-bandwidth products exceeding 10 Gb-km/s. In order to restrict the guide to single-mode operation, the core diameter must typically be 10 μm or less. This introduces stringent requirements for connectors and splices and increases the peak power density inside the guide. As will be discussed, this property of the single-mode fiber enhances optical nonlinearities which can act to either limit or increase the performance of an optical fiber system.

1.4 FIBER DISPERSION AND ATTENUATION

Attenuation

In most cases, the modes of interest exhibit a complex exponential behavior along the direction of propagation z.

$$Z(z) = \exp(i\tilde{\beta}z) \tag{9}$$

β is generally termed the propagation constant and may be a complex quantity. The real part of β is proportional to the phase velocity of the mode in question, and produces a phase shift on propagation which changes rather rapidly with optical wavelength. It is often expressed as an effective refractive index for the mode by normalizing to the vacuum wave vector:

$$N_{\text{eff}} = \frac{Re\{\tilde{\beta}\}}{k_0} \tag{10}$$

The imaginary part of β represents the loss (or gain) in the fiber and is a weak (but certainly not negligible) function of optical wavelength. Fiber attenuation occurs due to fundamental scattering processes (the most important contribution is Rayleigh scattering), absorption (both the OH-absorption and the long-wavelength vibrational absorption), and scattering due to inhomogeneities arising in the fabrication process. Attenuation limits both the short- and long-wavelength applications of optical fibers. Figure 6 illustrates the attenuation characteristics of a typical fiber.

The variation of the longitudinal propagation velocity with either optical frequency or path length introduces a fundamental limit to fiber communications. Since signaling necessarily requires a nonzero bandwidth, the dispersion in propagation velocity between different frequency components of the signal or between different modes of a multimode fiber produces a signal distortion and intersymbol interference (in digital systems) which is unacceptable. Fiber dispersion is commonly classified as follows.

Intermodal Dispersion

The earliest telecommunications links as well as many modern data communications systems have made use of multimode fiber. These modes (which we have noted have some connection to geometrical ray angles) will typically have a broad range of propagation velocities. An optical pulse which couples to this range of guided modes will tend to

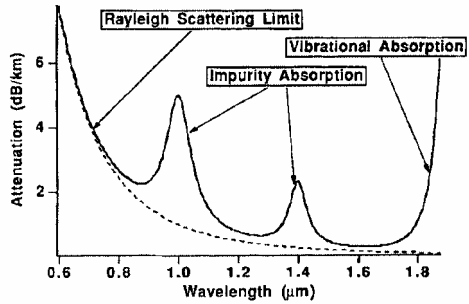

FIGURE 6 Attenuation characteristics of a typical fiber: (*a*) schematic, showing the important mechanisms of fiber attenuation.

broaden by an amount equal to the mean-squared difference in propagation time among the modes. This was the original purpose behind the gradient-index fiber; the geometrical illustrations of Figs. 1 and 2 show that, in the case of a step-index fiber, a higher-order mode (one with a steeper geometrical angle or a higher mode index m) will propagate by a longer path than an axial mode. A fiber with a suitable index gradient will support a wide range of modes with nearly the same phase velocity. Vassell was among the first to show this,[6] and demonstrated that a hyperbolic secant profile could very nearly equalize the velocity of all modes. The α-profile description eventually became the most popular due to the analytic expansions it allows (for certain values of α) and the fact that it requires the optimization of only a single parameter.

Multimode fibers are no longer used in long distance (>10 km) telecommunications due to the significant performance advantages offered by single-mode systems. Many short-link applications, for which intermodal dispersion is not a problem, still make use of multimode fibers.

Material Dispersion

The same physical processes which introduce fiber attenuation also produce a refractive index which varies with wavelength. This intrinsic, or material, dispersion is primarily a property of the glass used in the core, although the dispersion of the cladding will influence the fiber in proportion to the fraction of guided energy which actually resides outside the core. Material dispersion is particularly important if sources of broad spectral width are used, but narrow linewidth lasers which are spectrally broadened under modulation also incur penalties from material dispersion. For single-mode fibers, material dispersion must always be considered along with waveguide and profile dispersion.

Waveguide and Profile Dispersion

The energy distribution in a single-mode fiber is a consequence of the boundary conditions at the core-cladding interface, and is therefore a function of optical frequency. A change in frequency will therefore change the propagation constant independent of the dispersion of the core and cladding materials; this results in what is commonly termed *waveguide dispersion.* Since dispersion of the core and cladding materials differs, a change in frequency can result in a small but measurable change in index profile, resulting in *profile dispersion* (this contribution, being small, is often neglected). Material, waveguide, and profile dispersion act together, the waveguide dispersion being of opposite sign to that of the material dispersion. There exists, therefore, a wavelength at which the total dispersion will vanish. Beyond this, the fiber exhibits a region of anomalous dispersion in which the real part of the propagation constant increases with increasing wavelength. Anomalous dispersion has been used in the compression of pulses in optical fibers and to support long distance soliton propagation.

Dispersion, which results in a degradation of the signal with length, combines with attenuation to yield a length limit for a communications link operating at a fixed bandwidth. The bandwidth-length product is often cited as a practical figure of merit which can include the effects of either a dispersion or attenuation limit.

Normalized Variables in Fiber Description

The propagation constant and dispersion of guided modes in optical fibers can be conveniently expressed in the form of normalized variables. Two common engineering problems are the determination of mode content and the computation of total dispersion. For example, commonly available single-mode fibers are designed for a wavelength range of 1.3 to 1.55 μm.

TABLE 1 Normalized Variables in the Mathematical Description of Optical Fibers

Symbol	Description
$k_0 = \frac{2\pi}{\lambda}$	Vacuum wave vector
a	Core radius
n_0	Core index
n_1	Cladding index
$\tilde{\beta} = \beta' + i\beta''$	Mode propagation constant
$\alpha = 2\beta''$	Fiber attenuation
$N_{\text{eff}} = \beta'/k_0$	Effective index of mode
$\Delta = \frac{n_0^2 - n_1^2}{2n_1^2}$	Normalized core-cladding index differences
$V = \sqrt{2k_0}\, an_1\Delta$	Normalized frequency
$b = \left(\frac{N_{\text{eff}}}{n_1} - 1\right) \Big/ \Delta$	Normalized effective index
$f(r)$	Gradient-index shape factor
$\Gamma = \frac{\int_0^a f(r)\Psi^2(r) r\, dr}{\int_0^a \Psi^2(r) r\, dr}$	Profile parameter ($\Gamma = 1$ for step-index)

Shorter wavelengths will typically support two or more modes, resulting in significant intermodal interference at the output. In order to guarantee single-mode performance, it is important to determine the single-mode cut-off wavelength for a given fiber. Normalized variables allow one to readily determine the cut-off wavelength and dispersion limits of a fiber using universal curves.

The normalized variables are listed in Table 1 along with the usual designations for fiber parameters. The definitions here apply to the limit of the "weakly-guiding" fiber of Gloge,[7] for which $\Delta \ll 1$. The cutoff for single-mode performance appears at a normalized frequency of $V = 2.405$. For values of V greater than this, the fiber is multimode. The practical range of frequencies for good single-mode fiber operation lie in the range.

$$1.8 < V < 2.4 \tag{11}$$

An analytic approximation for the normalized propagation constant b which is valid for this range is given by

$$b(V) \approx \left(1 - 1.1428 - \frac{0.996}{V}\right)^2 \tag{12}$$

Operation close to the cutoff $V = 2.405$ risks introducing higher-order modes if the fiber parameters are not precisely targeted. A useful expression which applies to step-index fibers relates the core diameter and wavelength at the single-mode cutoff.[5]

$$\lambda_{\text{cutoff}} = \left(\frac{\pi}{2.405}\right)(2a)n_0\sqrt{2\Delta} \tag{13}$$

Evaluation of Fiber Dispersion

Evaluation of the fiber dispersion requires:

1. Detailed material dispersion curves such as may be obtained from a Sellmeier formula.[4] The Sellmeier constants for a range of silica-based materials used in fiber fabrication are contained in Chap. 33 of Vol. II, "Crystals and Glasses."

2. Complete information about the fiber profile, including compositional as well as refractive index information.

3. Numerical evaluation of the effective indices of the modes in question *and their first and second derivatives.* Several authors have noted the considerable numerical challenge involved in this,[8,9] particularly since measurements of the refractive index/composition possess intrinsic uncertainties.

Figure 7 shows an example of the dispersion exhibited by a step-index single-mode fiber. Different components of the dispersion are shown in order to illustrate the point of zero dispersion near 1.3 μm. The section devoted to fiber properties will describe how profile control can shift the minimum dispersion point to the very low-loss window near 1.55 μm.

1.5 POLARIZATION CHARACTERISTICS OF FIBERS

The cylindrical symmetry of an optical fiber leads to a natural decoupling of the radial and tangential components of the electric field vector. These polarizations are, however, so nearly degenerate that a fiber of circular symmetry is generally described in terms of orthogonal linear polarizations. This near-degeneracy is easily broken by any stresses or imperfections which break the cylindrical symmetry of the fiber. Any such symmetry breaking (which may arise accidentally or be introduced intentionally in the fabrication process) will result in two orthogonally polarized modes with slightly different propagation constants. These two modes need not be linearly polarized; in general, they are two elliptical polarizations. Such polarization splitting is referred to as *birefringence.*

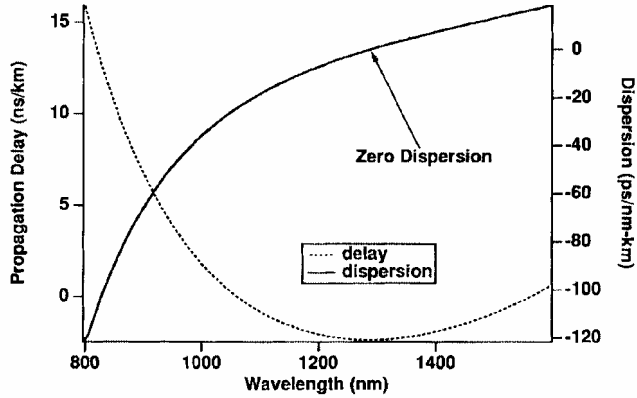

FIGURE 7 Dispersion of a typical single-mode fiber. The opposite contributions of the waveguide and material dispersion cancel near $\lambda = 1.3$ μm. (*Courtesy of Corning, Inc.*)

The difference in effective index between the two polarizations results in a state of polarization (SOP) which evolves through various states of ellipticity and orientation. After some propagation distance, the two modes will differ in phase by a multiple of 2π, resulting in a state of polarization identical to that at the input. This characteristic length is called the *beat length* between the two polarizations and is a measure of the intrinsic birefringence in the fiber. The time delay between polarizations is sometimes termed *polarization dispersion,* because it can have an effect on optical communication links which is similar to intermodal dispersion.

If this delay is much less than the coherence time of the source, coherence is maintained and the light in the fiber remains fully polarized. For sources of wide spectral width, however, the delay between the two polarizations may exceed the source coherence time and yield light which emerges from the fiber in a partially polarized or unpolarized state. The orthogonal polarizations then have little or no statistical correlation. The state of polarization of the output can have an important impact on systems with polarizing elements. For links producing an unpolarized output, a 3-dB power loss is experienced when passing through a polarizing element at the output.

The intentional introduction of birefringence can be used to provide polarization stability. An elliptical or double-core geometry will introduce a large birefringence, decoupling a pair of (approximately) linearly polarized modes.[10,11] It also will tend to introduce loss discrimination between modes. This combination of birefringence and loss discrimination is the primary principle behind polarization-maintaining fiber. As will be discussed in the description of optical fiber systems, there is a class of transmission techniques which requires control over the polarization of the transmitted light, and therefore requires polarization-maintaining fiber.

1.6 OPTICAL AND MECHANICAL PROPERTIES OF FIBERS

This section contains brief descriptions of fiber measurement methods and general information on fiber attenuation, dispersion, strength, and reliability. It should be emphasized that nearly all optical and mechanical properties of fibers are functions of chemistry, fabrication process, and transverse structure. Fibers are now well into the commercial arena and specific links between fiber structure, chemistry, and optical and mechanical properties are considered highly proprietary by fiber manufacturers. On the other hand, most fiber measurements now have established standards. We therefore give attention to the generic properties of fibers and the relevant evaluation techniques.

Attenuation Measurement

There are two general methods for the measurement of fiber attenuation. Source-to-fiber coupling must be taken into account in any scheme to measure attenuation, and destructive evaluation accomplishes this rather simply. The *cut-back method*[12,13] for attenuation measurement requires

1. Coupling light into a long length of fiber
2. Measuring the light output into a large area detector (so fiber-detector coupling remains constant)
3. Cutting the fiber back by a known distance and measuring the change in transmitted intensity

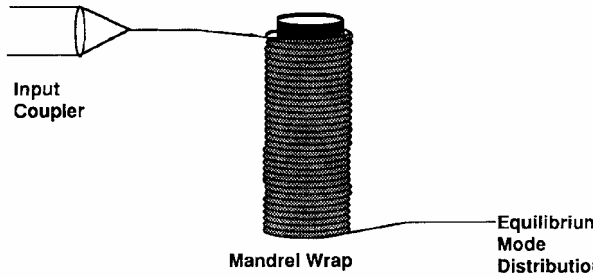

FIGURE 8 Mandrel wrap method of achieving an equilibrium mode distribution.

For single-mode fiber, the fiber can be cut back to a relatively short length provided that the cladding modes are effectively stripped. The concept of "mode stripping" is an important one for both attenuation and bandwidth measurements[14] (since modes near or just beyond cutoff can propagate some distance but with very high attenuation). If these modes are included in the measurement, the result yields an anomalously high attenuation. Lossy modes can be effectively stripped by a mandrel wrap or a sufficiently long length of fiber well-matched to the test fiber (see Fig. 8).

For multimode fiber (whether step-index or gradient-index) the excitation conditions are particularly important. This is because the propagating modes of a multimode fiber exhibit widely varying losses. If the laser used for performing the measurement is focused to a tight spot at the center of the core, a group of low-order modes may be initially excited. This group of lower-order modes will have lower loss and the first 10 to 1000 meters will show an anomalously low attenuation. As the propagation distance increases, lower-order modes gradually scatter into higher-order modes and the mode volume "fills up." The high-order modes are substantially lossier, so the actual power flow at equilibrium is that from the lower-order modes to the higher-order and out of the fiber. This process is illustrated in Fig. 9. It is easy to see that if the excitation conditions are set so that all modes guide approximately the same power at the input, the loss in the first hundred meters would be much higher than the equilibrium loss.

With modern single-mode splices, connectors, and couplers, it is sometimes possible to make nondestructive attenuation measurements simply by assuring that the connector loss is much less than the total loss of the fiber length being measured. With this method, care must be taken that the connector design exhibits no interference between fiber endfaces.

Connector loss measurements must have similar control over launch conditions. In addition, it is important to place a sufficiently long length of fiber (or short mandrel wrap) *after* the connector to strip the lossy modes. A slightly misaligned connector will often

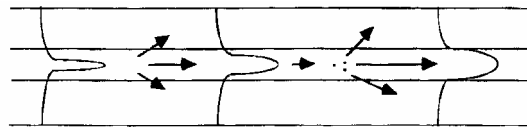

FIGURE 9 In a multimode fiber, low-order modes lose power to the high-order modes, and the high-order modes scatter into cladding and other lossy modes.

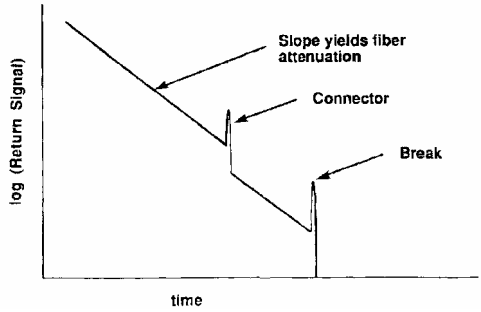

FIGURE 10 Typical OTDR signal. OTDR can be used for attenuation measurement, splice and connector evaluation, and fault location.

exhibit an extremely low loss prior to mode stripping. This is because power is coupled into modes which, while still guided, have high attenuation. It is important, in evaluation of fibers, to properly attribute this loss to the connector and not to the length of fiber which follows.

Another method of nondestructive evaluation of attenuation is optical time domain reflectometry (OTDR). The excitation of a fiber with a narrow laser pulse produces a continuous backscatter signal from the fiber. Assuming a linear and homogeneous scattering process, the reduction in backscattered light with time becomes a map of the round-trip attenuation versus distance. Sudden reductions in intensity typically indicate a splice loss, while a narrow peak will usually indicate a reflection. A typical OTDR signal is shown in Fig. 10. OTDR is extremely sensitive to excitation conditions—a fiber which is not properly excited will often exhibit anomalous behavior. Control of the launch conditions is therefore important for all methods of attenuation measurement.

A major theme of research and development in optical telecommunications has been the elimination of troublesome reflections from optical networks. In particular, high-return loss connectors have been developed which exhibit 30 to 40 dB of reflection suppression.[15–18] OTDR can be used to assess the reflection at network connections as well as perform on-line fault monitoring.

Dispersion and Bandwidth Measurement

The fiber has often been presented as the "multi-TeraHertz bandwidth transmission channel." While it is true that the total attenuation window of the fiber is extremely large by communications standards, the actual information bandwidth at any given wavelength is limited by the various sources of dispersion. The bandwidth of the fiber can be measured either in the time or frequency domain. Both measurements assume the fiber to be linear in its baseband (intensity) transfer characteristics. This assumption breaks down at very high powers and short pulses, but is nevertheless useful in most system applications.

The *time domain measurement*[19] measures the temporal broadening of a narrow input pulse. The ratio of the Fourier transform of the output intensity to that of the input yields a baseband transfer function for the fiber. If the laser and detector are linear, this transfer function relates the drive current of the laser to the photocurrent of the receiver and treats the fiber simply as a linear transmission channel of limited bandwidth. The use of the Fourier

transform readily allows the phase to be extracted from the baseband transfer function. For intermodal pulse broadening in multimode fibers, this phase can be a nonlinear function of frequency, indicating a distortion as well as a broadening of the optical pulse.

Swept-frequency methods[20] have also been used for fiber evaluation. A pure sinusoidal modulation of the input laser is detected and compared in amplitude (and phase, if a network analyzer is available). In principle, this yields a transfer function similar to the pulse method. Both rely on the linearity of the laser for an accurate estimation, but since the swept-frequency method generally uses a single tone, the harmonics produced by laser nonlinearities can be rejected. Agreement between the two methods requires repeatable excitation conditions, a nontrivial requirement for multimode fibers.

The usual bandwidth specification of a multimode fiber is in the form of a 3-dB bandwidth (for a fixed length) or a length-bandwidth product. A single-mode fiber is typically specified simply in terms of the measured total dispersion. This dispersion can be measured either interferometrically, temporally, or using frequency domain techniques.

The *interferometric measurement*[21,22] is appropriate for short fiber lengths, and allows a detailed, direct comparison of the optical phase shifts between a test fiber and a reference arm with a suitable delay. This approach is illustrated in Fig. 11, which makes use of a Mach-Zehnder interferometer. This requires a source which is tunable, and one with sufficient coherence to tolerate small path differences between the two arms. The advantage of the approach is the fact that it allows measurements of extremely small absolute delays (a shift of one optical wavelength represents less than 10 fs time delay). It tends to be limited to rather short lengths of fiber; if a fiber is used in the reference arm to balance the interferometer, the properties of that fiber must be known with some accuracy.

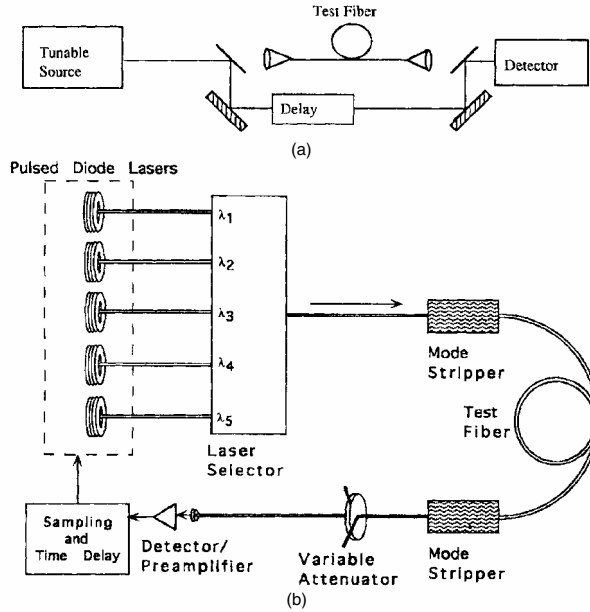

FIGURE 11 (*a*) Interferometric measurement of fiber dispersion; (*b*) time delay measurement of fiber dispersion.

Time-domain measurements[23] over a broad spectral range can be made provided a multiwavelength source is available with a sufficiently short optical pulse. One can make use of a series of pulsed diode lasers spaced at different wavelengths, use Raman scattering to generate many wavelengths from a single source, or make use of a tunable, mode-locked solid state laser. The relative delay between neighboring wavelengths yields the dispersion directly. This technique requires fibers long enough to adequately measure the delay, and the optical pulses must be weak enough not to incur additional phase shifts associated with fiber nonlinearities.

Frequency-domain or phase-shift measurements attempt to measure the effects of the dispersion on the baseband signal. A sinusoidally modulated signal will experience a phase shift with propagation delay; that phase shift can be readily measured electronically. This technique uses a filtered broadband source (such as an LED) or a CW, tunable, solid state source to measure the propagation delay as a function of wavelength.

Shifting and Flattening of Fiber Dispersion

A major dilemma facing system designers in the early 1980s was the choice between zero dispersion at 1.3 μm and the loss minimum at 1.55 μm. The loss minimum is an indelible consequence of the chemistry of silica fiber, as is the material dispersion. The waveguide dispersion can, however, be influenced by suitable profile designs.[24] Figure 12 illustrates a generic design which has been successfully used to shift the dispersion minimum to 1.55 μm.

The addition of several core and cladding layers to the fiber design allows for more complicated dispersion compensation to be accomplished. *Dispersion-flattened* fiber is designed for very low dispersion in an entire wavelength range; the spectral region from 1.3 to 1.6 μm is the usual range of interest. This is important for broadband WDM applications, for which the fiber dispersion must be as uniform as possible over a wide spectral region.

Reliability Assessment

The reliability of an optical fiber is of paramount importance in communications applications—long links represent large investments and require high reliability. There will, of course, always be unforeseen reliability problems. Perhaps the most famous such example was the fiber cable design on the first transatlantic link—the designers had not quite appreciated the Atlantic shark's need for a high-fiber diet. The sharks, apparently attracted by the scent of the cable materials, made short work of the initial cable installations. However, most of the stresses which an optical fiber will experience in the field can be replicated in the laboratory. A variety of accelerated aging models (usually relying on temperature as the accelerating factor) can be used to test for active and passive component reliability. In this section, we will review the reliability assessment of the fiber itself, referring interested readers to other sources for information on cable design.

Among the most important mechanical properties of the fiber in a wide range of applications is the tensile strength.[25] The strength is primarily measured destructively, by finding the maximum load just prior to fracture.[26] Full reliability information requires a knowledge of the maximum load, the relation between load and strain, a knowledge of the strain experienced by the fully packaged fiber, and some idea of how the maximum tolerable strain will change over long periods of time. One must finally determine the strain and associated failure probability for fibers with finite bends.

The tensile strength typically decreases slowly over time as the material exhibits fatigue, but in some cases can degrade rather rapidly after a long period of comparative strength. The former behavior is usually linked to fatigue associated with purely mechanical influences,

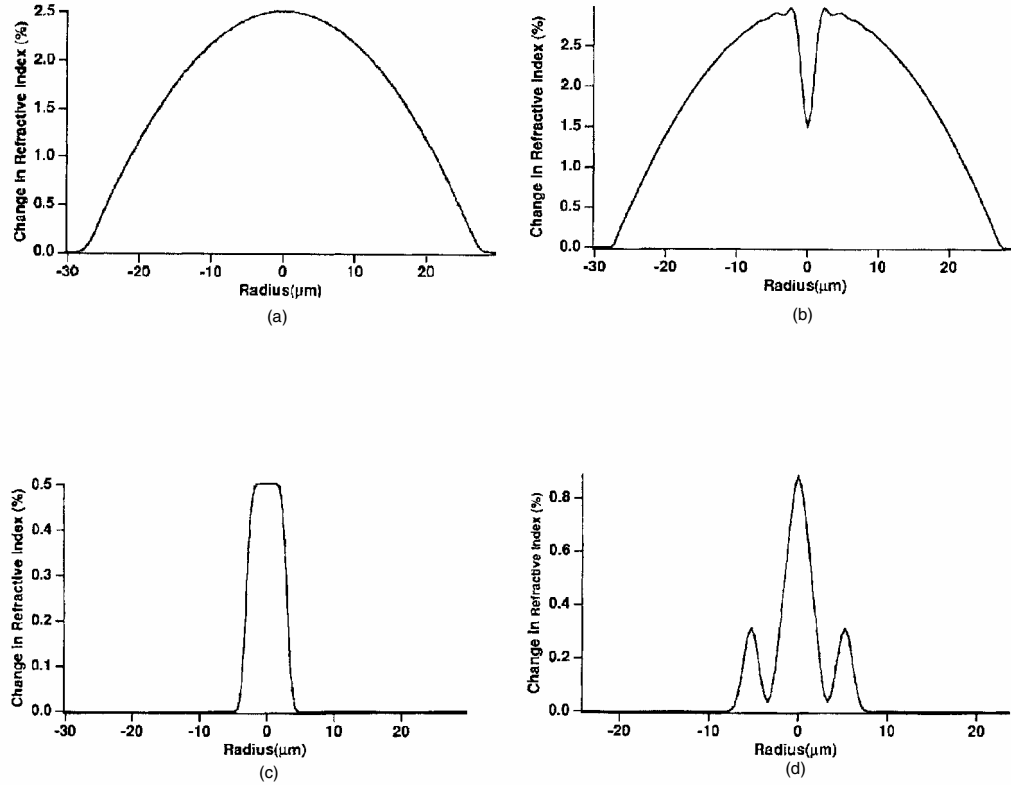

FIGURE 12 Typical index profiles for (*a*), (*b*) gradient-index multimode fiber; (*c*) step-index single-mode fiber; (*d*) dispersion-shifted fiber.

while the latter often indicates chemical damage to the glass matrix. The strain ε and tensile loading F are related through the fiber cross section and Young's modulus:[27]

$$\varepsilon = \frac{F}{\sum_i E_i A_i} \tag{14}$$

E_i and A_i represent the Young's modulus and cross-sectional area of the i_{th} layer of the fiber-jacketing combination. Thus, if the Young's moduli are known, a measurement of the load yields the strain.

It is sometimes helpful to measure the fiber strain directly in cases where either the load or Young's moduli are not known. For example, a fiber does not necessarily have a uniform load after jacketing, cabling, and pulling; the load would (in any case) be a difficult quantity to measure. Using the relation between the strain and the optical properties of the fiber it is possible to infer the fiber strain from optical measurements. These techniques have been

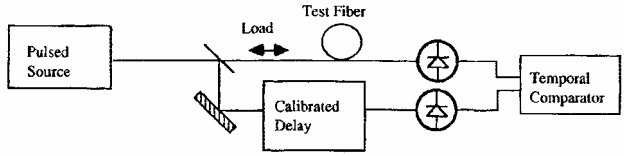

FIGURE 13 Single-pass technique for time-domain measurement of fiber strain.

successful enough to lead to the development of fiber strain gauges for use in mechanical systems.

Optical measurements of strain make use of the transit time of light through a medium of refractive index N_{eff}. (We will, for simplicity, assume single-mode propagation.) A change in length ΔL produced by a strain $\Delta L/L$ will yield a change in transit time

$$\frac{\Delta\tau}{\Delta L} = \frac{N_{\text{eff}}}{c}\left(1 + \frac{L}{N_{\text{eff}}} + \frac{dN_{\text{eff}}}{dL}\right) \tag{15}$$

For most cases of interest, the effective index is simply taken to be the value for that of the core. The ratio $\Delta\tau/\Delta L$ can be calculated (it is about 3.83 ns/m for a germania-silica fiber with $\Delta = 1\%$) or calibrated by using a control fiber and a measured load. It is important to note that this measurement yields only information on the *average* strain of a given fiber length.

There are three categories of optoelectronic techniques for measuring $\Delta\tau$; these are very similar to the approaches for dispersion measurement. A single-pass optical approach generally employs a short-pulse laser source passing through the fiber, with the delay of the transmitted pulse deduced by a comparison with a reference (which presumably is jitter-free). This is shown in Fig. 13. Figure 14*a* shows a multipass optoelectronic scheme, in which an optoelectronic oscillator circuit is set up with the fiber as a delay loop. The Q of the optoelectronic oscillator determines the effective number of passes in this measurement of optical delay. Finally, one can use an all-optical circuit in which the test fiber is placed in a fiber loop with weak optical taps to a laser and detector/signal processor (Fig. 14*b*). This "ring resonator" arrangement can also be set up with a fiber amplifier in the resonator to form the all-optical analog of the multipass optoelectronic scheme of Fig. 14*a*.

If the strain is being used to gain information about fiber reliability, it is necessary to understand how strain, load, and fiber failure are related. Fatigue, the delayed failure of the fiber, appears to be the primary model for fiber failure. One experimental evaluation of this process is to measure the mean time to failure as a function of the load on the fiber with the temperature, the chemical environment, and a host of other factors serving as control parameters.

Since the actual time to failure represents only the average of a performance distribution, the reliability of manufactured fibers is sometimes specified in terms of the two-parameter Weibull distribution[25,27–30]

$$P_f = 1 - \exp\left\{\left(\frac{l}{l_0}\right)\left(\frac{S}{S_0}\right)^m\right\} \tag{16}$$

where P_f denotes the cumulative failure probability and the parameters are as defined in Table 2. The Weibull exponent m is one of the primary descriptors of long-term fiber reliability. Figure 15 shows a series of Weibull plots associated with both bending and tensile strength measurements for low, intermediate, and high values of m.

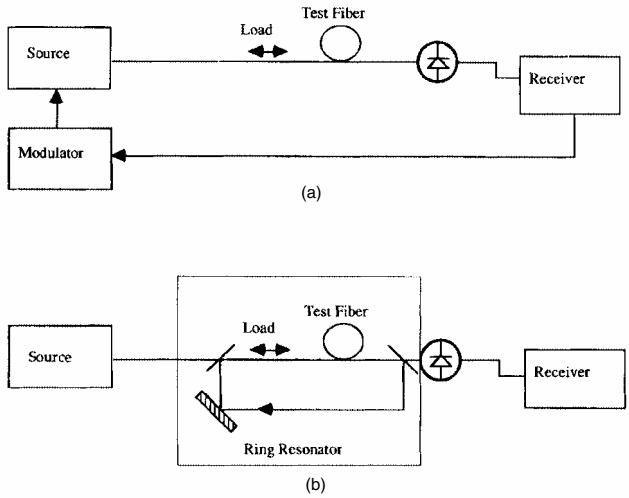

FIGURE 14 Multipass techniques for strain measurement. (*a*) Optoelectronic oscillator; (*b*) optical ring resonator.

One factor which has been shown to have a strong impact on reliability is the absolute humidity of the fiber environment and the ability of the protective coating to isolate the SiO_2 from the effects of H_2O. A recent review by Inniss, Brownlow, and Kurkjian[31] pointed out the correlation between a sudden change in slope, or "knee," in the time-to-failure curve and the H_2O content—a stark difference appeared between liquid and vapor environments. Before this knee, a combination of moisture and stress are required for fiber failure. In the case of fiber environments with a knee, a rather early mean time to failure will exist even for very low fiber stresses, indicating that chemistry rather than mechanical strain is responsible for the failure. The same authors investigated the effects of sodium solutions on the strength and aging of bare silica fibers.

1.7 OPTICAL FIBER COMMUNICATIONS

The optical fiber found its first large-scale application in telecommunications systems. Beginning with the first LED-based systems,[32,34,35] the technology progressed rapidly to longer

TABLE 2 Variables Used in the Weibull Distribution

l	Fiber length
l_0	Length normalization factor
S	Failure stress
S_0	Location parameter
m	Weibull exponent

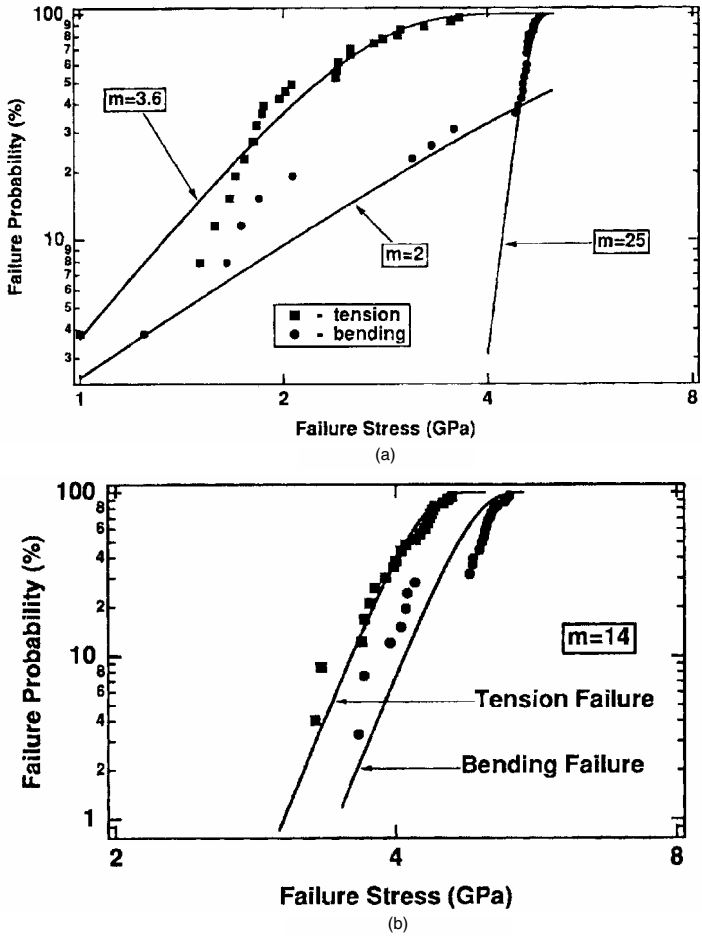

FIGURE 15 A series of Weibull plots comparing bending and tensile strength for (*a*) low, (*b*) intermediate, and (*c*) high values of the Weibull exponent *m*; (*d*) shows a typical mean time to failure plot. Actual fibers will often exhibit slope discontinuities, indicating a change in the dominant failure mechanism. (*Data Courtesy of Corning, Inc.*)

wavelengths and laser-based systems of repeater lengths over 30 km.[36] The first applications were primarily digital, since source nonlinearities precluded multichannel analog applications. Early links were designed for the 800- to 900-nm window of the optical fiber transmission spectrum, consistent with the emission wavelengths of the GaAs-AlGaAs materials system for semiconductor lasers and LEDs. The development of sources and detectors in the

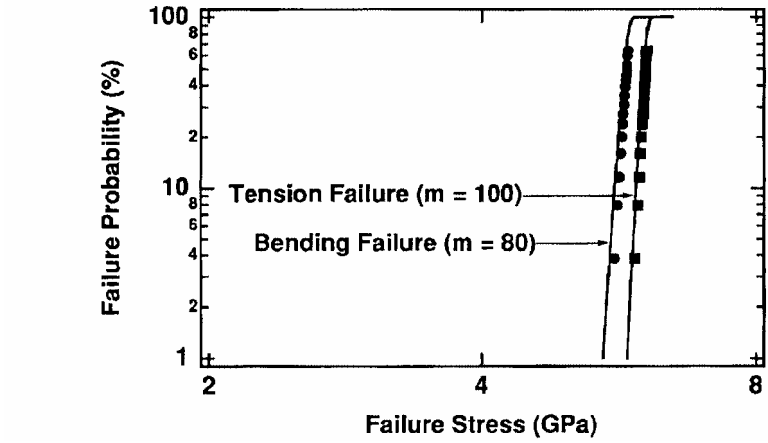

(c)

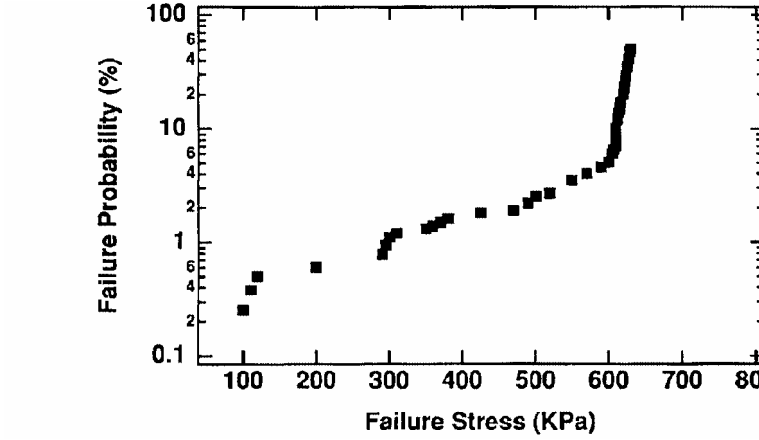

(d)

FIGURE 15 (*Continued*)

1.3- to 1.55-μm wavelength range and the further improvement in optical fiber loss over those ranges has directed most applications to either the 1.3-μm window (for low dispersion) or the 1.55-μm window (for minimum loss). The design of dispersion-shifted single-mode fiber along the availability of erbium-doped fiber amplifiers has solidified 1.55 μm as the wavelength of choice for high-speed communications.

The largest currently emerging application for optical fibers is in the local area network (LAN) environment for computer data communications, and the local subscriber loop for telephone, video, and data services for homes and small businesses. Both of these applications place a premium on reliability, connectivity, and economy. While existing systems still use point-to-point optical links as building blocks, there is a considerable range of networking components on the market which allow splitting, tapping, and multiplexing of optical components without the need for optical detection and retransmission.

Point-to-Point Links

The simplest optical communications system is the single-channel (no optical multiplexing) point-to-point digital link. As illustrated in Fig. 16, it consists of a diode laser (with associated driver circuitry and temperature control), optical fiber (with associated splices, connectors, and supporting material), and a detector (with appropriate electronics for signal processing and regeneration). The physics and principles of operation of the laser and detector are covered elsewhere in this collection (see Chap. 11 of Vol. I, "Lasers" Chap. 15 of Vol. I, "Photodetectors"), but the impact of certain device characteristics on the optical fiber communications link is of some importance.

Modulation and Source Characteristics. For information to be accurately transmitted, an appropriate modulation scheme is required. The most common modulation schemes employ direct modulation of the laser drive current, thereby achieving a modulation depth of 80 percent or better. The modulation depth is defined as

$$m = \frac{P_{\max} - P_{\min}}{P_{\max} + P_{\min}} \tag{17}$$

where $P_{\min}$ and $P_{\max}$ are the minimum and maximum laser power, respectively. The modulation depth is limited by the requirement that the laser always remain above threshold, since modulation near the lasing threshold results in a longer turn-on time, a broader spectrum, and higher source noise.

The transmitting laser contributes noise to the system in a fashion that is, generally speaking, proportional to the peak transmitted laser power. This noise is always evaluated as a fraction of the laser power and is therefore termed *relative intensity noise* (RIN). The RIN contribution from a laser is specified in dB/Hz, to reflect a spectral density which is approximately flat and at a fixed ratio (expressed in dB) to the laser power. Figure 17 shows a typical plot of the relative intensity noise of a source. The specification of RIN as a flat noise source is valid only at frequencies much less than the relaxation oscillation frequency and in situations where reflections are small.

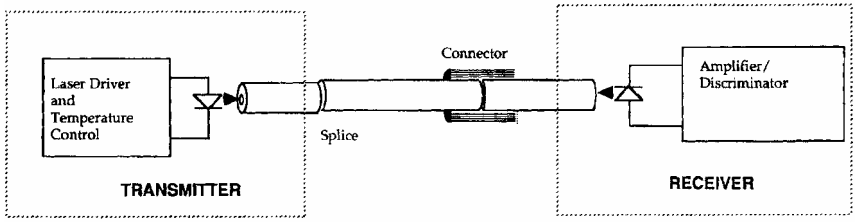

FIGURE 16 Typical point-to-point optical fiber communications link.

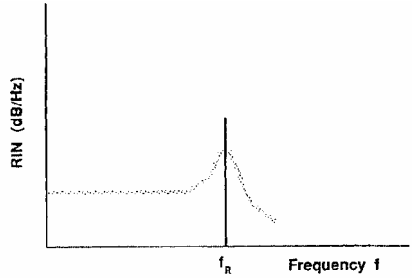

FIGURE 17 Typical RIN spectrum for a diode laser. The peak corresponds to the relaxation resonance frequency, f_R, of the laser.

The relative intensity noise is affected rather dramatically by the environment of the diode laser. A rather weak reflection back into the laser will both increase the magnitude of the relative intensity noise and modify its spectrum. As the reflection increases, it can produce self-pulsations and chaos in the output of the laser, rendering it useless for communications applications.[37] Thus, the laser cannot be thought of as an isolated component in the communications system. Just as RF and microwave systems require impedance matching for good performance, an optical communications system must minimize reflections. This is relatively easily accomplished for a long distance telecommunications link which makes use of low-reflection fusion splices. However, in a short link-network environment which must be modular, a small number of connectors can cause severe problems unless those connectors are designed to minimize reflections. It is now widely accepted that optical fiber connectors must be specified both in terms of insertion loss and reflection. A 1 percent reflection from a fiber connector can have far more serious implications for an optical fiber link than a 1 percent loss which is not reflected back to the laser. Optical isolators are available but only at considerable expense and are not generally considered economically realistic for network environments.

Impact of Fiber Properties on a Communications Link. For moderate power levels, the fiber is a passive, dispersive transmission channel. Dispersion can limit system performance in two ways. It results in a spreading of data pulses by an amount proportional to the spectral width of the source. This pulse spreading produces what is commonly termed "intersymbol interference." This should not be confused with an optical interference effect, but is simply the blurring of pulse energy into the neighboring time slot. In simple terms, it can be thought of as a reduction in the modulation depth of the signal as a function of link length. The effects of dispersion are often quantified in the form of a power penalty. This is simply a measure of the additional power required to overcome the effects of the dispersion, or bring the modulated power to what it would be in an identical link without dispersion. It is commonly expressed as a decibel ratio of the power required at the receiver compared to that of the ideal link.

Modulation-induced frequency chirp of the laser source will also result in pulse distortion. This is illustrated in Fig. 18, in which the drive current of the laser is modulated. The accompanying population relaxation produces a frequency modulation of the pulse. Upon transmission through a dispersive link, these portions of the pulse which are "chirped" will be advanced or retarded, resulting in both pulse distortion and intersymbol interference.

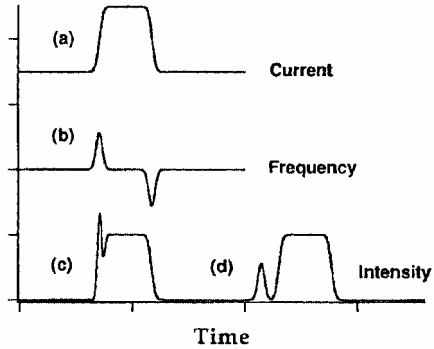

FIGURE 18 Modulation of the drive current in a semiconductor laser (*a*) results in both an intensity (*b*) and a frequency modulation (*c*). The pulse is distorted after transmission through the fiber (*d*).

System Design. The optical receiver must, within the signal bandwidth, establish an adequate signal-to-noise ratio (SNR) for accurate regeneration/retransmission of the signal. It must accomplish this within the constraints of the fiber dispersion and attenuation, the required system bandwidth, and the available source power. First-order system design normally requires the following steps:

1. Determine the maximum system bandwidth (or data rate for digital systems) and the appropriate transmission wavelength required for the system.

2. Find the maximum source RIN allowable for the system. For analog systems, in which a signal-to-noise ratio (SNR) must be specified in a bandwidth B_n, the RIN (which is usually specified in dB/Hz, indicating a measurement in a 1-Hz bandwidth) must obey the following inequality:

$$|\text{RIN(dB/Hz)}| \ll 10 \log (\text{SNR} \cdot B_n) \tag{18}$$

The SNR is specified here as an absolute ratio of carrier power to noise power. For an SNR specified as a decibel ratio,

$$|\text{RIN(dB/Hz)}| \ll \text{SNR(dB)} + 10 \log (B_n) \tag{19}$$

For digital systems, a Gaussian assumption allows a simple relationship between error probability (also termed bit error rate) and the signal-to-noise ratio:

$$P_E = 0.5 erfc[0.5(0.5\text{SNR})^{1/2}] \tag{20}$$

Where *erfc* denotes the complementary error function and the decision threshold is assumed to be midway between the on and off states. The maximum error probability due to source noise should be considerably less than the eventual target error probability. For system targets of 10^{-9} to 10^{-12}, the error probability due to source RIN should be considerably less than 10^{-20}. This will allow at least a 3-dB margin to allow for increases in RIN due to device aging.

3. Establish a length limit associated with the source frequency chirp and spectral width. The frequency chirp α_f is specified in GHz per milliampere change in the drive current of the laser. A total current modulation I_m therefore yields a frequency deviation Δf of

$$\Delta f = I_m \alpha_f \tag{21}$$

This frequency deviation translates into a propagation delay via the fiber intramodal dispersion D. This delay must be kept less than the minimum pulse width (data rate). With D specified in ps/nm-km, the length in kilometers must obey the following inequality to avoid penalties due to frequency chirp:

$$L \ll \frac{c}{B\Delta f D\lambda_0^2} = \frac{c}{\alpha_f I_m B D \lambda_0^2} \tag{22}$$

where B denotes the data rate and is the reciprocal of the pulse width for data pulses that fill up an entire time slot. (These signals are designated non-return-to-zero, or NRZ.)

The length limit due to source spectral width $\Delta\nu$ obeys a similar inequality—in this case, the delay associated with the spectral spread of the source must remain much less than one pulse width:

$$L \ll \frac{c}{\Delta\nu B D \lambda_0^2} \tag{23}$$

If the chirp is low and the unmodulated source bandwidth is less than the system bandwidth being considered, one must require that the delay distortion of the signal spectrum itself be small compared to a pulse width, requiring

$$L \ll \frac{c}{B^2 D \lambda_0^2} \tag{24}$$

For multimode fiber systems, the limiting length will generally be associated with the intermodal dispersion rather than the material and waveguide dispersion. A length-bandwidth product is generally quoted for such fibers. With the length and bandwidth limits established, it is now possible to design, within those limits, a receiver which meets the necessary specifications.

4. Determine the minimum power required at the receiver to achieve the target SNR or error probability. This minimum acceptable power (MAP) is first computed assuming an ideal source (no RIN contribution). A correction for the RIN can be carried out later. A computation of the MAP requires a knowledge of the noise sources and detector bandwidth. It is conventional to express the noise sources in terms of equivalent input noise current sources. The noise sources of importance for such systems are: the shot noise of the photocurrent, dark current, and drain current (in the case of a field effect transistor (FET) preamplifier); the Johnson noise associated with the load resistor or equivalent amplifier input impedance; 1/f noise from certain classes of FETs. The noise contributions from amplifiers other than the first stage are generally second-order corrections. Figure 19 shows a schematic of the receiver and relevant noise sources. Table 3 gives expressions for, and definitions of the important physical quantities which determine the receiver sensitivity.

Figure 20 illustrates two possible configurations for the detector/amplifier combination. Of these, the integrating front end is the simplest (particularly for high-frequency operation) but tends to be slower than a transimpedance amplifier with an equivalent load resistance. This is because the transimpedance amplifier reduces the effective input impedance of the circuit by $(A + 1)$, where A denotes the open loop gain of the amplifier.

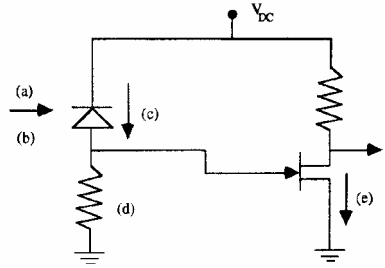

FIGURE 19 Schematic of the receiver, showing the introduction of noise into the system. Noise sources which may be relevant include (*a*) signal shot noise; (*b*) background noise (due to thermal background or channel crosstalk); (*c*) shot noise from the leakage current; (*d*) Johnson noise in the load resistor; (*e*) shot noise and 1/f noise in the drain current of the field effect transistor.

For equivalent bandwidth, the transimpedance amplifier exhibits a lower Johnson noise contribution since a higher feedback resistance is possible. It is worth mentioning that the transimpedance design tends to be much more sensitive to the parasitic capacitance which appears across the feedback resistor—small parasitics across the load resistor tend to be less important for the integrating front end.

The excess noise factor F_e is determined by the choice of detector. There are several choices over the wavelength range generally of interest for optical fiber transmission. (A detailed discussion of the principles of operation can be found in Chaps. 15–17 of Vol. I.)

TABLE 3 Symbols and Expressions for Receiver Noise

Symbol	Description
R_L	Load resistor
k	Boltzmann's constant
T	Temperature (Kelvin)
$\sigma_J^2 = \dfrac{4kT}{R_L} B_n$	Johnson noise power
R	Detector responsivity (A/W)
$P_g P$	Signal power
B_n	Noise bandwidth of amplifier
$\sigma_s^2 = 2eRP_sB_nFe$	Signal shot noise
i_d	Leakage current (dark)
$\sigma_d^2 = 2ei_dB_n$	Shot noise due to leakage current
$\sigma_R^2 = R^2P_s^2B_n \times 10^{-(\mathrm{RIN}/10)}$	Receiver noise due to source RIN
F_e	Excess noise factor (for APD)
σ_λ^2	Amplifier noise

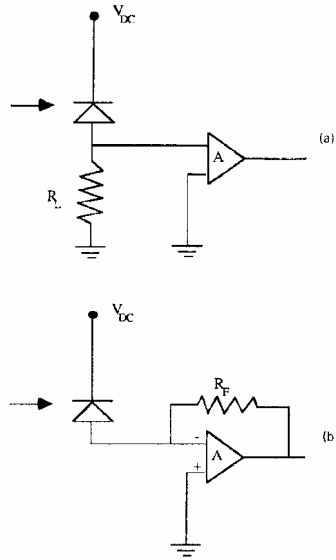

FIGURE 20 Two possible configurations for the detector/amplifier: (*a*) the integrating front end yields the simplest design for high speed operation; (*b*) the transimpedance amplifier provides an expansion of the receiver bandwidth by a factor of $A + 1$, where A is the open loop gain of the amplifier.

1. The p-i-n photodiode is described in some detail in Chap. 15 of Vol. I ("Photodetectors"). It can provide high quantum efficiencies and speeds in excess of 1 GHz. Dark currents range from less than 1 nA for silicon devices to 1 μA or more for Ge diodes. The dark current increases and the device slows down as the active area is increased.

2. The avalanche photodiode is a solid state device which exhibits internal multiplication of the photocurrent in a fashion that is sometimes compared with the gain in photomultiplier tubes. The multiplication does not come without a penalty, however, and that penalty is typically quantified in the form of an excess noise factor which multiplies the shot noise. The excess noise factor is a function both of the gain and the ratio of impact ionization rates between electrons and holes.

Figure 21 shows the excess noise factor for values of k ranging from 50 (large hole multiplication) to 0.03 (large electron multiplication). The former is claimed to be typical of certain III–V compounds while the latter is typical of silicon devices. Germanium, which would otherwise be the clear detector of choice for long wavelengths, has the unfortunate property of having k near unity. This results in maximum excess noise, and Ge avalanche photodiodes must typically be operated at low voltages and relatively small gains. The choice of a p-i-n detector, which exhibits no internal gain, yields $F_e = 1$.

3. The need for very high speed detectors combined with the fabrication challenges present in III-V detector technology has led to a renewed interest in Schottky barrier detectors for optical communications. A detector of considerable importance today is the metal-semiconductor-metal detector, which can operate at extremely high speed in an inter-

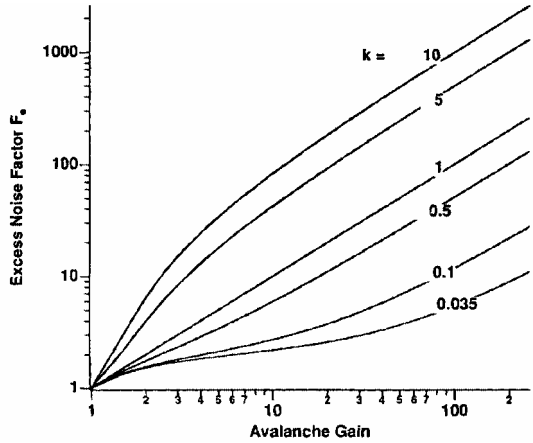

FIGURE 21 Excess noise factor for an avalanche photodiode with the electron/hole multiplication ratio k as a parameter. Small values of k indicate purely electron multiplication while large values of k indicate purely hole multiplication.

digitated electrode geometry. Chapter 17 of Vol. I provides further discussion of MSM detectors.

With all noise sources taken into account (see Table 3 for the relevant expressions), the signal-to-noise ratio of an optical receiver can be expressed as follows:

$$\mathrm{SNR} = \frac{R^2 P_S^2}{\sigma_s^2 + \sigma_T^2} \tag{25}$$

where σ_T^2 denotes the total signal-independent receiver noise:

$$\sigma_T^2 = \sigma_D^2 + \sigma_J^2 + \sigma_A^2 \tag{26}$$

and σ_s^2 is the signal shot noise as in Table 3. If the effects of RIN are to be included, the following correction to the SNR may be made:

$$\mathrm{SNR}^{-1} = \mathrm{SNR}^{-1} + \sigma_R^2 \tag{27}$$

With the signal-to-noise ratio determined, the error probability may be expressed in terms of the signal-to-noise ratio

$$P_E = 0.5 erfc[0.5(0.5 \times \mathrm{SNR})^{1/2}] \tag{28}$$

The just-noted expressions assume Gaussian distributed noise sources. This is a good assumption for nearly all cases of interest. The one situation in which the Gaussian assumption underestimates the effects of noise is for avalanche photodiodes with large excess noise. It was shown by McIntyre[38,39] and Personick[40] that the avalanche multiplication statistics are skewed and that the Gaussian assumption yields overly optimistic results.

5. Given the MAP of the receiver, the fiber attenuation and splice loss budget, and the available pigtailed laser power (the maximum power coupled into the first length of fiber by

the laser), it is possible to calculate a link loss budget. The budget must include a substantial power margin to allow for device aging, imperfect splices, and a small measure of stupidity. The result will be a link length which, if shorter than the dispersion limit, will provide an adequate signal-to-noise ratio.

For further link modeling, a variety of approaches can be used to numerically simulate the link performance and fully include the effects of fiber dispersion, a realistic detector-preamplifier combination, and a variety of other factors which the first-order design does not include. Nevertheless, a first-order design is necessary to reduce the range of free parameters used in the simulation.

The ultimate goal of the point-to-point link is to transparently transmit the data (or the analog signal) in such a way that standard communications techniques may be used in the optical link. Examples include the use of block or error-correcting codes in digital systems, standard protocols for point-to-point links between nodes of a network, or frequency allocation in the case of a multichannel analog link.

Advanced Transmission Techniques

The optical bandwidth available in either of the low-loss transmission windows of the fiber exceeds 10^{13} Hz. Two ways of taking full advantage of this bandwidth are through the use of ultrashort pulse transmission combined with time-division multiplexing or the use of wavelength/frequency-division multiplexing. Either technique can overcome the limits imposed by the channel dispersion, but both techniques have their limitations. The first technique seeks to turn fiber dispersion to advantage; the second attempts to simply reduce the negative effects of dispersion on a broadband optical signal.

Ultrashort Pulse Transmission. The most common form of multiplexing in digital communication systems is the combination of a number of low data rate signals into a single, high data rate signal by the use of time-division multiplexing. This requires much shorter optical pulses than are used in conventional transmission. As mentioned earlier, the normal (linear) limitation to the data rate is imposed by the fiber attenuation and dispersion. Both of these limits can be exceeded by the use of soliton transmission and optical amplification.

The physics of soliton formation[41–45] is discussed in "Nonlinear Optical Properties of Fibers," later in this chapter. Solitons, in conjunction with fiber amplifiers, have been shown to promise ultralong distance transmission without the need for optoelectronic repeaters/regenerators. Time-division multiplexing of optical solitons offers the possibility of extremely long distance repeaterless communications.

No communication technique is noise-free, and even solitons amplified by ideal amplifiers will exhibit phase fluctuations which broaden the spectrum and eventually cause the soliton to break up. This spontaneous-emission noise limit is known as the Gordon-Haus limit,[46] and had been thought to place a rather severe upper limit on the bit rate distance product for optical fiber systems. It has recently been noted,[47] that a unique series of linear filters can prevent the buildup of unwanted phase fluctuations in the soliton, thereby justifying amplified soliton transmission as a viable technology for undersea communications.

Such a communications system puts great demands on the signal processing both at the input and the output. For very high bit rates, one needs either all-optical demultiplexing or extremely fast electronic logic. Current limits on silicon logic are in the range of several Gb/s, which may be adequate for the first implementations of soliton transmission. It is anticipated that all-optical multiplexing and demultiplexing will be required in order to fully exploit the optical fiber bandwidth.

Solitons supported by an optical fiber bear a very specific relationship between pulse width T_0, peak power P_0, fiber dispersion D, effective area A_{eff}, and the intensity-dependent refractive index n_2. For a lowest-order ($N = 1$) soliton,

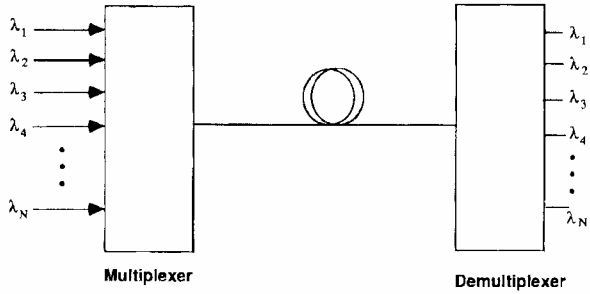

FIGURE 22 Schematic of a WDM transmission system. The main figures of merit are insertion loss (for both the multiplexer and demultiplexer) and channel crosstalk (for the demultiplexer).

$$T_0^2 = \frac{\lambda^3 D}{(2\pi)^2 n_2 (P_0/A_{\text{eff}})} \tag{29}$$

Under normal operation, a fiber will propagate lowest-order solitons of about 10 ps in duration. Even for a pulse train of comparatively high duty cycle, this represents less than 100 GHz of a much larger fiber bandwidth. To fully span the bandwidth requires wavelength-division multiplexing.

Wavelength-division Multiplexing (WDM). The troublesome delay between frequencies which is introduced by the fiber dispersion can also be overcome by division of the fiber transmission region into mutually incoherent (uncorrelated) wavelength channels. It is important for these channels to be uncorrelated in order to eliminate any worry about dispersion-induced delay between channels. Figure 22 shows a schematic picture of a WDM transmission system. The concept is quite simple, but reliable implementation can be a considerable challenge.

An attractive feature of WDM is the fact that the only active components of the system remain the optical sources and detectors. The multiplexers/demultiplexers are passive and are therefore intrinsically more reliable than active multiplexers. These schemes range from simple refractive/reflective beam combiners to diffractive approaches and are summarized in Fig. 23. For a multiplexing scheme, the key figure of merit is the insertion loss per channel. A simple 50-50 beam splitter for a two-channel combiner offers simple multiplexing with high insertion loss. If the beam splitter is coated to provide high reflectivity at one wavelength and high transmissivity at the other, the insertion loss is reduced, the coupler becomes wavelength-specific, and the element can act either as a multiplexer or demultiplexer.

Grating combiners offer an effective way to maximize the number of channels while still controlling the insertion loss. The grating shape must be appropriately designed—a problem which is easily solved for a single-wavelength, single-angle geometry. However, the diffraction efficiency is a function both of wavelength and angle of incidence. The optimum combination of a range of wavelengths over a wide angular range will typically require a tradeoff between insertion loss, wavelength range, and angular discrimination. Wavelength-division multiplexing technology has been greatly aided by the rapid advances in diffractive optics, synthetic holography, and binary optics in recent years. More on these subjects is included in Chap. 8 of Vol. II.

There have been considerable accomplishments in the past ten years in the fabrication of integrated optical components for WDM applications. Much of these involve the waveguide

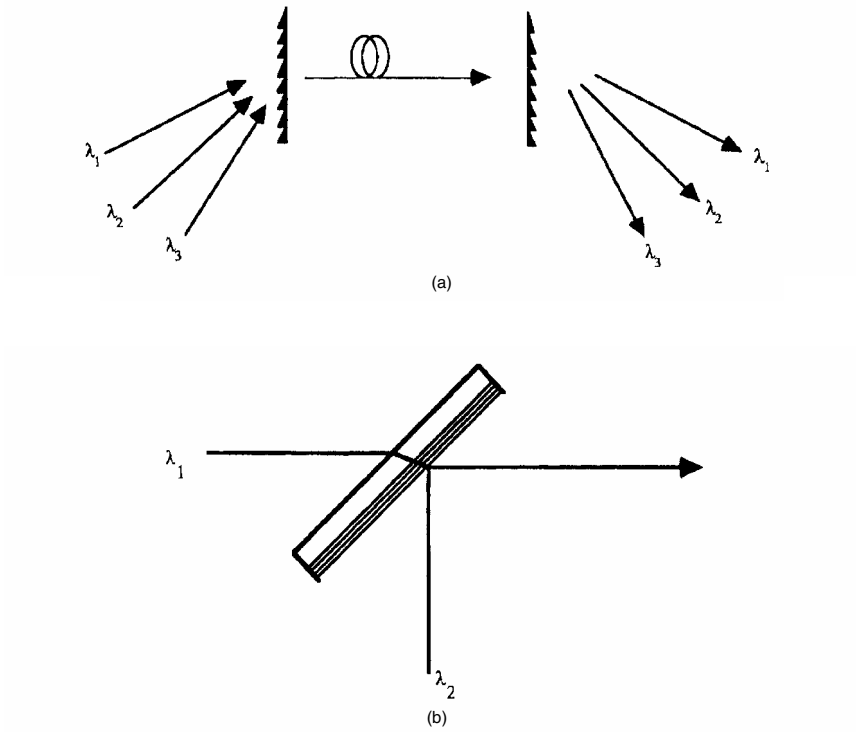

FIGURE 23 Multiplexing/demultiplexing schemes for WDM; (*a*) grating combiner (bulk optics); (*b*) wavelength selective beamsplitter (bulk optics); (*c*) directional coupler (integrated optics); (*d*) all-fiber multiplexer/demultiplexer.

equivalent of bulk diffractive optical elements. Since the optical elements are passive and efficient fiber coupling is required, glass waveguides have often been the medium of choice. A great variety of couplers, beam splitters, and multiplexer/demultiplexers have been successfully fabricated in ion-exchanged glass waveguides. Further details on the properties of these waveguides is contained in Chap. 36 of Vol. I. There has also been a major effort to fabricate low-cost polymer-based WDM components. These can be in the form of either waveguides or fibers.

From the point of view of connectivity and modular design, all-fiber WDM components are the most popular. Evanescent single-mode fiber couplers are inherently wavelength-sensitive and can be designed for minimum insertion loss. As with the bulk approaches, all-fiber components become more difficult to design and optimize as the number of channels increases. Most commercially available all-fiber components are designed for widely separated wavelength channels. For example, Corning, Inc. currently offers multiplexers designed for combining signals from 1.5-μm, 1.3-μm, and 0.8-μm sources.

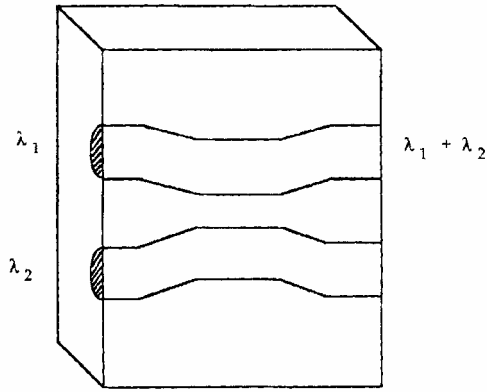

(c)



(d)

FIGURE 23 (*Continued*)

Advances in source fabrication technology in recent years have offered the possibility of fabricating diode laser arrays equipped with a controlled gradient in emission wavelength across the array. Such an array, equipped with appropriate beam-combining optics, could greatly reduce the packaging and alignment requirements in a large-scale WDM system. Minimizing crosstalk for closely spaced wavelength channels presents a significant challenge for demultiplexer design.

Coherent Optical Communications. Intensity modulation with direct detection remains the most popular scheme for optical communications systems. Under absolutely ideal transmission and detection conditions (no source RIN, perfect photon-counting detection, no background radiation), the probability of detecting n photons in a pulse train having an average of N_P photons per pulse would obey the Poisson distribution

$$p(n) = \frac{N_p^{\,n} e^{-N_P}}{n!} \tag{30}$$

The probability of an "error" P_E would be the detection of no photons during the pulse,

$$P_E = \exp(-N_P) \tag{31}$$

If we choose the benchmark error probability of 10^{-9}, we require an average of about 21 photons per pulse. This represents the quantum limit for the direct detection of optical signals. This limit can scarcely be reached, since it assumes no dark count and perfectly efficient photon counting.

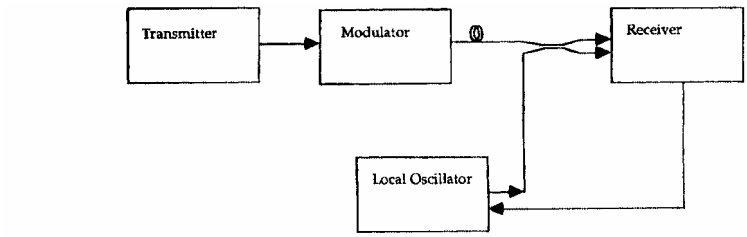

FIGURE 24 Generic coherent optical fiber communication link.

Current optical communication[48–54] offers a way to achieve quantum-limited receiver sensitivities even in the presence of receiver noise. By using either amplitude, phase, or frequency modulation combined with heterodyne or homodyne detection, it is possible to approach, and even exceed, the quantum limit for direct detection.

A generic coherent optical communication link is shown in Fig. 24. The crucial differences with direct detection lie in the role of the modulator in transmission and the presence of the local oscillator laser in reception. To understand the role of the modulator, we first consider the method of heterodyne detection. We will then discuss the component requirements for a coherent optical fiber communication link.

Heterodyne and Homodyne Detection. We consider the receiver shown in Fig. 25, in which an optical signal arriving from some distant point is combined with an intense local oscillator laser by use of a 2×2 coupler. The power $I(r)$ guided in the single-mode fiber due to the interfering amplitudes can be expressed as

$$I(r) = P_S(t)|\Psi_S(r)|^2 + P_{LO}|\Psi_{LO}(r)|^2 + 2e_S(t) \cdot e_{LO}\Psi_S(r)\Psi_{LO}(r)\sqrt{P_S(t)P_{LO}}\cos(\omega_{IF}t + \Delta\phi) \quad (32)$$

in which $e_{LO}(t)$ and $e_S(t)$ denote the polarizations of the local oscillator and signal, P_{LO} and $P_S(t)$ denote the powers of the local oscillator and signal, $\Psi_S(r)$ and $\Psi_{LO}(r)$ are the spatial amplitude distributions, and $\Delta\phi(t)$ denotes the phase difference between the two sources. The two sources may oscillate at two nominally different frequencies, the difference being labeled the *intermediate frequency* ω_{IF} (from heterodyne radio nomenclature). If the intermediate fre-

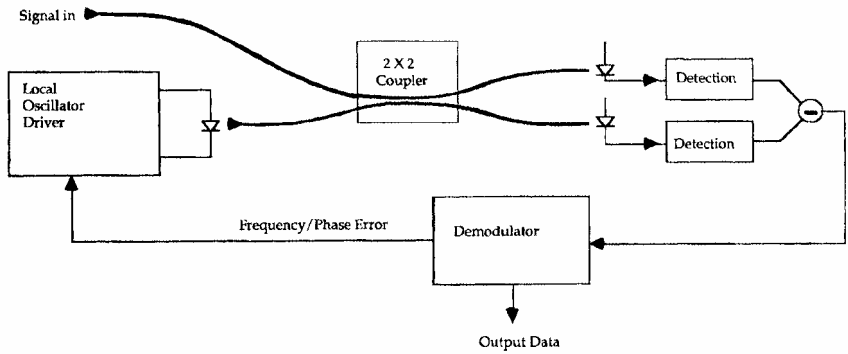

FIGURE 25 Heterodyne/homodyne receiver.

quency is zero, the detection process is termed *homodyne* detection; if a microwave or radio carrier frequency is chosen for postdetection processing, the detection process is referred to as *heterodyne* detection.

If the local oscillator power is much larger than the signal power, the first term is negligible. The second represents a large, continuous signal which carries no information but does provide a shot noise contribution. The third term represents the signal information. If the signal is coupled to a detector of responsivity R and ac-coupled to eliminate the local oscillator signal, the photocurrent $i(t)$ can be expressed as follows:

$$i(t) = 2R\eta_{\text{HET}}\sqrt{P_S(t)P_{LO}}\cos(\omega_{IF}t + \Delta\phi) \tag{33}$$

The heterodyne efficiency η_{HET} is determined by the spatial overlap of the fields and the inner product of the polarization components:

$$\eta_{\text{HET}} = (e_s(t) \cdot e_{LO}) \int_{\substack{\text{Fiber}\\ \text{Area}}} \Psi_S(r)\Psi_{LO}(r)\, d^2r \tag{34}$$

These results illustrate four principles of coherent optical fiber communications:

1. The optical frequency and phase of the signal relative to those of the local oscillator are preserved, including the phase and frequency fluctuations.

2. The local oscillator "preamplifies" the signal, yielding a larger information-carrying component of the photocurrent than would be detected directly.

3. The local oscillator and signal fields must occupy the same spatial modes. Modes orthogonal to that of the local oscillator are rejected.

4. Only matching polarization components contribute to the detection process.

The first principle allows the detection of frequency or phase information, provided the local oscillator has sufficient stability. The second provides an improvement of the signal-to-noise ratio in the limit of large local oscillator power. Both the first and fourth lead to component requirements which are rather more stringent than those encountered with direct detection. The following sections will discuss the source, modulator, fiber, and receiver requirements in a coherent transmission system.

Receiver Sensitivity. Let σ_T^2 represent the receiver noise described in Eq. (26). The signal-to-noise ratio for heterodyne detection may be expressed as

$$\text{SNR} = \frac{2\eta_{HET}R^2P_SP_{LO}}{2eRP_{LO}B_n + \sigma_T^2} \tag{35}$$

where B_n denotes the noise bandwidth of the receiver. (B_n is generally about half of the data rate for digital systems.) For homodyne detection, the signal envelope carries twice the energy, and

$$\text{SNR} = \frac{4\eta_{\text{HET}}R^2P_SP_{LO}}{2e\,RP_{LO}B_n + \sigma_T^2} \tag{36}$$

For a given modulation scheme, homodyne detection will therefore be twice as sensitive as heterodyne.

Modulation Formats. The modulation formats appropriate for coherent optical communications can be summarized as follows:

1. *Amplitude-Shift Keying (ASK).* This technique is simply on-off keying (similar to simple intensity modulation) but with the important constraint that the frequency and phase of the laser be kept constant. Direct modulation of ordinary semiconductor lasers produces a

frequency chirp which is unacceptable for ASK modulation. An external modulator such as an electro-optic modulator, a Mach-Zehnder modulator, or an electroabsorption modulator would therefore be appropriate for ASK.

2. *Phase-Shift Keying (PSK).* This technique requires switching the phase between two or more values. Any phase modulator can be suitable for phase-shift keying. Direct modulation of semiconductor lasers is not suitable for PSK for the same reasons mentioned for ASK.

3. *Frequency-Shift Keying (FSK).* FSK has received a good deal of attention[55] because it can be achieved by direct modulation of the source. It is possible to make use of the natural frequency chirp of the semiconductor laser to frequency modulate the laser simply by a small modulation of the drive current.

All of the modulation techniques can operate between two states (binary) or extend to four or more levels. The only technique which benefits from an increase in the number of channels is FSK. The sensitivity of PSK to source phase noise generally precludes higher-level signaling. Multilevel FSK, being a bandwidth expansion technique, offers a receiver sensitivity improvement over binary FSK without placing severe constraints on the source.

Table 4 gives expressions for the receiver error probability as a function of received power for each modulation technique. The right-hand column gives, for comparison purposes, the number of photons required per pulse to assure an error rate of better than 10^{-9}. PSK modulation with homodyne detection is the most sensitive, requiring only nine photons per pulse, which is below the quantum limit for direct detection.

Source Requirements. One of the ways coherent optical communications systems differ from their microwave counterparts is in the comparatively large phase noise of the source. Since the detection system is sensitive to the frequency and phase of the laser, the source linewidth is a major consideration. This is very different from intensity modulation/direct detection, in which the source spectral width limits the system only through the channel dispersion. When two sources are heterodyned to generate an intermediate frequency in the microwave region, the spectral spread of the heterodyned signal is the combined spectral spread of the signal and local oscillator. Thus, the rule of thumb for high-quality coherent detection is that the sum of the linewidths of the signal and local oscillator be much less than the receiver bandwidth.

TABLE 4 Receiver Sensitivities for a Variety of Modulation/Detection Schemes

Modulation/Detection Scheme	P_E	Photons per pulse @ $P_E = 10^{-9}$
ASK heterodyne	$0.5 erfc\left(\sqrt{\frac{\eta P_S}{4h\nu B}}\right)$	72
ASK homodyne	$0.5 erfc\left(\sqrt{\frac{\eta P_S}{2h\nu B}}\right)$	36
FSK heterodyne	$0.5 erfc\left(\sqrt{\frac{\eta P_S}{2h\nu B}}\right)$	36
PSK heterodyne	$0.5 erfc\left(\sqrt{\frac{\eta P_S}{h\nu B}}\right)$	18
PSK homodyne	$0.5 erfc\left(\sqrt{\frac{2\eta P_S}{h\nu B}}\right)$	9
Direction detection quantum limit	$0.5 \exp\left(\frac{-\eta P_S}{h\nu B}\right)$	21

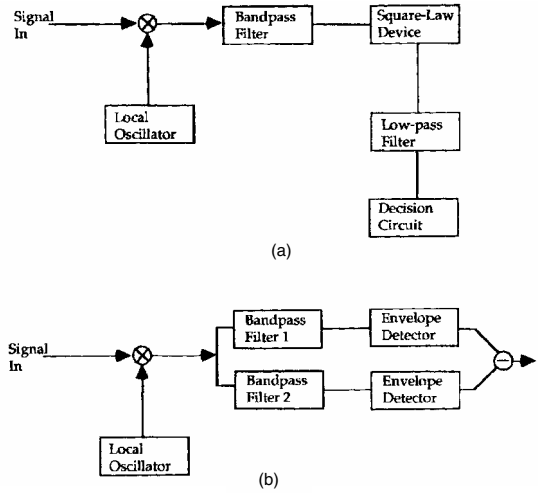

FIGURE 26 Noncoherent (asynchronous) demodulation schemes: (*a*) ASK envelope detection; (*b*) FSK dual filter detection, in which the signal is separated into complementary channels for ASK envelope detection.

Precisely how narrow the linewidth must be has been a topic of many papers.[49–52] The result varies somewhat with modulation scheme and varies strongly with the demodulation process. The general trends can be summarized as follows:

Incoherent Demodulation (Envelope Detection). Either ASK or FSK can be demodulated simply by using an appropriate combination of filters and nonlinear elements. The basic principle of incoherent ASK or dual-filter FSK detection is illustrated in Fig. 26. This type of detection is, in general, least sensitive to the spectral width of the source. The primary effect of a broad source is to broaden the *IF* signal spectrum, resulting in attenuation but not a catastrophic increase in bit error rate. Further, the receiver bandwidth can always be broadened to accommodate the signal. This yields a penalty in excess receiver noise, but the source spectral width can be a substantial fraction of the bit rate and still keep the receiver sensitivity within tolerable limits.

There are two approaches to PSK detection which avoid the need for a phase-locked loop. The first is differential phase-shift keying (DPSK), in which the information is transmitted in the form of phase *differences* between neighboring time slots. The second is phase diversity reception, in which a multiport interferometer is designed to yield signals proportional to the power in different phase quadrants.

Coherent Demodulation with Electronic Phase-Locked Loop. Some PSK signals cannot be demodulated incoherently and require careful receiver design for proper carrier recovery. Suppressed carrier communications schemes such as PSK require a nonlinear recovery circuit. The phase estimation required in proper carrier recovery is far more sensitive to phase noise than is the case with envelope detection. In contrast to incoherent demodulation, source spectral widths must generally be kept to less than 1 percent of the bit rate (10 percent of the phase-locked loop bandwidth) to maintain reliable detection.

Coherent Demodulation with Optoelectronic Phase-Locked Loop. Homodyne detection requires that an error signal be fed back to the local oscillator; phase and frequency errors

must be corrected optically in order to maintain precise frequency and phase matching between the two signals. This generally results in a narrower phase-locked loop bandwidth and a much narrower spectral width requirement for the transmitter and local oscillator. Homodyne systems therefore require considerably narrower linewidths than their heterodyne counterparts.

Fiber Requirements. Heterodyne or homodyne reception is inherently single-mode, and it is therefore necessary for coherent links to use single-mode fibers. Single-mode couplers can then be used to combine the signal and local oscillator lasers for efficient heterodyne detection.

As with other forms of fiber communications, fiber dispersion presents a degradation in the signal-to-noise ratio due to differential delay between different components of the signal spectrum. The power penalty associated with fiber dispersion is determined entirely by the dispersion, the fiber length, and the bit rate. Because of the stringent source linewidth requirements for coherent detection, the spectral broadening is entirely due to the signal itself. The coherent detection system is therefore inherently less sensitive to fiber dispersion.

One important requirement of any fiber that is to be used for coherent transmission is polarization control. As was discussed briefly under "Polarization Characteristics of Fibers" earlier in this chapter, the transmitted polarization of light from a single-mode fiber varies randomly with temperature, stress on the fiber, and other environmental influences. If heterodyning is attempted under these circumstances, the heat signal will fade in and out as the polarization of the signal changes.

Polarization fading can be controlled either by external compensation,[56] internal control,[11] or polarization diversity reception.[57] External compensation seeks to actively control the polarization of the output by sensing the error through a polarizer-analyzer combination and feeding back to correct the polarization. The latter can be accomplished through mechanical, electro-optical, or magneto-optical means.

There are classes of optical fiber sensors which have source and fiber requirements very similar to those of a coherent communication link. One of the most widely studied has been the optical fiber gyro, in which counterpropagating waves in a rotating fiber coil interfere with one another; the resulting beat frequency between the waves is proportional to the angular velocity of the coil. There are other interferometric sensors which make use of optical fibers. Most of them require polarization control and a high degree of frequency stability for the source. The relatively low frequencies and small bandwidths which are required for sensing represent the major difference between these applications and coherent data transmission.

1.8 NONLINEAR OPTICAL PROPERTIES OF FIBERS

Chapters and entire books have been devoted to the subject of optical nonlinearities in fibers. A selection of these are included in "Further Reading" at the end of this chapter. We will content ourselves with an overview of the subject, and consider nonlinear effects which are most important in either limiting or enhancing the performance of fibers. To date, most of the *applications* of nonlinear optics in fibers are in the area of ultralong distance telecommunications.[41,58–60] However, nonlinearities can limit the power-handling ability of fibers and can be an important limitation for certain medical/surgical applications.

Stimulated Scattering Processes

The low loss and long interaction length of an optical fiber makes it an ideal medium for stimulating even relatively weak scattering processes. Two important processes in fibers are: (1) stimulated Raman scattering, the interaction of the guided wave with high-frequency optical phonons in the material, and (2) stimulated Brillouin scattering, the emission, amplification,

and scattering of low-frequency acoustic waves. These are distinguished by the size of the frequency shift and the dynamics of the process, but both can act to limit the power available for transmission.

Stimulated Raman scattering (SRS) produces a frequency shift of about 400 cm^{-1} from the incident laser line. The equation governing the power growth of the Raman-shifted mode is as follows

$$\frac{dP_R}{dz} = -\alpha_R P_R + \frac{g_R}{a_P} P_P P_R \tag{37}$$

where P_R denotes the power of the Stokes-shifted light, P_P is the pump power (this is the power in the initially excited mode), and a_P is the effective area of the pump. The Raman gain g_R ultimately determines the SRS-limited light intensity. For typical single-mode silica fibers, g_R is about 10^{-11} cm/W, and yields a power limit of

$$P_{CR} = \frac{16\alpha a_P}{g_R} \tag{38}$$

beyond which the guided wave power will be efficiently Raman-shifted and excess loss will begin to appear at the pump wavelength.

Stimulated Brillouin scattering (SBS) can yield an even lower stimulated scattering threshold. Acoustic waves in the fiber tend to form a Bragg index grating, and scattering occurs primarily in the backward direction. The Brillouin gain g_B is much higher than Raman gain in fibers ($g_B = 5 \times 10^{-9}$ cm/W) and leads to a stimulated scattering threshold of

$$P_{CR} = \frac{25\alpha a_P}{g_B} \tag{39}$$

for a narrowband, CW input.

Either type of stimulated scattering process can be used as a source of gain in the fiber. Injecting a signal within the frequency band of the stimulated scattering process will provide amplification of the input signal. Raman amplification tends to be the more useful of the two because of the relatively large frequency shift and the broader-gain bandwidth. SBS has been used in applications such as coherent optical communications[48] where amplification of a pilot carrier is desired.

The gain bandwidth for SBS is quite narrow—100 MHz for a typical fiber. SBS is therefore only important for sources whose spectra lie within this band. An unmodulated narrow-band laser source such as would be used as a local oscillator in a coherent system would be highly susceptible to SBS, but a directly modulated laser with a 1-GHz linewidth under modulation (modulated laser linewidths can extend well into the GHz range due to frequency chirp) would have an SBS threshold about ten times that of the narrow linewidth source.

Pulse Compression and Soliton Propagation

A major accomplishment in the push toward short pulse propagation in optical fibers was the prediction and observation of solitary wave propagation. In a nonlinear dispersive medium, solitary waves may exist provided the nonlinearity and dispersion act to balance one another. In the case of soliton propagation, the nonlinearity is a refractive index which follows the pulse intensity in a nearly instantaneous fashion:

$$n(t) = n_0 + n_2 I(t) \tag{40}$$

For silica fibers, $n_2 = 3 \times 10^{-16}$ cm^2/W.

TABLE 5 Normalized Variables of the Nonlinear Schrödinger Equation

A	Pulse amplitude
z	Longitudinal coordinate
t	Time
P_0	Peak power
T_0	Pulse width
U	$A/\sqrt{P_0}$ normalized pulse amplitude
β_1	Propagation constant
β_2	Dispersion (2d order)
L_D	$T_0^2/\lvert\beta_2\rvert$ dispersion length
n_2	Nonlinear refractive index
τ	$\dfrac{t-\beta_1 z}{T_0}$ time normalized to moving frame
ξ	$\dfrac{z}{L_D}$ normalized distance
N	$n_2\beta_1 P_0 T_0^2/\lvert\beta_2\rvert$ Order of soliton

The scalar equation governing pulse propagation in such a nonlinear dispersive medium is sometimes termed the *nonlinear Schrödinger equation*

$$i\frac{dU}{d\xi} + \frac{1d^2U}{2d\tau^2} + N^2|U|^2U = 0 \tag{41}$$

where the symbols are defined in Table 5. Certain solutions of this equation exist in which the pulse propagates without change in shape; these are the soliton solutions. Solitons can be excited in fibers and propagate great distances before breaking up. This is the basis for fiber-based soliton communication.

Figure 27 illustrates what happens to a pulse which propagates in such a medium. The local refractive index change produces what is commonly known as *self phase modulation.* Since n_2 is positive, the leading edge of the pulse produces a local increase in refractive index. This results in a red shift in the instantaneous frequency. On the trailing edge, the pulse experiences a blue shift. If the channel is one which exhibits normal dispersion, the red-shifted edge will advance while the blue-shifted edge will retard, resulting in pulse spreading If, however, the fiber exhibits anomalous dispersion (beyond 1.3 μm for most single-mode fibers), the red-shifted edge will retard and the pulse will be compressed. Fibers have been used in this way as pulse compressors for some time. In the normal dispersion regime, the fiber nonlinearity is used to chirp the pulse, and a grating pair supplies the dispersion necessary for compression.

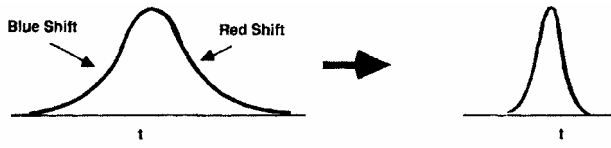

FIGURE 27 A pulse propagating through a medium with an intensity-dependent refractive index will experience frequency shifts of the leading and trailing edges of the pulse (*left*). Upon transmission through a fiber having anomalous dispersion, the pulse compresses (*right*).

In the anomalous dispersion regime, the fiber can act both to chirp and compress the pulse. Near the dispersion minimum, higher-order dependence of the group delay on wavelength becomes important, and simple pulse compression does not take place.

Pulse compression cannot continue indefinitely, since the linear dispersion will always act to spread the pulse. At a critical shape, the pulse stabilizes and will propagate without change in shape. This is the point at which a soliton forms. The lowest-order soliton will propagate entirely without change in shape, higher order solitons (which also carry higher energy) experience a periodic evolution of pulse shape.

A soliton requires a certain power level in order to maintain the necessary index change. Distortion-free pulses will therefore propagate only until the fiber loss depletes the energy. Since solitons cannot persist in a lossy channel, they were long treated merely as laboratory curiosities. This was changed by several successful demonstrations of extremely long distance soliton transmission by the inclusion of gain to balance the loss. The gain sections, which initially made use of stimulated Raman scattering, now consist of rare-earth doped fiber amplifiers. The record for repeaterless soliton transmission is constantly being challenged. At the time of this writing, distance of well over 10,000 km have been demonstrated in recirculating loop experiments.

In the laboratory, solitons have most often been generated by mode-locked laser sources. Mode-locked solid state laser sources are generally limited to low duty-cycle pulses, with repetition rates in the 1-GHz range or less. The mode-locked pulse train must then be modulated to carry data, a process which must be carried out externally. There is a high level of current interest in Erbium-doped fiber lasers as mode-locked sources for ultralong distance data communications. Despite the capability of high duty cycle, directly modulated semiconductor lasers are generally rendered unsuitable for soliton communications by the spectral broadening that occurs under modulation.

Four-Wave Mixing

The nonlinear refractive index is simply a degenerate case of a third-order optical nonlinearity, in which the polarization of the medium responds to the cube of the applied electric field. It is possible for widely separated frequencies to phase modulate one another via the fiber nonlinearity, generating sidebands which interfere with neighboring channels in a multiplexed system. This represents an important limit to channel capacity in either WDM or FDM systems. The simplest picture of the four-wave mixing process in fibers can be illustrated by the transmission and cross-phase modulation of four equally spaced channels shown in Fig. 28. Channels 1 and 2 interfere, producing an index of refraction which oscillates at the difference frequency. This modulation in refractive index modulates channel 4, producing sidebands at channels 3 and 5. This is only the simplest combination of frequencies. Four-wave mixing allows any combination of three frequencies beating together to produce a fourth. If the fourth frequency lies within a communication band, that channel can be rendered unusable.

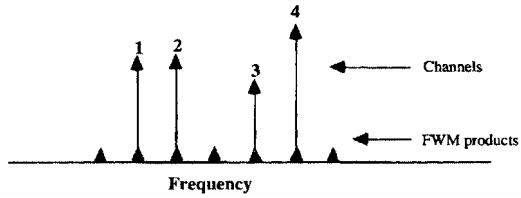

FIGURE 28 The effects of four-wave mixing on multichannel transmission through an optical fiber.

This channel interference can effect either closely spaced channels, as one encounters with coherent communications, or the rather widely separated channels of a WDM system. Efficient four-wave mixing requires phase matching of the interacting waves throughout the interaction length—widely separated channels will therefore be phase matched only in a region of low-fiber dispersion.

The communications engineer will recognize this as little more than the intermodulation products which must always be dealt with in a multichannel communications system with small nonlinearities. Four-wave mixing merely produces intermodulation products over an extremely wide bandwidth. Just as with baseband nonlinearities in analog communications systems, judicious allocation of channels can minimize the problem, but at the expense of bandwidth. The cumulative effect of the nonlinearities increases with interaction length and therefore imposes an important limit on frequency or wavelength-division multiplexed systems.

Photorefractive Nonlinearities in Fibers

There also exists a class of integrating, photorefractive nonlinearities in optical fibers which have been of some interest in recent years. We use the word photorefractive loosely here, simply to indicate a long-term change in either the first- or second-order susceptibility with light exposure. The effects appear strongest in fibers with a germania content, but the precise role of the glass constituents in these processes is still an area of active research.

Bragg Index Gratings. Photons of energy near a UV absorption edge can often write permanent phase gratings by photoionizing certain constituents or impurities in the material. This is the case for $LiNbO_4$ and certain other ferroelectric materials, and such effects have also been observed in germania-silica fibers. The effects were first observed in the process of guiding relatively high power densities of green light—it was found that a high backscatter developed over a period of prolonged exposure. The fiber then exhibited the transmission characteristics of a Bragg grating, with extremely high resonant reflectivities.

The writing of permanent gratings in fibers using UV exposure is now relatively commonplace. Bragg gratings can be used as filters in WDM systems, reflectors on fiber lasers, and possibly optical switches. For short lengths, the gratings are most easily formed holographically, by using two interfering beams from a pulsed UV source such as an excimer laser. The fiber is exposed from the side; by controlling the angle of the two interfering beams, any grating period may be chosen.

Frequency Doubling in Germania-Silica Fibers. While it is not surprising that UV exposure could produce refractive index changes, a rather unexpected discovery was the fact that strong optical fields inside the fiber could produce a second-order susceptibility, resulting in efficient frequency doubling. Electro-optic effects such as frequency doubling require that a crystalline material lack a center of symmetry while an amorphous material must lack a statistical center of symmetry. It has long been known that certain materials will develop an electro-optic effect under a suitable applied field. This process, known as *poling,* provides the necessary microscopic alignment of dipoles for development of the nonlinear susceptibility. In optical fibers, a type of self-poling occurs from the strong fundamental beam, resulting in a second-order susceptibility and efficient frequency doubling.

Efficient frequency doubling requires both a noncentrosymmetric material and adequate phase matching between the fundamental and second harmonic waves. The mechanism by which the fiber is both poled and phase matched is still not fully understood at the time of this writing, and it remains to be seen whether this represents an exciting, new application of germania-silica fibers or simply an internal damage mechanism which limits the ultimate power delivery of the fiber.

1.9 OPTICAL FIBER MATERIALS: CHEMISTRY AND FABRICATION

What is arguably the most important breakthrough in the history of optical fiber technology occurred in the materials development. Until 1970, many scientists felt that glasses of moderate softening points and smooth phase transitions would allow for easier drawing and better control. The choice of Corning Glass Works (now Corning, Inc.) to go to (what was then) the somewhat more difficult chemistry of the nearly pure silica fiber allowed both a dramatic reduction in fiber attenuation and a better understanding of the role of the chemical constituents in fiber loss. Researchers soon found that the best dopants for altering the refractive index were those which provided a weak index change without providing a large shift in the UV absorption edge. Conventional fiber chemistry consists of dopants such as GeO_2, P_2O_5 (for raising the refractive index) and B_2O_3 or SiF_4 (for lowering the refractive index).

Silica has both UV and mid-IR absorption bands; these two bands result in a fundamental limit to the attenuation which one can achieve in the silica system. This occurs despite the fact that the Rayleigh scattering contribution decreases as λ^{-4}, and the ultraviolet Urbach absorption edge decreases even faster with increasing λ. The infrared absorption increases with long wavelengths, and becomes dominant beyond wavelengths of about 1.6 μm, resulting in a fundamental loss minimum near 1.55 μm.

The promise of achieving a lower Rayleigh scattering limit in the mid-infrared (as well as the possible applications of fiber to the CO_2 laser wavelength range) have spurred a great deal of research in fiber materials which exhibit better infrared transparency. Two important representative materials are the heavy-metal fluoride glasses and the chalcogenide glasses. While both classes exhibit better infrared transparency, neither has yet improved to the point of serious competition with silica materials.

For a number of years, attenuation in optical fibers was limited by a strong absorption band near $\lambda = 1.4$ μm. (An examination of attenuation curves of early telecommunications-grade fiber shows it nearly unusable at what are now the wavelengths of prime interest—1.3 μm and 1.55 μm.) This absorption, which was linked to the presence of residual OH ions, grew steadily lower with the improvement of fiber fabrication techniques until the loss minimum at $\lambda = 1.55$ μm was eventually brought close to the Rayleigh scattering limit.

The low-cost, low-temperature processes by which polymers can be fabricated has led to continued research into the applications of plastic fiber to technologies which require low cost, easy connectivity, and that are not loss-limited. The additional flexibility of these materials makes them attractive for large-core, short-length applications in which one wishes to maximize the light insertion. Hybrid polymer cladding-silica core fibers have also received some attention in applications requiring additional flexibility.

The final triumph of fiber chemistry in recent years has been the introduction and successful demonstration of extremely long distance repeaterless fiber links using rare-earth doped fiber amplifiers. This represented the climax of a long period of research in rare-earth doped glasses which went largely unnoticed by the optics community. As a result, there has been an explosion of work in the materials science, materials engineering, and applications of rare-earth doped optical fibers.

Fabrication of Conventional Optical Fibers

Conventional fabrication of low-loss optical fibers requires two stages. The desired refractive index profile is first fabricated in macroscopic dimensions in a preform. A typical preform is several centimeters in width and a meter in length, maintaining the dimensions and dopant distribution in the core and cladding that will eventually form in the fiber.

Chemical vapor deposition (CVD) is the primary technology used in fiber manufacturing. The fabrication process must satisfy two requirements: (1) high purity, and (2) precise control

over composition (hence, refractive index) profiles. Manufacturing considerations favor approaches which provide a fast deposition rate and comparatively large preforms. In CVD processes, submicron silica particles are produced through one (or both) of the following chemical reactions

$$SiCl_4 + O_2 \rightarrow SiO_2 + 2Cl_2$$

$$SiCl_4 + 2H_2O \rightarrow SiO_2 + HCl$$

The reactions are carried out at a temperature of about 1800°C. The deposition leads to a high-purity silica soot which must then be sintered in order to form optical quality glass.

Modern manufacturing techniques, generally speaking, use one of two processes.[61] In the so-called "inside process," a rotating silica substrate tube is subjected to an internal flow of reactive gases. The two inside processes which have received the most attention are modified chemical vapor deposition (MCVD) and plasma-assisted chemical vapor deposition (PCVD). Both techniques require a layer-by-layer deposition, controlling the composition at each step in order to reach the correct target refractive index. Oxygen, as a carrier gas, is bubbled through $SiCl_4$, which has a relatively high vapor pressure at room temperature.

The PCVD process provides the necessary energy for the chemical reaction by direct RF plasma excitation. The submicron-sized particles form on the inner layer of the substrate, and the composition of the layer is controlled strictly by the composition of the gas. PCVD does not require the careful thermal control of other methods, but requires a separate sintering step to provide a pore-free preform. A final heating to 2150°C collapses the preform into a state in which it is ready to be drawn.

The MCVD process (Fig. 29) accomplishes the deposition by an external, local application of a torch. The torch has the dual role of providing the necessary energy for oxidation and the heat necessary for sintering the deposited SiO_2. The submicron particles are deposited on the "leading edge" of the torch; as the torch moves over these particles, they are sintered into a vitreous, pore-free layer. Multiple passes result in a layered, glassy deposit which should approximate the target radial profile of the fiber. As with PCVD, a final pass is necessary for collapse of the preform before the fiber is ready to be drawn. MCVD requires rather precise control over the temperature gradients in the tube but has the advantage of accomplishing the deposition and sintering in a single step.

In the "outside process," a rotating, thin cylindrical target (or mandrel) is used as the substrate for a subsequent chemical vapor deposition, and requires removal before the boule is sintered. Much of the control in these deposition techniques lies in the construction of the

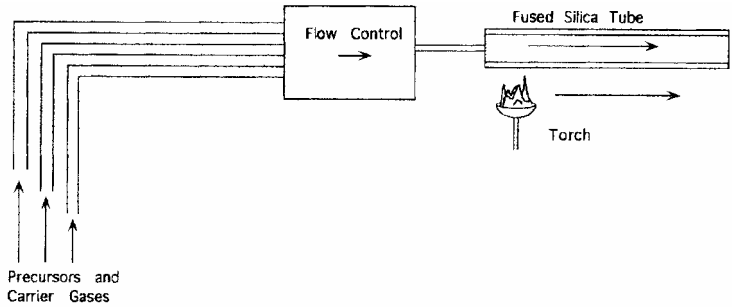

FIGURE 29 The modified chemical vapor deposition (MCVD) process for preform fabrication.

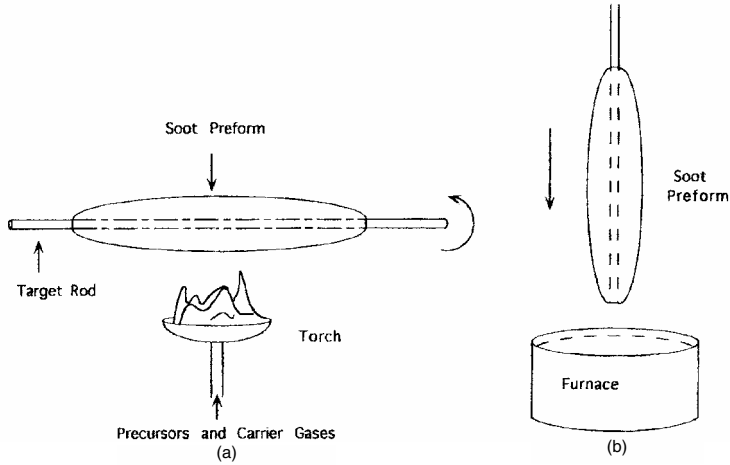

FIGURE 30 Outside method of preform fabrication. The soot deposition (*a*) is followed by sintering (*b*) to cast the preform.

torch. For an outside process, the torch supplies both the chemical constituents and the heat for the reaction.

Two outside processes which have been used a great deal are the outside vapor deposition (OVD) and the vapor axial deposition (VAD) techniques. Figure 30 illustrates a generic outside process. In the OVD process the torch consists of discrete holes formed in a pattern of concentric rings. The primary chemical stream is at the center, followed by O_2 (acting as a shield gas), premixed methane/oxygen, and another shield ring. The torch itself translates along the rotating boule and the dopants are dynamically controlled to achieve the necessary profiling.

The VAD torch is comprised of a set of concentric annular apertures, with a chemical sequence similar to the OVD. In contrast to the OVD method, the VAD torch is held stationary during the deposition; the rotating target is held vertically, and is lifted as the deposition continues.

Dopant Chemistry

Standard dopants for silica fiber include GeO_2, P_2O_5, B_2O_3, and SiF_4. The former two are used to increase the refractive index (and are therefore used in the core), while the latter decrease the index of refraction (and are therefore used in the cladding). The CVD processes will often use oxygen as a carrier gas with the high vapor pressure liquids $GeCl_4$, $POCl_3$, or SiF_4. The reaction which produces the dopant "soot" is then

$$GeCl_4 + O_2 \rightarrow GeO_2 + 2Cl_2$$

$$4POCl_3 + 3O_2 \rightarrow 2P_2O_5 + 6Cl_2$$

As noted in a recent article by Morse et al.,[62] "Nature has been kind in the creation of the high vapor pressure liquid precursors used in the fabrication of optical fibers for the transmission of telecommunication signals." This has been an extremely important factor in the

success of CVD fiber fabrication techniques. The problem of introducing more exotic dopants, such as the rare-earth elements, is not quite so straightforward and there does not appear to exist, at this time, a single, widely used technique. The problem of control over the rare-earth dopant profile is compounded by the fact that research in laser and amplifier design is ongoing, and the optimum dopant profile for rare-earth doped fibers and amplifiers is, in many cases, still unknown. Despite these uncertainties, rare-earth doped fibers have already been introduced into commercial products and promise to spearhead the next generation of long distance telecommunications systems.

Other Fabrication Techniques

There are other preform fabrication and fiber drawing techniques. These are not generally used in telecommunications-grade silica fiber, but can be of advantage for glass chemistries which do not easily lend themselves to chemical vapor deposition. Several examples of this will be described in the following section on infrared fiber fabrication.

CVD materials, while the most popular, are not the only methods for preform fabrication. Alternative methods of preform fabrication include both bulk casting and a class of non-CVD tubular casting techniques. One such technique is the "rod-in-tube" method, in which the core and cladding materials are cast separately and combined in a final melting/collapsing step. This method assures a homogeneous, low-impurity content core but risks introducing defects and bubbles into the core/cladding interface.

The most well-known method of *preform-free drawing* is the double crucible method, in which the core and cladding melts are formed separately and combined in the drawing process itself. This eliminates the need for a very large preform in the case of long lengths of fiber. The index profile is established in the drawing process itself, and index gradients are therefore difficult to establish unless additional crucibles are added. Another difficulty of the crucible method is the sometimes inadequate control of the concentricity of the core and cladding.

Infrared Fiber Fabrication

The major applications of interest for infrared optical fibers are as follows:

1. Ultra-low-loss communication links
2. CO_2 laser transmission for medical applications
3. Thermal imaging and remote temperature monitoring
4. Gas sensing

These may differ rather dramatically in their attenuation requirements and spectral region of interest. For example, an ultra-low-loss communications link requires attenuation somewhat less than 0.1 dB/km in order to be competitive with silica fiber. Typical medical applications simply require high-power handling capabilities of a CO_2 laser over meter lengths. All of these applications require a departure from the silica-based chemistry which has been so successful for applications in the near infrared and visible. Much of the generic chemistry of these glasses is covered in Chap. 33 of Vol. II, "Crystals and glasses." Our intent here is to give an overview of the fiber types and the general state of the materials technology in each case.

Chalcogenide Fibers. Sulfide, selenide, and telluride glasses have all been used for bulk infrared optics—particularly for applications involving CO_2 ($\lambda = 10.6\ \mu m$) or CO laser transmission ($\lambda = 5.4\ \mu m$). Infrared fibers have been drawn from these materials and yielded trans-

mission losses of the order of 1 dB/meter in the 5- to 7-μm region.[63] The preform fabrication and drawing of chalcogenide fibers is much more difficult than that of silica due primarily to its sensitivity both to oxygen and moisture. Both oxidation and crystallization can occur at the temperatures necessary to draw the fiber. Either will result in catastrophically high losses and fiber weakness.

Fluoride Fibers. Fluoride fibers have received the most attention for low-loss telecommunications applications, because the theoretical limit for Rayleigh scattering is considerably lower. This is due both to a higher-energy UV absorption edge and better infrared transparency. The difficulty is that excess absorption has proven rather difficult to reduce, and the lowest published losses to date have been near 1 dB/km for long fiber lengths.[64,65] The state-of-the-art in fluoride fiber fabrication is still well above the Rayleigh scattering limit but does show the expected improvement over silica fiber in wavelengths beyond 1.6 μm. Fabrication of very short fiber lengths has been somewhat more successful, with reported losses as low as 0.025 dB/km at 2.55 μm.[66]

The residual loss for longer fibers has been largely linked to extrinsic impurity/defect content. Recent articles by Takahashi and Sanghera[64,65] have noted the role of transition metal and rare-earth ions, submicron platinum particles, oxyfluoride particles, fluoride microcrystals, and bubbles as both extrinsic absorbers and scatterers. The defects of interest originate from a variety of sources, and there has been much discussion on which defects dominate the scattering process. To date, the consensus appears to be that impurity absorption does *not* adequately account for the current loss limits, but does account for residual losses in the neighborhood of 0.2 dB/km.

The classes of defects which have been blamed for the current loss limits are as follows:

Platinum particles. These arise from the use of platinum crucibles. The use of vitreous carbon crucibles eases this contamination.

Core bubbles. This is clearly a problem in the preform fabrication and appears in some of the bulk casting techniques.

Interfacial bubbles. Bubbles appearing at the core-cladding interface have been named as being a major cause of excess scattering. These appear to be a particular problem for those techniques which employ separate core and cladding melts. This unfortunately negates some of the advantages offered by the crucible techniques in fluoride fiber fabrication.

Fluoride microcrystals. Crystals can nucleate at a variety of defect sites. Many of these sites appear at the core-cladding interface, producing interface roughness and scattering. Since, for step-index fibers, the integrity of the core-cladding interface is essential to the confinement of the optical wave, a small amount of interface roughness can produce rather high excess losses.

Chapter 33 of Vol. II, "Crystals and glasses," gives information on the composition and properties of a single-mode fiber grade fluoride glass. This class of compositions has received the designation ZBLAN, after its heavy-metal constituents. The large number of components makes it immediately obvious that both phase separation and crystallization are important issues in fabrication. Either can produce catastrophic increases in loss as well as mechanical weakening of the fiber, and it is clear that many materials science challenges remain in the area of fluoride fiber fabrication.

1.10 REFERENCES

1. K. C. Kao and G. A. Hockham, "Dielectric Fibre Surface Waveguides for Optical Frequencies," *Proc. IEE,* **113**:1151–1158 (1966).
2. D. B. Keck, P. C. Schultz, and F. W. Zimar, U.S. Patent 3,737,393.

3. F. P. Kapron, D. B. Keck, and R. D. Maurer, "Radiation Losses in Glass Optical Waveguides" *Appl. Phys. Lett.* **17**:423 (1970).
4. M. J. Adams, *An Introduction to Optical Waveguides,* John Wiley and Sons, Chichester, 1981.
5. D. Davidson, "Single-Mode Wave Propagation in Cylindrical Optical Fibers," in E. E. Basch (ed.), *Optical Fiber Transmission,* Howard W. Sams, Indianapolis, 1987, 27–64.
6. M. O. Vassell, "Calculation of Propagating Modes in a Graded-Index Optical Fiber," *Optoelectronics* **6**:271–286 (1974).
7. D. Gloge, "Weakly Guiding Fibers," *Appl. Opt.* **10**:2252–2258 (1971).
8. R. W. Davies, D. Davidson, and M. P. Singh, "Single Mode Optical Fiber with Arbitrary Refractive Index Profile: Propagation Solution by the Numerov Method," *J. Lightwave Tech.* **LT-3**:619–627 (1985).
9. P. C. Chow, "Computer Solutions to the Schroedinger Problem," *Am. J. of Physics* **40**:730–734 (1972).
10. A. Kumar, R. K. Varshney, and K. Thyagarajan, "Birefringence Calculations in Elliptical-core Optical Fibers," *Electron. Lett.* **20**:112–113 (1984).
11. K. Sano and Y. Fuji, "Polarization Transmission Characteristics of Optical Fibers With Elliptical Cross Section," *Electron. Commun. Japan* **63**:87 (1980).
12. EIA-FOTP-46, *Spectral Attenuation Measurement for Long-Length, Graded-Index Optical Fibers, Procedure B,* Electronic Industries Association (Washington, D.C.).
13. EIA-FOTP-78, *Spectral Attenuation Cutback Measurement for Single Mode Optical Fibers,* Electronic Industries Association (Washington, D.C.).
14. EIA-FOTP-50, *Light Launch Conditions for Long-Length, Graded-Index Optical Fiber Spectral Attenuation Measurements, Procedure B,* Electronic Industries Association (Washington, D.C.).
15. A. W. Carlisle, "Small Size High-performance Lightguide Connector for LAN's," *Proc. Opt. Fiber Comm.* **TUQ 18**:74–75 (1985).
16. E. Sugita et al., "SC-Type Single-Mode Optical Fiber Connectors," *J. Lightwave Tech* **LT-7**:1689–1696 (1989).
17. N. Suzuki, M. Saruwatari, and M. Okuyama, "Low Insertion- and High Return-loss Optical Connectors with Spherically Convex-polished Ends," *Electron. Lett.* **22(2)**:110–112 (1986).
18. W. C. Young et al., "Design and Performance of the Biconic Connector Used in the FT3 Lightwave System," in *30th IWCS,* 1981.
19. EIA-FOTP-168, *Chromatic Dispersion Measurement of Multimode Graded-Index and Single-Mode Optical Fibers by Spectral Group Delay Measurement in the Time Domain,* Electronic Industries Association (Washington, D.C.).
20. R. Rao, "Field Dispersion Measurement—A Swept-Frequency Technique," in *NBS Special Publication 683,* Boulder, 1984, p. 135.
21. L. G. Cohen and J. Stone, "Interferometric Measurements of Minimum Dispersion Spectra in Short Lengths of Single-Mode Fiber," *Electron. Lett.* **18**:564 (1982).
22. L. G. Cohen, et al., "Experimental Technique for Evaluation of Fiber Transmission Loss and Dispersion," *Proc. IEEE* **68**:1203 (1980).
23. R. A. Modavis and W. F. Love, "Multiple-Wavelength System for Characterization of Dispersion in Single-Mode Optical Fibers," in *NBS Special Publication 683,* Boulder, 1984, p. 115.
24. T. Miya et al., "Fabrication of Low-dispersion Single-Mode Fiber Over a Wide Spectral Range," *IEEE J. Quantum Electronics,* **QE-17**:858 (1981).
25. R. Olshansky and R. D. Maurer, "Tensile Strength and Fatigue of Optical Fibers," *J. Applied Physics* **47**:4497–4499 (1976).
26. EIA-FOTP-28, *Method for Measuring Dynamic Tensile Strength of Optical Fibers,* Electronic Industries Association (Washington, D.C.).
27. M. R. Brininstool, "Measuring Longitudinal Strain in Optical Fibers," *Optical Engineering* **26**:1113 (1987).
28. M. J. Matthewson, C. R. Kurkjian, and S. T. Gulati, "Strength Measurement of Optical Fibers by Bending," *J. Am. Ceramic. Soc.* **69**:815 (1986).

29. W. Weibull, "A Statistical Distribution Function of Wide Applicability," *J. Appl. Mech.* **24**:293–297 (1951).
30. J. D. Helfinstine, "Adding Static and Dynamic Fatigue Effects Directly to the Weibull Distribution," *J. Am. Ceramic Soc.* **63**:113 (1980).
31. D. Inniss, D. L. Brownlow, and C. R. Kurkjian, "Effect of Sodium Chloride Solutions on the Strength and Fatigue of Bare Silica Fibers," *J. Am. Ceramic Soc.* **75**:364 (1992).
32. J. S. Cook and O. I. Scentesi, "North American Field Trials and Early Applications in Telephony," *IEEE J. Selected Areas in Communications* **SAC-1**:393–397 (1983).
33. H. Ishio "Japanese Field Trials and Early Applications in Telephony," *IEEE J. Selected Areas in Communications* **SAC-1**:398–403 (1983).
34. A. Moncolvo and F. Tosco, "European Field Trials and Early Applications in Telephony," *IEEE J. Selected Areas in Communications* **SAC-1**:398–403 (1983).
35. E. E. Basch, R. A. Beaudette, and H. A. Carnes, "Optical Transmission for Interoffice Trunks," *IEEE Trans. on Communications* **COM-26**:1007–1014 (1978).
36. G. P. Agrawal, *Fiber-Optic Communication Systems,* Wiley Series in Microwave and Optical Engineering, K. Chang (ed.), John Wiley and Sons, New York, 1992.
37. K. Petermann, *Laser Diode Modulation and Noise,* Kluwer Academic, Dordrecht, The Netherlands, 1991.
38. R. J. McIntyre, "Multiplication Noise in Uniform Avalanche Diodes," *IEEE Trans. Electron Devices* **ED-13**:164 (1966).
39. R. J. McIntyre, "The Distribution of Gains in Uniformly Multiplying Avalanche Photodiodes: Theory," *IEEE Trans. Electron Devices* **ED-19**:703–713 (1972).
40. S. D. Personick, "Statistics of a General Class of Avalanche Detectors with Applications to Optical Communications," *Bell System Technical Journal* **50**:167–189 (1971).
41. R. K. Dodd, et al., *Solitons and Nonlinear Wave Equations,* Academic Press, Orlando, Florida, 1984.
42. A. Hasegawa, *Solitons in Optical Fibers,* Springer-Verlag, Berlin, 1989.
43. L. F. Mollenauer, R. H. Stolen, and J. P. Gordon, "Experimental Observation of Picosecond Pulse Narrowing and Solitons in Optical Fibers," *Phys. Rev. Letters* **45**:1095 (1980).
44. L. F. Mollenauer et al., "Extreme Picosecond Pulse Narrowing by Means of Soliton Effect in Single-Mode Optical Fibers," *Opt. Lett.* **8**:289 (1983).
45. L. F. Mollenauer, R. H. Stolen, and M. N. Islam, "Experimental Demonstration of Soliton Propagation in Long Fibers: Loss Compensated by Raman Gain," *Opt. Lett.* **10**:229 (1985).
46. J. P. Gordon and H. A. Haus, *Opt. Lett.* **11**:665 (1986).
47. L. F. Mollenauer, J. P. Gordon, and S. G. Evangelides, "The Sliding Frequency Guiding Filter—an Improved Form of Soliton Jitter Control," *Opt. Lett.* **17**:1575 (1992).
48. A. R. Chraplyvy and R. W. Tkach, *Electron. Lett.* **22**:1084 (1986).
49. I. Garrett and G. Jacobsen, "Theoretical Analysis of Heterodyne Optical Receivers using Semiconductor Lasers of Non-negligible Linewidth," *J. Lightwave Technology* **4**:323 (1986).
50. B. Glance, "Performance of Homodyne Detection of Binary PSK Optical Signals," *J. Lightwave Technology* **4**:228 (1986).
51. L. G. Kazovsky, "Performance Analysis and Laser Linewidth Requirements for Optical PSK Heterodyne Communications," *J. Lightwave Technology* **4**:415 (1986).
52. K. Kikuchi, et al., *J. Lightwave Technology* **2**:1024 (1984).
53. T. Okoshi and K. Kikuchi, *Coherent Optical Fiber Communications,* Kluwer, Boston, 1988.
54. N. A. Olsson et al., "400 Mbit/s 372 = Km Coherent Transmission Experiment," *Electron. Lett.* **24**:36 (1988).
55. E. G. Bryant et al., "A 1.2 Gbit/s Optical FSK Field Trial Demonstration," *British Telecom Technology Journal* **8**:18 (1990).
56. T. Okoshi, "Polarization-State Control Schemes for Heterodyne of Homodyne Optical Fiber Communications," *J. Lightwave Technology* **3**:1232–1237 (1985).

57. B. Glance, "Polarization Independent Coherent Optical Receiver," *J. Lightwave Technology* **5**:274 (1987).
58. R. H. Stolen, "Nonlinear Properties of Optical Fibers," in S. E. Miller and A. G. Chynowth, eds., *Optical Fiber Telecommunications,* Academic Press, New York.
59. G. P. Agrawal, "Nonlinear Interactions in Optical Fibers," in G. P. Agrawal and R. W. Boyd, eds., *Contemporary Nonlinear Optics,* Academic Press, San Diego, California, 1992.
60. G. P. Agrawal, *Nonlinear Fiber Optics,* Academic Press, San Diego, California, 1989.
61. J. R. Bautista and R. M. Atkins, "The Formation and Deposition of SiO_2 Aerosols in Optical Fiber Manufacturing Torches," *J. Aerosol Science* **22**:667–675 (1991).
62. T. F. Morse et al., "Aerosol Transport for Optical Fiber Core Doping: A New Technique for Glass Formation," *J. Aerosol Science* **22**:657–666 (1991).
63. J. Nishii et al., "Recent Advances and Trends in Chalcogenide Glass Fiber Technology: A Review," *J. Noncrystalline Solids* **140**:199–208 (1992).
64. J. S. Sanghera, B. B. Harbison, and I. D. Aggarwal, "Challenges in Obtaining Low Loss Fluoride Glass Fibers," *J. Non-Crystalline Solids* **140**:146–149 (1992).
65. S. Takahashi, "Prospects for Ultra-low Loss Using Fluoride Glass Optical Fiber," *J. Non-Crystalline Solids* **140**:172–178 (1992).
66. I. Aggarwal, G. Lu, and L. Busse, *Materials Science Forum* **32 & 33**: Plenum, New York, 1988, p. 495.

1.11 FURTHER READING

Agrawal, G. P., *Fiber-Optic Communication Systems,* John Wiley and Sons, New York, 1992.
Baack, C. (ed.), *Optical Wideband Transmission Systems,* CRC Press, Boca Raton, Florida, 1986.
Baker, D. G., *Fiber Optic Design and Applications,* Reston Publishing, Reston, Virginia, 1985.
Barnoski, M. K. (ed.), *Fundamentals of Optical Fiber Communications,* Academic Press, New York, 1981.
Basch, E. E. (ed.), *Optical Fiber Transmission,* Howard W. Sams, Indianapolis, Indiana, 1987.
Chaffee, C. D., *The Rewiring of America: The Fiber Optics Revolution,* Academic Press, Boston, 1988.
Chaimowitz, J. C. A., *Lightwave Technology,* Butterworths, Boston, 1989.
Cheo, P. K., *Fiber Optics: Devices and Systems,* Prentice-Hall, Englewood Cliffs, New Jersey, 1985.
Cheo, P. K., *Fiber Optics and Optoelectronics,* Prentice-Hall, Englewood Cliffs, New Jersey, 1990.
Cherin, A. H., *An Introduction to Optical Fibers,* McGraw-Hill, New York, 1983.
Culshaw, B., *Optical Fibre Sensing and Signal Processing,* Peter Peregrinus, London, 1984.
Daly, J. C. (ed.), *Fiber Optics,* CRC Press, Boca Raton, Florida, 1984.
Day, G. W., *Measurement of Optical-Fiber Bandwidth in the Frequency Domain,* NBS Special Publication, No. 637, National Bureau of Standards, Boulder, 1983.
Edwards, T. C., *Fiber-Optic Systems: Network Applications,* John Wiley and Sons, New York, 1989.
Geckeler, S., *Optical Fiber Transmission Systems,* Artech House, Norwood, Massachusetts, 1987.
Gowar, J., *Optical Communications Systems,* Prentice-Hall, London, 1984.
Howes, M. J. and D. V. Morgan (eds.), *Optical Fiber Communications,* John Wiley and Sons, New York, 1980.
Jones, W. B., Jr., *Introduction to Optical Fiber Communications,* Holt, Rinehart and Winston, New York, 1988.
Kaiser, G. E., *Optical Fiber Communications,* McGraw-Hill, New York, 1991.
Kao, C. K., *Optical Fibre,* Peter Peregrinus, London, 1988.
Karp, S., R. Gagliardi et al., *Optical Channels: Fibers, Clouds, Water, and the Atmosphere,* Plenum Press, New York, 1988.
Killen, H. B., *Fiber Optic Communications,* Prentice-Hall, Englewood Cliffs, New Jersey, 1991.
Li, T., (ed.), *Optical Fiber Data Transmission,* Academic Press, Boston, 1991.

Lin, C. (ed.), *Optoelectronic Technology and Lightwave Communications Systems,* Van Nostrand Reinhold, New York, 1989.

Mahlke, G. and P. Gossing, *Fiber Optic Cables,* John Wiley and Sons, New York, 1987.

Miller, S. E. and J. P. Kaminow (eds.), *Optical Fiber Telecommunications II,* Academic Press, San Diego, California, 1988.

Okoshi, T. and K. Kikuchi, *Coherent Optical Fiber Communications,* Kluwer, Boston, 1988.

Palais, J. C., *Fiber-Optic Communications,* Prentice-Hall, Englewood Cliffs, New Jersey, 1988.

Personick, S. D., *Optical Fiber Transmission Systems,* Plenum Press, New York, 1981.

Personick, S. D., *Fiber Optics: Technology and Applications,* Plenum Press, New York, 1985.

Runge, P. K. and P. R. Trischitta (eds.), *Undersea Lightwave Communications,* IEEE Press, New York, 1986.

Senior, J. M., *Optical Fiber Communications,* Prentice-Hall, London, 1985.

Sharma, A. B., S. J. Halme, et al., *Optical Fiber Systems and Their Components,* Springer-Verlag, Berlin, 1981.

Sibley, M. J. N., *Optical Communications,* Macmillan, London, 1990.

Taylor, H. F. (ed.), *Fiber Optics Communications,* Artech House, Norwood, Massachusetts, 1983.

Taylor, H. F. (ed.), *Advances in Fiber Optics Communications,* Artech House, Norwood, Massachusetts, 1988.

Tsang, W. T. (ed.), *Lightwave Communications Technology,* Semiconductors and Semimetals. Academic Press, Orlando, Florida, 1985.

Fibers in Medicine

Harrington, J. A. (ed.), *Infrared Fiber Optics III,* SPIE, Bellingham, Washington, 1991.

Joffe, S. N., *Lasers in General Surgery,* Williams & Wilkins, Baltimore, 1989.

Katzir, A. (ed.), *Selected papers on optical fibers in medicine,* SPIE, Bellingham, Washington, 1990.

Katzir, A. (ed.), *Proc. Optical Fibers in Medicine VII,* Bellingham, Washington, SPIE, 1992.

Nonlinear Properties of Fibers

Agrawal, G. P., *Nonlinear Fiber Optics,* Academic Press, San Diego, California, 1989.

Agrawal, G. P., "*Nonlinear Interactions in Optical Fibers,*" in *Contemporary Nonlinear Optics,* Academic Press, San Diego, California, 1992.

Hasegawa, A., *Solitons in Optical Fibers,* Springer-Verlag, Berlin, 1989.

CHAPTER 2

OPTICAL FIBER COMMUNICATION TECHNOLOGY AND SYSTEM OVERVIEW

Ira Jacobs
Fiber and Electro-Optics Research Center
Virginia Polytechnic Institute and State University
Blacksburg, Virginia

2.1 INTRODUCTION

Basic elements of an optical fiber communication system include the transmitter [laser or light-emitting diode (LED)], fiber (multimode, single-mode, or dispersion-shifted), and the receiver [positive-intrinsic-negative (PIN) diode and avalanche photodetector (APD) detectors, coherent detectors, optical preamplifiers, receiver electronics]. Receiver sensitivities of digital systems are compared on the basis of the number of photons per bit required to achieve a given bit error probability, and eye degradation and error floor phenomena are described. Laser relative intensity noise and nonlinearities are shown to limit the performance of analog systems. Networking applications of optical amplifiers and wavelength-division multiplexing are considered, and future directions are discussed.

Although the light-guiding property of optical fibers has been known and used for many years, it is only relatively recently that optical fiber communications has become both a possibility and a reality.[1] Following the first prediction in 1966[2] that fibers might have sufficiently low attenuation for telecommunications, the first low-loss fiber (20 dB/km) was achieved in 1970.[3] The first semiconductor laser diode to radiate continuously at room temperature was also achieved in 1970.[4] The 1970s were a period of intense technology and system development, with the first systems coming into service at the end of the decade. The 1980s saw both the growth of applications (service on the first transatlantic cable in 1988) and continued advances in technology. This evolution continued in the 1990s with the advent of optical amplifiers and with the applications emphasis turning from point-to-point links to optical networks.

This chapter provides an overview of the basic technology, systems, and applications of optical fiber communication. It is an update and compression of material presented at a 1994 North Atlantic Treaty Organization (NATO) Summer School.[5]

Copyright 2001 by The McGraw-Hill Companies, Inc. Click Here for Terms of Use.

2.2 BASIC TECHNOLOGY

This section considers the basic technology components of an optical fiber communications link, namely the fiber, the transmitter, and the receiver, and discusses the principal parameters that determine communications performance.

Fiber

An optical fiber is a thin filament of glass with a central core having a slightly higher index of refraction than the surrounding cladding. From a physical optics standpoint, light is guided by total internal reflection at the core-cladding boundary. More precisely, the fiber is a dielectric waveguide in which there are a discrete number of propagating modes.[6] If the core diameter and the index difference are sufficiently small, only a single mode will propagate. The condition for single-mode propagation is that the normalized frequency V be less than 2.405, where

$$V = \frac{2\pi a}{\lambda}\sqrt{n_1^2 - n_2^2} \tag{1}$$

and a is the core radius, λ is the free space wavelength, and n_1 and n_2 are the indexes of refraction of the core and cladding, respectively. Multimode fibers typically have a fractional index difference (Δ) between core and cladding of between 1 and 1.5 percent and a core diameter of between 50 and 100 μm. Single-mode fibers typically have $\Delta \approx 0.3\%$ and a core diameter of between 8 and 10 μm.

The fiber numerical aperture (NA), which is the sine of the half-angle of the cone of acceptance, is given by

$$\text{NA} = \sqrt{n_1^2 - n_2^2} = n_1\sqrt{2\Delta} \tag{2}$$

Single-mode fibers typically have an NA of about 0.1, whereas the NA of multimode fibers is in the range of 0.2 to 0.3.

From a transmission system standpoint, the two most important fiber parameters are attenuation and bandwidth.

Attenuation. There are three principal attenuation mechanisms in fiber: absorption, scattering, and radiative loss. Silicon dioxide has resonance absorption peaks in the ultraviolet (electronic transitions) and in the infrared beyond 1.6 μm (atomic vibrational transitions), but is highly transparent in the visible and near-infrared.

Radiative losses are generally kept small by using a sufficiently thick cladding (communication fibers have an outer diameter of 125 μm), a compressible coating to buffer the fiber from external forces, and a cable structure that prevents sharp bends.

In the absence of impurities and radiation losses, the fundamental attenuation mechanism is Rayleigh scattering from the irregular glass structure, which results in index of refraction fluctuations over distances that are small compared to the wavelength. This leads to a scattering loss

$$\alpha = \frac{B}{\lambda^4}, \text{ with } B \approx 0.9\,\frac{dB}{\text{km}}\mu\text{m}^4 \tag{3}$$

for "best" fibers. Attenuation as a function of wavelength is shown in Fig. 1. The attenuation peak at $\lambda = 1.4$ μm is a resonance absorption due to small amounts of water in the fiber, although fibers now may be made in which this peak is absent. Initial systems operated at a wavelength around 0.85 μm owing to the availability of sources and detectors at this wave-

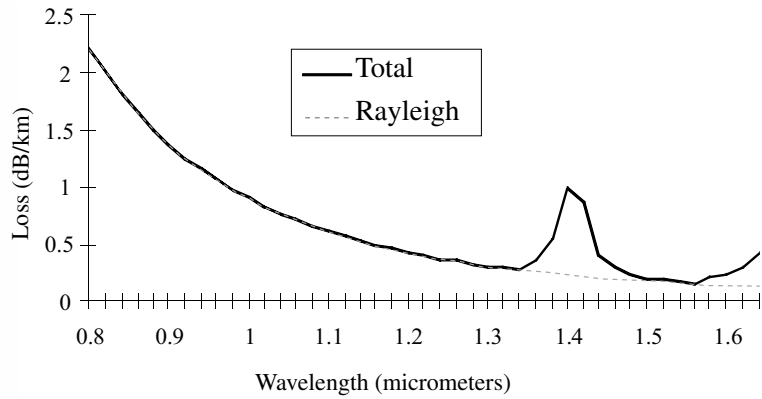

FIGURE 1 Fiber attenuation as a function of wavelength. Dashed curve shows Rayleigh scattering. Solid curve indicates total attenuation including resonance absorption at 1.38 μm from water and tail of infrared atomic resonances above 1.6 μm.

length. Present systems (other than some short-distance data links) generally operate at wavelengths of 1.3 or 1.55 μm. The former, in addition to being low in attenuation (about 0.32 dB/km for best fibers), is the wavelength of minimum intramodal dispersion (see the next section) for standard single-mode fiber. Operation at 1.55 μm allows even lower attenuation (minimum is about 0.16 dB/km) and the use of erbium-doped-fiber amplifiers (see Sec. 2.5), which operate at this wavelength.

Dispersion. Pulse spreading (dispersion) limits the maximum modulation bandwidth (or maximum pulse rate) that may be used with fibers. There are two principal forms of dispersion: intermodal dispersion and intramodal dispersion. In multimode fiber, the different modes experience different propagation delays resulting in pulse spreading. For graded-index fiber, the lowest dispersion per unit length is given approximately by[7]

$$\frac{\delta\tau}{L} = \frac{n_1\Delta^2}{10c} \text{ (intermodal)} \tag{4}$$

[Grading of the index of refraction of the core in a nearly parabolic function results in an approximate equalization of the propagation delays. For a step-index fiber, the dispersion per unit length is $\delta\tau/L = n_1\Delta/c$, which for Δ=0.01 is 1000 times larger than that given by Eq. (4).]

Bandwidth is inversely proportional to dispersion, with the proportionality constant dependent on pulse shape and how bandwidth is defined. If the dispersed pulse is approximated by a Gaussian pulse with $\delta\tau$ being the full width at the half-power point, then the –3-dB bandwidth B is given by

$$B = 0.44/\delta\tau \tag{5}$$

Multimode fibers are generally specified by their bandwidth in a 1-km length. Typical specifications are in the range from 200 MHz to 1 GHz. Fiber bandwidth is a sensitive function of the index profile and is wavelength dependent, and the scaling with length depends on whether there is mode mixing.[8] Also, for short-distance links, the bandwidth is dependent on

the launch conditions. Multimode fibers are generally used only when the bit rates and distances are sufficiently small that accurate characterization of dispersion is not of concern, although this may be changing with the advent of graded-index plastic optical fiber for high-bit-rate short-distance data links.

Although there is no intermodal dispersion in single-mode fibers,* there is still dispersion within the single mode (intramodal dispersion) resulting from the finite spectral width of the source and the dependence of group velocity on wavelength. The intramodal dispersion per unit length is given by

$$\begin{aligned} \delta\tau/L &= D\,\delta\lambda && \text{for } D \neq 0 \\ &= 0.2S_o\,(\delta\lambda)^2 && \text{for } D = 0 \end{aligned} \tag{6}$$

where D is the dispersion coefficient of the fiber, $\delta\lambda$ is the spectral width of the source, and S_o is the dispersion slope

$$S_o = \frac{dD}{d\lambda} \text{ at } \lambda = \lambda_0, \text{ where } D(\lambda_0) = 0 \tag{7}$$

If both intermodal and intramodal dispersion are present, the square of the total dispersion is the sum of the squares of the intermodal and intramodal dispersions. For typical digital systems, the total dispersion should be less than half the interpulse period T. From Eq. (5) this corresponds to an effective fiber bandwidth that is at least $0.88/T$.

There are two sources of intramodal dispersion: material dispersion, which is a consequence of the index of refraction being a function of wavelength, and waveguide dispersion, which is a consequence of the propagation constant of the fiber waveguide being a function of wavelength.

For a material with index of refraction $n(\lambda)$, the material dispersion coefficient is given by

$$D_{\text{mat}} = -\frac{\lambda}{c}\frac{d^2n}{d\lambda^2} \tag{8}$$

For silica-based glasses, D_{mat} has the general characteristics shown in Fig. 2. It is about –100 ps/km·nm at a wavelength of 820 nm, goes through zero at a wavelength near 1300 nm, and is about 20 ps/km·nm at 1550 nm.

For step-index single-mode fibers, waveguide dispersion is given approximately by[10]

$$D_{\text{wg}} \approx -\frac{0.025\lambda}{a^2 c n_2} \tag{9}$$

For conventional single-mode fiber, waveguide dispersion is small (about –5 ps/km·nm at 1300 nm). The resultant $D(\lambda)$ is then slightly shifted (relative to the material dispersion curve) to longer wavelengths, but the zero-dispersion wavelength (λ_0) remains in the vicinity of 1300 nm. However, if the waveguide dispersion is made larger negative by decreasing a or equivalently by tapering the index of refraction in the core the zero-dispersion wavelength may be shifted to the vicinity of 1550 nm (see Fig. 2). Such fibers are called *dispersion-shifted fibers* and are advantageous because of the lower fiber attenuation at this wavelength and the advent of erbium-doped-fiber amplifiers (see Sec. 8.5). Note that dispersion-shifted fibers have a smaller slope at the dispersion minimum ($S_0 \approx 0.06$ ps/km·nm^2 compared to $S_0 \approx 0.09$ ps/km·nm^2 for conventional single-mode fiber).

* A single-mode fiber actually has two degenerate modes corresponding to the two principal polarizations. Any asymmetry in the transmission path removes this degeneracy and results in polarization dispersion. This is typically very small (in the range of 0.1 to 1 ps/km$^{1/2}$), but is of concern in long-distance systems using linear repeaters.[9]

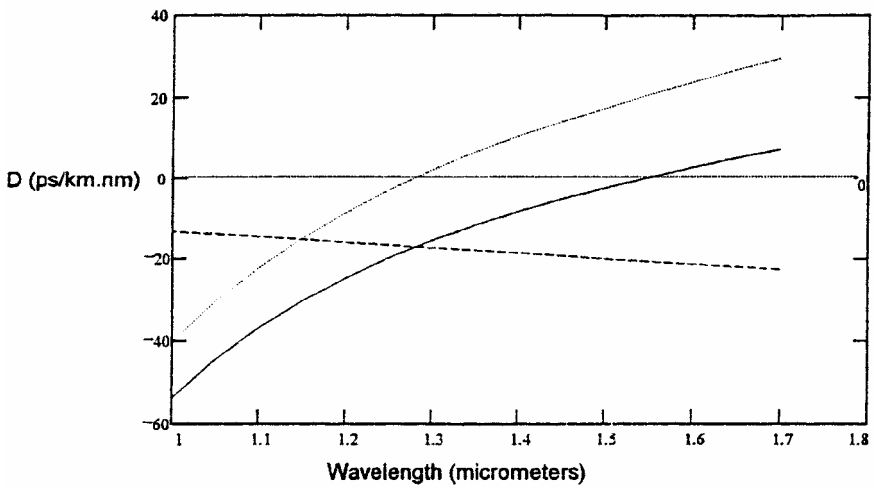

FIGURE 2 Intramodal dispersion coefficient as a function of wavelength. Dotted curve shows D_{mat}; dashed curve shows D_{wg} to achieve D (solid curve) with dispersion 0 at 1.55 μm.

With more complicated index of refraction profiles, it is possible, at least theoretically, to control the shape of the waveguide dispersion such that the total dispersion is small in both the 1300- and 1550-nm bands, leading to dispersion-flattened fibers.[11]

Transmitting Sources

Semiconductor light-emitting diodes (LEDs) or lasers are the primary light sources used in fiber-optic transmission systems. The principal parameters of concern are the power coupled into the fiber, the modulation bandwidth, and (because of intramodal dispersion) the spectral width.

Light-Emitting Diodes (LEDs). LEDs are forward-biased positive-negative (PN) junctions in which carrier recombination results in spontaneous emission at a wavelength corresponding to the energy gap. Although several milliwatts may be radiated from high-radiance LEDs, the radiation is over a wide angular range, and consequently there is a large coupling loss from an LED to a fiber. Coupling efficiency (η = ratio of power coupled to power radiated) from an LED to a fiber is given approximately by[12]

$$\eta \approx (\text{NA})^2 \text{ for } r_s < a$$

$$\eta \approx (a/r_s)^2 (\text{NA})^2 \text{ for } r_s > a \tag{10}$$

where r_s is the radius of the LED. Use of large-diameter, high-NA multimode fiber improves the coupling from LEDs to fiber. Typical coupling losses are 10 to 20 dB for multimode fibers and more than 30 dB for single-mode fibers.

In addition to radiating over a large angle, LED radiation has a large spectral width (about 50 nm at λ = 850 nm and 100 nm at λ = 1300 nm) determined by thermal effects. Systems employing LEDs at 850 nm tend to be intramodal-dispersion-limited, whereas those at 1300 nm are intermodal-dispersion-limited.

Owing to the relatively long time constant for spontaneous emission (typically several nanoseconds), the modulation bandwidths of LEDs are generally limited to several hundred MHz. Thus, LEDs are generally limited to relatively short-distance, low-bit-rate applications.

Lasers. In a laser, population inversion between the ground and excited states results in stimulated emission. In edge-emitting semiconductor lasers, this radiation is guided within the active region of the laser and is reflected at the end faces.* The combination of feedback and gain results in oscillation when the gain exceeds a threshold value. The spectral range over which the gain exceeds threshold (typically a few nanometers) is much narrower than the spectral width of an LED. Discrete wavelengths within this range, for which the optical length of the laser is an integer number of half-wavelengths, are radiated. Such a laser is termed a *multilongitudinal mode Fabry-Perot laser.* Radiation is confined to a much narrower angular range than for an LED, and consequently may be efficiently coupled into a small-NA fiber. Coupled power is typically about 1 mW.

The modulation bandwidth of lasers is determined by a resonance frequency caused by the interaction of the photon and electron concentrations.[14] Although this resonance frequency was less than 1 GHz in early semiconductor lasers, improvements in materials have led to semiconductor lasers with resonance frequencies (and consequently modulation bandwidths) in excess of 10 GHz. This not only is important for very high-speed digital systems, but now also allows semiconductor lasers to be directly modulated with microwave signals. Such applications are considered in Sec. 2.7.

Although multilongitudinal-mode Fabry-Perot lasers have a narrower spectral spread than LEDs, this spread still limits the high-speed and long-distance capability of such lasers. For such applications, single-longitudinal-mode (SLM) lasers are used. SLM lasers may be achieved by having a sufficiently short laser (less than 50 μm), by using coupled cavities (either external mirrors or cleaved coupled cavities[15]), or by incorporating a diffraction grating within the laser structure to select a specific wavelength. The latter has proven to be most practical for commercial application, and includes the distributed feedback (DFB) laser, in which the grating is within the laser active region, and the distributed Bragg reflector (DBR) laser, where the grating is external to the active region.[16]

There is still a finite line width for SLM lasers. For lasers without special stabilization, the line width is on the order of 0.1 nm. Expressed in terms of frequency, this corresponds to a frequency width of 12.5 GHz at a wavelength of 1550 nm. (Wavelength and frequency spread are related by $\delta f/f = -\delta\lambda/\lambda$, from which it follows that $\delta f = -c\delta\lambda/\lambda^2$.) Thus, unlike electrical communication systems, optical systems generally use sources with spectral widths that are large compared to the modulation bandwidth.

The finite line width (phase noise) of a laser is due to fluctuations of the phase of the optical field resulting from spontaneous emission. In addition to the phase noise contributed directly by the spontaneous emission, the interaction between the photon and electron concentrations in semiconductor lasers leads to a conversion of amplitude fluctuations to phase fluctuations, which increases the line width.[17] If the intensity of a laser is changed, this same phenomenon gives rise to a change in the frequency of the laser (*chirp*). Uncontrolled, this causes a substantial increase in line width when the laser is modulated, which may cause difficulties in some system applications, possibly necessitating external modulation. However, the phenomenon can also be used to advantage. For appropriate lasers under small signal modulation, a change in frequency proportional to the input signal can be used to frequency-modulate and/or to tune the laser. Tunable lasers are of particular importance in networking applications employing wavelength-division multiplexing (WDM).

* In vertical cavity surface-emitting lasers (VCSELs), reflection is from internal "mirrors" grown within the semiconductor structure.[13]

Photodetectors

Fiber-optic systems generally use PIN or APD photodetectors. In a reverse-biased PIN diode, absorption of light in the intrinsic region generates carriers that are swept out by the reverse-bias field. This results in a photocurrent (I_p) that is proportional to the incident optical power (P_R), where the proportionality constant is the responsivity ($\Re$) of the photodetector; that is, $\Re = I_P/P_R$. Since the number of photons per second incident on the detector is power divided by the photon energy, and the number of electrons per second flowing in the external circuit is the photocurrent divided by the charge of the electron, it follows that the quantum efficiency (η = electrons/photons) is related to the responsivity by

$$\eta = \frac{hc}{q\lambda}\frac{I_p}{P_R} = \frac{1.24\ (\mu\text{m}\cdot V)}{\lambda}\Re \tag{11}$$

For wavelengths shorter than 900 nm, silicon is an excellent photodetector, with quantum efficiencies of about 90 percent. For longer wavelengths, InGaAs is generally used, with quantum efficiencies typically around 70 percent. Very high bandwidths may be achieved with PIN photodetectors. Consequently, the photodetector does not generally limit the overall system bandwidth.

In an avalanche photodetector (APD), a larger reverse voltage accelerates carriers, causing additional carriers by impact ionization resulting in a current $I_{\text{APD}} = MI_p$, where M is the current gain of the APD. As noted in Sec. 2.3, this can result in an improvement in receiver sensitivity.

2.3 RECEIVER SENSITIVITY

The receiver in a direct-detection fiber-optic communication system consists of a photodetector followed by electrical amplification and signal-processing circuits intended to recover the communications signal. Receiver sensitivity is defined as the average received optical power needed to achieve a given communication rate and performance. For analog communications, the communication rate is measured by the bandwidth of the electrical signal to be transmitted (B), and performance is given by the signal-to-noise ratio (SNR) of the recovered signal. For digital systems, the communication rate is measured by the bit rate (R_b) and performance is measured by the bit error probability (P_e).

For a constant optical power transmitted, there are fluctuations of the received photocurrent about the average given by Eq. (11). The principal sources of these fluctuations are signal shot noise (quantum noise resulting from random arrival times of photons at the detector), receiver thermal noise, APD excess noise, and relative intensity noise (RIN) associated with fluctuations in intensity of the source and/or multiple reflections in the fiber medium.

Digital On-Off-Keying Receiver

It is instructive to define a normalized sensitivity as the average number of photons per bit ($\overline{N}_p$) to achieve a given error probability, which we take here to be $P_e = 10^{-9}$. Given $\overline{N}_p$, the received power when a 1 is transmitted is obtained from

$$P_R = 2\overline{N}_p R_b \frac{hc}{\lambda} \tag{12}$$

where the factor of 2 in Eq. (12) is because P_R is the peak power, and $\overline{N}_p$ is the average number of photons per bit.

Ideal Receiver. In an ideal receiver individual photons may be counted, and the only source of noise is the fluctuation of the number of photons counted when a 1 is transmitted. This is a Poisson random variable with mean $2\overline{N}_p$. No photons are received when a 0 is transmitted. Consequently, an error is made only when a 1 is transmitted and no photons are received. This leads to the following expression for the error probability

$$P_e = \tfrac{1}{2} \exp(-2\overline{N}_p) \tag{13}$$

from which it follows that $\overline{N}_p = 10$ for $P_e = 10^{-9}$. This is termed the *quantum limit.*

PIN Receiver. In a PIN receiver, the photodetector output is amplified, filtered, and sampled, and the sample is compared with a threshold to decide whether a 1 or 0 was transmitted. Let I be the sampled current at the input to the decision circuit scaled back to the corresponding value at the output of the photodetector. (It is convenient to refer all signal and noise levels to their equivalent values at the output of the photodetector.) I is then a random variable with means and variances given by

$$\mu_1 = I_p \qquad \mu_0 = 0 \tag{14a}$$

$$\sigma_1^2 = 2qI_pB + \frac{4kTB}{R_e} \qquad \sigma_0^2 = \frac{4kTB}{R_e} \tag{14b}$$

where the subscripts 1 and 0 refer to the bit transmitted, kT is the thermal noise energy, and R_e is the effective input noise resistance of the amplifier. Note that the noise values in the 1 and 0 states are different owing to the shot noise in the 1 state.

Calculation of error probability requires knowledge of the distribution of I under the two hypotheses. Under the assumption that these distributions may be approximated by gaussian distributions with means and variances given by Eq. (14), the error probability may be shown to be given by (Chap. 4 in Ref. 18)

$$P_e = K\left(\frac{\mu_1 - \mu_0}{\sigma_1 + \sigma_0}\right) \tag{15}$$

where

$$K(Q) = \frac{1}{\sqrt{2\pi}} \int_Q^\infty dx \exp(-x^2/2) = \frac{1}{2}\operatorname{erfc}(Q/\sqrt{2}) \tag{16}$$

It can be shown from Eqs. (11), (12), (14), and (15) that

$$\overline{N}_p = \frac{B}{\eta R_b} Q^2\left[1 + \frac{1}{Q}\sqrt{\frac{8\pi kTC_e}{q^2}}\right] \tag{17}$$

where

$$C_e = \frac{1}{2\pi R_e B} \tag{18}$$

is the effective noise capacitance of the receiver, and from Eq. (16), $Q = 6$ for $P_e = 10^{-9}$. The minimum bandwidth of the receiver is half the bit rate, but in practice B/R_b is generally about 0.7.

The gaussian approximation is expected to be good when the thermal noise is large compared to the shot noise. It is interesting, however, to note that Eq. (17) gives $\overline{N}_p = 18$ when $C_e = 0$, $B/R_b = 0.5$, $\eta = 1$, and $Q = 6$. Thus, even in the shot noise limit, the gaussian approximation gives a surprisingly close result to the value calculated from the correct Poisson distri-

bution. It must be pointed out, however, that the location of the threshold calculated by the gaussian approximation is far from correct in this case. In general, the gaussian approximation is much better in estimating receiver sensitivity than in establishing where to set receiver thresholds.

Low-input-impedance amplifiers are generally required to achieve the high bandwidths required for high-bit-rate systems. However, a low input impedance results in high thermal noise and poor sensitivity. High-input-impedance amplifiers may be used, but this narrows the bandwidth, which must be compensated for by equalization following the first-stage amplifier. Although this may result in a highly sensitive receiver, the receiver will have a poor dynamic range owing to the high gains required in the equalizer.[19] Receivers for digital systems are generally implemented with transimpedance amplifiers having a large feedback resistance. This reduces the effective input noise capacitance to below the capacitance of the photodiode, and practical receivers can be built with $C_e \approx 0.1$ pF. Using this value of capacitance and $B/R_b = 0.7$, $\eta = 0.7$, and $Q = 6$, Eq. (17) gives $\overline{N}_p \approx 2600$. Note that this is about 34 dB greater than the value given by the quantum limit.

APD Receiver. In an APD receiver, there is additional shot noise owing to the excess noise factor F of the avalanche gain process. However, thermal noise is reduced because of the current multiplication gain M before thermal noise is introduced. This results in a receiver sensitivity given approximately by*

$$\overline{N}_p = \frac{B}{\eta R_b} Q^2 \left[F + \frac{1}{Q} \sqrt{\frac{8\pi k T C_e}{q^2 M^2}} \right] \tag{19}$$

The excess noise factor is an increasing function of M, which results in an optimum M to minimize $\overline{N}_p$.[19] Good APD receivers at 1300 and 1550 nm typically have sensitivities of the order of 1000 photons per bit. Owing to the lower excess noise of silicon APDs, sensitivity of about 500 photons per bit can be achieved at 850 nm.

Impairments. There are several sources of impairment that may degrade the sensitivity of receivers from the values given by Eqs. (17) and (19). These may be grouped into two general classes: eye degradations and signal-dependent noise.

An eye diagram is the superposition of all possible received sequences. At the sampling point, there is a spread of the values of a received 1 and a received 0. The difference between the minimum value of a received 1 and the maximum value of the received 0 is known as the *eye opening.* This is given by $(1 - \varepsilon)I_p$ where ε is the eye degradation. The two major sources of eye degradation are intersymbol interference and finite laser extinction ratio. Intersymbol interference results from dispersion, deviations from ideal shaping of the receiver filter, and low-frequency cutoff effects that result in direct current (DC) offsets.

Signal-dependent noises are phenomena that give a variance of the received photocurrent that is proportional to I_p^2 and consequently lead to a maximum signal-to-noise ratio at the output of the receiver. Principal sources of signal-dependent noise are laser relative intensity noise (RIN), reflection-induced noise, mode partition noise, and modal noise. RIN is a consequence of inherent fluctuations in laser intensity resulting from spontaneous emission (Ref. 17; Chap. 4 in Ref. 18). This is generally sufficiently small that it is not of concern in digital systems, but is an important limitation in analog systems requiring high signal-to-noise ratios (see Sec. 2.7). Reflection-induced noise is the conversion of laser phase noise to intensity noise by multiple reflections from discontinuities (such as at imperfect connectors.) This may result in a substantial RIN enhancement that can seriously affect digital as well as analog systems.[20] Mode partition noise occurs when Fabry-Perot lasers are used with dispersive fiber.

* The gaussian approximation is not as good for an APD as for a PIN receiver owing to the nongaussian nature of the excess APD noise.

Fiber dispersion results in changing phase relation between the various laser modes, which results in intensity fluctuations. The effect of mode partition noise is more serious than that of dispersion alone.[21] Modal noise is a similar phenomenon that occurs in multimode fiber when relatively few modes are excited and these interfere.

Eye degradations are accounted for by replacing Eq. (14*a*) by

$$\mu_1 - \mu_0 = (1 - \varepsilon)I_p \tag{20a}$$

and signal-dependent noise by replacing Eq. (14*b*) by

$$\sigma_1^2 = 2qI_pB + \frac{4kTB}{R_e} + \alpha^2 I_p^2 B \qquad \sigma_0^2 = \frac{4kTB}{R_e} + \alpha^2 I_p^2 B \tag{20b}$$

and α^2 is the relative spectral density of the signal-dependent noise. (It is assumed that the signal-dependent noise has a large bandwidth compared to the signal bandwidth *B*.) With these modifications, the sensitivity of an APD receiver becomes

$$\overline{N}_p = \frac{\dfrac{B}{\eta R_b}\left(\dfrac{Q}{1-\varepsilon}\right)^2\left[F + \left(\dfrac{1-\varepsilon}{Q}\right)\sqrt{\dfrac{8\pi kTC_e}{q^2M^2}}\right]}{1 - \alpha^2 B\left(\dfrac{Q}{1-\varepsilon}\right)^2} \tag{21}$$

where the PIN expression is obtained by setting F = 1 and M = 1. It follows from Eq. (21) that there is a minimum error probability (*error floor*) given by

$$P_{e,\min} = K(Q_{\max}) \text{ where } Q_{\max} = \frac{1-\varepsilon}{\alpha\sqrt{B}} \tag{22}$$

The existence of eye degradations and signal-dependent noise causes an increase in the receiver power (called *power penalty*) required to achieve a given error probability.

2.4 BIT RATE AND DISTANCE LIMITS

Bit rate and distance limitations of digital links are determined by loss and dispersion limitations. The following example is used to illustrate the calculation of the maximum distance for a given bit rate. Consider a 2.5-Gbit/s system at a wavelength of 1550 nm. Assume an average transmitter power of 0 dBm coupled into the fiber. Receiver sensitivity is taken to be 3000 photons per bit, which from Eq. (12) corresponds to an average receiver power of –30.2 dBm. Allowing a total of 8 dB for margin and for connector and cabling losses at the two ends gives a loss allowance of 22.2 dB. If the cabled fiber loss, including splices, is 0.25 dB/km, this leads to a loss-limited transmission distance of 89 km.

Assuming that the fiber dispersion is $D = 15$ ps/km·nm and source spectral width is 0.1 nm, this gives a dispersion per unit length of 1.5 ps/km. Taking the maximum allowed dispersion to be half the interpulse period, this gives a maximum dispersion of 200 ps, which then yields a maximum dispersion-limited distance of 133 km. Thus, the loss-limited distance is controlling.

Consider what happens if the bit rate is increased to 10 Gbit/s. For the same number of photons per bit at the receiver, the receiver power must be 6 dB greater than that in the preceding example. This reduces the loss allowance by 6 dB, corresponding to a reduction of 24 km in the loss-limited distance. The loss-limited distance is now 65 km (assuming all other parameters are unchanged). However, dispersion-limited distance scales inversely with bit rate, and is now 22 km. The system is now dispersion-limited. Dispersion-shifted fiber would be required to be able to operate at the loss limit.

Increasing Bit Rate

There are two general approaches for increasing the bit rate transmitted on a fiber: time-division multiplexing (TDM), in which the serial transmission rate is increased, and wavelength-division multiplexing (WDM), in which separate wavelengths are used to transmit independent serial bit streams in parallel. TDM has the advantage of minimizing the quantity of active devices but requires higher-speed electronics as the bit rate is increased. Also, as indicated by the preceding example, dispersion limitations will be more severe.

WDM allows use of existing lower-speed electronics, but requires multiple lasers and detectors as well as optical filters for combining and separating the wavelengths. Technology advances, including tunable lasers, transmitter and detector arrays, high-resolution optical filters, and optical amplifiers (Sec. 2.5) are making WDM more attractive, particularly for networking applications (Sec. 2.6).

Longer Repeater Spacing

In principal, there are three approaches for achieving longer repeater spacing than that calculated in the preceding text: lower fiber loss, higher transmitter powers, and improved receiver sensitivity (smaller $\overline{N}_p$). Silica-based fiber is already essentially at the theoretical Rayleigh scattering loss limit. There has been research on new fiber materials that would allow operation at wavelengths longer than 1.6 μm, with consequent lower theoretical loss values.[22] There are many reasons, however, why achieving such losses will be difficult, and progress in this area has been slow.

Higher transmitter powers are possible, but there are both nonlinearity and reliability issues that limit transmitter power. Since present receivers are more than 30 dB above the quantum limit, improved receiver sensitivity would appear to offer the greatest possibility. To improve the receiver sensitivity, it is necessary to increase the photocurrent at the output of the detector without introducing significant excess loss. There are two main approaches for doing so: optical amplification and optical mixing. Optical preamplifiers result in a theoretical sensitivity of 38 photons per bit[23] (6dB above the quantum limit), and experimental systems have been constructed with sensitivities of about 100 photons per bit.[24] This will be discussed further in Sec. 2.5. Optical mixing (coherent receivers) will be discussed briefly in the following text.

Coherent Systems. A photodetector provides an output current proportional to the magnitude square of the electric field that is incident on the detector. If a strong optical signal (*local oscillator*) coherent in phase with the incoming optical signal is added prior to the photodetector, then the photocurrent will contain a component at the difference frequency between the incoming and local oscillator signals. The magnitude of this photocurrent, relative to the direct detection case, is increased by the ratio of the local oscillator to the incoming field strengths. Such a coherent receiver offers considerable improvement in receiver sensitivity. With on-off keying, a heterodyne receiver (signal and local oscillator frequencies different) has a theoretical sensitivity of 36 photons per bit, and a homodyne receiver (signal and local oscillator frequencies the same) has a sensitivity of 18 photons per bit. Phase-shift keying (possible with coherent systems) provides a further 3-dB improvement. Coherent systems, however, require very stable signal and local oscillator sources (spectral linewidths need to be small compared to the modulation bandwidth) and matching of the polarization of the signal and local oscillator fields.[25]

An advantage of coherent systems, more so than improved receiver sensitivity, is that because the output of the photodetector is linear in the signal field, filtering for WDM demultiplexing may be done at the difference frequency (typically in the microwave range). This allows considerably greater selectivity than is obtainable with optical filtering techniques. The advent of optical amplifiers has slowed the interest in coherent systems.

2.5 OPTICAL AMPLIFIERS

There are two types of optical amplifiers: laser amplifiers based on stimulated emission and parametric amplifiers based on nonlinear effects (Chap. 8 in Ref. 18). The former are currently of most interest in fiber-optic communications. A laser without reflecting end faces is an amplifier, but it is more difficult to obtain sufficient gain for amplification than it is (with feedback) to obtain oscillation. Thus, laser oscillators were available much earlier than laser amplifiers.

Laser amplifiers are now available with gains in excess of 30 dB over a spectral range of more than 30 nm. Output saturation powers in excess of 10 dBm are achievable. The amplified spontaneous emission (ASE) noise power at the output of the amplifier, in each of two orthogonal polarizations, is given by

$$P_{\text{ASE}} = n_{\text{sp}} \frac{hc}{\lambda} B_o(G-1) \tag{23}$$

where G is the amplifier gain, B_o is the bandwidth, and the spontaneous emission factor n_{sp} is equal to 1 for ideal amplifiers with complete population inversion.

Comparison of Semiconductor and Fiber Amplifiers

There are two principal types of laser amplifiers: semiconductor laser amplifiers (SLAs) and doped-fiber amplifiers. The erbium-doped-fiber amplifier (EDFA), which operates at a wavelength of 1.55 μm, is of most current interest.

The advantages of the SLA, similar to laser oscillators, are that it is pumped by a DC current, it may be designed for any wavelength of interest, and it can be integrated with electrooptic semiconductor components.

The advantages of the EDFA are that there is no coupling loss to the transmission fiber, it is polarization-insensitive, it has lower noise than SLAs, it can be operated at saturation with no intermodulation owing to the long time constant of the gain dynamics, and it can be integrated with fiber devices. However, it does require optical pumping, with the principal pump wavelengths being either 980 or 1480 nm.

Communications Application of Optical Amplifiers

There are four principal applications of optical amplifiers in communication systems:[26,27]

1. Transmitter power amplifiers
2. Compensation for splitting loss in distribution networks
3. Receiver preamplifiers
4. Linear repeaters in long-distance systems

The last application is of particular importance for long-distance networks (particularly undersea systems), where a bit-rate-independent linear repeater allows subsequent upgrading of system capacity (either TDM or WDM) with changes only at the system terminals. Although amplifier noise accumulates in such long-distance linear systems, transoceanic lengths are achievable with amplifier spacings of about 60 km corresponding to about 15-dB fiber attenuation between amplifiers.

However, in addition to the accumulation of ASE, there are other factors limiting the distance of linearly amplified systems, namely dispersion and the interaction of dispersion and nonlinearity.[28] There are two alternatives for achieving very long-distance, very high-bit-rate systems with linear repeaters: *solitons,* which are pulses that maintain their shape in a dispersive medium,[29] and dispersion compensation.[30]

2.6 FIBER-OPTIC NETWORKS

Networks are communication systems used to interconnect a number of terminals within a defined geographic area—for example, local area networks (LANs), metropolitan area networks (MANs), and wide area networks (WANs). In addition to the transmission function discussed throughout the earlier portions of this chapter, networks also deal with the routing and switching aspects of communications.

Passive optical networks utilize couplers to distribute signals to users. In an $N \times N$ ideal star coupler, the signal on each input port is uniformly distributed among all output ports. If an average power P_T is transmitted at a transmitting port, the power received at a receiving port (neglecting transmission losses) is

$$P_R = \frac{P_T}{N}(1 - \delta_N) \tag{24}$$

where δ_N is the excess loss of the coupler. If N is a power of 2, an $N \times N$ star may be implemented by $\log_2 N$ stages of 2×2 couplers. Thus, it may be conservatively assumed that

$$1 - \delta_N = (1 - \delta_2)^{\log_2 N} = N^{\log_2(1 - \delta_2)} \tag{25}$$

The maximum bit rate per user is given by the average received power divided by the product of the photon energy and the required number of photons per bit (N_p). The throughput Y is the product of the number of users and the bit rate per user, and from Eqs. (24) and (25) is therefore given by

$$\mathrm{Y} = \frac{P_T}{N_p}\frac{\lambda}{hc}N^{\log_2(1 - \delta_2)} \tag{26}$$

Thus, the throughput (based on power considerations) is independent of N for ideal couplers ($\delta_2 = 0$) and decreases slowly with N ($\sim N^{-0.17}$) for 10 log $(1 - \delta_2) = 0.5$ dB. It follows from Eq. (26) that for a power of 1 mW at $\lambda = 1.55$ μm and with $N_p = 3000$, the maximum throughput is 2.6 Tbit/s.

This may be contrasted with a tapped bus, where it may be shown that optimum tap weight to maximize throughput is given by $1/N$, leading to a throughput given by[31]

$$\mathrm{Y} = \frac{P_T}{N_p}\frac{\lambda}{hc}\frac{1}{Ne^2}\exp(-2N\delta) \tag{27}$$

Thus, even for ideal ($\delta = 0$) couplers, the throughput decreases inversely with the number of users. If there is excess coupler loss, the throughput decreases exponentially with the number of users and is considerably less than that given by Eq. (26). Consequently, for a power-limited transmission medium, the star architecture is much more suitable than the tapped bus. The same conclusion does not apply to metallic media, where bandwidth rather than power limits the maximum throughput.

Although the preceding text indicates the large throughput that may be achieved in principle with a passive star network, it doesn't indicate how this can be realized. Most interest is in WDM networks.[32] The simplest protocols are those for which fixed-wavelength receivers and tunable transmitters are used. However, the technology is simpler when fixed-wavelength transmitters and tunable receivers are used, since a tunable receiver may be implemented with a tunable optical filter preceding a wideband photodetector. Fixed-wavelength transmitters and receivers involving multiple passes through the network are also possible, but this requires utilization of terminals as relay points. Protocol, technology, and application considerations for gigabit networks (networks having access at gigabit rates and throughputs at terabit rates) is an extensive area of current research.[32,33]

2.7 ANALOG TRANSMISSION ON FIBER

Most interest in fiber-optic communications is centered around digital transmission, since fiber is generally a power-limited rather than a bandwidth-limited medium. There are applications, however, where it is desirable to transmit analog signals directly on fiber without converting them to digital signals. Examples are cable television (CATV) distribution and microwave links such as entrance links to antennas and interconnection of base stations in mobile radio systems.

Carrier-to-Noise Ratio (CNR)

Optical intensity modulation is generally the only practical modulation technique for incoherent-detection fiber-optic systems. Let $f(t)$ be the carrier signal that intensity modulates the optical source. For convenience, assume that the average value of $f(t)$ is equal to 0, and that the magnitude of $f(t)$ is normalized to be less than or equal to 1. The received optical power may then be expressed as

$$P(t) = P_o[1 + mf(t)] \tag{28}$$

where m is the optical modulation index

$$m = \frac{P_{\max} - P_{\min}}{P_{\max} + P_{\min}} \tag{29}$$

The carrier-to-noise ratio is then given by

$$\text{CNR} = \frac{\frac{1}{2}m^2\Re^2P_o^2}{\text{RIN}\,\Re^2P_o^2B + 2q\Re P_oB + \langle i_{th}^2\rangle B} \tag{30}$$

where $\Re$ is the photodetector responsivity, RIN is the relative intensity noise spectral density (denoted by α^2 in Sec. 2.3), and $\langle i_{th}^2\rangle$ is the thermal noise spectral density (expressed as $4kT/R_e$ in Sec. 2.3). CNR is plotted in Fig. 3 as a function of received optical power for a bandwidth of $B = 4$ MHz (single video channel), optical modulation index $m = 0.05$, $\Re = 0.8$ A/W, RIN = −155 dB/Hz, and $\sqrt{\langle i_{\text{th}}^2\rangle} = 7$ pA/$\sqrt{\text{Hz}}$. At low received powers (typical of digital systems) the CNR is limited by thermal noise. However, to obtain the higher CNR generally needed by analog systems, shot noise and then ultimately laser RIN become limiting.

Analog Video Transmission on Fiber[34]

It is helpful to distinguish between single-channel and multiple-channel applications. For the single-channel case, the video signal may directly modulate the laser intensity [amplitude-modulated (AM) system], or the video signal may be used to frequency-modulate an electrical subcarrier, with this subcarrier then intensity-modulating the optical source [frequency-modulated (FM) system]. Equation (30) gives the CNR of the recovered subcarrier. Subsequent demodulation of the FM signal gives an additional increase in signal-to-noise ratio. In addition to this FM improvement factor, larger optical modulation indexes may be used than in AM systems. Thus FM systems allow higher signal-to-noise ratios and longer transmission spans than AM systems.

Two approaches have been used to transmit multichannel video signals on fiber. In the first (AM systems), the video signals undergo electrical frequency-division multiplexing (FDM),

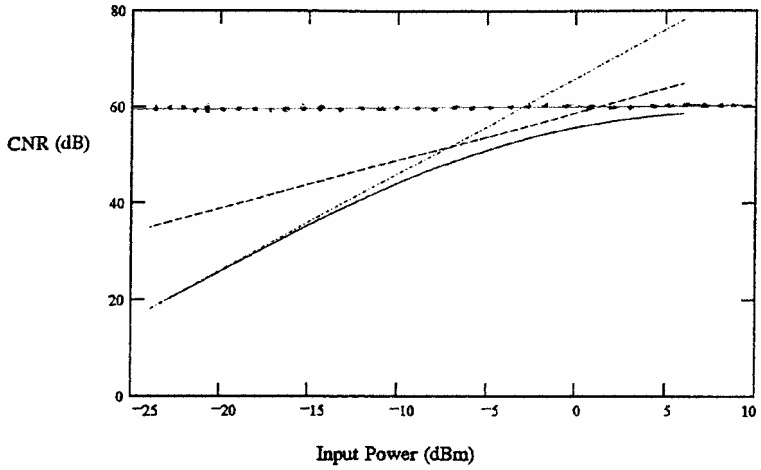

FIGURE 3 CNR as a function of input power. Straight lines indicate thermal noise (-.-.-), shot noise (–), and RIN (.....) limits.

and this combined FDM signal intensity modulates the optical source. This is conceptually the simplest system, since existing CATV multiplexing formats may be used.

In FM systems, the individual video channels frequency-modulate separate microwave carriers (as in satellite systems). These carriers are linearly combined and the combined signal intensity modulates a laser. Although FM systems are more tolerant than AM systems to intermodulation distortion and noise, the added electronics costs have made such systems less attractive than AM systems for CATV application.

Multichannel AM systems are of interest not only for CATV application but also for mobile radio applications to connect signals from a microcellular base station to a central processing station. Relative to CATV applications, the mobile radio application has the additional complication of being required to accommodate signals over a wide dynamic power range.

Nonlinear Distortion

In addition to CNR requirements, multichannel analog communication systems are subject to intermodulation distortion. If the input to the system consists of a number of tones at frequencies ω_i, then nonlinearities result in intermodulation products at frequencies given by all sums and differences of the input frequencies. Second-order intermodulation gives intermodulation products at frequencies $\omega_i \pm \omega_j$, whereas third-order intermodulation gives frequencies $\omega_i \pm \omega_j \pm \omega_k$. If the signal frequency band is such that the maximum frequency is less than twice the minimum frequency, then all second-order intermodulation products fall outside the signal band, and third-order intermodulation is the dominant nonlinearity. This condition is satisfied for the transport of microwave signals (e.g., mobile radio signals) on fiber, but is not satisfied for wideband CATV systems, where there are requirements on composite second-order (CSO) and composite triple-beat (CTB) distortion.

The principal causes of intermodulation in multichannel fiber-optic systems are laser threshold nonlinearity,[35] inherent laser gain nonlinearity, and the interaction of chirp and dispersion.

2.8 TECHNOLOGY AND APPLICATIONS DIRECTIONS

Fiber-optic communication application in the United States began with metropolitan and short-distance intercity trunking at a bit rate of 45 Mbit/s, corresponding to the DS-3 rate of the North American digital hierarchy. Technological advances, primarily higher-capacity transmission and longer repeater spacings, extended the application to long-distance intercity transmission, both terrestrial and undersea. Also, transmission formats are now based on the synchronous digital hierarchy (SDH), termed synchronous optical network (SONET) in the U.S. OC-48 systems* operating at 2.5 Gbit/s are widely deployed, with OC-192 10-Gbit/s systems also available as of 1999. All of the signal processing in these systems (multiplexing, switching, performance monitoring) is done electrically, with optics serving solely to provide point-to-point links.

For long-distance applications, dense wavelength-division multiplexing (DWDM), with channel spacings of 100 GHz and with upward of 80 wavelength channels, has extended the bit rate capability of fiber to greater than 400 Gbit/s in commercial systems and up to 3 Tbit/s in laboratory trials.[36] For local access, there is extensive interest in hybrid combinations of optical and electronic technologies and transmission media.[37,38] Owing to the criticality of communications, network survivability has achieved growing importance, with SONET rings being implemented so that no single cable cut will result in system failure.[39]

The huge bandwidth capability of fiber optics (measured in tens of terahertz) is not likely to be utilized by time-division techniques alone, and DWDM technology and systems are receiving considerable emphasis, although work is also under way on optical time-division multiplexing (OTDM) and optical code-division multiplexing (OCDM).

Nonlinear phenomena, when uncontrolled, generally lead to system impairments. However, controlled nonlinearities are the basis of devices such as parametric amplifiers and switching and logic elements. Nonlinear optics will consequently continue to receive increased emphasis.

2.9 REFERENCES

1. Jeff Hecht, *City of Light: The Story of Fiber Optics,* Oxford University Press, 1999.
2. C. K. Kao and G. A. Hockham, "Dielectric-Fiber Surface Waveguides for Optical Frequencies," *Proc. IEE* **113**:1151–1158 (July 1966).
3. F. P. Kapron et al., "Radiation Losses in Glass Optical Waveguides," *Appl. Phys. Lett.* **17**:423 (November 15, 1970).
4. I. Hayashi, M. B. Panish, and P. W. Foy, "Junction Lasers which Operate Continuously at Room Temperature," *Appl. Phys. Lett.* **17**:109 (1970).
5. Ira Jacobs, "Optical Fiber Communication Technology and System Overview," in O. D. D. Soares (ed.), *Trends in Optical Fibre Metrology and Standards,* NATO ASI Series, vol. 285, pp. 567–591, Kluwer Academic Publishers, 1995.
6. D. Gloge, "Weakly Guiding Fibers," *Appl. Opt.* **10**:2252–2258 (October 1971).
7. R. Olshansky and D. Keck, "Pulse Broadening in Graded Index Fibers," *Appl. Opt.* **15**:483–491 (February 1976).
8. D. Gloge, E. A. J. Marcatili, D. Marcuse, and S. D. Personick, "Dispersion Properties of Fibers," in S. E. Miller and A. G. Chynoweth (eds.), *Optical Fiber Telecommunications,* chap. 4, Academic Press, 1979.
9. Y. Namihira and H. Wakabayashi, "Fiber Length Dependence of Polarization Mode Dispersion Measurements in Long-Length Optical Fibers and Installed Optical Submarine Cables," *J. Opt. Commun.* **2**:2 (1991).
10. W. B. Jones Jr., *Introduction to Optical Fiber Communication Systems,* pp. 90–92, Holt, Rinehart and Winston, 1988.

* OC-*n* systems indicate optical channel at a bit rate of (51.84)*n* Mbit/s.

11. L. G. Cohen, W. L. Mammel, and S. J. Jang, "Low-Loss Quadruple-Clad Single-Mode Lightguides with Dispersion Below 2 ps/km·nm over the 1.28 μm–1.65 μm Wavelength Range," *Electron. Lett.* **18**:1023–1024 (1982).
12. G. Keiser, *Optical Fiber Communications,* 3d ed., chap. 5, McGraw-Hill, 2000.
13. N. M. Margalit, S. Z. Zhang, and J. E. Bowers, "Vertical Cavity Lasers for Telecom Applications," *IEEE Commun. Mag.* **35**:164–170 (May 1997).
14. J. E. Bowers and M. A. Pollack, "Semiconductor Lasers for Telecommunications," in S. E. Miller and I. P. Kaminow (eds.), *Optical Fiber Telecommunications II,* chap. 13, Academic Press, 1988.
15. W. T. Tsang, "The Cleaved-Coupled-Cavity (C^3) Laser," in *Semiconductors and Semimetals,* vol. 22, part B, chap. 5, pp. 257–373, 1985.
16. K. Kobayashi and I. Mito, "Single Frequency and Tunable Laser Diodes," *J. Lightwave Technol.* **6**:1623–1633 (November 1988).
17. T. Mukai and Y. Yamamoto, "AM Quantum Noise in 1.3 μm InGaAsP Lasers," *Electron. Lett.* **20**:29–30 (January 5, 1984).
18. G. P. Agrawal, *Fiber-Optic Communication Systems,* 2d ed., Wiley Interscience, 1997.
19. S. D. Personick, "Receiver Design for Digital Fiber Optic Communication Systems I," *Bell Syst. Tech. J.* **52**: 843–874 (July–August 1973).
20. J. L. Gimlett and N. K. Cheung, "Effects of Phase-to-Intensity Noise Conversion by Multiple Reflections on Gigabit-per-Second DFB Laser Transmission Systems," *J. Lightwave Technol.* **LT-7**:888–895 (June 1989).
21. K. Ogawa, "Analysis of Mode Partition Noise in Laser Transmission Systems," *IEEE J. Quantum Electron.* **QE-18**:849–855 (May 1982).
22. D. C. Tran, G. H. Sigel, and B. Bendow, "Heavy Metal Fluoride Fibers: A Review," *J. Lightwave Technol.* **LT-2**:566–586 (October 1984).
23. P. S. Henry, "Error-Rate Performance of Optical Amplifiers," *Optical Fiber Communications Conference (OFC'89 Technical Digest*), THK3, Houston, Texas, February 9, 1989.
24. O. Gautheron, G. Grandpierre, L. Pierre, J.-P. Thiery, and P. Kretzmeyer, "252 km Repeaterless 10 Gbits/s Transmission Demonstration," *Optical Fiber Communications Conference (OFC'93) Postdeadline Papers,* PD11, San Jose, California, February 21–26, 1993.
25. I. W. Stanley, "A Tutorial Review of Techniques for Coherent Optical Fiber Transmission Systems," *IEEE Commun. Mag.* **23**:37–53 (August 1985).
26. Bellcore, "Generic Requirements for Optical Fiber Amplifier Performance," Technical Advisory TA-NWT-001312, Issue 1, December 1992.
27. T. Li, "The Impact of Optical Amplifiers on Long-Distance Lightwave Telecommunications," *Proc. IEEE* **81**:1568–1579 (November 1993).
28. A. Naka and S. Saito, "In-Line Amplifier Transmission Distance Determined by Self-Phase Modulation and Group-Velocity Dispersion," *J. Lightwave Technol.* **12**:280–287 (February 1994).
29. G. P. Agrawal, *Nonlinear Fiber Optics,* chap. 5, Academic Press, 1989.
30. Bob Jopson and Alan Gnauck, "Dispersion Compensation for Optical Fiber Systems," *IEEE Commun. Mag.* **33**:96–102 (June 1995).
31. P. E. Green, Jr., *Fiber Optic Networks,* chap. 11, Prentice Hall, 1993.
32. M. Fujiwara, M. S. Goodman, M. J. O'Mahony, O. K. Tonguz, and A. E. Willner (eds.), Special Issue on Multiwavelength Optical Technology and Networks, *J. Lightwave Technology* **14**(6):932–1454 (June 1996).
33. P. J. Smith, D. W. Faulkner, and G. R. Hill, "Evolution Scenarios for Optical Telecommunication Networks Using Multiwavelength Transmission," *Proc. IEEE,* **81**:1580–1587 (November 1993).
34. T. E. Darcie, K. Nawata, and J. B. Glabb, Special Issue on Broad-Band Lightwave Video Transmission, *J. Lightwave Technol.* **11**(1) (January 1993).
35. A. A. M. Saleh, "Fundamental Limit on Number of Channels in SCM Lightwave CATV System," *Electron. Lett.* **25**(12):776–777 (1989).
36. A. R. Chraplyvy, "High-Capacity Lightwave Transmission Experiments," *Bell Labs Tech. J.* **4**:230–245 (January–March 1999).

37. C. Baack and G. Walf, "Photonics in Future Telecommunications," *Proc. IEEE* **81**:1624–1632 (November 1993).
38. Gordon C. Wilson et al., "FiberVista: An FTTH or FTTC System Delivering Broadband Data and CATV Services," *Bell Labs Tech. J.* **4**:300–322 (January–March 1999).
39. Bellcore (Telcordia), "SONET Bidirectional Line Switched Ring Equipment Generic Criteria," Bellcore GR-1230, December 1996.

CHAPTER 3
NONLINEAR EFFECTS IN OPTICAL FIBERS

John A. Buck
Georgia Institute of Technology,
School of Electrical and Computer Engineering
Atlanta, Georgia

Fiber nonlinearities are important in optical communications, both as useful attributes and as characteristics to be avoided. They must be considered when designing long-range high-data-rate systems that involve high optical power levels and in which signals at multiple wavelengths are transmitted. The consequences of nonlinear transmission can include (1) the generation of additional signal bandwidth within a given channel, (2) modifications of the phase and shape of pulses, (3) the generation of light at other wavelengths at the expense of power in the original signal, and (4) crosstalk between signals at different wavelengths and polarizations. The first two, arising from self-phase modulation, can be used to advantage in the generation of *solitons*—pulses whose nonlinear phase modulation compensates for linear group dispersion in the fiber channel[1] or in fiber gratings,[2] leading to pulses that propagate without changing shape or width (see Chap. 7). The third and fourth effects arise from stimulated Raman or Brillouin scattering or four-wave mixing. These can be used to advantage when it is desired to generate or amplify additional wavelengths, but they must usually be avoided in systems.

3.1 KEY ISSUES IN NONLINEAR OPTICS IN FIBERS

Optical fiber waveguides, being of glass compositions, do not possess large nonlinear coefficients. Nonlinear processes can nevertheless occur with high efficiencies since intensities are high and propagation distances are long. Even though power levels are usually modest (a few tens of milliwatts), intensities within the fiber are high due to the small cross-sectional areas involved. This is particularly true in single-mode fiber, where the LP_{01} mode typically presents an effective cross-sectional area of between 10^{-7} and 10^{-8} cm^2, thus leading to intensities on the order of MW/cm^2. Despite this, long interaction distances are usually necessary to achieve nonlinear mixing of any significance, so processes must be phase matched, or nearly so. Strategies to avoid unwanted nonlinear effects usually involve placing upper limits on optical power levels, and if possible, choosing other parameters such that phase mismatching occurs. Such choices may include wavelengths or wavelength spacing in wavelength-division multiplexed systems, or may be involved in special fiber waveguide designs.[3]

Copyright 2001 by The McGraw-Hill Companies, Inc. Click Here for Terms of Use.

The generation of light through nonlinear mixing arises through polarization of the medium, which occurs through its interaction with intense light. The polarization consists of an array of phased dipoles in which the dipole moment is a nonlinear function of the applied field strength. In the classical picture, the dipoles, once formed, reradiate light to form the nonlinear output. The medium polarization is conveniently expressed through a power series expansion involving products of real electric fields:

$$\mathcal{P} = \varepsilon_0[\chi^{(1)} \cdot \mathcal{E} + \chi^{(2)} \cdot \mathcal{E}\mathcal{E} + \chi^{(3)} \cdot \mathcal{E}\mathcal{E}\mathcal{E} + ...] = \mathcal{P}_L + \mathcal{P}_{NL} \tag{1}$$

in which the χ terms are the linear, second-, and third-order susceptibilities. Nonlinear processes are described through the product of two or more optical fields to form the nonlinear polarization $\mathcal{P}_{NL}$, consisting of all terms of second order and higher in Eq. (1).

The second-order term in Eq. (1) [involving $\chi^{(2)}$] describes three-wave mixing phenomena, such as second-harmonic generation. The third-order term describes four-wave mixing (FWM) processes and stimulated scattering phenomena. In the case of optical fibers, second-order processes are generally not possible, since these effects require noncentrosymmetric media.[4] In amorphous fiber waveguides, third-order effects [involving $\chi^{(3)}$] are usually seen exclusively, although second-harmonic generation can be observed in special instances.[5]

The interactions between fields and polarizations are described by the nonlinear wave equation:

$$\nabla^2\mathcal{E} + n_0^2\mu_0\varepsilon_0\frac{\partial^2\mathcal{E}}{\partial t^2} = \mu_0\frac{\partial^2\mathcal{P}_{NL}}{\partial t^2} \tag{2}$$

where $\mathcal{E}$ and $\mathcal{P}$ are the sums of all electric fields and nonlinear polarizations that are present, and where n_0 is the refractive index of the medium. The second-order differential equation is usually reduced to first order through the slowly varying envelope approximation (SVEA):

$$\left|\frac{\partial^2 E}{\partial z^2}\right| \ll \left|\frac{2\pi}{\lambda}\frac{\partial E}{\partial z}\right| \tag{3}$$

where E is the complex field amplitude. The interpretation of the SVEA is that the changes in field amplitude that occur over distances on the order of a wavelength are very large compared to variations in the rate of change over the same distance. The wave equation will separate according to frequencies or propagation directions, yielding sets of coupled differential equations that, under the SVEA, are first order. These describe the growth or decay of fields involved in the mixing process.

The requirement for phase matching is that the nonlinear polarization wave and the electric field associated with the generated wave propagate with the same phase constant; that is, their phase velocities are equal. Phase-matched processes in fiber include those that involve (1) interacting waves at the same wavelength and polarization, such as self- and cross-phase modulation, as well as other degenerate Kerr-type interactions; and (2) stimulated scattering processes (Raman and Brillouin), in addition to cross-phase modulation involving two wavelengths. Four-wave mixing processes involving light at different wavelengths can occur that are not precisely phase matched but that can nevertheless yield high efficiencies. Matters are further complicated by the fact that different nonlinear processes can occur simultaneously, with each affecting the performance of the other. Nonlinear effects are usually favored to occur under pulsed operation, since high peak powers can be achieved with comparatively modest average powers. Consequently, group velocity matching is desirable (although not always required) to achieve efficient mixing between pulses.

3.2 SELF- AND CROSS-PHASE MODULATION

Self-phase modulation (SPM) can occur whenever a signal having a time-varying amplitude is propagated in a nonlinear material. The origin of the effect is the refractive index of the medium, which will change with the instantaneous signal intensity. The complex nonlinear polarization for the process is:

$$P_{NL} = \tfrac{3}{4}\varepsilon_0\chi^{(3)}|E_0(z,\,t)|^2E_0(z,\,t)\exp[i(\omega t - \beta z)] \tag{4}$$

where $E_0(t)$ is the time-varying electric field amplitude that describes the pulse or signal envelope, and where the frequency ω is the same as that of the input light. Incorporating this polarization and the field into the wave equation leads to a modified refractive index over the original zero-field value n_0. The net index becomes:[6]

$$n = n_0 + n_2'|E_0(z,\,t)|^2 \tag{5}$$

where the nonlinear refractive index is given by $n_2' = Re\{3\chi^{(3)}/8n_0\}$. In fused silica it has the value $n_2' = 6.1 \times 10^{-23}\,m^2/V^2$.[7] Equation (5) can also be expressed in terms of light intensity through $n(I) = n_0 + n_2I(z,\,t)$, where $n_2 = 3.2 \times 10^{-20}\,m^2/W$. In optical fibers the index is modified from the effective mode index of the single-mode fiber n_{eff} (which assumes the role of n_0).

The complex field as it propagates through the medium can be expressed as:

$$E = E_0(z,\,t)\exp\{i[\omega_0 t - [n_0 + n_2I(z,\,t)]k_0z]\} \tag{6}$$

which exhibits phase modulation that follows the shape of the intensity envelope. The instantaneous frequency is found through the time derivative of the phase:

$$\omega' = \omega_0 - n_2k_0z\frac{\partial I}{\partial t} \tag{7}$$

The effects of self-phase modulation on pulse propagation can be qualitatively observed from Eqs. (6) and (7). First, additional frequency components are placed on the pulse, thus increasing its spectral width. Second, a frequency sweep (chirp) imposed on the pulse, the direction of which depends on the sign of $\partial I/\partial t$. The latter feature is particularly important in optical fibers, since the imposed frequency sweep from SPM will either add to or subtract from the chirp imposed by linear group dispersion. If the chirp directions for self-phase modulation and group dispersion are opposite, an effective cancellation may occur, leading to the formation of an optical soliton. In more conventional systems in which solitons are not employed, SPM must be considered as a possible benefit or detriment to performance, as some pulse shaping (which could include broadening or compression) can occur;[8,9] however, such systems can in theory yield excellent performance.[10] Furthermore, in systems employing fiber amplifiers, the change in refractive index associated with the signal-induced upper state population in erbium has been shown to be an important performance factor.[11] An additional effect can occur when pulse spectra lie within the anomalous group dispersion regime of the fiber; pulse breakup can occur as a result of *modulation instability,* in which the interplay between dispersive and nonlinear contributions to pulse shaping becomes unstable.[12]

Cross-phase modulation (XPM) is similar to SPM, except that two overlapping but distinguishable pulses (having, for example, different frequencies or polarizations) are involved. One pulse will modulate the index of the medium, which then leads to phase modulation of an overlapping pulse. XPM thus becomes a cross-talk mechanism between two channels if phase encoding is employed or if intensity modulation is used in dispersive systems.[13,14] No transfer of energy occurs between channels, however, which distinguishes the process from

other crosstalk mechanisms in which growth of signal power in one channel occurs at the expense of power in another. The strength of the effect is enhanced by a factor of 2 over that which can be obtained by a single field acting on itself (the nonlinear refractive index n_2 is effectively doubled in XPM).[15] The XPM process, while twice as strong as SPM, is effectively weakened by the fact that pulses of differing frequencies or polarizations are generally not group velocity matched, and so cannot maintain overlap indefinitely. The efficiency is further reduced if the interaction occurs between cross-polarized waves; in this case the nonlinear tensor element (and thus the effective nonlinear index) is a factor of ⅓ less than the tensor element that describes copolarized waves (pp. 164–165 in Ref. 6).

Self- and cross-phase modulation are analyzed by way of coupled equations of the *nonlinear Schrödinger* form,[16] which describes the evolution over time and position of the electric field envelopes of two pulses, E_{0a} and E_{0b}, where SVEA is used and where pulse widths are on the order of 1 ps or greater:

$$\frac{\partial E_{0a}}{\partial z} + \beta_{1a}\frac{\partial E_{0a}}{\partial t} = -\frac{i}{2}\beta_{2a}\frac{\partial^2 E_{0a}}{\partial t^2} + i\gamma_a|E_{0a}|^2E_{0a} + i\delta\gamma_a|E_{0b}|^2E_{0a} - \frac{\alpha_a}{2}E_{0a} \tag{8}$$

$$\frac{\partial E_{0b}}{\partial z} + \beta_{1b}\frac{\partial E_{0b}}{\partial t} = -\frac{i}{2}\beta_{2b}\frac{\partial^2 E_{0b}}{\partial t^2} + i\gamma_b|E_{0b}|^2E_{0b} + i\delta\gamma_b|E_{0a}|^2E_{0b} - \frac{\alpha_b}{2}E_{0b} \tag{9}$$

In these equations, β_{1j} ($j = a, b$) are the group delays of the pulses at the two frequencies or polarizations over a unit distance; β_{2j} are the group dispersion parameters associated with the two pulses; and $\gamma_j = n_2'\omega_j/(cA_{\text{eff}})$, where A_{eff} is the effective cross-sectional area of the fiber mode. The coefficient δ is equal to 2 for copolarized pulses of different frequencies and is ⅔ if the pulses are cross-polarized. Propagation loss characterized by coefficients α_j is assumed. The equation form that describes the propagation with SPM of a single pulse—E_{0a}, for example—is found from Eq. (8) by setting $E_{0b} = 0$. The terms on the right sides of Eqs. (8) and (9) describe in order the effects of group dispersion, SPM, XPM, and loss. The equations can be solved using numerical techniques that are described on pages 50–55 of Ref. 16.

For subpicosecond pulses, the accuracy of Eqs. (8) and (9) begins to degrade as pulse bandwidths increase with decreasing temporal width. Additional terms are usually incorporated in the equations as pulse widths are reduced to the vicinity of 100 fs. These embody (1) cubic dispersion, which becomes important as bandwidth increases, and (2) changes in group velocity with intensity. This latter effect can result in *self-steepening,* in which the pulse trailing edge shortens to the point of forming an optical shock front (pp. 113–120 of Ref. 16) under appropriate conditions. An additional consequence of broad pulse spectra is that power conversion from high-frequency components within a pulse to those at lower frequencies can occur via stimulated Raman scattering, provided the interacting components are sufficiently separated in wavelength. The effect is an overall red shift of the spectrum. At sufficiently high intensities, cross-coupling between pulses having different center wavelengths can also occur through Raman scattering, regardless of pulse width.

3.3 STIMULATED RAMAN SCATTERING

In *stimulated Raman scattering* (SRS), coupling occurs between copropagating light waves whose frequency difference is in the vicinity of resonances of certain molecular oscillation modes. In silica-based fibers, stretch vibrational resonances occur between Si and O atoms in several possible modes within the glass matrix (see Ref. 17 for illustrations of the important modes in pure silica). In the Stokes process, light at frequency ω_2 (pump wave) is downshifted to light at ω_1 (Stokes wave), with the excess energy being absorbed by the lattice vibrational modes (manifested in the generation of optical phonons). The process is either spontaneous,

in which the Stokes wave builds up from noise, or is stimulated, in which both waves are present in sufficient strength to generate a beat frequency that excites the oscillators and promotes coupling. A fiber Raman amplifier works on this principle, in which an input signal at ω_1 experiences gain in the presence of pump light at ω_2. Figure 1 shows the beam geometry in which an input wave at ω_1 and intensity I_{10} can emerge at the far end with amplified value I_{1L}. This occurs in the presence of the pump wave at ω_2 that has initial intensity I_{20} and that emerges with depleted intensity I_{2L}.

Back-conversion from ω_1 to ω_2 (the inverse Raman effect) will also occur once the Stokes wave reaches sufficient intensity, but gain will only occur for the Stokes wave. Both processes are phase matched, and so occur with high efficiency in long fibers. The back-conversion process is to be distinguished from anti-Stokes scattering, in which pump light at ω_2 is upshifted to frequency ω_3, with the additional energy being supplied by optical phonons associated with the previously excited medium. The anti-Stokes process is rarely seen in fiber transmission because (1) it is phase mismatched and (2) it requires a substantial population of excited oscillators, which is not the case at thermal equilibrium.

Figure 2 shows the measured Raman gain for the Stokes wave in fused silica. The gain is plotted as a function of difference frequency between the interacting waves measured in cm^{-1} (to convert this to wavelength shift, use the formula $\Delta\lambda = \lambda_p^2 \Delta f(cm^{-1})$, where λ_p is the pump wavelength). Other fiber constituents such as GeO_2, P_2O_5, and B_2O_3 exhibit their own Raman resonances, which occur at successively greater wavelength shifts;[19] the effects of these will be weak, since their concentration in the fiber is generally small. Thus the dominant Raman shifts in optical fiber are associated with SiO_2, and occur within the range of 440 to 490 cm^{-1}, as is evident in Fig. 2.

Nonlinear polarizations at frequencies ω_1 and ω_2 can be constructed that are proportional to products of the Stokes and pump fields, $E_1^{\omega_1}$ and $E_2^{\omega_2}$. These are of the form $P_{NL}^{\omega_1} \propto |E_2^{\omega_2}|^2 E_1^{\omega_1}$ (Stokes generation) and $P_{NL}^{\omega_2} \propto |E_1^{\omega_1}|^2 E_2^{\omega_2}$ (the inverse Raman effect). Substituting these polarizations and the two fields into the wave equation, using the SVEA, and assuming copolarized fields leads to the following coupled equations involving the Stokes and pump wave intensities I_1 and I_2:[18]

$$\frac{dI_1}{dz} = g_r I_1 I_2 - \alpha I_1 \tag{10}$$

$$\frac{dI_2}{dz} = -\frac{\omega_2}{\omega_1} g_r I_1 I_2 - \alpha I_2 \tag{11}$$

where the loss terms involving α (the fiber loss per unit distance) are added phenomenologically. The Raman gain function g_r is expressed in a general way as

$$g_r = \frac{A}{\lambda_2} f(\lambda_1 - \lambda_2) \tag{12}$$

where A is a function of the material parameters and $f(\lambda_1 - \lambda_2)$ is a normalized line shape function, which is either derived from theory or experimentally measured (determined from Fig. 2, for example). With λ_2 expressed in μm, $A = 1.0 \times 10^{-11}$ cm – μm/W.[20] The solutions of Eqs. (10) and (11) are:

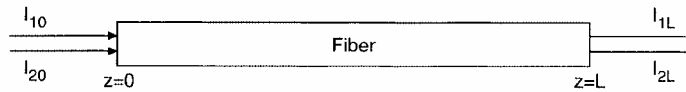

FIGURE 1 Beam geometry for stimulated Raman scattering in an optical fiber.

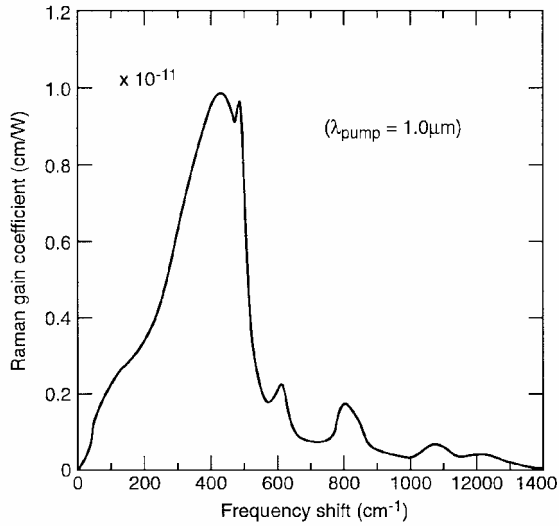

FIGURE 2 Raman gain spectrum in fused silica. (*Adapted from Ref. 22. © 1980 IEEE.*)

$$I_1(z) = \frac{\omega_1}{\omega_2} I_0 \exp(-\alpha z) \frac{\psi_r}{1 + \psi_r} \tag{13}$$

$$I_2(z) = I_0 \exp(-\alpha z) \frac{1}{1 + \psi_r} \tag{14}$$

In these equations, $I_0 = I_{20} + (\omega_1/\omega_2)I_{10}$, where I_{10} and I_{20} are the Stokes and pump intensities at the fiber input. The coupling parameter ψ_r assumes different forms, depending upon whether the input Stokes intensity I_{10} is present or not. If I_{10} is present, and if its magnitude is much greater than light from spontaneous Raman scattering, we have:

$$\psi_r = \frac{\omega_1}{\omega_2} \frac{I_{10}}{I_{20}} \exp(G_0) \tag{15}$$

When no Stokes input is present, the signal builds up from spontaneous Raman scattering, and the coupling parameter in this case becomes:

$$\psi_r = \frac{\hbar \omega_2 \Delta\omega_r}{4\sqrt{\pi}} \frac{1}{I_{20} A_{\text{eff}}} G_2^{-1/2} \exp(G_2) \tag{16}$$

with the gain parameters defined through $G_0 = g_r I_0 L_{\text{eff}}$ and $G_2 = g_r I_{20} L_{\text{eff}}$ The effective length of the fiber accounts for the reduction of Stokes and pump intensities as a result of loss, and is defined as

$$L_{\text{eff}} = \int_0^L \exp(-\alpha z) dz = \frac{1 - \exp(-\alpha L)}{\alpha} \tag{17}$$

The effective area of a single-mode fiber A_{eff} is calculated through πr_0^2, where r_0 is the mode field radius. For a multimode fiber, A_{eff} is usually taken as the core area, assuming that the power is uniformly distributed over the core. The power in the fiber is then $P_{1,2} = I_{1,2}A_{\text{eff}}$.

Two basic issues concerning SRS are of interest in fiber communication systems. First, pump-to-Stokes coupling provides a mechanism for crosstalk from short- to long-wavelength channels. This will occur most efficiently if the channel frequency spacing is in the vicinity of that associated with the maximum Raman gain. The Raman gain peak at approximately 500 cm^{-1} corresponds to a frequency spacing of 15 THz, meaning that operation at 1.55 μm produces a Stokes wave of about 1.67 μm wavelength. Two-channel operation at these wavelengths would lead to a maximum allowable signal level of about 50 mW.[21] In WDM systems, within the 1.53- to 1.56-μm erbium-doped fiber amplifier window, channel spacings on the order of 100 GHz are used. Raman gain is thus considerably reduced, but is still sufficient to cause appreciable crosstalk, which can lead to system penalties of between 1 and 3 dB depending on the number of channels.[22] Second, and of more importance to single-wavelength systems, is the conversion to Stokes power from the original signal—a mechanism by which signal power can be depleted. A related problem is walkoff[23] occurring between the signal and Stokes pulses, since these will have different group delays. Walkoff is a means for aliasing to occur in digital transmission, unless the signal is filtered at the output. If pulses are of subpicosecond widths, additional complications arise due to the increased importance of SPM and XPM.[24] In any event, an upper limit must be placed on the signal power if significant conversion to Stokes power is to be avoided. In single-wavelength systems, where crosstalk is not an issue, pulse peak powers must be kept below about 500 mW to avoid significant SRS conversion.[25]

A useful criterion is the so-called critical condition (or Raman threshold), defined as the condition under which the output Stokes and signal powers are equal. This occurs when $\psi_r = 1$, which, from Eq. (16), leads to $G_2 \approx 16$. SRS can also be weakened by taking advantage of the gain reduction that occurs as signal (pump) wavelengths increase, as shown in Eq. (12). For example, operation at 1.55 μm yields less SRS for a given signal power than operation at 1.3 μm.

Apart from the need to reduce SRS, the effect can be used to advantage in wavelength conversion and in amplification. Fiber Raman lasers have proven to be good sources of tunable radiation and operate at multiple Stokes wavelengths.[26] Specifically, a Stokes wave can serve as a pump to generate an additional (higher-order) Stokes wave at a longer wavelength.[27] Fiber Raman amplifiers have been demonstrated as repeaters in 1.3-μm wavelength systems.[28]

3.4 STIMULATED BRILLOUIN SCATTERING

The stimulated Brillouin scattering process (SBS) involves the input of a single intense optical wave at frequency ω_2, which initiates a copropagating acoustic wave at frequency ω_p. The acoustic wave is manifested as a traveling index grating in the fiber, which back-diffracts a portion of the original input. The backward (Stokes) wave is Doppler-shifted to a lower frequency ω_1 and is proportional to the phase conjugate of the input.[29] The backward wave is amplified as it propagates, with the gain increasing with increasing input (pump) power.

The beam interaction geometry is shown in Fig. 3. Usually, the Stokes wave builds up spontaneously, but can be inputted at the far end. The effect can be understood by considering a case in which counter-propagating Stokes and pump waves exist that together form a moving interference pattern whose velocity is proportional to the difference frequency $\omega_2 - \omega_1$. Coupling between the waves will occur via SBS when the interference pattern velocity is in the vicinity of the acoustic wave velocity v_p. It is the interference pattern that forms and reinforces the acoustic wave through electrostriction. With a single input, spontaneous scattering from numerous shock waves occurs, with preferential feedback from the acoustic wave that matches the condition just described. With the Stokes wave generated (although it is initially weak), the acoustic wave is reinforced, and so backscattering increases.

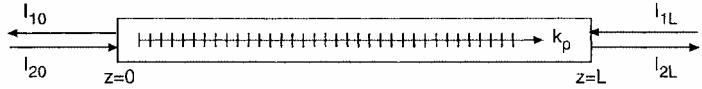

FIGURE 3 Beam geometry for stimulated Brillouin scattering in an optical fiber.

In terms of the wave vector magnitudes, the condition for phase matching is given by $k_p = k_1 + k_2$. Since the sound frequency is much less than those of the two optical waves, we can write $k_p \approx 2k_2$. Then, since $k_p = \omega_p/v_p$, it follows that $\omega_p \approx 2n\omega_2 v_p/c$, where n is the refractive index (assumed to be the same value at both optical frequencies). The Brillouin frequency shift under phase-matched conditions thus becomes

$$\omega_2 - \omega_1 \approx 2n\omega_2 \frac{v_p}{c} \tag{18}$$

This yields a value of about 11 GHz, with $v_p \approx 6$ km/s in fused silica and $\lambda_2 = 1.55$ μm.

The process can be described by the nonlinear polarization produced by the product of complex fields, E_1, E_2^*, and E_2; this yields a polarization at ω_1 that propagates with wave vector k_1 in the direction of the Stokes wave. Another polarization, describing back-coupling from Stokes to pump, involves the product $E_1 E_1^* E_2$. Substituting fields and polarizations into the wave equation yields the following coupled equations that describe the evolution of the optical intensities with distance (pp. 214–220 of Ref. 18):

$$\frac{dI_1}{dz} = -g_b I_1 I_2 + \alpha I_1 \tag{19}$$

$$\frac{dI_2}{dz} = -g_b I_1 I_2 - \alpha I_2 \tag{20}$$

where α is the linear loss coefficient. The Brillouin gain is given by

$$g_b = g_{b0}\left(1 + \frac{4(\omega_1 - \omega_{10})^2}{v_p^2 \alpha_p^2}\right)^{-1} \tag{21}$$

where ω_{10} is the Stokes frequency at precise phase matching, α_p is the loss coefficient for the acoustic wave, and the peak gain g_{b0} is a function of the material parameters. The Brillouin line width, defined as the full width at half-maximum of g_b, is $\Delta\omega_b = v_p\alpha_p$. In optical fibers, $\Delta f_b = \Delta\omega_b/2\pi$ is typically between 10 and 30 MHz (p. 374 of Ref. 16) and $g_{b0} = 4.5 \times 10^{-9}$ cm/W.[20] Signal bandwidths in high-data-rate communication systems greatly exceed the Brillouin line width, and so SBS is typically too weak to be considered a source of noise or signal depletion. This is to be compared to stimulated Raman scattering, which supports considerable gain over approximately 5 THz. Consequently, SRS is a much more serious problem in high-data-rate systems.

Using analysis methods similar to those employed in SRS, a critical condition (or threshold) can be defined for SBS, at which the backscattered power is equal to the input power:[30]

$$\frac{\omega_1 k_B T \Delta\omega_b}{4\sqrt{\pi}\omega_p I_{20} A_{\text{eff}}} G_b^{-3/2} \exp(G_b) = 1 \tag{22}$$

where k_B is Boltzmann's constant and T is the temperature in degrees Kelvin. The gain parameter is:

$$G_b = g_b I_{20} L_{\text{eff}} \tag{23}$$

with L_{eff} as defined in Eq. (17). Equation (22) is approximately satisfied when $G_b \approx 21$.[30] In practice, the backscattered power will always be less than the input power, since pump depletion will occur. Nevertheless, this condition is used as a benchmark to determine the point at which SBS becomes excessive in a given system.[31] In one study, it was found that $G_b \approx 21$ yields the pump power required to produce an SBS output that is at the level of Rayleigh backscattering.[32] Pump powers required to achieve threshold can be on the order of a few milliwatts for CW or narrowband signals, but these increase substantially for broadband signals.[33] Reduction of SBS is accomplished in practice by lowering the input signal power (I_{20}) or by taking advantage of the reduction in g_b that occurs when signal bandwidths ($\Delta\omega$) exceed the Brillouin line width. Specifically, if $\Delta\omega >> \Delta\omega_b$,

$$g_b(\Delta\omega) \approx g_b \frac{\Delta\omega_b}{\Delta\omega} \tag{24}$$

3.5 FOUR-WAVE MIXING

The term *four-wave mixing* in fibers is generally applied to wave coupling through the electronic nonlinearity in which at least two frequencies are involved and in which frequency conversion is occurring. The fact that the electronic nonlinearity is involved distinguishes four-wave mixing interactions from stimulated scattering processes because in the latter the medium was found to play an active role through the generation or absorption of optical phonons (in SRS) or acoustic phonons (in SBS). If the nonlinearity is electronic, bound electron distributions are modified according to the instantaneous optical field configurations. For example, with light at two frequencies present, electron positions can be modulated at the difference frequency, thus modulating the refractive index. Additional light will encounter the modulated index and can be up- or downshifted in frequency. In such cases, the medium plays a passive role in the interaction, as it does not absorb applied energy or release energy previously stored. The self- and cross-phase modulation processes also involve the electronic nonlinearity, but in those cases, power conversion between waves is not occurring—only phase modulation.

As an illustration of the process, consider the interaction of two strong waves at frequencies ω_1 and ω_2, which mix to produce a downshifted (Stokes) wave at ω_3 and an upshifted (anti-Stokes) wave at ω_4. The frequencies have equal spacing, that is, $\omega_1 - \omega_3 = \omega_2 - \omega_1 = \omega_4 - \omega_2$ (Fig. 4). All fields assume the real form:

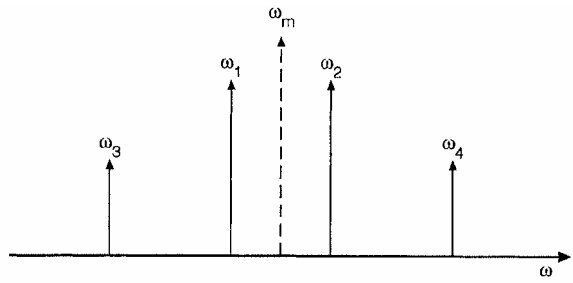

FIGURE 4 Frequency diagram for four-wave mixing, showing pump frequencies (ω_1 and ω_2) and sideband frequencies (ω_3 and ω_4).

$$\mathscr{E}_j = \tfrac{1}{2}E_{oj}\exp[i(\omega_j t - \beta_j z)] + c.c.\ j = 1 - 4 \tag{25}$$

The nonlinear polarization will be proportional to $\mathscr{E}^3$, where $\mathscr{E} = \mathscr{E}_1 + \mathscr{E}_2 + \mathscr{E}_3 + \mathscr{E}_4$. With all fields copolarized, complex nonlinear polarizations at ω_3 and ω_4 appear that have the form:

$$P_{\mathrm{NL}}^{\omega_3} = \tfrac{3}{4}\varepsilon_0\chi^{(3)}E_{01}^2E_{02}^*\exp[i(2\omega_1 - \omega_2)t]\exp[-i(2\beta^{\omega_1} - \beta^{\omega_2})z] \tag{26}$$

$$P_{\mathrm{NL}}^{\omega_4} = \tfrac{3}{4}\varepsilon_0\chi^{(3)}E_{02}^2E_{01}^*\exp[i(2\omega_2 - \omega_1)t]\exp[-i(2\beta^{\omega_2} - \beta^{\omega_1})z] \tag{27}$$

where $\omega_3 = 2\omega_1 - \omega_2$, $\omega_4 = 2\omega_2 - \omega_1$ and $\chi^{(3)}$ is proportional to the nonlinear refractive index n_2'. The significance of these polarizations lies not only in the fact that waves at the sideband frequencies ω_3 and ω_4 can be generated, but that preexisting waves at those frequencies can experience gain in the presence of the two pump fields at ω_1 and ω_2. The sideband waves will contain the amplitude and phase information on the pumps, thus making this process an important crosstalk mechanism in multiwavelength communication systems. Under phase-matched conditions, the gain associated with FWM is more than twice the peak gain in SRS.[34]

The wave equation, when solved in steady state, yields the output intensity at either one of the sideband frequencies.[35] For a medium of length L, having loss coefficient α, the sideband intensities are related to the pump intensities through

$$I^{\omega_3} \propto \left(\frac{n_2 L_{\mathrm{eff}}}{\lambda_m}\right)^2 I^{\omega_2}(I^{\omega_1})^2\eta\exp(-\alpha L) \tag{28}$$

$$I^{\omega_4} \propto \left(\frac{n_2 L_{\mathrm{eff}}}{\lambda_m}\right)^2 I^{\omega_1}(I^{\omega_2})^2\eta\ \exp(-\alpha L) \tag{29}$$

where L_{eff} is defined in Eq. (17), and where

$$\eta = \frac{\alpha^2}{\alpha^2 + \Delta\beta^2}\left(1 + \frac{4\exp(-\alpha L)\sin^2(\Delta\beta L/2)}{(1 - \exp(-\alpha L))^2}\right) \tag{30}$$

Other FWM interactions can occur, involving products of intensities at three different frequencies rather than two as demonstrated here. In such cases, the output wave intensities are increased by a factor of 4 over those indicated in Eqs. (28) and (29).

One method of suppressing four-wave mixing in WDM systems includes the use of unequal channel spacing.[36] This assures, for example, that $\omega_3 \neq 2\omega_1 + \omega_2$, where ω_1, ω_2, and ω_3 are assigned channel frequencies. Other methods involve phase-mismatching the process in some way. This is accomplished by increasing $\Delta\beta$, which has the effect of decreasing η in Eqs. (28) and (29). Note that in the low-loss limit, where $\alpha \to 0$, Eq. (30) reduces to $\eta = (\sin^2(\Delta\beta L/2))/(\Delta\beta L/2)^2$. The $\Delta\beta$ expressions associated with wave generation at ω_3 and ω_4 are given by

$$\Delta\beta(\omega_3) = 2\beta^{\omega_1} - \beta^{\omega_2} - \beta^{\omega_3} \tag{31}$$

and

$$\Delta\beta(\omega_4) = 2\beta^{\omega_2} - \beta^{\omega_1} - \beta^{\omega_4} \tag{32}$$

It is possible to express Eqs. (31) and (32) in terms of known fiber parameters by using a Taylor series for the propagation constant, where the expansion is about frequency ω_m as indicated in Fig. 4, where $\omega_m = (\omega_2 + \omega_1)/2$.

$$\beta \approx \beta_0 + (\omega - \omega_m)\,\beta_1 + \tfrac{1}{2}(\omega - \omega_m)^2\,\beta_2 + \tfrac{1}{6}(\omega - \omega_m)^3\beta_3 \tag{33}$$

In Eq. (33), β_1, β_2, and β_3 are, respectively, the first, second, and third derivatives of β with respect to ω, evaluated at ω_m. These in turn relate to the fiber dispersion parameter D (ps/nm·km) and its first derivative with respect to wavelength through $\beta_2 = -(\lambda_m^2/2\pi c)D(\lambda_m)$ and $\beta_3 = (\lambda_m^3/2\pi^2c^2)[D(\lambda_m) + (\lambda_m/2)(dD/d\lambda)|_{\lambda m}]$ where $\lambda_m = 2\pi c/\omega_m$. Using these relations along with Eq. (33) in Eqs. (31) and (32) results in:

$$\Delta\beta(\omega_3, \omega_4) \approx 2\pi c\frac{\Delta\lambda^2}{\lambda_m^2}\left[D(\lambda_m) \pm \frac{\Delta\lambda}{2}\frac{dD}{d\lambda}|_{\lambda m}\right] \tag{34}$$

where the plus sign is used for $\Delta\beta(\omega_3)$, the minus sign is used for $\Delta\beta(\omega_4)$, and $\Delta\lambda = \lambda_1 - \lambda_2$. Phase matching is not completely described by Eq. (34), since cross-phase modulation plays a subtle role, as discussed on pp. 410–411 of Ref. 16. Nevertheless, Eq. (34) does show that the retention of moderate values of dispersion D is a way to reduce FWM interactions that would occur, for example, in WDM systems. As such, modern commercial fiber intended for use in WDM applications will have values of D that are typically in the vicinity of 2 ps/nm·km.[37] With WDM operation in conventional dispersion-shifted fiber (with the dispersion zero near 1.55 μm), having a single channel at the zero dispersion wavelength can result in significant four-wave mixing.[38] Methods that were found to reduce four-wave mixing in such cases include the use of cross-polarized signals in dispersion-managed links[39] and operation within a longer-wavelength band near 1.6 μm[40] at which dispersion is appreciable and where gain-shifted fiber amplifiers are used.[41]

Examples of other cases involving four-wave mixing include single-wavelength systems, in which the effect has been successfully used in a demultiplexing technique for TDM signals.[42] In another case, coupling through FWM can occur between a signal and broadband amplified spontaneous emission (ASE) in links containing erbium-doped fiber amplifiers.[43] As a result, the signal becomes spectrally broadened and exhibits phase noise from the ASE. The phase noise becomes manifested as amplitude noise under the action of dispersion, producing a form of modulation instability.

An interesting application of four-wave mixing is spectral inversion. Consider a case that involves the input of a strong single-frequency pump wave along with a relatively weak wave having a spectrum of finite width positioned on one side of the pump frequency. Four-wave mixing leads to the generation of a wave whose spectrum is the "mirror image" of that of the weak wave, in which the mirroring occurs about the pump frequency. Figure 5 depicts a representation of this, where four frequency components comprising a spectrum are shown along

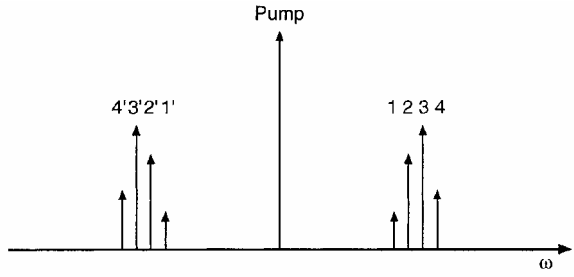

FIGURE 5 Frequency diagram for spectral inversion using four-wave mixing with a single pump frequency.

with their imaged counterparts. An important application of this is pulses that have experienced broadening with chirping after propagating through a length of fiber exhibiting linear group dispersion.[44] Inverting the spectrum of such a pulse using four-wave mixing has the effect of reversing the direction of the chirp (although the pulse center wavelength is displaced to a different value). When the spectrally inverted pulse is propagated through an additional length of fiber having the same dispersive characteristics, the pulse will compress to nearly its original input width. Compensation for nonlinear distortion has also been demonstrated using this method.[45]

3.6 CONCLUSION

An overview of fiber nonlinear effects has been presented here in which emphasis is placed on the basic concepts, principles, and perspectives on communication systems. Space is not available to cover the more subtle details of each effect or the interrelations between effects that often occur. The text by Agrawal[16] is recommended for further in-depth study, which should be supplemented by the current literature. Nonlinear optics in fibers and in fiber communication systems comprises an area whose principles and implications are still not fully understood. It thus remains an important area of current research.

3.7 REFERENCES

1. L. F. Mollenauer and P. V. Mamyshev, "Massive Wavelength-Division Multiplexing with Solitons," *IEEE J. Quantum Electron.* **34:**2089–2102 (1998).
2. C. M. de Sterke, B. J. Eggleton, and P. A. Krug, "High-Intensity Pulse Propagation in Uniform Gratings and Grating Superstructures," *IEEE J. Lightwave Technol.* **15:**1494–1502 (1997).
3. L. Clark, A. A. Klein, and D. W. Peckham, "Impact of Fiber Selection and Nonlinear Behavior on Network Upgrade Strategies for Optically Amplified Long Interoffice Routes," *Proceedings of the 10th Annual National Fiber Optic Engineers Conference,* vol. 4, 1994.
4. Y. R. Shen, *The Principles of Nonlinear Optics,* Wiley-Interscience, New York, 1984, p. 28.
5. R. H. Stolen and H. W. K. Tom, "Self-Organized Phase-Matched Harmonic Generation in Optical Fibers," *Opt. Lett.* **12:**585–587 (1987).
6. R. W. Boyd, *Nonlinear Optics,* Academic Press, San Diego, 1992, pp. 159 ff.
7. R. H. Stolen and C. Lin, "Self-Phase Modulation in Silica Optical Fibers," *Phys. Rev. A* **17:**1448–1453 (1978).
8. G. Bellotti, A. Bertaina, and S. Bigo, "Dependence of Self-Phase Modulation Impairments on Residual Dispersion in 10-Gb/s-Based Terrestrial Transmission Using Standard Fiber," *IEEE Photon. Technol. Lett.* **11:**824–826 (1999).
9. M. Stern, J. P. Heritage, R. N. Thurston, and S. Tu, "Self-Phase Modulation and Dispersion in High Data Rate Fiber Optic Transmission Systems," *IEEE J. Lightwave Technol.* **8:**1009–1015 (1990).
10. D. Marcuse and C. R. Menyuk, "Simulation of Single-Channel Optical Systems at 100 Gb/s," *IEEE J. Lightwave Technol.* **17:**564–569 (1999).
11. S. Reichel and R. Zengerle, "Effects of Nonlinear Dispersion in EDFA's on Optical Communication Systems," *IEEE J. Lightwave Technol.* **17:**1152–1157 (1999).
12. M. Karlsson, "Modulational Instability in Lossy Optical Fibers," *J. Opt. Soc. Am. B* **12:**2071–2077 (1995).
13. R. Hui, K. R. Demarest, and C. T. Allen, "Cross-Phase Modulation in Multispan WDM Optical Fiber Systems," *IEEE J. Lightwave Technol.* **17:**1018–1026 (1999).
14. S. Bigo, G. Billotti, and M. W. Chbat, "Investigation of Cross-Phase Modulation Limitation over Various Types of Fiber Infrastructures," *IEEE Photon. Technol. Lett.* **11:**605–607 (1999).

15. D. Marcuse, "Selected Topics in the Theory of Telecommunications Fibers," in *Optical Fiber Telecommunications II,* Academic Press, San Diego, 1988, p. 102.
16. G. P. Agrawal, *Nonlinear Fiber Optics,* 2d ed., Academic Press, San Diego, 1995, pp. 242–247.
17. G. Herzberg, *Infra-Red and Raman Spectroscopy of Polyatomic Molecules,* Van Nostrand, New York, 1945, pp. 99–101.
18. J. A. Buck, *Fundamentals of Optical Fibers,* Wiley-Interscience, New York, 1995, pp. 207–213.
19. F. L. Galeener, J. C. Mikkelsen Jr., R. H. Geils, and W. J. Mosby, "The Relative Raman Cross Sections of Vitreous SiO_2, GeO_2, B_2O_3, and P_2O_5," *Appl. Phys. Lett.* **32**:34–36 (1978).
20. R. H. Stolen, "Nonlinear Properties of Optical Fibers," in S. E. Miller and A. G. Chynoweth (eds.), *Optical Fiber Telecommunications,* Academic Press, New York, 1979.
21. A. R. Chraplyvy, "Optical Power Limits in Multi-Channel Wavelength Division Multiplexed Systems due to Stimulated Raman Scattering," *Electron. Lett.* **20**:58–59 (1984).
22. F. Forghieri, R. W. Tkach, and A. R. Chraplyvy, "Effect of Modulation Statistics on Raman Crosstalk in WDM Systems," *IEEE Photon. Technol. Lett.* **7**:101–103 (1995).
23. R. H. Stolen and A. M. Johnson, "The Effect of Pulse Walkoff on Stimulated Raman Scattering in Fibers," *IEEE J. Quantum Electron.* **22**:2154–2160 (1986).
24. C. H. Headley III and G. P. Agrawal, "Unified Description of Ultrafast Stimulated Raman Scattering in Optical Fibers," *J. Opt. Soc. Am. B* **13**:2170–2177 (1996).
25. R. H. Stolen, J. P. Gordon, W. J. Tomlinson, and H. A. Haus, "Raman Response Function of Silica Core Fibers," *J. Opt. Soc. Am. B* **6**:1159–1166 (1988).
26. L. G. Cohen and C. Lin, "A Universal Fiber-Optic (UFO) Measurement System Based on a Near-IR Fiber Raman Laser," *IEEE J. Quantum Electron.* **14**:855–859 (1978).
27. K. X. Liu and E. Garmire, "Understanding the Formation of the SRS Stokes Spectrum in Fused Silica Fibers," *IEEE J. Quantum Electron.* **27**:1022–1030 (1991).
28. T. N. Nielsen, P. B. Hansen, A. J. Stentz, V. M. Aguaro, J. R. Pedrazzani, A. A. Abramov, and R. P. Espindola, "8 × 10 Gb/s 1.3-μm Unrepeated Transmission over a Distance of 141 km with Raman Post- and Pre-Amplifiers," *IEEE Photonics Technology Letters,* vol. 10, pp. 1492–1494 (1998).
29. A. Yariv, *Quantum Electronics,* 3d ed., Wiley, New York, 1989, pp. 513–516.
30. R. G. Smith, "Optical Power Handling Capacity of Low Loss Optical Fibers as Determined by Stimulated Raman and Brillouin Scattering," *Appl. Opt.* **11**:2489–2494 (1972).
31. A. R. Chraplyvy, "Limitations on Lightwave Communications Imposed by Optical Fiber Nonlinearities," *IEEE J. Lightwave Technol.* **8**:1548–1557 (1990).
32. X. P. Mao, R. W. Tkach, A. R. Chraplyvy, R. M. Jopson, and R. M. Derosier, "Stimulated Brillouin Threshold Dependence on Fiber Type and Uniformity," *IEEE Photon. Technol. Lett.* **4**:66–68 (1992).
33. C. Edge, M. J. Goodwin, and I. Bennion, "Investigation of Nonlinear Power Transmission Limits in Optical Fiber Devices," *Proc. IEEE* **134**:180–182 (1987).
34. R. H. Stolen, "Phase-Matched Stimulated Four-Photon Mixing in Silica-Fiber Waveguides," *IEEE J. Quantum Electron.* **11**:100–103 (1975).
35. R. W. Tkach, A. R. Chraplyvy, F. Forghieri, A. H. Gnauck, and R. M. Derosier, "Four-Photon Mixing and High-Speed WDM Systems," *IEEE Journal of Lightwave Technology,* vol. 13, pp. 841–849 (1995).
36. F. Forghieri, R. W. Tkach, and A. R. Chraplyvy, and D. Marcuse, "Reduction of Four-Wave Mixing Crosstalk in WDM Systems Using Unequally-Spaced Channels," *IEEE Photon. Technol. Lett.* **6**:754–756 (1994).
37. AT&T Network Systems data sheet 4694FS-Issue 2 LLC, "TrueWave Single Mode Optical Fiber Improved Transmission Capacity," December 1995.
38. D. Marcuse, A. R. Chraplyvy, and R. W. Tkach, "Effect of Fiber Nonlinearity on Long-Distance Transmission," *IEEE J. Lightwave Technol.* **9**:121–128 (1991).
39. E. A. Golovchenko, N. S. Bergano, and C. R. Davidson, "Four-Wave Mixing in Multispan Dispersion Managed Transmission Links," *IEEE Photon. Technol. Lett.* **10**:1481–1483 (1998).
40. M. Jinno et al, "1580nm Band, Equally-Spaced 8X10 Gb/s WDM Channel Transmission Over 360km (3X120km) of Dispersion-Shifted Fiber Avoiding FWM Impairment," *IEEE Photon. Technol. Lett.* **10**:454–456 (1998).

41. H. Ono, M. Yamada, and Y. Ohishi, "Gain-Flattened Er^{3+}-Doped Fiber Amplifier for A WDM Signal in the 1.57–1.60μm Wavelength Region," *IEEE Photon. Technol. Lett.* **9**:596–598 (1997).
42. P. O. Hedekvist, M. Karlsson, and P. A. Andrekson, "Fiber Four-Wave Mixing Demultiplexing with Inherent Parametric Amplification," *IEEE J. Lightwave Technol.* **15**: 2051–2058 (1997).
43. R. Hui, M. O'Sullivan, A. Robinson, and M. Taylor, "Modulation Instability and Its Impact on Multispan Optical Amplified IMDD Systems: Theory and Experiments," *IEEE J. Lightwave Technol.* **15**: 1071–1082 (1997).
44. A. H. Gnauck, R. M. Jopson, and R. M. Derosier, "10 Gb/s 360 km Transmission over Dispersive Fiber Using Midsystem Spectral Inversion," *IEEE Photon. Technol. Lett.* **5**:663–666 (1993).
45. A. H. Gnauck, R. M. Jopson, and R. M. Derosier, "Compensating the Compensator: A Demonstration of Nonlinearity Cancellation in a WDM System," *IEEE Photon. Technol. Lett.* **7**:582–584 (1995).

CHAPTER 4

SOURCES, MODULATORS, AND DETECTORS FOR FIBER-OPTIC COMMUNICATION SYSTEMS

Elsa Garmire
Dartmouth College
Hanover, New Hampshire

4.1 INTRODUCTION

Optical communication systems utilize fiber optics to transmit the light that carries the signals. Such systems require optoelectronic devices as sources and detectors of such light, and they need modulators to impress the telecommunication signals onto the light. This chapter outlines the basics of these devices. Characteristics of devices designed for both high-performance, high-speed telecommunication systems (*telecom*) and for low-cost, more modest performance data communication systems (*datacom*) are presented. Sources for telecom are edge-emitting lasers, including double heterostructure (DH), quantum well (QW), strained layer (SL), distributed feedback (DFB), and distributed Bragg reflector (DBR) lasers. Operating characteristics of these edge-emitting lasers include threshold, light-out versus current-in, spatial, and spectral characteristics. The transient response includes relaxation oscillations, turn-on delay, and modulation response. The noise characteristics are described by relative intensity noise (RIN), signal-to-noise ratio (SNR), mode partition noise (in multimode lasers), and phase noise (which determines linewidth). Frequency chirping broadens the linewidth, described in the small and large signal regime; external optical feedback may profoundly disturb the stability of the lasers and may lead to coherence collapse.

Semiconductor lasers usually have a laser cavity in the plane of the semiconductor device, and emit light out through a cleaved edge in an elliptical output pattern. This output is not ideally suited to coupling into fibers, which have circular apertures. Low-cost systems, such as datacom, put a premium on simplicity in optical design. These systems typically use multimode fibers and surface-emitting light-emitting diodes (LEDs). The LEDs are less temperature dependent than lasers and are more robust, but they typically are slower and less efficient. Those LEDs applicable to fiber optics are described here, along with their operating and transient response characteristics. Edge-emitting LEDs have some niche fiber-optic applications and are briefly described.

Copyright 2001 by The McGraw-Hill Companies, Inc. Click Here for Terms of Use.

Recently, vertical cavity surface-emitting lasers (VCSELs) have been developed, which have vertical laser cavities that emit light normal to the plane of the semiconductor device. Fibers couple more easily to these surface-emitting sources, but their laser performance is usually degraded compared to that of the edge-emitting sources. This chapter outlines typical VCSEL designs (material, optical, and electrical); their spatial, spectral, and polarization characteristics; and their light-out versus current-in characteristics. While most VCSELs are GaAs-based, rapid progress is being made toward long-wavelength InP-based VCSELs.

The most common modulators used in fiber-optic systems today are external lithium niobate modulators. These are usually used in *Y*-branch interferometric modulators, created by phase modulation from the electro-optic effect. These modulators are introduced here, along with a discussion of high-speed modulation, losses, and polarization dependence, and a brief description of optical damage and other modulator geometries. These devices provide chirp-free modulation that can be made very linear for applications such as cable TV.

An alternative modulator uses semiconductors, particularly quantum wells. This design has the advantage of allowing for more compact devices and monolithic integration. Typically, these are intensity modulators using electroabsorption. By careful design, the chirp in these modulators can be controlled and even used to counteract pulse spreading from chromatic dispersion in fibers. The quantum-confined Stark effect is described, along with the *pin* waveguides used as modulators and techniques for their integration with lasers. Their operating characteristics as intensity modulators, their chirp, and improvements available by using strained quantum wells are presented.

Some semiconductor modulators use phase change rather than absorption change. The electro-optic effect in III-V semiconductors is discussed, along with the enhanced refractive index change that comes from the quantum-confined Stark effect, termed *electrorefraction.* Particularly large refractive index changes result if available quantum well states are filled by electrons. The field-dependent transfer of electrons in and out of quantum wells in a barrier, reservoir, and quantum well electron transfer (BRAQWET) structure enables a particularly large refractive index change modulation. Phase-change modulators based on this principle can be used in interferometers to yield intensity modulators.

Detectors used in fiber systems are primarily *pin* diodes, although short descriptions of avalanche photodetectors (APDs) and metal-semiconductor-metal (MSM) detectors are provided. The geometry, sensitivity, speed, dark current, and noise characteristics of the most important detectors used in fiber systems are described.

Most of the devices discussed in this chapter are based on semiconductors, and their production relies on the ability to tailor the material to design specifications through *epitaxial growth.* This technology starts with a bulk crystal substrate (usually the binary compounds GaAs or InP) and employs the multilayered growth upon this substrate of a few micrometers of material with a different composition, called a *heterostructure. Ternary* layers substitute a certain fraction x for one of the two binary components. Thus, $Al_xGa_{1-x}As$ is a common ternary alloy used in laser diodes. Another common ternary is $In_xGa_{1-x}As$. Layers are *lattice matched* when the ternary layers have the same size lattice as the binary; otherwise, the epitaxial layer will have *strain.* Lattice-matched epitaxial layers require that the substituting atom be approximately the same size as the atom it replaces. This is true of Al and Ga, so that $Al_xGa_{1-x}As$ ternary layers are lattice matched to GaAs. The lowest-cost lasers are those based on GaAs substrates with $Al_xGa_{1-x}As$ ternary layers surrounding the active layer. These lasers operate at wavelengths near the bandgap of GaAs, about 850 nm, and are typically used in low-cost data communications (as well as in CD players).

The wavelengths required for laser sources in telecommunications applications are those at which the fiber has the lowest loss and/or dispersion, traditionally 1.55 and 1.3 μm. There is no binary semiconductor with a bandgap at these wavelengths, nor is there a lattice-matched ternary. The $In_xGa_{1-x}As$ ternary will be strained under compression when it is grown on either GaAs or InP, because indium is a much bigger atom than gallium, and arsenic is much bigger than phosphorus. The way to eliminate this strain is to use a fourth small atom to reduce the size of the lattice back to that of the binary. This forms a *quaternary.* The hetero-

structure most useful for fiber-optics applications is based on InP substrates. The quaternary $In_xGa_{1-x}As_yP_{1-y}$ is commonly used, with the compositions x and y chosen to simultaneously provide the desired wavelength and lattice match. These quaternary heterostructures are the basis for much of the long-wavelength technology: sources, modulators, and detectors.

Earlier volumes of this handbook discuss the basics of lasers (Vol. I, Chap. 13), LEDs (Vol. I, Chap. 12), modulators (Vol. II, Chap. 13), and detectors (Vol. I, Chaps. 15 to 17). The reader is referred there for general information. This chapter is specific to characteristics that are important for fiber communication systems.

4.2 DOUBLE HETEROSTRUCTURE LASER DIODES

Telecommunications sources are usually edge-emitting lasers, grown with an active laser layer that has a bandgap near either 1.55 or 1.3 μm. These are quaternary layers consisting of $In_xGa_{1-x}As_yP_{1-y}$, grown lattice-matched to InP. The materials growth and fabrication technology had to be developed specifically for telecommunication applications and is now mature. These lasers are more temperature sensitive than GaAs lasers, and this fact has to be incorporated into their use. For telecom applications they are often provided with a thermoelectric cooler and are typically provided with a monitoring photodiode in the laser package, in order to provide a signal for temperature and/or current control.

Today's telecom systems use single-mode fibers, which require lasers with a single spatial mode. In order to avoid dispersion over long distances, a single frequency mode is necessary. These requirements constrain the geometry of laser diodes (LDs) used for telecom applications, as discussed in the next section. Following sections discuss the operating characteristics of these LDs and their transient response and noise characteristics, both as isolated diodes and when subject to small reflections from fiber facets. The modulation characteristics of these diodes are discussed, along with frequency chirping. Advanced laser concepts, such as quantum well lasers, strained layer lasers, and lasers with distributed reflection (DFB and DBR lasers), are also introduced.

A typical geometry of an edge-emitting InGaAsP/InP laser is shown in Fig. 1. The active quaternary laser region is shown crosshatched. It is from this region that light will be emitted. Traditionally, these active regions have uniform composition and are lattice matched to the substrate. More advanced laser diodes, often used for telecom applications, have active regions containing one or more quantum wells and may be grown to incorporate internal strain in the active region. Both these characteristics are described in a separate section later in this chapter.

The design of a double heterostructure laser diode requires optimization of the issues discussed in the following subsections.

Injection of a Population Inversion into the Active Region

This is necessary so that stimulated emission can take place. This is done by placing the active region between p and n layers, and forward-biasing the resulting diode. Electrons are injected into the active region from the n side and holes are injected from the p side; they become *free carriers.* Efficient electrical injection requires high-quality ohmic contacts attached to the n and p layers; electrical current through the junction then drives the laser.

Confinement of Carriers Within the Plane of the Active Layer

This is done by growing the active region as a thin layer of thickness d and surrounding it with layers of wider bandgap material, as shown in Fig. 2*a*. In quaternary lasers, wider bandgap

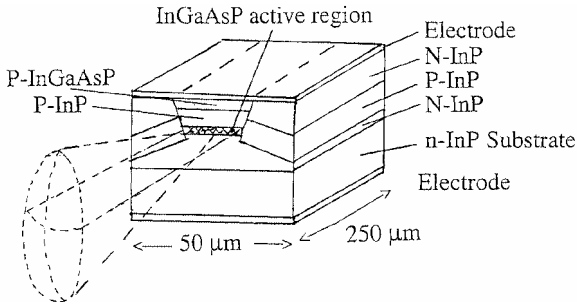

FIGURE 1 Typical geometry for an edge-emitting long-wavelength laser diode, as used in telecommunication systems. Light travels back and forth between cleaved mirror facets, confined to the active InGaAsP region by the buried heterostructure, and is emitted out of the crosshatched region, where it diffracts to the far-field. The current is confined to the stripe region by the current-blocking *npn* structure on either side.

material is provided by decreasing x and y relative to their values in the active region. Stimulated emission during electron-hole recombination in the narrow bandgap active layer provides the laser light. The thinner the active layer, the higher its gain. When the active layer thickness is as small as a few tens of nanometers, the free electron and hole energy levels become quantized in the growth direction, and the active layer becomes a *quantum well* (QW). Quantum wells have higher gain than bulk semiconductor active layers, and thus one or more quantum wells are often used as the active layers (see separate section later in this chapter).

Confinement of Light Near the Active Layer

Stimulated emission gain is proportional to the product of the carrier and photon densities, so that edge-emitting lasers require the highest possible light intensity. This is done by containing the light in an optical waveguide, with a typical light profile as shown in Fig. 2*b.* To achieve optical confinement, the layers surrounding the waveguide must have lower refractive index. It is fortunate that higher-bandgap materials that confine carriers also have smaller refractive index, and so the active layer automatically becomes a waveguide.

Proper optical confinement requires a single waveguide mode. This means that the waveguide layer must be thinner than the cutoff value for higher-order modes. The waveguide thickness d_g must be small enough that

$$d_g k_o \sqrt{n_g^2 - n_c^2} \equiv V < \pi \tag{1}$$

where n_g is the refractive index of the waveguide layer (usually the active layer), n_c is the refractive index of the surrounding cladding (usually the p and n layers), and $k_o = 2\pi/\lambda$, where λ is the free-space wavelength of the laser light. Typically, $n_g - n_c \sim 0.2$ and $d_g < 0.56$ μm for $\lambda = 1.3$ μm. The parameter V is usually introduced to characterize a waveguide.

If the waveguide is too thin, however, the waveguided optical mode spreads out beyond the waveguide layer. The fraction of optical power Γ_g (called the *waveguide confinement factor*) that remains in the waveguide layer of thickness d_g is given approximately by[1]:

$$\Gamma_g = \frac{V^2}{V^2 + 2} \tag{2}$$

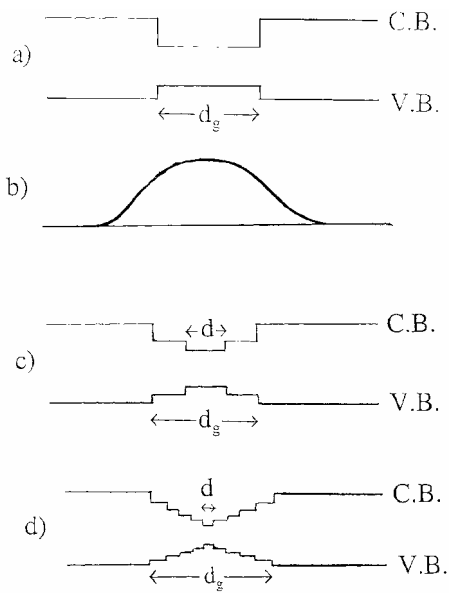

FIGURE 2 Conduction band (CB), valence band (VB), and guided optical mode as a function of position in the growth direction, near the active region in typical semiconductor laser geometries: (*a*) double heterostructure (DH) band structure, in which free carriers and light are both confined in the same region of small-bandgap material (of width d_g), surrounded by higher-bandgap cladding material; (*b*) near-field spatial profile for light guided in layer of width d_g; (*c*) separate confinement heterostructure (SCH) band structure, in which the free carriers are confined in a smaller active region (of width d) than the optical wave; and (*d*) graded index separate confinement heterostructure (GRINSCH), in which the composition of the cladding is graded in order to focus the light more tightly to the active region (deepest well) containing the free carriers.

As d_g becomes small, the confinement factor becomes small. When the carriers are confined in very thin layers, such as in quantum wells, the electrical carrier confinement layer cannot serve as an effective optical waveguide because the confinement factor is too small. Then a thicker waveguide region is used, and the photons and carriers are separately confined in a geometry called a *separate confinement heterostructure* (SCH), as shown in Fig. 2*c.* In this case the optical confinement factor, defined by the fraction of photons in the active layer of thickness d, is $\Gamma = \Gamma_g(d/d_g)$.

The light can be more effectively focused into a thin active layer by grading the refractive index in the separate confinement region, called a *graded index SCH* (GRINSCH) laser, shown in Fig. 2*d.* This graded refractive index is produced by growing material with varying bandgaps within the waveguide layer. Grading can be achieved by several discrete layers, as shown, or by grading many ultrathin layers with slight compositional differences. In either

case, the focusing property of a GRINSCH structure can be approximated by fitting the graded refractive index to a parabolic refractive index profile $n(x)$ such that:

$$n(x)^2 = n_g^2\left(1 - \frac{x^2}{x_o^2}\right)$$

where x_o is related to the curvature of the refractive index near $x = 0$: $x_o = (n_g/n'')^{1/2}$, where $n'' \equiv \partial^2 n/\partial x^2$ near $x = 0$. The mode guided by this profile has a gaussian beam-intensity profile:

$$I(x) = I_o \exp\left(\frac{-x^2}{w^2}\right)$$

where $w^2 = x_o/k_g$ and $k_g = 2\pi n_g/\lambda$

Limiting Carrier Injection to Stripe Geometry

Lasers are most efficient when the drive current is limited to the width of the optically active laser area. This requires defining a narrow stripe geometry electrode by means of a window etched in an isolating oxide layer or by ion implantation to render either side of the stripe resistive. More complex laser structures, such as those used in telecommunications applications, often define the conductive stripe electrode by using current-blocking *npn* layers grown on either side of the electrode, as shown in Fig. 1. The *npn* layers, consisting of back-to-back diodes, do not conduct current.

Injected carriers do not usually need lateral confinement, except to achieve the highest possible efficiency. Lateral free-carrier confinement will occur as a by-product of lateral optical confinement, which is discussed next.

Lateral Confinement of Light

The simplest laser diode structures do not specifically confine light laterally, except as the result of the stripe geometry carrier injection. These are called *gain-guided* lasers because high gain in the stripe region, due to the presence of free carriers, introduces a complex refractive index that guides the light laterally. Gain-guided lasers tend to be multimode (both lateral spatial modes and longitudinal frequency modes) unless the stripe is very narrow (<10 μm). In this case, the spatial far-field pattern has "rabbit ears," a double-lobed far-field pattern that is typically not very useful for coupling into single-mode fibers. Thus, gain-guided lasers are not usually used for telecommunications.

High-quality single-mode lasers for telecom applications typically require a means for creating a real refractive index difference laterally across the laser. The lowest threshold lasers use *buried heterostructure* (BH) lasers, the geometry shown in Fig. 1. After most of the layers are grown, the sample is taken out of the growth chamber and a stripe geometry mesa is etched. Then the sample is returned to the growth chamber, and one or more cladding layers with lower refractive index (higher bandgap) are grown, typically InP, as shown in Fig. 1. When the regrowth is planar, these are called *planar buried heterostructure* (PBH) lasers. The result is a real refractive index guide in the lateral dimension. The width of these *index-guided* laser stripes may be anything from 1 μm to more than 10 μm, depending on the refractive index difference between the active stripe and the lateral cladding material. Equation (1), which specifies the condition for single mode, applies here, with d_g as the width of the lateral index guide and n_c defined by the regrown material. A typical lateral width for low-threshold BH lasers is 3 μm.

A laser geometry that is much simpler to fabricate and has a higher reliability in production than that of BH lasers is the *ridge waveguide* (RWG) laser, shown in Fig. 3. The fabrication starts with the growth of a separate confinement heterostructure (sometimes with the addition of a thin etch-stop layer just after the top waveguide layer), followed by a stripe mesa etch down to the waveguide layer, finishing with planarization and contacting to the stripe. The etch leaves a ridge of *p*-cladding material above the waveguide layer, which causes *strip loading,* raising the effective refractive index locally in the stripe region, thereby creating lateral confinement of the light. Although the RWG laser is attractive because of its easy fabrication process, its threshold current is relatively high.

Retroreflection of Guided Light Along the Stripe

Light is usually reflected back and forth inside the laser cavity by Fresnel reflection from cleaved end facets. Since the waveguide refractive index is $n_g \sim 3.5$, the natural Fresnel reflectivity at an air interface, $R = [(n_g - 1)/(n_g + 1)]^2$, is ~0.3. This rather low reflectivity means that semiconductor lasers are high gain, requiring enough amplification that 70 percent of the light is regenerated on each pass through the active medium.

Relying on Fresnel reflection means that both facets emit light. The light emitted out the back facet may be recovered by including a high-reflectivity multilayer coating on the back facet, as is typically done in most telecom lasers. Sometimes a coating is also provided on the front facet in order to alter its reflectivity, typically to lower it, which increases the output power (as long as the gain is high enough to overcome the large loss upon reflection). The reflectivities must be such that the laser can obey the laser operating condition, which states that in a single round-trip through a laser of length L, the increase in optical power from gain must balance the reduction from finite reflectivity, so that their product is unity. That is,

$$R_1 R_2 \exp(2 g_L L) = 1 \tag{3}$$

where R_1 and R_2 are the reflectivities of the two facets and g_L is the *modal gain per unit length* (as experienced by the waveguided laser mode), with a subscript L to represent that the gain is measured with respect to length. If $R_1 = R_2 = 0.3$, then $g_L L = 1.2$. Typical laser diodes have lengths of 400 μm, so $g_L \sim 30\ \text{cm}^{-1}$.

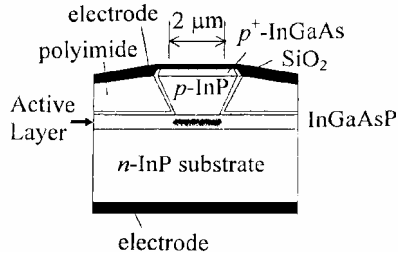

FIGURE 3 Geometry for a ridge waveguide (RWG) laser, fabricated by a single epitaxial growth followed by a mesa etch and planarization with polyimide. Light is confined to the region under the *p*-InP etched mesa by strip loading, which increases the effective refractive index in the waveguide region under the etched mesa.

In-plane retroreflection can also be achieved by using distributed feedback created from a grating impressed on top of the active layer. This method enables the construction of *distributed feedback* (DFB) lasers and *distributed Bragg reflector* (DBR) lasers, which are discussed later in a separate section.

Mounting so that Light is Edge-Emitted

Because the light is emitted out of the facet laterally, there must be a clear optical path for the light as it exits the laser. In many cases, the light is mounted with the active layer down, very close to the copper (or diamond) heat sink, in order to maximize cooling.[2] In this case, the laser chip must be placed at the very edge of the heat-sink block, as shown in Fig. 4*a.*

In some cases, the laser is mounted with its active region up with its substrate next to the heat sink. The edge alignment is not so critical in this case, but of course the laser light will still be emitted in a direction parallel to the plane of the heat sink. Because the thermal conductivity of the heat sink is much higher than that of the substrate, only the lowest threshold lasers, operating at moderate power levels, are operated with the active region up.

Suitable Packaging in a Hermetic Enclosure

Water vapor can degrade bare facets of a semiconductor laser when it is operating; therefore, LDs are usually passivated (i.e., their facets are coated with protective layers), and/or they are placed in sealed packages. The LD may be placed in a standard three-pin semiconductor device package, such as a TO-46 can with an optical window replacing the top of the can, as shown in Fig. 4*a.* The LD should be situated near the package window because the light diverges rapidly after it is emitted from the laser facet. The package window should be antireflection coated because any light reflected back into the laser can have serious consequences on the stability of the output (see Sec. 3.5).

Many high-end applications require an on-chip power monitor and/or a controllable thermoelectric cooler. In this case a more complex package will be used, typically a 14-pin "butterfly" package, often aligned to a fiber pigtail, such as is shown in Fig. 4*b.* In the less expensive datacom applications, nonhermetic packages may be acceptable with proper capping and passivation of the laser surfaces.

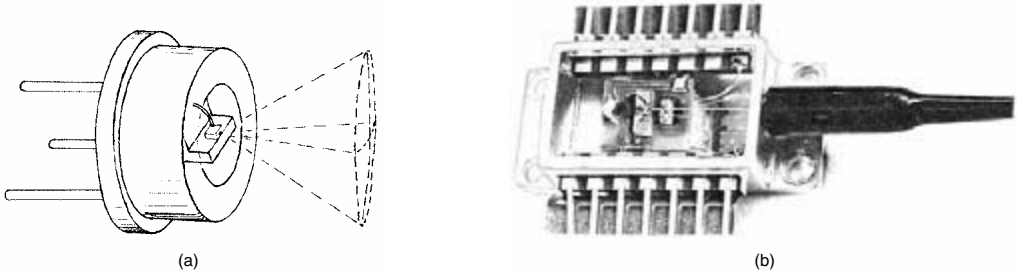

FIGURE 4 Packaging laser diodes: (*a*) typical hermetically sealed package showing heat sink and emission pattern for a laser diode with its active region placed down on a copper (or diamond) heat sink; and (b) typical butterfly package, showing laser in the middle, monitoring photodiode (behind), and fiber alignment chuck in front, all mounted on a thermoelectric cooler. Photo provided by Spectra-Diode Laboratories.

Fiber Pigtail Connection

Because light diverges at a rather large angle as it comes out of an edge-emitting laser (as discussed later), it is often desirable to use a laser provided with a *fiber pigtail,* which is a prealigned length of fiber that can be spliced or connected to the telecom fiber in the field. There will be an inevitable reduction in output power (compared to that of a laser with no pigtail) because of finite coupling efficiency into the pigtail, but the output will be immediately useful in a telecom system. The alternative to using a fiber pigtail is the use of a microlens—often a graded index (GRIN) lens, discussed elsewhere in this volume.

Long Life

Early lasers showed degradation with running time, but those problems have been solved, and it is expected that the semiconductor lasers used in telecom systems should last hundreds of thousands of hours. However, this requires that care be taken in their use. In particular, large reverse-bias static voltages can break down the *pn* diode. Thus, protection from electrostatic shock while handling and from reflected reverse-bias electrical currents during operation should be maintained. In addition, if LDs are driven with too much forward-bias current, the optical output can be so large that the light may erode the facet out of which it is emitted. Since the threshold is strongly temperature dependent, a laser driven at constant current that becomes too cold can emit too much light, with resulting optical damage. Thus, many telecom lasers have monitoring photodiodes to control the laser output and ensure that it stays within acceptable bounds.

4.3 OPERATING CHARACTERISTICS OF LASER DIODES

The principles of semiconductor laser operation are shown in Vol. I, Chap. 13 of this handbook. A forward-biased *pn* junction injects carriers into the active region. As the drive current increases, the carrier density in the active region increases. This reduces the absorption from an initially high value (at thermal equilibrium the absorption coefficient $\alpha \approx 500\ \text{cm}^{-1}$) to zero, at which point the active layer becomes transparent at the prospective laser wavelengths. An active layer is characterized by its carrier density at transparency N_{tr}. Typically, $N_{\text{tr}} \approx 10^{18}\ \text{cm}^{-3}$. Above this carrier density, stimulated emission occurs, with a gain proportional to the diode carrier density above transparency. The gain depends on the detailed device design, taking into account the issues enumerated in the previous section and the materials involved. The gain is sizeable only in direct-band semiconductors (semiconductors based on the III-V or II-VI columns of the periodic table).

Laser Threshold

Threshold is given by the requirement that the round-trip optical gain due to stimulated emission must equal the round-trip optical loss due to the sum of the transmission out the end facets and any residual distributed loss. Gain occurs only for light that is actually in the active region, and not for the fraction of waveguided light that extends outside the active region. Typically, the *local* gain per unit length G_L is defined as that experienced locally by light inside the active region. (The *modal* gain per unit length is $g_L = \Gamma\, G_L$.) Near transparency, the gain depends linearly on carrier density N:

$$G_L = a_L \frac{N - N_{\text{tr}}}{N_{\text{tr}}} \tag{4}$$

where a_L is the proportionality constant in units of length ($a_L \equiv N\,\partial G_L/\partial N$ near N_{tr}). When $N = 0$, $G_L = -a_L$, which is the loss per unit length in the unpumped active region (assuming the gain is linear in N). Typically, $a_L \sim 250\ \text{cm}^{-1}$.

The current density (J) is related to the carrier density through

$$J = \frac{eNd}{\tau} \tag{5}$$

where τ is the lifetime of the electron-hole pairs. The transparency current density for $d = 0.15$ μm, $N_{tr} = 10^{18}\ \text{cm}^{-3}$, and $\tau = 2$ ns is 1200 A/cm^2. The threshold condition can be found by taking the natural logarithm of Eq. (3):

$$g_{L,\text{th}} = G_{L,\text{th}}\Gamma = \alpha_i + \alpha_m \tag{6}$$

where α_m is the mirror reflectivity amortized over length, $2\alpha_m L = \ln(1/R_1R_2)$; and α_i represents any internal losses for the laser mode, also amortized over length.

Combining Eqs. (2) through (6), along with the fact that a laser diode with stripe width w and length L will have a current $I = JwL$, gives

$$I_{\text{th}} = I_{\text{tr}} + \frac{ewN_{\text{tr}}}{\tau a_L}\left[\frac{1}{2}\ln\left(\frac{1}{R_1R_2}\right) + \alpha_i L\right] d\left(1 + \frac{2}{V^2}\right) \tag{7}$$

where the waveguide V parameter is from Eq. (1) with $d = d_g$. Note that when the internal losses are small, the threshold current is independent of device length L, but depends on the reflectivity of the facets. Note also that the longer the spontaneous lifetime, the lower the threshold current density (although this may make a long turn-on delay, as discussed later). Finally, as expected by the relation between current and current density, a thinner stripe width w will lower the threshold current (consistent with appropriate spatial output, as discussed later). The current density at transparency N_{tr} is a basic property of the gain curve of the active region. It is smaller for quantum well lasers (discussed later) than for thicker active regions.

Note that because V is linearly proportional to d there is an optimal active layer thickness, a trade-off between increasing the carrier density as much as possible, but not so much as to lose optical confinement. The optimum thickness for 1.3-μm lasers is 0.15 μm; for 1.55-μm lasers it is comparable (0.15 – 0.18 μm). Threshold currents for broad-area DH lasers can be under ~500 A/cm^2 at 1.3 μm and ~1000 A/cm^2 at 1.55 μm. Confining carriers and light separately can beat this requirement, a trick used in designing quantum well lasers.

Light Out Versus Current In (the *L-I* Curve)

Below laser threshold only spontaneous emission is observed, which is the regime of the LED, as discussed in Sec. 4.8. In the spontaneous regime, the output varies linearly with input current and is emitted in all directions within the active region. As a result, a negligible amount of light is captured by the single-mode fiber of telecom below threshold.

Above threshold, the electrical power is converted to optical power. In general, the light will come out of both facets, and the amount of light reflected out the front facet depends on the rear facet reflectivity. When 100 percent mirror is placed on the back facet, the optical power at photon energy $h\nu$ (wavelength $\lambda = c/\nu$) emitted out the front facet is

$$\mathcal{P}_{\text{out}} = \frac{h\nu}{e}\,\frac{\alpha_m}{\alpha_m + \alpha_i}\,(I - I_{\text{th}} - I_L)\,\eta_i \tag{8}$$

where η_i is the *internal quantum efficiency,* which is the fraction of injected carriers that recombine by radiative recombination (usually close to unity in a well-designed semiconduc-

tor laser), and I_L is any leakage current. This equation indicates a linear dependence between light out and current above threshold (for constant quantum efficiency). The power out will drop by a factor of 2 if the back facet has a reflectivity equal to that of the front facet, since half the light will leave out the back.

From Eq. (8) can be calculated the *external slope efficiency* of the LD, given by $\partial \mathcal{P}_{\text{out}}/\partial I$. This allows the *differential quantum efficiency* η_D to be calculated:

$$\eta_D \equiv \frac{e}{h\nu} \frac{\partial \mathcal{P}_{\text{out}}}{\partial I} = \eta_i \frac{\alpha_m}{\alpha_m + \alpha_i} \tag{9}$$

This expression assumes that $\mathcal{P}_{\text{out}}$ includes the power out *both* facets.

The internal quantum efficiency depends on the modes of recombination for carriers. The rate of carrier loss is the sum of spontaneous processes, expressed in terms of carrier density divided by a lifetime τ_e, and stimulated emission, expressed in terms of gain per unit time G_T and photon density P:

$$R(N) = \frac{N}{\tau_e} + G_T(N)P \tag{10}$$

The spontaneous carrier lifetime is given by:

$$\frac{1}{\tau_e} = A_{\text{nr}} + BN + CN^2 \tag{11}$$

which includes spontaneous radiative recombination, given by BN. (The dependence on N results from needing the simultaneous presence of an electron and a hole, which have the same charge densities because of charge neutrality in undoped active regions.) The nonradiative recombination terms that decrease the quantum efficiency below unity are a constant term A_{nr} (that accounts for all background nonradiative recombination) and an Auger recombination term (with coefficient C) that depends on the square of the carrier density and comes from processes involving several carriers simultaneously. This term is particularly important in long-wavelength lasers where the Auger coefficient C is large. Stimulated emission is accounted for by gain in the time domain G_T, which depends on N (approximately linearly near threshold). The group velocity v_g converts gain per unit length G_L into a rate G_T (gain per unit time), $G_T \equiv v_g G_L$. We can define a gain coefficient in the time domain $a_T = v_g a_L$ so that

$$G_T = a_T \frac{N - N_{\text{tr}}}{N_{\text{tr}}} \tag{12}$$

The internal quantum efficiency in a laser is the fraction of the recombination processes that emit light:

$$\eta_i = \frac{BN^2 + G_T(N)P}{A_{\text{nr}}N + BN^2 + CN^3 + G_T(N)P} \tag{13}$$

Referring to Eq. (9), the external quantum efficiency depends on the sources of intrinsic loss. In long-wavelength lasers, this is primarily absorption loss due to intervalence band absorption. Another source of loss is scattering from roughness in the edges of the waveguide.

Figure 5 shows a typical experimental result for the light out of a laser diode as a function of applied current (the so-called *L-I* curve) for various temperatures. It can be seen that the linear relation between light out and current saturates as the current becomes large enough, particularly at high temperatures. Three main mechanisms have been proposed for the decrease in external slope efficiency with increasing current, each of which can be seen in the form of Eq. (9):

1. The leakage current increases with injection current.
2. Junction heating reduces recombination lifetime and increases threshold current.
3. The internal absorption increases with injection current.

When there is more than one laser mode (longitudinal or transverse) in the LD, the *L-I* curve has *kinks* at certain current levels. These are slight abrupt reductions in light out as the current increases. After a kink the external slope efficiency may be different, along with different spatial and spectral features of the laser. These multimode lasers may be acceptable for low-cost communication systems, but high-quality communication systems require single-mode lasers that do not exhibit such kinks in their *L-I* curves.

Temperature Dependence of Laser Properties

The long-wavelength lasers are more typically sensitive to temperature than are GaAs lasers. This sensitivity is usually expressed as an experimentally measured exponential dependence of threshold on temperature *T*:

$$I_{\text{th}}(T) = I_o \exp\left(\frac{T}{T_o}\right) \tag{14}$$

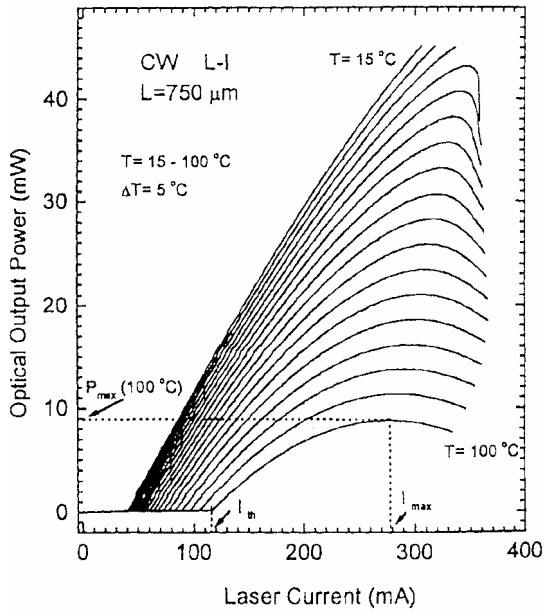

FIGURE 5 Typical experimental result for light out versus current in (the *L-I* curve). These results are for diodes operating at 1.3 μm, consisting of strained layer multiple quantum well InGaAsP lasers measured at a series of elevated temperatures.[3]

where T_o is a characteristic temperature (in degrees Kelvin) that expresses the measured thermal sensitivity. This formula is valid over only a limited temperature range, because it has no real physical derivation, but it has proved convenient and is often quoted. The data in Fig. 5 correspond to $T_o \approx 80$ K. The mechanisms for this sensitivity to temperature depend on the material system begin used. In long-wavelength double heterostructure lasers, T_o appears to be dominated by Auger recombination. However, in short-wavelength GaAs lasers and in strained layer quantum wells, where Auger recombination is suppressed, T_o is higher and is attributed to intervalence band absorption and/or carrier leakage over the heterostructure barrier, depending on the geometry. Typical long-wavelength DH lasers have T_o in the range of 50 to 70 K. Typical strained layer quantum well lasers have T_o in the range of 70 to 90 K, although higher T_o can be achieved by incorporating aluminum in barriers, with as high as 143 K reported.[4] This temperature dependence limits the maximum optical power that can be obtained because of the phenomenon of *thermal runaway,* as shown at the highest temperatures in Fig. 5. While the power is usually increased by increasing the current, the junction temperature also increases (due to ohmic losses), so the threshold may increase and the output power may tend to decrease.

Various means for increasing T_o have been explored. The most effective way to increase T_o has proven to be the use of tensile strained quantum wells (discussed in Sec. 3.6). The result has been to increase T_o from ~50 K to as high as 140 K, comparable to that measured in GaAs. In double heterostructures, losses by carrier leakage can be reduced by using a dual active region for double carrier confinement, which has been demonstrated to achieve T_o values as high as 180 K in 1.3-μm InP lasers.[5]

In practice, many long-wavelength lasers require thermoelectric coolers to moderate the temperature. The temperature dependence of long-wavelength lasers may limit their performance at high temperatures, which in turn limits where they can be used in the field.

Spatial Characteristics of Emitted Light

Light is emitted out of the facet of the laser diode after it has been guided in both directions. It will diverge by diffraction, more strongly in the out-of-plane dimension, where it has been more strongly waveguided. The diffracting output is sketched in Fig. 1. The spatial characteristics of the output can be estimated by fitting the guided light to a gaussian beam and then calculating the far-field pattern. The *out-of-plane* near-field profile for the lowest order mode in an optical confinement layer of width d_g can be fit to a gaussian distribution exp $(-x^2/w^2)$ by[6]:

$$w = d_g\left(0.321 + \frac{2.1}{V^{3/2}} + \frac{4}{V^6}\right) \qquad \text{for } 1.8 < V < 6 \tag{15}$$

where V is from Eq. (1). The far-field diffraction angle can be found from the Fourier transform multiplied by the obliquity factor, resulting in a slightly different gaussian fit. The gaussian half-angle in the far field is given by[6]:

$$\theta_{ff} = \tan^{-1}\left(\frac{\lambda}{\pi w_o}\right) \tag{16}$$

where

$$w_o = d_g\left(0.31 + \frac{3.15}{V^{3/2}} + \frac{2}{V^6}\right) \qquad \text{for } 1.5 < V < 6.$$

Experimental data can be compared to the gaussian beam formula by remembering that the full-width half-maximum power FWHM $= w(2 \ln 2)^{1/2}$. For a typical strongly index-guided

buried heterostructure laser, the far-field FWHM angle out of plane is ~1 rad and in-plane is ~1/2 rad. These angles are independent of current for index-guided lasers. Separate confinement heterostructure lasers can have smaller out-of-plane beam divergences, more typically ~30°.

Single-mode lasers that are index guided in the lateral direction (buried heterostructure and ridge waveguide) will obey the preceding equations, with lateral divergence angles varying from 30° to 10°, depending on design. This beam width will also be independent of current. When lasers are gain guided laterally, the spatial variation of the gain leads to a complex refractive index and a curved wavefront. The result is that the equivalent gaussian lateral beam seems to have been emitted from somewhere inside the laser facet. The out-of-plane beam, however, is still index guided and will appear to be emitted from the end facet. This means that the output of a gain-guided laser has *astigmatism,* which must be compensated for by a suitably designed external lens if the laser is to be focused effectively into a fiber (as discussed elsewhere in this handbook).

If the laser emits a diverging gaussian beam with waist w, a lens can be used to focus it into a fiber. An effective thin lens of focal length f placed a distance d_1 after the laser facet will focus to a new waist w' given by:

$$w'^2 = w^2 \frac{f^2}{b^2 + X_1^2} \tag{17}$$

where

$$X_1 \equiv d_1 - f$$

$$b \equiv \pi w^2/\lambda$$

The distance d_2 from the lens to the new beam waist is given by:

$$X_2 = X_1 \frac{f^2}{X_1^2 + b^2} \tag{18}$$

where $$X_2 \equiv d_2 - f$$

This new waist must be matched to the fiber mode. Because of the large numerical aperture of laser light, simple lenses exhibit severe spherical aberration. Fiber systems usually utilize pigtailed fiber, butt coupled as close as possible to the laser, without any intervening lens. Typical coupling efficiencies are only a few percent. Alternatively, a ball lens may be melted directly onto a fiber tip and placed near the laser facet. Sometimes *graded index* (*GRIN*) lenses are used to improve coupling into fibers.

Gain-guided lasers with electrode stripe widths of >5 μm usually emit multiple spatial modes in the in-plane direction. These modes interfere laterally, producing a spatial output with multiple maxima and nulls. Such spatial profiles are suitable for multimode fiber applications, but cannot be coupled into single-mode fibers with high efficiency. They will diffract at an angle given by setting w equal to the minimum near-field feature size. If the stripe is narrow enough, gain-guided lasers are always single mode, but the double-lobed far-field spatial profile (from the complex refractive index in the gain medium) cannot be conveniently coupled into single-mode fibers.

Spectral Characteristics of Laser Light

In principle, a Fabry-Perot laser has many frequency modes with frequencies ν_m, given by requiring standing waves within the laser cavity. Since the mth mode obeys $m\lambda/2n = L$, where n is the refractive index experienced by the guided laser mode, then

$$\nu_m = \frac{mc}{2nL} \tag{19}$$

Taking the differential, the frequency difference between modes is

$$\Delta\nu = \frac{c}{2n_{\text{eff}}L} \tag{20}$$

where the *effective group refractive index* $n_{\text{eff}} = n + \nu(\partial n/\partial\nu)$. For typical semiconductor lasers, $n = 3.5$ and $n_{\text{eff}} = 4$, so that when $L = 250$ μm, the frequency difference between modes is $\Delta\nu = 150$ GHz, and since $\Delta\lambda = (\lambda^2/c)\Delta\nu$, when $\lambda = 1.5$ μm, the wavelength spacing is $\Delta\lambda \approx 1$ nm.

At any given instant in time, a single spatial mode emits in only one spectral mode. However, in multimode lasers, considerable *mode hopping* occurs, in which the LD jumps from one spectral mode to another very rapidly. Most spectral measurements are time averages and do not resolve this mode hopping, which can occur in nanoseconds or less. Explanations for the mode-hopping typically involve *spatial hole burning* or *spectral hole burning*. Hole burning occurs when the available carrier density is momentarily depleted, either spatially or spectrally. At that time an adjacent mode with a different (longitudinal or lateral) spatial profile or a different resonance wavelength may be more advantageous for laser action. Thus, the laser jumps to this new mode. The competition between different modes for available gain is a strong mechanism for creating lasers with multiple wavelength modes.

One way to provide a single spectral mode is to ensure a single (lateral) spatial mode. It has been found that single spatial mode lasers usually have single spectral modes, at least at moderate power levels. The only way to *ensure* a single-frequency LD is to ensure a single longitudinal mode by using distributed feedback, as discussed in Sec. 5.7.

Polarization

The emitted light from a typical semiconductor laser is usually linearly polarized in the plane of the heterostructure. While the gain in a semiconductor has no favored polarization dependence, the *transverse electric* (*TE*) *waveguide mode* (polarized in-plane) is favored for two reasons. First, the TE mode is slightly more confined than the *transverse magnetic* (TM) mode (polarized out-of-plane). Second, the Fresnel reflectivity off the cleaved end facets is strongly polarization sensitive. As waveguided light travels along the active stripe region, it can be considered to follow a zig-zag path, being totally internally reflected by the cladding layers. The total internal reflection angle for these waves is about 10° off the normal to the cleaved facets of the laser. This is enough to cause the *TM waveguide mode* to experience less reflectivity, while the TE-polarized mode experiences more reflectivity. Thus, laser light from LDs is traditionally polarized in the plane of the junction.

However, the introduction of strain (Sec. 4.6) in the active layer changes the polarization properties, and the particular polarization will depend on the details of the device's geometry. In addition, DFB and DBR lasers (Sec. 4.7) do not have strong polarization preferences, and they must be carefully designed and fabricated if well-defined single polarization is required.

4.4 TRANSIENT RESPONSE OF LASER DIODES

When laser diodes are operated by direct current, the output is constant and follows the *L-I* curve discussed previously. When the LD is rapidly switched, however, there are transient phenomena that must be taken into account. Such considerations are important for any high-

speed communication system, especially digital systems. The study of these phenomena comes from solving the semiconductor rate equations.[7]

Turn-on Delay

When a semiconductor laser is turned on abruptly by applying forward-biased current to the diode, it takes time for the carrier density to reach its threshold value and for the photon density to build up, as shown in the experimental data of Fig. 6. This means that a laser has an unavoidable turn-on time. The delay time depends on applied current and on carrier lifetime, which depends on carrier density N, as shown in Eq. (11). Using a differential analysis, the turn-on time for a laser that is switched from an initial current I_i just below threshold to I just above threshold is

$$\tau_d = \tau'(N_{\text{th}}) \frac{I_{\text{th}} - I_i}{I - I_{\text{th}}} \tag{21}$$

where $\tau'(N)$ is a differential lifetime given by

$$\frac{1}{\tau'} = A_{\text{nr}} + 2BN + 3CN^2 \tag{22}$$

When $I_i = 0$ and $I >> I_{\text{th}}$, the turn-on delay has an inverse current dependence:

$$\tau_d = \tau_e(N_{\text{th}}) \frac{I_{\text{th}}}{I} \tag{23}$$

When radiative recombination dominates, then $1/\tau_e \approx BN$ and $1/\tau' \approx 2BN \approx 2/\tau_e$, as seen by comparing the middle terms of Eqs. (11) and (22). For a 1.3-μm laser, $A_{\text{nr}} = 10^8$/s, $B = 10^{-10}$ cm^3/s, $C = 3 \times 10^{-29}$ cm^6/s, and $N_{\text{th}} \approx N_{\text{tr}} = 10^{18}$ cm^{-3}. Thus, $\tau_e = 5$ ns and a typical turn-on time at 1.5 times threshold current is 3 ns. The increase in delay time as the current approaches threshold is clearly seen in the data of Fig. 6. As a result, to switch a laser rapidly, it is necessary to switch it from just below threshold to far above threshold. However, Fig. 6 shows that under these conditions there are large transient oscillations, discussed next.

Relaxation Oscillations

An important characteristic of the output of any rapidly switched laser (not just semiconductor lasers) is the *relaxation oscillations* that can be observed in Fig. 6. These overshoots occur as the photon dynamics and carrier dynamics are coming into equilibrium. Such oscillations are characteristic of the nonlinear coupled laser rate equations and can be found by simple perturbation theory. These relaxation oscillations have a radian frequency Ω_R given, to first order, by[9]:

$$\Omega_R^2 = \frac{1 + \chi}{\tau_e \tau_p} \frac{I - I_{\text{th}}}{I_{\text{th}}} \tag{24}$$

where I is the current, I_{th} is the current at threshold, τ_p is the photon lifetime in the cavity, given by

$$v_g \tau_p = \frac{1}{\alpha_i + \alpha_m} \tag{25}$$

and

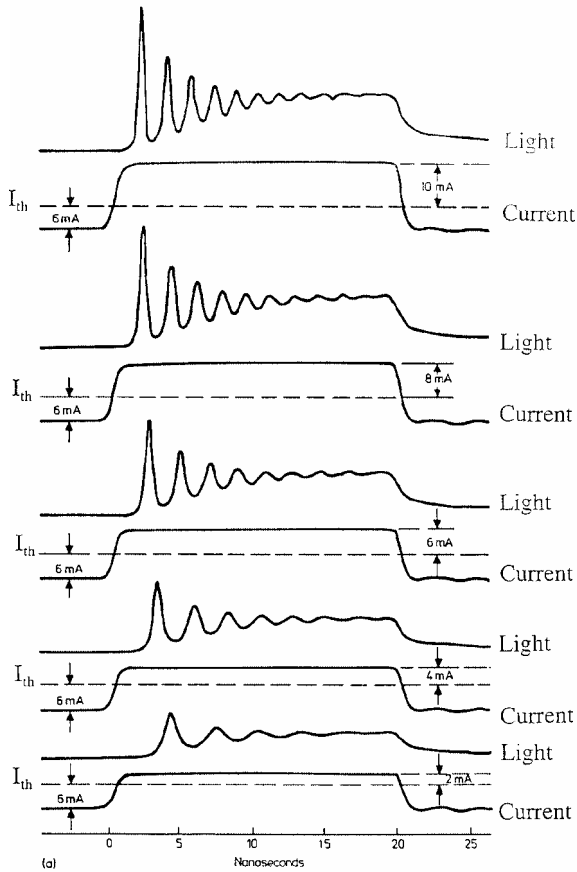

FIGURE 6 Experimental example of turn-on delay and relaxation oscillations in a laser diode when the operating current is suddenly switched from 6 mA below the threshold current of 177 mA to varying levels above threshold (from 2 to 10 mA). The GaAs laser diode was 50 μm long, with a SiO_2 defined stripe 20 μm wide. Light output and current pulse are shown for each case.[8]

$$\chi = \Gamma a_L v_g \tau_p = \Gamma a_T \tau_p = \Gamma \frac{a_L}{\alpha_i + \alpha_m} \tag{26}$$

where a_L is from Eq. (4). The factor χ is the ratio of the unpumped absorption loss to the cavity loss. For semiconductor lasers, χ is on the order of 1 to 3. It can also be shown that $\chi = I_{tr}/(I_{th} - I_{tr})$, where I_{tr} is the current at transparency.

When $\chi \approx 1$, at 1.5 times threshold current, where $(1 + \chi)(I - I_{th})/I_{th} \approx 1$, the time between successive relaxation oscillation maxima is approximately the geometric mean of the carrier and photon lifetimes: $\Omega_R^2 \approx 1/\tau_e \tau_p$. Typical numbers for semiconductor lasers are $\tau_e = 10$ ns, $\tau_p = 3$ ps,

so at 1.5 times threshold current, the relaxation oscillation frequency is $f_R = \Omega_R/2\pi = 1$ GHz, and the time between the relaxation oscillation peaks is 1 ns.

The decay rate of these relaxation oscillations γ_R is given by

$$2\tau_e\gamma_R = 1 + \chi\,\frac{I - I_{\text{th}}}{I_{\text{tr}}} = 1 + (1+\chi)\,\frac{I - I_{\text{th}}}{I_{\text{th}}} = 1 + \Omega_R^2\tau_e\tau_p \tag{27}$$

and is roughly 2 ns at twice threshold for typical heterostructure lasers. At 1.5 times threshold, when $\chi \approx 1$, $\gamma_R \approx 1/\tau_e$. The relaxation oscillations will last approximately as long as the spontaneous emission lifetime of the carriers.

This analysis employs several assumptions which do not seriously affect the relaxation oscillation frequency, but which will overestimate the time that relaxation oscillations will last. The analysis ignores *gain saturation,* which reduces gain with increased photon density P and is important at high optical powers. It also ignores the rate of spontaneous emission in the cavity R_{sp}, which is important at small optical powers. Finally, it ignores the impact of changing carrier density on spontaneous emission lifetime. A more exact formulation[10] includes these effects:

$$2\gamma_R = \frac{1}{\tau'} + P\left(\frac{\partial g_T}{\partial N} - \frac{\partial g_T}{\partial P}\right) + \frac{R_{\text{sp}}}{P} \tag{28}$$

where g_T is the modal gain per unit time. This more exact analysis increases the rate of decay, since the sign of $\partial g_T/\partial P$ is negative and also $1/\tau' \approx 2/\tau_e$. A more typical experimental decay rate for lasers at 1.3-μm wavelength is $\gamma \approx 3/\tau_e$.

The number of relaxation oscillations (before they die out) in an LD at 1.5 times threshold is proportional to $\Omega_R/\gamma_R \propto (\tau_e/\tau_p)$. The longer the carrier lifetime, the more relaxation oscillations will occur (because the carriers do not decay rapidly to steady state). Shorter carrier lifetimes also mean shorter turn-on times. Thus, achieving short carrier lifetimes by high carrier densities is important for high-speed semiconductor lasers. This can be achieved by using as small an active region as possible (such as quantum wells) and by reducing the reflectivity of the laser facets to raise the threshold carrier density.

The relaxation oscillations disappear if the current is just at threshold. However, we've also seen that under this situation the turn-on time becomes very long. It is more advantageous to turn the laser on fast, suffering the relaxation oscillations and using a laser designed to achieve a high decay rate, which means using the laser with the highest possible relaxation oscillation frequency.

Other useful forms for the relaxation oscillations are:

$$\Omega_R^2 = g_T g_T' P = \frac{g_T' P}{\tau_m} = g_T'\left(\frac{\mathcal{P}_{\text{out}}}{h\nu V_a}\,\frac{\alpha_m + \alpha_i}{\alpha_m}\right) \tag{29}$$

where $g_T' \equiv \partial g_T/\partial N = \Gamma a_T/N_{\text{tr}}$. These expressions can be found by inserting the following equations into Eq. (24):

$$I - I_{\text{th}} = \frac{\mathcal{P}_{\text{out}}}{h\nu}\,\frac{e}{\eta_D} \tag{30a}$$

$$\mathcal{P}_{\text{out}} = h\nu\left(\frac{P}{\tau_m}\right)V_a \tag{30b}$$

where $\tau_m = (v_g\alpha_m)^{-1}$ is the time it takes light to bleed out the mirror and

$$I_{\text{th}} = \frac{eN_{\text{th}}V_a}{\tau_e} \tag{30c}$$

$$g_T = \Gamma\, a_T \frac{(N - N_{\text{tr}})}{N_{\text{tr}}} \tag{30d}$$

so that $g_T' \equiv \partial g_T/\partial N = \Gamma\, a_T/N_{\text{tr}}$ and $N_{\text{tr}} = \Gamma a_T/g_T'$. Also

$$\chi = \frac{I_{\text{tr}}}{I_{\text{th}} - I_{\text{tr}}}, \qquad \text{so} \qquad 1 + \chi = \frac{I_{\text{th}}}{I_{\text{th}} - I_{\text{tr}}} \tag{30e}$$

$$\eta_D = \eta_i \left(\frac{\alpha_i}{\alpha_m + \alpha_i} \right) = \eta_i \left(\frac{\tau_p}{\tau_i} \right), \qquad \text{assuming} \qquad \eta_i \approx 1 \tag{30f}$$

Note that the relaxation oscillation frequency increases as the photon density increases, showing that smaller laser dimensions are better.

Relaxation oscillations can be avoided by biasing the laser just below threshold, communication systems often operate with a prebiased laser. In digital and high-speed analog systems, relaxation oscillations may limit speed and performance.

Modulation Response and Gain Saturation

The *modulation response* describes the amplitude of the modulated optical output as a function of frequency under small-signal current modulation. There is a resonance in the modulation response at the relaxation oscillation frequency, as indicated by the experimental data in Fig. 7. It is more difficult to modulate the laser, above the relaxation oscillation frequency. Carrying out a small-signal expansion of the rate equations around photon density P, the modulation response (in terms of current density J) is[12]:

$$\frac{\partial P}{\partial J} = \frac{(1/ed)(g_T' P + \beta_{\text{sp}}/\tau_e)}{(g_T' P/\tau_p + \beta_{\text{sp}}/\tau_e \tau_p - \omega^2) + j\omega\,(g_T' P + 1/\tau_e)} \tag{31}$$

where β_{sp} is the fraction of spontaneous emission that radiates into the mode ($\beta_{\text{sp}} = R_{\text{sp}}\tau_e/N$);

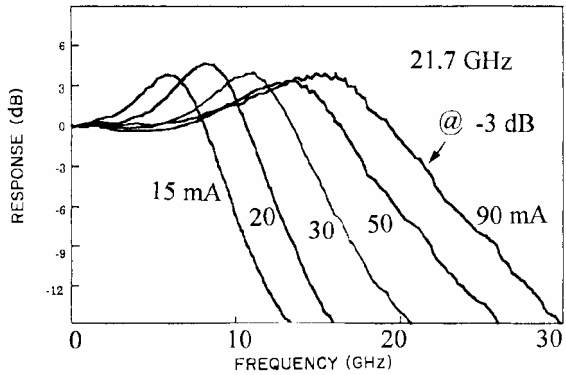

FIGURE 7 Measured small-signal modulation response of a high-speed DFB laser at several bias levels. Zero-dB modulation response is defined in terms of the low-frequency modulation response, Eq. (32).[11]

and, as before, τ_e is the spontaneous carrier lifetime, and $g_T' \equiv \partial g_T/\partial N = \Gamma a_T/N_{tr}$. This modulation response has the form of a second-order low-pass filter. Resonance occurs when $\omega^2 \approx g_T' P/\tau_p = \Omega_R^2$ (from Eq. (29), with negligible internal loss); that is, at the relaxation oscillation frequency.

The modulation response at a frequency well below the relaxation oscillation frequency can be expressed as the change in optical power $\mathcal{P}_{out}$ as a function of current I using the limit of Eq. (31) when $\omega \to 0$. From $\partial P/\partial J = \tau_p/ed$, and relating output power to photon density through $\mathcal{P}_{out} = (h\nu)(P/\tau_m)V_a$, the low frequency modulation response becomes

$$\frac{\partial \mathcal{P}_{out}}{\partial I} = \frac{h\nu}{\tau_m} V_a \frac{\partial P}{\partial J} \cdot \frac{1}{wL} = \frac{h\nu}{e} \cdot \frac{\tau_p}{\tau_m} = \frac{h\nu}{e} \cdot \frac{\alpha_m}{(\alpha_m + \alpha_i)} \tag{32}$$

which is expected from Eq. (8) when $\eta_i \to 1$.

The 3-dB modulation radian frequency bandwidth ω_B can be expressed in terms of the relaxation oscillation parameters by[13]:

$$\omega_B^2 = \Omega_R^2 - \gamma_R^2 + 2\sqrt{\Omega_R^2 (\Omega_R^2 + \gamma_R^2) + \gamma_R^4} \tag{33}$$

where the oscillation frequency Ω_R and damping rate γ_R are as previously described. The parameters are strongly power dependent and the bandwidth increases with optical power. When $\gamma_R << \Omega_R$, the 3-dB bandwidth $\omega_B \approx \sqrt{3}\,\Omega_R \propto \sqrt{P}$. At high optical powers the presence of gain saturation (reduced gain at high optical power densities) must be included; the modulation bandwidth saturates, and the limiting value depends on the way that the gain saturates with photon density. Using the following approximate expression for gain saturation:

$$g_T(N, P) = g_T' \frac{N - N_o}{\sqrt{1 + P/P_s}} \tag{34}$$

where N_o is the equilibrium carrier density and P_s is the saturation photon density, a simple expression can be found for the limiting value of the modulation bandwidth at high optical powers:

$$(\omega_{B,\max})^2 = \frac{3 g_T' P_s}{2\tau_p}$$

Typical numbers for a 1.55-μm InGaAsP laser are 20 to 40 GHz.

Frequency Chirping

When the carrier density in the active region is rapidly changed, the refractive index also changes rapidly, causing a frequency shift proportional to $\partial n/\partial t$. This broadens the laser linewidth from its original width of ~100 MHz into a double-peaked profile with a gigahertz linewidth, as shown in the experimental results of Fig. 8. The frequency spread is directly proportional to the dependence of the refractive index n on carrier density N. This is a complex function that depends on wavelength and degree of excitation, but for simplicity a Taylor expansion around the steady-state carrier density N_o can be assumed: $n = n_o + n_1(N - N_o)$, where $n_1 \equiv \partial n/\partial N$. The (normalized) ratio of this slope to that of the gain per unit length g_L is called the *linewidth enhancement factor* β_c.

$$\beta_c \equiv -2k_o \frac{\partial n/\partial N}{\partial g_L/\partial N} = -2k_o \frac{n_1}{g_L'} \tag{35}$$

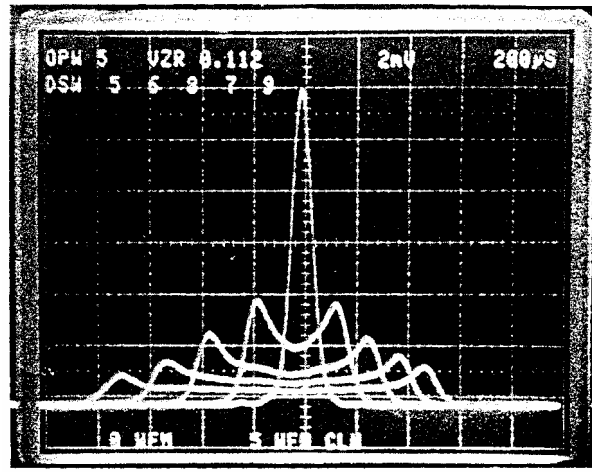

FIGURE 8 Time-averaged power spectra of 1.3 μm InGaAsP laser under sinusoidal modulation at 100 MHz. Horizontal scale is 0.05 nm per division. Spectrum broadens with increase in modulation current due to frequency chirping.[14]

The magnitude of the frequency spread between the double lobes of a chirped pulse, $2\delta\omega_{CH}$, can be estimated in the small-signal and large-signal regimes from analyzing the time dependence of a modulated pulse in terms of the sum of all frequency components.[15]

Small-Signal Modulation. For a modulation frequency ω_m that is less than the relaxation oscillation frequency, and assuming that $\gamma_R \ll \Omega_R$, a small modulation current I_m will cause a frequency chirp of magnitude

$$\delta\omega_{CH} = \frac{\beta_c I_m h_v}{2e\mathcal{P}_{out}} \left(\frac{\alpha_m}{\alpha_m + \alpha_i}\right)\sqrt{\omega_m^2 + \gamma_p^2} \tag{36}$$

where $\gamma_p = R_{sp}/P - (\partial g_T/\partial P)P$ (remembering that $\partial g_T/\partial P$ is negative). The origin of chirp is the linewidth enhancement factor β_c. It will be largest for gain-guided devices where β_c is a maximum. The chirp will be smaller in lasers with $\alpha_m \ll \alpha_i$, such as will occur for long lasers, where mirror loss is amortized over a longer length, but such lasers will have a smaller differential quantum efficiency and smaller relaxation oscillation frequency. Typical numbers at 25-mA modulation current can vary from 0.2 nm for gain-guided lasers to 0.03 nm for ridge waveguide lasers.

Large-Signal Modulation. There is a transient frequency shift during large-signal modulation given by:

$$\delta\omega_{CH} = \frac{\beta_c}{2}\left(\frac{1}{P}\frac{\partial P}{\partial t}\right) \tag{37a}$$

When a gaussian shape pulse is assumed, $\exp(-t^2/T^2)$, the frequency shift becomes

$$\delta\omega_{CH} \approx \beta_c/T \tag{37b}$$

The importance of the linewidth enhancement factor β_c is evident from this equation; its existence will inevitably broaden modulated laser linewidths.

4.5 NOISE CHARACTERISTICS OF LASER DIODES

Noise in LDs results from fluctuations in spontaneous emission and from the carrier generation-recombination process (shot noise). To analyze the response of LDs to noise, one starts with rate equations, introduces Langevin noise sources as small perturbations, and linearizes (performs a small-signal analysis). Finally, one solves in the frequency domain using Fourier analysis.[16, 17] Only the results are given here.

Relative Intensity Noise (RIN)

Noise at a given frequency is described in terms of *relative intensity noise,* defined by:

$$\text{RIN} = \frac{S_P(\omega)}{P_T^2} \tag{38}$$

where $S_P(\omega)$ is the photon noise spectral density (noise per unit frequency interval), and P_T is the total photon number, $P_T = PV_a$. The solution to the analysis for RIN is:

$$\text{RIN} = \frac{2\beta_{sp} I_{th}}{ePV_a} \cdot \frac{1/\tau'^2 + \omega^2 + (\partial g_T/\partial N)^2 \, P/(\beta_{sp} V_a)}{[(\Omega_R - \omega)^2 + \gamma_R^2][(\Omega_R + \omega)^2 + \gamma_R^2]} \tag{39}$$

where β_{sp} is the fraction of spontaneous emission emitted into the laser cavity, and is related to the spontaneous emission rate R_{sp} by $\beta_{sp}(I_{th}/eV_a) = R_{sp}$. As before, the photon density P can be related to the optical power out both facets by $\mathcal{P}_{out} = (h\nu)\, PV_a/\tau_m$. Note the significant enhancement of noise near the relaxation oscillation frequency $\omega = \Omega_R$ where the noise has its maximum value. An example of RIN as a function of frequency is shown in Fig. 9, for both low power and high power, showing that the RIN goes up as the total optical power decreases.

At low frequencies, and for $\gamma_R \ll \Omega_R$, the noise is proportional to the inverse fourth power of the relaxation oscillation frequency. Clearly, it is advantageous to use as high a relaxation oscillation frequency as possible to reduce RIN. Since the relaxation oscillation frequency is proportional to the square root of the power P, the RIN increases as $1/P^3$ as the power decreases. Inserting the expression for Ω_R into Eq. (39) gives:

$$\text{RIN}_{lf} = \frac{2\,\beta_{sp} I_{th} \tau_m^2 V_a^2}{eP_T^3 (\partial g_T/\partial N)^2} \left[\frac{1}{\tau'^2} + \left(\frac{\partial g_T}{\partial N} \right)^2 \frac{P}{\beta_{sp} V_a} \right] \tag{40}$$

Usually, the first term dominates. It can be seen that the volume of the active laser region V_a should be as small as possible, consistent with maintaining a significant power out.

Signal-to-Noise Ratio (SNR)

The *signal-to-noise ratio* (SNR) can be found in terms of the relaxation oscillation parameters using the expression for RIN (which assumes $\tau_e \Omega_R >> \gamma_R \Omega_R >> 1$) and the total photon number:

$$(\text{SNR})^2 = \frac{2\gamma_R e}{\beta_{sp} I_{th}} P_T = \frac{2\gamma_R e \tau_m}{\beta_{sp} I_{tr} h\nu} \mathcal{P}_{out} \tag{41}$$

As expected, the SNR increases with smaller spontaneous emission and larger laser power.

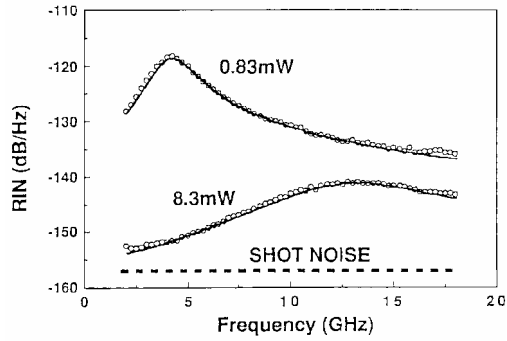

FIGURE 9 Measured relative intensity noise as a function of frequency in a multiple quantum well 1.5-μm laser diode, for optical power near threshold and high above threshold. The shot noise level for the higher power measurement is also shown.[18]

Far above threshold, inserting the value for the decay rate $\gamma_R \approx \tau_e/3$ gives

$$(\text{SNR})^2 = \frac{2e\tau_e\tau_m}{3\beta_{\text{sp}}I_{\text{th}}h\nu}\,\mathcal{P}_{\text{out}} \tag{42}$$

Gain saturation at high powers eventually limits the SNR to about 30 dB; while at powers of a few milliwatts it is 20 dB, with intensity fluctuation typically close to 1 percent.

Mode Partition Noise in Multimode Lasers

The preceding discussion of noise holds qualitatively for multimode lasers as long as all the laser modes are included. However, measurements made on any one mode show much more noise, particularly at low frequencies. This is due to the mode-hopping discussed previously, and is referred to as *mode partition noise.* That is, the power partitions itself between different laser modes in a way that keeps the overall intensity relatively constant, as shown by the solid line in Fig. 10. The power in each mode is not a steady function of time, because the power distribution among the modes changes with time. Whenever the distribution changes, the power output undergoes fluctuation, leading to a noise term on a nominally stable output. This leads to the enhanced RIN on the dominant mode in Fig. 10. Even an output whose spectrum looks nominally single mode, as shown in the inset of Fig. 10, can have a large RIN on the dominant mode. This is because the spectrum is time averaged. A side mode does not contain 5 percent of the power, for example; it contains 100 percent of the power for 5 percent of the time. This causes the very large RIN observed. The solution to avoiding this noise is to insist on a single longitudinal mode by using distributed feedback. Since lasers for telecommunication applications are typically single mode, we will not consider mode partition noise further. It becomes important for data communications based on multimode lasers, however, and it is crucial to gather all the light into the fiber.

Phase Noise—Linewidth

The fundamental linewidth of a laser is given by the stochastic process of spontaneous emission, as first derived by Schawlow and Townes in the very early days of lasers. In a semicon-

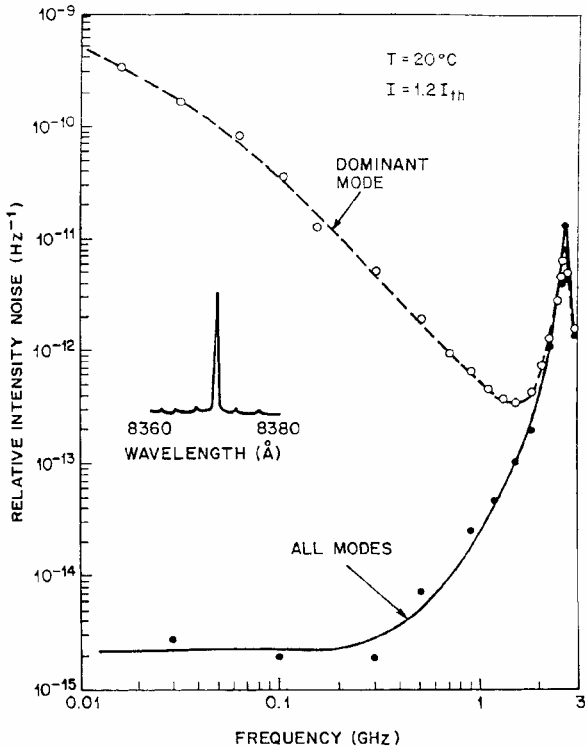

FIGURE 10 Effect of mode partition noise on relative intensity noise in multimode lasers. Experimentally observed intensity-noise spectra in all modes (solid curve) or in dominant mode (dashed curve). Inset shows spectrum of average mode power.[19]

ductor laser, additional noise enters from the stochastic process of carrier injection. Because the refractive index is a function of the carrier density, changes in carrier density cause changes in refractive index, which in turn create phase noise.

The formula for the radian frequency linewidth of a semiconductor laser includes the *linewidth enhancement factor* β_c (defined in Eq. (35):

$$\delta\omega = (1 + \beta_c^2)\, \delta\omega_o \tag{43}$$

where the original Schawlow-Townes linewidth is given by

$$\delta\omega_o = \frac{R_{sp}}{2P} = \frac{\beta_{sp} I_{th} h\nu \tau_m}{2e\mathcal{P}_{out}} \tag{44}$$

Typical values of the linewidth enhancement factor are $\beta_c = 5$. It can be seen that the linewidth decreases inversely as the laser power increases. However, as shown in the experimental data in Fig. 11, at high enough power (above 10 mW) the linewidth narrowing saturates at ~1 to 10 MHz and then begins to broaden again at even higher power levels. It is also possible to

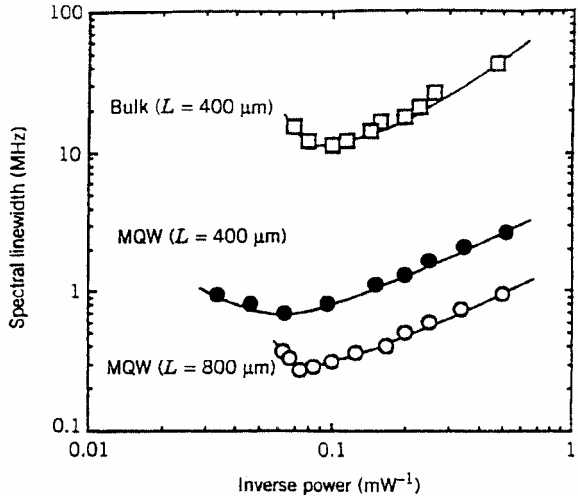

FIGURE 11 Linewidth of DFB lasers as a function of inverse power, comparing bulk active regions and multiple quantum well active regions.[20]

reduce the linewidth by using QWs and increasing the cavity length (to decrease N_{th} and increase P).

External Optical Feedback and Coherence Collapse

Semiconductor lasers are extremely sensitive to weak time-delayed feedback, such as from reflections off the front ends of fiber pigtails. These fed-back signals can result in mode hopping, strong excess noise, and chaotic behavior in the *coherence collapse* regime. Some of the features of feedback-induced noise are outlined here.

Regimes of Feedback. The following provides a useful classification scheme[21]:

Regime I. At the lowest levels of feedback, narrowing or broadening of the emission line is observed, depending on the phase of the feedback.

Regime II. At higher levels of feedback, mode hopping between different external cavity modes may appear.

Regime III. Further increasing the levels of feedback, the laser is observed to operate in the lowest linewidth mode.

Regime IV. At yet higher feedback levels, satellite modes appear, separated from the main mode by the relaxation oscillation frequency. These grow as the feedback increases and the laser line eventually broadens. This regime does not depend on the distance from the laser to the reflector. This is the regime of *coherence collapse.*

Regime V. A regime of stable operation that can be reached only with antireflection coating on the laser facet to ensure the largest possible coupling back into the laser.

These regimes of feedback are characterized by the value of a *feedback parameter C,* given by:

$$C = \sqrt{f_{\text{ext}}}\, C_e \frac{\tau_{\text{ext}}}{\tau_L} \sqrt{1 + \beta_c^2} \tag{45}$$

where f_{ext} is the ratio of the externally reflected power that enters back into the laser divided by the emitted power. Also, the external coupling factor $C_e = (1 - R)/\sqrt{R}$, where R is the reflectivity of the laser facet. As before, β_c is the linewidth enhancement factor. The external round-trip time delay is τ_{ext}, and the laser round-trip time is τ_L. The regimes have the following values of the feedback parameter:

Regime I. $C < 1$

Regime II. $C > 1$

Regime III. $C >> 1$

Regime IV. This is the so-called *coherence collapse* regime, where C is even larger.

Fig. 12 gives an example of the linewidth of a semiconductor laser versus the parameter C. A quantitative discussion of these regimes follows.[22]

Assume that the coupling efficiency from the laser into the fiber is η. Then, because feedback requires a double pass, the fraction of emitted light fed back into the laser is $f_{\text{ext}} = \eta^2 R_e$, where R_e is the reflectivity from the end of the fiber. The external reflection changes the overall reflectivity and therefore the required gain for threshold, depending on its phase ϕ_{ext}. Possible modes are defined by the threshold gain and the phase condition that requires an effective external round-trip phase for fed-back light $\delta\phi_L = m\pi$. But a change in the threshold gain also changes the refractive index and the phase through the linewidth enhancement factor β_c. The phase of the returning light is:

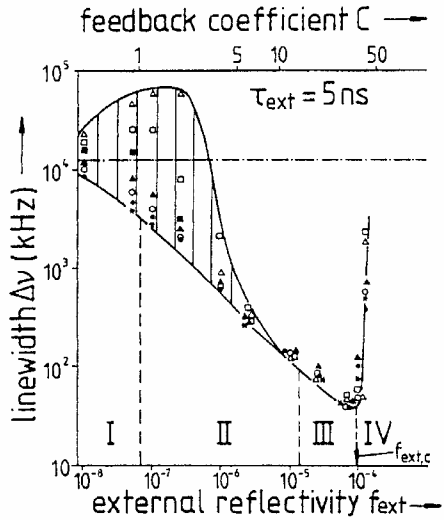

FIGURE 12 Linewidth versus feedback for a semiconductor laser and the corresponding feedback regimes.[22]

$$\delta\phi_L = \frac{\tau_L}{\tau_{\text{ext}}} [(\omega - \omega_{\text{th}})\tau_{\text{ext}} + C \sin (\omega\tau_{\text{ext}} + \tan^{-1} \beta_c)] \tag{46}$$

where ω_{th} is the frequency of the solitary laser at threshold.

Regime I. For very weak feedback, $C < 1$ and there is only one solution when $\delta\phi_L$ is set equal to $m\pi$, so that the frequency of the mode of the solitary laser ω is at most slightly changed. The line will be narrowed or broadened as the external reflection adds to or subtracts from the output of the laser.

The linewidth is:

$$\Delta\omega = \frac{\Delta\omega_o}{[1 + C \cos (\omega\tau_{\text{ext}} + \tan^{-1} \beta_c)]^2} \tag{47}$$

with maximum and minimum values given by:

$$\Delta\omega_{\text{min}} = \frac{\Delta\omega_o}{(1 + C)^2} \tag{47a}$$

$$\Delta\omega_{\text{max}} = \frac{\Delta\omega_o}{(1 - C)^2} \tag{47b}$$

This is regime I.

The system performance moves toward regime II as $C \to 1$. Note that at $C = 1$ the maximum value predicts an infinite linewidth. This indicates that even very small feedback can cause wide spectral response, as long as $C \sim 1$.

Regime II. For higher feedback with $C > 1$, several solutions with $\delta\phi_L = m\pi$ may exist. Linewidth broadening occurs because the single external cavity mode now has split into a dual mode, accompanied by considerable phase noise. Mode hopping gives linewidth broadening and intensity noise. This is a low-frequency noise with a cutoff frequency of about 10 MHz.

Regime III. As the system performance moves toward regime III with increasing feedback, the mode splitting increases up to a frequency $\Delta\omega = 1/\tau_{\text{ext}}$ and the cutoff frequency for mode hopping noise decreases until only one of the split modes survives. To understand which mode survives, it is important to realize that in regime III, stable and unstable modes alternate with increasing phase. Because $\beta_c \neq 0$, the mode with the best phase stability (corresponding to the minimum linewidth mode) does not coincide with the mode with minimum threshold gain. However, in feedback regime III, the mode with the minimum linewidth rather than the mode with the minimum gain is the predominant lasing mode. This has been understood by analyzing the importance of phase stability to laser operation. This minimum linewidth mode remains relatively stable in regime III and is at the emission frequency of the laser without feedback. The laser operates in the lowest linewidth mode as long as the inverse of the linewidth of the solitary laser is larger than the external cavity round-trip time. In this mode of operation, the laser is stably phase locked to the feedback.

Regime IV. The stable linewidth solution of regime III collapses as the fraction of power fed back f_{ext} increases to a critical value. There is considerable discussion of the physical mechanism that leads to this coherence collapse. The existence of this regime has been demonstrated by simulation, through numerical solution of the rate equations. Fitting to experimental results and theoretical analyses indicates that the onset of coherence collapse occurs when the feedback is larger than a critical value given by[23]:

$$C \geq C_{\text{crit}} = 2\gamma_R \tau_{\text{ext}} \frac{1 + \beta_c^2}{\beta_c^2} \tag{48}$$

where γ_R is the damping rate of the relaxation oscillations, as previously defined. As the feedback level approaches the critical value C, undamped relaxation oscillations appear, and oscillations of carrier density induce the phase of the field to oscillate through the linewidth enhancement factor β_c. To obtain an analytical result, it must be assumed that the external cavity round-trip time is larger than the time for relaxation oscillations to damp out.

As the feedback increases, the relaxation oscillation ceases to be damped, as a result of the interaction between the field amplitude in the semiconductor cavity and the carrier density, which shows up as a phase difference between the field in the semiconductor cavity and in the feedback field. The onset of coherence collapse is determined by the feedback parameter at which the relaxation oscillation ceases to be damped.

Regime V. This is a regime of stable operation that can only be achieved with an antireflection-coated laser output facet (such as a bare diode in an external cavity), and is not of concern here.

Cavity Length Dependence and RIN. In some regimes the regions of stability depend on the length of the external cavity, that is, the distance from the extra reflection to the laser diode. These regions have been mapped out for two different laser diodes, as shown in Fig. 13. The qualitative dependence on distance to reflection should be the same for all lasers.

The RIN is low for weak to moderate levels of feedback but increases tremendously in regime IV. The RIN and the linewidth are strongly related (see Fig. 12); the RIN is suppressed in regimes III and V.

Low-Frequency Fluctuations. When a laser operating near threshold is subject to a moderate amount of feedback, chaotic behavior evolves into *low-frequency fluctuations* (*LFF*). During LFF the average laser intensity shows sudden dropouts, from which it gradually recovers, only to drop out again after some variable time, typically on the order of tens of external cavity round-trips. This occurs in regimes of parameter space where at least one stable external cavity mode exists, typically at the transition between regimes IV and V. Explanations differ as to the cause of LFF, but it appears to originate in strong intensity pulses that occur during the buildup of average intensity, as a form of mode locking, being frustrated by the drive toward maximum gain. Typical frequencies for LFF are 20 to 100 MHz, although feedback from reflectors very close to the laser has caused LFF at frequencies as high as 1.6 GHz.

Conclusions. Semiconductor laser subject to optical feedback exhibits a rich and complex dynamic behavior that can enhance or degrade the laser's performance significantly. Feedback can occur through unwanted back reflections—for instance, from a fiber facet—and can lead to a severe degradation of the spectral and temporal characteristics, such as in the coherence collapse regime or in the LFF regime. In both regimes, the laser intensity fluctuates erratically and the optical spectrum is broadened, showing large sidebands. Because these unstable regimes can occur for even minute levels of feedback, optical isolators or some other means of prevention are usually used.

4.6 QUANTUM WELL AND STRAINED LASERS

Quantum Well Lasers

We have seen that the optimum design for low-threshold LDs uses the thinnest possible active region to confine free carriers, as long as the laser light is waveguided. When the active

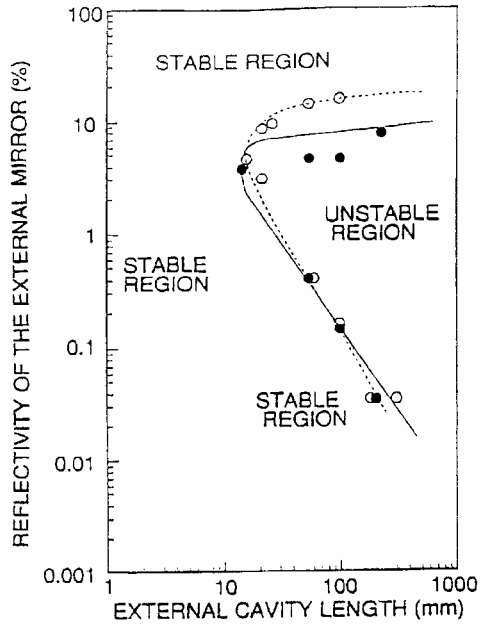

FIGURE 13 Regimes of stable and unstable operation for two laser diodes (○ and ●) when subject to external feedback at varying distances and of varying amounts.[24]

layer has a thickness less than a few tens of nanometers (hundreds of angstroms), it becomes a *quantum well* (QW). That is, the layer is so thin that the confined carriers have energies that are quantized in the growth direction z, as described in Vol. 1, Chap. 13 of this handbook. This changes the density of states and the gain (and absorption) spectrum. While bulk semiconductors have an absorption spectrum near the band edge that increases with photon energy above the bandgap energy E_g as $(h\nu - E_g)^{1/2}$, quantum wells have an absorption spectrum that is steplike in photon energy at each of the allowed quantum states. Riding on this steplike absorption is a series of exciton resonances at the absorption steps that occur because of the Coulomb interaction between free electrons and holes, which can be seen in the spectra of Fig. 14. These abrupt absorption features result in much higher gain for quantum well lasers than for bulk semiconductor lasers. The multiple spectra in Fig. 14 record the reduction in absorption as the QW states are filled with carriers. When the absorption goes to zero, transparency is reached. Figure 14 also shows that narrower wells push the bandgap to higher energies, a result of quantum confinement. The QW thickness is another design parameter in optimizing lasers for telecommunications.

Because a single quantum well (SQW) is so thin, its optical confinement factor is small. It is necessary either to use multiple QWs (separated by heterostructure barriers that contain the electronic wave functions within individual wells) or to use a guided wave structure that focuses the light into a SQW. The latter is usually a GRIN structure, as shown in Fig. 2*d*. Band diagrams as a function of distance in the growth direction for typical quantum well separate confinement heterostructures are shown in Fig. 15. The challenge is to properly confine carriers and light using materials that can be reliably grown and processed by common crystal growth methods.

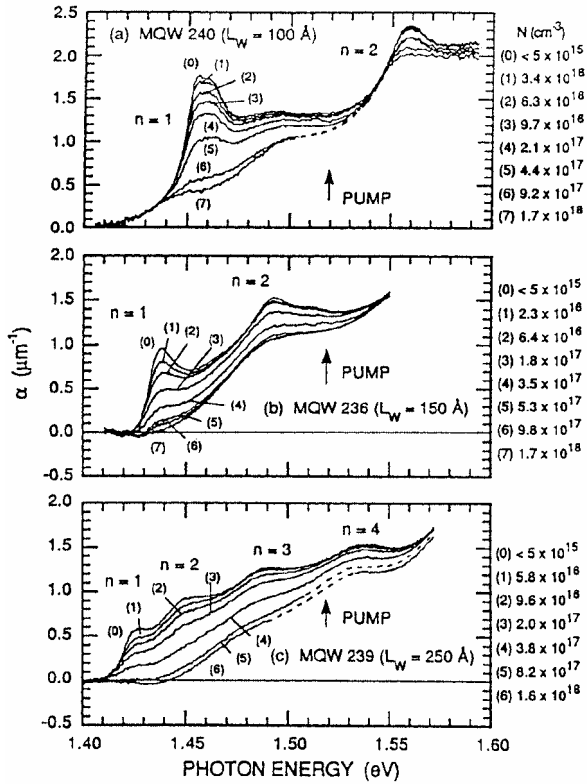

FIGURE 14 Absorption spectrum for multiple quantum wells of three different well sizes, for varying levels of optically induced carrier density, showing the decrease in absorption toward transparency. Note the stronger excitonic resonances and increased bandgap with smaller well size.[25]

Quantum wells have provided significant improvement over bulk active regions, as originally observed in GaAs lasers. In InP lasers, Auger recombination and other losses come into play at the high carrier densities that occur in quantum confined structures, which tends to degrade laser performance. However, it has been found that providing strain in the active region can improve the performance of QW InGaAsP lasers to a level comparable with GaAs lasers. Strained QW lasers are described in the next section.

The LD characteristics described in Secs. 5.2 to 5.5 hold for QW lasers as well as for bulk lasers. The primary difference is that the gain is larger and the optical confinement factor will be much smaller, because the light is not well confined in a single thin QW active region. The optical confinement factor in a typical QW of thickness d is dominated by the second term in the denominator of Eq. (2). When multiple quantum wells (MQWs) are used, d_g can be the thickness of the entire region containing the MQWs and their barriers, but Γ must now be multiplied by the filling factor Γ_f of the quantum wells within the MQW region—that is, if there are N_w wells, each of thickness d_w, then $\Gamma_f = N_w d_w / d_g$. When a GRINSCH structure is used, the optical confinement factor depends on the curvature of its refractive gradient near the center of the guide.

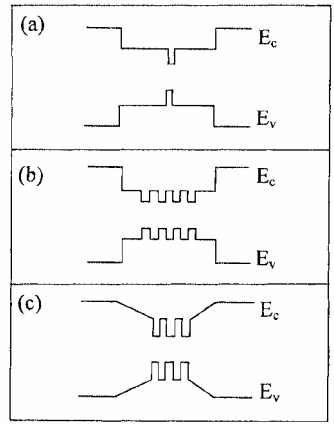

FIGURE 15 Typical band diagrams (energy of conduction band E_c and valence band E_v versus growth direction) for quantum wells in separate confinement laser heterostructures: (*a*) single quantum well; (*b*) multiple quantum wells; and (*c*) graded index separate confinement heterostructure (GRINSCH) and multiple quantum wells.

There are subtle differences in performance between different geometries, depending on how many QWs are used and the extent to which a GRINSCH structure is dominant. The lowest threshold current densities have been reported for the highest Q cavities (longest lengths or highest reflectivities) using single QWs. However, for lower Q cavities the lowest threshold current densities are achieved with MQWs, even though they require higher carrier densities to achieve threshold. This is presumably because Auger recombination depends on the cube of the carrier density, so that SQW lasers will have excess losses with their higher carrier densities. In general, MQWs are a better choice in long-wavelength lasers, while SQWs have the advantage in GaAs lasers. However, with MQW lasers it is important to realize that the transport of carriers moving from one well to the next during high-speed modulation must be taken into account. In addition, improvements through the use of strained layer QWs make single QW devices more attractive.

Strained Layer Quantum Well Lasers

Active layers containing *strained quantum wells* have proven to be an extremely valuable advance in high-performance long-wavelength InP lasers. They have lower thresholds, enhanced differential quantum efficiency η_D, larger characteristic temperature T_o, reduced linewidth enhancement factor β_c (less chirp), and enhanced high-speed characteristics (larger relaxation oscillation frequency Ω_R) compared to unstrained QW and bulk devices. This results from the effect of strain on the energy-versus-momentum band diagram. Bulk semiconductors have two valence bands that are degenerate at the potential well minimum, as shown in Fig. 16. They are called *heavy-hole* and *light-hole* bands, since the smaller curvature means a heavier effective mass. Quantum wells lift this degeneracy, and interaction between the two bands near momentum $k = 0$ causes a local distortion in the formerly parabolic bands, also shown in Fig. 16. As a result, the heavy hole effective mass becomes smaller, more nearly approaching that

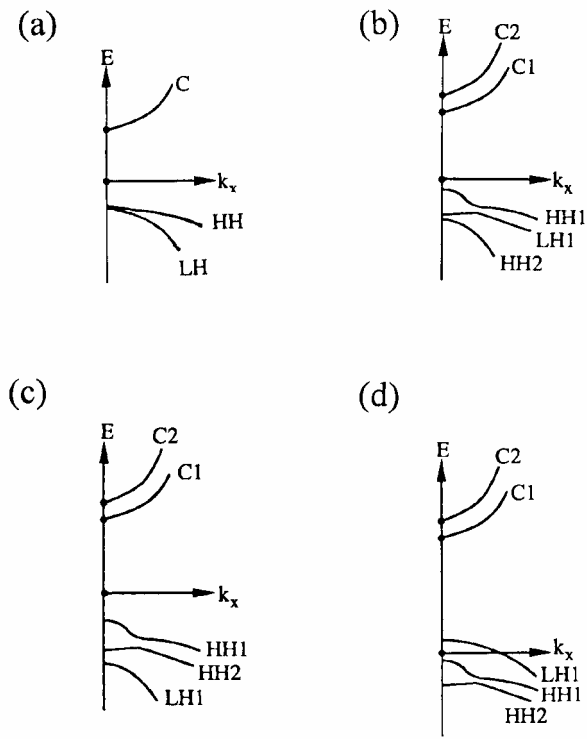

FIGURE 16 The effect of strain on the band diagram (energy E versus in-plane momentum k_x) of III-V semiconductors: (*a*) no strain, showing the degeneracy of the heavy holes HH and light holes LH at $k_x = 0$; (*b*) quantum wells, showing the separately quantized conduction bands (C_1 and C_2) and removal of the valence band degeneracy, with the lowest energy heavy holes HH_1 no longer having the same energy as the lowest energy light holes LH_1 at $k = 0$; (*c*) compressive strain, with enhanced separation between the light-hole and the lowest heavy-hole band; and (*d*) tensile strain, with light holes having the lowest energy.

of the conduction band. This allows population inversion to become more efficient, increasing the differential gain; this is one factor in the reduced threshold of QW lasers.[26]

Strain additionally alters this structure in a way that can improve performance even more. Compressive strain in the QW moves the heavy-hole and light-hole valence bands further apart and further reduces the hole effective mass. Strain also decreases the heavy-hole effective mass by a factor of two or more, further increasing the differential gain and reducing the threshold carrier density. Higher differential gain also results in a smaller linewidth enhancement factor. Tensile strain moves the heavy-hole and light-hole valence bands closer together. In fact, at one particular tensile strain value these bands become degenerate at $k = 0$. Further tensile strain results in the light hole having the lowest energy at $k = 0$. These lasers will be polarized TM, because of the angular momentum properties of the light-hole band. This polarization has a larger optical matrix element, which can enhance the gain over some wavelength regions.

In addition to the heavy- and light-hole bands, there is an additional, higher-energy valence band (called the *split-off band*) which participates in Auger recombination and intervalence band absorption, both of which reduce quantum efficiency. In unstrained material there is a near-resonance between the bandgap energy and the difference in energy between the heavy-hole and split-off valence bands, which enhances these mechanisms for nonradiative recombination. Strain removes this near-degeneracy and reduces those losses that are caused by Auger recombination and intervalence band absorption. This means that incorporating strain is essential in long-wavelength laser diodes intended to be operated at high carrier densities. The reliability of strained layer QW lasers is excellent, when properly designed. However, strain does increase the intraband relaxation time, making the gain compression factor worse, so strained lasers tend to be more difficult to modulate at high speed.

Specific performance parameters are strongly dependent on the specific material, amount of strain, size and number of QWs, and device geometry, as well as the quality of crystal growth. Calculations show that compressive strain provides the lowest transparency current density, but tensile strain provides the largest gain (at sufficiently high carrier densities), as shown in Fig. 17. The lowest threshold lasers, then, will typically be compressively strained. Nonetheless, calculations show that, far enough above the band edge, the differential gain is 4 times higher in tensile compared to compressive strain. This results in a smaller linewidth enhancement factor, even if the refractive index changes per carrier density are larger. It has also been found that tensile strain in the active region reduces the Auger recombination, decreasing the losses introduced at higher temperatures. This means that T_o can increase with strain, particularly tensile strain. Performance at 1.55 μm comparable with that of GaAs lasers has been demonstrated using strained layer QWs. Deciding between compressively and tensilely strained QWs will be a matter of desired performance for specific applications.

Threshold current densities under 200 A/cm^2 have been reported at 1.55 μm; T_o values on the order of 140 K have been reported, 3 times better than bulk lasers. Strained QW lasers have improved modulation properties compared with bulk DH lasers. Because the gain coefficient can be almost double, the relaxation oscillation frequency is expected to be almost 50 percent higher, enhancing the modulation bandwidth and decreasing the relative intensity noise for the same output power. Even the frequency chirp under modulation will be less, because the linewidth enhancement factor is less. The typical laser geometry, operating characteristics, transient response, noise, frequency chirping, and the effects of external optical feedback are all similar in the strained QW lasers to what has been described previously for bulk lasers. Only the experimentally derived numerical parameters will be somewhat different; strained long-wavelength semiconductor lasers have performance parameters comparable to those of GaAs lasers. One difference is that the polarization of the light emitted from

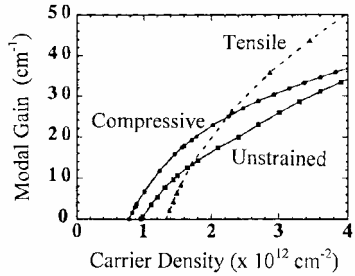

FIGURE 17 Modal gain at 1.55 μm in InGaAs QW lasers calculated as a function of the carrier density per unit area contained in the quantum well. Well widths were determined by specifying wavelength.[27]

strained lasers may differ from that emitted from bulk lasers. As explained in Sec. 3.3, the gain in bulk semiconductors is independent of polarization, but lasers tend to be polarized in-plane because of higher facet reflectivity for that polarization. The use of quantum wells causes the gain for the TE polarization to be slightly (~10 percent) higher than for the TM polarization, so lattice-matched QW lasers operate with in-plane polarization. Compressive strain causes the TE polarization to have significantly more gain than the TM polarization (typically 50 to 100 percent more), so these lasers are also polarized in-plane. However, tensile strain severely depresses the TE gain, and these lasers have the potential to operate in TM polarization.

Typical 1.3- and 1.5-μm InP lasers today use from 5 to 15 wells that are grown with internal strain. By providing strain-compensating compressive barriers, there is no net buildup of strain. Typical threshold current densities today are ~1000 A/cm^2, threshold currents ~10 mA, T_o ~ 50 to 70 K, maximum powers ~40 mW, differential efficiencies ~0.3 W/A, and maximum operating temperatures ~70°C before the maximum power drops by 50 percent. There are trade-offs on all these parameters; some can be made better at the expense of some of the others.

4.7 DISTRIBUTED FEEDBACK (DFB) AND DISTRIBUTED BRAGG REFLECTOR (DBR) LASERS

Rather than cleaved facets for feedback, some lasers use distributed reflection from corrugated waveguide surfaces. Each groove provides some slight reflectivity, which adds up coherently along the waveguide at the wavelength given by the corrugation. This has two advantages. First, it defines the wavelength (by choice of grating spacing) and can be used to fabricate single-mode lasers. Second, it is an in-plane technology (no cleaves) and is therefore compatible with monolithic integration with modulators and/or other devices.

Distributed Bragg Reflector (DBR) Lasers

The *distributed Bragg reflector* (DBR) laser replaces one or both laser facet reflectors with a waveguide diffraction grating located outside the active region, as shown in Fig. 18. The

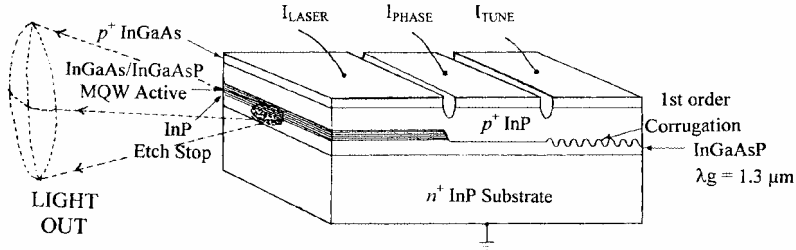

FIGURE 18 Schematic for DBR laser configuration in a geometry that includes a phase portion for phase tuning and a tunable DBR grating. Fixed-wavelength DBR lasers do not require this tuning region. Designed for 1.55-μm output, light is waveguided in the transparent layer below the MQW that has a bandgap at a wavelength of 1.3 μm. The guided wave reflects from the rear grating, sees gain in the MQW active region, and is partially emitted and partially reflected from the cleaved front facet. Fully planar integration is possible if the front cleave is replaced by another DBR grating.[28]

reflectivity of a Bragg mirror is the square of the reflection coefficient (given here for the assumption of lossless mirrors)[29]:

$$r = \frac{\kappa}{\delta - iS \coth (SL)} \tag{49}$$

where κ is the *coupling coefficient* due to the corrugation (which is real for corrugations that modify the effective refractive index in the waveguide, but would be imaginary for periodic modulations in the gain and could, indeed, be complex). Also, δ is a *detuning parameter* that measures the offset of the optical wavelength λ from that defined by the grating periodicity Λ. When the grating is used in the mth order,

$$\delta = \frac{2\pi n_g}{\lambda} - \frac{m\pi}{\Lambda} \tag{50}$$

where n_g is the effective group refractive index of the waveguide mode, and m is any integer. Also, S is given by:

$$S^2 = \kappa^2 - \delta^2 \tag{51}$$

The Bragg mirror has its maximum reflectivity on resonance when $\delta \to 0$ and the wavelength λ_m is determined by the mth order of the grating spacing Λ:

$$\Lambda = \frac{m\lambda_m}{2n_g} \tag{52}$$

The reflection coefficient on resonance is $r_{\max} = -i \tanh (KL)$ and the Bragg reflectivity is:

$$R_{\max} = \tanh^2 (KL) \tag{53}$$

where K is the coupling per unit length, $K = |\kappa|$, and is larger for deeper corrugations or when the refractive index difference between the waveguide and the cladding is larger. The reflectivity falls off as the wavelength moves away from resonance and the detuning increases.

When off resonance far enough that $|\delta| > |\kappa|$, it is more practical to define:

$$\sigma^2 = \delta^2 - \kappa^2 \tag{54}$$

and the reflectivity has the form:

$$R = \frac{(KL)^2}{(\delta L)^2 + (\sigma L)^2 \cot^2 (\sigma L)} \tag{55}$$

Note that when $\sigma \to 0$, $\delta = K$ and $R \to (KL)^2/[1 + (KL)^2]$. For moderate values of the grating coupling KL, this value of the reflectivity is not very different from that given by Eq. (53). Thus, $\sigma^2 > 0$ over most of the detuning range.

The half-width of the resonance can be found by noting that the reflectivity goes to zero when $\sigma L = \pi$, where the cotangent goes to infinity. This occurs at a cutoff detuning δ_c given by $\delta_c^2 L^2 = \pi^2 + K^2 L^2$. This fact allows us to define a reflection resonance half-width as $\delta_c/2$ and the full width as δ_o. The width of the resonance is constant ($\delta_c = \pi/L$) when $KL \ll \pi$, but broadens for large KL. Typical numbers are $2 < KL < 5$, so it is reasonable to take $\delta_c \approx \pi/L$. The detuning is related to the wavelength bandwidth of the mirror by differentiating Eq. (50): $\Delta\delta = 2\pi n_g (\Delta\lambda/\lambda_o^2)$. Then the wavelength bandwidth for $\delta_c = \pi/L$ is $\Delta\lambda = \lambda^2/(2Ln_g)$ and the width of the resonance is 0.5 nm (when $L = 500$ μm, $\lambda = 1.3$ μm, and $KL \ll \pi$). This narrow resonance, fixable by choosing the grating spacing and variable by varying the refractive index (with, for example, carrier injection) makes the DBR laser very favorable for use in optical communication systems.

The characteristics of Fabry-Perot lasers previously described still hold for DBR lasers, except that the narrow resonance can ensure that these lasers are single mode, even at high excitation levels.

Distributed Feedback (DFB) Lasers

When the corrugation is put directly on the active region or its cladding, this is called *distributed feedback* (*DFB*). One typical example is shown in Fig. 19. As before, the grating spacing is chosen such that, for a desired wavelength near λ_o, $\Lambda = m\lambda_o/2n_g$, where now n_g is the effective group refractive index of the laser mode inside its waveguiding active region, and m is any integer. A laser operating under the action of this grating has feedback that is distributed throughout the laser gain medium. In this case, Eq. (49) is generalized to allow for the gain: $\delta = \delta_o + ig_L$, where g_L is the laser gain and $\delta_o = 2\pi n_g/\lambda - 2\pi n_g/\lambda_o$. Equations (49) to (54) remain valid, understanding that now δ is complex.

The laser oscillation condition requires that after a round-trip inside the laser cavity, a wave must have the same phase that it started out with, so that successive reflections add in phase. Thus, the phase of the product of the complex reflection coefficients (which now include gain) must be an integral number of 2π. This forces r^2 to be a positive real number. So, laser oscillation requires that:

$$r^2 > 0 \tag{56}$$

On resonance $\delta_o = 0$ and $S_o^2 = \kappa^2 + g_L^2$, so that S_o is pure real for simple corrugations (κ real). Since the denominator in Eq. (49) is now pure imaginary, r^2 is negative and the round-trip condition of Eq. (56) cannot be met. Thus, there is no on-resonance solution to a simple DFB laser with a corrugated waveguide and/or a periodic refractive index.

DFB Threshold. We look for an off-resonance solution to the DFB laser with a corrugated waveguide in the active region (κ real). A laser requires sufficient gain that the reflection coefficient becomes infinite. That is,

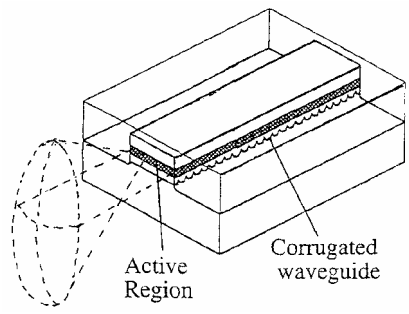

FIGURE 19 Geometry for a DFB laser, showing a buried grating waveguide that forms the separate confinement heterostructure laser, which was grown on top of a grating-etched substrate. The cross-hatched region contains the MQW active layer. A stripe mesa is etched and regrown to provide a buried heterostructure laser. Reflection from the cleaved facets must be suppressed by means of an antireflection coating.

$$\delta_{th} = iS_{th} \coth (S_{th}L) \tag{57}$$

where

$$S_{th}^2 = \kappa^2 - \delta_{th}^2 \tag{58}$$

By simple algebraic manipulation, Eq. (57) can be written as:

$$\exp (2S_{th}) \frac{S_{th} + i\delta_{th}}{S_{th} - i\delta_{th}} = -1 \tag{59}$$

Multiplying and dividing by $S_{th} + i\delta_{th}$ gives:

$$\exp (2S_{th}) \frac{(S_{th} + i\delta_{th})^2}{S_{th}^2 + \delta_{th}^2} = -1 \tag{60}$$

The denominator is κ^2, which, for pure corrugations, is K^2. For large gain, $\delta_{th}^2 >> K^2$, so that Eq. (58) gives $S_{th} = i\delta_{th} = i\delta_o - g_L$. Inserting this in the numerator, Eq. (60) becomes[30]:

$$\exp (2S_{th}) \frac{4(g_L - i\delta_o)^2}{K^2} = -1. \tag{61}$$

This is a complex eigenvalue equation that has both a real and an imaginary part, which give both the detuning δ_o and the required gain g_L. Equating the phases gives:

$$2 \tan^{-1} \left(\frac{\delta_o}{g_L} \right) - 2\delta_o L + \delta_o L \frac{K^2}{g_L^2 + \delta_o^2} = (2m + 1)\pi \tag{62}$$

There is a series of solutions, depending on the value of *m*.

For the largest possible gains,

$$\delta_o L = -(m + \tfrac{1}{2})\, \pi \tag{63}$$

There are two solutions, $m = -1$ and $m = 0$, giving $\delta_o L = -\pi/2$ and $\delta_o L = +\pi/2$. These are two modes equally spaced around the Bragg resonance. Converting to wavelength units, the mode detuning becomes $\delta_o L = -2\pi n_g L(\delta\lambda/\lambda^2)$, where $\delta\lambda$ is the deviation from the Bragg wavelength. Considering $\delta_o L = \pi/2$, for $L = 500$ μm, $n_g = 3.5$, and $\lambda = 1.55$ μm, this corresponds to $\delta\lambda = 0.34$ nm. The mode spacing is twice this, or 0.7 nm.

The required laser gain is found from the magnitude of Eq. (61) through

$$\frac{K^2}{4} = (g_L^2 L^2 + \delta_o^2 L^2) \exp (-2g_L L) \tag{64}$$

For detuning $\delta_o L = -\pi/2$, the gain can be found by plotting Eq. (64) as a function of gain g_L, which gives $K(g_L)$, which can be inverted to give $g_L(K)$.

These results show that there is a symmetry around $\delta_o = 0$, so that there will tend to be *two* modes, equally spaced around λ_o. Such a multimode laser is not useful for communication systems, so something must be done about this. The first reality is that there are usually cleaved facets, at least at the output end of the DFB laser. This changes the analysis from that given here, requiring additional Fresnel reflection to be added to the analysis. The additional reflection will usually favor one mode over the other, and the DFB will end up as a single mode. However, there is very little control over the exact positioning of these additional cleaved facets with respect to the grating, and this has not proven to be a reliable way to achieve single-mode operation. The most common solution to this multimode problem is to use a *quarter-wavelength-shifted grating,* as shown in Fig. 20. Midway along the grating, the phase changes by $\pi/2$ and the two-mode degeneracy is lifted. This is the way that DFB lasers are made today.

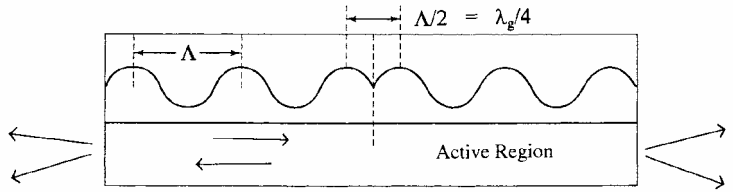

FIGURE 20 Side view of a quarter-wavelength-shifted grating, etched into a separate confinement waveguide above the active laser region. Light with wavelength in the medium λ_g sees a $\pi/4$ phase shift, resulting in a single-mode DFB laser operating on line-center.

Quarter-Wavelength-Shifted Grating. Introducing an additional phase shift of π to the round-trip optical wave enables an on-resonance DFB laser. Thus, light traveling in each direction must pass through an additional phase shift of $\pi/2$. This is done by interjecting an additional phase region of length $\Lambda/2$, or $\lambda/4n_g$, as shown in Fig. 20. This provides an additional $\pi/2$ phase in Eq. (63), so that the high-gain oscillation condition becomes:

$$\delta_o L = -m\pi \tag{65}$$

Now there is a unique solution at $m = 0$, given by Eq. (64) with $\delta_o = 0$:

$$KL = g_L L \exp(-g_L L) \tag{66}$$

Given a value for KL, the gain can be calculated. Alternatively, the gain can be varied, and the coupling coefficient used with that gain can be calculated. It can be seen that if there are internal losses α_i, the laser must have sufficient gain to overcome them as well: $g_L + \alpha_i$.

Quarter-wavelength-shifted DFB lasers are commonly used in telecommunications applications. There are a variety of ways in which the DFB corrugations are placed with respect to the active layer. Most common is to place the corrugations laterally on either side of the active region, where the evanescent wave of the guided mode experiences sufficient distributed feedback for threshold to be achieved. Alternative methods place the corrugations on a thin cladding above the active layer. Because the process of corrugation may introduce defects, it is traditional to avoid corrugating the active layer directly. Once a DFB laser has been properly designed, it will be single mode at essentially all power levels and under all modulation conditions. Then the single-mode laser characteristics described in the early part of this chapter will be well satisfied. However, it is crucial to avoid reflections from fibers back into the laser, because instabilities may arise, and the output may cease to be single mode.

A different technique that is sometimes used is to spatially modulate the gain. This renders κ complex and enables an on-resonance solution for the DFB laser, since S will then be complex on resonance. Corrugation directly on the active region makes this possible, but care must be taken to avoid introducing centers for nonradiative recombination.

There have been more than 35 years of research and development in semiconductor lasers for telecommunications. Today it appears that the optimal sources for telecommunications applications are strained quantum well distributed feedback lasers at 1.3 or 1.55 μm.

4.8 LIGHT-EMITTING DIODES (LEDS)

Sources for low-cost fiber communication systems, such as are used for communicating data, are typically light-emitting diodes (LEDs). These may be *edge-emitting LEDs* (*E-LEDs*),

which resemble laser diodes, or, more commonly, *surface-emitting LEDs* (*S-LEDs*), which emit light from the surface of the diode and can be butt-coupled to multimode fibers.

When a PN junction is forward biased, electrons are injected from the N region and holes are injected from the P region into the active region. When free electrons and free holes coexist with comparable momentum, they will combine and may emit photons of energy near that of the bandgap, resulting in an LED. The process is called *injection* (or *electro-*) *luminescence,* since injected carriers recombine and emit light by spontaneous emission. A semiconductor laser diode below threshold acts as an LED. Indeed, a semiconductor laser without mirrors is an LED. Because LEDs have no threshold, they usually are not as critical to operate and are usually much less expensive. Also, they do not need the optical feedback of lasers (in the form of cleaved facets or distributed feedback). Because the LED operates by spontaneous emission, it is an incoherent light source, typically emitted from a larger aperture (out the top surface) with a wider far-field angle and a much wider wavelength range (30 to 50 nm). In addition, LEDs are slower to modulate than laser diodes. Nonetheless, they can be excellent sources for inexpensive multimode fiber communication systems. Also, LEDs have the advantages of simpler fabrication procedures, lower cost, and simpler drive circuitry. They are longer lived, exhibit more linear input-output characteristics, are less temperature sensitive, and are essentially noise-free electrical-to-optical converters. The disadvantages are lower power output, smaller modulation bandwidths, and distortion in fiber systems because of the wide wavelength band emitted. Some general characteristics of LEDs are discussed in Vol. 1, Chap. 12 of this handbook (pp. 12.36–12.37).

In fiber communication systems, LEDs are used for low-cost, high-reliability sources typically operating with graded index multimode fibers (core diameters approximately 62 μm) at data rates up to 622 Mb/s. The emission wavelength will be at the bandgap of the active region in the LED; different alloys and materials have different bandgaps. For medium-range distances up to ~10 km (limited by modal dispersion), LEDs of InGaAsP grown on InP and operating at $\lambda = 1.3$ μm offer low-cost, high-reliability transmitters. For short-distance systems, up to 2 km, GaAs-based LEDs operating near 850 nm wavelength are used, because they have the lowest cost, both to fabricate and to operate, and the least temperature dependence. The link length is limited to ~2 km because of chromatic dispersion in the fiber and the finite linewidth of the LED. For lower data rates (a few megabits per second) and short distances (a few tens of meters), very inexpensive systems consisting of red-emitting LEDs with GaAlAs or GaInP active regions emitting at 650 nm can be used with plastic fibers and standard silicon detectors. The 650-nm wavelength is a window in the absorption in acrylic plastic fiber, where the loss is ~0.3 dB/m.

A typical GaAs LED heterostructure is shown in Fig. 21. The forward-biased *pn* junction injects electrons and holes into the GaAs active region. The AlGaAs cladding layers confine the carriers in the active region. High-speed operation requires high levels of injection (and/or doping) so that the recombination rate of electrons and holes is very high. This means that the active region should be very thin. However, nonradiative recombination increases at high carrier concentrations, so there is a trade-off between internal quantum efficiency and speed. Under some conditions, LED performance is improved by using quantum wells or strained layers. The improvement is not as marked as with lasers, however.

Spontaneous emission causes light to be emitted in all directions inside the active layer, with an internal quantum efficiency that may approach 100 percent in these direct band semiconductors. However, only the light that gets out of the LED and into the fiber is useful in a communication system, as illustrated in Fig. 21a. The challenge, then, is to collect as much light as possible into the fiber end. The simplest approach is to butt-couple a multimode fiber to the LED surface as shown in Fig. 21a (although more light is collected by lensing the fiber tip or attaching a high-index lens directly on the LED surface). The alternative is to cleave the LED, as in a laser (Fig. 1), and collect the waveguided light that is emitted out the edge. Thus, there are two generic geometries for LEDs: *surface-emitting* and *edge-emitting.* The edge-emitting geometry is similar to that of a laser, while the surface-emitting geometry allows light to come out the top (or bottom). Its inexpensive fabrication and integration process makes

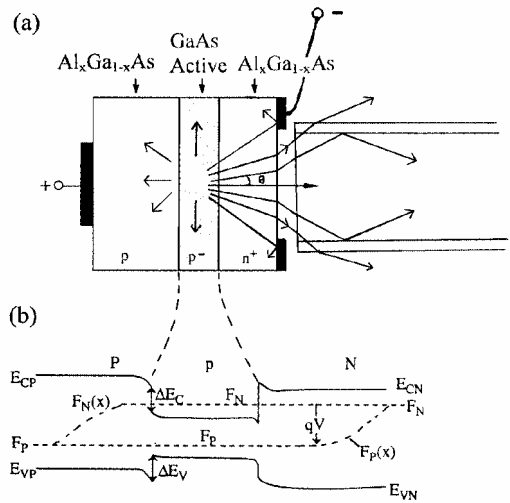

FIGURE 21 Cross-section of a typical GaAs light-emitting diode (LED) structure: (*a*) surface-emitting LED aligned to a multimode fiber, indicating the small fraction of spontaneous emission that can be captured by the fiber; (*b*) energy of the conduction band E_c and valence band E_v as a function of depth through the LED under forward bias V, as well as the Fermi energies that indicate the potential drop that the average electron sees.

the surface-emitting LED the most common type for inexpensive data communication; it will be discussed first. The edge-emitting LEDs have a niche in their ability to couple with reasonable efficiency into single-mode fibers. Both LED types can be modulated at bit rates up to 622 Mb/s, an ATM standard, but many commercial LEDs have considerably smaller bandwidths.

Surface-Emitting LEDs

The geometry of a surface-emitting LED butt-coupled to a multimode graded index fiber is shown Fig. 21*a*. The coupling efficiency is typically small, unless methods are employed to optimize it. Because light is spontaneously emitted in all internal directions, only half of it is emitted toward the top surface, so that often a mirror is provided to reflect back the downward-traveling light. In addition, light emitted at too great an angle to the surface normal is totally internally reflected back down and is lost. The critical angle for total internal reflection between the semiconductor of refractive index n_s and the output medium (air or plastic encapsulant) of refractive index n_o is given by $\sin \theta_c = n_o/n_s$. Because the refractive index of GaAs is $n_s \sim 3.3$, the internal critical angle with air is $\theta_c \sim 18°$. Even with encapsulation, the angle is only 27°. A butt-coupled fiber can accept only spontaneous emission at those external angles that are smaller than its numerical aperture. For a typical fiber $NA \approx 0.25$, this corresponds to an external angle (in air) of 14°, which corresponds to 4.4° inside the GaAs. This means that the cone of spontaneous emission that can be accepted by the fiber is only ~0.2 percent of the entire spontaneous emis-

sion. Fresnel reflection losses makes this number even smaller. Even including all angles, less than 2 percent of the total internal spontaneous emission will come out the top surface of a planar LED.

The LED source is incoherent, a Lambertian emitter, and follows the law of imaging optics: a lens can be used to reduce the angle of divergence of LED light, but will enlarge the apparent source. The use of a collimating lens means that the LED source diameter must be proportionally smaller than the fiber into which it is to be coupled. Unlike a laser, the LED has no modal interference, and the output of a well-designed LED has a smooth Lambertian intensity distribution that lends itself to imaging.

The coupling efficiency can be increased in a variety of ways, as shown in Fig. 22. The LED can be encapsulated in materials such as plastic or epoxy, with direct attachment to a focusing lens (Fig. 22*a*). Then the output cone angle will depend on the design of this encapsulating lens; the finite size of the emitting aperture and resulting aberrations will be the limiting consideration. In general, the user must know both the area of the emitting aperture and the angular divergence in order to optimize coupling efficiency into a fiber. Typical commercially available LEDs at 850 nm for fiber-optic applications have external half-angles of ~25° without a lens and ~10° with a lens, suitable for butt-coupling to multimode fiber.

Additional improvement can be achieved by lensing the pigtailed fiber to increase its acceptance angle (Fig. 22*b*). An alternative is to place a microlens between the LED and the fiber (Fig. 22*c*). Perhaps the most effective geometry for capturing light is the integrated domed surface fabricated directly on the back side of an InP LED, as shown in Fig. 22*d*. Because the refractive index of encapsulating plastic is <1.5, compared to 3.3 of the semi-conductor, only a semiconductor dome can entirely eliminate total internal reflection. Integrated semiconductor domes require advanced semiconductor fabrication technology, but have been proven effective. In GaAs diodes the substrate is absorptive, but etching a well and inserting a fiber can serve to collect backside emission. For any of these geometries, improvement in efficiency of as much as a factor of two can be obtained if a mirror is provided to reflect backward-emitted light forward. This mirror can be either metal or a dielectric stack at the air-semiconductor interface, or it can be a DBR mirror grown within the semiconductor structure.

Current must be confined to the surface area of emission, which is typically 25 to 75 μm in diameter. This is done by constricting the flow of injection current by mesa etching or by using an oxide-defined (reflective) electrode. Regrowth using *npn* blocking layers or semi-insulating material in the surrounding areas (as in lasers) has the advantage of reducing thermal heating. Surface-emitting LEDs require that light be emitted out of the surface in a gaussian-like pattern; it must not be obscured by the contacting electrode. Typically, a highly conductive cap layer brings the current in from a ring electrode; alternatively, when light is collected out of the substrate side rather than the top side, electrical contact may be made to the substrate.

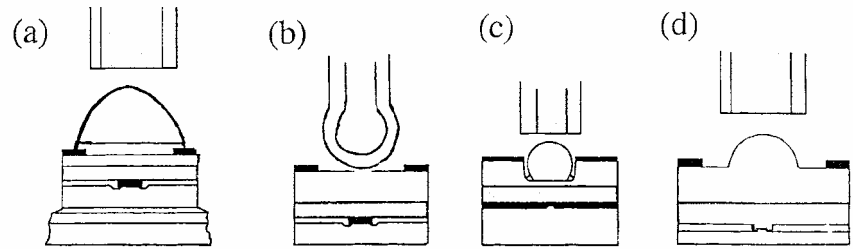

FIGURE 22 Typical geometries for coupling from LEDs into fibers: (*a*) hemispherical lens attached with encapsulating plastic; (*b*) lensed fiber tip; (*c*) microlens aligned through use of an etched well; and (*d*) spherical semiconductor surface formed on the substrate side of the LED.

Typical operating specifications for a surface-emitting LED at 1.3 μm pigtailed to a 62-μm core graded index fiber might be 15 μW at 100 mA input current, for ~0.02 percent efficiency,[31] with a modulation capability of 622 Mb/s. A factor of 2.5 times improvement in power can be achieved with a comparable reduction in speed. The LEDs are typically placed in lensed TO-18 cans, and a lens micromachined on the back of the InP die is used to achieve this output coupling efficiency. At 1.55 μm, the specifications are for 7 times less power and 3 times less speed.

Recently, improved S-LED performance has been obtained by using resonant cavities to reduce the linewidth and increase the bandwidth that can be transmitted through fibers. These devices have integral mirrors grown above and below the active region that serve to resonate the spontaneous emission. As such, they look very much like VCSELs below threshold (Sec. 4.9).

Edge-Emitting LEDs

Edge-emitting LEDs (E-LEDs or EELEDs) have a geometry that is similar to that of a conventional laser diode (Fig. 1), but without a feedback cavity. That is, light travels back and forth in the plane of the active region of an E-LED and it is emitted out one anti-reflection coated cleaved end. As in a laser, the active layer is 0.1 to 0.2 μm thick. Because the light in an E-LED is waveguided in the out-of-plane dimension and is lambertian in-plane, the output radiation pattern will be elliptical, with the largest divergence in-plane with a full width at half-maximum (FWHM) angle of 120°. The out-of-plane guided direction typically radiates with a 30° half-angle. An elliptical collimating lens will be needed to optimally couple light into a fiber. The efficiency can be doubled by providing a reflector on the back facet of the E-LED, just as in the case of a laser.

Edge-emitting LEDs can be coupled into fibers with greater efficiency because their source area is smaller than that of S-LEDs. However, the alignment and packaging is more cumbersome than with S-LEDs. Typically, E-LEDs can be obtained already pigtailed to fibers. Edge-emitting diodes can be coupled into *single-mode* fiber with modest efficiency. A single-mode fiber pigtailed to an E-LED can typically transmit 30 μW at 150 mA drive at 1 V, for an overall efficiency of 0.04 percent. This efficiency is comparable to the emission of surface-emitting lasers into *multimode* fiber with 50 times the area. Because of their wide emission wavelength bandwidth, E-LEDs are typically used as low-coherence sources for fiber sensor applications, rather than in communications applications.

Operating Characteristics of LEDs

In an LED, the output optical power P_{opt} is linearly proportional to the drive current; the relation defines the output efficiency η:

$$P_{out} = \frac{\eta h \nu I}{e} \tag{67}$$

This efficiency is strongly affected by the geometry of the LED. The power coupled into a fiber is further reduced by the coupling efficiency between the LED emitter and the fiber, which depends on the location, size, and numerical aperture of the fiber as well as on the spatial distribution of the LED output light and the optics of any intervening lens. The internal quantum efficiency (ratio of emitted photons to incident electrons) is usually close to 100 percent.

Figure 23 shows a typical result for power coupled into a graded index multimode fiber as a function of current for various temperatures. The nonlinearity in the light out versus current, which is much less than in a laser diode, nevertheless causes some nonlinearity in the modulation of LEDs. This LED nonlinearity arises both from material properties and device

configuration; it may be made worse by ohmic heating at high drive currents. The residual nonlinearity is an important characteristic of any LED used in communication systems. Edge emitters are typically less linear because they operate nearer the amplified spontaneous limit.

There is ~10 percent reduction in output power for a 25°C increase in temperature (compared to ~50 percent reduction for a typical laser). Unlike a laser, there is no temperature-dependent threshold. Also, the geometric factors that determine the fraction of light emitted from the LED are not temperature dependent. Nonetheless, the InP-based LEDs have a stronger temperature dependence than GaAs-based LEDs, because of the larger presence of nonradiative recombination, particularly at the high injection levels required by high-speed LEDs.

The spectrum of the incoherent light emitted from an LED is roughly gaussian with a FWHM around 40 nm in the case of a typical GaAs/AlGaAs LED operating around 0.8 μm. This bandwidth, along with chromatic dispersion in graded index fibers, limits the distance over which these LEDs can be used in fiber systems. InGaAsP/InP LEDs have wider linewidths (due to alloy scattering, heavy doping, and temperature fluctuations), which depend on the details of their design. As temperature increases, the peak of the spectrum shifts to longer wavelength and the spectrum widens. The variation of the central wavelength with temperature is ~5 meV/°C. However, at 1.3 μm, graded index fibers have negligible chromatic dispersion, so this usually is not a problem; if it is, heat sinking and/or cooling can be provided. Resonant cavity LEDs can provide narrower linewidths, but are more difficult to fabricate.

LEDs do not suffer from the catastrophic optical damage that lasers do, because of their lower optical power densities. However, they do degrade with time. Lifetimes of 10^6 to 10^9 hours can be expected. Because degradation processes have an exponential dependence on temperature, LED life can be shortened by operating at excessive temperatures. Using concepts of thermally accelerated life testing, the power out P varies with time t as:

$$P(t) = P(0) \exp(-qt) \tag{68}$$

where $q = q_o \exp(-W_a/k_B T)$, with W_a as the activation energy, k_B as Boltzman's constant, and T as temperature. In GaAs LEDs, W_a is 0.6 to 1 eV. Of course, this assumes that the LEDs are placed in a proper electrical circuit.

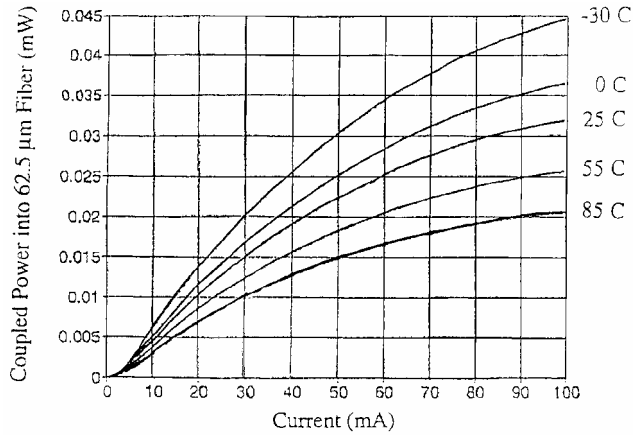

FIGURE 23 Optical power coupled from an *InGaAsP S–* LED into graded index fiber at 1.3 μm wavelength as a function of drive current, for several temperatures.[32]

LED light is typically unpolarized, since there is no preferred polarization for spontaneous emission.

Transient Response

Most LEDs respond in times faster than 1 μs; with optimization, they can reach the nanosecond response times needed for optical communication systems. To achieve the 125 Mb/s rate of the fiber distributed data interface (FDDI) standard requires a maximum rise time and fall time of 3.5 ns; to achieve the 622 Mb/s rate of the asynchronous transfer mode (ATM) standard, the necessary times drop to 0.7 ns.

The speed of an LED is limited by the lifetime of injected carriers; it does not have the turn-on delay of lasers, nor any relaxation oscillations, but it also does not have the fast decay of stimulated emission. The LED intrinsic frequency response (defined as the ratio of the AC components of the emitted light to the current) is[33]:

$$r(\omega) = (1 + \omega^2\tau^2)^{-1/2} \tag{69}$$

where τ is the minority carrier lifetime in the injected region. It can be seen that high-speed LEDs require small minority carrier lifetimes. The square-root dependence comes out of solving the rate equations.

When the active region is doped more highly than the density of injected carriers (the low-injection regime), the lifetime τ_L is determined by the background doping density N_o:

$$\frac{1}{\tau_L} = BN_o \tag{70}$$

The lifetime decreases as the doping increases. The challenge is to provide high levels of doping without increasing the fraction of nonradiative recombination. The fastest speeds that are usually obtained are ~1 ns, although doping with beryllium (or carbon) at levels as high as 7×10^{19} cm^{-3} has allowed speeds to increase to as much as 0.1 ns, resulting in a cutoff frequency of 1.7 GHz (at the sacrifice of some efficiency).[34]

When operating in the high-injection regime, the injected carrier density N can be much larger than the doping density, and $1/\tau_H = BN$. But N is created by a current density J such that $N = J\tau/ed$. Combining these two equations:

$$\frac{1}{\tau_H} = \left(\frac{BJ}{ed}\right)^{1/2} \tag{71}$$

The recombination time may be reduced by thinning the active region and by increasing the drive current. However, too much injection may lead to thermal problems, which in turn may cause modulation nonlinearity. LEDs with thin active layers operated in the high-injection regime will have the fastest response. Bandwidths in excess of 1 GHz have been achieved in practical LEDs.

Because LEDs have such wide wavelength spectra, frequency chirping is negligible. That is, LEDs cannot be modulated fast enough for their wavelengths to be affected by the modulation. Because LEDs do not have optical cavities, as do lasers, they will not have modal interference and noise. Also, there will not be strong feedback effects coming from external fiber facets, such as the coherence collapse. Because of their inherent light-current linearity, the modulation response of LEDs should be a direct measure of their frequency response. They add no noise to the circuit, and they add distortion only at the highest drive levels.

Drive Circuitry and Packaging

The LED is operated under sufficient forward bias to flatten the bands of the *pn* junction. This voltage depends on the bandgap and doping and is typically between 1 and 2 V. The current will be converted directly to light; typically, ~100 mA is required to produce a few milliwatts of output, with a series resistor used to limit the current.

The LED is modulated by varying the drive current. A typical circuit might apply the signal to the base circuit of a transistor connected in series with the LED and a current-limiting resistor. The variation in current flowing through the LED (and therefore in the light out) is proportional to the input voltage in the base circuit. LEDs are typically mounted on standard headers such as TO-18 or TO-46 cans; SMA and ST connectors are also used. The header is covered by a metal cap with a clear glass top through which light can pass.

4.9 VERTICAL CAVITY SURFACE-EMITTING LASERS (VCSELS)

The *vertical cavity surface-emitting laser* (VCSEL) has advantages for low-cost data transmission. The use of a laser means that multigigahertz modulation is possible, and the stimulated emission is directional, rather than the isotropic spontaneous emission of LEDs. Because the light is emitted directly from the surface, single or multimode fiber can be directly butt-coupled with an inexpensive mounting technology, and the coupling efficiency can be very high. The VCSELs can also be fabricated in linear arrays that can be coupled inexpensively to linear arrays of fibers for parallel fiber interconnects with aggregate bit rates of several gigabits per second, amortizing the alignment cost over the number of elements in the array. VCSELs lend themselves to two-dimensional arrays as well, which makes them attractive to use with smart pixels. The planar fabrication of VCSELs allows for wafer-scale testing, another cost savings.

The VCSEL requires mirrors on the top and bottom of the active layer, forming a vertical cavity, as shown in Fig. 24. These lasers utilize the fact that a DBR (multilayer quarter-wavelength dielectric stack) can make a very high reflectance mirror. Thus, the very short path length through a few quantum wells (at normal incidence to the plane) is sufficient to reach threshold.

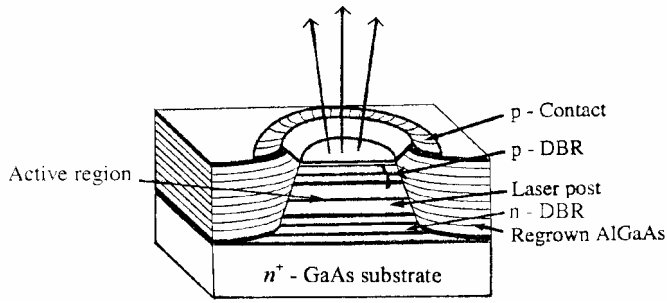

FIGURE 24 One example of a vertical cavity surface emitting laser (VCSEL) geometry. This is a passive antiguide region (PAR) VCSEL.[35] Light is reflected up and down through the active region by the two DBR mirrors. After the laser post is etched, regrowth in the region outside the mesa provides a high-refractive-index AlGaAs*nipi* region to stop current flow and to provide excess loss to higher-order modes.

In the 1990s, the only commercial VCSELs were based on GaAs: either GaAs active regions that emit at 850 nm, or strained InGaAs active regions that emit at 980 nm. The former are of greater interest in low-cost communication systems because they are compatible with inexpensive silicon detectors. This section describes the design of VCSELs and some of their key characteristics.

Number of Quantum Wells

A single quantum well of GaAs requires ~100 A/cm^2 to achieve transparency; N wells require N times this current. To keep the threshold current less than 1 kA/cm^2, then, means less than 10 QWs. The VCSEL provides an optical standing wave which, in GaAs, has a period of ~120 nm. The gain region should be confined to the quarter-wavelength region at the peak of the optical standing wave, a region of about 60 nm. Thus, a typical active region might consist of 3 QWs of 10 nm thickness, each separated by ~10 nm. The lowest threshold VCSELs are single quantum wells of InGaAs grown on GaAs, sacrificing power for threshold.

Mirror Reflectivity

When the mirror reflectivity R in a laser is very high, such that $R = 1 - \varepsilon$, a simple expression for the threshold gain-length product $G_L L$ is

$$G_L L = \varepsilon_1 \varepsilon_2 \tag{72}$$

Typical GaAs lasers have gains $G_L \sim 1000$ cm^{-1}. For a quantum well thickness of 10 nm, the gain per quantum well is 10^{-3} and reflectivities of ~98 percent for each mirror should be sufficient to achieve threshold for 3 QW. Very often, however, in order to lower the threshold much higher reflectivities are used, particularly on the back mirror.

The on-resonance Bragg mirror reflectivity is the square of the reflection coefficient r, given by:

$$r = \frac{1 - (n_f/n_i)(n_l/n_h)^{2N}}{1 + (n_f/n_i)(n_l/n_h)^{2N}} \tag{73}$$

where there are N pairs of quarter-wavelength layers that alternate high-index and low-index (n_h and n_l, respectively), and n_f and n_i are the refractive index of the final and initial media, respectively.[36]

For high-reflectance Bragg mirrors, the second term in the numerator and denominator is small, and the reflectivity can be simplified to:

$$\varepsilon = 1 - R = 1 - r^2 = 4\left(\frac{n_f}{n_i}\right)\left(\frac{n_l}{n_h}\right)^{2N} \tag{74}$$

Higher reflectivity (smaller ε) is provided by either more layer pairs or a larger refractive index difference between the two compositions in the layer pairs. Also, Eq. (74) shows that internal mirrors ($n_f = n_i$) will have a smaller reflectivity than external mirrors ($n_f = 1$) for the same number of layer pairs. If the layer pair is GaAs ($n \sim 3.6$) and AlAs ($n \sim 3.0$), a mirror consisting of 15 layer pairs will have an internal reflectivity $R = 98$ percent and external reflectivity $R = 99.5$ percent. Thirty layer pairs will increase the internal mirror reflectivity to 99.96 percent. Bragg mirrors with a smaller fraction of AlAs in the low-index layers will require more layer pairs to achieve the same reflectivity.

Some advanced technologies reduce the number of required layer pairs by selectively oxidizing the AlAs layers to lower their refractive index to $n \sim 1.5$. Using such techniques, reflec-

tivities as high as 99.95 and 99.97 percent can be achieved from mirrors grown with only 7 interior pairs and 5 outside pairs, respectively; these mirrors can be used in VSCELs, but do not easily conduct current.

Electrical Injection

There is difficulty in injecting carriers from the top electrode down through the Bragg reflector, even if it is *n*-doped, because the GaAs layers provide potential wells that trap carriers. Furthermore, *n*-doping increases the optical loss in the mirrors. Possible solutions include reducing the AlAs concentration to < 60 percent; using graded compositions rather than abrupt layer pairs; using lateral carrier injection (which increases the operating voltage); using a separately deposited dielectric mirror on top of a transparent electrode; or accepting the high resistivity of the Bragg mirror and operating the laser at relatively high voltage.

The major issue for VCSELs, then, is to inject carriers efficiently, without resistive loss and without carrier leakage. Because resistance in *n*-doped mirrors is less than in *p*-doped mirrors, typically the top mirror is doped *n*-type and carrier injection comes from a top electrode. Light is emitted through a window hole in this top electrode. Carrier injection into the active region often requires rather high voltages because it may be difficult to drive carriers across the Bragg mirrors. Transverse current injection typically requires even higher voltages, although this method has been proven useful when highly conductive layers are grown just above and below the active region.

Some VCSELs use GRINSCH structures (similar to the composition used in edge emitters) to reduce the resistivity in the active region. Typical thresholds for VCSELs are about 3.5 V. Because the drive is limited by resistance, thresholds are typically given as voltages, rather than currents.

Planar VCSELs of fairly large diameter (>10 μm) are straightforward to make, and are useful when a low threshold is not required and multispatial mode is acceptable. Ion implantation outside the VCSEL controls the current in this region; the light experiences gain guiding and perhaps thermal lensing. Smaller diameters (3 to 10 μm) require etching mesas vertically through the Bragg mirror in order to contain the laser light that tends to diffract away.

Higher injection efficiency is obtained by defining the active region through an oxide window just above the active layer. This uses a selective lateral oxidation process that can double the maximum conversion efficiency to almost 60 percent. A high-aluminum fraction AlGaAs layer (~98 percent) is grown. A mesa is etched to below that layer. Then a long, soaking, wet-oxidization process selectively creates a ring of native oxide that stops vertical carrier transport. The chemical reaction moves in from the side of an etched pillar and is stopped when the desired diameter is achieved. Such a current aperture confines current only where needed. Threshold voltages of <6 V are common in diameters ~12 μm. This geometry is shown in Fig. 25. This oxide-defined current channel increases the efficiency, but tends to cause multiple transverse modes due to relatively strong oxide-induced index guiding. Single-mode requirements force the diameter to be very small (below 4 to 5 μm).

Spatial Characteristics of Emitted Light

Single transverse mode remains a challenge for VCSELs, particularly at the larger diameters. When VCSELs are modulated, lateral spatial instabilities tend to set in, and spatial hole burning causes transverse modes to jump. This can introduce considerable modal noise in coupling VCSEL light into fibers. Techniques for mode selection include incorporating a spatial filter, using an antiguide structure where the losses are much higher for higher order modes, or using sidewall scattering losses that are higher for higher-order modes. The requirement is that the mode selective losses must be large enough to overcome the effects of spatial hole burning.

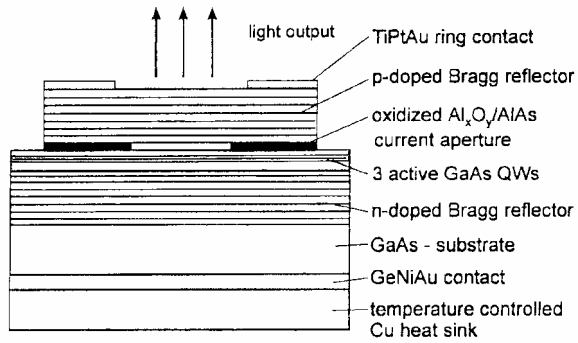

FIGURE 25 Cross-sectional view of an oxidized GaAs VCSEL. An AlGaAs layer with high aluminum content grown just above the active region is chemically oxidized into Al_xO_y by a process that moves in from the edge of the etched mesa with time. Controlling the oxidization rate and time results in a suitable current aperture to obtain high conversion efficiency.[37]

One approach to achieving single transverse mode output is to include a passive antiguide region (PAR), the geometry shown in Fig. 24.[35] The surrounding region has been etched and the sides backfilled with material of *higher* refractive index. This provides an *antiguide* for the laser, which has low loss only for the lowest order transverse mode. A single mode with a FWHM mode size of 7.4 μm (which matches single-mode fibers) can be achieved at 2.4 times threshold with VCSEL diameters of 15 μm. Current blocking outside the active area can be achieved by regrowing an *nipi*-doped antiguide. Typical thresholds for such lasers are 2 V (at 3 mA). A single-mode output of 1.7 mW with an input of 6.6 mA was reported, with more than 20 dB higher-order spatial mode suppression. Fixed polarization along one of the crystal orientations was observed during single-mode operation and attributed to asymmetry introduced in the etching and regrowth process. These structures have slightly higher thresholds than other geometries, but offer single-mode operation.

Other low-cost means of confining current are either proton implantation or etching mesas and then planarizing with polyimide. In both these cases, the regions surrounding the mesa will have a lower refractive index, which will cause the VCSEL to be a real index guide, which will tend toward multimode operation. This may introduce *modal noise* into fiber communication systems.

When the QWs are composed of InGaAs, the VCSELs will emit at 980 nm, and they can be designed to be bottom emitting, since the substrate is transparent. However, inexpensive silicon detectors can no longer be used at this wavelength, so these VCSELs offer fewer advantages in optical communication systems.

Light Out versus Current In

The VCSEL will, in general, have similar *L-I* performance to edge-emitting laser diodes, with some small differences. Because the acceptance angle for the mode is higher than in edge-emitting diodes, there will be more spontaneous emission, which will show up as a more graceful turn-on of light out versus voltage in. As previously mentioned, the operating voltage is 2 to 3 times that of edge-emitting lasers. Thus, Eq. (8) must be modified to take into account the operating voltage drop across the resistance R of the device. The operating power efficiency is:

$$P_{\text{eff}} = \eta_D \frac{I_{\text{op}} - I_{\text{th}}}{I_{\text{th}}} \frac{V_g}{V_g + I_{\text{op}}R} \tag{75}$$

Single-mode VCSELs of small diameter would typically have a 5 μm radius, a carrier injection efficiency of 80 to 90 percent, an internal optical absorption loss $\alpha_i L$ of 0.003, an optical scattering loss of 0.001, and a net transmission through the front mirror of 0.005 to 0.0095. Carrier losses reducing the quantum efficiency are typically due to spontaneous emission in the wells, spontaneous emission in the barriers, Auger recombination, and carrier leakage.

Typical VCSELs designed for a compatibility with single-mode fiber incorporate an 8-μm proton implantation window and 10-μm-diameter window in the top contact. Such diodes may have threshold voltages of ~3 V and threshold currents of a few milliamps. These lasers may emit up to ~2 mW maximum output power. Devices will operate in zero-order transverse spatial mode with gaussian near-field profile when operated with DC drive current less than about twice the threshold. Output optical powers in single mode as high as 4.4 mW have been reported.

When there is emission in more than one spatial mode, or with both polarizations, there will usually be kinks in the *L-I* curve, as with multimode edge-emitting lasers.

Spectral Characteristics

Since the laser cavity is short, the longitudinal modes are much farther apart in wavelength, typically $\delta\lambda \sim 50$ nm, so only one longitudinal mode will appear, and there is longitudinal mode purity. The problem is with spatial modes, since at higher power levels the laser does not operate in a single spatial mode. Each spatial mode will have slightly different wavelengths, perhaps 0.01 to 0.02 nm apart. There is nothing in a typical VCSEL that selects a given polarization state. Thus, the VCSEL tends to oscillate in both polarization states, also with slightly different wavelengths.

When modulated, lateral spatial instabilities may set in, and spatial hole burning may cause transverse modes to jump. This can cause spectral broadening. In addition, external reflections can cause instabilities and increased relative intensity noise, just as in edge-emitting lasers.[38] For very short cavities, such as between the VCSEL and a butt-coupled fiber (with ~4 percent reflectivity), instabilities do not set in, but the output power can be affected by the additional mirror, which forms a Fabry-Perot cavity with the output mirror and can reduce or increase its effective reflectivity, depending on the round-trip phase difference. When the external reflection comes from ~1 cm away, bifurcations and chaos can be introduced with a feedback parameter $F > 10^{-4}$, where $F = C_e \sqrt{f_{\text{ext}}}$, with C_e and f_{ext} as defined in the discussion surrounding Eq. (45). For $R_o = 0.995$, $R_{\text{ext}} = 0.04$, the feedback parameter $F \sim 10^{-3}$, and instabilities can be observed if one is not careful about back-reflections.

Polarization

Most VCSELs exhibit linear but random polarization states, which may wander with time (and temperature) and may have slightly different emission wavelengths. These unstable polarization characteristics are due to the in-plane crystalline symmetry of the quantum wells grown on (100) oriented substrates. Polarization-preserving VCSELs require breaking the symmetry by introducing anisotropy in the optical gain or loss. Some polarization selection may arise from an elliptical current aperture. The strongest polarization selectivity has come from growth on (311) GaAs substrates, which causes anisotropic gain.

VCSELs at Other Wavelengths

Long-wavelength VCSELs at 1.3 and 1.55 μm have been limited by their poor high-temperature characteristics and by the low reflectivity of InP/InGaAsP Bragg mirrors due to

low index contrast between lattice-matched layers grown on InP. These problems have been overcome by using the same InGaAsP/InP active layers as in edge-emitting lasers, but providing mirrors another way: dielectric mirrors, wafer fusion, or metamorphic Bragg reflectors. Dielectric mirrors have limited thermal dissipation and require lateral injection, although carrier injection through a tunnel junction has shown promise. More success has been achieved by wafer-fusing GaAs/AlGaAs Bragg mirrors (grown lattice-matched onto GaAs) to the InP lasers. Wafer fusion occurs when pressing the two wafers together (after removing oxide off their surfaces) at 15 atm and heating to 630°C under hydrogen for 20 min. Typically one side will have an integrally grown InP/InGaAsP lattice-matched DBR (GaAlAsSb/AlAsSb mirrors also work). Mirrors can be wafer-fused on both sides of the VCSEL by etching away the InP substrate and one of the GaAs substrates. An integrated fabrication technology involves growing metamorphic GaAs/AlGaAs Bragg reflectors directly onto the InP structure. These high-reflectivity mirrors, grown by molecular beam epitaxy, have a large lattice mismatch and a high dislocation density. Nonetheless, because current injection is based on majority carriers, these mirrors can still be conductive, with high enough reflectivity to enable promising long-wavelength VCSELs.[39]

4.10 LITHIUM NIOBATE MODULATORS

The most direct way to create a modulated optical signal for communications applications is to directly modulate the current driving the laser diode. However, as discussed in the sections on lasers, this may cause turn-on delay, relaxation oscillation, mode-hopping, and/or chirping of the optical wavelength. Therefore, an alternative often used is to operate the laser in a continuous manner and to place a modulator after the laser. This modulator turns the laser light on and off without impacting the laser itself. The modulator can be butt-coupled directly to the laser, located in the laser chip package and optically coupled by a microlens, or remotely attached by means of a fiber pigtail between the laser and modulator.

Lithium niobate modulators have become one of the main technologies used for high-speed modulation of continuous-wave (CW) diode lasers, particularly in applications (such as cable television) where extremely linear modulation is required, or where chirp is to be avoided at all costs. These modulators operate by the electro-optic effect, in which the applied electric field changes the refractive index. Integrated optic waveguide modulators are fabricated by diffusion into a lithium niobate substrate. The end faces are polished and butt-coupled (or lens-coupled) to a single-mode fiber pigtail (or to the laser driver itself). This section describes the electro-optic effect in lithium niobate, its use as a phase modulator and an intensity modulator, considerations for high-speed operation, and the difficulties in achieving polarization independence.[40]

The most commonly used modulator is the *Y*-branch interferometric modulator shown in Fig. 26, discussed in a following subsection. The waveguides that are used for these modulators are fabricated in lithium niobate either by diffusing titanium into the substrate from a metallic titanium strip or by using ion exchange. The waveguide pattern is obtained by photolithography. The standard thermal indiffusion process takes place in air at 1050°C over 10 h. An 8-μm-wide strip of titanium 50 nm thick creates a fiber-compatible single mode at 1.3 μm. The process introduces ~1.5 percent titanium at the surface, with a diffusion profile depth of ~4 μm. The result is a waveguide with increased extraordinary refractive index of 0.009 at the surface. The ordinary refractive index change is ~0.006. A typical modulator will use aluminum electrodes 2 cm long, etched on either side of the waveguides, with a gap of 10 μm.

In the case of ion exchange, the lithium niobate sample is immersed in a melt containing a large proton concentration (typically benzoic acid or pyrophosphoric acid at >170°C), with some areas protected from diffusion by masking; the lithium near the surface of the substrate is replaced by protons, which increases the refractive index. The ion-exchange process changes only the extraordinary polarization; that is, only light polarized parallel to the *Z* axis

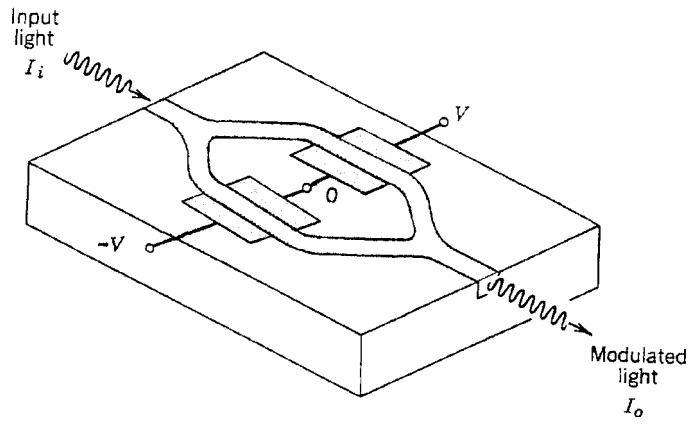

FIGURE 26 *Y*-branch interferometric modulator in the "push-pull" configuration. Center electrodes are grounded. Light is modulated by applying positive or negative voltage to the outer electrodes.

is waveguided. Thus, it is possible in lithium niobate to construct a polarization-independent modulator with titanium indiffusion, but not with proton-exchange. Nonetheless, ion exchange makes possible a much larger refractive index change (~0.12), which provides more flexibility in modulator design. Annealing after diffusion can reduce insertion loss and restore the electro-optic effect. Interferometric modulators with moderate index changes ($\Delta n < 0.02$) are insensitive to aging at temperatures of 95°C or below. Using higher index change devices, or higher temperatures, may lead to some degradation with time. Tapered waveguides can be fabricated easily by ion exchange for high coupling efficiency.[41]

Electro-Optic Effect

The *electro-optic effect* is the change in refractive index that occurs in a noncentrosymmetric crystal in the presence of an applied electric field. The linear electro-optic effect is represented by a third-rank tensor. However, using symmetry rules it is sufficient to define a reduced tensor r_{ij}, where $i = 1 \ldots 6$ and $j = x, y, z$, denoted as 1, 2, 3. Then, the linear electro-optic effect is traditionally expressed as a linear change in the inverse refractive index squared (see Vol. II, Chap. 13 of this handbook):

$$\Delta\left(\frac{1}{n^2}\right)_i = \sum_j r_{ij} E_j \qquad j = x, y, z \tag{76}$$

where E_j is the component of the applied electric field in the jth direction. The applied electric field changes the index ellipsoid of the anisotropic crystal into a new form based on Eq. (76):

$$a_1x^2 + a_2y^2 + a_3z^2 + 2a_4yz + 2a_5xz + 2a_6xy = 1 \tag{77}$$

where the diagonal elements are given by:

$$a_1 = \frac{1}{n_x^2} + \Delta\left(\frac{1}{n^2}\right)_1 \quad a_2 = \frac{1}{n_y^2} + \Delta\left(\frac{1}{n^2}\right)_2 \quad a_3 = \frac{1}{n_z^2} + \Delta\left(\frac{1}{n^2}\right)_3$$

and the cross terms are given by

$$a_4 = \Delta\left(\frac{1}{n^2}\right)_4 \quad a_5 = \Delta\left(\frac{1}{n^2}\right)_5 \quad a_6 = \Delta\left(\frac{1}{n^2}\right)_6$$

The presence of cross terms indicates that the ellipsoid is rotated and the lengths of the principal dielectric axes have changed.

Diagonalizing the ellipsoid of Eq. (77) will give the new axes and values. The general case is treated in Vol. II, Chap. 13. In lithium niobate, the material of choice for electro-optic modulators, the equations are simplified because the only nonzero components and their magnitudes are[42]:

$$r_{33} = 31 \times 10^{-12} \text{ m/V} \qquad r_{13} = r_{23} = 8.6 \times 10^{-12} \text{ m/V}$$

$$r_{51} = r_{42} = 28 \times 10^{-12} \text{ m/V} \qquad r_{22} = -r_{12} = -r_{61} = 3.4 \times 10^{-12} \text{ m/V}$$

The crystal orientation is usually chosen so as to obtain the largest electro-optic effect. This means that if the applied electric field is along *Z,* then light polarized along *Z* sees the largest field-induced change in refractive index. Since $\Delta(1/n^2)_3 = \Delta(1/n_z)^2 = r_{33}E_z$, performing the difference gives

$$\Delta n_z = -\frac{n_z^3}{2} r_{33} E_z \Gamma \tag{78}$$

We have included a filling factor Γ (also called an *optical-electrical field overlap parameter*) to include the fact that the applied field may not be uniform as it overlaps the waveguide, resulting in an effective field that is somewhat less than 100 percent of the maximum field.

In the general case for the applied electric field along *Z,* the only terms in the index ellipsoid will be $\Delta(1/n^2)_1 = r_{13}E_z = \Delta(1/n^2)_2 = r_{23}E_z$, and $\Delta(1/n^2)_3 = r_{33}E_z$. This means that the index ellipsoid has not rotated, its axes have merely changed in length. Light polarized along any of these axes will see a pure phase modulation. Because r_{33} is largest, polarizing the light along *Z* and providing the applied field along *Z* will provide the largest phase modulation. Light polarized along either *X* or *Y* will have the same (although smaller) index change, which might be a better direction if polarization-independent modulation is desired. However, this would require that light enter along *Z,* which is the direction in which the field is applied, so it is not practical.

As another example, consider the applied electric field along *Y.* In this case the nonzero terms are

$$\Delta\left(\frac{1}{n^2}\right)_1 = r_{12}E_y \quad \Delta\left(\frac{1}{n^2}\right)_2 = r_{22}E_y = -r_{12}E_y \quad \Delta\left(\frac{1}{n^2}\right)_4 = r_{42}E_y \tag{79}$$

It can be seen that now there is a *YZ* cross-term, coming from r_{42}. Diagonalization of the perturbed index ellipsoid finds new principal axes, only slightly rotated about the *Z* axis. Therefore, the principal refractive index changes are essentially along the *X* and *Y* axes, with the same values as $\Delta(1/n^2)_1$ and $\Delta(1/n^2)_2$ in Eq. (79). If light enters along the *Z* axis without a field applied, both polarizations (*X* and *Y*) see an ordinary refractive index. With a field applied, both polarizations experience the same phase change (but opposite sign). We later describe an interferometric modulator that does not depend on the sign of the phase change. This modulator is polarization independent, using this crystal and applied-field orientation, at the expense of operating at somewhat higher voltages, because $r_{22} < r_{33}$.

Since lithium niobate is an insulator, the direction of the applied field in the material depends on how the electrodes are applied. Fig. 27 shows a simple phase modulator. Electrodes that straddle the modulator provide an in-plane field as the field lines intersect the

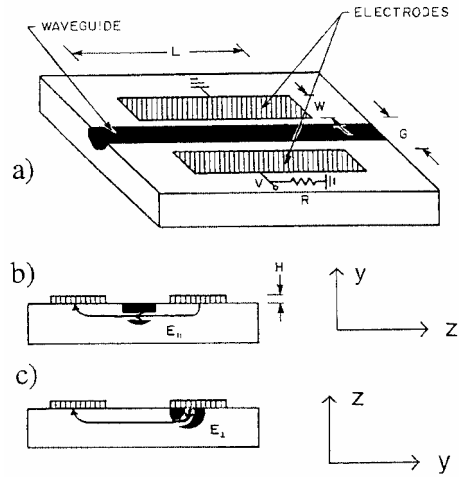

FIGURE 27 (*a*) Geometry for phase modulation in lithium niobate with electrodes straddling the channel waveguide. (*b*) End view of (*a*), showing how the field in the channel is parallel to the surface. (*c*) End view of a geometry placing one electrode over the channel, showing how the field in the channel is essentially normal to the surface.

waveguide, as shown in Fig. 27*b.* This requires the modulator to be *Y-cut* $LiNbO_3$ (the *Y* axis is normal to the wafer plane), with the field lines along the *Z* direction; *X-cut* $LiNbO_3$ will perform similarly. Figure 27*c* shows a modulator in *Z-cut* $LiNbO_3$. In this case, the electrode is placed over the waveguide, with the electric field extending downward through the waveguide (along the *Z* direction). The field lines will come up at a second, more distant electrode. In either case, the field may be fringing and nonuniform, which is why the filling factor Γ has been introduced.

Phase Modulation

Phase modulation is achieved by applying a field to one of the geometries shown in Figure 27. The field is roughly *V/G,* where *G* is the gap between the two electrodes. For an electrode length *L,* the phase shift is:

$$\Delta\phi = \Delta n_z kL = -\frac{n_o^3}{2} r_{33} \left(\frac{V}{G}\right) \Gamma\, kL \tag{80}$$

The refractive index for bulk $LiNbO_3$ is given by[43]:

$$n_o = 2.195 + \frac{0.037}{[\lambda\ (\mu m)]^2}$$

and

$$n_e = 2.122 + \frac{0.031}{[\lambda\ (\mu m)]^2}$$

Inserting numbers for a wavelength of 1.55 μm, $n_o = 2.21$. When $G = 10$ μm and $V = 5$ V, a π phase shift is expected in a length $L \sim 1$ cm.

It can be seen from Eq. (80) that the electro-optic phase shift depends on the product of the length and voltage. Longer modulators can use smaller voltages to achieve π phase shift. Shorter modulators require higher voltages. Thus, phase modulators typically use the product of the voltage required to reach π times the length as the figure of merit. The modulator just discussed has a 5 V · cm figure of merit.

The electro-optic phase shift has a few direct uses, such as providing a *frequency shifter* (since $\partial\phi/\partial t \propto \nu$). However, in communication systems this phase shift is generally used in an interferometric configuration to provide intensity modulation, discussed next.

Y-Branch Interferometric (Mach-Zehnder) Modulator

The *interferometric modulator* is shown schematically in Fig. 26. This geometry allows waveguided light from the two branches to interfere, forming the basis of an intensity modulator. The amount of interference is tunable by providing a relative phase shift on one arm with respect to the other. Light entering a single-mode waveguide is equally divided into the two branches at the *Y* junction, initially with zero relative phase difference. The guided light then enters the two arms of the waveguide interferometer, which are sufficiently separated that there is no coupling between them. If no voltage is applied to the electrodes, and the arms are exactly the same length, the two guided beams arrive at the second *Y* junction in phase and enter the output single-mode waveguide in phase. Except for small radiation losses, the output is equal in intensity to the input. However, if a π phase difference is introduced between the two beams via the electro-optic effect, the combined beam has a lateral amplitude profile of odd spatial symmetry. This is a second-order mode and is not supported in a single-mode waveguide. The light is thus forced to radiate into the substrate and is lost. In this way, the device operates as an electrically driven optical intensity on-off modulator. Assuming perfectly equal splitting and combining, the fraction of light transmitted is:

$$\eta = \left[\cos\left(\frac{\Delta\phi}{2}\right)\right]^2 \tag{81}$$

where $\Delta\phi$ is the difference in phase experienced by the light in the different arms of the interferometer: $\Delta\phi = \Delta n\, kL$, where $k = 2\pi/\lambda$, Δn is the difference in refractive index between the two arms, and L is the path length of the refractive index difference. The voltage at which the transmission goes to zero ($\Delta\phi = \pi$) is usually called V_π. By operating in a push-pull manner, with the index change increasing in one arm and decreasing in the other, the index difference Δn is twice the index change in either arm. This halves the required voltage.

Note that the transmitted light is periodic in phase difference (and therefore voltage). The response depends only on the integrated phase shift and not on the details of its spatial evolution. Therefore, nonuniformities in the electro-optically induced index change that may occur along the interferometer arms do not affect the extinction ratio. This property has made the interferometric modulator the device of choice in communications applications.

For analog applications, where linear modulation is required, the modulator is prebiased to the quarter-wave point (at voltage $V_b = \pi/2$), and the transmission efficiency becomes linear in $V - V_b$ (for moderate excursions):

$$\eta = \frac{1}{2}\left[1 + \sin\frac{\pi(V - V_b)}{2V_\pi}\right] \approx \frac{1}{2} + \frac{\pi}{4}\,\frac{(V - V_b)}{V_\pi} \tag{82}$$

The electro-optic effect depends on the polarization. For the electrode configuration shown here, the applied field is in the plane of the lithium niobate wafer, and the polarization

of the light to be modulated must also be in that plane. This will be the case if a TE-polarized semiconductor laser is butt-coupled (or lens-coupled) with the plane of its active region parallel to the lithium niobate wafer, and if the wafer is *Y*-cut. Polarization-independent modulation requires a different orientation, to be described later. First, however, we discuss the electrode requirements for high-speed modulation.

High-Speed Operation

The optimal modulator electrode design depends on how the modulator is to be driven. Because the electrode is on the order of 1 cm long, the fastest devices require traveling wave electrodes rather than lumped electrodes. Lower-speed modulators use lumped electrodes, in which the modulator is driven as a capacitor terminated in a parallel resistor matched to the impedance of the source line. The modulation speed depends primarily on the *RC* time constant determined by the electrode capacitance and the terminating resistance. To a smaller extent, the speed also depends on the resistivity of the electrode itself. The capacitance per unit length is a critical design parameter. This depends on the material dielectric constant and the electrode gap-to-width ratio *G/W*. The capacitance-to-length ratio decreases and the bandwidth-length product increases essentially logarithmically with increasing *G/W*. At $G/W = 1$, $C/L = 2.3$ pF/cm and $\Delta f_{RC} L = 2.5$ GHz · cm. The tradeoff is between large *G/W* to reduce capacitance and a small *G/W* to reduce drive voltage and electrode resistance. The ultimate speed of lumped electrode devices is limited by the electric transit time, with a bandwidth-length product of 2.2 GHz · cm. The way to achieve higher speed modulation is to use traveling wave electrodes.

The traveling wave electrode is a miniature transmission line. Ideally, the impedance of this coplanar line is matched to the electrical drive line and is terminated in its characteristic impedance. In this case, the modulator bandwidth is determined by the difference in velocity between the optical and electrical signals (velocity mismatch or walk-off), and any electrical propagation loss. Because of competing requirements between a small gap to reduce drive voltage and a wide electrode width to reduce RF losses, as well as reflections at any impedance transition, there are subtle trade-offs that must be considered in designing traveling-wave devices.

Lithium niobate modulators that operate at frequencies out to 8 GHz at 1.55 μm wavelength are commercially available, with operating voltages of <4 V.[44] Typical modulators have <5 dB insertion loss and >20 dB extinction ratio. To operate near quadrature, which is the linear modulation point, a bias voltage of ~10 V is required. Direct coupling from a laser or polarization-maintaining fiber is required, since these modulators are not independent of polarization. Traveling wave modulators operating well beyond 20 GHz have been reported in the research literature.

Insertion Loss

Modulator insertion loss can be due to Fresnel reflection at the lithium niobate–air interfaces, which can be reduced by using antireflection coatings or index matching (which only helps, but does not eliminate this loss, because of the very high refractive index of lithium niobate). The other cause of insertion loss is mode mismatch. The diffusion process must make a deep waveguide. Typically, the waveguide will be 9 μm wide and 5 μm deep. While the in-plane mode can be gaussian and can match well to the fiber mode, the out-of-plane mode tends to be asymmetric, and its depth must be carefully optimized. In an optimized modulator, the coupling loss per face is about 0.35 dB and the propagation loss is about 0.3 dB/cm. This result includes a residual index-matched Fresnel loss of 0.12 dB.

Misalignment can also cause insertion loss. An offset of 2 μm typically increases the coupling loss by 0.25 dB. The angular misalignment must be maintained below 0.5° in order to keep the excess loss below 0.25 dB.[40]

Propagation loss comes about from absorption, metallic overlay, scattering from the volume or surface, bend loss, and excess loss in the *Y*-branches. Absorption loss at 1.3- and 1.55-μm wavelengths appears to be <0.1 dB/cm. Bend loss can be large, unless any curvature of guides is small. The attenuation coefficient in a bend has the form:

$$\alpha = C_1 \exp(-C_2 R) \tag{83}$$

where $C_1 = 15\ \text{mm}^{-1}$ and $C_2 = 0.4\ \text{mm}^{-1}$ in titanium indiffused lithium niobate, at wavelengths around 1.3 to 1.5 μm. This means that a 5-mm-long section of constant radius 20 mm will introduce only 0.1 dB of excess loss.[45]

A final source of loss in *Y*-branches is excess radiation introduced by sharp transitions. These branches must be fabricated carefully to avoid such losses, since the tolerances on waveguide roughness are critically small.

Polarization Independence

As previously shown, if the light is incident along the *Z* axis and the field is along the *Y* axis, then light polarized along *X* and *Y* experience the same phase shift, but opposite signs. An *X*-cut crystal, with an in-plane field along *Y,* therefore, provides polarization-independent interferometric modulation at the sacrifice of somewhat higher half-wave voltage (e.g., 17 V).[46] Because of the difficulty of achieving exactly reproducible lengths in the two arms of the *Y*-branch interferometer, it has been found useful to do a postfabrication phase correction using laser ablation.

Photorefractivity and Optical Damage

Lithium niobate exhibits *photorefractivity,* also called *optical damage* when it is a nuisance. This phenomenon is a change in refractive index as a result of photoconduction originating in weak absorption by deep traps and a subsequent redistribution of charges within the lithium niobate. Because the photoconductive crystal is electro-optic, the change in electric field resulting from charge motion shows up as a change in refractive index, altering the phase shift as well as the waveguiding properties. While photorefractivity seriously limits the performance of lithium niobate modulators at shorter wavelengths (even at 850 nm),[47] it is not a serious concern at 1.3 and 1.55 μm.

However, partial screening by photocarriers may cause a drift in the required bias voltage of modulators, and systems designers may need to be sensitive to this.

Delta-Beta Reversal Modulators

Early designs for modulators used a configuration entitled the *delta-beta reversal modulator.* This is based on the concept of the *directional coupler.* When two parallel waveguides are situated close enough that their evanescent fields overlap, light couples between them. If they are identical, light can oscillate completely between them, similar to the coupling of energy between two coupled pendula. When they are not identical, the coupling occurs more rapidly, and there is not complete transfer of energy between the two guides. A modulator can be built, then, by using a field applied to one guide to destroy their synchronicity and therefore their coupling.[48] This has not proven to be practical, however, both because of fabrication difficulties and because of residual effects due to photorefractivity. These modulators are not discussed further here.

4.11 ELECTROABSORPTION MODULATORS FOR FIBER-OPTIC SYSTEMS

When modulators are composed of III-V semiconductors, they can be integrated directly on the same chip as the laser, or placed external to the laser chip. External modulators may be butt-coupled to the laser, coupled by means of a microlens, or coupled by means of a fiber pigtail.

Electroabsorption. Semiconductor modulators typically use *electroabsorption,* the electric field dependence of the absorption near the band edge of a semiconductor. Electroabsorption is particularly strong in quantum wells (QWs), where it is called the *quantum-confined Stark effect* (*QCSE*). An example of the frequency dependence of the QCSE is shown in Fig. 28. The absorption spectrum of QWs exhibits a peak at the *exciton resonance.* When a field is applied, the exciton resonance moves to longer wavelengths, becomes weaker, and broadens. This means that the absorption increases with field on the long-wavelength side, as the exciton resonance moves to longer wavelengths. At wavelengths closer to the exciton resonance, the absorption will first increase with field, then plateau, and finally decrease, as the field continues to grow. At wavelengths shorter than the zero-field exciton resonance, the absorption will decrease with increasing field, as the resonance moves to longer wavelengths.

While electroabsorption in QWs is much larger than in bulk, due to the sharpness of the excitonic-enhanced absorption edge, the useful absorption change must be multiplied by the filling factor of the QW in the waveguide, which reduces its effective magnitude. Under some conditions, electroabsorption near the band edge in bulk semiconductors (typically called the *Franz-Keldysh effect*) may also be useful in electroabsorption modulators.

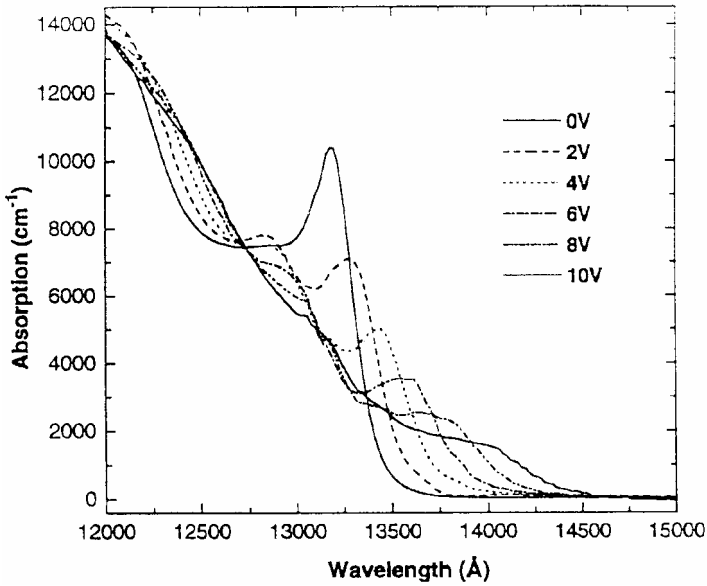

FIGURE 28 Spectrum of quantum-confined Stark effect (QCSE) in InAsP/InP strained MQWs. The absorption changes with applied field.[49]

Waveguide Modulators. When light traverses a length of QW material, the transmission will be a function of applied voltage. An electroabsorption modulator consists of a length of waveguide containing QWs. The waveguide is necessary to confine the light to the QW region so that it does not diffract away. Thus, low-refractive-index layers must surround the layer containing the QWs. Discrete electroabsorption modulators are typically made by using geometries very similar to those of edge-emitting lasers (Fig. 1). They are cleaved, antireflection coated and then butt-coupled to the laser chip. They are operated by a reverse bias, rather than the forward bias of a laser. Alternatively, the modulator is integrated on the laser chip, with the electroabsorption modulator region following a DFB or DBR laser in the optical train, as shown in Fig. 29. This figure shows the simplest electroabsorption modulator, with the same MQW composition as the DFB laser. This ridge waveguide device has been demonstrated with a 3-dB bandwidth of 30 GHz. The on-off contrast ratio is 12.5 dB for a 3-V drive voltage in a 90-μm-long modulator.[50] The use of the same QW is possible by setting the grating that determines the laser wavelength to well below the exciton resonance. Because of the inherently wide gain spectrum exhibited by strained layer MQWs, this detuning is possible for the laser and allows it to operate in the optimal wavelength region for the electroabsorption modulator.

Other integrated electroabsorption modulators use a QW composition in the electroabsorption region that is different from that of the laser medium. Techniques for integration are discussed later.

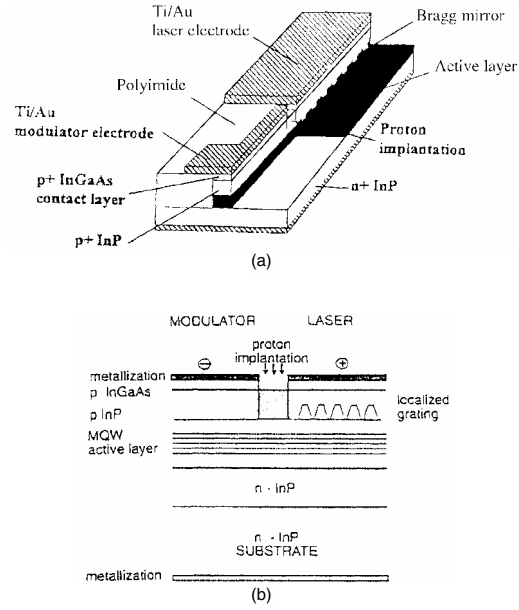

FIGURE 29 (*a*) Geometry for a channel electroabsorption modulator (foreground) integrated on the same chip with a DFB laser (background, under the Bragg mirror). (*b*) Side view, showing how the same MQW active layer can be used under forward bias with a grating to provide a DFB laser, and in a separate region under reverse bias for modulation, with the two regions electrically separated by proton implantation.[50]

Intensity Modulation by Electroabsorption

In an electroabsorption waveguide modulator of length L, where the absorption is a function of applied field E, the transmission is a function of field: $T(E) = \exp[-\alpha(E)L]$, where α is the absorption per unit length, averaging the QW absorption over the entire waveguide. (That is, α is the QW absorption multiplied by the filling factor of the QW in the waveguide.) Performance is usually characterized by two quantities: *insertion loss* (throughput at high transmission) and *contrast ratio* (ratio of high transmission to low transmission). Assume that the loss in the QW, initially at low value α_{-}, increases by $\delta\alpha$. The *contrast ratio* is given by:

$$\mathrm{CR} \equiv \frac{T_{\mathrm{high}}}{T_{\mathrm{low}}} = \exp(\delta\alpha L). \tag{84}$$

The *insertion loss* is given by

$$A \equiv 1 - T_{\mathrm{high}} = 1 - \exp(-\alpha_{-} L) \approx \alpha_{-} L \tag{85}$$

A long path length L means a high contrast ratio but also a large insertion loss and large capacitance, which results in a slower speed. Choosing the most practical length for any given application requires trading off the contrast ratio against insertion loss and speed.

To keep a moderate insertion loss, waveguide lengths should be chosen so that $L \approx 1/\alpha_{-}$. This sets the contrast ratio as

$$\mathrm{CR} = \exp\left(\frac{\delta\alpha}{\alpha_{-}}\right)$$

The contrast ratio depends on the ratio of the change in absorption to the absorption in the low-loss state; this fact is used to design the QW composition and dimensions relative to the wavelength of operation. In general, the contrast ratio improves farther from the band edge, but the maximum absorption is smaller there, so the modulator must be longer, which increases its capacitance, decreases its speed, and increases its loss. Contrast ratios may reach 10/1 or more with <2 V applied for optimized electroabsorption modulators. The contrast ratio does not depend on the filling factor of the QW in the waveguide, but the required length L does. Since high-speed modulators require small capacitance and small length, the filling factor should be as high as possible.

Waveguide modulators are used at wavelengths where the absorption is not too large, well below the band edge. In this wavelength region, electroabsorption at a fixed wavelength can be modeled by a pure quadratic dependence on field. Thus:

$$\alpha(E) \approx \alpha_o + \alpha_2 E^2 \tag{86}$$

where α_2 will typically depend on the wavelength, the QW and barrier dimensions and composition, and the waveguide filling factor. Intimately connected with this change in absorption is a change in refractive index with a similar field dependence:

$$\delta n(E) \approx n_2 E^2 \tag{87}$$

where n_2 is also strongly dependent on wavelength. Both electroabsorption and electrorefraction are about an order of magnitude larger in QWs than in bulk material. Specific numerical values depend on the detailed design, but typical values are on the order of $\alpha_o \sim 100\ \mathrm{cm}^{-1}$, $\delta\alpha \sim 1000\ \mathrm{cm}^{-1}$, $L \sim 200\ \mu\mathrm{m}$ for 2 V applied across an i region 2.5 μm thick, for a field of ~10 kV/cm. This means $\alpha_2 \sim 2 \times 10^{-5}\ \mathrm{cm/V^2}$. Also, $n_2 \sim 2 \times 10^{-11}\ \mathrm{V^{-2}}$.

Applying a Field in a Semiconductor

The electric field is usually applied by reverse biasing a *pin* junction. The electric field is supported by the semiconductor depletion region that exists within a *pin* junction, or at a metal-semiconductor junction (Schottky barrier). Charge carrier depletion in the *n* and *p* regions may play a role in determining the electric field across thin intrinsic regions. Taking this into account while assuming an undoped *i* region, the electric field across the *i* region of an ideally abrupt *pin* junction is given by[51]:

$$E = \frac{eN_d}{\varepsilon} \frac{-d_i + \sqrt{d_i^2 + 2(\varepsilon V_{\text{tot}}/eN_o)(1 + N_d/N_a)}}{1 + N_d/N_a} \tag{88}$$

where N_d is the (donor) doping density in the *n* region, N_a is the (acceptor) doping density in the *p* region, *e* is the elementary charge, ε is the dielectric constant, d_i is the thickness of the intrinsic region, and V_{tot} is the sum of the applied and built-in field (defined positive for reverse bias). When the *n* and *p* regions are highly doped and the *i* region is undoped, most of the voltage is dropped across the *i* region. When d_i is sufficiently large, the square root can be approximated, the d_i terms in the numerator cancel, and Eq. (88) becomes:

$$E = \frac{V_{\text{tot}}}{d_i}\left[1 - \frac{\varepsilon V_{\text{tot}}\,(1 + N_d/N_a)}{2\,eN_d d_i^2}\right] \tag{89}$$

which, to lowest order, is just the field across a capacitor of thickness d_i. For a typical applied voltage of 5 V and $d_i = 0.25$ μm, with $N_a = 10^{18}$ cm^{-3} and $N_d = 10^{18}$ cm^{-3}, $E = 2 \times 10^5$ V/cm. How much absorption and refractive index change this results in depends on wavelength and, of course, material design.

Integrating the Modulator

Stripe-geometry modulators can be cleaved from a wafer, antireflection coated, and butt-coupled to either a laser or a fiber pigtail. Typical insertion losses may be ~10 dB. Or, the modulator may be monolithically integrated with the laser. A portion of the same epitaxial layer grown for the laser active region can be used as an electroabsorption modulator by providing a separate contact and applying a reverse bias. When such a modulator is placed inside the laser cavity, a multielement laser results that can have interesting switching properties, including wavelength tunability. When the electroabsorption modulator is placed outside the laser cavity, it is necessary to operate an electroabsorption modulator at wavelengths well below the band edge. Then, the modulator region must have a higher energy bandgap than the laser medium. Otherwise, the incident light will be absorbed, creating free electron-hole pairs that will move to screen the applied field and ruin the modulator.

The integration of an electroabsorption modulator, therefore, usually requires that the light traverse some portion of the sample that has a different bandgap from that of the laser region. Four techniques have been developed: etching and regrowth, vertical coupling between layers, selective area epitaxy, and postgrowth well and barrier intermixing.

Etching and Regrowth. Typically, a first set of epitaxial layers is grown everywhere, which includes the laser structure up through the QW layer. Then the QW layer is etched away from the regions where it is not needed. The structure is then overgrown everywhere with the same upper cladding layers. This typically results in a bulk electroabsorption modulator, consisting of laser cladding material. A more complex fabrication process might mask the laser region during the regrowth process and grow a different QW composition that would provide an integrated butt-coupled modulator for the DFB (or DBR) QW laser.

Vertical Coupling Between Layers. This approach makes it possible to use a QW modulator as well as a QW laser, with a different QW composition in each. Two sets of QWs can be grown one on top of the other and the structures can be designed so that light couples vertically from one layer to the other, using, for example, grating assisted coupling. This may involve photolithographically defining a grating followed by a regrowth of cladding layers, depending on the design.

Selective Area Epitaxy. Growth on a patterned substrate allows the width of the QWs to be varied across the wafer during a single growth. The substrate is usually coated with a SiO_2 mask in which slots are opened. Under a precise set of growth conditions no growth takes place on top of the dielectric, but surface migration of the group III species (indium) can take place for some distance across the mask to the nearest opening. The growth rate in the opened area depends on the width of the opening and the patterning on the mask. Another approach is epitaxial growth on faceted mesas, making use of the different surface diffusion lengths of deposited atomic species on different crystal facets.

Well and Barrier Intermixing. The bandgap of a QW structure can be modified after growth by intermixing the well and barrier materials to form an alloy. This causes a rounding of the initially square QW bandgap profile and, in general, results in an increase of the bandgap energy. This provides a way to fabricate lasers and bandgap-shifted QCSE modulators using only one epitaxial step. Intermixing is greatly enhanced by the presence of impurities or defects in the vicinity of the QW interfaces. Then the bandgap is modified using impurity induced disordering, laser beam induced disordering, impurity-free vacancy diffusion, or ion implantation enhanced interdiffusion. The challenge is to ensure that the electrical quality of the *pin* junction remains after interdiffusion; sometimes regrowth of a top *p* layer helps.[52]

Operating Characteristics

In addition to contrast ratio, insertion loss, and required voltage, the performance of electroabsorption modulators depends on speed, chirp, polarization dependence, optical power-handling capabilities, and linearity. These factors all depend on the wavelength of operation, the materials, the presence of strain, the QW and waveguide geometry, and the device design. There will be extensive trade-offs that must be considered to achieve the best possible operation for a given application. Modulators will differ, depending on the laser and the proposed applications.

Chirp. Because a change in refractive index is simultaneous with any absorption change, electroabsorption modulators, in general, exhibit *chirp* (frequency broadening due to the time-varying refractive index, also observed in modulated lasers), which can seriously limit their usefulness. As with semiconductor lasers, the figure of merit is:

$$\beta = k_o \frac{\delta n}{\delta \alpha} \tag{90}$$

Unlike with lasers, however, there are particular wavelengths of sizable absorption change at which $\delta n = 0$. Studies have shown that these nulls in index change can be positioned where $\delta\alpha$ is large by using coupled quantum wells (CQWs).[53] These structures provide two, three, or more wells so closely spaced that the electron wave functions overlap between them. If desired, several sets of these CQWs may be used in a single waveguide, if they are separated by large enough barriers that they do not interact. Chirp-free design is an important aspect of electroabsorption modulators.

On the other hand, since the chirp can be controlled in electroabsorption modulators, there are conditions under which it is advantageous to provide a negative chirp to cancel out the positive chirp introduced by fibers. This allows 1.55-μm laser pulses to travel down normal dispensive fiber (zero material dispersion at 1.3 μm wavelength) without the pulses unduly spreading.

Polarization Dependence. In general, the quantum-confined Stark effect is strongly polarization dependent, although there may be specific wavelengths at which TE and TM polarized light experience the same values of electroabsorption (and/or electrorefraction). It turns out that polarization-independent modulation is more readily achieved by using strained QWs. In addition, the contrast ratio of electroabsorption change at long wavelengths can be improved by using strained QWs.

Optical Power Dependence. During the process of electroabsorption, the modulators can absorb some of the incident light. This will create electron-hole pairs. If these electron-hole pairs remain in the QWs, at high optical powers they will introduce a free carrier plasma field that can screen the exciton resonance. This broadens the absorption spectrum and reduces the contrast ratio. In some cases, electroabsorption modulators operating at the band edge of bulk semiconductors (the *Franz-Keldysh effect*) may be able to operate with higher laser power. A common approach is to use shallow QWs, so that the electrons and holes may escape easily.

Even when the electron-hole pairs created by absorption escape the QWs, they will move across the junction to screen the applied fields. This will tend to reduce the applied field, and the performance will depend on the magnitude of absorbed light. Photogenerated carriers must also be removed, or they will slow down the modulator's response time. Carriers may be removed by leakage currents in the electrodes or by recombination.

Built-in Bias. Because *pin* junctions have built-in fields, even at zero applied voltage, electroabsorption modulators have a prebias. Some applications use a small forward bias to achieve even larger modulation depths. However, the large forward current resulting from the forward bias limits the usefulness of this approach. There are, at present, some research approaches to remove the internal fields using an internal strain-induced piezoelectric effect to offset the *pn* junction intrinsic field.

Advanced Concepts for Electroabsorption in QWs

Coupled QWs offer the possibility of chirp control, and strained QWs offer the possibility of polarization independence, as previously explained. Adding these degrees of freedom to electroabsorption modulator design has been crucial in obtaining the highest performance devices.

High-performance Discrete Electroabsorption Modulators. A discrete modulator at 1.3 μm uses compressively strained InAsP wells grown on InP with InGaP barriers that are under tensile stress for strain compensation. High-speed operation with 3-dB bandwidth of >10 GHz and operating voltage of <2 V has been reported with a 20-dB on-off ratio.[54] The electroabsorptive layer contained five QWs, each 11 nm thick. The waveguide was an etched high-mesa structure 3 μm wide and 200 μm long. A modulator had a 10-dB insertion loss, and the measured electroabsorptive figure of merit was $\delta\alpha/\alpha_- = 10/1$.

A discrete modulator at 1.55 μm planned for polarization insensitivity and capable of handling high optical powers was designed with two strongly coupled tensilely strained QWs.[55] An 8-dB extinction ratio at 1.5-V drive voltage with a 3-dB bandwidth of 20 GHz was reported for average optical powers as high as 20 mW. Two InGaAs wells 5 nm thick with a 0.5-nm

InGaAlAs barrier between them were grown in pairs, with 9-nm barriers separating each pair. A total of 13 pairs of wells were grown and etched to form ridge waveguides 3 μm wide.

High-Performance Integrated Electroabsorption Modulators. When an electroabsorption modulator is integrated with a DFB laser, strain is not required because polarization insensitivity is not needed. Selective epitaxy has been used to grow a 200-μm-long modulator region consisting of lattice-matched quaternary wells ~5 nm in width. The reported extinction ratio was >13 dB at 1.5 V, with output powers in the on state of >4 mW, at a current of 100 mA.[56]

A two-step growth procedure provided a butt joint between a modulator and a DFB laser. Compressively strained wells were used to reduce the potential well that the hole sees, speeding the device.[57] Providing 3 V to a 200-μm-long modulator reduced the DFB laser output from 25 mW to 1 mW, for a 25/1 extinction ratio. The 3-dB bandwidth was 15 GHz. While there was a condition of zero chirp at –2 V, biasing to a regime of negative chirp allowed cancellation of the chromatic dispersion of fiber at the 1.55-μm laser wavelength. As a result, 10 Gb/s non-return-to-zero (NRZ) transmission was demonstrated over 60 km of standard fiber.

Wannier Stark Localization. A variation on the quantum-confined Stark effect uses an array of closely coupled quantum wells, which exhibit *Wannier Stark localization* (WSL). Because of the close spacing of the QWs, in the absence of a field, the electron wave function is free to travel across all wells, creating a miniband. When a field is applied, the wells decouple, and the electrons localize within individual wells. This removes the miniband, sharpening the absorption spectrum and creating a *decrease* in absorption below the band edge.[58]

Electron Transfer Modulators. A large absorption change can be created by filling the states near the edge of the semiconductor bands with electrons (or holes). This filling requires free carriers to be injected into the optical modulator. Quantum wells enhance the magnitude of this absorption change. Using applied voltage to transfer electrons from a reservoir across a barrier into a QW produces an effective long-wavelength modulator, termed a *barrier, reservoir, and quantum well electron transfer* (BRAQWET) modulator.[59] By changing the bias across the device, the bound states of the QW are moved above and below the Fermi level fixed by the electron reservoir. These states are then emptied or filled by a transfer of electrons to or from the reservoir region. Optical modulation is achieved due to state filling and by carrier screening of the coulombic interaction between the electrons and holes in the QW. The combined effects reduce the absorption as the QW fills with electrons. Since electron transfer across the spacer is a very fast process, these modulators can have high modulation speeds, demonstrated at almost 6 GHz.

4.12 ELECTRO-OPTIC AND ELECTROREFRACTIVE SEMICONDUCTOR MODULATORS

Some semiconductor modulators are based on phase modulation that is converted to amplitude modulation by using a Mach-Zehnder interferometer, in the same manner as discussed in Sec. 4.10. Such modulators can be integrated on the same substrate as the laser, but do not have the chirp issues that electroabsorption modulators exhibit.

Electro-Optic Effect in Semiconductors

The III-V semiconductors are electro-optic. Although they are not initially anisotropic, they become so when an electric field is applied, and so they can be used as phase modulators. Referring to the discussion of the electro-optic effect in Sec. 4.10 for definitions, the GaAs

electro-optic coefficients have only one nonzero term: $r_{41} = r_{52} = r_{63} = 1.4 \times 10^{-12}$ m/V. Crystals are typically grown on the (001) face, with the Z axis normal to the surface. This means that the field is usually applied along Z. The only electro-optically induced index change will be $\Delta(1/n^2)_4 = r_{41}E_z$. Inserting this into the equation for the index ellipsoid, the electric field causes a rotation of the index ellipsoid around Z. Performing the diagonalization shows that the new values of the index ellipsoid are: $1/n_{x'}^2 = 1/n_o^2 + r_{41}E_z$ and $1/n_{y'}^2 = 1/n_o^2 - r_{41}E_z$. These axes are at 45° to the crystal axes.

Performing the differential gives the refractive index changes at 45° to crystal axes:

$$n_{x'} = n_o + \frac{n_o^3}{2} r_{41}E_z \qquad \text{and} \qquad n_{y'} = n_o - \frac{n_o^3}{2} r_{41}E_z. \tag{91}$$

The direction of these new optic axes (45° to the crystal axes) turns out to be in the direction that the zincblende material cleaves. Thus, TE-polarized light traveling down a waveguide normal to a cleave experiences the index change shown here. Light polarized along Z will not see any index change. Depending on whether light is polarized along X' or Y', the index will increase or decrease.[60]

With an electro-optic coefficient of $r_{41} = 1.4 \times 10^{-10}$ cm/V, in a field of 10 kV/cm (2 V across 2 μm), and since $n_o = 3.3$, the index change for the TE polarization in GaAs will be 2.5×10^{-5}. The index change in InP-based materials is comparable. The phase shift in a sample of length L is ΔnkL. At 1-μm wavelength, this will require a sample of length 1 cm to achieve a π phase shift, so that the voltage-length product for electro-optic GaAs (or other semiconductor) will be ~20 V·mm. Practical devices require larger refractive index changes, which can be achieved by using quantum wells and choosing the exciton resonance at a shorter wavelength than that of the light to be modulated. These wells have an electrorefractive effect.

Electrorefraction in Semiconductors

Near the band edge in semiconductors, the change in refractive index with applied field can be particularly large, especially in quantum wells, and is termed *electrorefraction,* or the *electrorefractive effect.* Electrorefraction is calculated from the spectrum of electroabsorption using the Kramers-Kronig relations. Enhanced electroabsorption means enhanced electrorefraction at wavelengths below the band edge. Electrorefraction allows significant reductions in length and drive voltages required for phase modulation in waveguides. The voltage-length product depends on how close to the absorption resonance the modulator is operated. It also depends on device design. As with electroabsorption modulators, the field is usually applied across a *pin* junction. Some reported π voltage-length products are 2.3 V·mm in GaAs/AlGaAs QW (at 25-V bias), 1.8 V·mm in InGaAs/InAlAs QW and 1.8 V·mm in GaAs/AlGaAs double heterostructures.[61] These voltage-length products depend on wavelength detuning from the exciton resonance and therefore on insertion and electroabsorption losses. The larger the voltage-length product, the greater the loss.

Typical Performance. Electrorefraction is polarization dependent, because the quantum-confined Stark effect is polarization dependent. In addition, the TE polarization experiences the electro-optic effect, which may add to or subtract from the electrorefractive effect, depending on the crystal orientation. Typically, Δn for TE polarization (in an orientation that sums these effects) will be 8×10^{-4} at 82 kV/cm (7 V across a waveguide with an i layer 0.85 μm thick). Of this, the contribution from the electro-optic effect is 2×10^{-4}. Thus, electrorefraction is about 4 times larger than the electro-optic effect. The voltage-length product will thus be enhanced by a factor of four, reducing to 5 V·mm. Of course, this ratio depends on the field, since the electro-optic effect is linear in field and electrorefraction is quadratic in the field. This ratio also depends on wavelength; electrorefraction can be larger closer to the exci-

ton resonance, but the residual losses go up. The TM polarization, which experiences electrorefraction alone, will be 5×10^{-4} at the same field, slightly smaller than the TE electrorefraction, because QCSE is smaller for TM than TE polarization.[62]

Advanced QW Concepts. Compressive strain increases electrorefraction, as it does QCSE. Measurements at the same 82 kV/cm show an increase from 2.5×10^{-4} to 7.5×10^{-4} by increasing compressive strain.[63] Strained QWs also make it possible to achieve polarization-independent electrorefractive modulators (although when integrated with a semiconductor laser, which typically has a well-defined polarization, this should not be a necessity).

Advanced QW designs have the potential to increase the refractive index change below the exciton resonance. One example analyzes asymmetric coupled QWs and finds more than 10 times enhancement in Δn below the band edge, at least at small biases. However, when fabricated and incorporated into Mach-Zehnder modulators, the complex three-well structure lowered V_π by only a factor of 3, attributed to the growth challenges of these structures.[64]

Nipi *Modulators.* One way to obtain a particularly low voltage-length product is to use MQWs in a hetero-*nipi* waveguide. These structures incorporate multiple *pin* junctions (alternating *n-i-p-i-n-i-p*) and include QWs in each *i* layer. Selective contacts to each electrode are required, which limits how fast the modulator can be switched. A voltage-length product of 0.8 V·mm was observed at a wavelength 115 meV below the exciton resonance. The lowest voltage InGaAs modulator had $V_\pi = 0.5$ V, at speeds up to 110 MHz. Faster speeds require shorter devices and higher voltages.[61]

Band-Filling Modulators. When one operates sufficiently far from the band edge that the absorption is not large, then the electrorefractive effect is only 2 to 3 times larger than the bulk electro-optic effect. This is because oscillations in the change in absorption with wavelength tend to cancel out their contributions to the change in refractive index at long wavelengths. By contrast, the long-wavelength refractive index change during band filling is large because band filling decreases the absorption at all wavelengths. However, because band filling relies on real carriers, it lasts as long as the carriers do, and it is important to find ways to remove these carriers to achieve high-speed operation.

Voltage-controlled transfer of electrons into and out of QWs (BRAQWET modulator) can yield large electrorefraction by band filling (Sec. 4.11 discusses electroabsorption in this structure under "Electron Transfer Modulators"). The refractive index change at 1.55 μm can be as large as $\Delta n = 0.02$ for 6 V. One structure consists of 12 repeating elements,[65] with the single QW replaced by three closely spaced strongly coupled QWs, demonstrating $V_\pi L =$ 3.2 V·mm with negligible loss.

Semiconductor Interferometric Modulators

The issues for Mach-Zehnder modulators fabricated in semiconductors are similar to those for modulators in lithium niobate, but the design and fabrication processes in semiconductors are by no means as finalized. Fabrication tolerances, polarization dependence, interaction with lasers, and operation at high optical input powers are just some of the issues that need to be addressed. The interferometer can be composed of *Y* branches, fabricated by etching to form ridge waveguides. Alternatively, 3-dB couplers are often formed by a *multimode interferometer* (MMI), composed of two parallel waveguides placed very close together with a bridging region that introduces coupling between them. Proper choice of this coupling region yields a 3-dB coupler.

One example reports a Mach-Zehnder interferometer at 1.55 μm in InGaAlAs QWs with InAlAs barriers.[66] A polarization-independent extinction ratio of 30 dB was reported, over a

20-nm wavelength range without degradation at input powers of 18 dBm (63 mW). The interferometer phase-shifting region was 1000 μm long, and each MMI was 200 μm long. The insertion loss of 13 dB was due to the mismatch between the mode of the single-mode optical fiber and of the semiconductor waveguide, which was 2 μm wide and 3.5 μm high. Various semiconductor structures to convert spot size should bring this coupling loss down.

4.13 PIN *DIODES*

The detectors used for fiber-optic communication systems are usually *pin photodiodes.* In high-sensitivity applications, such as long-distance systems operating at 1.55-μm wavelength, *avalanche photodiodes* are sometimes used because they have internal gain. Occasionally, *metal-semiconductor-metal* (MSM) *photoconductive detectors* with interdigitated electrode geometry are used because of ease of fabrication and integration. For the highest speed applications, *Schottky photodiodes* may be chosen. This section reviews properties of *pin* photodiodes. The next section outlines the other photodetectors.

The material of choice for these photodiodes depends on the wavelength at which they will be operated. The short-wavelength *pin* silicon photodiode is perfectly suited for GaAs wavelengths (850 nm); these inexpensive photodetectors are paired with GaAs/AlGaAs LEDs for low-cost data communications applications. They are also used in the shorter-wavelength plastic fiber applications at 650 nm. The longer-wavelength telecommunication systems at 1.3 and 1.55 μm require longer-wavelength detectors. These are typically *pin* diodes composed of lattice-matched ternary $In_{0.47}Ga_{0.53}As$ grown on InP. Silicon is an indirect bandgap semiconductor while InGaAs is a direct band material; this affects each material's absorption and therefore its photodiode design. In particular, silicon photodiodes tend to be slower than those made of GaAs or InGaAs, because silicon intrinsic regions must be thicker. Speeds are also determined by carrier mobilities, which are higher in the III-V materials.

Previous volumes in this handbook have outlined the concepts behind the photodetectors discussed here. Volume I, Chap. 15 places *pin* photodetectors in context with other detectors, and gives specific characteristics of some commercially available detectors, allowing direct comparison of silicon, InGaAsP, and germanium detectors. Volume I, Chap. 16, describes the principles by which the *pin* and the avalanche photodiodes operate (Figure 6 of that chapter contains a misprint, in that the central portion of the top layer should be labeled p^+ InP, rather than n^+ InP). The properties of greatest interest to fiber communications are repeated here. Volume I, Chap. 17 concentrates on high-speed photodetectors and provides particularly useful information on their design for high-speed applications. Finally, some of the key issues for photodetectors in fiber-optic communication systems were outlined in Vol. II, Chap. 10. This chapter considers these issues in much more detail.

The *pin* junction consists of a thin, heavily doped *n* region, a near-intrinsic *n* region (the *i* region), and a heavily doped *p* region. When an incident photon has energy greater than or equal to the bandgap of the semiconductor, electron-hole pairs are generated. In a well-designed photodiode, this generation takes place in the space-charge region of the *pn* junction. As a result of the electric field in this region, the electrons and holes separate and drift in opposite directions, causing current to flow in the external circuit. This current is monitored as a change in voltage across a load resistor. The *pin* photo-diode is the workhorse of fiber communication systems.

Typical Geometry

Typically, the electric field is applied across the *pn* junction and photocarriers are collected across the diode. A typical geometry for a silicon photodiode is shown in Fig. 30*a.* A *pn* junction is formed by a thin p^+ diffusion into a lightly doped n^- layer (also called the *i* layer since

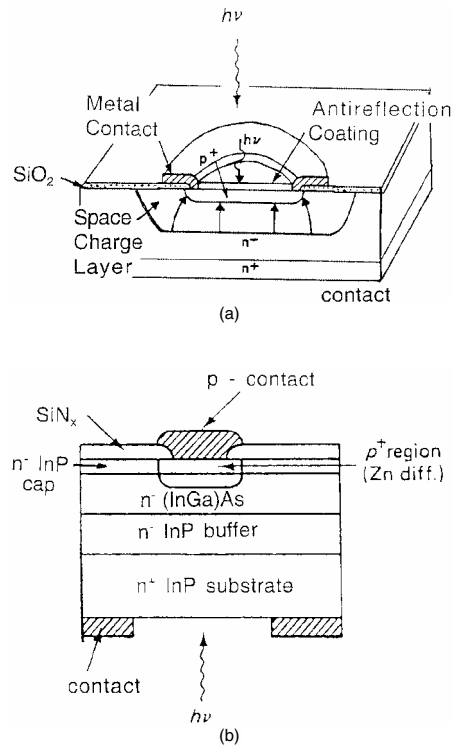

FIGURE 30 Geometry for *pin* photodiodes: (*a*) cutaway of silicon, illuminated from the top, showing the ring electrode and static electric field lines in the space-charge region; (*b*) cross-section of InGaAs/InP, illuminated from the bottom. The p^+ region is formed by diffusion. The low-doped n^- layer is the *i* or nearly intrinsic layer.

it is almost *intrinsic*) through a window in a protective SiO_2 film. The n^- region between the p^+ and n^+ regions supports a space-charge region, which, in the dark, is depleted of free carriers and supports the voltage drop that results from the *pn* junction. When light is absorbed in this space-charge region, the absorption process creates electron-hole pairs that separate in the electric field (field lines are shown in Fig. 30a), the electrons falling down the potential hill to the *n* region and the holes moving to the *p* region. This separation of charge produces a current in the external circuit, which is read out as a measure of the light level. Free carriers generated within a diffusion length of the junction may diffuse into the junction, adding to the measured current.

Long-wavelength detectors utilize n^- or *i* layers that are grown with a composition that will absorb efficiently in the wavelength region of interest. The ternary $In_{0.47}Ga_{0.53}As$ can be grown lattice-matched to InP and has a spectral response that is suitable for both the 1.3- and 1.55-μm wavelength regions. Thus, this ternary is usually the material of choice, rather than the more difficult to grow quaternary InGaAsP, although the latter provides more opportunity to tune

the wavelength response. Figure 30*b* shows a typical geometry. Epitaxial growth is used to provide lightly doped n^- layers on a heavily doped n^+ substrate. The InP buffer layers are grown to keep the dopants from diffusing into the lightly doped absorbing InGaAs layer. The required thin p region is formed by diffusion through a silicon nitride insulating window. Because InP is transparent to 1.3 and 1.55 μm, the photodiode can be back-illuminated, which makes electrical contacting convenient. In some embodiments, a well is etched in the substrate and the fiber is glued in place just below the photosensitive region.

Carriers generated outside the depletion region may enter into the junction by diffusion, and can introduce considerable time delay. In silicon, the diffusion length is as long as 1 cm, so any photocarriers generated anywhere within the silicon photodiode can contribute to the photocurrent. Because the diffusion velocity is much slower than the transit time across the space-charge region, diffusion currents slow down silicon photodiodes. This is particularly true in *pn* diodes. Thus, high-speed applications typically use *pin* diodes with absorption only in the *i* layer.

To minimize diffusion from the p^+ entrance region, the junction should be formed very close to the surface. The space-charge region should be sufficiently thick that most of the light will be absorbed (thickness $\approx 1/\alpha$). With sufficient reverse bias, carriers will drift at their scattering-limited velocity. The space-charge layer must not be too thick, however, or transit-time effects will limit the frequency response. Neither should it be too thin, or excessive capacitance will result in a large RC time constant. The optimum compromise occurs when the modulation period is on the order of twice the transit time. For example, for a modulation frequency of 10 GHz, the optimum space-charge layer thickness in silicon is about 5 μm. However, this is not enough thickness to absorb more than ~50 percent of the light at 850 nm. Thus, there is a trade-off between sensitivity and speed. If the wavelength drops to 980 nm, only 10 percent of the light is absorbed in a 10-μm thickness of silicon space-charge layer.

The doping must be sufficiently small that the low n^- doped region can support the voltage drop of the built-in voltage V_{bi} plus the applied voltage. When the doping density of the p^+ region is much higher than the doping density of the n^- layer, the thickness of the space-charge layer is:

$$W_s = \sqrt{\frac{2\varepsilon_s}{e}\frac{(V_{bi} - V)}{N_D}} \tag{92}$$

To achieve $W_s = 10$ μm in a silicon photodiode with 10 V applied requires $N_D \approx 10^{14}$ cm^{-3}. If the doping is not this low, the voltage drops more rapidly, and the field will not extend fully across the low-doped region.

In InGaAs photodiodes (also GaAs/AlGaAs photodiodes), the n^+ and p^+ layers are transparent, and no photocarriers are generated in them. Thus, no photocarriers will enter from the n^+ and p^+ regions, even though the diffusion length is ~100 μm. The thickness of the *i* layer is chosen thin enough to achieve the desired speed (trading off transit time and capacitance), with a possible sacrifice of sensitivity.

Typically, light makes a single pass through the active layer. In silicon photodiodes, the light usually enters through the p contact at the surface of the diode (Fig. 30a); the top metal contact must have a window for light to enter (or be a transparent contact). The InGaAs photodiodes may receive light from the p side or the n side, because neither is absorbing. In addition, some back-illuminated devices use a double pass, reflecting off a mirrored top surface, to double the absorbing length. Some more advanced detectors, *resonant photodiodes,* use integrally grown Fabry-Perot cavities (using DBR mirrors, as in VCSELs) that resonantly reflect the light back and forth across the active region, enhancing the quantum efficiency. These are typically used only at the highest bandwidths (>20 GHz) or for wavelength division multiplexing (WDM) applications, where wavelength-selective photodetection is required. In addition, photodiodes designed for integration with other components are illuminated through a waveguide in the plane of the *pn* junction. The reader is directed to Vol. I, Chap. 17 to obtain more information on these advanced geometries.

Sensitivity (Responsivity)

To operate a *pin* photodiode, it is sufficient to place a load resistor between ground and the *n* side and apply reverse voltage to the *p* side ($V < 0$). The photocurrent is monitored as a voltage drop across this load resistor. The photodiode current in the presence of an optical signal of power P_s is negative, with a magnitude given by:

$$I = \eta_D \left(\frac{e}{h\nu} \right) P_s + I_D \tag{93}$$

where I_D is the magnitude of the (negative) current measured in the dark. The detector *quantum efficiency* η_D (electron-hole pairs detected per photon) is determined by how much light is lost before reaching the space-charge region, how much light is absorbed (which depends on the absorption coefficient), and how much light is reflected from the surface of the photodiode (a loss which can be reduced by adding antireflective coatings). Finally, depending on design, there may be some loss from metal electrodes. These factors are contained in the following expression for the quantum efficiency:

$$\eta_D = (1 - R)T[1 - \exp(-\alpha W)] \tag{94}$$

where R is the surface reflectivity, T is the transmission of any lossy electrode layers, W is the thickness of the absorbing layer, and α is its absorption coefficient.

The *sensitivity* (or *responsivity* $\Re$) of a detector is the ratio of milliamps of current out per milliwatt of light in. Thus, the responsivity is:

$$\Re = \frac{I_{PD}}{P_S} = \eta_D \frac{e}{h\nu} \tag{95}$$

For detection of a given wavelength, the photodiode material must be chosen with a bandgap sufficient to provide suitable sensitivity. The absorption spectra of candidate detector materials are shown in Fig. 31. Silicon photodiodes provide low-cost detectors for most data communications applications, with acceptable sensitivity at 850 nm (absorption coefficient ~500 cm^{-1}). These detectors work well with the GaAs lasers and LEDs that are used in the inexpensive datacom systems and for short-distance or low-bandwidth local area network (LAN) applications. GaAs detectors are faster, both because their absorption can be larger and because their electron mobility is higher, but they are more expensive. Systems that require longer-wavelength InGaAsP/InP lasers typically use InGaAs photodiodes. Germanium has a larger dark current, so it is not usually employed for optical communications applications. Essentially all commercial photodetectors use bulk material, not quantum wells, as these are simpler, are less wavelength sensitive, and have comparable performance.

The spectral response of typical photodetectors is shown in Fig. 32. The detailed response depends on the detector design and on applied voltage, so these are only representative examples. Important communication wavelengths are marked.

Table 1 gives the sensitivity of typical detectors of interest in fiber communications, measured in units of amps per watt, along with speed and relative dark current.

Speed

Contributions to the speed of a *pin* diode come from the transit time across the space-charge region and from the *RC* time constant of the diode circuit in the presence of a load resistor R_L. Finally, in silicon there may be a contribution from the diffusion of carriers generated in undepleted regions.

In a properly designed *pin* photodiode, light should be absorbed in the space-charge region that extends from the p^+ junction across the low *n*-doped layer (the *i* layer). Equation

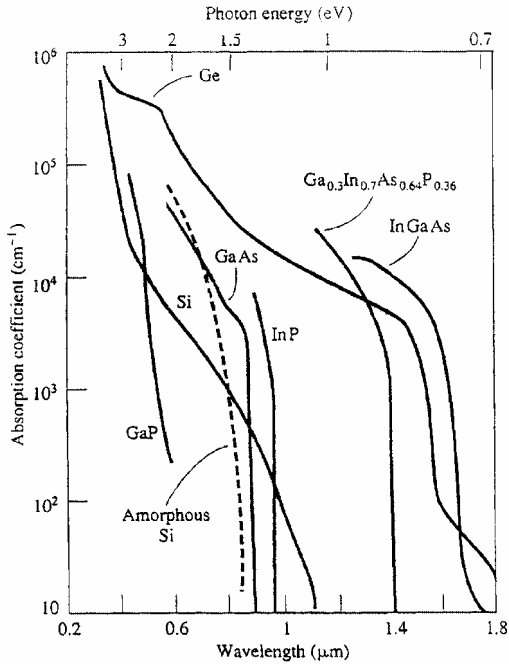

FIGURE 31 Absorption coefficient as a function of wavelength for several semiconductors used in *pin* diode detectors.

(92) gives the thickness of the space charge region W_s, as long as it is less than the thickness of the i layer W_i. Define V_i as that voltage at which $W_s = W_i$. Then

$$-V_i = W_i^2 \frac{eN_D}{2\varepsilon_s} - V_{\text{bi}}.$$

For any voltage larger than this, the space-charge width is essentially W_i, since the space charge extends a negligible distance into highly doped regions.

If the electric field across the space-charge region is high enough for the carriers to reach their saturation velocity v_s and high enough to fully deplete the i region, then the carrier transit time will be $\tau_i = W_i/v_s$. For $v_s = 10^7$ cm/s and $W_i = 4$ μm, the transit time $\tau_i = 40$ ps. It can be shown that a finite transit time τ_i reduces the response at modulation frequency ω[67]:

$$\Re(\omega) = \Re_o \frac{\sin(\omega\tau_i/2)}{\omega\tau_i/2} \tag{96}$$

Defining the 3-dB bandwidth as that modulation frequency at which the electrical power decreases by 50 percent, it can be shown that the transit-limited 3-dB bandwidth is $\delta\omega_i = 2.8/\tau_i = 2.8\ v_s/W_i$. (Electrical power is proportional to I^2 and $\Re^2$, so the half-power point is achieved when the current is reduced by $1/\sqrt{2}$.) There is a trade-off between diode sensitivity and diode transit time, since, for thin layers, from Eq. (94), $\eta_D \approx (1 - R)T\alpha W_i$. Thus, the quantum efficiency–bandwidth product is:

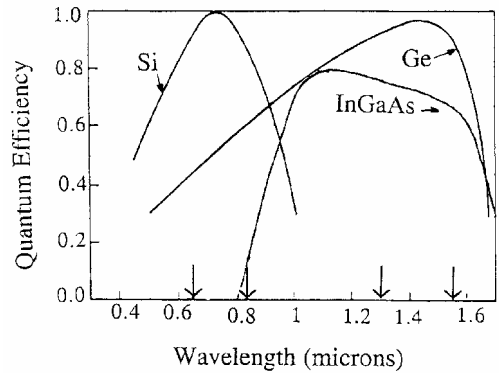

FIGURE 32 Spectral response of typical photodetectors.

$$\eta_D \, \delta\omega_i \approx 2.8\alpha v_s(1 - R)T \tag{97}$$

The speed of a *pin* photodiode is also limited by its capacitance, through the *RC* of the load resistor. Sandwiching a space-charge layer, which is depleted of carriers, between conductive *n* and *p* layers causes a diode capacitance proportional to the detector area *A:*

$$C_D = \frac{\varepsilon_s A}{W_i} \tag{98}$$

For a given load resistance, the smaller the area, the smaller the *RC* time constant, and the higher the speed. We will see also that the dark current I_s decreases as the detector area decreases. The detector should be as small as possible, as long as all the light from the fiber can be collected onto the detector. Multimode fibers easily butt-couple to detectors whose area matches the fiber core size. High-speed detectors compatible with single-mode fibers can be extremely small, but this increases the alignment difficulty; high-speed photodetectors can be obtained already pigtailed to single-mode fiber. A low load resistance may be needed to keep the *RC* time constant small, but this may result in a small signal that needs amplification. Speeds in excess of 1 GHz are straightforward to achieve, and speeds of 50 GHz are not uncommon.

Thicker space-charge regions provide smaller capacitance, but too thick a space charge region causes the speed to be limited by the carrier transit time. The bandwidth with a load resistor R_L is:

$$\omega_{3\,\mathrm{dB}} = \frac{2.8}{\tau_i} + \frac{1}{R_L C} = \frac{2.8 v_s}{W_i} + \frac{W_i}{\varepsilon_s A R_L} \tag{99}$$

TABLE 1 Characteristics of Typical Photodiodes

	Wavelength, μm	Sensitivity ℜ, As/W	Speed τ, ns	Dark current, normalized units
Sil	0.85	0.55	3	1
	0.65	0.4	3	
GaInAs	1.3–1.6	0.95	0.2	3
Ge (*pn*)	1.55	0.9	3	66

This shows that there is an optimum thickness W_i for high-speed operation. Any additional series resistance R_s or parasitic capacitance C_P must be added by using $R \rightarrow R_L + R_S$ and $C \rightarrow C + C_P$. The external connections to the photodetector can also limit speed. The gold bonding wire may provide additional series inductance. It is important to realize that the photodiode is a high impedance load, with very high electrical reflection, so that an appropriate load resistor must be used. As pointed out in Vol. I, Chap. 17, it is possible to integrate a matching load resistor inside the photodiode device, with a reduction in sensitivity of a factor of two (since half the photocurrent goes through the load resistor), but double the speed (since the *RC* time constant is halved). A second challenge is to build external bias circuits without high-frequency electrical resonances. Innovative design of the photodetector may integrate the necessary bias capacitor and load resistor, ensuring smooth electrical response.

Silicon photodetectors are inherently not as fast. Because their highly doped *p* and *n* regions are also absorbing, and because they are indirect bandgap materials and do not have as high an absorption coefficient, there will be a substantial contribution from carriers generated in undepleted regions. These carriers have to diffuse into the space charge region before they can be collected. Therefore, the photoresponse of the diode has a component of a slower response time governed by the carrier diffusion time:

$$T_D = \frac{W_D^2}{2D} \tag{100}$$

where W_D is the width of the absorbing undepleted region, and D is the diffusion constant for whichever carrier is dominant (usually holes in the *n* region). For silicon, $D = 12$ cm^2/s, so that when $W_D = 10$ μm, $\tau_D = 40$ ns.

Dark Current

Semiconductor diodes can pass current even in the dark, giving rise to *dark current* that provides a background present in any measurement. This current comes primarily from the thermally generated diffusion of minority carriers out of the *n* and *p* regions into the depleted junction region, where they recombine. The current-voltage equation for a *pn* diode (in the dark) is:

$$I = I_S \left[\exp\left(\frac{eV}{\beta kT} \right) - 1 \right] \tag{101}$$

where I_S is the *saturation current* that flows at large back bias (V large and negative). This equation represents the current that passes through any biased *pn* junction. Photodiodes use *pn* junctions reverse biased ($V < 0$) to avoid large leakage current.

Here β is the *ideality factor,* which varies from 1 to 2, depending on the diode structure. In a metal-semiconductor junction (Schottky barrier) or an ideal *pn* junction in which the only current in the dark is due to minority carriers that diffuse from the *p* and *n* regions, then $\beta = 1$. However, if there is thermal generation and recombination of carriers in the space-charge region, then β tends toward the value 2. This is more likely to occur in long-wavelength detectors.

The saturation current I_S is proportional to the area A of the diode in an ideal junction:

$$I_S = e \left(\frac{D_p p_{n0}}{L_p} + \frac{D_n n_{p0}}{L_n} \right) A \tag{102}$$

where D_n, D_p are diffusion constants, L_n, L_p are diffusion lengths, and n_{p0}, p_{n0} are equilibrium minority carrier densities, all of electrons and holes, respectively. The saturation current I_S can be related to the diode resistance measured in the dark when $V = 0$. Defining

$$\frac{1}{R_0} = -\frac{\partial I}{\partial V}\bigg|_{V=0}$$

then:

$$R_0 = \frac{\beta kT}{eI_S} \tag{103}$$

The dark resistance is inversely proportional to the saturation current, and therefore to the area of the diode.

The diffusion current in Eq. (101) has two components that are of opposite sign in a forward-biased diode: a forward current $I_S \exp(eV/\beta kT)$ and a backward current $-I_S$. Each of these components is statistically independent, coming from diffusive contributions to the forward current and backward current, respectively. This fact is important in understanding the noise properties of photodiodes.

In photodiodes, $V \le 0$. For clarity, write $V = -V'$ and use V' as a *positive* quantity in the equations that follow. For a reverse-biased diode in the dark, diffusion current flows as a negative *dark current,* with a magnitude given by

$$I_D = I_S\left[1 - \exp\left(\frac{-eV'}{\beta kT}\right)\right] \tag{104}$$

The negative dark current flows opposite to the current flow in a forward-biased diode. Holes move toward the *p* region and electrons move toward the *n* region; both currents are negative and add. This dark current adds to the negative photocurrent. The hole current must be thermally generated because there are no free holes in the *n* region to feed into the *p* region. By the same token, the electron current must be thermally generated since there are no free electrons in the *p* region to move toward the *n* region. The dark current at large reverse bias voltage is due to thermally generated currents.

Using Eq. (104) and assuming $eV' \gg kT$, the negative dark current equals the saturation current:

$$I_D = I_S \approx \left(\frac{\beta kT}{eR_0}\right) \tag{105}$$

It can be seen that the dark current increases linearly with temperature and is independent of (large enough) reverse bias. *Trap-assisted* thermal generation current increases β; in this process, carriers trapped in impurity levels can be thermally elevated to the conduction band. The temperature of photodiodes should be kept moderate in order to avoid excess dark current.

When light is present in a photodiode, the photocurrent is negative, in the direction of the applied voltage, and adds to the negative dark current. The net effect of carrier motion will be to tend to screen the internal field. Defining the magnitude of the photocurrent as $I_{PC} = \eta_D(e/h\nu)P_S$, then the total current is negative:

$$I = -[I_D + I_{PC}] = -I_S\left[1 - \exp\left(\frac{-eV'}{\beta kT}\right)\right] - I_{PC} \tag{106}$$

Noise in Photodiodes

Successful fiber-optic communication systems depend on a large signal-to-noise ratio. This requires photodiodes with high sensitivity and low noise. Background noise comes from shot noise due to the discrete process of photon detection, from thermal processes in the load

resistor (Johnson noise), and from generation-recombination noise due to carriers within the semiconductor. When used with a field-effect transistor (FET) amplifier, there will also be shot noise from the amplifier and $1/f$ noise in the drain current.

Shot Noise. *Shot noise* is fundamental to all photodiodes and is due to the discrete nature of the conversion of photons to free carriers. The shot noise current is a statistical process. If N photons are detected in a time interval Δt, Poisson noise statistics cause the uncertainty in N to be $\sqrt{N}$. Using the fact that N electron-hole pairs create a current I through $I = eN/\Delta t$, then the signal-to-noise ratio (SNR) is $N/\sqrt{N} = \sqrt{N} = \sqrt{(I\Delta t/e)}$. Writing the frequency bandwidth Δf in terms of the time interval through $\Delta f = 1/(2\Delta t)$ gives:

$$\text{SNR} = \sqrt{\frac{I}{2e\Delta f}}$$

The root mean square (rms) photon noise, given by $\sqrt{N}$, creates an rms shot noise current of:

$$i_{\text{SH}} = e\,\frac{\sqrt{N}}{\Delta t} = \sqrt{\frac{eI}{\Delta t}} = \sqrt{2eI\Delta f} \tag{107}$$

Shot noise depends on the average current I; therefore, for a given photodiode, it depends on the details of the current voltage characteristic. Expressed in terms of P_S, the optical signal power (when the dark current is small enough to be neglected), the rms shot noise current is

$$i_{\text{SH}} = \sqrt{2eI_{\text{PC}}\Delta f} = \sqrt{2e\Re P_S\Delta f} \tag{108}$$

where $\Re$ is the responsivity (or sensitivity), given in units of amps per watt.

The shot noise can be expressed directly in terms of the properties of the diode when all sources of noise are included. Since they are statistically independent, the contributions to the noise current will be additive. Noise currents can exist in both the forward and backward directions, and these contributions must add, along with the photocurrent contribution. The entire noise current squared becomes:

$$i_N^2 = 2e\left\{I_{\text{PC}} + \left(\frac{\beta kT}{eR_0}\right)\left[1 + \exp\left(\frac{-eV'}{\beta kT}\right)\right]\right\}\Delta f \tag{109}$$

Clearly, noise is reduced by increasing the reverse bias. When the voltage is large, the shot noise current squared becomes:

$$i_N^2 = 2e\,[I_{\text{PC}} + I_D]\,\Delta f \tag{110}$$

The dark current adds linearly to the photocurrent in calculating the shot noise.

In addition to shot noise due to the random variations in the detection process, the random thermal motion of charge carriers contributes to a *thermal noise* current, often called *Johnson* or *Nyquist noise.* It can be calculated by assuming thermal equilibrium with $V = 0$, $\beta = 1$, so that Eq. (109) becomes:

$$i_{\text{th}}^2 = 4\left(\frac{kT}{R_0}\right)\Delta f \tag{111}$$

This is just Johnson noise in the resistance of the diode. The noise appears as a fluctuating voltage, independent of bias level.

Johnson Noise from External Circuit. An additional noise component will be from the load resistor R_L and resistance from the input to the preamplifier, R_i:

$$i_{\mathrm{NJ}}^2 = 4kT\left(\frac{1}{R_L} + \frac{1}{R_i}\right)\Delta f \tag{112}$$

Note that the resistances add in parallel as they contribute to noise current.

Noise Equivalent Power. The ability to detect a signal requires having a photocurrent equal to or higher than the noise current. The amount of noise that detectors produce is often characterized by the *noise equivalent power* (NEP), which is the amount of optical power required to produce a photocurrent just equal to the noise current. Define the noise equivalent photocurrent I_{NE}, which is set equal to the noise current i_{SH}. When the dark current is negligible,

$$i_{\mathrm{SH}} = \sqrt{2eI_{\mathrm{NE}}\Delta f} = I_{\mathrm{NE}}$$

Thus, the noise equivalent current is $I_{\mathrm{NE}} = 2e\Delta f$, and depends only on the bandwidth Δf. The noise equivalent power can now be expressed in terms of the noise equivalent current:

$$\mathrm{NEP} = \frac{I_{\mathrm{NE}}}{\eta}\frac{h\nu}{e} = 2\frac{h\nu}{\eta}\Delta f \tag{113}$$

The second equality assumes the absence of dark current. In this case, the NEP can be decreased only by increasing the quantum efficiency (for a fixed bandwidth). In terms of sensitivity (amps per watt):

$$\mathrm{NEP} = 2\frac{e}{\Re}\Delta f = I_{\mathrm{NE}}\Delta f \tag{114}$$

This expression is usually valid for photodetectors used in optical communication systems, which have small dark currents.

When dark current is dominant, $i_N = \sqrt{2e\, I_D\, \Delta f}$, so that:

$$\mathrm{NEP} = \frac{I_{\mathrm{NE}}}{\eta}\frac{h\nu}{e} = \sqrt{\frac{2I_D\,\Delta f}{e}}\frac{h\nu}{\eta} \tag{115}$$

This is often the case in infrared detectors such as germanium. Note that the dark-current-limited noise equivalent power is proportional to the square root of the area of the detector because the dark current is proportional to the detector area. The NEP is also proportional to the square root of the bandwidth Δf. Thus, in photodetectors whose noise is dominated by dark current, NEP divided by the square root of area times bandwidth should be a constant. The inverse of this quantity has been called the *detectivity D** and is often used to describe infrared detectors. In photodiodes used for communications, dark current usually does not dominate and it is better to use Eq. (114), an expression which is independent of area, but depends linearly on bandwidth.

4.14 AVALANCHE PHOTODIODES, MSM DETECTORS, AND SCHOTTKY DIODES

Avalanche Detectors

When large voltages are applied to photodiodes, the avalanche process produces gain, but at the cost of excess noise and slower speed. In fiber telecommunications applications, where speed and signal-to-noise are of the essence, avalanche photodiodes (APDs) are frequently at a disadvantage. Nonetheless, in long-haul systems at 2488 Mb/s, APDs may provide up to 10

dB greater sensitivity in receivers limited by amplifier noise. While APDs are inherently complex and costly to manufacture, they are less expensive than optical amplifiers and may be used when signals are weak.

Gain (Multiplication). When a diode is subject to a high reverse-bias field, the process of impact ionization makes it possible for a single electron to gain sufficient kinetic energy to knock another electron from the valence to the conduction band, creating another electron-hole pair. This enables the quantum efficiency to be >1. This internal multiplication of photocurrent could be compared to the gain in photomultiplier tubes. The *gain* (or *multiplication*) M of an APD is the ratio of the photocurrent divided by that which would give unity quantum efficiency. Multiplication comes with a penalty of an excess noise factor, which multiplies shot noise. This excess noise is function of both the gain and the ratio of impact ionization rates between electrons and holes.

Phenomenologically, the low-frequency multiplication factor is:

$$M_{\mathrm{DC}} = \frac{1}{1 - (V/V_B)^n} \tag{116}$$

where the parameter n varies between 3 and 6, depending on the semiconductor, and V_B is the breakdown voltage. Gains of $M > 100$ can be achieved in silicon APDs, while they are more typically 10 to 20 for longer-wavelength detectors, before multiplied noise begins to exceed multiplied signal. A typical voltage will be 75 V in InGaAs APDs, while in silicon it can be 400 V.

The avalanche process involves using an electric field high enough to cause carriers to gain enough energy to accelerate them into ionizing collisions with the lattice, producing electron-hole pairs. Then, both the original carriers and the newly generated carriers can be accelerated to produce further ionizing collisions. The result is an avalanche process.

In an i layer (where the electric field is uniform) of width W_i, the gain relates to the fundamental avalanche process through $M = 1/(1 - aW_i)$, where a is the *impact ionization coefficient,* which is the number of ionizing collisions per unit length. When $aW_i \rightarrow 1$, the gain becomes infinity and the diode breaks down. This means that avalanche multiplication appears in the regime before the probability of an ionizing collision is 100 percent. The gain is a strong function of voltage, and these diodes must be used very carefully. The total current will be the sum of avalanching electron current and avalanching hole current.

In most *pin* diodes the i region is really low n-doped. This means that the field is not exactly constant, and an integration of the avalanche process across the layer must be performed to determine a. The result depends on the relative ionization coefficients; in III-V materials they are approximately equal. In this case, aW_i is just the integral of the ionizing coefficient that varies rapidly with electric field.

Separate Absorber and Multiplication (SAM) APDs. In this design the long-wavelength infrared light is absorbed in an intrinsic narrow-bandgap InGaAs layer and photocarriers move to a separate, more highly n-doped InP layer that supports a much higher field. This layer is designed to provide avalanche gain in a separate region without excessive dark currents from tunneling processes. This layer typically contains the *pn* junction, which traditionally has been diffused. Fabrication procedures such as etching a mesa, burying it, and introducing a guard ring electrode are all required to reduce noise and dark current. All-epitaxial structures provide low-cost batch-processed devices with high performance characteristics.[68]

Speed. When the gain is low, the speed is limited by the RC time constant. As the gain increases, the avalanche buildup time limits the speed, and for modulated signals the multiplication factor decreases. The multiplication factor as a function of modulation frequency is:

$$M(\omega) = \frac{M_{DC}}{\sqrt{1 + M_{DC}^2 \omega^2 \tau_1^2}} \tag{117}$$

where $\tau_1 = p\tau$, where τ is the multiplication-region transit time and p is a number that changes from 2 to ⅓ as the gain changes from 1 to 1000. The gain decreases from its low-frequency value when $M_{DC}\omega = 1/\tau_1$. It can be seen that it is the gain-bandwidth product that describes the characteristics of an avalanche photodiode in a communication system.

Noise. The shot noise in an APD is that of a *pin* diode multiplied by M^2 times an excess noise factor F_e:

$$i_S^2 = 2e\, I_{PC}\, \Delta f\, M^2\, F_e \tag{118}$$

where

$$F_e(M) = \beta M + (1 - \beta)\left(2 - \frac{1}{M}\right)$$

In this expression, β is the ratio of the ionization coefficient of the opposite type divided by the ionization coefficient of the carrier type that initiates multiplication. In the limit of equal ionization coefficients of electrons and holes (usually the case in III-V semiconductors), $F_e = M$ and $F_h = 1$. Typical numerical values for enhanced APD sensitivity are given in Vol. I, Chap. 17, Fig. 15.

Dark Current. In an APD, dark current is the sum of the unmultiplied current I_{du}, mainly due to surface leakage, and the bulk dark current experiencing multiplication I_{dm}, multiplied by the gain:

$$I_d = I_{du} + MI_{dm} \tag{119}$$

The shot noise from dark (leakage) current i_d:

$$i_d^2 = 2e\, [i_{du} + I_{dm} M^2\, F_e(M)]\, \Delta f \tag{120}$$

The proper use of APDs requires choosing the proper design, carefully controlling the voltage, and using the APD in a suitably designed system, since the noise is so large.

MSM Detectors

Volume I, Chap. 17, Fig. 1 of this handbook shows that interdigitated electrodes on top of a semiconductor can provide a planar configuration for electrical contacts. Either a *pn* junction or bulk semiconductor material can reside under the interdigitated fingers. The MSM geometry has the advantage of lower capacitance for a given cross-sectional area, but the transit times may be longer, limited by the lithographic ability to produce very fine lines. Typically, MSM detectors are photoconductive. Volume I, Chap. 17, Fig. 17 shows the geometry of high-speed interdigitated photoconductors. These are simple to fabricate and can be integrated in a straightforward way onto MESFET preamplifiers.

Consider parallel electrodes deposited on the surface of a photoconductive semiconductor with a distance L between them. Under illumination, the photocarriers will travel laterally to the electrodes. The photocurrent in the presence of P_s input optical flux at photon energy $h\nu$ is:

$$I_{ph} = q\eta GP\, h\nu \tag{121}$$

The photoconductive gain G is the ratio of the carrier lifetime τ to the carrier transit time τ_{tr}:

$$G = \frac{\tau}{\tau_{tr}}$$

Decreasing the carrier lifetime increases the speed but decreases the sensitivity.

The output signal is due to the time-varying resistance that results from the time-varying photoinduced carrier density $N(t)$:

$$R_s(t) = \frac{L}{eN(t)\ \mu w d_e} \tag{122}$$

where μ is the sum of the electron and hole mobilities, w is the length along the electrodes excited by light, and d_e is the effective absorption depth into the semiconductor.

Usually, MSM detectors are not the design of choice for high-quality communication systems. Nonetheless, their ease of fabrication and integration with other components makes them desirable for some low-cost applications—for example, when there are a number of parallel channels and dense integration is required.

Schottky Photodiodes

A Schottky photodiode uses a metal-semiconductor junction rather than a *pin* junction. An abrupt contact between metal and semiconductor can produce a space-charge region. Absorption of light in this region causes photocurrent that can be detected in an external circuit. Because metal-semiconductor diodes are majority carrier devices they may be faster than *pin* diodes (they rely on drift currents only, there is no minority carrier diffusion). Up to 100 GHz modulation has been reported in a 5- × 5-μm area detector with a 0.3-μm thin drift region using a semitransparent platinum film 10 nm thick to provide the abrupt Schottky contact. Resonance enhancement of the light has been used to improve sensitivity.

4.15 REFERENCES

1. D. Botez, *IEEE J. Quantum Electron.* **17**:178 (1981).
2. See, for example, E. Garmire and M. Tavis, *IEEE J. Quantum Electron.* **20**:1277 (1984).
3. B. B. Elenkrig, S. Smetona, J. G. Simmons, T. Making, and J. D. Evans, *J. Appl. Phys.* **85**:2367 (1999).
4. M. Yamada, T. Anan, K. Tokutome, and S. Sugou, *IEEE Photon. Technol. Lett.* **11**:164 (1999).
5. T. C. Hasenberg and E. Garmire, *IEEE J. Quantum Electron.* **23**:948 (1987).
6. D. Botez and M. Ettenberg, *IEEE J. Quantum Electron.* **14**:827 (1978).
7. G. P. Agrawal and N. K. Dutta, *Semiconductor Lasers,* 2d ed., Van Nostrand Reinhold, New York, 1993, Sec. 6.4.
8. G. H. B. Thompson, *Physics of Semiconductor Laser Devices,* John Wiley & Sons, New York, 1980, Fig. 7.8
9. K. Tatah and E. Garmire, *IEEE J. Quantum Electron.* **25**:1800 (1989).
10. Agrawal and Dutta, Sec. 6.4.3.
11. W. H. Cheng, A. Mar, J. E. Bowers, R. T. Huang, and C. B. Su, *IEEE J. Quantum Electron.* **29**:1650 (1993).
12. J. T. Verdeyen, *Laser Electronics,* 3d ed., Prentice Hall, Englewood Cliffs, N.J., 1995, p. 490.
13. Agrawal and Dutta, Eq. 6.6.32.
14. N. K. Dutta, N. A. Olsson, L. A. Koszi, P. Besomi, and R. B. Wilson, *J. Appl. Phys.* **56**:2167 (1984).
15. Agrawal and Dutta, Sec. 6.6.2.

16. Agrawal and Dutta, Sec. 6.5.2.
17. L. A. Coldren and S. W. Corizine, *Diode Lasers and Photonic Integrated Circuits,* John Wiley & Sons, New York, 1995, Sec. 5.5.
18. M. C. Tatham, I. F. Lealman, C. P. Seltzer, L. D. Westbrook, and D. M. Cooper, *IEEE J. Quantum Electron.* **28**:408 (1992).
19. H. Jackel and G. Guekos, *Opt. Quantum Electron.* **9**:223 (1977).
20. M. K. Aoki, K. Uomi, T. Tsuchiya, S. Sasaki, M. Okai, and N. Chinone, *IEEE J. Quantum Electron.* **27**:1782 (1991).
21. R. W. Tkach and A. R. Chaplyvy, *J. Lightwave Technol.* **LT-4**:1655 (1986).
22. K. Petermann, *IEEE J. Sel. Topics in Qu. Electr.* **1**:480 (1995).
23. T. Hirono, T. Kurosaki, and M. Fukuda, *IEEE J. Quantum Electron.* **32**:829 (1996).
24. Y. Kitaoka, *IEEE J. Quantum Electron.* **32**:822 (1996), Fig. 2.
25. M. Kawase, E. Garmire, H. C. Lee, and P. D. Dapkus, *IEEE J. Quantum Electron.* **30**:981 (1994).
26. Coldren and Corizine, Sec. 4.3.
27. S. L. Chuang, *Physics of Optoelectronic Devices,* John Wiley & Sons, New York, 1995, Fig. 10.33.
28. T. L. Koch and U. Koren, *IEEE J. Quantum Electron.* **27**:641 (1991).
29. B. G. Kim and E. Garmire, *J. Opt. Soc. Am.* **A9**:132 (1992).
30. A. Yariv, *Optical Electronics,* 4th ed., (Saunders, Philadelphia, Pa., 1991) Eq. 13.6-19.
31. Information from www.telecomdevices.com.
32. C. L. Jiang and B. H. Reysen, *Proc. SPIE* **3002**:168 (1997), Fig. 7.
33. See, for example, Pallab Bhattacharya, *Semiconductor Optoelectronic Devices,* Prentice-Hall, New York, 1998, App. 6.
34. C. H. Chen, M. Hargis, J. M. Woodall, M. R. Melloch, J. S. Reynolds, E. Yablonovitch, and W. Wang, *Appl. Phys. Lett.* **74**:3140 (1999).
35. Y. A. Wu, G. S. Li, W. Yuen, C. Caneau, and C. J. Chang-Hasnain, *IEEE J. Sel. Topics in Quantum Electron.* **3**:429 (1997).
36. See, for example, F. L. Pedrotti and L. S. Pedrotti, *Introduction to Optics,* Prentice-Hall, Englewood Cliffs, N.J., 1987.
37. B. Weigl, M. Grabherr, C. Jung, R. Jager, G. Reiner, R. Michalzik, D. Sowada, and K. J. Ebeling, *IEEE J. Sel. Top. in Quantum Electron.* **3**:409 (1997).
38. J. W. Law and G. P. Agrawal, *IEEE J. Sel. Top. Quantum Electron.* **3**:353 (1997).
39. J. Boucart et al., *IEEE J. Sel. Top. Quantum Electron.* **5**:520 (1999).
40. S. K. Korotky and R. C. Alferness, "Ti:$LiNbO_3$ Integrated Optic Technology," in (ed.), L. D. Hutcheson, *Integrated Optical Circuits and Components,* Dekker, New York, 1987.
41. G. Y. Wang and E. Garmire, *Opt. Lett.* **21**:42 (1996).
42. Yariv, Table 9.2.
43. G. D. Boyd, R. C. Miller, K. Nassau, W. L. Bond, and A. Savage, *Appl. Phys. Lett.* **5**:234 (1964).
44. Information from www.utocorp.com, June 1999.
45. F. P. Leonberger and J. P. Donnelly, "Semiconductor Integrated Optic Devices," in T. Tamir (ed.), *Guided Wave Optoelectronics,* Springer-Verlag, 1990, p. 340.
46. C. C. Chen, H. Porte, A. Carenco, J. P. Goedgebuer, and V. Armbruster, *IEEE Photon. Technol. Lett.* **9**:1361 (1997).
47. C. T. Mueller and E. Garmire, *Appl. Opt.* **23**:4348 (1984).
48. H. Kogelnik, "Theory of Dielectric Waveguides," in T. Tamir (ed.), *Integrated Optics,* Springer-Verlag, 1975.
49. H. Q. Hou, A. N. Cheng, H. H. Wieder, W. S. C. Chang, and C. W. Tu, *Appl. Phys. Lett.* **63**:1833 (1993).
50. A. Ramdane, F. Devauz, N. Souli, D. Dalprat, and A. Ougazzaden, *IEEE J. Sel. Top. in Quantum Electron.* **2**:326 (1996).

51. S. D. Koehler and E. M. Garmire, in T. Tamir, H. Bertoni, and G. Griffel (eds.), *Guided-Wave Optoelectronics: Device Characterization, Analysis and Design,* Plenum Press, New York, 1995.
52. See, for example, S. Carbonneau, E. S. Koteles, P. J. Poole, J. J. He, G. C. Aers, J. Haysom, M. Buchanan, Y. Feng, A. Delage, F. Yang, M. Davies, R. D. Goldberg, P. G. Piva, and I. V. Mitchell, *IEEE J. Sel. Top. in Quantum Electron.* **4**:772 (1998).
53. J. A. Trezza, J. S. Powell, and J. S. Harris, *IEEE Photon. Technol. Lett.* **9**:330 (1997).
54. K. Wakita, I. Kotaka, T. Amano, and H. Sugiura, *Electron. Lett.* **31**:1339 (1995).
55. F. Devaux, J. C. Harmand, I. F. L. Dias, T. Guetler, O. Krebs, and P. Voisin, *Electron. Lett.* **33**:161 (1997).
56. H. Yamazaki, Y. Sakata, M. Yamaguchi, Y. Inomoto, and K. Komatsu, *Electron. Lett.* **32**:109 (1996).
57. K. Morito, K. Sato, Y. Kotaki, H. Soda, and R. Sahara, *Electron. Lett.* **31**:975 (1995).
58. F. Devaux, E. Bigan, M. Allovon, et al., *Appl. Phys. Lett.* **61**:2773 (1992).
59. J. E. Zucker, K. L. Jones, M. Wegener, T. Y. Chang, N. J. Sauer, M. D. Divino, and D. S. Chemla, *Appl. Phys. Lett.* **59**:201 (1991).
60. M. Jupina, E. Garmire, M. Zembutsu, and N. Shibata, *IEEE J. Quantum Electron.* **28**:663 (1992).
61. S. D. Koehler, E. M. Garmire, A. R. Kost, D. Yap, D. P. Doctor, and T. C. Hasenberg, *IEEE Photon. Technol. Lett.* **7**:878 (1995).
62. A. Sneh, J. E. Zucker, B. I. Miller, and L. W. Stultz, *IEEE Photon. Technol. Lett.* **9**:1589 (1997).
63. J. Pamulapati, et al., *J. Appl. Phys.* **69**:4071 (1991).
64. H. Feng, J. P. Pang, M. Sugiyama, K. Tada, and Y. Nakano, *IEEE J. Quantum Electron.* **34**:1197 (1998).
65. J. Wang, J. E. Zucker, J. P. Leburton, T. Y. Chang, and N. J. Sauer, *Appl. Phys. Lett.* **65**:2196 (1994).
66. N. Yoshimoto, Y. Shibata, S. Oku, S. Kondo, and Y. Noguchi, *IEEE Photon. Technol. Lett.* **10**:531 (1998).
67. Yariv, Sec. 11.7.
68. E. Hasnain et al., *IEEE J. Quantum Electron.* **34**:2321 (1998).

CHAPTER 5
OPTICAL FIBER AMPLIFIERS

John A. Buck
School of Electrical and Computer Engineering
Georgia Institute of Technology
Atlanta, Georgia

5.1 INTRODUCTION

The development of rare-earth-doped fiber amplifiers has led to dramatic increases in the channel capacities of fiber communication systems, and has provided the key components in many new forms of optical sources and signal processing devices. The most widely used fiber amplifiers are formed by doping the glass fiber host with erbium ions, from which gain by stimulated emission occurs at wavelengths in the vicinity of 1.55 μm. The amplifiers are optically pumped using light at either 1.48-μm or 0.98-μm wavelengths. Other rare-earth dopants include praseodymium, which provides gain at 1.3 μm and which is pumped at 1.02 μm,[1] ytterbium, which amplifies from 975 to 1150 nm using pump wavelengths between 910 and 1064 nm,[2] and erbium-ytterbium codoping, which enables use of pump light at 1.06 μm while providing gain at 1.55 μm.[3] Additionally, thulium- and thulium/terbium-doped fluoride fibers have been constructed for amplification at 0.8, 1.4, and 1.65 μm.[4] Aside from systems applications, much development has occurred in fiber ring lasers based on erbium-doped-fiber amplifiers (EDFAs),[5] in addition to optical storage loops[6] and nonlinear switching devices.[7]

The original intent in fiber amplifier development was to provide a simpler alternative to the electronic repeater by allowing the signal to remain in optical form throughout a link or network. Fiber amplifiers as repeaters offer additional advantages, which include the ability to change system data rates as needed, or to simultaneously transmit multiple rates—all without the need to modify the transmission channel. A further advantage is that signal power at multiple wavelengths can be simultaneously boosted by a single amplifier—a task that would otherwise require a separate electronic repeater for each wavelength. This latter feature contributed to the realization of dense wavelength-division multiplexed (DWDM) systems, in which terabit/sec data rates have been demonstrated.[8] The usable gain in an EDFA occupies a wavelength range spanning 1.53 to 1.56 μm. In DWDM systems this allows, for example, the use of some 40 channels having 100-GHz spacing. A fundamental disadvantage of the fiber amplifier as a repeater is that dispersion is not reset. This requires additional network design efforts in dispersion management,[9] which may include optical equalization methods.[10] The deployment of fiber amplifiers in commercial networks demonstrates the move toward

Copyright 2001 by The McGraw-Hill Companies, Inc. Click Here for Terms of Use.

transparent fiber systems, in which signals are maintained in optical form, and in which multiple wavelengths, data rates, and modulation formats are supported.

Aside from rare-earth-doped glass fibers, which provide gain through stimulated emission, there has been renewed interest in fiber Raman amplifiers, in which gain at the signal wavelength occurs as a result of glass-mediated coupling to a shorter-wavelength optical pump.[11] Raman amplifiers have recently been demonstrated in DWDM systems that operate in the vicinity of 1.3 μm.[12] This chapter emphasizes the rare-earth systems—particularly erbium-doped fiber amplifiers, since these are the most important ones in practical use.

5.2 RARE-EARTH-DOPED AMPLIFIER CONFIGURATION AND OPERATION

Pump Configuation and Optimum Amplifier Length

A typical fiber amplifier configuration consists of the doped fiber positioned between polarization-independent optical isolators. Pump light is input by way of a wavelength-selective coupler which can be configured for forward, backward, or bidirectional pumping (see Fig. 1). Pump absorption throughout the amplifier length results in a population inversion that varies with position along the fiber; this reaches a minimum at the fiber end opposite the pump laser for unidirectional pumping, or minimizes at midlength for bidirectional pumping using equal pump powers. To achieve the highest overall gain, the length is chosen so that the fiber is transparent to the signal at the point of minimum pump power. For example, using forward pumping, the optimum fiber length is determined by requiring transparency to occur at the output end. If longer fiber lengths are used, some reabsorption of the signal will occur beyond the transparency point. With lengths shorter than the optimum, full use is not made of the available pump energy. Other factors may modify the optimum length, particularly if substantial gain saturation occurs, or if amplified spontaneous emission (ASE) is present, which can result in additional gain saturation and noise.[13]

Isolators maintain unidirectional light propagation so that, for example, backscattered or reflected light from further down the link cannot reenter the amplifier and cause gain quenching, noise enhancement, or possibly lasing. Double-pass and segmented configurations are also used; in the latter, isolators are positioned between two or more lengths of amplifying fiber that

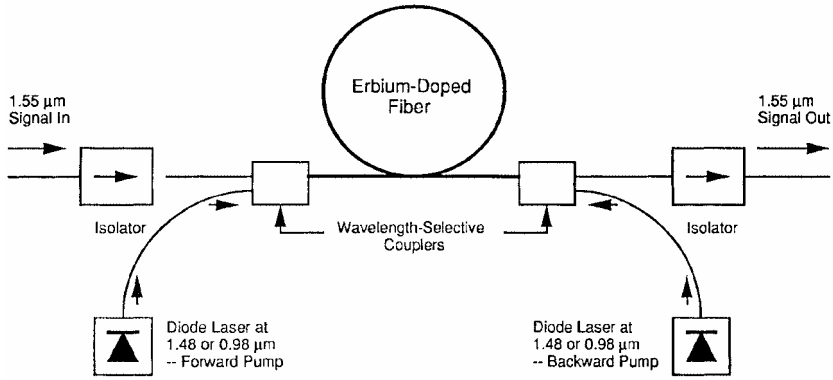

FIGURE 1 General erbium-doped fiber configuration, showing bidirectional pumping.

are separately pumped. The result is that gain quenching and noise arising from back-scattered light or from ASE can be lower than those of a single fiber amplifier of the combined lengths.

Regimes of Operation

There are roughly three operating regimes, the choice between which is determined by the use intended for the amplifier.[14, 15] These are (1) small-signal, or linear, (2) saturation, and (3) deep saturation regimes. In the linear regime, low input signal levels (<1 μW) are amplified with negligible gain saturation, assuming the amplifier length has been optimized. Amplifier gain in decibels is defined in terms of the input and output signal powers as $G(\text{dB}) = 10 \log_{10} (P_s^{\text{out}}/P_s^{\text{in}})$. EDFA small signal gains range between 25 and 35 dB.[15]

In the saturation regime, the input signal level is high enough to cause a measurable reduction in the net gain. A useful figure of merit is the *input saturation power,* defined as the input signal power required to reduce the net amplifier gain by 3 dB, assuming an optimized fiber length. Specifically, the gain in this case is $G = G_{\max} - 3$ dB, where $G_{\max}$ is the small-signal gain. A related parameter is the *saturation output power,* $P_{\text{sat}}^{\text{out}}$, defined as the amplifier output that is achieved when the overall gain is reduced by 3 dB. The two quantities are thus related through $G_{\max} - 3\text{dB} = 10 \log_{10} (P_{\text{sat}}^{\text{out}}/P_{\text{sat}}^{\text{in}})$. Using these parameters, the *dynamic range* of the amplifier is defined through $P_s^{\text{in}} \le P_{\text{sat}}^{\text{in}}$, or equivalently $P_s^{\text{out}} \le P_{\text{sat}}^{\text{out}}$. For an N-channel wavelength-division multiplexed signal, the dynamic range is reduced accordingly by a factor of 1/N, assuming a flat gain spectrum.[15]

With the amplifier operating in deep saturation, gain reductions on the order of 20 to 40 dB occur.[14] This is typical of *power amplifier* applications, in which input signal levels are high, and where the maximum output power is desired. In this application, the concept of *power conversion efficiency* (PCE) between pump and signal becomes important. It is defined as $\text{PCE} = (P_s^{\text{out}} - P_s^{\text{in}})/P_p^{\text{in}}$, where P_p^{in} is the input pump power. Another important quantity that is pertinent to the deep saturation regime is the *saturated output power,* P_s^{out} (max), not to be confused with the saturation output power previously described. P_s^{out} (max) is the maximum output signal power that can be achieved for a given input signal level and available pump power. This quantity would maximize when the amplifier, having previously been fully inverted, is then completely saturated by the signal. Maximum saturation, however, requires the input signal power to be extremely high, such that ultimately, P_s^{out} (max) $\approx P_s^{\text{in}}$, representing a net gain of nearly 0 dB. Clearly the more important situations are those in which moderate signal powers are to be amplified; in these cases the choice of pump power and pumping configuration can substantially influence P_s^{out} (max).

5.3 EDFA PHYSICAL STRUCTURE AND LIGHT INTERACTIONS

Energy Levels in the EDFA

Gain in the erbium-doped fiber system occurs when an inverted population exists between parts of the $^4I_{13/2}$ and $^4I_{15/2}$ states, as shown in Fig. 2*a.* This notation uses the standard form, $^{(2S+1)}L_J$, where *L, S,* and *J* are the orbital, spin, and total angular momenta, respectively. EDFAs are manufactured by incorporating erbium ions into the glass matrix that forms the fiber core. Interactions between the ions and the host matrix induce Stark splitting of the ion energy levels, as shown in Fig. 2*a.* This produces an average spacing between adjacent Stark levels of 50 cm^{-1}, and an overall spread of 300 to 400 cm^{-1} within each state. A broader emission spectrum results, since more deexcitation pathways are produced, which occur at different transition wavelengths.

Other mechanisms further broaden the emission spectrum. First, the extent to which ions interact with the glass varies from site to site, as a result of the nonuniform structure of the

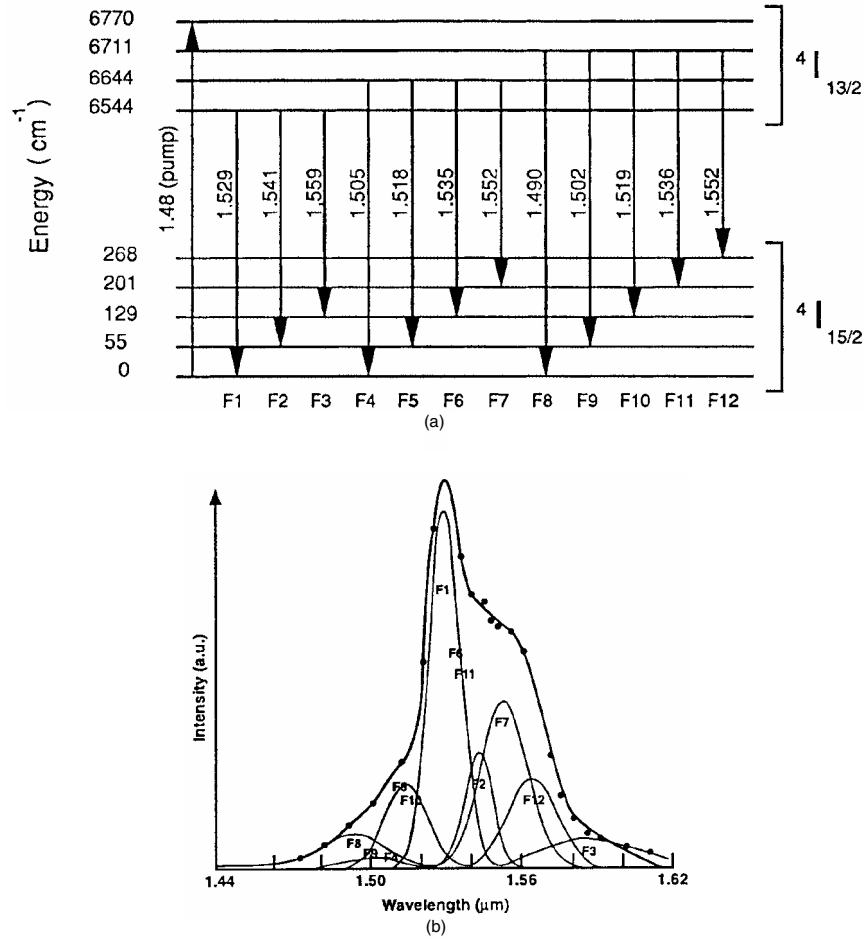

FIGURE 2 (*a*) Emissive transitions between Stark-split levels of erbium in an aluminosilicate glass host. Values on transition arrows indicate wavelengths in micrometers. *(Adapted from Ref. 19).* (*b*) EDFA fluorescence spectrum associated with the transitions in Figure 2*a. (Reprinted with permission from* Optical Fiber Amplifiers: Materials, Devices, and Applications*, by S. Sudo. Artech House Publishers, Norwood, MA, USA. www.artechhouse.com).*

amorphous glass matrix. This produces some degree of inhomogeneous broadening in the emission spectrum, the extent of which varies with the type of glass host used.[16] Second, thermal fluctuations in the material lead to homogeneous broadening of the individual Stark transitions. The magnitudes of the two broadening mechanisms are 27 to 60 cm^{-1} for inhomogeneous, and 8 to 49 cm^{-1} for homogeneous.[16] The choice of host material strongly affects the shape of the emission spectrum, owing to the character of the ion-host interactions. For example, in pure silica (SiO_2), the spectrum of the Er-doped system is narrowest and has the least

smoothness. Use of an aluminosilicate host (SiO_2-$A1_2O_3$) produces slight broadening and smoothing.[17] The broadest spectra, however, occur when using fluoride-based glass, such as ZBLAN.[18]

Gain Formation

Fig. 2*b* shows how the net emission (fluorescence) spectrum is constructed from the superposition of the individual Stark spectra; the latter are associated with the transitions shown in Fig. 2*a.* Similar diagrams can be constructed for the upward (absorptive) transitions, from which the absorption spectrum can be developed.[19] The shapes of both spectra are further influenced by the populations within the Stark split levels, which assume a Maxwell-Boltzman distribution. The sequence of events in the population dynamics is (1) pump light boosts population from the ground state, $^4I_{15/2}$, to the upper Stark levels in the first excited state, $^4I_{13/2}$; (2) the upper state Stark level populations thermalize; and (3) deexcitation from $^4I_{13/2}$ to $^4I_{15/2}$ occurs through either spontaneous or stimulated emission.

The system can be treated using a simple two-level (1.48-μm pump) or three-level model (0.98-μm pump), from which rate equations can be constructed that incorporate the actual wavelength- and temperature-dependent absorption and emission cross sections. These models have been formulated with and without inhomogeneous broadening, but in most cases excellent agreement with experiment has been achieved by assuming only homogeneous broadening.[20, 21, 22]

Pump Wavelength Options in EDFAs

The 1.48-μm pump wavelength corresponds to the energy difference between the two most widely spaced Stark levels, as shown in Fig. 2*a.* A better alternative is to pump with light at 0.98 μm, which boosts the ground state population to the second excited state, $^4I_{11/2}$, which lies above $^4I_{13/2}$. This is followed by rapid nonradiative decay into $^4I_{13/2}$ and gain is formed as before. The pumping efficiency suffers slightly at 0.98 μm, owing to some excited state absorption (ESA) from $^4I_{11/2}$ to the higher-lying $^4F_{7/2}$.[23] Use of 0.98-μm pump light as opposed to 1.48 μm will nevertheless yield a more efficient system, since the 0.98-μm pump will not contribute to the deexcitation process, which occurs when 1.48 μm is used.

The *gain efficiency* of a rare-earth-doped fiber is defined as the ratio of the maximum small signal gain to the input pump power, using the optimized fiber length. EDFA efficiencies are typically on the order of 10 dB/mW for pumping at .98 μm. For pumping at 1.48 μm, efficiencies are about half the values obtainable at .98 μm, and require about twice the fiber length. Other pump wavelengths can be used,[24] but with some penalty to be paid in the form of excited state absorption from the $^4I_{13/2}$ state into various upper levels, thus depleting the gain that would otherwise be available. This problem is minimized when using either 0.98 or 1.48 μm, and so these two wavelengths are almost exclusively used in erbium-doped fibers.

Noise

Performance is degraded by the presence of noise from two fundamental sources. These are (1) amplified spontaneous emission (ASE) and (2) Rayleigh scattering. Both processes lead to additional light that propagates in the forward and backward directions, and which can encounter considerable gain over long amplifier lengths. The more serious of the two noise sources is ASE. In severe cases, involving high-gain amplifiers of long lengths, ASE can be of high enough intensity to partially saturate the gain (self-saturation), thus reducing the available gain for signal amplification. Backward pumping has been found to reduce this effect.[25]

In general, ASE can be reduced by (1) assuring that the population inversion is as high as possible (ideally, completely inverted); (2) operating the amplifier in the deep saturation regime; or (3) using two or more amplifier stages rather than one continuous length of fiber, and positioning bandpass filters and isolators between stages. Rayleigh scattering noise can be minimized by using multistage configurations, in addition to placing adequate controls on dopant concentration and confinement during the manufacturing stage.[26]

The *noise figure* of a rare-earth-doped fiber amplifier is stated in a manner consistent with the IEEE standard definition for a general amplifier. This is the signal-to-noise ratio of the fiber amplifier input divided by the signal-to-noise ratio of the output, expressed in decibels, where the input signal is shot noise limited. Although this definition is widely used, it has recently come under some criticism, owing to the physical nature of ASE noise, and the resulting awkwardness in applying the definition to cascaded amplifier systems.[27] The best noise figures for EDFAs are obtained by using whatever pump configurations produce the highest population inversions. Again, use of .98-μm pumping is preferred, with noise figures of about 3 dB obtainable; using 1.48 μm yields best results of about 4 dB.[14]

Gain Flattening

The use of multiple wavelength channels motivates the need to effectively flatten the emission spectrum, and thus equalize the gain for all wavelengths. Flattening techniques can be classified into roughly three categories. First, intrinsic methods can be used; these involve choices of fiber host materials such as fluoride glass[28] that yield smoother and broader gain spectra. In addition, by carefully choosing pump power levels, a degree of population inversion can be obtained which will allow some cancellation to occur between the slopes of the absorption and emission spectra.[29] Second, spectral filtering at the output of a single amplifier or between cascaded amplifiers can be employed; this effectively produces higher loss for wavelengths that have achieved higher gain. Examples of successful filtering devices include long-period fiber gratings[30] and Mach-Zehnder filters.[31] Third, hybrid amplifiers that use cascaded configurations of different gain media can be used to produce an overall gain spectrum that is reasonably flat. Flattened gain spectra have been obtained having approximate widths that range from 12 to 85 nm. Reference 32 is recommended for an excellent discussion and comparison of the methods.

5.4 GAIN FORMATION IN OTHER RARE-EARTH SYSTEMS

Praseodymium-Doped Fiber Amplifiers (PDFAs)

In the praseodymium-doped fluoride system, the strongest gain occurs in the vicinity of 1.3 μm, with the pump wavelength at 1.02 μm. Gain formation is described by a basic three-level model, in which pump light excites the system from the ground state, $^3H_4$, to the metastable excited state, $^1G_4$. Gain for 1.3-μm light is associated with the downward $^1G_4 \rightarrow {}^3H_5$ transition, which peaks in the vicinity of 1.32 to 1.34 μm. Gain diminishes at longer wavelengths, principally as a result of ground state absorption from $^3H_4 \rightarrow {}^3F_3$.[23]

The main problem with the PDFA system is reduction of the available gain through the competing $^1G_4 \rightarrow {}^3F_4$ transition (2900 cm^{-1} spacing), occurring through multiphonon relaxation.[23] The result is that the *radiative quantum efficiency* (defined as the ratio of the desired transition rate to itself plus all competing transition rates) can be low enough to make the system impractical. The multiphonon relaxation rate is reduced when using hosts having low phonon energies, such as fluoride or chalcogenide glasses. Using these produces radiative quantum efficiencies on the order of 2 percent. For comparison, erbium systems exhibit quan-

tum efficiencies of nearly 100 percent for the 1.5-μm transition. Nevertheless, PDFAs have found practical use in 1.3-μm transmission systems, and have yielded net gains that are comparable to EDFAs, but of course with substantially higher pump power requirements. Other considerations such as broadening mechanisms and excited state absorption are analogous to the erbium system. References 1, 32, and 33 are recommended for further reading.

Erbium/Ytterbium-Doped Fiber Amplifiers (EYDFAs)

Erbium/ytterbium codoping offers special advantages in fiber amplifier performance. Ytterbium ions absorb very efficiently over the wavelength range of 800 to 1100 nm. Once excited, they transfer their energy to the erbium ions, and gain between 1.53 and 1.56 μm is formed as before.[3] Advantages of such a system include the following: With high pump absorption, side-pumping is possible, thus allowing the use of large-area diode lasers as pumps. In addition, high gain can be established over a shorter propagation distance in the fiber than is possible in a conventional EDFA. As a result, shorter-length amplifiers having lower ASE noise can be constructed. An added benefit is that the absorption band allows pumping by high-power lasers such as Nd:YAG (at 1.06 μm) or Nd:YLF (at 1.05 μm), and there is no excited state absorption. Currently, Yb-sensitized fibers are primarily attractive for use as power amplifiers, and in the construction of fiber lasers, in which a short-length, high-gain medium is needed.[35]

5.5 REFERENCES

1. Y. Ohishi et al., "Pr^{3+}-Doped Fluoride Fiber Amplifier Operation at 1.3 μm," *Optics Letters* **16**: 1747–1749 (1991).
2. R. Paschotta et al., "Ytterbium-Doped Fiber Amplifiers," *IEEE Journal of Quantum Electronics* **33**: 1049–1056 (1997).
3. J. E. Townsend et al., "Yb^{3+}-Sensitized Er^{3+}-Doped Silica Optical Fiber with Ultra High Efficiency and Gain," *Electronics Letters* **27**:1958–1959 (1991).
4. S. Sudo, "Progress in Optical Fiber Amplifiers," *Current Trends in Optical Amplifiers and their Applications,* T. P. Lee (ed.), World Scientific, New Jersey, 1996, 19–21.
5. I. N. Duling III, "Subpicosecond All-Fiber Erbium Laser," *Electronics Letters* **27**:544–545 (1991).
6. B. Moslehi and J. W. Goodman, "Novel Amplified Fiber Optic Recirculating Delay Line Processor," *IEEE Journal of Lightwave Technology* **10**:1142–1147 (1992).
7. R. H. Pantell, R. W. Sadowski, M. J. F. Digonnet, and H. J. Shaw, "Laser Diode-Pumped Nonlinear Switch in Erbium-Doped Fiber," *Optics Letters* **17**:1026–1028 (1992).
8. A. R. Chraplyvy and R. W. Tkach, "Terabit/Second Transmission Experiments," *IEEE Journal of Quantum Electronics* **34**:2103–2108 (1998).
9. A. R. Chraplyvy, A. H. Gnauck, R. W. Tkach, and R. M. Derosier, "8 × 10 Gb/s Transmission through 280 km of Dispersion-Managed Fiber," *IEEE Photonics Technology Letters* **5**:1233–1235 (1993).
10. *IEEE Journal of Lightwave Technology*—Special Miniissue on Dispersion Compensation **12**:1706–1765 (1994).
11. J. Auyeung and A. Yariv, "Spontaneous and Stimulated Raman Scattering in Long Low-Loss Fibers," *IEEE Journal of Quantum Electronics* **14**:347–352 (1978).
12. T. N. Nielsen, P. B. Hansen, A. J. Stentz, V. M. Aguaro, J. R. Pedrazzani, A. A. Abramov, and R. P. Espindola, "8 × 10 Gb/s 1.3-μm Unrepeatered Transmission over a Distance of 141 km with Raman Post- and Pre-Amplifiers," *IEEE Photonics Technology Letters,* **10**:1492–1494 (1998).
13. P. C. Becker, N. A. Olsson, and J. R. Simpson, *Erbium-Doped Fiber Amplifiers, Fundamentals and Technology,* Academic Press, San Diego, 1999, 139–140.
14. J.-M. P. Delavaux and J. A. Nagel, "Multi-Stage Erbium-Doped Fiber Amplifier Design," *IEEE Journal of Lightwave Technology* **13**:703–720 (1995).

15. E. Desurvire, *Erbium-Doped Fiber Amplifiers, Principles and Applications,* Wiley-Interscience, New York, 1994, 337–340.
16. S. Sudo, "Outline of Optical Fiber Amplifiers," *Optical Fiber Amplifiers: Materials, Devices, and Applications,* S. Sudo (ed.), Artech House, Boston, 1997, 81–83 and references therein.
17. W. J. Miniscalco, "Erbium-Doped Glasses for Fiber Amplifiers at 1500nm," *IEEE Journal of Lightwave Technology* **9**:234–250 (1991).
18. S. T. Davey and P. W. France, "Rare-Earth-Doped Fluorozirconate Glass for Fibre Devices," *British Telecom Technical Journal* **7**:58 (1989).
19. E. Desurvire, *Erbium-Doped Fiber Amplifiers, Principles and Applications,* Wiley-Interscience, New York, 1994, 238.
20. C. R. Giles and E. Desurvire, "Modeling Erbium-Doped Fiber Amplifiers," *IEEE Journal of Lightwave Technology* **9**:271–283 (1991).
21. E. Desurvire, "Study of the Complex Atomic Susceptibility of Erbium-Doped Fiber Amplifiers," *IEEE Journal of Lightwave Technology* **8**:1517–1527 (1990).
22. Y. Sun, J. L. Zyskind, and A. K. Srivastava, "Average Inversion Level, Modeling, and Physics of Erbium-Doped Fiber Amplifiers," *IEEE Journal of Selected Topics in Quantum Electronics* **3**:991–1007 (1997).
23. S. Sudo, "Outline of Optical Fiber Amplifiers," *Optical Fiber Amplifiers: Materials, Devices, and Applications,* S. Sudo (ed.), Artech House, Boston, 1997, 73.
24. M. Horiguchi et al., "Erbium-Doped Fiber Amplifiers Pumped in the 660- and 820-nm Bands," *IEEE Journal of Lightwave Technology,* **12**:810–820 (1994).
25. E. Desurvire, "Analysis of Gain Difference Between Forward- and Backward-Pumped Erbium-Doped Fibers in the Saturation Regime," *IEEE Photonics Technology Letters,* **4**:711–713 (1992).
26. M. N. Zervas and R. I. Laming, "Rayleigh Scattering Effect on the Gain Efficiency and Noise of Erbium-Doped Fiber Amplifiers," *IEEE Journal of Quantum Electronics* **31**:469–471 (1995).
27. H. A. Haus, "The Noise Figure of Optical Amplifiers," *IEEE Photonics Technology Letters* **10**:1602–1604 (1998).
28. D. Bayart, B. Clesca, L. Hamon, and J. L. Beylat, "Experimental Investigation of the Gain Flatness Characteristics for 1.55μm Erbium-Doped Fluoride Fiber Amplifiers," *IEEE Photonics Technology Letters* **6**:613–615 (1994).
29. E. L. Goldstein, L. Eskildsen, C. Lin, and R. E. Tench, "Multiwavelength Propagation in Lightwave Systems with Strongly-Inverted Fiber Amplifiers," *IEEE Photonics Technology Letters* **6**:266–269 (1994).
30. C. R. Giles, "Lightwave Applications of Fiber Bragg Gratings," *IEEE Journal of Lightwave Technology* **15**:1391–1404 (1997).
31. J.-Y. Pan, M. A. Ah, A. F. Elrefaie, and R. E. Wagner, "Multiwavelength Fiber Amplifier Cascades with Equalization Employing Mach-Zehnder Optical Filters," *IEEE Photonics Technology Letters* **7**:1501–1503 (1995).
32. P. C. Becker, N. A. Olsson, and J. R. Simpson, op. cit., 285–295.
33. T. J. Whitley et al., "Quarter-Watt Output from a Praseodymium-Doped Fluoride Fibre Amplifier with a Diode-Pumped Nd:YLF Laser," *IEEE Photonics Technology Letters* **5**:399–401 (1993).
34. T. J. Whitley, "A Review of Recent System Demonstrations Incorporating Praseodymium-Doped Fluoride Fiber Amplifiers," *IEEE Journal of Lightwave Technology* **13**:744–760 (1995).
35. G. G. Vienne et al., "Fabrication and Characterization of Yb^{3+}:Er^{3+} Phosphosilicate Fibers for Lasers," *IEEE Journal of Lightwave Technology* **16**:1990–2001 (1998).

CHAPTER 6

FIBER-OPTIC COMMUNICATION LINKS (TELECOM, DATACOM, AND ANALOG)

Casimer DeCusatis
IBM Corporation
Poughkeepsie, New York

Guifang Li
School of Optics/The Center for Research and Education in Optics and Lasers (CREOL)
University of Central Florida
Orlando, Florida

6.1 INTRODUCTION

There are many different applications for fiber-optic communication systems, and each has its own unique performance requirements. For example, analog communication systems may be subject to different types of noise and interference than digital systems, and consequently require different figures of merit to characterize their behavior. At first glance, telecommunication and data communication systems appear to have much in common, as both use digital encoding of data streams; in fact, both types can share a common network infrastructure. Upon closer examination, however, we find important differences between them. First, datacom systems must maintain a much lower bit error rate (BER), defined as the number of transmission errors per second in the communication link. (We will discuss BER in more detail in the following sections.) For telecom (voice) communications, the ultimate receiver is the human ear, and voice signals have a bandwidth of only about 4 kHz; transmission errors often manifest as excessive static noise such as encountered on a mobile phone, and most users can tolerate this level of fidelity. In contrast, the consequences of even a single bit error to a datacom system can be very serious; critical data such as medical or financial records could be corrupted, or large computer systems could be shut down. Typical telecom systems operate at a BER of about 10e-9, compared with about 10e-12 to 10e-15 for datacom systems. Another unique requirement of datacom systems is eye safety versus distance trade-offs. Most telecommunications equipment is maintained in a restricted environment

Copyright 2001 by The McGraw-Hill Companies, Inc. Click Here for Terms of Use.

and accessible only to personnel trained in the proper handling of high-power optical sources. Datacom equipment is maintained in a computer center and must comply with international regulations for inherent eye safety; this limits the amount of optical power that can safely be launched into the fiber, and consequently limits the maximum transmission distances that can be achieved without using repeaters or regenerators. For the same reason, datacom equipment must be rugged enough to withstand casual use, while telecom equipment is more often handled by specially trained service personnel. Telecom systems also make more extensive use of multiplexing techniques, which are only now being introduced into the data center, and more extensive use of optical repeaters. For example, commercial phone lines require repeaters spaced about every 12 km; optical links have increased this distance to around 40 km, and some recently installed systems (1997) extend the unrepeated distance up to 120 km or more.

In the following sections, we will examine the technical requirements for designing fiber optic communication systems suitable for these different environments. We begin by defining some figures of merit to characterize the system performance. Then, concentrating on digital optical communication systems, we will describe how to design an optical link loss budget and how to account for various types of noise sources in the link.

6.2 FIGURES OF MERIT: SNR, BER, MER, AND SFDR

Several possible figures of merit may be used to characterize the performance of an optical communication system. Furthermore, different figures of merit may be more suitable for different applications, such as analog or digital transmission. In this section we will describe some of the measurements used to characterize the performance of optical communication systems. Even if we ignore the practical considerations of laser eye safety standards, an optical transmitter is capable of launching only a limited amount of optical power into a fiber; similarly, there is a limit as to how weak a signal can be detected by the receiver in the presence of noise and interference. Thus, a fundamental consideration in optical communication systems design is the optical link power budget, or the difference between the transmitted and received optical power levels. Some power will be lost due to connections, splices, and bulk attenuation in the fiber. There may also be optical power penalties due to dispersion, modal noise, or other effects in the fiber and electronics. The optical power levels define the signal-to-noise ratio (SNR) at the receiver, which is often used to characterize the performance of analog communication systems. For digital transmission, the most common figure of merit is the bit error rate (BER), defined as the ratio of received bit errors to the total number of transmitted bits. Signal-to-noise ratio is related to the bit error rate by the Gaussian integral

$$\text{BER} = \frac{1}{\sqrt{2\pi}} \int_{Q}^{\infty} e^{-Q^2/2}\, dQ \cong \frac{1}{Q\sqrt{2\pi}}\, e^{-Q^2/2} \tag{1}$$

where Q represents the SNR for simplicity of notation.[1–4] From Eq. (1), we see that a plot of BER versus received optical power yields a straight line on semilog scale, as illustrated in Fig. 1. Nominally, the slope is about 1.8 dB/decade; deviations from a straight line may indicate the presence of nonlinear or non-Gaussian noise sources. Some effects, such as fiber attenuation, are linear noise sources; they can be overcome by increasing the received optical power, as seen from Fig. 1, subject to constraints on maximum optical power (laser safety) and the limits of receiver sensitivity. There are other types of noise sources, such as mode partition noise or relative intensity noise (RIN), which are independent of signal strength. When such noise is present, no amount of increase in transmitted signal strength will affect the BER; a noise floor is produced, as shown by curve B in Fig. 1. This type of noise can be a serious limitation on link performance. If we plot BER versus receiver sensitivity for increasing optical power, we obtain a curve similar to that in Fig. 2, which shows that for very high power levels

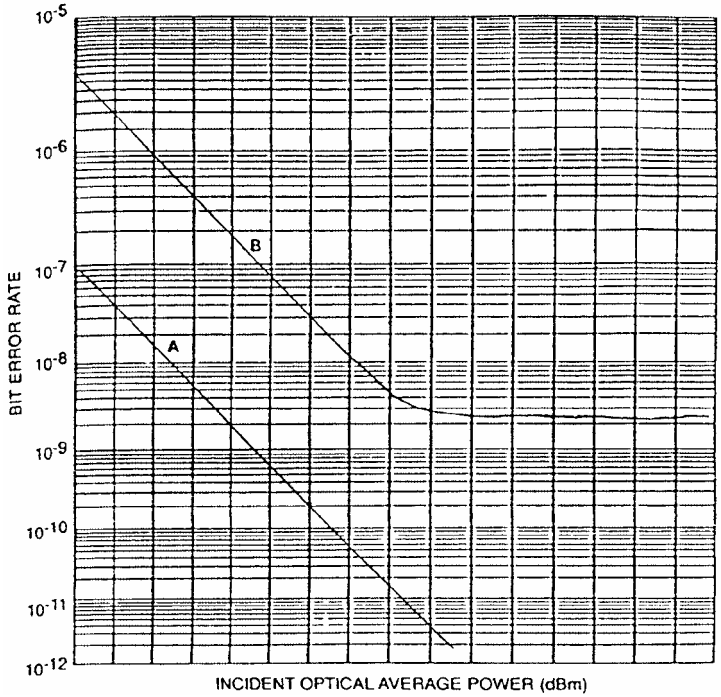

FIGURE 1 Bit error rate as a function of received optical power. Curve A shows typical performance, whereas curve B shows a BER floor [5].

the receiver will go into saturation. The characteristic bathtub-shaped curve illustrates a window of operation with both upper and lower limits on the received power. There may also be an upper limit on optical power due to eye safety considerations.

We can see from Fig. 1 that receiver sensitivity is specified at a given BER, which is often too low to measure directly in a reasonable amount of time (for example, a 200-Mbit/s link operating at a BER of 10e-15 will only take one error every 57 days on average, and several hundred errors are recommended for a reasonable BER measurement). For practical reasons, the BER is typically measured at much higher error rates (such as 10e-4 to 10e-8), where the data can be collected more quickly and then extrapolated to find the sensitivity at low BER. This assumes the absence of nonlinear noise floors, as cautioned previously. The relationship between optical input power, in watts, and the BER is the complimentary Gaussian error function

$$\text{BER} = 1/2 \text{ erfc } (\text{Pout} - \text{Psignal} / \text{RMS noise}) \quad (2)$$

where the error function is an open integral that cannot be solved directly. Several approximations have been developed for this integral, which can be developed into transformation functions that yield a linear least squares fit to the data.[1] The same curve-fitting equations can also be used to characterize the eye window performance of optical receivers. Clock position/phase versus BER data are collected for each edge of the eye window; these data sets are then

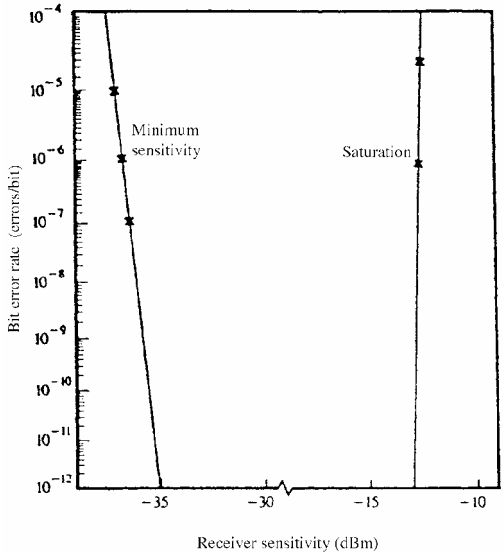

FIGURE 2 Bit error rate as a function of received optical power illustrating range of operation from minimum sensitivity to saturation.

curve-fitted with the previously noted expressions to determine the clock position at the desired BER. The difference in the two resulting clock positions, on either side of the window, gives the clear eye opening.[1–4]

In describing Figs. 1 and 2, we have also made some assumptions about the receiver circuit. Most data links are asynchronous and do not transmit a clock pulse along with the data; instead, a clock is extracted from the incoming data and used to retime the received data stream. We have made the assumption that the BER is measured with the clock at the center of the received data bit: ideally, this is when we compare the signal with a preset threshold to determine if a logical 1 or 0 was sent. When the clock is recovered from a receiver circuit such as a phase lock loop, there is always some uncertainty about the clock position; even if it is centered on the data bit, the relative clock position may drift over time. The region of the bit interval in the time domain where the BER is acceptable is called the *eyewidth;* if the clock timing is swept over the data bit using a delay generator, the BER will degrade near the edges of the eye window. Eyewidth measurements are an important parameter in link design, which will be discussed further in the section on jitter and link budget modeling.

In the designs of some analog optical communication systems, as well as of some digital television systems (for example, those based on 64-bit Quadrature Amplitude Modulation), another possible figure of merit is the modulation error ratio (MER). To understand this metric, we will consider the standard definition of the Digital Video Broadcasters (DVB) Measurements Group.[5] First, the video receiver captures a time record of N received signal coordinate pairs, representing the position of information on a two-dimensional screen. The ideal position coordinates are given by the vector (X_j, Y_j). For each received symbol, a decision is made as to which symbol was transmitted, and an error vector $(\Delta X_j, \Delta Y_j)$ is defined as the distance from the ideal position to the actual position of the received symbol. The MER is then

defined as the sum of the squares of the magnitudes of the ideal symbol vector divided by the sum of the squares of the magnitudes of the symbol error vectors:

$$\text{MER} = 10 \log \frac{\sum_{j=1}^{N} (X_j^2 + Y_j^2)}{\sum_{j=1}^{N} (\Delta X_j^2 + \Delta Y_j^2)} \text{ dB} \tag{3}$$

When the signal vectors are corrupted by noise, they can be treated as random variables. The denominator in Eq. (3) becomes an estimate of the average power of the error vector (in other words, its second moment) and contains all signal degradation due to noise, reflections, transmitter quadrature errors, and so forth. If the only significant source of signal degradation is additive white Gaussian noise, then MER and SNR are equivalent. For communication systems that contain other noise sources, MER offers some advantages; in particular, for some digital transmission systems there may be a very sharp change in BER as a function of SNR (a so-called *cliff effect*), which means that BER alone cannot be used as an early predictor of system failures. MER, on the other hand, can be used to measure signal-to-interference ratios accurately for such systems. Because MER is a statistical measurement, its accuracy is directly related to the number of vectors, *N,* used in the computation; an accuracy of 0.14 dB can be obtained with $N = 10{,}000$, which would require about 2 ms to accumulate at the industry standard digital video rate of 5.057 Msymbols/s.

In order to design a proper optical data link, the contribution of different types of noise sources should be assessed when developing a link budget. There are two basic approaches to link-budget modeling. One method is to design the link to operate at the desired BER when all the individual link components assume their worst-case performance. This conservative approach is desirable when very high performance is required, or when it is difficult or inconvenient to replace failing components near the end of their useful lifetimes. The resulting design has a high safety margin; in some cases it may be overdesigned for the required level of performance. Since it is very unlikely that all the elements of the link will assume their worst-case performance at the same time, an alternative is to model the link budget statistically. For this method, distributions of transmitter power output, receiver sensitivity, and other parameters are either measured or estimated. They are then combined statistically using an approach such as the Monte Carlo method, in which many possible link combinations are simulated to generate an overall distribution of the available link optical power. A typical approach is the 3-sigma design, in which the combined variations of all link components are not allowed to extend more than three standard deviations from the average performance target in either direction. The statistical approach results in greater design flexibility and generally increased distance compared with a worst-case model at the same BER.

Harmonic Distortions, Intermodulation Distortions, and Dynamics Range

Fiber-optic analog links are in general nonlinear. That is, if the input electrical information is a harmonic signal of frequency f_0, the output electrical signal will contain the fundamental frequency f_0 as well as high-order harmonics of frequencies nf_0 ($n > 2$). These high-order harmonics comprise the harmonic distortions of analog fiber-optic links.[6] The nonlinear behavior is caused by nonlinearities in the transmitter, the fiber, and the receiver.

The same sources of nonlinearities in the fiber-optic links lead to intermodulation distortions (IMD), which can best be illustrated in a two-tone transmission scenario. If the input electrical information is a superposition of two harmonic signals of frequencies f_1 and f_2, the output electrical signal will contain second-order intermodulation at frequencies $f_1 + f_2$ and $f_1 - f_2$ as well as third-order intermodulation at frequencies $2f_1 - f_2$ and $2f_2 - f_1$.

Most analog fiber-optic links require bandwidth of less than one octave ($f_{max} < 2f_{min}$). As a result, harmonic distortions as well as second-order IMD products are not important as they can be filtered out electronically. However, third-order IMD products are in the same fre-

quency range (between f_{min} and f_{max}) as the signal itself and therefore appear in the output signal as the spurious response. Thus the linearity of analog fiber-optic links is determined by the level of third-order IMD products. In the case of analog links where third-order IMD is eliminated through linearization circuitry, the lowest odd-order IMD determines the linearity of the link.

To quantify IMD distortions, a two-tone experiment (or simulation) is usually conducted, where the input RF powers of the two tones are equal. The linear and nonlinear power transfer functions—the output RF power of each of two input tones and the second- or third-order IMD product as a function of the input RF power of each input harmonic signal—are schematically presented in Fig. 3. When plotted on a log-log scale, the fundamental power transfer function should be a line with a slope of unity. The second- (third-) order power transfer function should be a line with a slope of two (three). The intersections of the power transfer functions are called *second-* and *third-order* intercept points, respectively. Because of the fixed slopes of the power transfer functions, the intercept points can be calculated from measurements obtained at a single input power level. Suppose that at a certain input level, the output power of each of the two fundamental tones, the second-order IMD product, and third-order IMD products are P_1, P_2, and P_3, respectively. When the power levels are in units of dB or dBm, the second-order and third-order intercept points are

$$IP_2 = 2P_1 - P_2 \tag{4}$$

and

$$IP_3 = (3P_1 - P_3)/2 \tag{5}$$

The dynamic range is a measure of an analog fiber-optic link's ability to faithfully transmit signals at various power levels. At the low input power end, the analog link can fail due to insufficient power level, so that the output power is below the noise level. At the high input power

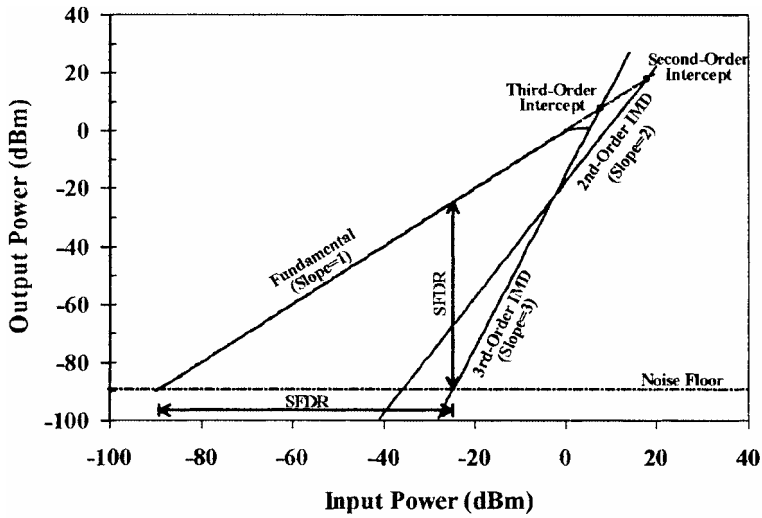

FIGURE 3 Intermodulation and dynamic range of analog fiber-optic links.

end, the analog link can fail due to the fact that the IMD products become the dominant source of signal degradation. In terms of the output power, the dynamic range (of the output power) is defined as the ratio of the fundamental output to the noise power. However, it should be noted that the third-order IMD products increase three times faster than the fundamental signal. After the third-order IMD products exceeds the noise floor, the ratio of the fundamental output to the noise power is meaningless, as the dominant degradation of the output signal comes from IMD products. So a more meaningful definition of the dynamic range is the so-called spurious-free dynamic range (SFDR),[6,7] which is the ratio of the fundamental output to the noise power at the point where the IMD products is at the noise level. The spurious-free dynamic range is then practically the maximum dynamic range. Since the noise floor depends on the bandwidth of interest, the unit for SFDR should be (dB $Hz^{2/3}$). The dynamic range decreases as the bandwidth of the system is increased. The spurious-free dynamic range is also often defined with reference to the input power, which corresponds to SFDR with reference to the output power if there is no gain compression.

6.3 LINK BUDGET ANALYSIS: INSTALLATION LOSS

It is convenient to break down the link budget into two areas: *installation loss* and *available power.* Installation or DC loss refers to optical losses associated with the fiber cable plant, such as connector loss, splice loss, and bandwidth considerations. Available optical power is the difference between the transmitter output and receiver input powers, minus additional losses due to optical noise sources on the link (also known as *AC losses*). With this approach, the installation loss budget may be treated statistically and the available power budget as worst case. First, we consider the installation loss budget, which can be broken down into three areas, namely transmission loss, fiber attenuation as a function of wavelength, and connector or splice losses.

Transmission Loss

Transmission loss is perhaps the most important property of an optical fiber; it affects the link budget and maximum unrepeated distance. Since the maximum optical power launched into an optical fiber is determined by international laser eye safety standards,[8] the number and separation between optical repeaters and regenerators is largely determined by this loss. The mechanisms responsible for this loss include material absorption as well as both linear and nonlinear scattering of light from impurities in the fiber.[1–5] Typical loss for single-mode optical fiber is about 2 to 3 dB/km near 800 nm wavelength, 0.5 dB/km near 1300 nm, and 0.25 dB/km near 1550 nm. Multimode fiber loss is slightly higher, and bending loss will only increase the link attenuation further.

Attenuation versus Wavelength

Since fiber loss varies with wavelength, changes in the source wavelength or use of sources with a spectrum of wavelengths will produce additional loss. Transmission loss is minimized near the 1550-nm wavelength band, which unfortunately does not correspond with the dispersion minimum at around 1310 nm. An accurate model for fiber loss as a function of wavelength has been developed by Walker[9]; this model accounts for the effects of linear scattering, macrobending, and material absorption due to ultraviolet and infrared band edges, hydroxide (OH) absorption, and absorption from common impurities such as phosphorus. Using this model, it is possible to calculate the fiber loss as a function of wavelength for different impu-

rity levels; the fiber properties can be specified along with the acceptable wavelength limits of the source to limit the fiber loss over the entire operating wavelength range. Design tradeoffs are possible between center wavelength and fiber composition to achieve the desired result. Typical loss due to wavelength-dependent attenuation for laser sources on single-mode fiber can be held below 0.1 dB/km.

Connector and Splice Losses

There are also installation losses associated with fiber-optic connectors and splices; both of these are inherently statistical in nature and can be characterized by a Gaussian distribution. There are many different kinds of standardized optical connectors, some of which have been discussed previously; some industry standards also specify the type of optical fiber and connectors suitable for a given application.[10] There are also different models which have been published for estimating connection loss due to fiber misalignment[11, 12]; most of these treat loss due to misalignment of fiber cores, offset of fibers on either side of the connector, and angular misalignment of fibers. The loss due to these effects is then combined into an overall estimate of the connector performance. There is no general model available to treat all types of connectors, but typical connector loss values average about 0.5 dB worst case for multimode, and slightly higher for single mode (see Table 1).

TABLE 1 Typical Cable Plant Optical Losses [5]

Component	Description	Size (μm)	Mean loss	Variance (dB^2)
Connector[a]	Physical contact	62.5–62.5	0.40 dB	0.02
		50.0–50.0	0.40 dB	0.02
		9.0–9.0[b]	0.35 dB	0.06
		62.5–50.0	2.10 dB	0.12
		50.0–62.5	0.00 dB	0.01
Connector[a]	Nonphysical contact (multimode only)	62.5–62.5	0.70 dB	0.04
		50.0–50.0	0.70 dB	0.04
		62.5–50.0	2.40 dB	0.12
		50.0–62.5	0.30 dB	0.01
Splice	Mechanical	62.5–62.5	0.15 dB	0.01
		50.0–50.0	0.15 dB	0.01
		9.0–9.0[b]	0.15 dB	0.01
Splice	Fusion	62.5–62.5	0.40 dB	0.01
		50.0–50.0	0.40 dB	0.01
		9.0–9.0[b]	0.40 dB	0.01
Cable	IBM multimode jumper	62.5	1.75 dB/km	NA
	IBM multimode jumper	50.0	3.00 dB/km at 850 nm	NA
	IBM single-mode jumper	9.0	0.8 dB/km	NA
	Trunk	62.5	1.00 dB/km	NA
	Trunk	50.0	0.90 dB/km	NA
	Trunk	9.0	0.50 dB/km	NA

[a] The connector loss value is typical when attaching identical connectors. The loss can vary significantly if attaching different connector types.

[b] Single-mode connectors and splices must meet a minimum return loss specification of 28 dB.

Optical splices are required for longer links, since fiber is usually available in spools of 1 to 5 km, or to repair broken fibers. There are two basic types, *mechanical splices* (which involve placing the two fiber ends in a receptacle that holds them close together, usually with epoxy) and the more commonly used *fusion splices* (in which the fibers are aligned, then heated sufficiently to fuse the two ends together). Typical splice loss values are given in Table 1.

6.4 LINK BUDGET ANALYSIS: OPTICAL POWER PENALTIES

Next, we will consider the *assembly loss budget,* which is the difference between the transmitter output and receiver input powers, allowing for optical power penalties due to noise sources in the link. We will follow the standard convention in the literature of assuming a digital optical communication link which is best characterized by its BER. Contributing factors to link performance include the following:

- Dispersion (modal and chromatic) or intersymbol interference
- Mode partition noise
- Mode hopping
- Extinction ratio
- Multipath interference
- Relative intensity noise (RIN)
- Timing jitter
- Radiation-induced darkening
- Modal noise

Higher order, nonlinear effects, including Stimulated Raman and Brillouin scattering and frequency chirping, will be discussed elsewhere.

Dispersion

The most important fiber characteristic after transmission loss is *dispersion,* or *intersymbol interference.* This refers to the broadening of optical pulses as they propagate along the fiber. As pulses broaden, they tend to interfere with adjacent pulses; this limits the maximum achievable data rate. In multimode fibers, there are two dominant kinds of dispersion, *modal* and *chromatic.* Modal dispersion refers to the fact that different modes will travel at different velocities and cause pulse broadening. The fiber's modal bandwidth, in units of MHz-km, is specified according to the expression

$$BW_{\text{modal}} = BW_1/L^{\gamma} \tag{6}$$

where BW_{modal} is the modal bandwidth for a length L of fiber, BW_1 is the manufacturer-specified modal bandwidth of a 1-km section of fiber, and γ is a constant known as the *modal bandwidth concatenation length scaling factor.* The term γ usually assumes a value between 0.5 and 1, depending on details of the fiber manufacturing and design as well as the operating wavelength; it is conservative to take $\gamma = 1.0$. Modal bandwidth can be increased by mode mixing, which promotes the interchange of energy between modes to average out the effects of modal dispersion. Fiber splices tend to increase the modal bandwidth, although it is conservative to discard this effect when designing a link.

The other major contribution is chromatic dispersion, BW_{chrom}, which occurs because different wavelengths of light propagate at different velocities in the fiber. For multimode fiber, this is given by an empirical model of the form

$$BW_{\text{chrom}} = \frac{L^{\gamma_c}}{\sqrt{\lambda_w}\,(a_0 + a_1|\lambda_c - \lambda_{\text{eff}}|)} \tag{7}$$

where L is the fiber length in km; λ_c is the center wavelength of the source in nm; λ_w is the source FWHM spectral width in nm; γ_c is the chromatic bandwidth length scaling coefficient, a constant; λ_{eff} is the effective wavelength, which combines the effects of the fiber zero dispersion wavelength and spectral loss signature; and the constants a_1 and a_0 are determined by a regression fit of measured data. From Ref. (13), the chromatic bandwidth for 62.5/125-micron fiber is empirically given by

$$BW_{\text{chrom}} = \frac{10^4 L^{-0.69}}{\sqrt{\lambda_w}\,(1.1 + 0.0189|\lambda_c - 1370|)} \tag{8}$$

For this expression, the center wavelength was 1335 nm and λ_{eff} was chosen midway between λ_c and the water absorption peak at 1390 nm; although λ_{eff} was estimated in this case, the expression still provides a good fit to the data. For 50/125-micron fiber, the expression becomes

$$BW_{\text{chrom}} = \frac{10^4 L^{-0.65}}{\sqrt{\lambda_w}\,(1.01 + 0.0177|\lambda_c - 1330|)} \tag{9}$$

For this case, λ_c was 1313 nm and the chromatic bandwidth peaked at $\lambda_{\text{eff}} = 1330$ nm. Recall that this is only one possible model for fiber bandwidth.[1] The total bandwidth capacity of multimode fiber BW_t is obtained by combining the modal and chromatic dispersion contributions, according to

$$\frac{1}{BW_t^2} = \frac{1}{BW_{\text{chrom}}^2} + \frac{1}{BW_{\text{modal}}^2} \tag{10}$$

Once the total bandwidth is known, the dispersion penalty can be calculated for a given data rate. One expression for the dispersion penalty in dB is

$$P_d = 1.22\left[\frac{\text{Bit Rate } (Mb/s)}{BW_t(\text{MHz})}\right]^2 \tag{11}$$

For typical telecommunication grade fiber, the dispersion penalty for a 20-km link is about 0.5 dB.

Dispersion is usually minimized at wavelengths near 1310 nm; special types of fiber have been developed which manipulate the index profile across the core to achieve minimal dispersion near 1550 nm, which is also the wavelength region of minimal transmission loss. Unfortunately, this dispersion-shifted fiber suffers from some practical drawbacks, including susceptibility to certain kinds of nonlinear noise and increased interference between adjacent channels in a wavelength multiplexing environment. There is a new type of fiber, called *dispersion-optimized fiber,* that minimizes dispersion while reducing the unwanted crosstalk effects. By using a very sophisticated fiber profile, it is possible to minimize dispersion over the entire wavelength range from 1300 to 1550 nm, at the expense of very high loss (around 2 dB/km); this is known as *dispersion-flattened fiber.* Yet another approach is called *dispersion-compensating fiber;* this fiber is designed with negative dispersion characteristics, so that when used in series with conventional fiber it will "undisperse" the signal. Dispersion-compensating fiber has a much narrower core than standard single-mode fiber, which makes it susceptible to nonlinear effects; it is also birefringent and suffers from polarization mode dispersion, in which different states of polarized light propagate with very different group velocities. Note

that standard single-mode fiber does not preserve the polarization state of the incident light; there is yet another type of specialty fiber, with asymmetric core profiles, capable of preserving the polarization of incident light over long distances.

By definition, single-mode fiber does not suffer modal dispersion. Chromatic dispersion is an important effect, though, even given the relatively narrow spectral width of most laser diodes. The dispersion of single-mode fiber corresponds to the first derivative of group velocity τ_g with respect to wavelength, and is given by

$$D = \frac{d\tau_g}{d\lambda} = \frac{S_0}{4}\left(\lambda_c - \frac{\lambda_0^4}{\lambda_c^3}\right) \tag{12}$$

where D is the dispersion in ps/(km-nm) and λ_c is the laser center wavelength. The fiber is characterized by its zero dispersion wavelength, λ_0, and zero dispersion slope, S_0. Usually, both center wavelength and zero dispersion wavelength are specified over a range of values; it is necessary to consider both upper and lower bounds in order to determine the worst-case dispersion penalty. This can be seen from Fig. 4, which plots D versus wavelength for some typical values of λ_0 and λ_c; the largest absolute value of D occurs at the extremes of this region. Once the dispersion is determined, the intersymbol interference penalty as a function of link length L can be determined to a good approximation from a model proposed by Agrawal[14]:

$$P_d = 5 \log [1 + 2\pi(BD\,\Delta\lambda)^2 L^2] \tag{13}$$

where B is the bit rate and $\Delta\lambda$ is the root mean square (RMS) spectral width of the source. By maintaining a close match between the operating and zero dispersion wavelengths, this penalty can be kept to a tolerable 0.5 to 1.0 dB in most cases.

Mode Partition Noise

Group velocity dispersion contributes to other optical penalties that remain the subject of continuing research—*mode partition noise* and *mode hopping.* These penalties are related to

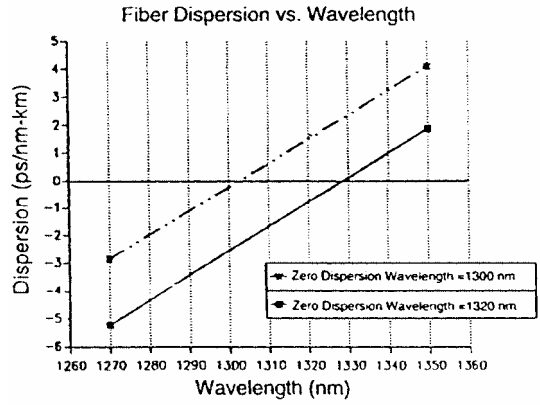

FIGURE 4 Single-mode fiber dispersion as a function of wavelength [5].

the properties of a Fabry-Perot type laser diode cavity; although the total optical power output from the laser may remain constant, the optical power distribution among the laser's longitudinal modes will fluctuate. This is illustrated by the model depicted in Fig. 5; when a laser diode is directly modulated with injection current, the total output power stays constant from pulse to pulse; however, the power distribution among several longitudinal modes will vary between pulses. We must be careful to distinguish this behavior of the instantaneous laser spectrum, which varies with time, from the time-averaged spectrum that is normally observed experimentally. The light propagates through a fiber with wavelength-dependent dispersion or attenuation, which deforms the pulse shape. Each mode is delayed by a different amount due to group velocity dispersion in the fiber; this leads to additional signal degradation at the receiver, in addition to the intersymbol interference caused by chromatic dispersion alone, discussed earlier. This is known as *mode partition noise;* it is capable of generating bit error rate floors such that additional optical power into the receiver will not improve the link BER. This is because mode partition noise is a function of the laser spectral fluctuations and wavelength-dependent dispersion of the fiber, so the signal-to-noise ratio due to this effect is independent of the signal power. The power penalty due to mode partition noise was first calculated by Ogawa[15] as

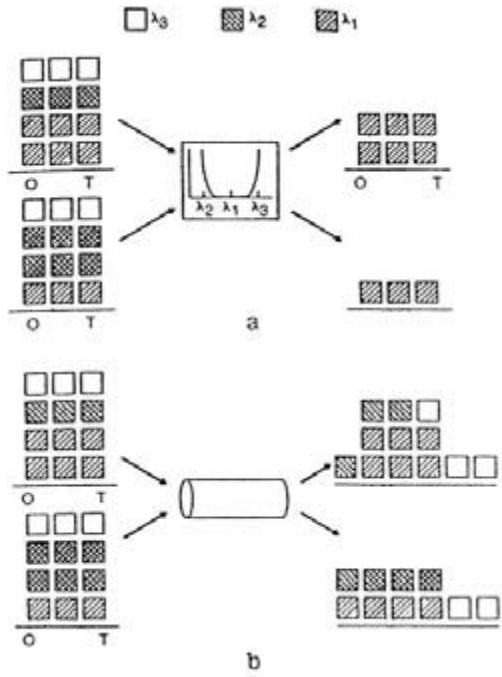

FIGURE 5 Model for mode partition noise; an optical source emits a combination of wavelengths, illustrated by different color blocks: (a) wavelength-dependent loss; (b) chromatic dispersion.

$$P_{mp} = 5 \log (1 - Q^2\sigma_{mp}^2) \tag{14}$$

where

$$\sigma_{mp}^2 = \tfrac{1}{2}\, k^2(\pi B)^4[A_1^4\Delta\lambda^4 + 42A_1^2A_2^2\Delta\lambda^6 + 48A_2^4\Delta\lambda^8] \tag{15}$$

$$A_1 = DL \tag{16}$$

and

$$A_2 = \frac{A_1}{2(\lambda_c - \lambda_0)} \tag{17}$$

The mode partition coefficient k is a number between 0 and 1 that describes how much of the optical power is randomly shared between modes; it summarizes the statistical nature of mode partition noise. According to Ogawa, k depends on the number of interacting modes and rms spectral width of the source, the exact dependence being complex. However, subsequent work has shown[16] that Ogawa's model tends to underestimate the power penalty due to mode partition noise because it does not consider the variation of longitudinal mode power between successive baud periods, and because it assumes a linear model of chromatic dispersion rather than the nonlinear model given in the just-cited equation. A more detailed model has been proposed by Campbell,[17] which is general enough to include effects of the laser diode spectrum, pulse shaping, transmitter extinction ratio, and statistics of the data stream. While Ogawa's model assumed an equiprobable distribution of zeros and ones in the data stream, Campbell showed that mode partition noise is data dependent as well. Recent work based on this model[18] has rederived the signal variance:

$$\sigma_{mp}^2 = E_{av}(\sigma_0^2 + \sigma_{+1}^2 + \sigma_{-1}^2) \tag{18}$$

where the mode partition noise contributed by adjacent baud periods is defined by

$$\sigma_{+1}^2 + \sigma_{-1}^2 = \tfrac{1}{2}\, k^2(\pi B)^4(1.25A_1^4\Delta\lambda^4 + 40.95A_1^2A_2^2\Delta\lambda^6 + 50.25A_2^4\Delta\lambda^8) \tag{19}$$

and the time-average extinction ratio $E_{av} = 10 \log (P_1/P_0)$, where P_1,P_0 represent the optical power by a 1 and 0, respectively. If the operating wavelength is far away from the zero dispersion wavelength, the noise variance simplifies to

$$\sigma_{mp}^2 = 2.25\, \frac{k^2}{2}\, E_{av}\, (1 - e^{-\beta L^2})^2 \tag{20}$$

which is valid provided that

$$\beta = (\pi BD\Delta\lambda)^2 << 1 \tag{21}$$

Many diode lasers exhibit mode hopping or mode splitting, in which the spectrum appears to split optical power between 2 or 3 modes for brief periods of time. The exact mechanism is not fully understood, but stable Gaussian spectra are generally only observed for CW operation and temperature-stabilized lasers. During these mode hops the previously cited theory does not apply, since the spectrum is non-Gaussian, and the model will overpredict the power penalty; hence, it is not possible to model mode hops as mode partitioning with $k = 1$. There is no currently published model describing a treatment of mode-hopping noise, although recent papers[19] suggest approximate calculations based on the statistical properties of the laser cavity. In a practical link, some amount of mode hopping is probably unavoidable as a contributor to burst noise; empirical testing of link hardware remains the only reliable way to

reduce this effect. A practical rule of thumb is to keep the mode partition noise penalty less than 1.0 dB maximum, provided that this penalty is far away from any noise floors.

Extinction Ratio

The receiver extinction ratio also contributes directly to the link penalties. The receiver BER is a function of the modulated AC signal power; if the laser transmitter has a small extinction ratio, the DC component of total optical power is significant. Gain or loss can be introduced in the link budget if the extinction ratio at which the receiver sensitivity is measured differs from the worst-case transmitter extinction ratio. If the extinction ratio E_t at the transmitter is defined as the ratio of optical power when a 1 is transmitted versus when a 0 is transmitted,

$$E_t = \frac{\text{Power}(1)}{\text{Power}(0)} \tag{22}$$

then we can define a modulation index at the transmitter M_t according to

$$M_t = \frac{E_t - 1}{E_t + 1} \tag{23}$$

Similarly, we can measure the linear extinction ratio at the optical receiver input and define a modulation index M_r. The extinction ratio penalty is given by

$$P_{er} = -10 \log \left(\frac{M_t}{M_r} \right) \tag{24}$$

where the subscripts t and r refer to specifications for the transmitter and receiver, respectively. Usually, the extinction ratio is specified to be the same at the transmitter and receiver, and is large enough that there is no power penalty due to extinction ratio effects.

Multipath Interference

Another important property of the optical link is the amount of light reflected from the fiber endfaces that returns up the link and back into the transmitter. Whenever there is a connection or splice in the link, some fraction of the light is reflected back; each connection is thus a potential noise generator, since the reflected fields can interfere with one another to create noise in the detected optical signal. The phenomenon is analogous to the noise caused by multiple atmospheric reflections of radio waves, and is known as *multipath interference noise.* To limit this noise, connectors and splices are specified with a minimum return loss. If there is a total of N reflection points in a link and the geometric mean of the connector reflections is alpha, then based on the model of Duff et al.[20] the power penalty due to multipath interference (adjusted for bit error rate and bandwidth) is closely approximated by

$$P_{mpi} = 10 \log (1 - 0.7N\text{a}) \tag{25}$$

Multipath noise can usually be reduced well below 0.5 dB with available connectors, whose return loss is often better than 25 dB.

Relative Intensity Noise (RIN)

Stray light reflected back into a Fabry-Perot type laser diode gives rise to intensity fluctuations in the laser output. This is a complicated phenomenon, strongly dependent on the type

of laser; it is called either *reflection-induced intensity noise* or *relative intensity noise* (RIN). This effect is important, since it can also generate BER floors. The power penalty due to RIN is the subject of ongoing research; since the reflected light is measured at a specified signal level, RIN is data dependent, although it is independent of link length. Since many laser diodes are packaged in windowed containers, it is difficult to correlate the RIN measurements on an unpackaged laser with those of a commercial product. There have been several detailed attempts to characterize RIN[21, 22]; typically, the RIN noise is assumed Gaussian in amplitude and uniform in frequency over the receiver bandwidth of interest. The RIN value is specified for a given laser by measuring changes in the optical power when a controlled amount of light is fed back into the laser; it is signal dependent, and is also influenced by temperature, bias voltage, laser structure, and other factors which typically influence laser output power.[22] If we assume that the effect of RIN is to produce an equivalent noise current at the receiver, then the additional receiver noise σ_r may be modeled as

$$\sigma_r = \gamma^2 S^{2g} B \tag{26}$$

where S is the signal level during a bit period, B is the bit rate, and g is a noise exponent that defines the amount of signal-dependent noise. If $g = 0$, noise power is independent of the signal, while for $g = 1$ noise power is proportional to the square of the signal strength. The coefficient γ is given by

$$\gamma^2 = S_i^{2(1-g)}\, 10^{(\mathrm{RIN}_i/10)} \tag{27}$$

where RIN_i is the measured RIN value at the average signal level S_i, including worst-case back-reflection conditions and operating temperatures. The Gaussian BER probability due to the additional RIN noise current is given by

$$P_{\text{error}} = \frac{1}{2}\left[P_e^1\left(\frac{S_1 - S_0}{2\sigma_1}\right) + P_e^0\left(\frac{S_1 - S_0}{2\sigma_0}\right)\right] \tag{28}$$

where σ_1 and σ_0 represent the total noise current during transmission of a digital 1 and 0, respectively and P_e^1 and P_e^0 are the probabilities of error during transmission of a 1 or 0, respectively. The power penalty due to RIN may then be calculated by determining the additional signal power required to achieve the same BER with RIN noise present as without the RIN contribution. One approximation for the RIN power penalty is given by

$$P_{\text{rin}} = -5 \log\left[1 - Q^2(BW)(1 + M_r)^{2g}(10^{\mathrm{RIN}/10})\left(\frac{1}{M_r}\right)^2\right] \tag{29}$$

where the RIN value is specified in dB/Hz, BW is the receiver bandwidth, M_r is the receiver modulation index, and the exponent g is a constant varying between 0 and 1 which relates the magnitude of RIN noise to the optical power level. The maximum RIN noise penalty in a link can usually be kept to below 0.5 dB.

Jitter

Although it is not strictly an optical phenomenon, another important area in link design deals with the effects of timing jitter on the optical signal. In a typical optical link, a clock is extracted from the incoming data signal which is used to retime and reshape the received digital pulse; the received pulse is then compared with a threshold to determine if a digital 1 or 0 was transmitted. So far, we have discussed BER testing with the implicit assumption that the measurement was made in the center of the received data bit; to achieve this, a clock transition at the center of the bit is required. When the clock is generated from a receiver timing recovery circuit, it will have some variation in time, and the exact location of the clock edge will be uncer-

tain. Even if the clock is positioned at the center of the bit, its position may drift over time. There will be a region of the bit interval, or eye, in the time domain where the BER is acceptable; this region is defined as the eyewidth.[1–3] Eyewidth measurements are an important parameter for evaluation of fiber-optic links; they are intimately related to the BER, as well as to the acceptable clock drift, pulse width distortion, and optical power. At low optical power levels, the receiver signal-to-noise ratio is reduced; increased noise causes amplitude variations in the received signal. These amplitude variations are translated into time domain variations in the receiver decision circuitry, which narrows the eyewidth. At the other extreme, an optical receiver may become saturated at high optical power, reducing the eyewidth and making the system more sensitive to timing jitter. This behavior results in the typical bathtub curve shown in Fig. 2; for this measurement, the clock is delayed from one end of the bit cell to the other, with the BER calculated at each position. Near the ends of the cell, a large number of errors occur; toward the center of the cell, the BER decreases to its true value. The eye opening may be defined as the portion of the eye for which the BER remains constant; pulse width distortion occurs near the edges of the eye, which denotes the limits of the valid clock timing. Uncertainty in the data pulse arrival times causes errors to occur by closing the eye window and causing the eye pattern to be sampled away from the center. This is one of the fundamental problems of optical and digital signal processing, and a large body of work has been done in this area.[23, 24] In general, multiple jitter sources will be present in a link; these will tend to be uncorrelated. However, jitter on digital signals, especially resulting from a cascade of repeaters, may be coherent.

International standards on jitter were first published by the CCITT (Central Commission for International Telephony and Telegraphy, now known as the International Telecommunications Union, or ITU). This standards body has adopted a definition of jitter[24] as short-term variations of the significant instants (rising or falling edges) of a digital signal from their ideal position in time. Longer-term variations are described as *wander;* in terms of frequency, the distinction between jitter and wander is somewhat unclear. The predominant sources of jitter include the following:

- Phase noise in receiver clock recovery circuits, particularly crystal-controlled oscillator circuits; this may be aggravated by filters or other components which do not have a linear phase response. Noise in digital logic resulting from restricted rise and fall times may also contribute to jitter.
- Imperfect timing recovery in digital regenerative repeaters, which is usually dependent on the data pattern.
- Different data patterns may contribute to jitter when the clock recovery circuit of a repeater attempts to recover the receive clock from inbound data. Data pattern sensitivity can produce as much as 0.5-dB penalty in receiver sensitivity. Higher data rates are more susceptible (>1 Gbit/s); data patterns with long run lengths of 1s or 0s, or with abrupt phase transitions between consecutive blocks of 1s and 0s, tend to produce worst-case jitter.
- At low optical power levels, the receiver signal-to-noise ratio, Q, is reduced; increased noise causes amplitude variations in the signal, which may be translated into time domain variations by the receiver circuitry.
- Low frequency jitter, also called *wander,* resulting from instabilities in clock sources and modulation of transmitters.
- Very low frequency jitter caused by variations in the propagation delay of fibers, connectors, etc., typically resulting from small temperature variations (this can make it especially difficult to perform long-term jitter measurements).

In general, jitter from each of these sources will be uncorrelated; jitter related to modulation components of the digital signal may be coherent, and cumulative jitter from a series of repeaters or regenerators may also contain some well-correlated components.

There are several parameters of interest in characterizing jitter performance. Jitter may be classified as either random or deterministic, depending on whether it is associated with pattern-

dependent effects; these are distinct from the duty cycle distortion that often accompanies imperfect signal timing. Each component of the optical link (data source, serializer, transmitter, encoder, fiber, receiver, retiming/clock recovery/deserialization, decision circuit) will contribute some fraction of the total system jitter. If we consider the link to be a "black box" (but not necessarily a linear system), then we can measure the level of output jitter in the absence of input jitter; this is known as the *intrinsic jitter* of the link. The relative importance of jitter from different sources may be evaluated by measuring the spectral density of the jitter. Another approach is the maximum tolerable input jitter (MTIJ) for the link. Finally, since jitter is essentially a stochastic process, we may attempt to characterize the jitter transfer function (JTF) of the link, or estimate the probability density function of the jitter. When multiple traces occur at the edges of the eye, this can indicate the presence of data-dependent jitter or duty cycle distortion; a histogram of the edge location will show several distinct peaks. This type of jitter can indicate a design flaw in the transmitter or receiver. By contrast, random jitter typically has a more Gaussian profile and is present to some degree in all data links.

The problem of jitter accumulation in a chain of repeaters becomes increasingly complex; however, we can state some general rules of thumb. It has been shown[25] that jitter can be generally divided into two components, one due to repetitive patterns and one due to random data. In receivers with phase-lock loop timing recovery circuits, repetitive data patterns will tend to cause jitter accumulation, especially for long run lengths. This effect is commonly modeled as a second-order receiver transfer function. Jitter will also accumulate when the link is transferring random data; jitter due to random data is of two types, *systematic* and *random.* The classic model for systematic jitter accumulation in cascaded repeaters was published by Byrne.[26] The Byrne model assumes cascaded identical timing recovery circuits, and then the systematic and random jitter can be combined as rms quantities so that total jitter due to random jitter may be obtained. This model has been generalized to networks consisting of different components,[27] and to nonidentical repeaters.[28] Despite these considerations, for well-designed practical networks the basic results of the Byrne model remain valid for N nominally identical repeaters transmitting random data; systematic jitter accumulates in proportion to $N^{1/2}$; and random jitter accumulates in proportion to $N^{1/4}$. For most applications, the maximum timing jitter should be kept below about 30 percent of the maximum receiver eye opening.

Modal Noise

An additional effect of lossy connectors and splices is modal noise. Because high-capacity optical links tend to use highly coherent laser transmitters, random coupling between fiber modes causes fluctuations in the optical power coupled through splices and connectors; this phenomena is known as *modal noise.*[29] As one might expect, modal noise is worst when using laser sources in conjunction with multimode fiber; recent industry standards have allowed the use of short-wave lasers (750 to 850 nm) on 50-micron fiber, which may experience this problem. Modal noise is usually considered to be nonexistent in single-mode systems. However, modal noise in single-mode fibers can arise when higher-order modes are generated at imperfect connections or splices. If the lossy mode is not completely attenuated before it reaches the next connection, interference with the dominant mode may occur. The effects of modal noise have been modeled previously,[29] assuming that the only significant interaction occurs between the LP01 and LP11 modes for a sufficiently coherent laser. For N sections of fiber, each of length L in a single-mode link, the worst-case sigma for modal noise can be given by

$$\sigma_m = \sqrt{2}\, N\eta(1-\eta)e^{-aL} \tag{30}$$

where a is the attenuation coefficient of the LP11 mode and η is the splice transmission efficiency, given by

$$\eta = 10^{-(\eta_0/10)} \tag{31}$$

where η_0 is the mean splice loss (typically, splice transmission efficiency will exceed 90 percent). The corresponding optical power penalty due to modal noise is given by

$$P = -5 \log (1 - Q^2\sigma_m^2) \tag{32}$$

where Q corresponds to the desired BER. This power penalty should be kept to less than 0.5 dB.

Radiation-Induced Loss

Another important environmental factor as mentioned earlier is exposure of the fiber to ionizing radiation damage. There is a large body of literature concerning the effects of ionizing radiation on fiber links.[30, 31] There are many factors that can affect the radiation susceptibility of optical fiber, including the type of fiber, type of radiation (gamma radiation is usually assumed to be representative), total dose, dose rate (important only for higher exposure levels), prior irradiation history of the fiber, temperature, wavelength, and data rate. Optical fiber with a pure silica core is least susceptible to radiation damage; however, almost all commercial fiber is intentionally doped to control the refractive index of the core and cladding, as well as dispersion properties. Trace impurities are also introduced which become important only under irradiation; among the most important are Ge dopants in the core of graded index (GRIN) fibers, in addition to F, Cl, P, B, OH content, and the alkali metals. In general, radiation sensitivity is worst at lower temperatures, and is also made worse by hydrogen diffusion from materials in the fiber cladding. Because of the many factors involved, a comprehensive theory does not exist to model radiation damage in optical fibers. The basic physics of the interaction have been described[30, 31]; there are two dominant mechanisms, *radiation-induced darkening* and *scintillation.* First, high-energy radiation can interact with dopants, impurities, or defects in the glass structure to produce color centers which absorb strongly at the operating wavelength. Carriers can also be freed by radiolytic or photochemical processes; some of these become trapped at defect sites, which modifies the band structure of the fiber and causes strong absorption at infrared wavelengths. This radiation-induced darkening increases the fiber attenuation; in some cases it is partially reversible when the radiation is removed, although high levels or prolonged exposure will permanently damage the fiber. A second effect is caused if the radiation interacts with impurities to produce stray light, or scintillation. This light is generally broadband, but will tend to degrade the BER at the receiver; scintillation is a weaker effect than radiation-induced darkening. These effects will degrade the BER of a link; they can be prevented by shielding the fiber, or partially overcome by a third mechanism, *photobleaching.* The presence of intense light at the proper wavelength can partially reverse the effects of darkening in a fiber. It is also possible to treat silica core fibers by briefly exposing them to controlled levels of radiation at controlled temperatures; this increases the fiber loss, but makes the fiber less susceptible to future irradiation. These so-called radiation-hardened fibers are often used in environments where radiation is anticipated to play an important role. Recently, several models have been advanced[31] for the performance of fiber under moderate radiation levels; the effect on BER is a power law model of the form

$$\text{BER} = \text{BER}_0 + \text{A}(\text{dose})^{\text{b}} \tag{33}$$

where BER_0 is the link BER prior to irradiation, the dose is given in rads, and the constants A and b are empirically fitted. The loss due to normal background radiation exposure over a typical link lifetime can be held below about 0.5 dB.

6.5 REFERENCES

1. S. E. Miller and A. G. Chynoweth (eds.), *Optical Fiber Telecommunications,* Academic Press, New York, 1979.

2. J. Gowar, *Optical Communication Systems,* Prentice Hall, Englewood Cliffs, New Jersey, 1984.
3. C. DeCusatis, E. Maass, D. Clement, and R. Lasky (eds.), *Handbook of Fiber Optic Data Communication,* Academic Press, New York, 1998; see also *Optical Engineering* special issue on optical data communication (December 1998).
4. R. Lasky, U. Osterberg, and D. Stigliani (eds.), *Optoelectronics for Data Communication,* Academic Press, New York, 1995.
5. "Digital Video Broadcasting (DVB) Measurement Guidelines for DVB Systems," European Telecommunications Standards Institute ETSI Technical Report ETR 290, May 1997; "Digital Multi-Programme Systems for Television Sound and Data Services for Cable Distribution," International Telecommunications Union ITU-T Recommendation J.83, 1995; "Digital Broadcasting System for Television, Sound and Data Services; Framing Structure, Channel Coding and Modulation for Cable Systems," European Telecommunications Standards Institute ETSI 300 429, 1994.
6. W. E. Stephens and T. R. Hoseph, "System Characteristics of Direct Modulated and Externally Modulated RF Fiber-Optic Links," *IEEE J. Lightwave Technol.,* **LT-5(3)**:380–387 (1987).
7. C. H. Cox, III, and E. I. Ackerman, "Some Limits on the Performance of an Analog Optical Link," *Proceedings of the SPIE—The International Society for Optical Engineering* **3463**:2–7 (1999).
8. Laser safety standards in the United States are regulated by the Department of Health and Human Services (DHHS), Occupational Safety and Health Administration (OSHA), Food and Drug Administration (FDA) Code of Radiological Health (CDRH) 21 Code of Federal Regulations (CFR) subchapter J; the relevant standards are ANSI Z136.1, "Standard for the Safe Use of Lasers" (1993 revision) and ANSI Z136.2, "Standard for the Safe Use of Optical Fiber Communication Systems Utilizing Laser Diodes and LED Sources" (1996–1997 revision); elsewhere in the world, the relevant standard is International Electrotechnical Commission (IEC/CEI) 825 (1993 revision).
9. S. S. Walker, "Rapid Modeling and Estimation of Total Spectral Loss in Optical Fibers," *IEEE Journ. Lightwave Tech.* **4**:1125–1132 (1996).
10. Electronics Industry Association/Telecommunications Industry Association (EIA/TIA) Commercial Building Telecommunications Cabling Standard (EIA/TIA-568-A), Electronics Industry Association/Telecommunications Industry Association (EIA/TIA) Detail Specification for 62.5 Micron Core Diameter/125 Micron Cladding Diameter Class 1a Multimode Graded Index Optical Waveguide Fibers (EIA/TIA-492AAAA), Electronics Industry Association/Telecommunications Industry Association (EIA/TIA) Detail Specification for Class IV-a Dispersion Unshifted Single-Mode Optical Waveguide Fibers Used in Communications Systems (EIA/TIA-492BAAA), Electronics Industry Association, New York.
11. D. Gloge, "Propagation Effects in Optical Fibers," *IEEE Trans. Microwave Theory and Tech.* **MTT-23**: p. 106–120 (1975).
12. P. M. Shanker, "Effect of Modal Noise on Single-Mode Fiber Optic Network," *Opt. Comm.* **64**: 347–350 (1988).
13. J. J. Refi, "LED Bandwidth of Multimode Fiber as a Function of Source Bandwidth and LED Spectral Characteristics," *IEEE Journ. of Lightwave Tech.* **LT-14**:265–272 (1986).
14. G. P. Agrawal et al., "Dispersion Penalty for 1.3 Micron Lightwave Systems with Multimode Semiconductor Lasers," *IEEE Journ. Lightwave Tech.* **6**:620–625 (1988).
15. K. Ogawa, "Analysis of Mode Partition Noise in Laser Transmission Systems," *IEEE Journ. Quantum Elec.* **QE-18**:849–855 (1982).
16. K. Ogawa, "Semiconductor Laser Noise; Mode Partition Noise," in *Semiconductors and Semimetals,* Vol. 22C, R. K. Willardson and A. C. Beer (eds.), Academic Press, New York, 1985.
17. J. C. Campbell, "Calculation of the Dispersion Penalty of the Route Design of Single-Mode Systems," *IEEE Journ. Lightwave Tech.* **6**:564–573 (1988).
18. M. Ohtsu et al., "Mode Stability Analysis of Nearly Single-Mode Semiconductor Laser," *IEEE Journ. Quantum Elec.* **24**:716–723 (1988).
19. M. Ohtsu and Y. Teramachi, "Analysis of Mode Partition and Mode Hopping in Semiconductor Lasers," *IEEE Quantum Elec.* **25**:31–38 (1989).
20. D. Duff et al., "Measurements and Simulations of Multipath Interference for 1.7 Gbit/s Lightwave Systems Utilizing Single and Multifrequency Lasers," *Proc. OFC:* 128 (1989).

21. J. Radcliffe, "Fiber Optic Link Performance in the Presence of Internal Noise Sources," IBM Technical Report, Glendale Labs, Endicott, New York (1989).
22. L. L. Xiao, C. B. Su, and R. B. Lauer, "Increase in Laser RIN Due to Asymmetric Nonlinear Gain, Fiber Dispersion, and Modulation," *IEEE Photon. Tech. Lett.* **4**:774–777 (1992).
23. P. Trischitta and P. Sannuti, "The Accumulation of Pattern Dependent Jitter for a Chain of Fiber Optic Regenerators," *IEEE Trans. Comm.* **36**:761–765 (1988).
24. CCITT Recommendations G.824, G.823, O.171, and G.703 on Timing Jitter in Digital Systems (1984).
25. R. J. S. Bates, "A Model for Jitter Accumulation in Digital Networks," *IEEE Globecom Proc.:* 145–149 (1983).
26. C. J. Byrne, B. J. Karafin, and D. B. Robinson, Jr., "Systematic Jitter in a Chain of Digital Regenerators," *Bell System Tech. Journal* **43**:2679–2714 (1963).
27. R. J. S. Bates and L. A. Sauer, "Jitter Accumulation in Token Passing Ring LANs," *IBM Journal Research and Development* **29**:580–587 (1985).
28. C. Chamzas, "Accumulation of Jitter: A Stochastic Mode," *AT&T Tech. Journal:* 64 (1985).
29. D. Marcuse and H. M. Presby, "Mode Coupling in an Optical Fiber with Core Distortion," *Bell Sys. Tech. Journal.* **1**:3 (1975).
30. E. J. Frieble et al., "Effect of Low Dose Rate Irradiation on Doped Silica Core Optical Fibers," *App. Opt.* **23**:4202–4208 (1984).
31. J. B. Haber et al., "Assessment of Radiation Induced Loss for AT&T Fiber Optic Transmission Systems in the Terestrial Environment," *IEEE Journ. Lightwave Tech.* **6**:150–154 (1988).

CHAPTER 7
SOLITONS IN OPTICAL FIBER COMMUNICATION SYSTEMS

P. V. Mamyshev
Bell Laboratories—Lucent Technologies
Holmdel, New Jersey

7.1 INTRODUCTION

To understand why optical solitons are needed in optical fiber communication systems, we should consider the problems that limit the distance and/or capacity of optical data transmission. A fiber-optic transmission line consists of a transmitter and a receiver connected with each other by a transmission optical fiber. Optical fibers inevitably have chromatic dispersion, losses (attenuation of the signal), and nonlinearity. Dispersion and nonlinearity can lead to the distortion of the signal. Because the optical receiver has a finite sensitivity, the signal should have a high-enough level to achieve error-free performance of the system. On the other hand, by increasing the signal level, one also increases the nonlinear effects in the fiber. To compensate for the fiber losses in a long distance transmission, one has to periodically install optical amplifiers along the transmission line. By doing this, a new source of errors is introduced into the system—an amplifier spontaneous emission noise. (Note that even ideal optical amplifiers inevitably introduce spontaneous emission noise.) The amount of noise increases with the transmission distance (with the number of amplifiers). To keep the signal-to-noise ratio (SNR) high enough for the error-free system performance, one has to increase the signal level and hence the potential problems caused by the nonlinear effects. Note that the nonlinear effects are proportional to the product of the signal power, P, and the transmission distance, L, and both of these multipliers increase with the distance. Summarizing, we can say that all the problems—dispersion, noise, and nonlinearity—grow with the transmission distance. The problems also increase when the transmission bit rate (speed) increases. It is important to emphasize that it is very difficult to deal with the signal distortions when the nonlinearity is involved, because the nonlinearity can couple all the detrimental effects together [nonlinearity, dispersion, noise, polarization mode dispersion (i.e., random birefringence of the fiber), polarization-dependent loss/gain, etc]. That happens when the nonlinear effects are out of control. The idea of soliton transmission is to guide the nonlinearity to the desired direction and use it for your benefit. When soliton pulses are used as an information carrier, the effects of dispersion and nonlinearity balance (or compensate) each other and thus don't degrade the signal quality with the propagation distance. In such a regime, the pulses propagate through the fiber without chang-

Copyright 2001 by The McGraw-Hill Companies, Inc. Click Here for Terms of Use.

ing their spectral and temporal shapes. This mutual compensation of dispersion and nonlinear effects takes place continuously with the distance in the case of "classical" solitons and periodically with the so-called dispersion map length in the case of dispersion-managed solitons. In addition, because of the unique features of optical solitons, soliton transmission can help to solve other problems of data transmission, like polarization mode dispersion. Also, when used with frequency guiding filters (sliding guiding filters in particular), the soliton systems provide continuous all-optical regeneration of the signal suppressing the detrimental effects of the noise and reducing the penalties associated with wavelength-division multiplexed (WDM) transmission. Because the soliton data looks essentially the same at different distances along the transmission, the soliton type of transmission is especially attractive for all-optical data networking. Moreover, because of the high quality of the pulses and return-to-zero (RZ) nature of the data, the soliton data is suitable for all-optical processing.

7.2 NATURE OF THE CLASSICAL SOLITON

Signal propagation in optical fibers is governed by the Nonlinear Schroedinger equation (NSE) for the complex envelope of the electric field of the signal.[1–3] This equation describes the combined action of the self-phase modulation and dispersion effects, which play the major role in the signal evolution in most practical cases. Additional linear and nonlinear effects can be added to the modified NSE.[4] Mathematically, one can say that solitons are stable solutions of NSE.[1,2] In this paper, however, we will give a qualitative physical description of the soliton regimes of pulse propagation, trying to avoid mathematics as much as possible.

Consider first the effect of dispersion. An optical pulse of width τ has a finite spectral bandwidth $BW \approx 1/\tau$. When the pulse is transform limited, or unchirped, all the spectral components have the same phase. In time domain, one can say that all the spectral components overlap in time, or sit on top of each other (see Fig. 1). Because of the dispersion, different spectral components propagate in the fiber with different group velocities, V_{gr}. As a result of the dispersion action alone, the initial unchirped pulse broadens and gets chirped (frequency modulated). The sign of the chirp depends on the sign of the fiber group velocity dispersion (see Fig. 1).

$$D = d\left(\frac{1}{V_{gr}}\right)/d\lambda \tag{1}$$

(λ is the light wavelength). A characteristic fiber length called the *dispersion length,* at which the pulse broadens by a factor sqrt(2), is determined both by the fiber dispersion and the pulse width:

$$z_d = \frac{2\pi c\ 0.322\tau^2}{\lambda^2 D} \tag{2}$$

(c is the speed of light). Note that the pulse spectral bandwidth remains unchanged because the dispersion is a linear effect.

Consider now the nonlinear effect of self-phase modulation (SPM).[5] Due to the Kerr effect, the fiber refractive index depends on the signal intensity, $n(I) = n_0 + n_2 I$, where n_2 is the nonlinear refractive index and intensity is $I = P/A$, P is the signal power and A is the fiber effective cross-section mode area. During a pulse propagation through the fiber, different parts of the pulse acquire different values of the nonlinear phase shift: $\phi(t) = 2\pi/\lambda\ n_2 I(t) L$. Here $I(t)$ is the intensity pulse shape in time domain and L is the transmission distance. This time-dependent nonlinear phase shift means that different parts of the pulse experience different frequency shifts:

$$\delta\omega(t) = \frac{d\phi}{dt} = -\frac{2\pi}{\lambda} n_2 L \frac{dI(t)}{dt} \tag{3}$$

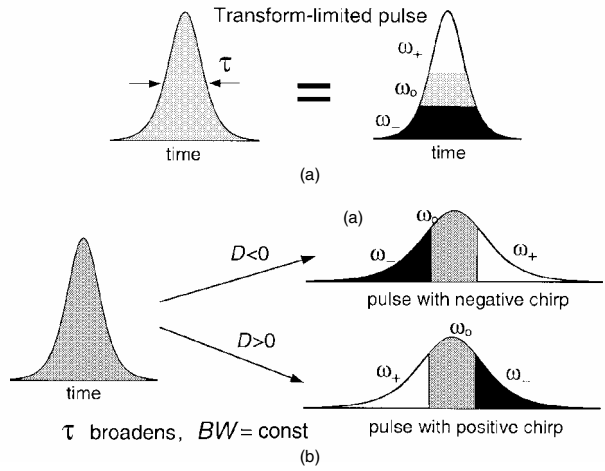

FIGURE 1 (*a*) Transform-limited pulse: all spectral components of the pulse "sit" on top of each other. (*b*) Effect of group velocity dispersion on a transform-limited pulse.

As one can see, the frequency shift is determined by the time derivative of the pulse shape. Because the nonlinear refractive index in silica-based fibers is positive, the self-phase modulation effect always shifts the front edge of the pulse to the "red" spectral region (downshift in frequency), and the trailing edge of the pulse to the "blue" spectral region (upshift in frequency). This means that an initially unchirped pulse spectrally broadens and gets negatively chirped (Fig. 2). A characteristic fiber length called the *nonlinear length,* at which the pulse spectrally broadens by a factor of two, is

$$z_{\mathrm{NL}} = \left(\frac{2\pi}{\lambda} n_2 I_0\right)^{-1} \tag{4}$$

Note that, when acting alone, SPM does not change the temporal intensity profile of the pulse.

As it was mentioned earlier, when under no control, both SPM and dispersion may be very harmful for the data transmission distorting considerably the spectral and temporal characteristics of the signal. Consider now how to control these effects by achieving the soliton

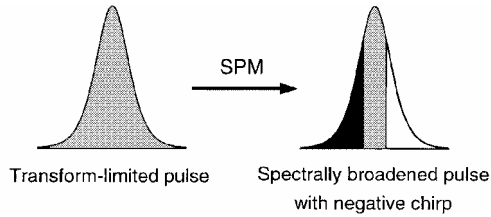

FIGURE 2 Effect of self-phase modulation on a transform-limited pulse.

regime of data transmission when the combined action of these effects results in a stable propagation of data pulses without changing their spectral and temporal envelopes.

In our qualitative consideration, consider the combined action of dispersion and nonlinearity (SPM) as an alternative sequence of actions of dispersion and nonlinearity. Assume that we start with a chirp-free pulse (see Fig. 3). The self-phase modulation broadens the pulse spectrum and produces a negative frequency chirp: The front edge of the pulse becomes red-shifted, and the trailing edge becomes blue-shifted. When positive GVD is then applied to this chirped pulse, the red spectral components are delayed in time with respect to the blue ones. If the right amount of dispersion is applied, the sign of the pulse chirp can be reversed to negative: The blue spectral components shift in time to the front pulse edge, while the red spectral components move to the trailing edge. When the nonlinearity is applied again, it shifts the frequency of the front edge to the red spectral region and upshifts the frequency of the trailing edge. That means that the blue front edge becomes green again, the red trailing edge also becomes green, and the pulse spectrum bandwidth narrows to its original width. The described regime of soliton propagation is achieved when the nonlinear and dispersion effect compensate each other exactly. In reality, the effects of dispersion and SPM act simultaneously, so that the pulse spectral and temporal widths stay constant with the distance, and the only net effect is a (constant within the entire pulse) phase shift of 0.5 rad per dispersion length of propagation.[6] The condition of the soliton regime is equality of the nonlinear and dispersion lengths: $z_d = z_{NL}$. One can rewrite this expression to find a relationship between the soliton peak power, pulse width, and fiber dispersion:

$$P_0 = \frac{\lambda^3 DA}{0.322\ 4\pi^2 c n_2 \tau^2} \tag{5}$$

Here, P_0 is the soliton peak power and τ is the soliton FWHM. Soliton pulses have a sech^2 form. Note that as it follows from our previous consideration, classical soliton propagation in fibers requires a positive sign of the fiber's dispersion, D (assuming that n_2 is positive). Consider a numerical example. For a pulse of width $\tau = 20$ ps propagating in a fiber with $D = 0.5$ ps nm^{-1} km^{-1}, fiber cross-section mode area $A = 50$ μm^2, $\lambda = 1.55$ μm, and typical value of $n_2 = 2.6$ cm^2/W, one can find the soliton peak power is 2.4 mW. The dispersion length is $z_d = 200$ km in this case.

7.3 PROPERTIES OF SOLITONS

The most important property of optical solitons is their robustness.[6–20] Consider what robustness means from a practical point of view. When a pulse is injected into the fiber, the pulse does not have to have the exact soliton shape and parameters (Eq. 5) to propagate as a soliton. As long as the input parameters are not too far from the optimum, during the nonlinear propagation the pulse "readjusts" itself, shaping into a soliton and shedding off nonsoliton components. For example, an unchirped pulse of width τ will be reshaped into a single soliton as long as its input

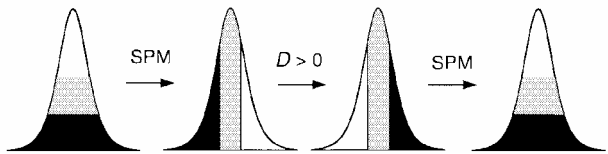

FIGURE 3 Qualitative explanation of classical soliton. Combined action of dispersion and nonlinearity (self-phase modulation) results in a stable pulse propagation with constant spectral and temporal widths. See text.

power, P, is greater than $P_0/4$ and less than $2.25P_0$. Here, P_0 is the soliton power determined by Eq. 5.[3]

Solitons are also robust with respect to the variations of the pulse energy and of the fiber parameters along the transmission line. As long as these variations are fast enough (period of perturbations is much smaller than the soliton dispersion length, z_d), the soliton "feels" only the average values of these parameters. This feature is extremely important for practical systems. In particular, it makes it possible to use solitons in long distance transmission systems where fiber losses are periodically compensated by lumped amplifiers. As long as the amplifier spacing is much less than the soliton dispersion length, $L_{amp} << z_d$, classical solitons work very well in these systems. Note that all soliton perturbations result in a loss of some part of the soliton energy, which is radiated into dispersive waves.

Consider now a case of slow variations of parameters along the transmission when a characteristic length at which a fiber parameter (or pulse energy) changes considerably is much longer than the soliton dispersion length. Soliton parameters follow adiabatically these changes. That means that all the parameters in Eq. 5 can be considered as distance dependent, and Eq. 5 remains valid. It can be rewritten in the following form:

$$\tau(z) = \text{const}\,\frac{D(z)A(z)}{P(z)\tau(z)} = \text{const}\,\frac{D(z)A(z)}{\text{Energy}(z)} \tag{6}$$

One can derive many important consequences from this equation.[13–22] One example would be the pulse broadening (and spectral narrowing) in a fiber with loss [assuming $D(z)$ and $A(z)$ are constant].[13–15] Note that the soliton broadening can be used in repeaterless data transmission systems when high-input signal power is required.[15] On the other hand, one can get a pulse compression in a fiber with adiabatic gain. Similar effects can be obtained by changing the fiber dispersion and/or mode area along the length. For example, adiabatic soliton compression can be obtained in a fiber with slowly decreasing dispersion (dispersion-tapered fiber).[16–22]

It is important to emphasize that the adiabatic soliton propagation does not necessarily require that each of these parameters—pulse energy, fiber dispersion, and mode area—changes adiabatically with the distance, as long as the whole expression, $[D(z)\ A(z)]/[\text{Energy}(z)]$ changes adiabatically with the distance. For example, soliton propagation in a dispersion-tapered fiber with losses is equivalent to transmission in a lossless, constant-dispersion fiber if the dispersion decreases with the same rate with the distance as the pulse energy [i.e., if $D(z)/\text{Energy}(z) = \text{const}$]. Note that this is true no matter what the fiber loss and the pulse width are.

So far, we've been discussing a single pulse propagation. In communication systems, one has to deal with streams of pulses. When two or more soliton pulses propagate in the fiber at the same wavelength, they can interact with each other: Tails from one soliton pulse may overlap with the other pulse. Due to the cross-phase modulation effect, this overlap leads to the frequency shifts of the interacting solitons. The signs of the frequency shifts are opposite for the two solitons. Through the fiber dispersion, the frequency changes result in the changes of the soliton group velocities. The strength of the interaction decreases very fast with the soliton separation and for most practical applications can be considered to be negligible when the separation is 4 to 5 times greater than the soliton pulse width, τ.[23,24] The character of interaction depends on the mutual optical phases of the solitons: When they are the same, the solitons attract to each other; when they are out of phase, the solitons repel from each other; when the phase difference is $\pi/2$, the solitons do not interact.

7.4 CLASSICAL SOLITON TRANSMISSION SYSTEMS

The soliton properties described earlier determine the engineering rules for designing the soliton-based transmission systems. First, to make sure that every individual pulse is stable in

the transmission line with constant fiber dispersion and loss periodically compensated by lump amplifiers, the amplifier spacing, L_{amp}, should be much smaller than the soliton dispersion length, z_d. To avoid considerable pulse-to-pulse interaction, the minimum distance between adjacent pulses should be $T \geq 4\tau$, where $1/T$ is the transmission bit rate and τ is the soliton pulse width. The pulse power determined from Eq. 5 should be considered as a path-average power, P_{av}. If the signal energy decreases with the distance in the fiber spans between the amplifiers as exp (γz) (here, γ is the loss rate), the path-average power is related to the pulse power at the output of each amplifier (input to the fiber span), P_{in}, as:

$$P_o = P_{in} \frac{1 - \exp(\gamma L_{amp})}{|\gamma| L_{amp}} \tag{7}$$

Here, L_{amp} is the amplifier spacing. As it was stated earlier, the dispersion and nonlinear effects "compensate" each other in the soliton regime of transmission, so that the pulses propagate practically without changing their temporal and spectral shapes. As long as the length scale of perturbations of the transmission parameters is much shorter than the soliton dispersion length, the pulses "feel" only the average parameters. Note, however, that perturbations may lead to shedding of dispersive waves by solitons.[12]

There are two main sources of errors in the soliton transmission systems: fluctuations of the pulse energies and fluctuations of the pulse arrival times.[25] The origin of the energy fluctuations is the same as in the other types of systems—spontaneous emission noise generated by the amplifiers. Each amplifier contributes a noise with a spectral density (power per unit bandwidth):

$$P_\nu = (G - 1)\, n_{sp} h\nu \tag{8}$$

Here, G is the power gain of the amplifier, $h\nu$ is the photon energy, and $n_{sp} \geq 1$ is the spontaneous emission factor that characterizes the quality of the amplifier. In the best case, when the amplifier is highly inverted, n_{sp} is close to unity. In a broadband transmission system (i.e., without in-line spectral filters), when the lumped amplifiers compensate exactly for the fiber loss, the noise grows linearly with the distance (with the number of amplifiers). At the output of a transmission line of length L, the path-averaged spectral density is:

$$P_{\nu\,av} = |\gamma|\, L\, n_{sp}\, h\nu\, F(G) \tag{9}$$

Here, function $F(G)$ describes the penalty one has to pay for having high-gain amplifiers (or long amplifier spacing):

$$F(G) = \frac{(G-1)^2}{G \ln^2 G} \tag{10}$$

The penalty function has its minimum [$F(G) = 1$] in the case of distributed amplification (when $G \to 1$) and grows with G. The SNR at the output of transmission should be high enough to have error-free transmission. Note that the noise spectral density, P_ν, has units of energy. It is also the noise energy received in any time, T, in a spectral bandwidth, $1/T$. That is why P_ν is also called the *equipartition energy.* To have the error probability less than 10^{-9} and 10^{-15}, the ratio of the pulse energy to the equipartition energy should be, correspondently, 100 and 160. For example, consider a transmission system with the average loss of 0.21 dB/km, $n_{sp} = 1.5$, amplifier spacing of 50 km. The minimum pulse energy at the input of each fiber span to have the error probability less than 10^{-9} in such a system of length $L = 5000$ km is 20 fJ, and for $L = 10{,}000$ km, it is 40 fJ.

Another type of error in the soliton systems is the fluctuation in the pulse arrival times, or timing jitter. The timing jitter can be caused by several factors. The adjacent pulse-to-pulse interactions can cause the pulses to shift in time. As we have stated earlier, interaction problems can be practically eliminated by spacing the solitons in time by more than 4 or 5 of their

width. A very important source of the timing jitter is the spontaneous emission noise. Every time the noise is added to the signal, it modulates the carrier frequencies of the solitons at random. The chromatic dispersion of the fiber then converts these frequency variations in a variation of the pulses' arrival times. This effect is known as the *Gordon-Haus effect.*[6,26] The variance of the timing jitter produced by the Gordon-Haus effect is:

$$\sigma_{GH}^2 \approx 0.2 n_2 h n_{sp} F(G) \frac{|\gamma|}{A} \frac{D}{\tau} L^3 \tag{11}$$

An error occurs when a pulse arrives outside of the acceptance time window, *W,* of the detection system (this window is usually slightly less than the bit slot, *T*). To have the error probability less than 10^{-9}, the acceptance window should be greater than 12 standard deviations of the timing jitter:

$$W \geq 12\sigma_{GH} \tag{12}$$

The Gordon-Haus jitter limits the maximum bit rate and transmission distance. As one can see from Eq. 11, the jitter increases very fast with the distance; it also increases when τ decreases. Another factor that limits the maximum transmission distance is that σ_{GH}^2 is proportional to the pulse energy [because the pulse energy is proportional to (D/τ)], and long-distance transmission systems should have high-enough pulse energies to keep the SNR high. Consider a numerical example, $L = 9{,}000$ km, $\tau = 20$ ps, $n_{sp} = 1.4$, $\gamma = -0.048$ km^{-1}, amplifier spacing = 30 km, $D = 0.5$ ps/(nm^{-1} km^{-1}), $A = 50$ μm^2. Equation 11 then gives the standard deviation of the Gordon-Haus timing jitter $\sigma = 11.7$ ps. As one can see, according to Eq. 12, this jitter is too high for 10 Gbit/s transmission ($1/T = 100$ ps) to be error-free, because $12\sigma_{GH} > 1/T$ in this case.

Another source of the timing jitter is the acoustic interaction of pulses.[27–30] Due to the electrostriction effect in the fiber, each propagating pulse generates an acoustic wave in the fiber. Other pulses experience the refractive index change caused by the acoustic wave. The resultant frequency changes of the pulses lead, through the effect of the fiber chromatic dispersion, to the fluctuation in the arrival times. The acoustic effect causes a "long-range" interaction: Pulses separated by a few nanoseconds can interact through this effect. One can estimate the acoustic timing jitter from the following simplified equation:

$$\sigma_a \approx 4.3 \frac{D^2}{\tau} (R - 0.99)^{1/2} L^2 \tag{13}$$

Here, standard deviation, σ_a, is in picoseconds; dispersion, *D,* is in picoseconds per nanometer per kilometer; the bit rate, $R = 1/T$, is in gigabits per second; and the distance, *L,* is in megameters. Equation 13 also assumes the fiber mode area of $A = 50$ μm^2. The acoustic jitter increases with the bit rate, and it has even stronger dependence on the distance than the Gordon-Haus jitter.

As it follows from the previous considerations, the timing jitter can impose severe limitations on the distance and capacity of the systems, and it has to be controlled.

7.5 FREQUENCY-GUIDING FILTERS

The Gordon-Haus and acoustic timing jitters originate from the frequency fluctuations of the pulses. That means that by controlling the frequency of the solitons, one can control the timing jitter as well. The frequency control can be done by periodically inserting narrowband filters (so-called frequency-guiding filters) along the transmission line, usually at the amplifier locations.[31,32] If, for some reason, the center frequency of a soliton is shifted from the filter

peak, the filter-induced differential loss across the pulse spectrum "pushes" the pulse frequency back to the filter peak. As a result, the pulse spectrum returns back to the filter peak in a characteristic damping length, Δ. If the damping length is considerably less that the transmission distance, *L,* the guiding filters dramatically reduce the timing jitter. To calculate the timing jitter in a filtered system, one should replace L^3 by $3L\Delta^2$ in Eq. 11, and L^2 in Eq. 13 should be replaced by $2L\Delta$. Then, we get the following expression for the Gordon-Haus jitter:

$$\sigma^2_{\mathrm{GH},f} \approx 0.6 n_2 h n_{\mathrm{sp}} F(G) \frac{|\gamma|}{A} \frac{D}{\tau} L\Delta^2 \tag{14}$$

The damping properties of the guiding filters are determined mainly by the curvature of the filter response in the neighborhood of its peak. That means that shallow Fabry-Perot etalon filters can be used as the guiding filters. Fabry-Perot etalon filters have multiple peaks, and different peaks can be used for different WDM channels. The ability of the guiding filters to control the frequency jitter is determined both by the filter characteristics and by the soliton spectral bandwidth. In the case of Fabry-Perot filters with the intensity mirror reflectivity, *R,* and the free spectral range (FSR), the damping length is:

$$\Delta = 0.483(\tau\ \mathrm{FSR})^2 \frac{(1-R)^2}{R} L_f \tag{15}$$

Here, L_f is the spacing between the guiding filters; usually, L_f equals the amplifier spacing L_{amp}.

Note that the Gordon-Haus and acoustic jitters are not specific for soliton transmission only. Any kind of transmission systems, including so-called linear transmission, are subject to these effects. However, the guiding filters can be used in the soliton systems only. Every time a pulse passes through a guiding filter, its spectrum narrows. Solitons can quickly recover their bandwidth through the fiber nonlinearity, whereas for a linear transmission the filter action continuously destroys the signal.

Note that even a more effective reduction of the timing jitter can be achieved if, in addition to the frequency-guiding filters, an amplitude and/or phase modulation at the bit rate is applied to the signal periodically with the distance. "Error-free" transmission over practically unlimited distances can be achieved in this case (1 million kilometers at 10 Gbit/s has been demonstrated).[33,34] Nevertheless, this technique is not passive, high-speed electronics is involved, and the clock recovery is required each time the modulation is applied. Also, in the case of WDM transmission, all WDM channels have to be demultiplexed before the modulation and then multiplexed back afterward; each channel has to have its own clock recovery and modulator. As one can see, this technique shares many drawbacks of the electronic regeneration schemes.

The frequency-guiding filters can dramatically reduce the timing jitter in the systems. At the same time, though, in some cases they can introduce additional problems. Every time a soliton passes through the filter, it loses some energy. To compensate for this loss, the amplifiers should provide an additional (excess) gain. Under this condition, the spontaneous emission noise and other nonsoliton components with the spectrum in the neighborhood of the filter peak experience exponential growth with the distance, which reduces the SNR and can lead to the soliton instabilities. As a result, one has to use weak-enough filters to reduce the excess gain. In practice, the filter strength is chosen to minimize the total penalty from the timing jitter and the excess gain.

7.6 SLIDING FREQUENCY-GUIDING FILTERS

As one can see, the excess gain prevents one from taking a full advantage of guiding filters. By using the sliding frequency-guiding filters,[35] one can essentially eliminate the problems asso-

ciated with the excess gain. The trick is very simple: The transmission peak of each guiding filter is shifted in frequency with respect to the peak of the previous filter, so that the center frequency slides with the distance with the rate of $f' = df/dz$. Solitons, thanks to the nonlinearity, can follow the filters and slide in frequency with the distance. But all unwanted linear radiation (e.g., spontaneous emission noise, nonsoliton components shedded from the solitons, etc.) cannot slide and eventually is killed by the filters. The sliding allows one to use strong guiding filters and even to reduce the amount of noise at the output of transmission in comparison with the broadband (no guiding filters) case. The maximum filter strength[36] and maximum sliding rate[35] are determined by the soliton stability. The error-free transmission of 10 Gbit/s signal over 40,000 km and 20 Gbit/s over 14,000 km was demonstrated with the sliding frequency-guiding filters technique.[37,38]

It is important to emphasize that by introducing the sliding frequency-guiding filters into the transmission line, one converts this transmission line into an effective, all-optical passive regenerator (compatible with WDM). Solitons with only one energy (and pulse width) can propagate stably in such a transmission line. The parameters of the transmission line (the filter strength, excess gain, fiber dispersion, and mode area) determine the unique parameters of these stable solitons. The system is opaque for a low-intensity radiation (noise, for example). However, if the pulse parameters at the input of the transmission line are not too far from the optimum soliton parameters, the transmission line reshapes the pulse into the soliton of that line. Note, again, that the parameters of the resultant soliton do not depend on the input pulse parameters, but only on the parameters of the transmission line. Note also that all nonsoliton components generated during the pulse reshaping are absorbed by the filters. That means, in particular, that the transmission line removes the energy fluctuations from the input data signal.[6] Note that the damping length for the energy fluctuations is close to the frequency damping length of Eq. 15. A very impressive demonstration of regenerative properties of a transmission line with the frequency-guiding filters is the conversion of a nonreturn-to-zero (NRZ) data signal (frequency modulated at the bit rate) into a clean soliton data signal.[39] Another important consequence of the regenerative properties of a transmission line with the frequency-guiding filters is the ability to self-equalize the energies of different channels in WDM transmission.[40] Negative feedback provided by frequency-guiding filters locks the energies of individual soliton channels to values that do not change with distance, even in the face of considerable variation in amplifier gain among the different channels. The equilibrium values of the energies are independent of the input values. All these benefits of sliding frequency-guiding filters are extremely valuable for practical systems. Additional benefits of guiding filters for WDM systems will be discussed later.

7.7 WAVELENGTH DIVISION MULTIPLEXING

Due to the fiber chromatic dispersion, pulses from different WDM channels propagate with different group velocities and collide with each other.[41] Consider a collision of two solitons propagating at different wavelengths (different channels). When the pulses are initially separated and the fast soliton (the soliton at shorter wavelength, with higher group velocity) is behind the slow one, the fast soliton eventually overtakes and passes through the slow soliton. An important parameter of the soliton collision is the collision length, L_{coll}, the fiber length at which the solitons overlap with each other. If we let the collision begin and end with the overlap of the pulses at half power points, then the collision length is:

$$L_{\text{coll}} = \frac{2\tau}{D\Delta\lambda} \tag{16}$$

Here, $\Delta\lambda$ is the solitons wavelengths difference. Due to the effect of cross-phase modulation, the solitons shift each other's carrier frequency during the collision. The frequency shifts for the two solitons are equal in amplitudes (if the pulse widths are equal) and have opposite

signs. During the first half of collision, the fast accelerates even faster (carrier frequency increases), while the slow soliton slows down. The maximum frequency excursion, δf_{max}, of the solitons is achieved in the middle of the collision, when the pulses completely overlap with each other:

$$\delta f_{max} = \pm \frac{1}{3\pi^2 0.322\, \Delta f \tau^2} = \pm \frac{1.18 n_2 \varepsilon}{A \tau D \lambda\, \Delta\lambda} \tag{17}$$

Here, $\Delta f = -c\, \Delta\lambda/\lambda^2$ is the frequency separation between the solitons, and $\varepsilon = 1.13 P_0 \tau$ is the soliton energy. In the middle of collision, the accelerations of the solitons change their signs. As a result, the frequency shifts in the second half of collision undo the frequency shifts of the first half, so that the soliton frequency shifts go back to zero when the collision is complete. This is a very important and beneficial feature for practical applications. The only residual effect of complete collision in a lossless fiber is the time displacements of the solitons:

$$\delta t_{cc} = \pm \frac{0.1786}{\Delta f^2\, \tau} = \pm \frac{2\varepsilon n_2 \lambda}{cDA\, \Delta\lambda^2} \tag{18}$$

The symmetry of the collision can be broken if the collision takes place in a transmission line with loss and lumped amplification. For example, if the collision length, L_{coll}, is shorter than the amplifier spacing, L_{amp}, and the center of collision coincides with the amplifier location, the pulses intensities are low in the first half of collision and high in the second half. As a result, the first half of collision is practically linear. The soliton frequency shifts acquired in the first half of collision are very small and insufficient to compensate for the frequency shifts of opposite signs acquired by the pulses in the second half of collision. This results in nonzero residual frequency shifts. Note that similar effects take place when there is a discontinuity in the value of the fiber dispersion as a function of distance. In this case, if a discontinuity takes place in the middle of collision, one half of the collision is fast (where D is higher) and the other half is slow. The result is nonzero residual frequency shifts. Nonzero residual frequency shifts lead, through the dispersion of the rest of the transmission fiber, to variations in the pulses arrival time at the output of transmission. Nevertheless, if the collision length is much longer than the amplifier spacing and of the characteristic length of the dispersion variations in the fiber, the residual soliton frequency shifts are zero, just like in a lossless uniform fiber. In practice, the residual frequency shifts are essentially zero as long as the following condition is satisfied:[41]

$$L_{coll} \geq 2L_{amp} \tag{19}$$

Another important case is so-called half-collisions (or partial collisions) at the input of the transmission.[42] These collisions take place if solitons from different channels overlap at the transmission input. These collisions result in residual frequency shifts of δf_{max} and the following pulse timing shifts, δt_{pc}, at the output of transmission of length L:

$$\delta t_{pc} \approx \delta f_{max} \frac{\lambda^2}{c} D(L - L_{coll}/4) = \pm \frac{1.18 \varepsilon n_2 \lambda}{c\tau A\, \Delta\lambda} (L - L_{coll}/4) \tag{20}$$

One can avoid half-collisions by staggering the pulse positions of the WDM channels at the transmission input.

Consider now the time shifts caused by all complete collisions. Consider a two-channel transmission, where each channel has a $1/T$ bit rate. The distance between subsequent collisions is:

$$l_{coll} = \frac{T}{D\, \Delta\lambda} \tag{21}$$

The maximum number of collisions that each pulse can experience is L/l_{coll}. This means that the maximum time shift caused by all complete collisions is:

$$\delta t_{\Sigma cc} \approx \delta t_{cc} L/l_{\text{coll}} = \pm \frac{2\varepsilon n_2 \lambda}{cTA\,\Delta\lambda} L \tag{22}$$

It is interesting to note that $\delta t_{\Sigma cc}$ does not depend on the fiber dispersion. Note also that Eq. 22 describes the worst case when the pulse experiences the maximum number of possible collisions. Consider a numerical example. For a two-channel transmission, 10 Gbit/s each (T = 100 ps), pulse energy (ε = 50 fJ), channel wavelength separation ($\Delta\lambda$ = 0.6 nm), fiber mode area (A = 50 μm^2 and L = 10 Mm), we find $\delta t_{\Sigma cc}$ = 45 ps. Note that this timing shift can be reduced by increasing the channel separation. Another way to reduce the channel-to-channel interaction by a factor of two is to have these channels orthogonally polarized to each other. In WDM transmission, with many channels, one has to add timing shifts caused by all other channels. Note, however, that as one can see from Eq. 22, the maximum penalty comes from the nearest neighboring channels.

As one can see, soliton collisions introduce additional jitter to the pulse arrival time, which can lead to considerable transmission penalties. As we saw earlier, the frequency-guiding filters are very effective in suppressing the Gordon-Haus and acoustic jitters. They can also be very effective in suppressing the timing jitter induced by WDM collisions. In the ideal case of parabolical filters and the collision length being much longer than the filter spacing, $L_{\text{coll}} >> L_f$, the filters make the residual time shift of a complete collision, δt_{cc}, exactly zero. They also considerably reduce the timing jitter associated with asymmetrical collisions and half-collisions. Note that for the guiding filters to work effectively in suppressing the collision penalties, the collision length should be at least a few times greater than the filter spacing. Note also that real filters, such as etalon filters, do not always perform as good as ideal parabolic filters. This is true especially when large-frequency excursions of solitons are involved, because the curvature of a shallow etalon filter response reduces with the deviation of the frequency from the filter peak. In any case, filters do a very good job in suppressing the timing jitter in WDM systems.

Consider now another potential problem in WDM transmission, which is the four-wave mixing. During the soliton collisions, the four-wave mixing spectral sidebands are generated. Nevertheless, in the case of a lossless, constant-dispersion fiber, these sidebands exist only during the collision, and when the collision is complete, the energy from the sidebands regenerates back into the solitons. That is why it was considered for a long time that the four-wave mixing should not be a problem in soliton systems. But this is true only in the case of a transmission in a lossless fiber. In the case of lossy fiber and periodical amplification, these perturbations can lead to the effect of the pseudo-phase-matched (or resonance) four-wave mixing.[43] The pseudo-phase-matched four-wave mixing lead to the soliton energy loss to the spectral sidebands and to a timing jitter (we called that effect an *extended Gordon-Haus effect*).[43] The effect can be so strong that even sliding frequency-guiding filters are not effective enough to suppress it. The solution to this problem is to use dispersion-tapered fiber spans. As we have discussed earlier, soliton propagation in the condition:

$$\frac{D(z)\,A(z)}{\text{Energy}(z)} = \text{const} \tag{23}$$

is identical to the case of lossless, constant-dispersion fiber. That means that the fiber dispersion in the spans between the amplifiers should decrease with the same rate as the signal energy. In the case of lumped amplifiers, this is the exponential decay with the distance. Note that the dispersion-tapered spans solve not just the four-wave mixing problem. By making the soliton transmission perturbation-free, they lift the requirements to have the amplifier spacing much shorter than the soliton dispersion length. The collisions remain symmetrical even when the collision length is shorter than the amplifier spacing. (Note, however, that the dispersion-

tapered fiber spans do not lift the requirement to have guiding filter spacing as short as possible in comparison with the collision length and with the dispersion length.) The dispersion-tapered fiber spans can be made with the present technology.[22] Stepwise approximation of the exact exponential taper made of fiber pieces of constant dispersion can also be used.[43] It was shown numerically and experimentally that by using fiber spans with only a few steps one can dramatically improve the quality of transmission.[44,45] In the experiment, each fiber span was dispersion tapered typically in three or four steps, the path-average dispersion value was 0.5 ± 0.05 ps nm^{-1} km^{-1} at 1557 nm. The use of dispersion-tapered fiber spans together with sliding frequency-guiding filters allowed transmission of eight 10-Gbit/s channels with the channel spacing, $\Delta\lambda = 0.6$ nm, over more than 9000 km. The maximum number of channels in this experiment was limited by the dispersion slope, $dD/d\lambda$, which was about 0.07 ps nm^{-2} km^{-1}. Because of the dispersion slope, different WDM channels experience different values of dispersion. As a result, not only the path average dispersion changes with the wavelength, but the dispersion tapering has exponential behavior only in a vicinity of one particular wavelength in the center of the transmission band. Wavelength-division multiplexed channels located far from that wavelength propagate in far from the optimal conditions. One solution to the problem is to use dispersion-flattened fibers (i.e., fibers with $dD/d\lambda = 0$). Unfortunately, these types of fibers are not commercially available at this time. This and some other problems of classical soliton transmission can be solved by using dispersion-managed soliton transmission.[46–63]

7.8 DISPERSION-MANAGED SOLITONS

In the dispersion-managed (DM) soliton transmission, the transmission line consists of the fiber spans with alternating signs of the dispersion. Let the positive and negative dispersion spans of the map have lengths and dispersions, L_+, D_+ and L_-, D_-, respectively. Then, the path-average dispersion, D_{av} is:

$$D_{av} = (D_+L_+ + L_-D_-)/L_{map} \tag{24}$$

Here, L_{map}, is the length of the dispersion map:

$$L_{map} = L_+ + L_- \tag{25}$$

Like in the case of classical soliton, during the DM soliton propagation, the dispersion and nonlinear effects cancel each other. The difference is that in the classical case, this cancellation takes place continuously, whereas in the DM case, it takes place periodically with the period of the dispersion map length, L_{map}. The strength of the DM is characterized by a parameter, S, which is determined as[47,50,52]

$$S = \frac{\lambda^2}{2\pi c} \frac{(D_+ - D_{av})L_+ - (D_- - D_{av})L_-}{\tau^2} \tag{26}$$

The absolute values of the local dispersion are usually much greater than the path average dispersion: $|D_+|$, $|D_-| >> |D_{av}|$. As one can see from Eq. 26, the strength of the map is proportional to the number of the local dispersion lengths of the pulse in the map length: $S \approx L_{map}/z_{d,\,local}$. The shape of the DM solitons are close to Gaussian. A very important feature of DM solitons is the so-called power enhancement. Depending on the strength of the map, the pulse energy of DM solitons, ε_{DM}, is greater than that of classical solitons, ε_0, propagating in a fiber with constant dispersion, $D = D_{av}$:[47,50]

$$\varepsilon_{DM} \approx \varepsilon_0 (1 + 0.7S^2) \tag{27}$$

Note that this equation assumes lossless fiber. The power enhancement effect is very important for practical applications. It provides an extra degree of freedom in the system design by

giving the possibility to change the pulse energy while keeping the path-average fiber dispersion constant. In particular, because DM solitons can have adequate pulse energy (to have a high-enough SNR) at or near zero path average dispersion, timing jitter from the Gordon-Haus and acoustic effects is greatly reduced (for example, the variance of the Gordon-Haus jitter, σ^2, scales almost as $1/\varepsilon_{DM}$).[49] Single-channel high-bit-rate DM soliton transmission over long distances with weak guiding filters and without guiding filters was experimentally demonstrated.[46,51]

Dispersion-managed soliton transmission is possible not only in transmission lines with positive dispersion, $D_{av} > 0$, but also in the case of $D_{av} = 0$ and even $D_{av} < 0$.[52] To understand this, consider qualitatively the DM soliton propagation (Fig. 4). Locally, the dispersive effects are always stronger than the nonlinear effect (i.e., the local dispersion length is much shorter than the nonlinear length). In the zero approximation, the pulse propagation in the map is almost linear. Let's call the middle of the positive D sections "point a," the middle of the negative sections "point c," transitions between positive and negative sections "point b," and transitions between negative and positive sections "point d." The chirp-free (minimum pulse width) positions of the pulse are in the middle of the positive- and negative-D sections (points a and c). The pulse chirp is positive between points a, b, and c (see Fig. 4). That means that the high-frequency (blue) spectral components of the pulse are at the front edge of the pulse, and the low-frequency (red) components are at the trailing edge. In the section c-d-a, the pulse chirp is negative. The action of the nonlinear SPM effect always downshifts in frequency the front edge of the pulse and up shifts in frequency the trailing edge of the pulse. That means that the nonlinearity decreases the spectral bandwidth of positively chirped pulses (section a-b-c) and increases the spectral bandwidth of negatively chirped pulses (section c-d-a). This results in the spectral bandwidth behavior also shown in Fig. 4: The maximum spectral bandwidth is achieved in the chirp-free point in the positive section, whereas the minimum spectral bandwidth is achieved in the chirp-free point in the negative section. The condition for the pulses to be DM solitons is that the nonlinear phase shift is compensated by the dispersion-induced

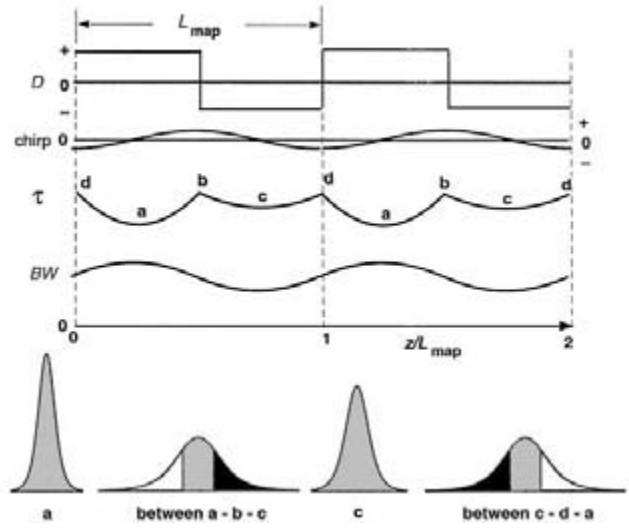

FIGURE 4 Qualitative description of dispersion-managed (DM) soliton transmission. Distance evolution of the fiber dispersion $[D(z)]$, pulse chirp, pulse width $[\tau(z)]$, and pulse bandwidth $[BW(z)]$. Evolution of the pulse shape in different fiber sections is shown in the bottom.

phase shift over the dispersion map length. That requires that $\int D\,BW^2\,dz > 0$ (here, BW is the pulse spectral bandwidth). Note that in the case of classical solitons, when spectral bandwidth is constant, this expression means that dispersion, D, must be positive. In the DM case, however, the pulse bandwidth is wider in the positive-D section than in the negative-D section. As a result, the integral can be positive, even when $D_{av} = \int Ddz/L_{map}$ is zero or negative. Note that the spectral bandwidth oscillations explain also the effect of power enhancement of DM solitons.

Consider interaction of adjacent pulses in DM systems.[54] The parameter that determines the strength of the interaction is the ratio τ/T (here, τ is the pulse width and T is the spacing between adjacent pulses). As in the case of classical soliton transmission, the cross-phase modulation effect (XPM) shifts the frequencies of the interacting pulses, Δf_{XPM}, which, in turn, results in timing jitter at the output of the transmission. As it was discussed earlier, the classical soliton interaction increases very quickly with τ/T. To avoid interaction-induced penalties in classical soliton transmission systems, the pulses should not overlap significantly with each other: τ/T should be less than 0.2 to 0.3. In the DM case, the situation is different. The pulse width in the DM case oscillates with the distance $\tau(z)$; that means that the interaction also changes with distance. Also, because the pulses are highly chirped when they are significantly overlapped with each other, the sign of the interaction is essentially independent of the mutual phases of the pulses. Cross-phase modulation always shifts the leading pulse to the red spectral region, and the trailing pulse shifts to the blue spectral region. The XPM-induced frequency shifts of interacting solitons per unit distance is:

$$\frac{d\,\Delta f_{XPM}}{dz} \approx \pm 0.15\,\frac{2\pi n_2 \varepsilon}{\lambda T^2 A}\,\Phi(\tau/T) \tag{28}$$

The minus sign in Eq. 28 corresponds to the leading pulse, and the plus sign corresponds to the trailing pulse. Numerically calculated dimensionless function, $\Phi(\tau/T)$, is shown in Fig. 5. As it follows from Eq. 28, $\Phi(\tau/T)$ describes the strength of the XPM-induced interaction of the pulses as a function of the degree of the pulse overlap. One can see that the interaction is very small when τ/T is smaller than 0.4 (i.e., when the pulses barely overlap), which is similar to the classical soliton propagation. The strength of the interaction of DM solitons also increases with τ/T, but only in the region $0 < \tau/T < 1$. In fact, the interaction reaches its maximum at $\tau/T \approx 1$ and then decreases and becomes very small again when $\tau/T >> 1$ (i.e., when the pulses overlap nearly completely). There are two reasons for such an interesting behavior at $\tau/T >> 1$. The XPM-induced frequency shift is proportional to the time derivative of the

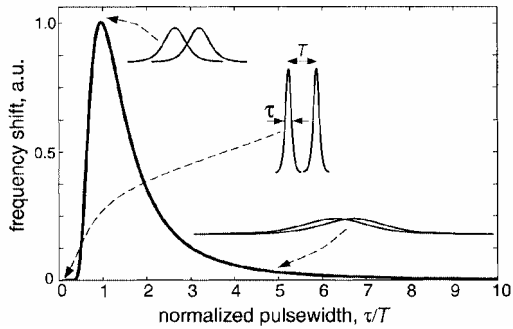

FIGURE 5 Dimensionless function, $\Phi(\tau/T)$, describing the XPM-induced frequency shift of two interacting chirped Gaussian pulses as a function of the pulse width normalized to the pulse separation.

interacting pulse's intensity, and the pulse derivative reduces with the pulse broadening. Also, when the pulses nearly completely overlap, the sign of the derivative changes across the region of overlap so that the net effect tends to be canceled out.

Based on Eq. 28 and Fig. 5, one can distinguish three main regimes of data transmission in DM systems. In all these regimes, the minimum pulse width is, of course, less than the bit slot, T. The regimes differ from each other by the maximum pulse breathing with the distance. In the first, "non-pulse-overlapped," regime, adjacent pulses barely overlap during most of the transmission, so that the pulse interaction is not a problem in this case. This is the most stable regime of transmission. In the "partially-pulse-overlapped" regime, the adjacent pulses spend a considerable portion of the transmission being partially overlapped [$\tau(z)$ being around T]. Cross-phase modulation causes the frequency and timing jitter in this case. In the third, "pulse-overlapped," regime, the adjacent pulses are almost completely overlapped with each other during most of the transmission [$\tau_{\min}\ (L_{\text{map}}/z_{\text{d, local}}) >> T$]. The XPM-induced pulse-to-pulse interaction is greatly reduced in this case in comparison with the previous one. The main limiting factor for this regime of transmission is the intrachannel four-wave mixing taking place during strong overlap of adjacent pulses.[54] The intrachannel four-wave mixing leads to the amplitude fluctuations of the pulses and "ghost" pulse generation in the "zero" slots of the data stream.

7.9 WAVELENGTH-DIVISION MULTIPLEXED DISPERSION-MANAGED SOLITON TRANSMISSION

One of the advantages of DM transmission over classical soliton transmission is that the local dispersion can be very high ($|D_+|, |D_-| >> |D_{\text{av}}|$), which efficiently suppresses the four-wave mixing from soliton-soliton collisions in WDM. Consider the timing jitter induced by collisions in the non-pulse-overlapped DM transmission. The character of the pulse collisions in DM systems is quite different from the case of a transmission line with uniform dispersion: In the former, the alternating sign of the high local dispersion causes the colliding solitons to move rapidly back and forth with respect to each other, with the net motion determined by D_{av}.[56–59] Because of this rapid breathing of the distance between the pulses, each net collision actually consists of many fast or "mini" collisions. The net collision length can be estimated as:[59]

$$L_{\text{coll}} \approx \frac{2\tau}{D_{\text{av}}\,\Delta\lambda} + \frac{(D_+ - D_{\text{av}})L_+}{D_{\text{av}}} \approx \frac{2\tau}{D_{\text{av}}\,\Delta\lambda} + \frac{\tau_{\text{eff}}}{D_{\text{av}}\,\Delta\lambda} \tag{29}$$

Here, τ is the minimum (unchirped) pulse width. Here, we also defined the quantity $\tau_{\text{eff}} \equiv L_+D_+\Delta\lambda$, which plays the role of an effective pulse width. For strong dispersion management, τ_{eff} is usually much bigger than τ. Thus, L_{coll} becomes almost independent of $\Delta\lambda$ and much longer than it is for classical solitons subject to the same D_{av}. As a result, the residual frequency shift caused by complete pulse collisions tends to become negligibly small for transmission using strong maps.[58] The maximum frequency excursion during the DM soliton collision is:[59]

$$\delta f_{\max} \approx \pm\frac{2n_2\varepsilon}{L_+D_+AD_{\text{av}}\lambda\,\Delta\lambda^2} = \pm\frac{2n_2\varepsilon}{A\,D_{\text{av}}\,\lambda\,\Delta\lambda\tau_{\text{eff}}} \tag{30}$$

Now, we can estimate the time shift of the solitons per complete collision:

$$\delta t_{\text{cc}} \approx D_{\text{av}}\,\lambda^2/c \int \delta f dz \approx \alpha D_{\text{av}}L_{\text{coll}}\,\delta f_{\max}\,\lambda^2/c \approx \pm\alpha\,\frac{2n_2\varepsilon\lambda}{cAD_{\text{av}}\,\Delta\lambda^2} \tag{31}$$

Here, $\alpha \le 1$ is a numerical coefficient that takes into account the particular shape of the frequency shift as a function of distance. Consider now the time shifts caused by all collisions. In

a two-channel transmission, the distance between subsequent collisions is $l_{coll} = T/(D_{av}\Delta\lambda)$. The maximum number of complete collisions at the transmission distance, L, is $(L - L_{coll})/l_{coll}$ (we assume that $L > L_{coll}$), and the number of incomplete collisions at the end of transmission is L_{coll}/l_{coll}. The timing shift caused by all these collisions can be estimated as

$$\delta t_{\Sigma c} \approx \delta t_{cc}\,(L - L_{coll}/2)/l_{coll} = \pm\alpha\,\frac{2n_2\varepsilon\lambda}{cAT\,\Delta\lambda}\,(L - L_{coll}/2) \tag{32}$$

Consider the problem of initial partial collisions. As it was discussed earlier for the case of classical solitons, initial partial collisions can be a serious problem by introducing large timing jitter at the output of transmission. On the other hand, for the classical case, one could avoid the half-collisions by staggering the pulse positions of the WDM channels at the transmission input. The situation is very different for the DM case. In the DM case, the collision length is usually longer than the distance between subsequent collisions (i.e., $L_{coll} > l_{coll}$). Thus, a pulse can collide *simultaneously* with several pulses of another channel. The maximum number of such simultaneous collisions is $N_{sc} \approx L_{coll}/l_{coll} = 2\tau/T + [(D_+ - D_{av})L_+\,\Delta\lambda]/T$. Note that N_{sc} increases when the channel spacing, $\Delta\lambda$, increases. The fact that the collision length is greater than the distance between collisions also means that initial partial collisions are inevitable in DM systems. Moreover, depending on the data pattern in the interacting channel, each pulse can experience up to N_{sc} initial partial collisions with that channel (not just one as in the classical case). As a consequence, the residual frequency shifts can be bigger than δf_{max}. The total time shift caused by the initial partial collisions at distance $L > L_{coll}$ can be estimated as:

$$\delta\tau_{pc} \approx \beta\delta f_{max} N_{sc}(L - L_{coll}/2)D_{av}\lambda^2/c \approx \pm\beta\,\frac{2n_2\varepsilon\lambda}{cAT\,\Delta\lambda}\,(L - L_{coll}/2) \tag{33}$$

Here, $\beta \le 1$ is a numerical coefficient that takes into account the particular shape of the frequency shift as a function of distance for a single collision.

Equations 32 and 33 assume that the transmission distance is greater than the collision length. When $L > L_{coll}$, these equations should be replaced by:

$$\delta t_{\Sigma c,\,pc} \approx (\alpha, \beta)\,D_{av}\delta f_{max}\,\frac{\lambda^2}{c}\,\frac{L^2}{2l_{coll}} \approx \pm(\alpha, \beta)\,\frac{n_2\varepsilon\lambda}{cAT\,\Delta\lambda}\,\frac{L^2}{L_{coll}} \tag{34}$$

Note that the signs of the timing shifts caused by initial partial collisions and by complete collisions are opposite. Thus, the maximum (worst-case) spread of the pulse arriving times caused by pulse collisions in the two-channel WDM transmission is described by:

$$\delta t_{max} = |\delta t_{pc}| + |\delta t_{\Sigma c}| \tag{35}$$

In a WDM transmission with more than two channels, one has to add contributions to the time shift from all the channels. Note that the biggest contribution makes the nearest neighboring channels, because the time shift is inversely proportional to the channel spacing, $\Delta\lambda$. Now, we can summarize the results of Eqs. 32 through 35 as follows. When $L > L_{coll}$ (Eqs. 32–33), corresponding to very long distance transmission, δt_{max} increases linearly with the distance and almost independently of the path-average dispersion, D_{av}. When $L < L_{coll}$ (Eq. 34), which corresponds to short-distance transmission and/or very low path-average dispersion, δt_{max} increases quadratically with the distance and in proportion to D_{av}. Note also that the WDM data transmission at near zero path-averaged dispersion, $D_{av} = 0$, may not be desirable, because $L_{coll} \to \infty$ and frequency excursions $\delta f_{max} \to \infty$ when $\overline{D} \to 0$ (see Eq. 30). Thus, even though Eq. 34 predicts the time shift to be zero when D_{av} is exactly zero, the frequency shifts of the solitons can be unacceptably large and Eq. 34 may be no longer valid. There are also practical difficulties in making maps with $D_{av} < 0.1$ ps nm^{-1} km^{-1} over the wide spectral range required for dense WDM transmission.

It is interesting to compare these results with the results for the case of classical solitons (Eqs. 17–22). The time shifts per complete collisions (Eqs. 18 and 31) are about the same, the time shifts from all initial partial collisions (Eqs. 20 and 33) are also close to each other. The total maximum time shifts from all collisions are also close to each other for the case of long distance transmission. That means that, similar to the classical case, one has to control the collision-induced timing jitter when it becomes too large. As it was discussed earlier, the sliding frequency-guiding filters are very effective in suppressing the timing jitter. Because the collision length in DM systems is much longer than in classical systems, and, at the same time, it is almost independent of the channel wavelength separation, the requirement that the collision length is much greater than the filter spacing, $L_{coll} >> L_f$, is easy to meet. As a result, the guiding filters suppress the timing jitter in DM systems even more effective than in classical soliton systems. The fact that the frequency excursions during collisions are much smaller in DM case, also makes the filters to work more effectively.

As we have discussed previously, many important features of DM solitons come from the fact that the soliton spectral bandwidth oscillates with the distance. That is why guiding filters alter the dispersion management itself and give an additional degree of freedom in the system design.[60] Note also that the position of the filters in the dispersion map can change the soliton stability in some cases.[61] It should also be noted that because of the weak dependence of the DM soliton spectral bandwidth on the soliton pulse energy, the energy fluctuations damping length provided by the guided filters is considerably longer than the frequency damping length.[62] This is the price one has to pay for many advantages of DM solitons. From the practical point of view, the most important advantage is the flexibility in system design and freedom in choosing the transmission fibers. For example, one can upgrade existing systems by providing an appropriate dispersion compensation with dispersion compensation fibers or with lumped dispersion compensators (fiber Bragg gratings, for example). The biggest advantage of DM systems is the possibility to design dispersion maps with essentially zero dispersion slope of the path-average dispersion, $dD_{av}/d\lambda$, by combining commercially available fibers with different signs of dispersion and dispersion slopes. (Note that it was a nonzero dispersion slope that limited the maximum number of channels in classical soliton long distance WDM transmission.) This was demonstrated in the experiment where almost flat average dispersion, $D_{av} = 0.3$ ps nm^{-1} km^{-1} was achieved by combining standard, dispersion-compensating, and True-Wave (Lucent nonzero dispersion-shifted) fibers.[63] By using sliding frequency-guiding filters and this dispersion map, "error-free" DM soliton transmission of twenty-seven 10-Gbit/s WDM channels was achieved over more than 9000 km without using forward error correction. It was shown that once the error-free transmission with about 10 channels is achieved, adding additional channels practically does not change performance of the system. (This is because, for each channel, only the nearest neighboring channels degrade its performance.) The maximum number of WDM channels in this experiment was limited only by the power and bandwidth of optical amplifiers used in the experiment. One can expect that the number of channels can be increased by a few times if more powerful and broader-bandwidth amplifiers are used.

7.10 CONCLUSION

We considered the basic principles of soliton transmission systems. The main idea of the "soliton philosophy" is to put under control, balance, and even to extract the maximum benefits from otherwise detrimental effects of the fiber dispersion and nonlinearity. The "soliton approach" is to make transmission systems intrinsically stable. Soliton technology is a very rapidly developing area of science and engineering, which promises a big change in the functionality and capacity of optical data transmission and networking.

7.11 REFERENCES

1. V. E. Zaharov and A. B. Shabat, "Exact Theory of Two Dimentional Self Focusing and One-Dimentional Self-Modulation of Waves in Nonlinear Media," *Zh. Eksp. Teor. Fiz.* **61**:118–134 (1971) [*Sov. Phys. JETP* **34**:62–69 (1972)].
2. A. Hasegawa and F. D. Tappert, "Transmission of Stationary Nonlinear Optical Pulses in Dispersive Dielectric Fibers. I. Anomalous Dispersion," *Applied Phys. Letters* **23**:142–144 (1973).
3. J. Satsuma and N. Yajima, "Initial Value Problem of One-Dimentional Self-Modulation of Nonlinear Waves in Dispersive Media," *Prog. Theor. Phys. Suppl.* **55**:284–306 (1980).
4. P. V. Mamyshev and S. V. Chernikov, "Ultrashort Pulse Propagation in Optical Fibers," *Optics Letters* **15**:1076–1078 (1990).
5. R. H. Stolen, in *Optical Fiber Telecommunications,* S. E. Miller and H. E. Chynoweth (eds.), Academic Press, New York, 1979, Chap. 5.
6. L. F. Mollenauer, J. P. Gordon, and P. V. Mamyshev, "Solitons in High Bit Rate, Long Distance Transmission," in *Optical Fiber Telecommunications III,* Academic Press, 1997, Chap. 12.
7. L. F. Mollenauer, J. P. Gordon, and M. N. Islam, "Soliton Propagation in Long Fibers with Periodically Compensated Loss," *IEEE J. Quantum Electron.* **QE-22**:157 (1986).
8. L. F. Mollenauer, M. J. Neubelt, S. G. Evangelides, J. P. Gordon, J. R. Simpson, and L. G. Cohen, "Experimental Study of Soliton Transmission Over More Than 10,000 km in Dispersion Shifted Fiber," *Opt. Lett.* **15**:1203 (1990).
9. L. F. Mollenauer, S. G. Evangelides, and H. A. Haus, "Long Distance Soliton Propagation Using Lumped Amplifiers and Dispersion Shifted Fiber," *J. Lightwave Technol.* **9**:194 (1991).
10. K. J. Blow and N. J. Doran, "Average Soliton Dynamics and the Operation of Soliton Systems with Lumped Amplifiers," *Photonics Tech. Lett.* **3**:369 (1991).
11. A. Hasegawa and Y. Kodama, "Guiding-Center Soliton in Optical Fibers," *Opt. Lett.* **15**:1443 (1990).
12. G. P. Gordon, "Dispersive Perturbations of Solitons of the Nonlinear Schroedinger Equation," *JOSA B* **9**:91–97 (1992).
13. A. Hasegawa and Y. Kodama, "Signal Transmission by Optical Solitons in Monomode Fiber," *Proc. IEEE* **69**:1145 (1981).
14. K. J. Blow and N. J. Doran, "Solitons in Optical Communications," *IEEE J. of Quantum Electronics,*" **QE-19**:1883 (1982).
15. P. B. Hansen, H. A. Haus, T. C. Damen, J. Shah, P. V. Mamyshev, and R. H. Stolen, "Application of Soliton Spreading in Optical Transmission," Dig. ECOC, Vol. 3, Paper WeC3.4, pp. 3.109–3.112, Oslo, Norway, September 1996.
16. K. Tajima, "Compensation of Soliton Broadening in Nonlinear Optical Fibers with Loss," *Opt. Lett.* **12**:54 (1987).
17. H. H. Kuehl, "Solitons on an Axially Nonuniform Optical Fiber," *J. Opt. Soc. Am. B* **5**:709–713 (1988).
18. E. M. Dianov, L. M. Ivanov, P. V. Mamyshev, and A. M. Prokhorov, "High-Quality Femtosecond Fundamental Soliton Compression in Optical Fibers with Varying Dispersion," Topical Meeting on Nonlinear Guided-Wave Phenomena: Physics and Applications, 1989, Technical Digest Series, vol. 2, OSA, Washington, D.C., 1989, pp. 157–160, paper FA-5.
19. P. V. Mamyshev, "Generation and Compression of Femtosecond Solitons in Optical Fibers," *Bull. Acad. Sci. USSR, Phys. Ser.,* **55**(2):374–381 (1991) [*Izv. Acad. Nauk, Ser. Phys.* **55**(2):374–381 (1991).
20. S. V. Chernikov and P. V. Mamyshev, "Femtosecond Soliton Propagation in Fibers with Slowly Decreasing Dispersion," *J. Opt. Soc. Am. B.* **8**(8):1633–1641 (1991).
21. P. V. Mamyshev, S. V. Chernikov, and E. M. Dianov, "Generation of Fundamental Soliton Trains for High-Bit-Rate Optical Fiber Communication Lines," *IEEE J. of Quantum Electron.* **27**(10):2347–2355 (1991).
22. V. A. Bogatyrev, M. M. Bubnov, E. M. Dianov, A. S. Kurkov, P. V. Mamyshev, A. M. Prokhorov, S. D. Rumyantsev, V. A. Semeonov, S. L. Semeonov, A. A. Sysoliatin, S. V. Chernikov, A. N. Gurianov, G. G. Devyatykh, S. I. Miroshnichenko, "Single-Mode Fiber with Chromatic Dispersion Varying along the Length," *IEEE J. of Lightwave Technology* **LT-9**(5):561–566 (1991).

23. V. I. Karpman and V. V. Solov'ev, "A Perturbation Approach to the Two-Soliton System," *Physica D* **3**:487–502 (1981).
24. J. P. Gordon, "Interaction Forces among Solitons in Optical Fibers," *Optics Letters* **8**:596–598 (1983).
25. J. P. Gordon and L. F. Mollenauer, "Effects of Fiber Nonlinearities and Amplifier Spacing on Ultra Long Distance Transmission," *J. Lightwave Technol.* **9**:170 (1991).
26. J. P. Gordon and H. A. Haus, "Random Walk of Coherently Amplified Solitons in Optical Fiber," *Opt. Lett.* **11**:665 (1986).
27. K. Smith and L. F. Mollenauer, "Experimental Observation of Soliton Interaction over Long Fiber Paths: Discovery of a Long-Range Interaction," *Opt. Lett.* **14**:1284 (1989).
28. E. M. Dianov, A. V. Luchnikov, A. N. Pilipetskii, and A. N. Starodumov, "Electrostriction Mechanism of Soliton Interaction in Optical Fibers," *Opt. Lett.* **15**:314 (1990).
29. E. M. Dianov, A. V. Luchnikov, A. N. Pilipetskii, and A. M. Prokorov, "Long-Range Interaction of Solitons in Ultra-Long Communication Systems," *Soviet Lightwave Communications* **1**:235 (1991).
30. E. M. Dianov, A. V. Luchnikov, A. N. Pilipetskii, and A. M. Prokhorov "Long-Range Interaction of Picosecond Solitons Through Excitation of Acoustic Waves in Optical Fibers," *Appl. Phys. B* **54**:175 (1992).
31. A. Mecozzi, J. D. Moores, H. A. Haus, and Y. Lai, "Soliton Transmission Control," *Opt. Lett.* **16**:1841 (1991).
32. Y. Kodama and A. Hasegawa, "Generation of Asymptotically Stable Optical Solitons and Suppression of the Gordon-Haus Effect," *Opt. Lett.* **17**:31 (1992).
33. M. Nakazawa, E. Yamada, H. Kubota, and K. Suzuki, "10 Gbit/s Soliton Transmission over One Million Kilometers," *Electron. Lett.* **27**:1270 (1991).
34. T. Widdowson and A. D. Ellis, "20 Gbit/s Soliton Transmission over 125 Mm," *Electron. Lett.* **30**:1866 (1994).
35. L. F. Mollenauer, J. P. Gordon, and S. G. Evangelides, "The Sliding-Frequency Guiding Filter: An Improved Form of Soliton Jitter Control," *Opt. Lett.* **17**:1575 (1992).
36. P. V. Mamyshev and L. F. Mollenauer, "Stability of Soliton Propagation with Sliding Frequency Guiding Filters," *Opt. Lett.* **19**:2083 (1994).
37. L. F. Mollenauer, P. V. Mamyshev, and M. J. Neubelt, "Measurement of Timing Jitter in Soliton Transmission at 10 Gbits/s and Achievement of 375 Gbits/s-Mm, error-free, at 12.5 and 15 Gbits/s," *Opt. Lett.* **19**:704 (1994).
38. D. LeGuen, F. Fave, R. Boittin, J. Debeau, F. Devaux, M. Henry, C. Thebault, and T. Georges, "Demonstration of Sliding-Filter-Controlled Soliton Transmission at 20 Gbit/s over 14 Mm," *Electron. Lett.* **31**:301 (1995).
39. P. V. Mamyshev and L. F. Mollenauer, "NRZ-to-Soliton Data Conversion by a Filtered Transmission Line," in *Optical Fiber Communication Conference OFC-95,* Vol. 8, 1995 OSA Technical Digest Series, OSA, Washington, D.C., 1995, Paper FB2, pp. 302–303.
40. P. V. Mamyshev and L. F. Mollenauer, "WDM Channel Energy Self-Equalization in a Soliton Transmission Line Using Guiding Filters," *Optics Letters* **21**(20):1658–1660 (1996).
41. L. F. Mollenauer, S. G. Evangelides, and J. P. Gordon, "Wavelength Division Multiplexing with Solitons in Ultra Long Distance Transmission Using Lumped Amplifiers," *J. Lightwave Technol.* **9**:362 (1991).
42. P. A. Andrekson, N. A. Olsson, J. R. Simpson, T. Tanbun-ek, R. A. Logan, P. C. Becker, and K. W. Wecht, *Electron. Lett.* **26**:1499 (1990).
43. P. V. Mamyshev, and L. F. Mollenauer, "Pseudo-Phase-Matched Four-Wave Mixing in Soliton WDM Transmission," *Opt. Lett.* **21**:396 (1996).
44. L. F. Mollenauer, P. V. Mamyshev, and M. J. Neubelt, "Demonstration of Soliton WDM Transmission at 6 and 7×10 GBit/s, Error-Free over Transoceanic Distances," *Electron. Lett.* **32**:471 (1996).
45. L. F. Mollenauer, P. V. Mamyshev, and M. J. Neubelt, "Demonstration of Soliton WDM Transmission at up to 8×10 GBit/s, Error-Free over Transoceanic Distances," OFC-96, Postdeadline paper PD-22.
46. M. Suzuki, I Morita, N. Edagawa, S. Yamamoto, H. Taga, and S. Akiba, "Reduction of Gordon-Haus Timing Jitter by Periodic Dispersion Compensation in Soliton Transmission," *Electron. Lett.* **31**:2027–2029 (1995).

47. N. J. Smith, N. J. Doran, F. M. Knox, and W. Forysiak, "Energy-Scaling Characteristics of Solitons in Strongly Dispersion-Managed Fibers," *Opt. Lett.* **21**:1981–1983 (1996).
48. I. Gabitov and S. K. Turitsyn, "Averaged Pulse Dynamics in a Cascaded Transmission System with Passive Dispersion Compensation," *Opt. Lett.* **21**:327–329 (1996).
49. N. J. Smith, W. Forysiak, and N. J. Doran, "Reduced Gordon-Haus Jitter Due to Enhanced Power Solitons in Strongly Dispersion Managed Systems," *Electron. Lett.* **32**:2085–2086 (1996).
50. V. S. Grigoryan, T. Yu, E. A. Golovchenko, C. R. Menyuk, and A. N. Pilipetskii, "Dispersion-Managed Soliton Dynamics," *Opt. Lett.* **21**:1609–1611 (1996).
51. G. Carter, J. M. Jacob, C. R. Menyuk, E. A. Golovchenko, and A. N. Pilipetskii, "Timing Jitter Reduction for a Dispersion-Managed Soliton System: Experimental Evidence," *Opt. Lett.* **22**:513–515 (1997).
52. S. K. Turitsyn, V. K. Mezentsev and E. G. Shapiro, "Dispersion-Managed Solitons and Optimization of the Dispersion Management," *Opt. Fiber Tech.* **4**:384–452 (1998).
53. J. P. Gordon and L. F. Mollenauer, "Scheme for Characterization of Dispersion-Managed Solitons," *Opt. Lett.* **24**:223–225 (1999).
54. P. V. Mamyshev and N. A. Mamysheva, "Pulse-Overlapped Dispersion-Managed Data Transmission and Intra-Channel Four-Wave Mixing," *Opt. Lett.* **24**:1454–1456 (1999).
55. D. Le Guen, S. Del Burgo, M. L. Moulinard, D. Grot, M. Henry, F. Favre, and T. Georges, "Narrow Band 1.02 Tbit/s (51×20 gbit/s) Soliton DWDM Transmission over 1000 km of Standard Fiber with 100 km Amplifier Spans," *OFC-99,* postdeadline paper PD-4.
56. S. Wabnitz, *Opt. Lett.* **21**:638–640 (1996).
57. E. A. Golovchenko, A. N. Pilipetskii, and C. R. Menyuk, *Opt. Lett.* **22**:1156–1158 (1997).
58. A. M. Niculae, W. Forysiak, A. G. Gloag, J. H. B. Nijhof, and N. J. Doran, "Soliton Collisions with Wavelength-Division Multiplexed Systems with Strong Dispersion Management," *Opt. Lett.* **23**:1354–1356 (1998).
59. P. V. Mamyshev and L. F. Mollenauer, "Soliton Collisions in Wavelength-Division-Multiplexed Dispersion-Managed Systems," *Opt. Lett.* **24**:448–450 (1999).
60. L. F. Mollenauer, P. V. Mamyshev, and J. P. Gordon, "Effect of Guiding Filters on the Behavior of Dispersion-Managed Solitons," *Opt. Lett.* **24**:220–222 (1999).
61. M. Matsumoto, *Opt. Lett.* **23**:1901–1903 (1998).
62. M. Matsumoto, *Electron. Lett.* **33**:1718 (1997).
63. L. F. Mollenauer, P. V. Mamyshev, J. Gripp, M. J. Neubelt, N. Mamysheva, L. Gruner-Nielsen, and T. Veng, "Demonstration of Massive WDM over Transoceanic Distances Using Dispersion Managed Solitons," *Optics Letters* **25**:704–706 (2000).

CHAPTER 8
TAPERED-FIBER COUPLERS, MUX AND DEMUX

Daniel Nolan
Corning Inc.
Corning, New York

8.1 INTRODUCTION

Fiber-optic couplers, including splitters and wavelength-division multiplexing (WDM) components, have been used extensively over the last two decades. This use continues to grow both in quantity and in the ways in which the devices are used. The uses today include, among other applications, simple splitting for signal distribution and wavelength multiplexing and demultiplexing multiple wavelength signals.

Fiber-based splitters and WDM components are among the simplest devices. Other technologies that can be used to fabricate components that exhibit similar functions include the planar waveguide and micro-optic technologies. These devices are, however, most suitable for integrated-optics in the case of planar or more complex devices in the case of micro-optic components. In this chapter, we will show the large number of optical functions that can be achieved with simple tapered fiber components. We will also describe the physics of the propagation of light through tapers in order to better understand the breadth of components that can be fabricated with this technology. The phenomenon of coupling includes an exchange of power that can depend both on wavelength and on polarization. Beyond the simple 1×2 power splitter, other devices that can be fabricated from tapered fibers include $1 \times N$ devices, wavelength multiplexing, polarization multiplexing, switches, attenuators, and filters.

Fiber-optic couplers have been fabricated since the early seventies. The fabrication technologies have included fusion tapering,[1–3] etching,[4] and polishing.[5–7] The tapered single-mode fiber-optic power splitter is perhaps the most universal of the single-mode tapered devices.[8] It has been shown that the power transferred during the tapering process involves an initial adiabatic transfer of the power in the input core to the cladding/air interface.[9] The light is then transferred to the adjacent core-cladding mode. During the up-tapering process, the input light will transfer back onto the fiber cores. In this case, it is referred to as a *cladding mode coupling device.* Light that is transferred to a higher-order mode of the core-cladding structure leads to an excess loss. This is because these higher-order modes are not bounded by the core and are readily stripped by the higher index of the fiber coating.

In the tapered fiber coupler process, two fibers are brought into close proximity after the protective plastic jacket is removed. Then, in the presence of a torch, the fibers are fused and

Copyright 2001 by The McGraw-Hill Companies, Inc. Click Here for Terms of Use.

stretched (see Fig. 1). The propagation of light through this tapered region is described using Maxwell's vector equations, but for a good approximation the scalar wave equation is valid. The scalar wave equation, written in cylindrical coordinates, is expressed as

$$[1/r\ d/dr\ r\ d/dr - \hat{v}^2/r^2 + k^2nl^2 - \beta^2 - (V/a)^2\ f(r/a)]\ \psi = \varepsilon\mu\ d^2\psi/dt^2 \tag{1}$$

In Eq. (1), $n1$ is the index value at $r = 0$, β is the propagation constant, which is to be determined, a is the core radius, $f(r/a)$ is a function describing the index distribution with radius, and V is the modal volume

$$V = 2\pi an1\ \frac{[\sqrt{[2\Delta]}]}{\lambda} \tag{2}$$

With

$$\Delta = \frac{[n1^2 - n2^2]}{[2n1^2]} \tag{3}$$

As light propagates in the single-mode fiber, it is not confined to the core region, but extends out into the surrounding region. As the light propagates through the tapered region, it is bounded by the shrinking, air-cladding boundary.

In the simplest case, the coupling from one cladding to the adjacent one can be described by perturbation theory.[10] In this case, the cladding air boundary is considered as the waveguide outer boundary, and the exchange of power along z is described as

$$P = \sin^2 [CZ] \tag{4}$$

$$C = 2\pi/[\lambda\alpha^2]\ \sqrt{[1 - (n1/n2)^2]} \tag{5}$$

$$[n1^2 - n2^2]/(n1^2 - n2^2)^{1.5}$$

$$\mathrm{K0}[2(\alpha + (2\pi d/\lambda))\ \sqrt{[n1^2 - n2^2]}]/$$

$$K1^2\left\{\alpha\sqrt{[n1^2 - n^2]}\right\}$$

with

$$\alpha = 2\pi n1/\lambda \tag{6}$$

It is important to point out that Eqs. (4) and (5) are only a first approximation. These equations are derived using first-order perturbation theory. Also, the scalar wave equation is not strictly

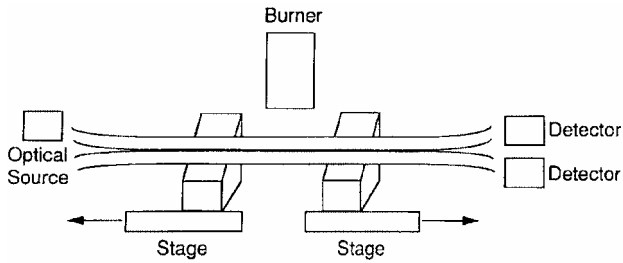

FIGURE 1 Fused biconic tapered coupler process. The fibers are stripped of their coating and fused and tapered using a heat source.

valid under the presence of large index differences, such as at a glass/air boundary. However, these equations describe a number of important effects. The sinusoidal dependence of the power coupled with wavelength, as well as the dependence of power transfer with cladding diameter and other dependencies, is well described with the model.

Equation (4) can be described by considering the light input to one core as a superposition of symmetric and antisymmetric modes.[10] These modes are eigen solutions to the composite two-core structure. The proper superposition of these two modes enables one to impose input boundary conditions for the case of a two-core structure. The symmetric and antisymmetric modes are written

$$\Psi s = \frac{[\psi 1 + \psi 2]}{\sqrt{2}} \tag{7}$$

$$\Psi a = \frac{[\psi 1 - \psi 2]}{\sqrt{2}} \tag{8}$$

Light input onto one core is described with $\Psi 1$ at $z = 0$,

$$\Psi 1 = \frac{[\psi s + \psi a]}{\sqrt{2}} \tag{9}$$

Propagation through the coupler is characterized with the superposition of Ψs and Ψa. This superposition describes the power transfer between the two guides along the direction of propagation.[10] The propagation constants of Ψs and Ψa are slightly different, and this value can be used to estimate excess loss under certain perturbations.

8.2 ACHROMATICITY

The simple sinusoidal dependence of the coupling with wavelength as just described is not always desired, and often a more achromatic dependence of the coupling is required. This can be achieved when dissimilar fibers[10] are used to fabricate the coupler. Fibers are characterized as dissimilar when the propagation constants of the guides are of different values. When dissimilar fibers (see Fig. 2) are used, Eqs. (4) and (5) can be replaced with

$$P1(z) = P1(0) + F^2 \{P2(0) - P1(0) + [(B_1 - B_2)/C]\,[P1(0)\,P2(0)]^5\}\,\sin^2(Cz/F) \tag{10}$$

where

$$F = 1./\left\{1 + \frac{B_1^2 - B_c^2}{4C^2}/[4\,C^2]\right\}^{1/2} \tag{11}$$

In most cases, the fibers are made dissimilar by changing the cladding diameter of one of the fibers. Etching or pre-tapering one of the fibers can do this. Another approach is to slightly change the cladding index of one of the fibers.[11] When dissimilar fibers are used, the total amount of power coupled is limited. As an example, an achromatic 3 dB coupler is made achromatic by operating at the sinusoidal maximum with wavelength rather than at the power of maximum power change with wavelength. Another approach to achieve achromaticity is to taper the device such that the modes expand well beyond the cladding boundaries.[12] This condition greatly weakens the wavelength dependence of the coupling. This has been achieved by encapsulating the fibers in a third matrix glass with an index very close to that of the fiber's cladding index. The difference in index between the cladding and the matrix glass is on the order of 0.001. The approach of encapsulating the fibers in a third-index material[13,14] is also

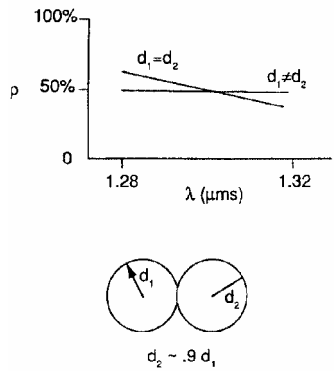

FIGURE 2 Achromatic couplers are fabricated by tapering two fibers with different propagating characteristics in the region of coupling.

useful for reasons other than achromaticity. One reason is that the packaging process is simplified. Also, a majority of couplers made for undersea applications use this method because it is a proven approach to ultra high reliability.

The wavelength dependence of the couplers just described is most often explained using mode coupling and perturbation theory. Often, numerical analysis is required in order to explain the effects that the varying taper angles have on the overall coupling. An important numerical approach is the beam propagation method.[15] In this approach, the propagation of light through a device is solved by an expansion of the evolution operator using a Taylor series and with the use of fast Fourier transforms to evaluate the appropriate derivatives. In this way, the propagation of the light can be studied as it couples to the adjacent guides or to higher order modes.

8.3 WAVELENGTH DIVISION MULTIPLEXING

Besides power splitting, tapered couplers can be used to separate wavelengths. To accomplish this separation, we utilize the wavelength dependence of Eqs. (4) and (5). By proper choice of the device length and taper ratio, two predetermined wavelengths can be put out onto two different ports. Wavelengths from 50 to 600 nms can be split using this approach. Applications include the splitting and/or combining of 1480 nm and 1550 nm light, as well as multiplexing 980 nm and 1550 nm onto an erbium fiber for signal amplification. Also important is the splitting of the 1310 to 1550 nm wavelength bands, which can be achieved using this approach.

8.4 1 × N POWER SPLITTERS

Often it is desirable to split a signal onto a number of output ports. This can be achieved by concatenating 1×2 power splitters. Alternatively, one can split the input simultaneously onto multiple output ports[16,17] (see Fig. 3). Typically, the output ports are of the form 2^N (i.e., 2, 4, 8, 16). The configuration of the fibers in the tapered region affects the distribution of the output power per port. A good approach to achieve uniform 1×8 splitting is described in Ref. 18.

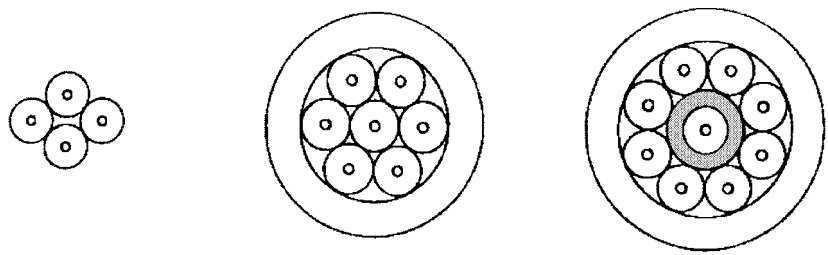

FIGURE 3 MXN couplers are fabricated by fusing and tapering fibers of the appropriate configuration. These configurations have been commercialized by Gould, BT&D, and Corning.

8.5 SWITCHES AND ATTENUATORS

In a tapered device, the power coupled over to the adjacent core can be significantly affected by bending the device at the midpoint. By encapsulating two fibers before tapering in a third index medium (see Fig. 4), the device is rigid and can be reliably bent in order to frustrate the coupling. The bending establishes a difference in the propagation constants of the two guiding media, preventing coupling or power transfer.

This approach can be used to fabricate both switches and attenuators. Switches with up to 30 dB crosstalk and attenuators with variable crosstalk up to 30 dB as well over the erbium wavelength band have been fabricated. Displacing one end of a 1-cm taper by 1 millimeter is enough to alter the crosstalk by the 30-dB value. Applications for attenuators have been increasing significantly over the last few years. An important reason is to maintain the gain in erbium-doped fiber amplifiers. This is achieved by limiting the amount of pump power into the erbium fiber. Over time, as the pump degrades, the power output of the attenuator is increased in order to compensate for the pump degradation.

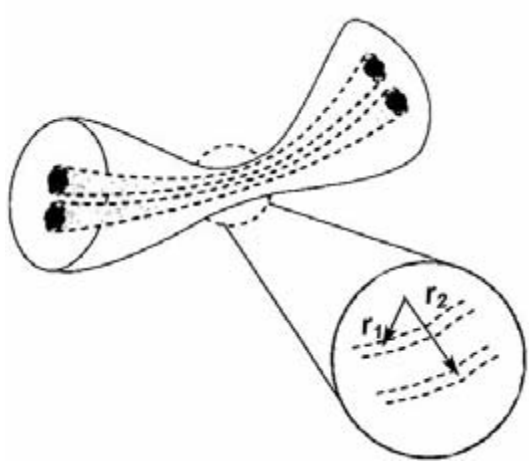

FIGURE 4 The coupling can be affected by bending the coupler at the midsection. Switched and variable attenuators are fabricated in this manner.

8.6 MACH-ZEHNDER DEVICES

Devices to split narrowly spaced wavelengths are very important. As previously mentioned, tapers can be designed such that wavelengths from 60 nm to 600 nm can be split in a tapered device. Dense WDM networks require splitting of wavelengths with separations on the order of nms. Fiber-based Mach-Zehnder devices enable such splitting. Monolithic fiber-based Mach-Zehnders can be fabricated using fibers with different cores (see Fig. 5),[20] (i.e., different propagation constants). Two or more tapers can be used to cause light from two different optical paths to interfere. The dissimilar cores enable light to propagate at different speeds between the tapers, causing the required constructive and destructive interference. These devices are environmentally stable due to the monolithic structure. Mach-Zehnders can also be fabricated using fibers with different lengths between the tapers. In this approach, it is the packaging that enables an environmentally stable device.

Multiple tapers can be used to fabricate devices with a wavelength spectra with higher-order Fourier components.[23] Figure 6 shows the spectrum of a three-tapered band splitter.

Mach-Zehnders and lattice filters can also be fabricated by tapering single-fiber devices.[24] In the tapered regions, the light couples to a cladding mode. The cladding mode propagates between tapers since a lower index overcladding replaces the higher index coating material. An interesting application for these devices is as gain-flattening filters for amplifiers.

8.7 POLARIZATION DEVICES

It is well-known that two polarization modes propagate in single-mode fiber. Most optical fiber modules allow both polarizations to propagate, but specify that the performance of the components be insensitive to the polarization states of the propagating light. However, this is often not the situation for fiber-optic sensor applications. Often, the state of polarization is important to the operation of the sensor itself. In these situations, polarization-maintaining fiber is used. Polarization components such as polarization-maintaining couplers and also single-

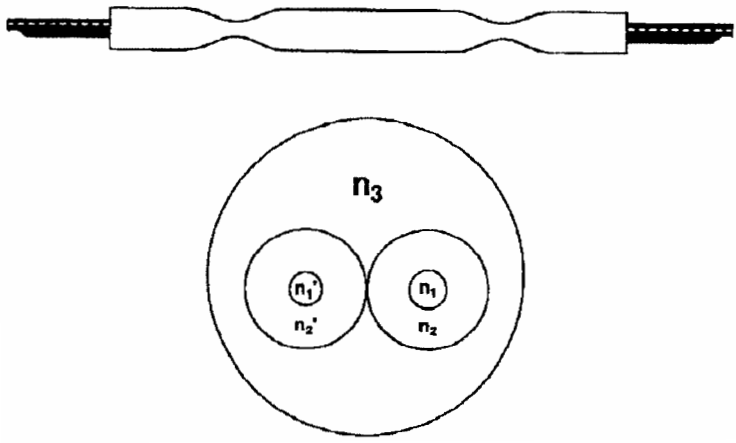

FIGURE 5 Narrow-band WDM devices can be fabricated by multiply tapering two fibers with different cores.

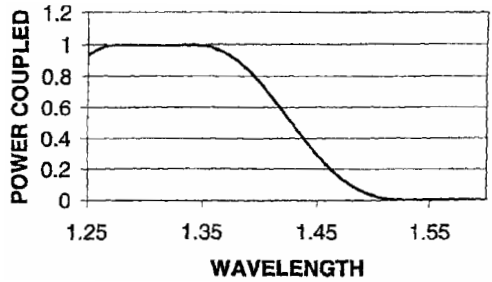

FIGURE 6 Band splitters are fabricated with three tapers.

polarization devices are used. In polarization-maintaining fiber, a difference in propagation constants of the polarization modes prevents mode coupling or exchange of energy. This is achieved by introducing stress or shape birefringence within the fiber core. A significant difference between the two polarization modes is maintained as the fiber twists in a cable or package.

In many fiber sensor systems, tapered fiber couplers are used to couple light from one core to another. Often the couplers are composed of birefringent fibers[24] (see Fig. 7). This is done in order to maintain the alignment of the polarizations to the incoming and outgoing fibers and also to maintain the polarization states within the device. The axes of the birefringent fibers are aligned before tapering, and care is taken not to excessively twist the fibers during the tapering process.

The birefringent fibers contain stress rods, elliptical core fibers, or inner claddings in order to maintain the birefringence. The stress rods in some birefringent fibers have an index higher than the silica cladding. In the tapering process, this can cause light to be trapped in these

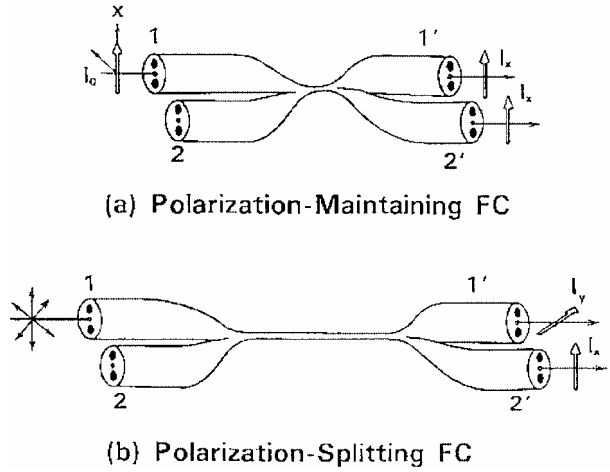

FIGURE 7 Polarization-maintaining couplers and polarization splitters are fabricated using polarization-maintaining fibers.

rods, resulting in an excess loss in the device. Stress rods with an index lower than that of silica can be used in these fibers, resulting in very low-loss devices.

8.8 SUMMARY

Tapered fiber couplers are extremely useful devices. Such devices include 1×2 and $1 \times N$ power splitters, wavelength-division multiplexers and filters, and polarization-maintaining and splitting components. Removing the fiber's plastic coating and then fusing and tapering two or more fibers in the presence of heat forms these devices. The simplicity and flexibility of this fabrication process is in part responsible for the widespread use of these components. The mechanism involved in the fabrication process is reasonably understood and simple, which is in part responsible for the widespread deployment of these devices. These couplers are found in optical modules for the telecommunication industry and in assemblies for the sensing industry. They are also being deployed as standalone components for fiber-to-the-home applications.

8.9 REFERENCES

1. T. Ozeki and B. S. Kawaski, "New Star Coupler Compatible with Single Multimode Fiber Links," *Elect. Lett.* **12**:151–152 (1976).
2. B. S. Kawaski and K. O. Hill, "Low Loss Access Coupler for Multimode Optical Fiber Distribution Networks," *Applied Optics* **16**:1794–1795 (1977).
3. G. E. Rawson and M. D. Bailey, "Bitaper Star Couplers with Up to 100 Fiber Channels," *Electron Lett.* **15**:432–433 (1975).
4. S. K. Sheem and T. G. Giallorenzi, "Single-Mode Fiber Optical Power Divided; Encapsulated Etching Technique," *Opt. Lett.* **4**:31 (1979).
5. Y. Tsujimoto, H. Serizawa, K. Hatori, and M. Fukai, "Fabrication of Low Loss 3 dB Couplers with Multimode Optical Fibers," *Electron Lett.* **14**:157–158 (1978).
6. R. A. Bergh, G. Kotler, and H. J. Shaw, "Single-Mode Fiber Optic Directional Coupler," *Electron Lett.* **16**:260–261 (1980).
7. O. Parriaux, S. Gidon, and A. Kuznetsov, "Distributed Coupler on Polished Single-Mode Fiber," *Appl. Opt.* **20**:2420–2423 (1981).
8. B. S. Kawaski, K. O. Hill, and R. G. Lamont, "Biconical—Taper Single-Mode Fiber Coupler," *Opt. Lett.* **6**:327 (1981).
9. R. G. Lamont, D. C. Johnson, and K. O. Hill, *Appl Opt.* **24**:327–332 (1984).
10. A. Snyder and J. D. Love, *Optical Waveguide Theory,* Chapman and Hall, 1983.
11. W. J. Miller, C. M. Truesdale, D. L. Weidman, and D. R. Young, U.S. Patent 5,011,251 (April 1991).
12. D. L. Weidman, "Achromat Overclad Coupler," U.S. Patent 5,268,979 (December 1993).
13. C. M. Truesdale and D. A. Nolan, "Core-Clad Mode Coupling in a New Three-Index Structure," European Conference on Optical Communications, Barcelona Spain, 1986.
14. D. B. Keck, A. J. Morrow, D. A. Nolan, and D. A. Thompson, *J. of Lightwave Technology* **7**:1623–1633 (1989).
15. M. D. Feit and J. A. Fleck, "Simple Spectral Method for Solving Propagation Problems in Cylcindrical Geometry with Fast Fourier Transforms," *Optics Letters* **14**:662–664 (1989).
16. D. B. Mortimore and J. W. Arkwright, "Performance of Wavelength-Flattened 1×7 Fused Couplers," Optical Fiber Conference, TUG6 (1990).
17. D. L. Weidman, "A New Approach to Achromaticity in Fused $1 \times N$ Couplers," Optical Fiber Conference, Post Deadline papers (1994).

18. W. J. Miller, D. A. Nolan, and G. E. Williams, "Method of Making a 1 × N Coupler," U.S. Patent 5,017,206.
19. M. A. Newhouse and F. A. Annunziata, "Single-Mode Optical Switch," *Technical Digest of the National Fiber Optic Conference,* 1990.
20. D. A. Nolan and W. J. Miller, "Wavelength Tunable Mach-Zehnder Device," Optical Fiber Conference (1994).
21. B. Malo, F. Bilodeau, K. O. Hill, and J. Albert, *Electron. Lett.* **25**:1416, (1989).
22. C. Huang, H. Luo, S. Xu, and P. Chen, "Ultra Low Loss, Temperature Insensitive 16 channel 100 Ghz Dense WDMs Based on Cascaded All Fiber Unbalanced Mach-Zehnder Structure," Optical Fiber Conference, TUH2 (1999).
23. D. A. Nolan, W. J. Miller, and R. Irion, "Fiber Based Band Splitter," Optical Fiber Conference (1998).
24. D. A. Nolan, W. J. Miller, G. Berkey, and L. Bhagavatula, "Tapered Lattice Filters," Optical Fiber Conference, TUH4 (1999).
25. I. Yokohama, M. Kawachi, K. Okamoto, and J. Noda, *Electron. Lett.* **22**:929, 1986.

This page intentionally left blank.

CHAPTER 9
FIBER BRAGG GRATINGS

Kenneth O. Hill
Communications Research Centre
Ottawa, Ontario, Canada

Nu-Wave Photonics
Ottawa, Ontario, Canada

9.1 GLOSSARY

FBG	fiber Bragg grating
FWHM	full width measured at half-maximum intensity
N_{eff}	effective refractive index for light propagating in a single mode
pps	pulses per second
β	propagation constant of optical fiber mode
Δn	magnitude of photoinduced refractive index change
κ	grating coupling coefficient
Λ	spatial period (or pitch) of spatial feature measured along optical fiber
λ	vacuum wavelength of propagating light
λ_B	Bragg wavelength
L	length of grating

9.2 INTRODUCTION

A fiber Bragg grating (FBG) is a periodic variation of the refractive index of the fiber core along the length of the fiber. The principal property of FBGs is that they reflect light in a narrow bandwidth that is centered about the Bragg wavelength, λ_B, which is given by $\lambda_B = 2N_{\text{eff}}\Lambda$, where Λ is the spatial period (or pitch) of the periodic variation and N_{eff} is the effective refractive index for light propagating in a single mode, usually the fundamental mode of a monomode optical fiber. The refractive index variations are formed by exposure of the fiber core to an intense optical interference pattern of ultraviolet light. The capability of light to induce permanent refractive index changes in the core of an optical fiber has been named photosensitivity. Photosensitivity was discovered by Hill et al. in 1978 at the Communications

Copyright 2001 by The McGraw-Hill Companies, Inc. Click Here for Terms of Use.

Research Centre in Canada (CRC).[1,2] The discovery has led to techniques for fabricating Bragg gratings in the core of an optical fiber and a means for manufacturing a wide range of FBG-based devices that have applications in optical fiber communications and optical sensor systems.

This chapter reviews the characteristics of photosensitivity, the properties of Bragg gratings, the techniques for fabricating Bragg gratings in optical fibers, and some FBG devices. More information on FBGs can be found in the following references, which are reviews on Bragg grating technology,[3,4] the physical mechanisms underlying photosensitivity,[5] applications for fiber gratings,[6] and the use of FBGs as sensors[7].

9.3 PHOTOSENSITIVITY

When ultraviolet light radiates an optical fiber, the refractive index of the fiber is changed permanently; the effect is termed *photosensitivity.* The change in refractive index is permanent in the sense that it will last for several years (lifetimes of 25 years are predicted) if the optical waveguide after exposure is annealed appropriately; that is, by heating for a few hours at a temperature of 50°C above its maximum anticipated operating temperature.[8] Initially, photosensitivity was thought to be a phenomenon that was associated only with germanium-doped-core optical fibers. Subsequently, photosensitivity has been observed in a wide variety of different fibers, many of which do not contain germanium as dopant. Nevertheless, optical fiber with a germanium-doped core remains the most important material for the fabrication of Bragg grating–based devices.

The magnitude of the photoinduced refractive index change (Δn) obtained depends on several different factors: the irradiation conditions (wavelength, intensity, and total dosage of irradiating light), the composition of glassy material forming the fiber core, and any processing of the fiber prior and subsequent to irradiation. A wide variety of different continuous-wave and pulsed-laser light sources, with wavelengths ranging from the visible to the vacuum ultraviolet, have been used to photoinduce refractive index changes in optical fibers. In practice, the most commonly used light sources are KrF and ArF excimer lasers that generate, respectively, 248- and 193-nm light pulses (pulse width ~10 ns) at pulse repetition rates of 50 to 100 pps. Typically, the fiber core is exposed to laser light for a few minutes at pulse levels ranging from 100 to 1000 mJ cm^{-2} $pulse^{-1}$. Under these conditions, Δn is positive in germanium-doped monomode fiber with a magnitude ranging between 10^{-5} and 10^{-3}.

The refractive index change can be enhanced (photosensitization) by processing the fiber prior to irradiation using such techniques as *hydrogen loading*[9] or *flame brushing.*[10] In the case of hydrogen loading, a piece of fiber is put in a high-pressure vessel containing hydrogen gas at room temperature; pressures of 100 to 1000 atmospheres (atm; 101 kPa/atm) are applied. After a few days, hydrogen in molecular form has diffused into the silica fiber; at equilibrium the fiber becomes saturated (i.e., loaded) with hydrogen gas. The fiber is then taken out of the high-pressure vessel and irradiated before the hydrogen has had sufficient time to diffuse out. Photoinduced refractive index changes up to 100 times greater are obtained by hydrogen loading a Ge-doped-core optical fiber. In flame brushing, the section of fiber that is to be irradiated is mounted on a jig and a hydrogen-fueled flame is passed back and forth (i.e., brushed) along the length of the fiber. The brushing takes about 10 minutes, and upon irradiation, an increase in the photoinduced refractive index change by about a factor of 10 can be obtained.

Irradiation at intensity levels higher than 1000 mJ/cm^2 marks the onset of a different nonlinear photosensitive process that enables a single irradiating excimer light pulse to photoinduce a large index change in a small localized region near the core/cladding boundary of the fiber. In this case, the refractive index changes are sufficiently large to be observable with a phase contrast microscope and have the appearance of physically damaging the fiber. This phenomenon has been used for the writing of gratings using a single-excimer light pulse.

Another property of the photoinduced refractive index change is *anisotropy.* This characteristic is most easily observed by irradiating the fiber from the side with ultraviolet light that is polarized perpendicular to the fiber axis. The anisotropy in the photoinduced refractive index change results in the fiber becoming birefringent for light propagating through the fiber. The effect is useful for fabricating polarization mode-converting devices or rocking filters.[11]

The physical processes underlying photosensitivity have not been fully resolved. In the case of germanium-doped glasses, photosensitivity is associated with GeO color center defects that have strong absorption in the ultraviolet (~242 nm) wavelength region. Irradiation with ultraviolet light bleaches the color center absorption band and increases absorption at shorter wavelengths, thereby changing the ultraviolet absorption spectrum of the glass. Consequently, as a result of the Kramers-Kronig causality relationship,[12] the refractive index of the glass also changes; the resultant refractive index change can be sensed at wavelengths that are far removed from the ultraviolet region extending to wavelengths in the visible and infrared. The physical processes underlying photosensitivity are, however, probably much more complex than this simple model. There is evidence that ultraviolet light irradiation of Ge-doped optical fiber results in structural rearrangement of the glass matrix leading to densification, thereby providing another mechanism for contributing to the increase in the fiber core refractive index. Furthermore, a physical model for photosensitivity must also account for the small anisotropy in the photoinduced refractive index change and the role that hydrogen loading plays in enhancing the magnitude of the photoinduced refractive change. Although the physical processes underlying photosensitivity are not completely known, the phenomenon of glass-fiber photosensitivity has the practical result of providing a means, using ultraviolet light, for photoinducing permanent changes in the refractive index at wavelengths that are far removed from the wavelength of the irradiating ultraviolet light.

9.4 PROPERTIES OF BRAGG GRATINGS

Bragg gratings have a periodic index structure in the core of the optical fiber. Light propagating in the Bragg grating is backscattered slightly by Fresnel reflection from each successive index perturbation. Normally, the amount of backscattered light is very small except when the light has a wavelength in the region of the Bragg wavelength, λ_B, given by

$$\lambda_B = 2N_{eff}\Lambda$$

where N_{eff} is the modal index and Λ is the grating period. At the Bragg wavelength, each back reflection from successive index perturbations is in phase with the next one. The back reflections add up coherently and a large reflected light signal is obtained. The reflectivity of a strong grating can approach 100 percent at the Bragg wavelength, whereas light at wavelengths longer or shorter than the Bragg wavelength pass through the Bragg grating with negligible loss. It is this wavelength-dependent behavior of Bragg gratings that makes them so useful in optical communications applications. Furthermore, the optical pitch ($N_{eff}\Lambda$) of a Bragg grating contained in a strand of fiber is changed by applying longitudinal stress to the fiber strand. This effect provides a simple means for sensing strain optically by monitoring the concomitant change in the Bragg resonant wavelength.

Bragg gratings can be described theoretically by using coupled-mode equations.[4, 6, 13] Here, we summarize the relevant formulas for tightly bound monomode light propagating through a uniform grating. The grating is assumed to have a sinusoidal perturbation of constant amplitude, Δn. The reflectivity of the grating is determined by three parameters: (1) the coupling coefficient, κ, (2) the mode propagation constant, $\beta = 2\pi N_{eff}/\lambda$, and (3) the grating length, L. The coupling coefficient, κ, which depends only on the operating wavelength of the light and the amplitude of the index perturbation, Δn, is given by $\kappa = (\pi/\lambda)\Delta n$. The most interesting case is when the wavelength of the light corresponds to the Bragg wavelength. The grating reflec-

tivity, R, of the grating is then given by the simple expression, $R = \tanh^2(\kappa L)$, where κ is the coupling coefficient at the Bragg wavelength and L is the length of the grating. Thus, the product κL can be used as a measure of grating strength. For $\kappa L = 1, 2, 3$, the grating reflectivity is, respectively, 58, 93, and 99 percent. A grating with a κL greater than one is termed a strong grating, whereas a weak grating has κL less than one. Figure 1 shows the typical reflection spectra for weak and strong gratings.

The other important property of the grating is its bandwidth, which is a measure of the wavelength range over which the grating reflects light. The bandwidth of a fiber grating that is most easily measured is its full width at half-maximum, $\Delta\lambda_{FWHM}$, of the central reflection peak, which is defined as the wavelength interval between the 3-dB points. That is the separation in the wavelength between the points on either side of the Bragg wavelength where the reflectivity has decreased to 50 percent of its maximum value. However, a much easier quantity to calculate is the bandwidth, $\Delta\lambda_0 = \lambda_0 - \lambda_B$, where λ_0 is the wavelength where the first zero in the reflection spectra occurs. This bandwidth can be found by calculating the difference in the propagation constants, $\Delta\beta_0 = \beta_0 - \beta_B$, where $\beta_0 = 2\pi N_{eff}/\lambda_0$ is the propagation constant at wavelength λ_0 for which the reflectivity is first zero, and $\beta_B = 2\pi N_{eff}/\lambda_B$ is the propagation constant at the Bragg wavelength for which the reflectivity is maximum.

In the case of weak gratings ($\kappa L < 1$), $\Delta\beta_0 = \beta_0 - \beta_B = \pi/L$, from which it can be determined that $\Delta\lambda_{FWHM} \sim \Delta\lambda_0 = \lambda_B^2/2N_{eff}L$; the bandwidth of a weak grating is inversely proportional to the grating length, L. Thus, long, weak gratings can have very narrow bandwidths. The first

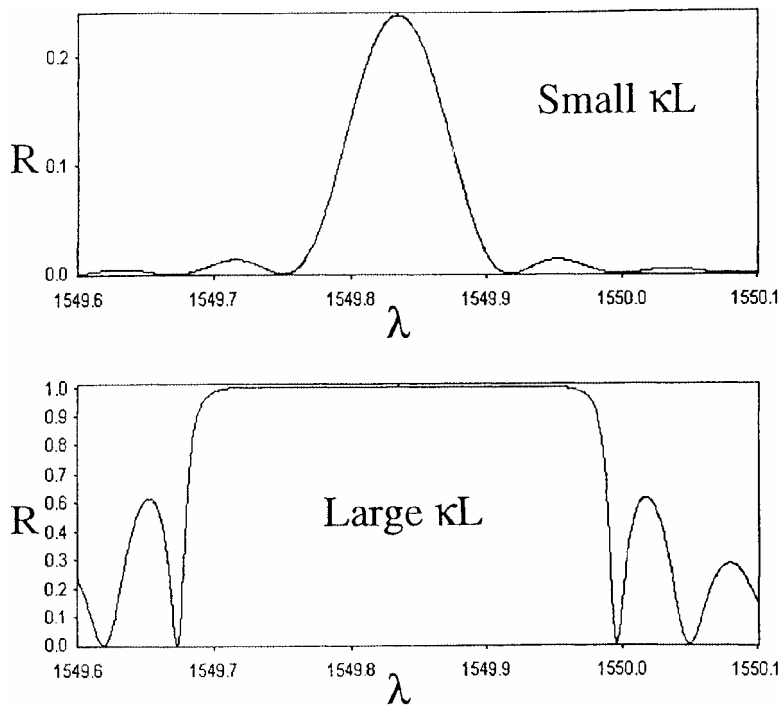

FIGURE 1 Typical reflection spectra for weak (small κL) and strong (large κL) fiber gratings.

Bragg grating written in fibers[1,2] was more than 1 m long and had a bandwidth less than 100 MHz, which is an astonishingly narrow bandwidth for a reflector of visible light. On the other hand, in the case of a strong grating ($\kappa L > 1$), $\Delta\beta_0 = \beta_0 - \beta_B = 4\kappa$ and $\Delta\lambda_{FWHM} \sim 2\Delta\lambda_0 = 4\lambda_B^2\kappa/\pi N_{eff}$. For strong gratings, the bandwidth is directly proportional to the coupling coefficient, κ, and is independent of the grating length.

9.5 FABRICATION OF FIBER GRATINGS

Writing a fiber grating optically in the core of an optical fiber requires irradiating the core with a periodic interference pattern. Historically, this was first achieved by interfering light that propagated in a forward direction along an optical fiber with light that was reflected from the fiber end and propagated in a backward direction.[1] This method for forming fiber gratings is known as the *internal writing technique,* and the gratings were referred to as *Hill gratings.* The Bragg gratings, formed by internal writing, suffer from the limitation that the wavelength of the reflected light is close to the wavelength at which they were written (i.e., at a wavelength in the blue-green spectral region).

A second method for fabricating fiber gratings is the *transverse holographic technique,*[14] which is shown schematically in Fig. 2. The light from an ultraviolet source is split into two beams that are brought together so that they intersect at an angle, θ. As Fig. 2 shows, the intersecting light beams form an interference pattern that is focused using cylindrical lenses (not shown) on the core of the optical fiber. Unlike the internal writing technique, the fiber core is irradiated from the side, thus giving rise to its name *transverse holographic technique.* The technique works because the fiber cladding is transparent to the ultraviolet light, whereas the core absorbs the light strongly. Since the period, Λ, of the grating depends on the angle, θ, between the two interfering coherent beams through the relationship $\Lambda = \lambda_{UV}/2 \sin(\theta/2)$, Bragg gratings can be made that reflect light at much longer wavelengths than the ultraviolet light that is used in the fabrication of the grating. Most important, FBGs can be made that function in the spectral regions that are of interest for fiber-optic communication and optical sensing.

A third technique for FBG fabrication is the *phase mask technique,*[15] which is illustrated in Fig. 3. The phase mask is made from a flat slab of silica glass, which is transparent to ultraviolet light. On one of the flat surfaces, a one-dimensional periodic surface relief structure is etched using photolithographic techniques. The shape of the periodic pattern approximates a square wave in profile. The optical fiber is placed almost in contact with and at right angles to the corrugations of the phase mask, as shown in Fig. 3. Ultraviolet light, which is incident normal to the

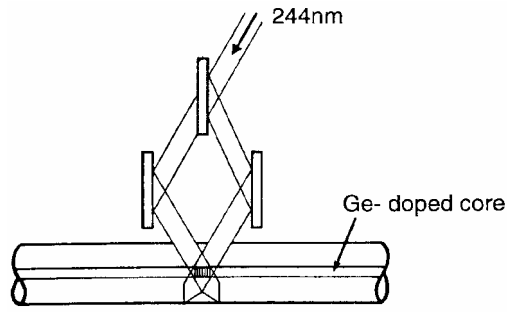

FIGURE 2 Schematic diagram illustrating the writing of an FBG using the transverse holographic technique.

phase mask, passes through and is diffracted by the periodic corrugations of the phase mask. Normally, most of the diffracted light is contained in the 0, +1, and −1 diffracted orders. However, the phase mask is designed to suppress the diffraction into the zero order by controlling the depth of the corrugations in the phase mask. In practice, the amount of light in the zero order can be reduced to less than 5 percent with approximately 80 percent of the total light intensity divided equally in the ±1 orders. The two ±1 diffracted-order beams interfere to produce a periodic pattern that photoimprints a corresponding grating in the optical fiber. If the period of the phase mask grating is Λ_{mask}, the period of the photoimprinted index grating is $\Lambda_{mask}/2$. Note that this period is independent of the wavelength of ultraviolet light that irradiates the phase mask.

The phase mask technique has the advantage of greatly simplifying the manufacturing process for Bragg gratings, while yielding high-performance gratings. In comparison with the holographic technique, the phase mask technique offers easier alignment of the fiber for photoimprinting, reduced stability requirements on the photoimprinting apparatus, and

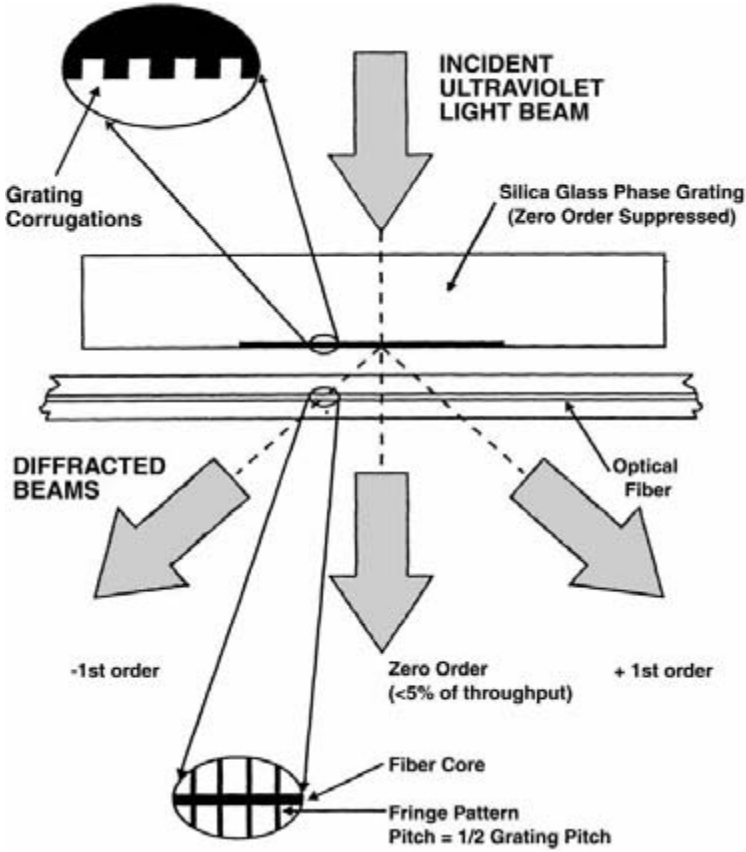

FIGURE 3 Schematic diagram of the phase mask technique for the manufacture of fiber Bragg gratings.

lower coherence requirements on the ultraviolet laser beam, thereby permitting the use of a cheaper ultraviolet excimer laser source. Furthermore, there is the possibility of manufacturing several gratings at once in a single exposure by irradiating parallel fibers through the phase mask. The capability to manufacture high-performance gratings at a low per-unit grating cost is critical for the economic viability of using gratings in some applications. A drawback of the phase mask technique is that a separate phase mask is required for each different Bragg wavelength. However, some wavelength tuning is possible by applying tension to the fiber during the photoimprinting process; the Bragg wavelength of the relaxed fiber will shift by ~2 nm.

The phase mask technique not only yields high-performance devices, but is also very flexible in that it can be used to fabricate gratings with controlled spectral response characteristics. For instance, the typical spectral response of a finite-length grating with a uniform index modulation along the fiber length has secondary maxima on both sides of the main reflection peak. In applications like wavelength-division multiplexing, this type of response is not desirable. However, if the profile of the index modulation, Δn, along the fiber length is given a bell-like functional shape, these secondary maxima can be suppressed.[16] The procedure is called *apodization.* Apodized fiber gratings have been fabricated using the phase mask technique, and suppressions of the sidelobes of 30 to 40 dB have been achieved,[17,18]

Figure 4 shows the spectral response of two Bragg gratings with the same full width at half-maximum (FWHM). One grating exhibits large sidebands, whereas the other has much-reduced sidebands. The one with the reduced sidebands is a little longer and has a coupling coefficient, κ, apodized as a second-degree cosine ($\cos^2$) along its length. Apodization has one disadvantage: It decreases the effective length of the Bragg grating. Therefore, to obtain fiber gratings having the same FWHM, the apodized fiber grating has a longer length than the equivalent-bandwidth unapodized fiber grating.

The phase mask technique has been extended to the fabrication of chirped or aperiodic fiber gratings. *Chirping* means varying the grating period along the length of the grating in order to broaden its spectral response. Aperiodic or chirped gratings are desirable for making dispersion compensators[19] or filters having broad spectral responses. The first chirped fiber gratings were made using a double-exposure technique.[20] In the first exposure, an opaque mask is positioned between the fiber and the ultraviolet beam blocking the light from irradiating the fiber. The mask is then moved slowly out of the beam at a constant velocity to increase continuously the length of the fiber that is exposed to the ultraviolet light. A continuous change in the photoinduced refractive index is produced that varies linearly along the fiber length with the largest index change occurring in the section of fiber that is exposed to ultraviolet light for the longest duration. In a second exposure, a fiber grating is photoimprinted in the fiber by using the standard phase mask technique. Because the optical pitch of a fiber grating depends on both the refractive index and the mechanical pitch (i.e., optical pitch = $N_{\text{eff}}\Lambda$), the pitch of the photoimprinted grating is effectively chirped, even though its mechanical period is constant. Following this demonstration, a variety of other methods have been developed to manufacture gratings that are chirped permanently[21,22] or that have an adjustable chirp.[23,24]

The phase mask technique can also be used to fabricate tilted or blazed gratings. Usually, the corrugations of the phase mask are oriented normal to the fiber axis, as shown in Fig. 3. However, if the corrugations of the phase mask are oriented at an angle to the axis of the fiber, the photoimprinted grating is tilted or blazed. Such fiber gratings couple light out from the bound modes of the fiber to either the cladding modes or the radiation modes. Tilted gratings have applications in fabricating fiber taps.[25] If the grating is simultaneously blazed and chirped, it can be used to fabricate an optical spectrum analyzer.[26]

Another approach to grating fabrication is the *point-by-point technique,*[27] also developed at CRC. In this method, each index perturbation of the grating is written point by point. For gratings with many index perturbations, the method is not very efficient. However, it has been used to fabricate micro-Bragg gratings in optical fibers,[28] but it is most useful for making coarse gratings with pitches of the order of 100 μm that are required for LP_{01} to LP_{11} mode

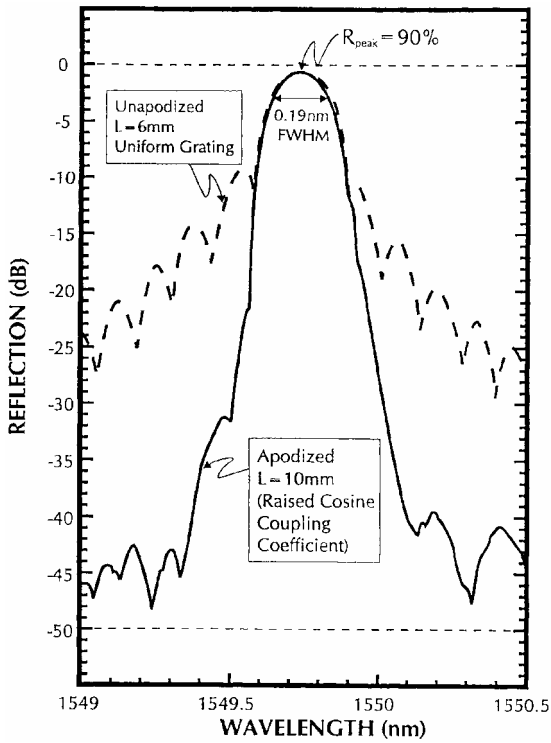

FIGURE 4 Comparison of an unapodized fiber grating's spectral response with that of an apodized fiber grating having the same bandwidth (FWHM).

converters[27] and polarization mode converters.[11] The interest in coarse period gratings has increased lately because of their use in long-period fiber-grating band-rejection filters[29] and fiber-amplifier gain equalizers.[30]

9.6 THE APPLICATION OF FIBER GRATINGS

Hill and Meltz[6] provide an extensive review of the many potential applications of fiber gratings in lightwave communication systems and in optical sensor systems. Our purpose here is to note that a common problem in using FBGs is that a transmission device is usually desired, whereas FBGs function as reflection devices. Thus, means are required to convert the reflection spectral response into a transmission response. This can be achieved using a Sagnac loop,[31] a Michleson (or Mach-Zehnder) interferometer,[32] or an optical circulator. Figure 5 shows an example of how this is achieved for the case of a multichannel dispersion compensator using chirped or aperiodic fiber gratings.

In Fig. 5*a,* the dispersion compensator is implemented using a Michelson interferometer. Each wavelength channel (λ_1, λ_2, λ_3) requires a pair of identically matched FBGs, one in each

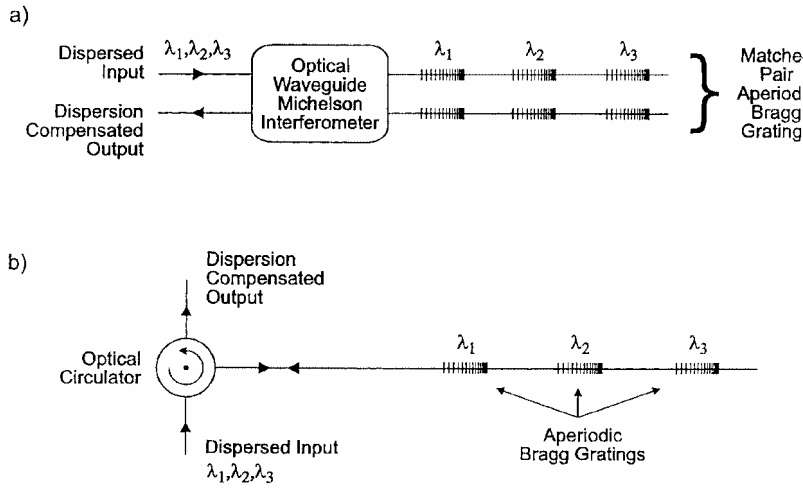

FIGURE 5 Schematic diagram of a multichannel dispersion compensator that is formed by using (*a*) a Michelson interferometer and (*b*) an optical circulator.

arm of the interferometer. Since it is difficult to fabricate identical Bragg gratings (i.e., having the same resonant wavelength and chirp), this configuration for the dispersion compensator has not yet been demonstrated. However, a wavelength-selective device that requires matched grating pairs has been demonstrated.[33,34] An additional disadvantage of the Michelson interferometer configuration being an interferometric device is that it would require temperature compensation. The advantage of using a Michelson interferometer is that it can be implemented in all-fiber or planar-integrated optics versions.

Figure 5*b* shows the dispersion compensator implemented using an optical circulator. In operation, light that enters through the input port is routed by the circulator to the port with the Bragg gratings. All of the light that is reflected by the FBGs is routed to the output channel. This configuration requires only one chirped FBG per wavelength channel and is the preferred method for implementing dispersion compensators using FBGs. The only disadvantage of this configuration is that the optical circulator is a bulk optic device (or microoptic device) that is relatively expensive compared with the all-fiber Michelson interferometer.

9.7 REFERENCES

1. K. O. Hill, Y. Fujii, D. C. Johnson, et al., "Photosensitivity in Optical Fiber Waveguides: Application to Reflection Filter Fabrication," *Applied Physics Letters* **32**(10)**:**647–649 (1978).
2. B. S. Kawasaki, K. O. Hill, D. C. Johnson, et al., "Narrow-Band Bragg Reflectors in Optical Fibers," *Optics Letters* **3**(8)**:**66–68 (1978).
3. K. O. Hill, B. Malo, F. Bilodeau, et al., "Photosensitivity in Optical Fibers," *Annual Review of Material Science* **23:**125–157 (1993).
4. I. Bennion, J. A. R. Williams, L. Zhang, et al., "Tutorial Review, UV-Written In-Fibre Bragg Gratings," *Optical and Quantum Electronics* **28:**93–135 (1996).

5. B. Poumellec, P. Niay, M. Douay, et al., "The UV-Induced Refractive Index Grating in Ge:SiO_2 Preforms: Additional CW Experiments and the Macroscopic Origin of the Change in Index," *Journal of Physics D, Applied Physics* **29:**1842–1856 (1996).
6. Kenneth O. Hill and Gerald Meltz, "Fiber Bragg Grating Technology Fundamentals and Overview," *Journal of Lightwave Technology* **15**(8)**:**1263–1276 (1997).
7. A. D. Kersey, M. A. Davis, H. J. Patrick, et al., "Fiber Grating Sensors," *Journal of Lightwave Technology* **15**(8)**:**1442–1463 (1997).
8. T. Erdogan, V. Mizrahi, P. J. Lemaire, et al., "Decay of Ultraviolet-Induced Fiber Bragg Gratings," *Journal of Applied Physics* **76**(1)**:**73–80 (1994).
9. P. J. Lemaire, R. M. Atkins, V. Mizrahi, et al., "High Pressure H_2 Loading as a Technique for Achieving Ultrahigh UV Photosensitivity and Thermal Sensitivity in GeO_2 Doped Optical Fibres," *Electronics Letters* **29**(13)**:**1191–1193 (1993).
10. F. Bilodeau, B. Malo, J. Albert, et al., "Photosensitization of Optical Fiber and Silica-on-Silicon/Silica Waveguides," *Optics Letters* **18**(12)**:**953–955 (1993).
11. K. O. Hill, F. Bilodeau, B. Malo, et al., "Birefringent Photosensitivity in Monomode Optical Fibre: Application to the External Writing of Rocking Filters," *Electronic Letters* **27**(17)**:**1548–1550 (1991).
12. Alan Miller, "Fundamental Optical Properties of Solids," in *Handbook of Optics,* edited by Michael Bass, McGraw-Hill, New York, 1995, vol. 1, pp. 9–15.
13. D. K. W. Lam and B. K. Garside, "Characterization of Single-Mode Optical Fiber Filters," *Applied Optics* **20**(3)**:**440–445 (1981).
14. G. Meltz, W. W. Morey, and W. H. Glenn, "Formation of Bragg Gratings in Optical Fibers by a Transverse Holographic Method," *Optics Letters* **14**(15)**:**823–825 (1989).
15. K. O. Hill, B. Malo, F. Bilodeau, et al., "Bragg Gratings Fabricated in Monomode Photosensitive Optical Fiber by UV Exposure Through a Phase Mask," *Applied Physics Letters* **62**(10)**:**1035–1037 (1993).
16. M. Matsuhara and K. O. Hill, "Optical-Waveguide Band-Rejection Filters: Design," *Applied Optics* **13**(12)**:**2886–2888 (1974).
17. B. Malo, S. Thériault, D. C. Johnson, et al., "Apodised In-Fibre Bragg Grating Reflectors Photoimprinted Using a Phase Mask," *Electronics Letters* **31**(3)**:**223–224 (1995).
18. J. Albert, K. O. Hill, B. Malo, et al., "Apodisation of the Spectral Response of Fibre Bragg Gratings Using a Phase Mask with Variable Diffraction Efficiency," *Electronics Letters* **31**(3)**:**222–223 (1995).
19. K. O. Hill, "Aperiodic Distributed-Parameter Waveguides for Integrated Optics," *Applied Optics* **13**(8)**:** 1853–1856 (1974).
20. K. O. Hill, F. Bilodeau, B. Malo, et al., "Chirped In-Fibre Bragg Grating for Compensation of Optical-Fiber Dispersion," *Optics Letters* **19**(17)**:**1314–1316 (1994).
21. K. Sugden, I. Bennion, A. Molony, et al., "Chirped Gratings Produced in Photosensitive Optical Fibres by Fibre Deformation during Exposure," *Electronics Letters* **30**(5)**:**440–442 (1994).
22. K. C. Byron and H. N. Rourke, "Fabrication of Chirped Fibre Gratings by Novel Stretch and Write Techniques," *Electronics Letters* **31**(1)**:**60–61 (1995).
23. D. Garthe, R. E. Epworth, W. S. Lee, et al., "Adjustable Dispersion Equaliser for 10 and 20 Gbit/s over Distances up to 160 km," *Electronics Letters* **30**(25)**:**2159–2160 (1994).
24. M. M. Ohn, A. T. Alavie, R. Maaskant, et al., "Dispersion Variable Fibre Bragg Grating Using a Piezoelectric Stack," *Electronics Letters* **32**(21)**:**2000–2001 (1996).
25. G. Meltz, W. W. Morey, and W. H. Glenn, "In-Fiber Bragg Grating Tap," presented at the Conference on Optical Fiber Communications, OFC'90, San Francisco, CA, 1990 (unpublished).
26. J. L. Wagener, T. A. Strasser, J. R. Pedrazzani, et al., "Fiber Grating Optical Spectrum Analyzer Tap," presented at the IOOC-ECOC'97, Edinburgh, UK, 1997 (unpublished).
27. K. O. Hill, B. Malo, K. A. Vineberg, et al., "Efficient Mode Conversion in Telecommunication Fibre Using Externally Written Gratings," *Electronics Letters* **26**(16)**:**1270–1272 (1990).
28. B. Malo, K. O. Hill, F. Bilodeau, et al., "Point-by-Point Fabrication of Micro-Bragg Gratings in Photosensitive Fibre Using Single Excimer Pulse Refractive Index Modification Techniques," *Electronic Letters* **29**(18)**:**1668–1669 (1993).

29. A. M. Vengsarkar, P. J. Lemaire, J. B. Judkins, et al., "Long-Period Fiber Gratings as Band-Rejection Filters," presented at the Optical Fiber Communication conference, OFC'95, San Diego, CA, 1995 (unpublished).
30. A. M. Vengsarkar, J. R. Pedrazzani, J. B. Judkins, et al., "Long-Period Fiber-Grating-Based gain equalizers," Optics Letters **21**(5)**:**336–338 (1996).
31. K. O. Hill, D. C. Johnson, F. Bilodeau, et al., "Narrow-Bandwidth Optical Waveguide Transmission Filters: A New Design Concept and Applications to Optical Fibre Communications," *Electronics Letters* **23**(9)**:**465–466 (1987).
32. D. C. Johnson, K. O. Hill, F. Bilodeau, et al., "New Design Concept for a Narrowband Wavelength-Selective Optical Tap and Combiner," *Electronics Letters* **23**(13)**:**668–669 (1987).
33. F. Bilodeau, K. O. Hill, B. Malo, et al., "High-Return-Loss Narrowband All-Fiber Bandpass Bragg Transmission Filter," *IEEE Photonics Technology Letters* **6**(1)**:**80–82 (1994).
34. F. Bilodeau, D. C. Johnson, S. Thériault, et al., "An All-Fiber Dense-Wavelength-Division Multiplexer/Demultiplexer Using Photoimprinted Bragg Gratings," *IEEE Photonics Technology Letters* **7**(4)**:**388–390 (1995).

This page intentionally left blank.

CHAPTER 10
MICRO-OPTICS-BASED COMPONENTS FOR NETWORKING

Joseph C. Palais
Department of Electrical Engineering
College of Engineering and Applied Sciences
Arizona State University
Tempe, Arizona

10.1 INTRODUCTION

The optical portion of many fiber networks requires a number of functional devices, some of which can be fabricated using small optical components (so-called *micro-optic* components). Micro-optic components are made up of parts that have linear dimensions on the order of a few millimeters. The completed functional device may occupy a space a few centimeters on a side. Components to be described in this section have the common feature that the fiber transmission link is opened and small (micro-optic) devices are inserted into the gap between the fiber ends to produce a functional component. Network components constructed entirely of fibers or constructed in integrated-optic form are described elsewhere in this Handbook.

The following sections describe, in order: a generalized component, specific useful network functions, microoptic subcomponents required to make up the final component, and complete components.

10.2 GENERALIZED COMPONENTS

A generalized fiber-optic component is drawn in Fig. 1. As indicated, input fibers are on the left and output fibers are on the right. Although some components have only a single input port and a single output port, many applications require more than one input and/or output ports. In fact, the number of ports in some devices can exceed 100. The *coupling loss* between any two ports is given, in decibels, by

$$L = -10 \log(P_{out}/P_{in}) \tag{1}$$

With respect to Fig. 1, P_{in} refers to the input power at any of the ports on the left, and P_{out} refers to the output power at any of the ports on the right. Because we are only considering

Copyright 2001 by The McGraw-Hill Companies, Inc. Click Here for Terms of Use.

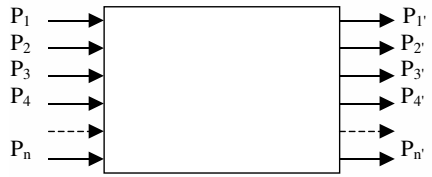

FIGURE 1 The generalized component.

passive components in this section, P_{out} will be less than P_{in}, and the loss will be a positive number.

Insertion loss refers to the coupling loss between any two ports where coupling is desired, and *isolation* (or *directionality*) refers to the coupling loss between any two ports where coupling is unwanted. *Excess loss* is the fraction of input power that does not emerge from any of the desired output ports, as expressed in decibels. It is the sum of all the useful power out divided by the input power.

10.3 NETWORK FUNCTIONS

Functions useful for many fiber-optic communications applications are described in the following paragraphs.

Attenuators

Attenuators reduce the amount of power flowing through the fiber system. Both fixed and variable attenuators are available. The applications include testing of receiver sensitivities (varying the attenuation changes the amount of power incident on the receiver) and protecting a receiver from saturating due to excess incident power. Attenuation from a few tenths of a dB to more than 50 dB are sometimes required.

Power Splitters and Directional Couplers

These devices distribute input power from a single fiber to two or more output fibers. The component design controls the fraction of power delivered to each of the output ports. Applications include power distribution in local area networks (LANs) and in subscriber networks. The most common splitters and couplers have a single input and equal distribution of power among each of two outputs, as shown schematically in Fig. 2*a.* For an ideal three-port splitter (one with no excess loss), half the input power emerges from each of the two output ports. The insertion loss, as calculated from Eq. 1 with a ratio of powers of 0.5, yields a 3 dB loss to each of the two output ports. Any excess loss is added to the 3 dB.

A splitter with more than two output ports can be constructed by connecting several three-port couplers in a tree pattern as indicated schematically in Fig. 2*b.* Adding more splitters in the same manner allows coupling from one input port to 8, 16, 32 (and more) output ports.

Adding a fourth port, as in Fig. 3, creates a *directional coupler.* The arrows in the figure show the allowed directions of wave travel through the coupler. An input beam is split between two output ports and is isolated from the fourth. By proper component design, any

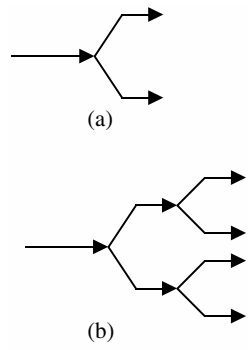

FIGURE 2 Power splitters: (*a*) 1:2 split and (*b*) 1:4 split.

desired power splitting ratio can be obtained. One application of the directional coupler is to the distribution network of a local area network, where simultaneous transmission and reception are required. Figure 4 illustrates this usage at one LAN terminal.

Isolators

An isolator is a one-way transmission line. It permits the flow of optical power in just one direction (the forward direction). Applications include protection of a transmitting laser diode from back reflections. Such reflections increase the noise in the system by disrupting the diode's operation. Isolators also improve the stability of fiber amplifiers by minimizing the possibility of feedback, which causes unwanted oscillations in such devices.

Circulators

In a circulator, power into the first port emerges from the second, while power into the second port emerges from a third. This behavior repeats at each successive input port until power into the last port emerges from the first. Practical circulators are typically three- or four-port devices.

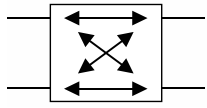

FIGURE 3 Four-port directional coupler.

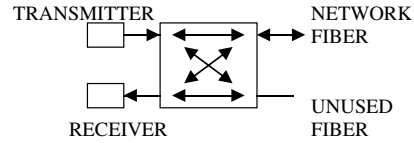

FIGURE 4 LAN terminal, illustrating application of the directional coupler.

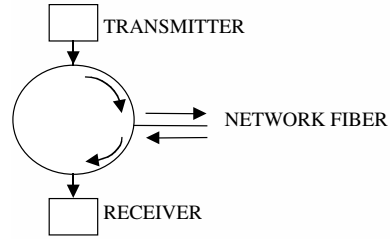

FIGURE 5 An optical circulator separates transmitted and received messages at a terminal.

Using a circulator, efficient two-way (*full-duplex*) transmission along a single fiber at a single wavelength is possible. The circulator separates the transmitting and receiving beams of light at each terminal, as illustrated in Fig. 5.

Multiplexers/Demultiplexers/Duplexers

The multiplexer and demultiplexer are heavily utilized in fiber-optic wavelength-division multiplexing (WDM) systems. The *multiplexer* combines beams of light from the different transmitters (each at a slightly shifted wavelength) onto the single transmission fiber. The *demultiplexer* separates the individual wavelengths transmitted and guides the separate channels to the appropriate optical receivers. These functions are illustrated in Fig. 6. Requirements for multiplexers/demultiplexers include combining and separating independent channels less than a nanometer apart, and accommodating numerous (in some cases over 100) channels. A frequency spacing between adjacent channels of 100 GHz corresponds to a

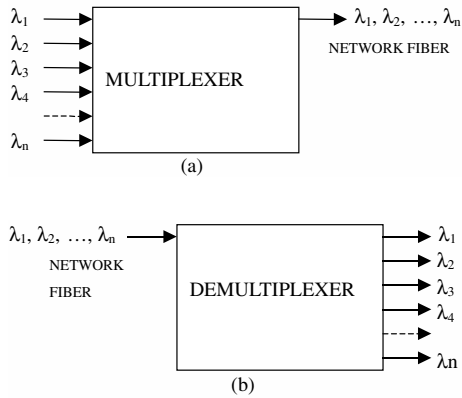

FIGURE 6 (*a*) A multiplexer combines different wavelength channels onto a single fiber for transmission. (*b*) A demultiplexer separates several incoming channels at different wavelengths and directs them to separate receivers.

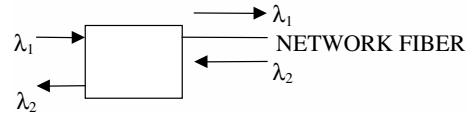

FIGURE 7 A duplexer allows two-way transmission along a single network fiber.

wavelength spacing of 0.8 nm for wavelengths near 1.55 μm. Insertion losses can be as low as a few tenths of a dB and isolations of 40 dB or more.

The *duplexer* allows for simultaneous two-way transmission along a single fiber. The wavelengths are different for the transmitting and receiving light beam. The duplexer separates the beams as indicated in Fig. 7, where λ_1 is the transmitting wavelength and λ_2 is the receiving wavelength.

Mechanical Switches

Operationally, an optical switch acts just like an electrical switch. Mechanical movement of some part (as implied schematically in Fig. 8) causes power entering one port to be directed to one of two or more output ports. Such devices are useful in testing of fiber components and systems and in other applications, such as bypassing inoperative nodes in a local area network. Insertion losses less than 0.10 dB and isolations greater than 50 dB are reasonable requirements.

10.4 SUBCOMPONENTS

Micro-optic subcomponents that form part of the design of many complete microoptic components are described in this section.

Prisms

Because of the dispersion in glass prisms, they can operate as multiplexers, demultiplexers, and duplexers. The dispersive property is illustrated in Fig. 9.

Right-angle glass prisms also act as excellent reflectors, as shown in Fig. 10, owing to perfect reflection (total internal reflection) at the glass-to-air interface. The critical angle for the glass-to-air interface is about 41°, and the incident ray is beyond that at 45°.

The beam-splitting cube, drawn in Fig. 11, consists of two right-angle prisms cemented together with a thin reflective layer between them. This beam splitter has the advantage over a flat reflective plate in that no angular displacement occurs between the input and output beam directions. This simplifies the alignment of the splitter with the input and output fibers.

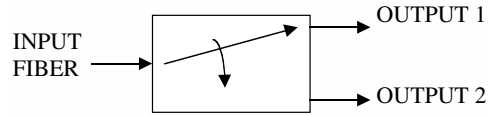

FIGURE 8 Mechanical optical switch.

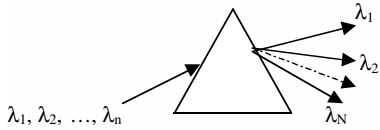

FIGURE 9 A dispersive prism spatially separates different wavelengths. This represents demultiplexing. Reversing the directions of the arrows illustrates combining of different wavelengths. This is multiplexing.

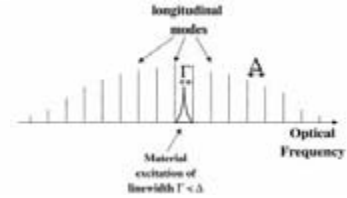

FIGURE 10 Totally reflecting prism.

Gratings

Ruled reflection gratings are also used in multiplexers and demultiplexers. As illustrated in Fig. 12, the dispersion characteristics of the grating perform the wavelength separation function required of a demultiplexer. The grating has much greater dispersive power than a prism, permitting increased wavelength spatial separation. The relationship between the incident and reflected beams, for an incident collimated light beam, is given by the diffraction equation

$$\sin \theta_i + \sin \theta_r = m\lambda/d \tag{2}$$

where θ_i and θ_r are the incident and reflected beam angles, d is the separation between adjacent reflecting surfaces, and m is the *order* of the diffraction. Typically, gratings are blazed so as to maximize the power into the first-order beams. As deduced from this equation for $m = 1$, the diffracted peak occurs at a different angle for different wavelengths. This feature produces the demultiplexing function needed in WDM systems. Reversing the arrows in Fig. 12 illustrates the multiplexing capability of the grating.

Filters

Dielectric-layered filters, consisting of very thin layers of various dielectrics deposited onto a glass substrate, are used to construct multiplexers, demultiplexers, and duplexers. Filters have unique reflectance/transmittance characteristics. They can be designed to reflect at certain wavelengths and transmit at others, thus spatially separating (or combining) different wavelengths as required for WDM applications.

Beam Splitters

A beam-splitting plate, shown in Fig. 13, is a partially silvered glass plate. The thickness of the silvered layer determines the fraction of light transmitted and reflected. In this way, the input beam can be divided in two parts of any desired ratio.

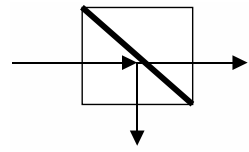

FIGURE 11 Beam-splitting cube.

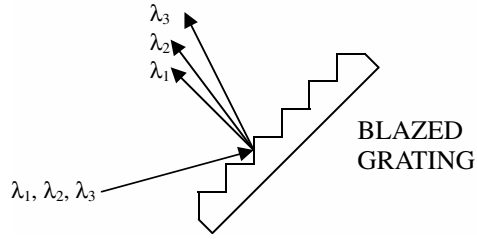

FIGURE 12 Blazed reflection grating operated as a demultiplexer.

Faraday Rotators

The Faraday rotator produces a nonreciprocal rotation of the plane of polarization. The amount of rotation is given by

$$\theta = VHL \tag{3}$$

where θ is the rotation angle, V is the *Verdet constant* (a measure of the strength of the Faraday effect), H is the applied magnetic field, and L is the length of the rotator. A commonly used rotator material is YIG (yttrium-iron garnet), which has a high value of V.

Figure 14 illustrates the nonreciprocal rotation of the state of polarization (SOP) of the wave. The rotation of a beam traveling from left-to-right is 45°, while the rotation for a beam traveling from right-to-left is an additional 45°.

The Faraday rotator is used in the isolator and the circulator.

Polarizers

Polarizers based upon dichroic absorbers and polarization prisms using birefringent materials are common. The polarizing beam splitter, illustrated in Fig. 15, is useful in microoptics applications such as the optical circulator. The polarizing splitter separates two orthogonally polarized beams.

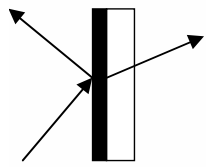

FIGURE 13 Beam-splitting plate.

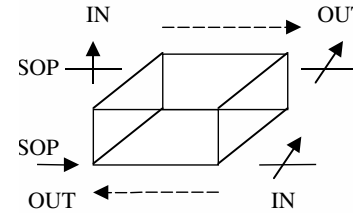

FIGURE 14 Faraday rotator. The dashed arrows indicate the direction of beam travel. The solid arrows represent the wave polarization in the plane perpendicular to the direction of wave travel.

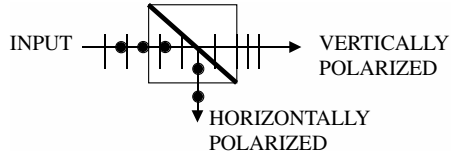

FIGURE 15 Polarizing beam splitter.

GRIN-Rod Lens

The subcomponents discussed in the last few paragraphs perform the operations indicated in their descriptions. The problem is that they cannot be directly inserted into a fiber transmission line. To insert one of the subcomponents into the fiber link requires that the fiber be opened to produce a gap. The subcomponent would then fit into the gap. Because the light emerging from a fiber diverges, with a gap present the receiving fiber does not capture much of the transmitted light. This situation is illustrated in Fig. 16. The emitted diverging light must be collimated, the required subcomponent (e.g., beam splitter, grating, etc.) inserted, and the light refocused. A commonly used device for performing this function is the *graded-index rod lens* (GRIN-rod lens). Its use is illustrated in Fig. 17. The diverging light emitted by the transmitting fiber is collimated by the first GRIN-rod lens. The collimated beam is refocused onto the receiving fiber by the second GRIN-rod lens. The collimation is sufficient such that a gap of 20 mm introduces less than 0.5 dB excess loss.[1] This allows for the insertion of beam-modifying devices of the types described in the preceding paragraphs (e.g., prisms, gratings, and beam splitters) in the gap with minimum added loss.

10.5 COMPONENTS

The subcomponents introduced in the last section are combined into useful fiber devices in the manner described in this section.

Attenuators

The simplest attenuator is produced by a gap introduced between two fibers, as in Fig. 18. As the gap length increases, so does the loss. Loss is also introduced by a lateral displacement. A variable attenuator is produced by allowing the gap (or the lateral offset) to be changeable. A disc whose absorption differs over different parts may also be placed between the fibers. The attenuation is varied by rotating the disk.

In another attenuator design, a small thin flat reflector is inserted at variable amounts into the gap to produce the desired amount of loss.[2]

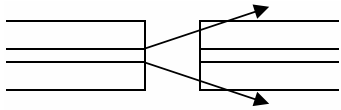

FIGURE 16 Diverging wave emitted from an open fiber couples poorly to the receiving fiber.

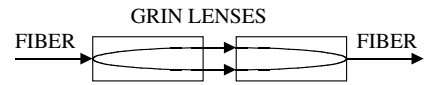

FIGURE 17 Collimating light between two fibers using GRIN-rod lenses.

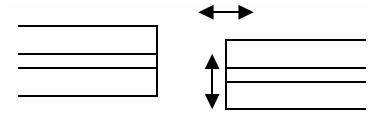

FIGURE 18 Gap attenuator showing relative displacement of the fibers to vary the insertion loss.

Power Splitters and Directional Couplers

A power splitter[3] can be constructed as illustrated in Fig. 19. A beam-splitting cube (or a beam-splitting plate) is placed in the gap between two GRIN-rod lenses to connect Ports 1 and 2. A third combination of lens and fiber collects the reflected light at Port 3. The division of power between the two output fibers is determined by the reflective properties of the splitter itself. Any desired ratio of outputs can be obtained.

If a fourth port is added (Port 4 in Fig. 19), the device is a four-port directional coupler.

Isolators and Circulators

The isolator combines the Faraday rotator and two polarizers[4] as indicated in Fig. 20. The input and output fibers can be coupled to the isolator using GRIN lenses. The vertically polarized beam at the input is rotated by 45° and passed through the output polarizer. Any reflected light is rotated an additional 45°, emerging cross-polarized with respect to the polarizer on the left. In this state, the reflected light will not pass back into the transmitting fiber. Similarly, a light beam traveling from right-to-left will be cross-polarized at the input polarizer and will not travel further in that direction. The polarizers can be polarizing beam splitters, dichroic polarizers, or polarizing fibers.

A circulator also requires a Faraday rotator and polarizers (polarizing beam splitters or polarizing fiber). Additional components include reflecting prisms, reciprocal 45° rotators, and fiber coupling devices such as GRIN-rod lenses.[5]

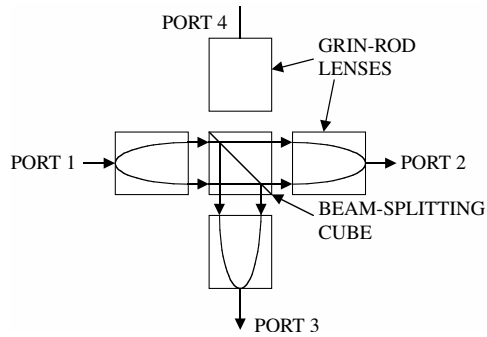

FIGURE 19 Three-power splitter and (with Port 4 added) four-port directional coupler.

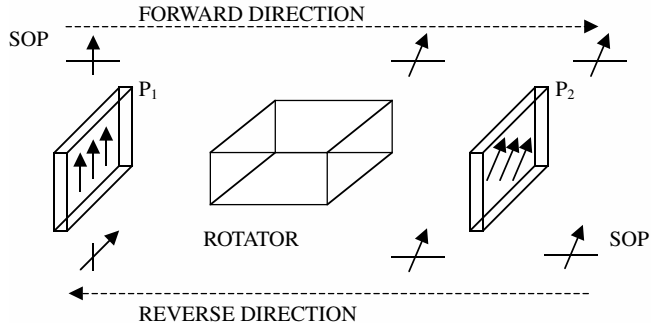

FIGURE 20 Optical isolator. P_1 and P_2 are polarizers.

Multiplexers/Demultiplexers/Duplexers

The multiplexer, demultiplexer, and duplexer are fundamentally the same device. The application determines which of the three descriptions is most appropriate. One embodiment is illustrated in Fig. 21 for a two-channel device. As a demultiplexer, the GRIN lens collimates the diverging beam from the network fiber and guides it onto the diffraction grating. The grating redirects the beam according to its wavelength. The GRIN lens then focuses the various wavelengths onto the output fibers for reception. As a multiplexer, the operation is just reversed with the *receiver fibers* replaced by transmitter fibers and all arrows reversed. As a duplexer, one of the two *receiver fibers* becomes a transmitter fiber.

Other configurations also use the diffraction grating, including one incorporating a concave reflector for properly collimating and focusing the beams between input and output fibers.[6] Microoptic grating-based devices can accommodate more than 100 WDM channels, with wavelength spacing on the order of 0.4 nm.

A filter-based multiplexer/demultiplexer appears in Fig. 22. The reflective coating transmits wavelength λ_1 and reflects wavelength λ_2. The device is illustrated as a demultiplexer. Again, by reversing the directions of the arrows, the device becomes a multiplexer. Filter-based multiplexers/demultiplexers can be extended to several channels in the microoptical form, essentially by cascading several devices of the type just described.

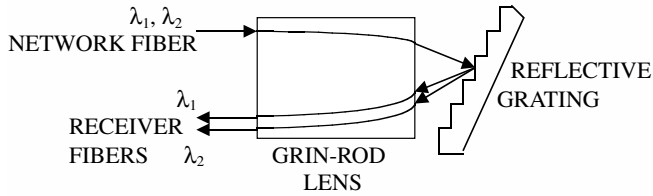

FIGURE 21 Two-channel demultiplexer. Only the beam's central rays are drawn. To operate as a multiplexer the arrows are reversed. To operate as a duplexer, the arrows for just one of the two wavelengths are reversed.

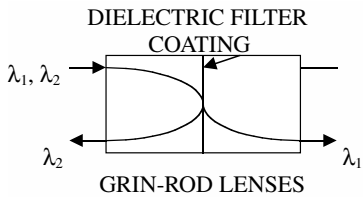

FIGURE 22 Filter-based multiplexer/demultiplexer.

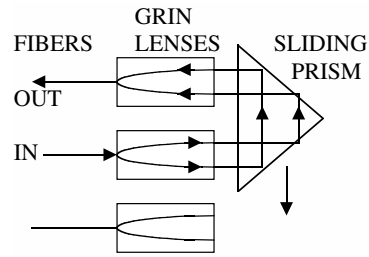

FIGURE 23 Moveable reflecting prism switch.

Mechanical Switches[7]

Switching the light beam from one fiber to another one is basically easy. Simply move the transmitting fiber to mechanically align it with the desired receiving fiber. The problem is that even very small misalignments between the two fiber cores introduce unacceptable transmission losses. Several construction strategies have been utilized. Some incorporate a moving fiber, and others incorporate a moveable reflector.[8] In a moveable fiber switch, the fiber can be positioned either manually or by using an electromagnetic force. The switching action in Fig. 23 occurs when the totally reflecting prism moves to align the beam with one or the other of the two output fibers.

10.6 REFERENCES

1. R. W. Gilsdorf and J. C. Palais, "Single-Mode Fiber Coupling Efficiency with Graded-Index Rod Lenses," *Appl. Opt.* **33:**3440–3445 (1994).
2. C. Marxer, P. Griss, and N. F. de Rooij, "A Variable Optical Attenuator Based on Silicon Micromechanics," *IEEE Photon. Technol. Lett.* **11:**233–235 (1999).
3. C.-L. Chen, *Elements of Optoelectronics and Fiber Optics,* Irwin, Chicago, 1996.
4. R. Ramaswami and K. N. Sivarajan, *Optical Networks: A Practical Perspective,* Morgan Kaufmann, San Francisco, 1998.
5. N. Kashima, *Passive Optical Components for Optical Fiber Transmission,* Artech House, Boston, 1995.
6. J. P. Laude and J. M. Lerner, "Wavelength Division Multiplexing/Demultiplexing (WDM) Using Diffraction Gratings," *SPIE-Application, Theory and Fabrication of Periodic Structures,* **503:**22–28 (1984).
7. J. C. Palais, *Fiber Optic Communications,* 4th ed., Prentice-Hall, Upper Saddle River, New Jersey, 1998.
8. W. J. Tomlinson, "Applications of GRIN-Rod Lenses in Optical Fiber Communications Systems," *Appl. Opt.* **19:**1123–1138 (1980).

This page intentionally left blank.

CHAPTER 11

SEMICONDUCTOR OPTICAL AMPLIFIERS AND WAVELENGTH CONVERSION

Ulf Österberg
Thayer School of Engineering,
Dartmouth College, Hanover, New Hampshire

11.1 GLOSSARY

B	photodetector bandwidth
d	active layer thickness
e	electronic charge
F	noise figure
G	amplifier gain
G_s	single-pass gain
g	gain per unit length
g_0	small-signal gain
$g(N)$	material gain coefficient
h	Planck's constant
I	light intensity
I_{sat}	saturated light intensity
J	current density
L	laser amplifier length
N	carrier density
N_0	transparency carrier density
N_{ph}	photon density
$N_{\text{ph, sat}}$	saturated photon density
n	refractive index

Copyright 2001 by The McGraw-Hill Companies, Inc. Click Here for Terms of Use.

P_{signal}	signal power
P_{shot}	shot noise power
$P_{thermal}$	thermal noise power
$P_{signal\text{-}sp}$	noise power from signal-spontaneous beating
$P_{sp\text{-}sp}$	noise power from spontaneous-spontaneous beating
R	reflectivity
$R(N)$	recombination rate
SNR	signal-to-noise ratio
V	volume of active layer
v_g	group velocity of light
w	laser amplifier stripe width
α	absorption coefficient
β	line width enhancement factor
Γ	optical confinement factor
γ	population inversion factor
λ_c	converted wavelength
λ_s	signal wavelength
ν	frequency
σ_g	differential gain
τ_s	carrier lifetime
Φ	phase shift
ω_a	angular frequency, anti-Stokes light
ω_{pump}	angular frequency, pump light
ω_s	angular frequency, Stokes light

11.2 WHY OPTICAL AMPLIFICATION?

Despite the inherently very low losses in optical glass fibers, it is necessary to amplify the light to maintain high signal-to-noise ratios (SNRs) for low bit error rate (BER) detection in communications systems and for sensor applications. Furthermore, as the bandwidth required is getting larger, it is also necessary to perform all-optical amplification using devices that are independent of bit rates and encoding schemes. In today's telecommunication systems (Chap. 10 in Ref. 1; Chaps. 1 and 2 in this book), optical amplifiers are typically utilized in the following three ways (Fig. 1):

- As power boosters immediately following the laser source
- To provide optical regeneration or in-line amplification for long-distance communications
- As preamplifiers at the receiver end

With the recent introduction of more complex local area networks, it has also become necessary to amplify the signal over short distances to allow it to be distributed to many users.

To characterize any optical amplifier, it is important to consider the following criteria:[2,3]

- Gain—depending on input power, can vary between 5 and 50 dB
- Bandwidth—varies between 1 and 10 THz or 30 and 100 nm

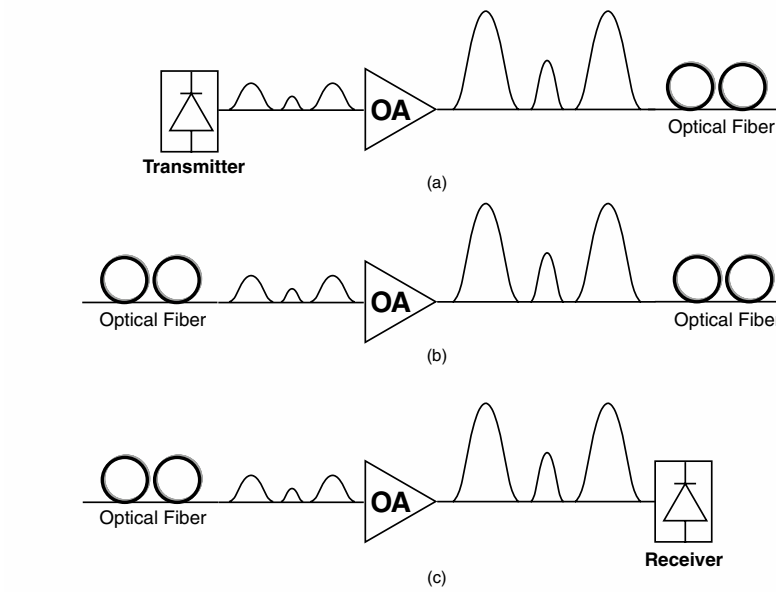

FIGURE 1 Applications of optical amplifiers.

- Pumping efficiency—varies between 1 and 10 dB/mW
- Gain saturation—on the order of 10 dBm for semiconductor amplifiers
- Noise—contributes a power penalty of at least 3 dB
- Polarization sensitivity
- Operating wavelength—most commonly 1.3 or 1.55 μm
- Crosstalk—occurs primarily in wavelength-division multiplexing (WDM) systems where many channels need to be amplified simultaneously
- Coupling loss—should be less than 0.3 dB

Naturally, these numbers are just estimates that can and will vary greatly depending on the exact operating wavelength used and the particular type of optical amplifier under consideration.

There are two main types of optical amplifiers: semiconductor and fiber. They each have strengths and weaknesses, and it becomes the task of the engineer to decide which type of amplifier to use with a specific application. This chapter is primarily about semiconductor amplifiers, but we will start with a short description of the salient features of fiber-optic amplifiers.

Fiber-optic Amplifiers

There are three types of fiber-optic amplifiers (Chap. 5): rare-earth-doped fiber amplifiers, Raman amplifiers, and Brillouin amplifiers (Chap. 38 in Ref. 1; Ref. 4; Chap. 5 in this book). Rare-earth-doped amplifiers are obtained by doping the fiberglass core with rare earth ions—neodymium for amplification around 1.06 μm, praseodynium for amplification around 1.3

μm, and erbium for amplification around 1.55 μm. An obvious advantage for optical fiber amplifiers is that they can be readily spliced to the main optical fiber, minimizing any coupling losses; furthermore, all types of fiber amplifiers are polarization insensitive. The Brillouin and Raman amplifiers rely on third-order nonlinearities in the glass to provide nonparametric interactions between photons and optical and acoustical phonons due to lattice or molecular vibrations within the core of the fiber. Brillouin amplification occurs when the pump and signal beams propagate in opposite directions. The gain is large but the bandwidth is very narrow (<100 MHz). Brillouin amplification is mostly used for receiver preamplification and for selective wavelength amplification for moderate-bit-rate communications systems (≤100 Mbit/s). Raman amplification is similar to Brillouin amplification. The most significant differences between Raman and Brillouin amplification are: (1) for Raman amplification, the pump and signal beam copropagate; (2) the Raman bandwidth is very large (>5 THz); and (3) the Stokes shift is orders of magnitude larger. Due to its broad bandwidth, Raman amplification can be used for very high-bit-rate communication systems. Unlike erbium-doped fiber amplifiers, Raman amplifiers can be used for any wavelength region, being limited only by the available pump sources.[5]

Semiconductor Amplifiers

Semiconductor laser amplifiers (SLAs) (Chap. 13 in Ref. 6) are most commonly divided into two types: (1) Fabry-Perot (FP) amplifiers and (2) traveling wave (TW) amplifiers. Both of these amplifier types are based on semiconductor lasers. The FP amplifier has facet reflectivities $R \approx 0.3$ (slightly less than the values for diode lasers) and the TW amplifier has $R \approx 10^{-3}$–10^{-4} (values as small as 10^{-5} have been reported[7]).

TW amplifiers whose bandwidth is >30 nm (bandwidth exceeding 150 nm has been obtained with the use of multiple quantum well structures[8]) are suitable for wavelength-division multiplexing (WDM) applications (Chap. 13). FP amplifiers have a very narrow bandwidth, typically 5 to 10 GHz (~0.1 nm at 1.5 μm). Due to the nonlinear properties of the semiconductor gain medium in conjunction with the feedback mechanism from the facet reflections, FP amplifiers are used for optical signal processing applications. In Fig. 2, the gain spectrum is shown for an SLA with two different facet reflectivities.

In Fig. 3 is a schematic of a typical amplifier design of length L (200 to 500 μm), thickness d (1 to 3 μm), and active region width w (10 μm). Amplification occurs when excited electrons in the active region of the semiconductor are stimulated to return to the ground level and excess energy is released as additional identical photons.

The connection between excited electrons (defined as number of electrons per cubic centimeter and referred to as the carrier density N) and the number of output photons N_{ph} is given by the rate equation

$$\frac{dN}{dt} = \frac{J}{ed} - R(N) - v_g \cdot g(N) \cdot N_{\text{ph}} \tag{1}$$

where J is the injection current density, v_g is the group velocity of light traveling through the amplifier, and $R(N)$ is the recombination rate (for a simple analytic analysis it is approximated to be linearly proportional to the carrier density, $R(N) \approx N/\tau_s$). For large injection currents this approximation breaks down and higher-order Auger recombination terms have to be incorporated.[9] $g(N)$ is the material gain coefficient, which depends on the light intensity and the specific band structure of the semiconductor used,

$$g(N) = \frac{\Gamma \cdot \sigma_g}{V} \cdot (N - N_0) \tag{2}$$

where Γ is the optical confinement factor, σ_g is the differential gain, $V = L \cdot d \cdot w$ is the volume of the active region, and N_0 is the carrier density needed for transparency—that is, no absorp-

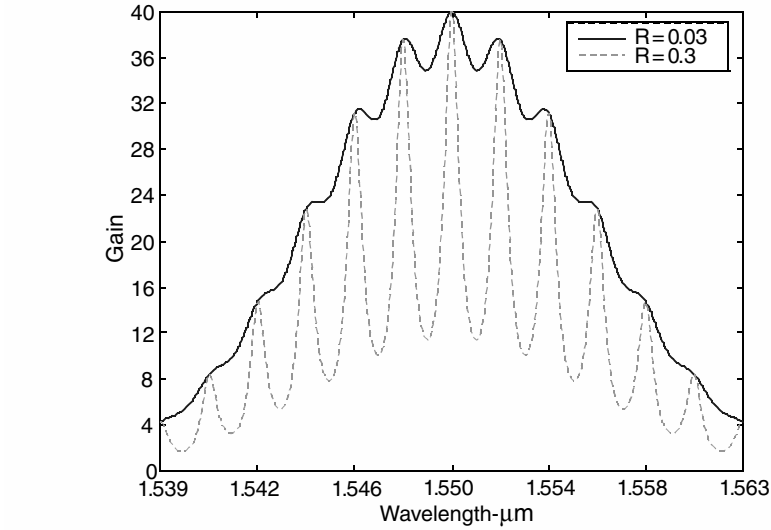

FIGURE 2 Gain spectrum for an SLA with two different facet reflectivities.

tion. The dependence on the band structure moves the peak wavelength of the gain peak toward shorter wavelengths as the carrier density is increased with increasing injection current.

The gain coefficient $g(N)$ is the parameter we wish to solve for in Eq. (1). We do that by setting the time derivative equal to 0 (steady state),

$$g(N) = \frac{g_0}{1 + \dfrac{N_{\text{ph}}}{N_{\text{ph, sat}}}} = \frac{g_0}{1 + \dfrac{I}{I_{\text{sat}}}} \tag{3}$$

where

$$g_0 = \frac{\Gamma \cdot \sigma_g}{V}\left(\frac{J}{ed} \cdot \tau_s - N_0\right) \tag{4}$$

$$I_{\text{sat}} = \frac{h\nu \cdot L \cdot d \cdot w}{\Gamma^2 \cdot \sigma_g \cdot \tau_s} \tag{5}$$

g_0 is referred to as the small-signal gain. From Eq. (5) we notice that for semiconductor materials with small differential gain coefficients and short recombination times we will obtain a large saturation intensity. For typical semiconductor materials the gain saturation is comparatively large.

The net gain per unit length for the amplifier is given by

$$g = \Gamma \cdot g(N) - \alpha \tag{6}$$

where α is the total loss coefficient per unit length. If we assume that g does not vary with distance along the direction of propagation within the active gain medium, we obtain through integration the single-pass gain G_s

$$G_s = \frac{I(L)}{I(0)} = e^{g \cdot L} = e(\Gamma \cdot g_0/1 + I/I_{\text{sat}} - \alpha)L \tag{7}$$

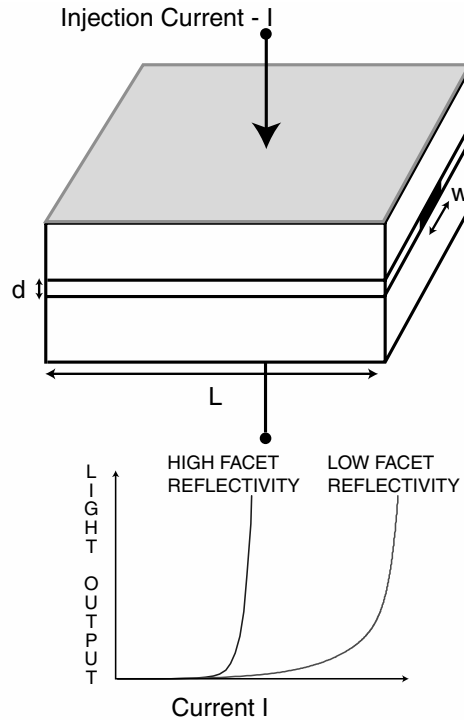

FIGURE 3 Schematic of an SLA and its light output versus injection current characteristics for two different facet reflectivities.

Notice that as the input intensity is increased above the saturation intensity the gain G_s starts to decrease rapidly. The reason for this is that there are not enough excited carriers to amplify all the incoming photons.

The phase shift for a single-pass amplifier is obtained by integrating the net gain g over the entire length L of the amplifier,[10]

$$\Phi = \frac{2\pi \cdot n \cdot L}{\lambda} + \frac{g_0 \cdot L \cdot \beta}{2}\left[\frac{I}{I + I_{\text{sat}}}\right] \tag{8}$$

where β is the line width enhancement factor and n is the refractive index. The second term, through gain saturation, will impose a frequency chirp on the amplified signal. The sign and linearity of this chirp in an SLA is such that the light pulse can be temporally compressed if it propagates in the anomalous dispersion regime of an optical fiber ($\lambda > 1.3$ μm).

From a systems point of view, noise is a very important design parameter. The noise for an amplifier is usually expressed using the noise figure F.[4,10]

$$F = \frac{SNR_{\text{in}}}{SNR_{\text{out}}} = \frac{SNR_b}{SNR_s} \tag{9}$$

where subscripts *b* and *s* refer to beat-noise-limited regime and shot-noise-limited regime, respectively.

The noise figure *F* is obtained by first calculating the *SNR* for an amplifier with gain *G* and for which the output light is detected with an ideal photodetector (bandwidth *B*) only limited by shot noise (Chaps. 17 and 18 in Ref. 1) and then calculating the *SNR* for a "real" amplifier for which the contribution from spontaneous emission is added as well as thermal noise for the photodetector. The SNR for the ideal case is

$$SNR_{\text{in}} = \frac{P_{\text{signal}}}{2 \cdot h\nu \cdot B} \tag{10}$$

and for the more realistic case it is

$$SNR_{\text{out}} = \frac{P_{\text{signal}}}{P_{\text{shot}} + P_{\text{thermal}} + P_{\text{sp-sp}} + P_{\text{signal-sp}}} \approx \frac{P_{\text{signal}}}{4 \cdot B \cdot h\nu \cdot \gamma} \cdot \frac{G}{G-1} \tag{11}$$

where γ is the population inversion factor,[4] and sp-sp and signal-sp are beating noise between either the spontaneously emitted light and itself or the spontaneously emitted light and the signal.

For large gain, $P_{\text{signal-sp}}$ dominates and

$$F = 2\gamma \cdot \frac{G}{G-1} \approx 2 \cdot \gamma \tag{12}$$

For an ideal amplifier, $\gamma = 1 \Rightarrow F = 3\text{dB}$; for most SLAs, $F > 5\text{dB}$.

11.3 WHY OPTICAL WAVELENGTH CONVERSION?

Wavelength-division multiplexed networks (Chap. 13) are already a reality, and as these networks continue to grow in size and complexity it will become necessary to use the same wavelengths in many different local parts of the network. To solve the wavelength contention problems at the connecting nodes, it is necessary to be able to perform wavelength conversion.

An optical wavelength converter should have the following characteristics:[11,12]

- Transparency to bit rates and coding schemes
- Fast setup time of output wavelength
- Conversion to both shorter and longer wavelengths
- Moderate input power levels
- Possibility for no wavelength conversion
- Polarization independence
- Small chirp
- High extinction ratio (power ratio between bit 0 and bit 1)
- Large SNR
- Simple implementation

Options for Altering Optical Wavelengths

There are two different techniques that have primarily been used for wavelength conversion. One is optoelectronic conversion (Chap. 13 in Ref. 6), in which the signal has to be converted

from optical to electrical format before being transmitted at a new optical wavelength. This technique is presently good up to bit rates of 10 Gbit/s.[11] The main drawbacks of this method are power consumption and complexity. The second method is all-optical, and it can further be divided into two different approaches—nonlinear optical parametric processes (Chap. 38 in Ref. 6; Chaps. 3 and 17 in this book) and cross-modulation using an SLA.

The most common nonlinear optical method is four-photon mixing (FPM). FPM occurs naturally in the optical fiber due to the real part of the third-order nonlinear polarization. When the signal beam is mixed with a pump beam, two new wavelengths are generated at frequencies ω_s and ω_a according to the phase-matching condition

$$\omega_s - \omega_{\text{pump}} = \omega_{\text{pump}} - \omega_a \tag{13}$$

where subscripts *s* and *a* stand for Stokes and anti-Stokes, respectively. Since the conversion efficiency is proportional to the square of the third-order nonlinear susceptibility, this is not a very efficient process. Furthermore, the FPM process is polarization sensitive and generates additional (satellite) wavelengths, which reduces the conversion efficiency to the desired wavelength and contributes to channel crosstalk. One major advantage is that no fiber splicing is necessary.

A similar nonlinear optical process that has also been used for wavelength conversion is difference-frequency generation (DFG). This process is due to the real part of the second-order nonlinear polarization and therefore cannot occur in the optical glass fiber. For DFG to be used, it is necessary to couple the light into an external waveguide, for example $LiNbO_3$. DFG does not generate any satellite wavelengths; however, it suffers from low conversion efficiency, polarization sensitivity, and coupling losses between fiber and external waveguide.

Semiconductor Optical Wavelength Converters

To date, the most promising method for wavelength conversion has been cross-modulation in an SLA in which either the gain or the phase can be modulated (XGM and XPM, respectively). A basic XGM converter is shown in Fig. 4*a*. The idea behind XGM is to mix the input signal with a cw beam at the new desired wavelength in the SLA. Due to gain saturation, the cw beam will be intensity modulated so that after the SLA it carries the same information as

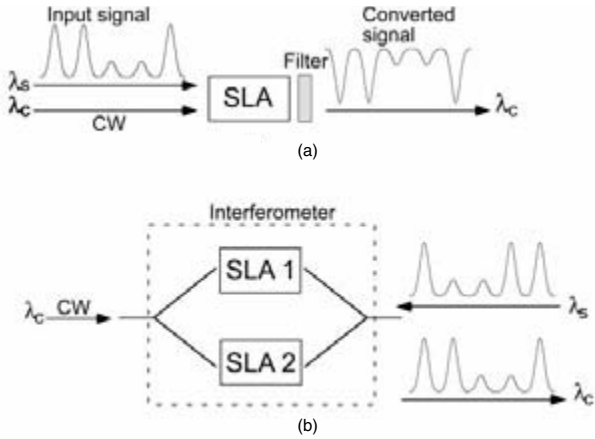

FIGURE 4 Use of an SLA for wavelength conversion. (*a*) Cross-gain modulation. (*b*) Cross-phase modulation.

the input signal. A filter is placed after the SLA to terminate the original wavelength λ_s. The signal and the cw beam can be either co- or counterpropagating. A counterpropagation approach has the advantage of not requiring the filter as well as making it possible for no wavelength conversion to take place. A typical XGM SLA converter is polarization independent but suffers from an inverted output signal and low extinction ratio.

Using an SLA in XPM mode for wavelength conversion makes it possible to generate a noninverted output signal with improved extinction ratio. The XPM relies on the fact that the refractive index in the active region of an SLA depends on the carrier density *N,* Eq. (1). Therefore, when an intensity-modulated signal propagates through the active region of an SLA it depletes the carrier density, thereby modulating the refractive index, which results in phase modulation of a CW beam propagating through the SLA simultaneously.

When the SLA is incorporated into an interferometer setup, the phase modulation can be transformed into an intensity modulated signal (Fig. 4*b*).

To improve the extinction ratio further, different setups using ring laser cavities[13] and nonlinear optical loop mirrors[14] have been proposed.

11.4 REFERENCES

1. M. Bass, E. W. Van Stryland, D. R. Williams, and W. L. Wolfe (eds.), *Handbook of Optics,* 2d ed., vol. II, McGraw-Hill, New York, 1995.
2. M. J. Mahony, "Semiconductor Laser Optical Amplifiers for use in Future Fiber Systems," *IEEE J. Light Tech.* **6**(4):531 (1988).
3. Max Ming-Kang Lin, *Principles and Applications of Optical Communications,* Irwin, 1996, chap. 17.
4. Govind P. Agrawal, *Fiber-Optic Communication Systems,* 2d ed., Wiley, New York, 1997, chap. 8.
5. M. J. Guy, S. V. Chernikov, and J. R. Taylor, "Lossless Transmission of 2 ps Pulses over 45 km of Standard Fibre at 1.3 μm using Distributed Raman Amplification," *Elect. Lett.* **34**(8):793 (1998).
6. M. Bass, E. W. Van Stryland, D. R. Williams, and W. L. Wolfe (eds.), *Handbook of Optics,* 2d ed., vol. I, McGraw-Hill, New York, 1995. [Chap 13 is P. L. Derry, L. Figueroa, and C.-S. Hong, "Semiconductor Lasers.")
7. T. Saitoh, T. Mukai, and O. Mikami, "Theoretical Analysis and Fabrication of Anti-Reflection Coatings on Laser Diode Facets," *IEEE J. Light. Tech.* **3**(2):288 (1985).
8. M. Tabuchi, "External Grating Tunable MQW Laser with Wide Tuning of 240 nm," *Elect. Lett.* **26**:742 (1990).
9. J. W. Wang, H. Olesen, and K. E. Stubkjaer, "Recombination, Gain, and Bandwidth Characteristics of 1.3 μm Semiconductor Laser Amplifiers," *Proc. IOOC-ECOC* 157 (1985).
10. I. Andonovic, "Optical Amplifiers," in O. D. D. Soares, ed., *Trends in Optical Fibre Metrology and Standards,* Kluwer, Dordrecht, 1995, sec. 5.1.
11. T. Durhuus, B. Mikkelsen, C. Joergensen, S. L. Danielsen, and K. E. Stubkjaer, "All-Optical Wavelength Conversion by Semiconductor Optical Amplifiers," *IEEE J. Light. Tech.* **14**(6):942 (1996).
12. M. S. Borella, J. P. Jue, D. Banerjee, B. Ramamurthy, and B. Mukherjee, "Optical Components for WDM Lightwave Networks," *Proc. IEEE* **85**(8):1274 (1997).
13. Y. Hibino, H. Terui, A. Sugita, and Y. Ohmori, "Silica-Based Optical Waveguide Ring Laser Integrated with Semiconductor Laser Amplifier on Si Substrate," *Elect. Lett.* **28**(20):1932 (1992).
14. M. Eiselt, W. Pieper, and H. G. Weber, "Decision Gate for All-Optical Retiming using a Semiconductor Laser Amplifier in a Loop Mirror Configuration," *Elect. Lett.* **29**:107 (1993).

This page intentionally left blank.

CHAPTER 12

OPTICAL TIME-DIVISION MULTIPLEXED COMMUNICATION NETWORKS

Peter J. Delfyett
School of Optics/The Center for Research and Education in Optics and Lasers (CREOL)
University of Central Florida
Orlando, Florida

12.1 GLOSSARY

Definitions

Bandwidth	A measure of the frequency spread of a signal or system—that is, its information-carrying capacity.
Chirping	The time dependence of the instantaneous frequency of a signal.
Commutator/decommutator	A device that assists in the sampling, multiplexing, and demultiplexing of time domain signals.
Homogeneous broadening	A physical mechanism that broadens the line width of a laser transition. The amount of broadening is exactly the same for all excited states.
Kerr effect	The dependence of a material's index of refraction on the square of an applied electric field.
Mode partion noise	Noise associated with mode competition in a multimode laser.
Multiplexing/demultiplexing	The process of combining and separating several independent signals that share a common communication channel.
Passband	The range of frequencies allowed to pass in a linear system.
Photon lifetime	The time associated with the decay in light intensity within an optical resonator.
Picosecond	One trillionth of a second.
p-n junction	The region that joins two materials of opposite doping. This occurs

Copyright 2001 by The McGraw-Hill Companies, Inc. Click Here for Terms of Use.

	when *n*-type and *p*-type materials are joined to form a continuous crystal.
Pockel's effect	The dependence of a material's index of refraction on an applied electric field.
Quantum confined Stark effect (QCSE)	Optical absorption induced by an applied electric field across a semiconductor quantum well.
Quantum well	A thin semiconductor layer sandwiched between material with a larger band gap. The relevant dimension of the layer is on the order of 10 nm.
Sampling	The process of acquiring discrete values of a continuous signal.
Spatial hole burning	The resultant nonuniform spatial distribution of optical gain in a material owing to standing waves in an optical resonator.
Spontaneous emission	An energy decay mechanism to reduce the energy of excited states by the emission of light.
Stimulated emission	An energy decay mechanism that is induced by the presence of light in matter to reduce the energy of excited states by the emission of light.
Terabit	1 trillion bits.

Abbreviations

ADC	analog-to-digital converter
APD	avalanche photodetector
CEPT	European Conference of Postal and Telecommunications Administrations
CMI	code mark inversion
DBR	distributed Bragg reflector
DFB	distributed feedback
DS	digital signal
EDFA	erbium-doped fiber amplifier
FDM	frequency-division multiplexing
FP	Fabry-Perot
LED	light-emitting diode
NRZ	non-return-to-zero
OC-*N*	optical carrier (*N*th level)
OOK	on-off keying
PAM	pulse amplitude modulation
PCM	pulse code modulation
PLL	phase-locked loop
PLM	pulse length modulation
PPM	pulse position modulation
RZ	return-to-zero
SDH	synchronous digital hierarchy
SLALOM	semiconductor laser amplifier loop optical mirror
SONET	synchronous optical network
SPE	synchronous payload envelope

STS	synchronous transmission signal
TDM	time-division multiplexing
TDMA	time-division multiple access
TOAD	terahertz optical asymmetric demultiplexer
UNI	unbalanced nonlinear interferometer
WDM	wavelength-division multiplexing
VCO	voltage-controlled oscillator

Symbols

B	number of bits respresenting N levels in an analog-to-digital converter
f_S	sampling frequency
N	number of levels in an analog-to-digital converter
n	index of refraction; integer
p_T	periodic sampling pulse train
$R_{1,2}$	mirror reflectivities
T	period
W (Hz)	bandwidth of a signal in hertz
$x_S(t)$	sampled version of a continuous function of time
$x(t)$	continuous analog signal
$X(\omega)$	frequency spectrum of the signal $x(t)$
δ	delta function
Λ	grating period
λ	wavelength
τ_D or τ_P	photon decay time or photon lifetime
τ_{RT}	round-trip propagation time of an optical cavity
ϕ	phase shift
ω	angular frequency (radians per second)

12.2 INTRODUCTION

Information and data services, such as voice, data, video, and the Internet, are integral parts of our everyday personal and business lives. By the year 2001, total information traffic on the phone lines will exceed 1 Tbit/s, with the Internet accounting for at least 50 percent of the total. More importantly, the amount of traffic is expected to grow to 100 Tbit/s by the year 2008. Clearly, there is a tremendous demand for the sharing, transfer, and use of information and related services. However, as the demand continues to increase, it should be noted that technology must evolve to meet this demand. This chapter discusses the current status of optical time-division multiplexed communication networks. This chapter is generally organized to initially provide the reader with a brief review of digital signals and sampling to show how and why time-division multiplexing (TDM) becomes a natural way of transmitting information. Following this introduction, time-division multiplexing and time-division multiple access (TDMA) are discussed in terms of their specific applications, for example voice communication/circuit-switched networks and data communication/packet-switched networks for TDM

and TDMA, respectively. These two sections provide the reader with a firm understanding of the overall system perspective as to how these networks are constructed and expected to perform. To provide an understanding of the current state of the art, a review of selected high-speed optical and optoelectronic device technology is given. Before a final summary and outlook toward future directions, a specific ultra-high-speed optical time-division optical link is discussed to coalesce the concepts with the discussed device technology.

Fundamental Concepts

Multiplexing is a technique used to combine the information of multiple communication sites or users over a common communication medium and to send that information over a communication channel where the *bandwidth,* or information-carrying capacity, is shared between each user. The reason for sharing the information channel is to reduce the cost and complexity of establishing a communication network for many users. In the case where the shared medium is time, a communication link is created by combining information from several independent sources and transmitting that information from each source simultaneously without the portions of information from each source interfering with each other. This is done by temporally interleaving small portions, or *bits,* of each source of information so that each user sends data for a very short period of time over the communication channel. The user waits until all other users transmit their data before being able to transmit another bit of information. At a switch or receiver end, the user for which the data was intended picks out, or *demultiplexes,* the data that is intended for that user, while the rest of the information on the communication channel continues to its intended destination.

Sampling

An important concept in time-division multiplexing is being able to have a simple and effective method for converting real-world information into a form that is suitable for transmission by light over an optical fiber or by a direct line-of-sight connection in free space. As networks evolve, the standard for information transmission is primarily becoming digital in nature—information is transmitted by sending a coded message using two symbols (e.g., a 1 or a 0) physically corresponding to light being either present or not on a detector at the receiving location. This process of transforming real signals into a form that is suitable for reliable transmission requires one to sample the analog signal to be sent and digitize and convert the analog signal to a stream of 1s and 0s. This process is usually performed by a sample-and-hold circuit, followed by an analog-to-digital converter (ADC). In this section the concepts of signal sampling and digitization are reviewed with the motivation to convey the idea of the robustness of digital communications. It should be noted, however, that pure analog time-division multiplexed systems can still be realized, as will be shown later, and it is necessary to review this prior to examining digital TDM networks.

Sampling Theorem

The key feature of time-division multiplexing is that it relies on the fact that an analog bandwidth-limited signal may be exactly specified by taking samples of the signal, if the samples are taken sufficiently frequently. Time multiplexing is achieved by interleaving the samples of the individual signals. It should be noted that since the samples are pulses, the system is said to be *pulse modulated.* An understanding of the fundamental principle of time-division multiplexing, called the *sampling theorem,* is needed to see that any signal, including a signal continuously varying in time, can be exactly represented by a sequence of samples or pulses. The theorem states that a real valued bandwidth-limited signal that has no spectral components above a frequency of W Hz is determined uniquely by its value at uniform intervals

spaced no greater than $1/(2W)$ s apart. This means that an analog signal can be completely reconstructed from a set of discrete samples uniformly spaced in time. The signal samples $x_S(t)$ are usually obtained by multiplying the signal $x(t)$ by a train of narrow pulses $p_T(t)$, with a time period $T = 1/f_S \leq \frac{1}{2}W$. The process of sampling can be mathematically represented as

$$\begin{aligned} x_S(t) &= x(t) \cdot p_T(t) \\ &= x(t) \cdot \sum_{n=-\infty}^{+\infty} \delta(t - nT) \\ &= \sum_{n=-\infty}^{+\infty} x(nT)\delta(t - nT) \end{aligned} \tag{1}$$

where it is assumed that the sampling pulses are ideal impulses and n is an integer. Defining the Fourier transform and its inverse as

$$X(\omega) = \int_{-\infty}^{+\infty} x(t) \exp(-j\omega t)dt \tag{2}$$

and

$$x(t) = \frac{1}{2\pi} \int_{-\infty}^{\infty} X(\omega) \exp(+j\omega t)d\omega \tag{3}$$

one can show that the spectrum $X_S(\omega)$ of the signal $x_S(t)$ is given by

$$\begin{aligned} X_S(\omega) &= \frac{1}{T} \sum P\left(\frac{2\pi n}{T}\right) \cdot X\left(\omega - \frac{2\pi n}{T}\right) \\ &= \frac{1}{T} P(\omega) \cdot \sum X\left(\omega - \frac{2\pi n}{T}\right) \end{aligned} \tag{4}$$

In the case of the sampling pulses p being perfect delta functions, and given that the Fourier transform of $\delta(t)$ is 1, the signal spectrum is given by

$$X_S = \sum X\left(\omega - \frac{2\pi n}{T}\right) \tag{5}$$

This is represented pictorially in Fig. 1*a–c.* In Fig. 1*a* and *b* is an analog signal and its sampled version, where the sample interval is ~8 times the nominal sample rate of $1/(2W)$. From Fig. 1*c* it is clear that the spectrum of the signal is repeated in frequency every $2\pi/T$ Hz if the sample rate T is $1/(2W)$. By employing (passing the signal through) an ideal rectangular low-pass filter—that is, a uniform (constant) passband with a sharp cutoff, centered at direct current (DC) with a bandwidth of $2\pi/T$ the signal can be completely recovered. This filter characteristic implies an impulse response of

$$h(t) = 2W \frac{\sin(2\pi Wt)}{(2\pi Wt)} \tag{6}$$

The reconstructed signal can now be given as

$$\begin{aligned} x(t) &= 2W \sum_{n=-\infty}^{+\infty} x(nT) \cdot \frac{\sin[2\pi W(t - nT)}{2\pi W(t - nT)} \\ &= x(t)/T,\ T = \frac{1}{2W} \end{aligned} \tag{7}$$

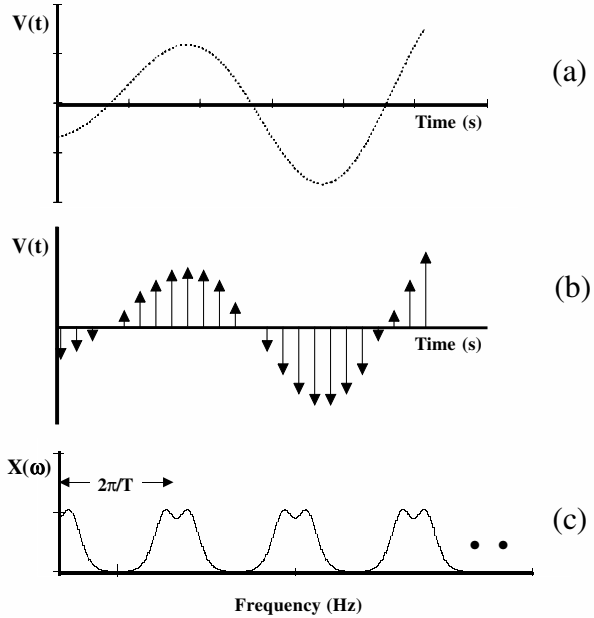

FIGURE 1 An analog bandwidth-limited signal (*a*), along with its sampled counterpart (*b*) sampled at a rate of ~8 times the Nyquist rate. (*c*) Frequency spectrum of a band-limited signal that has been sampled at a rate of $T = \frac{1}{2}W$, where W is the bandwidth of the signal.

This reconstruction is shown in Fig. 2. It should be noted that the oscillating nature of the impulse response $h(t)$ interferes destructively with other sample responses for times away from the centroid of each reconstructed sample. The sampling theorem now suggests three possibilities. (1) It is possible to interleave multiple sampled signals from several independent sources in time and transmit the total composite signal (time-division multiplexing). (2) Any parameter of the sampling train can be varied, such as its pulse length, pulse amplitude, or pulse position in direct accordance with the sampled values of the signal—that is, pulse length modulation (PLM), pulse amplitude modulation (PAM), and pulse position modulation (PPM). (3) The samples can be quantized and coded in binary or *m*-ary level format and transmitted as a digital signal, leading to pulse code modulation (PCM). Figure 3 shows an example of a sinusoidal signal and its representation in PAM, PPM, and PLM.

Interleaving

The sampling principle can be exploited in time-division multiplexing by considering the ideal case of a single point-to-point link connecting N users to N other users over a single communication channel, which is shown schematically in Fig. 4. At the transmitter end, a number of users with bandwidth-limited signals, each possessing a similar bandwidth, are connected to the contact points of a rotary switch called a *commutator.* For example, each user may be transmitting band-limited voice signals, each limited to 3.3 kHz. As the rotary arm of the

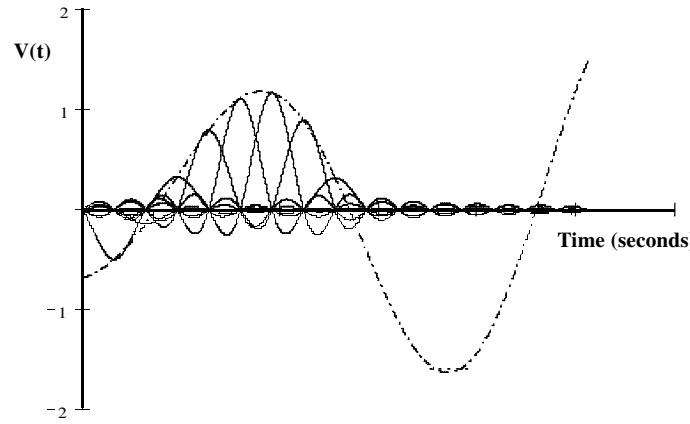

FIGURE 2 Temporal reconstruction of the sampled signal after passing the samples through a rectangular filter.

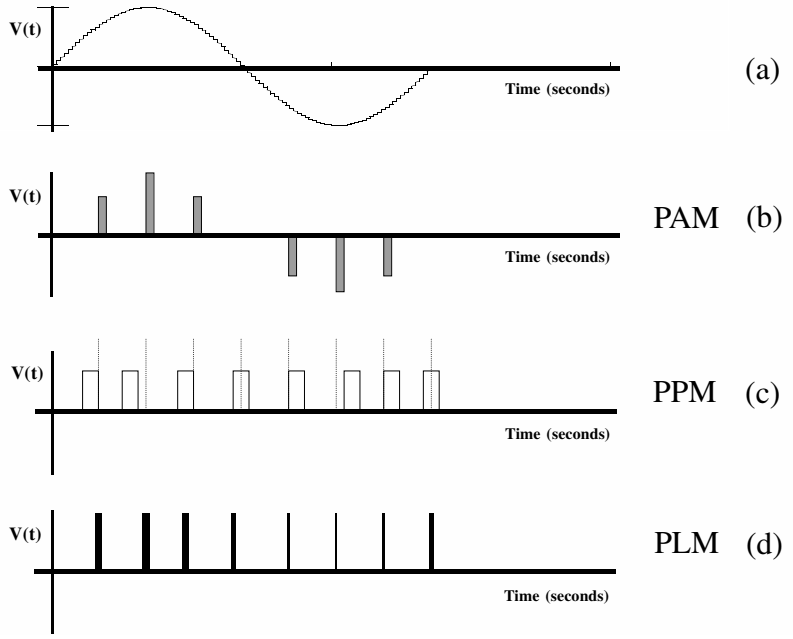

FIGURE 3 Schematic representation of three different possible methods of transmitting discrete samples of a continuous analog signal. (*a*) Analog sinusoidal. (*b*) Pulse amplitude modulation. (*c*) Pulse position modulation. (*d*) Pulse length modulation.

switch swings around, it samples each signal sequentially. The rotary switch at the receiving end is in synchrony with the switch at the sending end. The two switches make contact simultaneously at a similar number of contacts. With each revolution of the switch, one sample is taken of each input signal and presented to the correspondingly numbered contact of the switch at the receiving end. The train of samples at terminal 1 in the receiver passes through a low-pass filter and at the filter output the original signal $m(t)$ appears reconstructed. Of course, if f_M is the highest-frequency spectral component present in any of the input signals, the switches must make at least two f_M revolutions per second.

When the signals need to be multiplexed vary rapidly in time, electronic switching systems are employed, as opposed to the simple mechanical switches depicted in Fig. 4. The sampling and switching mechanism at the transmitter is called the *commutator;* while the sampling and switching mechanism at the receiver is called the *decommutator.* The commutator samples and combines samples, while the decommutator separates or *demultiplexes* samples belonging to individual signals so that these signals may be reconstructed.

The interleaving of the samples that allow multiplexing is shown in Fig. 5. For illustrative purposes, only two analog signals are considered. Both signals are repetitively sampled at a sample rate *T;* however, the instants at which the samples of each signal are taken are different. The input signal to receiver 1 in Fig. 4 is the train of samples from transmitter 1 and the input signal to receiver 2 is the train of samples from transmitter 2. The relative timing of the sampled signals of transmitter 1 has been drawn to be exactly between the samples of transmitter 2 for clarity; however, in practice, these samples would be separated by a smaller timing interval to accommodate additional temporally multiplexed signals.

In this particular case, it is seen that the train of pulses corresponding to the samples of each signal is modulated in amplitude in direct proportion to the signal. This is referred to as pulse amplitude modulation (PAM). Multiplexing of several PAM signals is possible because the various signals are kept distinct and are separately recoverable by virtue of the fact that they are

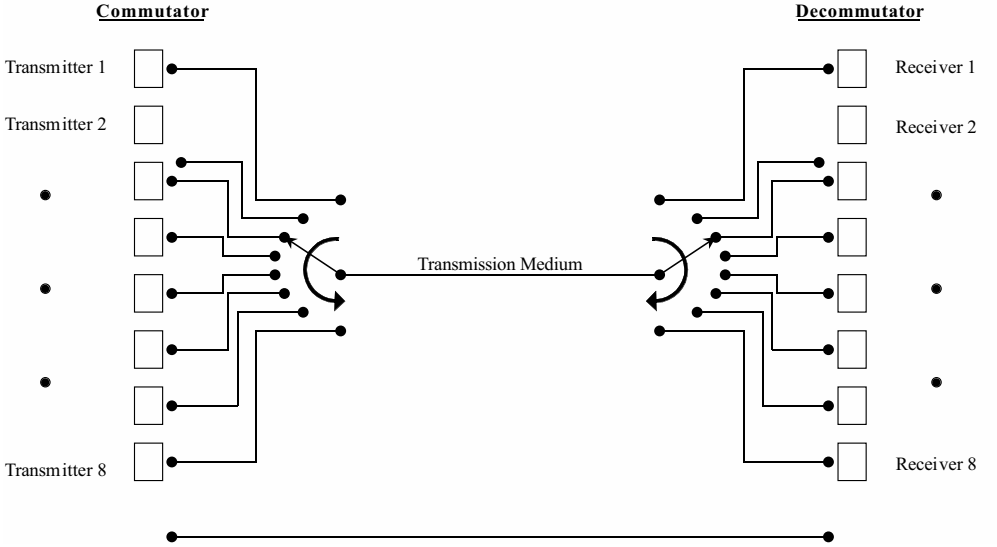

FIGURE 4 Illustration of a time multiplexer/demultiplexer based on simple mechanical switches called *commutators* and *decommutators.*

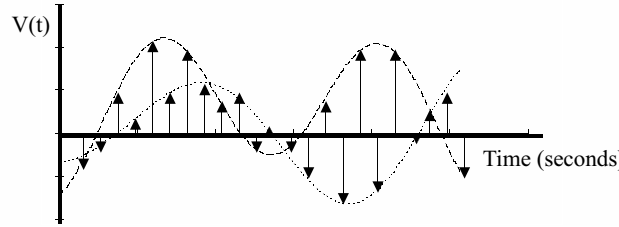

FIGURE 5 Two band-limited analog signals and their respective samples occurring at a rate of approximately 6 times the highest frequency, or 3 times the Nyquist rate.

sampled at different times; thus this is an example of a time-division multiplexed system. This is in contrast to systems that can keep the signals separable by virtue of their frequency (or optical wavelength) translation to different portions of the frequency (wavelength) domain. These systems are referred to as *frequency-division multiplexed* (FDM) or *wavelength-division multiplexed* (WDM).

In today's fiber-optic systems, formally, the sampled signals are transmitted on an optical carrier frequency, or *wavelength,* while older conventional electrical communication links transmit the multiplexed signals directly over a wire pair. It should be noted that the process of transmitting information on optical carriers is analogous to radio transmission, where the data is transmitted on carrier frequencies in the radio frequency range (kilohertz to gigahertz).

Demultiplexing—Synchronization of Transmitter and Receiver

In any type of time-division multiplexing system, it is required that the sampling at the transmitter end and the demultiplexing at the receiver end be *in step* (synchronized with each other). As an example, consider the diagram of the commutator in Fig. 4. When the transmitting multiplexer is set in a position that samples and transmits information from user 1, the receiving demultiplexer must be in a position to pick out, or *demultiplex,* and receive information that is directed for receiver 1. To accomplish this timing synchronization, the receiver has a local clock signal that controls the timing of the commutator as it switches from one time slot to the next. The clock signal may be a narrowband sinusoidal signal from which an appropriate clocking signal, with sufficiently fast rising edges of the appropriate signal strength, can be derived. The repetition rate of the clock in a simple configuration would then be equal to the sampling rate of an individual channel times the number of channels being multiplexed, thereby assigning one time slot per clock cycle.

At the receiver end, the clock signal is required to keep the decommutator synchronized to the commutator, that is, to keep both running at the same rate. As well, there must be additional timing information to provide agreement as to the relative positions or phase of the commutator-decommutator pair, which assures that information from transmitter 1 is guaranteed to be received at the desired destination of receiver 1. The time interval from the beginning of the time slot allocated to a particular channel until the next recurrence of that particular time slot is commonly referred to as a *frame.* As a result, timing information is required at both the bit (time slot) and frame levels. A common arrangement in time-division multiplexed systems is to allow for one or more time slots per frame to provide timing information, depending on the temporal duration of the transmitted frame. It should be noted that there are a variety of methods for providing timing information, such as directly using a portion of the allocated bandwidth, as just mentioned, or alternatively, recovering a clock signal by deriving timing information directly from the transmitted data.

Digital Signals—Pulse Code Modulation

In most applications that employ optical time-division multiplexing, signals are usually sent in a pulse-code-modulated format, as opposed to sending optical samples that are directly proportional to the analog signal amplitude (e.g., PAM, PPM, and PLM). The key feature of sending the information in the form of a digital code is that the analog form of the signal can be corrupted with noise that generally cannot be separated from the signal. The pulse code modulation format provides a mechanism by which the digitization and *quantization,* or coding, of the signal produces a signal that can be recovered from the noise introduced by the communication link.

The limitation of a simple analog communication system is that once noise is introduced onto the signal, it is impossible to remove. When quantization is employed, a new signal is created that is an approximation of the original signal. The main benefit of employing a quantization technique is that, in large part, the noise can be removed from the signal. The main characteristic of a general quantizer is it has an input-output characteristic that is in the form of a staircase, as shown in Fig. 6. It is observed that while the input signal $V_{in}(t)$ varies smoothly, the output $V_o(t)$ is held constant at a fixed level until the signal varies by an amount of $V_{\max}/N$, where N is the number of levels by which the output signal changes its output level. The output quantized signal represents the sampled waveform, assuming that the quantizer is linearly related to the input. The transition between one level and the next occurs at the instant when the signal is midway between two adjacent quantized levels. As a result, the quantized signal is an approximation of the original signal. The quality of the approximation may be improved by reducing the step size or increasing the number of quantized levels. With sufficiently small step size or number of quantized levels, the distinction between the original signal and the quantized signal becomes insignificant. Now, consider that the signal is transmitted and subsequently received, with the addition of noise on the received signal. If this signal is presented to the input of another identical quantizer, and if the peak value of the noise signal is less than half the step size of the quantizer, the output of the second quantizer is identical to the original transmitted quantized signal, without the noise that was added by the transmission channel! It should be noted that this example is presented only to illustrate the concept of noise removal via quantization techniques. In reality, there is always a finite probability—no matter how small—that the noise signal will have a value that is larger than half the step size, resulting in a detected error. While this example shows the benefits of quantization and digital transmission, the system trade-off is that additional bandwidth is required to transmit the coded signal.

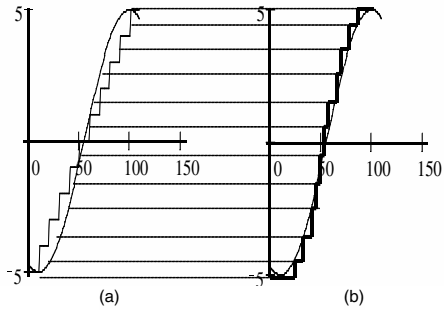

FIGURE 6 The input-output "staircase" transfer function of a digital quantizer. (*a*) Staircase function and sinusoid. (*b*) The resultant quantized function superimposed on the original sinusoid, showing a slight deviation of the quantized signal from the original sinusoid.

It should be noted that the resultant quantized signal shown in Fig. 6 possesses a slight distortion that results from the quantization process. This slight distortion generates a signal-to-noise ratio (SNR) that is not uniform for all values of received signals. This nonuniform SNR tends to increase the error in the transmitted signal due to quantization. One method of reducing this quantization error is to predistort the signal such that small-amplitude signals are received with the same SNR as large-amplitude signals. This process of predistorting the signal is called *compressing,* and is achieved in devices called *companders.* Obviously, on the receiver end, a similar process to invert the predistortion process is required, and is accomplished in an *expander.*

Pulse Code Modulation

A signal that is to be quantized prior to transmission has been sampled as well. The quantization is used to reduce the effects of noise, and the sampling allows us to time-division multiplex a number of users. The combined signal-processing techniques of sampling and quantizing generate a waveform composed of pulses whose amplitudes are limited to a discrete number of levels. Instead of these quantized sample values being transmitted directly, each quantized level can be represented as a binary code, and the code can be sent instead of the actual value of the signal. The benefit is immediately recognized when considering the electronic circuitry and signal processing required at the receiver end. In the case of binary code transmission, the receiver only has to determine whether one of two signals was received (e.g., a 1 or a 0), as compared to a receiver system, which would need to discern the difference between the N distinct levels used to quantize the original signal. The process of converting the sampled values of the signal into a binary coded signal is generally referred to as *encoding.* Generally, the signal-processing operations of sampling and encoding are usually performed simultaneously, and as such, the entire process is referred to as analog-to-digital (A-to-D) conversion.

Analog-to-Digital Conversion

The sampled signal, as shown in Fig. 5, represents the actual values of the analog signal at the sampling instants. In a practical communication system or in a realistic measurement setup, the received or measured values can never be absolutely correct because of the noise introduced by the transmission channel or small inaccuracies impressed on the received data owing to the detection or measurement process. It turns out that it is sufficient to transmit and receive only the quantized values of the signal samples. The quantized values of sampled signals, represented to the nearest digit, may be represented in a binary form or in any coded form using only 1s and 0s. For example, sampled values between 2.5 and 3.4 would be represented by the quantized value of 3, and could be represented as 11, using two bits (in base 2 arithmetic). This method of representing a sampled analog signal, as noted earlier, is known as pulse code modulation. An error is introduced on the signal by this quantization process. The magnitude of this error is given by

$$\varepsilon = \frac{0.4}{N} \tag{8}$$

where N is the number of levels determined by $N = 2^B$, and B is the B-bit binary code—for example, $B = 8$ for eight-bit words representing 256 levels. Thus one can minimize the error by increasing the number of levels, which is achieved by reducing the step size in the quantization process. It is interesting to note that using only four bits (16 levels), a maximum error of 2.5 percent is achieved, while increasing the number of bits to eight (256 levels) gives a maximum error of 0.15 percent.

Optical Representation of Binary Digits and Line Coding

The binary digits can be represented and transmitted on an optical beam and passed through an optical fiber or transmitted in free space. The optical beam is modulated to form pulses to represent the sampled and digitized information. A family of four such representations is shown in Fig. 7. There are two particular forms of data transmission that are quite common in optical communications owing to the fact that their modulation formats occur naturally in both direct and externally modulated optical sources. These two formats are referred to as *non-return-to-zero* (NRZ) and *return-to-zero* (RZ). In addition to NRZ and RZ data formats, pulse-code-modulated data signals are transmitted in other codes that are designed to optimize the link performance, owing to channel constraints. Some important data transmission formats for optical time-division multiplexed networks are code mark inversion (CMI) and Manchester coding or bi-phase coding. In CMI, the coded data has no transitions for logical 1 levels. Instead, the logic level alternates between a high and low level. For logical 0, on the other hand, there is always a transition from low to high at the middle of the bit interval. This transition for every logical 0 bit ensures proper timing recovery. For Manchester coding, logic 1 is represented by a return-to-zero pulse with a 50 percent duty cycle over the bit period (a half-cycle square wave), and logic 0 is represented by a similar return-to-zero waveform of opposite phase, hence the name *bi-phase.* The salient feature of both bi-phase and CMI coding is that their power spectra have significant energy at the bit rate, owing to the guarantee of a significant number of transitions from logic 1 to 0. This should be compared to the power spectra of RZ and NRZ data, which are shown in Fig. 8. The NRZ spectrum has no energy at the bit rate, while the RZ power spectrum does have energy at the bit rate—but the RZ spectrum is also broad, having twice the width of the NRZ spectrum. The received data power spectrum is important for TDM transmission links, where a clock or synchronization signal is required at the receiver end to demultiplex the data. It is useful to be able to recover a clock or synchronization signal derived from the transmitted data, instead of using a portion of the channel bandwidth to send a clock signal. Therefore, choosing a transmission format with a large power spectral component at the transmitted bit rate provides an easy method of recovering a clock signal.

Consider for example the return-to-zero (RZ) format just discussed. If the transmitted bits are random independent 1s and 0s with equal probability, the transmitted waveform can be

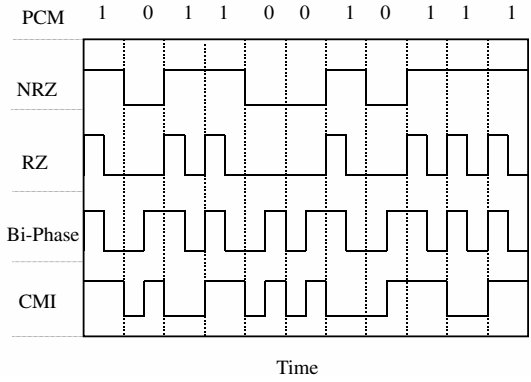

FIGURE 7 Line-coded representations of the pulse-code-modulated logic signal 10110010111. NRZ: non-return-to-zero format; RZ: return-to-zero format; bi-phase, also commonly referred to as Manchester coding; CMI: code mark inversion format.

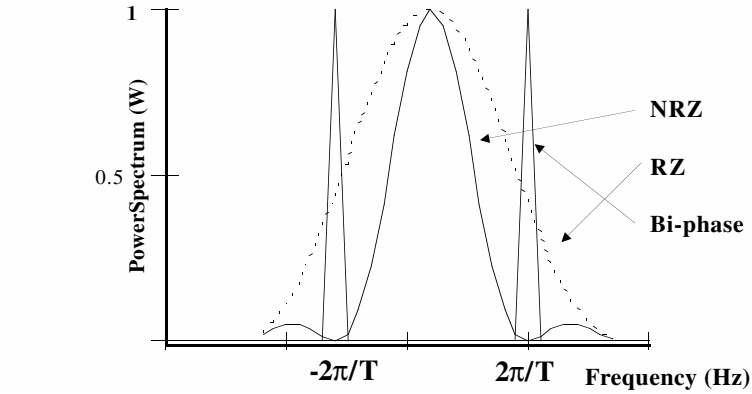

FIGURE 8 Power spectra of NRZ, RZ, and bi-phase line coded data. Note the relative power at the bit rate.

considered to be the sum of a periodic clock sequence with half of the amplitude and a random sequence with zero mean as shown in Fig. 9. The Fourier transform of the clock component has a peak at the bit frequency, and the Fourier transform of the random component is 0 at the bit frequency. Therefore, if there is a narrow-bandpass filter at the receiver with the received signal as the input, the clock component will pass through and the random part will be rejected. The output is thus a pure sinusoid oscillating at the clock frequency or bit rate. This concept of line filtering for clock recovery is schematically represented in Fig. 10.

Generally, pulse-code-modulated signals are transmitted in several different formats to fit within the constraints determined by the transmission channel (bandwidth and so on). It is clear from Fig. 8 that the power spectrum of return-to-zero PCM data has a spectral spread

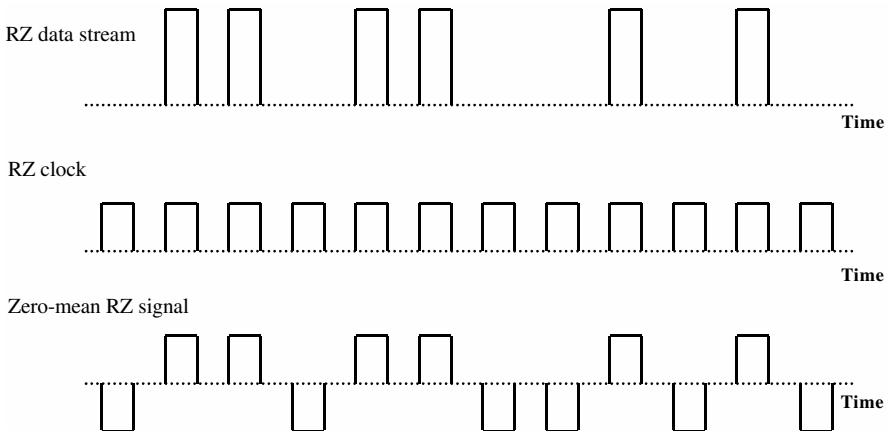

FIGURE 9 Illustration showing a random RZ data stream, along with its RZ clock component and its zero-mean counterpart. Note that the zero-mean signal results from the difference between the RZ data and the clock component.

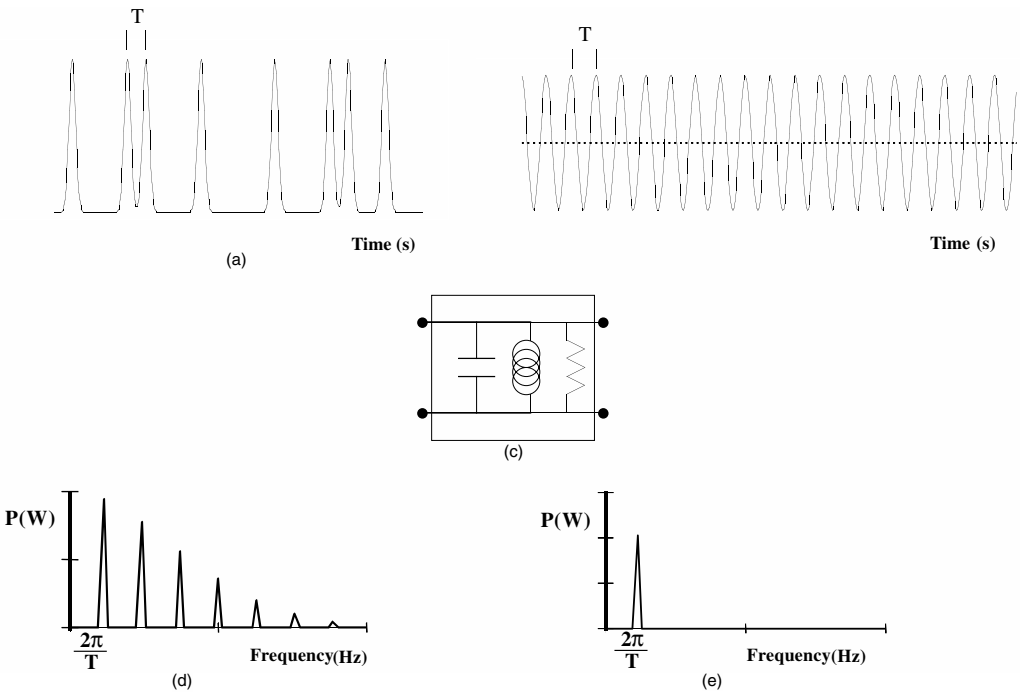

FIGURE 10 Principle of clock recovery using line filtering. (*a*) Input RZ data stream. (*b*) Filtered time-domain clock signal. (*c*) Schematic of an electrical tank circuit for realizing a bandpass filter. (*d*) Power spectrum of a periodic RZ sequence. (*e*) Power spectrum of the filtered signal.

that is approximately twice that of non-return-to-zero PCM data. Both formats have a large amount of power in the DC and low-frequency components of their power spectra. In contrast, the bi-phase code has very low power in the DC and low-frequency portion of the power spectrum, and as a result is a very useful format for efficient timing recovery.

Timing Recovery

Time-division multiplexing and time-division multiple-access networks inherently require timing signals to assist in demultiplexing individual signals from their multiplexed counterparts. One possible method is to utilize a portion of the communication bandwidth to transmit a timing signal. Technically, this is feasible; however (1) this approach requires hardware dedicated to timing functions distributed at each network node that performs multiplexing and demultiplexing functions, and (2) network planners want to optimize the channel bandwidth without resorting to dedicating a portion of the channel bandwidth to timing functions. The desired approach is to derive a timing signal directly from the transmitted data. This allows the production of the required timing signals for multiplexing and demultiplexing without the need to use valuable channel bandwidth.

As suggested by Fig. 10, a simple method for recovering a timing signal from transmitted return-to-zero data is to use a bandpass filter to pass a portion of the power spectrum of the transmitted data. The filtered output from the tank circuit is a pure sinusoid that provides the

timing information. An important parameter to consider in line filtering is the quality factor, designated as the filter Q. Generally, the Q factor is defined as

$$Q = \frac{\omega_o}{\Delta\omega}$$

where ω_o is the resonant frequency and $\Delta\omega$ is the bandwidth of the filter. It should also be noted that Q is a measure of the amount of energy stored in the bandpass filter, such that the output from the filter decays exponentially at a rate directly proportional to Q. In addition, for bandpass filters based on passive electrical circuits, the output peak signal is directly proportional to Q. These two important physical features of passive line filtering imply that the filter output will provide a large and stable timing signal if the Q factor is large. However, since Q is inversely proportional to the filter bandwidth, a large Q typically implies a small filter bandwidth. As a result, if the transmitter bit rate and the resonant frequency of the tank circuit do not coincide, the clock output could be zero. In addition, the clock output is very sensitive to the frequency offset between the transmitter and resonant frequency. Therefore, line filtering can provide a large and stable clock signal for large filter Q, but the same filter will not perform well when the bit rate of the received signal has a large frequency variation. In TDM bit timing recovery, the ability to recover the clock of an input signal over a wide frequency range is called *frequency acquisition* or *locking range,* and the ability to tolerate timing jitter and a long interval of zero transitions is called *frequency tracking* or *hold over time.* Therefore, the tradeoff exists between the locking range (low Q) and hold over time (large Q) in line filtering.

A second general scheme to realize timing recovery and overcome the drawbacks of line filtering using passive linear components is the use of a phase-locked loop (PLL) in conjunction with a voltage-controlled oscillator (VCO) (see Fig. 11*a*). In this case, two signals are fed into

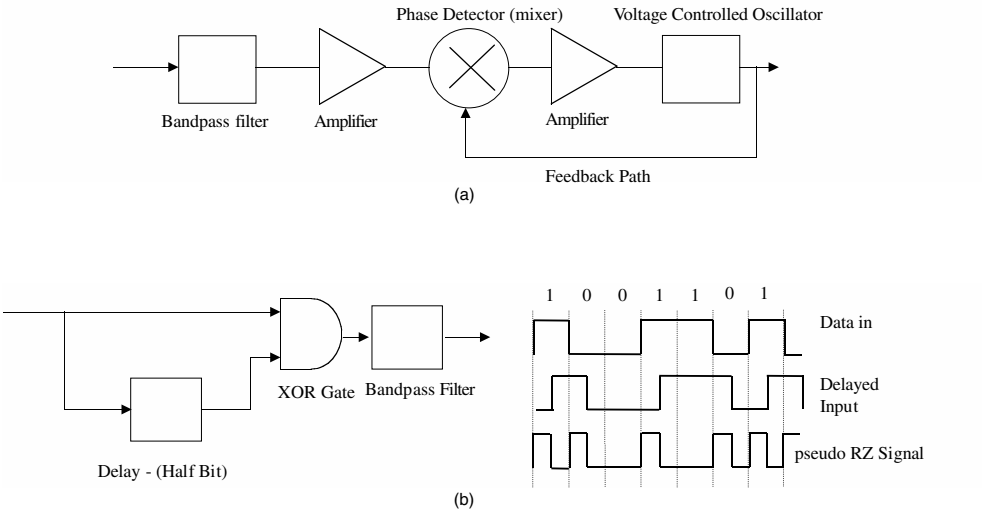

FIGURE 11 (*a*) Schematic diagram of a phase-locked loop using a mixer as a phase detector and a voltage-controlled oscillator to provide the clock signal that can track phase wander in the data stream. (*b*) Data format conversion between input NRZ data and RZ output data using an electronic logic gate. The subsequent RZ output is then suitable for use in a clock recovery device.

the mixer. One signal is derived from the data (e.g., from a line filtered signal possessing energy at the bit rate), while the second signal is a sinusoid generated from the VCO. The mixer is used as a phase detector and produces a DC voltage that is applied to the VCO to adjust its frequency of operation. The overall function of the PLL is to adjust its own voltage to track the frequency and phase of the input data signal. Owing to the active components in the PLL, this approach for timing recovery can realize a broad locking range, low insertion loss, and good phase-tracking capabilities. It should be noted that while the concepts for timing recovery described in this section were illustrated using techniques that are not directly applicable to ultra-high-speed optical networking, the underlying principles will still hold for high-speed all-optical techniques. These approaches are discussed in more detail later in the chapter.

While both these techniques require the input data to be in the return-to-zero format, many data transmission links use non-return-to-zero line coding owing to its bandwidth efficiency. Unfortunately, in the NRZ format there is no component in the power spectrum at the bit rate. As a result, some preprocessing of the input data signal is required before clock recovery can be performed. A simple method for achieving this is illustrated in Fig. 11*b*. The general concept is to present the data signal with a delayed version of the data at the input ports of a logic gate that performs the exclusive OR operation. The temporal delay, in this case, should be equal to half a bit. The output of the XOR gate is a pseudo-RZ data stream that can then be line filtered for clock recovery.

12.3 TIME-DIVISION MULTIPLEXING AND TIME-DIVISION MULTIPLE ACCESS

Overview

In today's evolving telecommunication (voice and real-time video) and data (e.g., Internet) networks, the general mode of transmitting information can be adapted to make maximum use of a network's bandwidth. In addition, the general characteristics of the user application may also require a specific mode of transmission format. For example, in classic circuit-switched voice communications, real-time network access is desired since voice communications are severely hampered in links that have large timing delays or *latency*. In contrast, data networks are not hampered if the communications link has small delays in the transmission of information. In this case, packet-switched data is sent in bursts, and the user does not require continuous, real-time access to the network. These two different ways of achieving access to the bandwidth are generally referred to as *time-division multiplexing* (TDM), typically used in circuit-switched voice communication networks, and *time-division multiple access* (TDMA), which is used in packet-switched data networks.

In communication links such as TDM and TDMA, since the transmission medium bandwidth is shared in the time domain, the transmitting node is required to know when (at what time) it can transmit, and the duration (or for how long) it can transmit the data. These two aspects of time multiplexing immediately imply constraints on the bit or frame synchronization and bit period or packet rate for TDM and TDMA, respectively. We will now review both TDM and TDMA access, emphasizing these two aspects.

Time-Domain Multiple Access

In time-domain multiple access (TDMA), communication nodes send their data to the shared medium during an assigned time slot. A key characteristic of TDMA is that it first stores lower-bit-rate signals in a buffer prior to transmission. As seen in Fig. 12, when a node is assigned a time slot and allowed to transmit, it transmits all the bits stored in the buffer at a high transmission rate. To relax the synchronization requirement, data bursts or time slots are

TDMA separated by a guard time. With this guard time, transmissions within different time slots may have different bit clocks. This key feature allows the simplification of the timing recovery process and removes the need for frequency justification.

Owing to the fact that there is no need for bit timing and synchronization between the multiple users, TDMA can be directly performed in the optical transmission domain. The user obtains access to the transmission medium by having an optical transmitter transmitting a burst of optical data in a pulse-code-modulation format within a time slot. It should be noted that in optical networking scenarios, optical TDMA (OTDMA) is preferred over optical TDM (OTDM), owing to the ease of implementation of OTDMA. However, it must be stressed that the OTDMA approach has a lower bandwidth efficiency because some of the time slots are required to realize required timing guard bands.

The TDMA frame in Fig. 12 consists of a reference burst and a specific number of time slots. The reference burst is used for timing and establishing a synchronization reference, in addition to carrying information regarding the signaling (the communication process that sets up the communication call and monitors the communication link). The rest of the frame, which contains additional guard bands and time slots, carries the data. The reference burst primarily contains three main components: (1) a preamble, (2) a start code, and (3) control data. The preamble is a periodic bit stream that provides bit timing synchronization. Depending on the technology employed, the temporal duration or number of bits required to establish synchronization is on the order of a few bit periods. Once bit timing is achieved, the content in the remaining reference burst can be read. Following the preamble is a unique start code indicating the end of the preamble and the start of the information portion of the reference burst. When the word is recognized, control data can be interpreted correctly. In general, control data carries information such as station timing, call setup status, and signal information.

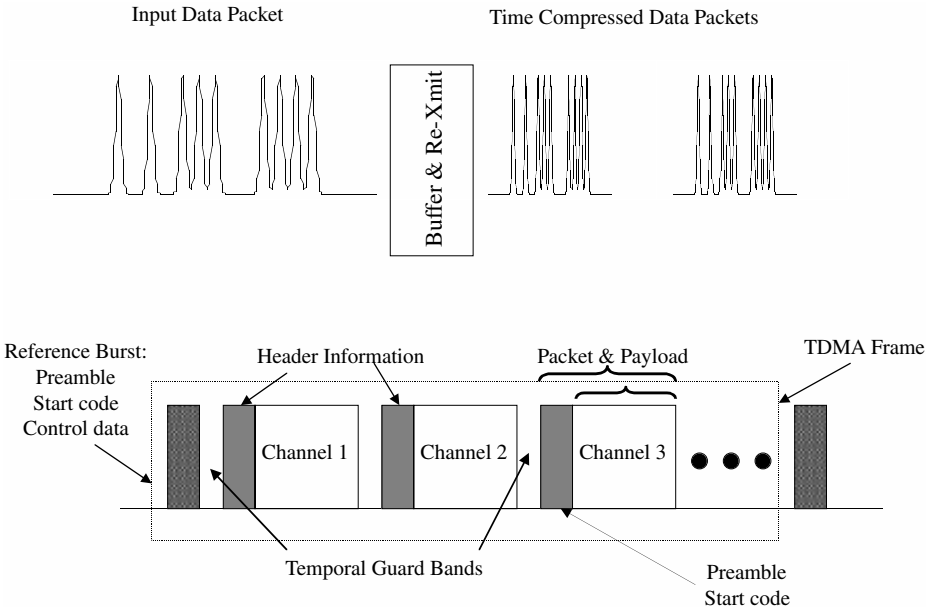

FIGURE 12 Representation illustrating the concepts of time-division multiple access, showing time-compressed data packets and the detailed layout of a TDMA packet, including header overhead and payload.

The reference burst in a TDMA frame is the overhead and occupies only a small portion of the frame. The remaining portion of the frame is divided into time slots separated by guard time bands. As in the reference burst, each time slot consists of a preamble, a unique start code, and the information payload. Owing to the different propagation delays between stations, the guard time between time slots is necessary to avoid overlap between two consecutive time slots. It should be noted that in TDMA networks, the transmitted data from the nodes must wait for time slots to become available. This occurs through an assigning process termed the *call setup.* Once a node obtains a time slot, it can use the same time slot in every frame for the duration of the communication session. In this case, the access is deterministic and as a result TDMA is generally used for constant-bit-rate transmission. While the node waits for the assigning of a time slot, the user stores its information into a buffer. Once the time slot is assigned, the bits are read out at a higher bit rate, and as a result the transmitted data bits have been compressed in time during the high-speed readout and transmission. When the input bits are stored and read out at a later time, a compression delay is introduced that is generally equal to the frame size. In real-time applications, it is critical to reduce the compression delay, and as a result the frame size should be as small as possible. However, since each frame has associated overhead in the preamble burst, the bandwidth or access efficiency is reduced. As a result, there is a trade-off between the network access efficiency and the compression delay.

Optical Domain TDMA

Even though there is an inherent trade-off between network access efficiency and compression delay, OTDMA is very attractive owing to the lack of any global, or network-wide, synchronization needs. As a result, the independent receiver nodes can have independent bit clocks. In an optical implementation, OTDMA bit rates are usually high, and this clock independence makes this approach attractive. One embodiment of an optical domain TDMA network is schematically illustrated in Fig. 13. To synchronize access, master frame timing needs to be distributed to all nodes. To achieve this, one of the nodes in the network, called the *master node,* generates a reference burst every T seconds, where T is the duration of a frame. Having the receiving nodes detect the reference burst means that the frame timing can be known at all receiving nodes; if the number of slots per frame is also known, the slot timing is obtained.

To allow the data to be received over a specific time slot in TDMA, a gate signal turns on during the slot interval, which is generated from the derived slot timing. As shown in Fig. 13, data in this slot interval can pass through the gate, be detected, and then be stored in the decompression buffer. The received slot timing derived is also sent to the local transmitter to determine its slot timing for transmission. The optical TDMA signal is first photodetected and then detected during a given slot interval. Data in all other time slots is suppressed by the gating operation. To preserve the received signal waveform, the bandwidth of the gating device is required to be much larger than the instantaneous bit rate. As a result, the bandwidth of the gate can limit the total TDMA throughput. To solve this problem, the gating function can be performed in the optical domain, whereby an electrooptical gate is used for a larger transmission bandwidth.

Time-Division Multiplexing

Historically, time-division multiplexing was first used in conventional digital telephony, where multiple lower-bit-rate digital data streams are interleaved in the time domain to form a higher-rate digital signal. These lower-bit-rate signals are referred to as *tributary signals.* Like TDMA, TDM is a time-domain multiple access approach, and each of its frames consists of a specific number of time slots. In contrast to the case with TDMA, data carried by different

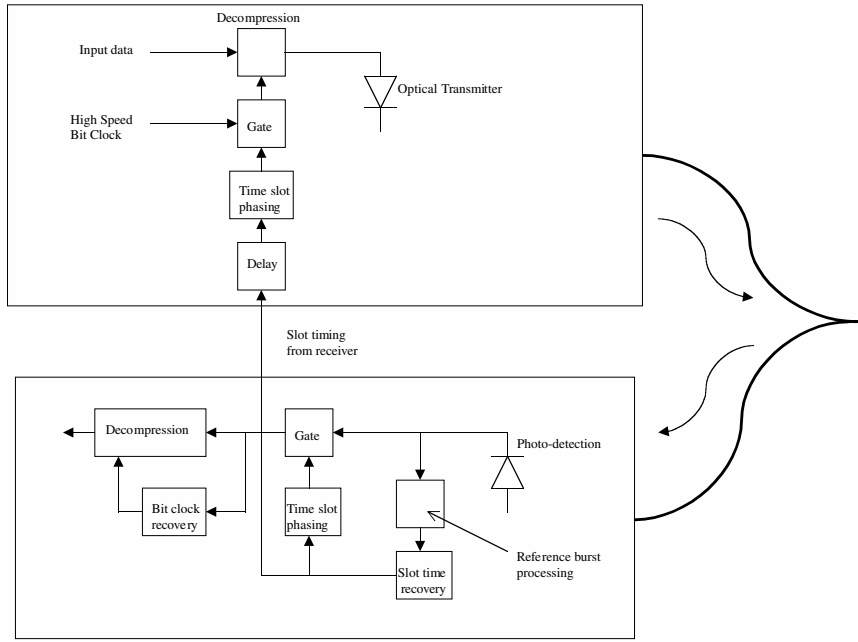

FIGURE 13 Optical implementation of a TDMA transmitter receiver.

slots is first synchronized in bit timing and then interleaved by a higher bit clock. This process of bit timing synchronization, called *frequency justification,* is necessary when upstream signals have different bit clock frequencies. Owing to the fact that all the tributary signals that feed into the overall network are synchronized at the bit level, no temporal guard band is required between different time slots, as is needed in the TDMA approach. In addition, a preamble signal at the beginning of each time slot is not required. As a result, if bit-level temporal synchronization is achievable, TDM is a better choice than TDMA, since the access and network bandwidth efficiency is higher (i.e., there are no wasted time slots used for preamble and guard band signals).

In TDM, lower-bit-rate signals are bit or byte interleaved into a higher-bit-rate signal. Accordingly, the multiplexed output consists of time slots, each of which carries one bit or byte for one input signal. To demultiplex time slots or to recognize which slots belong to which original inputs at the receiver end, time slots are grouped into frames that have additional overhead bits for frame and slot synchronization. As shown in Fig. 14, the number of time slots in a frame is equal to the total number of input signals, and when one input gets access to one slot, it continues to use the same slot in each frame for transmission. To multiplex a number of independent signals in TDM, the input signals must have the same bit clock. If there is any frequency mismatch between the bit rate of the independent signals, a premultiplexing signal processing step is required that adjusts the input bit rate of the signals to a common or master clock. This premultiplexing signal-processing step is referred to as *frequency justification* and can generally be achieved by adding additional bits to the frame, or by slip control, which may drop a byte and retransmit that byte in the next assigned time slot. These preprocessing steps of temporally aligning a number of independent signals to a com-

mon clock form one of the key challenges in high-bit-rate optical TDM systems, and for some applications this is a major drawback.

Owing to the fact that time-division multiplexing requires bit-timing synchronization, its implementation is more involved and complex. In order to synchronize the bit rates of the input signals, timing is generally performed at low bit rates directly on the input electrical signals. In order to facilitate the timing synchronization of the lower-bit-rate electrical signals that will ultimately be transmitted optically, an electronic synchronization standard has been developed that is referred to as the *synchronous optical network* (SONET) or the *synchronous digital hierarchy* (SDH). The key concept behind this synchronization process is the use of a floating payload, which eases the requirements of frequency justification, bit stuffing, and slip control.

Frame and Hierarchy

Like TDMA, TDM has a frame structure for data transmission and is composed of time slots that carry information, or data, from the lower-bit-rate or *tributary* signal. Since there is no temporal guard band or preamble signal for TDM time slots, the amount of data within a TDM time slot is generally one byte. While there is less overhead in TDM, this approach nonetheless does require the transmission of bits that assist in synchronization for the identification of frame boundaries and frequency justification, signaling for the setup and maintenance of the circuit connection, and maintenance bits for error correction and bit error rate monitoring.

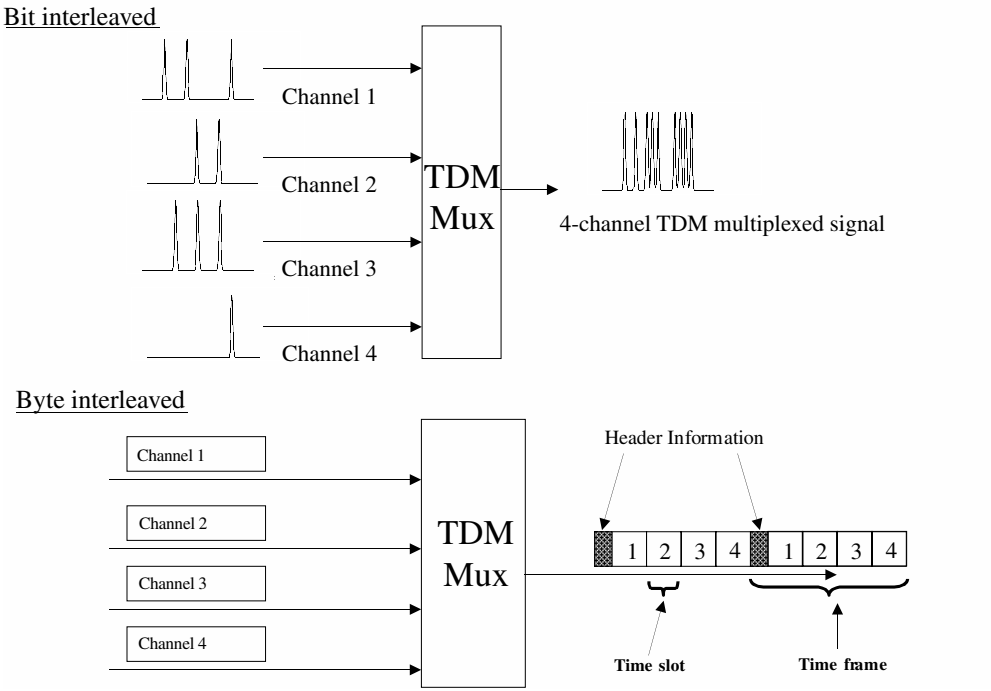

FIGURE 14 Representation illustrating the concepts of time-division multiplexing, showing schemes based on bit and byte interleaving.

In conventional TDM networks, two primary digital multiplexed systems are the 24- and 30-channel pulse-code-modulation formats for voice signals. In the 24-channel PCM-TDM format, 24 8-bit voice channels are time multiplexed to give 192 bits per frame, where each frame has a duration of 125 μs. One additional bit is inserted to provide frame synchronization, resulting in a total of 193 bits per frame. With a sampling rate of 8 kHz for standard voice communications, the overall clock rate is 1.544 Mbit/s; this is referred to as a *T1* signal or frame. Signaling information is usually transmitted over the eighth bit of the code word. A simplified block diagram of a 24-channel PCM coder/decoder is shown in Fig. 15.

A counterpart to the T1 frame of the 24-channel PCM-TDM is the 30-channel system, most generally deployed in Europe and referred to as the CEPT1 30-channel system. In this system, the frame size is also 125 μs, but each frame consists of 32 slots, with two slots (0 and 16) used for framing and signaling while the remaining 30 slots are used to carry 30 64kbit/s channels. From this design, the resulting bit rate of CEPT1 is 2.048 Mbit/s.

In TDM systems and telephony, the network is configured hierarchically—that is, higher-rate signals are multiplexed into continually higher-rate signals. In the AT&T digital hierarchy, the 24-channel PCM-TDM signals or T1 carriers are used as the basic system, and higher-order channel banks, referred to as T2, T3, and T4, are obtained by combining the lower-order channel banks. The multiplexing hierarchy is illustrated for both 24- and 30-channel systems in Fig. 16.

SONET and Frequency Justification

The synchronous optical network (SONET) is a TDM standard for transmission over optical fibers in the terrestrial United States. An international standard operating with the same

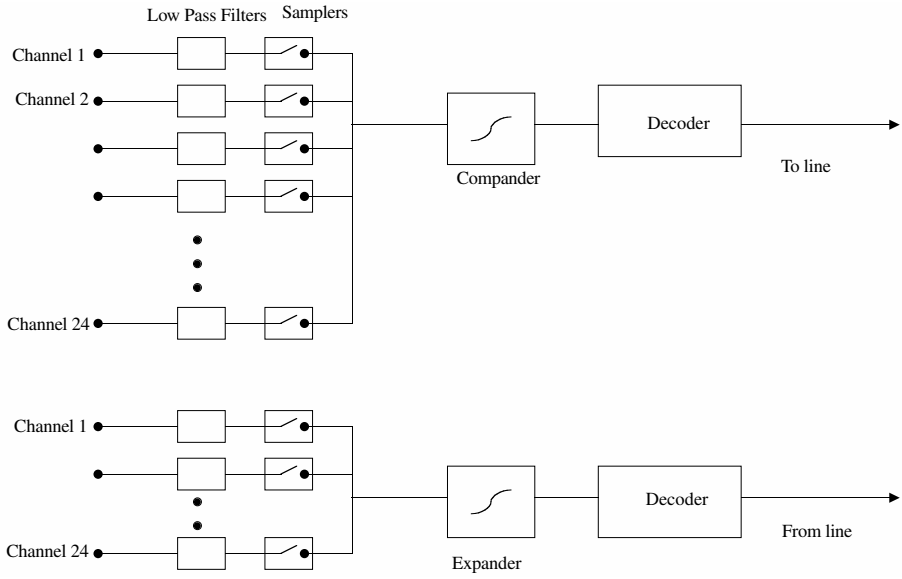

FIGURE 15 Schematic showing a 24-channel TDM transmitter/receiver. Included are compander/expander modules that compensate for quantization error and increase the system signal-to-noise ratio.

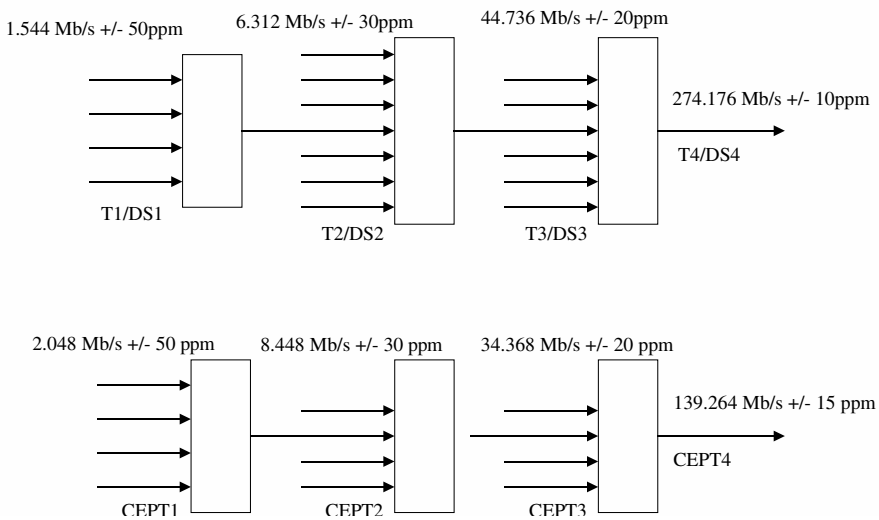

FIGURE 16 Schematic representation of the telephonic AT&T digital hierarchy and its European counterpart, CEPT.

underlying principles is called the *synchronous digital hierarchy* (SDH). These transmission standards were designed to simplify the process of frequency justification so that multiplexing and demultiplexing can be done at high speeds. To achieve this goal, SONET introduces the concept of a *floating payload,* where the information part of the packet floats with respect to the header information and the overall frame and the location of the payloads are identified by a process called *pointer processing.* A SONET frame has a two-dimensional frame structure to assist in examining its logical structure (see Fig. 17*a*). The sequence of data on the transmission line is obtained by traversing the table row by row, moving from left to right. The frame consists of 90 columns by nine rows. Since SONET transmission is to be compatible with voice communications, the frame duration is 125 μs, to be consistent with carrying at least one 8-bit digital sample of a voice channel. Therefore the basic bit rate of a SONET channel is $90 \times 9 \times 64$ kbit/s or 51.84 Mbit/s. This basic SONET signal is called synchronous transmission signal (STS)-1. STS-1 is the lowest rate in SONET, with all other SONET signals being multiples of this basic rate. It should be noted that the international version of SONET (SDH) has a two-dimensional frame structure of nine rows and 270 columns, existing for 125 μs, making the nominal SDH rate 3 times higher than that for SONET, or 155.52 Mbit/s. In this case STS-3 for SONET operates at the same rate as STS-1 (synchronous transport module) for SDH. When SONET signals are used to modulate a laser diode, the signals are then referred to as optical carrier (OC)-*N* signals.

In the SONET framing structure, the first four columns contain overhead information, and the remaining 86 columns contain the information payload. The fourth column and the remaining 86 columns make up a structure called the *synchronous payload envelope* (SPE). The salient feature of the SONET transmission is that the SPE can float with respect to the SONET frame—that is, the first byte of the SPE can be located anywhere within the 9×87 area. As one reads the SONET frame from left to right and top to bottom, the location of the overhead information is repeated in the same place in each frame. If these framing bytes continue to be present at the appropriate time, there is an extremely high probability that the signal is the framing signal and that the alignment of all other bytes is known. To identify the specific position of each payload, pointer processing becomes the critical aspect of SONET

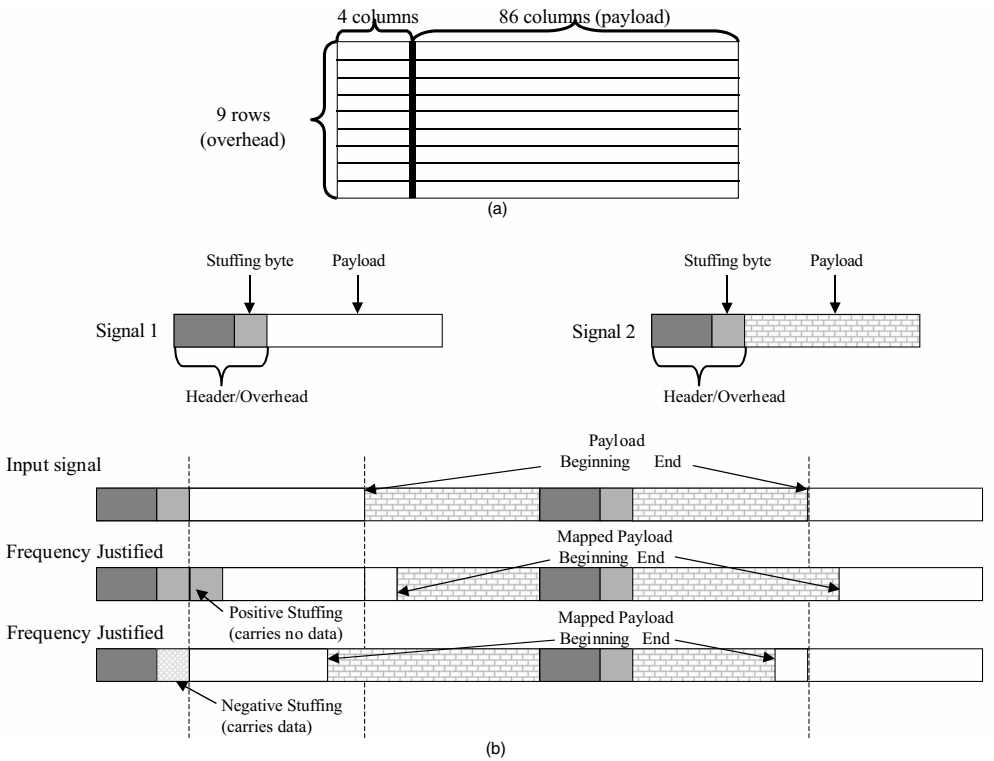

FIGURE 17 (*a*) The two-dimensional data structure of a TDM frame for SONET transmission. (*b*) The process of frequency justification, showing both positive and negative bit stuffing, to accommodate signals that are not at the same bit clock at a multiplexer.

transmission. In the classic T1 hierarchy, lower-speed signals generally arrive at the multiplexer at an arbitrary position with respect to their frame boundaries. The input data is then buffered to allow all the incoming signals to be aligned with the frame of the high-speed multiplex signal. These buffers were also necessary to allow for slight differences in clocks in the transmission lines that feed the multiplexer. The payload pointer eliminates the need for these buffers by providing a specific set of overhead bytes whose value can be used to determine the offset of the payload from the frame boundary.

The floating SPE concept and the use of pointer processing were developed to facilitate simpler implementation of frequency justification. In contrast to T carriers, where a tributary input at a multiplexer is frequency justified with respect to the frame of its next higher hierarchy, SONET performs frequency justification at the lowest STS-1 level. For example, when N STS-1 signals are multiplexed, the overhead of the input signals is removed, and the payloads of each input signal are mapped to the synchronous payload envelope (SPE) of the internal STS-1 signal of the multiplexer. Since each input signal is now synchronized and frequency justified after mapping to the internal STS-1 signal and its local clock, all N STS-1 signals can now be byte interleaved, resulting in a nominal outgoing bit rate of N times STS-1 for an STS-N signal. When M STS-N signals are multiplexed, each STS-N signal is first demultiplexed into N STS-1 signals, each of which is then frequency justified by the STS-1 clock of the multiplexer. Byte interleaving can then be done for the $M \times N$ STS-1 signals. It should be

noted that for T1 carriers, multiplexing occurs with four T1 signals to create a T2 signal, with seven T2 signals to create a T3 signal, and so on. This hierarchical multiplexing complicates the bit clock relationship at the different T-carrier levels.

To illustrate the process of frequency justification, consider the interleaving of a TDM packet with slightly different bit clocks as compared to the local bit clock of the multiplexer, as illustrated in Fig. 17*b.* In order to handle the possibility of each signal having a slightly different bit rate, the frame structure must possess extra space, or stuffing bits, to accommodate this difference. If the two signals, signal 1 and signal 2, have the same bit clock and as a result are frequency justified, only the payloads are copied to the outgoing frame. If the bit clocks are different, both payloads cannot fit within the outgoing frame, owing to bit conservation. In the case where the input bit clock of signal 1 has a higher bit rate than that of signal 2, the stuffing space from the header of signal 2 must be used to carry payload data from signal 1. Since the payloads of each signal possess the same number of bits, there is a one-byte shift in the mapping, that is, the start of the payload of signal 2 is advanced by one byte and floats with respect to the header. If, on the other hand, signal 1 has a lower bit rate than signal 2, an extra *dummy* byte is inserted into the payload of signal 2, and the mapping is delayed for one byte. Given these two extremes, it is clear that the payload floats with respect to the header within the TDM frame and can advance or be delayed to accommodate the timing difference between the signals.

12.4 INTRODUCTION TO DEVICE TECHNOLOGY

Thus far, a general description of the concepts of digital communications and the salient features of TDM and TDMA has been presented. Next we address specific device technology that is employed in OTDM networks (e.g., sources, modulators, receivers, clock recovery oscillators, demultiplexers, and so on) to provide an understanding of how and why specific device technology may be employed in a system to optimize network performance, minimize cost, or provide maximum flexibility in supporting a wide variety of user applications.

Optical Time-Division Multiplexing—Serial vs. Parallel

Optical time-division multiplexing can generally be achieved by two main methods. The first method is referred to as *parallel multiplexing;* the second method is classified as *serial multiplexing.* These two approaches are schematically illustrated in Fig. 18. The advantage of the parallel type of multiplexer is that it employs simple, linear passive optical components, not including the intensity modulator, and that the transmission speed is not limited by the modulator or any other high-speed switching element. The drawback is that the relative temporal delays between each channel must be accurately controlled and stabilized, which increases the complexity of this approach. Alternatively, the serial approach to multiplexing is simple to configure. In this approach a high-speed optical clock pulse train and modulation signal pulses are combined and introduced into an all-optical switch to create a modulated channel on the high-bit-rate clock signal. Cascading this process allows all the channels to be independently modulated, with the requirement that the relative delay between each channel must be appropriately adjusted.

Device Technology—Transmitters

For advanced lightwave systems and networks, it is the semiconductor laser that dominates as the primary optical source that is used to generate the light that is modulated and transmitted as information. The reason for the dominance of these devices is that they are very small, typically a few hundred micrometers on a side; that they achieve excellent efficiency in converting electrons to photons; and that their cost is low. In addition, semiconductor diode lasers

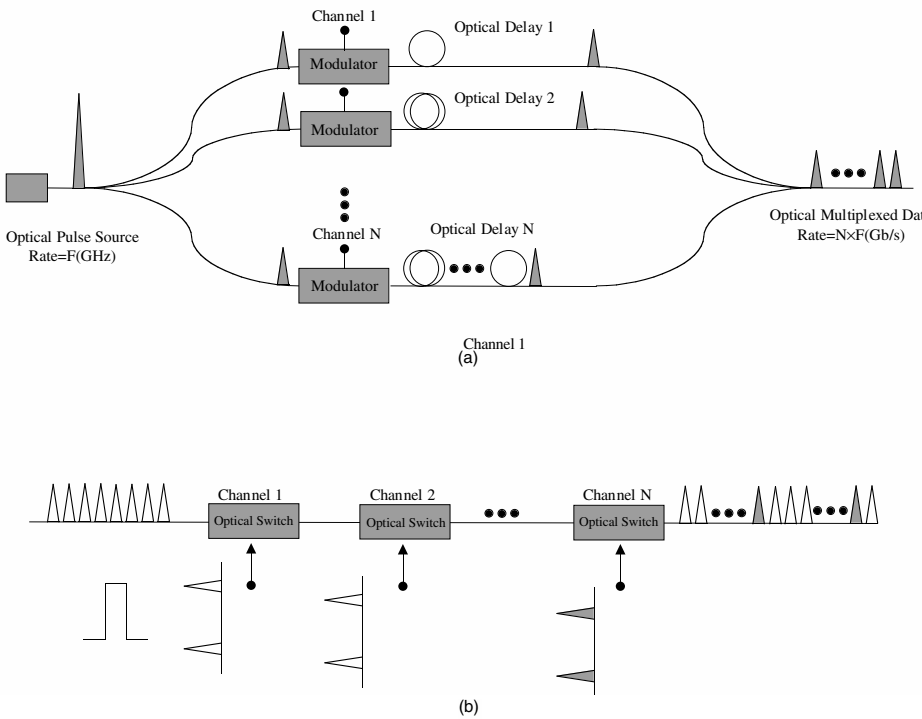

FIGURE 18 Schematic of optical time-division multiplexing for interleaving high-speed RZ optical pulses. (*a*) Parallel implementation. (*b*) Serial implementation.

can generate optical signals at wavelengths of 1.3 and 1.55 μm. These wavelengths are important because they correspond to the spectral regions where optical signals experience minimal dispersion (spreading of the optical data bits) and minimal loss.

These devices initially evolved from simple light-emitting diodes (LEDs) composed of a simple *p-n* junction, to Fabry-Perot (FP) semiconductor lasers, to distributed feedback (DFB) lasers and distributed Bragg reflector (DBR) lasers, and finally to mode-locked semiconductor diode lasers and optical fiber lasers. A simple description of each of these devices is given in the following text, along with advantages and disadvantages that influence how these optical transmitters are deployed in current optical systems and networks.

Fabry-Perot Semiconductor Lasers

Generally, the light-emitting diode is the simplest of all forms of all semiconductor light sources. These devices are quite popular for displays and indicator lights. Their use, however, is limited for communication and signal processing owing to the low modulation speeds and resulting low bandwidths achievable with these devices. In addition, owing to the fact that LEDs emit with a relatively broad optical spectrum, typically 10 to 30 nm, effects such as chromatic dispersion in the optical fiber tend to temporally broaden the optical bits and add additional constraints to the data transmission rates achievable with these devices. As a result, LEDs have a limited use in telecommunications, even though the device structure is quite

simple and the cost is very low. Given this, it is the simple Fabry-Perot semiconductor laser that will be initially considered as a potential source for OTDM systems and networks.

The Fabry-Perot semiconductor laser diode is made up of a semiconductor *p-n* junction that is heavily doped and fabricated from a direct-gap semiconductor material. The injected current is sufficiently large to provide optical gain. The optical feedback is provided by mirrors, which are usually obtained by cleaving the semiconductor material along its crystal planes. The large refractive index difference between the crystal and the surrounding air causes the cleaved surfaces to act as reflectors. As a result, the semiconductor crystal acts both as the gain medium and as an optical resonator or *cavity* (see Fig. 19). Provided that the gain coefficient is sufficiently large, the feedback transforms the device into an optical oscillator or laser diode. It should be noted that the laser diode is very similar to the light-emitting diode. Both devices have a source of pumping energy that is a small electric current injected into the *p-n* junction. To contrast the devices, the light emitted from the LED is generated from spontaneous emission, whereas the light produced from an FP laser diode is generated from stimulated emission.

To contrast semiconductor lasers with conventional gas laser sources, the spectral width of the output light is quite broad for semiconductor lasers owing to the fact that transitions between electrons and holes occur between two energy bands rather than two well-defined discrete energy levels. In addition, the energy and momentum relaxation processes in both conduction and valence band are very fast, typically ranging from 50 fs to 1 ps, and the gain medium tends to behave as a homogeneously broadened gain medium. Nonetheless, effects such as spatial hole burning allow the simultaneous oscillation of many longitudinal modes. This effect is compounded in semiconductor diode lasers because the cavity lengths are short and, as a result, have only a few longitudinal modes. This allows the fields of different longitudinal modes, which are distributed along the resonator axis, to overlap less, thereby allowing partial spatial hole burning to occur. Considering that the physical dimensions of the semiconductor diode laser are quite small, the short length of the diode forces the longitudinal mode spacing $c/2nL$ to be quite large. Here c is the speed of light, L is the length of the diode chip, and n is the refractive index. Nevertheless, many of these modes can generally fit within the broad gain bandwidth allowed in a semiconductor diode laser. As an example, consider an FP laser diode operating at 1.3 μm, fabricated from the InGaAsP material system. If $n = 3.5$ and $L = 400$ μm, the modes are spaced by 107 GHz, which corresponds to a wavelength spacing of 0.6 nm. In this device, the gain bandwidth can be 1.2 THz, corresponding to a wavelength spread of 7 nm, and as many as 11 modes can oscillate. Given that the mode spacing can be modified by cleaving the device so that only one axial mode exists within the gain bandwidth, the resulting device length would be approximately 36 μm, which is difficult to

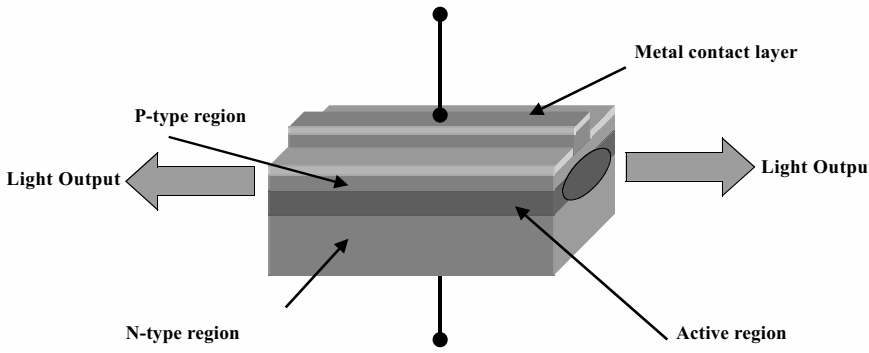

FIGURE 19 Schematic illustration of a simple Fabry-Perot semiconductor diode laser.

achieve. It should be noted that if the bias current is increased to well above threshold, the device can tend to oscillate on a single longitudinal mode. For telecommunications, it is very desirable to directly modulate the laser, thus avoiding the cost of an external modulator. However, in the case of direct modulation, the output emission spectrum will be multimode, and as a result, effects of dispersion will broaden the optical data bits and force the data rate to be reduced to avoid intersymbol interference. Given this effect, Fabry-Perot lasers tend to have a limited use in longer optical links.

Distributed Feedback Lasers

As indicated, the effects of dispersion and the broad spectral emission from semiconductor LEDs and semiconductor Fabry-Perot laser diodes tend to reduce the overall optical data transmission rate. Thus, methods have been developed to design novel semiconductor laser structures that will only operate on a single longitudinal mode. This will permit these devices to be directly modulated and allow for longer transmission paths since the overall spectral width is narrowed and the effect of dispersion is minimized.

There are several methods of achieving single-longitudinal-mode operation from semiconductor diode lasers. A standard semiconductor injection laser may be operated on a single transverse mode by reducing the waveguide's transverse dimensions, such as the width and height, while single-frequency operation may be obtained by reducing the length L of the diode chip so that the frequency spacing between adjacent longitudinal modes exceeds the spectral width of the gain medium. Other methods of single-mode operation include the use of a device known as a coupled-cleaved-cavity (C^3) laser, which is achieved by cleaving or etching a groove parallel to the end faces of the normal diode chip but placed between the end facets, thus creating two cavities. The standing-wave criteria must be satisfied by the boundary conditions at the surfaces of both cavities, and are generally only satisfied by a single frequency. In practice, however, the usefulness of this approach is limited by thermal drift, which results in both a wandering of the emission and abrupt, discrete changes in the spectral emission.

The preferred method of achieving single-frequency operation from semiconductor diode lasers is to incorporate frequency-selective reflectors at both ends of the diode chip, or alternately to fabricate the grating directly adjacent to the active layer. These two approaches result in devices referred to as *distributed Bragg reflector* (DBR) lasers and *distributed feedback* (DFB) lasers, respectively. In practice, it is easier to fabricate a single grating structure above the active layer as opposed to two separate gratings at each end. As a result, the DFB laser has become the laser of choice for telecommunications applications. These devices operate with spectral widths on the order of a few megahertz and have modulation bandwidths over 10 GHz. Clearly, the high modulation bandwidth and low spectral width make these devices well suited for direct modulation or on-off-keyed (OOK) optical networks. It should be noted that the narrow line width of a few megahertz is for the device operating in a continuous-wave mode, while modulating the device will necessarily broaden the spectral width.

In DFB lasers, Bragg reflection gratings are employed along the longitudinal direction of the laser cavity and are used to suppress the lasing of additional longitudinal modes. As shown in Fig. 20*a,* a periodic structure similar to a corrugated washboard is fabricated over the active layer, where the periodic spacing is denoted as Λ. Owing to this periodic structure, both forward- and backward-traveling waves must interfere constructively with each other. In order to achieve this constructive interference between the forward and backward waves, the round-trip phase change over one period should be $2\pi m$, where m is an integer and is called the order of the Bragg diffraction. With $m = 1$, the first-order Bragg wavelength λ_B is

$$2\pi = 2\Lambda(2\pi n/\lambda_B) \tag{9}$$

or

$$\lambda_B = 2\Lambda n \tag{10}$$

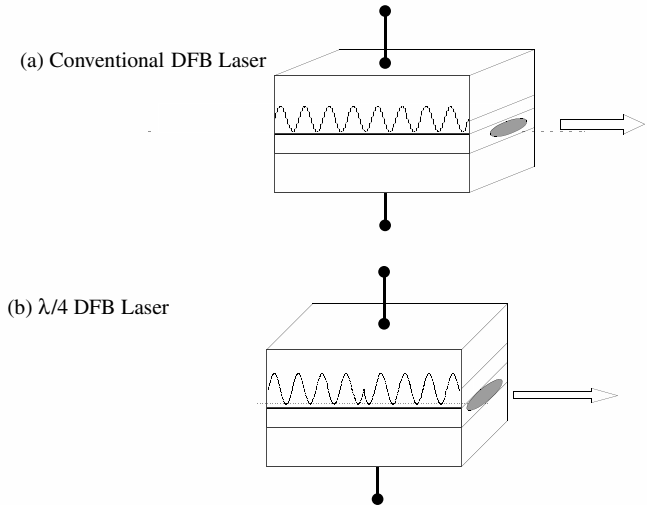

FIGURE 20 Schematic illustrations of distributed feedback (DFB) lasers. (*a*) Conventional DFB. (*b*) Quarter-wave DFB, showing the discontinuity of the Bragg grating structure to achieve single-wavelength operation.

where n is the refractive index of the semiconductor. Therefore, the period of the periodic structure determines the wavelength for the single-mode output. In reality, a periodic DFB structure generates two main modes symmetrically placed on either side of the Bragg wavelength λ_B. In order to suppress this dual-frequency emission and generate only one mode at the Bragg wavelength, a phase shift of $\lambda/4$ can be used to remove the symmetry. As shown in Fig. 20*b,* the periodic structure has a phase discontinuity of $\pi/2$ at the middle, which gives an equivalent $\lambda/4$ phase shift. Owing to the ability of the $\lambda/4$ DFB structure to generate a single-frequency, narrow spectral line width, these are the preferred devices for telecommunications at present.

Mode-locked Lasers

Mode-locking is a technique for obtaining very short bursts of light from lasers, and can be easily achieved employing both semiconductor and fiber gain media. As a result of mode-locking, the light that is produced is automatically in a pulsed form that produces return-to-zero (RZ) data if passed through an external modulator being electrically driven with non-return-to-zero data. More importantly, the temporal duration of the optical bits produced by mode-locking is much shorter than the period of the driving signal! In contrast, consider a DFB laser whose light is externally modulated. In this case, the temporal duration of the optical bits will be equal to the temporal duration of the electrical pulses driving the external modulator. As a result, the maximum possible data transmission rate achievable from the DFB will be limited to the speed of the electronic driving signal. With mode-locking, however, a low-frequency electrical drive signal can be used to generate ultrashort optical bits. By following the light production with external modulation and optical bit interleaving, one can realize the ultimate in OTDM transmission rates. To show the difference between a mode-locked pulse train and its drive, Fig. 21 plots a sinusoid and a mode-locked pulse train consisting of five locked optical modes.

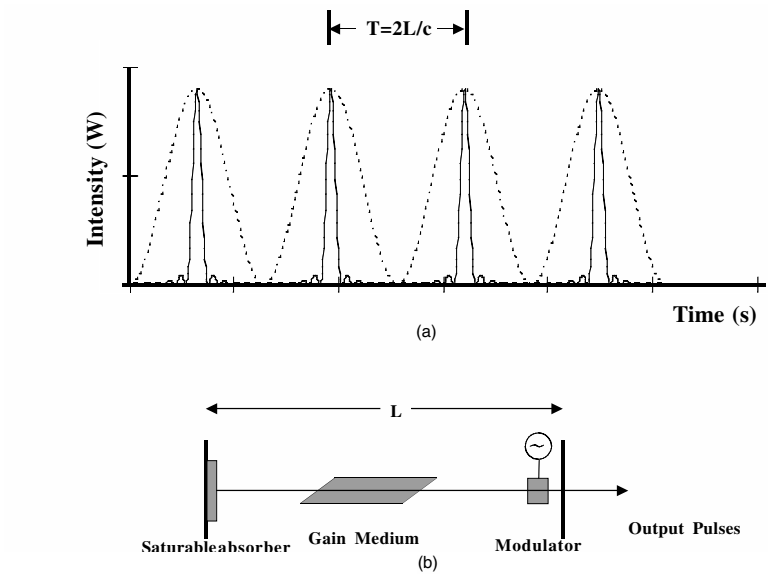

FIGURE 21 Optical intensity distribution of five coherent, phase-locked modes of a laser (*a*), and a schematic diagram of an external-cavity mode-locked laser (*b*). Superimposed on the optical pulse train is a typical sinusoid that could be used to mode-lock the laser, showing that much shorter optical pulses can be obtained from a low-frequency signal.

To understand the process of mode-locking, it should be recalled that a laser can oscillate on many longitudinal modes that are equally spaced by the longitudinal mode spacing $c/(2nL)$. Normally these modes oscillate independently; however, techniques can be employed to couple and lock their relative phases together. The modes can then be regarded as the components of a Fourier-series expansion of a periodic function of time of period $T = (2nL)/c$ that represents a periodic train of optical pulses. Consider for example a laser with multiple longitudinal modes separated by $c/2nL$. The output intensity of a perfectly mode-locked laser as a function of time t and axial position z with M locked longitudinal modes, each with equal intensity, is given by

$$I(t,z) = M^2|A|^2 \frac{\sin c^2[M(t - z/c)/T]}{\sin c^2[(t - z/c)T]} \tag{11}$$

where T is the periodicity of the optical pulses and $\sin c(x)$ is $\sin(x)/x$. In practice, there are several methods of generating optical pulse trains by mode-locking. These generally fall into two categories: (1) active mode-locking and (2) passive mode-locking. In both cases, to lock the longitudinal modes in phase, the gain of the laser is increased above its threshold for a short duration by opening and closing a shutter that is placed within the optical cavity. This allows a pulse of light to form. Allowing the light to propagate around the cavity and continually reopening and closing the shutter at a rate inversely proportional to the round-trip time forms a stable, well-defined optical pulse. If the shutter is realized by using an external modulator, the technique is referred to as *active mode-locking,* whereas if the shutter is realized by a device or material that is activated by the light intensity itself, the process is called *passive*

mode-locking. Both techniques can be used simultaneously; this is referred to as *hybrid mode-locking* (see Fig. 21*b*).

From the preceding equation, it is observed that the pulse duration is determined by the number of modes *M,* which in practice is generally limited by the gain bandwidth of the medium. Since the gain bandwidth of semiconductor and optical fiber lasers can be very broad, the resultant pulse width can be very short. In addition, since the modes are added coherently, the peak intensity is *M* times the average power, making these optical pulses sufficiently intense to induce nonlinear optical effects. Generally, high optical power in optical communication is useful for large signal-to-noise ratios in the detection process; however, other effects, such as nonlinear optical effects, can be detrimental. While nonlinear optical effects are typically avoided in data transmission, the peak intensity may exploit novel forms of optical propagation, such as optical soliton propagation. In addition, ultrafast all-optical switching and demultiplexing only become possible with such high-peak-intensity pulses. As a result, mode-locked semiconductor and fiber lasers may ultimately become the preferred laser transmitters for telecommunications.

Direct and Indirect Modulation

To transmit information in OTDM networks, the light output of the laser source must be modulated in intensity. Depending on whether the output light is modulated by directly modulating the current source to the laser or whether the light is modulated externally (after it has been generated), the process of modulation can be classified as either (1) direct or (2) indirect or external (see Fig. 22*a* and *b*). With direct modulation, the light is directly modulated inside the light source, while external modulation uses a separate external modulator placed after the laser source.

Direct modulation is used in many optical communication systems owing to its simple and cost-effective implementation. However, due to the physics of laser action and the finite response of populating the lasing levels owing to current injection, the light output under direct modulation cannot respond to the input electrical signal instantaneously. Instead, there are turn-on delays and oscillations that occur when the modulating signal, which is used as the pumping current, has large and fast changes. As a result, direct modulation has several undesirable effects, such as frequency chirping and line width broadening. In frequency chirping, the spectrum of the output generated light is time varying; that is, the wavelength and spectrum change over time. This is because as the laser is turned on and off, the gain is changed from a very low value to a high value. Since the index of refraction of the laser diode is closely related to the optical gain of the device, as the gain changes, so does its index. It is this time-varying refractive index that leads to frequency chirping, sometimes referred to as *phase modulation.* In addition, in Fabry-Perot lasers, if the device is turned on and off, the temporal behavior of the spectrum will vary from being multimode to nearly single mode within an optical bit, leading to line width broadening. The line width broadening results from measuring the time-integrated optical spectrum. In this case, since the instantaneous frequency or spectral width of the laser source varies rapidly over time, a measurement of the optical spectrum over a time interval that is long compared to the instantaneous frequency changes results in a broadened spectral width of the source as compared to a continuous wave measurement.

External Modulation

External modulation provides an alternative approach to achieving light modulation with the added benefit of avoiding the undesirable frequency chirping effects in DFB lasers and mode partition noise in FP lasers associated with direct modulation. A typical external modulator consists of an optical waveguide in which the incident light propagates through and the refrac-

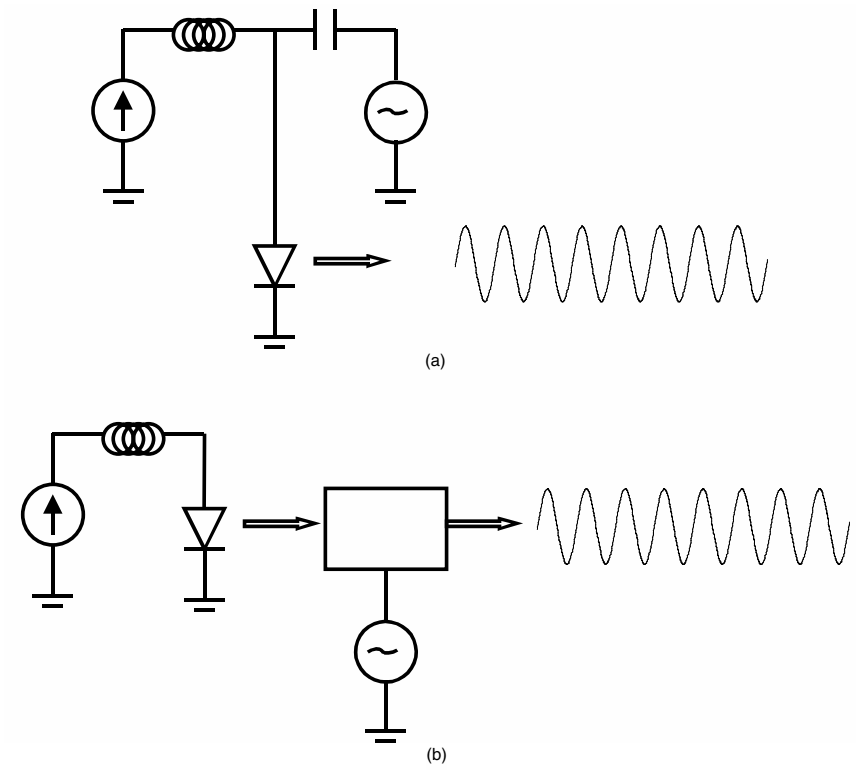

FIGURE 22 Illustrative example of direct modulation (*a*) and external modulation (*b*) of a laser diode.

tive index or absorption of the medium is modulated by a signal that represents the data to be transmitted. Depending on the specific device, three basic types of external modulators can be used: (1) electrooptic, (2) acoustooptic, and (3) electroabsorption (EA). Generally, acoustooptic modulators respond slowly—on the order of several nanoseconds—and as a result are not used for external modulators in telecommunications applications. Electroabsorption modulators rely on the fact that the band edge of a semiconductor can be frequency shifted to realize an intensity modulation for a well-defined wavelength that is close to the band edge of the modulator. Linear frequency responses up to 50 GHz are possible; however, the fact that the wavelength of the laser and the modulator must be accurately matched makes this approach more difficult to implement with individual devices. It should be noted, however, that EA modulators and semiconductor lasers can be integrated in the same devices, helping to remove restrictions on matching the transmitter's and modulator's wavelengths.

The typical desirable properties of an external modulator from a communications perspective are a large modulation bandwidth, a large depth of modulation, a small insertion loss (loss of the signal light passing through the device), and a low electrical drive power. In addition, for some types of communication TDM links, a high degree of linearity between the drive signal and modulated light signal is required (typical for analog links), and an independence of input polarization (polarization diversity) is desired. Finally, the low costs and small sizes of these devices make them extremely useful for cost-effective and wide-area deployment.

Electrooptic Modulators

An electrooptic modulator can be a simple optical channel or waveguide propagated by the light to be modulated. The material that is chosen to realize the electrooptic modulator must possess an optical birefringence that can be controlled or adjusted by an external electrical field that is applied along or transverse to the direction of propagation of the light to be modulated. This birefringence means that the index of refraction is different for light that propagates in different directions in the crystal. If the input light has a well-defined polarization state, this light can be made to see, or experience, different refractive indexes for different input polarization states. By adjusting the applied voltage to the electrooptic modulator, the polarization can be made to rotate or the speed of the light can be slightly varied. This modification of the input light property can be used to realize a change in the output light intensity by the use of a crossed polarizer or by interference of the modulated light with an exact copy of the unmodulated light. This can easily be achieved by using a waveguide interferometer, such as a Mach-Zehnder interferometer. If the refractive index is directly proportional to the applied electric field, the effect is referred to as *Pockel's effect.* In contrast, if the refractive index responds to the square of the applied electric field, the effect is referred to as the *Kerr effect.* This second effect has an interesting implication for all optical switching and modulation, since the intensity of a light beam is proportional to the square of the electric field and can therefore be used as a driving signal to modulate a second light beam.

Generally, for high-speed telecommunications applications, device designers employ the use of the electrooptic effect as a phase modulator in conjunction with an integrated Mach-Zehnder interferometer or an integrated directional coupler. Phase modulation (or delay/retardation modulation) does not affect the intensity of the input light beam. However, if a phase modulator is incorporated in one branch of an interferometer, the resultant output light from the interferometer will be intensity modulated. Consider an integrated Mach-Zehnder interferometer in Fig. 23. If the waveguide divides the input optical power equally, the transmitted intensity is related to the output intensity by the well-known interferometer equation $I_o = I_I \cos^2(\phi/2)$, where ϕ is the phase difference between the two light beams and the transmittance function is defined as $I_o/I_I = \cos^2(\phi/2)$.

Owing to the presence of the phase modulator in one of the interferometer arms, and with the phase being controlled by the applied voltage in accordance with a linear relation for

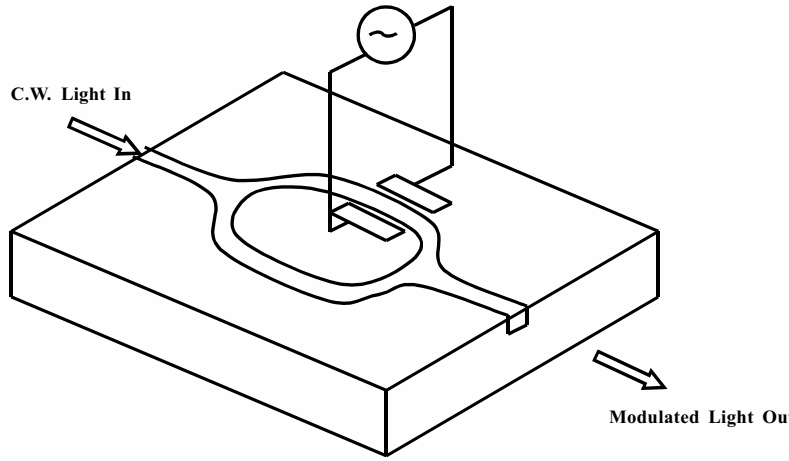

FIGURE 23 Illustration of an integrated lithium niobate Mach-Zehnder modulator.

Pockel's effect, $\phi = \phi_o - \pi V/V\pi$. In this equation, ϕ_o is determined by the optical path difference between the two beams and $V\pi$ is the voltage required to achieve a π phase shift between the two beams. The transmittance of the device therefore becomes a function of the applied voltage *V*,

$$T(V) = \cos^2(\phi/2 - \pi V/2V\pi) \tag{12}$$

This function is plotted in Fig. 24 for an arbitrary value of ϕ_o. The device can be used as a linear intensity modulator by adjusting the optical path difference so that $\phi_o = \pi/2$ and conducting operation in the linear region near $T = 0.5$. In contrast, the optical phase difference may be adjusted so that ϕ_o is a multiple of 2π. In this case, $T(0) = 1$ and $T(V\pi) = 0$, so that the modulator switches the light on and off as V is switched between 0 and $V\pi$, providing digital modulation of the light intensity, or on-off keying (OOK). Commercially available integrated devices operate at speeds of up to 40 GHz and are quite suitable for OTDM applications such as modulation and demultiplexing.

Electroabsorption Modulators

Electroabsorption modulators are intensity modulators that rely on the quantum confined Stark effect. In this device, thin layers of semiconductor material are grown on a semiconductor substrate to generate a multiplicity of semiconductor quantum wells, or multiple quantum wells (MQW). For telecommunication applications, the semiconductor material family that is generally used is InGaAsP/InP. The number of quantum wells can vary, but is typically on the order of 10, with an overall device length of a few hundred micrometers. Owing to the dimensions of the thin layers, typically 100 Å or less, the electrons and holes bind to form excitons. These excitons have sharp and well-defined optical absorption peaks that occur near the band gap of the semiconductor material. When an electric field or bias voltage is applied in a direction perpendicular to the quantum well layers, the relative position of the exciton absorption peak can be made to shift to longer wavelengths. As a result, an optical field that passes through these wells can be preferentially absorbed, if the polarization of the light field is parallel to the quantum well layers. Therefore, the input light can be modulated by modu-

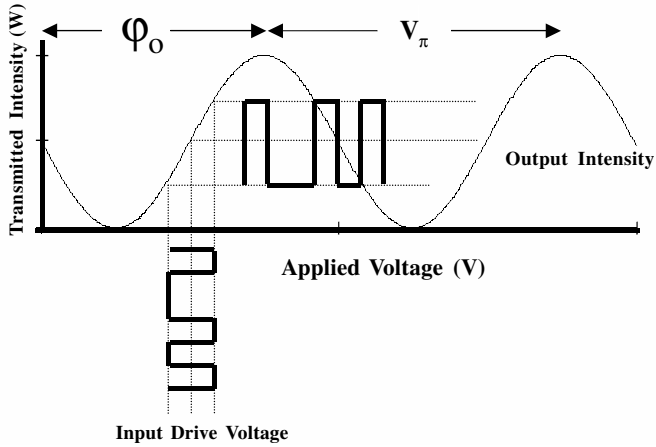

FIGURE 24 Input-output relations of an external modulator based on Pockel's effect. Superimposed on the transfer function is a modulated drive signal and the resultant output intensity from the modulator.

lating the bias voltage across the MQWs. These devices can theoretically possess modulation speeds as high as 50 GHz, with contrasts approaching 50 dB. A typical device schematic and absorption curve is shown in Fig. 25*a* and *b.*

Optical Clock Recovery

In time-division-multiplexed and multiple-access networks, it is necessary to regenerate a timing signal to be used for demultiplexing. A general discussion of clock extraction has already been given; in this section, an extension to those concepts is outlined for clock recovery in the optical domain. As in the conventional approaches to clock recovery, optical clock extraction has three general approaches: (1) the optical tank circuit, (2) high-speed phase-locked loops, and (3) injection locking of pulsed optical oscillators. The optical tank circuit can be easily real-

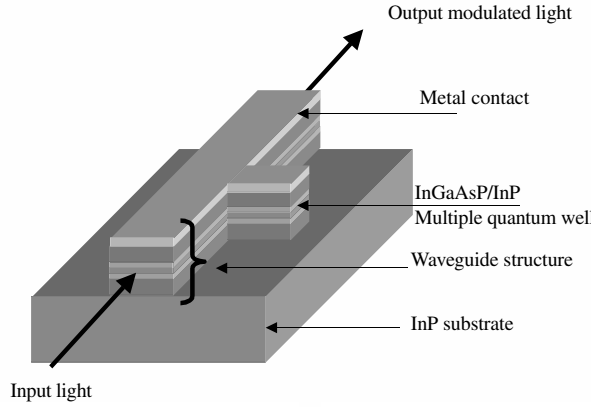

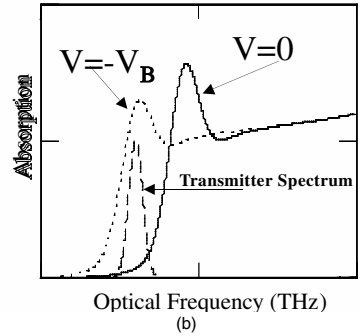

FIGURE 25 (*a*) Schematic diagram of an electroabsorption modulator. Light propagation occurs along the fabricated waveguide structure, in the plane of the semiconductor multiple quantum wells. (*b*) Typical absorption spectrum of a multiple quantum well stack under reverse bias and zero bias. Superimposed is a spectrum of a laser transmitter, showing how the shift in the absorption edge can either allow passage or attenuate the transmitted light.

ized by using a simple Fabry-Perot cavity. For clock extraction, the length L of the cavity must be related to the optical transmission bit rate. For example, if the input optical bit rate is 10 Gbit/s, the effective length of the optical tank cavity is 15 mm. The concept of the optical tank circuit is intuitively pleasing because it has many of the same features as electrical tank circuits—that is, a cavity Q and its associated decay time. In the case of a simple Fabry-Perot cavity as the optical tank circuit, the optical decay time or photon lifetime is given by

$$\tau_D = \frac{\tau_{RT}}{1 - R_1 R_2} \tag{13}$$

where τ_{RT} is the round-trip time given as $2L/c$, and R_1 and R_2 are the reflection coefficients of the cavity mirrors. One major difference between the optical tank circuit and its electrical counterpart is that the output of the optical tank circuit never exceeds the input optical intensity (see Fig. 26*a*).

A second technique that builds on the concept of the optical tank is optical injection seeding or injection locking. In this technique, the optical data bits are injected into a nonlinear device such as a passively mode-locked semiconductor laser diode (see Fig. 26*b*). The key difference between this approach and the optical tank circuit approach is that the injection-locking technique has internal gain to compensate for the finite photon lifetime, or decay, of the empty cavity. In addition to the gain, the cavity also contains a nonlinear element (e.g., a saturable absorber to initiate and sustain pulsed operation). Another important characteristic of the injection-locking technique using passively mode-locked laser diodes is that clock extraction can be prescaled—that is, a clock signal can be obtained at bit rates exactly equal to the input data bit rate or at harmonics or subharmonics of the input bit rate. In this case of generating a prescaled clock signal at a subharmonic of the input data stream, the resultant signal can be used directly for demultiplexing without any addition signal processing.

The operation of the injection seeded optical clock is as follows: The passively mode-locked laser produces optical pulses at its natural rate, which is proportional to the longitudinal mode spacing of the device cavity $c/(2L)$. Optical data bits from the transmitter are

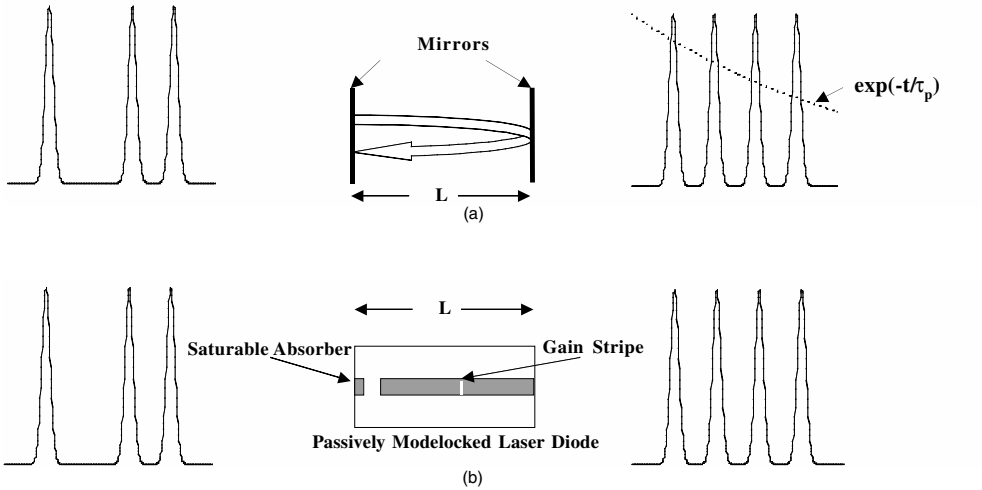

FIGURE 26 All-optical clock recovery based on optical injection of (*a*) an optical tank circuit (Fabry-Perot cavity) and (*b*) a mode-locked semiconductor diode laser.

injected into the mode-locked laser, where the data transmission rate is generally a harmonic of the clock rate. This criterion immediately provides the prescaling required for demultiplexing. The injected optical bits serve as a seeding mechanism to allow the clock to build up pulses from the injected optical bits. As the injected optical bits and the internal clock pulse compete for gain, the continuous injection of optical bits forces the internal clock pulse to evolve and shift in time to produce pulses that are synchronized with the input data. It should be noted that it is not necessary for the input optical bit rate to be equal to or greater than the nominal pulse rate of the clock—for example, the input data rate can be lower than the nominal bit rate of the clock. This is analogous to the transmitter sending data with primarily 0s, with logic 1 pulses occurring infrequently. The physical operating mechanism can also be understood by examining the operation in the frequency domain. From a frequency domain perspective, since the injected optical data bits are injected at a well-defined bit rate, the optical spectrum has a series of discrete line spectra centered around the laser emission wavelength and separated in frequency by the bit rate. Since the optical clock emits a periodic train of optical pulses, its optical spectrum is also a series of discrete line spectra separated by the clock repetition frequency. If the line spectra of the injected data bits fall within optical gain bandwidth of the optical clock, the injected line spectra will serve as seeding signals to force the optical clock to emit with line spectra similar to the injected signals. Since the injected data bits are repetitively pulsed, the discrete line spectra have the proper phase relation to force the clock to emit synchronously with the injected data.

It should be noted that the all optical clock recovery techniques discussed inherently rely on the fact that the transmitted optical data is in the return-to-zero (RZ) format. However, in present-day optical communication systems, non-return-to-zero (NRZ) is the line code that is primarily used. As shown in the preceding text, in the electrical domain there is a method to convert electrical NRZ signals to RZ signals by preprocessing using an exclusive OR logic function. In the optical domain, optical logic is possible but difficult to implement, so in theory a similar approach could be employed but would generally not be practical. Fortunately, by employing a simple optical interferometer, one can create a device that converts an optical NRZ signal to a pseudo-RZ signal that can be used for optical clock recovery. The pseudo-RZ signal is not an accurate transformation of the NRZ data, but only modifies the NRZ so that the resultant output RZ signal has the proper optical frequency components to allow for injection locking. To produce the required temporal delay, the format conversion uses a Mach-Zehnder interferometer that has an extra optical path in one arm. The interferometer is adjusted so that the output port is destructively interfering. Thus, when both signals are combined at the output, the output signal is zero. In contrast, when one signal or the other is present, a pulse exits the interferometer. This action nearly mimics the exclusive OR logic function. An example of how the format conversion is performed is schematically shown in Fig. 27; two optical configurations of its implementation are displayed in Fig. 28*a* and *b.* The benefit of this format conversion is that it employs simple linear optics; however, the interferometer is required to be stabilized for robust performance.

All-Optical Switching for Demultiplexing

In an all-optical switch, light controls light with the aid of a nonlinear optical material. It should be noted here that all materials will exhibit a nonlinear optical response, but the strength of the response will vary widely depending on the specific material. One important effect in an all-optical switch is the optical Kerr effect, whereby the refractive index of a medium is proportional to the square of the incident electric field. Since light is inducing the nonlinearity, or in other words providing the incident electric field, the refractive index becomes proportional to the light intensity. Since the intensity of a light beam can change the refractive index, the speed of a second, weaker beam can be modified owing to the presence of the intense beam. This effect is used extensively in combination with an optical interferometer to realize all-optical switching (see the section on electrooptic modulation using a Mach-Zehnder interferometer). Consider for example a Mach-Zehnder interferometer that

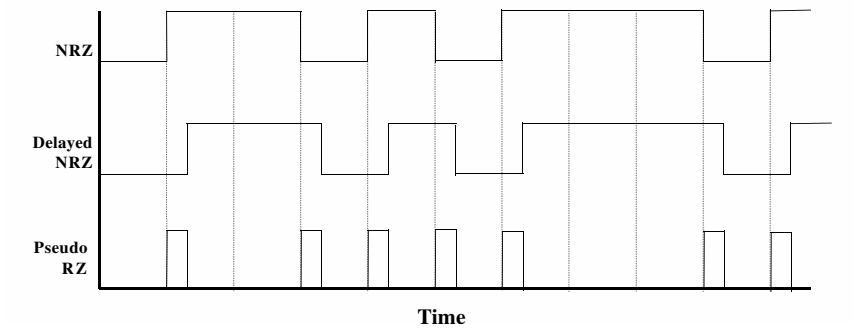

FIGURE 27 Illustration of format conversion between NRZ and RZ line codes. The resultant RZ code is not a representation of the NRZ data, but a pseudo-RZ code that has RZ pulses located at all NRZ transitions.

includes a nonlinear optical material that possesses the optical Kerr effect (see Fig. 29). If data to be demultiplexed is injected into the interferometer, the relative phase delay in each area can be adjusted so that the entire injected data signal is present only at one output port. If an intense optical control beam is injected into the nonlinear optical medium and synchronized with a single data bit passing through the nonlinear medium, that bit can be slowed down such that destructive interference occurs at the original output port and constructive interference

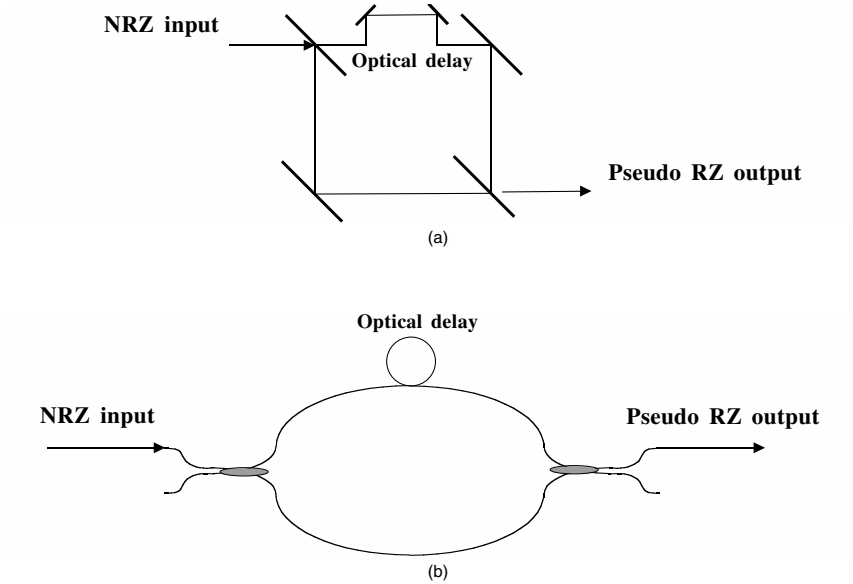

FIGURE 28 An optical implementation of an NRZ-to-RZ format converter, based on optical interference. (*a*) A simple interferometer demonstrating the operating principle. (*b*) A fiber-optic implementation of the format converter.

occurs at the secondary output port. In this case, the single bit has been switched out of the interferometer, while all other bits are transmitted.

Optical switches have been realized using optical fiber in the form of a Sagnac interferometer, and the fiber itself is used as the nonlinear medium. These devices are usually referred to as *nonlinear loop mirrors.* Other versions of all-optical switches may use semiconductor optical amplifiers as the nonlinear optical element. In this case, it is the change in gain induced by the control pulse that changes the refractive index owing to the Kramers-Kronig relations. Devices such as these are referred to as terahertz optical asymmetric demultiplexers (TOADs), semiconductor laser amplifier loop optical mirrors (SLALOMs), and unbalanced nonlinear interferometers (UNIs).

Receiver Systems

For high-speed optical time-division-multiplexed systems, key components are the optical receiver that detects the optical radiation, the associated electronic/optical circuitry that provides pre- or postamplification of the received signal, and the required clock recovery synchro-

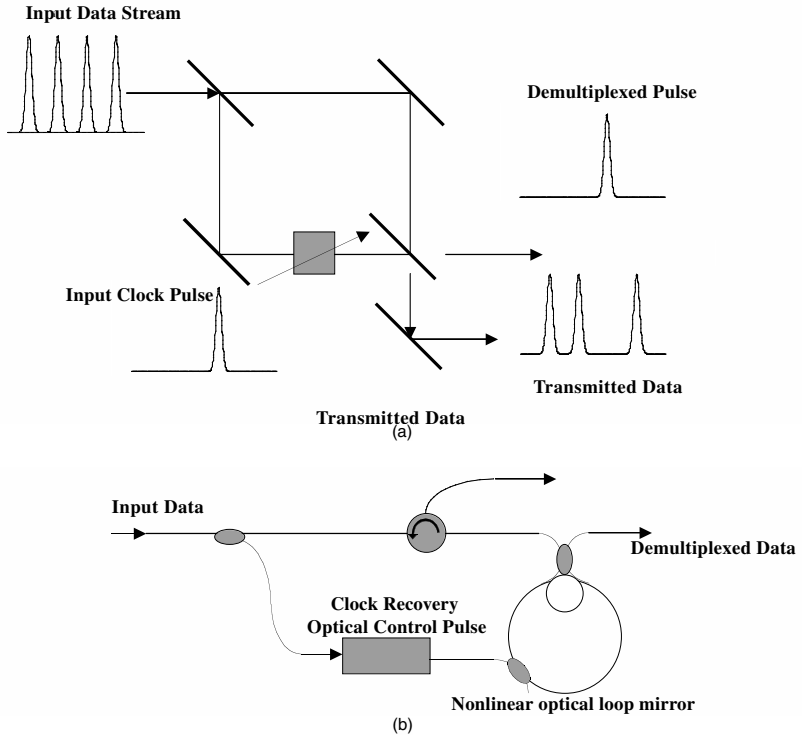

FIGURE 29 Schematic diagram of an all-optical switch. (*a*) A simple configuration based on a Mach-Zehnder interferometer and a separate nonlinear material activated by an independent control pulse. (*b*) An optical fiber implementation of an all-optical switch. This implementation relies on the inherent nonlinearity of the fiber that is induced by an independent control pulse.

nization for demultiplexing. In Fig. 30 is a typical arrangement for an optical receiver system. The incident lightwave signal is converted to an electrical signal by the optical receiver front end, which contains a photodetector and a preamplifier circuit. Usually, to enhance the receiver sensitivity, some means of increasing the average number of photoelectrons generated by the photodetector per incident photon is also included in the receiver setup. Schematically, this process is represented as a gain block G as shown in Fig. 30. This preamplification process can be accomplished in several ways. For example, in a direct detection system (i.e., one that directly detects the incident light), the most commonly adopted method is to use an avalanche photodiode (APD) as the photodetector. This type of detector provides a mechanism for electron multiplication that directly amplifies the detected signal electrically. Statistically, for every incident photon, the average number of photoelectrons generated by the APD is ηM, where η is the quantum efficiency of detection and M is the multiplication factor or avalanche gain, which is typically between 8 and 12 for most common receivers used in telecommunication systems.

An alternate method of realizing the preamplification process is to employ an optical amplifier, such as a semiconductor optical amplifier or an optical fiber amplifier, for example the erbium-doped fiber amplifier (EDFA). Owing to the large gain (which can be greater than 30 dB), the low noise characteristics, and the low insertion loss, the EDFA has been the predominant choice for implementing the optical preamplifier receiver in long-haul system experiments, particularly at high bit rates (>5 Gbit/s). The main disadvantage of employing EDFAs as optical preamplifiers are the high cost, high power consumption, and large size as compared to avalanche photodiodes. For moderate link lengths of less than 50 km, APDs are primarily employed.

In general, the preamplifier in the optical front end is an analog circuit. With a fixed-gain preamplifier, the front-end output signal level will follow the variation of the input optical power. This kind of signal level variation will impair the performance of the clock recovery and decision circuit subsystem, shown as the clock-data recovery block in Fig. 28. In addition, at low input power levels, the output signal level from the front end is usually not sufficiently high to be processed by the decision circuit, which typically requires an input peak-to-peak signal level of a few hundred millivolts. Therefore, a postamplifier is needed after the optical front end to minimize additional degradation in the performance of the CDR section. The main functions of this postamplifier are to provide an adequate signal amplification and to maintain a stable output signal level.

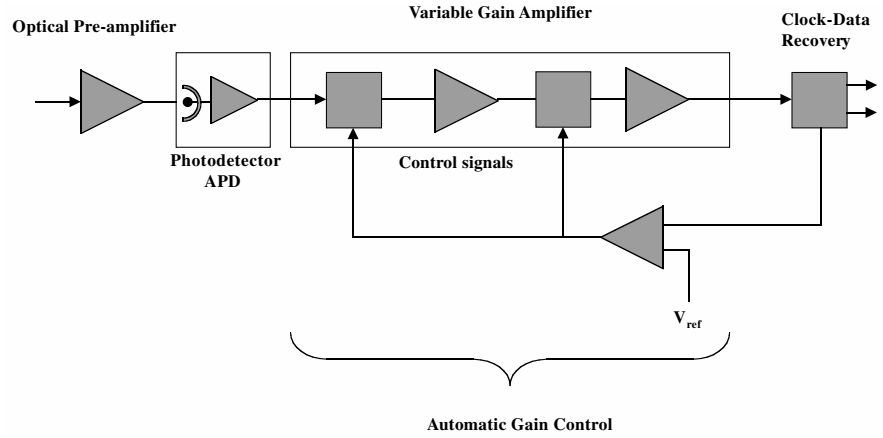

FIGURE 30 High-speed optical receiver showing input optical preamplification and control signals to achieve gain control to compensate for drift in received optical power.

There are two primary methods of creating an amplifier capable of providing the appropriate signal amplification and quantizing the required output signal level: (1) the use of a variable-gain amplifier (VGA) as a postamplifier and (2) the use of a limiting amplifier. When the variable-gain amplifier is employed as the postamplifier, its gain is adjusted according to the input signal power. This method is referred to as *automatic gain control* (AGC). An example of a variable-gain amplifier is created by cascading a chain of variable attenuators and fixed-gain amplifiers. A downstream power detector or peak detector is used to monitor the output signal level from the variable-gain amplifier. The power detector output is then compared with a predetermined reference voltage to generate the control signal, which will then adjust the amount of attenuation in the VGA. Therefore, under the closed-loop condition, the VGA automatically adjusts its overall gain to maintain a constant output signal level.

The second form of quantization amplifier is a limiting amplifier. The simplest form of the limiting amplifier can be pictured as a high-gain amplifier followed by a digital flip-flop. An ideal automatic-gain-controlled amplifier is, by definition, an analog circuit. The signal spectrum of an AGC output should be a scaled replica of that of the input signal. The limiting amplifier, on the other hand, is inherently a device with digital outputs. In practice, there are subtle differences in the rates at which errors may occur (*bit error rate*) and the distortion of the received bits (*eye margin*) between systems that use automatic-gain-controlled amplifiers and systems that employ limiting amplifiers.

While very high-speed optical fiber transmission experiments have been demonstrated, with data rates in excess of 100 Gbit/s (640 Gbit/s max for OTDM links), it should be noted that the key technologies that have made this possible are the use of optical amplifiers and all-optical multiplexers and demultiplexers. Nonetheless, electronic devices continue to have specific advantages over optical devices, such as high functionality, small size, low cost, and high reliability. In addition, as optics continues to push the limits of data transmission, integrated electronic technologies progress and have achieved integrated circuit performance in excess of 50 Gbit/s.

Ultra-High-Speed Optical Time-Division Multiplexed Optical Link—A Tutorial Example

To show how ultra-high-speed optoelectronic device technology can realize state-of-the-art performance in OTDM systems, an example is shown here that incorporates the system and device technology just discussed. While there are several groups that have created OTDM links operating in excess of 100 Gbit/s, generally using different device technology for pulse generation and subsequent demultiplexing, the basic concepts are consistent between each demonstration and are reproduced here to bring together the concepts of OTDM. In Fig. 31 is an ultra-high-speed optical data transmitter and demultiplexing system based on current research in Japan at NTT. To demonstrate the system performance, the transmitter was created by employing a 10-GHz mode-locked laser that uses an erbium-doped fiber as the gain medium and generates a 3-ps optical pulse. In this case, the laser is mode-locked by using a technique referred to as *regenerative mode-locking.* In regenerative mode-locking, the laser initiates mode-locking by using passive mode-locking techniques. A small portion of the resultant pulse train is detected and the subsequent electrical signal is then used to drive an active mode-locking device such as a $LiNbO_3$ modulator within the laser cavity. This approach derives the benefit of obtaining very short pulses that are typical of passively mode-locked lasers, but derives added temporal stability in the optical pulse train from the electrical drive signal. The data pulses are then modulated using a pseudorandom non-return-to-zero electrical signal that drives a 10-Gbit/s $LiNbO_2$ modulator. The optical pulses are then reduced in temporal duration using optical nonlinear effects in fiber (e.g., adiabatic soliton pulse compression), resulting in optical pulses of 250 fs in duration. The pulses are then temporally interleaved by a factor of 64 using a planar lightwave multiplexer. This device is simply a cascade of integrated Mach-Zehnder interferometers that employ a fixed delay equal to half of

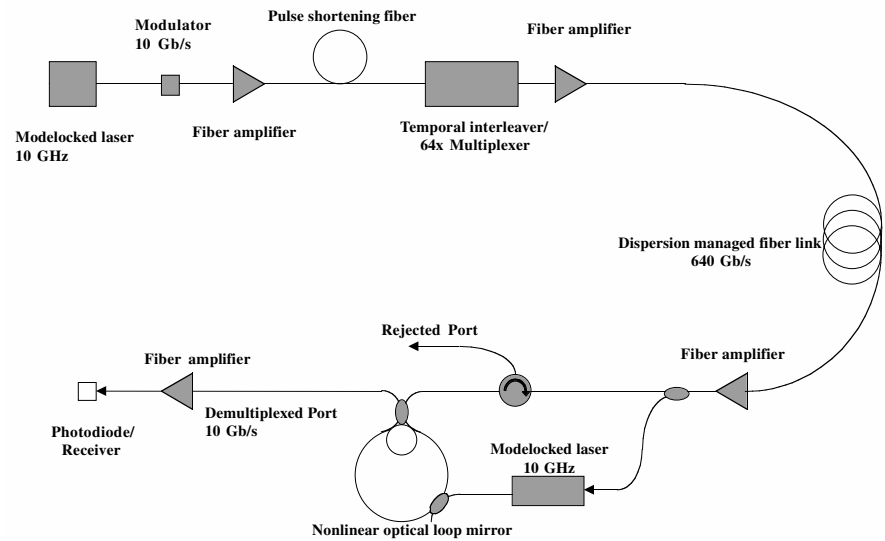

FIGURE 31 Schematic diagram of a 640-Gbit/s optical fiber link, using all the critical components described in this chapter—for example, mode-locked laser, high-speed modulator, temporal interleaver, optical clock recovery, all-optical switching for demultiplexing, and an optical photoreceiver.

the input repetition rate for each Mach-Zender stage. The resulting output from the planar lightwave circuit multiplexer (PLC MUX) is a pseudorandom modulated pulse train at 640 Gbit/s. It should be noted that, in a real system, the data from 64 individual users would need to be interleaved accurately for this scheme to work. However, this can be achieved by distributing or broadcasting the initial 10-Gbit/s pulse train to each user for modulation (recall Fig. 18*a*). Since the propagation distance to each user is fixed and deterministic, the return signals can be interleaved easily.

After the data has been generated and amplified in an EDFA to compensate for losses, the pulses are launched into a fiber span of approximately 60 km. It should be noted that the typical distance between central switching stations or central offices in conventional telecommunication networks is 40 to 80 km. The fiber span is composed of fiber with varying dispersion to reduce the effects of pulse broadening. The pulses at the demultiplexing end are initially amplified using an EDFA to again compensate for losses encountered in transmission. A portion of the data is extracted from the data line and is used to generate an optical clock signal that will be used as a control pulse in an all-optical switch/demultiplexer. The clock recovery unit is composed of a mode-locked laser that is electrically driven at a nominal data rate of 10 GHz. This clock signal could also be generated by injection locking of a passively mode-locked laser. Once the clock pulses are generated, they are injected into a nonlinear loop mirror, along with the data to provide all-optical demultiplexing at 10 Gbit/s. It should be noted that the clock and data pulses are at 1.533 and 1.556 μm, respectively. Owing to the wavelength difference between the clock data, a simple bandpass filter is used to pass the data stream and filter out the clock pulses after demultiplexing. Finally, after the data pulses are spectrally filtered, detection is performed with a photodetector, with the subsequent electrical signal analyzed by a bit-error-rate measurement system. The resulting performance of this system showed a bit error rate of 10^{-10}, that is, less than one error for every 10 billion bits received, with a received power of –23 dBm or 5 mW of average power.

12.5 SUMMARY AND FUTURE OUTLOOK

This chapter has reviewed the fundamental basics of optical time-division multiplexed communication networks, starting from an elementary perspective of digital sampling. The core basics of multiplexing and demultiplexing were then reviewed, with an emphasis on the difference between conventional time-division multiplexing for voice/circuit-switched networks versus data/packet-switched networks. Given this as an underlying background, specific device technology was introduced to show how the system functionality can be realized using ultra-high-speed optics and photonic technologies. Finally, as an example of how these system and device technologies are incorporated into a functioning ultra-high-speed optical time-division multiplexed system, a 640-Gbit/s link was discussed.

As we look toward the future and consider how the current state of the art will evolve to realize faster optical time-division networks and signal processing architectures, new concepts and approaches will be required. Several possible approaches may make use of optical solitons, which are optical pulses that can propagate without the detrimental effects of chromatic dispersion. An alternative approach for high-speed networking may incorporate a unique combination of both time-division multiplexing (TDM) and wavelength-division multiplexing (WDM), ushering in a new generation of hybrid WDM-TDM optical networking and signal processing devices and architectures. Generally speaking, however, in the present competitive industrial arena of telecommunications, there is always a technology-versus-cost tradeoff. As a result, the technology that is ultimately deployed will be application specific to maximize performance and minimize cost.

12.6 FURTHER READING

Joseph E. Berthold, "Sonet and ATM," in Ivan P. Kaminow and Thomas L. Koch (eds.), *Optical Fiber Telecommunications IIIA,* Academic Press, San Diego, 1997, pp. 2-13 to 2-41.

D. Cotter and A. D. Ellis, "Asynchronous Digital Optical Regeneration and Networks," *J. Lightwave Technol. IEEE* **16**(12):2068–2080 (1998).

J. Das, "Fundamentals of Digital Communication," in Bishnu P. Pal (ed.), *Fundamentals of Fiber Optics in Telecommunication and Sensor Systems,* Wiley Eastern, New Delhi, 1992, pp. 7-415 to 7-451.

S. Kawanishi, "Ultrahigh-Speed Optical Time-Division-Multiplexed Transmission Technology Based on Optical Signal Processing," *J. Quantum Electron. IEEE* **34**(11):2064–2078 (1998).

H. K. Lee, J. T. Ahn, M. Y. Jeon, K. H. Kim, D. S. Lim, and C. H. Lee, "All-Optical Clock Recovery from NRZ Data of 10 Gb/s," *Photon. Technol. Lett. IEEE* **11**(6):730–732 (1999).

Max Ming-Kang Liu, *Principles and Applications of Optical Communications,* Irwin, Chicago, 1996.

K. Ogawa, L. D. Tzeng, Y. K. Park, and E. Sano, "Advances in High Bit-Rate Transmission Systems," in Ivan P. Kaminow and Thomas L. Koch (eds.), *Optical Fiber Telecommunications IIIA,* Academic Press, San Diego, 1997, pp. 11-336 to 11-372.

CHAPTER 13

WAVELENGTH DOMAIN MULTIPLEXED (WDM) FIBER-OPTIC COMMUNICATION NETWORKS

Alan E. Willner and Yong Xie
Department of EE Systems
University of Southern California
Los Angeles, California

13.1 INTRODUCTION

Optical communications have experienced many revolutionary changes since the days of short-distance multimode transmission at 0.8 μm.[1] We have seen, with the advent of erbium-doped fiber amplifiers (EDFAs), single-channel repeaterless transmission at 10 Gb/s across over 8000 km.[2] We may consider single-channel point-to-point links to be state-of-the-art and an accomplished fact, albeit with many improvements possible. (Soliton transmission, which has the potential for much higher speeds and longer distances, is discussed in Chapter 7.) Although single-channel results are quite impressive, they nonetheless have two disadvantages: (1) they take advantage of only a very small fraction of the enormous bandwidth available in an optical fiber, and (2) they connect two distinct end points, not allowing for a multiuser environment. Since the required rates of data transmission among many users have been increasing at an impressive pace for the past several years, it is a highly desirable goal to eventually connect many users with a high-bandwidth optical communication system. By employing wavelength-division multiplexing (WDM) technology, a simple multiuser system may be a point-to-point link with many simultaneous channels, and a more complicated system can take the form of a local, metropolitan, or wide-area network with either high bidirectional connectivity or simple unidirectional distribution.[3]

Much technological progress has been achieved in WDM optical systems since the emergence of EDFAs, a key enabling technology for WDM. Some potential applications of WDM technology include a multiplexed high-bandwidth library resource system, simultaneous information sharing, supercomputer data and processor interaction, and a myriad of multimedia services, video applications, and additional previously undreamed-of services. As demands increase for network bandwidth, the need will become apparent for WDM optical networks, with issues such as functionality, compatibility, and cost determining which systems will eventually be implemented. This chapter will deal with the many technical issues, possi-

Copyright 2001 by The McGraw-Hill Companies, Inc. Click Here for Terms of Use.

ble solutions, and recent progress in the exciting area of WDM fiber-optic communication systems.

Fiber Bandwidth

The driving force motivating the use of multichannel optical systems is the enormous bandwidth available in the optical fiber. The attenuation curve as a function of optical carrier wavelength is shown in Fig. 1.[4] There are two low-loss windows, one near 1.3 μm and an even lower-loss one near 1.55 μm. Consider the window at 1.55 μm, which is approximately 25,000 GHz wide. (Note that due to the extremely desirable characteristics of the EDFA, which amplifies only near 1.55 μm, most systems would use EDFAs and therefore not use the dispersion-zero 1.3-μm band of the existing embedded conventional fiber base.) The high-bandwidth characteristic of the optical fiber implies that a single optical carrier at 1.55 μm can be baseband-modulated at ~25,000 Gb/s, occupying 25,000 GHz surrounding 1.55 μm, before transmission losses of the optical fiber would limit transmission. Obviously, this bit rate is impossible for present-day electrical and optical devices to achieve, given that even heroic lasers, external modulators, switches, and detectors all have bandwidths <100 GHz. Practical data links today are significantly slower, perhaps no more than 10 Gb/s per channel. Since a single high-speed channel only takes advantage of an extremely small portion of the available fiber bandwidth, an efficient multiplexing method is needed to take full advantage of the huge bandwidth offered by optical fibers. As we will see in this chapter, WDM has been proven to be the most appropriate approach.

Introduction to WDM Technology

In real systems, even a single channel will probably be a combination of many lower-speed signals, since very few individual applications today utilize this high bandwidth. These lower-speed channels are multiplexed together in time to form a higher-speed channel. This time-division multiplexing (TDM) can be accomplished in either the electrical or optical domain. In TDM, each lower-speed channel transmits a bit (or a collection of bits, known as a *packet*) in a given time slot and then waits its turn to transmit another bit (or packet) after all the other channels have had their opportunity to transmit. TDM is quite popular with today's electrical networks and is fairly straightforward to implement in an optical network at 10 Gb/s speeds. However, as was previously mentioned, this scheme by itself cannot hope to utilize

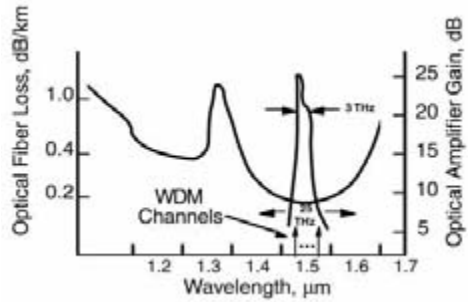

FIGURE 1 Fiber loss as a function of wavelength in conventional single-mode silica fiber. The gain spectrum of the EDFA is also shown.[4]

the available bandwidth because it is limited by the speed of the time-multiplexing and time-demultiplexing components. Moreover, ultra-high-speed transmission becomes severely limited by fiber dispersion and nonlinearities.[5]

To exploit more of the fiber's THz bandwidth, we seek solutions that complement or replace TDM. One obvious choice is WDM, in which several baseband-modulated channels are transmitted along a single fiber but with each channel located at a different wavelength (see Fig. 2.)[6–9] Each of *N* different-wavelength lasers is operating at the slower Gb/s speeds, but the aggregate system is transmitting at *N* times the individual laser speed, providing a significant capacity enhancement. The WDM channels are separated in wavelength in order to avoid crosstalk when they are (de)multiplexed by a nonideal optical filter. The wavelengths can be individually routed through a network or individually recovered by wavelength-selective components. WDM allows us to use much of the available fiber bandwidth, although various device, systems, and network issues will limit utilization of the full fiber bandwidth.

Figure 3 shows the continuous capacity growth in optical fiber systems over the past 15 years, where ETDM and OTDM represent electronic time-division multiplexing and optical time-division multiplexing, respectively. The highest demonstrated capacity has been achieved using WDM. One interesting point about this trend, predicted a decade ago by T. Li of AT&T Bell Labs, deserves mention. The trend, which has existed for more than a decade, is that the transmission capacity doubles every two years. WDM technology has provided the means for this trend to continue, and there is no reason to assume that WDM won't continue to produce dramatic progress. In fact, capacity of hundreds of Gb/s has recently been realized in commercial WDM systems.

13.2 FIBER IMPAIRMENTS

As was mentioned in Section 13.1, prior to the widespread use of EDFAs,[10] long-distance transmission required periodic regeneration of a signal. Such detection and retransmission compensate for both attenuation and fiber chromatic dispersion effects. However, when an EDFA is employed in the transmission line, it only compensates for attenuation, allowing other effects such as dispersion and nonlinearities to accumulate unimpeded along a transmission link. Although dispersion-shifted fiber (DSF) can be used in EDFA-based systems to minimize the effect of dispersion when channels are operated near the dispersion-zero wavelength, various nonlinear effects will also accumulate along the link and cause severe limitations in WDM transmission. These nonlinear effects include stimulated scattering processes (i.e., Raman and Brillouin scat-

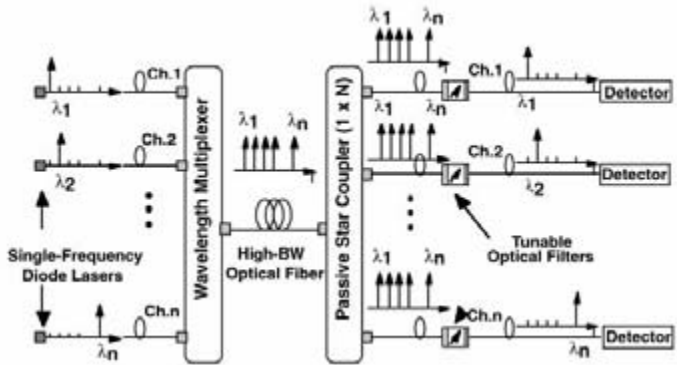

FIGURE 2 Many WDM channels propagating in a single optical fiber.

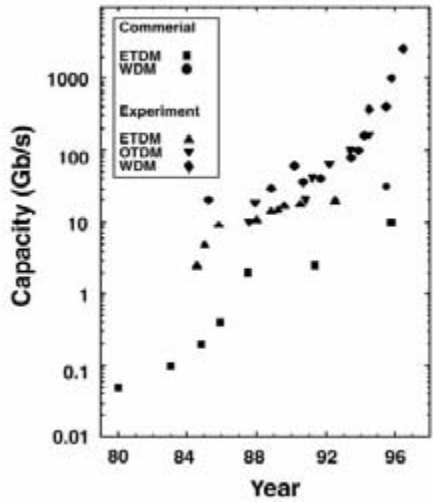

FIGURE 3 Continuous capacity growth in optical fiber transmission systems.

tering) and material refractive-index interactions [i.e., self- and cross-phase modulation (SPM and XPM) and four-wave mixing (FWM)].[11,12] The management of both fiber dispersion and nonlinearities is a key issue in optically amplified long-haul systems. In this section, we will describe these phenomena and discuss various techniques for compensating for their deleterious effects.

Chromatic Dispersion

Without fiber nonlinearity, the electric field of a linearly polarized signal propagating in single-mode fiber (SMF) can be described by

$$E(x, y, z, t) = \tfrac{1}{2}E(x, y, z_0, t_0)e^{i[[\beta(\omega) - \frac{\alpha}{2}]z - \omega t]} + \text{C.C.} \tag{1}$$

where z is the propagation direction, t is the time, α is the loss of the fiber, $\beta(\omega)$ is the propagation constant, ω is the angular frequency, and C.C. is the complex constant. The mode propagation constant $\beta(\omega)$ can be expanded in a Taylor series about the center frequency ω_0,[11]

$$\beta(\omega) = \beta_0 + \beta_1(\omega - \omega_0) + \tfrac{1}{2}\beta_2(\omega - \omega_0)^2 + \cdots \tag{2}$$

where

$$\beta_m = \left(\frac{d^m\beta}{d\omega^m}\right)_{\omega=\omega 0} \qquad (m = 0, 1, 2, \cdots) \tag{3}$$

ω_0/β_0 is the phase velocity, whereas $1/\beta_1$ is the group velocity, which is the speed of the energy (optical pulse) propagation. The term β_2 describing the frequency dependence of the group velocity is the chromatic dispersion (or group velocity dispersion) of the fiber.

Since an optical pulse consists of different frequency components that travel at different speeds in the fiber due to chromatic dispersion, the pulse will be broadened as it propagates through the fiber, as shown in Fig. 4.

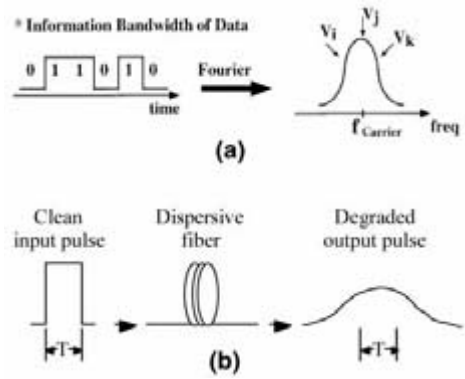

FIGURE 4 (*a*) Information bandwidth of data. (*b*) Broadening of an optical pulse propagating through a single-mode fiber.

In lightwave systems, it is more convenient to use

$$D = \frac{d}{d\lambda}\left(\frac{1}{v_g}\right) = \frac{d^2\beta}{d\lambda d\omega} \approx -\frac{2\pi c}{\lambda^2}\beta_2 \tag{4}$$

in units of ps/nm/km, which is the amount of broadening of a pulse with a bandwidth of 1 nm after propagating through 1 km of fiber, instead of β_2, to represent chromatic dispersion. For conventional SMF D is typically 17 ps/nm/km.

In fact, chromatic dispersion is also wavelength dependent. We define

$$\frac{dD}{d\lambda} = \frac{2\pi c}{\lambda^3}\left(2\beta_2 - \frac{2\pi c}{\lambda}\beta_3\right) \tag{5}$$

as the chromatic dispersion slope, which plays an important role in wide-band long-haul WDM systems.[13,14]

In a communication system, when a data stream composed of multiple optical pulses in series propagates through a dispersive fiber, each of the broadened pulses spreads into other time slots, causing intersymbol-inference after transmission, as shown in the simulation results for 10 Gb/s signal transmission in Fig. 5.

In Fig. 5, we can also see that the distortion due to chromatic dispersion is dependent on the data rates of the signal. Actually, fiber chromatic dispersion places limits on both channel data rates and transmission distance, since the pulse broadening is dependent on both of them. A simple estimation of the dispersion limit is:

$$L_D = \frac{1}{BD\Delta\lambda} \tag{6}$$

where L_D is the transmission distance at which the pulse broadening exceeds one bit-time, B is the data rate, and $\Delta\lambda$ is the bandwidth of the signal launched into the fiber. Since $\Delta\lambda$ is linearly proportional to the data rate B, the dispersion-limited transmission distance is inversely proportional to B^2. Using 2.5 Gb/s, 17 ps/nm/km, and 0.025 nm for B, D, and $\Delta\lambda$, we estimate the dispersion limit for 2.5 Gb/s chirp-free modulation systems would be around 1000 km. However, when the data rate increases to 10 Gb/s, the limit decreases to 60 to 70 km. Consequently, after 100 km SMF transmission, although there is no degradation at 2.5 Gb/s, 10 Gb/s pulses are seriously distorted.

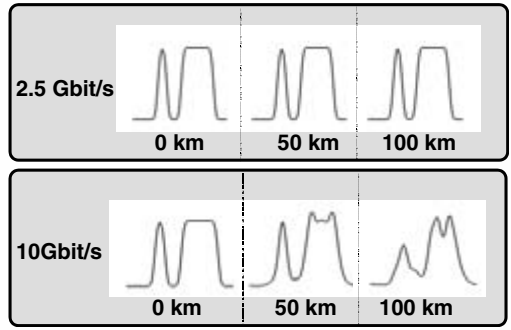

FIGURE 5 Signal waveform distortion due to fiber dispersion in 2.5 Gb/s and 10 Gb/s optical systems after 0, 50, and 100 km SMF transmission (assuming chirp-free modulation).

It is clear that in high data rate systems, fiber chromatic dispersion must be reduced to allow repeaterless long-haul transmission.[15] A straightforward way to overcome these dispersion limits is to shift the dispersion-zero wavelength of fiber to 1.55 μm.[16] The dispersion limit in DSF is dramatically increased compared to SMF. However, as we will discuss in next section, most fiber nonlinear effects would impose critical limitations on system performance when dispersion is low, which makes simultaneous management of both chromatic dispersion and fiber nonlinearities one of the most important issues in system design. Therefore, we will discuss dispersion compensation and management after a brief review of fiber nonlinearities.

Fiber Nonlinearities

Silica optical fiber has certain nonlinearities associated with it. The major nonlinear effects are each dependent on the power (i.e., intensity) of the propagating signals, with weak signals not incurring significant effects. Furthermore, these affects require a certain propagation distance to allow for the interactions to accumulate and become relevant.

A detailed discussion of fiber nonlinearities can be found in Chapter 3. In this section we will briefly describe system impairments due to some of the most important fiber nonlinearities.

Self-Phase Modulation and Cross-Phase Modulation The nonlinearities discussed in this section and the next all owe their origin to the fact that the index of refraction of an optical fiber varies nonlinearly with signal power:[11]

$$n = n_{\text{linear}} + \overline{n_2}\left(\frac{P}{A_{\text{eff}}}\right) \tag{7}$$

where $\overline{n_2}$ is the nonlinear index coefficient (3.2×10^{-16} cm^2/W for silica fiber), n_{linear} is the linear index of refraction, P is the optical power, and A_{eff} is the cross-sectional mode area.

Since the local refractive index is a function of the optical intensity of a propagating signal, a nonrectangular-shaped optical pulse will experience a varying refractive index depending on the optical power at each temporal location. As we know, the speed of an optical wave within a medium is dependent on the refractive index. Therefore, the varying refractive index will then cause the different intensities to propagate at different speeds along the fiber. Thus, optical power fluctuations are converted to phase fluctuations. This phase shift causes the pulse to temporally disperse in the fiber and limits transmission distance and signal speed.

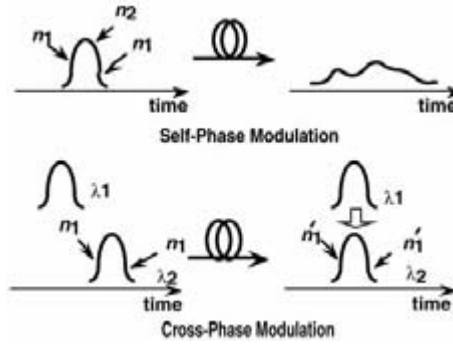

FIGURE 6 Pulse broadening due to SPM and XPM.

This effect for a single optical pulse is known as self-phase modulation (SPM) and will distort a transmitted optical pulse as shown in Fig. 6. Note that both temporal and spectral broadening result from this nonlinearity.

This effect of intensity-dependent propagation speeds is quite important when considering WDM transmission of several channels. The optical power from data pulses on one channel will affect the refractive index, propagation speed, and dispersion-induced distortion of data pulses on another channel if they are temporally colocated. Since each wave is located at a different transmission wavelength, the different channels will propagate at different speeds, and data pulses from one channel will propagate through the data pulses from another channel, causing an overall smearing of the distortion and dispersion from one channel to the next. This cross-channel interference is known as cross-phase modulation (XPM) (see Fig. 6). Note that XPM is not symmetric as two pulses pass through each other since optical power is not constant along a fiber span with lumped amplification. Moreover, the distortion caused by XPM is dependent on the local dispersion of fiber.[17] Increasing local dispersion can suppress the effects of XPM because the pulses on different channels tend to walk away faster, and the XPM can not accumulate.

Figure 7 shows the effects of XPM on the performance of 10 Gb/s systems. The signal-to-noise ratio (SNR) of the received signal is plotted as a function of the local dispersion in a

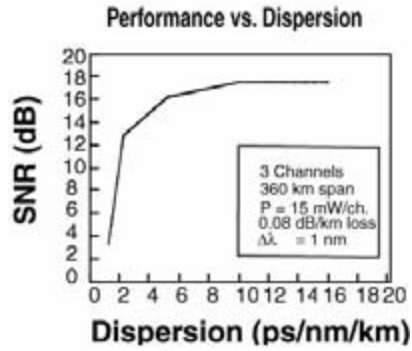

FIGURE 7 System performance in the presence of XPM.[17]

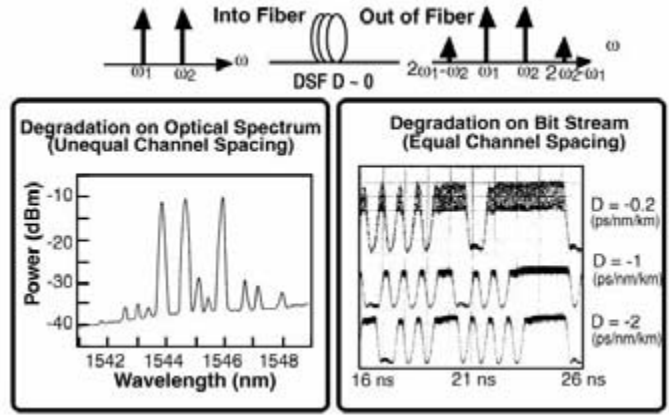

FIGURE 8 Four-wave mixing in WDM systems.[16]

dispersion-compensated system, showing that XPM effects could be suppressed by introducing an appropriate amount of local dispersion in the fiber.

Four-Wave Mixing Figure 8 shows the situation wherein two channels mix with each other, producing optical power at the sum and difference beat frequencies (see Chapter 3). It is important to note that FWM occurs only when (1) the two mixing channels are located near the dispersion-zero wavelength of the fiber, and (2) the channel spacing is less than a few 10s of GHz. These conditions exist since the two waves must maintain certain phase-matching requirements. The less critical effect of FWM is that the original channels suffer a power loss due to power transfer to the newly-generated products, and the more critical problem occurs when there are three or more original WDM signal channels producing many mixing products. It is quite probable that some of the products will appear at the same wavelength as one of the original signals. Then, when an optical filter ultimately recovers this original signal, both the original signal and a FWM product will be detected. The product has some modulation on it based on the combination of the channels that created it, and severe crosstalk results.[18,19] The equation describing the formation of FWM products between two waves A_1 and A_2 is:[20]

$$\frac{dA_1}{dz} = i\lambda_1 A_2^* A_3 A_4 e^{i\Delta kz}, \qquad \Delta k = k_3 + k_4 - k_1 - k_2 \tag{8}$$

where * denotes the complex conjugate, and k is the phase of the propagating wave.

Figure 8 also shows the dependence of FWM effects on fiber dispersion.[16] Increasing the local dispersion value in transmission fibers helps to suppress the FWM-induced crosstalk, since high dispersion may destroy the phase-matching condition required for FWM generation.

Dispersion Compensation and Management

In the previous section, we saw that although fiber dispersion is generally considered a negative characteristic, it does have the desirable effect of inhibiting FWM and XPM. Therefore, it may not be good to reduce the fiber dispersion to zero by using DSF in systems. As an alternative, we keep the local dispersion along the transmission link high enough to suppress nonlinear effects, while managing the total dispersion of the link to be close to zero, as shown in

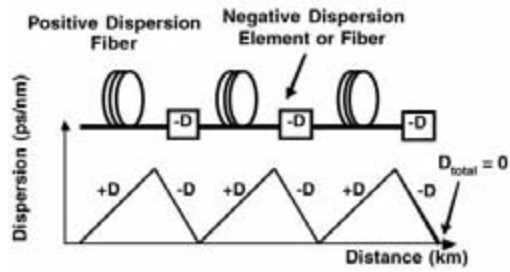

FIGURE 9 Sample dispersion map for a dispersion-managed system.

Fig. 9. We will introduce some of the most important dispersion compensation/management techniques in this section.

Dispersion Compensating Fiber Dispersion compensating fiber (DCF) has been the most successful method for dispersion compensation[21,22] because of its obvious advantage—wideband operation. Furthermore, as shown in Fig. 10, DCF can provide not only a very high negative dispersion, but also a negative dispersion slope,[21] which could mitigate the effect of dispersion accumulation on channels far from the dispersion-zero wavelength in WDM long-haul systems. The negative dispersion value for DCF is typically –80 to –100 ps/nm, so a relatively short length of DCF can compensate much longer lengths of SMF.

Tailoring the fiber's refractive index profile with the addition of germanium to the core generates the high negative dispersion of DCF. Therefore, losses in such fibers (typically 0.3 to 0.5 dB/km) are higher than standard SMF. Another approach for DCF is to guide the fundamental mode into the cladding to increase the waveguide dispersion, which minimizes the intrinsic loss. However, bending loss would be high for such designs, making it difficult to package the fibers for practical use. Moreover, the core size of DCF is usually much smaller than SMF (<4 μm compared to ~9 μm for SMF), leading to higher fiber-induced nonlinearity. Therefore, although DCF is commercially available and used in optical systems, people continue to seek better solutions to manage fiber dispersion.

Specialty Fibers for Dispersion Management A significant disadvantage of DCF is that it can not be employed as transmission fiber. Moreover, if DCF must be used, it would be better if the dispersion value of the transmission fiber were as small as possible to reduce the required DCF length, thus minimizing the induced loss and nonlinearity. The idea of dispersion management is to establish a long fiber link composed of alternating short lengths of two different types of fiber.[23] One type of fiber has the opposite sign but a similar dispersion mag-

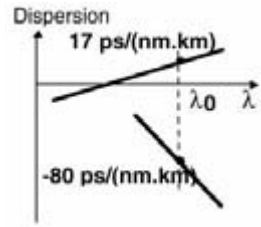

FIGURE 10 Dispersion compensating fiber.

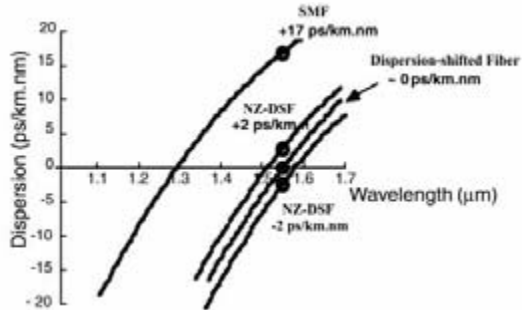

FIGURE 11 Dispersion of single-mode fibers.[15]

nitude as that of the other type of fiber for a given wavelength; note that these two types of fiber are similar except that their dispersion-zero wavelengths are shifted from each other. Each short length of fiber may have a dispersion value of, for instance, either +2 or –2 ps/(nm km), depending on which type of fiber is used. After a given distance of propagation, the total effective dispersion is close to zero, but there is an absolute value of dispersion at any given point along the fiber, reducing the impact of FWM and XPM.

Figure 11 shows the dispersion of non-zero dispersion-shifted fibers (NZ-DSF), which are specialty fibers designed for dispersion management. There are two types of NZ-DSF,[24] one having a dispersion-zero wavelength at about 1520 nm and another having a dispersion-zero wavelength at about 1580 nm. Their dispersion at 1550 nm is about +2 ps/nm/km or –2 ps/nm/km. These amounts of dispersion are lower than in standard SMF to mitigate the distortion due to accumulated dispersion, but higher than DSF to suppress fiber nonlinearities. Normally NZ-DSF has a smaller core area than SMF due to the different waveguide design, resulting in higher nonlinearity. However, with proper design, large-core NZ-DSF is also available.[25]

Some possible periodic dispersion maps for dispersion management include:[26,27]

- Positive NZ-DSF alternated with negative NZ-DSF
- Negative NZ-DSF alternated with standard SMF
- Positive NZ-DSF compensated with DCF

Chirped Fiber Bragg Grating In the past few years, chirped fiber Bragg gratings (FBGs) have become very attractive devices for dispersion compensation.[28–30] The grating period of a chirped FBG varies linearly along the grating, causing light with different wavelengths to be reflected at different points inside the FBG. Therefore, the optical pulses broadened during transmission can be recompressed using the chirped FBG as shown in Fig. 12.

Figure 13 shows the reflection and time delay of a chirped FBG. The slope of the time delay curve represents the amount of dispersion provided by the grating. Chirped FBGs are advantageous due to their low loss, compact size, and polarization insensitivity. Additionally, they do not induce additional optical nonlinearities, which is a main drawback of DCF.

Achieving wideband operation has been one of the most important issues for chirped FBGs. Let's consider a 10-cm-long grating. The maximum time delay that can be provided by the grating is ~1000 ps across the whole grating bandwidth. Assuming the grating bandwidth to be 0.2 nm for single-channel operation, the dispersion provided by the grating could be as high as ~5000 ps/nm. However, if the grating bandwidth increases to, say, 6 nm for multichannel operation, then the dispersion would be <200 ps/nm, which is too low for dispersion compensation. It is possible to make gratings as long as 1 m to obtain wideband operation.[31]

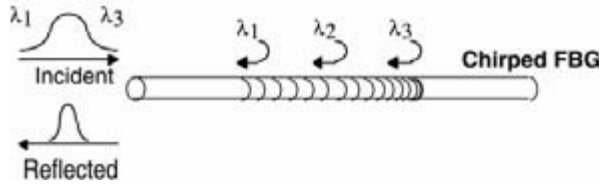

FIGURE 12 Dispersion compensation by a chirped FBG.

However, the fabrication process is difficult, and grating uniformity is hard to maintain. Another approach for wideband operation involves sampling the grating to generate multiple replicas of the grating reflection band.[32,33] Each of the replicas will have the same time-delay characteristics so that simultaneous dispersion compensation for multiple channels can be realized.

Tunable Dispersion Compensation All of the dispersion compensators previously discussed share one common feature—they are not tunable. However, the accumulated dispersion for a data channel may vary in time for (1) dynamically reconfigurable optical networks in which a given channel may originate locally or far away, and (2) transmission systems having changing operating conditions (i.e., due to laser or modulator chirp). For such dynamic systems, especially at data rates 10 Gb/s, dispersion compensation must be adjustable in order to track dynamically the accumulated dispersion. For DCF, there is no method at present for tuning *in situ* its dispersion. For linearly-chirped FBGs, simply stretching the grating only produces a shift in the resonant wavelength range of the reflected band but does nothing to change the induced dispersion.

A recent report used 21 separate stretching segments to asymmetrically stretch a uniform FBG to change the induced dispersion,[34] but in this case the grating bandwidth varied significantly during dispersion tuning.

Another approach is to use a nonlinearly-chirped FBG.[35] As shown in Fig. 14, the time delay induced by this nonlinearly-chirped FBG changes with wavelength in a nonlinear fashion. The time-delay characteristics, bandwidth, and spectral shape of the grating do not change when the grating is stretched by a linear stretcher, but the signal channel will experience a varying dispersion value during stretching. The tuning speed is on the order of a ms, which is fast enough for circuit-switched systems.

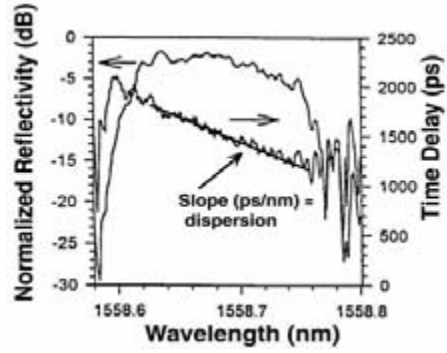

FIGURE 13 Reflection and time delay characteristics of a chirped FBG.

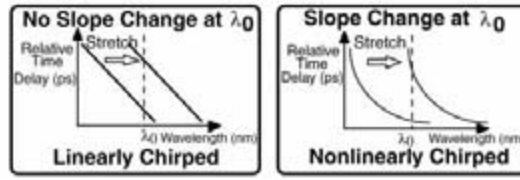

FIGURE 14 Concept of tunable dispersion compensation using a nonlinearly-chirped FBG.

Demonstration of dynamic dispersion compensation has also been accomplished by using a nonlinearly chirped FBG.[35] The eye diagrams before and after the dynamic dispersion compensation at both 50 and 104 km are shown in Fig. 15.

13.3 BASIC ARCHITECTURE OF WDM NETWORKS

We have explained how WDM enables the utilization of a significant portion of the available fiber bandwidth by allowing many independent signals to be transmitted simultaneously in one fiber, as well as the basic fiber impairments in WDM systems. Actually, the WDM channels can be routed and detected independently, with the wavelength determining the communication path by acting as the signature address of the origin, destination, or routing. Therefore, the basic system architecture that can take the full advantage of WDM technology is an important issue, and will be discussed in this section.

Point-to-Point Links

Figure 16 shows a simple point-to-point WDM system in which several channels are multiplexed at one node; the combined signals are transmitted across some distance of fiber; and the channels are demultiplexed at a destination node. This facilitates high-bandwidth fiber transmission. Add-drop multiplexers (ADMs) can be inserted in the transmission line to

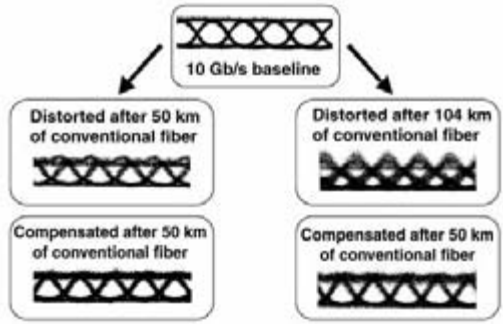

FIGURE 15 The results of tunable chromatic dispersion compensation with a nonlinearly-chirped FBG.

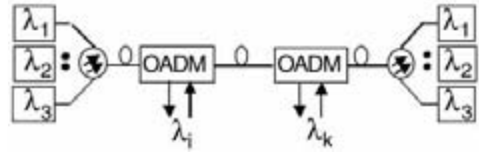

FIGURE 16 Point-to-point WDM links with optical ADMs.

allow the adding and dropping of one or more channels at specific nodes, forming a more efficient WDM link.

Wavelength-Routed Networks

Figure 17 shows a more complex multiuser WDM network structure, where the wavelength is used as the signature address for either the transmitters or the receivers, and determines the routing path through an optical network. In order for each node to be able to communicate with any other node and facilitate proper link setup, either the transmitters or the receivers must be wavelength tunable; we have arbitrarily chosen the transmitters to be tunable in this network example. Note that the wavelengths are routed passively in wavelength-routed networks.

WDM Stars, Rings, and Meshes

In this section, we will discuss three common network topologies that can use WDM, namely the *star, ring,* and *mesh* networks.[36–38]

In the star topology, each node has a transmitter and receiver, with the transmitter connected to one of the passive central star's inputs and the receiver connected to one of the star's outputs, as is shown in Fig. 18(*a*). Rings, as shown in Fig. 18(*b*), are also popular because (1) many electrical networks use this topology, and (2) rings are easy to implement for any geographical network configuration. In this example, each node in the unidirectional ring can transmit on a specific signature wavelength, and each node can recover any other node's wavelength signal by means of a wavelength-tunable receiver. Although not depicted in the figure, each node must recover a specific channel. This can be performed (1) where a small portion of the combined traffic is tapped off by a passive optical coupler, thereby allowing a tunable filter to recover a specific channel, or (2) in which a channel-dropping filter completely removes only the desired signal and allows all other channels to continue propagating around the ring. Furthermore, a synchronous optical network (SONET) dual-ring architecture, with one ring providing service and the other protection, can provide automatic fault detection and protection switching.[39]

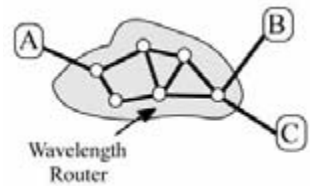

FIGURE 17 A wavelength-routed network.

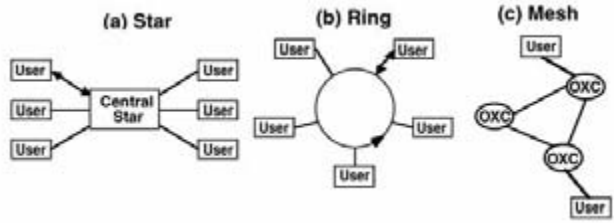

FIGURE 18 WDM stars, rings, and meshes.

In both the star and ring topologies, each node has a signature wavelength, and any two nodes can communicate with each other by transmitting and recovering that wavelength. This implies that N wavelengths are required to connect N nodes. The obvious advantage of this configuration, known as a *single-hop network,* is that data transfer occurs with an uninterrupted optical path between the origin and destination; the optical data starts at the originating node and reaches the destination node without stopping at any other intermediate node. A disadvantage of this single-hop WDM network is that the network and all its components must accommodate N wavelengths, which may be difficult (or impossible) to achieve in a large network.

An alternative is to have a mesh network, shown in Fig. 18(*c*), in which the nodes are connected by *reconfigurable optical crossconnects* (OXCs).[40] The wavelength can be dynamically switched and routed by controlling the OXCs. Therefore, the required number of wavelengths and the wavelength-tunable range of the components can be reduced in this topology. Moreover, the mesh topology can also provide multiple paths between two nodes to make network protection and restoration easier to realize. If a failure occurs in one of the paths, the system can automatically find another path and restore communications between any two nodes. However, OXCs with large numbers of ports are extremely difficult to obtain, which limits the scalability of the mesh network.

Network Reconfigurability

As mentioned in the previous section, a reconfigurable network will be highly desirable in future networks, in order to meet the requirements of high bandwidth and bursty traffic.[41]

A network is reconfigurable if it can provide the following functionality for multichannel operations:

- Channel add/drop
- Path reconfiguration for bandwidth allocation or restoration

These functions could be provided by using a reconfigurable optical crossconnect system as shown in Fig. 19.

A reconfigurable network allows dynamic network optimization to accommodate changing traffic patterns, which provides more efficient use of network resources. Figure 20 shows blocking probability as a function of call arrival rate in a WDM ring network with 20 nodes.[42] A configurable topology can support six times the traffic of a fixed WDM topology for the same blocking probability.

The key component technologies enabling network reconfigurability include:

- Wavelength-tunable lasers and laser arrays
- Wavelength routers

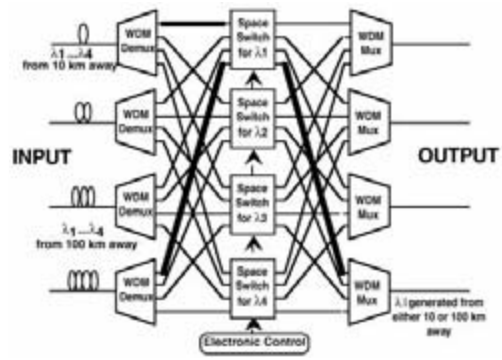

FIGURE 19 An optical crossconnect system in reconfigurable optical networks.

- Optical switches
- OXCs
- ADMs
- Tunable optical filters
- EDFAs

Although huge benefits are possible with a reconfigurable topology, the path to reconfigurability is paved with various degrading effects. As shown in Fig. 19, the signal may pass through different lengths of fiber links due to the dynamic routing, causing some degrading effects in reconfigurable networks to be more critical than in static networks, such as:

- Nonstatic dispersion and nonlinearity accumulation due to reconfigurable paths
- EDFA gain transients
- Channel power nonuniformity
- Crosstalk in optical switching and crossconnects
- Wavelength drift of components

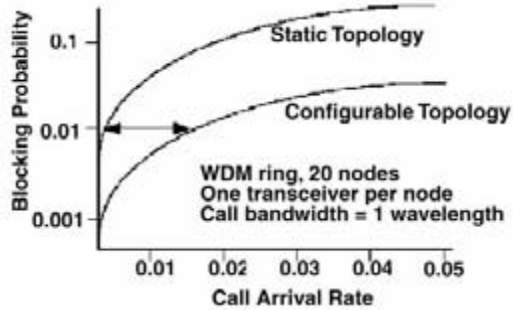

FIGURE 20 Blocking probability as a function of call arrival rate in a WDM ring.[42]

A detailed discussion on network reconfigurability can be found in Ref. 41. We note that dynamic optical routing and switching networks are still in the test-bed phase, for example, in the Multiwavelength Optical Network (MONET), the Optical Networks Technology Consortium (ONTC), and the wideband All-Optical Network (AON) Consortium.

Circuit and Packet Switching

Optical switching is one of the key components in reconfigurable optical networks. The two common schemes are (1) *circuit* and (2) *packet* switching.[43] Figure 21 shows the scenario for both these switching schemes in a simple 6-node network.

To begin with, it is important to realize that circuit switching is widely used and is the method typically used in the public switched telephone network. In circuit switching, if user A wishes to communicate with user E, user A sends a request signal to user E in order to initiate data transmission. If user E is available for interconnection, then it will acknowledge user A's original request, and then user A can begin data transmission. This process of request and acknowledgment is known as *handshaking.* Once transmission commences, a fixed path or circuit along the network is created between the two users until such time that the communications link is terminated by either user. The fiber medium on which the A-E circuit resides has a certain total bandwidth potential, and only a portion of this bandwidth is dedicated (i.e., reserved) for these two users. However, the medium bandwidth is reserved for the A-E circuit independent of whether a stream of bits is actually being transmitted (e.g., consider a pause in the conversation).

A circuit-switched network is quite easy to implement and control. Circuit switching emphasizes a transparent data pipe with a long set-up and tear-down time, and is more appropriate for low-speed transmission and long transmission time, such as a telephone call. Therefore, it has low component switching speed requirements (~ms), since the communications path is intended for minutes of transmission, as in a telephone call. In this case, the handshaking process between widely separated nodes may take only a short time compared to the slow data transfer speed. However, if the handshaking process takes a long time compared to the data transfer rate, then the link overhead due to handshaking is undesirably large. (Note that the switching speed discussed is the time it takes for a switch to change the routing of a data stream or packet, i.e., determining which output port of the switch is enabled for data arriving at a given input port.)

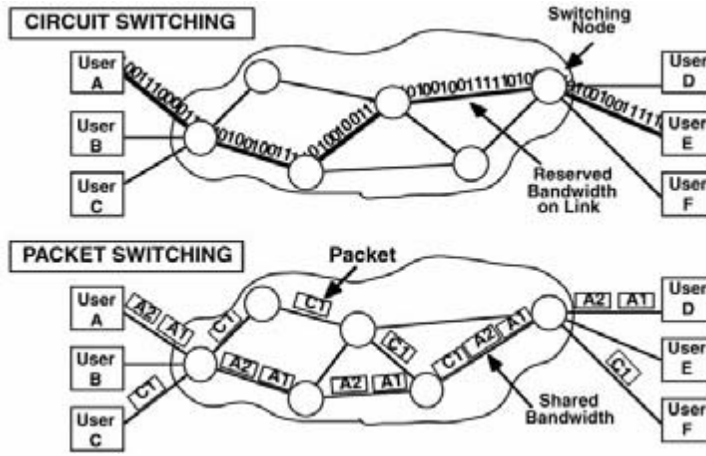

FIGURE 21 Circuit and packet switching systems for a simple 6-node network.

However, for high-speed (Gb/s) optical transmission, in which a user may require only a few seconds of transmission time, the more likely scenario to maximize system throughput is to implement a packet-switched network that does not require a link with dedicated bandwidth. Each user in such a network transmits data in the form of packets, as is depicted in Fig. 21. A data packet in a generic network is composed of (1) a flag (i.e., a unique set of bits) which is typically at the beginning of the packet in order to synchronize data recovery and alert a receiver that a packet is arriving, (2) header bits which contain destination and routing information for switching through the network, and (3) the user-generated end-to-end data payload.[44] A packet may be required to traverse many intermediate switching nodes before it is successfully routed to its destination. Depending on the network and on the available bandwidth on different lines, any packet may take several possible routes to reach a destination. In such a case, a sequence number is included in the packet to ensure that the packets will not be misinterpreted if they arrive out of order. Each transmitted packet uses some fraction of the bandwidth available in the fiber links. If no packets are transmitted, the bandwidth in the fiber links can be allocated to transmission of different packets, such as between users B and D. Therefore, packet switching efficiently uses the available bandwidth, since bandwidth is only used for transmitting high-speed data and the line will not be forced idle if a given user is not transmitting data (as is the case for circuit switching). Thus, bandwidth can be freely allocated in this system to where it is needed and is used quite efficiently, making it ideal for either bursty or uniform high-speed traffic. However, packet switching has much more stringent requirements on the switching technologies since switching must occur on the time scale of an individual packet. The component switching speed requirement is severe, with the range being μs to ns, depending on the specific system being implemented. Other critical issues in packet switching include:

- Header processing[45]
- Bit synchronization
- Variable bit rate processing
- Wavelength translation

13.4 ERBIUM-DOPED FIBER AMPLIFIERS IN WDM NETWORKS

Erbium-doped fiber amplifiers (EDFAs) are discussed in great detail in Chapter 5. In this section, we will consider some important issues about EDFAs with regard to their implementation in WDM systems. We emphasize that the EDFA has been perhaps the most important recent key enabling technology for WDM systems, because it can simultaneously amplify signals over a very wide bandwidth (~35 nm). EDFAs can be used in multichannel WDM systems to compensate for (1) fiber attenuation losses in transmission, (2) component excess losses, and (3) optical network splitting losses. These optical splitting losses can occur in a passive star, in which the optical power is divided by the number of users (N), or in a ring/bus, in which there may possibly be optical tapping losses at each node.

Figure 22(*a*) shows WDM transmission in a conventional electrically regenerated system. Regenerators can correct for fiber attenuation and chromatic dispersion by detecting an optical signal and then retransmitting it as a new signal using an internal laser. However, regenerators (being a hybrid of optics and electronics) are expensive, bit-rate and modulation-format specific, and waste much power and time in converting from photons to electrons and back again to photons. In contrast, as shown in Fig. 22(*b*), the EDFA is ideally a transparent box which is insensitive to the bit-rate, modulation-format, power, and wavelengths of the signal(s) passing through it, and, most important, provides gain for all the WDM channels simultaneously. Since all the channels remain in optical form during amplification, optically-amplified WDM systems are potentially cheaper and more reliable than electrically regenerated systems.

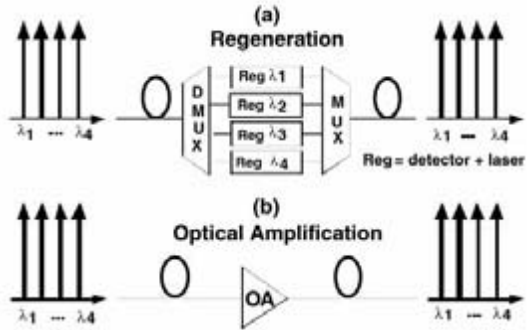

FIGURE 22 Wideband amplifiers enable WDM.

Gain Peaking in EDFA Cascades

The EDFA is an almost ideal optical amplifier for WDM systems, except for one major flaw: The gain is not uniform with wavelength, whereas the interamplifier losses are nearly wavelength independent.[46–49] For a single amplifier, as shown in Fig. 23, the gain exhibits a peak at 1530 nm and a relatively flat region near 1555 nm. Moreover, the gain shape of an EDFA is dependent on the inversion of Er^{3+} in the erbium-doped fiber.[16] When the inversion is low, which can be achieved by operating the amplifier in deep saturation, the gain peak at 1530 nm can be suppressed, and the gain flatness around 1555 nm would become quite flat.

If several channels are located on the relatively flat shoulder region of the gain spectrum, then the gain differential after a single amplifier will be within a few dB. However, when a cascade of EDFAs is used to periodically compensate for losses, the differential in gain and resultant SNR can become quite severe. A large differential in SNR among many channels can be deleterious for proper system performance. Figure 24 shows the gain spectrum after a single amplifier and after 13 cascaded amplifiers. The gain does not accumulate linearly from stage to stage, and the resultant wavelength-dependent gain shape dramatically changes in a cascade. Along the cascade, gain is gradually pulled away from the shorter wavelengths and made available at the longer wavelengths, resulting in a usable bandwidth of only several nm.

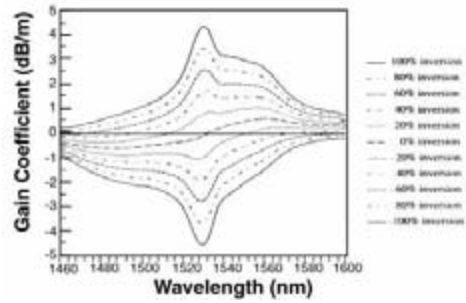

FIGURE 23 Nonuniform gain spectrum of an EDFA for different values of inversion.[16]

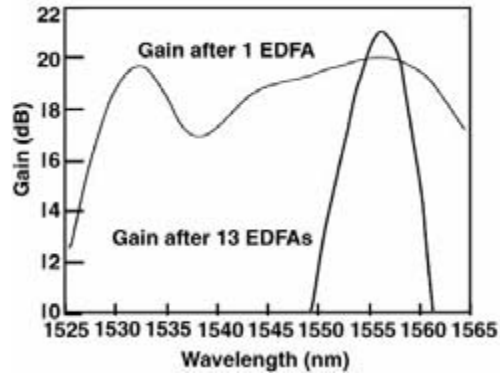

FIGURE 24 EDFA gain nonuniformity accumulation.

EDFA Gain Flattening

We have shown the bandwidth reduction due to nonuniform gain in a cascade of EDFAs. It is clear that gain flattening is an important issue in optically-amplified networks. Several methods have been reported for equalizing nonuniform EDFA gain. These methods include:

- *Long-period grating filters.* A long-period grating (LPG) with an index-varying period of ~100 μm provides coupling between the core modes and the cladding modes, creating a wavelength-dependent loss to equalize the EDFA gain shape.[50–53] The results in Reference 50 are shown in Fig. 25. (Note that in a recent report, similar bandwidth is obtained after more than 9000 km transmission.)
- *Mach-Zehnder filters.* The wavelength-dependent transmission characteristics of cascaded Mach-Zehnder filters can be tailored to compensate for the gain nonuniformity of EDFAs.[54–55]
- *Fluoride-based EDFAs.* A fluoride-based EDFA[56] can provide an intrinsically flat gain over a wide wavelength range from 1530 to 1560 nm, which is a much wider bandwidth than for a silica-based EDFA. However, the fluoride-based fiber is extremely difficult to splice to normal fibers, and mechanical connections result in high connection loss and instability.

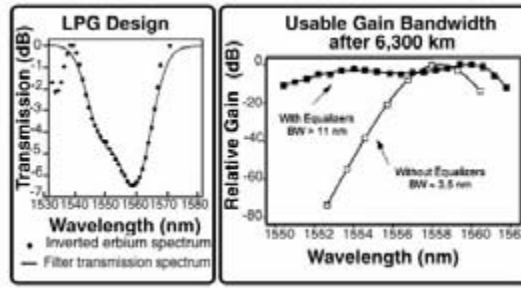

FIGURE 25 LPG design and gain equalization results.[50]

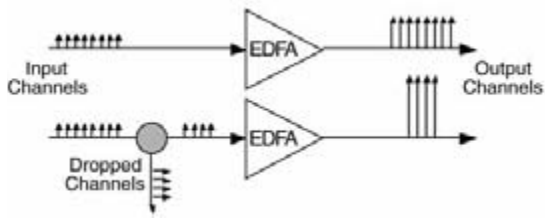

FIGURE 26 EDFA gain transients.

Fast Power Transients

The lifetime of a stimulated erbium ion is generally ~10 ms, which seems to be long enough to be transparent to signals modulated by data at the rates of several Gb/s or higher. However, the EDFAs could be critically affected by the adding/dropping of WDM channels, network reconfiguration, or link failures, as illustrated in Fig. 26. To achieve optimal channel SNRs, the EDFAs are typically operated in the gain-saturation regime where all channels must share the available gain.[57] Therefore, when channels are added or dropped, the power of the remaining channels will increase resulting transient effects.

The transients can be very fast in EDFA cascades.[58,59] As shown in Fig. 27, with an increase in the number of cascaded EDFAs, the transients can occur in ~2 μs. These fast power transients in chain-amplifier systems should be controlled dynamically, and the response time required scales as the size of the network. For large-scale networks, response times shorter than 100 ns may be necessary.

From a system point of view, fiber nonlinearity may become a problem when too much channel power exists, and a small SNR at the receiver may arise when too little power remains.[60] The corresponding fiber transmission penalty of the surviving channel is shown in Fig. 28 in terms of the Q-factor, for varying numbers of cascaded EDFAs. When 15 channels are dropped or added, the penalties are quite severe. Note that this degradation increases with the number of channels N simply because of enhanced SPM due to a large power excursion as a result of dropping $N - 1$ channels.

In order to maintain the quality of service, the surviving channels must be protected when channel add/drop or network reconfiguration occurs. The techniques include:

- Optical attenuation, by adjusting optical attenuators between the gain stages in the amplifier to control the amplifier gain[61]

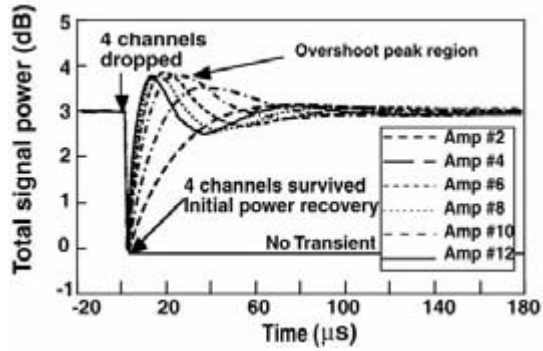

FIGURE 27 Fast power transients in EDFA cascades.[58]

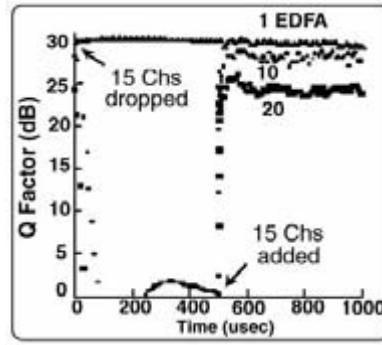

FIGURE 28 Q factor versus time for adding and dropping 15 channels of a 16-channel system at a bit rate of 10 Gb/sec.

- Pump control, by adjusting the drive current of the pump lasers to control the amplifier gain[62–64]
- Link control, using a power-variable control channel propagating with the signal channels to balance the amplifier gain[65]
- Gain clamping, with an automatic optical feedback control scheme to achieve all-optical gain clamping[66,67]

Ultrawideband EDFA

In Fig. 1 we saw that the bandwidth provided by conventional EDFAs is narrow compared to the low-loss window of the optical fiber. It is extremely important to broaden the gain spectrum of the optical amplifier to increase the transmission capacity of WDM systems.

Figure 29 shows a very promising scheme utilizing a parallel-type amplifier with both a 1550 nm-band and a 1580 nm-band EDFA.[68,69] The gain in the 1580 nm-band is provided by an underpumped EDFA, sometimes using an erbium-doped fiber of as long as ~200 m. The combined amplifier can offer a bandwidth of up to 80 nm, which is twice the bandwidth provided by conventional EDFAs.

In fact, the available bandwidth of amplified WDM systems can be further extended by combining this parallel configuration with other types of optical amplifiers, such as Raman amplifiers, as shown in Fig. 30. Moreover, the available bandwidth may exceed 25 THz (the low-loss window around 1.55 μm) by suppressing the high-loss peak around 1400 nm in the optical fiber. An additional bandwidth of more than 100 nm could be opened up by using this new type of fiber.[70]

13.5 DYNAMIC CHANNEL POWER EQUALIZATION

In Section 13.4 we discussed EDFA gain-flattening, which is a passive channel power equalization scheme effective only for a static link. However, as mentioned in Section 13.3, all optical networks are nonstatic, since the power in each channel suffers from dynamic network changes, including:

- Wavelength drift of components
- Changes in span loss
- Channel add/drop

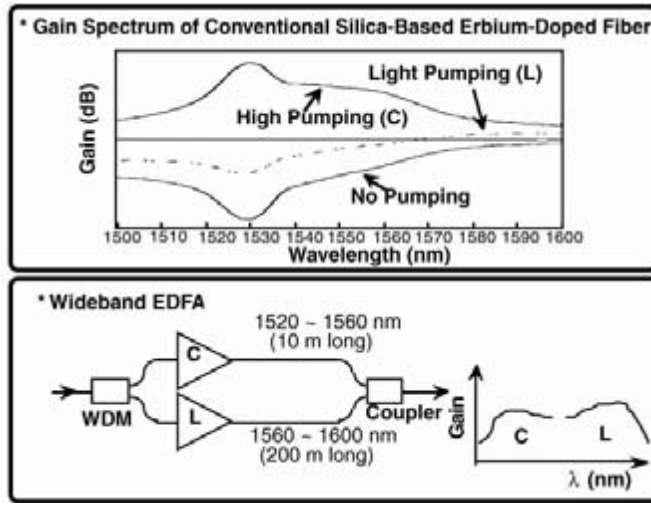

FIGURE 29 Ultrawideband silica-based EDFA.

As an example, consider Fig. 31, which shows how the gain shape of a cascaded EDFA chain varies significantly with link loss changes due to environmental problems. This is because the EDFA gain spectra are dependent on the saturation level of the amplifiers (see Fig. 23). The simulation results in Fig. 31 are for a cascade of 10 gain-flattened EDFAs, each with 20-dB gain, saturated by 16 input channels with –18 dBm per channel.

As illustrated in Fig. 32, system performance can be degraded due to unequalized WDM channel power. These degrading effects include:

- SNR differential (reduced system dynamic range)
- Widely varying channel crosstalk
- Nonlinear effects
- Low signal power at the receiver

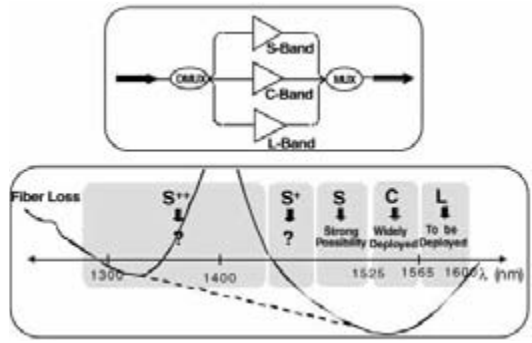

FIGURE 30 Potential wavelength regions for future WDM systems.

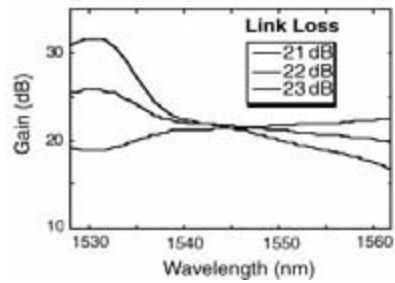

FIGURE 31 Gain spectra variation due to link loss changes for a cascade of 10 EDFAs.

Therefore, channel power needs to be equalized dynamically in WDM networks to ensure stable system performance. To obtain feedback for control purposes, a channel power monitoring scheme is very important. A simple way to accomplish this is to demultiplex all the channels and detect the power in each channel using different photodetectors or detector arrays. To avoid the high cost of many discrete components in WDM systems with large numbers of channels, other monitoring techniques that take advantage of wavelength-to-time mapping have also been proposed, including the use of concatenated FBGs[71] or swept acousto-optic tunable filters (AOTFs).[72]

Various techniques have been proposed for dynamic channel power equalization, including:

- Parallel loss elements[73]
- Individual bulk devices (e.g., AOTFs)[74]
- Serial filters[75]
- Micro-opto-mechanics (MEMS)[76]
- Integrated devices[77]

As an example, Fig. 33 shows the parallel loss element scheme, where the channels are demultiplexed and attenuated by separate loss elements. An additional advantage of this scheme is that ASE noise is reduced by the WDM multiplexer and demultiplexer. Possible candidates for the loss elements in this scheme include:

- Opto-mechanical attenuators
- Acousto-optic modulators
- FBG

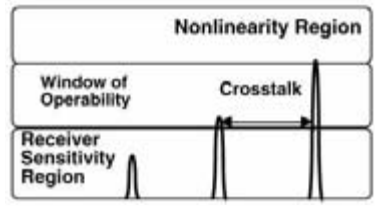

FIGURE 32 Degradation due to unequalized WDM channel power.

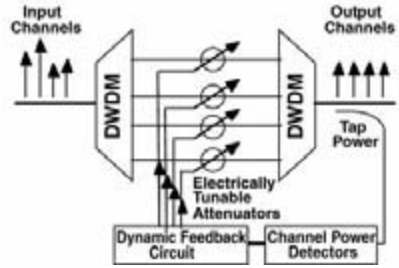

FIGURE 33 Parallel loss element scheme for dynamic channel power equalization.

13.6 CROSSTALK IN WDM NETWORKS

Incoherent and coherent crosstalk between adjacent channels are major problems that limit the density of WDM channels. In particular, coherent crosstalk in WDM ADMs and switches places severe requirements on the acceptable crosstalk-suppression levels provided by these components. In this section, we will introduce these two types of crosstalk and discuss their impact on system performance.

Incoherent Crosstalk

WDM channel crosstalk involves the most basic function of demultiplexing many WDM channels using an optical filter.[78] Figure 34 shows the demultiplexing of WDM channels by an optical filter so that only one channel is received and the other channel is blocked. However, the slowly diminishing spectral shape of the filter with long tails will induce crosstalk to the demultiplexed channel when the signals are detected at the photodetector.

In the case of incoherent crosstalk, the crosstalk level is determined by the channel spacing and channel powers. This interchannel crosstalk power P_{cr} will act to reduce the power extinction ratio of the selected recovered signal:

$$S = P_S - P_{cr} \tag{9}$$

where S is the effective recovered signal power, and P_S is the power in the selected wavelength that passes through the filter. The crosstalk due to power leakage from the adjacent channels may raise the level of a "zero," increasing the probability of errors. Although the tolerable amount of crosstalk depends on the specific WDM system, crosstalk should not exceed a few percent of the selected channel power in order to maintain good system performance.[79–81]

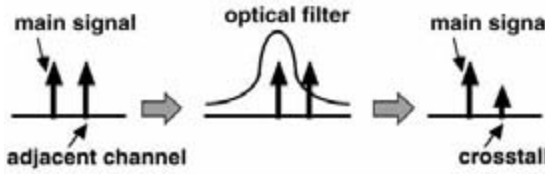

FIGURE 34 Incoherent crosstalk from adjacent channels.

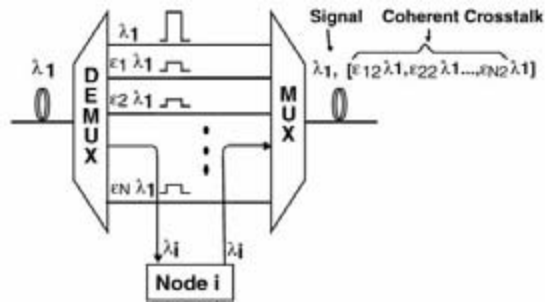

FIGURE 35 Coherent crosstalk in an ADM.

Coherent Crosstalk

Add-drop multiplexers are key subsystems in WDM networks.[82] They are typically composed of a wavelength demultiplexer followed by a wavelength multiplexer. Ideally, they allow a network node to have access to a single wavelength while allowing all other wavelengths to pass through the node unaffected (see Fig. 35). Unfortunately, wavelength (de)multiplexers[83] are not ideal and allow unwanted crosstalk of any input wavelength onto unintended output ports. For example, a small replica of the signal at wavelength λ_1 will appear at all the demultiplexer output ports, as shown in Fig. 35. If a nonideal demultiplexer and nonideal multiplexer are placed back-to-back, small replicas of the signal at λ_1 will recombine with the main signal at λ_1 at the multiplexer output.

This ADM structure with crosstalk represents an interferometer, since it consists of input and output ports connected by optical paths. Due to coherent interaction of the fields, the amplitude of the output signal will fluctuate as the signals' relative phases and polarization states change.[84,85]

Coherent crosstalk has been shown to be a serious limiting factor in scaleable WDM networks,[86,87] since the crosstalk signal has the same frequency as the main signal and the crosstalk is added to the main signal in the electric field. Let's consider the case shown in Fig. 36, where two signals with identical wavelengths enter an OXC and then are routed to different paths. Assuming the two channels have the same input power P and the power leakage of the OXC is ε, then the optical power at one of the output ports can be approximated by

$$P_0 \propto (\sqrt{P} + \sqrt{\varepsilon P})^2 = P \pm 2\sqrt{\varepsilon} P + \varepsilon P \tag{10}$$

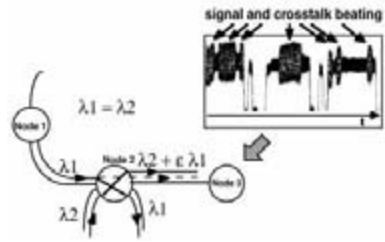

FIGURE 36 Power fluctuation due to coherent crosstalk.[86]

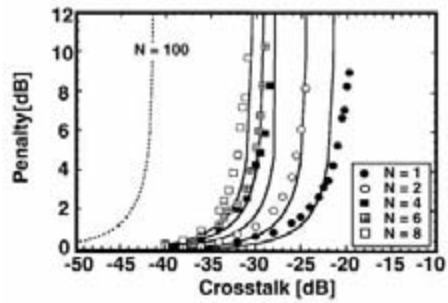

FIGURE 37 Scaling limitations due to coherent crosstalk.[86]

Therefore, the crosstalk power can be as high as 20 percent even when the power leakage ratio of the OXC is only 1 percent.

Figure 37 shows scaling limitations due to coherent crosstalk.[86] For the case of a single crosstalk channel, a coherent crosstalk of –25 dB will cause a power penalty of 1 dB, which is much more severe than the effects of incoherent crosstalk (1 dB power penalty at –8 dB crosstalk).[87] Because of the severity of this penalty, coherent crosstalk critically limits the scalability of an optical network employing ADMs and OXCs. If 100 channels are required, the crosstalk should be lower than –45 dB. However, the typical crosstalk of current components (WDM arrayed-waveguide gratings, switches, and modulators) is only –25 dB.

To mitigate the effects of coherent crosstalk in WDM networks, the following techniques have been proposed:

- *Architecture dilation.*[88] Purposely introducing fiber delays (on the order of a bit time) between different crosstalk paths decorrelates the bit pattern of the main signal from the interfering signals and places some of the crosstalk power in the "0" bits of the main signal instead of the "1" bits.
- *Low-coherence light sources.* Using *light-emitting diodes* (LEDs) or *chirped distributed feedback lasers* (DFBs) with coherence times less than a bit time can reduce coherent crosstalk, but the impact of dispersion would become more critical.
- *Polarization scrambling or modulation.* Polarization scrambling reduces the effect of coherent crosstalk, since interference between the crosstalk and signal decreases when their polarization states are not matched.
- *Phase modulation.* Modulating the phase of the signal at a rate greater than the bit rate averages out the crosstalk and improves performance, since signal degradation depends on the relative phase between the signal and crosstalk.

13.7 SUMMARY

In this chapter we have covered many different aspects of high-speed WDM fiber-optic communication networks. We have endeavored to treat the most important topics—those that will likely impact these networks for years to come. The enormous growth of these systems is all due to the revolutionary introduction of the EDFA. With increased knowledge, more development, higher data rates, and increasing channel count, WDM network limitations are being continually redefined. Network reconfigurability can offer great benefits for future WDM networks. However, a number of new degrading effects must be solved before recon-

figurable networks become a reality. Yet the push for more bandwidth in WDM systems continues due to the enormous inherent potential of the optical fiber.

13.8 ACKNOWLEDGMENTS

We are indebted to Steve Havstad for his generous help and valuable contributions to this chapter.

13.9 REFERENCES

1. F. P. Kapron, "Fiber-Optic System Tradeoffs," *IEEE Spectrum Magazine,* 60–75 (March 1985).
2. Y. K. Park, T. V. Nguyen, O. Mizuhara, C. D. Chen, L. D. Tzeng, P. D. Yeates, F. Heismann, Y. C. Chen, D. G. Ehrenbergh, and J. C. Feggeler, "Field Demonstration of 10-Gb/s Line-Rate Transmission on an Installed Transoceanic Submarine Lightwave Cable," *IEEE Photonics Technology Letters* **8**:425–427 (1996).
3. D. P. Berztsekas and R. G. Gallager, *Data Networks,* Prentice Hall, Englewood Cliffs, New Jersey, 1987.
4. P. Kaiser and D. B. Keck, "Fiber Types and Their Status," *Optical Fiber Telecommunications II,* S. E. Miller and I. P. Kaminow (eds.), Academic Press, New York, 1988.
5. A. R. Chraplyvy, "Limitations on Lightwave Communications Imposed by Optical Fiber Nonlinearities," *IEEE Journal of Lightwave Technology* **8**:1548–1557 (1990).
6. P. E. Green, Jr., *Fiber Optic Networks,* Prentice Hall, Englewood Cliffs, New Jersey, 1993.
7. Special Issue on Wavelength Division Multiplexing, *IEEE Journal on Selected Areas in Communications,* **8** (1990).
8. C. A. Brackett, "Dense Wavelength Division Multiplexing: Principles and Applications," *IEEE Journal on Selected Areas in Communications* **8**:948 (1990).
9. I. P. Kaminow, "FSK with Direct Detection in Optical Multiple-Access FDM Networks," *IEEE Journal on Selected Areas in Communications* **8**:1005 (1990).
10. T. Li, "The Impact of Optical Amplifiers on Long-Distance Lightwave Telecommunications," *Proceedings of the IEEE* **81**:1568–1579 (1993).
11. G. P. Agrawal, *Nonlinear Fiber Optics,* Academic Press, New York, 1990.
12. A. R. Chraplyvy and R. W. Tkach, "What Is the Actual Capacity of Single-Mode Fibers In Amplified Lightwave Systems?," *IEEE Photonics Technology Letters,* **5**:666–668 (1987).
13. N. S. Bergano, and C. R. Davidson, "Wavelength Division Multiplexing in Long-Haul Transmission Systems," *IEEE J. Lightwave Technology,* **14**:1299–1308 (1996).
14. H. Taga, "Technologies for Hundreds of Gb/s Capacities in Undersea Lightwave Systems," *Conference on Optical Fiber Communication,* paper TuD3 (1999).
15. T. Li, "The Impact of Optical Amplifiers on Long-Distance Lightwave Telecommunications," Proceedings of the IEEE **81**:1568, (1993).
16. I. Kaminow and T. Koch, *Optical Fiber Communications,* IIIA, Academic Press, 1997.
17. D. Marcuse, A. R. Chraplyvy, and R. W. Tkach, "Dependence of Cross-Phase Modulation on Channel Number in Fiber WDM Systems," *IEEE J. Lightwave Technology,* **12**:885–890 (1994).
18. R. G. Waarts and R. P. Braun, "System Limitations Due to Four-Wave Mixing In Single-Mode Optical Fibers," *Electronics Letters,* **22**:873 (1986).
19. M. W. Maeda, W. B. Sessa, W. I. Way, A. Yi-Yan, L. Curtis, R. Spicer, and R. I. Laming, "The Effect of Four Wave Mixing in Fibers on Optical Frequency-Division Multiplexed Systems," *IEEE J. Lightwave Technology* **8**:1402–1408 (1990).
20. K. O. Hill, D. C. Johnson, B. S. Kawasaki, and R. I. MacDonald, "CW Three-Wave Mixing In Single-Mode Optical Fibers," *J. Appl. Phys.,* **49**:5098 (1978).

21. A. M. Vengsarkar, "Dispersion Compensating Fibers," *Conference on Optical Fiber Communication,* paper ThA2 (1997).
22. A. J. Antos and D. K. Smith, "Design and Characterization of Dispersion Compensating Fiber Based on the LP_{01} Mode," *IEEE J. Lightwave Technology,* **12**:1739–1745 (1994).
23. C. Kurtzke, "Suppression of Fiber Nonlinearities By Appropriate Dispersion Management," *IEEE Photonics Technology Letters,* **5**:1250–1252 (1993).
24. A. R. Chraplyvy, "High-Capacity Lightwave Transmission Experiments," *Bell Labs Technical Journal* (January–March 1999).
25. Y. Liu and A. J. Antos, "Dispersion-Shifted Large-Effective-Area Fiber for Amplified High-Capacity Long-Distance Systems," *Conference on Optical Fiber Communication,* paper TuN5 (1997).
26. R. W. Tkach, A. R. Chraplyvy, F. Forghieri, A. H. Gnauck, and R. M. Derosier, "Four-Photon Mixing and High-Speed WDM Systems," *IEEE J. Lightwave Technology* **13**:841–849 (1995).
27. A. R. Chraplyvy, A. H. Gnauck, R. W. Tkach, and R. M. Derosier, "8 × 10 Gb/s Transmission Through 280 km of Dispersion Management," *IEEE Photonics Technology Letters,* **5**:1233–1235 (1993).
28. K. O. Hill, S. Theriault, B. Malo, F. Bilodeau, T. Kitagawa, D. C. Johnson, J. Albert, K. Takiguchi, T. Kataoka, and K. Hagimoto, "Chirped In-Fibre Bragg Grating Dispersion Compensators: Linearisation of Dispersion Characteristic and Demonstration of Dispersion Compensation in 100 km, 10 Gb/s Optical Fibre Link," *Electronics Letters,* **30**:1755–1756 (1994).
29. W. H. Loh, R. I. Laming, N. Robinson, A. Cavaciuti, F. Vaninetti, C. J. Anderson, M. N. Zervas, and M. J. Cole, "Dispersion Compensation Over Distances in Excess of 500 km for 10-Gb/s Systems Using Chirped Fiber Gratings," *IEEE Photonics Technology Letters,* **8**:944–946 (1996).
30. L. Dong, M. J. Cole, A. D. Ellis, N. Durkin, M. Ibsen, V. Gusmeroli, and R. I. Laming, "40 Gb/s 1.55 μm Transmission Over 109 km of Non-Dispersion Shifted Fiber with Long Continuous Chirped Fiber Gratings," *Conference on Optical Fiber Communication,* paper PD6 (1997).
31. M. Dukin, M. Ibsen, M. J. Cole, and R. I. Laming, "1m Long Continuously-Written Fiber Bragg Gratings for Combined Second- and Third-Order Dispersion Compensation," *Electron. Letters,* **33**:1891–1893 (1997).
32. M. Ibsen, M. K. Durkin, M. J. Cole, and R. I. Laming, "Sinc-Sampled Fiber Bragg Gratings for Identical Multiple Wavelength Operation," *IEEE Photonics Technology Letters,* **10**:842–845 (1998).
33. J.-X. Cai, K.-M. Feng, A. E. Willner, V. Grubsky, D. S. Starodubov, and J. Feinberg, "Simultaneous Tunable Dispersion Compensation of Many WDM Channels Using a Sampled Nonlinearly-Chirped Fiber-Bragg-Grating," *IEEE Photonics Technology Letters,* **11**:1455–1457, (1999).
34. M. M. Ohn, A. T. Alavie, R. Maaskant, M. G. Xu, F. Bilodeau, and K. O. Hill, "Tunable Fiber Grating Dispersion Using a Piezoelectric Stack," *Conference on Optical Fiber Communication,* paper WJ3 (1997).
35. K.-M. Feng, J.-X. Cai, V. Grubsky, D. S. Starodubov, M. I. Hayee, S. Lee, X. Jiang, A. E. Willner, and J. Feinberg, "Dynamic Dispersion Compensation in a 10-Gb/s Optical System Using a Novel Voltage Tuned Nonlinearly Chirped Fiber Bragg Grating," *IEEE Photonics Technology Letters,* **11**:373–375 (1999).
36. A. E. Willner, I. P. Kaminow, M. Kuznetsov, J. Stone, and L. W. Stulz, "1.2Gb/s Closely-Spaced FDMA-FSK Direct-Detection Star Network," *IEEE Photonics. Technology Letters,* **2**:223–226 (1990).
37. N. R. Dono, P. E. Green, K. Liu, R. Ramaswami, and F. F. Tong, "A Wavelength Division Multiple Access Network for Computer Communication," *IEEE Journal on Selected Areas in Communications,* **8**:983–994 (1990).
38. W. I. Way, D. A. Smith, J. J. Johnson, and H. Izadpanah, "A Self-Routing WDM High-Capacity SONET Ring Network," *IEEE Photonics Technology Letters* **4**:402–405 (1992).
39. T-H. Wu, *Fiber Network Service Survivability,* Boston: Artech House.
40. A. S. Acampora, M. J. Karol, and M. G. Hluchyj, "Terabit Lightwave Networks: The Multihop Approach," *AT&T Technical Journal,* **66**:21–34 (1987).
41. A. E. Willner, "Combating Degrading Effects in Non-Static and Reconfigurable WDM Systems and Networks," *Conference on Optical Fiber Communication,* Short Course SC114 (1999).
42. V. W. S. Chan, K. L. Hall, E. Modiano, and K. A. Rauschenbach, "Architectures and Technologies for High-Speed Optical Data Networks," *IEEE J. Lightwave Technology,* **16**:2146–2168 (1998).
43. J. Y. Hui, *Switching and Traffic Theory for Integrated Broadband Networks,* Kluwer Academic Publishers, Boston, 1990.

44. J. A. McEachern, "Gigabit Networking on the Public Transmission Network," *IEEE Communications Magazine,* 70–78 (April 1992).
45. M. C. Cardakli, S. Lee, A. E. Willner, V. Grubsky, D. Starodubov, and J. Feinberg, "All-Optical Packet Header Recognition and Switching in a Reconfigurable Network Using Fiber Bragg Gratings for Time-to-Wavelength Mapping and Decoding," *Conference on Optical Fiber Communications,* paper ThM4 (1999).
46. E. L. Goldstein, A. F. Elrefaie, N. Jackman, and S. Zaidi, "Multiwavelength Fiber-Amplifier Cascades in Unidirectional Interoffice Ring Networks," *Conference on Optical Fiber Communications,* paper TuJ3 (1993).
47. J. P. Blondel, A. Pitel, and J. F. Marcerou, "Gain-Filtering Stability in Ultralong-Distance Links," *Conference on Optical Fiber Communications '93,* paper TuI3 (1993).
48. H. Taga, N. Edagawa, Y. Yoshida, S. Yamamoto, and H. Wakabayashi, "IM-DD Four-Channel Transmission Experiment Over 1500 km Employing 22 Cascaded Optical Amplifiers," *Electron. Letters,* **29**:485 (1993).
49. A. E. Willner and S.-M. Hwang, "Transmission of Many WDM Channels Through a Cascade of EDFAs in Long-Distance Link and Ring Networks," *IEEE Journal of Lightwave Technology* **13**:802–816 (1995).
50. A. M. Vengsarkar, P. J. Lemaire, J. B. Judkins, V. Bhatia, T. Erdogan, and J. E. Sipe, "Long-Period Fiber Gratings as Band-Rejection Filters," *IEEE Journal of Lightwave Technology* **14**:58–65 (1996).
51. Y. Sun, J. B. Judkins, A. K. Srivastava, L. Garrett, J. L. Zyskind, J. W. Sulhoff, C. Wolf, R. M. Derosier, A. P. Gnauck, R. W. Tkach, J. Zhou, R. P. Espindola, A. M. Vengsarkar, and A. R. Chraplyvy, "Transmission of 32-WDM 10-Gb/s Channels Over 640 km Using Broad-Band, Gain-Flattened Erbium-Doped Silica Fiber Amplifiers," *IEEE Photonics Technology Letters* **9**:1652–1654 (1997).
52. A. M. Vengsarkar, P. J. Lemaire, J. B. Judkins, J. E. Sipe, and T. Erdogan, "Long-Period Fiber Gratings as Band-Rejection Filters," *Conference on Optical Fiber Communications,* paper PD4 (1995).
53. P. F. Wysocki, J. B. Judkins, R. P. Espindola, M. Andrejco, and A. M. Vengsarkar, "Broad-Band Erbium-Doped Fiber Amplifier Flattened Beyond 40 nm Using Long-Period Grating Filter," *IEEE Photonics Technology Letters* **9**:1343–1345 (1997).
54. K. Inoue, T. Kominato, and H. Toba, "Tunable Gain Equalization Using a Mach-Zehnder Optical Filter in Multistage Fiber Amplifiers," *IEEE Photonics Technology Letters,* **3**:718–720 (1991).
55. J. Y. Pan, M. A. Ali, A. F. Elrefaie, and R. E. Wagner, "Multiwavelength Fiber-Amplifier Cascades with Equalization Employing Mach-Zehnder Optical Filter," *IEEE Photonics Technology Letters* **7**:1501–1503 (1995).
56. M. Yamada, T. Kanamori, Y. Terunuma, K. Oikawa, M. Shimizu, S. Sudo, and K. Sagawa, "Fluoride-Based Erbium-Doped Fiber Amplifier with Inherently Flat Gain Spectrum," *IEEE Photonics Technology Letters* **8**:882–884 (1996).
57. E. Desurvire, R. Giles, and J. Simpson, "Gain Saturation Effects in High-Speed, Multi Channel Erbium-Doped Fiber Amplifiers at 1 = 1.53 mm," *IEEE Journal of Lightwave Technology* **7**:2095–2104 (1989).
58. J. Zyskind, Y. Sun, A. Srivastava, J. Sulhoff, A. Lucero, C. Wolf, and R. Tkach, "Fast Power Transients in Optically Amplified Multiwavelength Optical Networks," *Conference on Optical Fiber Communications,* paper PD-31 (1996).
59. Y. Sun, A. Saleh, J. Zyskind, D. Wilson, A. Srivastava, and J. Sulhoff, "Time Dependent Perturbation Theory and Tones in Cascaded Erbium-Doped Fiber Amplifier System," *IEEE Journal of Lightwave Technology* **15**:1083–1087 (1997).
60. M. Hayee and A. Willner, "Fiber Transmission Penalties Due to EDFA Power Transients Resulting from Fiber Nonlinearity and ASE Noise in Add/Drop Multiplexed WDM Networks," *IEEE Photonics Tech. Lett.* **11**:889–891 (1999).
61. J.-X. Cai, K.-M. Feng, and A. E. Willner, "Simultaneous Compensation of Fast Add/Drop Power-Transients and Equalization of Inter-Channel Power Differentials for Robust WDM Systems with EDFAs," *Conference on Optical Amplifiers and Their Applications, Victoria, Canada, paper MC6,* (July 1997).
62. K. Motoshima, L. Leba, D. Chen, M. Downs, T. Li and E. Desurvire, "Dynamic Compensation of Transient Gain Saturation in Erbium-Doped Fiber Amplifiers by Pump Feedback Control," *IEEE Photonics Technology Letters* **5**:1423–1426 (1993).

63. A. Srivastava, Y. Sun, J. Zyskind, J. Sulhoff, C. Wolf, and R. Tkach, "Fast Gain Control in an Erbium-Doped Fiber Amplifier," *Conference on Optical Amplifiers and Their Applications,* paper PD4 (1996).
64. C. Konishi, T. Yoshida, S. Hamada, K. Asahi, and S. Fujita, "Dynamic Gain-Controlled Erbium-Doped Fiber Amplifier Repeater for WDM Network," *Conference on Optical Fiber Communications,* paper TuE1 (1997).
65. A. Srivastava, J. Zyskind, Y. Sun, J. Ellson, G. Newsome, R. Tkach, A. Chraplyvy, J. Sulhoff, T. Strasser, C. Wolf, and J. Pedrazzani, "Fast-Link Control Protection of Surviving Channels in Multiwavelength Optical Networks," *IEEE Photonics Technology Letters* **9**:1667–1669 (1997).
66. B. Landousies, T. Georges, E. Delevaque, R. Lebref, and M. Monerie, "Low Power Transient in Multichannel Equalized and Stabilised Gain Amplifier Using Passive Gain Control," *Electronics Letters* **32**:1912–1913 (1996).
67. G. Luo, J. Zyskind, Y. Sun, A. Srivastava, J. Sulhoff, and M. Ali, "Performance Degradation of All-Optical Gain-Clamped EDFAs Due to Relaxation-Oscillations and Spectral-Hole Burning in Amplified WDM Networks," *IEEE Photonics Technology Letters* **9**:1346–1348 (1997).
68. Y. Sun, J. W. Sulhoff, A. K. Srivastava, J. L. Zyskind, T. A. Strasser, J. R. Pedrazzani, C. Wolf, J. Zhou, J. B. Jukins, R. P. Espindola, and A. M. Vengsarkar, "80 nm Ultra-Wideband Erbium-Doped Silica Fibre Amplifier," *Electronics Letters* **33**:1965–1967 (1997).
69. M. Yamada, H. Ono, T. Kanamori, S. Sudo, and Y. Ohishi, "Broadband and Gain-Flattened Amplifier Composed of a 1.55 μm-band and a 1.58 μm-band Er^{3+}-Doped Fibre Amplifier in a Parallel Configuration," *Electronics Letters* **33**:710–711 (1997).
70. Allwave Single-Mode Optical Fiber," *Bell Labs Technical Document* (June 1, 1999).
71. R. Giles, T. Strasser, K. Dryer, and C. Doerr, "Concatenated Fiber Grating Optical Monitor," *IEEE Photonics Technology Letters* **10**:1452–1454 (1998).
72. St. Schmid, S. Morasca, D. Scarano, and H. Herrmann, "High-Performance Integrated Acousto-Optic Channel Analyzer," *Conference on Optical Fiber Communications,* paper TuC3 (1997).
73. J. Cai, K. Feng, X. Chen, and A. Willner, "Experimental Demonstration of Dynamic High-Speed Equalization of Three WDM Channels Using Acousto-Optic Modulators and a Wavelength Demultiplexer," *IEEE Photonics Technology Letters* **9**:678–680 (1997).
74. S. Huang, X. Zou, A. Willner, Z. Bao, and D. Smith, "Experimental Demonstration of Active Equalization and ASE Suppression of Three 2.5 Gb/s WDM-Network Channels Over 2500 km Using AOTF as Transmission Filters," *IEEE Photonics Technology Letters* **9**:389–391 (1997).
75. D. Starodubov, V. Grubsky, J. Feinberg, J. Cai, K. Feng, and A. Willner, "Novel Fiber Amplitude Modulators for Dynamic Channel Power Equalization in WDM Systems," *Conference on Optical Fiber Communication,* paper PD-8 (1998).
76. J. Ford and J. Walker, "Dynamic Spectral Power Equalization Using Micro-Opto-Mechanics," *IEEE Photonics Technology Letters* **10**:1440–1442 (1998).
77. C. Doerr, C. Joyner, and L. Stulz, "Integrated WDM Dynamic Power Equalizer with Low Insertion Loss," *IEEE Photonics Technology Letters* **10**:1443–1445 (1998).
78. P. A. Humblet and W. M. Hamdy, "Crosstalk Analysis and Filter Optimization of Single- and Double-Cavity Fabry-Perot Filters," *IEEE Journal on Selected Areas of Communications* **8**:1095–1107 (1990).
79. I. P. Kaminow, P. P. Iannone, J. Stone, and L. W. Stulz, "FDMA-FSK Star Network with a Tunable Optical Fiber Demultiplexer," *J. Lightwave Technology* **6**:1406–1414 (1988).
80. A. E. Willner, "Simplified Model of a FSK-to-ASK Direct-Detection System Using a Fabry-Perot Demodulator," *IEEE Photonics Technology Letters* **2**:363–366 (1990).
81. A. E. Willner, I. P. Kaminow, M. Kuznetsov, J. Stone, and L. W. Stulz, "FDMA-FSK Noncoherent Star Network Operated at 600 Mb/s Using Two-Electrode DFB Lasers and a Fiber Optical Filter Demultiplexer," *Electronics Letters* **25**:1600–1601 (1989).
82. R. E. Wagner, R. C. Alferness, A. A. M. Saleh, and M. S. Goodman, "MONET: Multiwavelength Optical Networking," *J. Lightwave Technology* **14**:1349–1355 (1996).
83. C. Dragone, C. A. Edwards, and R. C. Kistler, "Integrated Optics N X N Multiplexer on Silicon," *IEEE Photonics Technology Letters* **3**:896–899 (1991).
84. A. Arie, M. Tur, and E. L. Goldstein, "Probability-Density Function of Noise at the Output of a Two-Beam Interferometer," *J. Opt. Soc. Am. A* **8**:1936–1941 (1991).

85. P. J. Legg, D. K. Hunter, I. Andonovic and P. E. Barnsley, "Inter-Channel Crosstalk Phenomena in Optical Time Division Multiplexed Switching Networks," *IEEE Photonics Technology Letters* **6**:661–663 (1994).

86. E. L. Goldstein and L. Eskildsen, "Scaling Limitations in Transparent Optical Networks Due to Low-Level Crosstalk," *IEEE Photonics Technology Letters* **7**:93–94 (1995).

87. E. L. Goldstein, L. Eskildsen, and A. F. Elrefaie, "Performance Implications of Component Crosstalk in Transparent Lightwave Networks," *IEEE Photonics Technology Letters* **6**:657–660 (1994).

88. R. Khosravani, M. I. Hayee, B. Hoanca, and A. E. Willner, "Reduction of Coherent Crosstalk in WDM Add/Drop Multiplexing Nodes by Bit Pattern Misalignment," *IEEE Photonics Technology Letters* **11**:134–136 (1999).

This page intentionally left blank.

CHAPTER 14
INFRARED FIBERS

James A. Harrington
Rutgers University
Piscataway, New Jersey

14.1 INTRODUCTION

Infrared (IR) optical fibers may be defined as fiber optics transmitting radiation with wavelengths greater than approximately 2 μm. The first IR fibers were fabricated in the mid-1960s from chalcogenide glasses such as arsenic trisulfide and had losses in excess of 10 dB/m.[1] During the mid-1970s, the interest in developing an efficient and reliable IR fiber for short-haul applications increased, partly in response to the need for a fiber to link broadband, long-wavelength radiation to remote photodetectors in military sensor applications. In addition, there was an ever increasing need for a flexible fiber delivery system for transmitting CO_2 laser radiation in surgical applications. Around 1975, a variety of IR materials and fibers were developed to meet these needs. These included the heavy metal fluoride glass (HMFG) and polycrystalline fibers as well as hollow rectangular waveguides. While none of these fibers had physical properties even approaching those of conventional silica fibers, they were nevertheless useful in lengths less than 2 to 3 m for a variety of IR sensor and power delivery applications.[2]

IR fiber optics may logically be divided into three broad categories: glass, crystalline, and hollow waveguides. These categories may be further subdivided based on fiber material, structure, or both, as shown in Table 1. Over the past 25 years many novel IR fibers have been made in an effort to fabricate a fiber optic with properties as close as possible to those of silica, but only a relatively small number have survived. A good source of general information on these various IR fiber types may be found in the literature.[3–6] In this review only the best, most viable, and, in most cases, commercially available IR fibers are discussed. In general, both the optical and mechanical properties of IR fibers remain inferior to those of silica fibers, and therefore the use of IR fibers is still limited primarily to nontelecommunication, short-haul applications requiring only tens of meters of fiber rather than the kilometer lengths common to telecommunication applications. The short-haul nature of IR fibers results from the fact that most IR fibers have losses in the range of a few decibels per meter. An exception is fluoride glass fibers, which can have losses as low as a few decibels per kilometer. In addition, IR fibers are much weaker than silica fiber and, therefore, more fragile. These deleterious features have slowed the acceptance of IR fibers and restricted their use today to applications in chemical sensing, thermometry, and laser power delivery.

Copyright 2001 by The McGraw-Hill Companies, Inc. Click Here for Terms of Use.

TABLE 1 Categories of IR Fibers with a Common Example to Illustrate Each Subcategory

Main	Subcategory	Examples
Glass	Heavy metal fluoride (HMFG)	ZrF_4-BaF_2-LaF_3-AlF_3-NaF (ZBLAN)
	Germanate	GeO_2-PbO
	Chalcogenide	As_2S_3 and AsGeTeSe
Crystal	Polycrystalline (PC)	AgBrCl
	Single crystal (SC)	Sapphire
Hollow waveguide	Metal/dielectric film	Hollow glass waveguide
	Refractive index < 1	Hollow sapphire at 10.6 μm

A key feature of current IR fibers is their ability to transmit longer wavelengths than most oxide glass fibers can. In some cases the transmittance of the fiber can extend well beyond 20 μm, but most applications do not require the delivery of radiation longer than about 12 μm. In Fig. 1 we give the attenuation values for some of the most common IR fibers as listed in Table 1. From the data it is clear that there is a wide variation in range of transmission for the different IR fibers and that there is significant extrinsic absorption that degrades the overall optical response. Most of these extrinsic bands can be attributed to various impurities, but, in the case of the hollow waveguides, they are due to interference effects resulting from the thin film coatings used to make the guides.

Some of the other physical properties of IR fibers are listed in Table 2. For comparison, the properties of silica fibers are also listed. The data in Table 2 and in Fig. 1 reveal that, compared to silica, IR fibers usually have higher losses, larger refractive indices and *dn/dT* values, lower melting or softening points, and greater thermal expansion. For example, chalcogenide and polycrystalline Ag halide fibers have refractive indices greater than 2. This means that the Fresnel loss exceeds 20 percent for two fiber ends. The higher *dn/dT* and low melting or softening point lead to thermal lensing and low laser-induced damage thresholds for some of the

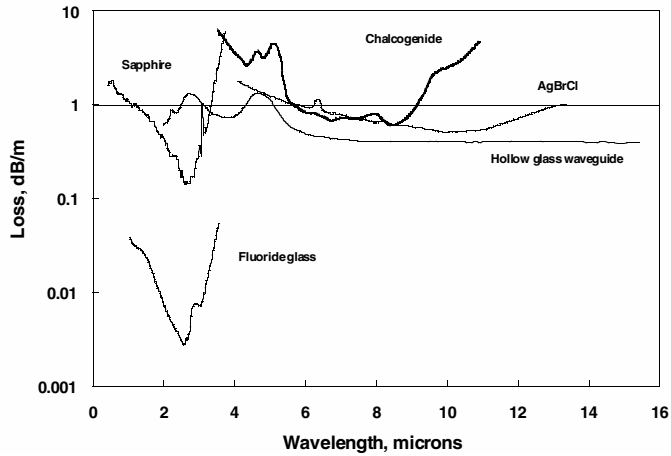

FIGURE 1 Composite loss spectra for some common IR fiber optics: ZBLAN fluoride glass,[7] SC sapphire,[8] chalcogenide glass,[9] PC AgBrCl,[10] and hollow glass waveguide.[11]

TABLE 2 Selected Physical Properties of Key IR Fibers Compared to Conventional Silica Fiber

	Glass			Crystal		Hollow
Property	Silica	HMFG ZBLAN	Chalcogenide AsGeSeTe	PC AgBrCl	SC Sapphire	Hollow Silica Waveguide
Glass transition or melting point, °C	1175	265	245	412	2030	150 (usable *T*)
Thermal conductivity, W/m °C	1.38	0.628	0.2	1.1	36	1.38
Thermal expansion coefficient, 10^{-6} °C^{-1}	0.55	17.2	15	30	5	0.55
Young's modulus, GPa	70.0	58.3	21.5	0.14	430	70.0
Density, g/cm^3	2.20	4.33	4.88	6.39	3.97	2.20
Refractive index (λ, μm)	1.455 (0.70)	1.499 (0.589)	2.9 (10.6)	2.2 (10.6)	1.71 (3.0)	NA
dn/dT, 10^{-5} °C^{-1} (λ, μm)	+1.2 (1.06)	−1.5 (1.06)	+10 (10.6)	−1.5 (10.6)	+1.4 (1.06)	NA
Fiber transmission range, μm	0.24–2.0	0.25–4.0	4–11	3–16	0.5–3.1	0.9–25
Loss* at 2.94 μm, dB/m	~800	0.08	5	3	0.4	0.5
Loss* at 10.6 μm, dB/m	NA	NA	2	0.5	NA	0.4

* Typical measured loss.
NA = not applicable.

fibers. Finally, a number of these fibers do not have cladding analogous to clad oxide glass fibers. Nevertheless, core-only IR fibers such as sapphire and chalcogenide fibers can still be useful because their refractive indices are sufficiently high. For these high-index fibers, the energy is largely confined to the core of the fiber as long as the unprotected fiber core does not come in contact with an absorbing medium.[12]

The motivation to develop a viable IR fiber stems from many proposed applications. A summary of the most important current and future applications and the associated candidate IR fiber that will best meet each need is given in Table 3. We may note several trends from this table. The first is that hollow waveguides are an ideal candidate for laser power delivery at all IR laser wavelengths. The air core of these special fibers or waveguides gives an inherent advantage over solid-core fibers, whose damage threshold is frequently very low for these IR-transmissive materials. The high refractive index of chalcogenide fibers is ideal for chem-

TABLE 3 Examples of IR Fiber Candidates for Various Sensor and Power Delivery Applications

Application	Comments	Suitable IR fibers
Fiber-optic chemical sensors	Evanescent wave principle—liquids	AgBrCl, sapphire, chalcogenide, HMFG
	Hollow core waveguides—gases	Hollow glass waveguides
Radiometry	Blackbody radiation, temperature measurements	Hollow glass waveguides, AgBrCl, chalcogenide, sapphire
Er:YAG laser power delivery	3-μm transmitting fibers with high damage threshold	Hollow glass waveguides, sapphire, germanate glass
CO_2 laser power delivery	10-μm transmitting fibers with high damage threshold	Hollow glass waveguides
Thermal imaging	Coherent bundles	HMFG, chalcogenide
Fiber amplifiers and lasers	Doped IR glass fibers	HMFG, chalcogenide

ical sensing via evanescent wave coupling of a small portion of the light from the core into an IR-absorbing medium. For the measurement of temperature through the simple transmission of blackbody radiation, IR fibers that transmit beyond about 8 μm, such as the Ag halide, chalcogenide, and hollow waveguides, are excellent candidates for use in measuring temperatures below 50°C. This is because the peak for room-temperature blackbody radiation is about 10 μm.

14.2 NONOXIDE AND HEAVY-METAL OXIDE GLASS IR FIBERS

There are two IR-transmitting glass fiber systems that are relatively similar to conventional silica-containing glass fibers. One is the HMFG and the other is heavy-metal germanate glass fibers based on GeO_2. The germanate glass fibers generally do not contain fluoride compounds; instead, they contain heavy metal oxides to shift the IR absorption edge to longer wavelengths. The advantage of germanate fibers over HMFG fibers is that germanate glass has a higher glass transition temperature and, therefore, higher laser damage thresholds. But the level of loss for the HMFG fibers is lower. Finally, chalcogenide glass fibers made from chalcogen elements such as As, Ge, S, and Te contain no oxides or halides, making them a good choice for nonlaser power delivery applications.

HMFG Fibers

Poulain et al.[13] discovered HMFGs or fluoride glasses accidentally in 1975 at the University of Rennes. In general, the typical fluoride glass has a glass transition temperature T_g four times less than that of silica, is considerably less stable than silica, and has failure strains of only a few percent compared to greater than 5 percent for silica. While an enormous number of multicomponent fluoride glass compositions have been fabricated, comparably few have been drawn into fiber. This is because the temperature range for fiber drawing is normally too small in most HMFGs to permit fiberization of the glass. The most popular HMFGs for fabrication into fibers are the fluorozirconate and fluoroaluminate glasses, of which the most common are ZrF_4-BaF_2-LaF_3-AlF_3-NaF (ZBLAN) and AlF_3-ZrF_4-BaF_2-CaF_2-YF_3, respectively. The key physical properties of these glasses are summarized in Table 4. An important feature of the fluoroaluminate glass is its higher T_g, which largely accounts for the higher laser damage threshold for the fluoroaluminate glasses compared to ZBLAN at the Er:YAG laser wavelength of 2.94 μm.

The fabrication of HMFG fiber is similar to any glass fiber drawing technology except that the preforms are made using some type of melt-forming method rather than by a vapor deposition process as is common with silica fibers. Specifically, a casting method based on first forming a clad glass tube and then adding the molten core glass is used to form either multimode or single-mode fluorozirconate fiber preforms. The cladding tube is made either by a

TABLE 4 Fluorozirconate vs. Fluoroaluminate Glasses

Property	Fluorozirconate (ZBLAN)	Fluoroaluminate (AlF_3-ZrF_4-BaF_2-CaF_2-YF_3)
Glass transition temperature, °C	265	400
Durability	Medium	Excellent
Loss at 2.94 μm, dB/m	0.01	0.1
Er:YAG laser peak output energy, mJ	300 (300-μm core)	850 (500-μm core)

Comparison between fluorozirconate and fluoroaluminate glasses of some key properties that relate to laser power transmission and durability of the two HMFG fibers. Other physical properties are relatively similar.

rotational casting technique in which the tube is spun in a metal mold or by merely inverting and pouring out most of the molten cladding glass contained in a metal mold to form a tube.[14] The cladding tube is then filled with a higher-index core glass. Other preform fabrication techniques include rod-in-tube and crucible techniques. The fluoroaluminate fiber preforms have been made using an unusual extrusion technique in which core and cladding glass plates are extruded into a core-clad preform.[15] All methods, however, involve fabrication from the melted glass rather than from the more pristine technique of vapor deposition used to form SiO_2-based fibers. This process creates inherent problems such as the formation of bubbles, core-cladding interface irregularities, and small preform sizes. Most HMFG fiber drawing is done using preforms rather than the crucible method. A ZBLAN preform is drawn at about 310°C in a controlled atmosphere (to minimize contamination by moisture or oxygen impurities, which can significantly weaken the fiber) using a narrow heat zone compared to silica. Either ultraviolet (UV) acrylate or Teflon coatings are applied to the fiber. In the case of Teflon, heat-shrink Teflon (FEP) is generally applied to the glass preform prior to the draw.

The attenuation in HMFG fibers is predicted to be about 10 times less than that for silica fibers.[16] Based on extrapolations of the intrinsic losses resulting from Rayleigh scattering and multiphonon absorption, the minimum in the loss curves or V-curves is projected to be about 0.01 dB/km at 2.55 μm. Recent refinements of the scattering loss have modified this value slightly to be 0.024 dB/km, or about eight times less than that for silica fiber.[7] In practice, however, extrinsic loss mechanisms still dominate fiber loss. In Fig. 2, losses for two ZBLAN fibers are shown. The data from British Telecom (BTRL) represents state-of-the-art fiber 110 m in length.[7] The other curve is more typical of commercially available (Infrared Fiber Systems, Silver Spring, Maryland) ZBLAN fiber. The lowest measured loss for a BTRL 60-m-long fiber is 0.45 dB/km at 2.3 μm. Some of the extrinsic absorption bands that contribute to the total loss shown in Fig. 2 for the BTRL fiber are Ho^{3+} (0.64 and 1.95 μm), Nd^{3+} (0.74 and 0.81 μm), Cu^{2+} (0.97 μm), and OH^- (2.87 μm). Scattering centers such as crystals, oxides, and bubbles have also been found in the HMFG fibers. In their analysis of the data in Fig. 2, the BTRL group separated the total minimum attenuation coefficient (0.65 dB/km at 2.59 μm)

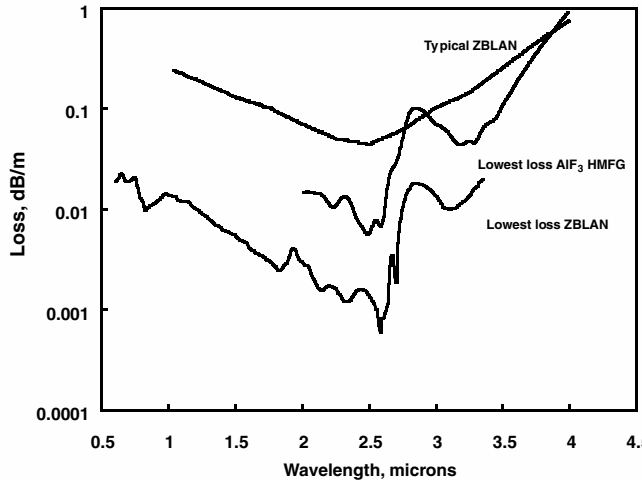

FIGURE 2 Losses in the best BTRL[7] and typical (Infrared Fiber Systems, Silver Spring, Maryland) ZBLAN fluoride glass fibers compared to those for fluoroaluminate glass fibers.[15]

into an absorptive loss component equal to 0.3 dB/km and a scattering loss component equal to 0.35 dB/km. The losses for the fluoroaluminate glass fibers are also shown for comparison in Fig. 2.[15] Clearly, the losses are not as low as for the BTRL-ZBLAN fiber, but the AlF_3-based fluoride fibers do have the advantage of higher glass transition temperatures and therefore are better candidates for laser power delivery.

The reliability of HMFG fibers depends on protecting the fiber from attack by moisture and on pretreatment of the preform to reduce surface crystallization. In general, the HMFGs are much less durable than oxide glasses. The leach rates for ZBLAN glass range between 10^{-3} and 10^{-2} g/cm^2/day. This is about five orders of magnitude higher than the leach rate for Pyrex glass. The fluoroaluminate glasses are more durable, with leach rates that are more than three times lower than those for the fluorozirconate glasses. The strength of HMFG fibers is less than that of silica fibers. From Table 2 we see that Young's modulus E for fluoride glass is 51 GPa compared to 73 GPa for silica glass. Taking the theoretical strength to be about one-fifth that of Young's modulus gives a theoretical value of strength of 11 GPa for fluoride glass. The largest bending strength measured has been about 1.4 Gpa, well below the theoretical value. To estimate the bending radius R, we may use the approximate expression $R = 1.198r(E/\sigma_{max})$, where σ_{max} is the maximum fracture stress and r is the fiber radius.[17]

Germanate Fibers

Heavy metal oxide glass fibers based on GeO_2 have recently shown great promise as an alternative to HMFG fibers for 3-μm laser power delivery.[18] Today, GeO_2-based glass fibers are composed of GeO_2 (30–76 percent)–RO (15–43 percent)–XO (3–20 percent), where R represents an alkaline earth metal and X represents an element of Group IIIA.[19] In addition, small amounts of heavy metal fluorides may be added to the oxide mixture. The oxide-only germanate glasses have glass transition temperatures as high as 680°C, excellent durability, and a relatively high refractive index of 1.84. In Fig. 3, loss data is given for a typical germanate glass fiber. While the losses are not as low as they are for the fluoride glasses shown in Fig. 2, these fibers have an exceptionally high damage threshold at 3 μm. Specifically, over 20 W (2 J at 10 Hz) of Er:YAG laser power has been launched into these fibers.

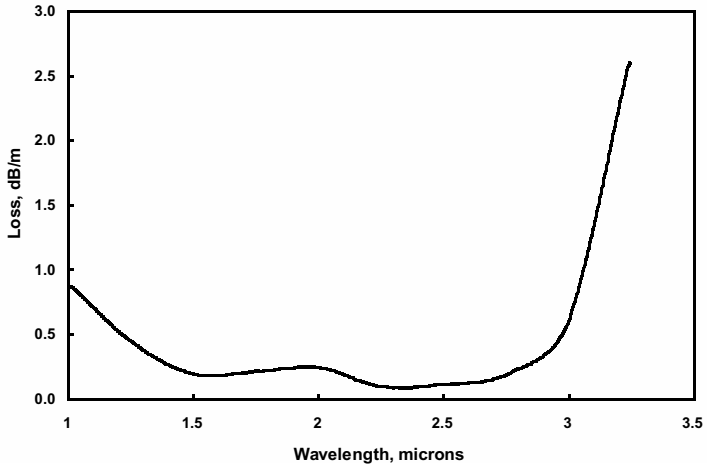

FIGURE 3 Germanate glass fiber manufactured by Infrared Fiber Systems, Silver Spring, Maryland.

Chalcogenide Fibers

Chalcogenide glass fibers were drawn into essentially the first IR fiber in the mid-1960s.[1] Chalcogenide fibers fall into three categories: sulfide, selenide, and telluride.[20] One or more chalcogen elements are mixed with one or more elements such as As, Ge, P, Sb, Ga, Al, Si, and so on to form a glass having two or more components. From the data in Table 2 we see that the glasses have low softening temperatures more comparable to those of fluoride glass than to those of oxide glasses. Chalcogenide glasses are very stable, durable, and insensitive to moisture. A distinctive difference between these glasses and the other IR fiber glasses is that they do not transmit well in the visible region and their refractive indices are quite high. Additionally, most of the chalcogenide glasses, except for As_2S_3, have a rather large value of dn/dT.[9] This fact limits the laser power handling capability of the fibers. In general, chalcogenide glass fibers have proven to be an excellent candidate for evanescent wave fiber sensors and for IR fiber image bundles.[21]

Chalcogenide glass is made by combining highly purified (>6 nines purity) raw elements in an ampoule that is heated in a rocking furnace for about 10 h. After melting and mixing, the glass is quenched and a glass preform is fabricated using rod-in-tube or rotational casting methods. Preform fiber draws involve drawing a core-clad preform or a core-only preform. For the core-only preform draw, either a soft chalcogenide cladding can be extruded over the fiber as it is drawn or the preform can be Teflon clad. Crucible drawing is also possible.

The losses for the most important chalcogenide fibers are given in Fig. 4. Arsenic trisulfide (As_2S_3) fiber, one of the simplest and oldest chalcogenide fibers, has a transmission range from 0.7 to about 6 μm.[20] This fiber is red in color and therefore transmits furthest into the visible region but cuts off in the long-wavelength end well before the heavier chalcogenide fibers.[9] Longer wavelengths are transmitted through the addition of heavier elements like Te, Ge, and Se, as shown in Fig. 4. A key feature of essentially all chalcogenide glasses is the strong extrinsic absorption resulting from the bonding of contaminants such as hydrogen, H_2O, and OH^- to the elemental cations. In particular, absorption peaks between 4.0 and 4.6 μm are due to S-H or Se-H bonds, and those at 2.78 and 6.3 μm are due to OH^- (2.78 μm) and/or molecular water. The hydride impurities are often especially strong and can be deleterious when these fibers are used in chemical sensing applications where the desired chemical signature falls in the region of extrinsic absorption. Another important feature of most of the chalcogenide fibers is that their

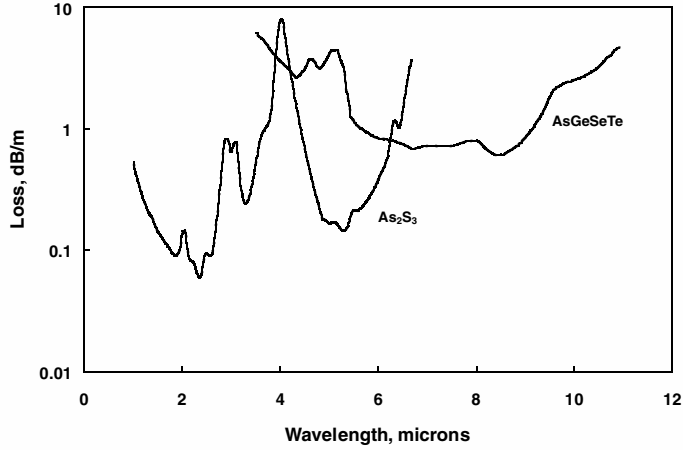

FIGURE 4 Two common chalcogenide glass fibers: As_2S_3 and an AsGeSeTe fiber.[9] Note the many impurity bands pervasive in these fiber systems.

losses are in general much higher than those of the fluoride glasses. In fact, at the important CO_2 laser wavelength of 10.6 μm, the lowest loss is still above 1 dB/m for the Se-based fibers.[20]

14.3 CRYSTALLINE FIBERS

Crystalline IR fibers are an attractive alternative to glass IR fibers because most nonoxide crystalline materials can transmit longer-wavelength radiation than IR glasses and, in the case of sapphire, exhibit some superior physical properties as well.[2] The disadvantage is that crystalline fibers are difficult to fabricate. There are two types of crystalline fiber: single-crystal (SC)[8] and polycrystalline (PC).[22,23] Historically, the first crystalline fiber made was hot-extruded KRS-5 fiber fabricated at Hughes Research Labs in 1975.[24] KRS-5 or TlBrI was chosen because it is very ductile and because it can transmit beyond the 20-μm range required for the intended military surveillance satellite application. In fact, crystalline fibers such as KRS-5 and other halide crystals were initially thought to hold great potential as next-generation ultra-low-loss fibers because their intrinsic loss was predicted to be as low as 10^{-3} dB/m.[24] Unfortunately, this loss was not only never achieved but not even approached experimentally.

PC Fibers

There are many halide crystals that have excellent IR transmission, but only a few have been fabricated into fiber optics. The technique used to make PC fibers is hot extrusion. As a result, only the silver and thallium halides have the requisite physical properties (such as ductility, low melting point, and independent slip systems) to be successfully extruded into fiber. In the hot extrusion process, a single-crystal billet or preform is placed in a heated chamber and the fiber is extruded to net shape through a diamond or tungsten carbide die at a temperature equal to about half the melting point. The final PC fibers are usually from 500 to 900 μm in diameter with no buffer jacket. The polycrystalline structure of the fiber consists of grains on the order of 10 μm or larger in size. The billet may be clad using the rod-in-tube method. In this method, a mixed silver halide such as AgBrCl is used as the core and then a lower-index tube is formed using a Cl^--rich AgBrCl crystal. The extrusion of a core-clad fiber is not as easy to achieve as it is in glass drawing, but Artjushenko et al.[10] at the General Physics Institute (GPI) in Moscow have achieved clad Ag halide fibers with losses nearly as low as those for the core-only Ag halide fiber. Today, the PC Ag halide fibers represent the best PC fibers. KRS-5 is no longer a viable candidate due largely to the toxicity of Tl and the greater flexibility of the Ag halide fibers.

The losses for the Ag halide fibers are shown in Fig. 5. Both the core-only and core-clad fibers are shown, and, as with the other IR fibers, we again see that there are several extrinsic absorption bands. Water is often present at 3 and 6.3 μm and there is sometimes an SO_4^{2-} absorption near 9.6 μm. Furthermore, we note the decreasing attenuation as the wavelength increases. This is a result of λ^{-2} scattering from strain-induced defects in the extruded fiber. An important feature of the data is that the loss at 10.6 μm can be as low as 0.2 dB/m for the core-only fiber and these fibers will transmit to almost 20 μm. These fibers have been used to transmit about 100 W of CO_2 laser power, but the safe limit seems to be 20 to 25 W.[25] This is due to the low melting point of the fibers.

There are several difficulties in handling and working with PC fibers. One is an unfortunate aging effect in which the fiber transmission is observed to decrease over time.[26] Normally the aging loss, which increases uniformly over the entire IR region, is a result of strain relaxation and possible grain growth as the fiber is stored. Another problem is that Ag halides are photosensitive; exposure to visible or UV radiation creates colloidal Ag, which in turn leads to increased losses in the IR. Finally, AgBrCl is corrosive to many metals. Therefore, the fibers should be packaged in dark jackets and connectorized with materials such as Ti, Au, or ceramics.

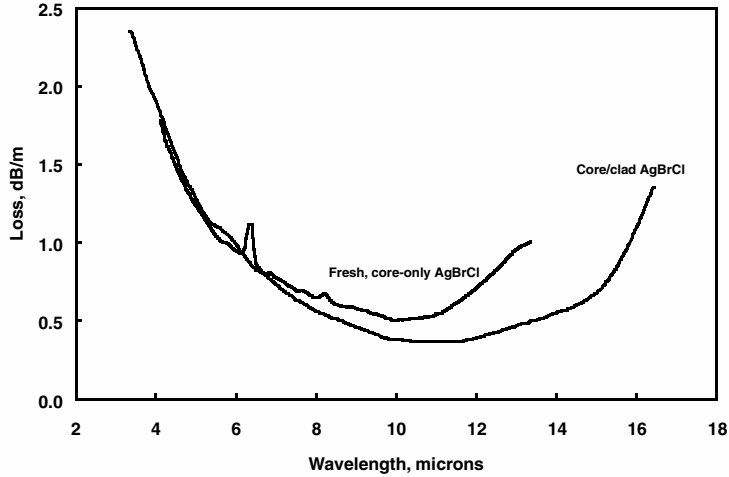

FIGURE 5 Losses in a typical PC silver halide fiber[22] compared to those in recently developed core-clad silver halide fiber.[10]

The mechanical properties of these ductile fibers are quite different from those of glass fibers. The fibers are weak, with ultimate tensile strengths of about 80 MPa for a 50-50 mixture of AgBrCl. However, the main difference between the PC and glass fibers is that the PC fibers plastically deform well before fracture. This plastic deformation leads to increased loss as a result of increased scattering from separated grain boundaries. Therefore, in use, the fibers should not be bent beyond their yield point; too much bending can lead to permanent damage and a region of high loss in the fiber.

SC Fibers

Meter-long lengths of SC fibers have been made from only a small number of the over 80 IR transmissive crystalline materials. Initially some SC fibers were grown by zone-refining methods from the same metal halides used to extrude PC fibers. The idea was that removal of the grain boundaries in the PC fibers would improve the optical properties of the fiber. This did not occur, so most of the crystalline materials chosen today for SC fiber fabrication have been oxides. Compared to halides, oxide materials like Al_2O_3 (sapphire) have the advantage of high melting points, chemical inertness, and the ability to be conveniently melted and grown in air. Currently, sapphire is the most popular SC fiber.[8,27,28]

Sapphire is an insoluble, uniaxial crystal (trigonal structure) with a melting point of over 2000°C. It is an extremely hard and robust material with a usable fiber transmission from about 0.5 to 3.2 μm. Other important physical properties shown in Table 2 include a refractive index equal to 1.75 at 3 μm, a thermal expansion about 10 times higher than that of silica, and a Young's modulus approximately six times greater than that of silica. These properties make sapphire an almost ideal IR fiber candidate for applications less than about 3.2 μm. In particular, this fiber has been used to deliver over 10 W of average power from an Er:YAG laser operating at 2.94 μm.[29]

Sapphire fibers are fabricated using either the edge-defined, film-fed growth (EFG) or the laser-heated pedestal growth (LHPG) techniques.[30] In either method, some or all of the

starting sapphire material is melted and an SC fiber is pulled from the melt. In the EFG method, a capillary tube is used to conduct the molten sapphire to a seed fiber, which is drawn slowly into a long fiber. Multiple capillary tubes, which also serve to define the shape and diameter of the fiber, may be placed in one crucible of molten sapphire so that many fibers can be drawn at one time. The LHPG process is a cruciibleless technique in which a small molten zone at the tip of an SC sapphire source rod (<2 mm diameter) is created using a CO_2 laser. A seed fiber slowly pulls the SC fiber as the source rod continuously moves into the molten zone to replenish the molten material. Both SC fiber growth methods are very slow (several millimeters per minute) compared to glass fiber drawing. The EFG method, however, has an advantage over LHPG methods because more than one fiber can be continuously pulled at a time. LHPG methods, however, have produced the cleanest and lowest-loss fibers owing to the fact that no crucible is used that can contaminate the fiber. The sapphire fibers grown by these techniques are unclad, pure Al_2O_3 with the *C*-axis usually aligned along the fiber axis. Fiber diameters range from 100 to 300 μm and lengths are generally less than 2 m. Postcladding techniques mostly involve a Teflon coating using heat-shrink tubing.

The optical properties of the as-grown sapphire fibers are normally inferior to those of the bulk starting material. This is particularly evident in the visible region and is a result of color-center-type defect formation during the fiber drawing. These defects and the resulting absorption can be greatly reduced if the fibers are postannealed in air or oxygen at about 1000°C. In Fig. 6, the losses for LHPG fiber grown at Rutgers University[8] and EFG fiber grown by Saphikon, Inc. (Milford, New Hampshire) are shown. Both fibers have been annealed at 1,000°C to reduce short-wavelength losses. We see that the LHPG fiber has the lowest overall loss. In particular, LHPG fiber loss at the important Er:YAG laser wavelength of 2.94 μm is less than 0.3 dB/m, compared to the intrinsic value of 0.15 dB/m. There are also several impurity absorptions beyond 3 μm that are believed to be due to transition metals like Ti or Fe. Sapphire fibers have been used at temperatures of up to 1400°C without any change in their transmission.

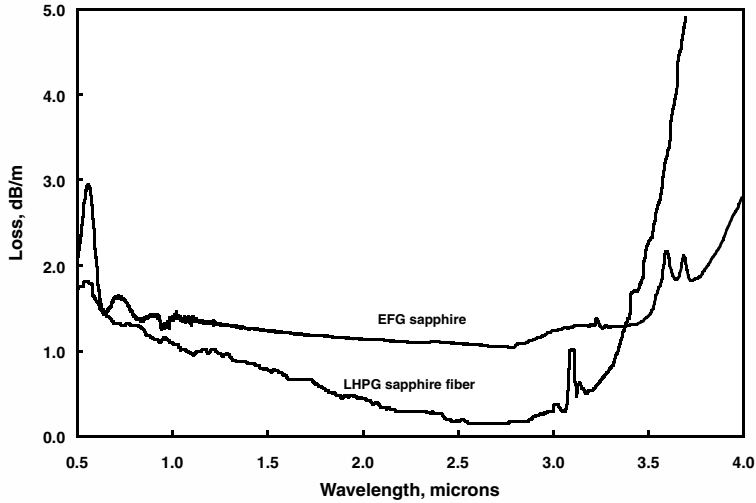

FIGURE 6 SC sapphire fibers grown by the EFG[30] (Saphikon, Inc., Milford, New Hampshire) and LHPG[29] methods.

14.4 HOLLOW WAVEGUIDES

The first optical-frequency hollow waveguides were similar in design to microwave guides. Garmire et al.[31] made a simple rectangular waveguide using aluminum strips spaced 0.5 mm apart by bronze shim stock. Even when the aluminum was not well polished, these guides worked surprisingly well. Losses at 10.6 μm were well below 1 dB/m, and Garmire early demonstrated the high power handling capability of an air-core guide by delivering over 1 kW of CO_2 laser power through this simple structure. These rectangular waveguides, however, never gained much popularity, primarily because their overall dimensions (about 0.5×10 mm) were quite large in comparison to circular-cross-section guides and also because the rectangular guides cannot be bent uniformly in any direction. As a result, hollow circular waveguides with diameters of 1 mm or less fabricated using metal, glass, or plastic tubing are the most common guides today. In general, hollow waveguides are an attractive alternative to conventional solid-core IR fibers for laser power delivery because of the inherent advantage of their air core. Hollow waveguides not only enjoy the advantage of high laser power thresholds but also low insertion loss, no end reflection, ruggedness, and small beam divergence. A disadvantage, however, is a loss on bending, which varies as $1/R$ where R is the bending radius. In addition, the losses for these guides vary as $1/a^3$ where a is the radius of the bore; therefore the loss can be arbitrarily small for a sufficiently large core. The bore size and bending radius dependence of all hollow waveguides are characteristics of these guides not shared by solid-core fibers. Initially these waveguides were developed for medical and industrial applications involving the delivery of CO_2 laser radiation, but more recently they have been used to transmit incoherent light for broadband spectroscopic and radiometric applications.[32–34] Today they are one of the best alternatives for power delivery in IR laser surgery and industrial laser delivery systems, with losses as low as 0.1 dB/m and transmitted CW laser powers as high as 2.7 kW.[35]

Hollow core waveguides may be grouped into two categories: (1) those whose inner core materials have refractive indices greater than 1 (leaky guides) and (2) those whose inner wall materials have refractive indexes less than 1 [attenuated total reflectance (ATR) guides]. Leaky or $n > 1$ guides have metallic and dielectric films deposited on the inside of metallic,[36] plastic,[37] or glass[11] tubing. ATR guides are made from dielectric materials with refractive indices of less than 1 in the wavelength region of interest.[38] Therefore, $n < 1$ guides are fiber-like in that the core index ($n \approx 1$) is greater than the clad index. Hollow sapphire fibers operating at 10.6 μm ($n = 0.67$) are an example of this class of hollow guide.[39]

Hollow Metal and Plastic Waveguides

The earliest circular-cross-section hollow guides were formed using metallic and plastic tubing as the structural members. Miyagi and colleagues in Japan used sputtering methods to deposit Ge,[40] ZnSe, and ZnS[36] coatings on aluminum mandrels. Then a final layer of Ni was electroplated over these coatings before the aluminum mandrel was removed by chemical leaching. The final structure was then a flexible Ni tube with optically thick dielectric layers on the inner wall to enhance the reflectivity in the infrared. Croitoru and colleagues[41] at Tel Aviv University applied Ag followed by AgI coatings on the inside of polyethylene and Teflon tubing to make a very flexible waveguide. Similar Ag and Ag halide coatings were deposited inside Ag tubes by Morrow and colleagues.[42]

Hollow Glass Waveguides

The most popular structure today is the hollow glass waveguide (HGW) developed initially at Rutgers University.[43] The advantage of glass tubing is that it is much smoother than either metal and plastic tubing and, therefore, the scattering losses are less. HGWs are fabricated

using wet chemistry methods to first deposit a layer of Ag on the inside of silica glass tubing and then to form a dielectric layer of AgI over the metallic film by converting some of the Ag to AgI. The silica tubing used has a polymer coating of UV acrylate or polyimide on the outside surface to preserve the mechanical strength. The thickness of the AgI is optimized to give high reflectivity at a particular laser wavelength or range of wavelengths. Using these techniques, HGWs have been fabricated with lengths as long as 13 m and bore sizes ranging from 250 to 1300 μm.

The spectral loss for an HGW with a 530-μm bore is given in Fig. 2. This HGW was designed for an optimal response at 10 μm. The peaks at about 3 and 5 μm are not absorption peaks but rather interference bands due to thin-film optical effects. For broadband applications and shorter-wavelength applications, a thinner AgI coating would be used to shift the interference peaks to shorter wavelengths. For such HGWs the optical response will be nearly flat without interference bands in the far IR fiber region of the spectrum. The data in Fig. 7 shows the straight loss measured using a CO_2 and Er:YAG laser for different bore sizes. An important feature of this data is the $1/a^3$ dependence of loss on bore size predicted by the theory of Marcatili and Schmeltzer.[44] In general, the losses are less than 0.5 dB/m at 10 μm for bore sizes larger than ~400 μm. Furthermore, the data at 10.6 μm agrees well with the calculated values, but at 3 μm the measured losses are somewhat above those predicted by Marcatili and Schmeltzer. This is a result of increased scattering at the shorter wavelengths from the metallic and dielectric films. The bending loss depends on many factors such as the quality of the films, the bore size, and the uniformity of the silica tubing. A typical bending loss curve for an HGW with a 530-μm bore measured with a CO_2 laser is given in Fig. 8. The losses are seen to increase linearly with increasing curvature as predicted. It is important to note that while there is an additional loss on bending for any hollow guide, it does not necessarily mean that this restricts the use of hollow guides in power delivery or sensor applications. Normally most fiber delivery systems have rather large bend radii and therefore a minimal amount of the guide is under tight bending conditions and the bending loss is low. From the

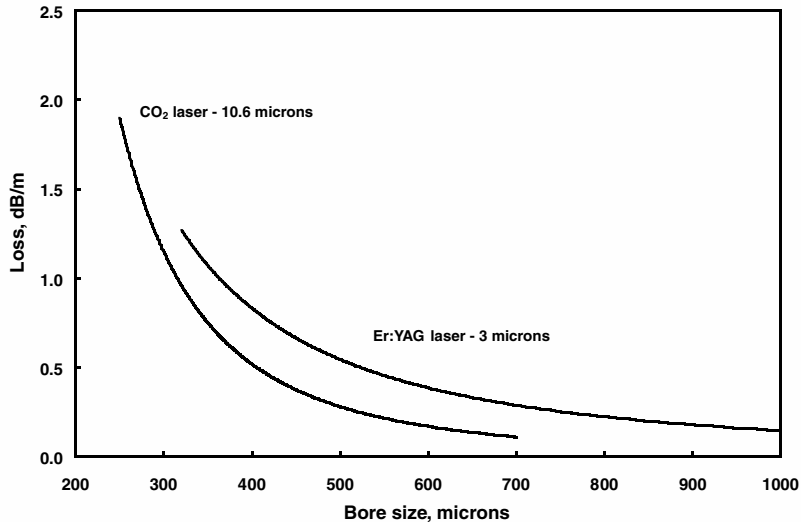

FIGURE 7 Straight losses measured in hollow glass waveguides with Ag/AgI films. The guide labeled "CO_2 laser" was designed for optimal transmission at 10.6 μm while that labeled "Er:YAG laser" was designed for optimal transmission at 3 μm. Note that the loss varies approximately as $1/a^3$.

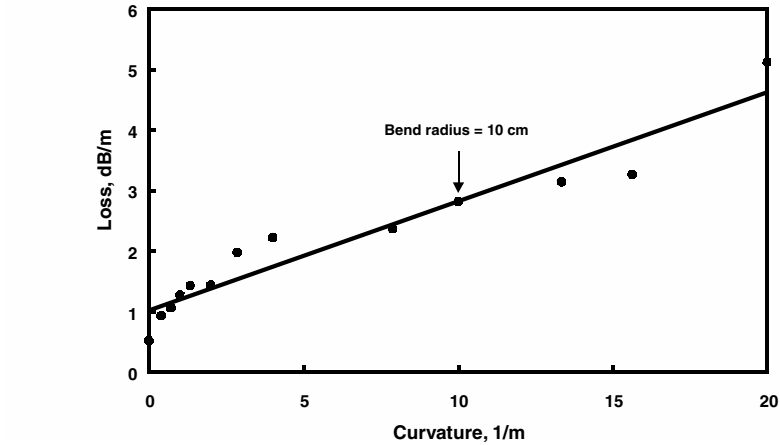

FIGURE 8 Additional loss on bending an HGW with a 530-μm bore, measured at 10.6 μm. The loss is seen to increase as the curvature increases.

data in Fig. 8 one can calculate the bending loss contribution for an HGW link by assuming some modest bends over a small section of guide length. An additional important feature of hollow waveguides is that they are nearly single mode. This is a result of the strong dependence of loss on the fiber mode parameter. That is, the loss of high-order modes increases as the square of the mode parameter, so even though the guides are very multimode, in practice only the lowest-order modes propagate. This is particularly true for the small-bore (<300 μm) guides, in which virtually only the lowest-order HE_{11} mode is propagated.

HGWs have been used quite successfully in IR laser power delivery and, more recently, in some sensor applications. Modest CO_2 and Er:YAG laser powers below about 80 W can be delivered without difficulty. At higher powers, water-cooling jackets have been placed around the guides to prevent laser damage. The highest CO_2 laser power delivered through a water-cooled hollow metallic waveguide with a bore of 1800 μm was 2700 W, and the highest power through a water-cooled HGW with a 700-μm bore was 1040 W.[45] Sensor applications include gas and temperature measurements. A coiled HGW filled with gas can be used in place of a more complex and costly White cell to provide an effective means for gas analysis. Unlike evanescent wave spectroscopy, in which light is coupled out of a solid-core-only fiber into media in contact with the core, all of the light is passing through the gas in the hollow guide cell, making this a sensitive, quick-response fiber sensor. Temperature measurements may be aided by using an HGW to transmit blackbody radiation from a remote site to an IR detector. Such an arrangement has been used to measure jet engine temperatures.

14.5 SUMMARY AND CONCLUSIONS

During the past 25 years of the development of IR fibers, there has been a great deal of fundamental research designed to produce a fiber with optical and mechanical properties close to those of silica. We can see that today we are still far from that Holy Grail, but some viable IR fibers have emerged that, as a class, can be used to address some of the needs for a fiber that can transmit greater than 2 μm. Yet we are still limited with the current IR fiber technology by high loss and low strength. Nevertheless, more applications are being found for IR

fibers as users become aware of their limitations and, more importantly, how to design around their properties.

There are two near-term applications of IR fibers: laser power delivery and sensors. An important future application for these fibers, however, may be more in active fiber systems like the Er- and Pr-doped fluoride fibers and emerging doped chalcogenide fibers. In regards to power delivery fibers, the best choice seems to be hollow waveguides for CO_2 lasers and SC sapphire, germanate glass, or HGWs for Er:YAG laser delivery. Chemical, temperature, and imaging bundles make use mostly of solid-core fibers. Evanescent wave spectroscopy (EWS) using chalcogenide and fluoride fibers is quite successful. A distinct advantage of an IR-fiber EWS sensor is that the signature of the analyte is often very strong in the infrared or fingerprint region of the spectrum. Temperature sensing generally involves the transmission of blackbody radiation. IR fibers can be very advantageous at low temperatures, especially near room temperature, where the peak in the blackbody radiation is near 10 μm. Finally, there is an emerging interest in IR imaging using coherent bundles of IR fibers. Several thousand chalcogenide fibers have been bundled by Amorphous Materials (Garland, Texas) to make an image bundle for the 3- to 10-μm region.

14.6 REFERENCES

1. N. S. Kapany and R. J. Simms, "Recent Developments of Infrared Fiber Optics," *Infrared Phys.* **5**:69 (1965).
2. J. A. Harrington, *Selected Papers on Infrared Fiber Optics,* Milestone Series, vol. MS-9, SPIE Press, Bellingham, Washington, 1990.
3. T. Katsuyama and H. Matsumura, *Infrared Optical Fibers,* Adam Hilger, Bristol, UK, 1989.
4. I. Aggarwal and G. Lu, *Fluoride Glass Optical Fiber,* Academic Press, San Diego, 1991.
5. P. France, M. G. Drexhage, J. M. Parker, M. W. Moore, S. F. Carter, and J. V. Wright, *Fluoride Glass Optical Fibers,* CRC Press, Boca Raton, Florida, 1990.
6. J. Sanghera and I. Aggarwal, *Infrared Fiber Optics,* CRC Press, Boca Raton, Florida, 1998.
7. S. F. Carter, M. W. Moore, D. Szebesta, D. Ransom, and P. W. France, "Low Loss Fluoride Fibre by Reduced Pressure Casting," *Electron. Lett.* **26**:2115–2117 (1990).
8. R. Nubling and J. A. Harrington, "Optical Properties of Single-Crystal Sapphire Fibers," *Appl. Opt.* **36**:5934–5940 (1997).
9. J. Nishii, S. Morimoto, I. Inagawa, R. Iizuka, T. Yamashita, and T. Yamagishi, "Recent Advances and Trends in Chalcogenide Glass Fiber Technology: A Review," *J. Non-Cryst. Sol.* **140**:199–208 (1992).
10. V. Artjushenko, V. Ionov, K. I. Kalaidjian, A. P. Kryukov, E. F. Kuzin, A. A. Lerman, A. S. Prokhorov, E. V. Stepanov, K. Bakhshpour, K. B. Moran, and W. Neuberger, "Infrared Fibers: Power Delivery and Medical Applications," *Proc. SPIE* **2396**:25–36 (1995).
11. Y. Matsuura, T. Abel, and J. A. Harrington, "Optical Properties of Small-Bore Hollow Glass Waveguides," *Appl. Opt.* **34**:6842–6847 (1995).
12. P. Kaiser, A. C. Hart Jr., and L. L. Blyler, "Low Loss FEP-clad Silica Fibers," *Appl. Opt.* **14**:156 (1975).
13. M. Poulain, M. Chanthanasinh, and J. Lucas, "New Fluoride Glasses," *Mat. Res. Bull.* **12**:151–156 (1977).
14. D. Tran, G. H. Sigel, and B. Bendow, "Heavy Metal Fluoride Glasses and Fibers: A Review," *J. Lightwave Technol.* **LT-2**:566–586 (1984).
15. K. Itoh, K. Miura, M. Masuda, M. Iwakura, and T. Yamagishi, "Low-Loss Fluorozirco-Aluminate Glass Fiber," in *Proceedings of 7th International Symposium on Halide Glass,* Center for Advanced Materials Technology, Monash University, Lorne, Australia, 1991, pp. 2.7–2.12.
16. P. W. France, S. F. Carter, M. W. Moore, and C. R. Day, "Progress in Fluoride Fibres for Optical Communications," *Brit. Telecom Tech. J.* **5**:28–44 (1987).
17. M. J. Matthewson, C. R. Kurkjian, and S. T. Gulati, "Strength Measurement of Optical Fibers by Bending," *J. Am. Cer. Soc.* **69**:815–821 (1986).

18. S. Kobayashi, N. Shibata, S. Shibata, and T. Izawa, "Characteristics of Optical Fibers in Infrared Wavelength Region," *Rev. Electrical Comm. Lab.* **26**:453–467, 1978.
19. D. Tran, Heavy Metal-Oxide Glass Optical Fibers for Use in Laser Medical Surgery, U.S. Patent 5,274,728, December 28, 1993.
20. Y. Kanamori, Y. Terunuma, and T. Miyashita, "Preparation of Chalcogenide Optical Fiber," *Rev. Electrical Comm. Lab.* **32**:469–477 (1984).
21. J. Nishii, T. Yamashita, T. Tamagishi, C. Tanaka, and H. Sone, "As_2S_3 Fibre for Infrared Image Bundle," *Int. J. Optoelectron.* **7**:209–216 (1992).
22. V. G. Artjushenko, L. N. Butvina, V. V. Vojtsekhovsky, E. M. Dianov, and J. G. Kolesnikov, "Mechanisms of Optical Losses in Polycrystalline KRS-5 Fibers," *J. Lightwave Technol.* **LT-4**:461–465 (1986).
23. A. Sa'ar, F. Moser, S. Akselrod, and A. Katzir, "Infrared Optical Properties of Polycrystalline Silver Halide Fibers," *Appl. Phys. Lett.* **49**:305–307 (1986).
24. D. A. Pinnow, A. L. Gentile, A. G. Standlee, A. J. Timper, and L. M. Hobrock, "Polycrystalline Fiber Optical Waveguides for Infrared Transmission," *Appl. Phys. Lett.* **33**:28–29 (1978).
25. K. Takahashi, N. Yoshida, and M. Yokota, "Optical Fibers for Transmitting High-power CO_2 Laser Beam," *Sumitomo Electric Tech. Rev.* **23**:203–210 (1984).
26. J. A. Wysocki, R. G. Wilson, A. G. Standlee, A. C. Pastor, R. N. Schwartz, A. R. Williams, G.-D. Lei, and L. Kevan, "Aging Effects in Bulk and Fiber TlBr-TlI," *J. Appl. Phys.* **63**:4365–4371 (1988).
27. D. H. Jundt, M. M. Fejer, and R. L. Byer, "Characterization of Single-Crystal Sapphire Fibers for Optical Power Delivery Systems," *Appl. Phys. Lett.* **55**:2170–2172 (1989).
28. R. S. F. Chang, V. Phomsakha, and N. Djeu, "Recent Advances in Sapphire Fibers," *Proc. SPIE* **2396**:48–53 (1995).
29. R. Nubling and J. A. Harrington, "Single-Crystal LHPG Sapphire Fibers for Er:YAG Laser Power Delivery," *Appl. Opt.* **37**:4777–4781 (1998).
30. H. E. LaBelle, "EFG, the Invention and Application to Sapphire Growth," *J. Cryst. Growth* **50**:8–17 (1980).
31. E. Garmire, T. McMahon, and M. Bass, "Flexible Infrared Waveguides for High-Power Transmission," *J. Quant. Elect.* **QE-16**:23–32 (1980).
32. S. J. Saggese, J. A. Harrington, and G. H. Sigel Jr., "Attenuation of Incoherent Infrared Radiation in Hollow Sapphire and Silica Waveguides," *Opt. Lett.* **16**:27–29 (1991).
33. M. Saito, Y. Matsuura, M. Kawamura, and M. Miyagi, "Bending Losses of Incoherent Light in Circular Hollow Waveguides," *J. Opt. Soc. Am. A* **7**:2063–2068 (1990).
34. M. Saito and K. Kikuchi, "Infrared Optical Fiber Sensors," *Opt. Rev.* **4**:527–538 (1997).
35. A. Hongo, K. Morosawa, K. Matsumoto, T. Shiota, and T. Hashimoto, "Transmission of Kilowatt-Class CO_2 Laser Light Through Dielectric-Coated Metallic Hollow Waveguides for Material Processing," *Appl. Opt.* **31**:5114–5120 (1992).
36. Y. Matsuura, M. Miyagi, and A. Hongo, "Fabrication of Low-Loss Zinc-Selenide Coated Silver Hollow Waveguides for CO_2 Laser Light," *J. Appl. Phys.* **68**:5463–5466 (1990).
37. M. Alaluf, J. Dror, R. Dahan, and N. Croitoru, "Plastic Hollow Fibers as a Selective Infrared Radiation Transmitting Medium," *J. Appl. Phys.* **72**:3878–3883 (1992).
38. C. C. Gregory and J. A. Harrington, "Attenuation, Modal, Polarization Properties of $n < 1$, Hollow Dielectric Waveguides," *Appl. Opt.* **32**:5302–5309 (1993).
39. J. A. Harrington and C. C. Gregory, "Hollow Sapphire Fibers for the Delivery of CO_2 Laser Energy," *Opt. Lett.* **15**:541–543 (1990).
40. M. Miyagi, Y. Shimada, A. Hongo, K. Sakamoto, and S. Nishida, "Fabrication and Transmission Properties of Electrically Deposited Germanium-Coated Waveguides for Infrared Radiation," *J. Appl. Phys.* **60**:454–456 (1986).
41. O. Morhaim, D. Mendlovic, I. Gannot, J. Dror, and N. Croitoru, "Ray Model for Transmission of Infrared Radiation Through Multibent Cylindrical Waveguides," *Opt. Eng.* **30**:1886–1891 (1991).
42. P. Bhardwaj, O. J. Gregory, C. Morrow, G. Gu, and K. Burbank, "Performance of a Dielectric-Coated Monolithic Hollow Metallic Waveguide," *Mat. Lett.* **16**:150–156 (1993).

43. T. Abel, J. Hirsch, and J. A. Harrington, "Hollow Glass Waveguides for Broadband Infrared Transmission," *Opt. Lett.* **19**:1034–1036 (1994).
44. E. A. J. Marcatili and R. A. Schmeltzer, "Hollow Metallic and Dielectric Waveguides for Long Distance Optical Transmission and Lasers," *Bell Syst. Tech. J.* **43**:1783–1809 (1964).
45. R. K. Nubling and J. A. Harrington, "Hollow-Waveguide Delivery Systems for High-Power, Industrial CO_2 Lasers," *Appl. Opt.* **34**:372–380 (1996).

CHAPTER 15
OPTICAL FIBER SENSORS

Richard O. Claus
Virginia Tech
Blacksburg, Virginia

Ignacio Matias and Francisco Arregui
Public University Navarra
Pamplona, Spain

15.1 INTRODUCTION

Optical fiber sensors are a broad topic. The objective of this chapter is to briefly summarize the fundamental properties of representative types of optical fiber sensors and how they operate. Four different types of sensors are evaluated systematically on the basis of performance criteria such as resolution, dynamic range, cross-sensitivity to multiple ambient perturbations, fabrication, and demodulation processes. The optical fiber sensing methods that will be investigated include well-established technologies such as fiber Bragg grating (FBG)–based sensors, and rapidly evolving measurement techniques such as those involving long-period gratings (LPGs). Additionally, two popular versions of Fabry-Perot interferometric sensors (intrinsic and extrinsic) are evaluated.

The outline of this chapter is as follows. The principles of operation and fabrication processes of each of the four sensors are discussed separately. The sensitivity of the sensors to displacement and simultaneous perturbations such as temperature is analyzed. The overall complexity and performance of a sensing technique depends heavily on the signal demodulation process. Thus, the detection schemes for all four sensors are discussed and compared on the basis of their complexity. Finally, a theoretical analysis of the cross-sensitivities of the four sensing schemes is presented and their performance is compared.

Measurements of a wide range of physical measurands by optical fiber sensors have been investigated for more than 20 years. Displacement measurements using optical fiber sensors are typical of these, and both embedded and surface-mounted configurations have been reported by researchers in the past.[1] Fiber-optic sensors are small in size, are immune to electromagnetic interference, and can be easily integrated with existing optical fiber communication links. Such sensors can typically be easily multiplexed, resulting in distributed networks that can be used for health monitoring of integrated, high-performance materials and structures.

Optical fiber sensors of displacement are perhaps the most basic of all fiber sensor types because they may be configured to measure many other related environmental factors. They

Copyright 2001 by The McGraw-Hill Companies, Inc. Click Here for Terms of Use.

should possess certain important characteristics. First, they should either be insensitive to ambient fluctuations in temperature and pressure or should employ demodulation techniques that compensate for changes in the output signal due to these additional perturbations. In an embedded configuration, the sensors for axial strain measurements should have minimum cross-sensitivity to other strain states. The sensor signal should itself be simple and easy to demodulate. Nonlinearities in the output require expensive decoding procedures or necessitate pre-calibration and sensor-to-sensor incompatibility. The sensor should ideally provide an absolute and real-time displacement or strain measurement in a form that can be easily processed. For environments where large strain magnitudes are expected, the sensor should have a large dynamic range while at the same time maintaining the desired sensitivity. We now discuss each of the four sensing schemes individually and present their relative advantages and shortcomings.

15.2 EXTRINSIC FABRY-PEROT INTERFEROMETRIC SENSORS

The extrinsic Fabry-Perot interferometric (EFPI) sensor, proposed by a number of groups and authors, is one of the most popular fiber-optic sensors used for applications in health monitoring of smart materials and structures.[3] As the name suggests, the EFPI is an interferometric sensor in which the detected intensity is modulated by the parameter under measurement. The simplest configuration of an EFPI is shown in Fig. 1.

The EFPI system consists of a single-mode laser diode that illuminates a Fabry-Perot cavity through a fused biconical tapered coupler. The cavity is formed between an input single-mode fiber and a reflecting target element that may be a fiber. Since the cavity is external to the lead-in/lead-out fiber, the EFPI sensor is independent of transverse strain and small ambient temperature fluctuations. The input fiber and the reflecting fiber are typically aligned using a hollow core tube as shown in Fig. 10. For optical fibers with uncoated ends, Fresnel reflection of approximately 4 percent results at the glass-to-air and air-to-glass interfaces that

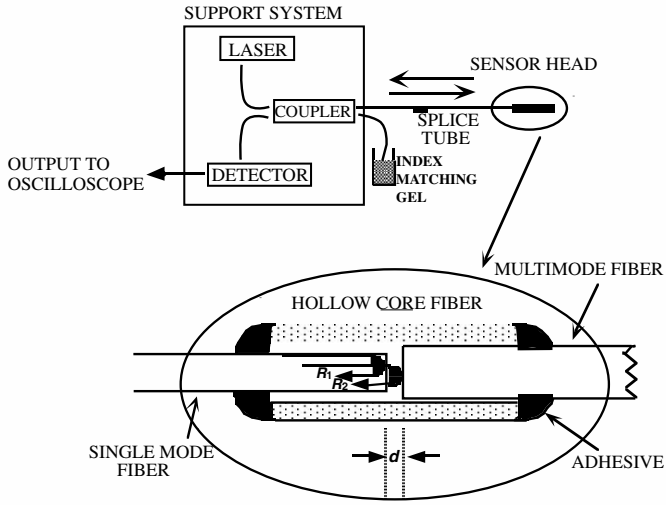

FIGURE 1 Extrinsic Fabry-Perot interferometric (EFPI) sensor and system.

define the cavity. The first reflection at the glass-air interface R_1, called the *reference reflection,* is independent of the applied perturbation. The second reflection at the air-glass interface R_2, termed the *sensing reflection,* is dependent on the length of the cavity *d,* which in turn is modulated by the applied perturbation. These two reflections interfere (provided $2d < L_c$, the coherence length of the light source) and the intensity I at the detector varies as a function of the cavity length,

$$I = I_0 \cos\left(\frac{4\pi}{\lambda} d\right) \tag{1}$$

where I_0 is the maximum value of the output intensity and λ is the center wavelength of the light source, here assumed to be a laser diode.

The typical intensity-versus-displacement transfer function curve [Eq.(1)] for an EFPI sensor is shown in Fig. 2. Small perturbations that result in operation around the quiescent or Q point of the sensor lead to an approximately linear variation in output intensity versus applied displacement. For larger displacements, the output signal is not a linear function of the input signal, and the output signal may vary over several sinusoidal periods. In this case, a *fringe* in the output signal is defined as the change in intensity from a maximum to a maximum, or from a minimum to a minimum, so each fringe corresponds to a change in the cavity length by half of the operating wavelength λ. The change in the cavity length Δd is then employed to calculate the strain using the expression

$$\varepsilon = \frac{\Delta d}{L} \tag{2}$$

where L is defined as the gauge length of the sensor and is typically the distance between two points where the input and reflecting fibers are bonded to the hollow-core support tube.

The EFPI sensor has been used for the analysis of materials and structures.[1,3] The relatively low temperature sensitivity of the sensor element, due to the opposite directional expansion of the fiber and tube elements, makes it attractive for the measurement of strain and displacement in environments where the temperature is not anticipated to change over a wide range.

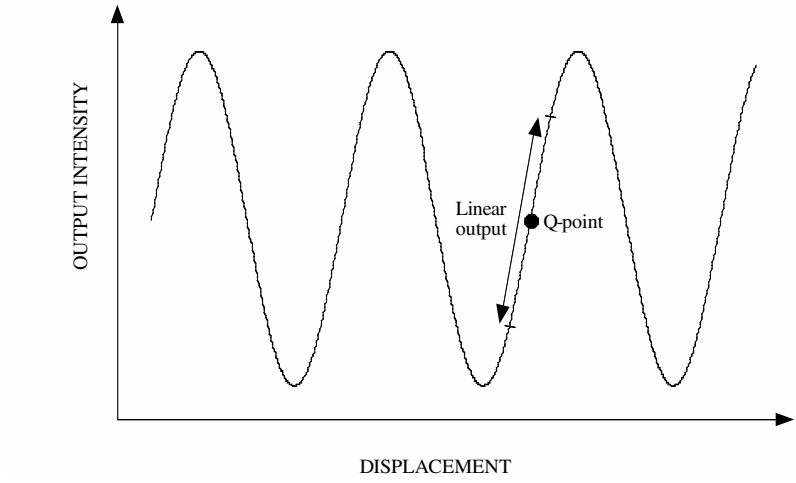

FIGURE 2 EFPI transfer function curve.

The EFPI sensor is capable of measuring subangstrom displacements with strain resolution better than 1 με and a dynamic range greater than 10,000 με. Moreover, the large bandwidth simplifies the measurement of highly cyclical strain. The sensor also allows single-ended operation and is hence suitable for applications where ingress to and egress from the sensor location are important. The sensor requires simple and inexpensive fabrication equipment and an assembly time of a few minutes. Additionally, since the cavity is external to the fibers, transverse strain components that tend to influence the response of similar intrinsic sensors through Poisson-effect cross-coupling have negligible effect on the EFPI sensor output.

15.3 INTRINSIC FABRY-PEROT INTERFEROMETRIC SENSORS

The intrinsic Fabry-Perot interferometric (IFPI) sensor is similar in operation to its extrinsic counterpart, but significant differences exist in the configurations of the two sensors.[4] The basic IFPI sensor is shown in Fig. 3. An optically isolated laser diode is used as the optical source to one of the input arms of a bidirectional 2×2 coupler. The Fabry-Perot cavity is formed internally by fusing a small length of single-mode fiber to one of the output legs of the coupler. As shown in Fig. 3, the reference (R) and sensing (S) reflections interfere at the detector to again provide a sinusoidal intensity variation versus cavity path length modulation. The cavity can also be implemented by introducing two Fresnel or other reflectors along the length of a single fiber. The photosensitivity effect in germanosilicate fibers has been used in the past to fabricate broadband grating-based reflector elements to define such an IFPI cavity.[5] Since the cavity is formed within an optical fiber, changes in the refractive index of the fiber due to the applied perturbation can significantly alter the phase of the sensing signal S. Thus the intrinsic cavity results in the sensor being sensitive to ambient temperature fluctuations and all states of strain.

The IFPI sensor, like all other interferometric signals, has a nonlinear output that complicates the measurement of large-magnitude strain. This can again be overcome by operating the sensor in the linear regime around the Q point of the sinusoidal transfer function curve. The main limitation of the IFPI strain sensor is that the photoelastic-effect-induced change in index of refraction results in a nonlinear relationship between the applied perturbation and the change in cavity length. For most IFPI sensors, the change in the propagation constant of the fundamental mode dominates the change in cavity length. Thus IFPIs are highly susceptible to temperature changes and transverse strain components.[6] In embedded applications, the sensitivity to all of the strain components can result in complex signal output. The process of fabricating an IFPI strain sensor is more complicated than that for the EFPI sensor since the sensing cavity of the IFPI sensor must be formed within the optical fiber by some special procedure. The strain resolution of IFPI sensors is approximately 1 με with an operating range

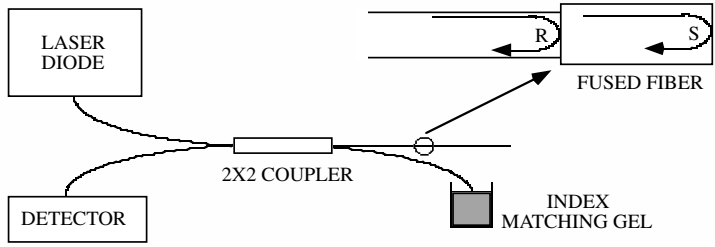

FIGURE 3 The intrinsic Fabry-Perot interferometric (IFPI) sensor.

greater than 10,000 με. IFPI sensors also suffer from drift in the output signal due to variations in the polarization state of the input light.

Thus the preliminary analysis shows that the extrinsic version of the Fabry-Perot optical fiber sensor seems to have an overall advantage over its intrinsic counterpart. The extrinsic sensor has negligible cross-sensitivity to temperature and transverse strain. Although the strain sensitivities, dynamic ranges, and bandwidths of the two sensors are comparable, the IFPIs can be expensive and cumbersome to fabricate due to the intrinsic nature of the sensing cavity.

The extrinsic and intrinsic Fabry-Perot interferometric sensors possess nonlinear sinusoidal outputs that complicate signal processing at the detector. Although intensity-based sensors have a simple output variation, they suffer from limited sensitivity to strain or other perturbations of interest. Grating-based sensors have recently become popular as transducers that provide wavelength-encoded output signals that can typically be easily demodulated to derive information about the perturbation under investigation. We next discuss the advantages and drawbacks of Bragg grating sensing technology. The basic operating mechanism of Bragg grating-based strain sensors is then reviewed and the expressions for strain resolution are obtained. These sensors are then compared to the recently developed long-period grating devices in terms of fabrication process, cross-sensitivity to multiple measurands, and simplicity of signal demodulation.

15.4 FIBER BRAGG GRATING SENSORS

The phenomenon of photosensitivity was discovered by Hill and coworkers in 1978.[7] It was found that permanent refractive index changes could be induced in optical fibers by exposing the germanium-doped core of a fiber to intense light at 488 or 514 nm. Hill found that a sinusoidal modulation of index of refraction in the core created by the spatial variation of such an index-modifying beam gives rise to refractive index grating that can be used to couple the energy in the fundamental guided mode to various guided and lossy modes. Later Meltz et al.[8] suggested that photosensitivity is more efficient if the fiber is side-exposed to a writing beam at wavelengths close to the absorption wavelength (242 nm) of the germanium defects in the fiber. The side-writing process simplified the fabrication of Bragg gratings, and these devices have recently emerged as highly versatile components for optical fiber communication and sensing systems. Recently, loading of the fibers with hydrogen prior to writing has been used to produce order-of-magnitude larger changes in index in germanosilicate fibers.[9]

Principle of Operation

Bragg gratings in optical fibers are based on a phase-matching condition between propagating optical modes. This phase-matching condition is given by

$$k_g + k_c = k_B \tag{3}$$

where k_g, k_c, and k_B are, respectively, the wave vectors of the coupled guided mode, the resulting coupling mode, and the grating. For a first-order interaction, $k_B = 2\pi/\Lambda$, where Λ is the spatial period of the grating. In terms of propagation constants, this condition reduces to the general form of interaction for mode coupling due to a periodic perturbation

$$\Delta\beta = \frac{2\pi}{\Lambda} \tag{4}$$

where $\Delta\beta$ is the difference in the propagation constants of the two modes involved in mode coupling, where both modes are assumed to travel in the same direction.

Fiber Bragg gratings (FBGs) involve the coupling of the forward-propagating fundamental LP_{01} in a single-mode fiber to the reverse-propagating LP_{01} mode.[10] Here, consider a single-mode fiber with β_{01} and $-\beta_{01}$ as the propagation constants of the forward- and reverse-propagating fundamental LP_{01} modes. To satisfy the phase-matching condition,

$$\Delta\beta = \beta_{01} - (-\beta_{01}) = \frac{2\pi}{\Lambda} \tag{5}$$

where $\beta_{01} = 2\pi n_{\text{eff}}/\lambda$, n_{eff} is the effective index of the fundamental mode, and λ is the free-space wavelength of the source. Equation (5) reduces to[10]

$$\lambda_B = 2\Lambda n_{\text{eff}} \tag{6}$$

where λ_B is termed the *Bragg wavelength*—the wavelength at which the forward-propagating LP_{01} mode couples to the reverse-propagating LP_{01} mode. Such coupling is wavelength dependent, since the propagation constants of the two modes are a function of the wavelength. Hence, if an FBG element is interrogated using a broadband optical source, the wavelength at which phase matching occurs is back-reflected. This back-reflected wavelength is a function of the grating period Λ and the effective index n_{eff} of the fundamental mode as shown in Eq. (6). Since strain and temperature effects can modulate both of these parameters, the Bragg wavelength is modulated by both of these external perturbations. The resulting spectral shifts are utilized to implement FBGs for sensing applications.

Figure 4 shows the mode-coupling mechanism in fiber Bragg gratings using a β-plot. Since the difference in propagation constants ($\Delta\beta$) between the modes involved in coupling is large, we see from Eq. (4) that only a small period, Λ, is needed to induce this mode coupling. Typically for optical fiber communication system applications the value of λ_B is approximately 1.5 μm. From Eq. (6), Λ is thus approximately 0.5 μm for $n_{\text{eff}} = 1.5$, the approximate index of refraction of the glass in a fiber. Due to the small period, on the order of 1 μm, FBGs are typically classified as short-period gratings (SPGs).

Bragg Grating Sensor Fabrication

Fiber Bragg gratings have commonly been manufactured using two side-exposure techniques, namely *interferometric* and *phase mask* methods. The interferometric method, shown in Fig. 5, uses an ultraviolet (UV) writing beam at 244 or 248 nm, split into two parts of approximately the same intensity by a beam splitter.[8] The two beams are focused on a portion of the Ge-doped fiber, whose protective coating has been removed using cylindrical lenses. The period of the resulting interference pattern, and hence the period of the Bragg grating element to be written, is varied by altering the mutual angle θ. A limitation of this method is that any relative vibration of the pairs of mirrors and lenses can lead to the degradation of the

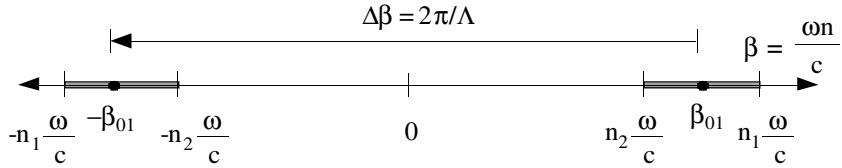

FIGURE 4 Mode-coupling mechanism in fiber Bragg gratings. The large value of $\Delta\beta$ in FBGs requires a small value of the grating periodicity Λ. The hatched regions represent the guided modes in the forward ($\beta > 0$) and reverse ($\beta > 0$) directions.

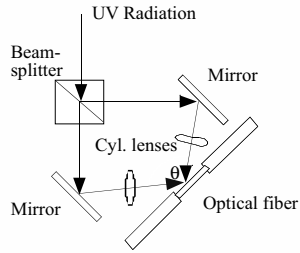

FIGURE 5 Fabrication of Bragg gratings using interferometric scheme.

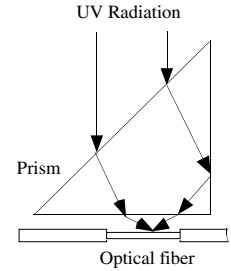

FIGURE 6 Bragg grating fabrication using prism method.

quality of the fringe pattern and the fabricated grating; thus the entire system has a stringent stability requirement. To overcome this drawback, Kashyap[10] proposed a novel interferometer technique in which the path difference between the interfering UV beams is produced by propagation through a right-angled prism, as shown in Fig. 6. This geometry is inherently stable because both beams are perturbed similarly by any prism vibration.

The phase mask technique has gained popularity as an efficient holographic side-writing procedure for grating fabrication.[11] In this method, shown in Fig. 7, an incident UV beam is diffracted into –1, 0, and +1 orders by a relief grating typically generated on a silica plate by electron beam exposure and plasma etching. The two first diffraction orders undergo total internal reflection at the glass-air interface of a rectangular prism and interfere at the location of the fiber placed directly behind the mask. This technique is wavelength specific, since the period of the resulting two-beam interference pattern is uniquely determined by the diffraction angle of –1 and +1 orders and thus the properties of the phase mask. Obviously, different phase masks are required for the fabrication of gratings at different Bragg wavelengths. A setup for actively monitoring the growth of a grating in the transmission mode during fabrication is shown in Fig. 8.

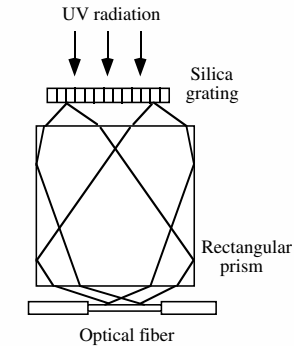

FIGURE 7 Phase mask method of fabricating Bragg gratings.

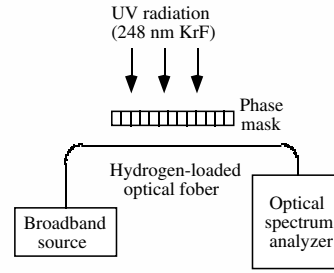

FIGURE 8 Setup to write Bragg gratings in germanosilicate fibers.

Bragg Grating Sensors

From Eq. (6) we see that a change in the value of n_{eff} and/or Λ can cause the Bragg wavelength λ to shift. This fractional change in the resonance wavelength $\Delta\lambda/\lambda$ is given by

$$\frac{\Delta\lambda}{\lambda} = \frac{\Delta\Lambda}{\Lambda} + \frac{\Delta n_{\text{eff}}}{n_{\text{eff}}} \tag{7}$$

where $\Delta\Lambda/\Lambda$ and $\Delta n_{\text{eff}}/n_{\text{eff}}$ are the fractional changes in the period and the effective index, respectively. The relative magnitudes of the two changes depend on the type of perturbation to which the grating is subjected. For most applications the effect due to change in effective index is the dominating mechanism.

An axial strain ε in the grating changes the grating period and the effective index and results in a shift in the Bragg wavelength, given by

$$\frac{1}{\lambda}\frac{\Delta\lambda}{\varepsilon} = \frac{1}{\Lambda}\frac{\Delta\Lambda}{\varepsilon} + \frac{1}{n_{\text{eff}}}\frac{\Delta n_{\text{eff}}}{\varepsilon} \tag{8}$$

The first term on the right side of Eq. (8) is unity, while the second term has its origin in the photoelastic effect. An axial strain in the fiber serves to change the refractive index of both the core and the cladding. This results in a variation in the value of the effective index of glass. The photoelastic or strain-optic coefficient is approximately –0.27. Thus, the variations in n_{eff} and Λ due to strain have contrasting effects on the Bragg peak. The fractional change in the Bragg wavelength due to axial strain is 0.73ε, or 73 percent of the applied strain. At 1550 and 1300 nm, the shifts in the resonance wavelength are 11 nm/%ε and 9 nm/%ε, respectively. An FBG at 1500 nm shifts by 1.6 nm for every 100°C rise in temperature.[7]

Limitations of Bragg Grating Strain Sensors

The primary limitation of Bragg grating sensors is the complex and expensive fabrication technique. Although side-writing is commonly being used to manufacture these gratings, the requirement of expensive phase masks increases the cost of the sensing system. In the interferometric technique, stability of the setup is a critical factor in obtaining high-quality gratings. Since index changes of the order of 10^{-3} are required to fabricate these gratings, laser pulses of high energy levels are necessary.

The second primary limitation of Bragg gratings is their limited bandwidth. The typical value of the full width at half-maximum (FWHM) is between 0.1 and 1 nm. Although higher bandwidths can be obtained by chirping the index or period along the grating length, this adds to the cost of the grating fabrication. The limited bandwidth requires high-resolution spectrum analysis to monitor the grating spectrum. Kersey and Berkoff[12] have proposed an unbalanced Mach-Zender interferometer to detect the perturbation-induced wavelength shift. Two unequal arms of the Mach-Zender interferometer are excited by the back reflection from a Bragg grating sensor element. Any change in the input optical wavelength modulates the phase difference between the two arms and results in a time-varying sinusoidal intensity at the output. This interference signal can be related to the shift in the Bragg peak and the magnitude of the perturbation can be obtained. Recently, modal interferometers have also been proposed to demodulate the output of a Bragg grating sensor.[13] The unbalanced interferometers are also susceptible to external perturbations and hence need to be isolated from the parameter under investigation. Moreover, the nonlinear output may require fringe counting, which can be complicated and expensive. Additionally, a change in the perturbation polarity at the maxima or minima of the transfer function curve will not be detected by this demodulation scheme. To overcome this limitation, two unbalanced interferometers may be employed for dynamic measurements.

Cross-sensitivity to temperature leads to erroneous displacement measurements in applications where the ambient temperature has a temporal variation. So a reference grating used to measure temperature change may be utilized to compensate for the output of the strain sensor. Recently, temperature-independent sensing has been demonstrated using chirped gratings written in tapered optical fibers.[14]

Finally, the sensitivity of fiber Bragg grating strain sensors may not be adequate for certain applications. This sensitivity of the sensor depends on the minimum detectable wavelength shift at the receiver. Although excellent wavelength resolution can be obtained with unbalanced interferometric detection techniques, standard spectrum analysis systems typically provide a resolution of 0.1 nm. At 1300 nm, this minimum detectable change in wavelength corresponds to a strain resolution of 111 με. Hence, in applications where strains smaller than 100 με are anticipated, Bragg grating sensors may not be practical. The dynamic range of strain measurement can be as much as 15,000 με.

15.5 LONG-PERIOD GRATING SENSORS

This section discusses the use of novel long-period gratings (LPGs) as displacement-sensing devices. We analyze the principle of operation of these gratings, their fabrication process, typical experimental evaluation, their demodulation process, and their cross-sensitivity to ambient temperature.

Principle of Operation

Long-period gratings that couple the fundamental guided mode to different guided modes have been demonstrated.[15,16] Gratings with longer periodicities that involve coupling of a guided mode to forward-propagating cladding modes were recently proposed by Vengsarkar et al.[17,18] As discussed previously, fiber gratings satisfy the Bragg phase-matching condition between the guided and cladding or radiation modes or another guided mode. This wavelength-dependent phase-matching condition is given by

$$\beta_{01} - \beta = \Delta\beta = \frac{2\pi}{\Lambda} \tag{9}$$

where Λ is the period of the grating and β_{01} and β are the propagation constant of the fundamental guided mode and the mode to which coupling occurs, respectively.

For conventional fiber Bragg gratings, the coupling of the forward-propagating LP_{01} mode occurs to the reverse-propagating LP_{01} mode ($\beta = -\beta_{01}$). Since $\Delta\beta$ is large in this case, as shown in Fig. 9*a,* the grating periodicity is small, typically on the order of 1 μm. Unblazed long-period gratings couple the fundamental mode to the discrete and circularly symmetric, forward-propagating cladding modes ($\beta = \beta^n$), resulting in smaller values of $\Delta\beta$, as shown in Fig. 9*b,* and hence periodicities ranging in the hundreds of micrometers.[17] The cladding modes attenuate rapidly as they propagate along the length of the fiber, due to the lossy cladding-coating interface and bends in the fiber. Since $\Delta\beta$ is discrete and a function of the wavelength, this coupling to the cladding modes is highly selective, leading to a wavelength-dependent loss. As a result, any modulation of the core and cladding guiding properties modifies the spectral response of long-period gratings, and this phenomenon can be utilized for sensing purposes. Moreover, since the cladding modes interact with the fiber jacket or any other material surrounding the cladding, changes in the index of refraction or other properties of these effective coatings materials can also be detected.

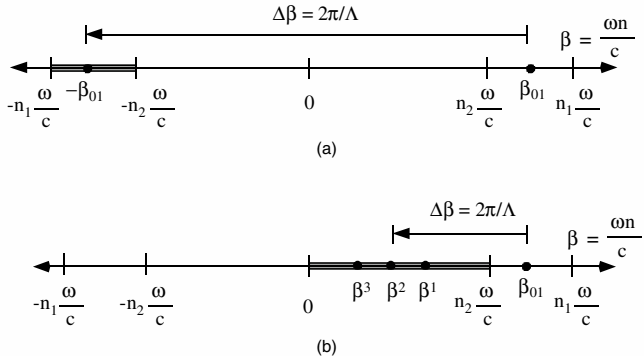

FIGURE 9 Depiction of mode coupling in (*a*) Bragg gratings and (*b*) long-period gratings. The differential propagation constant $\Delta\beta$ determines the grating periodicity.

LPG Fabrication Procedure

To fabricate long-period gratings, hydrogen-loaded (3.4 mole%), germanosilicate fibers may be exposed to 248-nm UV radiation from a KrF excimer laser through a chrome-plated amplitude mask possessing a periodic rectangular transmittance function. Figure 10 shows a typical setup used to fabricate such gratings. The laser is pulsed at approximately 20 Hz with a pulse duration of several nanoseconds. The typical writing times for an energy of 100 mJ/cm^2/pulse and a 2.5-cm exposed length vary between 6 and 15 min for different fibers. The coupling wavelength λ_p shifts to higher values during exposure due to the photoinduced enhancement of the refractive index of the fiber core and the resulting increase in β_{01}. After writing, the gratings are annealed at 150°C for several hours to remove the unreacted hydrogen. This high-temperature annealing causes λ_p to move to shorter wavelengths due to the decay of UV-induced defects and the diffusion of molecular hydrogen from the fiber. Figure 11 depicts the typical transmittance of a grating. Various attenuation bands correspond to coupling to discrete cladding modes of different orders. A number of gratings can be fabricated at the same time by placing more than one fiber behind the amplitude mask. Due to the relatively long spatial periods, the stability requirements during the writing process are not so severe as those for short-period Bragg gratings.

For coupling to the highest-order cladding mode, the maximum isolation (loss in transmission intensity) is typically in the 5- to 20-dB range on wavelengths depending on fiber param-

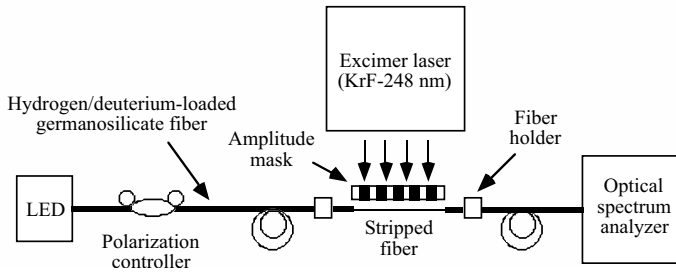

FIGURE 10 Setup to fabricate long-period gratings using an amplitude mask.

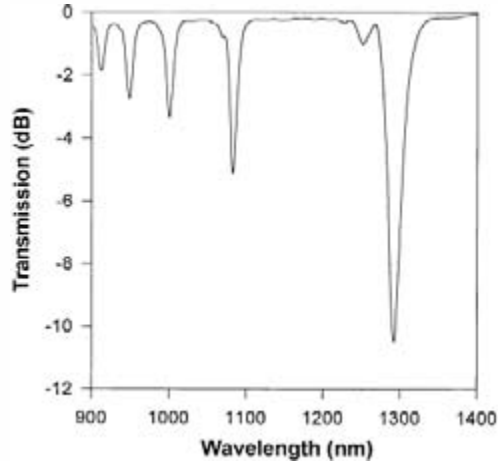

FIGURE 11 Transmission spectrum of a long-period grating written in Corning FLEXCOR fiber with period $\Lambda = 198$ μm. The discrete, spiky loss bands correspond to the coupling of the fundamental guided mode to discrete cladding modes.

eters, duration of UV exposure, and mask periodicity. The desired fundamental coupling wavelength can easily be varied by using inexpensive amplitude masks of different periodicities. The insertion loss, polarization mode dispersion, backreflection, and polarization-dependent loss of a typical grating are 0.2 dB, 0.01 ps, –80 dB, and 0.02 dB, respectively. The negligible polarization sensitivity and backreflection of these devices eliminates the need for expensive polarizers and isolators.

We now look at representative experiments that have been performed and discussed to examine the displacement sensitivity of long-period gratings written in different fibers.[19,20] For example, gratings have been fabricated in four different types of fibers—standard dispersion-shifted fiber (DSF), standard 1550-nm fiber, and conventional 980- and 1050-nm single-mode fibers. For the sake of brevity, these will be referred to as fibers A, B, C, and D, respectively. The strain sensitivity of gratings written in different fibers was determined by axially straining the gratings between two longitudinally separated translation stages. The shift in the peak loss wavelength of the grating in fiber D as a function of the applied strain is depicted in Fig. 12 along with that for a Bragg grating (about 9 nm/%ε at 1300 nm).[7] The strain coefficients of wavelength shift β for fibers A, B, C, and D are shown in Table 1. Fiber D has a coefficient of 15.2 nm/%ε, which gives it a strain-induced shift that is 50 percent larger than that for a conventional Bragg grating. The strain resolution of this fiber for a 0.1-nm detectable wavelength shift is 65.75 με.

TABLE 1 Strain Sensitivity of Long-Period Gratings Written in Four Different Types of Fibers

Type of fiber	Strain sensitivity (nm/%ε)
A—standard dispersion-shifted fiber (DSF)	–7.27
B—standard 1550-nm communication fiber	4.73
C—conventional 980-nm single-mode fiber	4.29
D—conventional 1060-nm single-mode fiber	15.21

Values correspond to the shift in the highest order resonance wavelength.

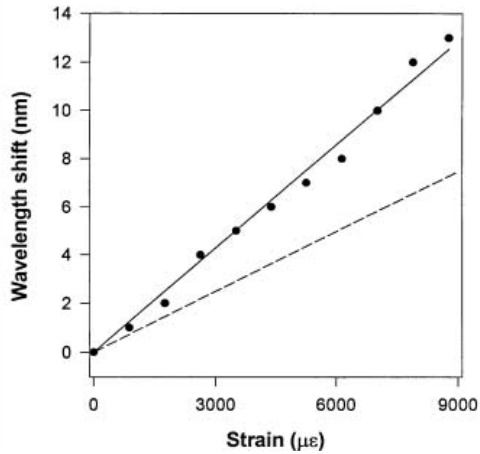

FIGURE 12 Shift in the highest order resonance band with strain for a long-period grating written in fiber D (circles). Also depicted is the shift for a conventional Bragg grating (dashed line).

The demodulation scheme of a sensor determines the overall simplicity and sensitivity of the sensing system. Short-period Bragg grating sensors were shown to possess signal processing techniques that are complex and expensive to implement. We now present a simple demodulation method to extract information from long-period gratings. The wide bandwidth of the resonance bands enables the wavelength shift due to the external perturbation to be converted into an intensity variation that can be easily detected.

Figure 13 shows the shift induced by strain in a grating written in fiber C. The increase in the loss at 1317 nm is about 1.6 dB. A laser diode centered at 1317 nm was used as the optical source, and the change in transmitted intensity was monitored as a function of applied strain. The transmitted intensity is plotted in Fig. 14 for three different trials. The repeatability of the experiment demonstrates the feasibility of using this simple scheme to utilize the high sensitivity of long-period gratings. The transmission of a laser diode centered on the slope of the grating spectrum on either side of the resonance wavelength can be used as a measure of the applied perturbation. A simple detector and amplifier combination at the output can be used to determine the transmission through the detector. On the other hand, a broadband source can also be used to interrogate the grating. At the output an optical bandpass filter can be used to transmit only a fixed bandwidth of the signal to the detector. The bandpass filter should again be centered on either side of the peak loss band of the resonance band. These schemes are easy to implement, and unlike the case for conventional Bragg gratings, complex and expensive interferometric demodulation schemes are not necessary.[20]

Temperature Sensitivity of Long-Period Gratings

Gratings written in different fibers were also tested for their cross-sensitivity to temperature.[20] The temperature coefficients of wavelength shift for different fibers are shown in Table 2. The temperature sensitivity of a fiber Bragg grating is 0.014 nm/°C. Hence the temperature sensitivity of a long-period grating is typically an order of magnitude higher than that of a Bragg grating. This large cross-sensitivity to ambient temperature can degrade the strain sens-

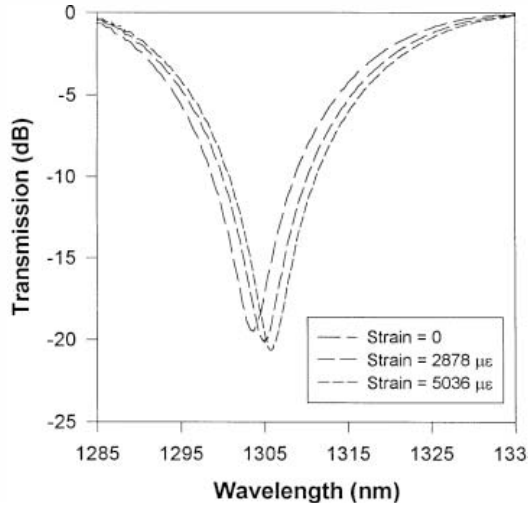

FIGURE 13 Strain-induced shift in a long-period grating fabricated in fiber C. The loss at 1317 nm increases by 1.6 dB due to the applied strain (5036 με).

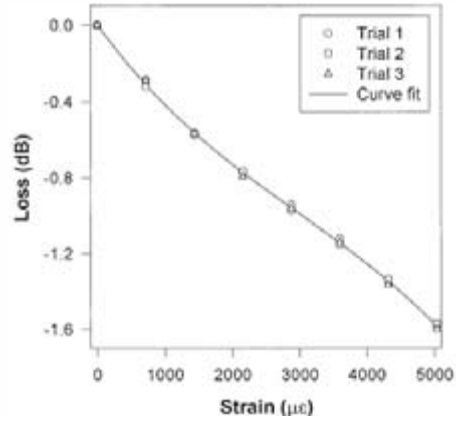

FIGURE 14 The change in the grating transmission at 1317 nm as a function of strain for three different trials. The increase in loss by 1.6 dB at 5036 με provides evidence of the feasibility of the simple setup used to measure strain.

TABLE 2 Temperature Sensitivity of Long-period Gratings Written in Four Different Types of Fibers

Type of fiber	Temperature sensitivity (nm/°C)
A—standard dispersion-shifted fiber (DSF)	0.062
B—standard 1550-nm communication fiber	0.058
C—conventional 980-nm single mode fiber	0.154
D—conventional 1060 nm single mode fiber	0.111

Values correspond to the shift in the highest order resonance wavelength.

ing performance of the system unless the output signal is adequately compensated. Multiparameter sensing using long-period gratings has been proposed to obtain precise strain measurements in environments with temperature fluctuations.[19]

In summary, long-period grating sensors are highly versatile. These sensors can easily be used in conjunction with simple and inexpensive detection techniques. Experimental results prove that these methods can be used effectively without sacrificing the enhanced resolution of the sensors. Long-period grating sensors are insensitive to input polarization and do not require coherent optical sources. Cross-sensitivity to temperature is a major concern while using these gratings for strain measurements.

15.6 COMPARISON OF SENSING SCHEMES

Based on these results, interferometric sensors have a high sensitivity and bandwidth but are limited by nonlinearity in their output signals. Conversely, intrinsic sensors are susceptible to ambient temperature changes, while grating-based sensors are simpler to multiplex. Each may be used in specific applications.

15.7 CONCLUSION

We have briefly summarized the performance of four different interferometric and grating-based sensors as representative of the very wide range of possible optical fiber sensor instrumentation and approaches. This analysis was based on the sensor head fabrication and cost, signal processing, cross-sensitivity to temperature, resolution, and operating range. Relative merits and demerits of the various sensing schemes were discussed.

15.8 REFERENCES

1. R. O. Claus, M. F. Gunther, A. Wang, and K. A. Murphy, "Extrinsic Fabry-Perot Sensor for Strain and Crack Opening Displacement Measurements from Minus 200 to 900°C," *Smart Mat. and Struct,* **1**:237–242 (1992).
2. K. A. Murphy, M. F. Gunther, A. M. Vengsarkar, and R. O. Claus, "Fabry-Perot Fiber Optic Sensors in Full-Scale Fatigue Testing on an F-15 Aircraft," *App. Opt.,* **31**:431–433 (1991).
3. V. Bhatia, C. A. Schmid, K. A. Murphy, R. O. Claus, T. A. Tran, J. A. Greene, and M. S. Miller, "Optical Fiber Sensing Technique for Edge-Induced and Internal Delamination Detection in Composites," *J. Smart Mat Strut.,* **4** (1995).
4. C. E. Lee and H. F. Taylor, "Fiber-Optic Fabry-Perot Temperature Sensor Using a Low-Coherence Light Source," *J. Lightwave Technol.,* **9**:129–134 (1991).

5. J. A. Greene, T. A. Tran, K. A. Murphy, A. J. Plante, V. Bhatia, M. B. Sen, and R. O. Claus, "Photo-induced Fresnel Reflectors for Point-Wise and Distributed Sensing Applications," in *Proceedings of the Conference on Smart Structures and Materials,* SPIE'95, paper 2444-05, February 1995.
6. J. Sirkis, "Phase-Strain-Temperature Model for Structurally Embedded Interferometric Optical Fiber Strain Sensors with Applications," *Fiber Opt. Smart Struct. Skins IV,* SPIE **1588** (1991).
7. K. O. Hill, Y. Fuiji, D. C. Johnson, and B. S. Kawasaki, "Photosensitivity in Optical Fiber Waveguides: Applications to Reflection Filter Fabrication," *Appl. Phys. Lett.* **32**:647 (1978).
8. G. Meltz, W. W. Morey, and W. H. Glenn, "Formation of Bragg Gratings in Optical Fibers by Transverse Holographic Method," *Opt. Lett.* **14**:823 (1989).
9. P. J. Lemaire, A. M. Vengsarkar, W. A. Reed, V. Mizrahi, and K. S. Kranz, "Refractive Index Changes in Optical Fibers Sensitized with Molecular Hydrogen," in *Proceedings of the Conference on Optical Fiber Communications,* OFC'94, Technical Digest, paper TuL1, 1994, p. 47.
10. R. Kashyap, "Photosensitive Optical Fibers: Devices and Applications," *Opt. Fiber Technol.* **1**:17–34 (1994).
11. D. Z. Anderson, V. Mizrahi, T. Ergodan, and A. E. White, "Phase-Mask Method for Volume Manufacturing of Fiber Phase Gratings," *in Proceedings of the Conference on Optical Fiber Communication,* post-deadline paper PD16, 1993, p. 68.
12. A. D. Kersey and T. A. Berkoff, "Fiber-Optic Bragg-Grating Differential-Temperature Sensor," *IEEE Phot. Techno. Lett.* **4**:1183–1185 (1992).
13. V. Bhatia, M. B. Sen, K. A. Murphy, A. Wang, R. O. Claus, M. E. Jones, J. L. Grace, and J. A. Greene, "Demodulation of Wavelength-Encoded Optical Fiber Sensor Signals Using Fiber Modal Interferometers," *SPIE Photon. East,* Philadelphia, PA, paper 2594–09, October 1995.
14. M. G. Xu, L. Dong, L. Reekie, J. A. Tucknott, and J. L. Cruz, "Chirped Fiber Gratings for Temperature-Independent Strain Sensing," in *Proceedings of the First OSA Topical Meeting on Photosensitivity and Quadratic Nonlinearity in Glass Waveguides: Fundamentals and Applications,* paper PMB2, 1995.
15. K. O. Hill, B. Malo, K. Vineberg, F. Bilodeau, D. Johnson, and I. Skinner, "Efficient Mode-Conversion in Telecommunication Fiber Using Externally Written Gratings," *Electron. Lett.,* **26**:1270–1272 (1990).
16. F. Bilodeau, K. O. Hill, B. Malo, D. Johnson, and I. Skinner, "Efficient Narrowband LP_{01} <–> LP_{02} Mode Converters Fabricated in Photosensitive Fiber: Spectral Response," *Electron. Lett.* **27**:682–684 (1991).
17. A. M. Vengsarkar, P. J. Lemaire, J. B. Judkins, V. Bhatia, J. E. Sipe, and T. E. Ergodan, "Long-Period Fiber Gratings as Band-Rejection Filters", in *Proceedings of Conference on Optical Fiber Communications,* OFC'95, post-deadline paper, PD4-2, 1995.
18. A. M. Vengsarkar, P. J. Lemaire, J. B. Judkins, V. Bhatia, J. E. Sipe, and T. E. Ergodan, "Long-Period Fiber Gratings as Band-Rejection Filters," *J. Lightwave Technol.,* accepted for publication, 1995.
19. V. Bhatia, M. B. Burford, K. A. Murphy, and A. M. Vengsarkar, "Long-Period Fiber Grating Sensors," in *Proceedings of the Conference on Optical Fiber Communication,* paper ThP1, February 1996.
20. V. Bhatia and A. M. Vengsarkar, "Optical Fiber Long-Period Grating Sensors," *Opt. Lett.* 1995, submitted.

15.9 FURTHER READING

Bhatia, V., M. J. de Vries, K. A. Murphy, R. O. Claus, T. A. Tran, and J. A. Greene, "Extrinsic Fabry-Perot Interferometers for Absolute Measurements," *Fiberoptic Prod. News* **9**:12–3, (December 1994).

Bhatia, V., M. B. Sen, K. A. Murphy, and R. O. Claus, "Wavelength-Tracked White Light Interferometry for Highly Sensitive Strain and Temperature Measurements", *Electron. Lett.,* 1995, submitted.

Butter, C. D., and G. B. Hocker, "Fiber Optics Strain Gage," *Appl. Opt.,* **17**:2867–2869 (1978).

J. S. Sirkis and H. W. Haslach, "Interferometric Strain Measurement by Arbitrarily Configured, Surface Mounted, Optical Fiber," *Lightwave Technol.,* **8**:1497–1503 (1990).

This page intentionally left blank.

CHAPTER 16
FIBER-OPTIC COMMUNICATION STANDARDS

Casimer DeCusatis
IBM Corporation
Poughkeepsie, New York

16.1 INTRODUCTION

In the past 10 years several international standards have been adopted for optical communications. This chapter presents a brief overview of several major industry standards, including the following:

- ESCON/SBCON (Enterprise System Connection / Serial Byte Connection)
- FDDI (Fiber Distributed Data Interface)
- Fibre Channel Standard
- ATM (Asynchronous Transfer Mode) / SONET (Synchronous Optical Network)
- Gigabit Ethernet

16.2 ESCON

The Enterprise System Connection (ESCON)* architecture was introduced on the IBM System/390 family of mainframe computers in 1990 as an alternative high-speed I/O channel attachment.[1,2] The ESCON interface specifications were adopted in 1996 by the ANSI X3T1 committee as the serial byte connection (SBCON) standard.[3]

The ESCON/SBCON channel is a bidirectional, point-to-point 1300-nm fiber-optic data link with a maximum data rate of 17 Mbytes/s (200 Mbit/s). ESCON supports a maximum unrepeated distance of 3 km using 62.5-micron multimode fiber and LED transmitters with an 8-dB link budget, or a maximum unrepeated distance of 20 km using single-mode fiber and laser transmitters with a 14-dB link budget. The laser channels are also known as the ESCON

* ESCON is a registered trademark of IBM Corporation, 1991

Copyright 2001 by The McGraw-Hill Companies, Inc. Click Here for Terms of Use.

extended distance feature (XDF). Physical connection is provided by an ESCON duplex connector, illustrated in Fig. 1. Recently, the single-mode ESCON links have adopted the SC duplex connector as standardized by Fibre Channel. With the use of repeaters or switches, an ESCON link can be extended up to 3 to 5 times these distances; however, performance of the attached devices typically falls off quickly at longer distances due to the longer round-trip latency of the link, making this approach suitable only for applications that can tolerate a lower effective throughput, such as remote backup of data for disaster recovery. ESCON devices and CPUs may communicate directly through a channel-to-channel attachment, but more commonly attach to a central nonblocking dynamic crosspoint switch. The resulting network topology is similar to a star-wired ring, which provides both efficient bandwidth utilization and reduced cabling requirements. The switching function is provided by an ESCON director, a nonblocking circuit switch. Although ESCON uses 8B/10B encoded data, it is not a packet-switching network; instead, the data frame header includes a request for connection that is established by the director for the duration of the data transfer. An ESCON data frame includes a header, payload of up to 1028 bytes of data, and a trailer. The header consists of a two-character start-of-frame delimiter, two-byte destination address, two-byte source address, and one byte of link control information. The trailer is a two-byte cyclic redundancy check (CRC) for errors, and a three-character end-of-frame delimiter. ESCON uses a DC-balanced 8B/10B coding scheme developed by IBM.

16.3 FDDI

The fiber distributed data interface (FDDI) was among the first open networking standards to specify optical fiber. It was an outgrowth of the ANSI X3T9.5 committee proposal in 1982 for a high-speed token passing ring as a back-end interface for storage devices. While interest in this application waned, FDDI found new applications as the backbone for local area networks (LANs). The FDDI standard was approved in 1992 as ISO standards IS 9314/1-2 and DIS 9314-3; it follows the architectural concepts of IEEE standard 802 (although it is controlled by ANSI, not IEEE, and therefore has a different numbering sequence) and is among the family of standards (including token ring and ethernet) that are compatible with a common IEEE 802.2 interface. FDDI is a family of four specifications, namely the physical layer (PHY), physical media dependent (PMD), media access control (MAC), and station management (SMT). These four specifications correspond to sublayers of the data link and physical layer of the OSI reference model; as before, we will concentrate on the physical layer implementation.

The FDDI network is a 100-Mbit/s token passing ring, with dual counterrotating rings for fault tolerance. The dual rings are independent fiber-optic cables; the primary ring is used for data transmission, and the secondary ring is a backup in case a node or link on the primary ring fails. Bypass switches are also supported to reroute traffic around a damaged area of the

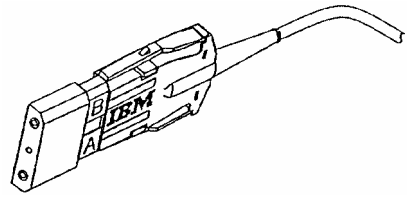

FIGURE 1 ESCON duplex fiber-optic connector.

network and prevent the ring from fragmenting in case of multiple node failures. The actual data rate is 125 Mbit/s, but this is reduced to an effective data rate of 100 Mbit/s by using a 4B/5B coding scheme. This high speed allows FDDI to be used as a backbone to encapsulate lower speed 4, 10, and 16 Mbit/s LAN protocols; existing ethernet, token ring, or other LANs can be linked to an FDDI network via a bridge or router. Although FDDI data flows in a logical ring, a more typical physical layout is a star configuration with all nodes connected to a central hub or concentrator rather than to the backbone itself. There are two types of FDDI nodes, either *dual attach* (connected to both rings) or *single attach;* a network supports up to 500 dual-attached nodes, 1000 single-attached nodes, or an equivalent mix of the two types. FDDI specifies 1300-nm LED transmitters operating over 62.5-micron multimode fiber as the reference media, although the standard also provides for the attachment of 50, 100, 140, and 85 micron fiber. Using 62.5-micron fiber, a maximum distance of 2 km between nodes is supported with an 11-dB link budget; since each node acts like a repeater with its own phase-lock loop to prevent jitter accumulation, the entire FDDI ring can be as large as 100 km. However, an FDDI link can fail due to either excessive attenuation or dispersion; for example, insertion of a bypass switch increases the link length and may cause dispersion errors even if the loss budget is within specifications. For most other applications, this does not occur because the dispersion penalty is included in the link budget calculations or the receiver sensitivity measurements. The physical interface is provided by a special media interface connector (MIC), illustrated in Fig. 2. The connector has a set of three color-coded keys which are interchangable depending on the type of network connection[1]; this is intended to prevent installation errors and assist in cable management.

An FDDI data frame is variable in length and contains up to 4500 8-bit bytes, or octets, including a preamble, start of frame, frame control, destination address, data payload, CRC error check, and frame status/end of frame. Each node has a MAC sublayer that reviews all the data frames looking for its own destination address. When it finds a packet destined for its node, that frame is copied into local memory; a copy bit is turned on in the packet; and it is then sent on to the next node on the ring. When the packet returns to the station that originally sent it, the originator assumes that the packet was received if the copy bit is on; the originator will then delete the packet from the ring. As in the IEEE 802.5 token ring protocol, a special type of packet called a *token* circulates in one direction around the ring, and a node can only transmit data when it holds the token. Each node observes a token retention time limit, and also keeps track of the elapsed time since it last received the token; nodes may be given the token in equal turns, or they can be given priority by receiving it more often or holding it longer after they receive it. This allows devices having different data requirements to be served appropriately.

Because of the flexibility built into the FDDI standard, many changes to the base standard have been proposed to allow interoperability with other standards, reduce costs, or extend FDDI into the MAN or WAN. These include a single-mode PMD layer for channel extensions up to 20 to 50 km. An alternative PMD provides for FDDI transmission over copper wire, either shielded or unshielded twisted pairs; this is known as *copper distributed data inter-*

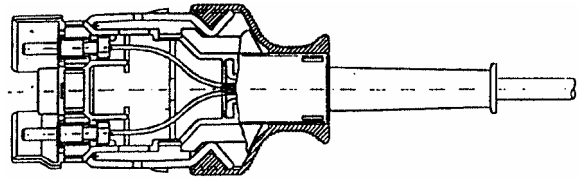

FIGURE 2 FDDI duplex fiber-optic connector.

face, or CDDI. A new PMD is also being developed to adapt FDDI data packets for transfer over a SONET link by stuffing approximately 30 Mbit/s into each frame to make up for the data rate mismatch (we will discuss SONET as an ATM physical layer in a later section). An enhancement called FDDI-II uses time-division multiplexing to divide the bandwidth between voice and data; it would accommodate isochronous, circuit-switched traffic as well as existing packet traffic. Recently, an option known as *low cost* (LC) FDDI has been adopted. This specification uses the more common SC duplex connector instead of expensive MIC connectors, and a lower-cost transceiver with a 9-pin footprint similar to the single-mode ESCON parts.

16.4 FIBRE CHANNEL STANDARD

Development of the ANSI Fibre Channel (FC) Standard began in 1988 under the X3T9.3 Working Group, as an outgrowth of the Intelligent Physical Protocol Enhanced Physical Project. The motivation for this work was to develop a scaleable standard for the attachment of both networking and I/O devices, using the same drivers, ports, and adapters over a single channel at the highest speeds currently achievable. The standard applies to both copper and fiber-optic media, and uses the English spelling *fibre* to denote both types of physical layers. In an effort to simplify equipment design, FC provides the means for a large number of existing upper-level protocols (ULPs), such as IP, SCI, and HIPPI, to operate over a variety of physical media. Different ULPs are mapped to FC constructs, encapsulated in FC frames, and transported across a network; this process remains transparent to the attached devices. The standard consists of five hierarchical layers,[4] namely a physical layer, an encode/decode layer which has adopted the DC-balanced 8B/10B code, a framing protocol layer, a common services layer (at this time, no functions have been formally defined for this layer), and a protocol-mapping layer to encapsulate ULPs into FC. The second layer defines the Fibre Channel data frame; frame size depends upon the implementation and is variable up to 2148 bytes long. Each frame consists of a 4-byte start-of-frame delimiter, a 24-byte header, a 2112-byte payload containing from 0 to 64 bytes of optional headers and 0 to 2048 bytes of data, a 4-byte CRC, and a 4-byte end-of-frame delimiter. In October 1994, the Fibre Channel physical and signaling interface standard FC-PH was approved as ANSI standard X3.230-1994.

Logically, Fibre Channel is a bidirectional point-to-point serial data link. Physically, there are many different media options (see Table 1) and three basic network topologies. The simplest, *default topology,* is a point-to-point direct link between two devices, such as a CPU and a device controller. The second, *Fibre Channel Arbitrated Loop* (FC-AL), connects between 2 and 126 devices in a loop configuration. Hubs or switches are not required, and there is no dedicated loop controller; all nodes on the loop share the bandwidth and arbitrate for temporary control of the loop at any given time. Each node has equal opportunity to gain control of the loop and establish a communications path; once the node relinquishes control, a fairness algorithm ensures that the same node cannot win control of the loop again until all other nodes have had a turn. As networks become larger, they may grow into the third topology, an *interconnected switchable network* or *fabric* in which all network management functions are taken over by a switching point, rather than each node. An analogy for a switched fabric is the telephone network; users specify an address (phone number) for a device with which they want to communicate, and the network provides them with an interconnection path. In theory there is no limit to the number of nodes in a fabric; practically, there are only about 16 million unique addresses. Fibre Channel also defines three classes of connection service, which offer options such as guaranteed delivery of messages in the order they were sent and acknowledgment of received messages.

As shown in Table 1, FC provides for both single-mode and multimode fiber-optic data links using longwave (1300-nm) lasers and LEDs as well as short-wave (780 to 850 nm) lasers. The physical connection is provided by an SC duplex connector defined in the standard (see

TABLE 1 Fiber Channel Standard Physical Layer

Media type	Data rate (Mbytes/s)	Maximum distance	Signaling rate (Mbaud)	Transmitter
SMF	100	10 km	1062.5	LW laser
	50	10 km	1062.5	LW laser
	25	10 km	1062.5	LW laser
50-μm multimode fiber	100	500 m	1062.5	SW laser
	50	1 km	531.25	SW laser
	25	2 km	265.625	SW laser
	12.5	10 km	132.8125	LW LED
62.5-μm multimode fiber	100	300 m	1062.5	SW laser
	50	600 m	531.25	SW laser
	25	1 km	265.625	LW LED
	12.5	2 km	132.8125	LW LED
105-Ω type 1 shielded twisted pair electrical	25	50 m	265.125	ECL
	12.5	100 m	132.8125	ECL
75 Ω mini coax	100	10 m	1062.5	ECL
	50	20 m	531.25	ECL
	25	30 m	265.625	ECL
	12.5	40 m	132.8125	ECL
75 Ω video coax	100	25 m	1062.5	ECL
	50	50 m	531.25	ECL
	25	75 m	265.625	ECL
	12.5	100 m	132.8125	ECL
150 Ω twinax or STP	100	30 m	1062.5	ECL
	50	60 m	531.25	ECL
	25	100 m	265.625	ECL

Here LW is long wavelength, SW is short wavelength, and ECL is emitter-coupled logic.

Fig. 3), which is keyed to prevent misplugging of a multimode cable into a single-mode receptacle. This connector design has since been adopted by other standards, including ATM, low-cost FDDI, and single-mode ESCON. The requirement for international class 1 laser safety is addressed using open fiber control (OFC) on some types of multimode links with shortwave lasers. This technique automatically senses when a full duplex link is interrupted, and turns off the laser transmitters on both ends to preserve laser safety. The lasers then transmit low-duty cycle optical pulses until the link is reestablished; a handshake sequence then automatically reactivates the transmitters.

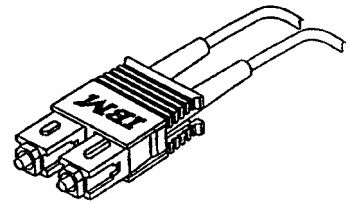

FIGURE 3 Single-mode SC duplex fiber-optic connector, per ANSI FC Standard specifications, with one narrow key and one wide key. Multimode SC duplex connectors use two wide keys.

16.5 ATM/SONET

Developed by the ATM Forum, this protocol has promised to provide a common transport media for voice, data, video, and other types of multimedia. ATM is a high-level protocol that can run over many different physical layers including copper; part of ATM's promise to merge voice and data traffic on a single network comes from plans to run ATM over the synchronous optical network (SONET) transmission hierarchy developed for the telecommunications industry. SONET is really a family of standards defined by ANSI T1.105-1988 and T1.106-1988, as well as by several CCITT recommendations.[5–8] Several different data rates are defined as multiples of 51.84 Mbit/s, known as OC-1. The numerical part of the OC-level designation indicates a multiple of this fundamental data rate, thus 155 Mbit/s is called OC-3. The standard provides for 7 incremental data rates, OC-3, OC-9, OC-12, OC-18, OC-24, OC-36, and OC-48 (2.48832 Gbit/s). Both single-mode links with laser sources and multimode links with LED sources are defined for OC-1 through OC-12; only single-mode laser links are defined for OC-18 and beyond. SONET also contains provisions to carry sub-OC-1 data rates, called *virtual tributaries,* which support telecom data rates including DS-1 (1.544 Mbit/s), DS-2 (6.312 Mbit/s), and 3.152 Mbit/s (DS1C). The basic SONET data frame is an array of nine rows with 90 bytes per row, known as a synchronous-transport signal level 1 (STS-1) frame. In an OC-1 system, an STS-1 frame is transmitted once every 125 microseconds (810 bytes per 125 microseconds yields 51.84 Mbit/s). The first three columns provide overhead functions such as identification, framing, error checking, and a pointer which identifies the start of the 87-byte data payload. The payload floats in the STS-1 frame, and may be split across two consecutive frames. Higher speeds can be obtained either by concatenation of *N* frames into an STS-Nc frame (the "c" stands for *concatenated*) or by byte-interleaved multiplexing of *N* frames into an STS-N frame.

ATM technology incorporates elements of both circuit and packet switching. All data is broken down into a 53-byte cell, which may be viewed as a short fixed-length packet. Five bytes make up the header, providing a 48-byte payload. The header information contains routing information (cell addresses) in the form of virtual path and channel identifiers; a field to identify the payload type; an error check on the header information; and other flow control information. Cells are generated asynchronously; as the data source provides enough information to fill a cell, it is placed in the next available cell slot. There is no fixed relationship between the cells and a master clock, as in conventional time-division multiplexing schemes; the flow of cells is driven by the bandwidth needs of the source. ATM provides bandwidth on demand; for example, in a client-server application the data may come in bursts; several data sources could share a common link by multiplexing during the idle intervals. Thus, the ATM adaptation layer allows for both constant and variable bit rate services. The combination of transmission options is sometimes described as a *pleisosynchronous network,* meaning that it combines some features of multiplexing operations without requiring a fully synchronous implementation. Note that the fixed cell length allows the use of synchronous multiplexing and switching techniques, while the generation of cells on demand allows flexible use of the link bandwidth for different types of data, characteristic of packet switching. Higher-level protocols may be required in an ATM network to ensure that multiplexed cells arrive in the correct order, or to check the data payload for errors (given the typical high reliability and low BER of modern fiber-optic technology, it was considered unnecessary overhead to replicate data error checks at each node of an ATM network). If an intermediate node in an ATM network detects an error in the cell header, cells may be discarded without notification to either end user. Although cell loss priority may be defined in the ATM header, for some applications the adoption of unacknowledged transmission may be a concern.

ATM data rates were intended to match SONET rates of 51, 155, and 622 Mbit/s; an FDDI-compliant data rate of 100 Mbit/s was added, in order to facilitate emulation of different types of LAN traffic over ATM. In order to provide a low-cost copper option and compatibility with 16-Mbit/s token ring LANs to the desktop, a 25-Mbit/s speed has also been

approved. For premises wiring applications, ATM specifies the SC duplex connector, color coded beige for multimode links and blue for single-mode links. At 155 Mbit/s, multimode ATM links support a maximum distance of 3 km while single-mode links support up to 20 km.

16.6 GIGABIT ETHERNET

Ethernet is a local area network (LAN) communication standard originally developed for copper interconnections on a common data bus; it is an IEEE standard 802.3.[9] The basic principle used in Ethernet is carrier sense multiple access with collision detection (CSMA/CD). Ethernet LANs are typically configured as a bus, often wired radially through a central hub. A device attached to the LAN that intends to transmit data must first sense whether another device is transmitting. If another device is already sending, then it must wait until the LAN is available; thus, the intention is that only one device will be using the LAN to send data at a given time. When one device is sending, all other attached devices receive the data and check to see if it is addressed to them; if it is not, then the data is discarded. If two devices attempt to send data at the same time (for example, both devices may begin transmission at the same time after determining that the LAN is available; there is a gap between when one device starts to send and before another potential sender can detect that the LAN is in use), then a collision occurs. Using CSMA/CD as the media access control protocol, when a collision is detected attached devices will detect the collision and must wait for different lengths of time before attempting retransmission. Since it is not always certain that data will reach its destination without errors or that the sending device will know about lost data, each station on the LAN must operate an end-to-end protocol for error recovery and data integrity. Data frames begin with an 8-byte preamble used for determining start-of-frame and synchronization, and a header consisting of a 6-byte destination address, 6-byte source address, and 2-byte length field. User data may vary from 46 to 1500 bytes, with data shorter than the minimum length padded to fit the frame; the user data is followed by a 2-byte CRC error check. Thus, an Ethernet frame may range from 70 bytes to 1524 bytes.

The original Ethernet standard, known also as 10Base-T (10 Mbit/s over unshielded twisted pair copper wires) was primarily a copper standard, although a specification using 850-nm LEDs was also available. Subsequent standardization efforts increased this data rate to 100 Mbit/s over the same copper media (100Base-T), while once again offering an alternative fiber specification (100Base-FX). Recently, the standard has continued to evolve with the development of Gigabit Ethernet (1000Base-FX), which will operate over fiber as the primary medium; this has the potential to be the first networking standard for which the implementation cost on fiber is lower than on copper media. Under development as IEEE 802.3z, the gigabit Ethernet standard was approved in late 1998. Gigabit Ethernet will include some changes to the MAC layer in addition to a completely new physical layer operating at 1.25 Gbit/s. Switches rather than hubs are expected to predominate, since at higher data rates throughput per end user and total network cost are both optimized by using switched rather than shared media. The minimum frame size has increased to 512 bytes; frames shorter than this are padded with idle characters (carrier extension). The maximum frame size remains unchanged, although devices may now transmit multiple frames in bursts rather than single frames for improved efficiency. The physical layer will use standard 8B/10B data encoding. The standard does not specify a physical connector type for fiber; at this writing there are several proposals, including the SC duplex and various small-form-factor connectors about the size of a standard RJ-45 jack. Transceivers may be packaged as gigabit interface converters, or GBICs, which allows different optical or copper transceivers to be plugged onto the same host card. There is presently a concern with proposals to operate long-wave (1300 nm) laser sources over both single-mode and multimode fiber. When a transmitter is optimized for a single-mode launch condition, it will underfill the multimode fiber; this causes some modes to be excited and propagate at different speeds than others, and the resulting differential mode

delay significantly degrades link performance. One proposed solution involves the use of special optical cables known as optical mode conditioners with offset ferrules to simulate an equilibrium mode launch condition into multimode fiber.

16.7 REFERENCES

1. D. Stigliani, "Enterprise Systems Connection Fiber Optic Link," Chapter 13 in *Handbook of Optoelectronics for Fiber Optic Data Communications,* C. DeCusatis, R. Lasky, D. Clement, and E. Mass (eds.) Academic Press, 1997.
2. "ESCON I/O Interface Physical Layer Document" (IBM document number SA23-0394), third edition, IBM Corporation, Mechanicsburg, Pennsylvania, 1995.
3. ANSI Single Byte Command Code Sets CONnection architecture (SBCON), draft ANSI standard X3T11/95-469 (rev. 2.2) 1996.
4. ANSI X3.230-1994 rev. 4.3, Fibre Channel—Physical and Signaling Interface (FC-PH), ANSI X3.272-199x, rev. 4.5, Fibre Channel—Arbitrated Loop (FC-AL), June 1995, ANSI X3.269-199x, rev. 012, Fiber Channel Protocol for SCSI (FCP), May 30, 1995.
5. ANSI T1.105-1988, Digital Hierarchy Optical Rates and Format Specification.
6. CCITT Recommendation G.707, Synchronous Digital Hierarchy Bit Rates.
7. CCITT Recommendation G.708, Network Node Interfaces for the Synchronous Digital Hierarchy.
8. CCITT Recommendation G.709, Synchronous Multiplexing Structure.
9. IEEE 802.3z, Draft Supplement to Carrier Sense Multiple Access with Collision Detection (CSMA/CD) Access Method and Physical Layer Specifications: Media Access Control (MAC) Parameters, Physical Layer, Repeater and Management Parameters for 1000 Mb/s Operation (June 1997).

P · A · R · T · 2

NONLINEAR AND QUANTUM OPTICS

Copyright 2001 by The McGraw-Hill Companies, Inc. Click Here for Terms of Use.

This page intentionally left blank.

CHAPTER 17
THIRD-ORDER OPTICAL NONLINEARITIES

Mansoor Sheik-Bahae
Department of Physics and Astronomy
University of New Mexico
Albuquerque, New Mexico

Michael P. Hasselbeck
Department of Physics and Astronomy
University of New Mexico
Albuquerque, New Mexico

17.1 INTRODUCTION

The subject of this chapter could well fill a textbook, and indeed the topic comprises a significant portion of the many books on nonlinear optics. A large (but by no means exhaustive or complete) list of texts that provide extensive discussion of high-order nonlinearities appears in Refs. 1 through 29. We have not attempted to write a review chapter nor mentioned or even listed every known third-order nonlinear optical phenomenon. Our aim is to illustrate important and representative third-order effects, emphasizing qualitative descriptions. Details can be found in the references. An exception is our discussion of the Kramers-Kronig relations in nonlinear optics. A fundamental premise of this transformation is the causal link between nonlinear refraction and nonlinear absorption, which is a key aspect of the third-order susceptibility. It has not been treated in most texts; some of the important mathematical steps are given here. Our treatment of third-order nonlinear optics assumes that the reader is familiar with electromagnetic theory, physical optics, and quantum mechanical energy level diagrams.

Any real, physical oscillating system will exhibit a nonlinear response when it is overdriven. In an optical system, a nonlinear response can occur when there is sufficiently intense illumination. The nonlinearity is exhibited in the polarization ($\vec{\mathcal{P}}$) of the material, which is often represented by a power series expansion of the total applied optical field ($\vec{\mathcal{E}}$):

$$\vec{\mathcal{P}} = \varepsilon_0\chi^{(1)}\vec{\mathcal{E}} + \varepsilon_0\chi^{(2)}\vec{\mathcal{E}}^2 + \varepsilon_0\chi^{(3)}\vec{\mathcal{E}}^3 + \ldots \tag{1}$$

Here $\chi^{(1)}$ is the linear susceptibility representing the linear response (i.e., linear absorption and the refractive index) of the material. The two lowest-order nonlinear responses are accounted for by the second- and third-order nonlinear susceptibilities $\chi^{(2)}$ and $\chi^{(3)}$. The subject of this chapter is third-order effects. Processes arising from the second-order response (including second-harmonic generation and optical parametric processes) are discussed elsewhere

Copyright 2001 by The McGraw-Hill Companies, Inc. Click Here for Terms of Use.

(see Vol. II, Chap. 38, and this vol., Chap. 22). We will, however, briefly consider the cascading of second-order nonlinearities that appear as an *effective* third-order process in Section 17.10.

Third-order optical nonlinearities cover a vast and diverse area in nonlinear optics. A simple illustration of this point is the reported range of magnitudes and response times for $\chi^{(3)}$ in various materials, which span 15 orders of magnitude! This has led to unavoidable inconsistency and confusion in the definition and interpretation of the nonlinear susceptibility. We will not be immune from such inconsistencies and errors. In that spirit, we note that the simple power series representation of the nonlinear optical response described by Eq. (1) is not rigorously correct because it assumes the response is instantaneous. In the case of the bound-electronic nonlinearity, for example, this assumption is excellent because the response is exceedingly fast. The response is not *infinitely* fast, however. Response times can vary by orders of magnitude depending on the physical mechanism and resonance conditions involved. Furthermore, Eq. (1) assumes locality, which implies that the nonlinear polarization at a given point in space depends on the magnitude of the electric field only at that point. This condition is not always satisfied. The electrostrictive nonlinearity, for example, is the result of physical displacement of charged particles in a material subject to the ponder-motive force due to the gradient of light irradiance. It is therefore nonlocal. It is nevertheless instructive to apply Eq. (1) to describe various third-order effects that are local and (single photon) nonresonant.

The nonlinear polarization represented in Eq. (1) excludes *effective* third-order nonlinear processes involving linear absorption ($\chi^{(1)}$ process) of one of the excitation beams. An example is the thermal nonlinearity resulting from linear absorption and heating that causes a change of refractive index. Although this is effectively a third-order nonlinear response, we group this and similar phenomena in Section 17.9 on cascaded $\chi^{(1)}$:$\chi^{(1)}$ effects.

The term involving $\tilde{\mathscr{E}}^3$ in Eq. (1) implies that three optical fields interact to produce a fourth field. The $\chi^{(3)}$ interaction is thus a four-photon process. This is a consequence of the quantum mechanical picture of the nonlinear susceptibility. Conservation of photon energy is always required to complete the interaction process. Assuming the applied optical fields are monochromatic plane waves, we write the total input electric field $\tilde{\mathscr{E}}$ as:

$$\tilde{\mathscr{E}}(r,t) = \tilde{\mathscr{E}}_1(r,t) + \tilde{\mathscr{E}}_2(r,t) + \tilde{\mathscr{E}}_3(r,t) \tag{2}$$

In general, each beam has a different frequency (ω) and wave vector ($\vec{k}$), represented in complex notation:

$$\tilde{\mathscr{E}}_j(r,t) = \frac{\vec{E}_j}{2} \exp\left(i\omega_j t - i\vec{k}_j \cdot r\right) + \text{c.c.} \quad \text{for } j = 1,2,3 \tag{3}$$

where c.c. stands for complex conjugate and $\vec{E}_j$ is a complex vector describing the amplitude, phase, and polarization of each beam. It is important to realize that there can be up to three different input laser frequencies, but there can also be as few as one. Ignoring the $\chi^{(1)}$ and $\chi^{(2)}$ components in Eq. (1), the nonlinear polarization resulting from the $\tilde{\mathscr{E}}^3$ interaction leads to a total of 108 terms involving all possible permutations of the fields at three frequencies. The nonlinear polarization occurs at frequencies given by:

$$\omega_4 = \pm\omega_i \pm\omega_j \pm\omega_k \quad \text{for } i,j,k = 1,2,3 \tag{4}$$

The existence of 108 terms does not mean there are as many distinct mechanisms involved. For instance, three terms give $\omega_4 = 3\omega_j$ for $j = 1,2,3$, describing exactly the same process of third-harmonic generation (THG). Furthermore, THG is a special case of sum frequency generation (SFG) involving one, two, or three different frequencies giving $\omega_4 = \omega_i + \omega_j + \omega_k$, $i,j,k = 1,2,3$ accounting for 27 terms.

One realizes 108 permutations with different time ordering of three different laser beams distinguished by frequency, and/or wave vector, and/or polarization. If only two distinguishable laser beams are available, the number of permutations decreases to 48. When the system

is driven by a single beam, the third-order response involves only four terms in three fields. In general, the $\chi^{(3)}$ coefficients associated with each term will be different due to the ever-present dispersion (i.e., frequency dependence) of the susceptibilities. The frequency dependence is a direct consequence of the finite response time of the interaction. We will expand on this subject in the discussion of the Kramers-Kronig dispersion relations in Section 17.4.

Another important property of nonlinear susceptibilities is their tensor nature. Because of the molecular or lattice structure of materials, the nonlinear response will depend on the state of polarization of the optical fields. For the sake of brevity, we neglect the tensor properties of $\chi^{(3)}$ and treat all the susceptibilities and electric fields as scalar quantities. The reader may consult textbooks on nonlinear optics for detailed discussions of this subject.

Propagation of interacting beams is also an important consideration, and one must account for wave vector summation (i.e., conservation of momentum) that results from the $\mathscr{E}^3$ operation. It is useful to invoke the four photon picture, recalling that the momentum of each photon is given by $\hbar k_j$. Taking the resultant nonlinear polarization to be a plane wave with a wave vector $\vec{k}_4$, momentum conservation requires that:

$$\vec{k}_4 = \pm\vec{k}_i \pm \vec{k}_j \pm \vec{k}_k \tag{5}$$

where $|\vec{k}_j| = n(\omega_j)\omega_j / c$. This phase-matching requirement is not necessarily satisfied in every interaction due to dispersion of the linear refractive index in the material. Phase matching can be a serious obstacle in interactions leading to new-frequency generation, that is, when $\omega_4 \neq \omega_1,\omega_2$, and ω_3 (e.g., Section 17.6 on THG). When the nonlinear polarization is at one of the driving frequencies, $\omega_4 = \omega_i$ for example, conservation of energy [Eq. (4)] implies that $\omega_j = -\omega_k$. In this case, Eq. (5) reduces to a vector-matching condition that depends only on the geometry (i.e., direction) of the beams (Sections 17.11 and 17.12).

The frequency terms arising from the third-order nonlinear polarization described by Eq. (1) are collected in Table 1. In the following section, we discuss the physical mechanisms and important features of these processes.

17.2 QUANTUM MECHANICAL PICTURE

The conservation of energy shown in the frequency summation of Eq. (4) contains both positive and negative signs from each of the input beams. A positive sign represents the annihilation (absorption) of a photon, while the negative sign is interpreted as the generation (gain) of a photon. Both annihilation and generation of photons involve atomic and/or molecular transitions from one state to another. It is instructive to use diagrams to keep track of transitions participating in the nonlinear interactions. Let us take the most general case, where four distinguishable beams (i.e., three input photons at ω_1, ω_2, ω_3, and the final photon at ω_4) are involved. The third-order nonlinear interaction follows a path corresponding to one of 14 sign-ordering possibilities, assuming emission at the photon frequency ω_4. All possible time-ordering sequences are illustrated in Fig. 1. In addition, the interacting photons are in general distinguishable; to preserve the clarity of presentation we have not shown this in Fig. 1. Because the photons are (in general) distinct, we must allow for permutation of frequencies in the diagrams. Assuming emission at ω_4 (i.e., we can only assign ω_4 to a downward-pointing arrow), we count up the various time-ordering permutations for each interaction path shown in Fig. 1. This gives a total of 168 terms! Little would be gained by a tedious analysis of all these terms, and such a task is far beyond the scope of this chapter. Instead, we illustrate some important third-order mechanisms and the role of resonances in Fig. 2, where we have labeled the three most important diagrams in Fig. 1. The energy level $|g\rangle$ is the ground state, while $|a\rangle$, $|u\rangle$, and $|b\rangle$ are intermediate states of the system in a sequence of transitions involving photons with frequencies ω_i, ω_j, ω_k, and ω_l (i,j,k,l = 1,2,3,4) such that $\pm\omega_i\pm\omega_j\pm\omega_k\pm\omega_l = 0$. The three time-ordering processes shown in the figure are:

TABLE 1 Frequency Terms Arising from Third-Order Nonlinear Polarization

Nonlinear process	$8P(\omega_4)/\varepsilon_0\chi^{(3)}$	ω_4
• Third harmonic generation (THG)	$E_j^3\ j = 1, \ldots 3$	$3\omega_1, 3\omega_2, 3\omega_3$
• Sum frequency generation (SFG)	$3E_iE_j^2\ i,j = 1,2,3\ i \neq j$	$2\omega_1 + \omega_2, 2\omega_1 + \omega_3,$ $2\omega_2 + \omega_3, 2\omega_2 + \omega_1,$ $2\omega_3 + \omega_1, 2\omega_3 + \omega_2,$
	$6E_1E_2E_3$	$\omega_1 + \omega_2 + \omega_3$
• Frequency mixing	$3E_i^*E_j^2\ i,j = 1,2,3\ i \neq j$	$2\omega_1 - \omega_2, 2\omega_1 - \omega_3,$
• Parametric amplification		$2\omega_2 - \omega_3, 2\omega_2 - \omega_1,$ $2\omega_3 - \omega_1, 2\omega_3 - \omega_2,$
• Coherent Stokes and anti-Stokes Raman scattering (CSRS and CARS)	$6E_i^*E_jE_k\ i,j,k = 1,2,3\ i \neq j \neq k$	$\omega_1 + \omega_2 - \omega_3,$ $\omega_1 - \omega_2 + \omega_3,$ $-\omega_1 + \omega_2 + \omega_3$
	$6E_i^*E_j^*E_k\ i,j,k = 1,2,3\ i \neq j \neq k$	$\omega_1 - \omega_2 - \omega_3,$ $-\omega_1 - \omega_2 + \omega_3,$ $-\omega_1 + \omega_2 - \omega_3$
• Bound-electronic optical Kerr effect	$3E_i^2E_i^*\ i = 1,2,3$	$\omega_1, \omega_2, \omega_3$
• Raman induced Kerr effect (RIKE)		
• Molecular orientational Kerr effect	$6E_iE_jE_j^*\ i,j = 1,2,3,\ i \neq j$	
• Two-photon absorption (2PA)		
• ac Stark effect		
• Stimulated Raman scattering (SRS)		
• Stimulated Rayleigh-Wing Scattering		

Figure 2(*a*). Consecutive absorption of three photons followed by the generation of the final photon, partly describing sum frequency generation and third-harmonic generation. The reverse process is third-order parametric amplification, which is the absorption of a photon together with emission of three photons.

Figure 2(*b*). An absorption-emission-absorption-emission sequence. Difference frequency generation and frequency mixing are examples of this type of interaction. Coherent anti-Stokes Raman spectroscopy (CARS) is also represented by this transition sequence.

Figure 2(*c*). Absorption of two photons followed by emission of the two photons. As can be seen in the third section of Table 1, a variety of physical mechanisms fall under this general description. Note that the essential difference between (*b*) and (*c*) is the time ordering of the transitions. This is extremely important in resonant cases: a Raman-type resonance occurs in (*b*), and a two-photon resonance exists in (*c*).

Energy conservation is strictly obeyed upon the completion of the interaction [as dictated by Eq. (4)] but may be violated in the time frame of intermediate state transitions. This is allowed by Heisenberg's Uncertainty Principle. In many cases, an intermediate state is a virtual state, which is a convenient way of stating that a real, intermediate state of the system does not exist to support the transition of a photon at the selected wavelength. The virtual, intermediate state allows for energy bookkeeping in transition diagrams, but a physical description of the optical interaction using quantum mechanics involves only real eigenstates of the system. In particular, there must be a dipole-allowed transition between the initial state

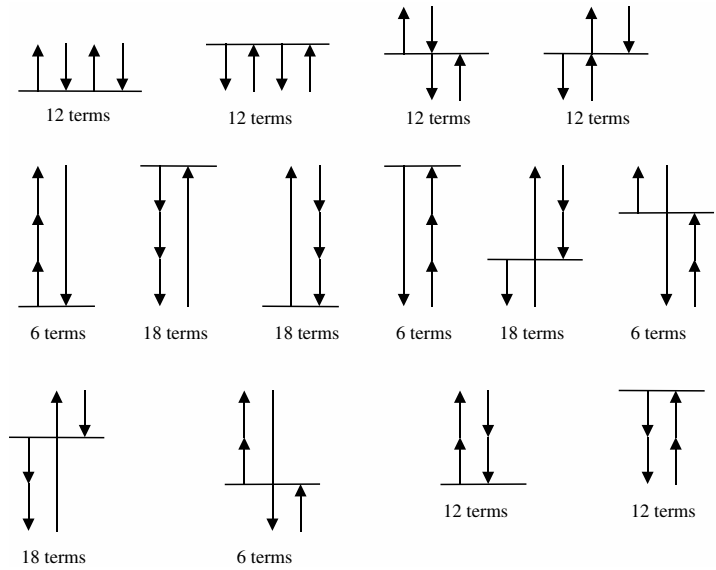

FIGURE 1 Time-ordering sequences illustrating all possible third-order paths. Arrows depict photons. Note that in general, the size of the arrows can be different provided their vector sum is zero. The number of terms is obtained assuming emission of a photon at ω_4. For clarity, arrows are not marked.

|g> and a real state *associated* with the virtual state. The time scale and strength of the interaction is partly determined by the energy mismatch between the virtual, intermediate state and an associated real, electronic state. This means a system can absorb a photon of energy $\hbar\omega_i$ and make a transition from the ground state |g> to a real intermediate state |a> even though there is insufficient photon energy to bridge the gap (i.e., there is an energy mismatch $\Delta E = |\hbar\omega_i - E_a + E_g| > 0$). This is possible, provided the interaction occurs in a time faster than the observation time $\Delta t \sim \hbar/\Delta E$ permitted by the Uncertainty Principle. Transitions of this type are called *virtual* transitions, as opposed to *real* transitions, where energy is conserved. In the former case, Δt is known as the virtual lifetime of the transition.

If the entire sequence of transitions comprising the third-order interaction is not completed within the virtual lifetime, the intermediate state collapses back to the ground state, and no nonlinear interaction occurs. In other words, all the required particles must be present in the system during the virtual lifetime. The longer the virtual lifetime, the greater the probability that the required photons will appear, allowing the multiparticle interaction to run to completion. A longer virtual lifetime translates to a larger third-order nonlinear susceptibility $\chi^{(3)}$. The closer an input photon moves to a dipole-allowed system resonance, the longer the virtual lifetime and the stronger the resulting $\chi^{(3)}$ will be.

These quantum mechanical issues are manifest in the mathematical formulation of $\chi^{(3)}$ derived from perturbation theory[1,3,17]:

$$\chi^{(3)}(\pm\omega_1,\pm\omega_2,\pm\omega_3) = \frac{N}{\hbar^3}\sum_{i,j,k,l}\sum_{a,u,b}\mu_{ga}\frac{\mu_{au}}{(\omega_{ag}\mp\omega_i)}\frac{\mu_{ub}}{(\omega_{ug}\mp\omega_i\mp\omega_j)}\frac{\mu_{bg}}{\underbrace{(\omega_{bg}\mp\omega_i\mp\omega_j\mp\omega_k)}_{\mp\omega_l}} \quad (6)$$

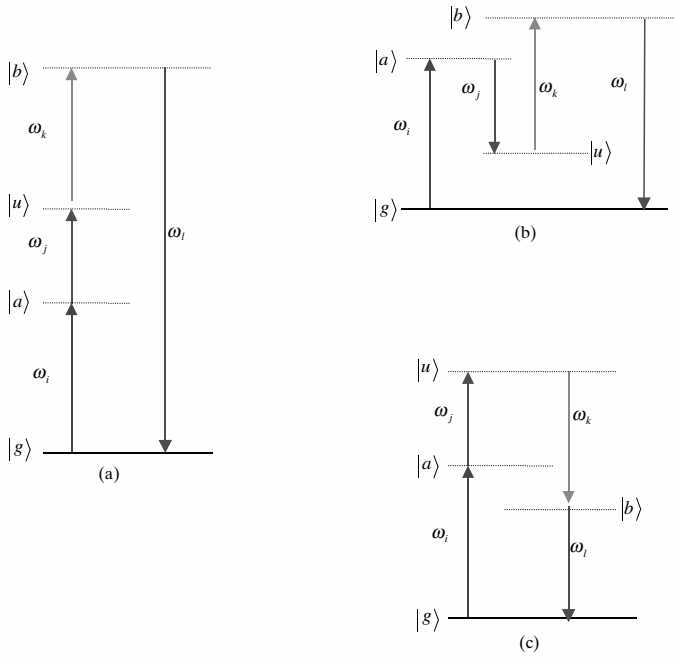

FIGURE 2 Energy level diagrams for some important third-order nonlinear optical processes: (*a*) third-harmonic generation (THG); (*b*) coherent anti-Stokes Raman scattering (CARS); (*c*) two-photon absorption (2PA).

In Eq. (6), N is the total population in the ground state $|g\rangle$, and μ's are dipole-moment matrix elements associated with each of the transitions. The first sum describes the frequency permutations: $i,j,k,$ and l can take any integer value 1,2,3,4, provided energy conservation ($\pm\omega_i \pm \omega_j \pm \omega_k \pm \omega_l = 0$) is obeyed. The second sum is over all possible real, intermediate quantum eigenstates of the system. This complicated-looking equation is nothing more than the sequence of optical transitions weighted by the appropriate virtual lifetime. The first coefficient represents the virtual transition initiated by a photon of energy $\hbar\omega_i$ from the ground state to the intermediate state $|a\rangle$ with strength given by the matrix element μ_{ga}. The next three matrix elements are weighted by the virtual lifetimes of their initial state. The virtual lifetimes are represented by energy (i.e., frequency) denominators; as the photon frequency approaches a system resonance, the virtual lifetime and magnitude of $\chi^{(3)}$ grow accordingly.

The ± signs in front of the frequency arguments in Eq. (6) indicate there is a physical significance to the time ordering of the participating photons. This representation distinguishes the various components of the third-order susceptibility. In many textbooks, a permutation of all the frequencies (including the signs) is already incorporated in the final calculation of $\chi^{(3)}$.[3,4] In that case, for a given ω_4, one obtains the total contribution to $\chi^{(3)}$ with the order of frequency arguments having no particular physical relevance.

We also point out that the nonlinear susceptibility described by Eq. (6) and shown in our example is *real.* A resonance condition occurs when any one of the energy/frequency denom-

inators approaches zero. This not only enhances $\chi^{(3)}$ but also makes it a complex quantity (i.e., a resonance condition introduces an imaginary component to $\chi^{(3)}$). This is better understood by making the following substitution:

$$\frac{1}{\Delta\omega} \rightarrow \frac{1}{\Delta\omega + i\Gamma} \tag{7}$$

where Γ represents a phenomenological broadening of the particular transition. This complex damping term accounts for the physical impossibility of the nonlinear susceptibility becoming infinite in a resonance condition. Even in the case of vanishing damping, a basic theorem of complex variables can be applied to Eq. (7):

$$\lim_{\Gamma \to 0} \frac{1}{\Delta\omega + i\Gamma} = \mathcal{P}\left(\frac{1}{\Delta\omega}\right) + i\pi\delta(\Delta\omega) \tag{8}$$

where $\mathcal{P}$ stands for the principle value and δ is the Dirac delta function. The important message is that in general, the nonlinear susceptibility $\chi^{(3)}$ is a complex quantity that will be dominated by its imaginary component when photon frequencies move into resonance with real eigenstates of the system. The resonance conditions leading to a strong imaginary $\chi^{(3)}$ are associated with one or more of the following processes: three-photon ($\omega_i + \omega_j + \omega_k = -\omega_l \approx \omega_{bg}$), two-photon ($\omega_i + \omega_j = -\omega_k - \omega_l \approx \omega_{ug}$), Raman-type ($\omega_i - \omega_j = \omega_l - \omega_k \approx \omega_{ug}$), and/or single-photon ($\omega_i \approx \omega_{ag}$) resonances. The latter cases (i.e., those having linear resonance) will be discussed in Section 17.9, which deals with cascaded $\chi^{(1)}$:$\chi^{(1)}$ nonlinearities. A special case of linear resonance can occur in Raman-type transitions where $\omega_{ug} = 0$ (i.e., when the second intermediate state is degenerate with the ground state). This corresponds to the optical Stark effect (ac Stark effect). The three-photon resonance that gives rise to an imaginary $\chi^{(3)}$ in third-harmonic generation does not have a significant physical implication. It only influences the phase of the interacting fields, similar to the case of second-order effects (e.g., second-harmonic generation).[1] The remaining two processes involving two-photon and Raman resonances are of significant interest and will be discussed in detail.

17.3 NONLINEAR ABSORPTION (NLA) AND NONLINEAR REFRACTION (NLR)

Just as the real and imaginary components of the linear susceptibility $\chi^{(1)}$ are associated with refraction and absorption, the real and imaginary parts of $\chi^{(3)}$ describe nonlinear refraction (NLR) and nonlinear absorption (NLA) or gain. This can be understood by considering situations in which the nonlinear polarization is at one of the driving frequencies. These are particular cases of Figs. 2(*b*) and 2(*c*), with corresponding polarization terms given in the third section of Table 1. Taking the interacting photons to have frequencies ω_a and ω_b, the total polarization (linear and third order) at ω_a can be written as:

$$P(\omega_a) = \varepsilon_0 \left\{ \frac{1}{2}\chi^{(1)}(\omega_a) E_a + \frac{3}{8}\chi^{(3)}(\omega_a,\omega_a,-\omega_a) E_a^2 E_a^* + \frac{6}{8}\chi^{(3)}(\omega_a,\omega_b,-\omega_b) E_a E_b E_b^* \right\} \tag{9}$$

For the sake of brevity, we ignore time-ordering in the frequency arguments of $\chi^{(3)}$. This means that the $\chi^{(3)}$ component in Eq. (9) is assumed to contain the various permutations of frequencies including, for example, two-photon as well as Raman transitions shown in Figs. 2(*b*) and 2(*c*). From Eq. (9), we introduce an effective susceptibility χ_{eff}:

$$\chi_{eff}(\omega_a) = \chi^{(1)}(\omega_a) + \frac{3}{4}\chi^{(3)}(\omega_a,\omega_a,-\omega_a)|E_a|^2 + \frac{6}{4}\chi^{(3)}(\omega_a,\omega_b,-\omega_b)|E_b|^2 \tag{10}$$

Deriving the coefficients of nonlinear absorption and refraction from Eq. (10) is now straightforward. The complex refractive index is defined as:

$$n + i\kappa = (1 + \chi_{\text{eff}})^{1/2} \tag{11}$$

Making the very realistic assumption that the nonlinear terms in Eq. (10) are small compared to the linear terms, we use the binomial expansion to simplify Eq. (11):

$$n + i\kappa \cong n_0 + i\frac{c}{2\omega_a}\,\alpha_0 + \Delta n + i\frac{c}{2\omega_a}\,\Delta\alpha \tag{12}$$

where $n_0 = (1 + \Re e\{\chi^{(1)}\})^{1/2}$. We also assume the background linear absorption coefficient is small, that is, $\alpha_0 \propto \Im m\{\chi^{(1)}\} << \Re e\{\chi^{(1)}\}$. We define the irradiance as $I_i = (1/2)c\varepsilon_0 n_0(\omega_i)|E_i|^2$ (i = a,b) and the nonlinear refraction coefficient n_2 and the nonlinear absorption coefficient α_2 as follows:

$$n_2(\omega_a;\omega_b) = \frac{3}{4\varepsilon_0 n_0(\omega_a) n_0(\omega_b) c}\,\Re e\{\chi^{(3)}(\omega_a, -\omega_b, \omega_b)\} \tag{13}$$

$$\alpha_2(\omega_a;\omega_b) = \frac{3\omega_a}{2\varepsilon_0 n_0(\omega_a) n_0(\omega_b) c^2}\,\Im m\{\chi^{(3)}(\omega_a, -\omega_b, \omega_b)\} \tag{14}$$

The change of refractive index due to the presence of fields E_a and E_b is:

$$\Delta n(\omega_a) = n_2(\omega_a;\omega_a) I_a + 2n_2(\omega_a;\omega_b) I_b \tag{15}$$

and the change of absorption is

$$\Delta\alpha(\omega_a) = \alpha_2(\omega_a;\omega_a) I_a + 2\alpha_2(\omega_a;\omega_b) I_b \tag{16}$$

where I_a and I_b are the irradiances of the two beams. Note that without loss of generality we assume the measurement is performed on the laser beam corresponding to field E_a, while the field E_b acts as an excitation source only. The first terms on the right-hand side of the just-noted equations correspond to self-action (i.e., commonly performed single-beam experiments). The second terms correspond to the case of an excite-probe experiment where the two beams are distinguishable either by frequency and/or wave vector. The factor of 2 in front of the second terms in Eqs. (15) and (16) arises from the larger number of permutations in this component of the nonlinear susceptibility.[3,4,31] The stronger nondegenerate response (i.e., distinguishable beams) is sometimes referred to as *weak-wave retardation.*[32] While most reported measurements and applications involve degenerate self-action processes (i.e., a single laser beam), the theoretical treatment presented in this chapter considers the more general nondegenerate case. One must keep in mind that degenerate third-order coefficients are only the limit of the nondegenerate case where $\omega_a = \omega_b$. The need for generality in the theoretical approach is very important for correct implementation of the Kramers-Kronig dispersion relations in nonlinear optics. This allows us to establish a rigorous mathematical relation between NLR and NLA, discussed in the next section.

Another commonly used coefficient for describing the nonlinear index is $\tilde{n}_2$ defined as:

$$n = n_0 + \tilde{n}_2(\omega_a;\omega_a)\,\frac{|E_a|^2}{2} + 2\tilde{n}_2(\omega_a;\omega_b)\,\frac{|E_b|^2}{2} \tag{17}$$

where $\tilde{n}_2$ is usually given in Gaussian units (esu). $\tilde{n}_2$ is related to n_2 by

$$\tilde{n}_2(\text{esu}) = \frac{cn}{40\pi}\,n_2(\text{SI}) \tag{18}$$

where the right-hand side is in SI/MKS units. The reader is cautioned that in the literature various symbols and definitions different from those given here are often used to describe the nonlinear refractive index. The symbol β is commonly used in place of α_2 to denote two-photon absorption (2PA).

The propagation of electromagnetic waves E_a and E_b through a nonlinear medium, ignoring the effect of diffraction and dispersion (i.e., pulse distortion), is governed by the following equations for the irradiance and phase of the probe beam (E_a):

$$\frac{dI_a}{dz} = -\alpha_0(\omega_a)I_a - \alpha_2(\omega_a;\omega_a)I_a^2 - 2\alpha_2(\omega_a;\omega_b)I_aI_b \tag{19}$$

and

$$\frac{d\phi_a}{dz} = \frac{\omega_a}{c}\left[n_0(\omega_a) + n_2(\omega_a;\omega_a)I_a + 2n_2(\omega_a;\omega_b)I_b\right] \tag{20}$$

The coefficient n_2 is often used to describe the nonlinear index change due to mechanisms such as thermally induced material changes, molecular orientation effects, saturation of absorption, and ultrafast $\chi^{(3)}$ processes. Here, consistent with our definition of $\chi^{(3)}$, we designate the n_2 notation for local and linearly nonresonant nonlinearities only. Processes that appear as an *effective* n_2 are treated separately as cascaded $\chi^{(1)}{:}\chi^{(1)}$ or $\chi^{(2)}{:}\chi^{(2)}$ phenomena.

As a consequence of the principle of causality, the real and imaginary parts of the linear susceptibility are connected through the Kramers-Kronig relations of linear optics. Equations (19) and (20) suggest a similar relation in nonlinear optics. We discuss the Kramers-Kronig relations of nonlinear optics and their underlying physics next.

17.4 KRAMERS-KRONIG DISPERSION RELATIONS

The complex response function of any linear, causal system obeys a dispersion relation linking its real and imaginary parts as Hilbert transform pairs. In linear optics, causality is manifest in the Kramers-Kronig (K-K) dispersion relations (Vol. II, Chap. 36) that tie the frequency-dependent refractive index, $n(\omega)$, to the absorption coefficient $\alpha(\omega)$ and vice-versa:

$$n(\omega) - 1 = \frac{c}{\pi}\,\mathcal{P}\int_0^\infty \frac{\alpha(\omega')}{\omega'^2 - \omega^2}\,d\omega' \tag{21}$$

where $\mathcal{P}$ denotes the Cauchy principal value. The principal value is really just a warning to be careful when integrating near the singularity in the denominator of the integrand. We drop the $\mathcal{P}$ notation for simplicity, although it is always implied. There is an equivalent relation for the real and imaginary parts of the linear susceptibility:

$$\Re e\{\chi^{(1)}(\omega)\} = \frac{1}{\pi}\int_{-\infty}^{\infty} \frac{\Im m\{\chi^{(1)}(\omega')\}}{\omega' - \omega}\,d\omega' \tag{22}$$

The K-K relation is the mathematical expression of causality, and a simple, intuitive derivation of these relations can be made.[33,34]

Causality clearly holds for any real, linear system. Real, nonlinear systems must also be causal—does that imply there are dispersion relations as well? If so, what form do they take? The Kramers-Kronig relations of linear optics are derived from linear dispersion theory, suggesting this procedure is completely inappropriate for a nonlinear system. Fortunately, this is not the case, and since the early days of nonlinear optics, many authors have addressed the K-K relations in the nonlinear regime.[35–39] The usefulness of these relations was not fully

appreciated until recently, however.[31,39,40] The key insight is that one can linearize the system; we view it as the material *plus* a strong perturbing light beam. This new linear system, which is different from the system in the presence of weak light, has a modified absorption spectrum. The linear Kramers-Kronig relation is applied in the presence of and in the absence of a high field perturbation, and we study the difference between these two regimes. It is important to appreciate the fact that our new system is causal even in the presence of an external perturbation. This allows us to write down a modified form of the Kramers-Kronig relation linking the index of refraction to the absorption[31,39]:

$$[n(\omega) + \Delta n(\omega;\zeta)] - 1 = \frac{c}{\pi} \int_{-\infty}^{\infty} \frac{\alpha(\omega') + \Delta\alpha(\omega';\zeta)}{\omega'^2 - \omega^2}\, d\omega' \tag{22}$$

After subtracting the linear terms n and α, we are left with a relationship between the changes in refractive index and change of absorption:

$$\Delta n(\omega;\zeta) = \frac{c}{\pi} \int_{0}^{\infty} \frac{\Delta\alpha(\omega';\zeta)}{\omega'^2 - \omega^2}\, d\omega' \tag{23}$$

where ζ denotes the perturbation. An equivalent relation also exists that allows calculation of the change in absorption coefficient, given the change in the refractive index. This relation is rarely used in practice for reasons described momentarily. In evaluating Eq. (23), it is essential that the perturbation be independent of the frequency of observation (ω'). In other words, the excitation ζ must remain constant as ω' is varied.

It is an interesting fact that calculation of the refractive index change from data obtained in nonlinear optics experiments is often easier than extracting the absolute refractive index from the K-K transform in linear optics! The reason is that absorption changes in nonlinear optics are usually strong only in a very limited frequency range; the integration range in Eq. (23) need only consider this spectrum. In contrast, evaluation of the linear index based on the linear absorption spectrum normally involves a much larger amount of data. One must take full account of the entire linear absorption data to obtain quantitative agreement with experiments that measure the refractive index. In the same way, the reverse transformation in nonlinear optics (obtaining $\Delta\alpha$ from Δn) is not as accommodating as the transformation of Eq. (23). Experiments show that irradiance-dependent changes of the refractive index occur over a relatively broad frequency spectrum. A large and impractical amount of nonlinear dispersion data must be collected and incorporated into a K-K calculation of nonlinear absorption. The reverse transformation is thus difficult to accomplish in practice.

Equation (23) has been used to determine refractive changes due to *real* excitations (i.e., $\chi^{(1)}$:$\chi^{(1)}$ cascaded processes) such as thermal and free-carrier nonlinearities in semiconductors.[41,42] In these examples, ζ denotes either change of temperature or change of free-carrier density, respectively. This K-K methodology has also been applied with great success to the situation where the perturbation is *virtual* or nonresonant. This work unified the bound-electronic Kerr effect in bulk semiconductors (i.e., the dispersive nonlinearity resulting from anharmonic motion of bound, valence electrons) to its absorptive counterparts: two-photon absorption, the electronic Raman effect, and the ac Stark effect.[31,39,43–45] The dispersion relation between α_2 and n_2 is given by:

$$n_2(\omega_a;\omega_b) = \frac{c}{\pi} \int_{0}^{\infty} \frac{\alpha_2(\omega';\omega_b)}{\omega'^2 - \omega_a^2}\, d\omega' \tag{24}$$

Note that in the general case we are dealing with two frequencies, ω_a and ω_b. Even in the degenerate situation (i.e., $n_2 = n_2(\omega_a;\omega_a)$) where we desire the nonlinear index coefficient at a single frequency ω_a, we are still required to provide the nondegenerate absorption spectrum $\alpha_2(\omega';\omega_b)$ at all frequencies ω' as input to the calculation. We also point out that Eq. (24) can

be used to derive relations linking the real and imaginary parts of the nonlinear susceptibility via Eq. (13) [the inverse transformation is obtained with Eq. (14)]:

$$\Re e\{\chi^{(3)}(\omega_a,\omega_b,-\omega_b)\} = \frac{2}{\pi}\int_0^{\infty}\frac{\omega'\Im m\{\chi^{(3)}(\omega',\omega_b,\omega_b)\}}{\omega'^2-\omega_a^2}\,d\omega' \tag{25}$$

Using the symmetry properties of $\chi^{(3)}$, an equivalent representation is:

$$\Re e\{\chi^{(3)}(\omega_a,\omega_b,-\omega_b)\} = \frac{1}{\pi}\int_{-\infty}^{\infty}\frac{\Im m\{\chi^{(3)}(\omega',\omega_b,\omega_b)\}}{\omega'-\omega_b}\,d\omega' \tag{26}$$

Equation (26) can be also be derived in a very general way from a first-principles approach that applies the causality condition directly in the temporal nonlinear response. In this way, one can obtain the dispersion relations for the n-th order optical susceptibility[39]:

$$\chi^{(n)}(\omega_1,\omega_2,\ldots,\omega_j,\ldots,\omega_n) = \frac{-i}{\pi}\int_{-\infty}^{\infty}\frac{\chi^{(n)}(\omega_1,\omega_2,\ldots,\omega',\ldots,\omega_n)}{\omega_j-\omega'}\,d\omega' \tag{27}$$

where $\chi^{(n)}$ is a complex quantity. By separating the real and imaginary parts of this equation, we get the generalized Kramers-Kronig relation for a nondegenerate, n-th order nonlinear susceptibility:

$$\Re e\,\chi^{(n)}(\omega_1,\omega_2,\ldots,\omega_j,\ldots,\omega_n) = \frac{1}{\pi}\int_{-\infty}^{\infty}\frac{\Im m\,\chi^{(n)}(\omega_1,\omega_2,\ldots,\omega',\ldots,\omega_n)}{\omega'-\omega_j}\,d\omega' \tag{28}$$

Note that for n = 3 with the substitutions $\omega_1 = \omega_a$, $\omega_2 = \omega_b$ and $\omega_3 = -\omega_b$, Eq. (28) becomes identical to Eq. (26). When the susceptibilities for generating frequency harmonics are included, Eq. (28) can be further generalized.[39] If we consider the $\chi^{(3)}$ associated with third-harmonic generation, it can be shown that:

$$\Re e\{\chi^{(3)}(+\omega,+\omega,+\omega)\} = \frac{1}{\pi}\int_{-\infty}^{\infty}\frac{\Im m\{\chi^{(3)}(+\omega',+\omega',+\omega')\}}{\omega'-\omega}\,d\omega' \tag{29}$$

Such relationships have been utilized in calculations of the total $\chi^{(3)}$ (THG) in semiconductors. It is computationally more convenient to first calculate the imaginary part because of the presence of δ-functions in its frequency domain. The real part is then calculated using the K-K dispersion relations.[46]

17.5 OPTICAL KERR EFFECT

The $\chi^{(3)}$ process leading to an intensity-dependent refractive index is known as the *optical Kerr effect* (OKE). Experimental observation is relatively straightforward, usually requiring just a single laser beam. The OKE is described by Eq. (15) where, for the sake of brevity, we ignore cross-modulation terms and drop the frequency terms to write:

$$n = n_0 + n_2 I \tag{30}$$

There are a variety of physical mechanisms that submit to this mathematical representation, many different ways to observe the effect experimentally, and an assortment of practical devices that can be built.

Optical transitions giving rise to a nonlinear susceptibility $\chi^{(3)}$ (see Figs. 1 and 2, for example) are intimately related to the energy eigenstates of the system. These eigenstates can be associated with bound electronic motion, molecular vibrations, or molecular rotations of the

system. Electronic transitions involve the largest energy separation and rotational transitions the smallest. In a given material (gas, liquid, or solid), one or more of these excitations may contribute to the optical Kerr effect. In general, the various contributions differ in their response time, magnitude, and frequency dependence. Referring to our earlier discussion of Eq. (6), the time response of an optical nonlinearity is governed by the virtual lifetime of the relevant transitions. This implies that the nonlinearities associated with the electronic transitions give the fastest response time because they possess large energy denominators. Experiments have shown that electronic nonlinearities are usually faster than the time resolution provided by the shortest optical pulses available at the time of this writing (< 10 fs). For practical purposes, then, the nonlinearity associated with the motion of bound electrons can be regarded as instantaneous. At the other extreme, the nonlinearity associated with rotational motion of molecules is relatively sluggish—response times in the picosecond regime have been measured. In the middle range are nonlinearities arising from molecular vibrations. For a Raman-type transition as shown in Fig. 2(*b*) this effect is manifest as the Raman Induced Kerr Effect (RIKE). We discuss two important cases of NLR: the bound electronic Kerr effect in solids (n_2), and the rotational (or orientational) Kerr effect in liquids.

Bound Electronic Optical Kerr Effect in Solids

The optical Kerr effect in solids has been extensively studied in materials ranging from large-gap dielectrics and glasses to narrow-gap semiconductors.[31,44,47–50] The fundamental energy gap E_g turns out to be a parameter of critical importance. Because of direct, linear absorption of the incident laser light, we are interested in the transparency regime where the photon frequency is less than the bandgap energy (i.e., $\omega < \omega_g = E_g/\hbar$). We estimate the response time (τ_r) of the nonlinearity using the virtual lifetime of the transition: $\tau_r \approx 1/|\omega - \omega_g|$. Far below the bandgap, where $\omega << \omega_g$, the response time can be very fast (<< 10 fs) and for most applications can be assumed as instantaneous. This ultrafast response has been exploited in soliton propagation in glass fibers[5,51] (Section 17.11) and in the generation of femtosecond pulses in solid-state lasers.[52] The optical Kerr effect also causes self-focusing, sometimes resulting in beam distortion and damage in transparent media (Section 17.11). Another significant application is the development of ultrafast all-optical-switching devices.[53,54] Although much progress has been made in this area of research, development of a practical switch has been hindered by the relatively small magnitude of bound-electronic nonlinearities.

The bound-electronic optical Kerr effect in optical solids has been analyzed using semi-empirical methods[55] and, more recently, by simple two-band models appropriate for semiconductors.[31,44] The latter treatment provides information about the dispersion, band-gap scaling, and the relationship between the NLA (e.g., two-photon absorption) and NLR through Kramers-Kronig transformation. The resulting simple formula allows one to predict the nonlinear refraction coefficient n_2 knowing only the photon frequency (ω), energy bandgap (E_g), and linear index (n_0):

$$n_2(m^2/W) = \frac{A}{n_0^2 E_g^4}\,\overline{G}_2\left(\frac{\hbar\omega}{E_g}\right) \tag{31}$$

where $A \approx 3 \times 10^{-35}$ (MKS); E_g is in Joules. The function $\overline{G}_2$ describes the normalized dispersion of the coefficient n_2 and is depicted in Fig. 3, along with the normalized two-photon absorption spectrum for bulk semiconductors (Section 17.8).

Recall that NLA and NLR correspond to the imaginary and real parts of the third-order susceptibility, respectively. The derivation of Eq. (31) by a Kramers-Kronig transformation required knowledge of the NLA spectrum. Three different mechanisms of NLA were employed in the analysis, corresponding to the three relevant time-ordering sequences depicted in Fig. 2: two-photon absorption, electronic Raman scattering, and the optical (ac) Stark shift of electronic states. The optical Stark effect is a change of the fundamental energy gap that

occurs when the oscillating laser field becomes comparable to the electric field binding valence electrons to the positively charge nuclei. In experiments where only a single beam is used (i.e., all the input frequencies are the same), the only observable NLA effect is two-photon absorption, which is discussed in Section 17.8.

The plot of the dispersion function $\overline{G}_2$ (Fig. 3) is consistent with our intuitive arguments about resonance enhancement presented in Section 17.2. At long wavelengths (i.e., for $\hbar\omega << E_g$), we are far from resonance so $\overline{G}_2 \approx 1$ and is nearly frequency independent (i.e., there is very weak dispersion). Approaching the two-photon resonance (i.e., as $2\hbar\omega$ gets close to E_g), there is an approximately fivefold enhancement of n_2. With increasing photon energy, the sign of n_2 reverses; this is a direct consequence of the sign change in the energy denominator associated with two-photon absorption. With further photon energy increase, there is enhancement due to resonances ascribed to two-photon absorption and the optical Stark effect. The inverse fourth-power bandgap scaling (i.e., E_g^{-4}) and the dispersion predicted by this simple expression display remarkable agreement with data obtained with many different semiconductors and dielectrics.[44]

Reorientational Kerr Effect in Liquids

The reorientational Kerr effect involves transitions between rotational energy levels of a molecule. It is nonresonant and therefore associated with the real part of $\chi^{(3)}$. The absorptive nonlinearity associated with these rotational levels gives an imaginary component to $\chi^{(3)}$; this is a Raman-type transition known as *Rayleigh-wing scattering*.[3,17] For simplicity, we make a classical description of this phenomenon. Consider a carbon disulfide (CS_2) molecule as shown in Fig. 4. This is a cigar-shaped molecule with different polarizabilities along its principal axes (here we show $\alpha_3 > \alpha_1$). As discussed in Section 17.7, the polarizability describes the propensity for an external field to produce a dipole in a molecule. In the first step of the interaction, the optical field polarizes this molecule (i.e., induces a dipole moment). The induced dipole interacts with the applied field and aligns itself along the direction of polarization. This molecular reorientation (rotation) causes a birefringence in an isotropic solution; initially, the

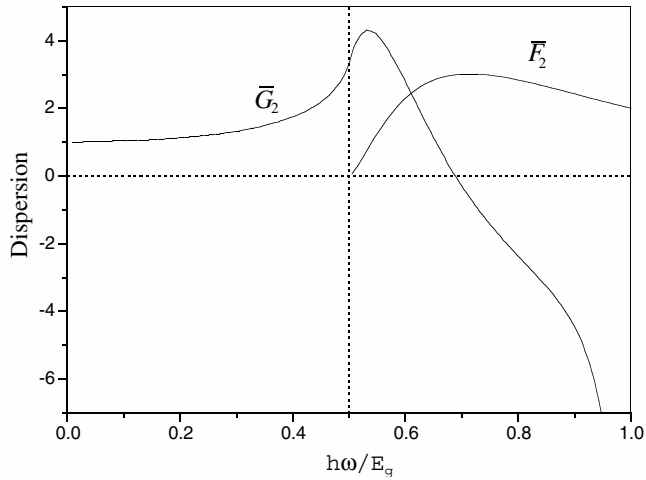

FIGURE 3 Calculated dispersion of nonlinear absorption. Also shown is the two-photon absorption spectrum.

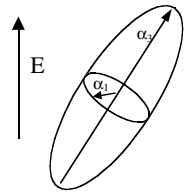

FIGURE 4 Simple picture of CS_2 molecule.

molecules were randomly oriented and there was no birefringence. The response time of the molecule depends on its mass: the heavier molecule, the slower the response. As an example, CS_2 has a reorientational $n_2 \approx 3.4 \times 10^{-18}$ m^2/W with a relaxation time $\tau \approx 1$ to 2 ps.[56]

17.6 THIRD-HARMONIC GENERATION

In crystals where there is no inversion symmetry, $\chi^{(2)}$ vanishes, making sum and difference frequency mixing impossible. The possibility of third-harmonic generation always exists in principle, although it usually suffers from practical drawbacks. Typical values of $\chi^{(3)}$ are orders of magnitude smaller than $\chi^{(2)}$ coefficients found in popular frequency conversion crystals. This means the laser irradiance must be increased to compensate, often leading to material damage. Moreover, third-harmonic generation in crystals is usually difficult to phase match. Because of these obstacles, cascading of two second-order effects (second-harmonic generation, followed by sum-frequency generation) in two separate crystals is usually the preferred method of obtaining high multiples of the pump laser frequency (see Section 17.10).

Gases do not have the damage limitations of crystals. Third-harmonic generation was extensively studied in many different gases around the time that high-power, Q-switched lasers became widely available, and conversion efficiencies as high as several percent were obtained. Studies of sodium vapor have been helpful in elucidating the resonant enhancement that occurs near ω, 2ω, and 3ω.

17.7 STIMULATED SCATTERING

Useful spectroscopic information can be obtained when light is scattered from material, often at frequencies far removed from absorption and emission resonances. Spontaneous scattering is a linear process, in which the material is unmodified by the probing light beam. The various forms of spontaneous scattering (Raman, Brillouin, and Rayleigh) have been known for the better part of a century. In the presence of a sufficiently intense laser beam, however, these scattering processes can be strongly amplified by a nonlinear interaction of the excitation beam with the material, resulting in stimulated scattering.

Raman scattering is most commonly described as the interaction of light with vibrational waves in a material. (Electronic and magnetic excitations can also be measured in Raman experiments.) These vibrational frequencies are typically in the infrared, meaning that Raman-scattered light can have a substantial spectral shift with respect to near-infrared or visible excitation light. Brillouin scattering involves the interaction of light with acoustic waves—waves associated with the propagation of pressure in the medium, leading to periodic density fluctuations. Acoustic waves occur at frequencies that are orders of magnitude smaller than material vibrations; Brillouin scattered light is therefore frequency-shifted from the incident light by a much smaller amount. Rayleigh scattering results from the interaction of light with stationary density variations—variations much smaller than the wavelength of

the incident light. Scattering takes place without any frequency shift relative to the incident light. Rayleigh scattering is of interest because of its strong wavelength dependence and polarization properties. Spontaneous scattering processes scale linearly with input irradiance.

Stimulated Raman Scattering

In Raman scattering (Fig. 5), a photon is absorbed by a material that makes a quantum-mechanical transition from a low energy state |1> to a high energy state |2>. At some short time later (i.e., not instantaneously), the material relaxes to a lower energy state |3> different from the original state, giving up its energy in the form of a photon of different energy than the excitation photon. If the lower state |3> is at a higher energy than state |1>, the emitted photon will be at a longer wavelength than the excitation light. This is called *Stokes shifted Raman scattering.* If the terminal state |3> is at a lower energy than state |1>, the emitted photon will be shorter in wavelength than the incident light, leading to *anti-Stokes shifted Raman scattering.* The difference between the incident and emitted light thus provides information about the relative positions of the different energy levels. Maintaining the same nomenclature, there is also Stokes and anti-Stokes shifted Brillouin scattering. Note that when state |1> and |3> are the same, there is no frequency shift and we have Rayleigh scattering.

The intermediate state can be a real state corresponding to a quantum mechanical energy level of the system; this is known as *resonant Raman scattering.* In the theme of this chapter, resonant Raman scattering is an example of a cascaded linear process leading to an effective $\chi^{(3)}$. More often, the intermediate level is not resonant with the photon, and the transition from |1> to |2> is virtual (illustrated by a horizontal dotted line in Fig. 5). The distinction between the resonant and nonresonant processes can be confusing because both are referred to as Raman scattering. To maintain consistency with standard nomenclature, we briefly depart from the logical organization of this chapter and discuss both resonant and nonresonant Raman scattering in this section.

The essential physics of Raman scattering can be understood from the classical picture of a diatomic molecule of identical atoms vibrating back and forth at frequency ω_L. The diatomic molecule is an illustrative example; in principle all Raman-active and some normal modes of vibration of a solid, liquid, or gas can be probed with Raman techniques.[57] We assume that the electronic charge distribution on the molecule is perfectly symmetric, hence there is no permanent dipole or a dipole moment modulated by the vibration. This normal mode is therefore not dipole active, that is, it cannot absorb electromagnetic radiation (see Vol. I, Chap. 9).

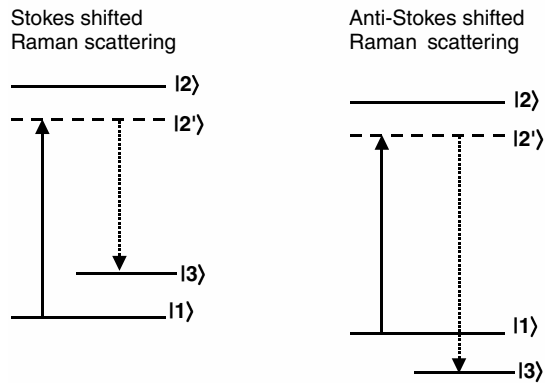

FIGURE 5 Raman scattering.

When an external electric field is applied, the situation changes. The field in an electromagnetic wave polarizes the charge distribution on the molecule and it acquires a dipole. If the induced dipole is also modulated by a normal mode of vibration, the mode is said to be Raman active. The extent to which an external field can polarize the molecule is quantified by the following equation:

$$\mathbf{p}(r,t) = \alpha \mathbf{E}(r,t) \tag{33}$$

where $\mathbf{p}(r,t)$ is the induced dipole moment, α is the polarizability, $\mathbf{E}(r,t)$ is the time- and spatially-varying electric field, and bold type denotes vector quantities. The polarizability is not constant, however, but rather is a function of the molecular separation distance q. Writing the first two terms of a Taylor series expansion of $\alpha(q)$ we have:

$$\alpha(q) = \alpha_o + \left(\frac{\partial \alpha}{\partial q}\right)_{qo} q \tag{33}$$

where α_0 is a constant representing the polarizability at the equilibrium position of the molecule (q_o). The molecule vibrates at a frequency $\pm\omega_L$, which is the energy difference between the states |1> and |3> in Fig. 5, hence:

$$q = q_o \exp(\pm i\omega_L t) \tag{34}$$

Inserting Eqs. (33) and (34) into (32), and realizing that the electromagnetic field varies sinusoidally at the optical frequency ω, we find that the second term in the polarizability expansion is responsible for the appearance of induced dipoles oscillating at a frequency offset from the incident electromagnetic wave by $\pm\omega_L$:

$$\mathrm{p}(r,t)_{\mathrm{Raman}} = \mathrm{E}_o(r)\left(\frac{\partial \alpha}{\partial q}\right)_{qo} q_o \exp(i\omega t \pm \mathrm{i}\omega_L t) \tag{35}$$

These dipoles can radiate and are the origin of spontaneous Raman scattering. There is also an oscillating dipole unaffected by the vibration corresponding to the term α_o. This dipole oscillation is exactly at the frequency of the incident light and corresponds to spontaneous Rayleigh scattering:

$$\mathrm{p}(r,t)_{\mathrm{Rayleigh}} = \mathrm{E}_o(r)\alpha_o \exp(i\omega t) \tag{36}$$

In stimulated scattering, we have to consider the force exerted on the vibrating molecule by the external field as a consequence of its polarizability. This force involves only the second term in Eq. (33):

$$F = \frac{1}{2}\left(\frac{\partial \alpha}{\partial q}\right)_{qo} \langle E^2(r,t)\rangle \tag{37}$$

where the angular brackets represent a time average over an optical period. In a dipole-active interaction, the lowest order forcing term is proportional to E, resulting in linear absorption of light. In the case of a Raman-active mode, Eq. (37) shows the force scales as E^2; therefore the force is nonlinear in the field. The forcing term is negligible at low light intensities, but becomes important when large electromagnetic field levels generated by lasers are encountered.

Because the Raman active mode of the molecule is subject to a force proportional to E^2, there must be two input photons driving the interaction. If the two photons are at different frequencies, the molecule will experience a force at the beat frequency of the two photons. If the wavelengths of the two photons are chosen so that their beat frequency equals that of the molecular vibration ω_L, strong amplification of all three waves (two input electromagnetic waves and the molecular vibration) can occur, resulting in stimulated scattering. The molecular polarizability thus acts as a nonlinear mixing term to reinforce and amplify the interacting

waves. It is important to realize this is of practical consequence only when the input electromagnetic fields are sufficiently high.

The nonlinear polarizability impresses sidebands on the pump light, resulting in three distinct electromagnetic waves (laser beam, Stokes shifted Raman, and anti-Stokes shifted Raman) propagating in the medium. The same nonlinear mixing process that led to the generation of the Raman sidebands in the first place can cause coherent excitation of additional molecules due to their polarizability. In this way, a coherent vibrational wave builds up, which in turn feeds more energy into the Raman-shifted components, thus amplifying them. In stimulated scattering, the fluctuations of the optical medium (vibrations, density variations, etc.) are *induced* and *amplified* by the external electromagnetic radiation. In contrast, spontaneous scattering originates from the naturally occurring (thermally driven, for example) fluctuations of the material. Because the linear optical properties of the medium are modified by the presence of an exciting laser beam (specifically its irradiance), the various stimulated scattering mechanisms are classified as third-order nonlinear optical processes.

In stimulated Raman scattering (SRS), one is most often looking for a new frequency generation at the wavelength corresponding to the energy difference of levels $|2'>$ (or $|2>$) and $|3>$ shown in Fig. 5. Stimulated Raman gain and loss applied to an input beam at this frequency can be obtained as well. Polarization effects occurring in the nonlinear wave mixing process can also be studied in what is known as *Raman-induced Kerr effect spectroscopy* (RIKES, see Vol. II, Chap. 36). We also mention two other classes of third-order nonlinear spectroscopy: coherent anti-Stokes Raman spectroscopy (CARS) and coherent Stokes Raman spectroscopy (CSRS). In these interactions, illustrated in Fig. 6, two external laser fields at frequencies ω_1 and ω_2 are supplied. There must be a third-order nonlinear polarization present as in SRS, leading to frequency mixing and new wavelengths.

The somewhat subtle differences distinguishing SRS, CARS, and CSRS are the number and location of intermediate levels (designated by dashed lines in Fig. 6). Consider two excitation frequencies with $\omega_1 > \omega_2$ probing a given material system with real energy levels separated by frequency ω_L in Fig. 6. In CARS, short-wavelength photons are detected at $\omega_{as} =$

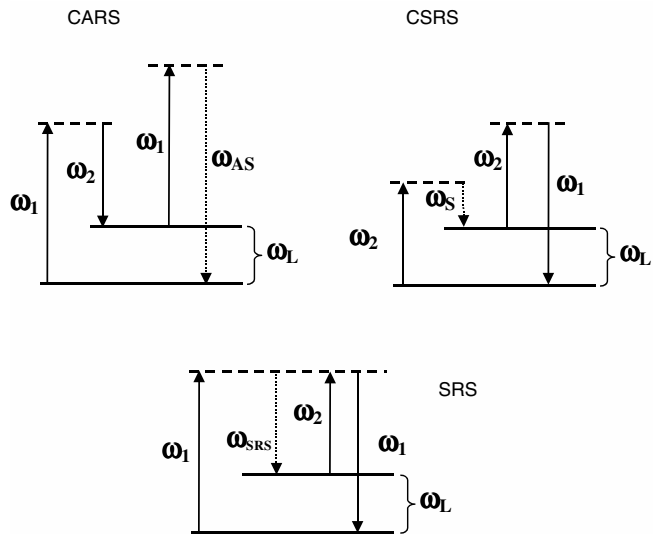

FIGURE 6 Stimulated Raman processes.

$2\omega_1 - \omega_2$. For the CSRS arrangement, the excited intermediate states are at lower energy and a longer-wavelength photon at frequency $\omega_s = 2\omega_2 - \omega_1$ is detected. Note that SRS is obtained when the intermediate levels are degenerate; SRS is thus a special case of the nonlinear interaction. In linear, spontaneous Raman scattering, a single exciting electromagnetic wave is required. In SRS, two input fields are involved; they just happen to be at the same frequency and invariably are supplied by a single laser source. Unlike spontaneous Raman scattering, however, SRS is a function of the third-order nonlinear susceptibility and hence depends nonlinearly on the irradiance of the excitation laser.

It is important to emphasize that all three of these stimulated Raman processes (SRS, CARS, and CSRS) are essentially a mixing of three waves to produce a fourth wave via the third-order nonlinear polarization. Analysis of the problem is made using second-order perturbation theory in quantum mechanics. The tensor nature of the third-order susceptibility and the multitude of ways the interacting waves of various polarization states can mix lead to complicated expressions. One finds resonance denominators quantifying the efficiency of the wave mixing process. The scattering efficiency is governed by the proximity of photon energies to real energy eigenstates in the system. In principle, SRS, CSRS, and CARS can all take place in an experiment; the various generated beams can be distinguished by substantially different angles of propagation when leaving the irradiated sample. These angles are readily determined by phase-matching conditions for the nonlinear interaction. The wave-vectors of the interacting photons can be arranged for maximum output signal of the desired Raman process. The phase-matching condition is obtained automatically in SRS, but careful orientation of the interacting beams can lead to very narrow linewidths and extremely accurate spectroscopic measurements. Some applications of stimulated Raman scattering include high-resolution spectroscopy of gases,[11,17,58,59] spin-flip Raman scattering, stimulated polariton (the quanta of photon-phonon coupling) scattering, and ultrafast time-resolved measurements.[60,61] The reader should also be aware that Raman spectroscopy beyond the third-order nonlinear susceptibility has been demonstrated. Further information can be obtained in texts on nonlinear laser spectroscopy.[3,6,10,16,62–65]

Stimulated Brillouin Scattering

Stimulated Brillouin scattering (SBS) is an important third-order nonlinear optical effect that has been widely used for efficient phase conjugate reflection of high-power lasers.[26] An incident laser beam can scatter with the periodic refractive index variations associated with a propagating acoustic wave. The scattered light, depending on the propagation direction of the acoustic wave, will be Stokes or anti-Stokes shifted by the frequency of the acoustic wave. The process is stimulated because the interference of the incident and scattered wave can lead to an amplification of the acoustic wave, which then tends to pump more energy into the scattered wave. This positive feedback process can cause an exponential growth of the SBS beam and very high efficiencies in the right circumstances. Optical feedback to the medium is accomplished in one of two ways: (1) *electrostriction* is local compression of the material in response to the strength of the electromagnetic field with a commensurate refractive index change; and (2) *linear optical absorption* by the laser field leads to local heating, expansion, density fluctuations, and thus periodic modulation of the refractive index. The latter effect is an example of a cascaded χ^{1}:χ^{1} process, which is the subject of Section 17.9. Electrostriction is usually associated with SBS, and we discuss it here.

Consider again the diatomic molecule that was used to illustrate the Raman effect. In the presence of an external electric field, it acquires a polarizability described by Eq. (33). As we have seen, the induced dipole can interact with the field. Electrostriction accounts for the ability of the electric field to do work on the polarized molecule—pulling and pushing it by electrostatic forces. The molecules will move and tend to pile up in regions of high field, increasing the local density. Associated with these density changes will be a change of refractive index. Density fluctuations can also be generated by the change in pressure that accompanies a propagating acoustic wave: Pressure nodes will exist in the peaks and valleys of the acoustic wave. Electrostriction therefore provides a coupling mechanism between acoustic waves and electromagnetic waves.

It is important to emphasize that the periodic modulations in an electrostrictive medium are propagating spatial fluctuations modulated at the frequency of traveling acoustic waves. When the density fluctuations are stationary, we can have stimulated Rayleigh scattering. A thorough, detailed discussion of the many (often intricate) issues in stimulated Brillouin and Rayleigh scattering can be found in textbooks on nonlinear optics.[3,11,16,17,28]

17.8 TWO-PHOTON ABSORPTION

Two-photon absorption (2PA) is the process by which the energy gap between two real states is bridged by the simultaneous (in the context of the Uncertainty Principle discussed in Section 17.2) absorption of two photons, not necessarily at the same frequency. Both photons have insufficient energy to complete the transition alone; 2PA is thus observed in the spectral range where the material is normally transparent. When the two photons are present together for a fleeting instant of time determined by the Uncertainty Principle, an optical transition can take place.

Quantum mechanically, we can think of the first photon making a virtual transition to a nonexistent state between the upper and lower levels [Fig. 2(*c*)]. If the second photon appears within the virtual lifetime of that state, the absorption sequence to the upper state can be completed. If not, the virtual transition collapses back to the ground state, and no absorption takes place. To have an appreciable rate of 2PA, photons must be supplied at a rate high enough that there is a reasonable probability two photons will both be present during the virtual lifetime. Because the virtual lifetime is so short, photon fluxes must be high, and therefore power levels from laser beams are required.

The efficiency of 2PA is affected by the proximity of the input photons to a real state of the system. It is important to note that there must be an allowed optical transition linking the initial state and this real state. The closer one of the input photons coincides with a real state, the stronger the 2PA. When the intermediate state of 2PA is also a system resonance, the situation is commonly referred to as *excited state absorption* (ESA)—a sequence of two linear absorption processes that leads to an effective third-order nonlinearity. Excited state absorption is thus a cascaded $\chi^{(1)}$:$\chi^{(1)}$ effect, giving rise to an effective third-order nonlinearity (Section 17.9). It has implications for optical power limiting and is discussed in Chap. 19 of this handbook.

In stimulated scattering, the *difference* frequency of two input electromagnetic fields $\hbar\omega_i - \hbar\omega_j$ equals a characteristic energy resonance of the material system. In 2PA, an energy resonance exists at the *sum* of the two input fields: $\hbar\omega_i + \hbar\omega_j$. In Sections 17.2 and 17.3, 2PA was shown to be associated with the imaginary part of $\chi^{(3)}$. This is because it is an absorption process (i.e., it is exactly resonant with two eigenstates of the system). It is the only NLA process (i.e., a process associated with the imaginary part of $\chi^{(3)}$) that can be simply studied with a single photon frequency.

Two-photon absorption in semiconductors is one of the most thoroughly studied subjects in the entire field of nonlinear optics.[66] The 2PA coefficient (often written β or α_2^{2PA}) of bulk semiconductors has been calculated using models involving only two parabolic bands and also with more complex band structure.[67] It is defined by the rate of electron-hole pair excitation: $dN/dt = \beta I^2/(2\hbar\omega)$. The two-parabolic band model gives a comparatively simple yet general and accurate description of 2PA for a large class of semiconductors. The theoretical result for single frequency excitation can be expressed as:

$$\beta(m/W) \simeq \frac{B}{n_0^2 E_g^3}\,\overline{F}_2\left(\frac{\hbar\omega}{E_g}\right) \tag{38}$$

where $\overline{F}_2(x) = 2(2x-1)^{3/2}/x^5$ and $B = 5.67 \times 10^{-66}$ ($x = \hbar\omega/E_g$ and the energy bandgap E_g is in Joules). The best empirical fit to experimental data is obtained with B adjusted to a slightly higher value of 9.06×10^{-66}. The function $\overline{F}_2$ describes the dispersion of 2PA and is plotted in

Fig. 3. The intimate relation between NLA and NLR and the role of 2PA in semiconductors is explored in Section 17.4 and in References 31 and 67 to 69. There are important practical implications for 2PA in semiconductors and dielectrics. It can enhance or degrade optical switching performance in semiconductor devices and lead to optical damage in laser window materials. 2PA is also the basis of Doppler-free spectroscopy of gases.[57,59]

17.9 EFFECTIVE THIRD-ORDER NONLINEARITIES; CASCADED $\chi^1{:}\chi^1$ PROCESSES

Effective third-order nonlinearities occur when one of the transitions in our four-photon interaction picture is resonant, providing a path of linear absorption. Linear absorption is a mechanism to directly couple laser light into the system—with sufficiently intense laser light, the linear optical properties of a material can be modified. An effective third-order nonlinearity occurs when linear absorption affects the refractive index. We give some examples here.

Optically Generated Plasmas

Optical generation of stable plasmas is readily obtained in semiconductors and most studies of this subject have been made with these materials (Vol. I, Chap. 9 and Vol. II, Chap. 36). For cascaded linear processes that we discuss here, the formation of a free electron-hole pair occurs by direct bandgap excitation by an incident photon. The optically produced carriers augment the background electron-hole density, and the plasma remains electrostatically neutral. If the generation of an excess amount of plasma exceeds the rate of loss (by recombination or diffusion) on the time scale of interest, the plasma will modify the linear optical properties of the semiconducting material. The simplest way to see this is via the classical Drude model, where the refractive index of a metal or semiconductor is[70,71]:

$$n = n_0 \sqrt{1 - \frac{\omega_p^{\,2}}{\omega^2}} \tag{39}$$

In this equation, ω is the angular frequency of the light, n_0 is the linear index in the absence of significant free carrier density, and ω_p is the density-dependent plasma frequency:

$$\omega_p = \sqrt{\frac{Ne^2}{m\varepsilon}} \tag{40}$$

where N is the electron-hole pair density, e is the electronic charge, m is the reduced mass of the positive and negative charge carriers (electrons, holes, or ions), and ε is an appropriate background dielectric constant. Note that as the carrier density increases, the refractive index decreases. The material is usually excited by a laser beam with a nonuniform spatial profile such as a Gaussian, giving rise to negative-lensing and self-defocusing, assuming $\omega < \omega_p$.

The situation becomes complicated at densities where many-body effects become important or when the Drude model ceases to be valid. We also note that optical generation of plasmas can also occur as the result of nonlinear mechanisms in the presence of high laser fields, and we aren't, of course, restricted only to solid-state plasmas. Examples of nonlinear plasma production are multiphoton absorption, laser-induced impact ionization, and tunneling. Because plasma generation and the concomitant refractive index modification are caused by a nonlinear optical process, the order of the nonlinearity is higher than three. Although high-order nonlinearities are a rich subset of the field, they are not dealt with in this chapter. A number of review articles and textbooks on laser-induced change to the refractive index due to plasma generation via linear absorption are available.[31,42,72–74]

Absorption Saturation

Absorption saturation is a well-known example of a cascaded linear process. Consider a homogeneously broadened system of two-level atoms (i.e., a system of identical two-level atoms) with the energy diagram shown in Fig. 7. The lower and upper states are resonant with a photon depicted by the vertical arrow, and there is linear absorption of incident light. Associated with the absorption is a spectral linewidth (with a Lorentzian shape for a homogeneous system), illustrated on the right side of the diagram in Fig. 7. An induced dipole or polarization is set up between the two states upon excitation by a photon. The states are coherently coupled, and this coherence is in phase with the exciting electromagnetic field. In a real system, this coherence will be quickly destroyed by collisions with other atoms. The rate at which the coherence is washed out determines the spectral width of the absorption profile and hence the frequency response of the imaginary component of the linear susceptibility. The real part of the linear susceptibility is obtained by the Kramers-Kronig transformation, giving rise to what is traditionally known as anomalous dispersion of the refractive index shown on the left side of Fig. 7. Note that the refractive index is positive for frequencies below resonance and negative at frequencies above it.

We have assumed that the rate at which photons are supplied to the system produces a negligible change of population in the upper and lower states. This means that the rate of population relaxation (recombination and diffusion, for example) is much faster than excitation. When the incident irradiance is sufficiently high, however, this may no longer be the case. The upper level can become appreciably occupied, reducing the availability of terminal states for optical transitions. The absorption thus decreases or bleaches, indicated by the dashed lines in Fig. 7. Associated with the change of absorption is a change of refractive index. The relationship between absorption and refraction can again be handled with the Kramers-Kronig transformation *provided* we consider the system as being composed of both the atoms *and* the input light beam, specifically the nonequilibrium change of population created by the input light. This is exactly the same mathematical formulation used in the description of nonresonant third-order nonlinearities introduced in Section 17.4. The difference here is that the absorption of photons is a resonant, linear process. The linear absorption of light then affects the linear optical properties of absorption and dispersion. Because the reduction of absorption depends directly on laser irradiance, it behaves like a third-order nonlinearity. We point out that the resonant nature of absorption saturation (and the associated nonlinear refraction) can lead to an unacceptable deviation from a third-order susceptibility description when the input irradiance goes even higher. In the high-power regime, a nonperturbative approach (i.e., not represented by a power series expansion) must be used.[75]

Absorption saturation spectroscopy (with emphasis on gases) is discussed at length in Ref. 59. It is also a principle nonlinear effect in bulk and quantum-confined semiconductors (where the simple two-level picture previously outlined must be substantially modified), having implications for optical switching and bistability.[42,53,72,76]

We briefly mention the density matrix (see Vol. II, Chap. 38[76], "Nonlinear Optics"). This is a powerful method of analysis for the resonant interaction of light with a two-level system. In

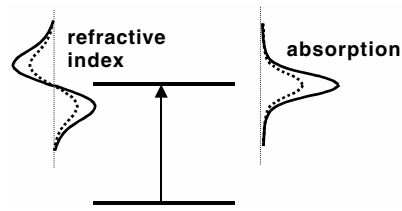

FIGURE 7 Absorption saturation and refraction of a two-level atomic system.

addition to absorption saturation, the nonlinear optical effects described by the density matrix include Rabi oscillations, photon echoes, optical nutation, superradiance, self-induced transparency, and optical-free induction decay, which are not immediately associated with a third-order nonlinearity derived from a perturbation expansion of the polarization. Experimental manifestations of these phenomena, however, can often be represented by an effective third-order nonlinearity. The nonlinear optics of the two-level system and the associated optical Bloch equations derived from the density matrix formulation of the problem are discussed in Chapter 24, "Coherent Optical Transients." The reader is also referred to many excellent textbooks and monographs.[3,11,24,77,78]

Thermal Effects

Linear absorption of light must result in energy deposition in the irradiated material. If the rate of energy deposition significantly exceeds its rate of removal, heating can take place. As the energy of a collection of atoms and molecules increases, it's easy to understand that their macroscopic optical properties will be altered. When there is a linear relationship between laser irradiance and the refractive index, an effective third-order nonlinearity will result. The thermo-optic effect has a relatively straightforward physical interpretation and is arguably one of the most important optical nonlinearities. It is often the power-limiting mechanism of a high-power solid-state laser—where excessive circulating optical flux can cause *thermal blooming* in the laser crystal. This heat-induced lensing effect can destroy the beam quality. Thermal-index coefficients have been extensively tabulated, and the reader is referred to Refs. 18 and 42.

Photorefraction

Photorefraction results from the spatial redistribution of electrons and/or holes in a solid (see Vol. II, Chap. 39, "Photorefractive Materials and Devices"). Electron-hole pairs are generated by linear absorption of laser light. If the excitation geometry produces a spatial modulation of irradiance such as a two-beam interference pattern, the electrons and holes will arrange themselves in accordance with the spatial irradiance profile. Often the linear absorption involves impurity levels. Mobile carriers tend to diffuse from the bright regions, leaving fixed charges behind. If a sinusoidally modulated, two-beam interference fringe pattern is written in a doped photorefractive crystal, for example, fixed charges of ionized states will be prevalent in the high irradiance regions while mobile charge carriers will tend to accumulate in regions with low light levels. A modulated space charge must exist, and therefore a modulated electric field pattern must be present as well. This field alters the refractive index via the linear electro-optic effect (i.e., Pockel's effect). The photorefractive nonlinearity is clearly nonlocal, as it requires a spatial modulation of charge density. Manipulation of the carriers can also be obtained with static electric fields, and the response time tends to be of the order of seconds.[3,18,79,80]

17.10 EFFECTIVE THIRD-ORDER NONLINEARITIES; CASCADED $\chi^{(2)}$:$\chi^{(2)}$ PROCESSES

Materials lacking a center of inversion symmetry have nonzero $\chi^{(2)}$ and exhibit a second-order nonlinear polarization. This is the second term in the polarization power series expansion of Eq. (1) that is responsible for the most well-known effects in nonlinear optics, including second-harmonic generation (sum and difference frequency generation, optical rectification), and

optical parametric processes (see Chap. 22, "Optical Parametric Oscillators"). It is also possible to cascade two $\chi^{(2)}$ processes to produce an effect that mimics a $\chi^{(3)}$ process. The most common and efficient way of producing THG, for example, is by a $\chi^{(2)}$ cascade process. In this interaction, an input source at ω generates SHG via the second-order susceptibility $\chi^{(2)}$ ($2\omega = \omega + \omega$); the second harmonic and fundamental then mix in a second (or the same) nonlinear crystal to produce the third harmonic by sum frequency generation $\chi^{(2)}(3\omega = 2\omega + \omega)$. This type of nonlinearity is nonlocal because the two processes (SHG and SFG) take place in spatially separate regions.

In addition to THG, all other $\chi^{(3)}$ effects have an analogous process in $\chi^{(2)}$:$\chi^{(2)}$ cascading. Consider the case where we have one frequency ω. The corresponding cascaded $\chi^{(2)}$ effects are depicted in Fig. 8. Recall that the intrinsic $\chi^{(3)}$ is manifest as: (1) THG, (2) 2PA, and (3) the ac Stark effect. The horizontal block arrows indicate the point of cascade (i.e., the propagation of the beams between the two $\chi^{(2)}$ interactions). There are always two distinguishable $\chi^{(2)}$ interaction regions; hence $\chi^{(2)}$:$\chi^{(2)}$ is clearly nonlocal. We also point out that in general the photon frequencies can be different.

Although the analogy is limited, cascaded $\chi^{(2)}$ effects exhibit NLA and NLR mimicking $\chi^{(3)}$. In the case of SHG, for example, the manifestation of $\chi^{(3)}$ NLA is depletion of the pump beam. The utility of cascaded $\chi^{(2)}$:$\chi^{(2)}$ for producing large nonlinear phase shifts has been realized only recently.[81–83] The analysis of $\chi^{(2)}$ is relatively straightforward, involving the coupled amplitude equations governing the propagation of the interacting beams. For example, the nonlinear phase shift imposed on a fundamental beam (ω) as it propagates through an SHG crystal of length L with a phase mismatch $\Delta k = k(2\omega) - 2k(\omega)$ and assuming small depletion is[82]:

$$\Delta\phi \approx \tan^{-1}\left(\frac{\Delta kL}{2}\,\frac{\tan(\beta L)}{\beta L}\right) - \frac{\Delta kL}{2} \tag{41}$$

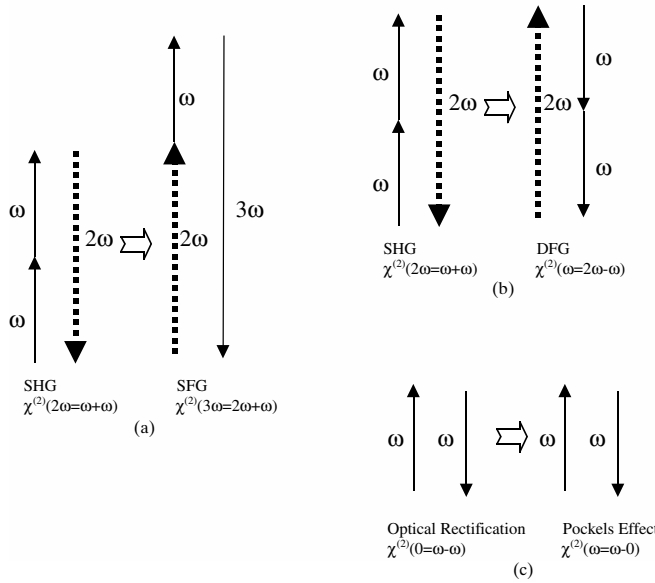

FIGURE 8 Cascaded $\chi^{(2)}$:$\chi^{(2)}$ effective third-order nonlinearities.

where $\beta = \sqrt{(\Delta kL/2)^2 + \Gamma^2}$, $\Gamma = \omega\chi^{(2)}\,|E_0|/2c\sqrt{n(2\omega)n(\omega)}$, and E_0 denotes the electric field of the fundamental beam. An effective $\chi^{(3)}$ can be obtained if we expand $\Delta\phi$ to lowest order in Γ and use $\Delta\phi = \omega L n_2^{\text{eff}}\, I/c$ to give[84]:

$$n_2^{\text{eff}} = \frac{8}{c^2 4\pi\varepsilon_0}\,\frac{\omega d_{\text{eff}}^2 L}{n^2(\omega)n(2\omega)}\left[\frac{\pi}{\Delta kL}\left(1 - \frac{\sin(\Delta kL)}{\Delta kL}\right)\right] \tag{42}$$

Here $d_{\text{eff}} = \chi^{(2)}(2\omega = \omega + \omega)/2$ is the effective tensor component of the second-order nonlinear susceptibility for a given experimental geometry.

Phase mismatch is represented by the bracketed term in Eq. (42), plotted in Fig. 9. Also shown in Fig. 9 is the depletion of the fundamental beam which, on the same level of approximation, can be regarded as an effective two-photon absorption coefficient that scales as $\beta^{\text{eff}} \sim \text{sinc}^2\,(\Delta kL)$. Cascaded $\chi^{(2)}$ leads to an effective refractive index modulation (n_2^{eff}) and two-photon absorption (β^{eff}), but one should not conclude that the material's index of refraction is altered or energy is deposited in the material. These coefficients describe only nonlinear phase shifts and the conversion of the fundamental beam to second-harmonic beams. The nonlinear phase shift from the $\chi^{(2)}$:$\chi^{(2)}$ process has been used to demonstrate nonlinear effects analogous to those observed previously with the intrinsic optical Kerr effect. These include self-focusing and self-defocusing,[81] all-optical switching,[85,86] soliton propagation,[87,88] and laser mode-locking.[89]

17.11 PROPAGATION EFFECTS

When the nonlinear optical polarization $P^{\text{NL}}(t)$ is known, the propagation of optical fields in a nonlinear medium can be analyzed with the aid of Maxwell's equations:

$$\nabla \times \nabla \times E + \frac{1}{c^2}\,\frac{\partial^2 E}{\partial t^2} = -\mu\,\frac{\partial^2 P}{\partial t^2} \tag{43}$$

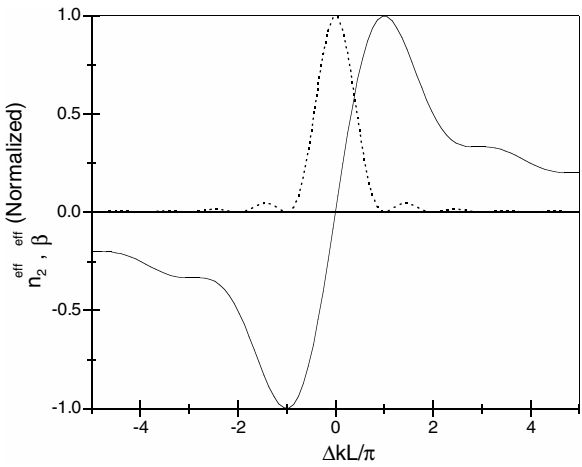

FIGURE 9 Calculated phase shifts in cascaded $\chi^{(2)}$:$\chi^{(2)}$.

where P(t) is the total polarization including the linear and nonlinear terms. The slowly varying envelope approximation is then usually made to reduce the above equation to a system of four coupled nonlinear differential equations for the four interacting fields. For *thin* nonlinear media, where there is no significant distortion of the spatial beam and temporal shape upon propagation, the problem simplifies greatly. Equations (19) and (20) were obtained with this approximation. For *thick* nonlinear media, however, linear and nonlinear diffraction as well as dispersion cannot be ignored. In this section, we discuss two important propagation phenomena: *self-focusing* and *soliton formation.*

Self-Focusing

Self-focusing occurs in materials with a positive intensity-dependent refractive index coefficient ($n_2 > 0$). Self-focusing (or *Kerr-lensing*) causes spatial collapse of the laser beam when it propagates through transparent optical materials, often leading to optical damage. It is a consequence of the nonuniform spatial profile of the laser beam.[2,3,17,18] For a *thin* nonlinear material, one makes the so-called parabolic approximation for the nonlinear phase shift to obtain an approximate Kerr-lens focal length, assuming a Gaussian beam of radius w (1/e of the electric field profile)[90]:

$$f_{\mathrm{NL}} \simeq \frac{aw^2}{4Ln_2I} \tag{44}$$

where L is the thickness of the medium, I is the irradiance, and $6 > a > 4$ is a correction term. Note that when n_2 is negative, Eq. (44) shows there will be a negative focal length and thus self-defocusing of the incident beam.

Equation (44) is valid for $f_{\mathrm{NL}} >> \mathrm{L}$ and $Z_0 >> \mathrm{L}$ where Z_0 is the diffraction length (Rayleigh range) of the incident beam. This is the so-called *external self-action* regime.[91] This approximation fails for thick nonlinear media and/or at high irradiance (i.e., *internal self-action*). Equation (43) must then be solved numerically. Analysis shows that self-lensing of a Gaussian beam overcomes diffraction at a distinct threshold power (i.e., the self-focusing threshold), given by the approximate formula[90,92]:

$$P_{\mathrm{cr}} \simeq \frac{a\lambda^2}{8\pi n_2 n_0} \tag{45}$$

Note that for sufficiently thick media, the self-focusing threshold occurs at a critical power, not at a threshold irradiance (i.e., the power at which the self-focusing overcomes diffraction). Self-focusing and diffraction both scale with beam area, thus canceling out the spot size dependence in Eq. (45). Self-focusing and self-defocusing (collectively called *self-action effects*) are often employed in optical limiting applications. Self-action is also the essential mechanism for mode-locking cw solid-state lasers, commonly known as *Kerr-lens mode-locking.*[93]

Solitons

Soliton waves are realized in many different physical circumstances, ranging from mechanical motion to light propagation. In general, they are robust disturbances that can propagate distortion-free for relatively long distances. The robustness of optical solitons can be manifest in the time domain (temporal solitons), transverse space (spatial solitons), or both (light bullets). Temporal solitons have been extensively studied in optical fibers because of their tremendous utility in long-distance optical communication. They exist as a consequence of a balance between the competing effects of linear refractive index dispersion and nonlinear phase modulation.

Assume a single beam propagating in a long nonlinear waveguide characterized by an instantaneous nonlinear index coefficient n_2 and a linear refractive index $n(\omega)$. Ignoring spatial effects (i.e., diffraction), we write the electric field as $\mathscr{E}(z,t) = A_0 u(z,t - z/v_g)\exp(i\omega_0 t - ik_0 z) + \text{c.c.}$. From Eq. (43), one derives a differential equation describing the evolution of the soliton field envelope $u(z,t)$[3,51,94]:

$$-i\frac{\partial u}{\partial z} + \frac{k_2}{2}\frac{\partial^2 u}{\partial \tau^2} = \Delta k_{NL}|u|^2 u \tag{46}$$

Here $v_g = d\omega/dk|_{\omega=\omega_0}$ is the soliton pulse group velocity, τ is a retarded time $\tau = t - z/v_g$, $k_2 = d^2k/d\omega^2|_{\omega=\omega_0}$ gives the group velocity dispersion (GVD), and $\Delta k_{NL} = n_2 I_0 \omega_0/c$ is the irradiance-dependent change of the propagation wave vector. In MKS units, the peak intensity of the soliton pulse is $I_0 = n_0\varepsilon_0 c|A_0|^2/2$. Equation (46) is called the *nonlinear Schrödinger equation* (NLSE) and can be solved exactly. One solution gives the fundamental soliton pulse:

$$u(z,\tau) = \sec h(\tau/\tau_0)e^{i\kappa z} \tag{47}$$

where $\tau_0^2 = -k_2/\Delta k_{NL}$ is the soliton pulsewidth and $\kappa = -k_2/2\tau_0^2$. Note that the modulus of the soliton pulse envelope $|u|$ remains unperturbed upon propagation. For this solution to exist, the GVD (k_2) and the nonlinear refraction (Δk_{NL}) must have opposite signs. For transparent optical solids, including silica glass optical fibers, the nonlinear index coefficient n_2 is almost always positive, which means that a negative GVD is required. In fused silica fibers, the point of balance is attained at a wavelength of $\lambda \approx 1.55$ μm. This is also a spectral region with very low absorption loss. This wavelength has become the standard for the telecommunications industry. Optical solitons in fibers were first reported by Mollenauer et al.[51]

Spatial solitons refer to the propagation of an optical beam without any change or distortion to its spatial irradiance distribution. In this type of soliton, a point of stability is achieved between linear diffraction (causing the beam to diverge) and nonlinear self-focusing. In the presence of a $\chi^{(3)}$ nonlinearity, a stable solution to the NLSE can be found in one spatial dimension only.[95,96] Using a cascaded $\chi^{(2)}{:}\chi^{(2)}$ nonlinearity, however, two-dimensional spatial solitons (or solitary waves) have been demonstrated.[87,88] Two-dimensional spatial solitons can be realized for a cascaded $\chi^{(2)}{:}\chi^{(2)}$ process because of its different behavior compared to $\chi^{(3)}$ at large nonlinear phase shifts. Specifically, cascaded $\chi^{(2)}{:}\chi^{(2)}$ exhibits a saturation of the nonlinear phase-shift that is a direct consequence of depletion of the fundamental beam.

17.12 COMMON EXPERIMENTAL TECHNIQUES AND APPLICATIONS

There are a variety of experimental methods for determining the characteristics (magnitude, response time, spectrum, etc.) of $\chi^{(3)}$ (or $\chi^{(3)}_{\text{eff}}$). The merit of a technique depends on the nature of the nonlinearity and/or the specific property that we wish to measure. An example is obtaining short-time resolution at the expense of sensitivity. Nonlinear optical coefficients can be determined absolutely or relative to a reference material. In the former case, accuracy is determined by the ability to precisely characterize the incident beams. There are many potential sources of error and misinterpretation in nonlinear optical measurements. In *thick* samples, for example, the phase shift that occurs during beam propagation can lead to varying irradiance at different points within the sample. This can be quite difficult to account for and properly model. It is usually best to work in the *external self-action* regime (i.e., thin-sample limit so that beam propagation effects can be ignored)[91] (see also Section 17.3). This greatly simplifies data analysis, since the equation describing nonlinear absorption can be separated from nonlinear refraction. Even if the thin-sample approximation is satisfied, nonlinear refraction can deflect light so strongly *after* the sample that the detector does not collect

all the transmitted energy. This will lead to an overestimation of the nonlinear loss. Particular care must be exercised when using ultrashort pulses. Pulse broadening effects due to group velocity dispersion, for example, may cast ambiguity on the magnitude as well as response time associated with a nonlinearity.

We briefly discuss a few of the commonly used experimental methods: four-wave mixing, excite-probe techniques, interferometry, and Z-scan. It is practically impossible for any single technique to unambiguously separate the different nonlinear responses. Experiments are generally sensitive to several different nonlinearities at once. Different measurements are usually required to unravel the underlying physics, by varying parameters such as irradiance and pulse width. Near-instantaneous nonlinearities such as two-photon absorption and the optical Kerr effect should be independent of pulse width. Slower nonlinear responses will change as the pulse width approaches the response time. Ultrafast and cumulative nonlinearities are often present simultaneously in experiments (e.g., semiconductors), thus hindering their experimental isolation.

Time-Resolved Excite-Probe Techniques

Pump-probe (excite-probe) measurements allow the study of temporal dynamics in nonlinear absorption.[27,60] In the usual implementation, a relatively strong pump pulse excites the sample and changes its optical properties (see Fig. 10). A weaker probe pulse interrogates the excitation region and detects changes. By varying the relative time separation of the two pulses (i.e., by appropriately advancing and delaying the probe pulse), the temporal response can be mapped out. Specifically, relatively slow and fast nonlinear responses can be identified. Often, but not always, the probe is derived from the excitation beam. In degenerate pump-probe (identical frequencies), the probe beam is isolated from the pump beam in a noncollinear geometry (i.e., spatial separation as in Fig. 10) or by orienting the probe with a different polarization.

Nondegenerate nonlinear absorption spectra can also be measured; one approach is to use a fixed-frequency laser pump and continuum (white light) probe such as the output of a flashlamp.[97] The temporal width of a flashlamp source is usually much longer than the laser pulse, which causes a convolution of the fast two-photon response with much longer-lived cumulative nonlinearities in the probe spectrum. The availability of femtosecond white-light continuum sources has allowed nondegenerate spectra to be obtained on short time scales where the ultrafast response dominates.[27,98]

Interpretation of the nonlinear response is complicated by the fact that pump-probe experimental methods are sensitive to any and all induced changes in transmission (or reflection); pump-induced phase shifts on the probe are not readily detected. A time-resolved technique that is very sensitive to index changes is the optical Kerr-gate. This is a form of the pump-probe experiment where induced anisotropy in a time-gated crystal leads to polariza-

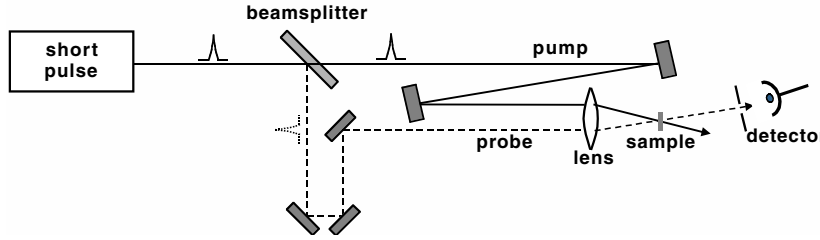

FIGURE 10 Pump-probe experiment.

tion changes.[99] Beyond the two-beam pump probe, three-beam interactions can produce a fourth beam through NLA and/or NLR. This is known as *four-wave mixing* and is discussed in the next section. The development of high-irradiance, femtosecond-pulsed laser systems has led to the evolution of pump-probe measurements that automatically yield the nondegenerate nonlinear absorption spectrum. The femtosecond pulse is split into two beams: one beam is used for sample excitation while the other beam is focused into an appropriate material to produce a white-light continuum for probing. This white-light continuum is used to measure the response over a range of frequencies ω'; this data is suitable for numerical evaluation via the K-K integral in Eq. (23). For a sufficiently broad spectrum of data, the K-K integration yields the nondegenerate n_2 coefficient.[100]

Four-Wave Mixing

The most general case of third-order interaction has all four interacting waves (three input and one scattered) at different frequencies. Generating and phase-matching three different laser wavelengths in an experiment is a formidable task; the benefit is often an improved signal-to-noise ratio.

The other extreme is when all four waves have identical frequency, a situation known as *degenerate four-wave mixing* (DFWM), although it is commonly (and less precisely) referred to as *four-wave mixing* (see Vol. II, Chap. 39, "Photorefractive Materials and Devices," and Vol. II, Chap. 36, "Optical Properties of Semiconductors"). DFWM is readily implemented in the laboratory, since only a single laser source is needed. There are two general cases: *nonresonant* and *resonant* DFWM. In transparent media (i.e., nonresonant) the index of refraction is usually a linear function of laser irradiance, and nonresonant DFWM (wavelength far from an absorption resonance) leads to optical phase conjugation. Phase conjugation by the optical Kerr effect (Section 17.5) is one of the most important applications involving third-order nonlinearities.[26] Nonresonant DFWM leads to the formation of a phase grating due the spatial modulation of the refractive index. Two of the beams write the phase grating while a third reads or probes the grating by diffracting from it, thereby generating a fourth beam (see Fig. 11). The diffracted beam can either be transmitted or reflected (i.e., a phase-conjugate beam) from the material in a direction determined by the wave vectors of the interacting photons. In some experiments, the writing beams also serve to read the grating. One of the difficulties in interpreting DFWM data for third-order nonlinearities is that the signal is proportional to $|\chi^{(3)}|^2 = |\Re e\{\chi^{(3)}\} + \Im m\{\chi^{(3)}\}|^2$ (i.e., NLA and NLR both contribute). Separating the effects is difficult without performing additional experiments. Techniques that study different polarizations can provide information on the symmetry properties of $\chi^{(3)}$.

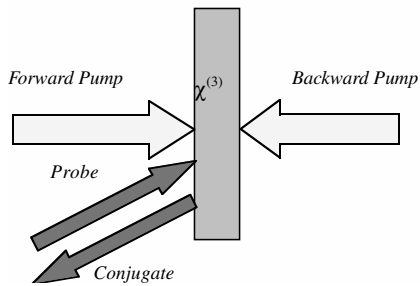

FIGURE 11 Schematic diagram of a four-wave mixing experiment.

In resonant DFWM, there is the added complication of optical absorption at the frequency of the interacting light beams.[101] This is an example of a cascaded $\chi^{(1)}$:$\chi^{(1)}$ effective third-order nonlinearity discussed in Section 17.9, where absorption causes population in excited states, resulting in a spatial grating due the spatial modulation of population. In principle, both phase and absorption gratings are present in resonant DFWM. In practice, it is usually the intensity-dependent changes of population (i.e., effective $\chi^{(3)}$) that dominate the nonlinear polarization, although this is not always the case.[76] For example, photocarrier generation in a semiconductor can alter the bulk plasma frequency and thus modulate the refractive index, leading to a strong phase grating (see Section 17.9).

The diffracted beam contains a wealth of information about the system under study. In nonresonant DFWM, the absolute magnitude and spectral width of the Kerr-effect nonlinearity (n_2) can be obtained. Even more can be deduced from time-resolved DFWM, where the interacting beams are short laser pulses. If the pulses (two and sometimes three separate pulses) are delayed with respect to each other, the dynamic response of the nonlinear polarization can be measured. In resonant DFWM, the diffracted beam measures the coherent response of the optically coupled eigenstates of the system. The linewidth of the diffracted beam indicates the rate at which various physical processes broaden the transition. The nonlinear polarization can be washed out by mechanisms such as population relaxation and diffusion and scattering events associated with optically coupled states. Because of selection rules linking resonant states, various polarization geometries can be employed to study specific transitions. This can be very useful in studies of a complex system such as a semiconductor. Time-resolved experiments with short pulses provide information that complements and elucidates spectral linewidth data obtained from measurements with long duration or continuous laser beams.[26,60,102]

Interferometry

Interferometric methods can be used to measure nonlinearly induced phase distortion.[103,104] One implementation of this approach places a sample in one path (e.g., arm) of an interferometer, and the interference fringes are monitored as a function of irradiance. If the interferometer is set up to give a series of straight-line interference fringes for low-input irradiance (linear regime), the fringes become curved near the region of high irradiance, such as the center of a Gaussian beam. The addition of a streak camera can add time resolution.[27] Alternatively, a third beam can be added to the experiment. The sample is in the path of one weak beam and the strong third beam. The fringe pattern of the two weak beams is monitored as a function of sample irradiance provided by the strong beam. The relative fringe shift observed when the strong beam is present and blocked gives the optical path length change. The nonlinear phase shift can thus be determined. Interferometric experiments require excellent stability and precise alignment. When these conditions are met, sensitivities of better than $\lambda/10^4$ induced optical path length change can be measured.

Z-Scan

The Z-scan was developed to measure the magnitude and sign of nonlinear refraction (NLR). It is also useful for characterizing nonlinear absorption (NLA) and for separating the effects of NLR from NLA.[105,106] The essential geometry is shown in Fig. 12. Using a single, focused laser beam, one measures the transmittance of a sample through a partially obscuring circular aperture (Z-scan) or around a partially obscuring disk (EZ-scan[107]) placed in the far field. The transmittance is determined as a function of the sample position (Z) measured with respect to the focal plane. Employing a Gaussian spatial profile beam simplifies the analysis.

We illustrate how Z-scan (or EZ-scan) data is related to the NLR of a sample. Assume, for example, a material with a positive nonlinear refractive index. We start the Z-scan far from

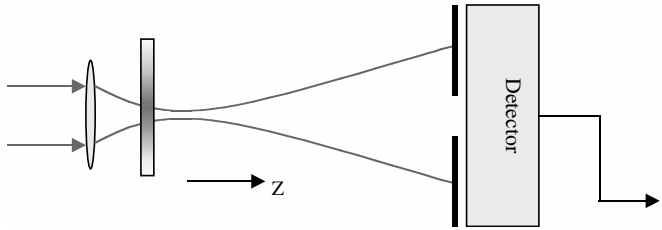

FIGURE 12 Z-scan experimental arrangement.

the focus at a large value of negative Z (i.e., close to the lens). The beam irradiance is low and negligible NLR occurs; the transmittance remains relatively constant near this sample position. The transmittance is normalized to unity in this linear regime as depicted in Fig. 13. As the sample is brought closer to focus, the beam irradiance increases, leading to self-focusing. This positive NLR moves the focal point closer to the lens, causing greater beam divergence in the far field. Transmittance through the aperture is reduced. As the sample is moved past the focus, self-focusing increasingly collimates the beam, resulting in enhanced transmittance through the aperture. Translating the sample farther toward the detector reduces the irradiance to the linear regime and returns the normalized transmittance to unity. Reading the data right to left, a valley followed by peak is indicative of positive NLR. In negative NLR, one finds exactly the opposite: a peak followed by a valley. This is due to laser-induced self-defocusing. Characteristic curves for both types of NLR are shown in Fig. 12. The EZ-scan reverses the peak and valley in both cases. In the far field, the largest fractional changes in

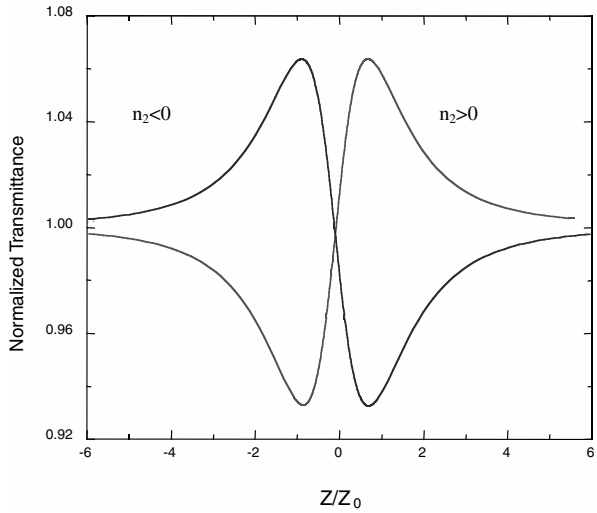

FIGURE 13 Representative curves depicting nonlinear refraction (both positive and negative) as measured by the Z-scan.

irradiance occur in the wings of a Gaussian beam. For this reason, the EZ-scan can be more than an order of magnitude more sensitive than the Z-scan.

We define an easily measurable quantity ΔT_{pv} as the difference between the normalized peak and valley transmittance: $T_p - T_v$. Analysis shows that variation of ΔT_{pv} is linearly dependent on the temporally averaged induced phase distortion, defined here as $\Delta\Phi_0$. If the Z-scan aperture is closed to allow linear transmission of less than 10 percent, and $\Delta T_{pv} < 1$[105,108]:

$$\Delta T_{pv} \cong 0.41|\Delta\Phi_0| \tag{48}$$

assuming cw illumination. If the experiment is capable of resolving transmission changes $\Delta T_{pv} \cong 1\%$, the Z-scan will be sensitive to wavefront distortion of less than $\lambda/250$ (i.e., $\Delta\Phi_0 = 2\pi/250$). The Z-scan has demonstrated sensitivity to a nonlinearly induced optical path length change of nearly $\lambda/10^3$, while the EZ-scan has shown a sensitivity of $\lambda/10^4$, including temporal averaging over the pulsewidth.

To this point in the discussion, we have assumed a purely refractive nonlinearity with no NLA. It has been shown that two-photon absorption will suppress the peak and enhance the valley. If NLA and NLR are present simultaneously, a numerical fitting procedure can extract both the nonlinear refractive and absorptive coefficients. Alternatively, a second Z-scan with the aperture removed (all the transmitted light collected) can independently determine the NLA. Considering 2PA only and a Gaussian input beam, the Z-scan traces out a symmetric Lorentzian shape. The so-called *open aperture* Z-scan is sensitive *only* to NLA. One can then divide the partially obscuring Z-scan data by the open aperture data to give a curve that shows only nonlinear refraction. By performing these two types of Z-scans, we can isolate NLR and NLA without the need for a complicated numerical analysis of a single data set obtained with an aperture.

All-Optical Switching and Optical Bistability

Since the early 1980s, there has been substantial interest in third-order nonlinear optical behavior in materials because of the potential for performing high-speed switching operations—gate speeds many orders of magnitude faster than conventional electronics have been demonstrated. The possibility of increasing data rates on information networks provides the obvious motivation for this research. A bistable optical switch has two stable output states for a given input (i.e., a specific optical power level). This has implications for applications such as optical data storage and power limiting. Both nonresonant $\chi^{(3)}$ and resonant effective $\chi^{(3)}$ processes have been extensively studied, primarily in semiconductors. The early work looked at bulk semiconductor behavior, but as the technology matured the emphasis shifted to specially designed optical waveguides made from suitable material. At the time of this writing, both resonant and nonresonant approaches have encountered problems that have limited practical use. The bound-electronic nonlinearity responds on a femtosecond timescale but is inherently weak. The laser irradiance must be increased to compensate, but this leads to the unwelcome presence of 2PA and associated losses. Resonant nonlinearities must involve the generation of carriers (electrons and holes). While such nonlinearities can be exceptionally strong, the speed of an optical switch depends crucially on the ability to manipulate the carriers. Generation of electron-hole pairs, for example, may dramatically affect the refractive index of a semiconductor and its ability to modulate light, but if the carriers have a long recombination lifetime the switch recovery time will be relatively slow. Other significant issues that must be weighed when comparing optical switching schemes to the all-electronic approach (i.e., transistors and integrated circuits) include device packaging density and heat removal.[18,42,53,72,109,110] For more detailed discussion, consult Chap. 21 on all-optical-switching.

17.13 REFERENCES

1. N. Bloembergen, *Nonlinear Optics,* Addison-Wesley, Redwood City, California, 1992.
2. S. A. Akhmanov and R. V. Khokhlov, *Problems of Nonlinear Optics: Electromagnetic Waves in Nonlinear Dispersive Media,* Gordon and Breach Science Publishers, New York, 1972.
3. R. W. Boyd, *Nonlinear Optics,* Academic Press, Boston, 1992.
4. P. N. Butcher and D. Cotter, *The Elements of Nonlinear Optics,* Cambridge University Press, Cambridge and New York, 1990.
5. G. P. Agrawal, *Nonlinear Fiber Optics,* 2nd ed., Academic Press, San Diego, California, 1995.
6. W. Demtröder, M. Inguscio, and North Atlantic Treaty Organization, Scientific Affairs Division, *Applied Laser Spectroscopy,* Plenum Press, New York, 1990.
7. D. C. Hanna, M. A. Yuratich, and D. Cotter, *Nonlinear Optics of Free Atoms and Molecules,* Springer-Verlag, Berlin and New York, 1979.
8. F. A. Hopf and G. I. Stegeman, *Applied Classical Electrodynamics,* Reprint ed., Krieger Pub. Co., Malabar, Florida, 1992.
9. I.-C. Khoo, J.-F. Lam, and F. Simoni, *Nonlinear Optics and Optical Physics,* World Scientific, Singapore and River Edge, New Jersey, 1994.
10. V. S. Letokhov and V. P. Chebotaev, *Nonlinear Laser Spectroscopy,* Springer-Verlag, Berlin and New York, 1977.
11. M. D. Levenson and S. Kano, *Introduction to Nonlinear Laser Spectroscopy,* Rev. ed., Academic Press, Boston, 1988.
12. S. R. Marder, J. E. Sohn, G. D. Stucky, American Chemical Society, Division of Organic Chemistry, American Chemical Society, Division of Inorganic Chemistry, and American Chemical Society, Meeting, *Materials for Nonlinear Optics: Chemical Perspectives,* American Chemical Society, Washington, DC, 1991.
13. D. L. Mills, *Nonlinear Optics: Basic Concepts,* 2nd enl. ed., Springer, New York, 1998.
14. A. C. Newell and J. V. Moloney, *Nonlinear Optics,* Addison-Wesley, Redwood City, California, 1992.
15. E. G. Sauter, *Nonlinear Optics,* John Wiley & Sons, New York, 1996.
16. M. Schubert and B. Wilhelmi, *Nonlinear Optics and Quantum Electronics,* John Wiley & Sons, New York, 1986.
17. Y. R. Shen, *The Principles of Nonlinear Optics,* John Wiley & Sons, New York, 1984.
18. R. L. Sutherland, *Handbook of Nonlinear Optics,* Marcel Dekker, New York, 1996.
19. P. Yeh, *Nonlinear Optics and Applications,* vol. 613, Society of Photo-Optical Instrumentation Engineers, Bellingham, Washington, 1986.
20. P. Yeh, *Introduction to Photorefractive Nonlinear Optics,* John Wiley & Sons, New York, 1993.
21. F. Zernike and J. E. Midwinter, *Applied Nonlinear Optics,* John Wiley & Sons, New York, 1973.
22. B. E. A. Saleh and M. C. Teich, *Fundamentals of Photonics,* John Wiley & Sons, New York, 1991.
23. A. Yariv, *Optical Electronics in Modern Communications,* 5th ed., Oxford University Press, New York, 1997.
24. A. Yariv, *Quantum Electronics,* 3rd ed., John Wiley & Sons, New York, 1989.
25. A. Yariv and P. Yeh, *Optical Waves in Crystals: Propagation and Control of Laser Radiation,* John Wiley & Sons, New York, 1984.
26. R. A. Fisher, *Optical Phase Conjugation,* Academic Press, New York, 1983.
27. J.-C. Diels and W. Rudolph, *Ultrashort Laser Pulse Phenomena: Fundamentals, Techniques, and Applications on a Femtosecond Time Scale,* Academic Press, San Diego, 1996.
28. B. I. A. Zel'dovich, N. F. Pilipetskii, and V. V. Shkunov, *Principles of Phase Conjugation,* Springer-Verlag, Berlin and New York, 1985.

29. B. S. Wherrett and P. G. Harper, *Nonlinear Optics,* Academic Press, London, 1977.
30. E. Garmire and A. Kost, "Nonlinear Optics in Semiconductors I & II," in *Semiconductors and Semimetals,* R. K. Wilardson and E. R. Webber, eds., Academic Press, 1999.
31. M. Sheik-Bahae and E. W. Van Stryland, "Optical Nonlinearities in the Transparency Region of Bulk Semiconductors," in *Nonlinear Optics in Semiconductors I,* vol. 58, *Semiconductors and Semimetals,* E. Garmire and A. Kost, eds., Academic Press, 1999.
32. E. W. Van Stryland, A. L. Smirl, T. F. Boggess, M. J. Soileau, B. S. Wherrett, and F. Hopf, "Weak-Wave Retardation and Phase-Conjugate Self-Defocusing in Si," in *Picosecond Phenomena III,* R. M. H. K. B. Eisenthal, W. Kaiser, and A. Laubereau, eds., Springer-Verlag, Berlin, 1982.
33. J. S. Toll, "Casaulity and Dispersion Relation: Logical Foundation," *Phys. Rev.* **104**:1760–1770 (1956).
34. H. M. Nussenzveig, *Causality and Dispersion Relations,* Academic Press, New York, 1972.
35. P. J. Caspers, "Dispersion Relations for Nonlinear Response," *Phys. Rev. A.* **133**:1249 (1964).
36. S. M. Kogan, "On the Electromagnetics of Weakly Nonlinear Media," *Sov. Phys. JETP* **16**:217 (1963).
37. P. J. Price, "Theory of Quadratic Response Functions," *Phys. Rev.* **130**:1792 (1964).
38. F. L. J. Ridener and R. H. J. Good, "Dispersion Relations for Nonlinear Systems or Arbitrary Degree," *Phys. Rev. B* **11**:2768 (1975).
39. D. C. Hutchings, M. Sheik-Bahae, D. J. Hagan, and E. W. Van Stryland, "Kramers-Kronig Relations in Nonlinear Optics," *Optical and Quantum Electronics* **24**:1–30 (1992).
40. F. Bassani and S. Scandolo, "Dispersion-Relations and Sum-Rules in Nonlinear Optics," *Phys. Rev. B-Condensed Matter* **44**:8446–8453 (1991).
41. D. A. B. Miller, C. T. Seaton, M. E. Prise, and S. D. Smith, "Band-Gap-Resonant Non-Linear Refraction in Iii-V Semiconductors," *Phys. Rev. Lett.* **47**:197–200 (1981).
42. B. S. Wherrett, A. C. Walker, and F. A. P. Tooley, "Nonlinear Refraction for CW Optical Bistability," in *Optical Nonlinearities and Instabilities in Semiconductors,* H. Haug, ed., Academic Press, Boston, 1988.
43. M. Sheik-Bahae, D. J. Hagan, and E. W. Van Stryland, "Dispersion and Band-Gap Scaling of the Electronic Kerr Effect in Solids Associated With 2-Photon Absorption," *Phys. Rev. Lett.* **65**:96–99 (1990).
44. M. Sheik-Bahae, D. C. Hutchings, D. J. Hagan, and E. W. Van Stryland, "Dispersion of Bound Electronic Nonlinear Refraction in Solids," *IEEE J. Quantum Electron.* **27**:1296–1309 (1991).
45. M. Sheik-Bahae, "Nonlinear Optics of Bound Electrons in Solids," in *Nonlinear Optical Materials,* J. V. Moloney, ed., Springer, New York, 1998.
46. D. J. Moss, E. Ghahramani, J. E. Sipe, and H. M. Van Driel, "Band-Structure Calculation of Dispersion and Anisotropy in $\chi^{(3)}$ For 3rd-Harmonic Generation in Si, Ge, and GaAs," *Phys. Rev. B* **41**: 1542–1560 (1990).
47. R. Adair, L. L. Chase, and S. A. Payne, "Nonlinear Refractive-Index Measurements of Glasses Using 3-Wave Frequency Mixing," *Journal of the Optical Society of America B-Optical Physics* **4**: 875–881 (1987).
48. R. Adair, L. L. Chase, and S. A. Payne, "Nonlinear Refractive-Index of Optical-Crystals," *Phys. Rev. B-Condensed Matter* **39**:3337–3350 (1989).
49. S. R. Friberg, A. M. Weiner, Y. Silberberg, B. G. Sfez, and P. S. Smith, "Femtosecond Switching in a Dual-Core-Fiber Nonlinear Coupler," *Opt. Lett.* **13**:904–906 (1988).
50. M. J. Weber, D. Milam, and W. L. Smith, "Non-Linear Refractive-Index of Glasses and Crystals," *Optical Engineering* **17**:463–469 (1978).
51. L. F. Mollenauer, R. H. Stolen, and J. P. Gordon, *Phys. Rev. Let.* **45**:1095 (1980).
52. D. E. Spence, P. N. Kean, and W. Sibbett, "60-Fsec Pulse Generation From a Self-Mode-Locked Ti-Sapphire Laser," *Optics Letters* **16**:42–44 (1991).
53. H. M. Gibbs, *Optical Bistability: Controlling Light with Light,* Academic Press, Orlando, Florida, 1985.

54. M. N. Islam, *Ultrafast Fiber Switching Devices and Systems,* Cambridge University Press, Cambridge and New York, 1992.
55. N. L. Boling, A. J. Glass, and A. Owyoung, "Empirical Relationships for Predicting Nonlinear Refractive Index Changes in Optical Solids," *IEEE J. Quantum Electron.* **QE-14**:601 (1978).
56. P. P. Ho and R. R. Alfano, "Optical Kerr Effect in Liquids," *Phys. Rev. A* **20**:2170 (1979).
57. F. A. Hopf and G. I. Stegeman, *Applied Classical Electrodynamics,* John Wiley & Sons, New York, 1985.
58. J. F. Reintjes, *Nonlinear Optical Parametric Processes in Liquids and Gases,* Academic Press, New York, 1984.
59. M. D. Levenson, *Introduction to Nonlinear Laser Spectroscopy,* Academic Press, New York, 1982.
60. W. Kaiser and D. H. Auston, *Ultrashort Laser Pulses: Generation and Applications,* 2nd ed., Springer, Berlin and New York, 1993.
61. M. Cardona and G. Güntherodt, *Light Scattering in Solids VI: Recent Results, Including High-Tc Superconductivity,* Springer-Verlag, Berlin and New York, 1991.
62. J. J. Valentini, "Laser Raman Techniques," in *Optical Engineering: Laser Spectroscopy and its Applications,* vol. 11, L. J. Radziemski, R. W. Solarz, and J. A. Paisner, eds., Dekker, New York, 1987.
63. D. A. Long, *Raman Spectroscopy,* McGraw-Hill, New York, 1977.
64. G. L. Eesley, *Cohernet Raman Spectroscopy,* Pergamon, Oxford, 1981.
65. L. A. Woodward, *Raman Spectroscopy: Theory and Practice,* H. A. Szymanski, ed., Plenum, New York, 1987.
66. E. W. Van Stryland and L. Chase, "Two-Photon Absorption: Inorganic Materials," in *Handbook of Laser Science and Technology, Supplement 2, Optical Materials,* M. Weber, ed., CRC Press, 1994.
67. E. W. Van Stryland, H. Vanherzeele, M. A. Woodall, M. J. Soileau, A. L. Smirl, S. Guha, and T. F. Boggess, "2 Photon-Absorption; Nonlinear Refraction; and Optical Limiting in Semiconductors," *Optical Engineering,* **24**:613–623 (1985).
68. E. W. Van Stryland, M. A. Woodall, H. Vanherzeele, and M. J. Soileau, "Energy Band-Gap Dependence of 2-Photon Absorption," *Opt. Lett.* **10**:490–492 (1985).
69. B. S. Wherrett, "Scaling Rules for Multiphoton Interband Absorption in Semiconductors," *Journal of the Optical Society of America B-Optical Physics* **1**:67–72 (1984).
70. J. I. Pankove, *Optical Processes in Semiconductors,* Dover, New York, 1971.
71. C. Kittel, *Introduction to Solid State Physics,* 7th ed., John Wiley & Sons, New York, 1996.
72. A. Miller, D. A. B. Miller, and S. D. Smith, "Dynamic Non-Linear Optical Processes in Semiconductors," *Advances in Physics* **30**:697–800 (1981).
73. H. Haug and S. W. Koch, *Quantum Theory of the Optical and Electronic Properties of Semiconductors,* 3rd ed., World Scientific, Singapore, 1994.
74. W. W. Chow, S. W. Koch, and M. Sargent, *Semiconductor-Laser Physics,* corrected printing ed., Springer-Verlag, Berlin and New York, 1997.
75. L. Banyai and S. W. Koch, "A Simple Theory for the Effects of Plasma Screening on the Optical-Spectra of Highly Excited Semiconductors," *Zeitschrift Fur Physik B-Condensed Matter* **63**:283–291 (1986).
76. R. K. Jain and M. B. Klein, "Degenerate Four-Wave Mixing in Semiconductors," in *Optical Phase Conjugation,* R. A. Fisher, ed., Academic Press, New York, 1983.
77. J. I. Steinfeld, *Laser and Coherence Spectroscopy,* Plenum Press, New York, 1978.
78. M. Sargent, M. O. Scully, and W. E. Lamb, *Laser Physics,* Addison-Wesley, Reading, Massachusetts and London, 1977.
79. J. Feinberg, "Optical Phase Conjugation in Photorefractive Materials," in *Optical Phase Conjugation,* R. A. Fisher, ed., Academic Press, New York, 1983.
80. J. E. Millard, M. Ziari, and A. Partovi, "Photorefractivity in Semiconductors," in *Nonlinear Optics in Semiconductors I, vol. 58, Semiconductors and Semimetals,* E. Garmire and A. Kost, eds., Academic Press, 1999.

81. R. DeSalvo, D. J. Hagan, M. Sheik-Bahae, G. Stegeman, E. W. Van Stryland, and H. Vanherzeele, "Self-Focusing and Self-Defocusing by Cascaded 2nd-Order Effects in Ktp," *Opt. Lett.* **17**:28–30 (1992).
82. N. R. Belashenkov, S. V. Gagarskii, and M. V. Inochkin, "Nonlinear Refraction of Light on Second-Harmonic Generation," *Opt. Spektrosk.* **66**:1383–1386 (1989).
83. G. I. Stegeman, M. Sheik-Bahae, E. Van Stryland, and G. Assanto, "Large Nonlinear Phase-Shifts in 2nd-Order Nonlinear-Optical Processes," *Opt. Lett.* **18**:13–15 (1993).
84. E. W. Van Stryland, "Third-Order and Cascaded Nonlinearities," presented at Laser Sources and Applications, 1996.
85. G. Assanto, G. Stegeman, M. Sheik-Bahae, and E. Van Stryland, "All-Optical Switching Devices Based on Large Nonlinear Phase-Shifts from 2nd Harmonic-Generation," *Appl. Phys. Lett.* **62**:1323–1325 (1993).
86. G. Assanto, G. I. Stegeman, M. Sheik-Bahae, and E. Van Stryland, "Coherent Interactions for All-Optical Signal-Processing Via Quadratic Nonlinearities," *IEEE J. Quantum Electron.* **31**:673–681 (1995).
87. W. Torruellas, B. Lawrence, and G. I. Stegeman, "Self-Focusing and 2d Spatial Solutions in Pts," *Electronics Letters* **32**:2092–2094 (1996).
88. W. E. Torruellas, Z. Wang, D. J. Hagan, E. W. Vanstryland, G. I. Stegeman, L. Torner, and C. R. Menyuk, "Observation of 2-Dimensional Spatial Solitary Waves in a Quadratic Medium," *Physical Review Letters* **74**:5036–5039, 1995.
89. L. J. Qian, X. Liu, and F. W. Wise, "Femtosecond Kerr-Lens Mode Locking with Negative Nonlinear Phase Shifts," *Optics Letters* **24**:166–168, 1999.
90. M. Sheik-Bahae, A. A. Said, D. J. Hagan, M. J. Soileau, and E. W. Van Stryland, "Nonlinear Refraction and Optical Limiting in Thick Media," *Optical Engineering* **30**:1228–1235 (1991).
91. A. E. Kaplan, "External Self-Focusing of Light by a Nonlinear Layer," *Radiophys. Quantum Electron.* **12**:692–696 (1969).
92. J. H. Marburger, in *Progress in Quantum Electronics,* J. H. Sanders and S. Stenholm, eds., Pergamon Press, New York, 1977.
93. H. A. Haus, J. G. Fujimoto, and E. P. Ippen, "Analytic Theory of Additive Pulse and Kerr Lens Mode-Locking," *IEEE J. Quantum Electron.* **28**:2086–2096 (1992).
94. G. P. Agrawal, *Nonlinear fiber optics.* Academic Press, Boston, 1989.
95. A. Barthelemy, S. Maneuf, and C. Froehly, "Soliton Propagation and Self-Confinement of Laser-Beams by Kerr Optical Non-Linearity," *Optics Communications* **55**:201–206 (1985).
96. S. Maneuf, A. Barthelemy, and C. Froehly, "Soliton Beam Propagation: Space-Time Behavior and Spectral Features," *Journal of Optics* **17**:139–145 (1986).
97. J. J. Hopfield, J. M. Worlock, and K. Park, "Two-Quantum Absorption Spectrum of KI," *Phys. Rev. Lett.* **11**:414 (1963).
98. J. A. Bolger, A. K. Kar, B. S. Wherrett, R. Desalvo, D. C. Hutchings, and D. J. Hagan, "Nondegenerate 2-Photon Absorption-Spectra of Znse; Zns and Zno," *Optics Communications* **97**:203–209 (1993).
99. P. Maker, R. Terhune, and C. Savage, "Intensity-Dependent Changes in the Refractive Index of Liquids," *Phys. Rev. Lett.* **12**:507 (1964).
100. D. J. Hagan, E. Miesak, R. Negres, S. Ross, J. Lim, and E. W. Van Stryland, "Nonlinear Spectrometry of Chromophores for Optical Limiting," *SPIE Proceedings* **3472**:80–90 (1998).
101. R. L. Abrams, J. F. Lam, R. C. Lind, D. G. Steel, and P. F. Liao, "Phase Conjugation and High Resolution Spectroscopy by Resonant Degenerate Four-Wave Mixing," in *Optical Phase Conjugation,* R. A. Fisher, ed., Academic Press, New York, 1983.
102. J. Shah, *Ultrafast Spectroscopy of Semiconductors and Semiconductor Nanostructures,* Springer, Berlin and New York, 1996.
103. M. J. Weber, D. Milam, and W. L. Smith, "Nonlinear Refractive Index of Glasses and Crystals," *Opt. Eng.,* 463 (1978).

104. M. J. Moran, C. Y. She, and R. L. Carmen, "Interferometric Measurements of the Nonlinear Refractive Index Coefficient Relative to CS2 in the Laser System Related Materials," *IEEE J. Quantum Electron.* **11**:259 (1975).

105. M. Sheik-Bahae, A. A. Said, T. H. Wei, D. J. Hagan, and E. W. Van Stryland, "Sensitive Measurement of Optical Nonlinearities Using a Single Beam," *IEEE J. Quantum Electron.* **26**:760–769 (1990).

106. E. W. Van Stryland and M. Sheik-Bahae, "Z-Scan," in *Characterization Techniques and Tabulations for Organic Nonlinear Optical Materials,* M. G. Kuzyk and C. W. Dirk, eds., Marcel Dekker, New York, 1998.

107. T. Xia, D. J. Hagan, M. Sheik-Bahae, and E. W. Van Stryland, "Eclipsing Z-Scan Measurement of Lambda/10(4) Wave-Front Distortion," *Opt. Lett.* **19**:317–319 (1994).

108. M. Sheik-Bahae, A. A. Said, and E. W. Van Stryland, "High-Sensitivity; Single-Beam N2 Measurements," *Opt. Lett.* **14**:955–957 (1989).

109. G. Stegeman and E. Wright, "All-Optical Waveguide Switching," *Optical and Quantum Electronics* **22**:95 (1990).

110. G. I. Stegeman, A. Villeneuve, J. Kang, J. S. Aitchison, C. N. Ironside, K. Alhemyari, C. C. Yang, C. H. Lin, H. H. Lin, G. T. Kennedy, R. S. Grant, and W. Sibbett, "AlGaAs Below Half Bandgap: The Silicon of Nonlinear-Optical Materials," *International Journal of Nonlinear Optical Physics* **3**:347–371 (1994).

CHAPTER 18
STIMULATED RAMAN AND BRILLOUIN SCATTERING

J. Reintjes and M. Bashkansky
Optical Sciences Division
Naval Research Laboratory
Washington, DC

18.1 INTRODUCTION

Raman and Brillouin scattering are inelastic scattering processes in which the wavelength of the scattered radiation is different from that of the incident light and a change in the internal energy of the scattering medium occurs. The main distinction between Raman and Brillouin scattering is the type of internal mode involved. Raman scattering involves nonpropagating collective modes in the material. Examples include electronic excitations and molecular vibrations and rotations in liquids and gases, electronic excitations and optical phonons in solids, and electron-plasma oscillations in plasmas. Brillouin scattering involves low-frequency propagating waves, for example acoustic waves in solids, liquids, and gases and ion-acoustic waves in plasmas. The two processes exhibit a range of similarities and differences in the properties of the scattering process as well as in the materials that are involved. General descriptions of Raman and Brillouin scattering are given in Refs. 1–8. Collections of papers on specific aspects of Raman and Brillouin scattering are contained in Refs. 9–11. Review articles are given in Refs. 12 and 13.

18.2 RAMAN SCATTERING

Raman scattering occurs in a wide variety of solids, liquids, gases, and plasmas. The most common form of Raman scattering is one in which the incident light, termed the *pump,* is scattered into light at a longer wavelength, termed the *Stokes wave,* with the energy difference between the incident and scattered photons being taken up in excitation of the appropriate mode of the material. The difference between the incident and scattered photon energy is termed the *Stokes shift.* The identification of the scattered wave as the Stokes wave is made in analogy with the Stokes shift to longer wavelengths in fluorescence, but the dynamics of the

Copyright 2001 by The McGraw-Hill Companies, Inc. Click Here for Terms of Use.

two processes are different except for interactions that are resonant with an allowed single-photon resonant transition. Raman scattering in which the incident light is scattered to a light wave at a shorter wavelength, accompanied by a deexcitation of an internal mode of the medium, is termed *anti-Stokes scattering,* and the scattered wave is termed the *anti-Stokes wave.* The difference between the anti-Stokes and pump photon energies is termed the *anti-Stokes shift.* Again, the analogy is with the corresponding process in fluorescence. Raman shifts can range from tens to tens of thousands of wavenumbers, and are determined entirely by the material and the mode involved.

Raman Interactions

Raman scattering can be viewed in the semiclassical model as a two-photon interaction in which the material makes a real transition from an initial to a final state and a pump photon is destroyed while a Stokes or anti-Stokes photon is created. Several types of Raman interactions are possible. These are illustrated in the level diagrams of Fig. 1, which show Stokes scattering, anti-Stokes scattering, anti-Stokes scattering with four-wave mixing, multiple Stokes scattering, and hyper-Raman scattering. Of these, the most common is Stokes scattering (Fig. 1*a*), in which the pump photon at frequency ω_L is scattered into a longer-wavelength Stokes photon ω_S, accompanied by the excitation of an internal mode of the medium at frequency ω_o.

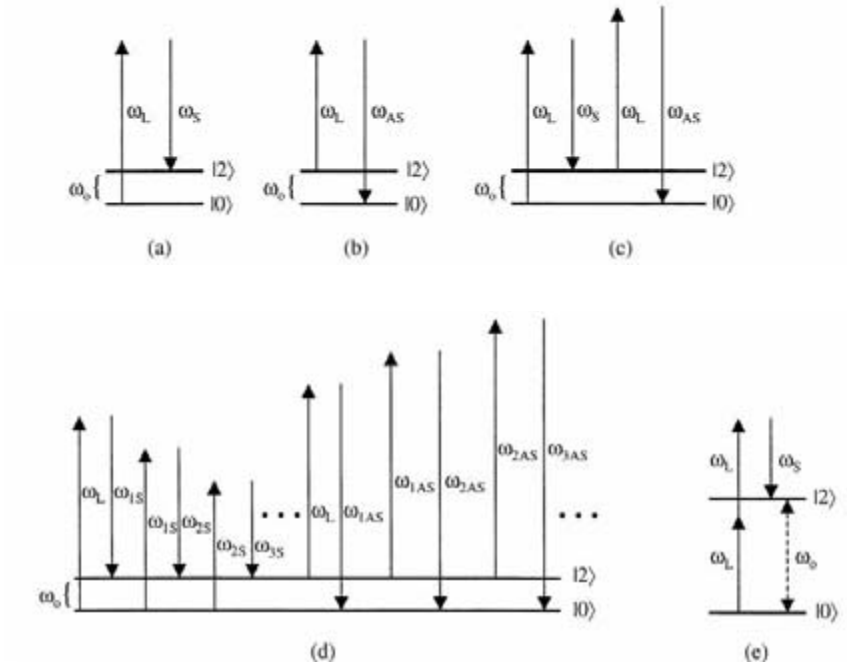

FIGURE 1 Level diagrams showing (*a*) stimulated Raman Stokes scattering, (*b*) stimulated Raman anti-Stokes scattering, (*c*) coherent anti-Stokes four-wave mixing, (*d*) multiple Stokes and anti-Stokes scattering, and (*e*) hyper-Raman scattering.

Anti-Stokes scattering (Fig. 1*b*), in which the pump photon is scattered into a shorter-wavelength anti-Stokes photon ω_{AS} accompanied by the deexcitation of an internal mode of the medium, requires initial excitation into upper levels of the medium. The anti-Stokes interaction illustrated in Fig. 1*b* is less common than the Stokes interaction, occurring most often in spontaneous Raman scattering when the levels are excited thermally. In stimulated processes, this interaction incurs exponential loss unless a population inversion is created between the initial and final states.

Anti-Stokes Raman scattering involving a four-wave mixing interaction, as illustrated in Fig. 1*c,* is much more common in Raman scattering. In this interaction, two pump photons are scattered into a Stokes and anti-Stokes interaction with no net excitation or deexcitation of the medium. This interaction requires perfect or approximate phase matching, depending on the conditions of the scattering interaction. Multiple Raman scattering (Fig. 1*d*) occurs when the Stokes wave becomes powerful enough to drive its own Raman interaction. This generally occurs when the pump wave is significantly above the stimulated Raman threshold. Under these conditions, multiple Stokes waves are generated, each one shifted from its effective pump wave by the frequency of the internal mode of the medium. Multiple Stokes and anti-Stokes waves can also be created through four-wave mixing processes involving one or more of the pump- or frequency-shifted waves. Hyper-Raman scattering (Fig. 1*e*) involves multiphoton interactions in which two or more pump photons are scattered into a single Stokes photon with excitation of an appropriate mode of the material.

In all of these interactions, energy is conserved among the incident and scattered photons and internal energy of the medium. The appropriate relations are summarized in Table 1.

Not all levels in a material can be involved in Raman scattering. In general, Raman scattering follows the rules for two-photon dipole transitions. In materials with inversion symmetry, the initial and final states must have the same parity, and therefore are mutually exclusive with absorptive transitions. In materials without inversion symmetry, internal levels can be both Raman and optically active.

Regimes of Raman Scattering

Raman scattering can occur in the spontaneous and stimulated regimes. In the spontaneous regime, the power of the Stokes and anti-Stokes waves is proportional to the power of the pump wave. The entire manifold of Raman-active internal modes is present in the scattered spectrum, with relative intensities of the Stokes components being determined by the relative Raman scattering cross sections for the various modes. Anti-Stokes scattering arises in spontaneous Raman scattering through thermal excitation of the internal modes. Therefore, the intensity of anti-Stokes modes is reduced from that of the Stokes modes for the same internal

TABLE 1 Frequency and *k*-Vector Relationships in Various Raman Interactions

Stokes scattering	$\omega_S = \omega_L - \omega_o$ $k_o = k_L - k_S$
Anti-Stokes scattering	$\omega_{AS} = \omega_L + \omega_o$ $k_o = k_{AS} - k_L$
Coherent anti-Stokes scattering	$\omega_S + \omega_{AS} = 2\omega_L$ $k_{AS} = 2k_L - k_S$
Multiple Stokes scattering	$\omega_{nS} = \omega_{(n-1)S} - \omega_o = \omega_L - n\omega_o$ $k_o = k_{(n-1)S} - k_{nS}$
Hyper-Raman scattering	$\omega_S = 2\omega_L - \omega_o$ $k_o = 2k_L - k_S$

level by the thermal excitation factor $e^{-\hbar\omega_o/kT}$. Anti-Stokes scattering in the spontaneous regime is generally less common than Stokes scattering, except when low-lying rotational levels of molecules or low-frequency phonons in solids are involved, because thermal excitation of the internal mode is required. Anti-Stokes scattering can be more prominent in stimulated or coherent scattering processes, as will be described in later sections. Spontaneous Raman scattering is used primarily for spectroscopic studies, especially for modes that are forbidden in single-photon absorption or emission measurements.

Stimulated Raman Scattering (SRS) occurs when the intensity of the incident pump wave is strong enough to initiate a positive feedback effect in the medium, resulting in exponential growth of the scattered wave. Stimulated Raman scattering is used for wavelength shifting of coherent light, amplification, improved optical beam properties, pulse compression, phase conjugation, and beam combining. Coherent Raman interactions are used for spectroscopy.

Stimulated Raman Scattering

In stimulated Raman scattering, the internal mode of the medium is driven by the interference of the pump and Stokes waves while the Stokes wave is driven by the modulation of the pump wave by the material oscillation. Thus, the growth rate of the Stokes wave, which is determined by the strength of the internal excitation, increases as the Stokes intensity increases. This is exactly the condition needed for exponential growth of the Stokes wave. Stimulated Raman scattering was observed soon after the development of Q-switched lasers.[14]

Stimulated Raman Geometries. Stimulated Raman scattering can occur in several geometries, each with its own applications. Stimulated Raman generators are illustrated in Figs. 2*a* and *b*. In this arrangement, only a pump wave is incident on the medium, and the Stokes wave grows from quantum noise. Forward scattering is the most common form of Raman generator (Fig. 2*a*), but backward wave generation can occur under some conditions (Fig. 2*b*). Single-pass Raman generators involve amplified spontaneous emission (ASE), and the coherence and divergence properties are characteristic of ASE devices. If the interaction is strong enough to involve pump depletion, the coherence of the Stokes wave can approach that of the pump wave. Raman generators are typically used for frequency conversion from the pump to the Stokes wavelength or for creation of a Stokes wave for other applications. Conversion to multiple Stokes or anti-Stokes waves can also be done with Raman generators. Mirrors can be used with the Raman generator to create a Raman oscillator as in Fig. 2*c*. This arrangement is used with low-intensity continuous-wave (cw) or pulsed pump lasers to reduce the Raman threshold.[13]

Raman amplification can be achieved with the arrangements shown in Figs. 2*d* and *e*, in which a Stokes wave is supplied along with the pump wave. The Stokes wave is amplified at the expense of the pump wave. The Stokes wave is usually created in a separate low-power Raman generator and may be spatially filtered for control of the spatial divergence. Raman amplification is used when a high-quality Stokes beam is desired or when highly efficient conversion of the pump energy is desired without creation of multiple Stokes components. Backward amplification (Fig. 2*e*) is used for Stokes amplification or for pulse compression. In Raman generators, usually only a single Stokes frequency is generated corresponding to the material mode with the highest gain. Amplification of any of the Raman modes is possible if a suitable input Stokes signal is provided.

Coherent anti-Stokes Raman scattering (CARS) is illustrated in Fig. 2*f*. Here the pump and Stokes waves are supplied, often having comparable intensities and propagating at the appropriate phase-matching angle. The anti-Stokes wave is created at the appropriate angle for phase matching. CARS is used for spectroscopy and other diagnostic applications.

Raman Susceptibilities. Classically, the Raman effect occurs because of modulation of the polarization in the medium induced by the pump at the difference frequency between the

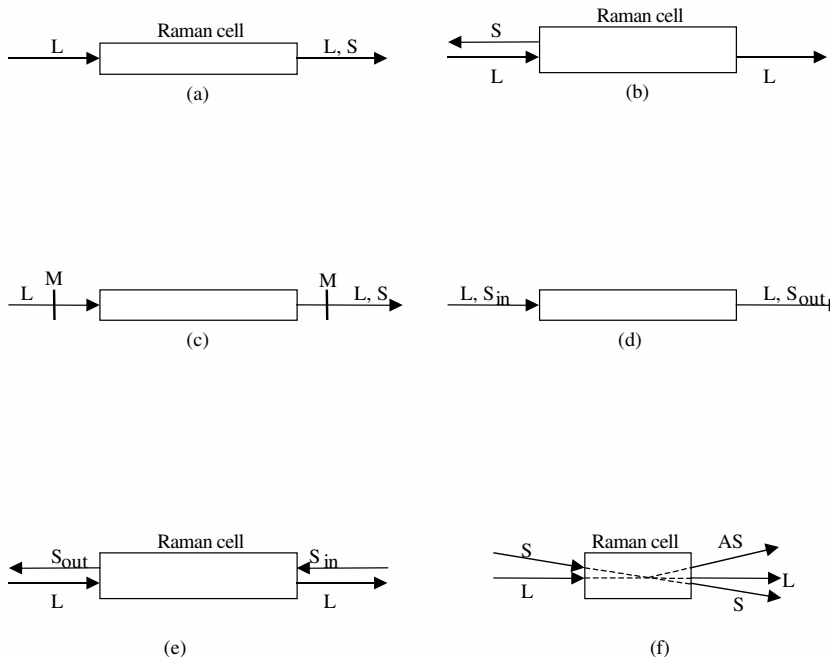

FIGURE 2 Schematic diagrams of various Raman interaction geometries. (*a*) Forward Raman generator. (*b*) Backward Raman generator. (*c*) Raman oscillator. (*d*) Forward Raman amplifier. (*e*) Backward Raman amplifier. (*f*) Coherent anti-Stokes four-wave mixing. AS, generated anti-Stokes mixing; L, pump laser; M, mirrors; S, Stokes wave; S_{in}, Stokes wave from Raman generator; S_{out}, amplified Stokes wave.

pump and material mode. This arises from the hyperpolarizability of the medium. The polarization of the medium is given by[6,7]

$$P = \varepsilon_o(\mu_o + \mu E + \frac{\partial \alpha}{\partial Q} QE + \ldots) \tag{1}$$

where μ_o is the permanent dipole moment of the material, μ is the first-order dipole moment, $(\partial\alpha/\partial Q)$ is the hyperpolarizability, and Q is the normal mode coordinate of the material oscillation. Spontaneous Raman scattering is given classically by the relation

$$P_S = NA \frac{\partial \sigma}{\partial \Omega} d\Omega \, P_L L \tag{2a}$$

where $d\sigma/d\Omega$ is the differential cross section of the Raman transition, L is the length of the scattering medium, A is the cross-sectional area, and $d\Omega$ is its solid angle. The Raman cross section is related to the hyperpolarizability by

$$\frac{\partial \sigma}{\partial \Omega} = \frac{\pi h n_S \nu_S^4}{4 n_L m \omega_o c^2} \left(\frac{\partial \alpha}{\partial Q} \right)^2 \tag{2b}$$

The Raman effect can also be analyzed quantum-mechanically through the use of the density matrix[15] using the third-order elements ρ_{0i} and ρ_{i2} and the second-order element ρ_{02}, where the subscripts 0 and 2 designate the initial and final Raman levels and the subscript i designates intermediate levels. The classical parameter Q is related to the off-diagonal density matrix element ρ_{02}, while the population density is related to the element ρ_{22}. Thus the normal mode coordinate of the material oscillation is associated with quantum mechanical transition probabilities and not directly with the population of the excited state of the material.

The Raman cross section can be related to the susceptibilities of nonlinear optics[15] through density matrix calculations involving the third-order elements ρ_{0i} and ρ_{i2} and the second-order element ρ_{02}. The nonlinear Raman polarization amplitude is

$$P(\omega_S) = \tfrac{3}{2}\,\varepsilon_o \chi^{(3)}(-\omega_S, \omega_L, -\omega_L, \omega_S)|A_L|^2 A_S \tag{3a}$$

and the Raman susceptibility per atom or molecule is:

$$\chi^{(3)}_{\text{Raman}} = \frac{1}{6\hbar^3\varepsilon_o}\,\frac{1}{\omega_{20} - (\omega_L - \omega_S) + i/T_2}\left|\sum_i \mu_{0i}\mu_{i2}\left(\frac{1}{\omega_{i0} - \omega_L} + \frac{1}{\omega_{i0} + \omega_S}\right)\right|^2 \tag{3b}$$

where T_2 is the homogeneous Raman dephasing time and μ_{ij} is the transition dipole moment between states i and j.

The Raman susceptibility has real and imaginary parts. The imaginary part, which is negative and proportional to T_2, is responsible for spontaneous and stimulated Raman scattering. The real part contributes to the nonlinear refractive index through Raman-type interactions. The Raman susceptibility is related to the hyperpolarizability as

$$\chi'' = -\frac{1}{12\Gamma m\omega_o}\left(\frac{\partial\alpha}{\partial Q}\right)^2 \tag{4}$$

where χ'' is the imaginary part of the Raman susceptibility, Γ is the inverse of the dephasing time, m is the effective mass of the material oscillator, and ω_o is the frequency of the material transition. The Raman susceptibility is defined only for steady-state interactions. In transient interactions, the Raman polarization must be solved for as a dynamic variable along with the optical fields.

SRS Equations. Stimulated Raman scattering is described in the most general form by the equations:[2]

$$\nabla_\perp^2 A_S + 2ik_S\left(\frac{\partial A_S}{\partial z} \pm \frac{1}{v_{gS}}\frac{\partial A_S}{\partial t}\right) = -\frac{\Delta N}{2}\frac{\omega_S^2}{c^2}\left(\frac{\partial\alpha}{\partial Q}\right)_S Q^* A_L \tag{5a}$$

$$\nabla_\perp^2 A_L + 2ik_L\left(\frac{\partial A_L}{\partial z} + \frac{1}{v_{gL}}\frac{\partial A_L}{\partial t}\right) = -\frac{\Delta N}{2}\frac{\omega_L^2}{c^2}\left[\left(\frac{\partial\alpha}{\partial Q}\right)_S Q A_S + \left(\frac{\partial\alpha}{\partial Q}\right)_{\text{AS}} Q^* A_{\text{AS}} e^{i\Delta kz}\right] \tag{5b}$$

$$\nabla_\perp^2 A_{\text{AS}} + 2ik_{\text{AS}}\left(\frac{\partial A_{\text{AS}}}{\partial z} \pm \frac{1}{v_{g\text{AS}}}\frac{\partial A_{\text{AS}}}{\partial t}\right) = -\frac{\Delta N}{2}\frac{\omega_{\text{AS}}^2}{c^2}\left(\frac{\partial\alpha}{\partial Q}\right)_{\text{AS}} Q A_L e^{-i\Delta kz} \tag{5c}$$

$$\frac{\partial Q^*}{\partial t} + \left[i\left(\frac{\omega_o^2 - \Omega^2}{2\Omega}\right) + \Gamma\right]Q^* = -\frac{i}{4\omega_o m}\left[\left(\frac{\partial\alpha}{\partial Q}\right)_S A_L^* A_S + \left(\frac{\partial\alpha}{\partial Q}\right)_{\text{AS}} A_{\text{AS}}^* A_L e^{-i\Delta kz}\right] \tag{5d}$$

$$\frac{\partial\Delta N}{\partial\tau} + \frac{1}{T_1}(\Delta N - N) = -i\,\frac{\Delta N\varepsilon_o}{4\hbar}\left[\left(\frac{\partial\alpha}{\partial Q}\right)_S (Q^* A_L A_S^* - Q A_L^* A_S) + \left(\frac{\partial\alpha}{\partial Q}\right)_{\text{AS}} (Q^* A_L^* A_{\text{AS}} e^{i\Delta kz} - Q\,A_L\,A_{\text{AS}}^* e^{-i\Delta kz})\right] \tag{5e}$$

where A_S, A_L, and A_{AS} are the slowly varying optical field amplitudes of the Stokes, laser (pump) and anti-Stokes waves given by:

$$E_{S,L,AS}(x, y, z, t) = \tfrac{1}{2}[A_{S,L,AS}(x, y, z, t)e^{-i(\omega_{S,L,AS}t - k_{S,L,AS}z)} + c.c.] \tag{6}$$

where $\omega_{S,L,AS}$ are the optical frequencies, $k_{S,L,AS}$ are the k vectors, $v_{S,L,AS}$ are the group velocities, ΔN is the difference in the population between the lower and the upper Raman transition levels, $\Delta N = N_0 - N_2$, N is the total population density, and Q is the amplitude of the normal mode coordinate of the material excitation defined by:

$$\mathbf{Q}(x, y, z, t) = \tfrac{1}{2}[Q(x, y, z, t)e^{-i(\Omega t - k_o z)} + cc] \tag{7}$$

$(\partial\alpha/\partial Q)_S$ and $(\partial\alpha/\partial Q)_{AS}$ are the hyperpolarizabilities for the Stokes and anti-Stokes waves, respectively, ω_o is the Raman transition frequency, and k_o is the nonpropagating k vector of the material excitation. Γ is the half-width at half-maximum of the Raman linewidth given by $\Gamma = 1/T_2$, Δk is the phase mismatch of the anti-Stokes scattering, m is the effective reduced mass of the material oscillation, and ε_o is the permitivity of the free space.

The relation between various frequencies and k vectors is:

$$\omega_S = \omega_L - \Omega \tag{8a}$$

$$\omega_{AS} = \omega_L + \Omega \tag{8b}$$

$$k_o = k_L - k_S \tag{8c}$$

$$\Delta k = k_S + k_{AS} - 2k_L \tag{8d}$$

The intensity of the various light waves is given by:

$$I_{S,L,AS} = \tfrac{1}{2}(cn\varepsilon_o)|A_{S,L,AS}|^2 \tag{9}$$

Phase matching, which is of central importance in many nonlinear interactions, is automatically satisfied in stimulated Raman scattering because k_o automatically adjusts to satisfy Eq. (8*c*). Phase matching in anti-Stokes scattering through four-wave mixing is not automatic, and phase-matching conditions determine many of the properties of the four-wave mixing anti-Stokes scattering interaction.

These equations describe most of the effects that are commonly encountered in Raman scattering, including amplification, diffraction, growth from noise, multiple Stokes generation, forward and backward interactions, coherent anti-Stokes interactions, and transient and steady-state interactions. Each of these will be discussed individually in subsequent parts of this chapter. In most of these effects the population of the ground state is undisturbed and the approximation $\Delta N = N$ is valid. In some situations involving high-power lasers or resonant interactions, ΔN will vary and Eq. (5*e*) must be used.

Steady-State Stokes Scattering. Many of the effects associated with stimulated Raman scattering can be illustrated by considering plane-wave steady-state forward Raman amplification. In this interaction, an incident Stokes wave at frequency ω_S is amplified by a pump wave at frequency ω_L in the geometry of Fig. 2*d*. The plane-wave steady-state Raman amplification equations are obtained from Eqs. (5*a* and *b*) by assuming that the time variation of the wave envelopes is slow compared to the dephasing time T_2, allowing the time derivatives to be neglected; by neglecting the transverse spatial derivative; and by assuming that the ground state population is unchanged, allowing Eq. (5*e*) to be neglected and the ground state population $N_o = N$ to be treated as a constant. The resulting equations are

$$\frac{dA_S}{dz} = i\kappa_2 Q^* A_L \tag{10a}$$

$$\frac{dA_L}{dz} = i\,\frac{\omega_L n_S}{\omega_S n_L}\,\kappa_2 A_S Q \tag{10b}$$

$$Q^* = -i\,\frac{1}{4\omega_o m}\left(\frac{\partial\alpha}{\partial Q}\right)\frac{1}{\Gamma + i(\omega_o - \Omega)}\,A_L^* A_S \tag{10c}$$

where

$$\kappa_2 = \frac{N\omega_S}{4n_S c}\left(\frac{\partial\alpha}{\partial Q}\right) \tag{11}$$

Equation (10*c*) results from solution of Eq. (5*d*) neglecting the time derivative and the anti-Stokes term.

Steady-State Gain. If the pump wave intensity is taken as a constant, then Eq. (10*a*) can be solved for the Stokes intensity:

$$I_S(L) = I_S(0)\,e^{g_{SS} I_L L} \tag{12}$$

where L is the length of the interaction region and g_{SS} is the steady-state Raman gain coefficient, given by

$$g_{SS} = \frac{N\omega_S}{4\Gamma n_S n_L m\omega_o c^2 \varepsilon_o}\left(\frac{\partial\alpha}{\partial Q}\right)^2 \tag{13}$$

This result is also written in the literature in the forms

$$I_S(L) = I_S(0)\,e^{G_{SS}} \tag{14a}$$

$$I_S(L) = I_S(0)\,e^{N\sigma_R I_L L} \tag{14b}$$

where

$$G_{SS} = g_{SS} I_L L \tag{15a}$$

is the total steady-state Raman gain and

$$\sigma_R = \frac{\omega_S}{4\Gamma n_S n_L m\omega_o c^2 \varepsilon_o}\left(\frac{\partial\alpha}{\partial Q}\right)^2 \tag{15b}$$

is the stimulated Raman cross section. The gain coefficient is given in terms of the Raman susceptibility as

$$g_{SS} = -\frac{3N\omega_S}{c^2 n_S n_L \varepsilon_o}\,\chi'' \tag{16}$$

The classical Raman scattering cross section is related to the Raman gain, given in Eq. (13), by

$$g_{SS} = \frac{2Nc^2}{\pi n_S^2 h\nu_S^3 \Delta\nu_R}\,\frac{\partial\sigma}{\partial\Omega} \tag{17}$$

where $\Delta\nu_R$ is the Raman linewidth [full width at half-maximum (FWHM)] related to the dephasing time as

$$\Delta\nu_R = \frac{1}{\pi T_2} \tag{18}$$

In transparent regions of the spectrum, the Raman cross section scales as ν_S^4 and the Raman gain coefficient scales as ν_S. In dispersive regions of the spectrum, as for example when the pump wavelength is in the ultraviolet, additional frequency variation in the Raman gain arises from the resonant term $1/(\omega_{i0} - \omega_L)$ in the susceptibility.

Initially, stimulated Raman gain coefficients were calculated from measurements of the spontaneous Raman scattering cross section or estimated from measurements of the Raman threshold. The most accurate determinations of Raman gain coefficients are now made with steady-state amplification measurements in the low-gain regime.

The conditions for steady-state Raman amplification are encountered when both the pump and incident Stokes radiation are either cw or narrowband pulses with pulse duration longer than a steady-state time given by:[16–19]

$$t_{SS} = G_{SS} T_2 \tag{19}$$

and contain no rapid internal temporal variation, requiring that the linewidths $\Delta\nu_L$ and $\Delta\nu_S$ satisfy the condition

$$\Delta\nu_{L(S)} \ll \Delta\nu_R \tag{20}$$

Raman Linewidths. The steady-state Raman gain scales as the medium density and inversely with the Stokes wavelength and the material linewidth. In materials such as some molecular gases, the linewidth is pressure dependent due to pressure broadening with a variation of the form:[20]

$$\Delta\nu_R = \Delta\nu_o + \beta\rho \tag{21}$$

where ρ is the density of the material and $\Delta\nu_o$ is the Raman linewidth at low pressures. In materials that exhibit this behavior, the gain increases at low pressures but levels off at higher pressures, becoming independent of pressure in the limit of high pressures. In hydrogen, for example, the steady-state gain for the Q(1) vibrational mode is effectively independent of pressure for pressures above about 10 atmospheres. The rotational lines in some gases such as hydrogen reach their pressure-broadened limit at lower pressures than do the vibrational lines. As a result, rotational Raman scattering in these materials is more prominent at low pressures, while the vibrational scattering is dominant at higher pressures.

The linewidth for forward scattering in some gases such as hydrogen exhibits Dicke narrowing,[21] in which inelastic collisions cause a narrowing of the linewidth at small but nonzero pressures before the material enters a pressure-broadened regime. The linewidth exhibits a variation in a region above some cutoff pressure of the form:[22]

$$\Delta\nu_R = \frac{A}{\rho} + B\delta\rho \tag{22}$$

This behavior is shown for hydrogen in Fig. 3. Raman frequency shifts for a number of materials are shown in Table 2. Linewidths and gain coefficients for selected materials are given in Table 3. The temperature dependence of the frequency shift parameters for hydrogen is given in Table 4. Temperature dependence of line-broadening parameters for hydrogen and nitrogen is given in Table 5. Formulas for quantities appropriate for Raman scattering in molecular gases are given in Table 6.

Pump Depletion. If the Stokes intensity becomes large enough, the depletion of the pump wave must be taken into account and Eqs. (10*a*) and (10*b*) must be solved together.

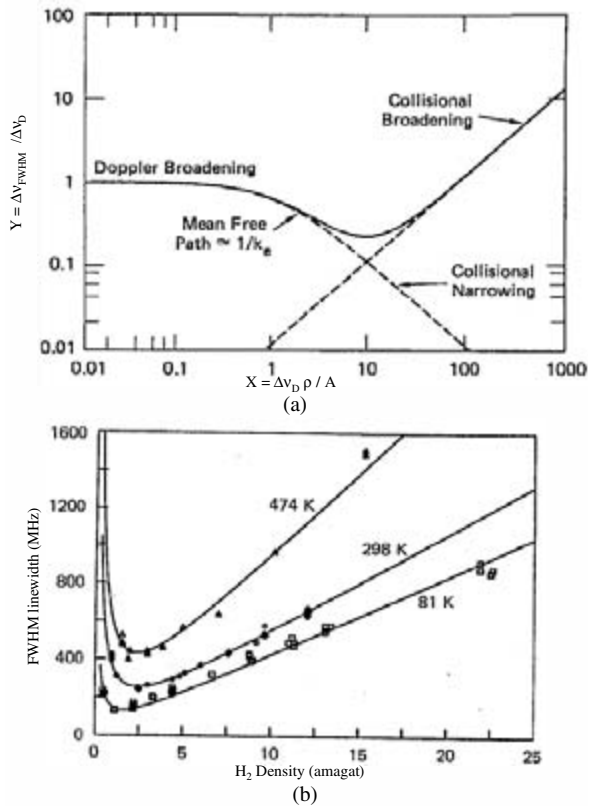

FIGURE 3 Calculated (*a*) and experimental (*b*) variation with pressure of the linewidth of the Q(1) transition in hydrogen gas showing Dicke narrowing and pressure broadening. (From Ref. 22; copyright 1986 by the American Physical Society.)

The solutions are

$$I_S(z) = \frac{\left[I_S(0) + \frac{\omega_S}{\omega_L} I_L(0)\right] \frac{\omega_L}{\omega_S} \frac{I_S(0)}{I_L(0)} e^{\left[I_L(0) + \frac{\omega_L}{\omega_S} I_S(0)\right] gz}}{1 + \frac{\omega_L}{\omega_S} \frac{I_S(0)}{I_L(0)} e^{\left[I_L(0) + \frac{\omega_L}{\omega_S} I_S(0)\right] gz}} \tag{23a}$$

$$I_L(z) = \frac{\left[1 + \frac{\omega_S}{\omega_L} \frac{I_L(0)}{I_S(0)}\right] I_L(0) e^{-\left[I_L(0) + \frac{\omega_L}{\omega_S} I_S(0)\right] gz}}{1 + \frac{\omega_S}{\omega_L} \frac{I_L(0)}{I_S(0)} e^{-\left[I_L(0) + \frac{\omega_L}{\omega_S} I_S(0)\right] gz}} \tag{23b}$$

TABLE 2 Raman Transition Frequencies of Selected Materials

Liquids		
Substance	ν_R (cm^{-1})	Reference
Bromoform	222	23
Tetrachloroethylene	448	24
Carbon tetrachloride[a]	460	25
Ethyl iodide	497	26
Hexafluorobenzene[a]	515	25
Bromoform	539	23
Chlorine	552	2
Methylene bromide	580	25
Trichloroethylene	640	23
Carbon disulfide	655	27
Ethylene bromide	660	28
Chloroform	667	23
o-Xylene	730	29
FC104[b]	757	30
Sulfur hexafluoride	775	31
α-Dimethylphenethylamine	836	32
Dioxane	836	23
Morpholine[a]	841	25
Thiophenol[a]	916	25
Nitromethane[a]	927	25
Deuterated benzene	944	14
Potassium dihydrogen phosphate	980	33
Cumene[a]	990	25
Pyridine	991	14
1.3-Dibromobenzene	992	24
Benzene	992	14
Aniline	997	34
Styrene	998	35
m-Toluidine[a]	999	25
Acetophenone	999	36
Bromobenzene	1000	34
Chlorobenzene[a]	1001	25
tert-Butylbenzene	1000	24
Benzaldehyde[c]	1001	24
Ethylbenzoate	1001	36
Benzonitrile	1002	34
Ethylbenzene	1002	29
Toluene	1004	14
Fluorobenzene	1012	37
γ-Picoline	1016	25
m-Cresol[a]	1029	25
m-Dichlorobenzene[a]	1034	25
1-Fluoro-2-chlorobenzene[d]	1034	24
Iodo-Benzene[a]	1070	25
Benzoyl chloride[a]	1086	25
Benzaldehyde[a]	1086	25
Anisole[a]	1097	25
Pyrrole[a]	1178	25
Furan[a]	1180	25
Nitrous oxide	1289	31
Styrene	1315	35

TABLE 2 Raman Transition Frequencies of Selected Materials (*Continued*)

Liquids (*Continued*)

Substance	ν_R (cm^{-1})	Reference
Nitrobenzene	1344	14
1-Bromonaphthalene	1363	14
1-Chloronaphthalene	1374	38
2-Ethylnaphthalene	1382	24
m-Nitrotoluene[a]	1389	25
Carbon dioxide	1392	31
Quinoline[a]	1427	25
Bromocyclohexane	1438	26
Furan[a]	1522	25
Methyl salicylate[a]	1612	25
Cinnamaldehyde	1624	38
Styrene	1631	35
3-Methylbutadiene	1638	39
Pentadiene	1655	39
Isoprene	1792	32
1-Hexyne	2116	24
Dimethyl sulfoxide[c]	2128	40
o-Dichlorobenzene[a]	2202	25
Benzonitrile	2229	38
Acetonitrile	2250	26
1,2-Dimethylaniline[a]	2292	25
Nitrogen	2327	41
Hydrobromic acid	2493	30
Hydrochloric acid	2814	42
Methylcyclohexane[a]	2817	25
Methanol	2831	23
cis,trans,1,3-Dimethylcyclohexane	2844	24
Tetrahydrofuran	2849	38
Cyclohexane	2852	14
cis-1,2-Dimethylcyclohexane	2853	24
α-Dimethylphenethylamine	2856	32
Dioxane	2856	23
Decahydronaphthalene	2860	30
Cyclohexane	2863	23
Cyclohexanone	2863	29
cis,trans-1,3-Dimethylcyclohexane	2866	24
cis,1,4-Dimethylcyclohexane	2866	24
Cyclohexane	2884	23
Dichloromethane[a]	2902	25
Dimethyl sulfoxide	2916	40
Morpholine[a]	2902	25
Cargille 5610[f]	2908	30
2,3-Dimethyl-1,5-hexadiene	2910	24
Limonene	2910	32
o-Xylene	2913	29
1-Hexyne	2916	24
cis-2-Heptene	2916	24
2-Octene	2918	24
Acetonitrile	2920	30
Mesitylene	2920	32
2-Bromopropane	2920	24

TABLE 2 Raman Transition Frequencies of Selected Materials (*Continued*)

Liquids (*Continued*)		
Substance	ν_R (cm^{-1})	Reference
Acetone	2921	29
Ethanol	2921	23
cis-1,2-Dimethylcyclohexane	2921	24
Carvone	2922	32
2-Chloro-2-methylbutane	2927	24
Dimethylformamide	2930	23
Cis,trans-1,3-Dimethylcyclohexane	2926	24
m-Xylene	2933	29
1,2-Diethyl tartrate	2933	32
o-Xylene	2933	29
Piperidine	2933	29
1,2-Diethylbenzene	2934	24
1-Bromopropane	2935	24
Piperidine	2936	29
Tetrahydrofuran	2939	38
Decahydronaphthalene	2940	30
Piperidine	2940	29
Cyclohexanone	2945	29
2-Nitropropane	2945	24
1,2 Diethyl carbonate[a]	2955	25
1,2 Dichloroethane[a]	2956	25
trans-Dichloroethylene	2956	23
Methyl fluoride	2960	31
1-Bromopropane	2962	24
2-Chloro-2-methylbutane	2962	24
α-Dimethylphenethylamine	2967	32
Dioxane	2967	23
Methyl chloride	2970	31
Cyclohexanol[a]	2982	25
Cyclopentane[a]	2982	25
Cyclopentanol[a]	2982	25
Bromocyclopentane[a]	2982	25
o-Dichlorobenzene[a]	2982	25
p-Chlorotoluene[a]	2982	25
α-Picoline[a]	2982	25
p-Xylene	2988	29
o-Xylene	2992	29
Dibutyl-phthalate[a]	2992	25
1, 1, 1-Trichloroethane	3018	23
Ethylene chlorohydrin[a]	3022	25
Isophorone[a]	3022	25
Nitrosodimethylamine[a]	3022	25
Propylene glycol[a]	3022	25
Cyclohexane[a]	3038	25
Styrene	3056	35
Pyridine	3058	24
Benzene	3064	14
tert-Butylbenzene	3065	24
1-Fluoro-2-chlorobenzene	3082	24
Turpentine[a]	3090	25
Pseudocumene[a]	3093	25

TABLE 2 Raman Transition Frequencies of Selected Materials (*Continued*)

Liquids (*Continued*)

Substance	ν_R (cm^{-1})	Reference
Acetic acid[a]	3162	25
Acetonylacetone[a]	3162	25
Methyl methacrylate[a]	3162	25
γ-Picoline[a]	3182	25
Aniline	3300	34
Water[a]	3651	25

Solids

Substance	ν_R (cm^{-1})	Reference
Quartz	128	43
Lithium niobate	152	44
α-Sulfur	216	45
Lithium niobate	248	44
Bromine	295	45
Bromine	303	45
Quartz	466	43
α-Sulfur	470	45
Chlorine	543	46
Lithium niobate	628	44
Carbon disulfide	656	46
Potassium iodate	746	47
Potassium bromate[d]	780	47
Potassium periodate	790	47
Potassium bromate	798	47
Potassium chromate	844	47
Sodium molybdate[d]	884	47
Potassium dichromate	906	47
Calcium tungstate	911	38
Potassium dihydrogen phosphate	915	33
Ammonium vanadate	915	47
Sodium tungstate	915	47
Potassium perchlorate[d]	936	47
Potassium chlorate[d]	938	47
Ammonium sulfate[d]	975	47
Potassium sulfate[d]	985	47
Stilbene	997	48
Polystyrene	1001	23
Calcium nitrate	1050	47
Calcium nitrate tetrahydrate[d]	1052	47
Potassium nitrate	1060	47
Magnesium nitrate dehydrate[d]	1060	47
Ammonium nitrate[d]	1062	47
Magnesium nitrate hexahydrate[d]	1063	47
Sodium nitrate	1075	47
77 K (not observed at 293 K)[d]		
Calcite	1086	45
Diamond	1332	45
Naphthalene	1380	38
Anthracene	1403	49
Stilbene	1591	48
Potassium thiocyanate	1040	47

TABLE 2 Raman Transition Frequencies of Selected Materials (*Continued*)

Solids (*Continued*)

Substance	ν_R (cm^{-1})	Reference
Potassium ferricyanide[d]	2100	47
Triglycine sulfate	2422	25
Triglycine sulfate	2702	25
Triglycine sulfate	3022	25
Polystyrene	3054	23

Gases

Substance	ν_R (cm^{-1})	Reference
Barium vapor[d]	IR[e]	50
Cesium vapor[d]	IR[e]	51, 52
Hydrogen fluoride	FIR[e]	53
Potassium vapor[d]	IR[e]	51, 52
Rubidium vapor[d]	IR[e]	54
ρ-H_2	354	55, 56
Carbon tetrafluoride	980	57
Oxygen	1552	29
Nitrogen	2331	58
Potassium vapor	2721	59
Methane	2916	60
Deuterium	2991	60
Hydrogen deuteride	3628	61
Hydrogen	4155	60

[a] Observed at low resolution.
[b] Product of 3M Co., St. Paul, Minnesota.
[c] 1:1 mixture with tetrachloroethylene.
[d] Stimulated electronic Raman scattering (SERS).
[e] Generally tunable transitions in the infrared (IR) and far infrared (FIR).

Reprinted with permission from M. J. Weber (ed.), *CRC Handbook of Laser Science and Technology: Optical Materials,* part 1, vol. III. Copyright CRC Press, Boca Raton, FL, 1988.

When $I_S(0) \ll I_L(0)$, the pump depletion solutions simplify to

$$I_S(z) = \frac{I_S(0)e^{I_L(0)gz}}{1 + \dfrac{\omega_L}{\omega_S}\dfrac{I_S(0)}{I_L(0)}e^{I_L(0)gz}} \tag{24a}$$

$$I_L(z) = \frac{\left[1 + \dfrac{\omega_S}{\omega_L}\dfrac{I_L(0)}{I_S(0)}\right]I_L(0)e^{-I_L(0)gz}}{1 + \dfrac{\omega_S}{\omega_L}\dfrac{I_L(0)}{I_S(0)}e^{-I_L(0)gz}} \tag{24b}$$

The conditions for exponential Raman amplification can now be identified. In order for the approximate solution of Eq. (12) to be valid, it is necessary for the condition

$$I_S(0)e^{g_{SS}I_Lz} \ll I_L(0) \tag{25}$$

to be satisfied. When the condition in Eq. (25) is not satisfied, the full solution of Eq. (23) [or Eq. (24), if $I_S(0) \ll I_L(0)$] must be used. The calculated behavior of the pump and Stokes waves in the depletion regime is shown in Fig. 4.

TABLE 3 Linewidths and Gain Coefficients for Selected Materials

Raman transition frequencies, linewidths, and gains of selected materials at room temperature[a]

Material	Mode	ν_0 (cm^{-1})	$\Delta\nu$ (MHz)	λ_L (nm)	g (cm/GW)	Reference
H_2 gas (20 atm)	Q(1)	4155	$309/\rho + 52.2\ \rho$	532	2.5	22, 62, 63
H_2 gas (high)	S(1)	587	$119\ \rho$	350	1.2	64
D_2 gas (60 atm)	Q(2)	2987	$101/\rho + 120\ \rho$	532	0.45	63, 65, 66, 67
D_2 gas	S(2)	414	$124\ \rho$	350		64
HD	Q(1)	3628	$693\ \rho$	532		68
HD	S(1)	443	$760\ \rho$	350	0.098	64
CH_4 (115 atm)	ν_1	2913	$8220 + 384\ \rho$	532	1.26	63, 65
N_2	Q	2327	$22.5\ (\rho < 10)$	248	0.3ρ	69
N_2	S(6)	60	$3570\ \rho$	566	0.0063	70
O_2	Q	1552	54	248	0.012ρ	69
SiH_4	Q	2186	15 (est.)	248	0.19ρ	69
GeH_4	ν_1	2111	15 (est.)	248	0.27ρ	69
CF_4	ν_1	908	21 (est.)	248	0.008ρ	69
SF_6	ν_1	775	30 (est.) (cm^{-1})	248	0.014ρ	69
Liquid N_2		2326.5	0.067	694	16 ± 5	2
Liquid O_2		1552	0.117	694	14.5 ± 4	2
H_2O		3290	200	694	0.14	1, 2, 71
Benzene		992	2.15		2.8	2
CS_2		655.6	0.50	694	24	2
Nitrobenzene		1345	6.6		2.1	2
Bromobenzene		1000	1.9		1.5	2
Chlorobenzene		1002	1.6		1.9	2
Toluene		1003	1.94		1.2	2
$LiNbO_3$		637	20	694	9.4	2
$Ba_2NaNb_5O_{15}$		650		694	6.7	2
$LiTaO_3$		201	22	694	4.4	2
SiO_2		467		694	0.8	2
$Ba(NO_3)_2$		1047	1.5 cm^{-1}	532	47	72–76

In the limit of large pump depletion, the Stokes intensity becomes

$$I_S(z) = I_S(0) + \frac{\omega_S}{\omega_L} I_L(0) \tag{26}$$

Equation (26) indicates that the maximum energy that can be added to the Stokes wave is reduced from the energy of the pump wave by the fraction (ω_S/ω_L). This ratio is termed the *Manly Rowe fraction.* The difference between the energy given up by the pump wave and that gained by the Stokes wave is taken up by energy deposited in the material excitation. Although complete energy conversion is not possible with Raman scattering, in principle 100 percent of the pump photons can be converted to the Stokes wave. In practice, high photon conversion efficiency to a single Stokes wave is limited in Raman generators by multiple Stokes or anti-Stokes scattering. High conversion efficiencies are generally obtained in practice in Raman amplifiers or in Raman generators where multiple Stokes generation is unfavorable because of energy level structure. Photon conversion efficiencies in excess of 90 percent have been reported with pulsed lasers.

Gain Narrowing. Gain narrowing can occur when the Raman gain varies in one of the parameters of the interaction—for example, time, because of pulsed radiation; space, because of a special mode profile; or spectrum, because of use of broadband light; or when a Raman generator is used.

TABLE 3 Linewidths and Gain Coefficients for Selected Materials (*Continued*)

Calculated[b] and measured gain (g_s) factor for stimulated Raman transitions in liquids (ℓ), gases (g), and solids (s)

Substance	Pump Wavelength (nm)	Frequency (cm^{-1})	Linewidth $\Delta\nu_R$ (cm^{-1})	Gain (g_s) $\times 10^9$ (cm/W)	g_s calc. $\times 10^9$ (cm/W)	g_s at 532 nm[c]	g_s Relative to $C_6H_6(\ell)$[d]	Reference
Benzene (ℓ)	532	992	2.15	5.5[e]		5.5	1.0	132
	532	992	2.15	5.5[f]		5.5		133
	532	992	2.15	4.3 ± 0.9[g]		4.3 ± 0.9		134
	694.3	992	2.15		2.8	5.9[h,i]		135
Oxygen (ℓ)	694.3	1552	0.117	16.0 ± 0.5	14.5 ± 0.4	21.5	3.9	135
Nitrogen (ℓ)	532	2327	0.067	30.0	24.0 ± 7.0	30.0	5.4	136
	694.3	2327	0.067	16.0 ± 0.55	17.0 ± 0.5	21.5	3.9	135
	1060	2327	0.067	10.0	9.0 ± 3.0	23.2	4.2	137
	1315	2327	0.067	5.0 ± 2.0	6.0 ± 2.0	15.6 ± 6.2	2.9	138
Carbon disulfide (ℓ)	694.3	655.6	0.50	24.0		32.2	5.9	135
Methanol (ℓ)	694.3	2837	18	0.4		0.53	0.10	139
Carbon tetrachloride (ℓ)	597.6	458		1.3		1.5	0.27	140
	532						0.12[j]	141
Acetone (ℓ)	532						0.20[j]	141
Cyclohexane (ℓ)	532						0.25[j]	141
Hydrogen[k] (g)	694.3	4155			1.5[l]	2.14		142
	694.3	4155		1.9 ± 0.3[l]	1.5[l]	2.7		142
	694.3	4155		1.5[l]		2.1		143
	353	4155		5.0[l]	5.7[l]			131
	308	4155			6.7[l]			131
	10600	354			0.07	0.09		144
Hydrogen deuteride (g)	353	3628		0.2				131
Nitrogen (g, 1 atm)	694.3	2330.7		0.0022		0.0030		128
	694.3	2330.7	0.075		0.0027[m]	0.0038		145
Carbon tetrafluoride (g, 500 atm)	532	980	0.17	24.6 ± 2[n]		2.46 ± 2[n]		127

TABLE 3 Linewidths and Gain Coefficients for Selected Materials (*Continued*)

Calculated[b] and measured gain (g_s) factor for stimulated Raman transitions in liquids (ℓ), gases (g), and solids (s) (*Continued*)

Substance	Pump Wavelength (nm)	Frequency (cm^{-1})	Linewidth $\Delta\omega_R$ (cm^{-1})	Gain (g_s) $\times 10^9$ (cm/W)	g_s calc. $\times 10^9$ (cm/W)	g_s at 532 nm[c]	g_s Relative to $C_6H_6(\ell)$[d]	Reference
Calcite (s)	532	1086	1.2	5.5		5.5		146
Fused quartz (s)	495.4	420		0.017		0.016		147
Potassium dihydrogen phosphate (s)	532	918	18	0.21 ± 0.05[g]		0.21 ± 0.05		134

[a] ρ is measured in amagats (1 amagat = 2.68×10^{-19} cm^{-3}).
[b] Only those supporting measured values of special interest are given.
[c] Except where noted, $g_s/532 = (\omega_s/532)/(\omega_s/\text{meas})\ g_s/\text{meas}$.
[d] For qualitative use only; see previous text.
[e] Estimated from stimulated threshold.
[f] Estimated from stimulated conversion.
[g] Direct measurements with single-frequency lasers.
[h] Extrapolated using $I\alpha\ \omega_s^4(\omega_a - \omega_\ell)^{-2}$; $\omega_a = 39{,}000$ cm^{-1}.
[i] See Ref. 77 for discussion of peak cross section measurements.
[j] Relative threshold measurement.
[k] For detailed analysis of H_2 cross-section pump frequency dependence, see Ref. 63.
[l] Pressure independent gain; Q(1) transition.
[m] Corrected using linewidth of Ref. 58; Q(6) transition.
[n] Transient gain.

Reprinted with permission from M. J. Weber (ed.), *CRC Handbook of Laser Science and Technology: Optical Materials*, suppl. 2, copyright CRC Press, Boca Raton, FL, 1988; R. W. Boyd, *Nonlinear Optics,* Academic Press, New York, 1992; M. J. Weber (ed.), *CRC Handbook of Laser Science and Technology: Optical Materials*, part 1, vol. III, copyright CRC Press, Boca Raton, FL, 1988.

TABLE 4 Temperature Dependence of Line Shift Parameters for H_2

T (°K)	Transition	$\nu_R(0)$ (cm^{-1})	C (MHz/amagat)	D (MHz/amagat^2)	Reference
474	Q(1)	4155	9.5 ± 0.9	0.51 ± 0.07	22
298	Q(1)		–96 ± 1		22
298	Q(0)		–64 ± 5		22
81	Q(1)		–305 ± 10		22
81	Q(0)		–250 ± 10		22
81	Q(0)		–336 ± 10		22
p-H_2					
295	S(0)		6.5 ± 3		78
	S(1)		5.9 ± 1		78
80	S(0)		–22.3 ± 0.6		78
	S(1)		–23 ± 0.6		78

Line shift parameters: $\nu_R = \nu_R(0) + C\rho + D\rho^2$

Reprinted with permission from M. J. Weber (ed.), *CRC Handbook of Laser Science and Technology: Optical Materials,* suppl. 2. Copyright CRC Press, Boca Raton, FL, 1988.

TABLE 5 Temperature Dependence of Line Broadening Parameters for H_2 and N_2

H_2

T (°K)	Transition	A (MHz – amagat)	B (MHz/amagat)	ρ_c (amagat)	Reference
474	Q(1)	508 ± 29	94.0 ± 2.0	1.23	22
298	Q(1)	309 ± 11	52.2 ± 0.5	0.92	22
298	Q(0)	257 ± 12	76.6 ± 0.8	0.79	22
81	Q(1)	107 ± 20	41.5 ± 0.6	0.63	22
81	Q(0)	189 ± 40	29 ± 1	1.1	22
81	Q(0)	76 ± 6	45.4 ± 0.8	0.45	22
p-H_2					
295	S(1)	6.15	114 ± 5	0.134	78
	S(0)	1.87	77 ± 2	0.068	78
80	S(1)	2.1	110 ± 3	0.088	78
	S(0)	1.37	67 ± 2	0.095	78

N_2

T (°K)	Transition	ν_R (cm^{-1})	λ_s (nm)	B_0 (MHz/amagat)	γ	$\Delta N/N$	g (cm/GW)	Reference
298								
	S(6)	60	568	3560	0.26 ± .04	0.0282	0.0036	70, 78
	S(8)	76	568	3270	0.33 ± .004	0.0337	0.0046	70, 78
	S(10)	92	568	3060	0.35 ± .002	0.0335	0.0048	70, 78
	S(12)	108	568	2870	0.39 ± .03	0.0289	0.0043	70, 78
195								
	S(6)		568	3070		0.0485	0.0072	70, 78
	S(8)		568	2860		0.0491	0.0076	70, 78
	S(10)		568	2660		0.0399	0.0065	70, 78
	S(12)		568	2340		0.0271	0.0049	70, 78

TABLE 5 Temperature Dependence of Line Broadening Parameters for H_2 and N_2 (*Continued*)

N_2 *(Continued)*								
T (°K)	Transition	ν_R (cm^{-1})	λ_s (nm)	B_0 (MHz/amagat)	γ	$\Delta N/N$	g (cm/GW)	Reference
80								
	S(6)		568	2520		0.0897	0.0161	70, 78
	S(8)		568	2120		0.0452	0.0093	70, 78
	S(10)		568	1940		0.0156	0.0034	70, 78
	S(12)		568	1690		.00378	0.00091	70, 78

Broadening coefficients for H_2: $\Delta\nu_R = A/\rho + B\rho$
$A = 309/\rho\ (T/298)^{0.92}$ $B = [51.8 + 0.152(T - 298) + 4.85 \times 10^{-4}\ (T - 298)]\ \rho$
Broadening coefficients for N_2: $\Delta\nu_R = B_0\rho(T/295)^{\gamma}$

Reprinted with permission from M. J. Weber (ed.), *CRC Handbook of Laser Science and Technology: Optical Materials,* suppl. 2. Copyright CRC Press, Boca Raton, FL, 1988.

TABLE 6 Formula Summary for SRS in Molecules 1

Quantity	Formula	Reference
$\partial\sigma/\partial\Omega$ (vibrational, averaged over rotational levels)	$(2\pi\nu_s)^4\ (\alpha_{01}^2 + 7/45 \sum_j f_j b_{jj} \gamma_{01}^2)$	62
$\partial\sigma/\partial\Omega$ (vibrational, single rotational level)	$(2\pi\nu_s)^4\ (\alpha_{01}^2 + 4/45\ b_{jj}\gamma_{01}^2)$	62
	$B_{jj} = J(J+1)(2J-1)(2J+1)$ f_j–relative population of level J For hydrogen: $\alpha_{01} = 1.11 \times 10^{-25}$ cm^{-3} $\gamma_{01} = 0.951 \times 10^{-25}$ for $\lambda_L = 500$ nm	
$\partial\sigma/\partial\Omega$ (vibrational, wavelength dependence for hydrogen)	$A\ \nu_s^4/(\nu_i^2 - \nu_L^2)^2$	62
	$A = 8.74 \times 10^{-28}$ cm^2/sr; $\nu_i = 8.48 \times 10^4$ cm^{-1}	
ν_R (Raman shift in H2, pressure dependence)	$\nu_R\ (0) + C\rho + \Delta\rho^2$ (ρ in amagats)	62
$\Delta\nu_R$ (linewidth of H2, pressure and temperature dependence)	$(309/\rho)(T/298)^{0.92} + [51.8 + 0.152(T - 298) + 4.85 \times 10^{-4}(T - 298)^2\rho]$ (ρ in amagats)	62
$\partial\sigma/\partial\Omega$ (rotational scattering in linear molecules)	$(2/15)(2\pi\nu_s/c)^4\gamma^2[(J+1)(J+2)]/[(2J+1)(2J+3)]$	70
	J is lower-state rotational number $\gamma(\nu) = \alpha_{S\|\|}\ [\nu_{i\|\|}^2/(\nu_{i\|\|}^2 - \nu^2)] - \alpha_{S\perp}\ [\nu_{i\perp}^2/(\nu_{i\perp}^2 - \nu^2)]$ For nitrogen: $\nu_{i\|\|} = 1.26 \times 10^5$ cm^{-1} $\nu_{i\perp} = 1.323 \times 10^5$ cm^{-1} $\alpha_{S\|\|} = 2.2 \times 10^{-24}$ cm^{-3} $\alpha_{S\perp} = 1.507 \times 10^{-24}$ cm^{-3}	

Reprinted with permission from M. J. Weber (ed.), *CRC Handbook of Laser Science and Technology, Optical Materials,* suppl. 2. Copyright CRC Press, Boca Raton, FL, 1988.

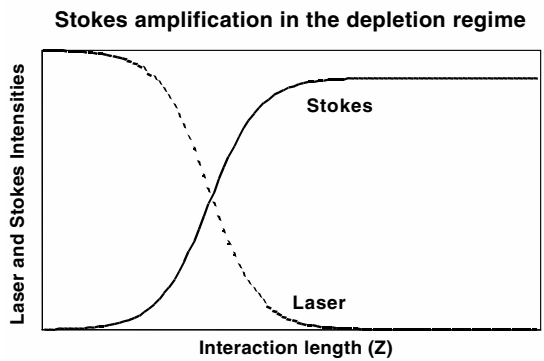

FIGURE 4 Calculated pump and Stokes dependence on interaction length in pump depletion regime.

Spectral Gain Narrowing. Spectral gain narrowing is commonly encountered in Raman generators. The spontaneous Stokes emission has the spectral variation of the appropriate Raman transition. For a lorentzian line shape, this variation is given by

$$P_S(\Delta\omega) = P_S(0)\,\frac{1}{\Delta\omega^2 T^2 + 1} \tag{27}$$

where $\Delta\omega = \omega_o - (\omega_L - \omega_S)$.

This variation with detuning also appears in the Raman gain of Eq. (13) or (15). The Stokes light generated from such a signal can be represented approximately as

$$I(\Delta\omega, L) = I(0)\,\frac{1}{\Delta\omega^2 T^2 + 1}\,\exp\left[\frac{G(0)}{\Delta\omega^2 T^2 + 1}\right] \tag{28}$$

The reduced gain at nonzero detunings from the Raman resonance leads to narrowing of the amplified Stokes spectrum relative to the spontaneous spectrum.[22] If we use the quantity $\Delta\omega(G)$ to describe the spectral width (FWHM) of the generated or amplified Stokes light, then the spectral width of the amplified Stokes light is

$$\Delta\omega(G) = \Delta\omega(0)\,\sqrt{\frac{\ln 2/G(0)}{1 - \ln 2/G(0)}} \tag{29}$$

where $G(0)$ is the gain at the center of the line. If we consider the range of values of G that can be achieved without driving the interaction into saturation to be $23 < G_{\max} < 40$, then the maximum gain narrowing that can be experienced without driving the interaction into saturation is on the order of 5.5 to 7.5.

Photon Description. The steady-state Raman gain can be recast in the formulation of photon interactions. In this situation, the pump and Stokes intensities are given by

$$I_S = h\nu_S n_S \tag{30a}$$

$$I_L = h\nu_L n_L \tag{30b}$$

where n_S and n_L are the photon flux densities (photons per square centimeter per second), which are related to the corresponding photon densities (photons per cubic centimeter) without dispersion as

$$n_S = N_S c \tag{31a}$$

$$n_L = N_L c \tag{31b}$$

Equations for the growth of pump and Stokes photon densities can be derived from quantum mechanical rate equations as:[7]

$$\frac{dN_S}{dt} = K(N_S + 1)N_L \tag{32a}$$

$$\frac{dN_L}{dt} = -K(N_L + 1)N_S \tag{32b}$$

where K is the appropriate transition rate for the Raman interaction.

These can be converted to the spatial gain equations for the photon flux density through the relations

$$\frac{dN_S}{dt} = \frac{dn_S}{dz} \tag{33a}$$

$$\frac{dN_L}{dt} = \frac{dn_L}{dz} \tag{33b}$$

giving

$$\frac{dn_S}{dz} = K(n_S + 1)n_L \tag{34a}$$

$$\frac{dn_L}{dt} = -K(n_L + 1)n_S \tag{34b}$$

The 1 in Eqs. (34*a* and *b*) arises from quantum mechanical commutators and represents spontaneous Raman scattering. When the number of Stokes photons per mode is small compared to unity, the spontaneous Raman emission result is obtained:

$$n_S = Kn_L L \tag{35}$$

where L is the length of the scattering medium. When $n_S \gg 1$, the exponential gain of stimulated Raman scattering is obtained:

$$n_S(L) = n_S(0)e^{Kn_L z} \tag{36}$$

where $K = h\nu g_{SS}$. The relation of spontaneous and stimulated Raman scattering will be discussed again later in the chapter.

Transient Effects. When the temporal structure of the pump or Stokes wave varies on a time scale comparable to or shorter than the steady-state time given in Eq. (19), transient effects must be taken into account. In this situation, the integrating effects of the material excitation affect the properties of the Raman interaction. Depending on the situation, this can result in reduced Raman gain for pulses of a given intensity or alteration of the coherence properties of the Stokes radiation. Transient effects can occur for short pump pulses or broadband pump and/or Stokes waves.

Pulsed Transient Effects. Transient Raman scattering with pulsed Raman radiation is described by the equations

$$\frac{\partial A_S(z,t)}{\partial z} + \frac{n_S}{c}\frac{\partial A_S(z,t)}{\partial t} = i\kappa_2 Q^*(z,t)A_L(z,t) \tag{37a}$$

$$\frac{\partial A_L(z,t)}{\partial z} + \frac{n_L}{c}\frac{\partial A_L(z,t)}{\partial t} = i\frac{\omega_L n_S}{\omega_S n_L}\kappa_2 Q(z,t)A_S(z,t) \tag{37b}$$

$$\frac{\partial Q^*(z,t)}{\partial t} + \Gamma Q^* = -i\kappa_1 A_S(z,t)A_L^*(z,t) \tag{37c}$$

where

$$\kappa_1 = \frac{1}{4\omega_0 m}\left(\frac{\partial \alpha}{\partial Q}\right) \tag{38}$$

and κ_2 is given in Eq. (11).

In the most general form, when pump depletion is involved, these equations must be solved numerically. When pump depletion and dispersion can be neglected, the pump field can be taken as a prescribed function of z and t, and the equations take on the form

$$\frac{\partial A_S(z',\tau)}{\partial z'} = i\kappa_2 Q^*(z',\tau)A_L(\tau) \tag{39a}$$

$$\frac{\partial Q^*(z',\tau)}{\partial \tau} + \Gamma Q^*(z',\tau) = -i\,\kappa_1 A_S(z',\tau)A_L^*(\tau) \tag{39b}$$

where z' and τ are coordinates moving with the common velocity of the pump and Stokes pulses:

$$z' = z \tag{40a}$$

$$\tau = t - z/c \tag{40b}$$

An integral solution for these equations can be written as:[16–19]

$$A_S(z,\tau) = A_S(0,\tau) + \sqrt{\kappa_1\kappa_2 z}\,A_L(\tau)\int_{-\infty}^{\tau}\frac{e^{-\Gamma(\tau-\tau')}A_L^*(\tau')A_S(0,\tau')\,I_1\left(\sqrt{4\kappa_1\kappa_2 z[p(\tau)-p(\tau')]}\right)}{\sqrt{p(\tau)-p(\tau')}}\,d\tau' \tag{41a}$$

$$Q^* = -i\kappa_2\int_{-\infty}^{\tau} e^{-\Gamma(\tau-\tau')}\,A_L^*(\tau')\,A_S(0,\tau')\,I_0\left(\sqrt{4\kappa_1\kappa_2 z[p(\tau)-p(\tau')]}\right)d\tau' \tag{41b}$$

where I_0 and I_1 are modified Bessel functions and

$$p(\tau) = \int_{-\infty}^{\tau}|A_L(\tau')|^2\,d\tau' \tag{42}$$

is proportional to the total pump energy integrated to time τ.

In the extreme transient regime, when $t_p \ll T_2$, and when the incident Stokes pulse has the same functional form as the pump, an analytic solution for the Stokes intensity can be found:

$$I_S(z,\tau) = I_S(0,\tau)I_0^2(u(z,\tau)) \tag{43}$$

where

$$u(z, \tau) = \sqrt{4\kappa_1\kappa_2 z p(\tau)} = \sqrt{2g_{ss}\Gamma z \int_{-\infty}^{\tau} I_L(\tau')\, d\tau'} \tag{44}$$

and g_{ss} is the steady-state gain coefficient as given in Eq. (13).

When the conditions for Eq. (43) are valid, the solution can be approximated for values of u greater than about 3, corresponding to intensity amplifications of about 24, with the first term in the asymptotic expansion:

$$I_S(z, \tau) = I_S(0, \tau)\, \frac{e^{2u}}{2\pi u} \tag{45}$$

Quantities other than the instantaneous intensity, such as power density, energy density, or total pulse energy, are useful for characterizing transient Raman measurements done with short pulses. Expressions corresponding to Eq. (45) and for the first and second terms of the expansion of Eq. (43) in u are given in Table 7. The variation of these quantities with the transient gain parameter u is shown in Fig. 5. These solutions are useful for modeling the approximate properties of transient interactions. However, in most practical situations the incident pump and Stokes pulses do not have the same functional form, and the more general integral solution of Eq. (41*a*) must be used for accurate results, taking into account the specific variation of the Stokes amplitude and phase and the relative timing between the incident Stokes and pump pulses. An approximate analytic expression has been given in the limit of high conversion in which the Stokes pulse evolves to an approximate constant form and the pump pulse is described by regular Bessel functions.[79]

In the extreme transient regime $t_p \ll T_2$, growth of the Stokes pulse in the leading part of the pulse is dominated by the Bessel function and the Stokes pulse rises more slowly than the pump. In the trailing part of the pulse, the integral contribution remains fairly constant and the Stokes amplitude follows the pump amplitude.[17] The result is that the Stokes pulse is delayed relative to the pump and is shorter than the pump. Ideal square pulses can be shortened by an arbitrarily large factor, while more realistic gaussian pulses can be shortened by about a factor of 2.[17,80] The transient response for square and gaussian pulses is illustrated in Fig. 6. Optimal amplification of the Stokes pulse has been shown to require that the incident

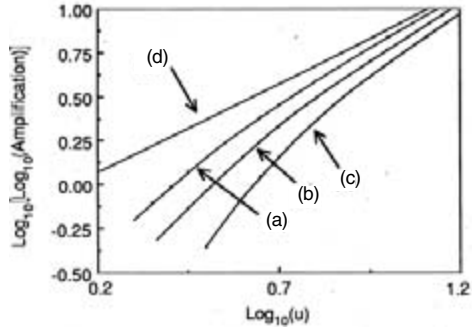

FIGURE 5 Theoretical dependence of the small-signal amplification on the transient gain parameter u for (*a*) the intensity, (*b*) the energy density or power, and (*c*) the energy as predicted by the exact Bessel function solution. The exponential form exp(2*u*) is shown for comparison in (*d*). (From Ref. 19.)

TABLE 7 Analytic Expressions and High-Gain Limiting Forms for Small-Signal Transient Raman Amplification of Various Quantities.[19,a]

	Intensity, I_S[b]	Energy Density, $\mathcal{W}_S$[c]	Power, $\mathcal{P}_S$[d]	Energy, $\mathcal{E}_S$[e]
Approximation	$I_S(r, z, t) = \dfrac{I_S(r, z, t)}{I_S(r, 0, t)}$	$\mathcal{W}_S(r,z) = \dfrac{\int_{-\infty}^{\infty} I_S(r, z, t')dt'}{\int_{-\infty}^{\infty} I_S(r, 0, t')dt'}$	$\mathcal{P}_S(r,z) = \dfrac{\int_0^{\infty} I_S(r, z, t)dr^2}{\int_0^{\infty} I_S(r, 0, t)dr^2}$	$\mathcal{E}_S(r,z) = \dfrac{\int_0^{\infty}\int_{-\infty}^{\infty} I_S(r, z, t')dt'\, dr^2}{\int_0^{\infty}\int_{-\infty}^{\infty} I_S(r, 0, t')dt'\, dr^2}$
Exact	$I_0^2(u)$	$I_0^2(u) - I_1^2(u)$	$I_0^2(u) - I_1^2(u)$	$I_0^2(u) - 2I_1^2(u) + I_0(u)I_2(u)$
High-gain limit (1st term)	$e^{2u}/2\pi u$	$e^{2u}/2\pi u^2$	$e^{2u}/2\pi u^2$	$e^{2u}/2\pi u^3$
High-gain limit (1st 2 terms)	$(e^{2u}/2\pi u)(1 + 1/4u)$	$(e^{2u}/2\pi u^2)(1 + 1/4u)$	$(e^{2u}/2\pi u^2)(1 + 1/4u)$	$(e^{2u}/2\pi u^3)(1 + 3/4u)$

[a] $u = u_m(r, z, t) = 2[\kappa_1\kappa_2 z \int_{-\infty}^{t} |A_L(r, t')|^2\, dt']^{1/2}$
[b] $u = u_m(r, z, t)$
[c] $u = u_m(r, z, \infty)$
[d] $u = u_m(0, z, t)$
[e] $u = u_m(0, z, \infty)$

Stokes pulse arrive earlier than the pump by about half the pulse duration.[19] An example of experimentally measured transient Raman amplification is given in Fig. 7 along with a theoretical comparison. The theoretical curve was obtained by integrating the square magnitude of Eq. (41*a*) over space and time using the experimentally measured amplitude and phase variations of the incident Stokes pulse. Agreement between experiment and theory was obtained over approximately eight orders of magnitude using one adjustable parameter in the region below pump depletion.

The peak intensity amplification in the extreme transient limit is reduced from the steady-state amplification for pump pulses with the same peak intensity. The intensity amplification grows as the pulse length increases, approaching the steady-state value when $t_p \gg G_{ss}T_2$. For pulses of a given energy, the total integrated energy amplification increases steadily as the pulse duration decreases, reaching a maximum in the extreme transient regime.

Phase Pulling. There is a tendency for the Stokes phase to become locked to the pump phase in the transient regime. This can be seen from the equations for the phases of the pump and Stokes pulses:[19]

$$\frac{\partial\phi_S}{\partial z} = -\kappa_2 \frac{A_L}{A_S} Q \sin\Phi \tag{46a}$$

$$\frac{\partial\phi_L}{\partial z} = -\kappa_2 \frac{n_S\omega_L}{n_L\omega_S} \frac{A_S}{A_L} Q \sin\Phi \tag{46b}$$

$$\frac{\partial\phi_Q}{\partial z} = -\kappa_1 \frac{A_L A_S}{Q} \sin\Phi \tag{46c}$$

where $\Phi = \phi_S + \phi_Q - \phi_L$.

The phase driving terms vanish for the condition $\Phi = 0$ or π, which are the conditions for optimum power transfer from the pump beam and to the pump beam, respectively. Phase pulling occurs only when $\Phi \neq 0$ or π and when the time derivatives are important. When the time derivatives are not important, ϕ_Q automatically adjusts itself so that the condition $\Phi = 0$ is satisfied. When the transient response is important, phase pulling occurs whenever ϕ_S and

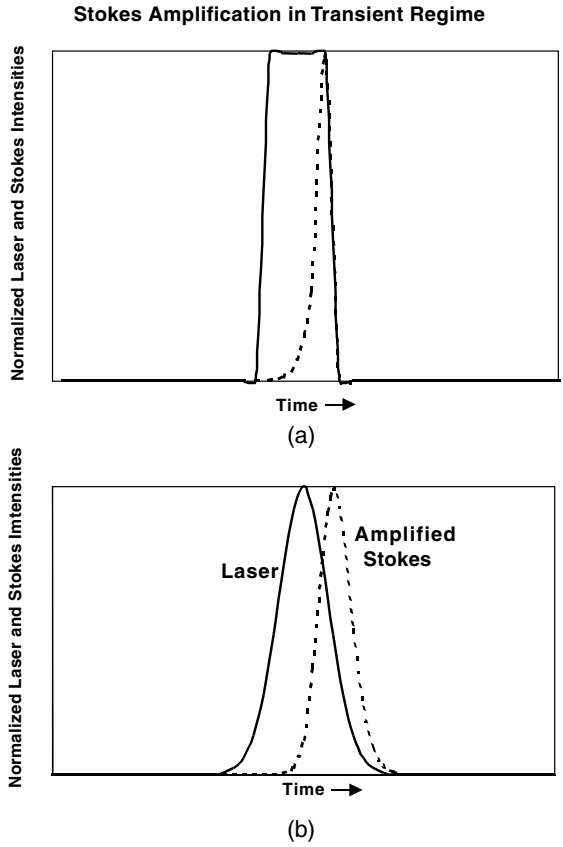

FIGURE 6 Calculated Stokes intensity (dotted line) and pump (solid line) for square pump pulses (*a*) and gaussian pump pulses (*b*). The input Stokes signal was assumed to be constant in both cases.

ϕ_L have different time dependencies. If the amplitude of the initial Stokes wave is small compared to that of the pump, the phase of the material excitation will be established at some constant value early in the pulse after the material excitation has been amplified above the noise level. At later times the phase of the Stokes wave will be driven according to Eq. (46a) so as to establish the condition $\Phi = 0$. In the early stages of the amplification, the corresponding driving term for the pump phase is much smaller, so that the Stokes phase becomes effectively locked to that of the incident pump, with a possible constant offset due to the phase of the material excitation. If the amplitude of the incident Stokes wave is comparable to that of the pump, the phases of all of the waves can evolve during the interaction, and the transfer of power from the pump to the Stokes wave can be affected or greatly reduced. An example of phase pulling in short-pulse Raman interactions is shown in Fig. 8.

Solitons. Soliton and other self-similar solutions to the transient Raman equations can also be derived. Using Eq. (37) in the form

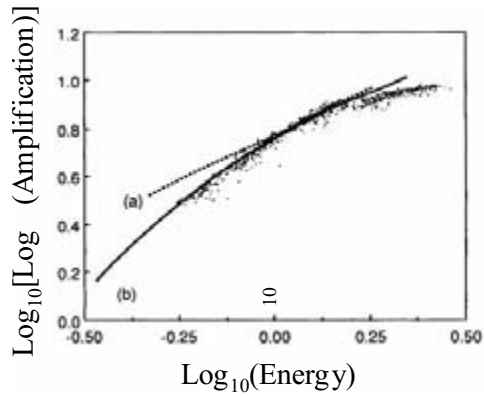

FIGURE 7 Experimental measurement of transient Stokes amplification in hydrogen gas. Solid line includes measured phase and amplitude structure of incident Stokes pulse. Dotted line was calculated for the same conditions, neglecting the phase structure of the incident Stokes pulse. The deviation of the solid curve from the measurements at the high end is due to pump depletion. (From Ref. 19.)

$$\frac{\partial A_S}{\partial \xi} = i\kappa_2 A_L Q^* \tag{47a}$$

$$\frac{\partial A_L}{\partial \xi} = i\frac{\omega_L}{\omega_S}\,\kappa_2 A_S Q \tag{47b}$$

$$\frac{\partial Q}{\partial \tau} + \Gamma Q = i\kappa_1 A_L A_S^* \tag{47c}$$

where κ_1 and κ_2 are given in Eqs. (38) and (11), respectively, and ξ and τ are moving coordinates related to the laboratory coordinates by

$$\xi = z \tag{48a}$$

$$\tau = t - zn/c \tag{48b}$$

In the extreme transient limit, the term with Γ in Eq. (47*c*) can be neglected and the equations can be expressed in normalized quantities as

$$\frac{\partial A_1}{\partial \chi} = -A_2 X \tag{49a}$$

$$\frac{\partial A_2}{\partial \chi} = A_1 X^* \tag{49b}$$

$$\frac{\partial X}{\partial \tau'} = A_1 A_2^* \tag{49c}$$

where $A_1 = \sqrt{\omega_S n_L\ \kappa_1/\omega_L n_S \kappa_2}A_L$, $A_2 = \sqrt{\kappa_1/\kappa_2}A_S$, and $X = -i\sqrt{\omega_L n_S/\omega_S n_L}Q$, $\chi = \kappa_2\xi$, $\tau' = (\omega_L n_S/\omega_S n_L)\kappa_2\,\tau$.

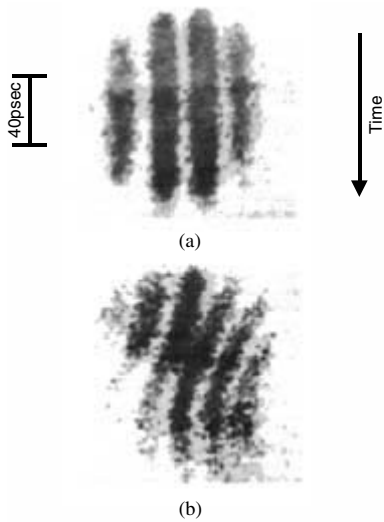

FIGURE 8 Experimental demonstration of phase pulling in transient Raman amplification. The pump beam and incident Stokes beam both carry phase modulation due to the nonlinear index in the laser. The measurement shows time-dependent interference between the incident and amplified Stokes waves. When the incident Stokes phase structure is aligned with the pump phase structure, no phase pulling is observed (*a*). When the incident Stokes pulse is advanced to misalign the pump and Stokes phase structure, phase pulling is observed (*b*). (From Ref. 19.)

The soliton solutions are:[81]

$$A_1(\chi, \tau) = K(\tau)\left(1 - \frac{a^2}{4\alpha^2}\right)^{1/2} \exp(i\alpha\chi/2)\,\mathrm{sech}\left\{\left(\alpha^2 - \frac{a^2}{4}\right)^{1/2}\left[\chi - \frac{I(\tau)}{\alpha^2}\right]\right\} \tag{50a}$$

$$A_2(\chi, \tau) = K(\tau)\left(1 - \frac{a^2}{4\alpha^2}\right)^{1/2} \tanh\left\{\left(\alpha^2 - \frac{a^2}{4}\right)^{1/2}\left[\chi - \frac{I(\tau)}{\alpha^2}\right]\right\} \tag{50b}$$

$$X(\chi, \tau) = \left(\alpha^2 - \frac{a^2}{4}\right)^{1/2} \exp(i\alpha\chi/2)\,\mathrm{sech}\left\{\left(\alpha^2 - \frac{a^2}{4}\right)^{1/2}\left[\chi - \frac{I(\tau)}{\alpha^2}\right]\right\} \tag{50c}$$

where $K^2(\tau) = |A_1(\chi, \tau)|^2 + |A_2(\chi, \tau)|^2$, $I(\tau) = \int_{-\infty}^{\tau} K^2(\tau')d\tau'$ and a and α are arbitrary parameters such that $a > \alpha/2$.

These are transient solutions in which the Stokes pulse is large everywhere except for a dip centered on the position $\chi = I(\tau)/\alpha^2$. The Stokes pulse also has a phase shift at its center. When $a = 0$, the phase shift is π, and when $a \neq 0$ it is smaller. The pump intensity is small except for a narrow region centered about $\chi = I(\tau)/\alpha^2$, and the behavior of the material excitation is similar to that of the pump.

The form of these solutions is opposite to those normally encountered in Raman interactions. Once they are established, they propagate in self-similar form at a speed that is slower than that of the optical pulses, gradually "walking" backward in the optical pulse and eventually disappearing. However, the pulse shapes necessary for soliton formation do not occur in all experimental situations. In normal transient experiments, with the incident Stokes wave weak and the pump strong, the Stokes phase will lock to the pump phase, and solitons cannot develop. They have been produced with a phase shift introduced onto the Stokes pulse externally.[82] In this situation, the soliton pulse of Eq. (50*a*), which is significantly shorter than T_2, evolves from longer pulses and damping plays a central role in its formation. An experimental demonstration of this behavior has been done by Druhl et al.[82] and their results are reproduced in Fig. 9. Conditions for soliton formation can also be encountered in growth from noise using narrowband pump pulses due to phase fluctuations in the zero point starting signal of the Stokes field. Other self-similar solutions are possible as well. Forms with damped oscillations, termed *accordion solutions,* have been described by Menyuk.[83]

Broadband Effects. Transient effects also appear in the conversion of broadband radiation, which is produced, for example, in many types of pulsed lasers, when the overall pulse duration is longer than T_2 but the pump linewidth is wider than the Raman linewidth:[84–99]

$$t_p \gg T_2 \tag{51a}$$

$$\Delta\nu_L > \frac{1}{\pi T_2} \tag{51b}$$

The equations for the Stokes and material excitation are as given in Eq. (37). The interaction can be modeled in the time domain, or in the frequency domain using a mode model for the laser radiation.

In the mode picture, the pump and Stokes radiation is modeled as being made up of a combination of randomly phased modes separated by an amount Δ, shown in Fig. 10:

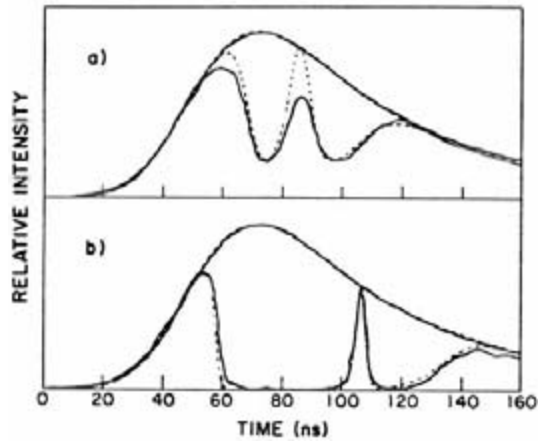

FIGURE 9 Experimental (solid curves) and theoretical (dashed curves) behavior of Raman soliton formation in hydrogen gas showing the input (upper curves) and output (lower curves) pump pulses. The soliton was initiated by introducing a phase shift on the incident Stokes pulse. The overall pulse duration was about 70 ns. The curves in (*b*) were obtained with higher pump power than the curves in (*a*). (From Ref. 82; copyright 1983 by American Physical Society.)

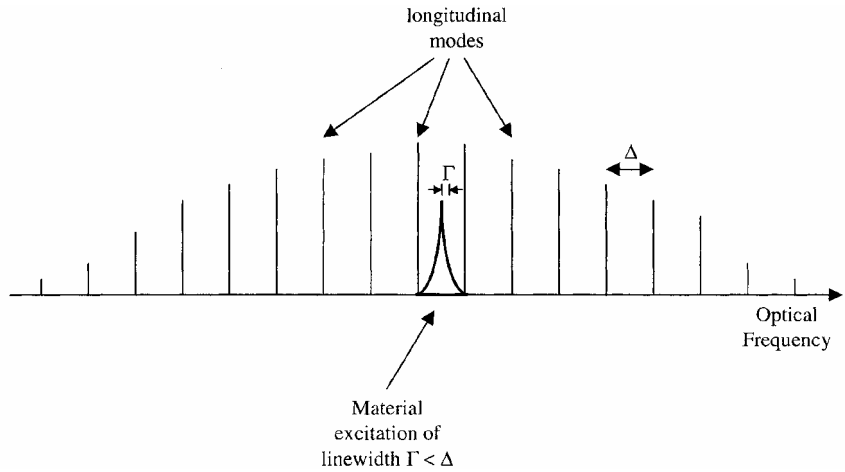

FIGURE 10 Mode structure used to model the broadband Raman scattering. The laser and Stokes modes are spaced by frequency Δ, and, for approximations of Eq. (56), the Raman linewidth is narrower than the mode spacing.

$$E_S = \tfrac{1}{2} \sum_m A_{S,m} e^{-i(m\Delta t + \phi_{S,m})}\, e^{-i(\omega_S t - k_S z)} \tag{52a}$$

$$E_L = \tfrac{1}{2} \sum_m A_{L,m}\, e^{-i(m\Delta t + \phi_{L,m})}\, e^{-i(\omega_L t - k_L z)} \tag{52b}$$

In the absence of dispersion, Eq. (37*c*) can be solved in the frequency domain:

$$Q_k^* = i\kappa_2 \sum_m \frac{A^*_{L,\,m+k} A_{S,\,m}}{\Gamma - im\Delta} \tag{53}$$

The average Stokes intensity is given by:[93]

$$\bar{I}_S(z) = \bar{I}_S(0) + \bar{I}_S(0) \sum_k \left[\frac{|\sum_m A_{L,\,m+k} A^*_{S,\,m}(0)|^2}{\sum_m A_{L,\,m} A^*_{L,\,m} \sum_m A_{S,\,m}(0) A^*_{S,\,m}(0)} \right] \left\{ \exp\left[\frac{\bar{I}_L g z}{1 + (k\Delta/\Gamma)^2} \right] - 1 \right\} \tag{54}$$

where the bar symbol denotes the average intensity given by

$$\bar{I}_S = \tfrac{1}{2} c n_S \varepsilon_o \sum_m A^*_{S,\,m} A_{S,\,m} \tag{55}$$

If the longitudinal mode spacing is much wider than the Raman linewidth and the pump linewidth is broad enough, the material excitation Q will not be able to follow the temporal variations of the light due to the mode structure. This is equivalent to the steady-state approximation. Only the $k = 0$ term survives in Eq. (54), and the average intensity is given by:

$$\bar{I}_S(z) = \bar{I}_S(0)\, [1 + R(e^{g\bar{I}_L z} - 1)] \tag{56}$$

where R is the field cross-correlation function given by

$$R = \frac{|\sum_n A_{S,\,n}(0) A^*_{P,\,n}(0)|^2}{\sum_n |A_{S,\,n}|^2 \sum_n |A_{L,\,n}|^2} \tag{57}$$

In this approximation the double summation in the product of the Stokes and pump waves has collapsed to a single sum. Each Stokes mode m interacts only with the corresponding pump mode m.

When the Stokes field is correlated with the pump, the correlation function is unity and the broadband Stokes light has the same exponential gain as in a narrowband interaction with the same average pump intensity. When the incident Stokes wave is not fully correlated with the pump, the component of the Stokes wave that is correlated with the pump has the largest gain, while Stokes components that are not correlated with the pump ($R = 0$) do not receive amplification.[86–88] The Stokes wave thus becomes more correlated with the pump wave as it is amplified. This behavior is equivalent to the phase-pulling effects discussed earlier. The effective Stokes input signal to the amplifier is reduced by the factor $1/M$, where M is the number of spectral modes of the Stokes wave. However, when growth from noise is considered, the total input Stokes signal increases in proportion to the Stokes bandwidth and the effective Stokes input is one photon per mode independent of the Stokes bandwidth. The threshold for growth from noise is therefore the same for broadband and narrowband interactions.

When dispersion is taken into account,[84,88,96] the exponential gain becomes:

$$G = G_0 - \frac{4\tau_w^2}{G_0\tau_c^2} \tag{58}$$

where G_0 is the gain without dispersion, τ_c is the correlation time of the laser radiation, defined by $\tau_c = [1/\delta\omega_L^2]^{1/2}$ where $\delta\omega_L^2$ is the variance of the laser spectrum, and τ_w is the beam walkoff time, given by

$$\tau_w = z\Delta(1/v) \tag{59}$$

where $\Delta(1/v) = 1/v_{gL} - 1/v_{gS}$.

Solutions also exist for pump depletion when the mode spacing is large and the dispersion can be neglected:[98]

$$I_S(z) = I_S(0)\,\frac{1+\alpha}{2}\,\frac{(1+\beta)\gamma + (1-\beta)e^{-\beta\left[I_L(0)+\frac{\omega_L}{\omega_S}I_S(0)\right]gz}}{\gamma + e^{-\beta\left[I_L(0)+\frac{\omega_L}{\omega_S}I_S(0)\right]gz}} \tag{60}$$

where

$$\alpha = \frac{\omega_S}{\omega_L}\,\frac{I_L(0)}{I_S(0)} \tag{61}$$

$$\beta = \left[\left(I_S(0) - \frac{\omega_S}{\omega_L}I_L(0)\right)^2 + 4\,\frac{\omega_S}{\omega_L}I_L(0)I_S(0)R\right]^{1/2} \Big/ \left[I_S(0) - \frac{\omega_S}{\omega_L}I_L(0)\right] \tag{62}$$

$$\gamma = \frac{(1+\beta) - \alpha(1-\beta)}{\alpha(1+\beta) - (1-\beta)} \tag{63}$$

Broadband Raman scattering has also been analyzed within the time domain.[99] Here the starting point is Eqs. (39*a* and *b*). The average of quantities is calculated as

$$\langle f(t)\rangle = \frac{1}{T}\int_t^{t+T} f(t')\,dt' \tag{64}$$

where the interval T is chosen to be large enough to provide a stationary average of the temporal structure in the signal. Generally speaking,

$$T \gg \frac{1}{\Delta\nu_L} \tag{65}$$

If $\Delta\nu_L \gg \Delta\nu_R$, again the material excitation cannot follow the time variations of the optical signals and Eq. (39*b*) can be solved as

$$\langle Q^*(t)\rangle = -\frac{i\kappa_1}{\Gamma}\langle A_S(t)A_L^*(t)\rangle \tag{66}$$

$\langle Q^*(t)\rangle$ is a slowly varying quantity even though $A_S(t)$ and $A_L(t)$ individually have rapid time variations. The equation for the average Stokes intensity is

$$\frac{\partial}{\partial z}\langle A_S(t)A_S^*(t)\rangle = i\kappa_2\langle A_S^*(t)A_L(t)Q^*(t) - A_S(t)A_L^*(t)Q(t)\rangle \tag{67}$$

Making use of the fact that Q is not correlated with A_L or A_S and using Eq. (66) gives

$$\frac{\partial}{\partial z}\langle A_S(t)A_S^*(t)\rangle = i\kappa_2[\langle A_S^*(t)A_L(t)\rangle\langle Q^*(t)\rangle - \langle A_S(t)A_L^*(t)\rangle\langle Q(t)\rangle] \tag{68}$$

$$\frac{\partial}{\partial z}\langle A_S(t)A_S^*(t)\rangle = \frac{\kappa_1\kappa_2}{\Gamma}[\langle A_S^*(t)A_L(t)\rangle\langle A_S(t)A_L^*(t)\rangle] \tag{69}$$

The Stokes intensity is given by

$$\langle I_S(z,\,t)\rangle = \langle I_S(0,\,t)\rangle\,[1 + R(e^{g(I_L)L} - 1)] \tag{70a}$$

where R is the normalized Stokes pump cross-correlation function at the input:

$$R = \frac{\langle A_S(0,\,t)A_L^*(0,\,t)\rangle\langle A_S^*(0,\,t)A_L(0,\,t)\rangle}{\langle|A_S(0,\,t)|^2\rangle\langle|A_L(0,\,t)|^2\rangle} \tag{70b}$$

The result of Eq. (70*a*) has the same form as that of Eq. (56). Akhmanov et al.[99] have discussed the statistical properties of stimulated Raman scattering with broadband radiation under a number of other conditions.

Spectral Properties. As described, the Stokes radiation produced in a Raman generator in the steady-state regime is expected to be a gain-narrowed version of the spontaneous Stokes emission. Druhl et al.[82] have shown that when narrowband pump radiation is used, the linewidth of the generated Stokes radiation with single pulses varies randomly from the same width as the pump radiation to a value several times greater than the spontaneous Raman linewidth. Only in the ensemble average does the linewidth of the generated Stokes radiation coincide with the gain-narrowed spontaneous line. Individual pulses exhibit considerable spectral structure. This behavior is traceable to the stochastic nature of the damping process, by which the Raman coherence has decreased to $1/e$ of its initial value on a statistical basis.

When broadband radiation is used, the Stokes wave has a tendency to be pulled into correlation with the pump and the Stokes spectral variation matches that of the pump. Duncan et al.[100] have shown that the spectrum of transient spontaneous Raman scattering matches that of the pump.

Anti-Stokes Raman Scattering. Anti-Stokes scattering produces a scattered wave at a shorter wavelength than the pump with frequency

$$\omega_{AS} = \omega_L + \omega_o \tag{71}$$

Anti-Stokes scattering can occur either as a two-photon transition between an upper and lower state, as illustrated in Fig. 1*b,* or as a resonant four-wave mixing process, as illustrated in Fig. 1*c.* The first interaction is directly analogous with the transitions involved in stimulated Stokes Raman scattering that have been discussed in previous sections. For a normal thermal distribution of population, the stimulated version of the anti-Stokes interaction incurs exponential loss.

Anti-Stokes components are produced in the spontaneous Raman spectrum. When a population inversion is created between the upper and lower states, the anti-Stokes process has exponential gain, with properties similar to those of normal stimulated Stokes Raman scattering. This interaction, termed an *anti-Stokes Raman laser,* has been described by several authors.[101–104]

Anti-Stokes radiation can also be produced through a four-wave mixing process, illustrated in Fig. 1*c* Refs. (1, 71, 105–107, 107a, 107b). In this interaction, two pump wave photons are converted to one Stokes and one anti-Stokes photon with the relation

$$2\omega_L = \omega_S + \omega_{AS} \tag{72a}$$

The process is sensitive to the phase mismatch given by

$$\Delta k = k_{AS} - 2k_L + k_S \tag{72b}$$

Usually, four-wave mixing processes are optimized when the phase mismatch is zero. For materials with normal dispersion, this occurs when the Stokes and anti-Stokes waves propagate at angles to the pump light, as shown in Fig. 11. The angles θ_S and θ_{AS} are given in the small angle and small Δk approximation by

$$\theta_S = \sqrt{\frac{2(k_S + k_{AS} - 2k_L)}{k_S(1 + k_S/k_{AS})}} \tag{73a}$$

$$\theta_{AS} = \sqrt{\frac{2(k_S + k_{AS} - 2k_L)}{k_{AS}(1 + k_{AS}/k_S)}} \tag{73b}$$

When the dispersion of the material is small, so that the refractive indexes at the various wavelengths can be approximated as $n_S = n_L - \delta$ and $n_{AS} = n_L + \delta$, the phase-matching angles are given by

$$\theta_S = \sqrt{\frac{2(\lambda_S - \lambda_{AS})\delta}{n_L\lambda_{AS}(1 + \lambda_{AS}/\lambda_S)}} \tag{74a}$$

$$\theta_{AS} = \sqrt{\frac{2(\lambda_S - \lambda_{AS})\delta}{n_L\lambda_S(1 + \lambda_S/\lambda_{AS})}} \tag{74b}$$

The plane-wave steady-state equations describing anti-Stokes generation with four-wave mixing are

$$\frac{dA_S^*}{dz} = K_3 |A_L|^2 A_S^* + K_2 \left(\frac{\omega_S n_{AS}}{\omega_{AS} n_S}\right) A_L^{*2} A_{AS} e^{i\Delta kz} \tag{75a}$$

$$\frac{dA_{AS}}{dz} = -K_1 |A_L|^2 A_{AS} - K_2 A_L^2 A_S^* e^{-i\Delta kz} \tag{75b}$$

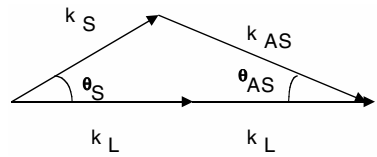

FIGURE 11 *k* vector diagram for coherent anti-Stokes Raman scattering showing laser and Stokes and anti-Stokes propagation directions for a medium with positive dispersion.

where $K_1 = -iK_{AS}\chi_{AS}$; $K_2 = -iK_{AS}\sqrt{\chi_{AS}\chi_S^*}$; $K_3 = -i\,K_S\chi_S^*$; χ_S and χ_{AS} are nonlinear susceptibilities for stimulated growth of the Stokes and anti-Stokes waves, respectively; $K_{S(AS)} = N\omega_{S(AS)}/n_{S(AS)}c$; N is the number density, and $\Delta k = k_S + k_{AS} - 2k_L$ is the phase mismatch.

General solutions have been discussed by Bloembergen and Shen.[105] These have shown that the Stokes and anti-Stokes waves grow as part of a mixed mode with amplitudes

$$A_{\text{Raman}} = \begin{pmatrix} A_S \\ A_{AS} \end{pmatrix} \tag{76}$$

One mode is primarily anti-Stokes in character and has exponential loss. The other mode is primarily Stokes in character and has exponential gain given by

$$A_{\text{Raman}} = \begin{pmatrix} A_S \\ A_{AS} \end{pmatrix} e^{gz} \tag{77}$$

where g is given by

$$\begin{aligned} g = Re\{&(1/2)(K_3 - K_1)|A_L|^2 \\ &-(i/2)[\Delta k^2 + 2i\Delta k(K_3 + K_1)\,|A_L|^2 - (K_1 - K_3)^2\,|A_L|^4]^{1/2}\} \end{aligned} \tag{78}$$

The exponential gain for the coupled mode is zero for exact phase matching, $\Delta k = 0$, and increases for nonzero Δk until it reaches its full decoupled value for $\Delta k > 2g_{SS}$, where g_{SS} is the steady-state gain coefficient. For nonzero Δk, the maximum gain occurs at small detunings from exact resonance. The ratio of anti-Stokes to Stokes intensities is given by

$$\frac{|A_{AS}|^2}{|A_S|^2} = \left(\frac{\omega_S^2}{c^2 k_{Sz}}\right)^2 |\chi_S|^2\,|A_L|^4 \Delta k^{-2} \tag{79}$$

Solutions for phase-matched conditions have been discussed by Duncan et al.[106] They have the form

$$\begin{aligned} A_S(z) = A_S(0)&\left\{\frac{K_1}{K_1 - K_3} - \left(\frac{K_3}{K_1 - K_3}\right)\exp[-(K_1 - K_3)\,|A_L|^2 z]\right\} \\ &+ \left(\frac{\omega_S n_{AS}}{\omega_{AS} n_S}\right)\left(\frac{K_2}{K_1 - K_3}\right) A_{AS}(0)\,\{1 - \exp[-(K_1 - K_3)\,|A_L|^2 z]\} \end{aligned} \tag{80}$$

$$\begin{aligned} A_{AS}(z) = A_{AS}(0)&\left\{\left(\frac{K_1}{K_1 - K_3}\right)\exp[-(K_1 - K_3)\,|A_L|^2 z] - \left(\frac{K_3}{K_1 - K_3}\right)\right\} \\ &- \left(\frac{K_2}{K_1 - K_3}\right)\, A_S(0)\,\{1 - \exp[-(K_1 - K_3)\,|A_L|^2 z]\} \end{aligned} \tag{81}$$

Initially the Stokes and anti-Stokes amplitudes grow linearly in z with opposite phases. The growth slows down as z increases and the condition

$$\frac{A_{AS}(z)}{A_S(z)} = -\frac{K_2}{K_1} = \sqrt{\frac{\chi_S^*}{\chi_{AS}}} \tag{82}$$

is approached asymptotically in the limit of large z. This ratio is approximately equal to unity except when there is strong resonant enhancement of the anti-Stokes susceptibility. The maximum value of the anti-Stokes amplitude is

$$A_{AS,\,\max}(z) = -A_{AS}(0)\,\frac{K_3}{K_1 - K_3} - A_S(0)\,\frac{K_2}{K_1 - K_3} \tag{83a}$$

$$\approx -A_{AS}(0)\frac{\omega_S}{\omega_{AS}-\omega_S} - A_S(0)\frac{\omega_{AS}}{\omega_{AS}-\omega_S} \tag{83b}$$

where the second of these relations is approximately valid when $\chi_S^* \approx \chi_{AS}$ and $n_{AS} \approx n_S$.

If the initial Stokes amplitude is small, as for example in a Raman generator, the limiting value of the anti-Stokes amplitude will be small and the predominant anti-Stokes generation will occur at small but finite phase mismatches. For Raman generators, the anti-Stokes radiation is produced in a cone about the phase-matching angle with a dark ring at exact phase matching. Experimental limitations can make the phase-matching minimum difficult to observe, but measurements of the dark ring in the phase-matching cone have been reported, as shown in Fig. 12. If the incident Stokes intensity is comparable to the pump intensity, considerable conversion can be made to the anti-Stokes wave at exact phase matching.[107]

In spectroscopic applications of CARS,[108] the usual input condition is for approximately equal pump and Stokes amplitudes with no anti-Stokes input. These experiments are usually performed under conditions of low exponential gain well below the limiting conditions of Eq. (82). Under these conditions, the anti-Stokes generation is maximized at the phase-matching conditions.

Growth from Noise. The most common configuration for Stokes Raman interactions is a Raman generator in which only a pump signal is provided at the input, as shown in Fig. 1*a*. The Stokes wave is generated in the interaction. The Stokes generation process can be viewed as one in which the effective Stokes noise at the beginning of the cell is amplified in the stimulated Raman interaction as described in the previous sections.

Classically, the Stokes noise is considered as arising from the spontaneous Raman scattering that is produced at the beginning of the cell. If we consider the effective spontaneous Stokes radiation that serves as a source for amplification to be that generated in the first *e*-folding length of the Raman generator, the Stokes intensity at the output is

$$I_S = \frac{\partial\sigma}{\partial\Omega}\, d\Omega NA(e^{N\sigma I_L L} - 1) \tag{84}$$

where N is the number density of the medium, A is the cross sectional area, and $d\Omega$ is the solid angle of the gain column.

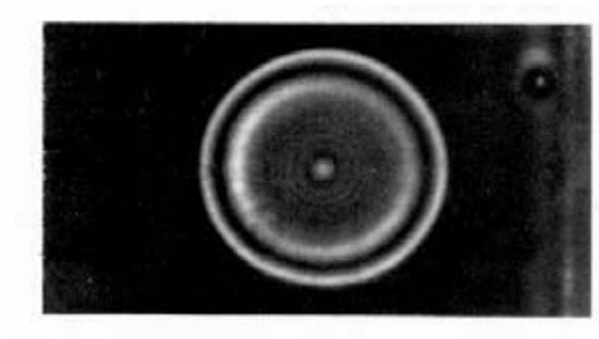

FIGURE 12 Photograph of the far field of the anti-Stokes emission pattern in hydrogen gas at a pressure of 14 atm. The anti-Stokes radiation is emitted in a cone about the phase-matching angle. The dark ring in the center of the cone is due to parametric gain suppression. (From Ref. 106.)

The growth from noise has been modeled more rigorously in terms of quantum fluctuations of the Stokes field amplitude and material excitation.[97,100,109–112] In this treatment, the Stokes and material oscillators are described by quantum mechanical creation and annihilation operators while the pump field is treated classically. The equations for the Stokes and material oscillators are:[97]

$$\frac{\partial}{\partial z}\hat{A}_S^{(-)}(z,\tau) = i\kappa_2 A_L(t)\hat{Q}^{(+)}(z,\tau) \tag{85a}$$

$$\frac{\partial}{\partial \tau}\hat{Q}^{(+)}(\tau) + \Gamma\hat{Q}^{(+)}(\tau) = -i\kappa_1 A_L^*(\tau)\hat{A}_S^{(-)}(z,\tau) + \hat{F}^{(+)}(z,\tau) \tag{85b}$$

where the symbol ^ indicates a quantum mechanical operator, the symbols (–) and (+) indicate creation and annihilation operators, respectively, and $\hat{F}$ is a Langevin operator that ensures the correct longtime behavior of Q.

The initial fluctuations of the Stokes and material oscillators satisfy the conditions:

$$\langle \hat{A}_S^{(+)}(0,t)\hat{A}_S^{(-)}(0,t')\rangle = \frac{2\hbar\omega_S}{cn_S\varepsilon_o a}\,\delta(t-t') \tag{86a}$$

$$\langle \hat{A}_S^{(-)}(0,t)\hat{A}_S^{(+)}(0,t')\rangle = 0 \tag{86b}$$

$$\langle \hat{Q}^{(+)}(z,0)\hat{Q}^{(-)}(z',0)\rangle = \frac{1}{\rho}\,\delta(z-z') \tag{86c}$$

$$\langle \hat{Q}^{(-)}(z,0)\hat{Q}^{(+)}(z',0)\rangle = 0 \tag{86d}$$

$$\langle \hat{F}^{(+)}(z,t)\hat{F}^{(-)}(z',t')\rangle = \frac{2\Gamma}{\rho}\,\delta(z-z')\,\delta(t-t') \tag{86e}$$

$$\langle \hat{F}^{(-)}(z,t)\hat{F}^{(+)}(z',t')\rangle = 0 \tag{86f}$$

where a is the cross sectional area of the beam. The average Stokes intensity is given by the expectation of the normally ordered number operator:

$$I_S(z,\tau) = \tfrac{1}{2}\,cn_S\varepsilon_o\,\langle A_S^{(+)}(z,\tau)A_S^{(-)}(z,\tau)\rangle \tag{87}$$

The formal solution is:[97]

$$\begin{aligned}\hat{A}_s^{(-)}(z,\tau) &= \hat{A}_s^{(-)}(0,\tau)\\ &+ (\kappa_1\kappa_2 z)^{1/2}\,A_L(\tau)\int_{-\infty}^{\tau} d\tau'\,\hat{A}_s^{(-)}(0,\tau')A_L^*(\tau')e^{-\Gamma(\tau-\tau')}\,\frac{I_1(\{4\kappa_1\kappa_2 z[p(\tau)-p(\tau')]\}^{1/2})}{[p(\tau)-p(\tau')]^{1/2}}\\ &- i\kappa_2 A_L(\tau)e^{-\Gamma\tau}\int_0^z dz'\hat{Q}^{+}(z',0)I_0(\{4\kappa_1\kappa_2(z-z')p(\tau)\}^{1/2})\\ &- i\kappa_2 A_L(\tau)\int_{-\infty}^{\tau} d\tau'\int_0^z dz'\,\hat{F}^{+}(z',\tau')e^{-\Gamma(\tau-\tau')}I_0(\{4\kappa_1\kappa_2(z-z')[p(\tau)-p(\tau')]\}^{1/2})\end{aligned} \tag{88}$$

The Stokes intensity obtained from use of Eq. (87) is

$$I_S(z,\tau) = \tfrac{1}{2}\,cn_S\varepsilon_o\,|\kappa_2 A_L(\tau)|^2\,z\{e^{-2\Gamma\tau}(I_o^2([4\kappa_1\kappa_2 z p(\tau)]^{1/2}) - I_1^2([4\kappa_1\kappa_2 z p(\tau)]^{1/2})$$

$$+ 2\Gamma \int_{-\infty}^{\tau} e^{-2\Gamma(\tau-\tau')} \left(I_o^2 (4\kappa_1\kappa_2\, z[p(\tau) - p(\tau')])^{1/2}\right) - I_1^2(\{4\kappa_1\kappa_2\, z[p(\tau) - p(\tau')]\}^{1/2})]\, d\tau'\} \tag{89}$$

In this formulation, only the third and fourth terms of Eq. (88) survive because the expectation values on the right side are taken over the initial state, which contains no quanta in either the Stokes or molecular fields. The first and second terms involve a Stokes annihilation operator acting on the Stokes ground state and return zero. The third term returns a nonzero result because it involves a creation operator acting on the molecular ground state, as discussed by Raymer.[97] In this treatment the Stokes light is generated entirely from fluctuations in the material oscillators, while the material excitation is generated from zero-point fluctuations in the material oscillators.

In the extreme transient regime, this result reduces to

$$I_S(z, \tau) = \tfrac{1}{2}\, \Gamma g_{ss} I_L(\tau) z\, \{I_o^2\, ((2g_{ss} z I_L \Gamma\tau)^{1/2}) - I_1^2\, ((2g_{ss} z I_L \Gamma\tau)^{1/2})\} \tag{90}$$

Comparison of this result with that of Eq. (43) shows a different functional dependence on the modified Bessel functions, which reflects the effects of buildup of the signal from the distributed noise source.

In the steady state, Eq. (89) reduces to

$$I_S(z, \tau = \infty) = \tfrac{1}{2}\, \Gamma g_{ss} I_L z[I_o(g_{ss} I_L z/2) - I_1(g_{ss} I_L z/2)]\, e^{g_{ss} I_L z/2} \tag{91}$$

An alternative analysis for transient scattering has been presented using antinormal ordering of the creation and annihilation operators for the intensity.[109] In this formalism, the zero-point term must be subtracted explicitly. The intensity is given by

$$I_S(z, \tau) = \tfrac{1}{2}\, cn_s\varepsilon_o\{\langle \hat{A}_S^{(+)}(z, \tau)\hat{A}_S^{(-)}(z, \tau)\rangle - \langle \hat{A}_S^{(-)}(0, \tau)\hat{A}_S^{(+)}(0, \tau)\rangle \tag{92}$$

The Stokes intensity is given by

$$\begin{aligned} I_S\,(z, \tau) = {} & \tfrac{1}{2}\, cn_s\varepsilon_o\{\, \kappa_2^2 |A_L(\tau)|^2 \iint dz'dz''\, I_o(\sqrt{4\kappa_1\kappa_2(z - z')p(\tau)})\, I_o(\sqrt{4\kappa_1\kappa_2(z - z'')p(\tau)}) \\ & \times \langle \hat{Q}^{(-)}(z', 0)\hat{Q}^{(+)}(z'', 0)\rangle + \kappa_1\kappa_2 z |A_L(\tau)|^2 \iint I_1(\sqrt{4\kappa_1\kappa_2 z\, [p(\tau) - p(\tau')]}) \\ & \times I_1(\sqrt{4\kappa_1\kappa_2 z[p(\tau) - p(\tau'')]})/\sqrt{[p(\tau) - p(\tau')][\, p(\tau) - p(\tau'')]} \\ & \times A_L(\tau')A_L^*(\tau'')\, \langle \hat{A}_S^{(+)}(0, \tau')\, \hat{A}_S^{(-)}(0, \tau'')\rangle d\tau' d\tau'' + \sqrt{\kappa_1\kappa_2 z}\, \Big\{(A_L^*(\tau) \int_{-\infty}^{t} A_L(\tau')\langle \hat{A}_S^{(+)}(0, \tau')\hat{A}_S^{(-)}(0, \tau)\rangle \\ & \times I_1(\sqrt{4\kappa_1\kappa_2 z[p(\tau) - p(\tau')]})/\sqrt{p(\tau) - p(\tau')}\, d\tau' + A_L(\tau) \int_{-\infty}^{t} A_L^*(\tau') \\ & \times \langle \hat{A}_S^{(+)}(0, \tau)\hat{A}_S^{(-)}(0, \tau')\rangle\, I_1(\sqrt{4\kappa_1\kappa_2 z[p(\tau) - p(\tau')]}/\sqrt{p(\tau) - p(\tau')}\, d\tau')\Big\} \end{aligned} \tag{93}$$

Here the first term in Q is 0 because it represents an annihilation operator operating on the ground state. Further analysis shows that this result is identical to the one in Eq. (90). The second term gives the transient stimulated Raman signal, and the last two terms in brackets describe spontaneous Raman scattering. In this formalism, the Stokes wave is started by its own zero-point motion and does not involve the zero-point motion of the molecular oscillators. The zero-point motion of the molecular oscillators is responsible for the initiation of the

molecular excitation. Further analysis has shown that the Stokes signal can be viewed as arising from quantum fluctuations of the Stokes radiation,[97] the material oscillator,[109] or a combination of both.[100]

The effective Stokes noise amplitude corresponds to one Stokes photon at the input of the generator. This result is expected for this model, which assumes plane wave propagation, effectively assuming a single mode in the amplifier. In a more general case, the effective Stokes noise level will be one Stokes photon for each temporal and spatial mode of the amplifier. The number of spatial modes is given by the square of the effective Fresnel number of the amplifier:[113]

$$N_{\text{spatial modes}} = F^2 \tag{94}$$

where

$$F = \frac{A}{\lambda L} \tag{95}$$

where A is the effective area of the gain region and L is the interaction length. Because of spatial gain narrowing, the effective area of the generator can be significantly less than the nominal diameter of the pump beam and can depend on the gain level. The number of temporal modes depends on the relation of the pump pulse duration to the dephasing time T_2. A single temporal mode will be present when $t_p \ll T_2$. For longer pulses, the number of temporal modes has been modeled as[110]

$$N_{\text{temporal modes}} = 1, \qquad t_p < t_{\text{ss}} \tag{96a}$$

$$N_{\text{temporal modes}} = \frac{t_p}{G_{\text{ss}} T_2}, \qquad t_p > t_{\text{ss}} \tag{96b}$$

or alternatively as[114]

$$N_{\text{temporal modes}} = \sqrt{\frac{ln2/G_{\text{ss}}}{1 - ln2/G_{\text{ss}}}} \frac{t_p}{\pi T_2} \tag{97}$$

The first of these derives the number of temporal modes from the steady-state time of Eq. (19) and the second from the gain-narrowing formula of Eq. (29).

Raman Threshold. Generation of first Stokes radiation from noise in a single-pass generator passes smoothly from exponential amplification of noise to depletion of the pump radiation without a true threshold. Thresholdlike behavior has been reported in some situations but has been due to multimode structure of the radiation or secondary reflections. A Raman threshold is, however, commonly associated with a single-pass gain. This is done by assigning the threshold to a pump value (intensity or energy) at which the Stokes signal from a Raman generator is an arbitrary fraction of the incident pump (typically of the order of 1 percent). At this level, pump saturation is generally not important, but for higher pump powers the process rapidly transitions to saturation. Thus, the concept of Raman threshold in Raman generators is reasonably practical, if not technically precise. The gain that is required to reach threshold depends on the number of noise modes present in the generator. For typical geometries of long, narrow interaction lengths, the Raman gain at threshold is of the order of e^{23} to e^{40}. Raman amplifiers are typically operated at gain levels below threshold. Stable amplifier gains of the order of e^{19} are achievable.

Quantum Fluctuations. Macroscopic manifestations of the stochastic nature of the Raman initiating fluctuations have been reported in spatial fluctuations of the output Stokes intensity profile, in the pointing of the Stokes beam, and in the spectral and temporal structure of the Stokes signal generated by narrowband radiation.[110,111,115–120] The stochastic nature of the starting signal is manifest in the pulse energy statistics of Raman generators operated below

threshold. In this regime, the statistical distribution of the Stokes pulse energy is of the form $p(W_S) = \exp\{-W_S/\langle W_S\rangle\}$, where W_S is the energy of a Stokes pulse and $\langle W_S\rangle$ is the average energy over an ensemble. When the Raman generator is operated below threshold, energy of the output pulses fluctuates in accordance with this distribution. As the generator approaches pump depletion, the Stokes pulse energy distribution approaches one that is peaked about the average value. Statistical distributions of pulse radiation in short pulse experiments show exponential behavior characteristic of stochastic input for gains below threshold, and a gradual evolution to coherent behavior as saturation is approached.

Competition of the quantum noise with real Stokes signals in Raman amplifiers at the quantum level has been reported by Duncan et al.[113] Their results show experimentally that the effective initiating signal is consistent with a noise level of one photon per mode of the amplifier. When the incident Stokes signal exceeds the noise level of one photon per mode by a sufficient amount, the fluctuations are effectively suppressed in both the spatial profile and the pulse energy statistics. An example of the evolution of the amplified Stokes signal from one dominated by quantum noise to one dominated by the coherent Stokes input signal in the image of bars in a resolution chart is shown in Fig. 13.

Multiple Stokes Generation. Once a significant signal is produced in the first Stokes wave, it can serve as a pump wave for a second Raman process, generating a second Stokes wave at

$$\omega_{2S} = \omega_S - \omega_o = \omega_L - 2\omega_o \tag{98}$$

This usually occurs at a pump power such that significant Stokes conversion occurs within the first half of the Raman cell, allowing generation of the second Stokes wave in the last part of the cell. Once the first Stokes wave is generated, the second Stokes radiation can also arise from a four-wave mixing interaction of the form

$$\omega_{2S} = 2\omega_S - \omega_L \tag{99a}$$

which has properties similar to the anti-Stokes four-wave mixing interaction.

The four-wave mixing interaction is a coherent one and will produce second Stokes radiation with coherent statistics when the first Stokes radiation has saturated the pump. The second Stokes radiation generated from stimulated scattering will exhibit the stochastic behavior characteristic of growth from quantum noise. The relative importance of the two sources of second Stokes radiation is affected by the phase mismatch for the four-wave mixing interaction and depends on the density of the material.

Still higher pump powers can result in conversion to third or higher Stokes orders. Each of the orders involves a frequency shift due to the same material transition, rather than higher excitation of the material system. In most materials, conditions for multiple Stokes generation are sufficient to produce significant amounts of anti-Stokes energy through the four-wave mixing interaction. Multiple-order anti-Stokes energy can also be generated using various combinations of Stokes and anti-Stokes orders of the form

$$\omega_{n\mathrm{AS}} = \omega_{mS} - \omega_{(m+1)S} + \omega_{(n-1)\mathrm{AS}} \tag{99b}$$

where n and m are orders of Stokes and anti-Stokes radiation and $\omega_{0S} = \omega_{0\mathrm{AS}} = \omega_L$. Multiple-order Stokes radiation can also be produced through four-wave mixing involving similar terms.

An ideal progression of Raman scattering through multiple Stokes modes is shown in Fig. 14*a.* Such a progression is seldom seen in practice because of the onset of anti-Stokes and four-wave mixing interactions. Higher-order Stokes energy can be suppressed through choice of resonant structure in the material or through use of high pressures that suppress four-wave mixing through disruption of phase matching. An example of second Stokes generation in hydrogen is shown in Fig. 14*b,* in which initiation through four-wave mixing occurs at low powers and initiation through a stimulated process, evidenced by the wide scatter of points, occurs at higher powers.[122]

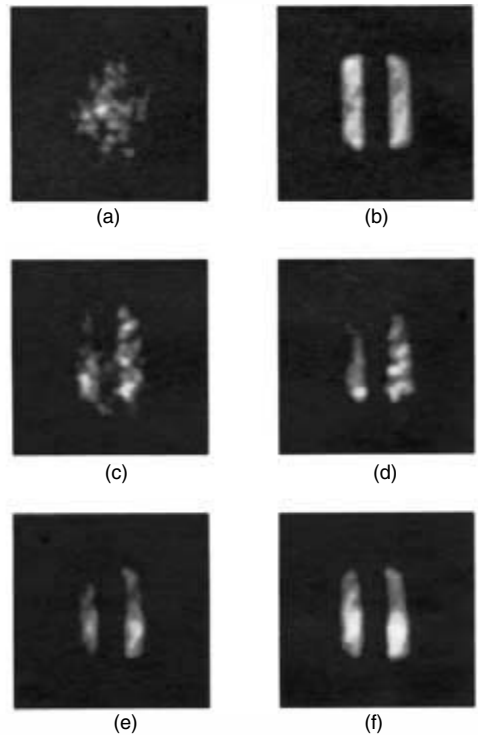

FIGURE 13 Images of bars in a resolution chart from a Stokes amplifier with amplification of 1.4×10^4 for different levels of incident Stokes energy, showing effects of competition between incident Stokes energy and quantum noise. (*a*) Incident Stokes wave blocked. (*b*) Incident Stokes wave. (*c*) 210 seed Stokes photons, camera sensitivity 1. (*d*) 800 seed Stokes photons, camera sensitivity 0.3. (*e*) 3.2×10^4 seed Stokes photons, camera sensitivity 7.4×10^{-3}. (*f*) 1.5×10^{10} seed Stokes photons, camera sensitivity 3.2×10^{-8}. (From Ref. 121.)

Focused Beams. The effects of focusing are described by the spatial derivative in Eqs. (5*a* and *b*). When the pump intensity varies with z, the gain must be integrated over the interaction length. For steady-state interactions, the Stokes intensity takes the form

$$I_S(r, z) = I_S(r, 0) \exp[g \int_0^L I_L \, dz] \tag{100}$$

The profile of a gaussian beam is described by a $1/e$ field radius w, given by

$$w(z) = w_o \sqrt{1 + \xi^2} \tag{101}$$

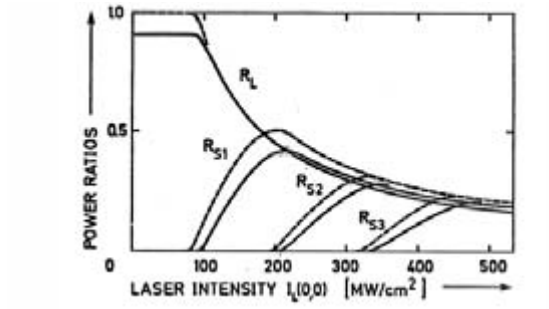

(a)

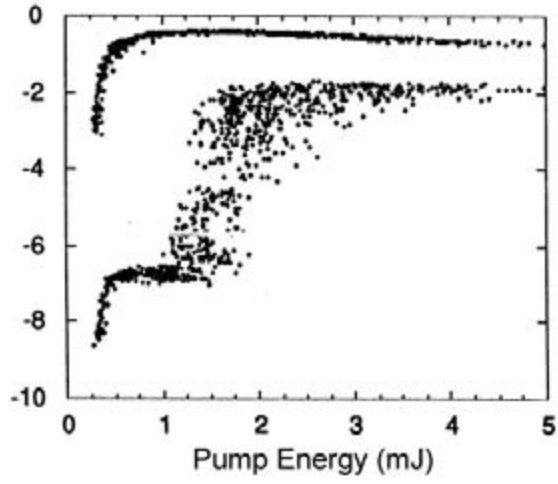

(b)

FIGURE 14 (*a*) Theoretical calculation of multiple Stokes generation for gaussian pulses. (From Ref. 2.) (*b*) Second Stokes generation (lower curve) in hydrogen at 1600 psi showing growth from four-wave mixing at low pump energies and the transition to stimulated emission from quantum fluctuations at higher pump energies. The first Stokes wave is shown in the upper curve. (From Ref. 122.)

where w_o is the radius of the beam waist, $\xi = 2z/b$, and $b = 2\pi w_o^2/\lambda$ is the confocal parameter. When $b \gg L$, the pump beam is collimated over the interaction length and the primary effect of the gaussian profile is to produce gain narrowing, effectively confining the Stokes intensity near the beam axis. When the beam is tightly focused, so that $b \ll L$, the integrated gain is independent of the interaction length and depends only on the total pump power:

$$G = g \int I_L dz = g4P/b\lambda \tag{102}$$

where P is the total pump power. Amplification or generation with focused beams can result in changes of the Stokes beam divergence and displacements of the apparent source point for divergence of the Stokes beam.

Backward Raman Scattering. Stimulated Raman scattering also occurs in the backward direction, for which the Stokes and pump waves travel in opposite directions.[2,69] This type of interaction is much more dependent on the geometry and the laser linewidth than the forward interaction. Backward interaction can involve growth from noise (Fig. 2*b*) or amplification (Fig. 2*d*). Generally, it occurs for sufficiently narrow linewidths that the coherence length of the radiation is longer than the interaction length. One of the characteristic differences of the backward interaction is that the growing Stokes wave continually interacts with undepleted pump as it propagates. Thus, for conditions in which the Stokes wave can grow to saturate the Raman interaction, the Stokes wave continually experiences the full pump intensity rather than a continually decreasing intensity as in the forward direction. One consequence of this property is that the intensity of the backward Stokes pulse can grow to be much higher than the initial pump intensity, while the pulse duration decreases, producing pulse compression, one of the common applications for backward Raman scattering.[69] For this application, the optimal duration for the pump pulse is twice the length of the Raman cell. The Stokes wave grows to depletion level in the first half of the pump pulse and depletes the pump in the second half. Factors affecting pulse compression have been discussed in Ref. 69, where designs of systems to give a factor-of-10 shortening were described.

Backward scattering also results in Stokes pulses of higher spatial quality than are obtained in the forward direction. If the backward Stokes wave depletes the pump pulse too much before it travels an entire cell length, the initiating signal for Stokes radiation in subsequent parts of the pulse can be suppressed and oscillations can result.[123]

Polarization Dependence. The Raman gain for various polarizations depends on the symmetry of the Raman transition and is governed by the depolarization ratio. For many materials and transitions, the maximum gain occurs for pump and Stokes polarizations that are linear and parallel. For other types of transitions—for example, rotational transitions in diatomic molecules—circular polarization is preferred with the pump and Stokes waves polarized in the opposite sense. The relative gains for various polarization combinations are shown in Table 8.[124]

Applications

The earliest and most common application of stimulated Raman scattering is the production of coherent sources at wavelengths different from those of the pump laser. Prior to the introduction of tunable lasers, this was one of the few methods available for obtaining coherent radiation at any but a small number of wavelengths at which fixed-frequency lasers existed. This application remains an important one today for extending the versatility of tunable lasers, and for generation of radiation at wavelengths required for specific applications such

TABLE 8 Polarization Dependence of Relative Gain for SRS

	Laser polarization	Stokes polarization	Relative gain
Rotational	Linear	Linear, parallel	1
scattering,	Linear	Linear, perpendicular	0.75
linear	Circular	Circular, same sense	0.25
molecules	Circular	Circular, opposite sense	1.5

as the eye-safe region around 1.5 μm. Other applications of Raman scattering include Raman beam cleanup, pulse compression, time-gated imaging, and coherent spectroscopy. Two of these are described in the following text.

Coherent Spectroscopy. Several Raman interactions are used for coherent spectroscopy.[108,125] These interactions have the advantage of producing a stronger signal than incoherent spectroscopy under some conditions. These advantages occur primarily when prominent Raman modes are studied in pure materials or the dominant constituent of a mixture. A summary of interactions used in coherent spectroscopy along with names given to them is given in Table 9. The most common of these is coherent anti-Stokes Raman scattering (CARS). A typical CARS spectroscopic interaction is shown in Fig. 11. Incident light at both the pump and Stokes wavelengths is supplied. The anti-Stokes signal is measured as the wavelength of the Stokes light is varied. The spectral structure is recorded as the frequency difference $\omega_L - \omega_S$ is tuned through Raman resonances of the material.

The anti-Stokes intensity is given in a steady-state plane-wave approximation as

$$I_{\mathrm{AS}} = |\chi_R + \chi_{\mathrm{NR}}|^2 I_L^2 I_S \tag{103}$$

where χ_R is the Raman susceptibility that carries the resonance and χ_{NR} is the nonresonant nonlinear susceptibility due to electronic or other transitions in the medium. The Raman susceptibility exhibits resonant behavior as $\omega_L - \omega_S$ is tuned through the Raman resonance ω_o, while the nonresonant susceptibility is generally constant through the resonance region. The wavelength variation of the anti-Stokes intensity reflects the influence of the interference between the resonant and nonresonant susceptibilities. In particular, the anti-Stokes intensity goes through zero when $\chi_R = -\chi_{NR}$, which always occurs on the high-frequency side of the resonance. Depending on the situation, the anti-Stokes intensity can exhibit a resonant-like peak if χ_{NR} is small compared to χ_R at the resonance or a dispersive-like behavior if χ_{NR} is larger than χ_R. Intermediate behavior between these two extremes is also possible depending on the relative magnitudes of χ_R and χ_{NR}. Dispersive-like behavior can occur for relatively weak Raman transitions, or for Raman transitions in materials that are minor constituents in mixtures. An example of CARS spectral behavior for various conditions is shown in Fig. 15.

Time-Gated Imaging. Raman amplification has also been applied to time-gated imaging to suppress background light in highly scattering materials, for example biological tissue or materials such as ceramics.[127–129] Time gating with Raman scattering can be done with either short pulses, in which case the gate time is comparable to the pulse duration, or with broadband radiation, in which case the time gate is determined by the coherence time of the pulse. In pulsed gating, only that part of the signal that overlaps with the pump pulse in time is amplified, and light that is delayed through multiple scattering is suppressed. In coherence gating, only the Stokes components that are coherent with the pump are amplified, and com-

TABLE 9 Raman Interactions Used for Coherent Spectroscopy

Interaction	Frequency relations	Measured quantity
Coherent anti-Stokes Raman scattering (CARS)	$\omega_{\mathrm{AS}} = 2\omega_L - \omega_S$	Anti-Stokes power
Coherent Stokes Raman spectroscopy (CSRS)	$\omega_S = \omega_L - \omega_o$	Amplified Stokes power
Raman-induced Kerr effect (RIKES)	$\omega_S = \omega_L - \omega_o$	Stokes power in orthogonal polarization component

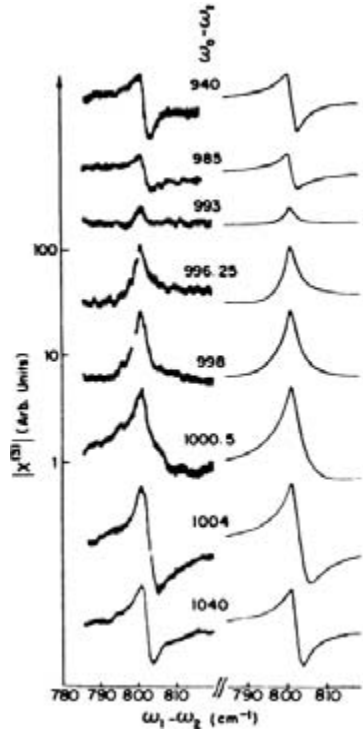

FIGURE 15 Signal from coherent anti-Stokes Raman scattering showing variation of line shape due to interference of Raman and nonresonant susceptibilities. (From Ref. 126; copyright 1976 by American Physical Society.)

ponents that are decorrelated because of multiple-path scattering are suppressed. Gate contrasts of the order of 10^9 are possible with pulse gating, while contrasts of the order of 10^6 can be obtained with correlation gating. An example of the use of pulsed gating for imaging in a scattering solution is shown in Fig. 16.

18.3 STIMULATED BRILLOUIN SCATTERING

Brillouin scattering involves low-frequency propagating waves—for example, acoustic waves in solids, liquids, and gases and ion-acoustic waves in plasmas. Again, scattering can be to a longer or shorter wavelength than the incident radiation, with the long-wavelength scattered wave being termed the *Stokes wave* and the short-wavelength scattered wave termed the *anti-Stokes wave.* The difference between the incident and scattered frequencies is again termed the *Stokes shift* or *anti-Stokes shift* as appropriate. For Brillouin scattering, the energies of the modes are much lower than for Raman scattering, and anti-Stokes radiation is much more common. Common Brillouin shifts are typically on the order of 0.1 to 100 GHz, and depend on the excitation

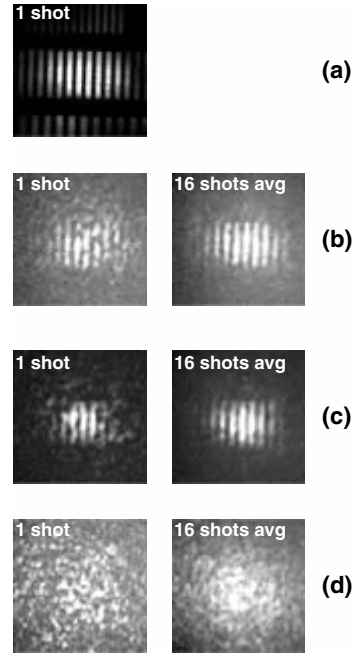

FIGURE 16 Use of Raman amplification with short pulses for time gating to photograph objects through scattering materials. (*a*) image of bar chart, no scatterer. The relative timing of the pump and Stokes pulses were (*b*) –16 ps, (*c*) 0 ps, and (*d*) +24 ps. (From Ref. 128.)

wavelength and interaction geometry as well as on material properties. Brillouin scattering is used most commonly for phase conjugation and pulse compression. It is also prominent as a limiting process for intensity in fiber-optic systems.

The equations for Stokes Brillouin scattering for forward ($+v_g$) and backward ($-v_g$) waves are[2,6,7]

$$\frac{\partial A_S}{\partial z} \pm \frac{1}{v_g}\frac{\partial A_S}{\partial t} = i\frac{\omega_S}{4n_S c}\gamma\frac{\Delta\rho^*}{\rho_o}A_L \tag{104a}$$

$$-2i\Omega\frac{\partial\Delta\rho^*}{\partial t} + (v^2q^2 - \Omega^2 + iq^2\Gamma'\Omega)\Delta\rho^* + 2iqv^2\frac{\partial\Delta\rho^*}{\partial z} - \frac{v_S^2q^2\beta_p\rho_o}{\gamma}\Delta T^* + 2iq\frac{v_S^2\beta_p\rho_o}{\gamma}\frac{\partial\Delta T^*}{\partial z} = q^2\gamma A_L^* A_S \tag{104b}$$

$$\rho_o C_v\frac{\partial\Delta T^*}{\partial t} - i\Omega\rho_o C_v\Delta T^* - \frac{C_v(\gamma-1)}{\beta_p}\frac{\partial\Delta\rho}{\partial t} + i\Omega\frac{C_v(\gamma-1)}{\beta_p}\Delta\rho + \kappa q^2(\Delta T) = cn\varepsilon_o\alpha A_L^* A_S \tag{104c}$$

where v_s is the sound velocity and

$$\Gamma' = \frac{1}{\rho}\left[\frac{4}{3}\eta_s + \eta_b + \frac{\kappa}{C_p}\left(\frac{C_p}{C_v} - 1\right)\right] \tag{105}$$

and η_s is the coefficient of shear viscosity, η_b is the coefficient of bulk viscosity, κ is the thermal conductivity, C_p is the specific heat at constant pressure, and C_v is the specific heat at constant volume.

The fields are described by the equations

$$E_L(z, t) = \tfrac{1}{2}\left[A_L(z, t)e^{-i(\omega_L t - k_L z)} + \text{cc.}\right] \tag{106a}$$

$$E_S(\xi, t) = \tfrac{1}{2}\left[A_S(z, t)e^{-i(\omega_S t - k_S \xi)} + \text{cc.}\right] \tag{106b}$$

$$\rho(\zeta, t) = \rho_o + \tfrac{1}{2}\left[\Delta\rho e^{-i(\Omega t - q\zeta)} + \text{cc}\right] \tag{106c}$$

where A_L, A_S, and ρ are the amplitudes of the laser, scattered optical wave, and sound wave density, respectively, and ω_L, ω_S, Ω_L, and k_L, k_S, and q are the frequencies and k vectors of the various waves. The scattered optical wave propagates along the direction ξ and the sound wave propagates along direction ζ, neither of which is required to coincide with z. The frequencies and k vectors obey the following relations:

$$\omega_L - \omega_S = \Omega \tag{107a}$$

$$\vec{k}_L - \vec{k}_S = \vec{q} \tag{107b}$$

$$q = \frac{2\pi}{\Lambda_s} \tag{107c}$$

where Λ_s is the sound wavelength. The k vectors of the various waves are arranged according to the diagram in Fig. 17.

Because the sound frequency is much less than the optical frequency, $|k_L| \approx |k_S|$ and

$$q \approx 2k_L \sin(\theta/2) \tag{108}$$

The Brillouin frequency shift can then be written as

$$\Omega_B = 2n_L\omega_L \frac{v_s}{c} \sin(\theta/2) \tag{109}$$

Unlike the Raman frequency shift, the Brillouin frequency shift depends on the laser frequency and the interaction geometry. It has its maximum value for backward scattering ($\theta = 180°$).

The Brillouin interaction involves both electrostrictive and thermal effects. Equation (104*c*) was obtained from the equation for the low-frequency acoustic and thermal response

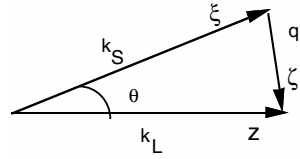

FIGURE 17 k vector diagram for stimulated Brillouin scattering showing k vectors for laser k_L Stokes k_S and sound wave q.

of liquids and gases to optical radiation:[2,6,7]

$$-\frac{\partial^2\Delta\rho}{\partial t^2}+\frac{v_S^2}{\gamma}\nabla^2(\Delta\rho)+\frac{2\eta_s+\eta_b}{\rho_o}\nabla^2\frac{\partial\Delta\rho}{\partial t}+\frac{v_S^2\beta_p\rho_o}{\gamma}\nabla^2(\Delta T)=\frac{1}{2}cn\varepsilon_o\gamma_e\nabla^2\langle E_{\text{tot}}\rangle^2 \quad (110a)$$

$$\rho_o C_v\frac{\partial\Delta T}{\partial t}-\frac{C_v(\gamma-1)}{\beta_p}\frac{\partial\Delta\rho}{\partial t}-\kappa\nabla^2(\Delta T)=cn\varepsilon_o\alpha\langle E_{\text{tot}}\rangle^2 \quad (110b)$$

where $\gamma = C_p/C_v$ is the ratio of specific heats at constant pressure and volume, η_s is the coefficient of shear viscosity, η_b is the coefficient of bulk viscosity, β_p is the thermal expansion coefficient at constant pressure, $\gamma_e = \rho(\partial\varepsilon/\partial\rho)$ is the electrostrictive constant, α is the absorption coefficient, κ is the thermal conductivity, $E_{\text{tot}} = E_L + E_S$ is the total optical field, and ΔT is the change in temperature. The following form for the temperature

$$T = T_o + \tfrac{1}{2}\left[\Delta T e^{-i(\Omega t - qz)} + \text{cc}\right] \quad (111)$$

can be used to reduce Eqs. (110*a* and *b*) to first order, giving Eqs. (104*b* and *c*).

The Brillouin equations can be solved under various approximations. The propagating terms in $\partial\Delta\rho/\partial z$ and $\partial\Delta T/\partial z$ are usually neglected because the sound waves are strongly damped. The steady-state solution for the Stokes intensity is

$$I_S(L) = I_S(0)\, e^{gIL} \quad (112)$$

where the gain coefficient g is given by $g = g^e + g^a$, where g^e is the electrostrictive gain coefficient given by

$$g^e = \frac{\omega_S\gamma_e^2\Omega_B}{n_S n_L c^2\varepsilon_o\rho_o\Gamma_B v_s^2}\,\frac{1}{1+\left(\dfrac{2\delta\Omega}{\Gamma_B}\right)^2} \quad (113a)$$

and g^a is the absorptive Brillouin gain coefficient given by

$$g^a = \frac{\omega_S\gamma_e\gamma_a\Omega_B}{2n_S n_L c^2\varepsilon_o\rho_o\Gamma_B v_s^2}\,\frac{4\delta\Omega/\Gamma_B}{1+\left(\dfrac{2\delta\Omega}{\Gamma_B}\right)^2} \quad (113b)$$

where $\gamma_a = 2\alpha n v^2\beta_p/C_p\Omega_B$,

$$\Omega_B = v_s q \quad (114)$$

is the Brillouin frequency shift, $\delta\Omega = \Omega - \Omega_B$, and

$$\Gamma_B = q^2\left[\frac{1}{\rho}(2\eta_s+\eta_b)+\frac{\kappa}{C_p}\left(\frac{C_p}{C_v}-1\right)\right] \quad (115a)$$

$$= q^2\Gamma'' \quad (115b)$$

is the Brillouin damping constant.

The gain due to the electrostrictive interaction is peaked about the Brillouin frequency shift $\Omega = \Omega_B$ with a linewidth (FWHM) of $\Delta\nu_B = \Gamma_B/2\pi$. The acoustic energy damping time is given by

$$\tau_B = 1/2\pi\Delta\nu_B \quad (116)$$

The electrostrictive gain coefficient g can also be written as

$$g^e = \frac{2\omega_S \gamma_e^2 \omega_L}{n_S c^3 \varepsilon_o \rho_o \Gamma_B v_s} \sin(\theta/2) \frac{1}{1 + \left(\dfrac{\delta\Omega}{\Gamma_B/2}\right)^2} \tag{117a}$$

$$= \frac{\omega_S \gamma_e^2}{2\omega_L n_S n_L^2 c \varepsilon_o \rho_o \Gamma'' v_s} \frac{1}{\sin(\theta/2)} \frac{1}{1 + \left(\dfrac{\delta\Omega}{\Gamma_B/2}\right)^2} \tag{117b}$$

The maximum steady-state gain is

$$g^e_{\mathrm{B,\,max}} = \frac{\omega_S \omega_L \gamma_e^2}{\pi n_S c^3 \varepsilon_o \rho_o v_s \Delta\nu_B} \tag{118}$$

and occurs for backward scattering ($\theta = 180°$). The frequency shift for backward scattering is

$$\Omega_B(180°) = 2n\omega_L \frac{v_s}{c} \tag{119}$$

Since the Brillouin frequency shift is small, $\omega_S \approx \omega_L$ and the maximum Brillouin gain apparently scales as ω_L^2. However, the linewidth also scales as ω_L^2 [see Eq. (115*b*)], leaving the maximum Brillouin gain independent of wavelength as indicated in Eq. (117*b*).

The dependence of the linewidth on q^2 causes the steady-state gain in the forward direction to go to infinity [Eq. (117*b*)] rather than to zero [Eq. (117*a*)]. However, the forward interaction is always transient because the steady-state time for forward scattering also goes to infinity. As a result, the forward gain is zero. Brillouin scattering at 90° is important in propagation of high-power laser radiation through large-diameter optics.

Transient Brillouin scattering has been described by Kroll[16] and Faris et al.[130] The transient solutions to the stimulated Brillouin scattering are formally similar to those for Raman scattering and can be written as

$$A_S(z, \tau) = A_S(0, \tau) + \sqrt{\Gamma_B g_B z / c n_L \varepsilon_o}\, A_L(\tau) \int_{-\infty}^{\tau} \frac{e^{-(\tau - \tau')/T_2} A_L^*(\tau') A_S(0, \tau')\, I_1(\sqrt{\Gamma_B g_B z [p(\tau) - p(\tau')]/c v_L \varepsilon_o})}{\sqrt{p(\tau) - p(\tau')}}\, d\tau \tag{120}$$

Again, the transient gain depends on the time integral of the laser intensity, and the scattered intensity grows as a Bessel function. The steady-state solution of Eq. (112) applies when the pulse duration is greater than the steady-state time given by

$$t_{\mathrm{SS}} = \frac{G_{\mathrm{SS}}}{\Gamma_B} \tag{121}$$

where $G_{\mathrm{SS}} = GI_L L$.

Brillouin scattering in solids has been discussed in Refs. 131–134. The formal equations for electrostrictive Brillouin scattering are similar to those for liquids and gases. However, the gain coefficient depends on the polarization of the laser and scattered light, and Brillouin resonances exist for both longitudinal and shear acoustic waves. The Brillouin gain is given by

$$g^e = \frac{\omega_S \Omega_B n_S^3 n_L^4 p'^2}{n_S n_L c^2 \varepsilon_o \rho_o \Gamma_B v_s^2} \frac{1}{1 + \left(\dfrac{2\delta\Omega}{\Gamma_B}\right)} \tag{122}$$

where p' is the photoelastic constant appropriate for the specific combination of polarizations for the optical and acoustic waves. For longitudinal acoustic waves in isotropic materials:[134]

$$p' = p_{12}(\hat{\varepsilon}_L \cdot \hat{\varepsilon}_S) + p_{44}[(\hat{\varepsilon}_L \cdot \hat{\kappa}_a)(\hat{\varepsilon}_L \cdot \hat{\varepsilon}_S) + (\hat{\varepsilon}_L \cdot \hat{\varepsilon}_a)(\hat{\varepsilon}_S \cdot \hat{\kappa}_a)] \tag{123a}$$

while for shear acoustic waves

$$p' = p_{44}[(\hat{\varepsilon}_L \cdot \hat{\kappa}_a)(\hat{\varepsilon}_S \cdot \hat{\varepsilon}_a) + (\hat{\varepsilon}_L \cdot \hat{\varepsilon}_a)(\hat{\varepsilon}_S \cdot \hat{\kappa}_a)] \tag{123b}$$

where $\hat{\varepsilon}_{L(S)(a)}$ is the unit polarization vector of the pump (Stokes)(acoustic) wave and κ_a is the unit propagation vector of the acoustic wave.

Buildup of noise in a generator with Brillouin scattering is similar in principle to buildup with Raman scattering. However, the primary noise source for Brillouin scattering is the thermally excited acoustic phonons. As a result, the equivalent noise level for Brillouin scattering can be several orders of magnitude larger than the Raman noise level.[135–137] The noise power into a given solid angle $d\Omega = \pi\theta^2/4$ is given by:[135]

$$p_{\text{noise}} = \frac{\omega_S}{\Omega} k_B T \Delta\nu_B \left(\frac{\theta}{2\theta_D}\right)^2 \tag{124}$$

where $\theta_D = \lambda/2\pi D$ is the diffraction angle that can be resolved by a gain column of diameter D. Brillouin scattering with broadband radiation is discussed in Refs. 138 and 139. Multiline Brillouin scattering is treated in Ref. 140. As with backward Raman scattering, the gain decreases when the coherence length becomes comparable to or shorter than the interaction length.

Thermal Brillouin scattering is driven by nonuniform heating due to absorption and is described by g^a in Eq. (113*b*). The gain shows a dispersive behavior with frequency, with zero gain at the Brillouin frequency, gain for frequencies less than Ω_B, and loss for frequencies greater than Ω_B. Brillouin scattering parameters for various materials are listed in Table 10.

Brillouin Phase Conjugation

One of the major uses of stimulated Brillouin scattering (SBS) is phase conjugation.[140a] Phase conjugation is also possible with stimulated Raman scattering, but SRS is not used for this purpose as much as SBS. Phase conjugation is used to correct distortions on optical beams that arise from propagation through nonideal optical media, such as the atmosphere or low-quality optical components. It can also be used for correcting or stabilizing aiming errors that arise from motion of components in an optical train, for improving the beam quality of laser oscillators and oscillator amplifier systems, and for beam combining.

A typical arrangement for phase conjugation is shown in Fig. 18. The distorting medium impresses a transverse phase variation on the optical beam propagating from left to right that can result in increased divergence, intensity structure, or reduced focal plane intensity if focused by a subsequent lens or mirror. If the beam entering the distorting material carried an initial distortion that would be undone by the material, then the beam would emerge from the medium undistorted. The general concept is that the initial distortion required for this compensation is the inverse of the distortion imposed by the medium. However, determining precisely what that distortion is and imposing it on the initial beam is the heart of the matter in phase compensation.

The arrangement shown in Fig. 19 illustrates how this is done with nonlinear optical phase conjugation. The beam propagating from left to right is initially undistorted. It emerges from the medium at point B with a complete record of the distortion imposed by the medium. In the nonlinear medium, the beam undergoes a backward nonlinear optical interaction in which a second beam is generated that travels in the opposite direction and has phase variations that are reversed from the original distorted beam. When this beam propagates through the distorting medium again from right to left, the medium again impresses a phase variation on it, but this time the process simply undoes the initial phase distortion instead of creating one. The beam emerging from the distorting medium at point A is undistorted.

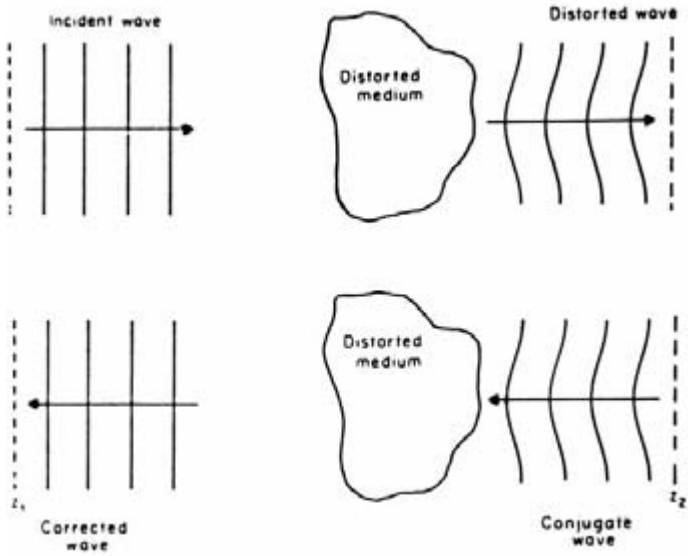

FIGURE 18 Schematic diagram for correction of phase distortions caused by distorting medium with double-pass propagation.

Several types of nonlinear interactions have been used for phase conjugation, including degenerate and nondegenerate four-wave mixing, stimulated Brillouin scattering, Brillouin-enhanced four-wave mixing, and stimulated Raman scattering. Of these, degenerate four-wave mixing is used most often for low-power interactions and stimulated Brillouin scattering is used for high-power applications. Brillouin-enhanced four-wave mixing provides a high-gain Brillouin system.

Phase conjugation with SBS is the result of mode competition in which the mode that corresponds to the conjugate of the pump has higher gain than other possible modes. The gain for the backward-generated beam involves a sum over all possible spatial modes of the backward Stokes wave. The mode that matches the pump wave has the highest gain because the

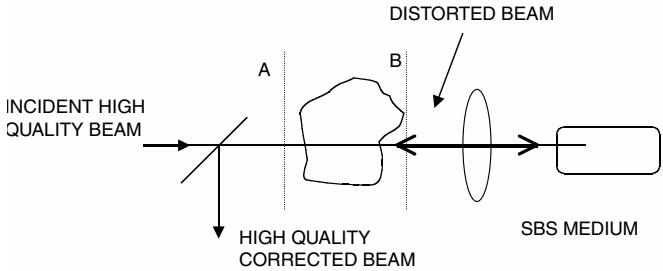

FIGURE 19 Schematic diagram of use of stimulated Brillouin scattering for phase distortion correction with phase conjugation.

TABLE 10 Brillouin Parameters for Various Materials

Liquids								
	Laser Wavelength (nm)	Frequency Shift (GHz)	Δν (MHz)	τ_B (ns)	g_B (cm/GW)	n	Density (g/cm^3)	Reference
Acetone	1059	2.987	119 ± 5	1.34	15.8	1.355	0.791	141
	532	5.93	361	0.44	12.9	1.359(Na-D)		142
	532	6.0	320	0.497	20			138
Benzene	1059	4.124	228	0.7	9.6	1.4837	0.879	141
	532	8.33	515	0.31	12.3	1.501(Na-D)	0.874	142
Benzyl alcohol	532	9.38	2120	0.08	5.75	1.54(Na-D)	1.045	142
Butyl acetate	532	6.23	575	0.28	9.13	1.394(Na-D)	0.882	142
CS_2	1060	3.761	50	3.2	68	1.595	1.262	141
	532	7.7	120	1.9	130			138
CCl_4	1060	2.772	528	0.3	3.8	1.452	1.595	141
	532	5.72	890	0.18	8.77	1.4595	1.594	142
Chloroform	532	5.75	635	0.25	11.7	1.446(Na-D)	1.492	142
Cyclohexane	532	7.19	1440	0.11	5.8	1.426(Na-D)	0.779	142
N,N-Dimethyl formamide	532	7.93	615	0.26	7.8	1.431(Na-D)	0.944	142
Dichloromethane	532	5.92	255	0.62	16.8	1.424	1.325	142
o-Dichlorobenzene	532	8.03	1340	0.12	4.7	1.551	1.306	142
Ethanol	532	5.91	546	0.29		1.36	0.785	142
Ethylene glycol	532	10.2	3630	0.04	0.85	1.431	1.113	142
Freon 113	532	3.72	865	0.18	5.5	1.3578	1.575	142
n-Hexane	532	5.64	580	0.27	8.8	1.379	0.67	142
Nitrobenzene	1060	4.255	396	0.4	7.2	1.5297	1.206	141
Methanol	532	5.47	325	0.49	10.6	1.329	0.791	142
	530	5.6	210	0.334	13			138
Pyridine	532	8.92	746	0.21	14	1.51	0.978	142
Tin tetrachloride	1064	2.21 ± 0.02	182 ± 12	0.874	11.2 ± 0.5	1.36	2.226	143
	532	4.71	357	0.45				
Titanium tetrachloride	1060	3.070	216	0.735	14.2	1.577	1.73	141
Toluene	532	7.72	1314	0.12	8.4	1.496	0.867	142
Trichloroethylene	532	5.94	765	0.21	12	1.4755	1.464	142
Water	1060	3.703	170	0.935	3.8	1.324	1	141
	532	7.4	607	0.26	2.94	1.333	1	142
Xylenes	532	7.74	1211	0.13	9.3	1.497	0.86	142

TABLE 10 Brillouin Parameters for Various Materials (*Continued*)

Gases

	Laser Wavelength (nm)	Frequency Shift (GHz)	Δν (MHz)	τ_B (ns)	g_B (cm/GW)	n	Density (g/cm^3)	Reference
Xenon								
7599 Torr	532	0.654 ± 0.024	98.1 ± 8.9		1.38 ± .19	1.0069	0.05767	134
6840 Torr	532	0.627 ± 0.030	107.4 ± 16.9			1.0062	0.05159	134
				0.65 $\lambda_P^2 P$				144
$CClF_3$								
3310 kPa (liquid)	1060		305					145
3860	1060		155					145
3950	1060		200					145
32 atm (liquid)				6.2 ± 0.4				146
Gas				$(4.78 \times 10^9/\rho\lambda_L^2 + 3.25 \times 10^5)^{-1}$				144
SF_6				$(5.9 \times 10^9/\rho\lambda_L^2 + 1.6 \times 10^5)^{-1}$				144

P in atmospheres, ρ in bg/m^3

Solids

Substance	Polarization P	Polarization k	Laser Wavelength (nm)	Frequency Shift (GHz)	Δν (MHz)	τ_B (ns)	g_B (cm/GW)	n	Density (g/cm^3)	Reference
d-LAP			1053		28.9 (θ = 180°)	5.5 (θ = 180°)	18 (θ = 180°)			147
					14.4 (θ = 90°)	11 (θ = 90°)	26 (θ = 90°)			147
	x	$y = b = Y$	532	25.374 ± 0.051	84.1 ± 3.5		20.7 ± 2.99	1.5090	1.600	134
	x	z	532	25.207 ± 0.042	100.4 ± 7.5		10.99 ± 1.88	1.5090	1.600	134
	y	x	532	19.590 ± 0.087	79.8 ± 6.3		27.96 ± 2.85	1.5764	1.600	134
	y	z	532	26.415 ± 0.009	104.1 ± 5.2		12.25 ± 0.93	1.5764	1.600	134
	z	x	532	19.644 ± 0.048	82.3 ± 6.2		29.85 ± 2.4	1.5847	1.600	134
	z	y	532	26.709 ± 0.039	91.9 ± 5.1		24.33 ± 3.26	1.5847	1.600	134
	THG		532	25.149 ± 0.072	94.8 ± 8.4		17.45 ± 3.41			134
			351		261 (θ = 180°)	0.61 (θ = 180°)	22 (θ = 180°)			147
					132 (θ = 90°)	1.2 (θ = 90°)	31 (θ = 90°)			147
Fused silica			1053		40.8 (θ = 180°)	3.9 (θ = 180°)	4.8 (θ = 180°)		2.202	147
			1053		20.4 (θ = 90°)	7.8 (θ = 90°)	6.8 (θ = 90°)			147
			532	32.65 ± 0.054	163 ± 7.6		2.9 ± 0.015	1.4607		134
			532	32.62	167.6 ± 13.5		2.69 ± 0.22			134
			351		370 (θ = 180°)	0.43 (θ = 180°)	5.4 (θ = 180°)			147
			351		185 (θ = 90°)	0.86 (θ = 90°)	7.6 (θ = 90°)			147

KD*P	$x = c = Z$	$z = Y$	532	29.763 ± 0.06	101.5 ± 7.5	3.53 ± 0.31	1.4683	2.355	134
	z	x	532	27.627 ± 0.087	120.0 ± 6.9	4.57 ± 0.38	1.5073	2.355	134
	z	z	532	30.525 ± 0.156	107.4 ± 7.2	5.09 ± 0.40	1.5073	2.355	134
KDP, THG			532	28.554 ± 0.036	72.9 ± 5.7	6.5 ± 0.95	1.5073	2.355	134
LAA	y	b	532	20.892 ± 0.009	100.4 ± 7.6	24.9 ± 3.75			134
BK 3			532	31.383 ± 0.036	198.6 ± 6.6	1.78 ± 0.13	1.5008	2.37	134
LHG-8			532	27.786 ± 0.024	219.0 ± 6.2	2.74 ± 0.23	1.5316	2.83	134
BK 7			532	34.65 ± 0.039	165.0 ± 8.6	2.15 ± 0.21	1.5195	2.51	134
CaF_2			532	37.164 ± 1.185	45.6 ± 8.8	4.11 ± 0.65	1.4354	3.179	134
Plexiglas			532	15.687 ± 0.036	253.7 ± 12.6		1.4938	1.19	134
GGG			532	26.283 ± 0.005	12.5 ± 6.9	1.02 ± 0.5	1.9788	7.09	134

Glasses

	Laser Wavelength (nm)	Frequency Shift (GHz)	Δν (MHz)	v_s (m/s)	g_B (cm/GW)	n	Density (g/cm^3)	Reference
SiO_2	488	35.6	156	5944.2	4.482	1.462	2.203	132
ZBL	488	25.0	213.6	3979.0	2.832	1.530	4.672	132
ZBLA	488	25.2	98.7	3968.4	1.713	1.548	4.579	132
ZBLAN	488	26.6	96.0	4270	3.608	1.521	4.301	132
HBL	488	22.4	151.4	3608.9	1.127	1.514	5.78	132
HBLA	488	22.1	162.3	3470	0.96	1.554	5.83	132
HBLAPC	488	25.2	179.5	4035	1.023	1.524	5.1	132
BeF_2	488	24.3	52.5	4634.1	16.06	1.28	2.01	132
$95BeF_2$-$5THF_4$	488	24.9	74.8	4638.5	11.54	1.31	2.1	132
4.97 Li_2O 94.27 B_2O_3 0.13 Al_2O_3	488	26.9	100	4364	12.88	1.5056	1.9434	132
4.97 Li_2O 94.27 B_2O_3 0.13 Al_2O_3	488	26.8	116	4351	14.29	1.5053	1.9439	132
4.97 Li_2O 94.27 B_2O_3 0.13 Al_2O_3	488	24.8	113	4050	11.74	1.4946	1.9025	132
4.97 Li_2O 94.27 B_2O_3 0.13 Al_2O_3	488	32.1	124	5109	10.93	1.5324	2.0753	132
4.97 Li_2O 94.27 B_2O_3 0.13 Al_2O_3	488	29.0	138	4662	12.66	1.5189	1.9823	132
4.97 Li_2O 94.27 B_2O_3 0.13 Al_2O_3	488	33.0	104	5205	3.441	1.5455	2.0541	132
6 K_2O-94SiO_2 673° C 78.56 h	488	33.1	184	5458	3.905	1.4781	2.2416	132
6 K_2O-94SiO_2 604.8°C 231.8 h	488	33.1	186	5465	2.783	1.4781	2.2519	132
8 K_2O-92SiO_2 547° C	488	32.4	175	5330	3.354	1.4845	2.2703	132
8 K_2O-92SiO_2 603.5°C 103.42 h	488	32.5	190	5335	3.587	1.4844	2.2725	132
8 K_2O-92SiO_2 589.5°C 141.79 h	488	32.4	177	5332	5.181	1.4846	2.2716	132
8 K_2O-92SiO_2 574.3°C 345.68 h	488	32.4	170	5321	3.704	1.4844	2.2696	132
8 K_2O-92SiO_2 573.4°C 84.66 h	488	32.5	187	5339	4.038	1.4846	2.2702	132
10 K_2O-90SiO_2	488	30.8	208	5039	3.122	1.4923	2.2991	132
10 K_2O-90SiO_2	488	25.8	104	4190	8.169	1.5037	2.0281	132
30 K_2O-70SiO_2	488	30.2	134	4839	4.675	1.5231	2.2699	132

Reprinted with permission from M. J. Weber (ed.), *CRC Handbook of Laser Science and Technology: Optical Materials,* suppl. 2. Copyright CRC Press, Boca Raton, FL, 1988.

high- and low-intensity points coincide, providing reinforcement of that mode over the entire interaction length. The exponential gain for this mode is twice that for the noncorrelated modes when the pump beam carries a large number of spatial modes.

In order for the conjugate mode to dominate over the other modes, it is necessary that it experience preferential gain over an extended region. Essentially, it is required that the Stokes beam diffract across the entire pump beam in the interaction region before it grows to a saturation level. This has been accomplished by using a light guide to confine the beams. In free-focused interactions, it requires that the divergence of the pump beam be sufficient to provide a wide focal area relative to its depth. An example of phase conjugate correction in a two-pass Q-switched Nd:YAG amplifier system is shown in Fig. 20 using liquid Freon-113 as the conjugating medium.[148] Properties of phase-conjugated beams, quality of correction, and efficiency of conversion are given in Ref. 10.

Brillouin-Enhanced Four-Wave Mixing. Brillouin-enhanced four-wave mixing (BEFWM) is a nearly degenerate four-wave mixing process where the four waves are coupled by the Brillouin nonlinearity as shown schematically in the Fig. 21. BEFWM was first observed and explained by Basov et al.[149] In addition to the beam to be conjugated, two oppositely propagating pump beams are provided at frequency ω_L. In general, the two pump beams do not need to be at the same frequency, but in practice they usually are. The signal beam k_s at a frequency $\omega_S = \omega_P - \Delta\omega_B$ interacts with the laser beam k_1 at a frequency ω_P to produce an acoustic wave that moves in the direction of the laser beam. The second laser beam k_2 scatters from the moving grating to generate the conjugated anti-Stokes beam k_{AS} at a frequency $\omega_{AS} = \omega_P + \Delta\omega_B$. The phase-conjugated beam, traveling in the opposite direction of the signal beam, can be amplified when the pump beams do not interact with each other. Therefore, BEFWM represents a mirror with reflectivity greater than 1. The pump beams are usually decoupled by

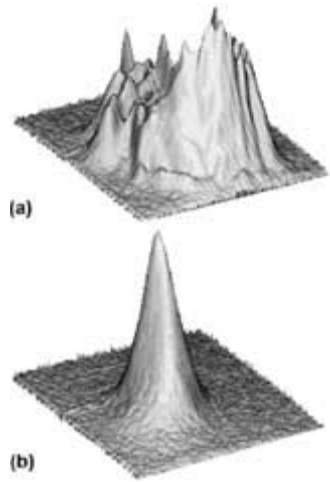

FIGURE 20 Spatial beam profiles of a Q-switched Nd:YAG oscillator-amplifier system using a two-pass amplifier configuration with a conventional mirror in the two-pass amplifier (*a*) and an SBS mirror (*b*). The Brillouin mirror was a cell of liquid Freon-113. (From Ref. 148.)



FIGURE 21 *k* vector diagram for Brillouin-enhanced four-wave mixing.

frequency or polarization control. A reflectivity as high as $\sim 7 \times 10^5$ has been observed.[150] The process can also be done with the anti-Stokes wave as the signal beam. The signal Stokes beam is usually generated externally via a separate SBS process. The angles between the beams can be adjusted to make the phase matching possible. Various aspects of BEFWM are described in detail in Ref. 151.

18.4 REFERENCES

1. N. Bloembergen, *Nonlinear Optics,* Benjamin, New York, 1965.
2. W. Kaiser and M. Maier, "Stimulated Rayleigh, Brillouin and Raman Spectroscopy," in F. T. Arecchi and E. O. Schulz-DuBois (eds.), *Laser Handbook,* vol. 2, North-Holland, Amsterdam, New York, 1972, pp. 1077–1150.
3. C. S. Wang, "The Stimulated Raman Process," in Herbert Rabin and C. L. Tang (eds.), *Quantum Electronics: A Treatise,* vol. 1, part A, Academic Press, New York, 1975.
4. A. Penzkofer, A. Laubereau, and W. Kaiser, "High Intensity Raman Interactions," *Prog. Quant. Elec.* **6**:55–140 (1979).
5. F. Milanovich, "Stimulated Raman Scattering," in M. J. Weber (ed.), *Handbook of Laser Science and Technology: Optical Materials,* vol. III, CRC, Boca Raton, FL, 1986.
6. Y. R. Shen, *Principles of Nonlinear Optics,* Wiley, New York, 1984.
7. R. W. Boyd, *Nonlinear Optics,* Academic, New York, 1992.
8. John F. Reintjes, "Stimulated Raman and Brillouin Scattering," in M. J. Weber (ed.), *Handbook of Laser Science and Technology: Optical Materials,* suppl. 2, CRC, Boca Raton, FL, 1995, pp. 334–364.
9. "Stimulated Raman and Brillouin Scattering for Laser Beam Control," special issue of *JOSA B* **3** (October 1986).
10. J. Reintjes (ed.), "Laser Wavefront Control," *SPIE* **1000** (1988).
11. D. Levi, C. R. Menyuk, and P. Winternitz (eds.), *Self-Similarity in Stimulated Raman Scattering,* Les Publications CRM, Montreal, Canada, 1994.
12. N. Bloembergen, "The Stimulated Raman Effect," *Am. J. Phys.* **35**:989 (1967).
13. A. Z. Grasyuk, "Raman Lasers (Review)," *Sov. J. Quant. Electron.* **4**:269 (1974).
14. G. Eckardt, R. W. Hellwarth, F. J. McClung, S. E. Schwarz, and D. Weiner, "Stimulated Raman Scattering from Organic Liquids," *Phys. Rev. Lett.* **9**:455 (1962).
15. Y. R. Shen and N. Bloembergen, "Theory of Stimulated Raman and Brillouin Scattering," *Phys. Rev.* **137**:A1787 (1965).
16. N. M. Kroll, "Excitation of Hypersonic Vibrations by Means of Photoelastic Coupling of High Intensity Light Waves to Elastic Waves," *J. Appl. Phys.* **36**:34 (1965).
17. R. L. Carman, F. Shimizu, C. S. Wang, and N. Bloembergen, "Theory of Stokes Pulse Shapes in Transient Stimulated Raman Scattering," *Phys. Rev. A* **2**:60 (1970).
18. C. S. Wang, "Theory of Stimulated Raman Scattering," *Phys. Rev.* **182**:482 (1969).

19. M. D. Duncan, R. Mahon, L. L. Tankersley, and J. Reintjes, "Transient Stimulated Raman Amplification in Hydrogen," *JOSA B* **5**:37 (1988).
20. J. R. Murray and A. Javan, "Effects of Collisions on Raman Line Profiles of Hydrogen and Deuterium Gas," *J. Mol. Spectrosc.* **42**:1–26 (1972).
21. R. H. Dicke, *Phys. Rev.* **89**:472 (1953).
22. W. K. Bischel and M. J. Dyer, "Temperature Dependence of the Raman Linewidth and Lineshift for the Q(1) and Q(0) Transitions in Normal and Para H_2," *Phys. Rev. A* **33**:3113 (1986).
23. S. Kern and B. Feldman, *Stimulated Raman Emission,* vol. 3, Massachusetts Institute of Technology, Lincoln Laboratory, Bedford, MA, 1974, p. 18.
24. J. J. Barrett and M. C. Tobin, "Stimulated Raman Emission Frequencies in 21 Organic Liquids," *J. Opt. Soc. Am.* **56**:129 (1966).
25. M. D. Martin and E. L. Thomas, "Infrared Difference Frequency Generation," *IEEE J. Quant. Electron.* **QE-2**:196 (1966).
26. M. A. El-Sayed, F. M. Johnson, and J. Duardo, "A Comparative Study of the Coherent Raman Processes Using the Ruby and the Second Harmonic Neodymium Giant-Pulsed Lasers," *J. Chem. Phys.* **1**:227 (1967).
27. J. A. Giordmaine and J. A. Howe, "Intensity-Induced Optical Absorption Cross Section in CS_2," *Phys. Rev. Lett.* **11**:207 (1963).
28. T. A. Prasada Rao and N. Seetharaman, "Amplification of Stimulated Raman Scattering By a Dye," *Ind. J. Pure Appl. Phys.* **13**:207 (1975).
29. M. Geller, D. P. Bortfeld, and W. R. Sooy, "New Woodbury-Raman Laser Materials," *Appl. Phys. Lett.* **3**:36 (1963).
30. W. L. Smith and F. P. Milanovich, Lawrence Livermore National Laboratory, Livermore, CA, private communication, 1983.
31. J. R. Maple and J. T. Knudtson, "Transient Stimulated Vibrational Raman Scattering in Small Molecule Liquids," *Chem. Phys. Lett.* **56**:241 (1978).
32. J. K. Wright, C. H. H. Carmichael, and B. J. Brown, "Narrow Linewidth Output from a Q-switched Nd 3-/Glass Laser," *Phys. Lett.* **16**:264 (1965).
33. M. K. Srivastava and R. W. Crow, "Raman Susceptibility Measurements and Stimulated Raman Effect in KDP," *Opt. Commun.* **8**:82 (1973).
34. P. D. Maker and R. W. Terhune, "Study of Optical Effects Due to an Induced Polarization Third Order in the Electric Field Strength," *Phys. Rev.* **137**:A801 (1965).
35. D. P. Bortfeld, M. Geiller, and G. Eckhardt, "Combination Lines in the Stimulated Raman Spectrum of Styrene," *J. Chem. Phys.* **40**:1770 (1964).
36. V. A. Orlovich, "Measurement of the Coefficient of Stimulated Raman Scattering in Organic Liquids with the Aid of an Amplifier with Transverse Pumping," *Zh. Prikl. Spektrosk.* **23**:224 (1975).
37. J. A. Calvieilo and Z. H. Heller, "Raman Laser Action in Mixed Liquids," *Appl. Phys. Lett.* **5**:112 (1964).
38. G. Eckhardt, "Selection of Raman Laser Materials," *IEEE J. Quant. Electron.* **QE-2**:1 (1966).
39. V. A. Subov, M. M. Sushchinskii, and I. K. Shuvalton, "Investigation of the Excitation Threshold of Induced Raman Scattering," *J. Exp. Theor. Phys. USSR* **47**:784 (1964).
40. C. D. Decker, "High-Efficiency Stimulated Raman Scattering/Dye Radiation Source," *Appl. Phys. Lett.* **33**:323 (1978).
41. B. P. Stoicheff, "Characteristics of Stimulated Raman Radiation Generated by Coherent Light," *Phys. Lett.* **7**:186 (1963).
42. D. Cotter, D. C. Hanna, and R. Wyatt, "A High Power, Widely Tunable Infrared Source Based on Stimulated Electronic Raman Scattering in Caesium Vapour," *Opt. Commun.* **16**:256 (1976).
43. P. E. Tannenwaid and J. B. Thaxter, "Stimulated Brillouin and Raman Scattering in Quartz at 2.1 to 293 Kelvin," *Science* **134**:1319 (1966).
44. J. Gelbwachs, R. H. Pantell, H. E. Puthoff, and J. M. Yarborough, "A Tunable Stimulated Raman Oscillator," *Appl. Phys. Lett.* **14** (1969).

45. G. Eckhardt, D. P. Bortfeld, and M. Geller, "Stimulated Emission of Stokes and Anti-Stokes Raman Lines from Diamond, Calcite and α-sulfur Single Crystals," *Appl. Phys. Lett.* **3**:137 (1963).
46. I. V. Aleksandrov, Y. S. Bobovitch, A. V. Bortkevich, and M. Y. Tsenter, "Raman Scattering in Crystalline Chlorine and Bromine," *Opt. Spektrosk.* **36**:150 (1974).
47. I. I. Kondilenko, P. A. Korotkov, and V. I. Maly, "Temperature Dependence of SRS Thresholds for Some Salts of Inorganic Acids in the Crystalline Phase," *Opt. Commun.* **10**:50 (1974).
48. D. L. Weinberg, "Stimulated Raman Emission in Crystals and Organic Liquids," *Mass. Inst. Technol. Lincoln Lab. Solid-State Res. Rep.* **3**:31 (1965).
49. O. S. Avanesyan, V. A. Benderskii, V. K. H. Brikenshtein, V. L. Broude, A. G. Lavrushko, I. I. Tartakovskii, and P. V. Filippov, "Characteristics of Stimulated Light Generation and Stimulated Raman Scattering in Anthracene Crystals," *Sov. J. Quant. Electron.* **7**:403 (1977).
50. J. L. Carlsten and P. C. Dunn, "Stimulated Stokes Emission with a Dye Laser: Intense Tunable Radiation in the Infrared," *Opt. Commun.* **14**:8 (1975).
51. D. Cotter, D. C. Hanna, P. A. Kärkkäinen, and R. Wyatt, "Stimulated Electronic Raman Scattering as a Tunable Infrared Source," *Opt. Commun.* **15**:143 (1975).
52. P. P. Sorokin, J. J. Wynne, and J. R. Landkard, "Tunable Coherent IR Source Based Upon Four-Wave Parametric Conversion in Alkali Metal Vapors," *Appl. Phys. Lett.* **22**:342 (1973).
53. A. DeMartino, R. Frey, and F. Pradere, "Tunable Far Infrared Generation in Hydrogen Fluoride," *Opt. Commun.* **27**:262 (1978).
54. P. May, P. Bernage, and H. Boequet, "Stimulated Electronic Raman Scattering in Rubidium Vapour," *Opt. Commun.* **29**:369 (1979).
55. R. L. Byer and W. R. Trutna, "16-μm Generation by CO_2-Pumped Rotational Raman Scattering in H_2," *Opt. Lett.* **3**:144 (1978).
56. P. Rabinowitz, A. Stein, R. Brickman, and A. Kaldor, "Efficient Tunable H_2 Raman Laser," *Appl. Phys. Lett.* **35**:739 (1979).
57. E. Pochon, "Determination of the Spontaneous Raman Linewidth of CF_4 by Measurements of Stimulated Raman Scattering in Both Transient and Steady States," *Chem. Phys. Lett.* **77**:500 (1981).
58. B. E. Kinkaid and J. R. Fontana, "Raman Cross-Section Determination by Direction Stimulated Raman Gain Measurements," *Appl. Phys. Lett.* **28**:12 (1975).
59. M. Rokni and S. Yatsiv, "Resonance Raman Effects in Free Atoms of Potassium," *Phys. Lett.* **24**:277 (1967).
60. R. W. Minek, R. W. Terhune, and W. G. Rado, "Laser-Stimulated Raman Effect and Resonant Four-Photon Interactions in Gases H_2, D_2, and CH_4," *Appl. Phys. Lett.* **3**:181 (1963).
61. H. Komine, Northrop Corp., Palos Verdes, Calif., private communication, 1983.
62. W. K. Bischel and M. J. Dyer, "Wavelength Dependence of the Absolute Raman Gain Coefficient for the Q(1) Transition in H_2," *JOSA* **B5**:677 (1986).
63. W. K. Bischel and G. Black, "Wavelength Dependence of Raman Scattering Cross Sections from 200–600 nm," in C. K. Rhodes, H. Egger, and H. Pummer (eds.), *Excimer Lasers—1983,* AIP, New York, 1983.
64. W. K. Bischel, "Stimulated Raman Gain Processes in H_2, HD and D_2," unpublished data.
65. J. J. Ottusch and D. A. Rockwell, "Measurement of Raman Gain Coefficients of Hydrogen, Deuterium and Methane," *IEEE J. Quant. Elect.* **QE-24**:2076 (1988).
66. D. A. Russel and W. B. Roh, "High Resolution CARS Measurements of Raman Linewidths of Deuterium," *J. Mol. Spect.* **24**:240 (1987).
67. K. C. Smyth, G. J. Rosasco, and W. S. Hurst, "Measurements and Rate Law Analysis of D2 Q-Branch Line Broadening Coefficients for Collisions with D_2, He, Ar, H_2 and CH_4," *J. Chem. Phys.* **87**:1001 (1987).
68. D. Haner and I. S. McDermid, "Stimulated Raman Shifting of the Nd:YAG Fourth Harmonic (266 nm) in H_2, HD and D_2," *IEEE J. Quant. Electron.* **QE-26**:1292 (1990).
69. J. R. Murray, J. Goldhar, D. Eimerl, and A. Szoke, "Raman Pulse Compression of Excimer Lasers for Application to Laser Fusion," *IEEE J. Quant. Elect.* **QE-15**:342 (1979).

70. G. C. Herring, M. J. Dyer, and W. K. Bischel, "Temperature and Wavelength Dependence of the Rotational Raman Gain Coefficient in N_2," *Opt. Lett.* **11**:348 (1986).
71. A. P. Hickman, J. A. Paisner, and W. K. Bischel, *Phys. Rev. A* **33**:1788 (1986).
72. H. Chuan and T. H. Chyba, "Solid-State Barium Nitrate Raman Laser in the Visible Region," *Opt. Commun.* **135**:273 (1997).
73. P. G. Zverev, T. T. Basiev, V. V. Osiko, A. M. Kulkov, V. N. Voitsekhovskii, and V. E. Yakobsen, "Physical, Chemical and Optical Properties of Barium Nitrate Raman Crystal," *Opt. Mat.* **11**:315 (1999).
74. P. G. Zverev and T. T. Basiev, "Investigation of the Line Broadening of an SRS-Active Vibration in a Barium Nitrate Crystal by Two-Photon Raman Amplification Spectroscopy," *Quant. Electron.* **25**:1204 (1995).
75. V. N. Voitsekhovskii, S. N. Karpukhin, and V. E. Yakobson, "Single-Crystal Barium Nitrate and Sodium Nitrate as Efficient Materials for Laser-Radiation Frequency Conversion Based on Stimulated Raman Scattering," *J. Opt. Tech.* **62**:770 (1995).
76. P. G. Zverev, J. T. Murray, R. C. Powell, R. J. Reeves, and T. T. Basiev, "Stimulated Raman Scattering of Picosecond Pulses in Barium Nitrate Crystals," *Opt. Commun.* **97**:59 (1993).
77. A. Owyoung and P. S. Percy, "Precise Characterization of the Raman Nonlinearity in Benzene Using Nonlinear Interferometry," *J. Appl. Phys.* **48**:674 (1977).
78. G. C. Herring, M. J. Dyer, and W. K. Bischel, "Temperature and Density Dependence of the Linewidths and Lineshifts of the Rotational Raman Lines in N_2 and H_2," *Phys. Rev. A* **34**:1944 (1986).
79. G. Hilfer and C. R. Menyuk, "Stimulated Raman Scattering in the Transient Limit," *J. Opt. Soc. Am. B* **7**:739–749 (1990).
80. M. J. Colles, *Appl. Phys. Lett.* **19**:23 (1971).
81. C. R. Menyuk, in D. Levi, C. R. Menyuk, and P. Winternitz (eds.), *Self-Similarity in Stimulated Raman Scattering,* Les Publications CRM, Montreal, Canada, 1994.
82. K. J. Druhl, R. G. Wenzel, and J. L. Carlsten, *Phys. Rev. Lett.* **51**:1171 (1983).
83. C. R. Menyuk, *Phys. Rev. A*. **47**:2235 (1993).
84. W. R. Trutna, Y. K. Park, and R. L. Byer, *IEEE J. Quant. Elect.* **QE-15**:648 (1979).
85. M. G. Raymer, J. Mostowski, and J. L. Carlsten, "Theory of Stimulated Raman Scattering with Broadband Lasers," *Phys. Rev. A* **19**:2304 (1979).
86. J. Eggleston and R. L. Byer, *IEEE J. Quant. Elect.* **QE-16**:850 (1980).
87. E. A. Stappaerts, W. H. Long Jr., and H. Komine, *Opt. Lett.* **5**:4 (1980).
88. A. Flusberg, D. Korff, and C. Duzy, "The Effect of Weak Dispersion on Stimulated Raman Scattering," *IEEE J. Quant. Elect.* **QE-21**:232 (1985).
89. K. A. Druhl, "Coherence Properties of Stokes Beams for Incoherent Broadband Pumps," *JOSA B* **3**:1363 (1986).
90. D. Korff, E. Mazur, C. Duzy, and A. Flusberg, "Raman Conversion Using Crossed Broadband Pump Beams and Bisecting Stokes," *JOSA B* **3**:1333 (1986).
91. G. C. Lombardi and H. Injeyan, "Phase Correlation Effects in a Raman Amplifier," *JOSA B* **3**:1461 (1986).
92. M. Bashkansky and J. Reintjes, "Correlation Effects in Pump-Depleted Broad-band Stimulated Raman Amplification," *Opt. Commun.* **83**:103 (1991).
93. M. Bashkansky and J. Reintjes, "Incoherent Multimode Raman Amplification Theory," *JOSA B* **8**: 1843 (1991).
94. M. D. Skeldon and R. Bahr, "Stimulated Rotational Raman Scattering in Air with a High Power Broadband Laser," *Opt. Lett.* **16**:366 (1991).
95. M. Trippenbach, K. Rzazewski, and M. G. Raymer, "Stimulated Raman Scattering of Colored Light," *JOSA B* **1**:671 (1984).
96. B. W. Shore, S. Lowder, and M. A. Johnson, "Some General Properties of Stimulated Raman Propagation with Pump Depletion, Transiency and Dispersion," LLNL Report No. UCRL-ID-1-7967 R 1, 1991.

97. M. G. Raymer and J. Mostowski, "Stimulated Raman Scattering: Unified Treatment of Spontaneous Initiation and Spatial Propagation," *Phys. Rev. A* **24**:1980 (1981).
98. G. P. Dzhotyan, Y. E. D'yakov, I. G. Zubarev, A. B. Mironov, and S. I. Mikhailov, "Amplification During Stimulated Raman Scattering in a Nonmonochromatic Pump Field," *Sov. Phys. JETP* **46**:431 (1978).
99. S. A. Akhmanov, Y. E. D'yakov, and L. I. Pavlov, "Statistical Phenomena in Raman Scattering Stimulated by a Broad-band Pump," *Sov. Phys. JETP* **39**:249 (1975).
100. M. D. Duncan, R. Mahon, L. L. Tankersley, and J. Reintjes, "Spectral and Temporal Characteristics of Spontaneous Raman Scattering in the Transient Regime," *JOSA B* **8**:300 (1991).
101. J. C. White and D. Henderson, "Anti-Stokes Raman Lasers," *AIP Conf. Proc.* **90**:117–127 (1982).
102. J. C. White and D. Henderson, "TI: Threshold and Dispersion Effects in the Anti-Stokes Raman Laser," *Opt. Lett.* **7**:517 (1982).
103. K. Ludewigt, R. Dierking, W. Pfingsten, and B. Wellegehausen, "Vacuum Ultraviolet Anti-Stokes Raman Lasers," *IEEE J. Quant. Electron.* **QE 22**:1967–1974 (1986).
104. A. Z. Grasyuk, L. L. Losev, A. P. Lutsenko, and S. N. Sazonov, "Parametric Raman anti-Stokes Laser," *Sov. J. Quant. Electron.* **20**:1153–1155 (1990).
105. N. Bloembergen and Y. R. Shen, "Coupling Between Vibrations and Light Waves in Raman Laser Media," *Phys. Rev. Lett.* **12**:504 (1964).
106. M. D. Duncan, R. Mahon, L. L. Tankersley, and J. Reintjes, "Parametric Raman Gain Suppression in D2 and H2," *Opt. Lett.* **11**:803 (1986).
107a. K. Leung, M. Oron, D. Klimek, R. Holmes, and A. Flusberg, "Observation of Parametric Gain Sup pression in Rotational Raman Transitions in N2 and H2." *Opt. Lett.* **13**:33 (1988).
107b. B. N. Perry, P. Raninowitz, and O. S. Bomse, *Opt. Lett.* **10**:146 (1985).
107. C. Reiser, T. D. Raymond, R. B. Michie, and A. P. Hickman, "Efficient Anti-Stokes Raman Conversion in Collimated Beams," *JOSA B,* **6**:1859 (1989).
108. M. D. Levenson, "Coherent Raman Spectroscopy" (see also included references), *Phys. Today* (May 1977).
109. C. M. Bowden and J. C. Englund, "Macroscopic Manifestation of Quantum Noise," *Opt. Commun.* **67**:71 (1988).
110. M. G. Raymer, I. A. Walmsley, J. Mostowski, and B. Sobolewska, "Quantum Theory of Spatial and Temporal Coherence Properties of Stimulated Raman Scattering," *Phys. Rev. A* **32**:332 (1985).
111. M. G. Raymer, Z. W. Li, and I. A. Walmsley, "Temporal Quantum Fluctuations in Stimulated Raman Scattering," *Phys. Rev. Lett.* **63**:1586 (1989).
112. M. G. Raymer and L. A. Westling, "Quantum Theory of Stokes Generation with a Multimode Laser," *JOSA B* **2**:1417 (1985).
113. M. D. Duncan, R. Mahon, L. L. Tankersley, and J. Reintjes, "Low-Light Level, Quantum-Noise-Limited Amplification in a Stimulated Raman Amplifier," *JOSA B* **9**:2107 (1992).
114. R. C. Swanson, P. R. Battle, and J. Carlsten, "Interferometric Measurement of Quantum Noise in a Raman Amplifier," *Phys. Rev. Lett.* **67**:38 (1991).
115. N. Fabriucius, K. Nattermann, and D. von der Linde, "Macroscopic Manifestation of Quantum Fluctuations in Transient Stimulated Raman Scattering," *Phys. Rev. Lett.* **52**:113 (1984).
116. K. Nattermann, N. Fabricius, and D. von der Linde, "Observation of Transverse Effects on Quantum Fluctuations in Stimulated Raman Scattering," *Opt. Commun.* **57**:212 (1986).
117. M. G. Raymer, K. Rzazewski, and J. Mostowski, "Pulse Energy Statistics in Stimulated Raman Scattering," *Opt. Lett.* **7**:71 (1982).
118. K. Rzazewski, M. Lewenstein, and M. G. Raymer, "Statistics of Stimulated Stokes Pulse Energies in the Steady State Regime," *Opt. Commun.* **43**:451 (1982).
119. D. C. MacPherson, R. C. Swanson, and J. L. Carlsten, "Quantum Fluctuations in the Stimulated Scattering Linewidth," *Phys. Rev. Lett.* **61**:66 (1988).
120. M. G. Raymer and I. A. Walmsley, "Quantum Statistics of Stimulated Raman Scattering," in L. Mandel (ed.), *Coherence and Quantum Optics,* vol. V, Plenum, New York, 1983, p. 63.

121. M. D. Duncan, R. Mahon, L. L. Tankersley, and J. Reintjes, "Imaging Through a Low Light Level Amplifier," *SPIE* **1409**:127–134 (1991).
122. M. D. Duncan, R. Mahon, L. L. Tankersley, and J. Reintjes, "Second Stokes Generation in Deuterium and Hydrogen," *Opt. Commun.* **86**:538–546 (1991).
123. G. I. Kachen and W. H. Lowdermilk, "Subnanosecond Pulsations in Forward and Backward Stimulated Raman Scattering," *Opt. Commun.* **18**:112 (1976).
124. M. Rokni and A. Flusberg, "Stimulated Rotational Raman Scattering in the Atmosphere," *IEEE J. Quant. Elect.* **QE-22**:1102 (1986).
125. M. D. Levenson, *Introduction to Nonlinear Laser Spectroscopy,* Academic Press, New York, 1982.
126. H. Lotem and R. T. Lynch Jr., *Phys. Rev. Lett.* **37**:334 (1976).
127. M. D. Duncan, R. Mahon, L. L. Tankersley, and J. Reintjes, "Time-Gated Imaging Through Scattering Media Using Stimulated Raman Amplification," *Opt. Lett.* **16**:1868–1870 (1991).
128. R. Mahon, M. D. Duncan, L. L. Tankersley, and J. Reintjes, "Time-Gated Imaging Through Dense Scatterers with a Raman Amplifier," *Appl. Opt.* **32**:7425–7433 (1993).
129. M. Bashkansky, P. R. Battle, R. Mahon, and J. Reintjes, "Subsurface Defect Detection in Ceramic Materials Using Ultrafast Optical Techniques," *22nd Ann. Rev. of Prog. in Quantitative Nondestructive Evaluation,* Seattle, WA, 1995.
130. G. W. Faris, M. J. Dyer, and A. Peet Hickman, "Transient Effects on Stimulated Brillouin Scattering," *Opt. Lett.* **17**:1049 (1992).
131. L. G. Hwa, J. Schroeder, and X.-S. Zhao, "Intrinsic Brillouin Linewidths and Stimulated Brillouin Coefficients in Glasses Studied by Inelastic Light Scattering," *JOSA B* **6**:833 (1989).
132. J. Schroeder, L. G. Hwa, G. Kendall, C. S. Dumais, M. C. Shyong, and D. A. Thompson, "Inelastic Light Scattering in Halide and Oxide Glasses: Intrinsic Brillouin Linewidths and Stimulated Brillouin Gain," *J. Noncryst. Solids* **102**:240 (1988).
133. G. W. Faris, L. E. Jusinski, M. J. Dyer, W. K. Bischel, and A. Peet Hickman, "High Resolution Brillouion Gain Spectroscopy in Fused Silica," *Opt. Lett.* **15**:703 (1990).
134. G. W. Faris, L. E. Jusinski, and A. Peet Hickman, "High Resolution Stimulated Brillouin Gain Spectroscopy in Glasses and Crystals," *JOSA B* **10**:587 (1990).
135. A. M. Scott, D. E. Watkins, and P. Tapster, "Gain and Noise Characteristics of Brillouin Amplifier and Their Dependence on the Spatial Structure of the Pump Beam," *JOSA B* **7**:929 (1990).
136. R. W. F. Gross, S. T. Amimoto, and L. Garman-DuVall, "Gain and Phase Conjugation Fidelity of a Four Wave Brilluoin Mirror Based on Methane," *Opt. Lett.* **16**:94 (1991).
137. V. I. Bespalov, O. V. Kulagin, A. I. Makarov, G. A. Pasmanik, A. K. Potjomkin, P. B. Potlov, and A. A. Shilov, "High-Sensitivity Optical System with Laser Amplifiers and Phase Conjugating Mirrors," *Opt. Acoust. Rev.* **1**:71 (1989).
138. P. Narum, M. D. Skeldon, and R. W. Boyd, "Effect of Laser Mode Structure on Stimulated Brillouin Scattering," *IEEE J. Quant. Electron.* **QE-22**:2161 (1986).
139. G. C. Valley, "A Review of Stimulated Brilluoin Scattering Excited with a Broad Pump Laser," *IEEE J. Quant. Electron.* **QE-22**:704 (1986).
140. W. T. Whitney, M. T. Duignan, and B. J. Feldman, "Stimulated Brilluoin Scattering and Phase Conjugation of Multiline Hydrogen Fluoride Laser Radiation," *JOSA B* **7**:2160 (1990).
140a. Robert A. Fisher (ed.), *Optical Phase Conjugation,* Academic Press, New York, 1983.
141. A. I. Erohkin, V. I. Kovalev, and F. S. Faizullov, "Determination of the Parameters of a Nonlinear Response of Liquids in an Acoustic Resonance Region by the Method of Nondegenerate Four Wave Interaction," *Sov. J. Quant. Electron.* **16**:872 (1986).
142. M. J. Dyer and W. K. Bischel, unpublished data.
143. S. T. Amimoto, R. W. F. Gross, L. Garman-DuVall, T. W. Good, and J. D. Piranian, "Stimulated Brillouin-Scattering Properties of SnCL4," *Opt. Lett.* **16**:1382 (1991).
144. M. J. Damzen, M. H. R. Hutchinson, and W. A. Schroeder, "Direct Measurement of the Acoustic Decay Times of Hypersonic Waves Generated by SBS," *IEEE J. Quant. Electron.* **QE-23**:328 (1987).
145. F. E. Hovis and J. D. Kelley, "Phase Conjugation by Stimulated Brilluoin Scattering in $CC1F_3$ Near the Gas-Liquid Critical Temperature," *JOSA B* **6**:840 (1989).

146. S. Y. Tang, C. Y. She, and S. A. Lee, "Continuous Wave Rayleigh-Brillouin Gain Spectroscopy in SF_6," *Opt. Lett.* **12** (1987).

147. D. Milam, LLNL Report No. 90-011/6330K.

148. P. Klovekom and J. Munch, "Variable Stimulated Brillouin Scattering Pulse Compressor for Nonlinear Optical Measurements," *Appl. Opt.* **36**:5913 (1997).

149. N. G. Basov, I. G. Zubarev, A. V. Kotov, S. I. Mikhailov, and M. G. Smirnov, "Small-Signal Wavefront Reversal in Non-threshold Reflection from a Brillouin Mirror," *Sov. J. Quant. Electron.* **9**:237–239, 1979.

150. N. F. Andreev, V. I. Bespalov, A. M. Kiselev, A. Z. Matreev, G. A. Pasmanik, and A. A. Shilov, "Wavefront Inversion of Weak Optical Signals with a Large Reflection Coefficient," *JETP Lett.* **32**:625–629, 1980.

151. A. M. Scott and K. D. Ridley, "A Review of Brillouin-Enhanced Four-Wave Mixing," *IEEE J. Quant. Electron.* **25**:438–459 (1989).

18.5 ADDITIONAL REFERENCES

S. A. Akmanov, B. V. Zhdanov, A. I. Kovrigin, and S. A. Pershin, "Effective Stimulated Scattering in the Ultraviolet and Dispersion of Gain in the 1.06–0.26 μ Band," *JETP Lett.* **15**:185 (1972).

F. Ausenegg and V. Deserno, "Stimulated Raman Scattering Excited by Light of 5300 Å," *Opt. Commun.* **2**:295 (1970).

G. Bisson and G. Mayer, "Effets Raman stimulés dans la calcite," *Crit. Acad. Sci. Paris* **265**:397 (1967).

N. Bloembergen, B. P. Lallemand, A. Pine, and P. Simova, "Controlled Stimulated Raman Amplification and Oscillation in Hydrogen Gas," *IEEE J. Quant. Electron.* **QE-3**:197 (1967).

R. L. Byer, "A 16-μm Source for Laser Isotope Enrichment," *IEEE J. Quant. Electron.* **QE-12**:732 (1976).

M. J. Colles, "Efficient Stimulated Raman Scattering from Picosecond Pulses," *Opt. Commun.* **1**:169 (1969).

J. Gazengel, N. P. Xuan, and G. Rivoire, "Stimulated Raman Scattering Thresholds for Ultra-Short Excitation," *Opt. Acta* **26**:1245 (1979).

H. Gorner, M. Maier, and W. Kaiser, "Raman Gain in Liquid Core Fibers," *J. Raman Spectrosc.* **2**:363 (1974).

A. Z. Grasyuk, V. F. Erinkov, I. G. Zubarev, V. I. Mishin, and V. G. Smirnov, "Laser Based on Raman Scattering in Liquid Nitrogen," *JETP Lett.* **8**:291 (1968).

J. B. Grun, A. K. McQuillan, and B. P. Stoicheff, "Intensity and Gain Measurements on the Stimulated Raman Emission in Liquid O_2 and N_2," *Phys. Rev.* **181**:61 (1969).

E. E. Hagenlocker, R. W. Minck, and W. G. Rado, "Effects of Phonon Lifetime on Stimulated Optical Scattering in Gases," *Phys. Rev.* **154**:226 (1967).

E. P. Ippen, "Low-Power Quasi-cw Raman Oscillator," *Appl. Phys. Lett.* **16**:303 (1970).

R. W. Minck, E. E. Hagenlocker, and W. G. Rado, "Consideration and Evaluation of Factors Influencing the Stimulated Optical Scattering in Gases," Scientific Laboratory, Ford Motor Company, Dearborn, MI, SC66-24, 1966.

I. Reinhold and M. Maier, "Gain Measurements of Stimulated Raman Scattering Using a Tunable Dye Laser," *Opt. Commun.* **5**:31 (1972).

W. L. Smith, F. P. Milanovich, and M. Henesian, Lawrence Livermore National Laboratory, private communication, 1983.

M. B. Vakhonev, V. N. Volkov, A. Z. Grasyuk, and A. N. Kirkin, "Determination of the Gain in Stimulated Raman Scattering Under Spatially Inhomogeneous Pumping Conditions," *Sov. J. Quant. Electron.* **6**:1369 (1976).

This page intentionally left blank.

CHAPTER 19
OPTICAL LIMITING

David J. Hagan
School of Optics/The Center for Research and Education in Optics and Lasers (CREOL)
University of Central Florida
Orlando, Florida

19.1 INTRODUCTION

As the name implies, an optical limiter is a device designed to keep the power, irradiance, energy, or fluence transmitted by an optical system below some specified maximum value, regardless of the magnitude of the input. It must do this while maintaining high transmittance at low input powers. The most important application of such a device is the protection of sensitive optical sensors and components from laser damage. There are many other potential applications for such devices, including laser power regulation or stabilization, or restoration of signal levels in optical data transmission or logic systems, but this chapter will primarily concentrate on devices for sensor protection.

Perhaps the most obvious way of achieving optical limiting is by active control, where input light levels are monitored by a sensor, which through some processor activates a modulator or shutter that in turn limits the transmitted light. The best-known examples of these are the iris and blink response of the eye. However, these are limited in speed to about 0.1 seconds, so that any intense pulse of light shorter than this can get past these defense mechanisms and damage the retina before they can respond. Speed is an issue with most active control systems for optical limiting. To protect sensors, the transmittance must be reduced in a time much shorter than the width of the potentially damaging pulse. Even very fast electro-optic shutters are limited to rise times on the order of 1 ns, which may be insufficient to adequately block Q-switched pulses shorter than 50 ns or so in duration. Even for protection against longer pulses, cost and complexity are disadvantages of active optical limiting systems. Another direct way to protect sensors against high-power lasers is to use narrow-line spectral filters. These can work well when the laser wavelength is known, such as in laboratory laser safety goggles, but would be largely ineffective against tunable lasers.

Passive systems, on the other hand, use a nonlinear optical material that functions as a combined sensor, processor, and modulator. This offers the potential for high speed, simplicity, compactness, and low cost. However, passive systems place severe requirements on the nonlinear medium.[1,2,3] While many materials exhibit the type of effects that produce optical

Copyright 2001 by The McGraw-Hill Companies, Inc. Click Here for Terms of Use.

limiting, usually these effects prove not to be large enough. Because of this, all prototype passive systems demonstrated to date place the nonlinear optical component in or near a focal plane. In a focal plane, the energy density of a beam from a distant laser source is $10^5 \sim 10^8$ times greater than in a pupil plane. Even in this focused geometry, material nonlinearities are barely large enough, and systems that adequately protect eyes and other common sensors over a broad wavelength band have yet to be demonstrated, at least in the visible and near-infrared. The idea of using a nonlinear material in a pupil plane (e.g., a coating on the surface of goggles) is therefore far from reality. For mid-infrared (3–12 μm wavelength range), optical nonlinearities are typically much larger than in the visible and results have been more promising than in the visible.[4,5,6] Still, however, limiting elements must be placed near a focal plane. Hence, research to date on optical limiting has predominantly focused on the search for new or modified materials with stronger nonlinearities, and on how to optimally use the best available nonlinear materials. This chapter will concentrate on passive devices.

The response of an *ideal* optical limiter is shown in Fig. 1, along with some typical responses of passive limiters. Clearly, an optical sensor requires high linear transmittance, T_L, at low input light levels for the transmission of images. Meanwhile, for higher inputs the limiter must clamp the transmitted energy below some maximum value, E_{max}, up to the maximum energy the limiter can withstand, E_D. This is usually the energy damage threshold for the limiting material itself. Usually the minimum transmittance of the device, T_{min}, occurs at this energy. Often, the performance of a limiting system or device is characterized by some type of figure of merit (FOM).[7,8] One of the most commonly used is FOM = T_L/T_{min}, which states that a large linear transmittance combined with a low minimum transmittance is desirable.[8] A slightly different way of expressing this is in terms of the optical density (OD), defined as OD = $-\log_{10}(T)$, so that the FOM may be reexpressed as the change in OD, or ΔOD =

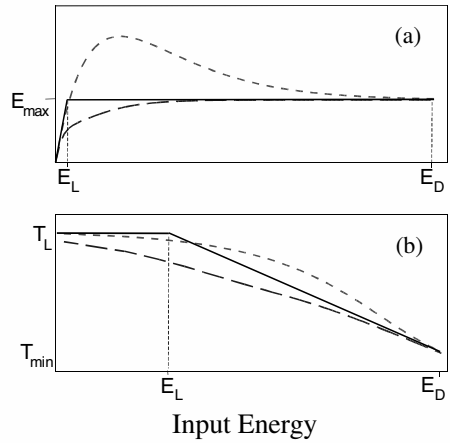

FIGURE 1 Typical limiting curves, drawn as (*a*) transmitted energy versus input energy, and (*b*) transmittance versus input energy, on a log-log scale. The solid line is the *ideal* optical limiter response, while the short- and long-dashed lines are typical of real systems. E_D is the energy at which the limiter undergoes irreversible laser damage. E_{max} is the maximum transmitted energy, here measured at the maximum input energy E_D. E_L is the limiting threshold for the ideal limiter, T_L is the linear transmittance and T_{min} is the minimum transmittance, usually obtained for the maximum input energy, E_D.

$\log_{10}(T_L/T_{min})$. For the ideal limiter shown in Fig. 1, the FOM is equivalent to the *dynamic range,* which is defined as D.R. = E_D/E_L.[7] However, although such merit figures are of some use, it is usually necessary to separately specify parameters such as linear transmittance, maximum transmitted energy, and damage energy. For example, in some applications, a linear transmittance of >50 percent could be an absolute requirement that cannot be offset by an improvement in protection. In addition, for nonideal limiting responses, the FOM may not give a clear indication of whether a device provides adequate protection at all input energies. For example, the dashed curves in Fig. 1 (*b*) look very similar when plotted as transmittance versus input energy. Although they have the same FOM, when plotted as transmitted versus input energy, it is clear that the long-dashed curve provides considerably better protection than the short-dashed curve.

The maximum permissible transmitted energy is highly dependent on the threat laser wavelength and pulse width, on the sensor to be protected, and on the *f*-number (defined as the ratio of focal length to lens diameter) of the imaging system. Most practical imaging systems use an *f*-number of 5 or less. However, one very common sensor for which we can specify maximum safe exposure levels is the human eye.[9] Mostly, we are concerned with retinal damage. Visible or near-infrared radiation is not absorbed in the cornea or lens of the eye, and the focusing of light onto the retina produces an optical gain on the order of 10^4 [i.e., the fluence (incident energy/unit area) at the retina is ~10^4 times that incident on the cornea]. Hence for visible or near-infrared radiation, damage will always occur first at the retina. For wavelengths in the UV and further into the infrared, light does not reach the retina, as it is absorbed in the lens or cornea where the fluence is much lower. If necessary, damage may be avoided by use of optical elements that simply block those wavelengths by reflection or absorption, as the eye cannot detect those wavelengths anyway. As shown in Fig. 2, the ANSI standard for the maximum safe energy entering the eye for pulse lengths less than 17 μs is 0.2 μJ.[10] However, larger energies may be tolerated where there is a finite probability of a retinal lesion but little chance of retinal hemorrhaging. For example, the ED-50 exposure level, for which there is a 50 percent chance of a retinal lesion but little chance of permanent damage, corresponds to ~1 μJ in the visible. Therefore ideally one would desire $E_{max} \ll 1$ μJ for an eye-protection limiter. However, since no practical prototype limiter so far has come close to this value, a more common target value for E_{max} in recent literature has been ~1 μJ.[11,12] As will be subsequently described, the total energy entering the eye is not a complete measure of performance, as many nonlinear optical mechanisms that give rise to limiting strongly distort a laser beam as well as controlling its total transmitted energy. Therefore, a better measure of limiting performance is the focus-

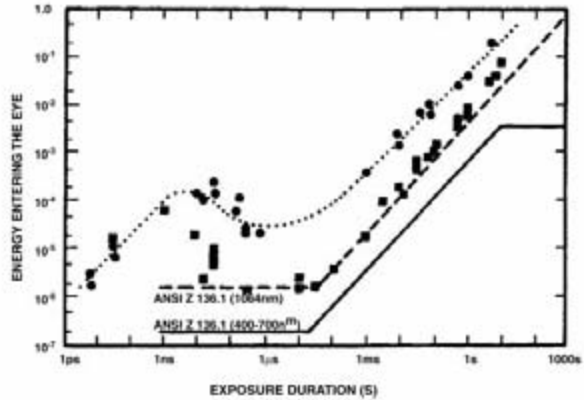

FIGURE 2 Damage thresholds for the eye. *(After Ref. 10.)*

able component of the energy entering the eye, E_{foc}. E_{foc} is defined as the energy falling within a 1.5-mrad-diameter circle in the retinal plane.[13] The accepted value for the minimum resolution of the eye is 1.5 mrad. Should the limiter defocus the beam enough that the focused beam significantly exceeds 1.5 mrad, an E_{max} of >1 μJ may be tolerable as long as $E_{foc} < 1$ μJ.

In the remainder of this chapter, we describe some of the fundamental principles of passive optical limiting, including nonlinear mechanisms and optimization of geometry. We also present a few examples of experimental demonstrations of some types of optical limiters, although this is by no means intended to be a comprehensive review. Rather, this chapter is intended as a starting point for newcomers to the field of optical limiting. For more detailed surveys of published research in this field, the reader is referred to the review papers,[1,3,12] journal special issues,[14] and conference proceedings[15–22] on the subject.

19.2 BASIC PRINCIPLES OF PASSIVE OPTICAL LIMITING

By way of an introduction to passive optical limiting, we briefly describe five of the most common nonlinear mechanisms used. As summarized in Fig. 3, these are (*a*) nonlinear absorption, (*b*) nonlinear refraction, (*c*) nonlinear scattering, (*d*) photorefraction, and (*e*) optically induced phase transitions. There have been many other schemes proposed for passive optical limiting, but those mentioned here form the basis for the vast majority of practical limiting devices that have appeared in the literature. A common theme to all schemes is that they each require the nonlinear optical material to be placed in or near a focal plane. Here we concentrate on how each nonlinear optical property results in limiting and we avoid detailed descriptions of the nonlinear mechanisms. For a more complete description of nonlinear optical phenomena and mechanisms, the reader is referred to Chapter 17 of this handbook.

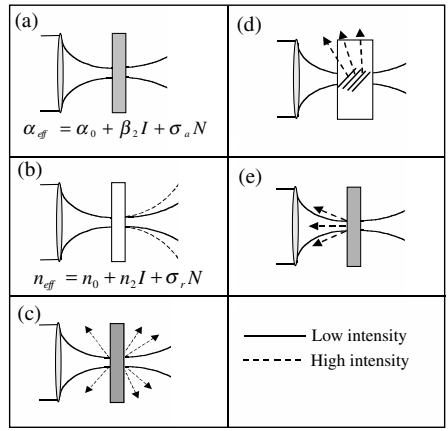

FIGURE 3 Fundamental mechanisms for passive optical limiting: (*a*) nonlinear absorption, (*b*) nonlinear refraction, (*c*) nonlinear scattering, (*d*) photorefraction, and (*e*) optically induced phase transitions.

Limiting via Nonlinear Absorption

Perhaps the most obvious and direct way to produce passive optical limiting is via nonlinear absorption (NLA), where we require the absorption to increase with increasing incident pulse fluence or irradiance. This can occur in a number of ways, as illustrated in Fig. 4, which shows some of the possible optical transitions for a generic material system. These could represent electronic transitions in many different material types (for example, an organic molecule or a semiconductor crystal).

Two-photon absorption (2PA) is a third-order nonlinear optical process that involves the simultaneous absorption of two photons.[23] For 2PA, the absorption increases in proportion to the incident irradiance, I. Another possibility is a two-step absorption process, where linear absorption populates excited states, from which a second absorption to a higher-lying energy state is possible.[24,25] If the excited state cross section, σ_{ex}, exceeds the ground state cross section, σ_g, then the absorption will increase with increasing excited state population density, N_{ex}, and hence with increasing incident fluence. This is usually referred to as *excited state absorption* (ESA) or *reverse-saturable absorption* (RSA). The latter nomenclature grew out of the more commonly observed *saturable absorption,* where $\sigma_{ex} < \sigma_g$ and the absorption decreases with increasing fluence. In materials with suitable energy levels, it is also possible to populate the excited state by two-photon absorption, and still produce excited state absorption at the excitation wavelength.[23,26] For any of these cases, we may write an approximate effective absorption coefficient, α_{eff},

$$\alpha_{eff} = \alpha + \beta I + \sigma_{ex} N_{ex} = \sigma_g N_g + \beta I + \sigma_{ex} N_{ex} \tag{1}$$

where β is the 2PA coefficient and N_g and N_{ex} are the ground state and excited state absorption cross sections, respectively. For a laser pulse shorter than the excited state lifetime, τ_1, and for low excitation levels, N_{ex} is directly proportional to the incident fluence. However, an optical limiter is required to work under high levels of excitation, so usually rate equations must

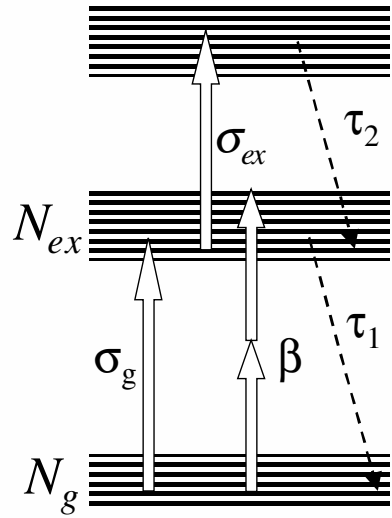

FIGURE 4 Nonlinear absorption processes.

be solved to determine the overall transmittance. Nevertheless, it is clear that a large ratio of σ_{ex}/σ_g is desirable, as we want large ESA, but small linear absorption. However, σ_g cannot be too small, as N_{ex} must become large enough to produce a strong limiting effect. The minimum achievable transmittance should occur when all molecules have been promoted to the first excited state, so that the transmittance is $T_{min} = \exp(-\sigma_{ex}NL)$, where N is the total molecular density and L is the material thickness. Hence the maximum achievable FOM is $T_{min}/T_L = \exp[-(\sigma_{ex} - \sigma_g)NL]$.[27] However, it is not practical to expect such a physical situation. Before such a high excitation is reached, other effects, including ionization, heating, and so forth will occur.[11]

In theory, 2PA is ideal for optical limiting, as the linear absorption is zero. Moreover, it can be shown that there is an absolute upper limit to the irradiance that can propagate through a two-photon absorber, given by $I_{max} = (\beta L)^{-1}$. 2PA also may populate excited states without the inconvenience of linear absorption, so that one can obtain limiting due to both 2PA and ESA. However, it is difficult to find materials with sufficiently large and broadband 2PA coefficients to work well with nanosecond or longer pulses.[26,28,29]

Regardless of the excitation mechanism, it is desirable to have an excited state lifetime, τ_1, longer than the laser pulse width, so that each electron or molecule need only be excited one time per pulse. A short upper excited state lifetime, τ_2, is required to reduce saturation of the excited state absorption, which detracts from limiting performance.

Optimization of NLA Limiters. While NLA gives the best optical limiting by placing the nonlinear material in a focal plane, this is also where the damage energy threshold of the nonlinear material is lowest. Very often, this gives an unacceptably low FOM. The damage threshold may be greatly increased by placing another nonlinear absorber in front of the one at focus, hence protecting it from damage. In the case of 2PA, this can be achieved by using a *thick* 2PA material, as illustrated in Fig. 5(*a*).[7,28,30] Here, the term *thick* means that the material thickness is much greater than the depth of focus of the beam. The front surface is far from focus, and the 2PA away from focus protects the material near focus. Theoretically, this can be done with no reduction in T_L, as there need be no linear absorption. In reality, parasitic linear transmittance and scatter may reduce T_L. For RSA materials, the intrinsic linear absorption does not permit us to

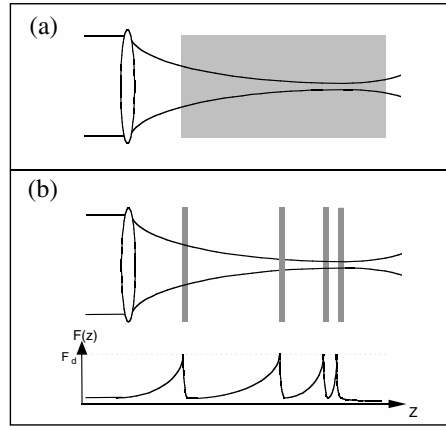

FIGURE 5 Optimization of limiter geometry: (*a*) for a 2PA limiter, (*b*) for an RSA limiter. The graph in (*b*) is a sketch of the on-axis fluence through the limiter near the maximum operating energy.

use an arbitrarily thick medium. Instead, discrete elements can be used. This geometry is usually referred to a *cascaded* or *tandem* limiter.[31] In the simplest case, this can consist of two or more elements in tandem, as illustrated in Fig. 5(*b*). The elements can be positioned so that the damage fluence, F_d, is reached simultaneously by all elements. This gives the maximum damage energy.[8,11,27] It has been shown that the total FOM of the limiter is given by the product of the FOMs of each individual element. However, because of beam distortion due to NLA or to any NLR that may be present in the material, the FOM of an individual element in a cascaded geometry does not usually approach the FOM of the same element when used alone. Miles[11] pointed out that this geometry helps keep the fluence high through the length of the limiter, by balancing the decrease in fluence due to absorption with the increase in fluence due to focusing. This is illustrated in Fig. 5(*b*), which shows a sketch of on-axis fluence versus distance for a four-element tandem limiter. This can be understood by considering the example of a limiter with $T_{min} = 10^{-4}$. If such a limiter were to have only a single element, the fluence on the front surface of the cell would have to exceed that on the rear surface by 10^4. If damage to the front of the cell were to be avoided, the fluence on the rear surface would be so low that the molecules near the rear surface could not contribute significantly to the limiting. Therefore, these molecules only serve to reduce the linear transmittance. However, for a 4-cell tandem limiter, $T_{min} = 0.1$ for each element, and the net value of T_{min} for the tandem limiter is 10^{-4}. This is much easier to achieve. The greater the number of cells, the larger the average fluence in each cell, and the separation of the cells is proportional to the square of the distance from focus, Z.[8] This can be extended to the limiting case of a single element with a graded molecular density, $N(z) \approx 1/\sigma_{ex}|Z|$.[11,32] In this case, the on-axis fluence would remain constant through the RSA material at some designed value of the input energy, usually just below the damage threshold. To avoid problems of generating the exact molecular density distribution, approximating the distribution with a steplike series of adjacent cells of different thickness and density has also been proposed. Like the tandem devices, these designs must be modified to account for beam distortion.[27]

Limiting via Nonlinear Refraction

From Kramers-Krönig relations, we know that all materials exhibiting nonlinear absorption must also exhibit nonlinear refraction.[33] A consequence of this is that each process that gives rise to optically induced changes in absorption must also result in changes to the refractive index. This can usually be expressed as,

$$n_{eff} = n_0 + n_2 I + \sigma_r N_{ex} \tag{2}$$

where n_2 describes instantaneous index changes proportional to incident irradiance and σ_r describes the change in index due to population of excited states. As described in Chapter 17 of this handbook and in Refs. 33 and 34, n_2 is related to the 2PA coefficient, β, by Kramers-Krönig relations. σ_r and σ_{ex} are related in a similar manner. Such index changes can occur even at wavelengths where there is no change in absorption.

As a focused beam has a spatially varying irradiance, then the induced index change varies across the beam profile, causing the beam to be strongly distorted upon propagation. Near focus, the beam is usually brightest in the center, so for a negative index change (where the index decreases with increasing irradiance or fluence), the nonlinear material will behave like a lens with negative focal length, and the beam is defocused. This process is referred to as *self-defocusing*. If the sign of the index change is positive, *self-focusing* results. Both of these effects can cause the beam to spread in the far field and hence limit the energy density in the far field, although the geometrical alignment may be different for optimal limiting in each case.[35] This means that E_{foc} may be strongly limited without necessarily limiting E_{max}. The presence of pupil-plane apertures in the imaging system combined with the beam distortion may also result in limiting of E_{max}. An advantage of this method over nonlinear absorption devices is that there is no need to absorb large amounts of energy in the nonlinear material,

which could cause thermal damage problems. A potential problem is that inadvertent refocusing of the eye could reduce the defocusing effect of the limiter. However, the nonlinear refraction usually aberrates the beam sufficiently that this is not a concern.

In terms of NLR, a *thick* limiter is defined as one where the propagation path in the nonlinear material is long enough that the index changes cause the beam to change its size inside the material. This process is sometimes refers to as *internal self-action*.[36] In this situation, the limiting behavior differs considerably between positive and negative index changes. Self-focusing causes the irradiance to be increased, causing more self-focusing, which becomes a catastrophic effect once a critical input power is reached.[37] This results in breakdown of the medium, which can strongly scatter the light and hence effectively limit the transmitted energy. It also causes damage to the material, but this is not a problem if the nonlinear medium is a liquid. Self-defocusing, on the other hand, reduces the irradiance, so that the limiting occurs more gradually as the input energy is increased.

Thermally induced index changes are also important in optical limiters. In liquids, where the thermal expansion is large, the index change results from the change in density upon heating due to laser absorption.[38] Hence the index decreases with temperature, giving a self-defocusing effect. The turn-on time for defocusing is dictated by the time taken for the liquid to expand across the width of the laser beam, which is roughly given by the beam radius divided by the speed of sound.[39] The turn-off time is dictated by thermal diffusion. In solids, thermal expansion is much smaller, but other effects, such as temperature dependence of the absorption edge, can cause thermally induced index changes. These usually result in an increase in index with temperature. As this is a local effect, the turn-on time is usually very fast, but turn-off times depend again on thermal diffusion. Thermal self-focusing in solid-state limiters can be a problem, leading to optical damage. Although thermal defocusing in liquids can be used to produce limiting, and some of the first passive optical limiters were based on this effect,[38] it usually degrades the performance of limiters based on NLA. This is one reason to use solid polymer host matrices for RSA dyes.[40]

Limiting via Nonlinear Scattering

Like absorption, scattering is also capable of strongly attenuating a transmitted beam. Nonlinear scattering is possible by laser-induced creation of new scatter centers, or by laser-induced changes in the refractive index difference between existing scatter centers and their surroundings. In the latter case, glass scatterers (such as small particles, a rough surface, highly porous glass, or a regular array of holes in glass) are index-matched by immersion in a liquid.[41–43] In this state, the composite material is clear and highly transparent. A small amount of absorber dye is dissolved in the liquid, so that when illuminated by a strong laser pulse, the solvent is heated and the index matching is lost, resulting in strong scattering.

In the former case, new scatter centers can be created when small particles, such as carbon black, molecular clusters, or other absorbing particles, are exposed to intense laser radiation.[44,45] In their normal state, such particles are very small, and although they may have a very strong optical absorption coefficient, due to their small size they neither absorb nor scatter much radiation. Upon absorption of radiation, the particles rapidly heat and ionize. This can cause the formation of microplasmas, which grow rapidly and strongly scatter the laser radiation. If the particles are suspended in a liquid, the heating can cause subsequent formation of microbubbles, which also strongly scatter light.[46,47] In either event, the scattering produces strong optical limiting. As the size of the scattering particles approaches the wavelength, the scattering is predominantly in the forward direction, which could reduce performance for low *f*-number imaging systems. Another problem is that the limiting process destroys the particles, making this mechanism unsuited to protection against high repetition-rate lasers. This might be overcome by flowing the suspensions. It has been shown that nonlinear scattering may also be an important yet unintentional mechanism in the operation of RSA limiters based on

organic molecules.[47] It is likely that that this is due to incomplete dissolution of the organic material, which leaves small clusters of undissolved material in suspension in the solvent.

Other Mechanisms

While the majority of the results reported on passive limiting employ one of the three previously noted mechanisms, many other schemes have been proposed and demonstrated. Most of these may involve some sort of change in refractive index or absorption, but they may use the change in a manner different from those just described. Although such schemes are too numerous to fully document here, the two following examples are worthy of mention.

Photorefraction. Photorefractives change their index when exposed to light, and they do so in such a way that the index change is in proportion to the gradient of light intensity. This is achieved by a complex process involving photoexcitation of charge carriers and diffusion of those carriers that results in a space charge field.[48] This field in turn causes an index change via the electro-optic effect. Due to the dependence on the gradient of intensity, the photorefractive effect is usually employed in situations where a periodic modulation of the irradiance induces a phase grating (a periodic modulation of the index). For optical-limiting applications, the interference is obtained by picking off a portion of the input laser beam with a beam splitter and overlapping it with the original beam in a photorefractive crystal.[49] Alternatively, a reflection from the rear surface of the crystal is used to interfere with the forward-going beam.[50] In both cases, a grating is produced that, via *two-beam coupling,* strongly scatters the incoming laser beam, limiting the transmitted energy.[51] An interesting side effect of this mechanism is that the limiting is coherence-dependent as well as intensity-dependent. Due to the requirement for charge diffusion, the turn on time is relatively slow, so that this type of limiter is usually only suitable for pulses of millisecond or longer duration.

Optically Induced Phase Change. A number of materials show a reversible, thermally induced semiconductor-metal phase transition upon illumination with strong laser radiation.[52] These materials are transparent to infrared radiation in their semiconducting state but highly reflective in their metallic state. Hence, in the infrared these materials may be transparent for low powers, while at high powers, weak optical absorption and subsequent heating may induce the strongly reflecting metallic phase, blocking the transmitted light. Some examples of materials of this type are Ag_2S, $TmSe_xTe_{1-x}$, and vanadium oxides, V_xO_{2x-1}. To be effective, such a material must be stable in its transparent state, have a small latent heat associated with the phase transition, and require a reasonably small temperature change (~100 K) to induce the phase transition. Vanadium oxides with compositions close to VO_2 or V_2O_3 comprise the most-studied class of these materials for optical limiting, having a phase transition temperature at around 70°C. In thin-film form and with appropriate antireflection coatings, these materials have high broadband transmission through the infrared (3 to 12 μm) which drops to around 1 percent in the metallic phase.[52]

19.3 EXAMPLES OF PASSIVE OPTICAL LIMITING IN SPECIFIC MATERIALS

Unavoidably, most of the materials used for passive optical limiting exhibit a combination of the nonlinear properties previously described. This usually complicates matters, but in some cases the different nonlinearities may be used to complement each other. In this section, we briefly present a few specific examples of limiting devices that illustrate how some of the principles just described may be applied in practice.

Semiconductors

Semiconductors exhibit a variety of strong nonlinear absorption and refraction effects.[53] Due to their broad absorption bands, they are capable of producing 2PA over a broad wavelength range where the linear absorption is low. Moreover, the carriers excited by 2PA produce very strong absorption and negative nonlinear refraction. The wavelength range of operation for 2PA, avoiding linear interband absorption, is $E_g/2 < h\nu < E_g$. E_g is the bandgap of the semiconductor and $h\nu$ is the photon energy. For example, in ZnSe, this corresponds to an operating wavelength range of about 480 nm to 900 nm, while in InSb the range is 7 to 14 μm at room temperature. Over this range, the combined effects of 2PA and free carrier absorption and refraction are more or less constant for a given semiconductor. However, the nonlinearities scale very strongly with bandgap. If we keep the ratio of photon energy to bandgap energy fixed, 2PA scales as E_g^{-3} and free carrier absorption and refraction scale approximately as $E^{-2}{}_g$.[6,23] Hence, semiconductors work significantly better for the infrared than for the visible. A problem with semiconductors is that they tend to have low damage thresholds. It was shown by Van Stryland et al.[28] that this can be overcome by the use of the thick-limiter geometry. In this case, a thick sample of the large-gap semiconductor ZnSe was used to demonstrate limiting of 30-ps pulses at a wavelength of 532 nm, as shown in Fig. 6. Due to a combination of 2PA and free-carrier absorption and refraction that occurs prior to focus, it was not possible to damage the ZnSe in the bulk. Hence, these devices were labeled *self-protecting* limiters. The FOM was measured as 2×10^4. The linear transmittance was 40 percent, probably due to a combination of scatter and parasitic absorption. Despite this good performance with ps pulses, the self-protection does not prevail for nanosecond pulses. This is thought to be due to the effects of carrier recombination and diffusion, which reduce the carrier defocusing effect, allowing positive thermal index changes to dominate.

Organics

Organic molecules have attracted interest for optical limiting for their attractive NLA properties in the visible and near-infrared. While some materials have shown promise for their combined 2PA and excited-state absorption properties,[26,29] so far these effects have not proven large enough over a sufficiently broad wavelength band to be practical. By far the

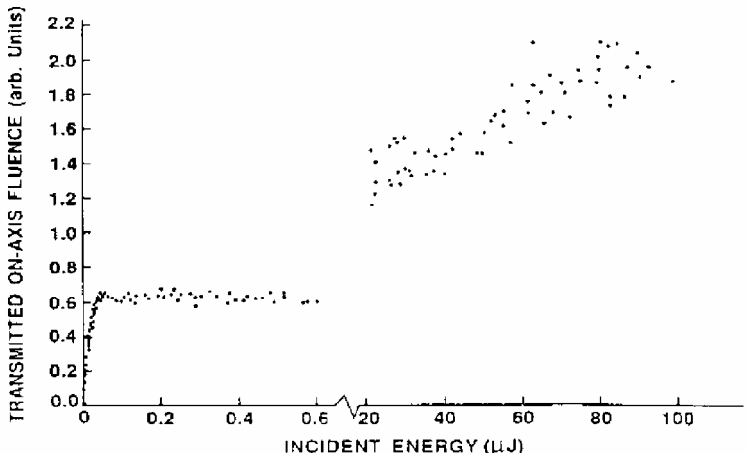

FIGURE 6 Limiting curve for ZnSe thick limiter for 30 ps, 532 nm. (*After Ref. 28.*)

most attention has been paid to organics for their RSA properties.[25,54] Generally, the mechanism is as shown in Fig. 4, but often the excited states may also relax into long-lived triplet states. This effectively increases the lifetime of the highly absorbing excited state. The transfer to triplet states may be enhanced by the addition of heavy atoms or paramagnetic groups to the molecule or solvent.[55] Several groups have demonstrated promising results with optimized limiting devices using phthalocyanines or other similar RSA molecules.[40,56] One example of an optimized limiter based on this type of material is that of Perry et al.[40] Here an indium phthalocyanine chloride (InClPc) was incorporated into a PMMA polymer host to make a solid-state limiting material. Slices of this material were used to make a three-element tandem limiter. The device, which had a linear transmittance of about 55 percent (70 percent internal transmittance), was designed to operate with a maximum fluence of 3 J/cm^2 in an *f*/5 focusing geometry. The combination of solid-state host and low design fluence helps minimize the detrimental effects of thermally induced refractive index changes. The device had a minimum transmittance of 0.185 percent at the maximum input energy of 6.5 mJ, corresponding to a maximum output energy of 12 μJ. This was a factor of four greater than predicted by simple design models, which assume a constant beam shape. This discrepancy is small compared with similar liquid-based limiters, which suffer from much greater thermal refraction. To properly design limiters of this type, propagation codes have been developed that account for all NLA and NLR mechanisms, including thermal refraction, and that are capable of modeling internal self-action.[57]

Carbon-Black Suspensions

It was shown by Mansour et al.[44] that dilute ink exhibits very strong, broadband optical limiting properties for nanosecond pulses. Ink is a liquid suspension of amorphous carbon particles. Figure 7 shows an example of limiting of 14-ns, 532-nm pulses using a carbon-black

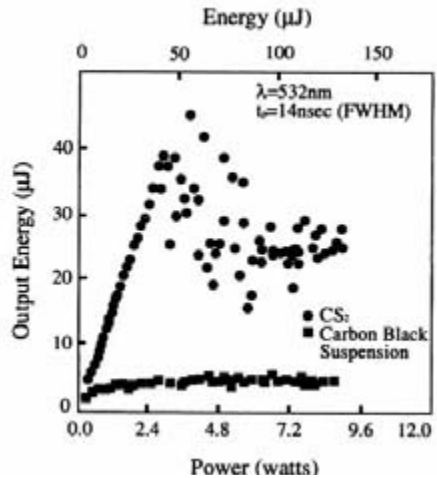

FIGURE 7 Optical limiting of 14-ns pulses at 532-nm wavelength in 1-cm thick, 70 percent linear transmittance CBS. Also shown are results of limiting in CS_2, for comparison. *(After Ref. 44.)*

suspension (CBS) in a 50:50 water/ethanol mixture with $T_L = 70$ percent. Similar results are obtained with a 1064-nm laser wavelength, indicating an extremely broadband limiting response. By observing scattered light intensity as a function of input irradiance, it was clearly shown that the incident light becomes very strongly scattered as the incident energy increases. Measurements of the angular distribution of scattered light show a Mie scattering pattern typical of scattering particles a factor of ≈3 larger than the original carbon-black particles. Similar results were found for a layer of small carbon particles deposited on a glass surface. It was concluded from this that the limiting is a result of scattering and absorption by microplasmas formed after thermionic emission from the laser-heated carbon particles. Later studies have indicated that the nonlinear scattering may result from microbubbles formed in the solvent by heating of the carbon. There is clear evidence that for longer pulses, the limiting is dependent on the volatility of the solvent,[46] and imaging techniques have shown that bubbles may persist in the focal volume 100 ns after the pulse.[47] It is quite feasible that microplasmas may be responsible for limiting on shorter (<10 ns) time scales, while bubbles play a more important role for longer (~100 ns) pulses.

Photorefractives

Although it has been shown that the photorefractive effect can occur over a vast range of time scales, effects large enough for practical devices typically have millisecond and longer response times. Cook et al.[50] exploited the large photorefractive two-beam coupling gain in Fe:$LiNbO_3$ to demonstrate strong optical limiting for millisecond pulses or c.w. lasers. A weak reflection of the input beam from the rear surface of the lithium niobate crystal was sufficient to initiate the two-beam coupling. As shown in Fig. 8, this produced a change in OD of up to 4 with a response time of about 2 ms. The linear transmittance for these samples is typically in the range of 30 to 60 percent. The limiting effect is not strongly sensitive to wavelength, operating between 420 and 670 nm. It is found that the optimum *f*-number for limiting was about *f*/20, and limiting performance drops off rapidly as the *f*-number is decreased. This results from the trade-off between the high irradiance produced by small focused spot sizes and the long interaction length produced by large spot sizes.

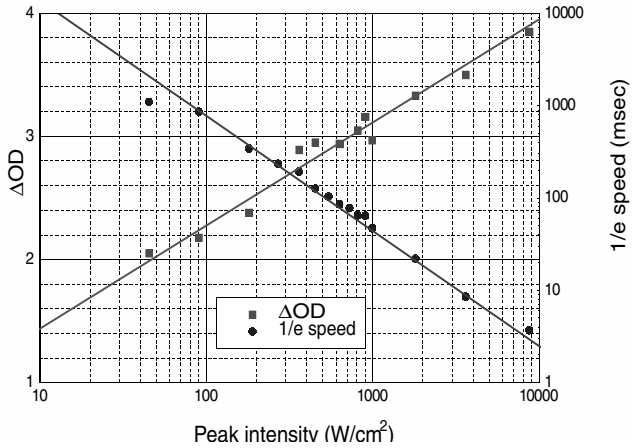

FIGURE 8 Far-field optical limiting and response time in a 3.4-mm path crystal of 0.03 percent Fe + 0.05 percent Tb:$LiNbO_3$ at 523.5 nm. *(After Ref. 50.)*

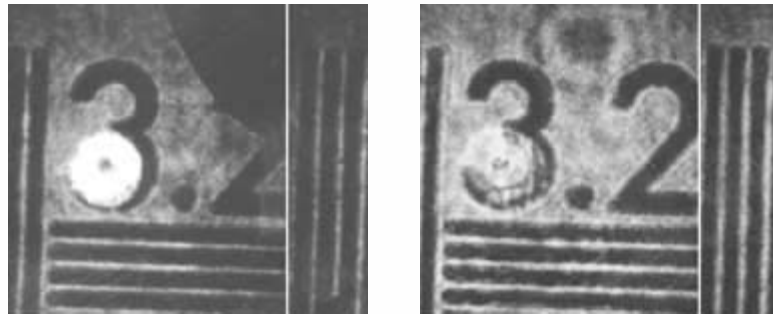

FIGURE 9 Suppression of a c.w. visible laser beam while transmitting the image of a resolution test chart, using a dye-doped nematic liquid crystal passive limiter. (*a*) Low laser intensity, showing no limiting effect, and (*b*) above the limiting threshold. *(After Ref. 59.)*

Liquid Crystals

Liquid crystals are composed of highly anisotropic molecules. By illuminating a nematic liquid crystal with a linearly polarized laser beam, the molecules can align with the electric field in the beam, inducing an irradiance-dependent birefringence in the bulk liquid. These effects are large, but typically take milliseconds to seconds for the realignment process. Recently, it has been shown that doping a liquid crystal with certain dyes can induce molecular reorientation at extremely low powers.[58] Khoo et al.[59] have shown that this effect may be used to achieve extremely low-power c.w. limiting. Using a twisted nematic 5CB film with 1 percent methyl red doping, between crossed polarizers, the maximum transmitted energy of a c.w. argon ion laser beam was kept below 13 μW for inputs up to 140 mW, with $T_L = 10$ percent, including Fresnel reflections and losses at the polarizers. Figure 9 shows a photograph of the transmitted beam for low and high powers, with an image that was simultaneously transmitted by the system. An advantage of liquid crystals is that they can be highly transparent across the entire visible spectrum.

19.4 REFERENCES

1. L. W. Tutt and T. F. Boggess, "A Review of Optical Limiting Mechanisms and Devices Using Organics, Fullerenes, Semiconductors and Other Materials," *Prog. Quant. Electr.* **17:**299–338 (1993).
2. G. L. Wood, W. W. Clark, M. J. Miller, G. J. Salamo, and E. J. Sharp, "Evaluation of Passive Optical Limiters and Switches," *Proceedings of SPIE Conference on Materials for Optical Switches, Isolators and Limiters,* **1105** (1989).
3. E. W. Van Stryland, M. J. Soileau, S. Ross, and D. J. Hagan, "Passive Optical Limiting: Where Are We?" *Nonlinear Optics* **21:**29–38 (1998).
4. M. Sheik-Bahae, D. C. Hutchings, D. J. Hagan, and E. W. Van Stryland, "Dispersion of Bound Electronic Nonlinear Refraction in Solids," *IEEE J. Quantum Electron.* **27:**1296–1309 (1991).
5. A. A. Said, M. Sheik-Bahae, D. J. Hagan, T. H. Wei, J. Wang, J. Young, and E. W. V. Stryland, "Determination of Bound and Free-Carrier Nonlinearities in ZnSe, GaAs, CdTe and ZnTe," *J. Opt. Soc. Am. B* **9:**409 (1991).
6. B. S. Wherrett, "Scaling Rules for Multiphoton Interband Absorption in Semiconductors," *J. Opt. Soc. Am. B-Optical Physics* **1:**67–72 (1984).
7. D. J. Hagan, E. W. Van Stryland, M. J. Soileau, Y. Y. Wu, and S. Guha, "Self-Protecting Semiconductor Optical Limiters," *Opt. Lett.* **13:**315–317 (1988).

8. D. J. Hagan, T. Xia, A. A. Said, T. H. Wei, and E. W. V. Stryland, "High Dynamic Range Passive Optical Limiters," *Int. J. Nonlin. Opt. Phys.* **2:**483–501 (1993).
9. D. H. Sliney and M. L. Wolbarsht, *Safety with Lasers and Other Optical Sources,* Plenum, New York, 1980.
10. D. H. Sliney, "Retinal Damage from Laser Radiation," *Nonlinear Optics,* **21:**1–18 (1998).
11. P. A. Miles, "Bottleneck Optical Limiters: The Optimal Use of Excited-State Absorbers," *Appl. Opt.* **33:**6965 (1994).
12. R. C. Hollins, "Optical Limiters, Spatial, Temporal and Spectral Effects," *Nonlinear Optics* **21:**39–48 (1998).
13. J. A. Zuclich, D. J. Lund, P. R. Edsall, R. C. Hollins, P. A. Smith, B. E. Stuck, and L. N. McLin, "Experimental Study of the Variation of Laser-Induced Retinal Damage Threshold with Retinal Image Size," *Nonlinear Optics* **21:**19–28 (1998).
14. J. A. Hermann and J. Staromlynska, "Special Issue on Optical Limiters, Switches and Discriminators," *J. Nonlinear Optical Phys. and Materials* **2** (1993).
15. F. Kajzar, "Proceedings of First International Workshop on Optical Power Limiting, Cannes, France," in *Nonlinear Optics, Principles, Materials, Phenomena, Devices,* Gordon & Breach, 1998.
16. C. M. Lawson, "Nonlinear Optical Liquids," *Proceedings of SPIE*, SPIE, **2853**, Denver, 1996.
17. C. M. Lawson, "Nonlinear Optical Liquids for Power Limiting and Imaging," *Proceedings of SPIE*, SPIE, **3472**, San Diego, 1998.
18. C. M. Lawson, "Power Limiting Materials and Devices," *Proceedings of SPIE*, SPIE, **3798**, Denver, 1999.
19. M. J. Soileau, "Materials for Optical Switches, Isolators and Limiters," *Proceedings of SPIE*, SPIE, **1105**, Orlando, 1989.
20. M. J. Soileau, *Electro-Optical Materials for Switches, Coatings, Sensor Optics and Detectors,* vol. 1307, SPIE, Orlando, 1990.
21. R. Crane, K. Lewis, E. W. Van Stryland, and M. Khoshnevisan, *Materials for Optical Limiting,* vol. 374, MRS, Boston, 1994.
22. R. Sutherland, R. Pachter, P. Hood, D. J. Hagan, K. Lewis, and J. Perry, *Materials for Optical Limiting II,* vol. 479, MRS, San Francisco, 1997.
23. E. W. Van Stryland, H. Vanherzeele, M. A. Woodall, M. J. Soileau, A. L. Smirl, S. Guha, and T. F. Boggess, "2 Photon-Absorption; Nonlinear Refraction; and Optical Limiting in Semiconductors," *Optical Engineering,* **24:**613–623 (1985).
24. C. R. Guliano and L. D. Hess, "Nonlinear Absorption of Light: Optical Saturation of Electronic Transitions in Organic Molecules with High Intensity Laser Radiation," *IEEE J. Quantum Electron.* **QE-3:**358–367 (1967).
25. T. H. Wei, D. J. Hagan, M. J. Sence, E. W. V. Stryland, J. W. Perry, and D. R. Coulter, "Direct Measurements of Nonlinear Absorption and Refraction in Solutions of Phthalocyanines," *Appl. Phys.* **B54:**46 (1992).
26. A. A. Said, C. Wamsley, D. J. Hagan, E. W. V. Stryland, B. A. Reinhardt, P. Roderer, and A. G. Dillard, "Third and Fifth Order Optical Nonlinearities in Organic Materials," *Chem. Phys. Lett.* **228:**646–650 (1994).
27. T. Xia, D. J. Hagan, A. Dogariu, A. A. Said, and E. W. V. Stryland, "Optimization of Optical Limiting Devices Based on Excited-State Absorption," *Applied Optics* **36:**4110–4122 (1997).
28. E. W. Van Stryland, Y. Y. Wu, D. J. Hagan, M. J. Soileau, and K. Mansour, "Optical Limiting with Semiconductors," *J. Opt. Soc. Am. B* **5:**1980–1989 (1988).
29. M. Albota, D. Beljonne, J. L. Brédas, J. Ehrlich, J. Fu, A. Heikal, T. Kogej, M. Levin, S. R. Marder, D. McCord-Maughon, J. W. Perry, H. Röckel, M. Rumi, G. Subramaniam, W. W. Webb, X. L. Wu, and C. Xu, "Design of Organic Molecules with Large Two-Photon Absorption Cross Sections," *Science* **281:**1653–1656 (1998).
30. M. Sheik-Bahae, A. A. Said, D. J. Hagan, M. J. Soileau, and E. W. Van Stryland, "Nonlinear Refraction and Optical Limiting in Thick Media," *Optical Engineering* **30:**1228–1235 (1991).
31. A. A. Said, R. DeSalvo, M. Sheik-Bahae, D. J. Hagan, and E. W. V. Stryland, "Self Protecting Optical Limiters Using Cascading Geometries," *Proceedings of SPIE,* SPIE, Orlando, Florida, 1992.

32. S. W. McCahon and L. W. Tutt, "Optical Limiter Including Optical Congruence and Absorbing Body with Inhomogeneous Distribution of Reverse Saturable Absorption," U.S. Patent 5,080,469, 1992.
33. D. C. Hutchings, M. Sheik-Bahae, D. J. Hagan, and E. W. Van Stryland, "Kramers-Kronig Relations in Nonlinear Optics," *Optical and Quantum Electronics* **24:**1–30 (1992).
34. M. Sheik-Bahae, D. J. Hagan, and E. W. V. Stryland, "Dispersion of Bound Electronic Nonlinear Refraction in Solids," *Phys. Rev. Lett.* **65:**96–99 (1990).
35. M. Sheik-Bahae, A. A. Said, and E. W. V. Stryland, "High-sensitivity, Single-Beam n_2 Measurements," *Opt. Lett.* **14:**955–957 (1989).
36. A. E. Kaplan, "External Self-focusing of Light by a Nonlinear Layer," *Radiophys. Quantum Electron.* **12:**692–696 (1969).
37. M. J. Soileau, W. E. Williams, and E. W. Van Stryland, "Optical Power Limiter with Picosecond Response Time," *IEEE J. Quantum Electron.* **QE-19:**731–735 (1983).
38. R. C. Leite, S. P. S. Porto, and T. C. Damen, *Appl. Phys. Lett.* **10:**100 (1967).
39. D. I. Kovsh, D. J. Hagan, and E. W. V. Stryland, "Numerical Modeling of Thermal Refraction in Liquids in the Transient Regime," *Optics Express* **4** (1999).
40. J. W. Perry, K. Mansour, I.-Y. S. Lee, X.-L. Wu, P. V. Bedworth, C.-T. Chen, D. Ng, S. R. Marder, P. Miles, T. Wada, M. Tian, and H. Sasabe, "Organic Optical Limiter with a Strong Nonlinear Absorptive Response," *Science* **273:**1533 (1996).
41. B. L. Justus, A. J. Campillo, and A. L. Huston, "Thermal-Defocusing/Scattering Optical Limiter," *Opt. Lett.* **19:**673 (1994).
42. H.-B. Lin, R. J. Tonucci, and A. J. Campillo, "Two-Dimensional Photonic Bandgap Optical Limiter in the Visible," *Opt. Lett.* **23:**94–96 (1998).
43. D. J. Hagan, S. S. Yang, C. Basanez, E. W. Van Stryland, W. Moreshead, and J. L. Nogues, "Optical Limiting via Nonlinear Scattering with Solgel Hosts," *Proceedings of SPIE Conf. on Power Limiting Materials and Devices,* SPIE, **3798**, Denver, Colorado, 1999.
44. K. Mansour, E. W. V. Stryland, and M. J. Soileau, "Nonlinear Properties of Carbon Black Suspensions," *J. Opt. Soc. Am. B* **9:**1100 (1992).
45. T. Xia, A. Dogariu, K. Mansour, D. J. Hagan, A. A. Said, E. W. V. Stryland, and S. Shi, "Nonlinear Optical Properties of Inorganic Metallic Clusters," *J. Opt. . Soc. Am B* **15:**1497 (1998).
46. K. J. McEwan, P. K. Milsom, and D. B. James, "Nonlinear Optical Effects in Carbon Suspensions," *Proceedings of Nonlinear Optical Liquids for Power Limiting and Imaging,* SPIE, **3472**, San Diego, California, 1998.
47. R. V. Goedert, R. J. Becker, A. Clements, and T. A. Whitaker III, "Overview of the Shadowgraphic Imaging Technique and Results for Various Materials," *Proceedings of Nonlinear Optical Liquids for Power Limiting and Imaging,* SPIE, **3472**, San Diego, California, 1998.
48. M. Cronin-Golumb and A. Yariv, "Optical Limiters Using Photorefractive Limiters," *J. Appl. Phys.* **57:**4906 (1985).
49. S. W. McCahon and M. V. Klein, "Coherent Beam Excisors Using the Photorefractive Effect in $BaTiO_3$," *Proceedings of SPIE Conference on Materials for Optical Switches, Isolators and Limiters,* SPIE, **1105**, Orlando, Florida, 1989.
50. G. Cook, D. C. Jones, C. J. Finnan, L. L. Taylor, and T. W. Vere, "Optical Limiting with Lithium Niobate," *Proceedings of Power-Limiting Materials and Devices,* SPIE, **3798**, Denver, Colorado, 1999.
51. R. W. Boyd, *Nonlinear Optics,* Academic Press, Boston, 1992.
52. K. L. Lewis, A. M. Pitt, T. Wyatt-Davies, and J. R. Milward, "Thin Film Thermochromic Devices for Non-Linear Optical Devices," *Proceedings of MRS Symposium on Materials for Optical Limiting,* MRS, Boston, 1994.
53. N. Peyghambarian, S. W. Koch, and A. Mysyrowicz, *Introduction to Semiconductor Optics,* Prentice Hall, Englewood Cliffs, New Jersey, 1993.
54. J. S. Shirk, R. G. S. Pong, F. J. Bartoli, and A. W. Snow, "Optical Limiter Using a Lead Phthalocyanine," *Appl. Phys. Lett.* **63:**1880 (1993).

55. J. W. Perry, "Organic and Metal-Containing Reverse Saturable Absorbers for Optical Limiters," in *Nonlinear Optics of Organic Molecules and Polymers,* H. S. Nalwa and S. Miyata, ed., CRC Press, New York, 1997.

56. A. A. Said, T. Xia, D. J. Hagan, A. Wajsgrus, S. Yang, D. Kovsh, and E. W. V. Stryland, "Liquid-Based Multicell Optical Limiter," *Proceedings of SPIE Conference on Nonlinear Optical Liquids,* SPIE, **2853**, Denver, Colorado, 1996.

57. D. Kovsh, S. Yang, D. J. Hagan, and E. W. Van Stryland, "Nonlinear Optical Beam Propagation for Optical Limiting," *Applied Optics* **38:**5168–5180 (1999).

58. L. Marrucci, D. Paparo, G. Abbate, E. Santamo, M. Kreuzer, P. Lehnert, and T. Vogeler, "Enhanced Optical Nonlinearity by Photoinduced Molecular Orientation in Absorbing Liquids," *Physical Review A,* **58:**4926 (1998).

59. I. C. Khoo, M. V. Wood, M. Y. Shih, and P. H. Chen, "Extremely Nonlinear Photosensitive Liquid Crystals for Image Sensing and Sensor Protection," *Opt. Exp.,* **4:**432–442 (1999).

CHAPTER 20
PHOTONIC BANDGAP MATERIALS

Pierre R. Villeneuve*
Department of Physics
Massachusetts Institute of Technology
Cambridge, Massachusetts

20.1 GLOSSARY

a	lattice constant of the periodic structure
c	speed of light in vacuum
E	energy
$\boldsymbol{E}$	electric field
f	frequency
f_0	center frequency of the cavity resonance
$\boldsymbol{H}$	magnetic field
$\boldsymbol{k}$	wavevector
L	cavity length
n	index of refraction
P	power
Q	quality factor
$\boldsymbol{r}$	position vector
V_m	modal volume
Δf	frequency width of the cavity resonance
ε	macroscopic dielectric function
η	enhancement factor of the spontaneous emission rate
λ	wavelength in vacuum
ω	angular frequency
Θ	differential operator

* Current address: Clarendon Photonics, Inc., Boston, Massachusetts.

Copyright 2001 by The McGraw-Hill Companies, Inc. Click Here for Terms of Use.

20.2 INTRODUCTION

Electromagnetic waves inside quarter-wave dielectric stacks undergo partial reflection at the different dielectric interfaces. The destructive interference of the waves leads to the formation of bands of forbidden electromagnetic states. When light is incident at frequencies lying within the forbidden bands, it is prevented from propagating inside the stack; instead it is reflected and its amplitude decays exponentially through successive layers.

The operational principle behind fiber Bragg gratings[1], interference filters[2], and distributed feedback lasers[3] is also based on the multiple scattering that occurs inside periodic dielectric materials. The range of frequencies over which light is reflected (i.e., over which wave propagation is forbidden) defines a stop band, or bandgap, the size of which is proportional to the grating strength (i.e., to the effective index contrast between the different materials). The range is typically less than 1 percent of the midgap frequency, and in some cases is much less than 1 percent.

In addition to being forbidden over a small range of frequencies, propagation in dielectric stacks is also forbidden over a small range of angles from normal incidence. This small range of angles defines a cone with its principal axis normal to the surface. Light incident at an angle outside the cone is not reflected, but rather is transmitted through the stack. To increase the size of the reflection cone, one can increase the index contrast between the different dielectric layers. It has been demonstrated recently that the cone can be made to extend as far as 90°, allowing light to be reflected off the stack from *any* angle of incidence.[4] Stacks that reflect light from every direction are referred to as *omnidirectional reflectors.*

The existence of omnidirectional reflectors does not necessarily imply the existence of omnidirectional bandgaps. In fact, omnidirectional reflectors do not have complete three-dimensional bandgaps. Electromagnetic states exist inside the reflectors at every frequency, but incident light cannot couple to them; the wave vector of the incident light cannot be matched to the wave vector of the electromagnetic states inside the reflector. However, if light were to be generated from *within* the reflector, light could propagate along the dielectric planes—hence the absence of a three-dimensional bandgap.

In order to create a complete three-dimensional bandgap and prevent light from propagating anywhere inside the material, periodic structures must possess a three-dimensional periodicity. The principal feature of three-dimensional (3D) bandgap materials is their ability to suppress the density of electromagnetic states everywhere inside the materials over a given range of frequencies. Since the rate of spontaneous radiative decay of an atom or molecule scales with the density of allowed states at the transition frequency, photonic bandgap (PBG) materials can be used to greatly affect the radiative dynamics of materials and lead to significant changes in the properties of optical devices.

In addition to affecting the radiative properties of atoms, PBG materials can also be used to control the flow of light by allowing states to exist within the bandgap. This novel feature has triggered the imagination of many researchers as it promises to enable the very large scale integration of photonic components.

Though three-dimensional PBG materials can completely suppress the density of states, some three-dimensional structures possess partial gaps (i.e., gaps that do not extend along every direction). These pseudogaps can lead to small (but nonzero) densities of states and can lead to significant changes in the radiative properties of materials. Moreover, dielectric stacks, in effect one-dimensionally periodic structures, can reduce the density of states by suppressing states with wave vectors normal to the layers but they cannot eliminate every state along every direction.

In this chapter, we discuss the radiative properties of emitters and the control of light flow in PBG materials with pseudogaps and complete gaps. An in-depth review of PBG materials can be found in Ref. 5. Early fabrication efforts of 3D PBG materials are described in Ref. 6; a more recent review of PBG materials at near-infrared frequencies is presented in Ref. 7.

20.3 MAXWELL'S EQUATIONS

Although the word *photon* is used, the appearance of bandgaps arises from a strictly classical treatment of the problem. The properties of PBG materials can be determined from the classical vector wave equation with a periodic index of refraction. If the fields are expanded in a set of harmonic modes, in the absence of external currents and sources, Maxwell's equations can be written in the following form:

$$\nabla \times \left[\frac{1}{\varepsilon(\boldsymbol{r})} \nabla \times \boldsymbol{H}(\boldsymbol{r}) \right] = \frac{\omega^2}{c^2} \boldsymbol{H}(\boldsymbol{r}) \tag{1}$$

where $\boldsymbol{H}(\boldsymbol{r})$ is the magnetic field, $\varepsilon(\boldsymbol{r})$ is the macroscopic dielectric function equal to the square of the index of refraction, $\boldsymbol{r}$ is the position vector, ω is the angular frequency, and c is the speed of light in vacuum. The macroscopic dielectric function has a periodic spatial dependence. Equation (1) is an eigenvalue problem; it can be rewritten as:

$$\Theta \boldsymbol{H}_i = \frac{\omega_i^2}{c^2} \boldsymbol{H}_i \tag{2}$$

where

$$\Theta = \nabla \times \frac{1}{\varepsilon(\boldsymbol{r})} \nabla \times \tag{3}$$

is a periodic Hermitian differential operator and ω_i^2/c^2 is the ith eigenvalue. The solutions $\boldsymbol{H}_i$ and ω_i are determined entirely from the strength and symmetry properties of $\varepsilon(\boldsymbol{r})$. The solutions are characterized by a wave vector $\boldsymbol{k}$ and a band number i. The region of all allowed wave vectors is called a *Brillouin zone,* and the collection of all solutions is termed a *band structure.*

Equation (2) closely resembles Schrödinger's equation for the problem of an electronic wave function inside a periodic atomic potential. Since the solutions of Schrödinger's equation lead to band diagrams for allowed and forbidden electronic states in crystalline structures, and since PBG materials have similar effects on electromagnetic waves, PBG materials are often referred to as *photonic crystals.* In this chapter, the terms *PBG material* and *photonic crystal* are used interchangeably.

An interesting feature of Eq. (1) is that there is no fundamental constant with dimensions of length, hence no fundamental length scale other than the assumption that the system is macroscopic. The solution at one length scale determines the solutions at all other length scales, assuming a frequency-independent dielectric function. This simple fact is of considerable practical importance as it allows results to be scaled from one wavelength to another, from the ultraviolet to microwaves and beyond, simply by expanding all distances.

The solutions $\boldsymbol{H}_i$ and ω_i provide information about the frequency of the allowed electromagnetic modes in a PBG structure and their polarization, symmetry, and field distribution. Although Eq. (1) can be applied to any dielectric structure—the only assumptions made were the absence of external currents and sources—early work in this field focused on the search for a complete bandgap, that is, a range of frequencies with no allowed electromagnetic mode for any wave vector $\boldsymbol{k}$ inside the Brillouin zone[6]. A review of three-dimensional photonic crystals follows.

Several numerical methods have been used to solve Maxwell's equations in periodic structures, including the use of a variational approach[8] where each eigenvalue in Eq. (2) is computed separately by minimizing the functional $\langle \boldsymbol{H}_i | \Theta | \boldsymbol{H}_i \rangle$. In this method, fast Fourier transforms are used repeatedly to switch back and forth between real and reciprocal space to avoid storing large matrices.

Other methods include the transfer matrix method[9] and the finite-difference time-domain (FDTD) method,[10] to name but two. In the former, Maxwell's equations are solved at a fixed

frequency by stepping the fields forward in space, one plane at a time, satisfying the continuity conditions at every step. The transfer matrix method is well-suited for transmission and reflection computations in photonic crystals. By imposing Bloch conditions, the transfer matrix method can also be used to compute the band structure. In the case of the FDTD method, Maxwell's equations are discretized on a three-dimensional grid, and the derivatives are approximated at each grid point by a corresponding centered difference. Maxwell's equations are solved everywhere in the computational cell at every time step, allowing the temporal response of the fields to be determined inside photonic crystals.

20.4 THREE-DIMENSIONAL PHOTONIC CRYSTALS

Criteria for 3D Bandgaps

The existence of bandgaps in periodic structures is determined entirely from the symmetry and strength of the periodic dielectric function. Since photonic crystals do not occur naturally, somehow one must arrange dielectric material in a 3D periodic structure, and, as with multilayer dielectric stacks, the length of the repeating unit must be on the order of one-half the wavelength in the material. Most structures exhibiting 3D bandgaps satisfy the following three general criteria: The periodic structure has a spherelike Brillouin zone; the refractive index contrast between the different materials is typically larger than 2; and the high and low dielectric materials form connected networks.

Spherelike Brillouin Zone. Waves propagating inside a periodic structure sense a periodicity that leads to the formation of stop bands at the edges of the irreducible Brillouin zone. Since the waves sense a different periodicity along the different directions, the wave vectors at the different points on the surface of the Brillouin zone have different magnitudes. Hence, the gaps are likely to be centered at different frequencies. Spherical Brillouin zones (if they were possible) would guarantee the overlap of all the gaps along every direction, since every point on the surface of a sphere is equidistant from the center—but crystal geometries do not allow for spherical Brillouin zones.

Several hundred years of mineralogy and crystallography have led to the classification of the various three-dimensionally periodic lattice geometries. The Brillouin zone of the face-centered-cubic (fcc) lattice is closer to a sphere than any other common crystal geometry. However, despite having the most spherelike Brillouin zone, the farthest point on the surface of the fcc Brillouin zone (i.e., the point with the largest wave vector, the so-called W point) lies 29 percent farther from the origin than the closest point, the L point. For a gap to open along every direction, the gaps at W and L must be large enough to overlap.

Large Index Contrast. The size of the bandgap at each point on the surface of the Brillouin zone scales with the index contrast between the different materials. For the different gaps to overlap over the entire Brillouin zone the refractive index contrast must be large, typically 2 to 1 or greater. Semiconductor materials such as Si ($n = 3.5$ at $\lambda = 1.5$ μm) and GaAs ($n = 3.4$) in combination with air or low-index oxides are excellent candidates for the fabrication of photonic crystals at infrared wavelengths.

A large index contrast and a spherelike Brillouin zone, however, are not sufficient to guarantee the formation of a bandgap in 3D structures. It is not sufficient to specify the structure in reciprocal space—there are essentially an infinite number of structures with an fcc lattice, since anything can be put inside the fundamental repeating unit. One must also specify the dielectric structure in real space. An example of a successful 3D photonic crystal is shown in the forthcoming section labeled "Examples of 3D Crystals."

Connected Networks. To appreciate the importance of having a connected network, it is useful to consider a one-dimensionally periodic structure such as a multilayer dielectric stack. The energy density of the mode below the stop band is more strongly localized in the high-

index layers than the mode above the stop band. The more strongly the energy density of the lower mode is localized in the high-index material and the more strongly the energy density of the upper mode is localized in the low-index material, the larger the bandgap.

In 3D periodic structures, it is generally advantageous for the high-index material to be fully connected to allow the electric field of the mode in the lower band to run through the high-index material as much as possible without having to go through the low-index material. One should be able to connect any point in the high-index material to any other point without having to cross over into the low-index material. The same also holds for the low-index material. Moreover, the low-index material should occupy typically over 50 percent of the total volume. A detailed discussion of the nature of bandgaps in periodic structures is given in Refs. 5 and 11.

The three general criteria just presented should serve only as guidelines. They do not constitute necessary conditions for the creation of 3D bandgaps. For example, though the fcc lattice is the most spherelike, other lattice geometries have been shown to generate 3D bandgaps.

Examples of 3D Crystals

The earliest antecedent to photonic bandgaps is the observation by Sir Lawrence Bragg of narrow stop bands in crystals from x-ray diffraction. The refractive index contrast, however, was very small, typically less than 1.001 to 1, and produced only narrow rings on the surfaces of the Brillouin zone.

The first structure with a full 3D bandgap was discovered by K. M. Ho et al. in 1990 and consisted of a diamond lattice of air spheres (i.e., a fcc lattice with two air spheres per unit cell) inside a high-index material.[12] Since then, there has been considerable effort to develop a process for the manufacturing of diamond (or diamondlike) structures at micrometer wavelengths. One such approach consists of etching a large number of hole triplets at off-vertical angles in a slab[13,14]; another consists of building an orderly stacking of dielectric rods[15]; yet another consists of etching a series of horizontal grooves into sequentially grown layers and etching vertical holes.[16] These structures are variations of the same diamond lattice grown along either the (1, 1, 1), (0, 0, 1) or (1, 1, 0) directions, respectively.

An example of the structure grown along the (0, 0, 1) direction is shown in Fig. 1. It consists of multiple layers of polycrystalline silicon rods with a stacking sequence that repeats itself every

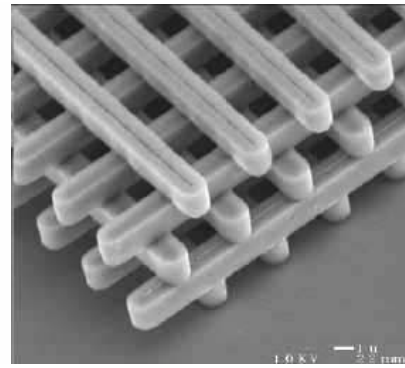

FIGURE 1 Scanning electron micrograph of a three-dimensional photonic crystal built at Sandia National Laboratories. The crystal consists of five layers of polycrystalline silicon rods. The width of the rods is 1.2 μm. The photonic bandgap is centered around a wavelength of 10 μm.

four layers. Within each layer, the rods are parallel to each other; the rods are shifted by half a period every other layer. Only five layers are shown. The structure was fabricated by S. Y. Lin et al. at Sandia National Laboratories in 1998 using a process that involves the repetitive deposition and etching of multiple dielectric films.[17] The width of each rod is roughly 1.2 micrometer. The bandgap is centered at a wavelength of 10 μm. In addition to fabricating this structure, the researchers also fabricated a structure at shorter wavelengths centered at $\lambda = 1.5$ μm.[7]

An overview of the recent progress in the fabrication of 3D PBG materials at micrometer and submicrometer length scales can be found in Ref. 7.

20.5 MICROCAVITIES IN THREE-DIMENSIONAL PHOTONIC CRYSTALS

From Fermi's golden rule, we know that the rate of spontaneous radiative decay of an atom scales with the density of allowed states at the atomic transition frequency. In free space, the density of states scales quadratically with frequency, and the probability of finding an atom in an excited state simply decays exponentially with time.

The introduction of boundaries in the vicinity of the atom has the effect of changing the density of allowed states. For example, in the case of a bounded system with reflecting walls—such as a laser cavity—the density of states is reduced to a spectrally discrete set of peaks, each corresponding to a resonant longitudinal mode of the cavity. When no mode falls within the emission linewidth of the atomic transition, atomic radiative decay is essentially suppressed. However, if the transition frequency overlaps one of the resonant frequencies, the density of available modes for radiative decay becomes very large, which in turn enhances the rate of spontaneous emission. In conventional solid-state lasers, several modes fall within the atomic emission linewidth. The free spectral range of the modes is given by $c/2nL$, where n is the refractive index of the host material and L is the distance between the reflectors. If L was made very small, it would be possible to increase the mode spacing such that only one (or even zero) mode would fall within the emission linewidth.

An example of a small laser cavity is the distributed feedback (DFB) laser consisting of a spatially corrugated waveguide with a quarter-wave phase shift. The phase shift defines a cavity, and the grating on either side acts like a mirror. The length L of the cavity is characterized by the decay length of the evanescent field along the axis of the grating and typically extends over hundreds of wavelengths in the material. The grating creates a stop band along the periodic axis. While the absence of longitudinal modes inside the stop gap reduces the total density of states, the presence of a quarter-wave phase shift generates a resonant mode inside the gap and increases the density of states. The increase is sufficiently large to allow single-mode action of the laser at the resonant frequency. Though DFB lasers have longitudinal stop bands, the total density of states is not zero, since the stop band extends only inside a small cone along one direction. Leaky radiation modes exist along every other direction.

3D PBG materials have the ability to open 3D stop bands that reflect light along every direction in space and that completely eliminate the density of states for a given range of frequencies. In the case where the radiative transition frequency of an atom falls within the frequency gap of the crystal, spontaneous radiative decay is essentially suppressed.

If a small defect (or phase shift) is introduced in the photonic crystal, a mode can be created within the structure at a frequency that lies inside the gap. If the size of the defect is such that it supports a mode, the defect behaves like a microcavity surrounded by reflecting walls. If the radiative transition frequency of the atom matches that of the defect mode, the rate of spontaneous emission can be enhanced.

Figure 2 shows the vector plot of a resonant mode in a 3D photonic crystal similar to the one shown in Fig. 1. The defect is located at the center of the crystal and consists of a broken high-index rib. (The defect could be introduced, for instance, in one of the layers during the growth of the crystal.) The electric field is shown in the vertical plane through the middle of the defect. The mode is strongly localized in all three dimensions, and its amplitude falls off

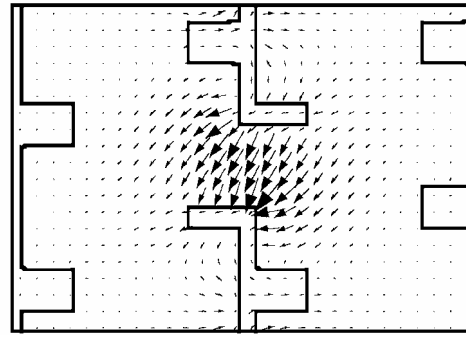

FIGURE 2 Vector plot of the electric field in a 3D PBG with a defect. The overlay indicates the edges of the high-dielectric material. The defect, located at the center of the figure, is fabricated by breaking one of the dielectric ribs. The defect supports a localized resonant mode inside the crystal.

sharply away from the defect. The electric field *jumps* from one edge of the broken rib to the other, while the magnetic field (not shown) has the shape of a torus and runs around the electric field. The frequency of the mode is $f = 0.59c/a$ where a is the lattice constant (i.e., the length of the repeating unit cell) of the crystal. In this particular example, the high-index material has a refractive index of 3.4; the low-dielectric material has an index of 1.0; and the gap extends from $f = 0.52c/a$ to $0.66c/a$.

In contrast to defects in one-dimensional periodic structures (such as DFB lasers), arbitrarily small defects in 3D crystals do not necessarily lead to the creation of localized modes. The volume of the defect must reach a certain threshold to sustain a resonant mode. Furthermore, quarter-wave shifts in DFB lasers lead to resonant modes at the center of the gap. There is no simple equivalent in 3D crystals.

The frequency of the resonant mode changes with the size and shape of the defect. The simple action of adjusting the defect size provides tunability of the resonant mode and affects the localization strength. The field attenuation through successive unit cells is stronger for modes lying near the center of the gap than for those lying near the edges.

Although the microcavity in the just-noted example was created by removing part of a high-index rib, a cavity could equally have been created either by adding material between ribs or by changing the shape of one or more ribs. Also, multiple high-order localized modes may appear inside the crystal as the size of the defect is made bigger.

Quality Factor

One important aspect of microcavities in finite-sized crystals is the quality factor Q of the resonator defined as[18]:

$$Q = \frac{2\pi f_0 E}{P} = -\frac{2\pi f_0 E}{dE/dt} \tag{4}$$

where f_0 is the resonant frequency, E is the energy stored inside the resonator, and $P = -dE/dt$ is the dissipated power. Hence, a resonator can sustain Q oscillations before its energy decays by a factor of $e^{-2\pi}$ (i.e., a reduction of 99.8 percent) of its initial value. In the specific case where the lineshape of the resonance is a Lorentzian, Eq. (4) reduces to $f_0/\Delta f$ where Δf is the width of the resonance.

Since the quality factor is a measure of the optical energy stored in the microcavity over the cycle-average power radiated out of the cavity, Q is expected to be largest for modes lying near the center of the gap where the field attenuation is strongest. Q is also expected to increase with the size of the crystal, since the reflectivity increases with the number of periods (i.e., the leakage from the edges of the crystal becomes progressively smaller). The quality factor of the mode shown in Fig. 2 is plotted in Fig. 3 as a function of the size of the crystal. The quality factor is computed using the finite-difference time-domain method described in Section 20.3. First the resonant mode is excited and the total energy is monitored as a function of time. Then the time required for 99.8 percent of the energy to escape is recorded. Results are shown for crystal sizes of dimension $2N \times 2N \times 2N$. In each case, the defect is surrounded by N unit cells along every direction. Q increases exponentially with the size of the crystal and reaches a value close to 10^4 with as little as four unit cells on either side of the defect. The steepness of the slope in Fig. 3 follows directly from the field attenuation through each successive lattice of the crystal. Since the only energy loss in the structure occurs from tunneling through the walls of the finite-sized crystal (i.e., intrinsic losses due to material absorption is not considered), Q does not saturate even for a large number of unit cells. A more detailed description of the properties of resonant modes in photonic crystals can be found in Ref. 19.

Enhancement of Spontaneous Emission

By coupling an optical transition to the microcavity resonance, the spontaneous emission rate can be enhanced by a factor η over the rate without a cavity. The expression for η is given by[20]:

$$\eta = \frac{2Q}{\pi V_m}\left(\frac{\lambda}{2n}\right)^3 \tag{5}$$

where V_m is the modal volume, n is the refractive index of the medium, and λ is the free-space wavelength of the optical transition. Photonic crystals have the ability to enhance the rate of spontaneous emission by enabling microcavities with large quality factors and small modal volumes. In the case where the modal volume is on the order of a cubic half-wavelength in the material [i.e., $V_m \sim (\lambda/2n)^3$], the enhancement factor is on the order of Q. A detailed example is provided in the following section.

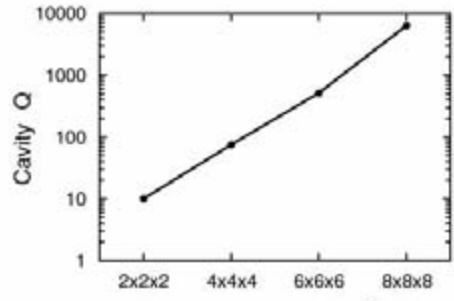

FIGURE 3 Quality factor of the resonant cavity shown in Fig. 2 as a function of the size of the 3D photonic crystal, given in units of cubic lattice constants.

20.6 MICROCAVITIES IN PHOTONIC CRYSTALS WITH TWO-DIMENSIONAL PERIODICITY

Three-dimensional field confinement can be achieved in dielectric structures, in part by the effect of a photonic bandgap, and in part by index confinement. An example was given in Section 20.5 for the case of a DFB laser (i.e., a structure with a one-dimensional periodicity). One important aspect of structures with dimensional periodicity lower than three is the coupling to radiation modes. By reducing the dimensionality of the periodicity and by resorting to standard index guiding to confine light along the nonperiodic direction(s), one no longer has the ability to contain light completely, and leaves open possible decay pathways through which light can escape.

In this section, we consider a dielectric slab waveguide with a two-dimensional periodic lattice. The periodic lattice is used to confine light in the plane of the waveguide (the xy-plane, say), and the slab keeps the light from escaping along the transverse direction (the z-direction). It is useful to begin with a uniform waveguide, and consider the effect of adding a periodic array of holes. The slab is chosen to have a large refractive index ($n = 3.4$) and, for simplicity, is assumed to lie in air. The thickness of the slab is set equal to $0.5a$ where a is a scaling parameter as defined in the text that follows. The use of a high-index waveguide is twofold: first, the high index provides strong field confinement along the z-direction (i.e., the extent of the guided modes outside the waveguide is small), allowing a large fraction of each mode to interact with the photonic crystal; and second, the high-index contrast between the dielectric material and the holes will increase the likelihood of having a bandgap in the xy-plane.

The waveguide is shown in Fig. 4(a). Its corresponding dispersion relation is shown in Fig. 4(b). The solid lines correspond to guided modes, and the shaded region corresponds to the continuum of radiation (i.e., nonguided) modes. The guided modes are labeled TE and TM with respect to the xy-plane of symmetry in the middle of the waveguide. TE (TM) modes are characterized by the absence of electric field components in the z (x and y) direction at the center of the waveguide.

The dispersion relation shown in Fig. 4(b) extends to the right of the figure; there is no upper bound on the wave vector. The introduction of a periodic array of holes in the waveguide has the effect of limiting the wave vector, folding the dispersion relation into the first Brillouin zone, and splitting the guided-mode bands. Figure 4(c) shows a waveguide with a triangular array of holes. The holes have a radius of $0.30a$, where a is the lattice constant of the array. The associated dispersion relation is shown in Fig. 4(d). Again, the shaded region above the light line corresponds to the continuum of radiation modes. The solid lines below the light line correspond to guided modes. These modes remain perfectly guided in spite of the holes and propagate in the waveguide with no loss. A bandgap can be seen between the first and second TE bands. An experimental observation of bandgaps in this type of structure is described in Ref. 21.

The introduction of holes in the waveguide also creates a frequency cutoff for guided modes. Every mode above the frequency $0.66c/a$ is folded into the radiation continuum, and is Bragg-scattered out of the slab. The cutoff frequency is independent of the refractive index of the slab or the size of the holes, and depends only on the lattice geometry of the array of holes.

If a defect is introduced in the PBG structure shown in Fig. 4(c), localized modes can be formed in the vicinity of the defect. Since each localized mode has a specific polarization, it is possible to create a TE mode between the first and second TE bands, orthogonal to TM modes. If, for example, light were to originate from a quantum well located at the middle of the waveguide, atomic transitions could be made to couple only to TE modes.

Two competing decay mechanisms contribute to the overall decay rate of the localized mode; horizontal in-plane coupling to guided modes at the edges of the crystal in the unperturbed (i.e., holeless) waveguide, and vertical coupling to radiation modes. For some applications (such as photonic integrated circuits) it may be preferable for the localized mode to decay primarily into guided modes, while for other applications (such as off-chip emission) it

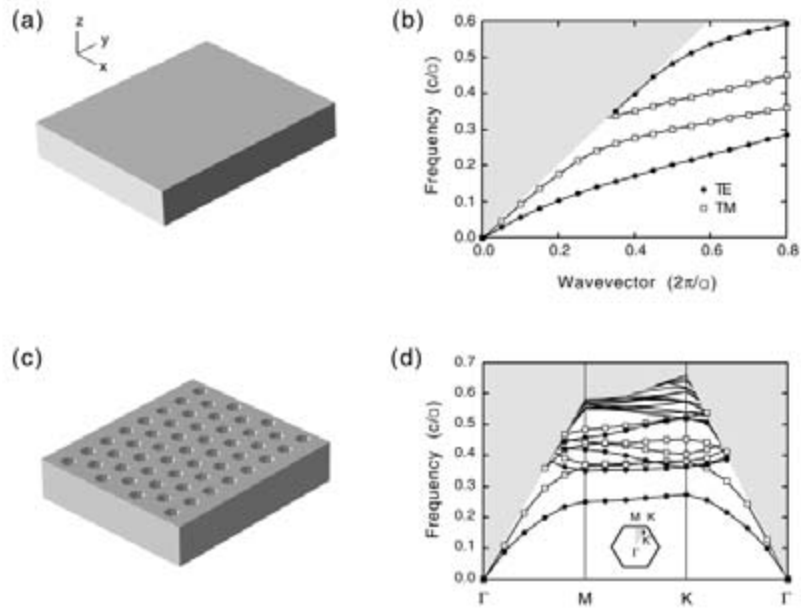

FIGURE 4 (*a*) Schematic diagram of a dielectric slab waveguide of thickness 0.5*a* and refractive index 3.4. (*b*) Band diagram of the slab waveguide shown in (*a*). The solid lines correspond to guided modes; the shaded region corresponds to the continuum of radiation modes. The guided modes are labeled TE or TM with respect to the *xy*-plane of symmetry in the middle of the slab. (*c*) Schematic diagram of a slab waveguide with a two-dimensional triangular array of holes with radius 0.3*a,* where *a* is the lattice constant of the periodic array. The parameters of the slab are identical to those in (*a*). (*d*) Band diagram for the slab waveguide shown in (*c*). Only the lowest nine bands are labeled TE and TM. Guided modes do not exist above the cut-off frequency of 0.66*c/a.* The inset shows the Brillouin zone and symmetry points for a triangular lattice, with the irreducible zone shaded.

may be preferable for the mode to decay primarily into the radiation continuum. These two cases are considered separately in the following text.

The total quality factor of the resonant mode, Q_{tot}, is given by[22]:

$$\frac{1}{Q_{\text{tot}}} = \frac{1}{Q_{\text{wg}}} + \frac{1}{Q_{\text{rad}}} \tag{6}$$

where $1/Q_{\text{wg}}$ is a measure of the coupling to waveguide modes and $1/Q_{\text{rad}}$ is a measure of the coupling to radiation modes. The strength of the two competing coupling mechanisms depends on the size of the crystal (i.e., the total number of holes around the defect), the modal volume, and the choice of substrate.

In-Plane Coupling

We present the case of an array of 45 holes with a missing hole at the center (i.e., one hole is filled). The structure supports a localized mode inside the TE bandgap. The total quality factor of the mode is computed using the finite-difference time-domain method described in Section 20.3 and is found to be 240. The modal volume, V_{m}, is defined as[23]:

$$V_m = \frac{\int \varepsilon(\boldsymbol{r})|\boldsymbol{E}(\boldsymbol{r})|^2 \, d^3\boldsymbol{r}}{(\varepsilon(\boldsymbol{r})|\boldsymbol{E}(\boldsymbol{r})|^2)_{\max}} \tag{7}$$

where $\boldsymbol{E}(\boldsymbol{r})$ is the electric field distribution of the mode. The computed modal volume is only three cubic half-wavelengths in the material. The spontaneous emission rate enhancement factor, computed from Eq. (5), is equal to 50.

Since the structure does not have a complete three-dimensional bandgap, Q_{tot} cannot be made arbitrarily large. While the addition of extra holes would reduce the coupling to the guided modes outside the crystal, light could not be prevented from coupling to radiation modes. Any significant increase in the number of holes would cause the mode to primarily radiate outside of the waveguide. Moreover, coupling to radiation modes would be enhanced if the waveguide was positioned on a substrate. The substrate would provide a favorable pathway for radiation loss. It has been shown, however, that the adverse effects of a substrate could be minimized with the use of a low-index insulating layer between the waveguide and the substrate.[24,25]

The coupling to radiation modes is also enhanced by reducing the modal volume. The more tightly a mode is confined, the more likely it is to radiate out of the waveguide. Conversely, if the modal volume is made larger, the coupling to radiation modes can be reduced, and, provided the coupling to guided modes remains largely unchanged, Q_{tot} can be increased. To increase the modal volume, one could create a different type of defect in the structure. If, instead of removing a single hole from the two-dimensional array, the radius of seven nearest-neighbor holes was reduced from $0.3a$ to $0.2a$ while otherwise leaving the structure unchanged, the localized mode would become more extended—the modal volume would increase by 20 percent to $3.6(\lambda/2n)^3$—and Q_{tot} would increase by more than one order of magnitude to 2500. The frequency of the new localized mode would remain unchanged, and the enhancement factor would exceed 400.

Out-of-Plane Coupling

While it may be possible to fabricate high-Q cavities that couple predominantly to guided modes, some applications (such as light-emitting diodes) may require a large fraction of the emitted light to be extracted from the high-index guiding layer. As mentioned previously, the emitted radiation can be made to decay primarily into radiation modes by increasing the total number of holes surrounding the defect. In this case, Q_{wg} would essentially be infinite, and $Q_{\text{tot}} \sim Q_{\text{rad}}$. For simplicity, in this example, we write $Q_{\text{tot}} = Q_{\text{rad}} = Q$.

Light-emitting diodes (LEDs) are widely used as incoherent light sources in applications such as lighting and short-distance fiber communications. Two important performance characteristics of LEDs are the output efficiency (i.e., the amount of light extracted from the structure for a given injection current) and the modulation rate (i.e., the information emission capacity).

Photonic crystals with two-dimensional periodicity can lead to the enhancement of the rate of spontaneous emission and consequently to higher modulation rates. However, photon reabsorption and nonradiative recombination can affect the performance of LEDs by reducing the extraction efficiency and the modulation rate. High-Q cavities, though seemingly favorable for the enhancement of the rate of spontaneous emission, may cause severe reabsorption in certain material systems, since the likelihood of observing photon reabsorption increases with the photon lifetime inside the cavity.

Display Applications. For display applications, it is usually desired to get as much light as possible out of the high-index material over the entire spontaneous emission bandwidth for a constant applied current. If all emitted frequencies fall inside the guided-mode bandgap, all available optical modes can contribute to the output signal. In the ideal case where there are

no nonradiative recombination processes, the extraction efficiency is unity; every photon escapes from the high-index waveguide. Even photons reabsorbed by the atomic system, if given enough time, eventually get reemitted and contribute to the output signal. However, when nonradiative processes are present, reabsorbed photons can be lost. In order to achieve high output efficiency, the effective spontaneous emission rate—the spontaneous emission rate reduced by photon reabsorption—has to dominate over the nonradiative recombination rate. The relative rate of the radiative and nonradiative processes can be controlled by modifying the quality factor of the cavity.

Two limit cases are identified: the case where photon reabsorption is negligible, and the case where it is important. The former arises in certain organic emitters, where the energy levels of the molecules are such that absorption and spontaneous emission are spectrally separated. The latter arises in most semiconductor systems, where both absorption and emission processes occur between the conduction and valence bands.

In the case of low reabsorption, if the cavity linewidth is larger than the emission linewidth, an increase of the cavity Q can result in an increase of the effective spontaneous emission rate and of the output efficiency. However, a reduction of the cavity linewidth beyond the material emission linewidth does not further enhance the spontaneous emission rate or output efficiency. In the case of large reabsorption, the rate of spontaneous emission and the output efficiency reach a maximum when the cavity linewidth is comparable to the material linewidth, but fall to zero when the cavity linewidth becomes much smaller than the material linewidth. A more detailed description of these conditions can be found in Ref. 26.

Communications Applications. For communications applications, it is advantageous to reduce the emission linewidth below the material emission linewidth to improve the temporal coherence of the emitted light. It is also advantageous to increase the modulation speed to improve the information emission capacity. If a time-varying current is applied to the LED, the response time of the electron-photon system will be determined by the slowest of the different relaxation processes.

While electronic recombination lifetimes are typically on the order of a few nanoseconds in both semiconductors and organic dyes, the photon lifetime in a cavity depends on the cavity Q and, in the case where, say, Q = 1000, is on the order of several picoseconds. Since the modulation speed is limited by the slower of the two processes, the electronic recombination rate, which is a sum of the effective spontaneous emission rate and the nonradiative recombination rate, constitutes the limiting factor. To achieve high modulation speeds, it is therefore necessary to increase the spontaneous emission rate.

In the case where photon reabsorption is small, such as in organic dyes, the rate of spontaneous emission and the modulation speed increase with the cavity Q. Conversely, when photon reabsorption is large, such as in semiconductors, the maximum rate of spontaneous emission and the maximum modulation rate are achieved when the cavity linewidth is comparable to the material linewidth. These conclusions are similar to those found for display applications.

Examples of Low-Q and High-Q Cavities. Low-Q cavities can be fabricated in high-index dielectric waveguides by introducing an array of holes with no defects. The absence of defects ensures that photons inside the waveguide—emitted from a quantum well, say—spend as little time as possible inside the waveguide and minimize the risk of being reabsorbed. The cavity is defined by the waveguide itself, which provides vertical field confinement. To avoid removing active material, the holes can be made to extend only partly into the guiding layer so as to not penetrate into the quantum well. Bandgaps for guided modes can be generated even when the holes do not extend through the entire thickness of the waveguide. The waveguide can also be positioned on a dielectric or metallic mirror to ensure that the output radiation escapes through the top surface.

High-Q cavities can be fabricated in structures similar to those used for low-Q cavities except that, in the case of high-Q cavities, defects are introduced in the periodic array. The

introduction of defects creates highly confined modes in the area of the defects, hence only a small fraction of the quantum well overlaps with the resonant modes (i.e., only a fraction of the electron-hole pairs contributes to the emitted signal). To eliminate this problem, high-Q cavities could be generated by placing the dielectric layer between two vertical Bragg mirrors—in analogy to resonant-cavity LEDs—and by getting rid of the defects. The entire active region would then overlap with the resonant cavity mode.

Experimental results of quantum-well emitters and dyes in photonic crystals with two-dimensional periodicity can be found in Refs. 27 through 31. A detailed analysis of the output efficiency and modulation rate of LEDs can be found in Refs. 26 and 32.

20.7 WAVEGUIDES

While three-dimensional field confinement can be achieved by introducing local-point defects in photonic crystals, two-dimensional field confinement can be achieved by introducing extended line defects. Both point defects and line defects can generate localized modes with frequencies that lie inside the bandgap. However, unlike point defects, line defects can generate modes that propagate along the lines with nonzero group velocity. Line defects can be made, for example, by *carving* channels in photonic crystals or by creating line dislocations. Electromagnetic waves propagating along the lines are guided not from total internal reflection but from the bandgap effect; they are prevented from leaking into the crystal since their frequencies lie inside the bandgap.

The absence of radiation modes in three-dimensional photonic crystals suggests that it may also be possible to create waveguides with very sharp bends. Since electromagnetic waves are prevented from propagating inside photonic crystals, the waves would only either propagate through the bend or be reflected back. It will be shown in the subsection labeled "Waveguide Bends" that, for certain frequencies, reflection may be eliminated altogether, leading to complete transmission. In three-dimensional crystals, waveguide bends could extend along any direction and could be used for the implementation of interconnected integrated optical circuits on multiple planes. In this chapter, however, we focus only on line defects in photonic crystals with two-dimensional periodicity.

Waveguides in Photonic Crystals with Two-Dimensional Periodicity

As we saw in Section 20.6, photonic crystals with two-dimensional periodicity rely on the existence of bandgaps to control propagation in the plane and on index guiding to confine electromagnetic fields along the third dimension. An example of a photonic crystal with two-dimensional periodicity was shown in Fig. 4(c); its corresponding dispersion relation was shown in Fig. 4(d). In the bandgap, no *guided* mode existed for TE polarization.

In this section, a line defect is introduced in the photonic crystal shown in Fig. 4(c) by increasing the radius of a line of nearest-neighbor holes along the Γ-K direction from $0.30a$ to $0.45a$. The resulting dispersion relation is shown in Fig. 5. The dispersion relation is computed using the plane-wave expansion method described in Section 20.3. The wave vector along the line defect is plotted on the abscissa.

In this structure, it is necessary to distinguish between the modes which are guided inside the dielectric slab [the so-called bulk crystal modes that correspond to the different bands in Fig. 4(d)] and the modes which are guided along the line defect. The dispersion relation is obtained from Fig. 4(d) by projecting the wave vector of every mode along the Γ-K direction; the dark gray regions correspond to the continuum of bulk crystal modes and the light gray region corresponds to the continuum of radiation modes. The bulk crystal modes and radiation modes are depicted with a uniform shading despite the nonuniform density of states in these regions. Since the structure retains an inherent periodicity along the line defect, the

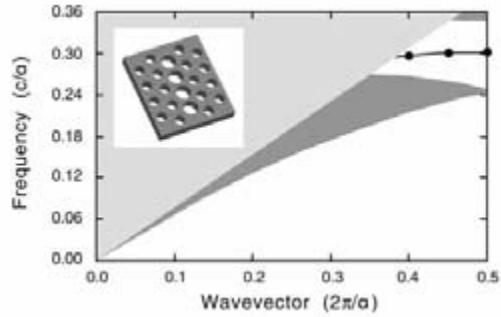

FIGURE 5 Projected dispersion relation of the TE modes in the waveguide structure shown in the inset. The dispersion relation is projected along the axis of the waveguide (i.e., along the line defined by the series of larger holes). The light gray region corresponds to the continuum of radiation modes, and the dark gray regions correspond to modes inside the bulk PBG dielectric slab. The thickness of the slab is 0.5*a,* the refractive index is 3.4, the radius of the small holes is 0.3*a,* and the radius of the large holes is 0.45*a.* The figure is to be compared with Fig. 4(*d*) along the Γ-K direction.

wave vector has an upper limit. However, although the line defect extends along the Γ-K direction, K is not the point at the edge of the dispersion relation. The boundary is located at the projected M point along the Γ-K direction, labeled K′ as shown in the inset of Fig. 4(*d*).

Only modes lying outside the shaded regions are truly guided along the line defect. A single guided mode appears inside the bandgap. Since the line defect consists of a series of larger holes, the effective index of the waveguide is lower than that of the surrounding photonic crystal. Hence, the mode is not index-guided in the plane; it is constrained horizontally by the bandgap. The effective index, however, is higher in the waveguide than in the regions above and below the slab, allowing the mode to be guided vertically by index confinement. The electric field of the guided mode is mostly concentrated in the dielectric material. The fraction of electric-field energy inside the high-dielectric material at K′, for example, is close to 75 percent.

Alternatively, a line defect could have been created by reducing the radius of a series of holes, or by creating lattice dislocations. Also, instead of using a high-index slab with holes, one could have used an array of high-index posts. High-index posts can generate dispersion relations similar to the one shown in Fig. 4(*c*) except that the open (solid) circles would now correspond to TE (TM) polarization. A more detailed analysis of these and other structures can be found in Refs. 33 and 34.

Waveguide Bends

If a sharp bend is introduced in a PBG waveguide—with a radius of curvature on the order of a few lattice constants—it may be possible to obtain high transmission through the bend for a wide range of frequencies. To obtain high transmission, the waveguide must support a single mode at the frequency of interest, and the radiation losses must be small, since coupling to high-order guided modes and to radiation modes reduces the transmission and increases the reflection.

While it may be possible to obtain 100 percent transmission in photonic crystals with two-dimensional periodicity, we choose to consider waveguide bends in purely two-dimensional

crystals. Two-dimensional crystals can be viewed either as flat structures in a two-dimensional Cartesian space or as structures of infinite thickness with no field variation along the vertical direction. Since there is no index confinement along the vertical direction, there are no radiation modes and no light cone. The bandgap in a 2D structure is analogous to a three-dimensional bandgap in that there are truly no modes inside the bandgap.

For simplicity, we consider a 2D photonic crystal of dielectric columns on a square lattice, surrounded by air. The refractive index of the rods is chosen to be 3.4 and the radius 0.20*a,* where *a* is the lattice constant of the array. A large bandgap appears in this structure for TM polarization (electric field parallel to the axis of the columns). A line defect is created inside the crystal by removing a row of rods. The line defect introduces a single guided TM mode inside the gap, similar to the one shown in Fig. 5. The main difference between the dispersion relation for this 2D crystal and the one shown in Fig. 5 is the absence of radiation modes in the 2D crystal. The bandgap extends over the entire range of wave vectors. If a bend is introduced in the waveguide, light will either travel through the bend or be reflected back, since there are no radiation modes to which light can couple. Only back reflection can hinder perfect transmission.

The transmission and reflection can be studied using the finite-difference time-domain method described in Section 20.3. In this method, a dipole located at the entrance of the waveguide creates a pulse with a Gaussian envelope in time. The field amplitude is monitored inside the waveguide at two points, one before the bend and one after the bend. The pulses are then Fourier-transformed to obtain the reflection and transmission coefficients for each frequency. A detailed description of this method and computational results are presented in Ref. 35.

The electric field pattern of a mode propagating through the bend is shown in Fig. 6. The mode is strongly guided inside the photonic crystal. One hundred percent of the light travels through the bend despite a radius of curvature on the order of one wavelength.

The transmission through the bend can be modeled as a simple one-dimensional scattering process. The bend can be broken down into three separate waveguide sections: the input

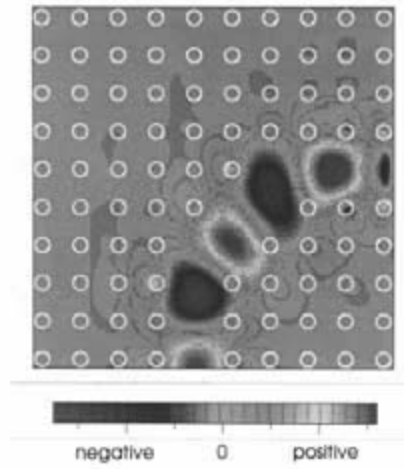

FIGURE 6 Electric field pattern of a guided mode in a photonic crystal in the vicinity of a bend. The white circles indicate the position of the high dielectric columns. The electric field is polarized along the axis of the columns. The mode is strongly confined inside the guide and is completely transmitted through the bend. The radius of curvature of the bend is on the order of the wavelength of the guided mode.

waveguide in the (01) direction; the output waveguide in the (10) direction; and a short waveguide section in the (11) direction, connecting the input and output waveguides. Each section supports a single guided mode with wavevector $\boldsymbol{k}_1(f)$ for propagation along the (01) or (10) direction, and $\boldsymbol{k}_2(f)$ for propagation along (11). These wave vectors are given by dispersion relations similar to the one shown in Fig. 5. The mode propagating along the (01) direction is scattered into the mode propagating along (11), then into the mode propagating along (10). At the interfaces, the fields and their derivatives must be continuous. By complete analogy with the one-dimensional Schrödinger equation for a square potential well, the transmission through the sharp bend can be mapped onto that of a wave propagating in a square *dielectric potential.* This potential consists of three constant pieces corresponding to the (01), (11), and (10) directions, respectively. The model differs from the standard one-dimensional scattering problem in that the depth of the well, determined by the difference $|\boldsymbol{k}_1(f)|^2 - |\boldsymbol{k}_2(f)|^2$, now depends on the frequency of the traveling wave. The scattering model correctly predicts the general quantitative features of the transmission spectrum obtained from the FDTD method, as well as the frequencies where the reflection coefficient vanishes.[35]

The results have been experimentally confirmed using a structure consisting of a square array of tall circular rods.[36] The rods were made of alumina with a refractive index of 3.0 and a radius of 0.25 mm. The lattice constant was chosen to be 1.27mm and the rods were close to 10 cm in length. The large aspect ratio between the length and the lattice constant provided a good approximation of a two-dimensional system. Because of the absence of vertical confinement, the waveguides were made to extend over less than 100 lattice constants to minimize loss in the vertical direction. The bandgap extended from 76 GHz to 105 GHz. The experiment was carried out at millimeter-wave frequencies to facilitate the fabrication of structures with a large aspect ratio.

To test the PBG structure, millimeter-wave transmitters and receivers were placed next to the entrance and exit of the PBG waveguide. This coupling scheme closely resembled the setup used in the computational simulations. The transmitted signal is shown in Fig. 7. The signal is normalized to the transmitted signal of a straight waveguide. The PBG bend exhibits near-perfect transmission around 87 GHz and 101 GHz. The two arrows indicate the expected positions of the reflection nodes computed from the one-dimensional scattering model. The positions of the nodes confirm a subtle and important point about PBG wave-

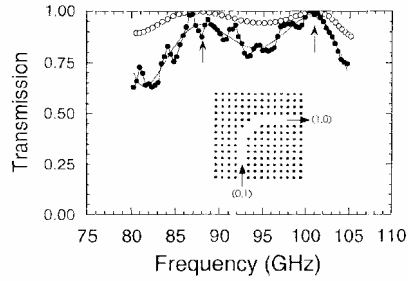

FIGURE 7 Normalized transmission spectrum for the PBG structure shown in the inset. The solid circles correspond to experimental data; the open circles are computed from the one-dimensional scattering model. Near-perfect transmission is observed through the bend near 87 GHz and 101 GHz. The arrows indicate the positions of the reflection nodes from theory. The experimental data is fitted with a polynomial curve.

guides: The detection of light at the end of a straight waveguide would not be a sufficient condition, in itself, to confirm PBG guiding. It is the existence of transmission peaks around the sharp bend, along with the specific position of these peaks, that confirms PBG guiding.

Waveguide Intersections

In addition to sharp bends, photonic crystals can be used to fabricate waveguide intersections with low crosstalk. If two waveguides intersect each other on the same plane, light traveling along one waveguide typically leaks into the second waveguide, causing signal loss and crosstalk. The insertion of a microcavity at the center of the intersection of two PBG waveguides can reduce the crosstalk and increase the throughput. If the resonant mode inside the cavity is such that it can couple only to one waveguide, the crosstalk can be essentially eliminated. In this case, the problem reduces to the well-known phenomenon of resonant tunneling through a cavity.

Figure 8(*a*) shows two intersecting waveguides in a two-dimensional photonic crystal identical to the one shown in Fig. 7. At the center of the intersection, a microcavity is created by adding rods inside the waveguides and by increasing the radius of one rod by 60 percent. The cavity is outlined by a dashed box. The cavity supports two degenerate modes with opposite symmetry at a frequency lying inside the bandgap. From symmetry, each resonant mode can couple to only one waveguide, as shown schematically in Fig. 8(*b*). Therefore, under the approximation that the waveguides couple to one another only through the resonant cavity, crosstalk is prohibited. The throughput in each waveguide is described by resonant tunneling; the throughput spectrum is a Lorentzian function with 100 percent transmission at resonance. The width of the resonance is given by the inverse of the quality factor of the microcavity.

In general, large throughput and low crosstalk can be achieved if each waveguide has a single guided mode in the frequency range of interest, and if the microcavity supports two resonant modes, each mode having even symmetry with respect to the mirror plane along one waveguide and odd symmetry with respect to the other mirror plane. The presence of radiation loss would reduce the throughput and increase the crosstalk. A detailed description of PBG waveguide intersections can be found in Ref. 37.

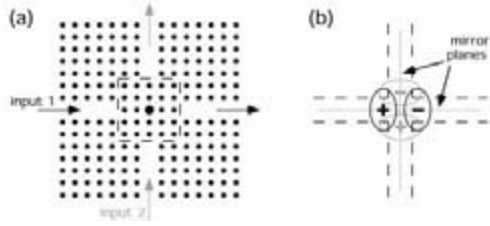

FIGURE 8 (*a*) Diagram of two intersecting waveguides inside a photonic crystal. The two waveguides are aligned along the (10) and (01) directions. A microcavity—outlined by the dashed line—is created at the center of the intersection by adding columns inside the waveguides and by increasing the size of the dielectric column at the center. The microcavity supports two degenerate modes with opposite symmetry. The mode contours are shown schematically in (*b*). By symmetry, the modes corresponding to the black contour lines cannot couple to even modes in the waveguide along the (01) direction, and the modes corresponding to the gray contour lines cannot couple to even modes in the waveguide along the (10) direction.

20.8 CONCLUSION

The routing and interconnection of optical signals through narrow channels and around sharp bends are important for large-scale all-optical circuit applications. In addition to sharp bends and low-crosstalk intersections, photonic bandgap materials can also be used for narrowband filters, add/drop filters, light emitters, low-threshold lasers, and modulators. PBG materials may enable the high-density integration of optical components on a single chip.

While this chapter focuses mostly on applications for high-density optical circuits, many other applications have been proposed for PBG materials. One such application is the PBG fiber.[38] While photonic crystals can guide light along a periodic plane (as shown in Section 20.7), they can also guide light along the direction perpendicular to the plane of periodicity. A PBG fiber is a two-dimensional periodic structure that essentially extends to infinity along the nonperiodic direction. Light is confined inside the fiber by a defect located at the center. PBG fibers may have interesting features such as single-mode operation over a large bandwidth and preferred dispersion compensation properties. Other applications can be found in Ref. 39.

20.9 REFERENCES

1. Alan Michette, "Zone and Phase Plates, Bragg-Fresnel Optics," in *Handbook of Optics,* vol. III, McGraw-Hill, New York, 2000.
2. J. A. Dobrowolski, "Optical Properties of Films and Coatings," in *Handbook of Optics,* vol. I, McGraw-Hill, New York, 1978.
3. T. L. Koch, F. J. Leonberger, and P. G. Suchoski, "Integrated Optics," in *Handbook of Optics,* vol. II, McGraw-Hill, New York, 1995.
4. J. N. Winn, Y. Fink, S. Fan, and J. D. Joannopoulos, "Omnidirectional Reflection from a One-Dimensional Photonic Crystal," *Opt. Lett.* **23**:1573–1575 (1998).
5. J. D. Joannopoulos, R. D. Meade, and J. N. Winn, *Photonic Crystals,* Princeton Press, Princeton, New Jersey, 1995.
6. E. Yablonovitch, "Photonic Band-Gap Structures," *J. Opt. Soc. Am. B* **10**:283–295 (1993).
7. B. Goss Levi, "Visible Progress Made in Three-Dimensional Photonic 'Crystals'," *Phys. Today,* January, 17–19 (1999).
8. R. D. Meade, A. M. Rappe, K. D. Brommer, and J. D. Joannopoulos, "Accurate Theoretical Analysis of Photonic Band-Gap Materials," *Phys. Rev. B* **48**:8434–8437 (1993). Erratum: S. G. Johnson, *Phys. Rev. B* **55**:15942 (1997).
9. J. B. Pendry, "Photonic Band Structures," *J. Mod. Optics* **41**:209–229 (1994).
10. K. S. Kunz and R. J. Luebbers, *The Finite-Difference Time-Domain Method for Electronics,* CRC Press, Boca Raton, Florida, 1993.
11. R. D. Meade, K. D. Brommer, A. M. Rappe, and J. D. Joannopoulos, "Nature of the Photonic Band Gap: Some Insights from a Field Analysis," *J. Opt. Soc. Am. B* **10**:328–332 (1993).
12. K. M. Ho, C. T. Chan, and C. M. Soukoulis, "Existence of a Photonic Gap in Periodic Dielectric Structures," *Phys. Rev. Lett.* **65**:3152–3155 (1990).
13. E. Yablonovitch, T. J. Gmitter, and K. M. Leung, "Photonic Band Structure: The Face-Centered-Cubic Case Employing Nonspherical Atoms," *Phys. Rev. Lett.* **67**:2295–2298 (1991).
14. C. C. Cheng and A. Scherer, "Fabrication of Photonic Band-Gap Crystals," *J. Vac. Sci. Technol. B* **13**:2696–2700 (1995).
15. E. Ozbay, A. Abeyta, G. Tuttle, M. Tringides, R. Biswas, C. T. Chan, C. M. Soukoulis, and K. M. Ho, "Measurement of a Three-Dimensional Photonic Band Gap in a Crystal Structure Made of Dielectric Rods," *Phys. Rev. B* **50**:1945–1948 (1994).
16. S. Fan, P. R. Villeneuve, R. D. Meade, and J. D. Joannopoulos, "Design of Three-Dimensional Photonic Crystals at Submicron Lengthscales," *Appl. Phys. Lett.* **65**:1466–1468 (1994).

17. S. Y. Lin, J. G. Fleming, D. L. Hetherington, B. K. Smith, R. Biswas, K. M. Ho, M. M. Sigalas, W. Zubrzycki, S. R. Kurtz, and J. Bur, "A Three-Dimensional Photonic Crystal Operating at Infrared Wavelengths," *Nature* **394**:251–253 (1998).
18. A. Yariv, *Optical Electronics,* Saunders, Philadelphia, Pennsylvania, 1991.
19. P. R. Villeneuve, S. Fan, and J. D. Joannopoulos, "Microcavities in Photonic Crystals: Mode Symmetry, Tunability, and Coupling Efficiency," *Phys. Rev. B* **54**:7837–7842 (1996).
20. H. Yokoyama and S. D. Brorson, "Rate Equation Analysis of Microcavity Lasers," *J. Appl. Phys.* **66**:4801–4805 (1989).
21. T. F. Krauss, R. M. De La Rue, and S. Band, "Two-Dimensional Photonic Bandgap Structures Operating at Near-Infrared Wavelengths," *Nature* **383**:699–702 (1996).
22. H. A. Haus, *Waves and Fields in Optoelectronics,* Prentice Hall, Englewood Cliffs, New Jersey, 1984.
23. R. Coccioli, M. Boroditsky, K. W. Kim, Y. Rahmat-Samii, and E. Yablonovitch, "Smallest Possible Electromagnetic Mode Volume in a Dielectric Cavity," *IEE Proc.-Optoelectron.* **145**:391–397 (1998).
24. P. R. Villeneuve, S. Fan, S. G. Johnson, and J. D. Joannopoulos, "Three-Dimensional Photon Confinement in Photonic Crystals of Low-Dimensional Periodicity," *IEE Proc.-Optoelectron.* **145**:384–390 (1998).
25. J. S. Foresi, P. R. Villeneuve, J. Ferrera, E. R. Thoen, G. Steinmeyer, S. Fan, J. D. Joannopoulos, L. C. Kimerling, Henry I. Smith, and E. P. Ippen, "Photonic-Bandgap Microcavities in Optical Waveguides," *Nature* **390**:143–145 (1997).
26. S. Fan, P. R. Villeneuve, and J. D. Joannopoulos, "Rate-Equation Analysis of Output Efficiency and Modulation Rate of Photonic-Crystal Light Emitting Diodes," *IEEE J. Quantum Electron,* **36:** October (2000).
27. R. K. Lee, O. J. Painter, B. D'Urso, A. Scherer, and A. Yariv, "Measurement of Spontaneous Emission from a Two-Dimensional Photonic Band Gap Defined Microcavity at Near-Infrared Wavelengths," *Appl. Phys. Lett.* **74**:1522–1524 (1999).
28. M. Meier, A. Mekis, A. Dodabalapur, A. Timko, R. E. Slusher, J. D. Joannopoulos, and O. Nalamasu, "Laser Action from Two-Dimensional Feedback in Photonic Crystals," *Appl. Phys. Lett.* **74**:7–9 (1999).
29. K. Inoue, M. Sasada, J. Kawamata, K. Sakoda, and J. Haus, "A Two-Dimensional Photonic Crystal Laser," *Jpn. J. Appl. Phys.* **38**:L157–L159 (1999).
30. T. Baba and T. Matsuzaki, "Fabrication and Photoluminescence Studies of GaInAsP/InP 2-Dimensional Photonic Crystals," *Jpn. J. Appl. Phys.* **35**:1348–1352 (1996).
31. P. L. Gourley, J. R. Wendt, G. A. Vawter, T. M. Brennan, and B. E. Hammons, "Optical Properties of Two-Dimensional Photonic Lattices Fabricated as Honeycomb Nanostructures in Compound Semiconductors," *Appl. Phys. Lett.* **64**:687–689 (1994).
32. M. Boroditsky, R. Vrijen, T. F. Krauss, R. Coccioli, R. Bhat, and E. Yablonovitch, "Spontaneous Emission Extraction and Purcell Enhancement from Thin-Film 2-d Photonic Crystals," *J. Lightwave Technol.* **17:** 2096–2112 (1999).
33. S. G. Johnson, S. Fan, P. R. Villeneuve, and J. D. Joannopoulos, "Guided Modes in Photonic Crystal Slabs," *Phys. Rev. B* **60**:5751–5758 (1999).
34. S. G. Johnson, P. R. Villeneuve, S. Fan, and J. D. Joannopoulos, "Linear Waveguides in Photonic-Crystal Slabs," *Phys. Rev. B* **62:** September (2000).
35. A. Mekis, J. C. Chen, I. Kurland, S. Fan, P. R. Villeneuve, and J. D. Joannopoulos, "High Transmission Through Sharp Bends in Photonic Crystal Waveguides," *Phys. Rev. Lett.* **77**:3787–3790 (1996).
36. S. Y. Lin, E. Chow, V. Hietala, P. R. Villeneuve, and J. D. Joannopoulos, "Experimental Demonstration of Guiding and Bending of Electromagnetic Waves in a Photonic Crystal," *Science* **282**:274–276 (1998).
37. S. G. Johnson, C. Manolatou, S. Fan, P. R. Villeneuve, J. D. Joannopoulos, and H. A. Haus, "Elimination of Cross Talk in Waveguide Intersections," *Opt. Lett.* **23**:1855–1857 (1998).
38. J. C. Knight, J. Broeng, T. A. Birks, and P. St. J. Russel, "Photonic Band Gap Guidance in Optical Fibers," *Science* **282**:1476–1478 (1998).
39. C. M. Soukoulis, ed., *Photonic Band Gap Materials,* NATO ASI Series E: Applied Sciences, Kluwer Academic, Dordrecht, 1996.

This page intentionally left blank.

CHAPTER 21
ALL-OPTICAL SWITCHING

George I. Stegeman
School of Optics/The Center for Research and Education in Optics and Lasers (CREOL)
University of Central Florida
Orlando, Florida

21.1 INTRODUCTION

All-optical switching is a process by which light, usually in the form of digital communications signals, is routed from one transmission channel to another, or *modulated,* without intermediate conversion to another format. Previous options in this process have included the following sequence of events: detection of an optical signal, an electronic routing decision, electronic triggering of a laser in the appropriate output channel, and generation of a new optical pulse. In the all-optical switching format, the signal remains in the optics domain and its properties are altered so that it is routed to a specific output.

The term *all-optical switching* has now taken on two separate meanings. In the first, the switching operation is controlled electrically—for example, via the electro-optic effect—and the induced phase changes are used interferometrically in a 2×2 switch. Switching between more than two channels is implemented by ganging together multiple 2×2 switches.

The second use for this term is when the operation is controlled optically. That is, an optical beam (rather than an electrical signal) changes the optical properties of the medium and leads to interferometric control of the output. This approach typically utilizes an intensity (I)-controlled change in the refractive index $\Delta n(I)$. In the simplest case, $\Delta n = n_2 I$, where n_2 is the Kerr coefficient.[1]

Both all-optical approaches require an externally induced change in the refractive index so that the device geometries and their applications are very similar. Electro-optic modulators, principally using ferroelectric materials, are already in system use, whereas the development of the completely optical concept is still futuristic and depends strongly on continuing materials development. The electro-optic approach is discussed in Chap. 4, Vol. 4.

The nonlinear optics option has certain features that make it attractive, and perhaps the only viable solution as data rates climb into the terabit range and higher. All-optical switching with light beams relies on the response of the third-order nonlinear properties of materials, which can be as short as femtoseconds.

Copyright 2001 by The McGraw-Hill Companies, Inc. Click Here for Terms of Use.

21.2 HOW DO YOU SWITCH?

Any optical signal can be characterized by its spatial location, its arrival time at a specific location, its phase, and its polarization. An optically induced change in any one of these properties can lead to identification and subsequent rerouting of the modified pulse. Linear optical elements such as polarizing beam splitters, interferometers, and so on are frequently used to reroute the modified pulse.[1]

The simplest example of an all-optical switching device is the Mach-Zehnder interferometer, usually in a guided wave format as shown in Fig. 1. It consists of six distinct elements, two of which constitute the input and output channels. The first Y-junction splits the input signal into equal signals in the two intermediate channels. In the absence of illumination by an intense optical beam, the two signals propagate in their separate and identical channels and acquire equal phase shifts in each one. Therefore, at the second Y-junction, the two signals recombine in phase and the input signal emerges unaltered in the output channel. If one arm is illuminated with a control beam of intensity I_c, and that channel has some characteristic nonlinearity n_2, there is an index change $\Delta n = n_2 I_c$ induced in the illuminated region. Therefore, there is an additional phase shift in the signal beam introduced into that arm over an illuminated distance L given by $\Delta\phi = k_{vac} n_2 I_c L$, and the signals in the two arms are no longer in phase at the output Y-junction and hence the resulting partial destructive interference reduces the transmitted signal. (The missing power is radiated away out of the waveguide system.) When $\Delta\phi = \pi$, complete destructive interference can occur—this actually corresponds to all-optical modulation, the most simple form of switching. It is important to note that the control beam does not have to be incident from outside the waveguides. This switch can also be implemented with control beams that are guided, traveling either in the same or opposite direction as the signal, usually in only one of the two arms.

This is an example of control signal switching. That is, a control beam is needed to switch a signal beam. This is the most useful operation. However, it is also possible that an intense beam can switch itself—that is, self-switching. This could be achieved in the Mach-Zehnder device by making the Y-junctions asymmetric such that a larger fraction of the input light would propagate in one channel than the other. Thus the nonlinear phase shift in the two arms would be unequal, again leading to partial or complete destructive interference.

21.3 REAL MATERIALS

The materials used for switching purposes can be divided into generic categories. The first utilizes the instantaneous (femtosecond time scale) response of the material, that is, $\Delta n(t) = n_2 I_c(t)$. That is, the index change induced in the material follows precisely in time the intensity profile of the control pulse. This usually requires third-order nonlinearities far from any dipole-allowed transitions between electronic or vibrational states in the material. This very



FIGURE 1 A guided wave Mach-Zehnder interferometer switch.

fast response offers the promise of multiterabit signal processing. The price to be paid for this speed is that unfortunately, nonresonant nonlinearities are typically small, so that acquiring the necessary nonlinear phase shift requires either high intensities I_c or long interaction regions L.

All-optical devices have been implemented successfully to date in primarily two material systems: semiconductors (in integrated optics waveguides) and glass (fibers). The nonlinearity in silica fibers is $n_2 = 2.45 \times 10^{-16}$ cm^2/W—very small.[2] However, given that the propagation losses are a fraction of a decibel per kilometer in the communications bands, switching can be achieved with subwatt power levels if long enough fiber is used. With the easy availability of erbium-doped fiber amplifiers, such power levels are quite realistic.

There has also been progress in developing new glasses for fibers with much larger nonlinearities and concurrently larger propagation losses. Chalcogenide glasses with $n_2 \cong 4 \times 10^{-14}$ cm^2/W at 1320 nm have been fabricated into fibers with losses in the range of 0.2 m^{-1}.[3] These have provided a useful alternative to silica glass, although their application has been hindered by the large mismatch between the core diameters needed for single-mode operation.

In semiconductors, for photon energies less than half the semiconductor's bandgap, both linear (<0.5 dB/cm) and nonlinear absorption are sufficiently small to allow essentially lossless propagation in channel waveguides a few centimeters long.[4] For $Al_xGa_{1-x}As$ with $x \cong 0.20$, half the bandgap is around 1500 nm, which allows switching operations in that communications window. However, the nonlinearity is small, $n_2 \cong 2 \times 10^{-13}$ cm^2/W.

The second option available with different (non-Kerr response) materials is to create index changes that follow the leading edge of the control pulse but relax slowly over time. The most obvious approach is to use resonant or near-resonant nonlinearities, which are orders of magnitude larger than the nonresonant ones. The index change typically decays on time scales τ_r of nanoseconds or longer. Furthermore, the effective nonlinearity operative for short control pulses ($\tau_r > \Delta t_c$) is reduced by approximately the ratio $\Delta t_c/\tau_r$. For this case the index change is directly proportional to the number of photons absorbed, and the steady state, for which n_2 is defined, is only reached for $\Delta t_c > \tau_r$.

Semiconductors such as AlGaAs have proven very interesting for wavelengths around 850 nm using resonant and near-resonant nonlinearities.[5] The near-resonant nonlinearities are large ($n_2 \cong -10^{-11}$ cm^2/W). The important trade-off needed for high-contrast switching is that between the nonlinearity (n_2) and the linear absorption ($L \cong \alpha^{-1}$), both of which decrease with increasing wavelength below the semiconductor bandgap. It is important to note that near the bandgap it is carrier generation subsequent to the absorption of photons that leads to the index change. These carriers recombine with nanosecond times, although carrier sweep-out with applied electric fields has reduced this time to 10 ps.[6]

Many of the recent all-optical devices have been based on semiconductor amplifiers.[7] They are pumped either optically (holding beam) or electrically. At the transparency point, there is neither gain nor loss for the signal and many ultrafast, but weak, mechanisms contribute to an index change. In the gain region, the response is dominated by changes in the carrier population due to light emission stimulated by the incident signal pulse, and it is this case that has proven most useful. That is, an incident photon stimulates the emission of additional photons, which drops electrons from the conduction band back to the valence band. This not only leads to an index change, but also to gain in the optical beam, which "feels" the index change and thus experiences a net phase change. The recovery time is limited by the rate at which electrons can be pumped back to the conduction band. Times as short as tens of picoseconds have been demonstrated.

21.4 HOW MATERIAL PROPERTIES AFFECT SWITCHING IN COMMUNICATIONS

How such materials can be used for all-optical switching can be illustrated with the Mach-Zehnder switch just discussed. Consider first the case of a Kerr material and pulsed signals typical of data streams in communications. To get complete switching, the induced nonlinear

phase shift $\Delta\phi(t) = \pi$ must be uniform across the temporal profile of the signal to achieve complete switching of the signal—that is, I_c must be constant over the signal pulse. If the signal pulse has a rectangular temporal profile of width Δt_s, then I_c must be constant over Δt_s for codirectional propagation in a waveguide and must be exactly coincident with it in time. Otherwise, a longer control pulse duration $\Delta t_c > \Delta t_s$ is required. For rectangular control pulses, this reduces the timing problem. For other (more realistic) pulse shapes, it is difficult to maintain $\Delta\phi(t) = \pi$ across the signal pulse and usually $\Delta t_c >> \Delta t_s$ is required to optimize the direct tradeoff between the control pulse width and the fraction of power switched.

In many applications, a single pulse or a few pulses from a long sequence of successive pulses need to be switched. In this case, although the control pulse needs to interact with multiple pulses, it does not lessen the timing problem, because usually a precise number of pulses is to be switched. That is, the precise timing of the trailing and leading edges of the control pulse is important, unless the pulses come in bursts for a time Δt_b with successive bursts well separated in time. If the control pulse is not rectangular in shape, then $\Delta t_c >> \Delta t_b$ is required so that the rate at which bursts can be processed is limited by the control pulse width Δt_c. In any case, if the control pulse significantly overlaps a wrong signal pulse, it will be switched erroneously.

The preceding simplest case dealt with control and signal pulses traveling at the same speed, v_c and v_s, respectively. A better approach is to use codirectional beams that travel with different group velocities, for example, because they have different frequencies or polarizations. In this case, clearly any pulse shape will suffice as long as $\pi \propto k_{\text{vac}} n_2 \int I_c(t) dt L_{\text{eff}}$ where $L_{\text{eff}} \propto |(v_c - v_s)^{-1}|$ is the effective distance over which the pulses overlap. The timing requirement is reduced somewhat as long as the pulses pass completely through each other, although the data rate is somewhat compromised. For sequences of successive pulses, the timing requirements are also relaxed, although they can limit the rate at which bursts are processed. The main limitation here is that usually the differences between the signal and control velocities are small, thus requiring long device lengths.

Counterpropagating signal and control beams pass completely through each other, substantially reducing timing requirements but requiring very long control pulses to maintain a long enough effective length L so that the required switching intensities do not become prohibitively large (i.e., $\Delta\phi \propto I_c L$). Since the pulses pass completely through each other, the net phase shift experienced by any point on the signal pulse is the same, so that switching can be complete.

There is one scenario in which the control pulse profiles are not an issue. In fibers, it is possible to generate temporal solitons and any nonlinear phase modulation imparted to a soliton is spread uniformly over its temporal profile (because it is a soliton). Such soliton pulses self-switch completely for a net π phase shift.[8]

Now consider the case of semiconductors operated either with passive nonlinearities or with gain at wavelengths near or at the bandgap.[7] A single control pulse creates an index change, and the signal pulse, or a sequence of signal pulses, could arrive over a large time window of order τ_r and still be switched. This reduces the timing requirements significantly, at the price of the rate ($\propto 1/\tau_r$) at which multiple single pulses or pulse bursts could be processed. In most cases, the index change would decay exponentially. Here the relative directions of the beams are not a major consideration and timing requirements are reduced as long as the signal pulse(s) follows the control pulse in time.

Various tricks can be used to overcome the long decay times associated with the index change. In the case of semiconductors where index change is due to carrier excitation, electric fields can be used to sweep the carriers responsible for the index change out of the waveguide regions. An alternate and very powerful approach is to use two successive control pulses separated in time by Δt. The first pulse creates a nonlinear phase shift in channel one of the Mach-Zehnder switch, and the second, a time Δt, later creates an equal phase shift in the second channel. Therefore the two signals recombined at the second Y-junction only experience a differential phase shift of π for the time Δt; otherwise the phase shifts are equal and constructive interference occurs. In this way single pulses can be switched and the timing requirements are determined by the rate of arrival of, for example, temporal spacing between subsequent pulses. Switching of pulse sequences may require periodic refreshing of one or both control pulses. An

attractive feature of this approach is that the shape of the control pulses (assuming that they are short enough) is not important, nor is the relative distribution of the index change along the waveguides. Only the integral that produces the net phase shift is important.

Although this discussion has dealt with a specific example, the same considerations are important for all all-optical switching devices.

21.5 OTHER DEVICE GEOMETRIES

There have been a large number of different device geometries studied to date for all-optical switching.[1] However, here the discussion is limited to a few important examples in addition to the Mach-Zehnder interferometer discussed previously. The nonlinear directional coupler (NLDC), the nonlinear loop mirror (NOLM), and combinations of these have proven both popular and useful. These two devices are shown schematically in Fig. 2.

NLDCs have been implemented in fiber and integrated optics formats.[9,10] As shown in Fig. 2*a,* they consist of two parallel waveguide channels placed in such close proximity (a few micrometers apart) that the fields guided by one channel overlap in space the second channel. This field overlap provides the coupling that allows power to flow between channels. In a fashion similar to coupled equivalent pendulums, when light is excited in one channel it transfers periodically back and forth between the two channels. The NLDC can be used as guided wave beam splitter by choosing different channel lengths. For switching, the device is terminated after all of the input power is transferred from the input to the neighboring channel. Therefore light incident in one channel is normally displaced (routed) spatially to the neighboring channel. This is called a *half-beat-length coupler.* The key to its linear operation is that the propagation wave vectors (β) of the two channels are equal, which is equivalent to the two pendulums being identical.

The introduction of a high-intensity control beam into one arm (channel) changes the propagation wave vector ($\Delta\beta \propto n_2 I_c$) of that arm. This inhibits power transfer to the neighboring channel, similar but not equivalent to the pendulum case because in the NLDC, power transfer changes the wave vector difference between the channels with distance, whereas in

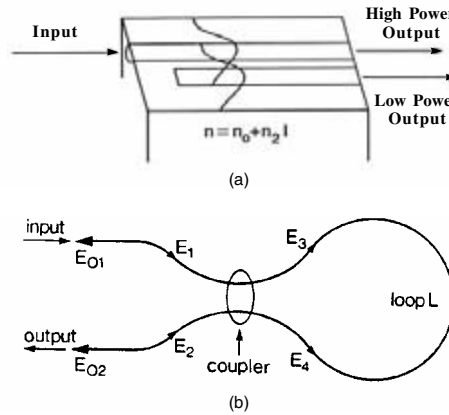

FIGURE 2 Two nonlinear guided wave switching devices: (*a*) the nonlinear directional coupler (NLDC); (*b*) the nonlinear optical loop mirror (NOLM).

the mismatched pendulum case the lengths stay the same during power transfer. In summary, the control beam inhibits switching and therefore controls the spatial location of the output.

In fact, the NLDC is a very versatile all-optical element because it is a "four-port" device. It can be used not just for routing but also for all-optical logic operations, limiting, and so on.[1]

The NOLM is at least as versatile as the NLDC, with the added advantage that it is completely compatible with transmission fibers, erbium-doped amplifiers, and temporal solitons. As shown in Fig. 2*b,* it consists of a loop of fiber with the two ends coupled together as in a linear directional coupler. In the simplest case the input power is split 50:50 into the two counterpropagating directions in the loop and then recombined when the two beams arrive back at the coupler. In the linear case, with the 50:50 splitter, the beam is reflected back into the input fiber and the device is essentially a mirror. When an additional phase shift of π is introduced into one of the counterpropagating beams by a control beam (example given later), the output signal is transferred to the output fiber. With splices, erbium-doped amplifiers, and other elements added judiciously in the right places, this device can perform routing with gain, signal regeneration, timing, logic, and so on.[1]

21.6 EXAMPLES OF OPERATION OF ALL-OPTICAL DEVICES

Two examples of operational switching devices, one in fiber and one in integrated optics formats, will now be discussed to indicate how all-optical switching concepts are implemented for specific device functions.

The first example (Fig. 3) shows a layout of a NOLM used for time-domain demultiplexing of a data train.[11] The goal is to remove selected pulses from the data stream by clocking them out with a sequence of control pulses. The loop itself is made from polarization-preserving fiber and the data and control pulses are orthogonally polarized. This allows the control pulses to be inserted into and extracted from the fiber loop with polarization-sensitive couplers without disturbing the data pulses. The data pulse to be extracted and the control pulse co-propagate and a nonlinear phase shift is imparted to the desired data pulse by cross-phase modulation. Because the fiber is polarization preserving, the data and control pulse pass through each other. At the positions marked by $\otimes$, the fiber is broken and respliced rotated by 90° so that the relative velocities of the control and data are periodically reversed. The two pulses pass through each other again and again. This trick is used to accumulate nonlinear phase shift without the need for precision timing. At the 50:50 splitter (coupler), the data pulse is extracted from the loop and the rest of the data returns back along its incidence path. Therefore, a single data pulse is extracted and rerouted.

The second example (Fig. 4) shows how semiconductor amplifiers (SOAs) can also be used for demultiplexing.[12,13] The data signal is split 50:50 with a directional coupler into both arms of the interferometer. There is a fixed phase shift bias between 0 and π introduced between the two interferometer arms, usually via the electro-optic effect. This phase bias is adjusted until there is no output, for example, in the bottom data output channel, and the data emerges from the top channel. A control pulse that lies within the gain region is introduced and split in two by the directional coupler and excites the two SOAs. This control beam results in an

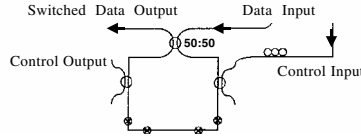

FIGURE 3 A NOLM used as a demultiplexer.

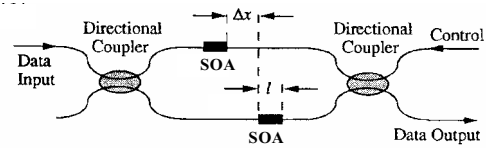

FIGURE 4 A switching device based on two semiconductor optical amplifiers (SOAs) in a Mach-Zehnder geometry.

additional π phase shift for the data pulse traveling in the opposite direction in the upper channel relative to the lower channel, but only within the temporal window created by the time it takes the control pulse to effectively travel the Δx between the SOAs. A pulse falling in that window gets switched out into the lower output channel. By offsetting the SOAs, the width of this window can be controlled, reducing the need for exact coincidence of the control and demultiplexed pulses by increasing the size of the temporal window at the expense of processing speed. Demultiplexing in the 100-Gbit/s range has been realized with picojoule switching energies.[12,13]

This device can also be used for all optical modulation or frequency shifting. If the data stream is replaced by, for example, a continuous-wave (cw) beam, then before the control pulses arrive at either amplifier there is a cw beam output in the upper channel only. During the time that one amplifier is excited by a control pulse and the other is not, an additional phase shift of π is produced on one beam and there is an output into the lower output channel. As soon as the second amplifier is excited, the phase shifts become equal again, switching the output back to the upper channel. Thus a pulse is created whose duration is given primarily by the SOA offset. In this mode of operation, the pulse train of the control beam is imparted onto the signal beam. If they have different wavelengths, this is a wavelength shifter.[1] Some other examples of SOA applications include optical sampling, tunable-wavelength filters, all-optical AND gates (devices that output a signal when two signals are inputted simultaneously) photonic packet switches, Asynchronous Transfer Mode (ATM) switching, clock recovery, time slot interchange, and so on.[1]

21.7 SUMMARY

All-optical switching of signal beams is implemented by using control beams to introduce a change in the refractive index into a signal beam's propagation path. This refractive index change is then used in a variety of guided wave structures to modify the output state of the signal beam, which in turn is translated into a change in signal routing, wavelength, modulation, and so on. Such devices have been successfully implemented both in optical fibers and in semiconductor integrated optics waveguides.

21.8 REFERENCES

1. Reviewed in G. I. Stegeman and A. Miller, "Physics of All-Optical Switching Devices," in *Photonic Switching,* vol. I, J. Midwinter (ed.), Academic Press, Orlando, FL, 1993, pp. 81–146; partially updated in G. I. Stegeman and G. Assanto, "Nonlinear Integrated Optical Devices," in *Design and Applications of Integrated Optical Circuits and Components,* E. Murphy (ed.), Marcel Dekker Inc., 1999, pp. 381–418.
2. R. H. Stolen, W. A. Reed, K. S. Kim, and G. T. Harvey, "Measurement of the Nonlinear Refractive Index of Long Dispersion-Shifted Fibers by Self-Phase Modulation at 1.55 Microns," *J. Lightwave Technol.* **16**:1006–1012 (1998).

3. M. Asobe, H. Kobayashi, and H. Itoh, "Laser-Diode Driven Ultrafast All-Optical Switching by Using Highly Nonlinear Chalcogenide Glass Fiber," *Opt. Lett.* **18**:1056–1058 (1993).
4. G. I. Stegeman, A. Villeneuve, J. Kang, J. S. Aitchison, C. N. Ironside, K. Alhemyari, C. C. Yang, C.-H. Lin, H.-H. Lin, G. T. Kennedy, R. S. Grant, and W. Sibbett, "AlGaAs Below Half Bandgap: The Silicon of Nonlinear Optical Materials," *Int. J. Nonlinear Opt. Phys.* **3**:347–371 (1994).
5. H. M. Gibbs, G. Khitrova, and N. Peyghamberian (eds.), *Nonlinear Photonics,* Springer-Verlag, Berlin, 1990.
6. A. Cavailles, D. A. B. Miller, J. E. Cunningham, P. LiKamWa, and A. Miller, "Simultaneous Measurements of Electron and Hole Sweep-Out From Quantum Wells and Modeling of Photoinduced Field Screening Dynamics," *IEEE J. Quant. Electron.* **28**:2486–2497 (1992).
7. For example, M. J. Adams, D. A. O. Davies, M. C. Tatham, and M. A. Fisher, "Nonlinearities in Semiconductor Amplifiers," *Opt. Quant. Electron.* **27**:1–13 (1995).
8. K. J. Blow, N. J. Doran, and B. K. Nayer, "Experimental Demonstration of Optical Soliton Switching in an All-Fiber Nonlinear Sagnac Interferometer," *Opt. Lett.* **14**:754–756 (1989).
9. P. LiKamWa, J. E. Stich, N. J. Mason, J. S. Roberts, and P. N. Robson, "All-Optical Multiple-Quantum-Well Waveguide Device," *Electron. Lett.* **21**:26–28 (1985).
10. S. R. Friberg, A. M. Weiner, Y. Silberberg, B. G. Sfez, and P. S. Smith, "Femtosecond Switching in a Dual-Core Fiber Nonlinear Coupler," *Opt. Lett.* **13**:904–906 (1998).
11. N. A. Whitaker Jr., H. Avramopoulos, P. M. W. French, M. C. Gabriel, R. E. LaMarche, D. J. Di Giovanni, and H. M. Presby, "All-Optical Arbitrary Demultiplexing at 2.5 Gbits/s with Tolerance to Timing Jitter," *Opt. Lett.* **16**:1838–1840 (1991).
12. K. I. Kang, T. G. Chang, I. Glesk, P. R. Prucnall, and R. K. Boncek, "Demonstration of Ultrafast, All-Optical, Low Control Energy, Single Wavelength, Polarization Independent, Cascadable and Integratable Switch," *Appl. Phys. Lett.* **67**:605–607 (1995).
13. E. Jahn, N. Agrawal, M. Arbert, H.-J. Ehrke, D. Franke, R. Ludwig, W. Pieper, H. G. Weber, and C. M. Weinert, "40 Gbit/s All-Optical Demultiplexing Using a Monolithically Integrated Mach-Zehnder Interferometer with Semiconductor Laser Amplifiers," *Electron. Lett.* **31**:1857–1858 (1995).

CHAPTER 22
OPTICAL PARAMETRIC OSCILLATORS

M. Ebrahimzadeh and M. H. Dunn
School of Physics and Astronomy
University of St. Andrews
Fife, United Kingdom

22.1 INTRODUCTION

The potential of nonlinear optical phenomena as a means of providing coherent radiation was realized nearly four decades ago, soon after the invention of the laser. Nonlinear effects in electromagnetism had been observed as early as the late nineteenth century by Kerr, Roentgen, Kundt, and Pockels, and later by Raman in 1927 when he discovered spontaneous scattering of light into new wavelengths in passing through a transparent medium. However, it was not until 1961 that the first observation of coherent nonlinear optical effects was made by Franken et al.,[1] who demonstrated second-harmonic generation of light in the crystal of quartz. This demonstration, which was made possible by the unprecedented optical intensities available from the laser, propelled the field of nonlinear optics and led the way for intensive theoretical and experimental efforts in this field. Soon after, the importance of optical parametric generation and amplification as powerful techniques for the generation of tunable coherent light in new spectral regions was recognized[2–4] and the first experimental device based on this concept was reported in 1965.[5] This demonstration initiated an intense surge of research interest in parametric devices and prompted an extensive search for nonlinear materials and laser pump sources. During this period, rapid progress was made in the development of parametric devices and intensive efforts were directed at the fundamental level toward the studies of crystal optics and the understanding of parametric processes and many aspects of nonlinear interaction of light with matter. This period laid the foundations for the field of parametric frequency conversion and established many of the fundamental principles and practical benchmarks for this subject area.

Following the initial rapid progress, however, research in parametric devices was hampered by several obstacles, most notably a lack of suitable nonlinear materials. Combined with the absence of laser sources of high spatial and spectral coherence and sufficient intensity in the desired spectral regions, these difficulties compounded to render parametric devices inconvenient sources of coherent light with limited practical utility. These factors led to a conspicuous decline of research interest in parametric devices and a long period of qui-

Copyright 2001 by The McGraw-Hill Companies, Inc. Click Here for Terms of Use.

escence in this field until, in the 1980s, the advent of new nonlinear materials once again prompted a major resurgence of interest in the field. The emergence of a new generation of nonlinear optical crystals such as β-BaB_2O_4 (BBO), LiB_3O_5 (LBO), and $KTiOPO_4$ (KTP), among others, with damage thresholds far exceeding those of the more classical materials and superior linear and nonlinear optical properties, provided new impetus for intensive research efforts in this field. Since then, there have been unparalleled advances in this area and parametric devices have been transformed from proof-of-principle demonstrations to viable sources of coherent light for practical applications. The operating domain of parametric devices, once confined to selected spectral and temporal regimes, now extends across spectral regions all the way from the near-ultraviolet well into the mid-infrared and encompasses all time scales from continuous-wave (CW) to the ultrafast femtosecond regime. New design concepts based on refined resonator and phase-matching geometries and novel pumping schemes have led to the realization of practical devices with much improved performance characteristics. At the same time, the availability of high-power laser sources with enhanced spectral and spatial coherence has enabled the development of parametric devices at unprecedented power levels. More recently, the advent of quasi-phase-matched (QPM) nonlinear materials such as periodically poled $LiNbO_3$ (PPLN) with large nonlinearity and widespread availability has led to minimal pump power requirements, bringing the operation of parametric devices within the reach of commonly available laser pump sources. The remarkable advances in this field over the past decade have now firmly established parametric devices as an important class of practical coherent light sources with many advantages over conventional lasers. These devices offer exceptional tunability and provide access to spectral regions not available to other laser sources, are solid state in design, and can deliver practical output powers at high efficiency in all time scales.

The aim of this chapter is to provide an overview of parametric devices from basic operation principles to the important recent developments in the field. The treatment includes a description of the fundamental concepts of optical parametric generation and amplification, design issues and optimization of parametric devices, material and pump laser selection criteria, and cavity and pumping architectures, as well as a review of pertinent device characteristics. However, in the treatment we do not concern ourselves with the background of the origin of the nonlinear optical effects or a discussion of crystal optics, which can be found in other reference texts.[6–9] While much of the discussion in this chapter is relevant to parametric devices of all types, particular emphasis is placed on optical parametric oscillators (OPOs), which represent the majority of the parametric devices developed to date. Other reviews on OPOs can be found elsewhere in the literature.[9–13] We will adopt SI units throughout the discussion.

22.2 BASIC PRINCIPLES

Optical parametric generation is a second-order nonlinear process involving the interaction of three optical fields at frequencies ω_3, ω_2, and ω_1, such that

$$\omega_3 = \omega_2 + \omega_1 \tag{1}$$

The field at ω_3 generally corresponds to an intense input optical *pump* field, giving rise to a pair of generated fields at frequencies ω_2 and ω_1. The generated field at the higher frequency—ω_2, say—is usually referred to as the *signal,* while the field at the lower frequency ω_1 is termed the *idler,* although variations in this nomenclature are also frequently used in the literature. The underlying physical principles responsible for the parametric process relate to the second-order susceptibility $\chi^{(2)}$ in a nonlinear crystalline medium. In such a medium, the induced polarization **P** due to an input optical field **E** is in its most general form given by

$$\mathbf{P} = \varepsilon_0 [\chi^{(1)} \cdot \mathbf{E} + \chi^{(2)} : \mathbf{EE} + \chi^{(3)} \vdots \mathbf{EEE} + \cdots] \tag{2}$$

where $\chi^{(1)}$ is the linear susceptibility and $\chi^{(2)}$, $\chi^{(3)}$, . . . are the nonlinear susceptibilities of the medium. The linear susceptibility is related to the refractive index through $\chi^{(1)} = n^2 - 1$ and is responsible for the linear optical properties of the medium such as refraction, dispersion, absorption, and birefringence. The second-order susceptibility $\chi^{(2)}$ gives rise to familiar nonlinear optical processes such as second-harmonic generation (SHG), sum- and difference-frequency mixing, the linear electro-optic (Pockels) effect, and, most importantly in the context of this treatment, optical parametric generation and amplification. The third-order nonlinear susceptibility $\chi^{(3)}$ is responsible for the phenomena of third-harmonic generation, optical bistability, phase conjugation, and the optical Kerr effect. The susceptibilities $\chi^{(1)}$, $\chi^{(2)}$, $\chi^{(3)}$, . . . are tensors of the second, third, fourth, and higher rank, respectively. In writing Eq. (2), we have used a tensor notation because most crystalline media that exhibit second-order nonlinearity are optically anisotropic, so that **P** and **E** are generally not parallel in such media. The magnitude of the susceptibility tensors decreases rapidly with increasing rank of nonlinearity [$\chi^{(1)}$:$\chi^{(2)}$:$\chi^{(3)}$ ~ 1:10^{-8}:10^{-16}]. It is thus not surprising that the observation of nonlinear optical effects only became possible after the invention of the laser. In this treatment, we are concerned only with the second-order nonlinear susceptibility $\chi^{(2)}$ and focus on the implications of this property only in relation to the parametric generation and amplification process. More extensive treatments of other $\chi^{(2)}$ and higher-order nonlinear processes can be found in numerous texts and review articles in the nonlinear optics literature.[6,9] In its most general form, the $\chi^{(2)}$ tensor has 27 elements, but in practice many of the components vanish under certain symmetry conditions, so the total number of independent components is generally far fewer. The tensor is nonzero only in media that lack inversion symmetry in their crystalline structure. In centrosymmetric media, $\chi^{(2)}$ and all other even-order susceptibilities reduce to zero, and so Eq. (2) involves only the odd-order terms in such media. In the definition of the induced polarization through Eq. (2), the units of $\chi^{(2)}$ in SI system are meters per volt.

In order to describe the parametric generation process, we need to consider the propagation of three optical fields—the pump, signal, and idler—at respective frequencies ω_3, ω_2, and ω_1 in a noncentrosymmetric medium exhibiting second-order nonlinear susceptibility $\chi^{(2)}$. More rigorous treatment of this problem can be found elsewhere.[7,9,14,15] Here, we only describe the essential features of this treatment and restrict our attention to the main results of the analysis. The propagation of an optical field in a $\chi^{(2)}$ nonlinear medium involves the solution of Maxwell's nonlinear wave equation. The formalism is developed by first separating the total induced polarization, as described by Eq. (2), into its constituent linear and nonlinear components as

$$\mathbf{P} = \mathbf{P}^{(1)} + \mathbf{P}^{(2)} + \mathbf{P}^{(3)} + \cdots \tag{3}$$

where $\mathbf{P}^{(1)} = \varepsilon_0 \chi^{(1)}$. **E** is the linear polarization, $\mathbf{P}^{(2)} = \varepsilon_0 \chi^{(2)} : \mathbf{EE}$ is the second-order nonlinear polarization, $\mathbf{P}^{(3)} = \varepsilon_0 \chi^{(3)} \vdots \mathbf{EEE}$ is the third-order nonlinear polarization, and so on. Since in the discussion of the parametric generation process only the role of the second-order nonlinear polarization is of importance, the linear and higher-order polarization terms in Eq. (3) may be ignored in the analysis. We must therefore seek solutions to Maxwell's wave equation with $\mathbf{P}^{(2)} = \varepsilon_0 \chi^{(2)} : \mathbf{EE}$ as the polarization source term in a dielectric medium. We also assume that the medium is lossless, nonconducting, and nonmagnetic. Since the parametric process involves the interaction of three optical fields, we consider a total field **E** comprising three monochromatic harmonic waves representing the pump, signal, and idler, so that $\mathbf{E} = \mathbf{E}_1(\omega_1) + \mathbf{E}_2(\omega_2) + \mathbf{E}_3(\omega_3)$. To simplify the discussion, we also assume that the optical fields are infinite uniform plane waves propagating in the z-direction, and define each harmonic field as

$$\mathbf{E}_j(\omega_j) = \left(\frac{1}{2}\right)\{E_j(z)[\exp i(k_j z - \omega_j t)] + \text{cc}\}$$

where $j = 1, 2, 3$ and $E_j(z)$ represents the complex field amplitude. We then substitute for $\mathbf{P}^{(2)}$ and **E** in Maxwell's wave equation and separate the resulting equation into three components

at three different frequencies ω_1, ω_2, ω_3, each of which must separately satisfy the wave equation. Now, by considering the three separate wave equations at each frequency and assuming that the field amplitudes vary only slowly over distances compared to a wavelength, after some manipulation, we arrive at

$$\frac{dE_1(z)}{dz} = i\kappa_1 E_3(z)E_2^*(z)e^{i\Delta kz} \tag{4a}$$

$$\frac{dE_2(z)}{dz} = i\kappa_2 E_3(z)E_1^*(z)e^{i\Delta kz} \tag{4b}$$

$$\frac{dE_3(z)}{dz} = i\kappa_3 E_1(z)E_2(z)e^{-i\Delta kz} \tag{4c}$$

where $\kappa_j = [\omega_j \chi_{\text{eff}}^{(2)}/2n_j c]$, with $j = 1, 2, 3$, n is the refractive index, and $\Delta k = k_3 - k_2 - k_1$ is the phase-mismatch parameter, which will be discussed in more detail in Sec. 22.3. These are the *coupled-wave equations* governing the parametric interaction of the pump, signal, and idler in a dielectric medium exhibiting second-order nonlinear susceptibility. In writing Eqs. (4*a*)–(4*c*), we have reverted to a scalar notation for convenience, with $\chi_{\text{eff}}^{(2)}$, representing the appropriate combination of the nonlinear tensor coefficients taking part in the parametric interaction process. The coupled-wave equations are the starting point in the analysis of a wide range of nonlinear optical effects and apply universally to any three-wave mixing process involving the second-order susceptibility, where the frequencies of the fields satisfy Eq. (1). Several familiar second-order processes are associated with the different combinations of ω_1, ω_2, and ω_3. These include sum-frequency mixing ($\omega_1 + \omega_2 \rightarrow \omega_3$), difference-frequency mixing ($\omega_3 - \omega_2 \rightarrow \omega_1$), second harmonic generation ($\omega_1 + \omega_2 \rightarrow \omega_3$, with $\omega_1 = \omega_2 = \omega$ and $\omega_3 = 2\omega$), and, most importantly in the context of this discussion, optical parametric generation ($\omega_3 \rightarrow \omega_2 + \omega_1$). We notice from Eqs. (4*a*)–(4*c*) that the amplitudes of the three optical fields are coupled to one another through the second-order susceptibility $\chi_{\text{eff}}^{(2)}$. Physically, this coupling provides the mechanism for the exchange of energy among the interacting fields as they propagate through the nonlinear medium. The direction of energy flow in a given three-wave mixing process depends on the relative phase and the intensity of the input fields.

We can use a phasor model to gain an insight into the nonlinear frequency conversion processes described by the coupled-wave equations Eqs. (4*a*) to (4*c*). In particular, we can use such a model to illustrate the role of phase in determining how the frequency conversion proceeds. To do this, we express the relationships between the fields in terms of small incremental changes rather than in terms of the differential equations. Consider Eq. (4*a*). Then the incremental change in the idler field δE_1 for propagation over a small distance δz is given by rearranging this equation to give

$$\delta E_1 = i\,\kappa_1 E_3 E_2^*\,\delta z$$

For the present we have assumed that the process is phase matched, that is $\Delta k = 0$ (see Sec. 22.3). The Es, and also the δEs, in the equation are of course complex quantities carrying information about the phases of the fields as well as their magnitudes. We can thus represent the Es as phasors in a phasor diagram (see Fig. 1*a*), where the length of the phasor (vector) represents the magnitude of the field and the angle the phasor (vector) makes with the X axis represents the phase of the field. The question now is how we compute the increment δE_1 from a knowledge of the two fields involved and using such phasor diagrams.

Without any loss of generality, we can choose to reference all phases to that of the pump field (see Fig. 1*b*), and thus draw the phasor representing this field along the X axis. Then the signal field phasor can be entered onto the diagram at an angle to the pump field phasor that represents the relative phase of the two fields. The question now is: what is the procedure for computing the direction of the phasor representing the increment in the idler field? According to the prescription given by $\delta E_1 = i\,\kappa_1 E_3 E_2^*\,\delta z$, we must first determine the complex conjugate of the signal field, which is designated by the dashed arrow in Fig. 1*b,* and then rotate this

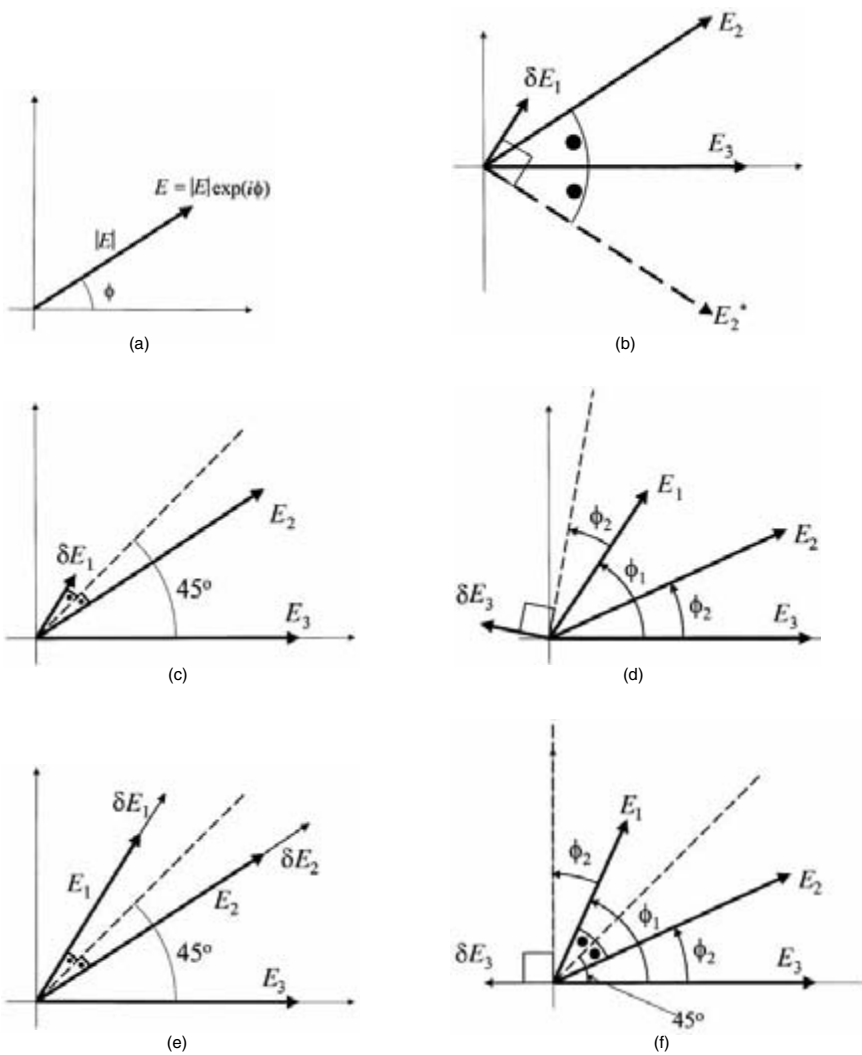

FIGURE 1 (*a*) Phasor representation of the (complex) amplitude of an optical wave. (*b*) Phase of signal wave referenced relative to the pump wave. (*c*) Procedure for determining the incremental phasor for the idler wave, generated from pump and signal waves. (*d*) Procedure for determining the incremental phasor for the pump wave, generated from the signal and idler waves. (*e*) Phasor geometry corresponding to optimum downconversion. (*f*) Depletion of pump wave during downconversion.

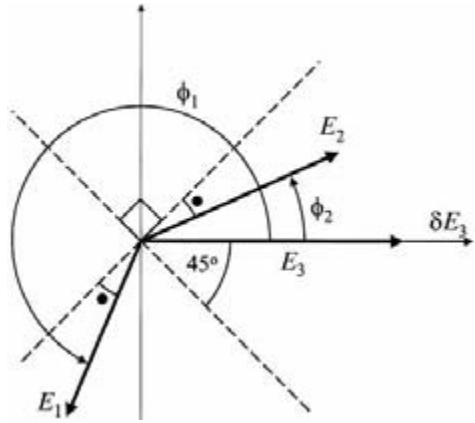

(g)

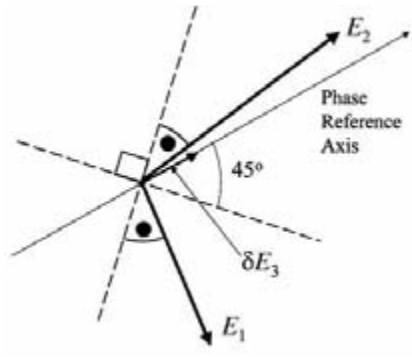

(h)

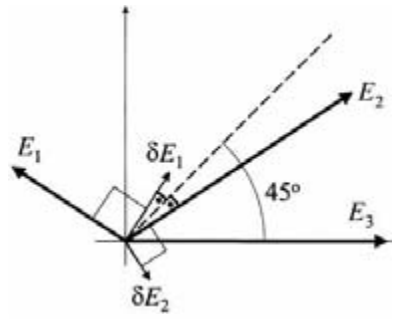

(i)

FIGURE 1 (*Continued*) (*g*) Phasor geometry corresponding to optimum upconversion. (*h*) Generation of pump wave during upconversion. (*i*) Nonlinear dispersion effects.

through +90° (+π/2), as prescribed by the complex i [= exp ($i\pi$/2)] in the equation. A little thought will show that the direction in which we then finish up is at an angle to the 45° diagonal in the phasor diagram equal to the angle made by the signal phasor with this diagonal, but now measured on the other side of the diagonal. We thus have an easy geometrical prescription for determining the phase of the incremental idler phasor, as summarized in Fig. 1*c.* (The length of the incremental idler phasor is, of course, just proportional to the product of the magnitudes of the signal and pump phasors.)

Using similar arguments in relation to the second coupled-wave equation describing the growth of the signal field [Eq. (4*b*)], we can show that simply by interchanging the roles of the signal and idler fields we can determine the incremental signal phasor.

To complete the description, we need to consider the phasor for the incremental change in the pump field. From the third coupled-wave equation [Eq. (4*c*)], which we can write in incremental form as $\delta E_3 = i\,\kappa_3 E_2 E_1$, the phasor geometry for the change in the pump field, as shown in Fig. 1*d,* readily follows.

Having introduced the technique, we can now explore the role of relative phase in determining the manner in which the nonlinear conversion proceeds. Suppose we wish to optimize the process of downconversion. We then require that the incremental phasor representing the newly generated idler wave is exactly in phase with the idler wave already present, as shown in Fig. 1*e.* However, we must further ask the question of how the mixing of the idler with the pump, in order to generate more signal, proceeds under such circumstances. From the geometry of Fig. 1*e* it may readily be seen that for an arrangement of signal and idler fields such as that previously prescribed, the incremental phasor representing the newly generated signal wave is also in exact phase with signal field already present. So both processes are optimized simultaneously. There is obviously an infinite number of combinations of signal and idler wave phasors that satisfy the condition of optimum downconversion (i.e., a unique phase between either the signal or the idler and the pump is not required). However, it is also apparent that signal and idler phasors must be symmetrically placed about the 45° phase line (diagonal line) for optimum downconversion. This is a useful rule that can also be stated in an equivalent way, remembering that the pump field provides the phase reference, as ($\phi_2 + \phi_1 - \phi_3 = \pi/2$).

If either of the downconverted fields (signal or idler) is initially absent, then the fields will evolve with optimum phasing for downconversion as just described, the initially absent field automatically being generated with the correct phase. We must also explore what is happening to the pump field under the above conditions. From the symmetry of the fields as shown in Fig. 1*f,* it can be seen that the incremental phasor representing the component of pump field generated by the interaction of the signal and idler fields is now in antiphase with the existing pump field phasor. Thus this is also a condition of maximum depletion of the pump field, as expected.

In a similar manner, we can deduce the condition for optimum upconversion (sum-frequency mixing) under the condition when all three fields are present, as shown in Fig. 1*g.* The equivalent condition to ($\phi_2 + \phi_1 - \phi_3 = \pi/2$) for this case is readily seen from the diagram to be ($\phi_2 + \phi_1 - \phi_3 = -\pi/2$).

As shown in Fig. 1*h,* in the case when only the idler and signal are present initially, the pump field is generated in just the right phase for the upconversion process to proceed under optimum conditions.

From the preceding discussion, the importance of phase-matching can be readily appreciated. In the absence of phase matching the relative phases of the pump, signal, and idler fields evolve in time rather than remaining static. Optimum phasings for frequency downconversion as best suits an OPO, and as given by ($\phi_2 + \phi_1 - \phi_3 = \pi/2$), can then evolve with propagation into phasings appropriate to frequency upconversion, so that the generation process reverses (referred to as *backconversion* in the context of the OPO) and generation efficiency is reduced. It is also apparent from the preceding discussion that if total depletion of the pump field occurs in an OPO before the signal and idler fields have exited the nonlinear medium, then backconversion will start to occur even with phase matching. The pump wave will thus be regenerated from the signal and idler, again with a consequent reduction in the downconversion efficiency.

It is also possible to find self-consistent conditions under which neither upconversion nor downconversion proceeds, even though all three fields are present together within the nonlinear medium. This state of affairs is illustrated in Fig. 1*i.* The effect of the nonlinear interaction is to produce only dispersive effects, in which the nonlinear process modifies the refractive indexes experienced by the different waves (cross-modulation of refractive index). The phase relation required for such a state of affairs is $\phi_2 + \phi_1 - \phi_3 = \pi$.

When the fields are present with phasings that do not correspond to either ($\phi_2 + \phi_1 - \phi_3 = \pi/2$) or ($\phi_2 + \phi_1 - \phi_3 = -\pi/2$), then the up- or downconversion process is not optimized, and the fields present will experience both gain or loss and also dispersion.

22.3 OPTICAL PARAMETRIC GENERATION AND AMPLIFICATION

As outlined earlier, optical parametric generation is a three-wave mixing process involving the interaction of three optical fields, the pump, signal, and idler, with frequencies satisfying Eq. (1), in a $\chi^{(2)}$ nonlinear medium. In practice, the process is initiated by a single intense pump field at frequency ω_3 at the input to a nonlinear crystal. This field, which is provided by a laser source, in turn mixes, through the nonlinear susceptibility, with a signal field at ω_2 to give rise to an idler field at $\omega_1 = \omega_3 - \omega_2$. The idler field so generated in turn mixes back with the pump to produce additional signal and the regenerated signal remixes with the pump to produce more idler. The process continues in this way until power is gradually transferred from the strong pump to the initially weak signal and idler fields through the nonlinear interaction mediated by $\chi^{(2)}$. Under suitable (phase-matched) conditions, as described in Sec. 22.2 and further discussed later in this section the generated signal and idler fields can undergo macroscopic amplification by continually draining power from the input pump field as they propagate through the nonlinear crystal.

In the absence of a coherent source of signal or idler (or both) beams at the input, the initial supply of signal and idler photons for mixing with the input pump is provided by the spontaneous breakup of pump photons through spontaneous parametric emission. This process, also referred to as *parametric noise* or *parametric fluorescence,* may be viewed to arise from the mixing of the zero-point flux of the electromagnetic field at the signal and idler frequency, quantized within the volume of the crystal, with the incoming pump photons, through the nonlinear polarization.[16–18] The effective zero-point flux at the signal and idler is obtained by allowing one half-photon of energy at both ω_2 and ω_1 or one photon of energy at either frequency to be present in each blackbody mode of the quantizing volume.

Having established the basic principles of parametric interactions, we can now go on to consider the gain and amplification factor for the growth of the signal and idler fields in such a process. The detailed mathematical treatment of this problem is beyond the scope of the present discussion and can be found elsewhere.[15] Essentially, the treatment involves the solution of the coupled-wave equations Eqs. (4*a*) to (4*c*). The general solution of these equations is difficult, but if it is assumed that the input pump field does not undergo strong depletion with propagation through the medium, then $dE_3/dz = 0$ in Eq. (4*c*), and the coupled-wave equations are reduced to two, involving Eqs. (4*a*) and (4*b*), with E_3 independent of z in both equations. Subject to the initial condition of zero input idler field $E_1(z = 0) = 0$ and nonzero input signal $E_2(z = 0) \neq 0$, the net fractional gain in signal intensity with propagation through the nonlinear crystal can be derived as

$$G_2(\ell) = \frac{I_2(z = \ell)}{I_2(z = 0)} - 1 = \Gamma^2 \ell^2 \frac{\sinh^2 [\Gamma^2 \ell^2 - (\Delta k \ell/2)^2]^{1/2}}{[\Gamma^2 \ell^2 - (\Delta k \ell/2)^2]} \tag{5}$$

where ℓ is the interaction length; $I = nc\varepsilon_0 EE^*/2$ is the intensity or flux, W/m^2; Δk is the phase mismatch; and Γ is the gain factor defined as

$$\Gamma^2 = \frac{8\pi^2 d_{\text{eff}}^2}{c\varepsilon_0 n_1 n_2 n_3 \lambda_1 \lambda_2} I_3(0) \tag{6}$$

Here, n refers to the refractive index and λ is the wavelength of the respective waves in vacuum; $I_3(0)$ is the input pump intensity; and $d_{\text{eff}} = \chi^{(2)}_{\text{eff}}/2$ is the effective nonlinear coupling coefficient, which is most commonly used in place of $\chi^{(2)}_{\text{eff}}$ in the discussion of nonlinear optical processes. As with $\chi^{(2)}_{\text{eff}}$, the units of d_{eff} in the SI system are meters per volt. From the same analysis, an expression similar to Eq. (5) may be derived for the growth of the idler field from its initial zero value at the input to the nonlinear crystal.[14] The case of nonzero input idler as well as signal can also be treated similarly,[12] and results analogous to Eq. (5) can be derived for the amplification of the generated fields. It is often useful to express the gain factor in the form

$$\Gamma^2 = \frac{8\pi^2 d_{\text{eff}}^2}{c\varepsilon_0 n_0^2 n_3 \lambda_0^2} (1 - \delta^2)\, I_3(0) \tag{7}$$

where δ is the degeneracy factor defined through

$$1 + \delta = \frac{\lambda_0}{\lambda_2}; \qquad 1 - \delta = \frac{\lambda_0}{\lambda_1} \qquad (0 \le \delta \le 1) \tag{8}$$

$\lambda_0 = 2\lambda_3$ is the degenerate wavelength, and n_0 is the refractive index at degeneracy, with $n_0 \sim n_1 \sim n_2$ assumed. It is clear from Eq. (7) that the gain in a parametric amplification process has a maximum value at degeneracy, where $\delta \sim 0$, and the gain decreases for operation away from degeneracy as $\delta \to 1$.

Gaussian Beams and Focusing

The preceding discussion of parametric amplification and gain has been based on a simplified plane-wave model in which the pump, signal, and idler fields are assumed to be infinite uniform plane waves. In practice, however, the beams are often focused to increase the parametric gain, so it is useful to include the effects of focusing and crystal double refraction in the analysis. While a more rigorous treatment of parametric interactions in the presence of gaussian beams, double refraction, and focusing is beyond the scope of this treatment, for convenience the expressions for the parametric gain factor Γ are summarized in Table 1. The expressions may be derived using a similar analysis to that in the plane-wave limit by including the gaussian transverse dependence of the pump, signal, and idler beams in the coupled-wave equations.[10–12] The solution of the modified coupled-wave equations, in the limit of negligible pump depletion and zero input idler, will then yield the relevant expressions for the gain factor.

Boyd and Ashkin[19] have considered the problem of focusing in the near-field limit. In the case where the crystal length is small compared with the confocal parameters of the interacting beams ($\ell \ll b$), the solution of the coupled-wave equations results in a gain factor represented by Eq. (T1) in Table 1. On the other hand, in the limit of confocally focused beams ($\ell \lesssim b$), the near-field approximation yields Eqs. (T2) and (T3) in Table 1. The near-field analysis has been further extended by Boyd and Kleinman to arbitrary tightly focused beams ($\ell \gtrsim b$) and generalized to include the effects of diffraction and crystal double refraction.[20] The results of their analysis yields a parametric gain factor represented by Eq. (T4) in Table 1. It can be seen that the gain factor in this case is modified from the confocal near-field limit by the gain reduction factor $\bar{h}_m(B, \xi)$, which includes the double-refraction parameter B and the focusing parameter $\xi = \ell/b$. The exact analysis of Boyd and Kleinman[20] shows that in the absence of double refraction ($B = 0$), the maximum value of $\bar{h}_m(B, \xi) = 1.068$, and hence maximum parametric gain, occurs for $\xi = 2.84$. Under this condition, parametric gains of the same order as the near-field confocal limit are available, and no penalty is incurred in using tightly focused beams. In the presence of double refraction, however, the peak value of $\bar{h}_m(B, \xi)$ rapidly decreases from 1.068 to ~0.1 for increasing values of B from 0 to ~3, thus severely

TABLE 1 Parametric Gain Factor in the Nondepleted Pump Approximation in the Presence of Gaussian Beams, Focusing, and Double Refraction

Arbitrary near-field gaussian beams:

$$\Gamma^2 = \frac{16\pi^2 d_{\text{eff}}^2}{c\varepsilon_0 n_0^2 n_3 \lambda_0^2} (1 - \delta^2)\,(4w_3^2 M^2)\, I_3(0) \tag{T1}$$

where

$$M = \frac{w_1 w_2 w_3}{w_1^2 w_2^2 + w_2^2 w_3^2 + w_1^2 w_3^2}$$

Near-field confocally focused gaussian beams:

$$\Gamma^2 = \frac{16\pi^2 d_{\text{eff}}^2}{c\varepsilon_0 n_0^2 n_3 \lambda_0^2} (1 - \delta^2)\,(4w_3^2 M_{\max}^2)\, I_3(0) \tag{T2}$$

where

$$M_{\max}^2 = \frac{1}{4} \frac{1}{w_1^2 + w_2^2} = \frac{\pi}{4\ell} \frac{n_0}{\lambda_0} (1 - \delta^2)$$

or

$$\Gamma^2 = \frac{16\pi^2 d_{\text{eff}}^2}{c\varepsilon_0 n_0 n_3 \lambda_0^3} (1 - \delta^2)^2 \frac{\pi w_3^2}{\ell}\, I_3(0) \tag{T3}$$

Optimized tightly focused gaussian beams in the presence of double refraction:

$$\Gamma^2 = \frac{16\pi^2 d_{\text{eff}}^2}{c\varepsilon_0 n_0 n_3 \lambda_0^3} (1 - \delta^2)^2\, \bar{h}_m(B, \xi) \frac{\pi w_3^2}{\ell}\, I_3(0) \tag{T4}$$

Note: w_1, w_2, and w_3 are the idler, signal, and pump gaussian beam waists, respectively; $h_m(B, \xi)$ is the gain reduction factor defined in Ref. 20; and $n_1 \sim n_2 \sim n_0$.

hampering parametric gain. The peak values of $\bar{h}_m(B, \xi)$ now also occur for optimum values of ξ lower than 2.84, decreasing to $\xi \sim 1.5$ at $B \sim 3$. However, the analysis also reveals that for a given crystal double refraction, the reduction in gain in moving from optimized tightly focused beams to confocal focusing ($\xi \sim 1$) is no more than ~20 percent. Therefore, the near-field limit is generally a good approximation for the optimization of parametric gain and is applicable to most situations of practical interest.

Phase Matching

It can be seen from Eq. (5) that in the presence of a strong input pump field, the signal and idler fields in the parametric process can experience growth as they propagate through the nonlinear crystal. It is also clear from Eq. (6) that the magnitude of nonlinear gain depends on material parameters such as the refractive index, interaction length, nonlinear coefficient, and the signal and idler wavelengths, as well as the pump intensity at the input to the nonlinear crystal. More important, however, close inspection of Eq. (5) reveals that the amplification of the signal and idler is also strongly dependent on the phase-mismatch parameter Δk. For $\Delta k = 0$, the generated fields experience maximum gain, whereas the growth of the parametric waves is severely hampered by an increase in the magnitude of Δk.

The general functional dependence of $G_2(\ell)$ on Δk can be found in a number of reference texts.[9,10,12,14] In most situations of practical interest, however, we are concerned with small

gains, for which $\Gamma^2\ell^2 \ll (\Delta k\ell/2)^2$. Under this condition, the net single-pass signal gain, given by Eq. (5), is modified to yield a small-signal gain as

$$G_2^{ss}(\ell) \cong \Gamma^2\ell^2\left[\frac{\sin(\Delta k\ell/2)}{(\Delta k\ell/2)}\right]^2 \tag{9}$$

which has a *sinc*^{2} dependence on the $\Delta k\ell/2$, as shown graphically in Fig. 2. Physically, the phase-mismatch parameter $\Delta k = k_3 - k_2 - k_1$ represents the degree of phase velocity mismatch between the pump, signal, and idler as they propagate through the nonlinear medium. In general, because of material dispersion, the three optical fields at different frequencies cannot maintain velocity synchronism, so that usually $\Delta k \neq 0$. Under this condition, the interacting fields periodically step out of phase and interfere constructively and destructively as they travel through the medium. This causes the pump and the parametric fields to exchange energy back and forth, with the net result that the intensity of the generated fields undergoes oscillations with a spatial period known as the *coherence length.* The coherence length is thus a measure of the maximum interaction length over which amplification of the parametric fields can be sustained in the presence of dispersion. Typical values of coherence length range from ~5 μm for visible to ~50 μm for infrared parametric generation in most nonlinear materials.

Clearly, for any meaningful growth of the parametric waves, phase velocity synchronism must be maintained over interaction lengths significantly longer than the coherence length. In fact, in order to exploit the full length of the nonlinear crystal, the necessary length for velocity synchronism must be comparable to or longer than the crystal length. This requirement can be met by exploiting the technique of *phase matching,* which permits the condition $\Delta k = 0$ to be satisfied, thus allowing the coherence length to become infinite, and phase velocity synchronism between the interacting fields to be maintained indefinitely. Under this condition, the signal and idler fields undergo macroscopic amplification over the crystal interaction length, and coherent output at ω_2 and ω_1 can be extracted from the device. The conventional method for achieving phase matching is to use the birefringence of optically anisotropic media to compensate for dispersion.[21,22] An alternative technique, known as *quasi–phase matching,*[15,23] relies on the periodic reversal of the sign of the nonlinear susceptibility tensor along the interaction length to obtain $\Delta k \sim 0$. In practice, this is most commonly achieved by periodic reversal of crystal domains every coherence length by electric field poling through the sample.

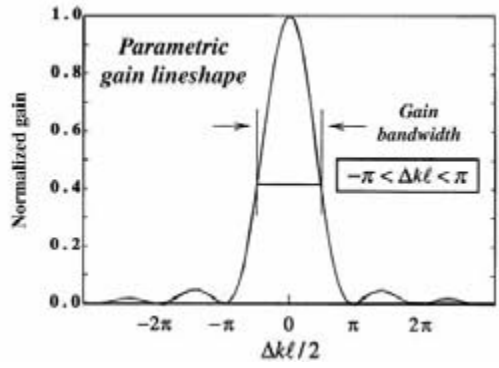

FIGURE 2 The dependence of parametric gain on the phase-mismatch parameter $\Delta k\ell/2$. In analogy to a conventional laser gain medium, the *sinc*^{2} function describes the *gain lineshape* of the parametric amplifier. The full-width at half-maximum gain bandwidth of the amplifier is defined by $|\Delta k\ell| \cong 2\pi$.

Detailed description of birefringent and quasi-phase-matching techniques and the different classifications and types of phase-matching schemes are not within the scope of this treatment and can be found in many other reference texts.[6,9] While birefringence phase matching has been the traditional approach most commonly employed in nonlinear optics, the remarkable success in the development of practical poling techniques in recent years has established quasi–phase matching as a powerful technique with great practical utility in new types of parametric devices.[24] The phase-match condition $\Delta k = 0$ is also the mechanism responsible for frequency tuning of the signal and idler in the parametric generation process. Since for a given crystal temperature and propagation direction, the phase-match condition $\Delta k = k_3 - k_2 - k_1$ may be satisfied only for one combination of frequencies (ω_3, ω_2, ω_1), then by altering the dispersion parameters of the material through changes in the crystal orientation or temperature, it is possible to tune ω_2 and ω_1 to new frequencies satisfying Eq. (1), while maintaining the phase-match condition. Alternatively, for a fixed crystal orientation and temperature, pump tuning may be used as a means of altering the signal and idler frequencies. In the case of quasi–phase matching, additional tuning flexibility is also provided by the poling period, where by using several uniform gratings or fanned grating structures on a single crystal, it is possible to achieve frequency tuning through simple mechanical translation of the crystal across the input pump beam.[25]

22.4 OPTICAL PARAMETRIC DEVICES

From the preceding discussion, we may conclude that macroscopic amplification of signal and idler in the parametric generation process can occur only if the phase-match condition $\Delta k \sim 0$ is satisfied. This is almost universally true in all parametric devices of practical interest. We must therefore consider the growth of the signal field under the phase-matched condition by setting $\Delta k = 0$ in Eq. (5). This yields the net single-pass signal gain as

$$G_2(\ell) = \sinh^2(\Gamma\ell) \tag{10}$$

which, for low gains ($\Gamma\ell \lesssim 1$), approximates to

$$G_2(\ell) \cong \Gamma^2\ell^2 \tag{11}$$

and, for high gains ($\Gamma\ell \gg 1$), reduces to

$$G_2(\ell) \cong \tfrac{1}{4}e^{2\Gamma\ell} \tag{12}$$

Therefore, under the phase-match condition ($\Delta k = 0$), the single-pass signal gain has a quadratic dependence on $\Gamma\ell$ in the low-gain limit, whereas it increases exponentially with $2\Gamma\ell$ in the high-gain limit.

Experimentally, the low-gain limit corresponds to parametric generation when using CW or low- to moderate-peak-power pulsed pump sources. As an example, let us consider near-degenerate parametric generation at ~2 μm ($\lambda_2 \sim \lambda_1 \sim 2$ μm) using a 5-W CW Nd:YAG pump laser at 1.064 μm. Taking typical experimental values of $\ell = 10$ mm and a near-optimum confocally focused pump waist radius of $w_3 \sim 20$ μm, typical material parameters, $n_3 \sim n_2 \sim n_1 \sim 1.5$ and $d_{\text{eff}} \sim 3$ pm/V, and assuming no double-refraction, Eq. (T4) in Table 1 yields $\Gamma\ell \sim 0.04$, resulting in a net single-pass power gain, calculated from Eq. (10), of only ~0.2 percent. A similar calculation can be performed for a Q-switched Nd:YAG laser delivering 10-mJ pulses of 10 ns duration. If the beam is focused to a typical beam waist radius $w_3 \sim 1$ mm, with $w_3 \sim w_2 \sim w_1$, then the near-field condition defined by Eq. (T1) in Table 1 yields $\Gamma\ell \sim 0.73$ and a net gain of ~62 percent. Here, we have used a pump beam radius of 1 mm due to considerations of optical damage to coatings or nonlinear material. In experiments involving Q-switched

pump pulses, the large energy fluence associated with such pulses generally prevents the use of tight focusing (see Sec. 22.9). It can thus be seen that both cases correspond to the low-gain limit, with $\Gamma\ell \lesssim 1$, and so Eq. (11) can be readily used as a good approximation for the single-pass gain. However, direct application of this type of single-pass gain to calculations of threshold and efficiency in pulsed nanosecond OPOs requires caution. As will be discussed in more detail in Sec. 22.7, the finite pump pulse duration in this type of OPO allows for only a limited number of round-trips in the cavity, hence presenting an effective *rise-time* loss to the generated waves. Considerations of rise-time loss dictate that for practical OPO cavity lengths of a few centimeters, average single-pass gains per round-trip somewhat larger than the low-gain limit ($\Gamma\ell > 1$) may often be necessary to reach oscillation threshold. Under these conditions, it is more appropriate to use the exact expression for the single-pass gain defined by Eq. (10), or the high-gain limit defined by Eq. (12) for larger gains.

On the other hand, the high-gain limit is valid for parametric generation using high-intensity, pulsed, and amplified laser pump sources. We can similarly consider an example of such an experiment involving a mode-locked and amplified titanium sapphire pump laser at ~1 μm for degenerate parametric amplification at ~2 μm. If the laser produces pulses of 10 μJ energy and 200 fs duration, and the beam is focused to a typical waist radius $w_3 = 15$ μm in a 1-mm crystal, then Eq. (T3) in Table 1 yields $\Gamma\ell \sim 38$, resulting in a net single-pass gain of $\sim 3.1 \times 10^{32}$, as calculated from Eq. (10). It can thus be seen that such an experiment corresponds to the high-gain limit, with $\Gamma\ell \gg 1$, and the single-pass parametric gain can be conveniently approximated by the exponential function represented by Eq. (12).

In the intermediate regime of moderate gain ($\Gamma\ell \gtrsim 1$), however, Eq. (10) must be used directly to obtain the net single-pass gain. Such a regime corresponds to nonamplified, high-repetition-rate, mode-locked laser pump sources. As an example, a typical Kerr-lens mode-locked titanium sapphire laser of 15 nJ pulse energy and 100 fs duration, focused to a 15-μm beam radius in a 1-mm-long crystal, with all other experimental parameters as before, will result in $\Gamma\ell \sim 2$, yielding a net single-pass gain of ~14.5, as calculated from Eq. (10). It should be noted that short crystal lengths of ~1 mm are typical in experiments involving femtosecond pulses. Here, the temporal synchronism (or *group velocity walkoff*) between the pump, signal, and idler imposes an additional upper limit (in addition to spatial walkoff) to the useful interaction length available for parametric generation (see Sec. 22.9). The short crystal length, together with considerations of optical damage, in turn set an upper limit to the strongest focusing that can be used in practice, so that the near-field confocal limit is generally a good approximation in such experiments.

22.5 OPTICAL PARAMETRIC OSCILLATORS

Of the different types of parametric devices studied and developed to date, the considerable majority conform to the low- to moderate-gain operating limit. This is the regime most frequently encountered in practice when commonly available laser pump sources and nonlinear materials are deployed. From the preceding discussion, it may be concluded that the small-signal gains available in such devices are on the order of 0.1 to 1000 percent for typical nonlinear materials and pumping intensities. Clearly, such gains are not sufficient to achieve macroscopic amplification of parametric waves from noise in a single pass through the nonlinear crystal. Therefore, the majority of parametric devices of this type are operated in an oscillator configuration, as in a conventional laser, by enclosing the nonlinear gain medium within an optical cavity to provide feedback at the generated waves. In this way, the amplification of parametric waves to macroscopic levels is achieved by successive passes through the nonlinear crystal, and coherent output can be extracted from the oscillator. This type of device is known as an *optical parametric oscillator* (OPO).

The high-gain limit, on the other hand, corresponds to devices where the available nonlinear gains are large enough to permit macroscopic amplification of the parametric waves in a

few passes through the nonlinear crystal. These types of devices, which do not require optical cavities for the attainment of discernible output, are generally referred to as *optical parametric generators* (OPGs) and *amplifiers* (OPAs). In this treatment, we are concerned mainly with a description of OPO devices and their operating characteristics. While many of the design criteria and operating principles are equally applicable to OPGs and OPAs, more extensive treatments of these devices can be found elsewhere in the literature.[26]

In the discussion of CW OPOs to follow, we also use the plane-wave analysis of parametric interactions. This model is valid when the sizes of the interacting beams are comparable to the crystal length and the effects of double refraction can be ignored. Although this may not always be the case in practice, the plane-wave model adequately describes the essential features of the parametric generation process and provides the fundamental criteria for the design and optimum operation of parametric devices with good accuracy.

The successful operation of an OPO necessitates the attainment of sufficient gain at the parametric waves, for a given pump power, to overcome parasitic losses in the cavity. This can be achieved by providing feedback at the generated waves using various configurations of the optical cavity. Figure 3 summarizes the principal cavity geometries that have been explored along with variants developed to address particular issues. Since two downconverted waves are generated within an OPO, the signal and the idler, there is the choice of resonating just one or the other of these two waves [singly resonant oscillator (SRO); see Fig. 3*a*], or to resonate both simultaneously [doubly resonant oscillator (DRO); see Fig. 3*b*]. Insofar as the latter results in two intense fields being present within the nonlinear crystal at the same time, rather than just one as in the former, the threshold of this OPO with regard to required pump power is reduced. However, the issues of both the stability and attainment of smooth tuning

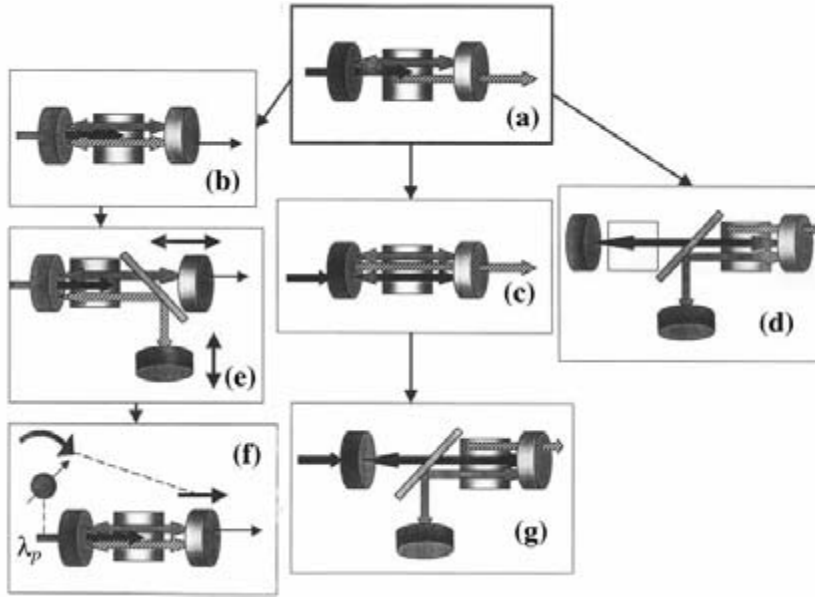

FIGURE 3 Cavity configurations for CW OPOs: (*a*) singly resonant; (*b*) doubly resonant; (*c*) pump enhanced; (*d*) intracavity; (*e*) dual cavity, doubly resonant; (*f*) doubly resonant, with pump tuning; and (*g*) dual cavity, pump enhanced. Black, gray, and striped arrows indicate pump, signal, and idler waves, respectively. Nonlinear media and gain media are shown by darker and lighter shading, respectively.

in such a doubly resonant cavity arise. An alternative approach is based on retaining just one intense downconverted wave in the cavity (i.e., an SRO), but now using a resonance to increase the pump wave intensity within the nonlinear medium. There are two approaches as to how this might be done. One is based on using a pump enhancement cavity to resonate the pump wave, from a separate pump laser, within the nonlinear medium [pump-enhanced singly resonant oscillator (PESRO); see Fig. 3*c*]. The other involves placing the nonlinear medium within the cavity of the pump laser itself, where there is a high circulating intensity [intracavity singly resonant oscillator (ICSRO); see Fig. 3*d*]. Other options, that we will consider briefly later, include a DRO with pump enhancement, leading to a triply resonant oscillator (TRO), or a DRO placed within the cavity of the pump laser (ICDRO).

22.6 CONTINUOUS-WAVE OPTICAL PARAMETRIC OSCILLATORS

The operation of a CW OPO was first reported in 1968 in the nonlinear crystal barium sodium niobate.[27] Operation of this device was confined to the near infrared. This was soon followed by operation in the visible, in both standing-wave and traveling-wave devices based on $LiNbO_3$.[28,29] Progress toward practical devices was slow in the early years following these demonstrations. However, the advent of improved pump lasers, in particular those based on diode-laser-pumped solid-state gain media, along with new nonlinear materials, in particular the new QPM materials such as PPLN, has resulted in accelerating progress in this area in the last five years or so. Improved pump lasers and nonlinear materials allow a wide variety of cavity geometries to be explored for CW OPOs, and this section is structured around such options. We first consider the SRO and DRO options, starting with an analysis of threshold conditions and conversion efficiencies.

Steady-State Threshold in SROs and DROs

In these analyses we assume the following conditions apply: (1) plane waves for all three waves, pump, signal, and idler; (2) single pass of the pump through the nonlinear crystal so that downconversion takes place only in the forward direction; (3) phase-matched interaction ($\Delta k = 0$); (4) negligible pump depletion through the nonlinear crystal (appropriate close to threshold). Under these conditions, only the first two coupled-wave equations, Eqs. (4*a*) and (4*b*) for the signal and idler waves, are required, and E_3 may be assumed constant throughout the length of the nonlinear medium.

Singly Resonant Oscillator. In this arrangement only one of the downconverted waves is resonant in the nonlinear medium, and we assume it to be the signal wave. We further assume that the idler wave leaves the nonlinear medium after a single pass. Since the pump is propagating only in the forward direction through the medium, parametric gain occurs for propagation of the signal in this direction only. We further assume that the losses of the signal wave from the cavity (described by α_2, the round-trip fractional power loss at the signal) are small, so that to a first approximation we may assume the signal wave (electric field) to be constant throughout the nonlinear medium. Hence, the coupled-wave equation Eq. (4*a*) for the change of the idler field with propagation through the nonlinear medium becomes

$$\frac{dE_1}{dz} = \left[\frac{id_{\text{eff}}\omega_1}{(cn_1)}\right] E_3 E_2^* = \text{constant} \tag{13}$$

Hence, the electric field of the idler wave grows linearly with distance (Z axis) through the nonlinear crystal, starting from zero at the input face of the crystal since the idler wave is not back-reflected, according to

$$E_1(z) = i\kappa_1 E_3 E_2^* z \tag{14}$$

The preceding expression can now be substituted into the coupled-wave equation for the signal wave (Eq. 4*b*) to give the increment in the electric field of the signal wave on propagation through the nonlinear medium as

$$\frac{\delta E_2}{E_2} = \frac{\kappa_2 \kappa_1 E_3 E_3^* \ell^2}{2} \tag{15}$$

where ℓ is the length of the nonlinear medium. Using the relation between increment in electric field and increment in intensity, namely $\delta I_2/I_2 = 2\delta E_2/E_2$, the increment in the intensity of the signal wave after propagation through the nonlinear medium can hence be calculated as

$$\frac{\delta I_2}{I_2} = \kappa_2 \kappa_1 \ell^2 (E_3 E_3^*) \tag{16}$$

This may be written in terms of the pump intensity using the relation

$$E_3 E_3^* = \frac{2 Z_o I_3}{n_3} \tag{17}$$

where $Z_o = (\mu_o/\varepsilon_o)^{1/2}$ is the permittivity of free space, when we obtain

$$\frac{\delta I_2}{I_2} = \frac{2 Z_o \kappa_2 \kappa_1 \ell^2 I_3}{n_3} \tag{18}$$

The fractional round-trip gain in intensity given by the preceding is now equated to the fractional round-trip loss in intensity, given by $\alpha_2 I_2$, where α_2 is the fractional round-trip power loss for the signal wave. The threshold condition hence becomes

$$\frac{2 Z_o \kappa_2 \kappa_1 \ell^2 I_3}{n_3} = \alpha_2 \tag{19}$$

On substitution of the values for κ_2 and κ_1 in the preceding, we obtain the following expression for the SRO threshold:

$$\frac{2 Z_o \omega_2 \omega_1 \ell^2 d_{\text{eff}}^2 I_{\text{th}}}{(c^2 n_3 n_2 n_1)} = \alpha_2 \tag{20}$$

An alternative form of the preceding is

$$\frac{8\pi^2 \ell^2 d_{\text{eff}}^2 I_{\text{th}}}{(c\varepsilon_o n_3 n_2 n_1 \lambda_2 \lambda_1)} = \alpha_2 \tag{21}$$

where I_{th} is the pump intensity required to reach oscillation threshold, and λ_2 and λ_1 are the free-space wavelengths of the signal and idler waves, respectively.

Doubly Resonant Oscillator. In this case, both the signal and the idler waves experience small fractional power losses on each round-trip, and so each may be considered to be constant throughout the length of the nonlinear medium when calculating the increment in the other. Further, since we are considering operation close to threshold, we assume that both the signal and idler fields, even though resonant, are much smaller than the pump field. In this case, any backconversion in the absence of the pump, which would occur on backward propagation of these fields through the nonlinear medium, may be ignored. This allows the changes in the electric fields of each wave per round-trip to be calculated as

$$\delta E_2 = i\kappa_2 E_3 E_1^* \ell \tag{22a}$$

$$\delta E_1 = i\kappa_1 E_3 E_2^* \ell \tag{22b}$$

Under optimum relative phasing between the interacting waves, the increment in the electric field of one or other of the down converted waves is in phase with the existing field associated with that wave (see Sec. 22.2). In this case, the following relation between increment in electric field and increment in intensity applies:

$$\delta I = \left(\frac{n}{Z_o}\right) |E|\,|\delta E| \tag{23}$$

Using this relation and also equating round-trip gain to round-trip loss of intensity, the following are readily obtained:

$$\delta I_2 = \left(\frac{n_2}{Z_o}\right) |E_3|\,|E_2|\,|E_1|\kappa_2 \ell = \alpha_2 I_2 \tag{24a}$$

$$\delta I_1 = \left(\frac{n_1}{Z_o}\right) |E_3|\,|E_2|\,|E_1|\kappa_1 \ell = \alpha_1 I_1 \tag{24b}$$

Taking the product of these two equations and evaluating the fields in terms of their intensities, we obtain for the threshold of the DRO the following expression:

$$\frac{2Z_o\omega_2\omega_1\ell^2 d_{\text{eff}}^2 I_{\text{th}}}{(c^2 n_3 n_2 n_1)} = \frac{\alpha_2\alpha_1}{4} \tag{25}$$

or the alternative form:

$$\frac{8\pi^2\ell^2 d_{\text{eff}}^2 I_{\text{th}}}{(c\varepsilon_o n_3 n_2 n_1 \lambda_2 \lambda_1)} = \frac{\alpha_2\alpha_1}{4} \tag{26}$$

Hence, we see that the threshold of the DRO, when compared to that of SRO, is reduced by a factor of $(\alpha_1/4)$. In the case when low loss cavities are being considered, the substantial reduction in threshold of the DRO compared to the SRO is apparent. For example, if the additional resonance has an associated round-trip power loss of 0.04 (4 percent), then threshold, in terms of required pump power, is reduced a hundredfold.

Conversion Efficiency in SROs and DROs

Doubly Resonant Oscillator. We now analyze the downconversion efficiency of the CW DRO as a function of pump power and, in particular, explore those processes limiting maximum attainable efficiency in a number of geometries. Our analysis throughout is limited to the case of plane waves, with uniform intensity across a wavefront, although we will review the consequences of deviating from this condition, for example in the case of gaussian beams. We first analyze the case when there is no backconversion of the signal and idler waves so as to regenerate the pump wave. Backconversion will always occur in a standing-wave cavity through which the pump wave propagates in one direction only. In this case, the backward-traveling signal and idler waves are unaccompanied by a pump wave, and hence they can regenerate the pump wave through sum-frequency mixing as they return through the nonlinear medium. In a traveling-wave cavity, on the other hand, the pump wave always accompanies the propagation of the signal and idler waves through the nonlinear medium, since backward-propagating signal and idler waves are now absent. Our analysis is therefore more appropriate to this latter case of the traveling-wave cavity. However, backconversion will still need to be considered even in this case if the pump wave is totally depleted

before it leaves the nonlinear medium. The efficiency of the traveling-wave DRO was first analyzed in 1969.[30]

If the losses of the doubly resonant cavity for both signal and idler waves are assumed to be small and if optimum phasing between the three fields is maintained (through phase matching), then the field amplitudes of both these waves may be assumed constant throughout the cavity length. Hence, we can write

$$\frac{dE_3}{dz} = i\kappa_3 E_2 E_1 = \text{constant} \tag{27}$$

and

$$E_3 \sim i\kappa_3 E_2 E_1 z \tag{28}$$

If the relative phases between the fields are appropriate to maximum downconversion (see Sec. 22.2), the preceding expression may be evaluated between the input face and the output face of the nonlinear medium (of length ℓ), to obtain

$$|E_{3,\,\text{in}} - E_{3,\,\text{out}}| = \kappa_3 |E_2|\,|E_1|\ell \tag{29}$$

where $E_{3,\,\text{in}}$ and $E_{3,\,\text{out}}$ are the pump field amplitudes at the input to and output from the crystal. The preceding may now be written in terms of the associated intensities of the various waves as

$$(I_{\text{in}})^{1/2} - (I_{\text{out}})^{1/2} = \kappa_3 \left[\frac{2Z_o n_3}{(n_2 n_1)}\right]^{1/2} (I_2)^{1/2}(I_1)^{1/2}\ell \tag{30}$$

where I_{in} and I_{out} are the pump intensities at the input to and the output from the nonlinear medium, respectively. In the process of downconversion, one pump photon creates one idler photon and one signal photon, and hence we can write

$$\begin{aligned}\text{Total loss rate of signal photons} &= \left[\frac{\alpha_2 I_2}{(\hbar\omega_2)}\right] \\ &= \text{total loss rate of idler photons} = \left[\frac{\alpha_1 I_1}{(\hbar\omega_1)}\right] \\ &= \text{total loss rate of pump photons} = \left[\frac{I_{\text{out}} - I_{\text{in}}}{(\hbar\omega_3)}\right]\end{aligned} \tag{31}$$

where α_2 and α_1 are the round-trip total fractional power losses of the signal and idler waves, respectively. We can use the preceding relations to substitute for the idler and signal intensities in Eq. (30) in terms of the pump intensities, and hence obtain an equation relating the pump output intensity to the pump input intensity. After some rearrangement of this equation, and using the threshold equation for the DRO, Eq. (26), we finally obtain

$$I_{\text{out}} = [(4I_{\text{th}})^{1/2} - (I_{\text{in}})^{1/2}]^2 \tag{32}$$

The total downconverted pump intensity may be calculated from the preceding as

$$I_{\text{DC}} = [I_{\text{in}} - I_{\text{out}}] = 4(I_{\text{th}})^{1/2}[(I_{\text{in}})^{1/2} - (I_{\text{th}})^{1/2}] \tag{33}$$

Thus, we conclude that in a DRO in the absence of backconversion (i.e., in a ring cavity geometry), 100 percent pump depletion (and hence 100 percent internal downconversion) occurs when the input pump intensity is 4 times that at threshold. The analysis, as presented, holds only up to the point where the pump intensity just reaches zero at the output face of the non-

linear medium. If the input pump intensity is further increased, then the pump wave will be totally depleted at some point within the crystal. In the remaining length of the crystal, the signal and idler waves are then able to regenerate the pump through sum-frequency mixing. As a result, pump intensity once again now exits the crystal, and the downconversion efficiency is reduced. There is hence an optimum value of the pump intensity, which we have shown to be 4 times threshold, and which we have shown to yield 100 percent downconversion. In fact, it may be shown with some additional analysis that the expressions given are valid also in this latter situation in which pump light is regenerated during forward propagation.

In the case of a standing-wave cavity and where the pump wave is a traveling wave passing through the nonlinear medium only in the forward direction, the pump wave is regenerated through sum-frequency mixing of the signal and idler waves on their backward propagation through the nonlinear medium. A component of the pump wave is reflected from the nonlinear medium, which hence limits the downconversion efficiency. We can readily extend the preceding analysis to include the backward regeneration of the pump wave. Applying Eq. (30) to the backward-propagating signal and idler waves, the intensity of the backward-regenerated pump wave may be shown to be

$$I_{\mathrm{BC}} = \frac{2Z_o\kappa_3^2\ell^2 n_3 I_2 I_1}{(n_2 n_1)} \tag{34}$$

In addition, we now write photon conservation (power conservation) so as to allow for the backward-generated pump wave as follows:

$$\frac{\alpha_2 I_2}{(\hbar\omega_2)} = \frac{\alpha_1 I_1}{(\hbar\omega_1)} = \frac{[I_{\mathrm{in}} - I_{\mathrm{out}}]}{(\hbar\omega_3)} - \frac{I_{\mathrm{BC}}}{(\hbar\omega_3)} \tag{35}$$

In this way, we obtain the following expression for the downconverted intensity:

$$I_{\mathrm{DC}} = 2(I_{\mathrm{th}})^{1/2}[(I_{\mathrm{in}})^{1/2} - (I_{\mathrm{th}})^{1/2}] \tag{36}$$

From this we see that maximum downconversion still occurs when pumping at 4 times the threshold intensity, but now this maximum is limited to only 50 percent of the incident intensity because of the backconversion. This backconversion leads to regeneration of the pump wave in the counterpropagating direction, which hence appears as a reflected component of the pump wave. Using Eqs. (34) and (35), the intensity of this wave can readily be shown to be

$$I_{\mathrm{BC}} = [(I_{\mathrm{in}})^{1/2} - (I_{\mathrm{th}})^{1/2}]^2 \tag{37}$$

We can then calculate the transmitted intensity of the pump wave I_{out} explicitly as

$$I_{\mathrm{out}} = I_{\mathrm{th}} \tag{38}$$

From the preceding equations we may draw the following important conclusions regarding the behavior of the standing-wave DRO when operating above threshold. First of all, the OPO acts as an intensity (or power) limiter in that the transmitted pump intensity is clamped to the threshold intensity no matter how much the input pump intensity is increased. Second, the maximum downconversion efficiency is limited to 50 percent, this being reached at 4 times threshold pumping. Third, as the input pump intensity is progressively increased, an increasing fraction of it is back-reflected from the OPO, rather than being either transmitted or downconverted. These important conclusions were first drawn by Siegman in a classic 1962 paper in which the DRO was first analyzed with respect to efficiency.[31]

In another classic paper in 1970, Bjorkholm et al. considered the consequences of double-passing the pump wave through the standing-wave DRO.[32] If the pump wave is reflected back through the medium by a mirror of unity reflectivity, then the threshold of the OPO may be reduced by a factor of 4 (equivalent to doubling the length of the nonlinear medium), and 100

percent downconversion efficiency may be attained, again at 4 times the (new and reduced) threshold intensity. However, since the downconversion process is dependent on the relative phases of the three interacting waves, optimum phasing (see Sec. 22.2) must be maintained between these waves on their back-reflection. This requires some care with regard to mirror design, or for a separate mirror to be employed for one or another of the three waves.

Singly Resonant Oscillator. In the singly resonant OPO and for the situation in which the round-trip losses of the resonant wave (the signal wave, say) are small, we can treat the complex field amplitude of this wave as being constant throughout the length of the nonlinear medium. However, the nonresonant idler wave grows from zero at that end of the medium where the pump wave enters, and exits at the far end after a single pass. We assume that the pump wave transits the nonlinear medium only in the forward direction, so that the idler wave is generated only in this direction. Since only the resonant signal wave returns through the nonlinear medium, the pump-wave regeneration on backward propagation does not arise here. Since in this case the idler wave is generated from zero at the beginning of the medium, a phase relation between the waves appropriate to maximum downconversion is acquired from the start (see Sec. 22.2), and, with phase matching, is maintained throughout the nonlinear process. The propagation of the pump wave is hence described by

$$\frac{dE_3}{dz} = i\kappa_3 E_2 E_1 \tag{39}$$

where E_2 is a constant. We also require the equation describing the propagation of the idler wave, which is

$$\frac{dE_1}{dz} = i\kappa_1 E_3 E_2^* \tag{40}$$

where E_2^* is similarly constant. To proceed, we differentiate the first of the preceding two equations with respect to distance z, and then use the second equation to eliminate the idler wave field amplitude, so as to obtain

$$\frac{d^2E_3}{dz^2} = -\kappa_3\kappa_1(E_2E_2^*)E_3 = -\left(\frac{2Z_o\kappa_3\kappa_1 I_2}{n_2}\right)E_3 \tag{41}$$

This harmonic oscillator–type equation may now be integrated to give

$$E_3 \sim A \sin(\Omega z) + B \cos(\Omega z) \tag{42}$$

where

$$\Omega = \left[\frac{2Z_o\kappa_3\kappa_1 I_2}{n_2}\right]^{1/2} \tag{43}$$

Applying the boundary conditions that at the entrance to the nonlinear crystal ($z = 0$), both E_1 and hence also (dE_3/dz) are zero, and using Eq. (35) to write the signal intensity I_2 in terms of the change in the pump intensity, we finally obtain

$$I_{\text{out}} = I_{\text{in}} \cos^2\left[\left(\frac{I_{\text{in}} - I_{\text{out}}}{I_{\text{th}}}\right)^{1/2}\right] \tag{44}$$

where I_{th} is the pump intensity required to bring the SRO to threshold, and was derived previously [see Eq. (21)]. The condition for 100 percent downconversion (total depletion of the pump, $I_{\text{out}} = 0$) is hence

$$I_{\text{in}} = \left(\frac{\pi}{2}\right)^2 I_{\text{th}} = 2.47 I_{\text{th}} \tag{45}$$

An analysis of the SRO with regard to efficiency was first reported by Kreuzer,[33] who identified the preceding condition for optimum downconversion. In 1970, Bjorkholm et al.[32] considered further aspects. They showed that the threshold could be halved in a standing-wave configuration by double-passing the pump wave through the nonlinear medium. However, they further showed that the attainment of the maximum efficiency of 100 percent still required the same absolute pump intensity as when the pump passed through the nonlinear medium only in the forward propagation direction (i.e., 2.47 times the threshold intensity for single passing of the pump wave). They also showed that the threshold could be reduced by a factor of 4 overall if both the pump wave and the nonresonant wave were to be double-passed through the nonlinear medium. However, to achieve this reduction the appropriate relative phases between the three waves must be maintained on reflection. [If optimum phase relations are maintained, the procedure is equivalent to doubling the length of the nonlinear medium, and from Eq. (21) a factor of 4 reduction in threshold is to be expected.]

More recently, Breitenbach et al.[34] have reported a systematic study of down-conversion efficiency in a DRO in which the pump wave was double-passed through the nonlinear medium. Based on MgO:$LiNbO_3$ as the nonlinear medium, pumped at 532 nm by a frequency-doubled Nd:YAG laser, a threshold of 28 mW was reported. At 4 times threshold a pump depletion of 95 percent was obtained, as expected. The paper also includes a comprehensive extension of the theory to the more realistic case of gaussian beam profiles for the interacting waves, rather than the plane-wave assumption that has been the basis of the discussion here.

In considering particular OPO devices shortly, experimentally determined OPO efficiencies, where reported, will be related to the previous discussion. Table 2 summarizes thresholds and efficiencies for both SROs and DROs in a variety of configurations.

Tuning Behavior and Stabilization of DROs and SROs

In the previous section concerning the thresholds and efficiencies of both SROs and DROs, the advantage of the latter in terms of a much reduced threshold compared to the former

TABLE 2 Theoretical Thresholds and Efficiencies of Various CW OPO Configurations

	Configuration						
	Singly resonant type				Doubly resonant type		
	Standing-wave cavity			Ring cavity	Standing-wave cavity		
	Single-pass pump	Double-pass pump					
Parameter	SP NR wave	SP NR wave	DP NR wave	SP NR wave	Single-pass pump	Double-pass pump	Ring cavity
Threshold	I_o	$\frac{I_o}{2}$	$\frac{I_o}{4}$	I_o	$\frac{\alpha I_o}{4}$	$\frac{\alpha I_o}{16}$	$\frac{\alpha I_o}{4}$
Max. efficiency	100%	100%	100%	100%	50%	100%	100%
Pump intensity	$2.46\, I_o$	$2.46\, I_o$	$\frac{2.46\, I_o}{4}$	$2.46\, I_o$	αI_o	$\frac{\alpha I_o}{4}$	αI_o
Phase	X	X	✓	X	X	✓	X

Note: SP = single pass; DP = double pass; NR = nonresonant; I_o = pump intensity to reach threshold in an SRO with single-pass pump and nonresonant wave; α = round-trip power loss of second resonator.

becomes apparent. However, stabilization and tuning, particularly smooth single-frequency tuning, are also important considerations. We now present a comprehensive introduction to the principles involved, in particular contrasting the behavior of DROs and SROs in these respects. Such considerations will provide a perspective to the progress that has been made in the development of practical devices.

The crux of the matter lies in the resonance requirements associated with the signal and idler waves within the two configurations. In addition to these resonance conditions, there are also the twin constraints of phase matching (which may be regarded as a manifestation of momentum conservation) and frequency conservation between the pump, signal, and idler waves (which may be regarded as a manifestation of energy conservation at the single-photon level). These ideas can be most simply understood from a frequency diagram, as shown in Fig. 4, the principles behind which we now discuss.

If we first consider the situation with regard to the generic DRO cavity as shown in Fig. 3*b,* then the resonance conditions for the signal and idler waves that must be simultaneously satisfied in this case are as follows:

$$\nu_2 = \frac{q_2 c}{[2L + 2(n_2 - 1)\ell]} \tag{46a}$$

$$\nu_1 = \frac{q_1 c}{[2L + 2(n_1 - 1)\ell]} \tag{46b}$$

where (q_2, q_1) are a pair of integers defining a particular signal and idler mode pair of the common cavity of length L. Since the nonlinear medium, of length ℓ, in general exhibits different refractive indexes to the signal and idler waves, the effective optical lengths of this cavity as exhibited to the two waves are different, which accounts for the different denominators in the preceding expressions. As a result, the free spectral ranges of the cavity as experienced by the signal and idler waves are different, being given as usual by

$$\Delta\nu_2 = \frac{c}{[2L + 2(n_2 - 1)\ell]} \tag{47a}$$

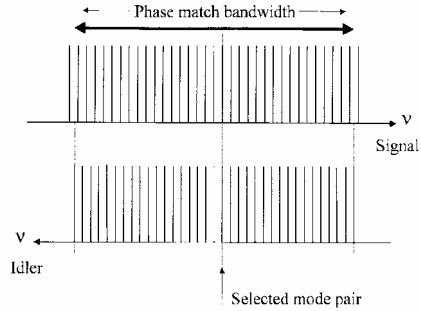

FIGURE 4 Signal and idler mode spectrum in a doubly resonant oscillator. At all points across the diagram the sum of the signal and idler frequencies is equal to the pump frequency. The slightly different free spectral ranges between the signal and idler modes means, in this example, that only one mode pair within the phase-match bandwidth, as indicated, can resonate.

$$\Delta\nu_1 = \frac{c}{[2L + 2(n_1 - 1)\ell]} \tag{47b}$$

respectively. [Note that in Eqs. (47*a*) and (47*b*) we have neglected the frequency dependence of the refractive indexes, which if included do modify the values for the free spectral ranges. In many cases the changes are not negligible, but need not concern us further here.] From our energy conservation condition, Eq. (1), we also require that $\nu_3 = \nu_2 + \nu_1$. We also require that for the down conversion process to take place efficiently, the three fields involved satisfy phase matching. There are thus four constraints placed on the operation of the DRO.

These may be summarized in a frequency diagram (Fig. 4). In this diagram, frequency is displayed on horizontal scales. The signal and idler modes are displayed as vertical lines, corresponding to the resonance conditions stated above, but lines for the adjacent modes have different frequency spacings in the case of the signal and idler modes because of the different free spectral ranges associated with these modes. In order to satisfy the frequency conservation condition, we plot the frequency scale for the signal modes, say, increasing from left to right, and the frequency scale for the idler modes correspondingly increasing from right to left. We can then arrange that at any point along these scales the sum of the signal and idler frequencies is equal to the pump frequency. The phase-matching requirement defines an envelope within which the mode pairs must lie in order to reach oscillation threshold.

It is apparent from the preceding discussion that if the pump frequency is changed, then one frequency scale (say, the signal scale) slides over the other frequency scale (the idler scale) so as to continue to satisfy $\nu_3 = \nu_2 + \nu_1$. However, the mode frequencies (the vertical lines) stay attached to their respective scales in this case, since the mode frequencies are not themselves altered by the process. As the pump frequency is changed, the center frequency of the phase-match envelope may also change, in a manner that can be calculated from the appropriate dispersion relations. Indeed, the envelope center may move much further in frequency than the change in the pump frequency itself.

If, however, the cavity length is changed, then the mode frequencies themselves change relative to what are now fixed frequency scales. The changes in the signal and idler mode frequencies for a change in the cavity length of δL are given by the usual expressions, obtained by appropriate differentiation of Eq. (46), namely

$$\delta\nu_2 = -\frac{\nu_2 \delta L}{[2L + 2(n_2 - 1)\ell]} \tag{48a}$$

$$\delta\nu_1 = -\frac{\nu_1 \delta L}{[2L + 2(n_1 - 1)\ell]} \tag{48b}$$

Thus, if the cavity length is increased, say, then both the signal mode frequencies and the idler mode frequencies decrease. In terms of the diagram in Fig. 4, it means that the signal modes move to the left against their frequency scale, and the idler modes move to the right against their frequency scale. If the length change is not too great, the free spectral ranges of either set of modes is little affected, so that each set of modes moves as a whole, with the spacings between adjacent modes of either set remaining unaltered.

The criterion for a particular signal and idler mode pair (given set of *q*s) to oscillate in a doubly resonant cavity is that the modes of the pair must line up, one under the other, in the diagram, and this must occur under the phase-matching envelope, preferably toward the center of this envelope for maximum gain. We can hence deduce the following. First, because of the different free spectral ranges associated with the idler and signal mode sets, when we arrange for one mode pair to line up, the other mode pairs in general will not (similar to the operation of a vernier). Hence, we deduce that the DRO has the potential for strong frequency selection to the single mode-pair level (single frequency signal, single frequency

idler), a very useful attribute if it can be exploited. We can arrange for a particular mode pair to line up either by adjusting the pump frequency or by adjusting the cavity length. However, if having done so we now alter the cavity length with the intent of smoothly tuning the frequencies of the selected mode pair in the usual manner, we will find that this will not happen. The alignment between the chosen signal and idler mode pair will not be maintained, since one mode of the selected pair will move toward one side of the diagram, while the other mode will move toward the other side of the diagram. In general, a condition is likely to appertain where no mode pairs line up under the phase-match bandwidth for an arbitrary spacing of the mirrors—in other words, the OPO ceases to oscillate. So although the DRO has the important attribute of specific mode-pair selection, it lacks the capability of smooth frequency tuning through the adjustment of a single parameter.

We now consider the nature of the tuning that does take place on altering the cavity length, and thereby introduce the ideas of mode hopping and cluster hopping. We also discuss the stability requirements placed on the cavity length and the frequency of the pump if selection of a specific signal and idler mode pair is to be maintained.

The two types of behavior on cavity length tuning are contrasted in Figs. 5 and 6. When the difference in free spectral range between signal and idler cavities compared to the phase-match bandwidth is as shown in Fig. 4, then the mode pair for which the signal and idler mode frequencies are closest to summing to the pump frequency is immediately adjacent to the selected mode pair (where, of course, the mode frequencies sum exactly to the pump frequency). It therefore follows that on changing the length of the common cavity, which causes one set of modes to slip relative to the other set of modes, the coincidence condition will move to this adjacent mode pair, as shown in detail in Fig. 5. This is referred to as a *mode hop,* and both the signal and idler mode frequencies will change by one free spectral range of the common cavity; one increasing, one decreasing. It is also apparent that if the length of the cavity continues to be changed, repeated mode hopping will continue until the coincident mode pair exits the phase-match bandwidth.

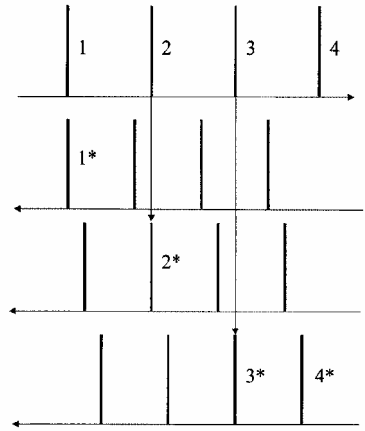

FIGURE 5 Mode hopping. As the cavity length (or pump frequency) is progressively changed, the signal and idler modes are progressively displaced relative to one another. The selected mode pair then hops from one adjacent mode pair to the next, as shown.

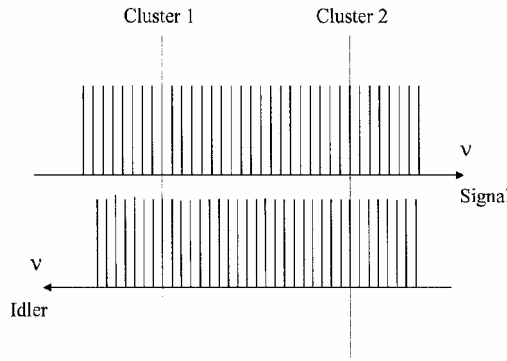

FIGURE 6 Cluster hopping. The difference in the free spectral ranges of signal and idler cavities is such that two near coincidences of mode pairs (clusters) occur within the phase-match bandwidth. On changing the cavity length, the mode pair that is actually selected is likely to hop from one cluster to the other, and then back again.

However, as Fig. 6 shows, if either the difference in free spectral range or the phase-match bandwidth is increased, then a different situation appertains. The mode pair for which the signal and idler frequencies are closest to summing to the pump frequency (after the exact summation associated with the currently selected mode pair) is now well removed from this currently selected mode pair. On changing the cavity length, the frequencies of both the signal and the idler will hence hop many free spectral ranges, the exact number depending on the particular circumstances. This effect is referred to as *cluster hopping.*

An estimate of the frequency interval associated with a cluster hop can readily be obtained by a consideration of the diagrams. The number N of free spectral ranges associated with a cluster hop is such that the accumulated frequency difference between signal and idler modes is equal to a free spectral range. The frequency difference encountered per free spectral range is just equal to the frequency difference between the signal and idler free spectral ranges, given by

$$\Delta\nu = \Delta\nu_2 - \Delta\nu_1 \tag{49}$$

Hence

$$N = \frac{\Delta\nu_2}{\Delta\nu} \tag{50}$$

So the frequency interval for a cluster hop becomes

$$\Delta\nu[\text{cluster}] = \frac{(\Delta\nu_2)^2}{\Delta\nu} \tag{51}$$

(Since the signal and idler free spectral ranges are very nearly equal, either may be substituted into the preceding expression.)

For a cluster hop to be possible, this value must be less than the phase-match bandwidth. Alternatively, if the phase-match bandwidth is kept below the cluster hop interval, then the more systematic behavior of mode hopping is likely to take place. It will have become apparent from the preceding discussion that the tuning behavior under conditions where cluster

hopping can occur can be quite complex. Different combinations of mode and cluster hopping can arise depending on the exact values of the various parameters involved. From the point of view of ease of selection and tuning, a situation where there is only one cluster under the phase-match bandwidth is to be preferred.

We now go on to consider stability requirements with regard to the operation of the DRO. So far we have treated cavity modes as lines in the frequency diagram, implying an infinitely narrow range over which coincidence can occur between signal and idler mode resonances. In practice, the cavity exhibits a finite resonance linewidth dependent on the finesse of the cavity, namely

$$\Delta\nu[\text{resonance}] = \frac{\Delta\nu_2}{F_2} \tag{52}$$

where the width is the half width to half maximum, and F_2 is the finesse, which is given by

$$F_2 = \frac{2\pi[1 - (\alpha_2/2)]^{1/2}}{\alpha_2} \tag{53}$$

where α_2 is the round-trip power loss of the cavity. For doubly resonant oscillation to be maintained, the coincidence of the signal mode and the idler mode must be to within the resonance linewidths, as shown in Fig. 7. Hence, we deduce that the pump frequency must be stable to better than

$$\Delta\nu[\text{pump}] = \pm\Delta\nu_2\left(\frac{1}{F_2} + \frac{1}{F_1}\right) \tag{54}$$

and, bearing in mind that a cavity mode tunes through one free spectral range of the cavity for a length change of one half a wavelength, we deduce that the length of the cavity must be stable to better than

$$\Delta L[\text{cavity}] = \pm\left(\frac{\lambda_3}{2}\right)\left(\frac{1}{F_2} + \frac{1}{F_1}\right) \tag{55}$$

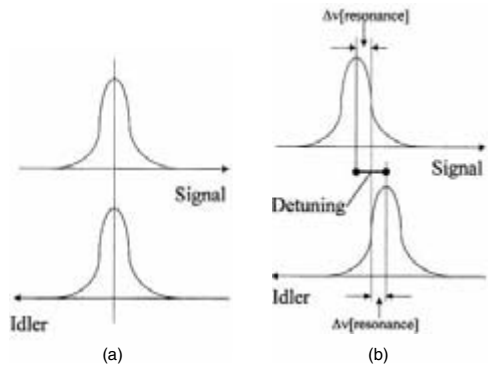

FIGURE 7 (*a*) Perfect coincidence of the signal and idler cavity resonances ensures oscillation with low threshold. (*b*) The detuning is such that coincidence occurs halfway down the resonance curve for each cavity, and the oscillation threshold will be accordingly increased.

if oscillation is to be maintained on the selected signal and idler mode pair. Given that cavity finesses are typically of the order of 200 to 300 in the case of DROs with low thresholds, it is apparent that these stability requirements are stringent ones. Cavity lengths must be held stable to tolerances on the order of $\lambda_3/400$ to $\lambda_3/600$ (i.e., on the order of 2 nm), and pump frequency on the order of several hundred megahertz. For this reason, well-designed servocontrol systems are required.

A further important consideration in relation to both stabilization and tuning is how well-defined a particular signal and idler mode coincidence is as the cavity length is scanned. In Fig. 8*a,* where the difference in free spectral range between signal and idler cavities $\Delta\nu$ is greater than the sum of the cavity bandwidths, it is apparent that on changing the cavity length, the initially selected mode pair will cease oscillation following a mode hop before oscillation starts on the next mode pair. In this case, well-defined double resonances will be observed, greatly facilitating servo locking. On the other hand, in Fig. 8*b,* where the difference in free spectral ranges is now less than the cavity bandwidth, it is apparent that oscillation on the next mode pair is likely to commence immediately as oscillation on the initially selected mode pair ceases. In this

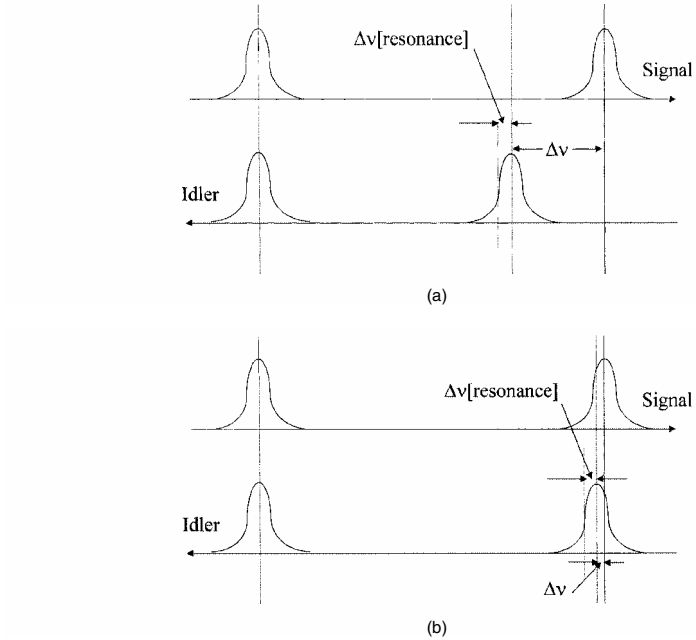

FIGURE 8 (*a*) Signal and idler resonances of the mode pair adjacent to the selected one are widely separated, due to a large difference $\Delta\nu$ in the free spectral ranges of the cavities, compared to their resonance widths $\Delta\nu$[resonance]. On tuning the cavity, oscillation is most likely to cease on the initially selected mode pair, with a gap during which the OPO may not oscillate, before oscillation begins on the adjacent mode pair. (*b*) The difference in the free spectral ranges is small compared to the resonance widths. On tuning the cavity, the OPO is most likely to remain above threshold for all cavity lengths, with mode hopping from one mode pair to the next taking place without a gap in the output.

case a continuous, albeit modulated, output is maintained as the cavity length is tuned. The double-resonance condition is now much less well defined, making servo control more difficult, but not impossible. Given comparable cavity parameters, the former condition of clearly resolved mode-pair resonances will hold when the difference in free spectral ranges is large—for example, in a type II phase-match geometry or where signal and idler wavelengths are markedly different, corresponding to operation well removed from degeneracy (see Fig. 9). On the other hand, in type I geometries operating close to degeneracy, where the difference in free spectral ranges between signal and idler waves is small, the OPO will not cease to oscillate as the cavity length changes (see also Fig. 9). The difference in free spectral ranges between signal and idler cavities can be calculated from the Sellmeier relations for the nonlinear material used.

Two approaches to smooth frequency fine-tuning have been demonstrated. One is to split the doubly resonant cavity into two separate cavities—one for the signal, the other for the idler, hence referred to as a *dual-cavity DRO.* This allows the signal and idler waves to be tuned independently, so that the frequency constraint from Eq. (1), in which the pump frequency is maintained constant, may be satisfied throughout by appropriate choice of the ratio of the mirror movements associated with the signal and idler cavities. The other approach is to simultaneously tune the pump frequency as the common cavity is tuned, hence referred to as *pump tuning.* The frequency constraint $\nu_3 = \nu_2 + \nu_1$ can hence continue to be satisfied if the change in the pump frequency is such as to accommodate the simultaneous increase (or decrease) in both the signal and idler frequencies associated with the movement of a common mirror. Both methods are examples of two-parameter tuning. Specific systems are discussed in the next sections.

DRO Devices

The early CW OPOs employed DRO cavities for reasons of the much lower threshold as compared to SROs, as previously discussed.[27–29] Some important characteristics of the early

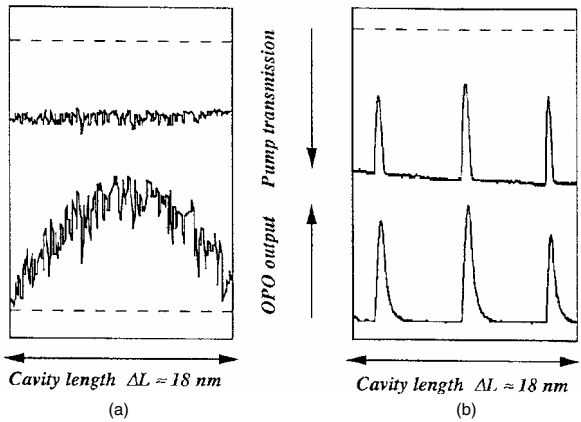

FIGURE 9 Experimental results corresponding to the two types of tuning behavior described in Fig. 8; in each case the lower trace is the OPO output and the upper trace is the pump transmission as a function of cavity length change: (*a*) the difference in free spectral ranges of the signal and idler cavities is small compared to the resonance widths, and hence the OPO output is maintained continuously as mode hopping takes place (corresponding to the situation described in Fig. 8*b*); (*b*) the much larger difference in free spectral ranges means that oscillation on one mode pair ceases for a period before recommencing on the next mode pair (corresponding to the situation described in Fig. 8*a*).

devices are summarized in Table 3. The first CW OPO was reported by Smith et al.[27] and was based on $Ba_2NaNb_5O_{15}$, pumped by a frequency-doubled Nd:YAG laser at 532 nm. Operating close to degeneracy, a threshold of 15 mW was inferred for a DRO cavity with round-trip losses for both the signal and idler waves of around 1 percent. The pump laser employed produced a multilongitudinal mode output, and the threshold power was that estimated to be associated with only the one pump mode coupling into the signal and idler mode pair selected by the doubly resonant cavity. Later in the same year, Byer et al.[28] reported a CW OPO based on $LiNbO_3$ pumped by a multilongitudinal mode argon ion laser at 514.5 nm. Matching the frequency spacing of the idler modes in the OPO cavity to the frequency spacing of the pump laser modes allowed the comb of pump modes to feed power into a single signal mode, with the complementary comb of idler modes, all resonant, taking up the frequency differences. In

TABLE 3 Parameters and Thresholds of Some Experimental DROs

Nonlinear medium, length, and phase match	Pump, signal, and idler wavelengths	Effective nonlinear coefficient	Signal and idler losses	Experimental threshold and waist	Calculated threshold	Source
$Ba_2NaNb_2O_5$, 5 mm	532 nm 980 nm 1160 nm	d_{31}	0.6–1% 0.6–1%	15 mW 30 μm		R. G. Smith et al., *Appl. Phys. Lett.* **12**:308 (1968).
$LiNbO_3$	514.5 nm 672 nm 2200 nm	6 pm/V	10.8% 4%	410 mW 34 μm		R. L. Byer et al., *Appl. Phys. Lett.* **13**:109 (1968). (Standing wave, multimode pump)
$LiNbO_3$, 34 mm	514.5 nm 660 nm 2000 nm	6 pm/V	2% 2%	150 mW 40 μm	3 mW	R. L. Byer et al., *Appl. Phys. Lett.* **15**:136 (1969). (Single-pass, ring)
MgO:$LiNbO_3$ 12.5 mm	532 nm 1007 nm 1129 nm	6 pm/V	0.6% 0.6%	12 mW 27 μm	3.2 mW	C. D. Nabors et al., *Opt. Lett.* **14**:1134 (1989). (Monolithic)
KTP, 8 mm, type II	531 nm 1062 nm 1062 nm	3 pm/V	1.0% 1.0%	22 mW	30 mW	D. Lee & N. C. Wong, *Opt. Lett.* **17**:13 (1992). (Standing wave)
LBO, 20 mm type I	514.5 nm 970 nm 1100 nm	1.2 pm/V	0.5% 0.5%	50 mW 45 μm	12 mW	F. G. Colville et al., *Opt. Lett.* **18**:205 (1993). (Standing wave)
LBO, 20 mm, type II	364 nm 500 nm 1350 nm	1.2 pm/V	2.0% 2.0%	115 mW 30–50 μm	96 mW	F. G. Colville et al., *Opt. Lett.* **18**:1065 (1993). (UV pumped)
LBO, 20 mm, type II	364 nm 500 nm 1350 nm	1.2 pm/V	2.0% 2.0%	200 mW		F. G. Colville et al., *Appl. Phys. Lett.* **64**:1490 (1994). (Dual cavity)
KTP, 6 mm type II	523 nm 900 nm 1100 nm	3 pm/V	3.0% 3.0%	30 mW 40 μm		G. M. Gibson et al., *Opt. Lett.* **23**:40 (1998). (Standing wave)
PPKTP, 9 mm, QPM	523 nm 766 nm 1650 nm	8 pm/V	3.0% 4.0%	25 mW 40 μm	50 mW	G. M. Gibson et al., *Opt. Lett.* **24**:397 (1999). (Standing wave)

Note: Not all of the tabulated parameters have been reported in all the papers. Calculated thresholds are only estimates based on both published and inferred data.

this fashion, all of the pump power became available for pumping the DRO. The device was operated far from degeneracy, with a signal output in the visible at 670 nm, representing the first report of a visible CW OPO. Other features of this device are summarized in Table 3. True single-frequency pumping of a CW OPO was first reported in 1969, when a single-frequency argon ion laser at 514.5 nm was used to pump a DRO based on $LiNbO_3$ within a ring cavity.[29] Traveling-wave resonators have advantages over standing-wave resonators in relation to maximum attainable pump depletions, as discussed in Sec. 22.6. Parameters associated with this OPO are summarized in Table 3, from which, by using Eq. (26), the expected threshold is calculated to be 3 mW, compared to an observed threshold of 150 mW. These measurements clearly illustrate why DROs were favored. On the basis of the calculated threshold for the DRO, the anticipated threshold for the equivalent SRO is 200 times greater at 0.6 W. However, this rises to 30 W based on the observed threshold. In 1971, Laurence and Tittel reported the extension of the operation of CW OPO based on $Ba_2NaNb_5O_{15}$ to the visible spectral region around 650 nm.[35]

Problems regarding both the stability and tuning behavior of DROs were recognized early on. Falk[36] provided a comprehensive study in 1971, while Weller et al.[37] investigated cluster effects in the mode selection behavior of CW DROs. Bjorkholm's comparative studies of pulsed SROs and DROs had provided a useful perspective for this later work on CW devices.[38,39] In 1973, a comprehensive study by Smith was published exploring the roles of the frequency stability of the pump laser and of cavity length changes on the spectral and tuning properties of DROs.[40]

Following the development of practical diode-pumped solid-state lasers, particularly the neodymium laser, in the late 1980s, there was a resurgence of interest in the experimental development of CW DROs. The greatly improved spectral and spatial properties of the radiation from these all-solid-state lasers, in particular the frequency stability associated with monolithic designs, provided pump sources for CW OPOs par excellence for the first time. In 1989, Nabors et al. reported a monolithic DRO based on $MgO:LiNbO_3$. Pumped by a frequency-doubled diode-pumped Nd:YAG laser, a 12-mW threshold was demonstrated.[41] Other parameters of this device are summarized in Table 3, along with the threshold calculated according to Eq. (26). In association with the practical realization of these stable monolithic OPOs, in 1991 Eckardt et al. carried out a comprehensive study of the tuning and control properties of DROs, including proposals relating to multiparameter tuning in order to overcome mode- and cluster-hopping effects.[42] In 1993, Lee and Wong extended studies to a type II KTP DRO pumped by a single-frequency krypton ion laser at 531 nm and operating close to degeneracy, with the aim of developing a tunable optical frequency divider.[43] Parameters for this device are also included for comparison purposes in Table 3. In 1993, Colville et al.[44,45] reported the first CW OPO using LBO as the nonlinear material. The first device was based on LBO in a type I phase-match geometry, was pumped by a single-frequency argon ion laser at 514.5 nm, and operated close to degeneracy.[44] The second device was based on LBO in a type II geometry, was pumped in the ultraviolet by a single-frequency argon ion laser operating at 364 nm, and was tunable in the visible over the signal wave range from 494 nm to 502 nm.[45] Parameters for these two lasers are also summarized in Table 3, along with experimental and calculated thresholds. Overall, by this stage progress had resulted in devices with lower thresholds, operating over extended wavelength ranges with greater stability and reliability than in the early days, and researchers had achieved a fuller understanding of the cavity, pump, and nonlinear material constraints limiting stability and smooth tuning.

In 1994, Colville et al. reported a CW DRO based on LBO that employed a dual-cavity scheme, allowing the signal and idler waves to be resonated in separate cavities, in order to overcome mode- and cluster-hopping effects.[46] Also, by appropriate choice of the now independently variable cavity lengths, the difference in free spectral ranges between signal and idler modes could be selected to give well-defined peaks on which to lock. In the dual-cavity approach, the two cavities still share a common section in which the nonlinear crystal is located, so that the signal, idler, and pump waves overlap there to provide efficient downconversion through the nonlinear process (see Figs. 3*e* and 10). However, by use of an appropri-

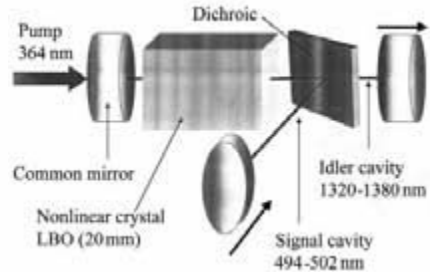

FIGURE 10 A doubly resonant OPO in which the signal and idler cavities terminate on different mirrors, hence referred to as a *dual-* (or *twin-*) *cavity OPO.* The independent tuning of the two cavities means that continuous tuning of the signal and idler frequencies can be accomplished with a fixed-frequency pump.

ate beam splitter, the signal and idler waves may now be routed to separate mirrors terminating the other, none common, ends of their respective cavities. Two-parameter tuning is now possible since the signal and idler waves may be independently tuned by appropriate movement of their separate mirrors. For example, one cavity may be reduced in length to increase the frequency of its associated wave, while the other is increased in length to decrease the frequency of its associated wave. Overall, the sum of the frequencies of the two waves can hence be maintained equal to the pump frequency, thereby preserving oscillation throughout with smooth tuning. In the scheme of Colville et al., a 20-mm-long crystal of LBO was pumped in a type II phase-matching geometry by single-frequency radiation at 364 nm from an argon ion laser. By use of a beam splitter, the signal wave, temperature tunable around 494 to 502 nm, was reflected into one cavity arm, while the idler wave, tunable over 1.32 to 1.38 μm, was transmitted into the other cavity arm. A servocontrol system was then employed on the idler cavity to change its length as the length of the signal cavity was externally changed, in order to maintain the double resonance condition throughout. Other parameters of the device are summarized in Table 3. The experimentally determined threshold was 200 mW, and smooth tuning was obtained over 0.4 GHz on both the signal and idler waves. Pump resonance effects within the idler cavity limited the tuning range.

In 1995, Henderson et al.[47] reported an alternative scheme for the extended smooth tuning of the single-frequency signal and idler waves. Here a single cavity for resonating both signal and idler waves was retained, but by simultaneously controlling the length of the OPO cavity as the frequency of the pump laser (frequency-doubled diode-pumped Nd:YLF laser) was tuned, the output frequency of the OPO could be continuously scanned. This is most effectively carried out by using a servo-locking scheme to hold the cavity on double resonance, and then to tune the pump, with the servo ensuring that the cavity length changes to maintain the double resonance. Extensive tuning of the pump laser is not necessary with this approach. Provided that the pump laser is able to tune the OPO to just over one free spectral range of the signal or idler cavities, repeated locking to adjacent signal and idler mode pairs allows a continuous single-frequency spectrum to be built up at either the signal or the idler wavelength. The device reported by Henderson et al. was based on a 10-mm KTP in a type II phase-match geometry as the nonlinear medium, pumped at 523 nm by a frequency-doubled, diode-pumped Nd:YLF laser. A spectral range from 900 to 1100 nm could be accessed by coarse angle tuning. Following servo locking, the device could then be continuously scanned over approximately 5 GHz by tuning the pump over 10 GHz (the latter being modest compared to a gain bandwidth of >100 GHz for Nd:YLF). Gibson et al.[48] subsequently demon-

strated the technique of mode hopping so as to cover a total frequency range of 220 GHz by interleaving successive scans. To move from one selected signal and idler mode pair to the next required a cavity length change of 8 nm. With the servo lock on, it was found that a light tap on one of the mirrors caused the OPO to reliably hop from one mode pair to the adjacent one. It proved possible in this way to reliably hop over 25 mode pairs. Since the free spectral range of the OPO cavity was 9 GHz, this corresponded to a total tuning range of 220 GHz. Other parameters of this system are summarized in Table 3. High-resolution spectroscopy of the cesium dimer has been carried out with this device over an extended spectral range around 1 μm. A further development reported by Gibson et al.[49] is the use of periodically poled KTP (PPKTP) as the nonlinear medium in a DRO pumped by the same pump laser as before. The PPKTP crystal had a grating period of 9.55 μm and was 9 mm long when a threshold of 25 mW for pumping at 523 nm was obtained (see Table 3). This grating period was chosen to provide an idler wavelength around 1.649 μm, suitable for carrying out absorption spectroscopy in methane. Particular care was taken in the choice of cavity parameters in this device to ensure that the difference in the free spectral ranges of the signal and idler cavities exceeded the cavity bandwidths, so as to ensure distinct double-resonance conditions on which to lock the OPO. Since the phase match bandwidth of PPKTP at the pump wavelength used (523 nm) was such that only one cluster was present, cluster-hopping effects were avoided. A microchip version of this device has also been demonstrated.[50]

In 1998, Bode et al.[51] reported a semimonolithic DRO based on MgO:$LiNbO_3$ and pumped by a frequency-doubled single-frequency Nd:YAG miniature ring laser at 532 nm. Operating close to degeneracy, 400 mW of combined signal and idler wave output power was obtained for a pump power of 1 W. Using an FM sideband-locking technique, the OPO could be tuned over a range of 8 GHz without mode hops, by tuning the pump laser frequency.

Al-Tahtamouni et al.[52] have reported the frequency stabilization of a DRO to attain an absolute frequency instability of <1 kHz. This involved the locking of the OPO to an ultrastable, cryogenic, sapphire Fabry-Perot cavity contained within an optical cryostat.

The advent of QPM nonlinear materials, in particular PPLN, has led to the development of CW DROs pumped directly by laser diodes.[53] The use of diode lasers as pumps for OPOs offers the attractive practical features of simplicity, low cost, compact solid-state design, and a significant pump tuning capability. Myers et al. have reported the use of a commercial diode laser (master oscillator/power amplifier configuration), while Lindsay et al. have used injection-locked broad area or single-stripe laser diodes to achieve single-frequency output for pumping PPLN DROs.[53]

SRO Devices

The advantages of the SRO with regard to stability and tuning were recognized from early days.[33,54] However, as we discussed previously, high oscillation thresholds precluded their operation except in pulsed mode (see Sec. 22.7) until more recently. In 1988, Kozlovsky et al.[55] reported the operation of long-pulse monolithic SROs based on MgO:$LiNbO_3$ in both standing-wave and ring configurations. The OPOs were pumped by an amplified single-mode diode-pumped Nd:YAG laser which was frequency doubled, and which provided square-top pulses at 532 nm of 0.5 μs duration at power up to 800 W. Within this time scale the SRO reached steady-state operation, and so may be regarded as operating in a quasi-CW mode. Both standing-wave and ring cavity geometries could be accessed within the same monolithic structure by appropriate launch of the pump wave. The signal wave at 900 nm was resonated in a cavity with a round-trip output coupling loss of 10 percent, while the idler at 1320 nm exited on a single pass. In the ring configuration, where the effective path length in the nonlinear gain medium was 13 mm, and where the signal and pump spot sizes were comparable at around 36 μm, a threshold for oscillation of 37 W was observed, with 60 percent pump depletion for pumping at 120 W. Spectral coverage from 850 to 1500 nm was obtained through temperature tuning. Other parameters of this system, for which the calculated threshold was 35 W, are given in Table 4.

TABLE 4 Parameters and Thresholds of Some Experimental SROs

Nonlinear medium, length, and phase match	Pump, signal, and idler wavelengths	Effective nonlinear coefficient	Signal and idler losses	Experimental threshold and waist	Calculated threshold	Source
$MgO:LiNbO_3$, 13 mm	532 nm 900 nm 1320 nm	5.9 pm/V	10%	37 W (3.5 μm)	35W	W. J. Kozlovsky et al., *Opt. Lett.* **13**:1102 (1988). (Monolithic ring, long pulse only)
KTP, 10 mm, type II	532 nm 1039 nm 1090 nm	3 pm/V	0.85%	1.4 W (20–30 μm)	1.8W	S. T. Yang et al., *Opt. Lett.* **19**:475 (1994). (Double pass of both pump and idler phase control)
PPLN, 50 mm, QPM: 29.7 μm	1064 nm 1570 nm 3250 nm	14.4 pm/V	2.2%	3.6 W (64–68 μm)	0.6W	W. R. Bosenberg et al., *Opt. Lett.* **21**:1336 (1996). (Ring)
PPLN	925 nm 1600 nm 2100 nm	14.4 pm/V	1.0%	1.7 W		M. E. Klein et al., *Opt. Lett.* **24**:1142 (1999). (Ring)

Note: Not all of the tabulated parameters have been reported in all the papers. Calculated thresholds are only estimates, based on both published and inferred data.

The first truly singly resonant CW OPO was reported by Yang et al. in 1993.[56] This device was based on KTP as the nonlinear medium employed in a type II noncritical phase-matching (NCPM) geometry. Pump light was provided by an injection-locked Nd:YAG laser, the output from which was resonantly frequency doubled to provide up to 4 W of single-frequency radiation at 532 nm. A standing-wave cavity, resonant for the signal wave (1039 nm), was employed based on bulk optical components; the pump wave and signal wave waists in the nonlinear crystal (of length 10 mm) were 21 and 31 μm, respectively. The idler wave was retroreflected at one end of the cavity, and so double-passed the nonlinear medium. For the case where the pump single-passed the nonlinear medium, and where the signal cavity had a round-trip power loss of 0.85 percent, the calculated threshold was 7.2 W. This was greater than the pump power available. However, by double-passing the pump and ensuring that the correct phase relationship between the three waves is maintained on their reflection, it has been shown by Bjorkholm[32] that threshold may be reduced by a factor of 4 (see Sec. 22.6). Under these conditions, the experimentally determined threshold was 1.4 W (see Table 4), somewhat less than expected. When pumped at 3.2 W, just over twice threshold, 1.07 W of idler power at 1090 nm was measured along with 36 mW of signal, corresponding to an efficiency of 35 percent. The low power in the signal wave is a result of this wave being resonant in a cavity with low output coupling loss compared to parasitic loss, in order to keep the oscillation threshold low. On the other hand, the nonresonant idler wave exits the nonlinear medium after only a double pass. In 1994, Yang et al.[57] reported a ring version of this device based around a 15-mm-long KTP crystal. A threshold of 4.3 W was reported (in the ring geometry the pump only single-passes the nonlinear medium), with 1.9 W of idler generated at a pumping level of 6.7 W.

The advent of QPM nonlinear materials around 1995 had a substantial impact on the development of SROs. This was particularly the case for OPOs based on PPLN and operating in the mid-infrared. In 1996, Bosenberg et al.[58,59] reported a number of innovative devices, two versions of which are illustrated in Fig. 11. One of these employed a ring cavity, the other a standing-wave cavity. A diode-pumped Nd:YAG laser, which operated in single transverse mode ($M^2 = 1.1$) and multiaxial mode (linewidth 2.2 GHz), provided up to 13.5 W of pump

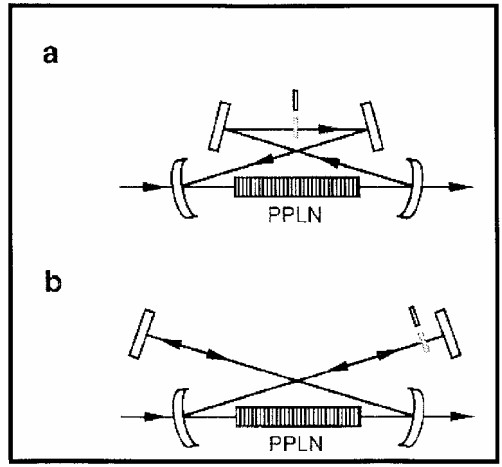

FIGURE 11 Two singly resonant cavity geometries for OPOs based on periodically poled lithium niobate (PPLN): (*a*) ring cavity, and (*b*) standing-wave cavity. (*From Refs. 58 and 59, Bosenberg et al., 1996. Reproduced with permission.*)

power at 1064 nm in a beam waist of 64 μm. In both devices the nonlinear gain medium was a 50-mm-long PPLN crystal incorporating a 29.7 μm grating. The ring cavity OPO, in which the signal wave at 1.57 μm was resonant with a round-trip loss on the order of 2.2 percent, exhibited a threshold of 3.6 W. At pump powers approaching 2.4 times threshold, pump depletions on the order of 93 percent were obtained, beyond which the pump depletion was observed to saturate. This behavior is consistent with theoretical predictions discussed earlier in Sec. 22.6. Some 3.55 W of power were coupled out in the nonresonant idler wave for a pump power of 13.5 W, the maximum available. The associated signal wave power was 1.6 W, much less than that generated since the signal wave is resonant in a cavity with low output coupling, in order to keep the threshold down, and hence is subject to high parasitic losses. By using a crystal with multiple parallel gratings with periods varying from 28 to 30 μm, an idler tuning range from 3.2 to 4.1 μm was accessed. In general, single longitudinal mode operation on the resonant signal wave was obtained without the use of any additional tuning elements. Under this condition the idler wave acquires the linewidth of the pump laser, in this particular case around 2 GHz. (The use of a single-frequency pump laser would result in single-frequency idler output.) By tilting an etalon (1 mm thick, fused silica, uncoated) placed in the signal cavity, the signal wave was tuned over 150 GHz by repeated mode hops and without the need to adjust any other system parameter.

In 1998, Batchko et al.[60] reported a SRO which was based on PPLN pumped at 532 nm. The pump laser was a multiaxial mode neodymium vanadate laser with intracavity frequency doubling which provided up to 5 W of pump power. Quasi–phase matching at this pump wavelength to provide a signal and idler tuning range of 917 to 1266 nm required a particularly short grating period in the PPLN of 6.5 μm. An oscillation threshold of around 1 W was reported, with 0.82 W of idler power being generated for pump power of 3.3 W. The study highlighted two important limitations of PPLN. First, thermal lensing, to which PPLN is particularly prone, meant that the device could only be operated at the reported pumping levels with a 50 percent duty cycle because of beam-pointing stability problems. Second, green-induced infrared absorption effects were experienced. In the presence of 532-nm radiation (1 W focused to 64 μm waist), the absorption shown by the 53-mm-long PPLN crystal to 1064-

nm radiation increased from an initial 0.5 percent in the absence of such radiation to 4.5 percent when it was present. This, of course, exacerbates the thermal lensing problem due to the increased power dissipation in the crystal in such circumstances.

A further development by Powers et al.[25] in 1998 was the replacement of the multiple gratings normally fabricated within PPLN crystals by a single grating with a continuously changing period across the width of the crystal—i.e., a fan-out grating whose period in this case changed progressively from 29.3 to 30.1 μm. By translating such a grating across the cavity axis, some 350 cm^{-1} of continuous tuning was obtained without changing the crystal temperature in a CW OPO pumped at around 1 μm and where the signal wave was resonant. This is equivalent to around 80 nm of tuning at the signal wavelength of 1.5 μm. By incorporating an etalon into the cavity of such a device, three levels of tuning could be accomplished so as to give continuous spectral coverage with single-frequency resolution across the whole of the 350 cm^{-1}. Translating the grating provided the coarse tuning across 350 cm^{-1}; rotating the etalon provided finer tuning across some 6 cm^{-1}; and fine-tuning of the single-mode signal was carried out in the usual way across a free spectral range of the signal cavity (0.05 cm^{-1}) by scanning the cavity length.

Given the flexibility inherent in quasi–phase matching due to the ability to fabricate different grating periods, it is possible to make one crystal serve two purposes by incorporating two grating periods in series within its length. In this way, Bosenberg et al.[61] described a device in 1998 that efficiently generated tunable high-power radiation around 629 nm. Of the two separate gratings in series in the one crystal, one grating acted to phase match a CW SRO pumped at 1064 nm and generating a signal wave at 1540 nm, while the second grating acted to phase match the sum-frequency mixing process between the generated (and resonant) signal wave and the pump wave. The overall result was to attain a 21 percent conversion efficiency from the pump wave at 1064 nm to the final output at 629 nm, so that some 11.8 W of input power at 1064 nm resulted in 2.5 W at 629 nm being generated.

In 1999, Klein et al.[62] reported a CW SRO pumped by a high-power diode laser. The MOPA configuration employed was based on InGaAs diode lasers in which an external cavity master oscillator in a Littman configuration pumped a flared amplifier and delivered up to 2.5 W at 925 nm with an $M^2 < 1.2$. The OPO was based on PPLN as the nonlinear medium and employed a ring cavity with round-trip losses on the order of 1 percent for the resonant signal wave. The oscillation threshold was 1.7 W and 480 mW of idler was generated when pumping at 2.5 W, corresponding to a pump depletion of 55 percent. A particular feature of this scheme is the flexibility afforded by pump tuning. Tuning the pump over the range 924 to 925.4 nm resulted in signal tuning of 1550 to 1700 nm and idler tuning of 2030 to 2290 nm. Appropriate synchronization of pump tuning and cavity length scanning results in a wide, continuous, single-frequency tuning range.

At the present time substantial progress continues to be made in the development of SROs based on QPM nonlinear materials such as PPLN. Such OPOs developed to the point where they generate widely tunable, stable, single-frequency coherent radiation at both signal and idler wavelengths will be valuable spectroscopic sources for the mid-infrared in the near future. However, the oscillation thresholds of singly resonant devices are still high, thus requiring substantial pump lasers. Also, PPLN itself suffers serious disadvantages with regard to both thermal effects and green-induced infrared absorption, which impede progress toward effective frequency control. For these reasons other QPM materials, such as the periodically poled phosphates and arsenates of the KTP type, are attractive options. However, all alternative QPM nonlinear materials to date exhibit effective nonlinear coefficients that are lower than that of PPLN itself, and so singly resonant devices based on them show yet higher oscillation thresholds. Hence, other approaches, such as pump-enhanced OPOs and intracavity OPOs, are of continuing interest if compact sources are required.

Pump-Enhanced Optical Parametric Oscillators

In the pump-enhanced optical parametric oscillator, the cavity is made resonant at the pump wavelength as well as at either the signal or idler wavelength. In this way, it is possible to

greatly enhance the circulating pump intensity within the nonlinear crystal. Although two waves are resonant in this type of oscillator, and in this respect they are similar to the DROs discussed previously, there are important differences when only one of the downconverted waves is resonated as here, compared to when both are resonated, as discussed previously. For example, the alignment procedures required to bring the pump field into resonance can be carried out with the OPO below threshold; hence, since the pump field is always present, being generated by a separate source, the cavity can be readily locked up and stabilized. Further, with common mirrors defining the pump cavity and the resonant downconverted wave cavity, the OPO is then also aligned for the latter as well as the former. On increasing the pump power to above the threshold value, the OPO oscillates regardless of the mirror spacing since the device is not overconstrained as is the DRO. Thus, there are considerable advantages in terms of ease of alignment associated with the pump-enhanced OPO. Another attribute is that stabilizing the cavity length on the pump field resonance allows the stability of the pump laser frequency to be transferred to the resonant downconverted wave which shares the common cavity. Similarly, if the pump frequency is tuned, so scanning the cavity length, the resonant wave frequency tunes in step, at least until a mode hop occurs.

A generic arrangement for a pump-enhanced OPO is shown in Figs. 3*c* and 12. The nonlinear medium is incorporated into a two-mirror cavity, where the left-hand mirror of (power) reflectivity r_1 and transmittance t_1 serves as the input mirror for the pump wave. If the effective transmission of the crystal to linear loss is t (round-trip) and to nonlinear loss (due to parametric downconversion) is t_{opo}, and if the reflectivity of the back mirror is r, then defining

$$r_m = (tt_{opo}r) \tag{56}$$

the circulating power P_c at the pump wavelength in the resonant cavity may be readily determined by the usual procedures to be

$$P_c = \frac{t_1 P_1}{[1 - (r_1 r_m)^{1/2}]^2} \tag{57}$$

where P_1 is the incident pump power. (Note that we have made the simplifying assumption that the circulating power is constant throughout the cavity on the basis that the fractional round-trip loss is small.) Now at and above OPO threshold, P_c is clamped to its value at threshold P_{cc} determined by the condition that the OPO gain equals OPO loss, namely

$$\beta P_{cc} = \alpha_{opo} \tag{58}$$

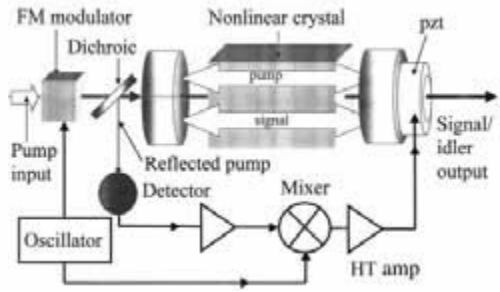

FIGURE 12 The basic layout of the pump-enhanced OPO. The Pound-Drever servo loop maintains the cavity on resonance with the single-frequency pump laser as the latter is tuned. Since the resonant (signal) wave shares a common cavity with the pump wave, it tunes in step with the pump wave.

where α_{opo} is the round-trip linear loss of the resonated downconverted wave in the OPO, and β is a constant depending on the effective nonlinear coefficient, focusing arrangement of the pump, and so on. The preceding equation should be compared with that derived previously for the threshold of the SRO, Eq. (21), in order to evaluate the constants it contains. However, it needs to be borne in mind that in the pump-enhanced OPO, the pump wave double-passes the nonlinear medium—in other words, the resonant wave experiences optical gain on backward as well as forward propagation through the cavity. This presents no difficulty with regard to the phasing of the three waves involved, since the nonresonant wave is assumed to exit the cavity after a single pass. In this case the only modification required is to equate the single-pass gain, as determined previously, to the single-pass loss (which is equal to half the double-pass loss). The round-trip loss α_{opo} is equal to either α_2 or α_1, depending on whether the signal or idler wave is being resonated, and it then follows that

$$\beta = \frac{16\pi \ell^2 d_{\text{eff}}^2}{[n_3 n_2 n_1 c \varepsilon_o \lambda_2 \lambda_1 w_o^2]} \tag{59}$$

where w_o is the radius of the pump beam in the nonlinear medium. (Note that the analysis applies to the case of plane waves of uniform intensity.)

Once the incident pump power is fixed, all quantities in Eq. (57) are fixed except for t_{opo}, which hence is determined by this equation. However, the downconverted power is given by

$$P_{DC} = (1 - t_{opo})\, P_{cc} \tag{60}$$

Hence we obtain

$$P_{DC} = P_{cc} \left\{ 1 - (r_1 rt)^{-1} \left[1 - \left(\frac{t_1 P_I}{P_{cc}} \right)^{1/2} \right]^2 \right\} \tag{61}$$

If we restrict attention to the case of a perfect input mirror (i.e., that $r_1 + t_1 = 1$), then on differentiating the preceding equation with respect to t_1, the optimum transmission required for the pump input mirror and the optimum downconverted power thereby generated under such conditions can be determined as

$$t_1^{\text{opt}} = \frac{P_I}{P_{cc}} \tag{62}$$

and

$$P_{DC}^{\text{opt}} = P_{cc} \left[1 - (rt)^{-1} \left(1 - \frac{P_I}{P_{cc}} \right) \right] \tag{63}$$

respectively.

From the preceding it is apparent that if

$$rt = 1 \tag{64}$$

that is, there is no parasitic loss experienced by the pump either due to leakage through the back mirror or through linear absorption within the cavity, then the downconverted power under optimum pump coupling conditions becomes equal to the input pump power. Hence, the pump-enhanced OPO is capable of exhibiting 100 percent efficiency for parametric downconversion (internal) if there is no parasitic linear loss of the pump wave from the cavity.

As an example of the effects of such parasitic loss in a real system, suppose that a pump source is available that provides 300 mW, and that the OPO requires 6 W in the nonlinear medium in order to reach threshold. Further suppose that round-trip losses (linear) due to all causes apart from the transmission of the input mirror are 2 percent. Then in this case rt =

0.98. From Eq. (62), it can be seen that the optimum transmission of the input mirror t_1^{opt} (assumed to be lossless) should be chosen to be 0.05 (i.e., 5 percent transmitting), resulting in a twentyfold enhancement of the intracavity field on resonance and *with the OPO oscillating.* (Interestingly, prior to the pump wave being of sufficient power for the OPO to reach oscillation threshold, the field enhancement is greater since there is then no nonlinear loss from the cavity.) It then follows from Eq. (63) that 180 mW of downconverted power is generated, corresponding to an efficiency of around 60 percent. The remaining pump power of 120 mW is lost parasitically, as may be seen by multiplying the intracavity power of 6 W by the parasitic loss of 2 percent. (Note that if this calculation is done more precisely, the sum of the downconverted pump power and the pump power lost parasitically exceeds the input pump power. The discrepancy lies in our earlier assumption of a constant intracavity pump power throughout the round trip, which is clearly only an approximation in a cavity with localized losses). It should be noted that under the conditions discussed the cavity is impedance matched with no back reflection of the incident pump wave.

The conditions for efficient downconversion with the pump-enhanced geometry should be contrasted with those in the case of the singly or doubly resonant OPOs discussed previously. SROs or DROs require significant depletion of the pump within the nonlinear medium for efficient operation. In the cases of the SRO or the ring DRO, and assuming plane-wave conditions apply, total depletion of the pump on a single pass through the cavity is possible, resulting in 100 percent downconversion. In the case of the standing-wave DRO or when gaussian beams are involved in either the SRO or the DRO, backconversion is detrimental in restricting optimum downconversion to below this level. In the case of the pump-enhanced OPO, the single-pass depletion of the pump within the resonant cavity is small, even under optimum conditions, as has been demonstrated. Therefore, backconversion does not limit the attainment of 100 percent downconversion efficiency in the case of the pump-enhanced OPO. The preceding expressions may readily be extended to the case in which the input coupling mirror exhibits pump-wave absorption.

In 1994, Robertson et al. demonstrated a CW OPO with pump enhancement based on LBO, operating in a type II noncritical phase-matching (NCPM) configuration.[63] The cavity length was controlled by a servo to maintain pump resonance when pumped by a single-frequency argon ion laser at 514.5 nm. The cavity was configured to be resonant also at the idler wavelength only (i.e., singly resonant with regard to the downconverted waves), as well as to provide the pump enhancement. The device reached threshold for an input pump power of 1 W (pump beam waist of 36 μm radius, LBO crystal length 25 mm), and generated in excess of 1 W of downconverted power in signal (946 nm) and idler (1130 nm) together when pumped at 3 W. Temperature tuning of the phase matching over 20°C from room temperature gave a signal tuning range of 930 to 950 nm and a corresponding idler tuning range of 950 to 1150 nm; ranges proportionally extendable by increasing the temperature range. The signal wave was observed to be single frequency most of the time without the need to introduce frequency-selective elements into the cavity. The intracavity pump power required to reach oscillation threshold may be determined using Eq. (21), but bearing in mind that both pump and nonresonant wave double-pass the crystal (see Table 2). For a round-trip loss at the idler frequency (resonant wave) estimated as 3 percent, this power is calculated to be 15 to 30 W, depending on the relative phases of the pump, signal, and idler. The pump enhancement cavity had an input coupling mirror transmission of 5 percent, while the other mirror of the cavity showed a residual transmission of 0.25 percent. According to Eq. (57), these figures are consistent with the measured enhancement factor of 76 times. This enhancement factor was observed to fall to around 30 times when the crystal was inserted, but with the OPO still below threshold. This reduced enhancement is consistent with the estimated crystal losses of 2 percent per round-trip. The measured external power to reach threshold of 1 W implies a circulating power within the cavity of 30 W, which is reasonably consistent with the threshold calculated. As we have discussed earlier, when the OPO is operated above threshold, the circulating pump power within the enhancement cavity is clamped to the threshold value by the nonlinear losses associated with the downconversion process. The total downconverted

power of 1 W, for pumping at 3 W, should be compared to the 1.9 W predicted by Eq. (61), and to that expected under optimum pump coupling ($t_1 = 0.1$, compared to the value of 0.05 used) of 2.2 W, as predicted by Eq. (63).

In 1995, Scheidt et al.[64] reported a pump-enhanced OPO pumped directly by a diode laser. Based on KTP under conditions of type II phase matching, a threshold of <50 mW was obtained for pumping at 769 nm using a single-stripe, single-frequency GaAlAs diode laser. The input coupling mirror of the OPO cavity was 2 percent transmitting at the pump wavelength, implying a pump-enhancement factor of around 160. The signal wave at 1093 nm was resonant (round-trip cavity loss of signal cavity on the order of 0.5 percent) and the idler wave at 2494 nm double-passed the cavity. Further developments of this approach by Scheidt et al.[65] included the use of a diode oscillator and tapered amplifier combination to increase the available pump power to 600 mW, and the replacement of KTP by $RbTiOAsO_4$ (RTA) as the nonlinear medium. At a pump power of 405 mW, and with pump and idler resonant, some 84 mW were generated in the signal wave at 1240 nm. Servo control of the cavity length to maintain resonance of the pump wave resulted in stable, single signal mode operation with measured linewidths of <10 MHz. Other parameters associated with this laser are given in Table 5, including calculated threshold estimates. A dual-cavity version, in which the resonant signal and pump cavities were partially separated, was also reported.

In 1997, Schneider et al.[66] reported a pump-enhanced CW OPO based on PPLN, including its application to spectroscopy. Pumped by a single-frequency miniature Nd:YAG laser at 1064 nm, and singly resonant at the signal wavelength, an external pump power of 250 mW was required to reach oscillation threshold. When pumped at a pump power of 800 mW, some 140 mW of idler wave power was generated. By a combination of temperature tuning and grating period tuning, tuning ranges of 1450 to 1990 nm for the signal and 2290 to 2960 nm for the idler were attained. When the cavity was servo locked to the pump frequency, a frequency stability in the single-frequency idler and signal waves of <10 MHz/min was obtained, demonstrating the particular advantage of the pump-enhanced OPO in this respect, as previously discussed. It proved possible, through tuning of the pump frequency and careful temperature control of the crystal, to tune the single-frequency idler output continuously through 2 GHz, allowing a number of mid-infrared spectroscopy experiments to be carried out. Schneider et al.[67] also reported a similar pump-enhanced OPO based on $MgO:LiNbO_3$ and pumped by a frequency-doubled Nd:YAG laser at 532 nm in 1997. This device exhibited a low pump power threshold of 200 mW, a phase-match tuning range of 1100 to 1135 nm, and single-frequency output continuously tunable over 2.3 GHz with a linewidth of <160 kHz. Downconversion efficiencies into the signal and idler wave together of around 33 percent were obtained when pumping at 1.5 times oscillation threshold.

In 1999, a comprehensive theory of an OPO with resonant pump and signal wave sharing a common cavity was reported by Schiller et al.[68] Oscillation thresholds and conversion efficiencies and their dependence on wavelength as a result of mode shape changes, and on mirror transmissions were explored. Spiking effects on the signal wave in a pump-enhanced idler resonant OPO have been observed by Scheidt et al.[69] and their properties confirmed by numerical modeling.

Because of their wide spectral coverage, OPOs are attractive sources for the generation of interrelated frequency standards across wide frequency ranges. A step toward the practical realization of such schemes is the recent demonstration by Lee et al. of 3:2:1 frequency division using self-injection locking in a pump-enhanced OPO.[70] The OPO was based on PPLN, and was pumped at 812 nm by a AlGaAs diode-laser MOPA system. Pump enhancement resulted in only a low external pump power of 150 mW being required in order to reach oscillation threshold. By using two in-line gratings with different periods in PPLN, the nonlinear medium performed the dual functions of parametric downconversion in a pump-enhanced OPO cavity, as well as intracavity frequency doubling of the resonant idler wave thereby generated. When the frequency of the doubled idler wave was close to the frequency of the signal wave, self-injection locking of the downconversion process was observed to occur, as a result of the enhancement of the signal wave. The device hence locks with the pump to signal

TABLE 5 Parameters and Performance Characteristics of Some Experimental Pump-Enhanced OPOs

Nonlinear material and length	Pump, signal, and idler wavelengths	Nonlinear coefficient d_{eff}	Resonant wave loss	Threshold and waist	t_1	r_1, t, and r	Enhancement factor	P_I at threshold (cold cavity)	P_{DC} and P_I	Source
LBO,	514.5 nm	0.7	3% (idler)	15–30 W	0.05	0.95	30	1W	1W	G. Robertson et al.
25 mm	946 nm	pm/V		36 μm		0.98			3W	*Opt. Lett.* **19**:1735 (1994).
	1130 nm					0.99				(Double-pass idler)
RTA,	800 nm	3	1.3% (idler)	7.3 W*	0.04	0.96	64*	225 mW	347 mW	M. Scheidt et al.
12 mm	1230 nm	pm/V		35 μm		0.996			1.03 W	*Opt. Lett.* **22**:1287 (1997).
	2250 nm					0.99				
PPLN,	1064 nm	15	2.5%	8.6 W	0.08	0.92	32	200 mW	400 mW	K. Schneider et al.
19 mm	1450 nm	pm/V	(signal)	29 μm		0.99			800 mW	*Opt. Lett.* **22**:1293 (1997).
	2960 nm					0.997				
MgO:	532 nm	4.7	2%	3.3 W	0.08	0.92	22	200 mW	100 mW	K. Schneider et al.
$LiNbO_3$,	1100 nm	pm/V	(signal)	18 μm		—			300 mW	*Appl. Phys. B* **65**:775 (1997).
7.5 mm	1135 nm					0.98				(Double-pass idler)

* Internal thresholds and enhancement factors are those quoted in references, except for these values, which were calculated from given parameters. For explanation and definition of symbols used, see main text.

and idler frequencies in the ratios 3:2:1, providing a comb of widely spaced but precisely interrelated frequencies. A locking bandwidth of 500 kHz was observed.

In the common cavity, pump-enhanced OPO, the extent of the continuous tuning range available at the signal or idler wavelength is limited by mode-hopping effects. If the center of the phase-match bandwidth is assumed to be independent of the pump wavelength, then in the case where the signal wave is resonant, a mode hop is to be expected after the signal wave has tuned through one free spectral range of the cavity. Since the signal tuning range is related to the pump tuning range, in the absence of mode hops, by

$$\Delta\nu_2 = \frac{\nu_2 \Delta\nu_3}{\nu_3} \tag{65}$$

then the associated pump tuning before a mode hop occurs is given by

$$\left| \frac{\nu_2 \Delta\nu_3}{\nu_3} \right| < \mathrm{FSR} \tag{66}$$

The idler tuning range associated with this pump tuning range is given by

$$\Delta\nu_1 = \frac{\nu_1 \Delta\nu_3}{\nu_3} = \frac{\lambda_3 \Delta\nu_3}{\lambda_1} \tag{67}$$

and hence the tuning range of the idler wave is given by

$$\Delta\nu_1 = \left[\frac{\nu_1}{\nu_2} \right] \times \mathrm{FSR} = \left[\frac{\lambda_2}{\lambda_1} \right] \times \mathrm{FSR} \tag{68}$$

Because the idler wavelength is greater than the signal wavelength, the idler tuning range is less than a free spectral range of the cavity. However, in practice the limitation is even more severe, since the center of the phase-match bandwidth can change very rapidly with change in the pump wavelength under certain circumstances. Defining $\partial\nu_2/\partial\nu_3$ as the ratio of the change of the center of the phase-match bandwidth as seen by the signal to the change in the pump wavelength, then the pump tuning range before a mode hop occurs now becomes

$$\left| \left[\frac{\nu_2}{\nu_3} - \left(\frac{\partial\nu_2}{\partial\nu_3} \right) \right] \Delta\nu_3 \right| < \mathrm{FSR}. \tag{69}$$

Generally the term in square brackets is nonzero, and indeed in many cases may be in excess of 4 or 5. Hence, the pump tuning range can become limited to only a small fraction of an FSR of the cavity, with an even more deleterious effect on the tuning range of the idler. For example, this limitation is particularly severe when pumping a PPLN-based OPO around 800 nm. Turnbull et al.[71] have shown that such limitations can be avoided by resonating the pump and signal waves in separate cavities. A suitable beam splitter is incorporated into the OPO cavity so that the (resonated) signal wave is directed to one mirror, while the resonated pump wave is directed to a separate mirror (see Fig. 13). In this way, the pump and signal resonance conditions may be adjusted independently. Pump and signal waves, and of course the idler wave, still share a common arm of the cavity in which the nonlinear medium is located, and where downconversion takes place. As well as providing independent control of the signal and idler cavities, this arrangement allows frequency-selective elements to be incorporated into one of the cavities without thereby affecting the wave in the other cavity. Two ways of attaining wide tuning ranges with this arrangement have been identified. In one, mode hopping is suppressed by placing a frequency-selective element, such as an etalon, into that arm of the signal wave cavity not common with the pump cavity. In this way, mode hopping due to separation of the signal mode frequency from the (possibly) shifting center of the phase-match bandwidth can be suppressed,

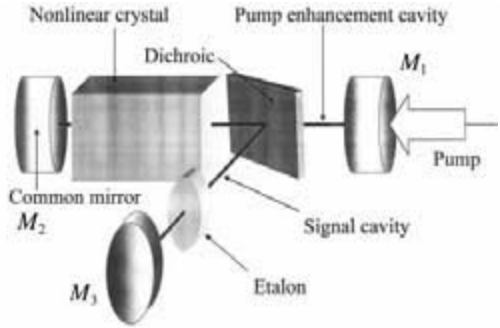

FIGURE 13 A dual-cavity, pump-enhanced OPO, in which the pump-enhancement cavity and the resonant (signal) wave cavity terminate on different mirrors. In this case, the signal wave frequency can be held constant, by the inclusion of an etalon, as the pump frequency is tuned, thereby ensuring that the total frequency shift of the pump wave is transferred to the idler wave.

and signal wave oscillation is constrained to a selected mode of the signal wave cavity. The frequency of the signal wave is hence held constant, so that as the pump wave is tuned, the pump enhancement being maintained throughout by appropriate adjustment of the independent pump wave cavity, all of the pump wave tuning range is transferred to the idler wave. By this means idler tuning ranges in excess of 10 GHz, corresponding to the tuning range of the pump laser, have recently been demonstrated in a pump-enhanced OPO based on PPLN and pumped by a titanium sapphire laser. An alternative approach is to scan the signal wave cavity as the pump laser is tuned, so as to maintain the selected single mode of the signal wave at the center of the phase-match bandwidth, and hence eliminate mode hopping. The signal wave will now tune in frequency at a substantially greater rate than the tuning rate of the pump, since the ratio of the signal tuning rate to the pump tuning rate is given by $(\partial\nu_2/\partial\nu_3)$.

As a result, the idler wave tunes over a range

$$\Delta\nu_1 = \left[1 - \left(\frac{\partial\nu_2}{\partial\nu_3}\right)\right]\Delta\nu_3 \tag{70}$$

Since the term in square brackets may be of the order of 5 or more, there is a significant enhancement of the idler tuning range compared to the pump tuning range.

Intracavity Optical Parametric Oscillators

By placing the OPO within the cavity of the pump laser itself, access is gained to a high-intensity pump field. Such a configuration is referred to as an *intracavity OPO* (ICOPO), see Figs. 3*d* and 14. The device may be either singly or doubly resonant with regard to the down-converted waves (the latter, of course, showing yet further reduction in threshold). In 1968, Oshman and Harris[72] demonstrated that the doubly resonant ICOPO encounters a number of stability problems, including both an inefficient operating regime and self-pulsing even at moderate pumping levels. In a recent (1998) analysis of the ICSRO, Turnbull et al.[73] have shown theoretically, and subsequently confirmed experimentally, that this device in contrast operates without such instabilities or inefficiencies at all pump power levels above threshold. The generic arrangement of the intracavity OPO is shown in Fig. 14. The nonlinear crystal is

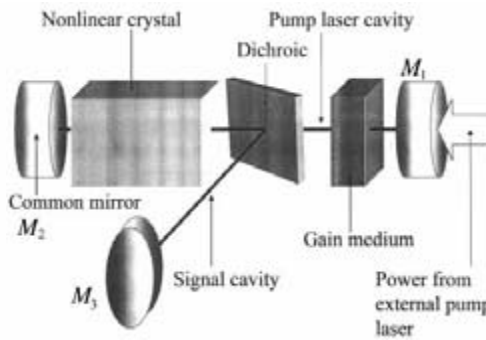

FIGURE 14 The basic layout of the intracavity OPO. In this arrangement, the gain medium of the pump laser and the nonlinear medium of the OPO are within the common cavity of the pump laser. The gain medium is excited either by another external pump laser (not shown) or by some other means (such as electrical excitation, for example).

located within the cavity of the pump laser formed by mirrors M_1 and M_2. The beam splitter is highly transmitting at the pump wavelength, but highly reflecting at the wavelength of the downconverted wave that is to be resonated—in the case illustrated, the signal wave. The signal wave cavity is then completed by mirror M_3, sharing a common mirror M_2 with the pump cavity.

Three distinct operating regimes of the device are illustrated in Fig. 15. In regime I, the external pump power P—we use the term *external* to designate that this is the pump power from another unspecified laser that is being employed to excite the pump laser itself—is below that value P_{th}^{L} required for the pump laser itself to reach oscillation threshold. No intracavity field develops, and hence no down-converted power is generated. In regime II, the external pump power exceeds P_{th}^{L}, and is hence sufficient to bring the pump laser into oscillation. As a result, an intracavity field within the pump laser develops, and increases linearly with the external pump power. However, within this regime the strength of this intracavity field is insufficient to bring the OPO itself above threshold, so downconverted power is not generated. In regime III, the external pump power now exceeds the critical value $P_{\text{th}}^{\text{SRO}}$, such that the associated intracavity pump field is now sufficient to bring the OPO above threshold. At this point, downconverted power begins to be generated, thereafter increasing linearly with pump power. Since the OPO operates under steady-state conditions throughout, the nonlinear gain must saturate with further increase in external pump power so as to remain equal to the cavity loss, which is constant. Since the intracavity field intensity determines the nonlinear gain, this field intensity is clamped to its value at the OPO threshold. The mechanism of the clamping is an increasing nonlinear loss associated with the OPO within the cavity of the pump laser. As the external pump power is increased, the intensity of the resonant downconverted wave in the OPO cavity increases, thereby bringing about this increase in nonlinear loss.

We now develop these ideas to determine the dependence of the total downconverted power P_{DC} (i.e., total signal power plus total idler power generated) on the external pump power P. The round-trip saturated gain G_{sat} of the pump may be described by

$$G_{\text{sat}} = \frac{KP}{(1 + P_{\text{IC}}/P_{\text{sat}})} \tag{71}$$

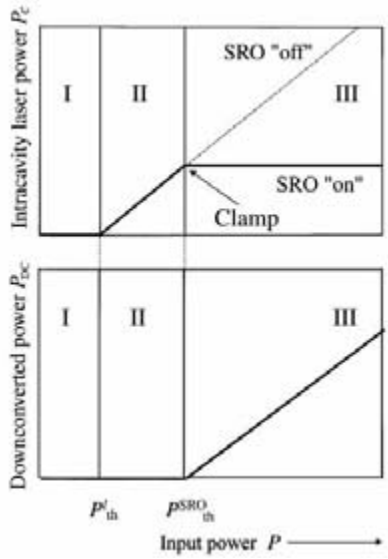

FIGURE 15 Operating regimes of the intracavity OPO as a function of the external (input) power applied. In region I, both the pump laser and the OPO are below threshold; hence, the intracavity power and downconverted power are both zero. In region II, the pump laser is above threshold, but the OPO is still below threshold. Hence, the intracavity power increases with increasing input power, while the downconverted power remains at zero. In region III, the OPO is now also above threshold. The intracavity power is hence clamped by the OPO such that the OPO gain just equals the losses of the OPO cavity. The clamping mechanism is an increasing nonlinear loss experienced by the pump laser due to the increasing downconverted power.

where K and P_{sat} are scaling parameters relating to the small-signal gain and the saturation of the gain respectively, P_{IC} is the circulating intracavity power in the pump laser, P is the external pump power available from the (unspecified) laser used to excite the pump laser, and homogeneous broadening of the pump laser transition has been assumed. Under steady-state operation of the pump laser, this saturated gain equals the total (round-trip) loss of the pump laser cavity, this loss being made up of the usual linear loss of the cavity ζ_{lin} but also the nonlinear loss associated with the operation of the OPO ζ_{nonlin}. Thus we can write

$$\frac{KP}{(1 + P_{IC}/P_{sat})} = \zeta_{lin} + \zeta_{nonlin} \tag{72}$$

The gain experienced by the downconverted wave, which is resonant in the OPO cavity, depends linearly on the circulating pump power P_{IC} present in that cavity. Further, when the OPO is operating above threshold, this gain is clamped so as to equal the loss (round-trip) associated with the OPO cavity. Hence, we can write

$$G_{\text{opo}} = g_{\text{opo}} P_{\text{IC}} = \alpha_{\text{opo}} \tag{73}$$

where g_{opo} is a parameter describing the OPO gain (and includes such parameters as d_{eff} and the cross-sectional area of the downconverted wave), and α_{opo} is the (round-trip) linear loss of the resonant downconverted wave from the OPO cavity. The generated downconverted power is given by

$$P_{\text{DC}} = P_{\text{IC}} \zeta_{\text{nonlin}} \tag{74}$$

(Note that this power will be split between the signal and the idler waves in the usual way in proportion to their relative frequencies. Further, not all downconverted power may be extracted usefully; in particular, the resonant downconverted wave power will partition between parasitic loss and useful output loss. On the other hand, most of the power in the nonresonant downconverted wave may be extracted efficiently since this wave exits the nonlinear medium on a single transit.)

We can use Eq. (73) to evaluate P_{IC} for substitution into Eq. (72) in order to determine ζ_{nonlin}, allowing the generated downconverted power to be calculated from Eq. (74) so as to obtain

$$P_{\text{DC}} = \left(\frac{\alpha_{\text{opo}}}{g}\right)\left\{\frac{KP}{[1 + (\alpha_{\text{opo}})/(gP_{\text{sat}})] - \zeta_{\text{lin}}}\right\} \tag{75}$$

From Eq. (72), we can determine the external pump power required to bring the pump laser to threshold P_{th}^{L} by putting the nonlinear loss and circulating intracavity power to zero, hence obtaining

$$P_{\text{th}}^{L} = \frac{\zeta_{\text{lin}}}{K} \tag{76}$$

Further, from Eq. (75) we can determine the external pump power required to bring the intracavity OPO to threshold $P_{\text{th}}^{\text{SRO}}$ by putting the term in braces to zero, hence obtaining

$$P_{\text{th}}^{\text{SRO}} = P_{\text{th}}^{L}\left[1 + \frac{(\alpha_{\text{opo}})}{(gP_{\text{sat}})}\right] \tag{77}$$

We can now write the expression for the downconverted power in terms of these thresholds, rather than in terms of the parameters of the pump laser and the OPO. We hence obtain the linear increase in the total downconverted power P_{DC} with the external pump power P as

$$P_{\text{DC}} = \sigma_{\max}(P - P_{\text{th}}^{\text{SRO}})\left[1 - \left(\frac{P_{\text{th}}^{L}}{P_{\text{th}}^{\text{SRO}}}\right)\right] \tag{78}$$

where $\sigma_{\max} = KP_{\text{sat}}$. The significance of $\sigma_{\max}$ becomes apparent by examining Eq. (72) describing the operation of the pump laser. Rearranging this equation, we obtain an expression for the steady-state circulating intracavity power in the absence of nonlinear downconversion as

$$P_{\text{IC}} = P_{\text{sat}}\left[\left(\frac{KP}{\zeta_{\text{lin}}}\right) - 1\right] \tag{79}$$

If an output coupler is used on this laser so as to extract the pump wave as useful output, then the output power extracted at the pump wavelength is

$$P_{\text{out}}^{L} = \zeta_{o} P_{\text{IC}} = \zeta_{o} P_{\text{sat}}\left[\left(\frac{KP}{\zeta_{\text{lin}}}\right) - 1\right] \tag{80}$$

From this it is apparent that the slope efficiency of the pump laser, defined as the ratio of the change in output power to the change in input power, is

$$\eta = \left(\frac{\zeta_o}{\zeta_{\text{lin}}}\right) KP_{\text{sat}} \tag{81}$$

Now the total linear loss ζ_{lin} is made up from the useful output coupling loss ζ_o and the parasitic loss ζ_p, namely

$$\zeta_{\text{lin}} = \zeta_o + \zeta_p \tag{82}$$

Hence, we see that $\sigma_{\max}$ is the slope efficiency of the pump laser itself when the total linear loss of that laser is equal to the useful output coupling loss—that is, when the parasitic loss is negligible in comparison to the useful output coupling loss. This is the maximum possible slope efficiency.

The total downconverted power P_{DC} may be optimized by suitable choice of the parameters in Eq. (78). In doing this, the first requirement is to minimize the threshold of the pump laser itself by making the linear loss of the pump laser cavity as low as possible. Obviously, this loss would now be entirely parasitic loss since output coupling of the pump wave is not required (i.e., $\zeta_{\text{lin}} = \zeta_p$). Given that it is required to operate the OPO at some fixed external pump power, we maximize the downconverted power by adjustment of the threshold of the OPO itself. By differentiating Eq. (78) with respect to $P_{\text{th}}^{\text{SRO}}$, it may readily be shown that this optimization occurs when

$$P_{\text{th}}^{\text{SRO}} = (P_{\text{th}}^{L}\, P)^{1/2} \tag{83}$$

In other words, optimization occurs when the external pump power required for the intracavity OPO to reach threshold is equal to the geometric mean of the external pump power for the pump laser itself to reach threshold and the available external pump power at which it is required to operate the OPO. By substituting this condition into Eq. (78), it may readily be shown that the total downconverted power thereby generated is given by

$$(P_{\text{DC}})_{\max} = \sigma_{\max}[(P)^{1/2} - (P_{\text{th}}^{L})^{1/2}]^2 \tag{84}$$

In the preceding $\sigma_{\max}$ is the maximum slope efficiency (i.e., where $\zeta_{\text{lin}} = \zeta_o$), and P_{th}^{L} is the minimum threshold (i.e. where the only linear loss is the unavoidable parasitic loss so that $\zeta_{\text{lin}} = \zeta_p$) of the pump laser. This expression is exactly the same as that describing the maximum output power that can be directly coupled out of the pump laser at the pump wavelength by optimizing the linear output coupling of that laser. (This later expression may readily be derived from Eq. (80) by differentiation of the output power with respect to ζ_o in order to derive first of all the optimum output coupling required, and then, by substitution, the value of the output power under such conditions.)

Thus, in an optimized intracavity OPO, the downconverted power generated is equal to the power that could have been coupled out of the pump laser itself under conditions of optimal (linear) output coupling. *Hence, the intracavity OPO has the potential for being 100 percent efficient with regard to the downconverted power that it generates.*

So far we have considered only the optimization of the downconverted power that is generated. Not all of this power can be extracted as useful output power, and indeed, as we shall see shortly, the optimization condition is not necessarily the same when it is required to maximize the extraction efficiency for a specific downconverted wave. In what follows we shall assume for convenience that the idler wave is the nonresonant wave and that it therefore exits the nonlinear crystal on a single pass, while the signal wave is the resonant wave. If the roles of the two waves are interchanged, analogous expressions for extraction efficiency can be readily deduced from the relations we are now about to derive.

The condition for maximum extracted idler wave power is the same as that given in Eq. (83) since this wave leaves the cavity on a single pass, and is therefore a fixed fraction of the

total downconverted power. Making due allowance for single-pass losses and for the fraction of the downconverted power that is internally generated as idler wave, we obtain

$$[P_1]_{\max} = \eta_1 \left(\frac{\omega_1}{\omega_3}\right) \sigma_{\max} [(P)^{1/2} - (P_{\text{th}}^L)^{1/2}]^2, \tag{85}$$

where η_1 is the fixed fraction of the idler that is transmitted out of the nonlinear medium in the presence of linear losses such as absorption and reflection.

The situation with regard to the signal wave is somewhat more complicated. Being the resonant wave in the OPO cavity, it is subject to both parasitic linear loss α_p that does not contribute usefully to the output, as well as the useful output coupling loss α_o (where $\alpha_{\text{lin}} = \alpha_o + \alpha_p$). Increasing the latter to diminish the effects of the former raises the threshold of the OPO, which then changes the downconversion efficiency. We must hence revert to a general expression for extracted signal power, and then seek a new optimization condition. The extracted signal power is readily derivable from Eq. (78) as

$$P_2 = \left(\frac{\omega_2}{\omega_3}\right) \left[\frac{\alpha_o}{(\alpha_o + \alpha_p)}\right] \sigma_{\max} (P - P_{\text{th}}^{\text{SRO}}) \left[1 - \left(\frac{P_{\text{th}}^L}{P_{\text{th}}^{\text{SRO}}}\right)\right] \tag{86}$$

where the first term describes the fraction of the downconverted power that goes into the signal wave, while the second term, the first one in square brackets, is the fraction of the signal wave power that is extracted usefully from the OPO cavity. We can relate the various linear losses in Eq. (86) to the external pump power required to reach their associated OPO thresholds by using Eq. (75), obtaining

$$P_2 = \left(\frac{\omega_2}{\omega_3}\right) \sigma_{\max} (P - P_{\text{th}}^{\text{SRO}}) \left\{1 - \left[\frac{(P_{\text{th}}^{\text{SRO}})_{\min}}{P_{\text{th}}^{\text{SRO}}}\right]\right\} \tag{87}$$

This equation differs from Eq. (78) only in that P_{th}^L is now replaced by $(P_{\text{th}}^{\text{SRO}})_{\min}$, where this latter is the OPO threshold when the linear loss from the signal cavity is parasitic loss α_p only—i.e., the useful output coupling loss α_o is zero. By comparison of Eqs. (78) and (87), it is apparent that the extracted signal power is a maximum when

$$P_{\text{th}}^{\text{SRO}} = [(P_{\text{th}}^{\text{SRO}})_{\min} P]^{1/2} \tag{88}$$

and that the signal power extracted under such conditions is

$$(P_2)_{\max} = \left(\frac{\omega_2}{\omega_3}\right) \sigma_{\max} \{(P)^{1/2} - [(P_{\text{th}}^{\text{SRO}})_{\min}]^{1/2}\}^2 \tag{89}$$

For the OPO to attain the highest possible efficiency as a downconverter of external power into useful signal wave power, the threshold of the OPO as determined solely by its parasitic loss must first be made as close as possible to the pump laser threshold. (This condition can only be approached rather than actually achieved.) Then the output coupling of the resonant signal wave must be increased to the point where the OPO threshold becomes the geometric mean of the external pump power at which it is required to operate the OPO and the minimum OPO threshold, as defined previously. If this condition, which is stated in Eq. (88), is fulfilled, Eq. (89) provides a measure of the overall efficiency of the intracavity OPO. We now summarize the various options for optimizing useful output from the intracavity OPO as follows:

For all of the options, the threshold of the pump laser should be made as low as possible by both minimizing parasitic losses and by avoiding any linear output coupling of the pump wave. Then one or other of the following procedures should be adopted depending on the type of output required.

1. If maximum idler (nonresonant) wave power is required, the threshold of the OPO should be arranged to be the geometric mean of the maximum external pump power available and the external pump power required to reach the oscillation threshold of the pump laser.
2. If maximum downconverted power is required, regardless of whether it is all usefully extracted, then the conditions appertaining to procedure 1 also apply.
3. If maximum useful signal (resonant) wave power is required, then the OPO threshold in the absence of useful output coupling of the resonant wave should first be minimized by eliminating parasitic losses as far as possible, and so on. Then the useful output coupling of the resonant wave should be increased to the point where the OPO threshold now becomes equal to the geometric mean of the pump laser threshold and the previous minimum OPO threshold.
4. If it is required to maximize the usefully extracted downconverted power regardless of whether it is in the idler wave or the signal wave, then it may be shown that following minimization of the external pump power required to reach oscillation threshold of the OPO in the absence of useful output coupling (as in procedure 3), the useful output coupling for the resonant (signal) wave should be increased to the point where the external pumping power required to reach OPO oscillation threshold becomes

$$P_{\text{th}}^{\text{SRO}} = \left[\left(\frac{\omega_2}{\omega_3} \right) P (P_{\text{th}}^{\text{SRO}})_{\min} + \left(\frac{\omega_1}{\omega_3} \right) P_{\text{th}}^{L} P \right]^{1/2} \tag{90}$$

In 1998 Edwards et al.[74] demonstrated just such high efficiencies in a practical device in which KTA was used as the nonlinear crystal within the cavity of a CW titanium sapphire laser. An argon ion laser provided the external pump power to pump the titanium sapphire laser. The KTA crystal used was of length 11.5 mm and was cut for type II NCPM for propagation along the optical X axis, with anti-reflection-coated end faces for both the pump and resonated signal wave. Fig. 16 shows the operating characteristics of the device. The titanium sapphire laser itself reaches threshold at an external pump power from the argon ion laser of about 0.8 W. The intracavity power within the titanium sapphire laser, which is the pump power for the OPO itself, then increases linearly with external pump power until the OPO reaches oscillation threshold at an intracavity pump power of around 15 W, corresponding to an external pump power of about 3 W from the argon ion laser. As the external pump power is further increased, the intracavity pump power becomes clamped to the threshold value, in contrast to the linear increase it would continue to show with increasing external pump power if the OPO were maintained in the off condition. At the same time, the downconverted power rises linearly with the external pump power. In Fig. 16*b* this experimentally observed downconverted power is plotted as a function of the external pump power (circles), along with the output power expected from the titanium sapphire laser when operated at the pump wavelength under conditions of optimal output coupling $(P_{\text{out}}^{L})_{\max}$ (solid line) and the downconverted power expected to be generated by the OPO according to Eq. (78). As predicted by Eq. (83), these latter two quantities are the same at an external pump power of 12 W. It may be seen from the figure that the observed downconverted power closely approaches the 100 percent efficiency value expected.

Figure 17 illustrates the tuning and output power behavior of the intracavity OPO as the titanium sapphire laser is tuned across part of its gain bandwidth (760 to 860 nm) and where the external pump power from the argon ion laser is 14 W. Both signal and idler powers simultaneously remain in excess of 0.5 W for tuning ranges of 1120 to 1200 nm and 2450 to 2850 nm, respectively.

In this particular device the pump wave (intracavity field of the titanium sapphire laser) was multimode (20 GHz), while the resonated signal wave was generally single frequency, with the idler wave hence acquiring the linewidth of the pump. An OPO with a ring configuration (traveling wave) for both the titanium sapphire and OPO cavities has been demonstrated. This facilitates attaining single-frequency oscillation of the pump wave through the

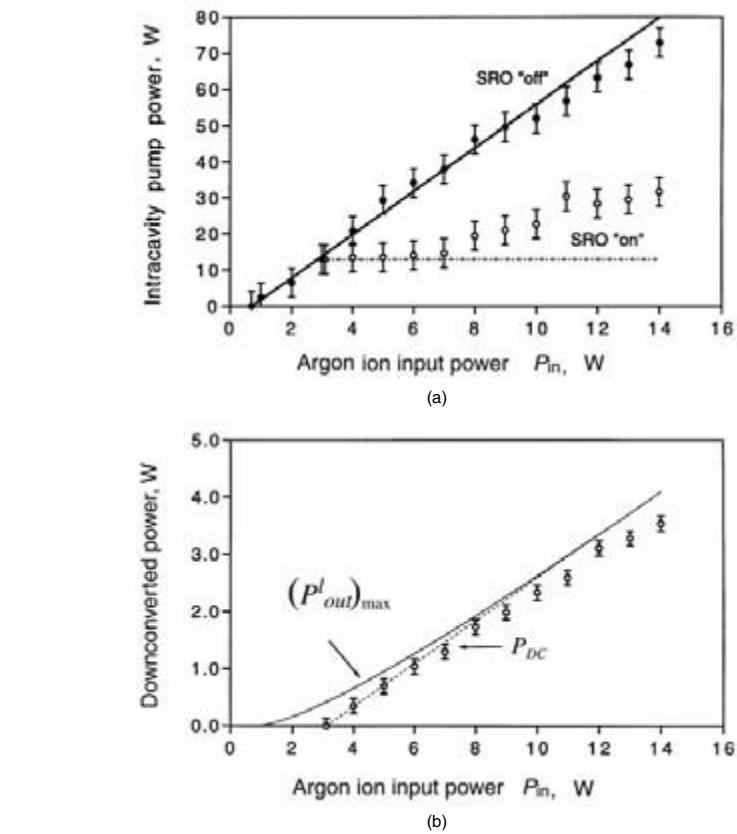

FIGURE 16 Operating characteristics of an intracavity OPO based on KTA as the nonlinear medium within the cavity of a titanium:sapphire laser. The titanium:sapphire laser is itself pumped by an argon ion laser. (*a*) Behavior of the intracavity power as the input power is increased, with the OPO both on and off. In the former case, the intracavity power is clamped as the OPO comes above threshold. Solid and dashed lines correspond to the theoretical predictions, whereas the points correspond to the experimental measurements. (*b*) Total downconverted power as a function of input power. The dashed line is the theoretical prediction, and the points correspond to the experimental measurements. Also shown is the maximum fundamental power that could be coupled out of the pump laser under optimum output (linear) coupling.

avoidance of spatial hole burning, and results in the idler wave also becoming single frequency.

The described use of a traditional birefringent material in the intracavity OPO highlights an important advantage of this approach. The threshold of the SRO based on such nonlinear materials when operated outside of the pump laser cavity is prohibitively high, being on the order of 15 W. On the other hand, this threshold can be exceeded when the device is operated

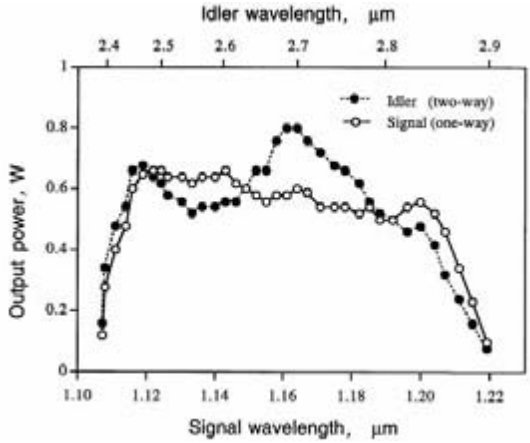

FIGURE 17 Signal and idler tuning ranges and output powers as a function of the pump wavelength for an intracavity OPO based on KTA within the cavity of a titanium:sapphire laser.

intracavity with only 3 W of pump power from the primary pump (the argon ion) laser. Intracavity SROs within titanium sapphire lasers based on KTP,[75] PPLN,[76] PPRTA,[77] and PPKTP,[78] in addition to the KTA just described, have now been demonstrated.

Devices in which the OPO is placed within the cavity of CW neodymium lasers pumped by laser diodes have also been demonstrated. In this context, both birefringently phase-matched materials such as KTA and QPM materials such as PPLN[79] have been used as nonlinear gain media. In the former case, output powers on the order of 1 W in the idler wave at 3.5 μm have been demonstrated when pumping a Nd:YVO_4 gain medium with 8 W of external pump power from a diode laser. In the latter case, a 1 W diode laser also pumping Nd:YVO_4 as the gain medium sufficed to generate in excess of 70 mW in an idler wave that could be tuned over 3 to 4 μm in a compact device. A review of the current progress on intracavity CW OPOs can to be found in Ref. 78.

22.7 PULSED PARAMETRIC OSCILLATORS

One of the main results of the preceding analyses is that the SRO configuration, in which only one of the generated waves is resonant, represents the simplest and most practical device configuration for an OPO, because of its minimal demands on pump beam coherence, high passive stability, and reduced complexity in spectral and temporal behavior. Yet, the SRO configuration yields the highest threshold of all cavity configurations. The most important implication of this result is that the attainment of oscillation threshold in SROs using conventional external pumping schemes is generally beyond the reach of commonly available CW pump lasers, particularly when conventional birefringent materials are employed. Given this restriction, practical operation of these devices has historically necessitated the use of high-peak-power pulsed pump sources. In the following discussion, we provide an overview of OPO devices operating in the nanosecond, picosecond, and femtosecond temporal domain and review some of the most important recent developments in this field. The discussion is focused mainly on SRO device configurations, as most of the practical devices developed to date conform to this operating regime.

Nanosecond Optical Parametric Oscillators

Because of their high peak powers, nanosecond pulsed lasers represent the most viable choice of pump for SROs. Combined with the widespread availability of such laser sources, OPOs operating in the nanosecond pulsed regime have traditionally been the most extensively developed of all parametric devices. Indeed, the first successful demonstration of an OPO was a nanosecond oscillator based on $LiNbO_3$ and pumped by a frequency-doubled, Q-switched Nd:$CaWO_4$ laser at 0.529 μm.[5] Although this device was a DRO, the development of pulsed SROs based on $LiNbO_3$ soon followed.[80,81] Subsequently, several devices based on other classical materials such as $LiIO_3$,[82] CdSe,[83] Ag_3AsS_3,[84] and $AgGaS_2$[85] were developed, covering wavelength regions mainly in the infrared spectrum. The pump sources were predominantly Q-switched neodymium lasers and their harmonics, although pulsed ruby lasers[82] and chemical lasers such as the HF laser[86] were also used as pumps for these devices.

The basic operation principles in nanosecond OPOs are the same as in CW oscillators. However, the steady-state threshold analysis used earlier in the treatment of CW OPOs is not strictly applicable here, because the instantaneous nature of parametric gain does not allow steady-state conditions to be reached within the finite temporal window of the pump pulse. This situation is markedly different from that in a conventional laser, where under pulsed excitation the gain storage capability of the gain medium generally permits amplification after the pump pulse excitation for a time determined by the upper-state lifetime of the transition. In the parametric process, the electronic susceptibility is effectively instantaneous, so that the nonlinear medium has no gain storage capacity. This means that coherent amplification of the parametric waves has to occur in the presence of the pump and that no gain is available outside the temporal window of the pump pulse. Given the finite duration of the pump pulse, only a limited number of round-trips for the parametric waves can be made available through the nonlinear crystal in OPO cavities of practical length, thus preventing the establishment of steady-state conditions. Therefore, nanosecond pulsed OPOs generally operate in a transient regime, and a modified model taking account of the dynamic behavior of OPO is thus necessary for the analysis of such devices.

By using a time-dependent gain analysis, Brosnan and Byer have derived the equations governing the threshold pump energy fluence in pulsed SROs.[87] The model assumes a gaussian temporal profile for the incident pump pulse and a gaussian spatial distribution for the pump and the resonant signal, with an idler wave that is unconstrained by the optical cavity. The model also includes the effects of mode overlap and spatial walkoff. The threshold condition is then derived from the solution of the coupled-wave equations Eqs. (4*a*) to (4*c*) in the limit of low pump depletion and zero input idler field, by allowing the resonant signal wave to be amplified from the initial parametric noise power to a detectable level by successive transits through the SRO cavity. By defining the SRO threshold as a signal energy of ~100 μJ, corresponding to a threshold signal power to parametric noise power of $\ln (P_s^{\text{th}}/P_n) = 33$, the threshold energy fluence (energy/area) is derived as

$$J_{\text{th}} \cong \frac{2.25}{\gamma g_s \zeta} \tau \left[\frac{L}{2\tau c} \ln \frac{P_s^{\text{th}}}{P_n} + 2\alpha\ell + \ln \frac{1}{\sqrt{R}} + \ln 2 \right]^2 \tag{91}$$

where τ is the $1/e^2$ intensity half-width of the pump pulse, L is the cavity length, α is the signal field amplitude loss coefficient within the crystal, R is the mirror reflectivity coefficient, and ℓ is the crystal length. The parameter γ is a modified gain coefficient, which is related to the gain factor Γ defined in Eq. (6) by

$$\gamma = \frac{\Gamma^2}{I_3(0)} = \frac{2\omega_2\omega_1 d_{\text{eff}}^2}{n_3 n_2 n_1 \varepsilon_o c^3} \tag{92}$$

The factor g_s is the spatial coupling coefficient describing the mode overlap between the signal and pump field. It is defined as

$$g_s = \frac{w_3^2}{w_3^2 + w_2^2} \tag{93}$$

where w_3 and w_2 are the gaussian mode electric field radii of the pump and signal, respectively. The parameter ζ is the effective parametric gain length given by

$$\zeta = \ell_w \operatorname{erf}\left(\frac{\sqrt{\pi}}{2}\frac{\ell}{\ell_w}\right) \tag{94}$$

where ℓ_w is the walkoff length defined as

$$\ell_w = \frac{\sqrt{\pi}}{2}\frac{w_3}{\rho}\sqrt{\frac{w_3^2 + w_2^2}{w_3^2 + w_2^2/2}} \tag{95}$$

where ρ is the double-refraction angle (see Sec. 22.9). The walkoff length ℓ_w is closely related to the aperture length defined in Sec. 22.9 and accounts for spatial walkoff between the gaussian pump and signal fields. In the absence of spatial walkoff, $\ell_w \to \infty$ and the crystal length ℓ becomes the effective parametric gain length.

The main conclusions of the time-dependent model relate to the strong dependence of pulsed OPO threshold on the characteristic *rise time* of the oscillator. This is a measure of the time required for the parametric gain to build up from noise to oscillation threshold.[88] In order for the OPO to switch on, it is essential that the oscillator rise time is shorter than the pump pulse duration. For efficient operation, however, the *rise time* must be minimized so that the parametric waves are rapidly amplified above the threshold level in a time significantly shorter than the pump pulse interval. Therefore, the rise time represents an effective loss for pulsed OPOs, with a direct impact on oscillation threshold. To exploit maximum gain, it is essential that the parametric waves be amplified in as short a time interval as possible in the presence of the pump pulse. In practice, this can be achieved by minimizing the OPO cavity length to allow maximum number of round-trips over the pump pulse interval. This is also evident from the direct dependence of J_{th} on the cavity length L in Eq. (91). In nanosecond OPOs, cavity lengths of a few centimeters or shorter are often practicable, yielding as many as 100 round-trips for pump pulses of 1 to 50 ns duration. As can be verified from Eq. (91), the pulsed OPO threshold can also be further reduced by using longer pump pulse durations τ (provided the peak pump pulse intensity is not diminished) and by lowering the intracavity parasitic losses through minimizing α and maximizing R. Above threshold, the operation of pulsed OPOs is characterized by the extraction of energy from the pump pulse and saturation of nonlinear gain, in a similar manner to CW OPOs discussed earlier. This is often observed in the form of depletion toward the trailing edge of pump pulse. The signal (and idler) pulse is then amplified with a characteristic delay from the pump pulse by a time interval determined by the OPO rise time.[81,89,90]

We can obtain a measure of the threshold fluence in pulsed SROs by considering a typical example based on a 10-mm-long KTP crystal under type II NCPM, pumped by 10-ns pulses from a Q-switched Nd:YAG laser at 1.064 μm. We assume a practical cavity length $L = 20$ mm, mirror reflectivities $R \sim 99.5$ percent, an effective nonlinear coefficient $d_{\text{eff}} \sim 3$ pm/V, refractive indexes $n_3 \sim n_2 \sim n_1 \sim 1.5$, and mode radii $w_3 \sim w_2$. For near-degenerate operation with $\lambda_1 \sim \lambda_2 \sim 2$ μm and for $\alpha \sim 2\%$ and $\rho = 0$, substitution of these parameters into Eqs. (92) to (95) and then into Eq. (91) yields a threshold pump energy fluence $J_{\text{th}} \sim 1.2$ J/cm^2. This translates into a threshold pump pulse energy of $E_{\text{th}} \sim 37$ mJ for a focused pump mode radius $w_3 \sim 1$ mm. The threshold energy can, of course, be substantially reduced by using tighter focusing. For example, the use of a pump beam waist of $w_3 \sim 0.5$ mm will lead to a nearly fourfold reduction in threshold energy to ~9 mJ, whereas reducing the focused radius to $w_3 \sim 0.1$ mm will result in nearly a tenfold threshold reduction to ~0.4 mJ. It should, however, be noted that considerations of material damage in the presence of nanosecond pulses present a practical upper limit to the minimum

focused pump spot radii that can be used in such devices (see Sec. 22.9). Therefore, the optimum choice of experimental parameters for the attainment of minimum operation threshold in pulsed OPOs is often compromised by material damage threshold. Material damage remained a major limitation to the operation of early devices, even at moderate power levels, and for many years hampered the development of practical nanosecond OPOs.

Nanosecond OPO Devices

With the emergence of a new generation of nonlinear materials in the 1980s with unprecedented damage thresholds, the development of practical nanosecond OPOs capable of providing high-power and widely tunable radiation in new spectral regions became possible. The predominant pump sources have continued to be frequency-converted, flashlamp-pumped, *Q*-switched neodymium-based lasers, but ultraviolet excimer lasers have also been shown to be attractive as OPO pumps, particularly given their higher average-power capability. Of the numerous new devices demonstrated, the type I phase-matched BBO OPO pumped by frequency-tripled Nd:YAG laser at 355 nm[91] or by the XeCl excimer laser at 308 nm[92,93] has been established as the most versatile and practical source of broadly tunable nanosecond pulses from the near-ultraviolet to the near-infrared. These devices can provide tunable nanosecond pulses over continuous range from typically 400 nm to 2.5 μm with a single crystal and only one or two sets of optimally designed cavity mirrors to resonate the short-wavelength branch of the tuning range up to degeneracy.[91,93] Output pulse energies from a few millijoules to tens of millijoules can currently be made available from these devices in pulses of 1 to 10 ns duration, at up to ~100-Hz repetition rates and with extraction efficiencies in excess of 30 percent. Because of the high optical damage threshold of the crystal, energy scaling of BBO OPOs to the multijoule level is also attainable with the use of high-energy pulsed pump sources. The upper limit to the conversion efficiency and output pulse energy in BBO OPOs is generally set by damage to the OPO mirrors and crystal coatings, which can be caused either by the pump pulses or by the circulating signal intensities. However, these may be circumvented by using novel pumping and crystal configurations,[94,95] longer pump pulse durations, and shorter cavity lengths. One of the major drawbacks of the type I BBO OPO, however, is the spectral linewidth of the output. Without any bandwidth control, the linewidth of the BBO OPO typically varies from 0.1 nm to as much as 12 nm near wavelength degeneracy,[93,95] which can limit the use of the device in spectroscopic applications. However, by employing techniques such as grating feedback[95] or external injection-seeding[96] it is possible to achieve linewidth reduction to below 0.1 nm across the tuning range of BBO OPO. The use of type II phase-matching and walkoff compensated geometries[97] and manipulation of pump laser spatial profile and filtering of the output[98] have also been shown to yield major improvements in the linewidth of BBO OPOs.

In addition to the BBO OPO, numerous nanosecond oscillators based on other nonlinear crystals including LBO, $KNbO_3$ (KNB), and KTP and its new arsenate isomorphs such as $KTiOAsO_4$ (KTA) have been developed using a variety of phase-matching geometries and pumping configurations. In particular, because of its temperature-tuning capability, versatile phase-matching characteristics, broad transparency (160 nm to 2.6 μm), and high damage threshold, LBO has proved to be highly attractive for use in nanosecond OPOs operating in the ultraviolet, visible, and near-infrared wavelength regions. While the effective nonlinear coefficient of LBO (~1 pm/V) is considerably lower than that of BBO (~3 pm/V), its NCPM capability and small double-refraction allow the use of longer interaction lengths, thus permitting comparable efficiencies to be maintained. The crystal has been used for parametric generation under both type I and type II temperature-tuned NCPM with XeCl excimer lasers[99] and frequency-tripled flashlamp-pumped Nd:YAG lasers.[100] The small spatial walkoff in LBO has also enabled the development of an all-solid-state, widely tunable OPO under type I critical phase matching (CPM) using frequency-tripled, *Q*-switched, diode-pumped Nd:YAG lasers.[101]

Other nonlinear crystals such as KTP, KNB, and KTA have been of particular interest for wavelength generation in the difficult 3- to 5-μm spectral range in the mid-infrared, because of

their longer infrared transmission beyond 5 μm. While these materials display lower optical damage thresholds than LBO, they possess considerably larger nonlinear coefficients. Of these, KTP has been perhaps the most extensively used material; nanosecond parametric oscillation out to 3.2 μm has been demonstrated with the fundamental of the Nd:YAG laser at 1.064 μm.[102] Under type II NCPM, all-solid-state pumping of a nanosecond KTP OPO has also been reported with a diode-pumped, *Q*-switched Nd:YAG laser.[103] However, an infrared cutoff wavelength of ~4.3 μm as well as absorption bands near 2.8 and 3.2 μm has limited the scope for use of KTP over the whole of its transmission window. On the other hand, the arsenate isomorphs of KTP such as KTA exhibit increased transparency with little or no absorption up to ~5.3 μm, while maintaining similarly attractive phase matching and nonlinear optical properties to KTP. As in KTP, the most efficient interaction in KTA is type II, which is possible under CPM in any of the principal planes or under NCPM along a principal axis. The potential of this material for mid-infrared parametric generation was demonstrated with the use of a flashlamp-pumped Nd:YAG laser at 1.064 μm as the pump source.[104] By using type II CPM in the *xz* plane, continuously tunable output in the 1.5- to 5-μm spectral range was generated at conversion efficiencies of up to 20 percent. The nonlinear crystal KNB has also been successfully used for nanosecond pulse generation in the 2- to 4-μm spectral range. However, the relatively high optical damage threshold, superior optical and mechanical properties, and availability in large size and good optical quality makes KTA a superior choice of material for practical near- to mid-infrared nanosecond OPOs at the present time. Other arsenate crystals such as RTA and $CsTiOAsO_4$ (CTA) also hold promise for parametric generation in the important 3- to 5-μm spectral region.

The recent development of QPM nonlinear materials such as PPLN, periodically poled KTP, and its arsenate isomorphs, PPRTA and PPKTA, has also had a widespread impact on pulsed OPOs. The large optical nonlinearity, combined with a NCPM capability, long interaction lengths, and widespread availability, particularly in the case of PPLN, has enabled the realization of pulsed OPOs at considerably lower pump pulse energies than are practicable with birefringent materials. This has facilitated the development of pulsed SROs using high-repetition-rate or long-pulse, diode-laser-based pump sources with low peak powers.[105,106] Average output power in excess of 1 W, repetition rates higher than 10 kHz, and tunability in the 2- to 5-μm spectral range are now routinely available from such PPLN-based SROs. The use of other newly developed QPM materials such as PPKTP have also enabled the development of pulsed SROs for the near-infrared with low pump thresholds and high conversion efficiencies.[107] Because of the temperature-tuning potential offered through periodic poling, wavelength tuning in PPKTP can be achieved under NCPM without resort to angle tuning. On the other hand, the large nonlinear gain of PPKTP allows critical phase matching with the use of large pump beam waists, so that angle tuning may also be used as a means of wavelength tuning without drastic declines in SRO performance. At present, however, extended angle-tuned phase matching in OPOs based on QPM materials is limited by the small crystal apertures (0.5 to 1 mm in PPLN and 1 to 2 mm in PPKTP and its arsenate analogs). This limitation, combined with consideration of material damage, has presented an obstacle to energy scaling of such devices; therefore, the development of large-aperture QPM crystals is currently an area of active research interest. Recently, however, the operation of a nanosecond OPO based on large-aperture (3 mm × 3 mm) PPRTA was demonstrated, with up to 17 mJ of signal pulse energy obtained at 26 percent conversion efficiency.[108] The large nonlinear gain of PPLN has also enabled fiber laser pumping of nanosecond OPOs[109] and the development of new types of single-pass parametric generators using nanosecond pulse pumping.[110]

22.8 SYNCHRONOUSLY PUMPED PARAMETRIC OSCILLATORS

Optical parametric oscillators are also highly effective for the generation of optical pulses with picosecond and femtosecond temporal durations. The high peak pulse intensities available from mode-locked picosecond and femtosecond laser sources can facilitate the attainment of

sufficient nonlinear gain in an OPO to overcome threshold, even in SRO configurations. However, unlike nanosecond devices, operation of ultra-short-pulse OPOs of this type is attainable only under *synchronous pumping* conditions. This is because the temporal window of the pump pulses in this case is too narrow to allow a sufficient number of round-trips for the build up of the parametric waves over the pump envelope, even for OPO cavity lengths as short as a few millimeters. To circumvent this difficulty, the OPO resonator length is matched to the length of the pump laser, so that the round-trip transit time in the OPO cavity is equal to the repetition period of the pump pulse train. In this way, the resonated parametric pulses experience amplification with consecutive coincidences with the input pump pulses as they make successive transits through the nonlinear crystal. In practice, the technique of synchronous pumping is restricted to relatively high pulse repetition rates (>50 MHz). At lower repetition frequencies, the required cavity lengths for synchronous pumping become too cumbersome to be practical for most purposes. The synchronously pumped parametric oscillator (SPPO) offers a number of advantages over conventional mode-locked lasers. In addition to wavelength flexibility and broad tuning range, the output pulses from the SPPO exhibit lower timing jitter relative to the pump pulses than other synchronously pumped lasers with gain storage, because of the instantaneous nature of parametric gain. This makes the SPPO highly suitable for applications such as high-resolution time-domain spectroscopy.

In general, SPPOs may be classified as either CW or pulsed devices. In CW SPPOs, the input pump radiation comprises a continuous train of ultrashort pulses, whereas in pulsed SPPOs the pump consists of trains of ultrashort pulses contained within a nanosecond or microsecond envelope. With regard to their operating characteristics, CW SPPOs may be treated as steady-state devices in the same way as CW OPOs, but with the peak pump pulse intensity determining the nonlinear gain. As such, the steady-state analysis of CW OPOs is similarly applicable to CW SPPOs by using the peak pulse intensity as the incident pump intensity. On the other hand, the operating dynamics of pulsed SPPOs is analogous to nanosecond oscillators, where a transient analysis taking account of rise-time effects is necessary to adequately describe the SPPO behavior.[87] In pulsed SPPOs, the nonlinear gain is similarly determined by the peak pulse intensity, but rise-time effects arising from the finite duration of the pulse envelope lead to an additional loss mechanism. In either case, however, additional effects pertinent to the operation of SPPOs including temporal walkoff (see Sec. 22.9) and group velocity dispersion also have to be included in the model. In picosecond SPPOs where pulse durations of >1 ps are involved, such temporal effects can generally be neglected for practical crystal lengths of up to 20 mm. However, they become increasingly important in femtosecond SPPOs involving pulses of 100 fs or shorter, as discussed in Sec. 22.9.

The plane-wave analysis of SPPOs under steady-state and transient operation has been presented by Becker et al.[111] and by Cheung and Liu[112] for CW singly resonant SPPOs with gaussian beams. One of the main conclusions of their analyses is that in the absence of group velocity dispersion and temporal walkoff, the output pulses from a SPPO are always shorter than the input pump pulses, with the parametric pulses broadening toward the pump pulse length with increasing pump depletion. They also show that it is possible to obtain conversion efficiencies as high as ~70 percent in such devices with suitable choice of design parameters. The analysis of CW singly resonant SPPOs also shows that for high efficiency and short pulses, the oscillator should be designed to operate with a peak pump intensity that is approximately twice the steady-state threshold value. For a given pump intensity and nonlinear material parameters, the output coupling mirror can therefore be adjusted to allow this condition to be met. Near threshold, the effects of temporal walkoff can be almost perfectly compensated by fine-tuning the cavity length.

Picosecond Optical Parametric Oscillators

For most practical applications, the CW SPPO is the most desired device configuration because the output consists of a truly continuous train of identical pulses. In pulsed SPPOs, on

the other hand, the amplitude, intensity, and duration of the output pulses can vary across the pulse envelope, and the output does not constitute a truly repetitive pulse train. However, because of the significantly higher peak powers available from pulsed mode-locked than from the equivalent CW mode-locked pump lasers, operation of SPPOs is more readily attainable under pulsed conditions, particularly in SRO configurations of practical interest. For this reason, most of the earlier SPPOs based on birefringent materials have been pulsed oscillators, pumped predominantly by the mode-locked and *Q*-switched (MLQS) neodymium laser and its harmonics. Of these, the type I singly resonant BBO SPPO pumped by the second and third harmonics of the MLQS flashlamp-pumped Nd:YAG laser has been shown to be a versatile source of picosecond pulses across a broad spectral range from 400 nm to 3 μm.[113,114] Output pulses with durations of 10 to 100 ps in *Q*-switched envelopes of a few millijoules energy at conversion efficiencies approaching 30 percent have been obtained from these devices. In addition to BBO, the crystals of KTP and LBO have also been successfully used in pulsed SPPOs pumped by the second harmonic of MLQS Nd:YAG and Nd:YLF lasers in the green. In particular, the use of type I temperature-tuned NCPM in LBO has enabled the development of widely tunable picosecond SPPOs in all-solid-state SRO configurations by using the frequency-doubled output of a MLQS diode-pumped Nd:YLF laser at 523 nm.[115] In addition to SRO devices, a number of pulsed doubly resonant SPPOs based on BBO, KTP, LBO, and $Ba_2NaNb_5O_{15}$ have also been reported with the use of MLQS Nd:YAG pump lasers.

In the meantime, considerable advances have been made in the development of practical CW picosecond SPPOs. Because of the relatively low peak powers available from CW mode-locked picosecond pump lasers, the early attempts in this area were confined to DRO devices, with the concomitant disadvantages of amplitude and spectral instabilities of the output. However, with the availability of high-power CW mode-locked laser sources and the emergence of novel mode-locking techniques, the operation of CW SPPOs in SRO configurations has become a practical reality. The majority of the CW singly resonant SPPOs demonstrated to date have been based on the CW mode-locked neodymium laser and its second harmonic as the pump source. In most cases, the attainment of short pump pulses of sufficient intensity has necessitated the use of coupled-cavity techniques or external pulse compression. Particularly noteworthy has been the development of all-solid-state CW singly resonant SPPOs based on KTP[116] and LBO[117,118] and pumped by the frequency-doubled output of coupled-cavity mode-locked Nd:YLF lasers. These oscillators have been shown to provide truly continuous and highly stable output pulses with durations of 1 to 5 ps at repetition rates as high as 130 MHz. The LBO SPPO can generate continuously tunable output from 650 nm to above 2.5 μm with a single crystal, while the KTP device is tunable over 900 nm to 1.2 μm. Average output powers of tens of milliwatts at efficiencies of up to 30 percent are routinely available from these devices. High-power operation of CW singly resonant SPPOs has also been reported with the use of flashlamp-pumped CW mode-locked neodymium lasers. By using the fundamental output of a Nd:YLF laser at 1.053 μm, total average output powers of up to 2.8 W have been obtained from a KTP SPPO for 14 W of pump, with 800 mW in the idler beam near 3.2 μm.[119] This device generated signal pulses of 12 ps duration for 40-ps input pump pulses at a 76-MHz repetition rate. A similar mid-infrared oscillator was also demonstrated by using temporally compressed output pulses from a Nd:YAG laser at 1.064 μm to pump a KTP SPPO.[120] Average output powers of up to 350 mW in pulses of 2 to 3 ps at 75 MHz were generated for 4 W of pump power. Picosecond pulse generation in the visible has also been demonstrated in LBO using the third harmonic of a CW mode-locked Nd:YLF laser.[121] Average output powers of 275 mW in the blue spectral range of 453 to 472 nm were obtained in 15-ps pulses at a 75-MHz repetition rate.

More recently, the operation of CW singly resonant picosecond SPPOs has been achieved with the use of the Kerr-lens mode-locked (KLM) titanium sapphire laser as the pump source. A particularly attractive feature of this approach is that the tunability of the titanium sapphire pump source allows wavelength tuning in the SPPO without resort to angle phase matching. This minimizes intracavity reflection losses caused by crystal rotation, thus maintaining max-

imum efficiency across the available tuning range. By using type II NCPM in KTP and a KLM titanium sapphire pump laser, tunable picosecond pulses in the 1- to 1.2-μm and 2.3- to 2.9-μm spectral ranges have been generated by tuning the titanium sapphire laser over 720 to 853 nm.[122] Average output powers of up to 700 mW in 1.2-ps pulses at a 82-MHz repetition rate were produced for 1.6 W of pump. The combination of a tunable titanium sapphire laser with temperature-tuned LBO under type I NCPM has also been shown to provide a versatile source of picosecond pulses with continuous tunability over 1 to 2.4 μm.[123] This SPPO could generate output powers of up to 325 mW for 1.2 W of pump in pulses of ~1 to 2 ps durations at a 81-MHz repetition rate. For wavelength coverage further into the infrared, the arsenate isomorphs of KTP, namely KTA and RTA, represent excellent material candidates because of their extended transparencies beyond those of KTP and LBO, as well as their NCPM capability under titanium sapphire pump tuning. The use of type II NCPM in KTA has enabled the generation of picosecond pulses out to 3.6 μm, with average power of up to 400 mW in 1- to 3-ps pulses.[124] The extension of tuning range of titanium-sapphire-pumped picosecond SPPOs to the visible has also been demonstrated by intracavity frequency doubling of signal pulses. By using LBO as the nonlinear material, visible pulses of ~1 ps duration in the 584- to 771-nm spectral range have been obtained at 320 mW average power with this technique.[125]

The availability of QPM nonlinear materials has also brought about new opportunities for the development of CW singly resonant picosecond SPPOs with improved performance characteristics. The large nonlinear optical coefficient of these materials combined with NCPM capability and broad infrared transparency has enabled the development of picosecond SROs with minimal pump power requirements, high output efficiency, practical output power, and extended tunability into the difficult mid-infrared spectral range. In particular, compact all-solid-state SPPOs based on PPLN or PPRTA and pumped by mode-locked Nd:YLF and titanium sapphire lasers have been shown to be versatile sources of picosecond pulses with tunability across the entire range of 1.5 to 6 μm.[126,127] These devices exhibit average pump power thresholds as low as 10 mW, and can provide signal output power of up to ~400 mW in pulses of ~1 to 5 ps duration, with >10 mW of idler available beyond 5 μm. Output power of >2 W has also been made available in PPLN-based devices by using high-power flashlamp-pumped picosecond Nd:YAG lasers. Substantial enhancement in the mid-infrared output power has been shown to be attainable by using intracavity difference-frequency-mixing techniques.[128]

Figure 18 provides a summary of the performance characteristics of singly resonant picosecond SPPOs developed to date.

Femtosecond Optical Parametric Oscillators

The high peak powers available from ultrashort femtosecond pulses are particularly suited to the exploitation of the small nonlinear gain in parametric devices. However, because of the short temporal duration (typically <100 fs) and large spectral content (typically >10 nm) associated with femtosecond pulses, additional effects such as group velocity dispersion, temporal walkoff, and spectral acceptance bandwidths play an important role in the operation of these devices. Group velocity dispersion often leads to pulse broadening in the SPPO, while temporal walkoff can degrade nonlinear gain or even modify the temporal characteristics of the output pulses. The spectral acceptance bandwidth of the crystal can also reduce gain as well as set a lower limit to the minimum attainable pulse duration from the SPPO. The influence of temporal walkoff and spectral acceptance bandwidth can be minimized by using short crystal lengths of typically 1 to 2 mm, while the effects of group velocity dispersion can be overcome by the inclusion of dispersion compensation in the SPPO cavity, as in conventional femtosecond lasers. Therefore, the choice of nonlinear crystal requires a trade-off with the crystal length. The need for large nonlinear figures of merit (see Sec. 22.9) for low oscillation thresholds must be traded against the desire for large phase-matching bandwidths and low temporal walkoffs for optimum design. While crystal lengths of 1 to 2 mm are too short to provide sufficient gain in picosecond and nanosecond oscillators, the substantially higher peak power avail-

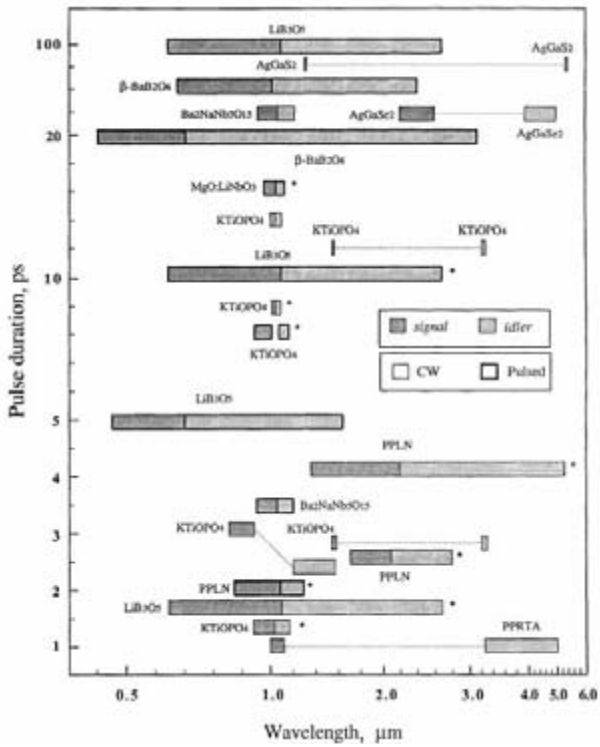

FIGURE 18 Summary of the temporal and tuning characteristics of several picosecond optical parametric oscillators synchronously pumped by neodymium and titanium:sapphire laser sources. The average output power from these OPOs ranges from ~1 mW to ~3 W, depending on the output wavelength range and the pump source used, and pulse repetition rates typically range from ~70 to ~360 MHz. The asterisk denotes all-solid-state pumping configurations.

able with femtosecond pulses can adequately compensate for this shortfall in gain. However, the high in-crystal peak intensities (typically >10 GW/cm^2) can also induce additional higher-order nonlinear effects such as self–phase modulation in femtosecond SPPOs. Such effects, which are not generally present in picosecond and nanosecond oscillators, often lead to spectral broadening and chirping of the output pulses and become more pronounced with longer interaction lengths. The spectral broadening due to self–phase modulation can, however, be exploited for subsequent compression of output pulses. Interestingly, the high intensities in femtosecond SPPOs can also result in non-phase-matched mixing processes over a coherence length of the crystal where, in addition to the signal and idler beams, several other wavelengths are also generated at a detectable level. The design of femtosecond SPPOs involves a careful consideration of the additional temporal and spectral effects as well as other phase-matching and material parameters relevant to the operation of parametric devices.

Optical parametric oscillators operating in the femtosecond time domain represent the newest class of parametric devices. The first report of a femtosecond SPPO was by Edelstein et al.,[129] who demonstrated a CW oscillator based on a 1.4 mm crystal of KTP and pumped by 170-fs pulses from a colliding-pulse mode-locked dye laser at 620 nm. To access the high peak

intensities necessary for oscillation, the KTP crystal was pumped at the intracavity focus of the dye laser in a noncollinear phase-matching geometry. This singly resonant device produced 220-fs signal pulses at milliwatt average power levels in the near infrared. The approach was subsequently extended to an externally pumped oscillator, where increased signal powers of up to 30 mW were generated.[130] In the meantime, a pulsed femtosecond SPPO based on noncollinearly phase-matched BBO and pumped by microsecond pulse trains from a frequency-doubled neodymium glass laser at 527 nm was also reported.[131] Output pulses with durations of ~90 fs over the range of 700 nm to 1.8 μm were obtained for 800-fs input pump pulses. Soon after, the availability of the KLM titanium sapphire laser provided a laser source capable of pumping CW femtosecond SPPOs at significantly higher powers and many times above threshold; at the present time, this laser still represents the primary pump source for femtosecond SPPOs. The availability of the KLM titanium sapphire laser enabled the development of a KTP-based femtosecond SPPO capable of producing 175 mW of average power in near-infrared 62-fs pulses at a 76-MHz repetition rate.[132] At the same time, a similar device generating hundreds of milliwatts of average power in 135-fs pulses in the near infrared was demonstrated by using a 2.5-W titanium sapphire laser.[133] This arrangement was soon extended to a KTP-based SPPO with tunability out to 4 μm[134] and to KTA,[135,136] CTA,[137,138] RTA,[139] and KNB[140] with the aim of providing high-repetition-rate femtosecond pulses further into the infrared spectral range. Average output power of hundreds of milliwatts in <100-fs pulses and tuning beyond 5 μm have been demonstrated from these devices. By using alternative collinear NCPM schemes in combination with titanium sapphire pump tuning, the operation of a femtosecond near-infrared SPPO based on KTP was achieved, generating 40-fs output pulses,[141] while a similar device based on RTA was reported as having a pump power threshold as low as 50 mW.[142] A device based on type I temperature-tuned LBO was also demonstrated, providing ~500 mW in ~100-fs pulses from the 1.1- to 2.4-μm range.[143]

The spectral range of titanium-sapphire-pumped femtosecond SPPOs has also been extended to the visible by using two different approaches. The first approach relies on the intracavity second harmonic generation of SPPO signal pulses by exploiting the high signal intensities internally available in the SPPO cavity.[144] Using a 47-μm BBO doubling crystal placed at an additional intracavity focus, output powers of 240 mW in <100-fs pulses were obtained over a wavelength range of 580 to 657 nm. A similar device based on RTA was later demonstrated, generating tunable 70-fs pulses in the 620- to 660-nm spectral range at 170 mW average power.[145] An extension of this approach to intracavity sum-frequency mixing between the pump and signal pulses in BBO has also been used in a KTP-based SPPO to provide <100-fs pulses in the blue spectral range from 426 to 483 nm at ~200 mW average power.[146] Intracavity second harmonic generation and parametric generation has also been achieved simultaneously in a SPPO based on a single KTP crystal, providing visible femtosecond pulses in the 530- to 580-nm range with up to 200 mW average power.[147] A similar oscillator based on sum-frequency mixing of the pump and signal in KTP was also reported, with a tunable range from 484 to 512 nm.

The second approach to visible femtosecond pulse generation has been the use of frequency-doubled output of the titanium sapphire laser at ~400 nm to directly pump a visible femtosecond SPPO based on BBO as the nonlinear crystal.[148] This device generated 30-fs signal pulses with average power of up to 100 mW from 566 to 676 nm. More recently, ultrashort femtosecond pulses with durations as short as 13 fs have been generated from such a device.[149] An interesting feature of femtosecond SPPOs, which has also been observed in other ultra-short-pulse picosecond oscillators, is the wavelength tuning available through cavity length mismatch. The wavelength tuning occurs because the cavity length detuning introduces a loss at the signal wavelength by reducing the synchronism between the pump and signal pulses. To maintain synchronism and optimize gain, the signal shifts to a more favorable wavelength with a group velocity that satisfies a constant round-trip time. This cavity length tuning, which was observed in the first demonstration of a femtosecond SPPO,[129] is a useful mechanism for tuning the output wavelength, often by as much as 50 nm in devices based on birefringent materials.

More recently, the introduction of QPM nonlinear materials has led to further advances in femtosecond SPPOs. Devices based on PPLN, PPRTA, and PPKTP have been shown to be highly versatile sources of femtosecond pulses, offering minimum pump thresholds, high out-

put power, and vast spectral coverage from a single device. Operation of femtosecond SPPOs based on QPM materials has been demonstrated over a wide spectral range from <1 to >5 μm using noncollinear CPM or collinear NCPM schemes.[150–153] Because of the large nonlinear gains available, these oscillators exhibit pump power thresholds typically below 100 mW, enabling the use of all-solid-state KLM titanium sapphire lasers as the pump source.[150,152] These devices can readily provide practical power in excess of 100 mW in the 1- to 4-μm range, with milliwatt-level output available in the difficult spectral regions beyond 5 μm. Output pulse durations of 100 to 200 fs at a ~80-MHz repetition rate are typically available. Because of the large nonlinear gain and wide phase-matching bandwidth of periodically poled crystals, combined with the short interaction lengths employed in femtosecond SPPOs, devices based on such materials have been shown to be particularly flexible in providing extensive wavelength coverage only through cavity length tuning.[151,152,154] This provides a highly convenient method for wavelength tuning without the need for pump, angle, or temperature tuning.

Figure 19 provides a summary of the performance characteristics of several titanium-sapphire-pumped femtosecond optical parametric oscillators demonstrated to date.

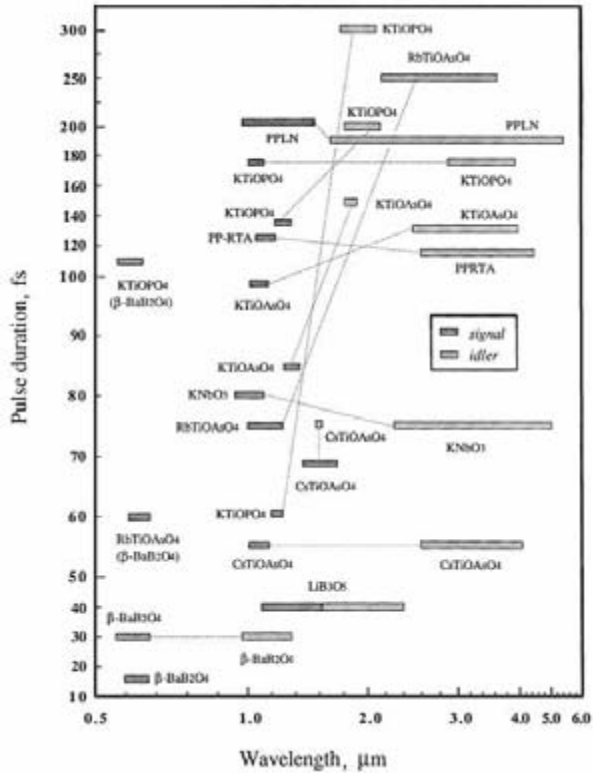

FIGURE 19 Summary of the temporal and tuning characteristics of a number of titanium-sapphire-laser-pumped CW femtosecond optical parametric oscillators developed to date. The average pump power available from these oscillators is between ~1 and 500 mW, at pulse repetition rates ranging from ~80 to ~350 MHz.

Finally, it is important to note that as well as OPOs, there have also been major advances in the development of parametric devices in resonator-free single-pass or traveling-wave configurations over the past few years. As discussed previously in Sec. 22.4, the operation of such devices is attainable by using large pumping intensities on the order of 1 to 100 GW/cm^2 to reach the threshold for coherent parametric generation. This is the basic principle of operation in OPA and traveling-wave OPG devices.[26] The pump sources for OPAs and OPGs generally comprise regenerative, multipass, and chirped pulse amplification schemes to provide pulses of sufficiently high energy (1 μJ to 1 mJ) and peak power (10 MW to 10 GW) to allow large parametric gains (typically >10^{10}) to be achieved in a single or double pass through the crystal. However, the large pumping intensities in this case place even more stringent demands on material damage, so that practical operation of these devices generally requires crystals with high optical damage thresholds such as BBO and LBO. At present, OPA and traveling-wave OPG systems can provide output pulses with picosecond and femtosecond temporal durations over a wide spectral range from the near ultraviolet to the infrared and pulse energies from a few microjoules to hundreds of microjoules are available at repetition rates of up to 250 kHz.

For a comprehensive overview of the advances in the field of optical parametric devices, processes, and applications, the reader is also referred to the three feature issues of the *Journal of the Optical Society of America B*.[155–157]

22.9 PARAMETRIC OSCILLATOR DESIGN ISSUES

The principal design criterion for optimum operation of parametric devices of all types, including OPOs, is the maximization of parametric gain through the suitable choice of the nonlinear material and laser pump source and the optimization of phase-matching, cavity design, and focusing parameters.

Laser Pump Source

The choice of laser pump source is determined principally by phase-matching requirements to access the wavelength regions of interest, and the pump wavelength should obviously be within the transparency range of the nonlinear material. The pump source must also be of sufficient intensity, as is evident from Eq. (6), to provide appreciable nonlinear gain for the OPO to reach operation threshold. This, in turn, necessitates a sufficiently low beam divergence to allow high focused intensities and depth of focus within the nonlinear material. Considerations of phase mismatch place further demands on the spectral and spatial coherence of the pump beam. As outlined in Sec. 22.3, parametric gain is strongly dependent on the phase-mismatch parameter Δk. Maximum gain occurs for $\Delta k = 0$, while increases in the magnitude of Δk result in severe reductions in nonlinear gain (see Fig. 2). Despite the use of phase-matching techniques, the attainment of perfect phase matching $\Delta k = 0$ remains difficult in practice. This is because practical laser pump sources exhibit finite spectral bandwidth and spatial divergence, so that all the spectral and spatial components of the beam can not be brought into perfect phase unison simultaneously. This leads to an increase in the magnitude of Δk, with the net result that the parametric gain is reduced from its peak value at $\Delta k = 0$. The maximum allowable pump bandwidth and divergence can be calculated from considerations of phase mismatch.[93] As will be discussed in more detail in this section, such limitations to pump beam quality can equivalently be considered in terms of the sensitivity of the nonlinear material to phase-mismatch effects. To maintain high parametric gains, it is therefore important to employ laser pump sources of narrow linewidth and low beam divergence.

Nonlinear Material

The selection of nonlinear material is governed by several factors, including a broad transparency range and phase matchability in the wavelength regions of interest, large nonlinear drive, high optical damage threshold, and favorable phase-matching properties such as small spatial and temporal walkoff and, preferably, a NCPM capability. Other important material requirements include high optical quality and low absorption loss; mechanical, chemical, and thermal stability; and availability in bulk form and large size.

The phase-matching behavior and tuning characteristics of the material can be derived from the wave-vector conservation condition $\Delta k = k_3 - k_2 - k_1 = 0$, using the dispersion relations for the nonlinear material. Noting from Eq. (1), that the frequency condition is given by $\omega_3 = \omega_2 + \omega_1$, the phase-match condition may be written as

$$\frac{n_3}{\lambda_3} - \frac{n_2}{\lambda_2} - \frac{n_1}{\lambda_1} = 0 \tag{96}$$

Since parametric gain has its maximum value at $\Delta k = 0$, Eq. (96) defines the wavelengths of the generated waves λ_2 and λ_1, which experience maximum growth for a given set of refractive indexes and pump wavelength λ_3. The signal and idler wavelengths so determined will therefore correspond to the macroscopic output from the OPO. Using the Sellmeier relations for the material, Eq. (96) may be solved to provide the tuning curves for the oscillator. For a fixed pump wavelength, any process that can alter the refractive indexes of the material results in a change in λ_2 and λ_1 to maintain the phase-match condition, Eq. (96). This is most commonly achieved by varying the propagation direction through the nonlinear crystal (*angle tuning*) or the crystal temperature (*temperature tuning*). Alternatively, for a fixed propagation angle and crystal temperature, *pump tuning* can be used to alter the signal and idler wavelengths to new values satisfying Eq. (96). Using these techniques, the generated signal and idler wavelengths can be tuned over extensive spectral ranges within the transparency range of the nonlinear crystal, and coherent output can be extracted from the OPO. Other less common tuning methods include electro-optic or pressure tuning by applying an external electric field or mechanical stress to the nonlinear material. These methods are particularly useful for fine-tuning of the OPO output. Detailed calculations of OPO tuning curves and the exact expressions for different types of phase matching in various nonlinear materials can be found in a number of reference texts.[6,9]

Another highly important material parameter is clearly a large optical nonlinearity, particularly when low pumping intensities are available. As is evident from Eq. (6), the parametric gain coefficient Γ is directly proportional to the effective nonlinear coefficient d_{eff} while, at the same time, it has an inverse-square-root dependence on the refractive indexes. It is often customary to describe the efficiency of the nonlinear material from Eq. (6) in terms of a *figure of merit* (FOM) defined as

$$\text{FOM} \equiv \frac{d_{\text{eff}}}{\sqrt{n_1 n_2 n_3}} \tag{97}$$

In general, infrared materials exhibit higher refractive indexes, and so from Eq. (97) one would expect a lower FOM in such materials. However, considerations of Miller's rule imply that $d_{\text{eff}} \propto n^6$, so that $\text{FOM} \propto n^{9/2}$. Hence, the FOM has a strong and direct dependence on the refractive index of material, and so infrared materials with higher indexes exhibit larger nonlinear efficiencies. However, it is equally important to note that this advantage is partly offset by the inverse-root dependence of Γ on the wavelengths, as is evident from Eq. (6), where for infrared generation, the longer signal and idler wavelengths result in lower nonlinear gain. However, the overall contributions of refractive indexes and wavelength factors, mean that infrared materials generally exhibit significantly higher FOM values than do visible and ultraviolet materials.

As well as a high nonlinear efficiency, it is also desirable for the material to display large tolerances to possible deviations in the spectral and spatial quality of the pump. As noted earlier, such deviations arise in practice from the finite bandwidth and divergence of the pump beam. The tolerance of the nonlinear crystal to such effects is measured in terms of the *spectral* and *angular acceptance bandwidths,* which can be calculated from the rate of change of phase mismatch with the wavelength and angular spread of the pump, using Taylor series expansion of Δk.[6,158] The acceptance bandwidths can then be obtained by solving for $\Delta\lambda$ and $\Delta\theta$. Noting from Fig. 2 that the parametric gain bandwidth may be defined by $|\Delta k\ell| \sim 2\pi$, the quantities $\Delta\lambda \cdot \ell$ and $\Delta\theta \cdot \ell$, under this boundary condition, then provide the full width at half-maximum (FWHM) spectral and angular acceptance bandwidth of the crystal. Thus, for a given crystal length ℓ, the acceptance bandwidths set an upper limit to the maximum allowable pump linewidth and divergence before parametric gain is severely diminished. Equivalently, for a given pump linewidth and angular divergence, the acceptance bandwidths determine the maximum length of the nonlinear crystal that can effectively contribute to the nonlinear gain. Since the crystal length follows an inverse relationship with the maximum allowable pump bandwidth and divergence, for shorter crystal lengths larger deviations in pump beam quality can be tolerated and vice versa.

The detailed calculations of acceptance bandwidths depend on the type of phase matching and dispersion properties of the nonlinear material and can be found elsewhere.[6,9] For example, the spectral acceptance bandwidth of LBO crystal under type I NCPM and pumped at 800 nm with a titanium:sapphire laser is $\Delta\lambda \cdot \ell \sim 5$ nm · cm. Thus, a crystal length of 1 cm can support pump bandwidths of up to ~5 nm without serious reductions in parametric gain. The spectral acceptance bandwidth requirements become more important in the presence of ultrashort femtosecond pulses, where the large spectral bandwidths impose severe restrictions on the maximum usable crystal length. However, this limitation is offset by the substantially higher peak powers available in such pulses, so that significant parametric gains can still be maintained in crystal lengths of ~1 mm or shorter. While maximization of spectral acceptance bandwidth does not follow a general prescription, the angular acceptance bandwidth can generally be maximized under NCPM because of the low sensitivity of refractive indexes in this geometry to beam propagation angle. Therefore, in the presence of pump beams of low spatial quality, it is highly beneficial to employ the NCPM geometry. For nonlinear materials that exhibit temperature-dependent refractive indexes and hence a temperature-tuning capability, one can similarly define a *temperature-acceptance bandwidth* $\Delta T \cdot \ell$, which is a measure of the sensitivity of phase matching, and thus parametric gain, to changes in the crystal temperature. As a general rule, for the attainment of maximum nonlinear gain and minimum OPO threshold, it is advantageous to use materials with large spectral, angular, and temperature-acceptance bandwidths.

Another important consideration in the choice of suitable nonlinear materials is crystal double refraction. The main consequence of this effect is spatial walkoff, which can result in major reductions in energy exchange among the interacting fields along the direction of propagation. Under this condition, the strength of coupling can rapidly diminish, and the interaction can become ineffective after a finite distance through the medium. It is convenient to define the effective crystal length in the presence of double refraction as $\ell_a = w_3\sqrt{\pi}/\rho$, where ℓ_a is known as the *aperture length,* w_3 is the pump beam waist radius, and ρ is the double-refraction angle.[159] It is clear that for longer aperture lengths, it is desirable to use nonlinear crystals with small double refraction. In practice, it is necessary to make $\ell_a > \ell$, so that the entire available crystal length contributes to parametric gain. Clearly, for a given ρ the aperture length may be increased by using larger pump beam waists. However, this may not always be possible in practice in the presence of low- to moderate-power laser sources, where tightly focused pump intensities are necessary for the attainment of sufficient parametric gain. One technique to avoid the effects of spatial walkoff is to use a NCPM geometry, corresponding to propagation along a principal dielectric axis. Under this condition, $\rho = 0$, spatial walkoff is eliminated, and $\ell_a \to \infty$. Other techniques for partial compensation of walkoff include elliptical focusing,[160] noncollinear phase matching,[136,139,161] and two-crystal configura-

tions.[95] We may thus conclude that in the presence of double refraction, in addition to acceptance bandwidth considerations, spatial walkoff places a further restriction on the maximum crystal length that can effectively contribute to parametric gain.

In parametric generation of ultrashort femtosecond and picosecond pulses, there is yet another limiting factor to the maximum useful crystal length, which is imposed by the difference in the group velocity between the pump, signal, and idler. This effect, which is the temporal analog of spatial walkoff, is commonly referred to as *group velocity walkoff* and is characterized by a so-called *pulse splitting length* given by $\ell_s = \Delta\tau/(1/v_g - 1/v'_g)$, where $\Delta\tau$ is the pulse width, and v_g and v'_g refer to group velocities of the respective waves.[26] In analogy with the aperture length in spatial walkoff, ℓ_s here provides an estimate of the useful crystal length before pulse walkoff renders parametric interaction ineffective. In a SPPO, group velocity mismatch between the pump and the resonated signal wave generally has a first-order effect on parametric gain, whereas that between the pump and the nonresonant idler or between the signal and idler has a second-order effect on oscillator performance.

Typical values of group velocity walkoff in commonly available nonlinear materials range from <10 fs/mm to >100 fs/mm. For example, in type II noncritically phase matched KTP under titanium:sapphire pumping, the temporal walkoff between the pump and signal can be as high as ~100 fs/mm, resulting in $\ell_s \sim 1$ mm. Therefore, if pump pulses of ~100 fs duration or shorter are to be used, the maximum useful crystal length will be limited to ~1 mm. On the other hand, in type I temperature-phase-matched LBO under NCPM, the walkoff between the pump and signal can be as low as ~20 fs/mm, so that interaction lengths of up to 5 mm may be utilized for 100-fs pump pulses.[143] Clearly, the maximum usable crystal length increases for longer pump pulses, but this advantage is brought about at the expense of a drop in the peak pumping intensity and hence a lowering of gain. It is therefore desirable, in the context of ultrashort pulse parametric generation, to use materials with low temporal walkoff, so that longer interaction lengths can be exploited for the attainment of maximum nonlinear gain. The effects of group velocity walkoff can be reduced, however, by using noncollinear phase-matching.[162]

In addition to the foregoing requirements, one of the most important properties that can ultimately limit practical operation of parametric devices is material damage threshold. Because of the high pumping intensities in the parametric process, the materials must withstand power densities typically >10 MW/cm^2 and often many times this value. Optical damage may be caused by several different mechanisms and can be of various types. The most predominant type is the irreversible damage, which can take the form of surface or bulk damage. It can be caused by thermal heating, induced absorption, self-focusing, stimulated Brillouin scattering, dielectric breakdown, or by several other mechanisms. Accurate determination of damage threshold is often difficult as it depends on the wavelength of the radiation and the exact experimental conditions. However, as a general trend, material damage tolerance is found to decrease for increasing pump energy fluence and with shorter pumping wavelengths. As a result, material damage becomes more important in the presence of nanosecond pulses than with picosecond or femtosecond pulses and CW pumping and also in the presence of ultraviolet and visible radiation. It is also found that the surface preparation and cleanliness as well as the presence of inclusions or impurities in the material can strongly affect the damage threshold. As such, one often finds conflicting values of the optical damage threshold for a given material in the literature. The experimentally observed optical damage thresholds for a variety of nonlinear materials have been tabulated in Ref. 6.

Laser-induced damage has also been argued to be a probabilistic effect based on an avalanche optical AC breakdown similar to DC dielectric breakdown.[163] Another type of optical damage that has been observed in $LiNbO_3$ is a reversible form, which results from illumination by visible radiation. This type of damage, known as *photorefractive damage,* manifests itself as inhomogeneities in the refractive index, which can lead to beam distortions and nonuniformities in birefringence and phase matching. The induced damage can be reversed by ultraviolet illumination of the crystal or by elevating its temperature. The subject of material damage is of great importance to the design and successful operation of parametric devices and has been extensively studied and reported in the literature. Yet, the exact evalu-

ation of damage thresholds and identification of the mechanisms responsible for optical damage in different materials remains a difficult task.

From the preceding considerations, it is clear that the optimum operation of parametric devices, and in particular OPOs, necessitates the attainment of several important pump laser and nonlinear material parameters. In practice, it is often difficult to fulfill all such requirements simultaneously, so that practical design and operation of parametric devices often necessitates a compromise among the many different design criteria. Such compromises depend on the particular device configuration and the output requirements for a given application.

22.10 CONCLUSIONS

This chapter has been concerned with a description of optical parametric devices, with particular emphasis on OPOs operating from the CW and nanosecond pulse to the picosecond and femtosecond temporal domain. In the discussion, we have described the basic principles of optical parametric generation and amplification, material and pump laser selection criteria, operating characteristics of OPO devices, and the latest advances in the field. The unprecedented level of research interest and the rapid progress in materials science and laser technology over the recent years have established parametric devices as truly practical tunable light sources, nearly four decades after their potential was first recognized. Many of the devices demonstrated as laboratory prototypes have found their way to the commercial marketplace in a period of only a few years and continue to find numerous new applications, from spectroscopy and environmental studies to optical frequency synthesis and quantum optics. The current efforts in this area are directed toward the development of devices for new spectral regions that have so far not been accessed, particularly the mid-infrared. Further refinements in the performance characteristics of parametric sources with regard to output power and energy, spectral and spatial coherence, and ruggedness and versatility continue to be driven by the need for such devices in applications where other alternatives cannot be made available. Future trends in this area point to the development of novel devices based on integrated quasi-phase-matched structures and semiconductor nonlinear optics.

22.11 REFERENCES

1. P. A. Franken, A. E. Hill, C. W. Peters, and G. Weinreich, "Generation of Optical Harmonics," *Phys. Rev. Lett.* **7**:118–119 (1961).
2. R. H. Kingston, "Parametric Amplification and Oscillation at Optical Frequencies," *Proc. IRE* **50**:472–473 (1962).
3. N. M. Kroll, "Parametric Amplification in Spatially Extended Media and Application to the Design of Tuneable Oscillators at Optical Frequencies," *Phys. Rev.* **127**:1207–1211 (1962).
4. S. A. Akhmanov and R. V. Khokhlov, "Concerning One Possibility of Amplification of Light Waves," *Sov. Phys. J. Exp. Theor. Phys.* **16**:252–254 (1963).
5. J. A. Giordmaine and R. C. Miller, "Tunable Coherent Parametric Oscillation in $LiNbO_3$ at Optical Frequencies," *Phys. Rev. Lett.* **14**:973–976 (1965).
6. V. G. Dimitriev, G. G. Gurzadyan, and D. N. Nikogosyan, *Handbook of Nonlinear Optical Crystals,* Springer-Verlag, Berlin, 1991.
7. M. Ebrahimzadeh and A. I. Ferguson, "Novel Nonlinear Crystals," in *Principles and Applications of Nonlinear Optical Materials,* Chapman and Hall, London, 1993, pp. 99–142.
8. C. L. Tang, "Nonlinear Optics," in *Handbook of Optics,* McGraw-Hill, New York, 1995, pp. 38.3–38.26.
9. R. L. Sutherland, *Handbook of Nonlinear Optics,* Marcel Dekker, New York, 1996.

10. S. E. Harris, "Tunable Optical Parametric Oscillators," *Proc. IEEE* **57**:2096–2113 (1969).
11. R. L. Byer, "Optical Parametric Oscillators," in H. Rabin and C. L. Tang (eds.), *Treatise in Quantum Electronics,* Academic Press, New York, 1973, pp. 587–702.
12. R. G. Smith, "Optical Parametric Oscillators," in A. K. Levine and A. J. DeMaria (eds.), *Lasers,* Marcel Dekker, New York, 1976, pp. 189–307.
13. M. H. Dunn and M. Ebrahimzadeh, "Parametric Generation of Tunable Light from Continuous-Wave to Femtosecond Pulses," *Science* **286**:1513–1517 (1999).
14. R. W. Boyd, *Nonlinear Optics,* Academic Press, New York, 1992.
15. J. A. Armstrong, N. Bloembergen, J. Ducuing, and P. S. Pershan, "Interaction Between Light Waves in a Nonlinear Dielectric," *Phys. Rev.* **127**:1918–1939 (1962).
16. W. H. Louisell, A. Yariv, and A. E. Siegman, "Quantum Fluctuations and Noise in Parametric Processes," *Phys. Rev.* **124**:1646 (1961).
17. Y. R. Shen, *Principles of Nonlinear Optics,* John Wiley, New York, 1984.
18. A. Yariv, *Quantum Electronics,* John Wiley, New York, 1989.
19. G. D. Boyd and A. Ashkin, "Theory of Parametric Oscillator Threshold with Single-Mode Optical Masers and Observation of Amplification in $LiNbO_3$," *Phys. Rev.* **146**:187–198 (1966).
20. G. D. Boyd and D. A. Kleinman, "Parametric Interaction of Focused Gaussian Light Beams," *J. Appl. Phys.* **39**:3597–3639 (1968).
21. J. A. Giordmaine, "Mixing of Light Beams in Crystals," *Phys. Rev. Lett.* **8**:19–20 (1962).
22. P. D. Maker, R. W. Terhune, M. Nissenoff, and C. M. Savage, "Effects of Dispersion and Focusing on the Production of Optical Harmonics," *Phys. Rev. Lett.* **8**:21–22 (1962).
23. M. M. Fejer, G. A. Magel, D. H. Jundt, and R. L. Byer, "Quasi-Phase-Matched Second Harmonic Generation: Tuning and Tolerances," *IEEE J. Quantum Electron.* **28**:2631–2654 (1992).
24. L. E. Myers, R. C. Eckardt, M. M. Fejer, R. L. Byer, W. R. Bosenberg, and J. W. Pierce, "Quasi-Phase-Matched Optical Parametric Oscillators in Bulk Periodically Poled $LiNbO_3$,"20*J. Opt. Soc. Am.* **B 12**:2102–2116 (1995).
25. P. E. Powers, T. J. Kulp, and S. E. Bisson, "Continuous Tuning of a Continuous-Wave Periodically Poled Lithium Niobate Optical Parametric Oscillator by Use of a Fan-Out Grating Design," *Opt. Lett.* **23**:159–161 (1998).
26. R. Danielius, A. Piskarskas, A. Stabinis, G. P. Banfi, P. Di Trapani, and R. Righini, "Traveling-Wave Parametric Generation of Widely Tunable, Highly Coherent Femtosecond Light Pulses," *J. Opt. Soc. Am. B* **10**:2222–2231 (1995).
27. R. G. Smith, J. E. Geusic, H. J. Levinstein, J. J. Rubin, S. Singh, and L. G. Van Uitert, "Continuous Optical Parametric Oscillation in $Ba_2NaNb_5O_{15}$," *Appl. Phys. Lett.* **12**:308–310 (1968); R. G. Smith et al., *J. Appl. Phys.* **39**:4030 (1968).
28. R. L. Byer, M. K. Oshman, J. F. Young, and S. E. Harris, "Visible CW Parametric Oscillator," *Appl. Phys. Lett.* **13**:109–111 (1968).
29. R. L. Byer et al., *Appl. Phys. Lett.* **15**:136 (1969).
30. J. E. Bjorkholm, "Analysis of the Doubly Resonant Optical Parametric Oscillator Without Power-Dependent Reflections," *IEEE J. Quantum. Electron.* **QE5**:293–295 (1969).
31. A. E. Siegman, "Nonlinear Optical Effects: An Optical Power Limiter," *Appl. Opt.* **1**:739–744 (1962).
32. J. E. Bjorkholm et al., *IEEE J. Quantum. Electron.* **QE6**:797 (1970).
33. L. B. Kreuzer, *Proc. Joint. Conf. on Lasers and Optoelectronics,* University of Southampton, England, pp. 52–63 (1969).
34. G. Breitenbach et al., *J. Opt. Soc. Am. B* **12**:2095 (1995).
35. C. Laurence and F. Tittel, *J. Appl. Phys.* **42**:2137 (1971).
36. J. Falk, *IEEE J. Quantum. Electon,* **QE7**:230 (1971).
37. J. F. Weller et al., *J. Appl. Phys.* **43**:4650 (1972).
38. J. E. Bjorkholm, "Efficient Optical Parametric Oscillation Using Doubly and Singly Resonant Cavities," *Appl. Phys. Lett.* **13**:53–56 (1968).

39. J. E. Bjorkholm, *Appl. Phys. Lett.* **13**:399 (1968).
40. R. G. Smith, "A Study of Factors Affecting the Performance of a Continuously Pumped Doubly Resonant Optical Parametric Oscillator," *IEEE J. Quantum. Electron.* **QE9**:530–541 (1973).
41. C. D. Nabors, R. C. Eckardt, W. J. Kozlovsky, and R. L. Byer, "Efficient, Single-Axial-Mode Operation of a Monolithic MgO:$LiNbO_3$ Optical Parametric Oscillator," *Opt. Lett.* **14**:1134–1136 (1989).
42. R. C. Eckardt, C. D. Nabors, W. J. Kozlovsky, and R. L. Byer, "Optical Parametric Oscillator Frequency Tuning and Control," *J. Opt. Soc. Am. B* **8**:646 (1991).
43. D. Lee and N. C. Wong, *Opt. Lett.* **17**:13 (1993).
44. F. G. Colville, A. J. Henderson, M. J. Padgett, J. Zhang, and M. H. Dunn, "Continuous-Wave Parametric Oscillation in Lithium Triborate," *Opt. Lett.* **18**:205–207 (1993).
45. F. G. Colville, M. J. Padgett, A. J. Henderson, J. Zhang, and M. H. Dunn, "Continuous-Wave Parametric Oscillator Pumped in the Ultraviolet," *Opt. Lett.* **18**:1065–1067 (1993).
46. F. G. Colville, M. J. Padgett, and M. H. Dunn, "Continuous-Wave, Dual-Cavity, Doubly Resonant, Optical Parametric Oscillator," *Appl. Phys. Lett.* **64**:1490–1492 (1994).
47. A. J. Henderson, M. J. Padgett, J. Zhang, W. Sibbett, and M. H. Dunn, "Continuous Frequency Tuning of a CW Optical Parametric Oscillator Through Tuning of Its Pump Source," *Opt. Lett.* **20**:1029–1031 (1995).
48. G. M. Gibson, M. J. Padgett, and M. H. Dunn, "Application of a Continuously Tunable, CW Optical Parametric Oscillator for High-Resolution Spectroscopy," *Opt. Lett.* **23**:40–42 (1998).
49. G. M. Gibson, M. Ebrahimzadeh, M. J. Padgett, and M. H. Dunn, "Continuous-Wave Optical Parametric Oscillator Based on Periodically Poled $KTiOPO_4$ and Its Application to Spectroscopy," *Opt. Lett.* **24**:397–399 (1999).
50. G. M. Gibson, R. S. Conroy, A. J. Kemp, B. D. Sinclair, M. J. Padgett, and M. H. Dunn, "Microchip Laser-Pumped Continuous-Wave Doubly Resonant Optical Parametric Oscillator," *Opt. Lett.* **23**:517–518 (1998).
51. M. Bode et al., *Opt. Commun.* **148**:117 (1998).
52. R. Al-Tahtamouni et al., *Appl. Phys. B* **66**:733 (1998).
53. L. E. Myers et al., *J. Opt. Soc. Am. B* **12**:2102 (1995); I.D. Lindsay et al. *Opt. Lett.* **23:** 1889 (1998).
54. G. P. Dzhotyan and Yu.E. D'yakov, *Sov. J. Quantum Electron.* **7**:1337 (1997).
55. W. J. Kozlovsky et al., *Opt. Lett.* **13**:1102 (1988).
56. S. T. Yang, R. C. Eckardt, and R. L. Byer, "Continuous-Wave Singly Resonant Optical Parametric Oscillator Pumped by a Single-Frequency Resonantly Doubled Nd:YAG Laser," *Opt. Lett.* **18**:971–973 (1993).
57. S. T. Yang et al., *Opt. Lett.* **19**:475 (1994).
58. W. R. Bosenberg, A. Drobshoff, J. I. Alexander, L. E. Myers, and R. L. Byer, "Continuous-Wave Singly Resonant Optical Parametric Oscillator Based on Periodically Poled $LiNbO_3$," *Opt. Lett.* **21**:713–715 (1996).
59. W. R. Bosenberg, A. Drobshoff, J. I. Alexander, L. E. Myers, and R. L. Byer, "93% Pump Depletion, 3.5-W Continuous-Wave, Singly Resonant Optical Parametric Oscillator," *Opt. Lett.* **21**:1336–1338 (1996).
60. R. G. Batchko et al., *Opt. Lett.* **23**:168 (1998).
61. W. R. Bosenberg, J. I. Alexander, L. E. Myers, R. W. Wallace, "2.5-W, Continuous-Wave, 629-nm Solid-State Laser Source," *Opt. Lett.* **23**:207–209 (1998).
62. M. E. Klein et al., *Opt. Lett.* **24**:1142 (1999).
63. G. Robertson, M. J. Padgett, and M. H. Dunn, "Continuous-Wave Singly Resonant Pump-Enhanced Type II Optical Parametric Oscillator," *Opt. Lett.* **19**:1735–1737 (1994).
64. M. Scheidt, B. Beier, R. Knappe, K.-J. Boller, and R. Wallenstein, "Diode-Laser-Pumped Continuous-Wave KTP Optical Parametric Oscillator," *J. Opt. Soc. Am. B* **12**:2087–2094 (1995).
65. M. Scheidt, B. Beier, K.-J. Boller, and R. Wallenstein, "Frequency-Stable Operation of a Diode-Pumped Continuous-Wave $RbTiOAsO_4$ Optical Parametric Oscillator," *Opt. Lett.* **22**:1287–1289 (1997).

66. K. Schneider, P. Kramper, S. Schiller, and J. Mlynek, "Toward an Optical Synthesizer: A Single-Frequency Parametric Oscillator Using Periodically Poled $LiNbO_3$," *Opt. Lett.* **22**:1293–1295 (1997).
67. K. Schneider and S. Schiller, "Narrow-Linewidth, Pump-Enhanced Singly-Resonant Optical Parametric Oscillator Pumped at 532 nm," *Appl. Phys. B* **65**:775–777 (1997).
68. S. Schiller, K. Schneider, and J. Mlynek, "Theory of an Optical Parametric Oscillator with Resonant Pump and Signal," *J. Opt. Soc. Am. B* **16**:1512–1524 (1999).
69. M. Scheidt et al., *Opt. Commun.* (1997).
70. D.-H. Lee, M. E. Klein, J.-P. Meyn, P. Groß, R. Wallenstein, and K.-J. Boller, "Self-Injection-Locking of a CW-OPO by Intracavity Frequency-Doubling of the Idler Wave," *Opt. Exp.* **5**:114–119 (1999).
71. G. A. Turnbull, D. McGloin, I. D. Lindsay, M. Ebrahimzadeh, and M. H. Dunn, "Extended Mode-Hop-Free Tuning Using a Dual-Cavity, Pump-Enhanced Optical Parametric Oscillator," *Opt. Lett.* **25**:341–343 (2000).
72. M. K. Oshman and S. E. Harris, "Theory of Optical Parametric Oscillation Internal to the Laser Cavity," *IEEE J. Quantum. Electron.* **QE4**:491–502 (1968).
73. G. A. Turnbull, M. H. Dunn, and M. Ebrahimzadeh, "Continuous-Wave, Intracavity Optical Parametric Oscillators: An Analysis of Power Characteristics," *Appl. Phys. B* **66**:701–710 (1998).
74. T. J. Edwards, G. A. Turnbull, M. H. Dunn, and M. Ebrahimzadeh, and F. G. Colville, "High-Power, Continuous-Wave, Singly Resonant Intracavity Optical Parametric Oscillator," *Appl. Phys. Lett.* **72**:1527–1529 (1998).
75. F. G. Colville, M. H. Dunn, and M. Ebrahimzadeh, "Continuous-Wave, Singly Resonant Intracavity Parametric Oscillator," *Opt. Lett.* **22**:75–79 (1997).
76. G. A. Turnbull, T. J. Edwards, M. H. Dunn, and M. Ebrahimzadeh, "Continuous-Wave Singly-Resonant Intracavity Optical Parametric Oscillator Based on Periodically-Poled $LiNbO_3$," *Electron. Lett.* **33**:1817–1818 (1997).
77. T. J. Edwards, G. A. Turnbull, M. H. Dunn, M. Ebrahimzadeh, H. Karlsson, G. Arvidsson, and F. Laurell, "Continuous-Wave Singly Resonant Optical Parametric Oscillator Based on Periodically Poled $RbTiOAsO_4$," *Opt. Lett.* **23**:837–839 (1998).
78. M. Ebrahimzadeh, G. A. Turnbull, T. J. Edwards, D. J. M. Stothard, I. D. Lindsay, and M. H. Dunn, "Intracavity Continuous-Wave Singly Resonant Optical Parametric Oscillators," *J. Opt. Soc. Am. B* **16**:1499–1511 (1999).
79. D. J. M. Stothard, M. Ebrahimzadeh, and M. H. Dunn, "Low-Pump-Threshold, Continuous-Wave, Singly Resonant Optical Parametric Oscillator," *Opt. Lett.* **23**:1895–1897 (1998).
80. R. W. Wallace, "Stable, Efficient Optical Parametric Oscillator Pumped with Doubled Nd:YAG," *Appl. Phys. Lett.* **17**:497–499 (1970).
81. J. E. Bjorkholm, "Efficient Optical Parametric Oscillation Using Doubly and Singly Resonant Cavities," *Appl. Phys. Lett.* **13**:53–55 (1968).
82. L. S. Goldberg, "Optical Parametric Oscillation in Lithium Iodate," *Appl. Phys. Lett.* **17**:489–491 (1970).
83. R. L. Herbst and R. L. Byer, "Singly Resonant CdSe Infrared Optical Parametric Oscillator," *Appl. Phys. Lett.* **21**:189–191 (1972).
84. D. C. Hanna, B. Luther-Davis, and R. C. Smith, "Singly Resonant Proustite Parametric Oscillator Tuned from 1.22 to 8.5 μm," *Appl. Phys. Lett.* **22**:440–442 (1973).
85. Y. X. Fan, R. C. Eckardt, R. L. Byer, R. K. Route, and R. S. Feigelson, "$AgGaS_2$ Infrared Optical Parametric Oscillator," *Appl. Phys. Lett.* **45**:313–315 (1984).
86. J. A. Weiss and L. S. Goldberg, "Singly Resonant CdSe Parametric Oscillator Pumped by an HF Laser," *Appl. Phys. Lett.* **24**:389–391 (1974).
87. S. J. Brosnan and R. L. Byer, "Optical Parametric Oscillator Threshold and Linewidth Studies," *IEEE J. Quantum Electron.,* **QE15**:415–431 (1979).
88. J. E. Pearson, U. Ganiel, and A. Yariv, "Rise Time of Pulsed Parametric Oscillators," *IEEE J. Quantum Electron.* **QE8**:433–440 (1972).
89. L. B. Kreuzer, "High-Efficiency Optical Parametric Oscillation and Power Limiting in $LiNbO_3$," *Appl. Phys. Lett.* **13**:57–59 (1968).

90. J. E. Bjorkholm, "Some Effects of Spatially Nonuniform Pumping in Pulsed Optical Parametric Oscillators," *IEEE J. Quantum Electron.,* **QE7**:109–118 (1971).
91. L. K. Cheng, W. R. Bosenberg, and C. L. Tang, "Broadly Tunable Optical Parametric Oscillation in β-BaB_2O_4," *Appl. Phys. Lett.* **53**:175–177 (1988).
92. H. Komine, "Optical Parametric Oscillation in Beta-Barium Borate Crystal Pumped by an XeCl Excimer Laser," *Opt. Lett.* **13**:643–645 (1988).
93. M. Ebrahimzadeh, A. J. Henderson, and M. H. Dunn, "An Excimer-Pumped β-BaB_2O_4 Optical Parametric Oscillator Tunable from 354 nm to 2.370 μm," *IEEE J. Quantum Electron.* **26**:1241–1252 (1990).
94. W. R. Bosenberg, L. K. Cheng, and C. L. Tang, "Ultraviolet Optical Parametric Oscillation in β-BaB_2O_4," *Appl. Phys. Lett.* **54**:13–15 (1989).
95. W. R. Bosenberg, W. S. Pelouch, and C. L. Tang, "High-Efficiency and Narrow-Linewidth Operation of a Two-Crystal β-BaB_2O_4 Optical Parametric Oscillator," *Appl. Phys. Lett.* **55**:1952–1954 (1989).
96. J. M. Boon-Engering, W. E. van der Veer, and J. W. Gerritsen, "Bandwidth Studies of an Injection-Seeded β-Barium Borate Optiocal Parametric Oscillator," *Opt. Lett.* **20**:380–382 (1995).
97. W. R. Bosenberg and C. L. Tang, "Type II Phase Matching in β-Barium Borate Optical Parametric Oscillator," *Appl. Phys. Lett.* **56**:1819–1821 (1990).
98. J. G. Haub, M. J. Johnson, A. J. Powell, and B. J. Orr, "Bandwidth Characteristics of a Pulsed Optical Parametric Oscillator: Application to Degenerate Four-Wave Mixing Spectroscopy," *Opt. Lett.* **20**:1637–1639 (1995).
99. M. Ebrahimzadeh, G. Robertson, and M. H. Dunn, "Efficient Ultraviolet LiB_3O_5 Optical Parametric Oscillator," *Opt. Lett.* **16**:767–769 (1991).
100. F. Hanson and D. Dick, "Blue Parametric Generation from Temperature-Tuned LiB_3O_5," *Opt. Lett.,* **16**:205–207 (1991).
101. Y. Cui, D. E. Withers, C. F. Rae, C. J. Norrie, Y. Tang, B. D. Sinclair, W. Sibbett, and M. H. Dunn, *Opt. Lett.,* **18**:122–124 (1993).
102. K. Kato, "Parametric Oscillation at 3.2 μm in KTP Pumped at 1.064 μm," *IEEE J. Quantum Electron.* **27**:1137–1140 (1991).
103. L. R. Marshall, J. Kasinski, A. D. Hays, and R. L. Burnham, "Efficient Optical Parametric Oscillation at 1.6 μm," *Opt. Lett.* **16**:681–683 (1991).
104. W. R. Bosenberg, L. K. Cheng, and J. D. Bierlein, "Optical Parametric Frequency-Conversion Properties of $KTiOAsO_4$," *Appl. Phys. Lett.* **65**:2765–2767 (1994).
105. L. E. Myers and W. R. Bosenberg, "Periodically Poled Lithium Niobate and Quasi-Phase-Matched Optical Parametric Oscillators," *IEEE J. Quantum Electron.* **33**:1663–1672 (1997).
106. U. Bader, J. Bartschke, I. Klimov, A. Borsutzky, and R. Wallenstein, "Optical Parametric Oscillator of Quasi-Phase-Matched $LiNbO_3$ Pumped by a Compact High Repetition Rate Single-Frequency Passively *Q*-Switched Nd:YAG Laser," *Opt. Commun.* **147**:95–98 (1998).
107. J. Hellstrom, V. Pasiskevicius, F. Laurell, and H. Karlsson, "Efficient Nanosecond Optical Parametric Oscillators Based on Periodically Poled KTP Emitting in the 1.8–2.5 μm Spectral Range," *Opt. Lett.* **24**:1233–1235 (1999).
108. H. Karlsson, M. Olson, G. Arvidsson, F. Laurell, U. Bader, A. Borsutzky, R. Wallenstein, S. Wickstrom, and M. Gustafsson, "Nanosecond Optical Parametric Oscillator Based on Large-Aperture Periodically Poled $RbTiOAsO_4$," *Opt. Lett.* **24**:330–332 (1999).
109. P. E. Britton, H. L. Offerhaus, D. J. Richardson, P. G. R. Smith, G. W. Ross, and D. C. Hanna, "Parametric Oscillator Directly Pumped by a 1.55-μm Erbium-Fibre Laser," *Opt. Lett.* **24**:975–977 (1999).
110. M. J. Missey, V. Dominic, P. E. Powers, and K. L. Schepler, "Periodically Poled Lithium Niobate Monolithic Nanosecond Optical Parametric Oscillators and Generators," *Opt. Lett.* **24**:1227–1229 (1999).
111. M. F. Becker, D. J. Kuizanga, D. W. Phillion, and A. E. Siegman, "Analytic Expressions for Ultrashort Pulse Generation in Mode-Locked Optical Parametric Oscillators," *J. Appl. Phys.* **45**:3996–4005 (1974).
112. E. C. Cheung and J. M. Liu, "Theory of a Synchronously Pumped Optical Parametric Oscillator in Steady-State Operation," *J. Opt. Soc. Am.* **B 7**:1385–1401 (1991); E. C. Cheung and J. M. Liu, "Effi-

cient Generation of Ultrashort, Wavelength-Tunable Infrared Pulses," *J. Opt. Soc. Am.* **B 8**:1491–1506 (1991).

113. L. J. Bromley, A. Guy, and D. C. Hanna, "Synchronously Pumped Optical Parametric Oscillation in KTP," *Opt. Commun.* **70**:350–354 (1989).
114. S. Burdulis, R. Grigonis, A. Piskarskas, G. Sinkevicius, V. Sirutkaitis, A. Fix, J. Nolting, and R. Wallenstein, "Visible Optical Parametric Oscillation in Synchronously Pumped Beta-Barium Borate," *Opt. Commun.,* **74**:398–402 (1990).
115. M. Ebrahimzadeh, G. J. Hall, and A. I. Ferguson, "Broadly Tunable, All-Solid-State, Visible and Infrared Picosecond Optical Parametric Oscillator," *Opt. Lett.* **18**:278–280 (1993).
116. M. J. McCarthy and D. C. Hanna, "Continuous-Wave Mode-Locked Singly Resonant Optical Parametric Oscillator Synchronously Pumped by a Laser-Diode-Pumped Nd:YLF Laser," *Opt. Lett.* **17**:402–404 (1992).
117. G. J. Hall, M. Ebrahimzadeh, A. Robertson, G. P. A. Malcolm, and A. I. Ferguson, "Synchronously Pumped Optical Parametric Oscillators Using All-Solid-State Pump Lasers," *J. Opt. Soc. Am. B,* **10**:2168–2179 (1993).
118. S. D. Butterworth, M. J. McCarthy, and D. C. Hanna, "Widely Tunable Synchronously Pumped Optical Parametric Oscillator," *Opt. Lett.* **18**:1429–1431 (1993).
119. C. Grasser, D. Wang, R. Beigang, and R. Wallenstein, "Singly Resonant Optical Parametric Oscillator of $KTiOPO_4$ Synchronously Pumped by the Radiation from a Continuous-Wave Mode-Locked Nd:YLF Laser," *J. Opt. Soc. Am. B* **10**:2218–2221 (1993).
120. J. Chung and A. E. Siegman, "Singly Resonant Continuous-Wave Mode-Locked $KTiOPO_4$ Optical Parametric Oscillator Pumped by a Nd:YAG Laser," *J. Opt. Soc. Am. B* **10**:2201–2210 (1993).
121. D. Wang, C. Grasser, R. Beigang, and R. Wallenstein, "The Generation of Tunable Blue ps-Light-Pulses from a CW Mode-Locked LBO Optical Parametric Oscillator," *Opt. Commun.* **138**:87–90 (1997).
122. A. Nebel, C. Fallnich, R. Beigang, and R. Wallenstein, "Noncritically Phase-Matched Continuous-Wave Mode-Locked Singly Resonant Optical Parametric Oscillator Synchronously Pumped by a Ti:Sapphire Laser," *J. Opt. Soc. Am. B* **10**:2195–2200 (1993).
123. M. Ebrahimzadeh, S. French, and A. Miller, "Design and Performance of a Singly Resonant Picosecond LiB_3O_5 Optical Parametric Oscillator Synchronously Pumped by a Self-Mode-Locked Ti:Sapphire Laser," *J. Opt. Soc. Am. B,* **12,** 2180–2191 (1995).
124. S. French, M. Ebrahimzadeh, and A. Miller, "High-Power, High-Repetition-Rate Picosecond Optical Parametric Oscillator for the Near- to Mid-Infrared," *Opt. Lett.* **21**:131–133 (1996).
125. S. French, M. Ebrahimzadeh, and A. Miller, "High-Power, High-Repetition-Rate Picosecond Optical Parametric Oscillator Tunable in the Visible," *Opt. Lett.* **21**:976–978 (1996).
126. G. T. Kennedy, D. T. Reid, A. Miller, M. Ebrahimzadeh, H. Karlsson, G. Arvidsson, and F. Laurell, "Broadly Tunable Mid-Infrared Picosecond Optical Parametric Oscillator Based on Periodically Poled $RbTiOAsO_4$," *Opt. Lett.* **23**:503–505 (1998).
127. L. Lefort, K. Peuch, G. W. Ross, Y. P. Svirko, and D. C. Hanna, "Optical Parametric Oscillation Out to 6.3 μm in Periodically Poled Lithium Niobate Under Strong Idler Absorption," *Appl. Phys. Lett.* **73**:1610–1612 (1998).
128. M. E. Dearborn, K. Koch, G. T. Moore, and J. C. Diels, "Greater than 100% Photon-Conversion Efficiency from an Optical Parametric Oscillator with Intracavity Difference-Frequency Mixing," *Opt. Lett.* **23**:759–761 (1998).
129. D. C. Edelstein, E. S. Wachman, and C. L. Tang, "Broadly Tunable High Repetition Rate Femtosecond Optical Parametric Oscillator," *Appl. Phys. Lett.* **54**:1728–1730 (1989).
130. G. Mak, Q. Fu, and H. M. van Driel, "Externally Pumped High Repetition Rate Femtosecond Infrared Optical Parametric Oscillator," *Appl. Phys. Lett.* **60**:542–544 (1992).
131. R. Laenen, H. Graener, and A. Laubereau, "Broadly Tunable Femtosecond Pulses Generated by Optical Parametric Oscillation," *Opt. Lett.* **15**:971–973 (1990).
132. Q. Fu, G. Mak, and H. M. van Driel, "High-Power, 62-fs Infrared Optical Parametric Oscillator Synchronously Pumped by a 76-MHz Ti:Sapphire Laser," *Opt. Lett.,* **17**:1006–1008 (1992).
133. W. S. Pelouch, P. E. Powers, and C. L. Tang, "Ti:Sapphire-Pumped, High-Repetition-Rate Femtosecond Optical Parametric Oscillator," *Opt. Lett.* **17**:1070–1072 (1992).

134. S. W. McCahon, S. A. Anson, D.-J. Jang, and T. F. Boggess, "Generation of 3-4 μm Femtosecond Pulses from a Synchronously Pumped, Critically Phase-Matched $KTiOPO_4$ Optical Parametric Oscillator," *Opt. Lett.* **22**:2309–2311 (1995).
135. P. E. Powers, S. Ramakrishna, C. L. Tang, and L. K. Cheng, "Optical Parametric Oscillation with $KTiOAsO_4$," *Opt. Lett.* **18**:1171–1173 (1993).
136. D. T. Reid, C. McGowan, M. Ebrahimzadeh, and W. Sibbett, "Characterization and Modeling of a Noncollinearly Phase-Matched Femtosecond Optical Parametric Oscillator Based on KTA and Operating Beyond 4 μm," *IEEE J. Quantum Electron.* **33**:1–9 (1997).
137. P. E. Powers, C. L. Tang, and L. K. Cheng, "High-Repetition-Rate Femtosecond Optical Parametric Oscillator Based on $CsTiOAsO_4$," *Opt. Lett.* **19**:37–39 (1994).
138. G. R. Holtom, R. A. Crowell, and L. K. Cheng, "Femtosecond Mid-Infrared Optical Parametric Oscillator Based on $CsTiOAsO_4$," *Opt. Lett.* **20**:1880–1882 (1995).
139. P. E. Powers, C. L. Tang, and L. K. Cheng, "High-Repetition-Rate Femtosecond Optical Parametric Oscillator Based on $RbTiOAsO_4$," *Opt. Lett.* **19**:1439–1441 (1994).
140. D. E. Spence, S. Wielandy, and C. L. Tang, "High Average Power, High Repetition Rate Femtosecond Pulse Generation in the 1–5 μm Region Using an Optical Parametric Oscillator," *Appl. Phys. Lett.* **68**:452–454 (1996).
141. J. M. Dudley, D. T. Reid, M. Ebrahimzadeh, and W. Sibbett, "Characteristics of a Noncritically Phase-Matched Ti:Sapphire-Pumped Femtosecond Optical Parametric Oscillator," *Opt. Commun.* **104**:419–430 (1994).
142. D. T. Reid, M. Ebrahimzadeh, and W. Sibbett, "Noncritically Phase-Matched Ti:Sapphire-Pumped Femtosecond Optical Parametric Oscillator based on $RbTiOAsO_4$," *Opt. Lett.* **20**:55–57 (1995).
143. J. D. Kafka, M. L. Watts, and J. W. Pieterse, "Synchronously Pumped Optical Parametric Oscillators with LiB_3O_5," *J. Opt. Soc. Am. B* **12**:2147–2157 (1995).
144. R. J. Ellingson and C. L. Tang, "High-Power, High-Repetition-Rate Femtosecond Pulses Tunable in the Visible," *Opt. Lett.,* **18**:438–440 (1993).
145. D. T. Reid, M. Ebrahimzadeh, and W. Sibbett, "Efficient Femtosecond Pulse Generation in the Visible in a Frequency-Doubled Optical Parametric Oscillator Based on $RbTiOAsO_4$," *J. Opt. Soc. Am. B* **12**:1157–1163 (1995).
146. A. Shirakawa, H. W. Mao, and T. Kobayashi, "Highly Efficient Generation of Blue-Orange Femtosecond Pulses from Intracavity-Frequency-Mixed Optical Parametric Oscillator," *Opt. Commun.* **123**:121–128 (1996).
147. T. Kartaloglu, K. G. Koprulu, and O. Aytur, "Phase-Matched Self-Doubling Optical Parametric Oscillator," *Opt. Lett.* **22**:280–282 (1997).
148. T. J. Driscoll, G. M. Gale, and F. Hache, "Ti:Sapphire Second-Harmonic-Pumped Visible Range Femtosecond Optical Parametric Oscillator," *Opt. Commun.* **110**:638–644 (1994).
149. G. M. Gale, F. Hache, and M. Cavallari, "Broad-Bandwidth Parametric Amplification in the Visible: Femtosecond Experiments and Simulations," *IEEE J. Sel. Top. Quantum Electron.* **4**:224–229 (1998).
150. K. C. Burr, C. L. Tang, M. A. Arbore, and M. M. Fejer, "Broadly Tunable Mid-Infrared Femtosecond Optical Parametric Oscillator Using All-Solid-State-Pumped Periodically Poled Lithium Niobate," *Opt. Lett.* **22**:1458–1460 (1997).
151. D. T. Reid, Z. Penman, M. Ebrahimzadeh, W. Sibbett, H. Karlsson, and F. Laurell, "Broadly Tunable Infrared Femtosecond Optical Parametric Oscillator Based on Periodically Poled $RbTiOAsO_4$," *Opt. Lett.* **22**:1397–1399 (1997).
152. D. T. Reid, G. T. Kennedy, A. Miller, W. Sibbett, and M. Ebrahimzadeh, "Widely Tunable Near- to Mid-Infrared Femtosecond and Picosecond Optical Parametric Oscillators Using Periodically Poled $LiNbO_3$ and $RbTiOAsO_4$," *IEEE J. Sel. Top. Quantum Electron.* **4**:238–248 (1998).
153. T. Kartaloglu, K. G. Koprulu, O. Aytur, M. Sundheimer, W. P. Risk, "Femtosecond Optical Parametric Oscillator Based on Periodically Poled $KTiOPO_4$," *Opt. Lett.* **23**:61–63 (1998).
154. C. McGowan, D. T. Reid, Z. E. Penman, M. Ebrahimzadeh, W. Sibbett, and D. T. Jundt, "Femtosecond Optical Parametric Oscillator Based on Periodically Poled Lithium Niobate," *J. Opt. Soc. Am. B* **15**:694–701 (1998).

155. R. L. Byer and A. Piskarskas (eds.), "Optical Parametric Oscillation and Amplification," *J. Opt. Soc. Am. B* **10**:1656–1791, 2148–2243 (1993).

156. W. R. Bosenberg and R. C. Eckardt (eds.), "Optical Parametric Devices," *J. Opt. Soc. Am. B* **12**:2084–2322 (1995).

157. M. Ebrahimzadeh, R. C. Eckardt, and M. H. Dunn (eds.), "Optical Parametric Devices and Processes," Special Issue, *J. Opt. Soc. Am. B* **16**(9) (1999).

158. N. P. Barnes and V. J. Corcoran, "Parametric Generation Processes: Spectral Bandwidth and Acceptance Angles," *Appl. Opt.* **15**:696–699 (1976).

159. G. D. Boyd, A. Ashkin, J. M. Dziedzic, and D. A. Kleinman, "Second Harmonic Generation of Light with Double Refraction," *Phys. Rev.* **137**:A1305–A1320 (1965).

160. D. J. Kuizenga, "Optimum Focusing Conditions for Parametric Gain in Crystals with Double Refraction," *Appl. Phys. Lett.* **21**:570–572 (1972).

161. E. S. Wachman, W. S. Pelouch, and C. L. Tang, "CW Femtosecond Pulses Tunable in the Near- to Mid-Infrared," *J. Appl. Phys.* **70**:1893–1895 (1992).

162. P. Di Trapani, A. Andreoni, C. Solcia, P. Foggi, R. Danielius, A. Dubeitis, and A. Piskarskas, "Matching of Group Velocities in Three-Wave Parametric Interaction with Femtosecond Pulses and Application to Travelling-Wave Generators," *J. Opt. Soc. Am. B* **12**:2237–2244 (1995).

163. M. Bass and D. W. Fradin, "Surface and Bulk Laser-Damage Statistics and the Identification of Intrinsic Breakdown Processes," *IEEE J. Quantum Electron.* **9**:890–896 (1973).

CHAPTER 23
ELECTROMAGNETICALLY INDUCED TRANSPARENCY

J.P. Marangos
Laser Optics and Spectroscopy Group
Blackett Laboratory, Imperial College
London, United Kingdom

23.1 GLOSSARY

Terms and Acronyms

CPT	coherent population trapping
EIT	electromagnetically induced transparency
IR	infrared
Ladder scheme	three coupled atomic levels with the initial state below the intermediate state which is below the final state
Λ (Lambda) scheme	three coupled atomic levels with the initial and final states at lower energy than the intermediate state
Metastable state	an excited state of an atom which has no allowed channels of radiative decay to other states
Raman	a two-photon process coupling two levels of opposite parity in a Λ configuration
STIRAP	Stimulated Raman Adiabatic Passage
V (Vee) scheme	three coupled atomic levels with the initial and final states at higher energy than the intermediate state
VUV	vacuum ultraviolet radiation

Symbols

$\|a\rangle$	quantum state of atom
E_a	energy of atomic state $\|a\rangle$

Copyright 2001 by The McGraw-Hill Companies, Inc. Click Here for Terms of Use.

ω	angular frequency of field (rad s^{-1})
I	laser irradiance (intensity) in Wm^{-2} (invariably given in Wcm^{-2} in literature)
E	electric field strength (Vm^{-1})
$\mathrm{Re}\chi^{(1)}$	real part of linear susceptibility (dispersion)
$\mathrm{Im}\chi^{(1)}$	imaginary part of linear susceptibility (absorption)
$\chi^{(3)}$	nonlinear susceptibility
P	macroscopic polarization (Cm^{-2})
Ω	Rabi frequency; $\Omega = E \cdot \mu_{ab}/\hbar$ (rad s^{-1})
μ_{ab}	transition dipole moment between states |a> and |b> (Cm)
Γ_a	decay rate from state |a> (rad s^{-1})
ρ_{ab}	density matrix element
γ_{ab}	coherence dephasing rate ρ_{ab} (e.g. due to radiative decays or collisions) (rad s^{-1})
$\gamma_{\mathrm{Doppler}}$	Doppler (inhomogeneous) line width (rad s^{-1})
Δ_{ab}	detuning of a field from the |a> to |b> transition frequency (rad s^{-1})
σ_{ion}	photo-ionisation cross-section (cm^2)

23.2 INTRODUCTION

Electromagnetically induced transparency (EIT) is a quantum interference phenomenon that arises when coherent optical fields couple to the states of an atomic or molecular system. In EIT the interference is between alternative transition pathways that are induced by the fields within the internal states of the atom or molecule. These effects arise because in quantum mechanics it is probability amplitudes (which may be positive or negative in sign), rather than probabilities, that must be summed and squared to obtain the total transition probability of a process. Interference between the amplitudes may lead to either an enhancement (constructive interference) or a complete cancellation (destructive interference) in the total probability of the process. A profound modification of the optical and nonlinear optical properties of a medium can result from this interference.

Interference effects of this kind are well known in physics; these occur naturally if there are two transition pathways available to the same final state. Fano interference is an example of interference between two transition pathways; a direct photoionization path interferes with another path to the same continuum state that goes via an intermediate autoionizing state.[1,2] It leads to asymmetric resonances in the photoionization spectrum, with vanishing photoionization cross sections possible at certain frequencies where complete destructive interference occurs. This process is well known for radiative transitions to autoionizing states in atoms and also predicted to occur in semiconductor quantum wells.[3]

Interfering transition pathways can also be deliberately induced by application of resonant laser fields to multilevel atomic systems. The cancellation of absorption for a probe field tuned in resonance to an atomic transition, for which strong absorption would normally be expected, is perhaps the most striking example of the manifestation of this type of interference. This process has been termed *electromagnetically induced transparency* (EIT),[4,5] the effect being so named as it is caused by the interference between the quantum coherences *induced* in the atom by the *electromagnetic* fields that lead to an initially highly opaque medium being rendered almost *transparent.* Similarly the refractive properties of the medium may be greatly modified[6,7]; for instance, the usual correlation of high refractive index with high absorption can be broken, leading to the creation of media with unique optical properties.

There has been a considerable research effort devoted to EIT and related topics over the last few years. This has been motivated by the recognition of a number of new potential applications (e.g., lasers without inversion, high-efficiency nonlinear optical processes, lossless propagation of laser beams through optically thick media, and high-efficiency population transfer via coherent adiabatic processes). Electromagnetically induced transparency is one of an interrelated group of processes—including coherent population trapping (CPT) and coherent adiabatic population transfer—that result from externally induced quantum mechanical coherence and interference. In contrast, the earlier ideas associated with CPT (first observed in 1976) had found application mostly as a tool of high-resolution spectroscopy, rather than as a new direction in nonlinear optics. Therefore the concept of EIT has contributed a distinctive new thrust to work on atomic coherence and its applications, and one that is of direct interest to optical scientists and engineers.

To explain and calculate EIT phenomena, an equivalent picture to that of interfering transition pathways is that of *laser dressed states*. These states are *coherent superpositions* of the atomic states that are created when the atom couples to a field. The coherent superpositions have well-defined amplitudes and phases that describe the relationship between the atomic states in the superposition. The reader is referred to *Theory of Coherent Atomic Excitations* by Shore[8] for a complete account of these ideas. An important feature of EIT experiments is the creation of large populations of these coherently driven, uniformly phased atoms (a medium termed *phasesonium* by Scully[6] to convey this idea). The optical properties (both linear and nonlinear) of this (coherent) medium are very different from those of a normal (incoherent) medium. In this laser-dressed medium the language of linear and nonlinear susceptibilities can be retained only to the extent that it is recognized that all these resonant processes are highly nonperturbative (i.e., even the "linear" processes involve the coupling of atoms with many photons). An important consequence of this is that the magnitudes of linear and nonlinear susceptibilities can reach equality in a phase-coherent medium. This is in marked contrast to the normal situation, in which the nonlinear susceptibility gives rise to effects that are many orders of magnitude weaker than those arising from the linear susceptibility.

The exceptionally high efficiency nonlinear optical processes that become possible in a *gas phase* medium therefore constitute an important feature of EIT. The high nonlinear conversion efficiencies are of a magnitude usually associated with nonlinear frequency mixing in optical crystals. Thus a renewed interest in gas phase nonlinear optical devices possessing unique capabilities (e.g., high conversion efficiencies into the VUV and far-IR) has occurred. There have been a number of notable recent demonstrations of the consequences of EIT. A near-unity frequency conversion into the far-UV was reported for a four-wave mixing scheme in lead vapor in which maximal coherence was created by an EIT-type process. This uniquely high conversion efficiency arises since the nonlinear terms become equal in magnitude to the linear terms in this system. In laser-cooled atoms EIT can be achieved using very weak laser couplings, with the result that in the vicinity of the frequency of maximum transparency there is an extremely steep dispersion as a function of frequency. The consequence of this is very slow group velocities ($<20 ms^{-1}$) for optical pulses propagating through the medium at this frequency.[9] Massive optical nonlinearities accompany the steep dispersion. These are manifested as very large nonlinear refractive indices that are many orders of magnitude larger than any previously observed. These huge nonlinearities are the subject of current research activity because they offer the likelihood of efficient nonlinear optical processes at the few photon level.

Another of the consequences of the coherence and interference effects related to EIT is the possibility of building a short-wavelength laser operating without the need to achieve population inversion in the atomic medium.[10–15] Lasing without inversion (LWI) has been demonstrated in sodium (Na) and rubidium (Rb) in the visible range.[16] The prospect that this might lead to the construction of lasers able to circumvent the usual constraints placed on achieving inversion in short wavelength lasers (due to the ω^3 scaling of the spontaneous emission) has been much discussed.[18,19] Related lasing without inversion and EIT effects in semiconductor quantum wells have also been theoretically explored using laser-induced processes[20] or band-gap engineering[21] to create the necessary coherences.

It is the aim of this chapter to provide an accessible summary of electromagnetically induced transparency and to present some of the main results obtained in recent research. It is not possible in the space available to cover all work in this field, and we apologize to authors whose important contributions are not directly mentioned. An extensive review of all theoretical and experimental work on related atomic coherence phenomena is also beyond the scope of the present article. The reader is advised to look at a number of reviews on lasing without inversion,[18,19] coherent population trapping,[8,22–24] including a very comprehensive recent review on this subject[25] and laser-induced continuum structure,[26,27] to find these topics presented in detail. The theory pertinent to EIT is sketched in the text, but again the reader is referred to the more detailed treatments published in the literature references to which will be given as they arise. The purposes of the chapter are (a) to communicate the underlying physical principles of EIT and related effects, (b) to describe the manifestations of EIT and to summarize the conditions required to create EIT, and (c) to introduce some potential applications in optical technology.

23.3 COHERENCE IN TWO- AND THREE-LEVEL ATOMIC SYSTEMS

The first experimental work on laser-induced atomic coherence was carried out in the 1970s. Earlier relevant work includes the investigation of dressing two-level systems by strong microwave fields (Autler-Townes splitting)[28] and work on photon echoes in two-level systems.[29] Mollow[30,31] reported novel features, subsequently termed the Mollow triplet, of resonance fluorescence in a two-level system driven by a strong resonant laser. Much work on two-level systems has been carried out since,[8,32,33] but although two-level systems remain a subject of considerable interest (e.g., in dressed-state lasers and quantum optics experiments), our concern here is primarily with three-level systems (and in some cases four-level systems).

Atomic coherence and interference in three-level systems was first seen experimentally in the work of Alzetta et al.[34–36] in Pisa and by Gray et al.[37] in Rochester. The Pisa group performed experiments that established coherence between the Zeeman split lower levels of a sodium atom using a multimode laser. By employing a spatially varying magnetic field they were able to observe a series of spatially separated dark lines (resonances) corresponding to the locations where the Zeeman splitting matched the frequency difference between modes of the coupling laser. This situation corresponds to a two-photon (Raman) resonant Λ scheme, and thus this was the first experimental observation of CPT. The experiments of Gray et al.[37] were similar to this but involved establishing coherence between the hyperfine lower levels of Na.

In essence in these experiments the laser fields are coupled to the three-level Λ configuration atomic levels to create superpositions of the two lower states $|1\rangle$ and $|2\rangle$ (see Fig. 1). One of the superpositions created can interact with the fields [see Eq. (1) in Section 4], a so-called *bright* state (i.e., the coupled state $|C\rangle$), but the other cannot due to interference causing cancellation of the two driven dipoles, and is thus termed a *dark* state (i.e., the noncoupled state $|NC\rangle$). Once the coherent states are formed, the population in the system will all be "optically pumped" into this dark state through spontaneous emission from the intermediate state in a matter of a few times the radiative decay rate. Once in the dark state there is no process to remove the population, and so there is a *trapping* of the population in this state.

Recently the basic idea of CPT has been utilized in systems with time-varying optical fields to yield very efficient excitation of atomic and molecular states.[38–40] In these coherent adiabatic population transfer schemes (e.g., stimulated raman adiabatic passage or STIRAP) the noncoupled ground state superposition $|NC\rangle$ of CPT is evolved in time from being composed purely of the lowest state $|1\rangle$ to being composed purely of the upper state $|2\rangle$ as the relative strengths of the laser couplings vary. This is achieved by employing counterintuitive pulse sequences, typically with identical Gaussian pulses, in which the coupling Ω_2 reaches its peak value around the time Ω_1 is just switching on and has decreased back to almost zero when the

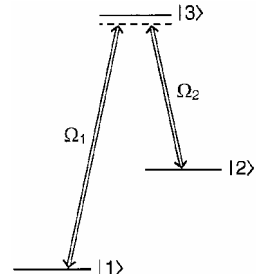

FIGURE 1 Coherent population trapping in a three-level Λ configuration. Fields are applied close to resonance with the |1>-|3> and |1>-|2> transitions with Rabi couplings Ω_1 and Ω_2 respectively.

latter is still just passing its peak. In this way the dark state |NC> is initially almost purely bare state |1> (the initial state of the system), then evolves through being an admixture of |1> and |2> while both fields are strong, and finally corresponds to being purely state |2>. The bright state |C> remains unpopulated throughout the process. The time scale for this adiabatic population transfer process is determined by the evolution of the laser pulse and not (as in conventional CPT) by the spontaneous emission time scale. Recently work has been performed that demonstrates the utility of these effects in laser cooling and manipulation of trapped atoms in a technique called *velocity-selective coherent population trapping* (VSCPT).[41–43]

In conventional CPT, the states |1> and |2> are usually initially populated (since they are typically sublevels of the atomic ground state); in contrast for EIT processes only state |1> needs to be populated initially and can remain the only state with significant population throughout the process. In CPT experiments the concern is primarily with the changes within the state *populations* of essentially individual atoms; for EIT the interest is more generally in the *optical response* of the entire medium. This optical response is determined by the coherences rather than the populations. Within the language of density matrices for CPT the pertinent quantities are the on-diagonal elements (populations), while in EIT they are the off-diagonal elements (coherences). Most important, in the limit of a strong coupling field (Ω_2) and the population initially in the ground state, the coherences leading to EIT are almost instantaneously established on a time scale of $\sim 1/\Omega_2$, which is typically a few picoseconds in a pulsed laser experiment. For creation of population trapping a time scale of several optical pumping times is required (typically many nanoseconds).

23.4 THE PHYSICAL BASIS OF ELECTROMAGNETICALLY INDUCED TRANSPARENCY

As was explained in the preceding section, there is a close link between electromagnetically induced transparency (EIT) and other atomic coherence phenomena such as coherent population trapping[25,34,44,45] and coherent adiabatic population transfer processes.[38–40,46] In all these processes, three-level atomic systems are involved—that is, systems that can be adequately reduced to three levels when the interactions with the pertinent electromagnetic fields are considered. The usual atomic dipole selection rules normally require that two pairs of levels are dipole-coupled, while the transition between the third pair is dipole-forbidden. In Fig. 2 we show the three basic level schemes for three-level atoms; all of the level schemes involved in the experiments discussed in this chapter can be reduced to one or another of these schemes.

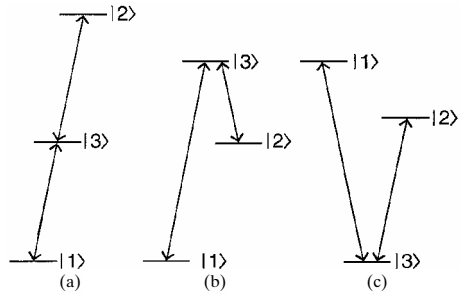

FIGURE 2 The three basic three-level schemes: (*a*) A Ladder (or Cascade) scheme with $E_1 < E_3 < E_2$. (*b*) A Λ (Lambda) scheme with $E_1 < E_2 < E_3$. (*c*) A V (Vee) scheme with $E_3 < E_1$ and E_2.

We label the levels |1>, |2>, and |3>, where |1> – |3> and |2> – |3> are dipole-allowed but |1> – |2> is not (this nomenclature follows Harris[5]). Classification of the schemes then depends upon the relative energies of the three states[31]: (a) in a *Ladder* (or *Cascade*) scheme $E_1 < E_3 < E_2$, (b) in a Λ (*Lambda*) scheme $E_1 < E_2 < E_3$ (although in a symmetric Lambda scheme E_1 and E_2 are almost degenerate), and (c) in a V (*vee*) scheme $E_3 < E_1$ and E_2 (although again in a symmetric vee scheme E_1 and E_2 are almost degenerate). EIT has been extensively studied in all three of these configurations. In a Λ or ladder scheme |1> is normally the ground state of the atom and is where the majority of the population (initially) resides. In EIT there is no need for significant population transfer, so states |2> and |3> can remain (essentially) unpopulated throughout the process. It should be noted that the Λ (lambda) scheme has a special importance due to the metastability of |2>. As a consequence of this metastability it is possible for the coherence between |1> and |2> to be very long-lived, which leads to near-perfect EIT conditions.

To understand more clearly how laser fields interact with a three-level atom and create coherent superpositions of the atomic basis states, we will first consider coherent population trapping (CPT) in a Λ scheme. A three-level Λ system (see Fig. 1) comprising states |1>, |2>, and |3> is coupled by two near-resonant laser fields of strengths (in terms of the Rabi frequency) Ω_1 (at frequency ω_1) and Ω_2 (at frequency ω_2). Defining the frequency of transitions between states as $\omega_{12} = (E_2 - E_1)/\hbar$, $\omega_{23} = (E_2 - E_3)/\hbar$, and $\omega_{13} = (E_3 - E_1)/\hbar$, we can further define one-photon frequency detunings as $\Delta_{13} = \omega_{13} - \omega_1$, $\Delta_{23} = \omega_{23} - \omega_2$ and two-photon (Raman) frequency detunings as $\Delta = [(\omega_{13} - \omega_{23}) - (\omega_1 - \omega_2)]$. The Hamiltonian of the bare atom H_0 should be modified to include the interactions due to the two couplings; that is, $H = H_0 + V_1 + V_2$ (where the interaction $V_j = \hbar\Omega_j$). The eigenstates of this new Hamiltonian will be linear superpositions of the bare atomic states |1>, |2>, and |3> (see Refs. 8, 24, and 47). For the situation of exact two-photon resonance ($\Delta = 0$), two of these eigenstates of the total Hamiltonian ($H_0 + V_1 + V_2$) turn out to be symmetric and antisymmetric coherent superpositions of the two *lower states* of the bare atom basis that are of the form:

$$|+\rangle = [\Omega_1|1\rangle + \Omega_2|2\rangle]/\Omega' \tag{1a}$$

$$|-\rangle = [\Omega_2|1\rangle - \Omega_1|2\rangle]/\Omega' \tag{1b}$$

where $\Omega' = \sqrt{(\Omega_1^2 + \Omega_2^2)}$. It is important to appreciate that no component of the bare atom state |3> appears in these superpositions. These form eigenstates of the atom-field system of which one (|+>) is coupled to the intermediate state |3> via the electric dipole interaction while the other state (|–>) becomes decoupled (a so-called *dark* or *trapped* state). This can be seen if we form the dipole moment between |+> or |–> with the remaining bare atom state |3>.[8]

If the magnitudes of the coupling fields Ω_1 and Ω_2 are appropriately balanced, the negative sign in the superposition of |1> and |2> which form |–> will ensure that the corresponding dipole moment will vanish. In effect, the two terms that are summed to give the transition amplitude between |3> and |–> are of equal and opposite magnitude, and hence the total amplitude will vanish. This can be viewed classically as driving the electron in the system with two fields, both of which may be strong, but which exert forces of exactly equal magnitude and opposite directions, leading to zero net force and hence an electron that doesn't move. State |–> is often referred to as a *noncoupled* state (|NC>), while |+> remains *coupled* (|C>) to the electromagnetic fields.

In the previous description the situation has been simplified by ignoring the fast time development (at frequencies $E_1/\hbar$ and $E_3/\hbar$) of the states in the superposition in Eq. (1) (these terms will in fact disappear when the dipole moments are formed). In conventional CPT, assuming a steady-state situation has been reached, the superposition state |NC> will acquire all of the population of the system through the action of optical pumping (i.e., spontaneous emission from |3> will populate |NC>), but there is no absorption process from |NC> to |3> to depopulate it.

In the usual CPT scheme $\Omega_1 \approx \Omega_2$ (i.e., both coupling strengths are of comparable magnitude) and the fields are also strong enough to reach the two-photon transition saturation condition. The two-photon transition saturation condition does not necessarily require that the fields are sufficient to saturate the single-photon transitions |1> – |3> and |3> – |2>. Under the two-photon resonance condition, state |3> can be adiabatically eliminated[8] so does not enter into the consideration of the coupling between atoms and fields. This latter point is very important in experiments where neither field is in single-photon resonance, but they are in Raman (two-photon) resonance so that large coherence effects are still induced.

In the CPT system, interference effects arise from both the coupling fields since they are of comparable strength. If only one of the fields (i.e., Ω_2) is strong such that $\Omega_1 \ll \Omega_2$, then only interference effects due to processes driven by Ω_2 will be important. This is the situation in many EIT schemes and this close connection between EIT and CPT is discussed by a number of authors (see for example Refs. 25 and 48). In EIT experiments Ω_2 is usually called the *coupling field* and labeled Ω_C, and Ω_1 is a weaker probe field labeled Ω_p. Typically in a CPT scheme, the states |1> and |2> are Zeeman or hyperfine sublevels of the ground state and are thus both initially populated. In contrast, in many EIT schemes |2> is an excited state and has no population at any time during the process. Unlike the case of CPT, where the time scale for population trapping in the |NC> state is several radiative lifetimes, in the case of EIT the effect is established (within a single atom) in a time of the order of $1/\Omega_2$, which is generally much faster. Comparison with coherent adiabatic population transfer schemes (e.g., stimulated Raman adiabatic passage or STIRAP)[38,39] also shows that the EIT situation is equivalent to the initial stages in the population transfer process when the counterintuitively sequenced laser pulses satisfy the condition $\Omega_1 \ll \Omega_2$.

The interference associated with EIT arises because the transition amplitude between |1> and |3> includes, as well as a term due only to the resonant field Ω_1, an additional amplitude due to the presence of the other field Ω_2 (see Fig. 3). This additional term and similar higher-order terms have a negative sign with respect to the first and hence in an ideal situation will cancel completely the first term. In the case of EIT, since the field Ω_2 is large, it is logical to choose the dressed-state basis[14] to analyze this system (see Fig. 4). In this basis, states |2> and |3> form a coherent superposition, which for a strong resonant coupling $\Delta_{23} = 0$ is of the form:

$$|a\rangle = 1/\sqrt{2}(|2\rangle + |3\rangle) \tag{2a}$$

$$|b\rangle = 1/\sqrt{2}(|2\rangle - |3\rangle) \tag{2b}$$

The transition amplitude at the (undressed) resonant frequency $(E_3 - E_1)/\hbar$ from the ground state |1> to the dressed states will be the sum of the contributions to states |a> and |b>. If |2> is metastable, then the contributions from the $|1\rangle \rightarrow |3\rangle$ transition cancel since they enter the sum with opposite signs. This cancellation of absorption on the $|1\rangle \rightarrow |3\rangle$ transition can also be viewed in terms of the Fano-type interference previously discussed.[14,48–50]

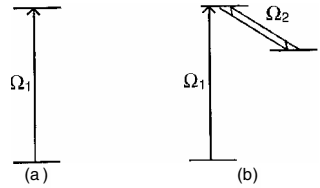

FIGURE 3 Electromagnetically induced transparency in a Λ scheme viewed in terms of Fano-type interference: (a) shows the direct channel for excitation from |1> → |3>, (b) shows the lowest-order additional channel introduced by the coupling field, |1> → |3> → |2> → |3>, interference between pathway (a) and (b) (plus higher-order terms) occurs.

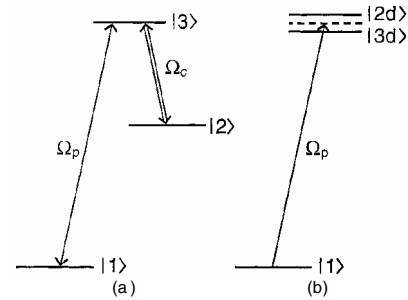

FIGURE 4 Electromagnetically induced transparency in a Λ scheme (cf. Fig. 3) viewed in terms of (*a*) bare atomic states with a probe field of strength Ω_p and a strong coupling Ω_C, (*b*) laser dressed states (dressed by Ω_C) |2d> and |3d> [corresponding to |a> and |b> in Eq. (2)] with the probe field in resonance with their center frequency.

The connection between EIT and the coupled and noncoupled states of Eq. (1) (where |3> has been adiabatically eliminated) can also be made. The states |NC> and |C> [i.e., |+> and |–> in Eq. (1)] in the case of two-photon (Raman) resonance are related to the bare atomic states by:

$$|C\rangle = [\Omega_1|1\rangle + \Omega_2|2\rangle]/\Omega' \tag{3a}$$

$$|NC\rangle = [\Omega_2|1\rangle - \Omega_1|2\rangle]/\Omega' \tag{3b}$$

or alternatively we can define the bare atomic states in terms of |NC> and |C>. From Eq. (3) we see, for example, that state |1> (atom ground state) can be written:

$$|1\rangle = [\Omega_2|NC\rangle + \Omega_1|C\rangle]/\Omega' \tag{4}$$

For the case $\Omega_1 \ll \Omega_2$ it is clear from Eq. (4) that |1> will be almost equivalent to |NC> (i.e., the noncoupled state) and thus absorption vanishes (i.e., EIT).

Equivalently within the picture of EIT in terms of the interfering pathways between the bare atomic states EIT, the so-called *coherences* are the quantities pertinent to the interference. Coherences can be thought of, in a semiclassical picture, as associated with the oscillating electric dipoles driven by the coupling fields applied between pairs of quantum states of the system (e.g., |i> – |j>). Strong excitation of these dipoles occurs whenever electromagnetic fields are applied close to resonance with an electric dipole transition between two states. If there are several ways to excite the oscillating dipole associated with |i> – |j>, then it is possible for interference to arise between the various contributions to this dipole, and these must be summed to give the total electric dipole oscillation between |i> and |j> (see Fig. 3). This is directly analogous to the Fano effect in autoionization[1] and to effects discussed in the context of laser-induced continuum structure (LICS).[27]

Formally coherences are identified with the off-diagonal density matrix elements ρ_{ij} formed by taking bilinear combinations of probability amplitudes of two quantum states of the system (i.e., the weighting factors associated with the outer products such as |i><j|).[51] Off-diagonal elements of the density matrix play a critical role in the evolution of an atom coupled to electromagnetic fields.[52] Many calculations of atomic coherence effects and of EIT (as well as general nonlinear optics and laser action) in three-level systems are therefore developed in terms of the density matrix.[7,53–55] The magnitudes of the relevant density matrix elements can be com-

puted from the basic coupled evolution equations (the Liouville equations)[8,51] and are found to depend upon parameters that are controllable within an experiment (e.g., detunings and laser intensities). This approach also naturally lends itself to the inclusion of dampings that cause the decay of populations and coherences (e.g., radiative decay and collisions).[46] EIT will manifest itself in the value of the density matrix element ρ_{13}, whose real and imaginary parts should both vanish at zero detuning (i.e., the coherence is cancelled by the interference of the pathways that can excite it). A set of coupled equations connecting the density matrix elements (e.g., ρ_{12}, ρ_{23}, and ρ_{13}) and their temporal derivatives can be written down and solved for various sets of conditions by either analytical or numerical means. Interference that leads to EIT arises from the existence of coherences ρ_{23} and ρ_{12} that are coupled to ρ_{13}. The coherence ρ_{12} between the ground state |1> and state |2> is present due only to the additional laser coupling. The contribution to the coherence ρ_{13} from the coherences ρ_{23} and ρ_{12} cancels with the direct contribution driving this coherence due to the applied probe field (at frequency ω_1).

Although this use of a density matrix approach is convenient, it is by no means essential, and many theoretical treatments that give clear physical insight have been performed in terms of probability amplitudes (see, for example, Refs. 5, 13, and 14). Additional physical insights have been obtained by adopting alternative approaches, for instance by a careful consideration of the Feynman diagrams representing the various processes involved that lead to interference,[48,50] or by applying a quantum jump approach.[56] In all cases the predictions are essentially identical.

Analytical solutions are generally only possible for steady-state conditions (corresponding to CW laser fields). A time-dependent calculation of the density matrix is of course appropriate if there are time-dependent laser pulses coupling with the atom. This is vital for modeling the results of pulsed laser experiments and correctly accounting for transient effects. Some time-dependent calculations have been made, but unless restrictive simplifying assumptions are applied[57] these calculations must be performed numerically rather than analytically. In most cases the results of the time-dependent calculation will be comparable to those of the steady-state method, at least in so far as qualitative trends are concerned. In calculating the results of propagation of pulses through an extended ensemble of atoms the time-dependent density matrix equations must also be coupled to Maxwell's equations. This is necessary, for instance, in computing the propagation of matched pulses[58–60] and in computing preparation losses and pulse shape modifications.[61]

23.5 ELECTROMAGNETICALLY INDUCED TRANSPARENCY PHENOMENA

The macroscopic polarization P at the transition frequency ω_{13} can be related to the microscopic coherence ρ_{13} via the expression:

$$P_{13} = N\mu_{13}\rho_{13} \tag{5}$$

where N is the number of equivalent atoms per unit volume in the ground state within the medium, and μ_{13} is the dipole matrix element associated with the (undressed) transition.[52] In this way imaginary and real parts of the linear susceptibility at frequency ω can be directly related to ρ_{13} via the macroscopic polarization,[52] since the latter can be defined as:

$$P_{13}(\omega) = \varepsilon_0\chi(\omega)E \tag{6}$$

The microscopic coherences are treated quantum mechanically, while the electromagnetic fields are treated classically using Maxwell's equations and these susceptibilities. This semiclassical approach is not essential, and fully quantum treatments for CPT (see, for example, Ref. 23) and EIT[62–64] have been developed. These fully quantum approaches are appropriate for cases such as the coupling of atoms to modes in cavities,[62,63] or when the statistical proper-

ties of the light are of interest as they are in proposals to generate squeezed light using EIT.[64] For relatively large fields, present in most laser experiments, a semiclassical treatment (with spontaneous decay added as a phenomenological damping) proves adequate.

The real and imaginary parts of the (dressed) linear susceptibility, associated with the dispersion and absorption of the medium respectively, will be given by expressions of the form[5]:

$$\mathrm{Re}\chi^{(1)}{}_{\mathrm{D}}(-\omega_1, \omega_1) = \frac{|\mu_{13}|^2 N}{\varepsilon_0 \hbar}\left[\frac{-4\Delta_{21}(|\Omega_2|^2 - 4\Delta_{21}\Delta_{32}) + 4\Delta_{31}\Gamma_2^2}{(4\Delta_{31}\Delta_{21} - \Gamma_3\Gamma_2 - |\Omega_2|^2)^2 + 4(\Gamma_3\Delta_{21} + \Gamma_2\Delta_{31})^2}\right] \tag{7a}$$

$$\mathrm{Im}\chi^{(1)}{}_{\mathrm{D}}(-\omega_1, \omega_1) = \frac{|\mu_{13}|^2 N}{\varepsilon_0 \hbar}\left[\frac{8\Delta_{21}{}^2\Gamma_3 + 2\Gamma_2(|\Omega_2|^2 + \Gamma_3\Gamma_2)}{(4\Delta_{31}\Delta_{21} - \Gamma_3\Gamma_2 - |\Omega_2|^2)^2 + 4(\Gamma_3\Delta_{21} + \Gamma_2\Delta_{31})^2}\right] \tag{7b}$$

Equations of this form can be derived in a steady-state situation using either the atomic bare state amplitudes or a density matrix approach. For these expressions, monochromatic coupling fields and no collisional or Doppler broadening were assumed. These susceptibilities (along with the nonlinear susceptibility) are plotted in Fig. 5 from Ref. 5 (see caption for explanation of labeling) as a function of detuning Δ_{13}, with $\Delta_{23} = 0$ (coupling field resonant). This is a striking result when compared to the case when no coupling field is present ($\Omega_2 = 0$),[5] the absorption vanishes at exact resonance (if |2> is perfectly metastable, that is, $\Gamma_2 = 0$). Simultaneously the dispersion is modified so that, although still zero at line center, as in the uncoupled case, the group velocity (dependent upon the slope of $\mathrm{Re}\chi^{(1)}$) can become anomalously low[65] where absorption has vanished. Inclusion of finite laser line widths and collisional and Doppler broadening is straightforward.[5] If this is done it is found that the dressed susceptibilities retain the key modifications providing the conditions discussed in the following paragraphs are met.

The medium that would in the absence of the coupling field be optically thick is now rendered transparent. The reduction in absorption is not merely that caused by the effective detuning induced by the Autler-Townes splitting of the dressed state absorption peaks (i.e., the absorption that would be measured if the probe field were interrogating the absorption coefficient of the medium in the wing of the absorption profile at a detuning $\Omega_2/2$). Additionally, there is *destructive* interference at the ω_{13} transition frequency that leads to complete cancellation of all absorption if there are no additional dephasing channels operating in the system (see Sec. 23.6). Even if the |1> → |2> transition dipole moment is not zero (i.e., if there is a spontaneous decay rate Γ_2), the absorption will be reduced compared to the weak field absorption at the detuning $\Omega_2/2$ in the ratio of Γ_2/Γ_3.[5]

In the preceding case it was implicitly assumed that the upper state probability amplitudes remain close to zero (i.e., the probe field is always very weak). If there is an incoherent population pump into the upper states, such that these no longer remain negligible, then gain on the |3> → |1> transition can result (see Sec. 23.8). The remarkable feature of this gain is that under the circumstances in which EIT occurs (i.e., when absorption is cancelled) the gain can be present without the requirement of population inversion in the bare atomic states. This is an example of *amplification without inversion.* This process has successfully been incorporated into a *laser without inversion* in a V scheme in Rb[16] and a Λ scheme in Na.[17] Much theoretical work[10–15] has been reported on this effect (earlier predicted by Arkhipkin and Heller,[12] and then further elucidated by Harris,[13] Kocharovskaya and Khanin,[10] and Scully et al.[11]). A long-term objective in this work is the prospect of overcoming the familiar difficulties of constructing short wavelength lasers (i.e., very high energy density pump requirements).

As well as leading to gain without population inversion, any incoherent pumping of population into the upper states also modifies the dispersive behavior. In particular, it is then possible to have spectral regions for which the refractive index is very high (with values comparable to those normally encountered at the half-widths of the absorption profile) while the absorption vanishes.[7] The prospects for engineering the refractive properties of media to give novel combinations of absorption/gain and dispersion have been explored in a number of theoretical[66–72] and experimental studies (see Sec. 23.9).

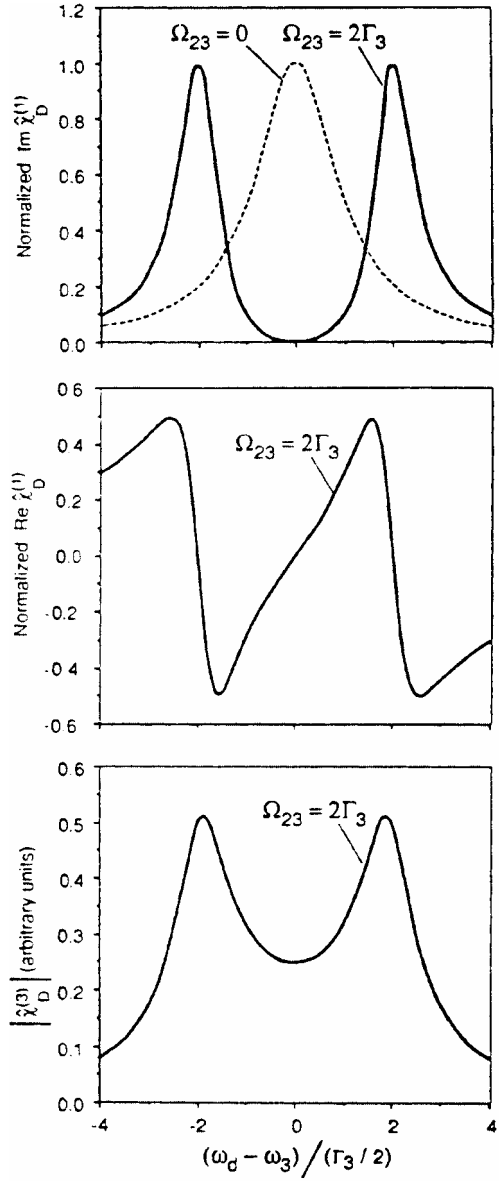

FIGURE 5 The dressed susceptibilities in terms of the normalized detuning $(\omega_d - \omega_3)/(\Gamma_3/2)$ [in the notation of this article this is $\Delta_{13}/)(\Gamma_3/2)$] for a value of the coupling Rabi field $\Omega_{23} = 2\,\Gamma_3$ ($\Omega_C = 2\,\Gamma_3$ in our notation). (Source: *S.E. Harris, J.E. Field, and A. Imamoglu, "Non-Linear Optical Processes Using Electromagnetically Induced Transparency,"* Phys.Rev.Lett. ***64****:1107 [1990].*)

Achievement of EIT depends upon a number of critical atomic and laser parameters. A correct choice of atomic energy level configuration is essential with states satisfying the dipole coupling conditions (|1> – |3> and |2> – |3> allowed; |1> – |2> not dipole-allowed). Radiative couplings to other energy levels outside of these three, which lead to the system being open, and additional hyperfine structure must also be considered. The coherence ρ_{12} is essential to EIT and so environmental factors that cause additional decays of this coherence, such as collisions with other species in the medium and photoionization, must be minimized. The laser couplings can be either pulsed or CW; in both cases they must have sufficient strength to overcome the inhomogeneous broadening and be sufficiently monochromatic (transform-limited in the pulsed case) so as not to dephase the ρ_{12} coherence. These critical parameters are summarized in Table 1. In the following section we deal in more detail with the most critical factors for obtaining EIT.

Intrinsic Dephasing of Atomic Coherence

For laser-induced atomic coherence processes in a real medium the maintenance of the phase of the coherence during the interaction is essential for effective interference. Any dephasing of the coherence will reduce and eventually nullify the interference effects. Dephasing can arise from a variety of different sources; for example the excitation of several closely spaced hyperfine or Zeeman components (see, for example, Refs. 8, 16, and 73), radiative decays of state |2> (e.g., on the |2> – |1> channel), the existence of additional photoionization channels,[74] and collisions.[5,75] In a ladder scheme perfect transparency is not usually achieved because state |2> is not metastable and can undergo spontaneous emission to |3> (as well as to other states in an open system). At finite density, collisional broadening with atoms of the same and other species is also critical and places strict limits on sample purity (for foreign gas broadening) and possibly on sample density. Also, at higher densities the local field effects due to nearest neighbor dipole-dipole couplings may be important,[75,76] and the simple relationship between macroscopic polarization and the coherences in Eq. (5) may break down.

Dephasing due to Laser Fields

In general, experiments with CW lasers, in which phase fluctuations can be made small with laser bandwidths reduced to the 1-MHz level or less, most fully approach the steady-state monochromatic limit explored in the elementary steady-state theory of these processes. Laser

TABLE 1 Summary of Atomic and Laser Parameters Critical to EIT

Physical parameter	Constraint	Typical values
|3> radiative decay Γ_3	—	1–50 MHz
|2> radiative decay Γ_2	$\Gamma_2 \ll \Gamma_3$	0–1 MHz
Photoionization rate Γ_{ion}	$\Gamma_{ion} \ll \Gamma_3$	$\Gamma_{ion} = \sigma_{ion} I$
Coherence dephasing γ_{ij}	$\gamma_{12} < \gamma_{13}, \gamma_{23}$	0–1 MHz
Laser linewidth γ_{laser}	$\gamma_{laser} < \Gamma_3$	<1 MHz (CW) or $\tau_{pulse} < 1/\gamma_{12}$ (pulsed)
Doppler linewidth $\gamma_{Doppler}$	$\gamma_{Doppler} < \Omega_C$	~ 1 GHz
Rabi frequency Ω_C	$\Omega_C > \gamma_{12}$	$\Omega_C = E.\mu_{23} / \hbar$
Pulse energy	$> NL\hbar\omega$	

line broadening, due to phase-diffusion processes[77–81] that gives rise to line widths above those of the allowed radiative decays, will destroy EIT. For EIT with pulsed lasers, although pulsed laser bandwidths are inevitably larger than those of CW lasers, the EIT effect is not reduced providing that the laser pulse is transform-limited. A single-mode laser pulse that is transform-limited (i.e., without excess phase fluctuation) will introduce insufficient dephasing during the interaction time (i.e., the duration of the pulse τ_{pulse}) to disturb the phases of the atomic coherences responsible for interference. It should also be appreciated that hyperfine sublevels will in general cause dephasing of coherences on a time scale given by the inverse of their frequency separation ($\Delta\omega_{hf}$).[8] In a pulsed excitation the dephasing due to hyperfine levels within the laser bandwidth will therefore be negligible, provided $\tau_{pulse} < 1/\Delta\omega_{hf}$ (i.e., if the hyperfine splittings are sufficiently small).

Inhomogeneous Broadening

In many experiments (inhomogeneous) Doppler broadening presents a serious limit since it introduces a randomization in the effective laser detunings over the ensemble of atoms in the sample.[5,82,83] Various methods have been employed to eliminate this effect (i.e., working in Doppler-free configurations[84,85] and using cooled atoms trapped in a magneto-optical trap[86,87]). Alternatively, by working with a coupling Rabi frequency larger than the width of the (Gaussian) Doppler profile, the influence of inhomogeneous broadening can, in effect, be overcome.[5] To generate Rabi couplings of greater than the Doppler width (~0.03 cm^{-1}) a CW laser, with a power typically of 1 W or less, must be tightly focused. This may lead to undesirable effects such as defocusing due to the interplay between the dressed refractive index and the transverse intensity variation across the beam waist in the region of the focus.[85] For pulsed lasers, with intrinsically high peak power, it is not generally necessary to focus the laser to achieve the required intensity. Thus the defocusing effects are not important, and there is also the important advantage that large numbers of atoms will be within the dressed ensemble.

EIT in solid-state systems has been observed by a number of workers.[88–91] For instance, in ruby the EIT was induced by a microwave field and probed optically.[88] We note also recently reported observations of related quantum interference effects between three states in a quantum well structure.[91] In general, however, it is the case that the large inhomogeneous broadening in solids leads to the requirement of large laser intensities for the creation of EIT, and this greatly increases the risk of optical damage to the sample. An exception to this is the work on solid H_2 (produced in cryogenic conditions), where exceptionally small inhomogeneous widths are encountered.[92]

Coupling Laser Power

In addition to the previously described condition that the coupling laser Rabi frequency should exceed the Doppler width, there are other constraints on the coupling laser power. In Raman schemes the laser powers must be sufficiently high to cause an EIT transparency with a width greater than the line width of the Raman (two-photon) transition to which the lasers are coupled. In Raman schemes operated far off single-photon resonance[92] this may require large laser powers. A preparation energy condition for EIT was established by Harris and Luo[61] which states that in a laser pulse there must be a sufficient number of photons to match the number of atoms (weighted by the transition oscillator strength) in the laser path (see Sec. 23.10). For a pulse to establish EIT in the adiabatic limit, it is essential that the pulse duration be long enough to significantly exceed $1/\Omega_C$.

23.6 ELECTROMAGNETICALLY INDUCED TRANSPARENCY WITH LASER PULSES

In the earliest work on electromagnetically induced transparency in the pulsed regime, the linear optical response of an extended ensemble of atoms was investigated. In these experiments measurements were made of the transmission of a weak probe field through an otherwise optically deep medium that was made possible by the presence of a strong coupling laser inducing EIT. In pulsed laser experiments there is usually no difficulty in producing laser pulses with a peak power sufficient to induce transparency in an inhomogeneously broadened medium. It is essential, however, that the laser be at the transform limit. Single-mode transform-limited nanosecond lasers are required; typically these are provided by injection-seeding an amplifier or optical parametric oscillator with narrow-band CW light of the correct frequency.

The first demonstration of pulsed EIT was by the group of Harris at Stanford in two atomic systems, Sr[93] and Pb.[94] In both of these experiments narrow-band pulsed laser radiation was used. In the strontium experiment (see Fig. 6) the atoms are initially pumped into an excited state by a pulsed laser. It is the transition (at 337.1 nm) between this 5s5p $^1P_1$ excited state (|1>) and the 4d5d $^1D_2$ autoionizing (|3>) state that was rendered transparent. A coupling laser (at 570.3 nm), derived from a single-mode Littman dye laser, was applied between this autoionizing state and a metastable bound state 4d5p $^1D_2$ (|2>). As in the prototypical scheme, the probe field excited the system to a state |3> with a large decay, and in the absence

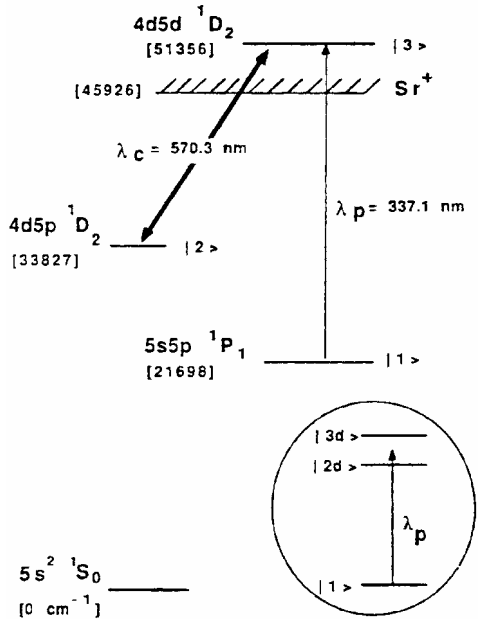

FIGURE 6 Energy-level diagram of neutral Sr used in the first demonstration of EIT. Inset: Dressed state picture. (Source: *K.J. Boller, A. Imamoglu, and S.E. Harris, "Observation of Electromagnetically Induced Transparency,"* Phys.Rev.Lett. ***66****:2593 [1991].*)

of the coupling laser there was a strong absorption; the Sr vapor was completely opaque at resonance, with an inferred transmission of $\exp(-20 \pm 1)$. When the coupling laser was applied the transmission at line center increased by a large factor to $\exp(-1 \pm 0.1)$. It was pointed out by the authors that for this large transparency, the interference effect is essential and that the detuning from line center induced by the Rabi splitting alone would only account for an increase in transmission to a value $\exp(-7.0)$.

A second experiment in lead vapor[94] demonstrated transparency within the bound states of a collisionally broadened system. The three levels were in a ladder configuration with the probe between the $6s^2 6p^2\ ^3P_0$ ground state $|1\rangle$ and the $6s^2 6p7s\ ^3P_1{}^0$ excited state $|3\rangle$, with the coupling field between $|3\rangle$ and the $6s^2 6p7p\ ^3D_1$ state $|2\rangle$. This scheme was chosen because of approximate coincidence with the frequency of the injection-seeded 1064-nm Nd:YAG laser used and the $|2\rangle - |3\rangle$ transition frequency. There was a 6-cm^{-1} detuning of the laser field from exact resonance. An important feature of this experiment was the role of resonance broadening, which was the dominant broadening channel for state $|3\rangle$ (about 40 times larger than the radiative width). Due to the destructive interference between the components of $|3\rangle$ in the two dressed states, these collisions have no effect on transparency. In contrast, the collisions that dephase state $|2\rangle$ (and which will affect the degree of transparency) are not resonance collisions and hence have a smaller magnitude for this scheme. The reduction in opacity induced when the transform-limited coupling laser was applied was by a factor of $\exp(-10)$.

Both experiments serve to demonstrate the principle of EIT in a three-level system. They also indicate how EIT can occur in situations where $|3\rangle$ is autoionizing or is collisionally broadened. In both cases the coupling laser was near transform-limited but the probe laser needed no special characteristics to demonstrate the effect, although the laser bandwidth must be less than the width of the transparency feature. Experiments using pulsed lasers continue to be important, most especially in the context of nonlinear optics and matched pulse propagation. A related resonant EIT scheme in Pb has been explored by Kasapi as a technique for enhanced isotope discrimination.[95] This method utilized the resonant opacity of a low-abundance isotope (Pb^{207}) at the frequency where the commonest isotope in their sample (Pb^{208}) is transparent. Work has also recently illustrated how EIT can be established in the Pb^{207} isotope despite the presence of hyperfine structure. This was done by adjusting the laser frequencies to coincide with the center of gravity of the hyperfine split transitions.[96,97] Under this condition, interference of the manifold of hyperfine states occurs to give EIT.

23.7 STEADY-STATE ELECTROMAGNETICALLY INDUCED TRANSPARENCY WITH CW LASERS

Steady-state EIT can be achieved using continuous wave (CW) lasers. This is an excellent regime for testing the theoretical understanding of EIT against experimental data from near-ideal systems. Investigation of new effects in the CW regime are straightforwardly suited to comparison with theoretical predictions. A monochromatic laser is required with a line width significantly less than the radiative decay Γ_3 (i.e., in the range 1 MHz to 10 kHz or less). This can be provided by either dye and titanium sapphire ring lasers or more cheaply (but with more limited wavelength coverage and power) by external cavity stabilized laser diodes. A more difficult condition to meet with CW lasers is to reach sufficient powers to give coupling strengths Ω_C that exceed the inhomogeneous broadening. This has required the employment of both Doppler-free techniques and the reduction of the Doppler width by atom cooling methods.

Much work has been carried out in Rb vapor samples due to suitability of the Rb atoms' energy level configuration for EIT (see Fig. 7), the possibility of near-complete elimination of Doppler effects in certain configurations, and the ease of handling the vapor. Groups in Arkansas in the United States and in St. Andrews, Scotland, have performed important demonstrations of steady-state EIT in this atom. A near-ideal Λ scheme is formed in the Rb

atom (see Fig. 7*a*) between the ground state $5S_{1/2}$ F = 1 and F = 2 states and the $5P_{1/2}$ F = 1 state; the transitions in this case are at 780 nm (separated by the 6837-MHz ground state hyperfine splitting). In a detailed theoretical treatment of this system it is necessary to include all the hyperfine sublevels of the three states, but in essence the behavior is that of a three-level system. Likewise a ladder scheme is formed in this atom between the $5S_{1/2} - 5P_{3/2} - 5D_{5/2}$ states (see Fig. 7*b*) with the transition wavelengths at 780 and 775 nm. Excitation of the transition at these wavelengths was easily achieved using either CW Ti:Sapphire ring lasers or grating-stabilized laser diodes. These schemes in Rb have the additional advantage that they can be operated with nearly perfect elimination of the Doppler width of the two-photon transition. These researchers have studied transparency,[82,98,99] refractive index modification,[84] and propagation effects.[85,100]

Observation of EIT in the Rb ladder scheme showed good agreement with a steady-state calculation in which the residual effects of inhomogeneous (Doppler) broadening were included.[82] Due to the near frequency coincidence between the 780 nm and 775 nm transitions in this scheme, the effect of inhomogeneous broadening on the experiment was almost eliminated by using counterpropagating beams. This elimination of broadening meant that relatively low power (< 10 mW) grating-stabilized laser diodes could be used to provide both probe and coupling fields in these experiments.

Results of experiments on the Rb Λ scheme also prove to be consistent with theory, with transparency being observed at the probe line center with a width and depth in reasonable agreement with the steady-state calculation.[98] In the case of the Λ scheme, copropagating beams leads to a Doppler-free situation, possible again because of the near equality of the probe and coupling laser wavelengths. As mentioned before, because of the elimination of

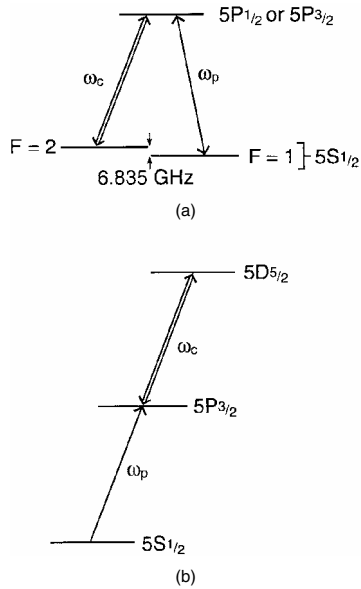

FIGURE 7 Rubidium atom EIT schemes: (*a*) A Λ scheme involving the hyperfine sublevels of the ground state (|1> and |2>) of ^{87}Rb (or ^{85}Rb) and the $5P_{1/2}$ or $5P_{3/2}$ excited state (|3>); (*b*) a Ladder scheme involving the $5S_{1/2}$ ground state |1>, $5P_{3/2}$ excited state |3>, and $5D_{5/2}$ excited state |2>.

Doppler broadening it was possible to employ very low power coupling lasers in these experiments. This was exploited by the same authors to perform an experiment that stresses the quantum interference nature of the EIT effect. By employing a coupling laser strength $\Omega_C < \Gamma_3$ (i.e., the Rabi splitting is too small to give rise, on its own, to any significant absorption reduction), a well-developed transparency, with a depth limited only by the laser line widths, was reported.[99] This experiment illustrates clearly how the additional coherence due to the coupling laser causes interference that cancels the effect of probe absorption.

The limit on probe laser power has been examined for steady-state EIT in the Rb ladder scheme just discussed.[101] When the coupling laser was strong, but the probe relatively weak, EIT was induced as usual. In the case of a strong probe with a power comparable to the coupling laser ($\Omega_P \sim \Omega_C$), the EIT was destroyed and replaced by enhanced absorption (electromagnetically induced absorption). This is explained by the opening of additional pathways in the absorption process (due to higher-order interactions with the probe field) leading to constructive interference in absorption. This result has implications in certain nonlinear frequency mixing schemes where a strong field is to be generated at the probe frequency and suggests there may be a limitation to the strength of fields that can be generated (see Sec. 23.12).

Laser cooling of the atoms can be used to fully eliminate Doppler broadening and to create steady-state EIT in systems where ω_P and ω_C differ significantly. Recently work has been reported on EIT (and CPT) in Rb and Cs Λ schemes for cold atoms confined in a magneto-optical trap (MOT).[86,87] In the Rb system a Zeeman scheme has also been studied.[102] These systems are close to ideal as the trapped atoms are very cool (i.e., Doppler broadening is almost absent) and the system is very low density and hence collisionless. If required, larger densities of trapped atoms can be provided by using *dark-spot* trap techniques.[103] Work has been carried out that exploits the characteristics of cold-confined atoms to study the nonlinear absorption and dispersion of cold Rb atoms.[104] Also temporal evolution of EIT in the transient regime has been investigated in a Rb MOT.[105] In cold Cs atoms in a MOT the nonlinear sum rule[106] for EIT-type situations has been experimentally verified.[107]

23.8 GAIN AND LASING WITHOUT INVERSION

If there is an incoherent pump into the excited states of an EIT system, producing a small population in the upper state of the probe transition, then inversionless gain of the probe can occur. The reader is referred to the extensive literature on this subject for further discussion (see, for example, Ref. 18). In studying gain without inversion, precautions should be taken to confirm that the system is indeed noninverted. This in practice is rather difficult, and experimenters often need to go to some trouble to confirm that there is (a) clear evidence for gain on the probe, and (b) truly no population inversion on this transition.

Gao and coworkers in Changchun[108] performed an early experiment that stimulated discussion and subsequent work. A Raman-driven four-level scheme was investigated in Na between the F = 1 and F = 2 hyperfine levels of the $3S_{1/2}$ ground state and the $3P_{3/2}$ and $3P_{1/2}$ states. A pulsed laser beam excited the transition between the ground state levels and $3P_{1/2}$, and this created a coherence between the two hyperfine states. A CW probe laser tuned around the wavelength of 589 nm of the other transition saw amplification when it was tuned to certain frequencies if a small amount of population is pumped into the $3P_{3/2}$ state. The incoherent pumping was achieved in this case by running a DC discharge through the sodium vapor. Amplification was seen, and the authors claimed that this was inversionless. There was initial criticism that there was no independent monitoring of the excited-state populations in this experiment, but with subsequent work this issue was addressed and firmer evidence for inversionless conditions were established by accompanying measurements of absorption.[109] A similar scheme in potassium vapor was reported by Kleinfeld and Streater.[110] Amplification of the probe laser was again seen, and the authors performed a careful numerical analysis that supports their claims that this is indeed amplification without inversion.

Further evidence for amplification without inversion has been found in several systems. Working with a Λ scheme in Na, with additional incoherent pumping into the upper state, Fry et al.[111] saw atomic coherence effects leading to amplification without inversion. The role of atomic coherence was confirmed by switching the coupling field on or off; amplification was only observed when the field was present, and when it was absent the large population always present in the lowest state led to absorption of the probe. In another demonstration, picosecond pulses were used to excite atomic coherence among the Zeeman sublevels of the Na ground state, and amplification without inversion was seen and unambiguously confirmed by Nottelmann et al.[112] Amplification without inversion was also demonstrated in a transient scheme in Cd[112] through the formation of a linear superposition of coherently populated Zeeman sublevels by van de Veer et al.[113] In this case nanosecond dye lasers were used. The coherent nature of the process was proven by the dependence of the gain on the time delay between the coherence preparation and probe pulse and the magnitude of the Zeeman splitting which controlled the period for coherent transfer of population in the atom. Recently a double Λ scheme in He, driven by 877.9-nm radiation in a He-Ne discharge, was used to observe amplification at both 1079.8 nm and 611 nm (up-conversion), and here the evidence for amplification without inversion rests on comparison to calculation.[114]

To demonstrate lasing without inversion, the gain medium must be placed within an optical cavity. In the two experiments[16,17] where this has so far been demonstrated, amplification without inversion was first proved using a probe through the medium and then the cavity was formed and lasing observed even under conditions where no inversion was possible. The first of these experiments (Zibrov et al.[16]) was in a V scheme formed on the D1 and D2 lines of Rb^{87}, with incoherent pumping from the F = 2 hyperfine level into the upper state of the D1 transition (lasing transition). Laser diodes were used for all the coherent and incoherent fields. The incoherent pump was generated by injecting white noise into an acousto-optic modulator (AOM) modulating one of the diodes. This work was therefore also the first experiment to achieve amplification without inversion using laser diodes. An important conceptual advantage of the V scheme is that there is no dressed basis within which a hidden inversion might reside; thus there is in principle true inversionless gain. This scheme can be considered in a simplified form as a four-level system (three levels coherently coupled and a fourth coupled via the incoherent field). There are, however, 32 hyperfine sublevels that must be considered in a detailed analysis of this system, which was carried out by the authors to yield predictions in good agreement with their experiment. Subsequently work was reported by Padmabandu et al.[17] demonstrating lasing without inversion in the Λ scheme in Na considered by the same authors in Ref. 111.

23.9 REFRACTIVE INDEX MODIFICATIONS FOR DRESSED ATOMS

As well as changes to opacity, the refractive index of the medium is also modified by EIT. Figure 5 shows the dependence of the $\mathrm{Re}\chi^{(1)}$ (which determines the refractive index) on the probe laser detuning. The dispersion is most significantly modified between the absorption peaks (i.e., for probe laser detunings in the range between $\Delta\omega_P = \Omega_c/2$). In the absence of a coupling field the usual form of $\mathrm{Re}\chi^{(1)}$ for an atom leads to anomalous dispersion (a negative slope in $\mathrm{Re}\chi^{(1)}$) in the vicinity of the resonance ($\Delta\omega_P = \pm\Gamma_3$) and to a vanishing dispersion $\mathrm{Re}\chi^{(1)}$ at exact resonance. In the usual case, however, the behavior is not significant for the optical properties of the medium since it is highly opaque in this frequency range. In contrast, in an EIT medium the transparency is nearly complete near resonance, and the modified dispersion can have a large effect on the refractive properties of the medium.

In a medium with EIT, $\mathrm{Re}\chi^{(1)} = 0$ at resonance, and so the refractive index will attain the vacuum value (n = 1) where the medium is fully transparent. As the assumption of a three-level atomic system is only an approximation, there will always be a background contribution to the refractive index due to the many other levels of the atom. These other levels, however,

are typically far from resonant with the fields and so lead to relatively small contributions to the dispersion. In nonlinear frequency mixing, the vanishing dispersion results in near-perfect phase-matching, which is essential for efficient frequency up-conversion (see Sec. 23.12). A second important modification to the dispersion in the frequency range between $\Delta\omega_P = \pm\Omega_C/2$ is that the medium is normally dispersive (a positive slope in $\mathrm{Re}\chi^{(1)}$). The value of the dispersion in this frequency range will depend on the shape of the curve and hence on the laser intensity which determines Ω_C. In Sec. 23.11 the situation when Ω_C is small will be examined; in this case the dispersion profile can be very steep, and consequently very low group velocities result. The intensity dependence of $\mathrm{Re}\chi^{(1)}$ leads also to the strong position dependence of the refractive index across the intensity profile of a focused laser beam.

Investigations have been carried out for steady-state schemes with CW lasers of the dispersion (refractive index) modification induced by EIT effects.[84,85,100] Direct measurements have been made of the modified refractive index that confirm the theoretical predictions. In a Rb scheme the Arkansas group measured the dispersive properties of EIT by incorporating the Rb vapor within a Mach-Zehnder interferometer.[84] The dispersion measured at the center frequency was inferred to be equivalent to a group velocity of $v_g = c/13.2$.

Observations of electromagnetically induced focusing/defocusing have been made that have implications for both future CW EIT experiments and potential applications. A wavelength-dependent induced focusing or defocusing was reported by the St. Andrews group[85,100] employing the Rb atomic scheme. Constraints are introduced to the tightness of focusing by these effects, but also there is the possibility of potential applications where control of the spatial properties of a beam at one frequency by a beam at another (perhaps widely different) frequency might be feasible.

In a scheme where a small amount of population is incoherently pumped into the excited state, it was predicted[7] that at $\Delta\omega_P = 0$ there will be gain (a negative $\mathrm{Im}\chi^{(1)}$) and at nearby frequencies where $\mathrm{Im}\chi^{(1)} = 0$ (absorption vanishes) the value of $\mathrm{Re}\chi^{(1)}$ can be high, a situation termed *enhanced refraction.* Enhanced refraction has been observed in the Rb Λ scheme when there is an additional pumping field between hyperfine sublevels that results in a small (noninverted) population in the upper state $|3\rangle$ of the system.[115] In this experiment an enhanced index of refraction was found at frequencies where the absorption was zero. A proposed application for refractive index modifications of this kind was for a high-sensitivity magnetometer.[116] The large dispersion at the point of vanishing absorption could, it was suggested, be used to detect, with high sensitivity, magnetic level shifts via optical phase measurements in a Mach-Zehnder interferometer.

23.10 PULSE PROPAGATION EFFECTS

Propagation of pulses is significantly modified in the presence of EIT. Figure 5(*b*) shows the changes to $\mathrm{Re}\chi^{(1)}$ that arise. An analysis of the refractive changes has been provided by Harris et al.[65], who expanded the susceptibilities (both real and imaginary parts) of the dressed atom, in a series around the resonance frequency to determine various terms in $\mathrm{Re}\chi^{(1)}$. The first term of the series (zero order) $\mathrm{Re}\chi^{(1)}(\omega_{13}) = 0$ corresponds to the vanishing dispersion at resonance. The next term $\partial\mathrm{Re}\chi^{(1)}(\omega)/\partial\omega$ gives the slope of the dispersion curve; at ω_{13} this takes the value:

$$\frac{\partial \mathrm{Re}\chi^{(1)}_{(\omega)}}{\partial\omega} = |\mu_{13}|^2 \frac{N4(\Omega_C{}^2 - \Gamma_2{}^2)}{\hbar\varepsilon_0(\Omega_C{}^2 + \Gamma_2\Gamma_3)^2} \tag{8}$$

This expression shows the dependence of the slope of $\mathrm{Re}\chi^{(1)}$ on Ω_C, and it is this parameter that controls the group velocity of a pulse at frequency ω_{13} propagating through the medium. Higher-order terms in the expansion lead to pulse distortions (group velocity dispersion) but at resonance the next nonvanishing term is third-order.

The first experimental studies of the influence of dispersive properties on pulse propagation in an EIT system were made by the Stanford group in 1995.[117] Working in the ^{208}Pb Λ scheme, they measured the delay of a probe pulse for various coupling laser strengths. Whilst still with high (55 percent) transmission through the medium, pulses were found to propagate with velocities as low as c/165. The authors showed that the delay time for the pulse in the medium compared to vacuum τ_{delay} was connected to the attenuation of the transmitted pulse and the Lorentzian linewidth of the forbidden |1> – |2> transition via the relation $\ln(E_{out}/E_{in}) = -\gamma_{12}\tau_{delay}$ (where E_{out} and E_{in} are the energies of the pulse leaving and entering the medium). This idea was subsequently demonstrated as a method for measuring Lorentzian linewidths.[118] It was also demonstrated[117] that the presence of the coupling pulse leads to a near diffraction-limited transmitted beam quality for a strong probe field under conditions where, in the absence of the coupling laser, severe spatial distortion was present. The situation where probe and coupling pulses were both strong was studied in a subsequent experiment that investigated further the elimination of optical self-focusing and filamentation that afflict a strong probe field.[119]

The prospects of controlling refractive index using strong off-resonant pulses was examined theoretically for a Λ scheme.[72] In this treatment it was shown that the off-resonant bound and continuum states lead to Stark shifts of the |2> and |1> states that can be compensated by detuning the lasers from exact (low-field) Raman resonance. If this is done correctly, the additional coherence ρ_{12} will lead to EIT-like modification of the refractive index experienced by both pulses. This extends to the situation for which the probe pulse is also strong. With both the laser pulses strong, off-resonant coherent population trapping is possible. Formation of an off-resonance population-trapped state is an important aspect of the experiment investigating the elimination of optical-self focusing[119] in which nonlinear refractive index effects would otherwise lead to self-focusing, filamentation, and beam breakup of the strong probe field. Off-resonant coherent population trapping is also important in nonlinear frequency mixing experiments in Raman systems in Pb[120] and solid H_2.[96] In this case the condition $\Omega' > \sqrt{(\Delta\gamma_{12})}$ must be met, where Δ is the detuning of the fields from the intermediate resonances, and this leads to the requirement of high peak powers if the detunings are large.

Propagation of two coupled strong pulses in a Λ (Raman) type system was discussed by Harris et al.[58,59] and Eberly and his coworkers.[24,60] This Raman scheme is equivalent to EIT, but if both fields (Ω_1 and Ω_2) are strong the dressed atomic system reacts back on the field modes in such a way as to result in lossless propagation through the medium for both the fields. For laser pulses with matched intensity envelopes (i.e., an identical form of temporal variation), any losses are minimal. If two initially matched pulses are simultaneously launched into a medium comprising atoms in their ground state, the system will self-organize so as to preserve the matched pulses and generate coherent population-trapped states. As the atoms are in |1> to begin with, the probe pulse will initially experience loss and will have a lower group velocity than the coupling pulse. It will then start to lag the coupling pulse and so the pulse pair will automatically satisfy the condition for adiabatic preparation of population-trapped states (i.e., a counterintuitive pulse sequence). So, following the initial loss of probe pulse energy, the medium is set up for lossless transmission.

A proper insight into this process is best obtained by thinking in terms of the formation of coherent population-trapped states by the laser pulses. Essentially the laser fields cause the formation in the atomic system of coupled |C> and uncoupled |NC> coherent superpositions of the bare atom lower states. However, the atoms in the phase-coherent medium that is formed are also responsible for driving the two fields, and this means that even intensity envelopes which are initially different will evolve into matched pulses. This process results in the self-consistent formation of stable normal modes of the driving fields, one of which is uncoupled from the "uncoupled" atomic state and the other of which is "uncoupled" from the coupled atomic state. These new field modes result in the lossless propagation of pulses through a normally lossy medium once a certain preparation energy has been extracted from the laser fields.[61]

An important point is that in the adiabatic limit [i.e., pulses that are sufficiently intense that the envelope evolution is slow compared to $1/\sqrt{(\Omega_2^2 + \Omega_1^2)}$] the time-scale to establish transparency for the whole medium is fast. Indeed, it can be much faster than the time scale

required to establish population-trapped states in an individual atom (since the latter process requires transfer of population; that is, irreversible exchange of energy between the field and the medium). In fact the transparency preparation time is equivalent to a preparation energy condition. The energy required to prepare the medium in a transparent state is essentially the coupling photon energy multiplied by the oscillator strength-weighted number of atoms:[61]

$$E_{\text{preparation}} = \frac{f_{13}}{f_{23}} NL\hbar\omega \tag{9}$$

Once the coupling laser pulse has been on sufficiently long for this condition to be achieved, the medium will be rendered transparent for all subsequent times. The possibility of applying this to the propagation of even sufficiently strong picosecond and femtosecond pulses can therefore be considered. This preparation energy is not transferred irreversibly to the medium but is stored reversibly in the coherent excitation of state |2> and in the coupling field.

23.11 ULTRASLOW LIGHT PULSES

The slope of the dispersion profile leads to a reduced group velocity v_g:

$$\frac{1}{v_g} = \frac{1}{c} + \frac{\pi}{\lambda} \frac{\partial\chi^{(1)}}{\partial\omega} \tag{10}$$

From the expression for $\partial\chi^{(1)}/\partial\omega$ [Eq. (8)] we see that this slope is steepest (and so v_g smallest) in the case where $\Omega_C \gg \Gamma_2$ and $\Omega_C^2 \gg \Gamma_2\Gamma_3$, but when Ω_C is still small compared to Γ_3 (i.e., $\Omega_C < \Gamma_3$) and hence $\partial\chi^{(1)}/\partial\omega \propto 1/\Omega_C^2$. In the limit of small Ω_C the following expression for v_g therefore holds:

$$v_g = \frac{\hbar c \varepsilon_0 [\Omega_C]^2}{2\omega_P |\mu_{13}|^2 N} \tag{11}$$

In an inhomeogenously broadened system the requirement for transparency is that $\Omega_C > \gamma_{\text{Doppler}}$, which usually means also that $\Omega_C > \Gamma_3$, and this constrains the group velocity reduction to relatively modest factors. Thus in the experiments in Pb (see Sec. 23.10), group velocities were clearly modified but the minimum reached was only $v_g = c/165$. Further reductions in v_g can be achieved by reducing γ_{Doppler} and therefore allowing lower values of Ω_C to be used such that $\Omega_C \ll \Gamma_3$. This reduction in γ_{Doppler} can be made by using an atom with an energy level configuration that gives $\omega_C \approx \omega_P$ and employing a Doppler-free geometry for the laser beams (i.e., copropagating in a V or Λ scheme and counterpropagating in a Ladder scheme). Alternatively, laser cooled and trapped atomic samples can be used that result in atoms for which $\gamma_{\text{Doppler}} \ll \Gamma_3$. The advantage of this is that schemes can then be investigated for which $\omega_C \neq \omega_P$, and there are no restrictions on beam geometry.

A limiting factor is the bandwidth of the light pulse that can be propagated at ultraslow velocity. This is set by the width of the transparency and by increased group velocity dispersion away from exact resonance $\omega_P = \omega_{13}$, and these factors limit the bandwidth of the pulse to values significantly less than Ω_c. The consequence is that pulses must be of sufficiently long duration that they contain no significant contribution from frequency components outside of this limited bandwidth.

A number of experimental observations of ultraslow group velocity have been reported. In a Doppler-free CPT scheme in a Cs atomic vapor the dispersion profile near the resonance was determined using a Mach-Zehnder interferometer.[121] From the steep normal dispersion measured, $v_g = c/3000$ was inferred. A Doppler-free experiment in Rb vapor was carried out that directly measured a much larger group velocity reduction. Here an amplitude-modulated

(modulation frequency up to 10 kHz) probe beam was passed through the sample and the phase lag of the modulation referenced to the input was used to measure the group velocity. Values of $v_g = 90 \text{ms}^{-1}$ were determined even though the temperature of the sample was as high as 360 K.[122] A Λ-scheme between Zeeman sublevels in Rb was recently investigated and a magnetic field dependent group velocity as low as 8 ms^{-1} was measured.[123]

The most dramatic demonstration of ultraslow light propagation to date was provided by Hau and coworkers.[9] They employed a laser-cooled Na sample trapped in a novel magnetic trap. Evaporative cooling of this could be used to prepare this sample in the Bose-Einstein condensed (BEC) state. Experiments were performed (see Fig. 8) to investigate the delay in propagation of a 2.5-μs duration probe light pulse when a coupling laser was applied to the sample in the perpendicular direction. The reduced group velocity was studied both above and below the BEC transition temperature. The lower group velocities found below T_c were due to the increased density of the sample when in this state. The lowest value of v_g that was measured was just 17 ms^{-1}.

23.12 ELECTROMAGNETICALLY INDUCED TRANSPARENCY IN NONLINEAR FREQUENCY MIXING

The nonlinear response of a medium is also significantly modified by EIT; this has been shown to lead to frequency mixing with greatly enhanced efficiencies and to large Kerr type nonlinearities. This is because in addition to the dressed linear susceptibility, given by Eqs. 7, there is also a dressed nonlinear susceptibility. This describes the coupling of the atom to other fields. For example, in the four-wave mixing process (see Fig. 9), three fields at frequencies ω_a, ω_b, and ω_2 couple together via the nonlinear response of the medium to generate a new field ω_1:$\omega_1 = \omega_a \pm \omega_b \pm \omega_2$. If ω_2 and ω_1 are as for the Lambda or Ladder scheme (Fig. 2), then ω_a and ω_b will be close to two-photon resonance between |1> and |2>. The nonlinear susceptibility is calculated from Eqs. (5) and (6) in the same way as the linear susceptibilities in Eq. (7), however now terms in ρ_{13} involving the fields at frequencies at ω_a and ω_b are also included. This gives:

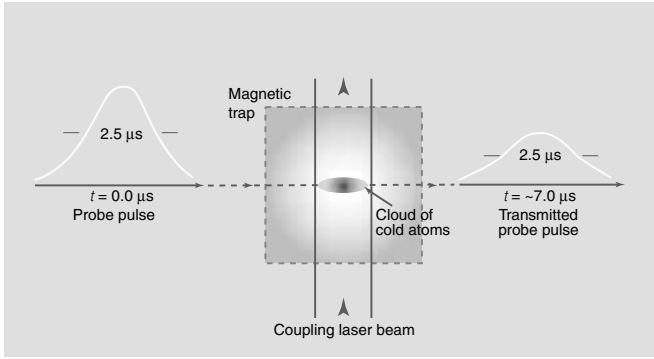

FIGURE 8 A schematic of the experimental setup of Hau et al.[9] The circularly polarized probe pulse takes ~7 μ to traverse the 0.2 mm-long cloud of cold atoms—this is one ten-millionth of the speed of light in a vacuum. (Source: *By permission of Macmillan Publishing, from* Nature, *volume 397.*)

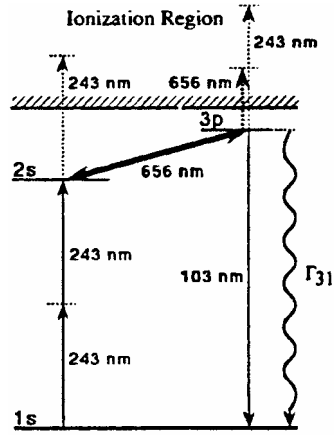

FIGURE 9 Four-wave mixing scheme in H. In this scheme EIT was created by the 656 nm field between the 2s and 3p states and a field was generated at 103 nm on the transition between 3p and 1s states (the "probe") due to four-wave mixing of the 656 nm with an additional field at 243 nm in two-photon resonance with the 1s-2s transition. (Source: *G.Z. Zhang, K. Hakuta, and B.P. Stoicheff, "Nonlinear Optical Generation Using Electromagnetically Induced Transparency in Hydrogen,"* Phys.Rev.Lett. ***71****:3099 [1993].*)

$$\chi_D^{(3)}(-\omega_1, \omega_a, \omega_b, \omega_2) = \frac{\mu_{23}\mu_{13}N}{6\varepsilon_0\hbar^3[(\Delta_{21} - j\Gamma_2/2)(\Delta_{31} - j\Gamma_3/2) - (|\Omega_C|^2/4)]^*} \sum_i \mu_{i1}\mu_{i3}\left(\frac{1}{\omega_i - \omega_a} + \frac{1}{\omega_i - \omega_b}\right) \quad (12)$$

Where the sum on the right-hand side represents the contribution to the nonlinear susceptibility of all the states of the atom, the fields at frequencies ω_a and ω_b are close to two-photon resonance with $|1> - |2>$ and are necessary to complete a four-wave mixing scheme with ω_2 in order to generate a field at frequency ω_1. The modulus of this nonlinear susceptibility is plotted in Fig. 5(*c*); although superficially similar to $\mathrm{Im}\chi_D^{(1)}$ [Fig. 5(*a*)] in the sense that the response displays the familiar Autler-Townes splitting, there is a fundamental difference. Paying attention to the center of the profile at detuning $\Delta_{13} = 0$ we see that instead of destructive interference there is constructive interference at this point.

Constructive interference in the nonlinear response of the atom is one of the most significant consequences of EIT. It accompanies the destructive interference which causes transparency at the same frequencies. In 1990 Harris et al. recognized how this could be used to greatly improve four-wave-mixing efficiencies into the VUV in atomic gases.[5] Enhancement of frequency-mixing schemes by atomic coherence and interference has been examined theoretically by a number of authors (see, for example, Refs. 5, 124, and 125). The interference effects lead to improved frequency mixing in resonant systems because of three connected factors: (a) There is reduced resonant reabsorption in the medium due to the creation of transparency; (b) the phase matching is optimized since near resonance the dispersion is zero;

and (c) although the coupling field causes some reduction in the value of the nonlinear susceptibility at resonance, it is subject to constructive rather than destructive interference. For a medium with a large density × length (NL) product, such that the uncoupled system is optically thick, there will be a large enhancement in the four-wave-mixing conversion efficiency. This persists in a Doppler-broadened medium, providing that the coupling-field strength exceeds the Doppler width.

In a finite medium a calculation including absorption and phase-matching must be performed to predict the enhancement and the frequency dependence of the nonlinear response.[5,80,81,125] In the limit of an optically deep medium and considering plane wave fields, the figure of merit determining the conversion efficiency is given by $|\chi_D^{(3)}|/\chi_D^{(1)}$. This is physically reasonable since $\chi_D^{(1)}$ characterizes the reabsorption and wave-vector mismatch in the medium, and $\chi_D^{(3)}$ the coupling strength that generates the new field. Thus we can see the importance of the destructive interference in the value of $\chi_D^{(1)}$ over the frequency range where $\chi_D^{(3)}$ experiences constructive interference. This enhances the generation efficiency in a Doppler-broadened medium by many orders of magnitude when the coupling field exceeds the Doppler width. Modifications of $\chi_D^{(1)}$ result in reduced absorption and the imposition of essentially perfect phase matching for all the resonant fields, and residual mismatch then appears only because of the dispersion caused by the remaining off-resonant states.

Electromagnetically induced phase matching was observed in an off-resonance four-wave mixing scheme in ^{208}Pb.[126] In this experiment, the $\Delta = 6$ cm^{-1} detuning from resonance meant that transparency played little role in the enhancement (since the sample was optically thin). However, once the coupling laser strength satisfied the inequality $\Omega_C > \sqrt{(\gamma^2_{\text{doppler}} + \Delta^2)}$, the dispersion (integrated across the Doppler profile) became effectively zero, leading to perfect phase matching and enhanced conversion efficiency.

In the first experiment to demonstrate the EIT enhancement effect, Hakuta, Stoicheff, and their coworkers investigated three-wave mixing (normally forbidden) in hydrogen when a DC electric field was applied to the sample.[127,128] This experiment can be viewed in the context of EIT by considering the DC field as a zero-frequency electromagnetic field that dresses the atom, creating two Stark states between which absorption cancellation occurs through interference. Second harmonic generation from a field at 243 nm, resonantly enhanced by the 1s-2s two-photon resonance, can then occur without the generated radiation at 121.6 nm (Lyman-α) being reabsorbed. Further experiments by the same group then demonstrated EIT enhancement of a resonant four-wave mixing scheme in H.[129] This was achieved in a scheme involving the 1s, 2s, and 3p levels, with the coupling laser at 656 nm applied between the 2s-3p states mixing with two-photons from a field at 243 nm (in two-photon resonance with 1s-2s) generating a field at 103 nm (see Fig. 9). Both of the laser fields used in the frequency mixing were derived from single-mode pulsed-dye lasers. In this scheme photoionization of the 3p state was an order of magnitude greater than that from the 2s state; this is important since the 1s-2s coherence must be preserved for the EIT effect to survive, and so decay due to photoionization is a critical impediment. However, so long as this decay rate is significantly less than that affecting the 3p state, the destructive interference in the absorption will persist and still lead to enhancement of the frequency mixing.

High conversion efficiencies require that the density × path length product (NL) is large enough to ensure that the medium is initially strongly opaque. An atomic hydrogen beam was specially constructed for these experiments in order to increase the beam density and path length so that these effects could be studied from the optically thin to the optically thick limits.[74,130] Working with NL up to 10^{16} cm^{-2}, conversion efficiencies of $>10^{-3}$ were found. There was, however, a limit to the obtainable conversion efficiency in this scheme, due to the large value of the Doppler width of the transitions (a consequence of the low mass of H and the elevated temperatures in the discharge used to produce the atoms). The coupling Rabi frequency Ω_C had to exceed the large Doppler width, leading to large Autler-Townes splittings and the reduction in the magnitude of $\chi^{(3)}$ available for mixing. To overcome this, four-wave mixing schemes in atoms with smaller Doppler widths (e.g., Kr) have been studied. Work with

a four-wave mixing scheme at a high NL (5×10^{16} cm^{-2}) in room-temperature Kr has recently demonstrated a conversion efficiency of 10^{-2} when generating a field at 123.6 nm.[131] Quantum interference effects arising from the generated field itself have been reported to lead to a limiting density for resonantly enhanced four-wave mixing. In a scheme in Rb,[132] at higher density the field generated was strong enough that it would itself cause a significant perturbation to the driven coherences in the system. This latter work, however, did not employ a single-mode coupling laser, and the low limiting rubidium density ($<10^{15}$ cm^{-3}) found may not be reflected in situations where EIT is present.

Frequency mixing in a Λ system has a number of special features. The metastability of state $|2\rangle$ is often almost complete, and this leads to intrinsically low decay rates for the ρ_{12} coherence; thus near-perfect transparency can result. Also in some systems (e.g., Rb and Na), where the two lower states are hyperfine sublevels, Doppler-free configurations can be employed. Figure 10 shows a general configuration for nonlinear interaction between four fields in a Λ system. The field at ω_1 is applied so as to create EIT, but there are then a number of different possible frequency-mixing scenarios for the other fields. Fields at frequencies ω_2 or ω_3 can be applied to the system to generate new fields. The sign of the detuning from resonance Δ for the applied or generated fields ω_3 and ω_4 can be positive or negative. Also, an additional state $|4\rangle$ may be present (at detuning Δ') so that the scheme becomes a double-Λ. If two fields ω_1 and ω_2 are applied, they will create the coherence ρ_{12} that can give rise, via a stimulated Raman process, to Stokes and anti-Stokes fields if it mixes again with ω_1 and ω_2. If fields are applied at ω_1 and ω_3 and a weak probe is applied at ω_4, then very efficient nondegenerate four-wave mixing can occur to generate a field that is phase conjugate to ω_4 at frequency ω_2.

Nondegenerate four-wave mixing (NDFWM) based on EIT in Λ schemes has been studied. For example, in an experiment in Rb[133] a coupling field was applied resonantly (ω_1) while a second field was applied at ω_3 and a weak probe at ω_4, both with a detuning of 450 MHz from resonance with $|3\rangle$. A phase-conjugate field was generated at frequency w_4. Due to EIT, absorption of this generated field vanished, but the nonlinearity remained resonantly enhanced. Measurements were made independently of $\mathrm{Im}\chi^{(1)}$ and $\chi^{(3)}$ under optically thin conditions, confirming that $\chi^{(3)}$ was indeed enhanced by constructive interference. If an optically dense medium was used, a significant enhancement in NDFWM was observed. High phase-conjugate gain was also recently observed with very low laser powers arising from the presence of population trapping in a double-Λ scheme in Na.[134,135] Continuous wave resonant four-wave mixing[136] and frequency up-conversion[137] have been observed in an experiment investigating a double-Λ scheme in Na dimers.

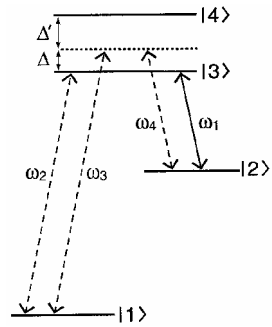

FIGURE 10 A generic four-wave mixing scheme within a Λ scheme. See text for additional description.

23.13 NONLINEAR OPTICS AT MAXIMAL ATOMIC COHERENCE

Under the conditions for matched pulse propagation, large populations of coherent population-trapped states are created. To achieve this situation the laser electric field strength must be large enough to create couplings that will ensure adiabatic atomic evolution, and laser pulses that are sufficiently energetic to prepare all of the atoms in the beam path. The ρ_{12} coherence thus created will have a maximum magnitude $|\rho_{12}| \cong 0.5$ (i.e., all the atoms are in the coherent state) and negative sign (i.e., all the atoms are in the population-trapped |NC> state). Under these circumstances, mixing of additional fields with the atom will become extremely efficient.

Imagine that in Fig. 10 the fields at frequencies ω_1 and ω_2 have created a maximum coherence of this type. Then the mixing of the fields ω_3 and ω_4 can occur with high efficiency since the nonlinear susceptibility governing the coupling for this system has only a single nonresonant denominator due to the detuning Δ. The nonlinear susceptibility for the fields at frequencies ω_3 and ω_4 is thus of the same order as the linear susceptibility (governing absorption and dispersion), as they share the same single-frequency detuning. A consequence of this is that complete nonlinear frequency conversion of the fields can occur in a distance of the order of the optical coherence length (determined by the real part of the susceptibility). This is equivalent to having near-vacuum conditions for the dispersion (and absorption) of the medium while the nonlinearity is large.

The preparation of coherent population-trapped states leading to the formation of a large atomic coherence has been used by the group in Stanford to produce very efficient nonlinear frequency conversion.[120] A Λ scheme in ^{208}Pb was used with two strong lasers (coupling at 406 nm and probe at 283 nm) introduced into the sample; these created a near-maximal coherence between the |1> and |2> states (see Fig. 11). The phase-coherent atoms formed acted as a local oscillator that mixed with a third laser field at 425 nm (1112 cm^{-1} off resonance). This generated a new field at 293 nm with an exceptionally high conversion efficiency of ~40 percent, as was inferred from the portion of energy from each beam known to be avail-

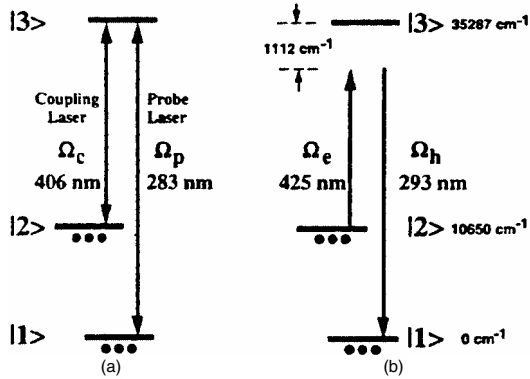

FIGURE 11 Nonlinear optics at maximal atomic coherence in a Pb vapor: (*a*) a large atomic coherence, ρ_{12}, was prepared by the probe and coupling lasers (at 283 nm and 406 nm respectively), (*b*) the 425-nm laser mixes with this coherence to generate a sum frequency at 293 nm. (Source: *M. Jain, H. Xia, G.Y. Yin, A.J. Merriam, and S.E. Harris, "Efficient Non-Linear Frequency Conversion with Maximal Atomic Coherence,"* Phys.Rev.Lett. ***77****:4326 [1996].*)

able for frequency mixing. The high conversion efficiency occurs since in this system the preparation of the optimal coherence ρ_{12} means that the nonlinear susceptibility is of the same size as the linear susceptibility. The same scheme was used, this time mixing with a field at 233 nm, to generate a field in the far-UV at 186 nm. In this case the nonresonant detuning from the fourth state in Pb was ~40cm^{-1} and near-unity conversion efficiencies were demonstrated.[138]

The Pb system was recently the subject of a proposal for a broad-band, high-efficiency, optical parametric oscillator (OPO).[139,140] In this case, optimal coherence between |1> and |2> was created in the same fashion as discussed in Ref. 120. This coherence then acts as the local oscillator in an optical parametric down-conversion scheme generating signal and idler waves in the IR to far-IR. In this system the nonlinear and linear responses of the medium were calculated to be of the same order and high conversion efficiencies up to 10 percent were predicted for the middle of the tuning range. Furthermore the device was predicted to be able to generate fields over the entire spectrum from IR out to almost DC fields.

Atomic coherence in solid hydrogen has recently been used to eliminate phase-mismatch in a Stokes or anti-Stokes stimulated Raman frequency-conversion scheme.[92] In this scheme, the hydrogen molecule electronic ground state $v = 0$ and $v = 1$ vibrational states form the lower states of a Raman scheme, and since the |1> -|2> dephasing rate is very small in appropriately prepared samples of solid hydrogen, interference can occur that causes the dispersion to become negligible. Because of the removal of the usual phase mismatch, efficient operation of this frequency conversion scheme over a broad range of frequencies (infrared to vacuum UV) has been predicted.

Another recent prediction is of broadband spectral generation associated with strong-field refractive index control.[141] In this case a pair of lasers slightly detuned from Raman resonance are used to establish adiabatically a superposition of two molecular states. This superposition then mixes with the applied fields to form a broad spectrum of sidebands. Applying this idea to a molecular system has recently been modeled,[142,143] and the self-phasing of the broad spectrum of sidebands has been predicted to lead to the generation of subfemtosecond pulses.

23.14 NONLINEAR OPTICS AT THE FEW PHOTON LEVEL

As we have noted, one of the most remarkable features of EIT is that the nonlinear susceptibility undergoes constructive interference while the linear susceptibility undergoes destructive interference. In a system without inhomogeneous broadening, perfect transparency can be induced with $\Omega_C \ll \Gamma_3$, so that the medium becomes nonabsorbing. Due to the small size of Ω_C relative to Γ_3 the nonlinear susceptibility will, because of the constructive interference, have a value essentially identical to that of the unmodified resonant atomic system. Since atomic resonances are generally much narrower than those of a solid-state system, the magnitudes of the nonlinearity in this case can be many orders of magnitude larger than that of any solid-state system. For instance, a very large nonlinear refractive index was reported by Hau et al.[9] for EIT in an ultracold Na vapor. They measured a value for the nonlinear refractive index that was 0.18 cm^{2}W^{-1}; this was 10^6 times larger than that measured for cold Cs atoms in a non-EIT system,[144] which itself was much greater than the nonlinear refractive index in a solid-state system. For comparison, the largest nonlinear refractive indices of solid-state materials are $< 10^{-12}$ cm^{2}W^{-1}.[145]

An important class of nonlinearity in this regime is the Kerr-type nonlinearity. This can be understood from examination of Fig. 10. If fields at frequencies ω_1, ω_2, and ω_4 are considered, the Kerr-type nonlinearity describes the coupling between the fields at ω_2 and ω_4. The detuning between ω_4 and state |4>, Δ', is generally smaller than Δ. The field at ω_4 causes a cross-modulation, via $\mathrm{Re}\chi^{(3)}$, with the field at ω_2. This effect was recently predicted to lead to a giant Kerr nonlinearity if ω_1 is of moderate strength viable even using extremely low-power laser fields at ω_2 and ω_4.[146] In the analysis of Ref. 146, values of $\mathrm{Re}\chi^{(3)}$ of 3×10^{-6} m^{2}V^{-2} are found.

These are large enough to give rise to the possibility of imposing measurable cross-phase modulations between fields containing only a few photons.

In the experiments of Hau et al.[9] under the same conditions where ultraslow light pulse propagation was measured, a large nonlinearity was deduced. This was extrapolated from the measurement of the AC Stark shift of the transparency minimum due to the interaction between the field at ω_1 and state |4>. This interaction is equivalent to that of the Kerr nonlinearity discussed in Ref. 146 with the field at ω_1 assuming also the role of the additional field (previously $Z\omega_4$). The connection between the large nonlinearity and the ultraslow light propagation condition has been discussed by several authors.[147,122] In the case of the experiments discussed here, the connection is seen clearly to arise through the AC Stark-shift of the steep dispersion curve responsible for ultralow group velocities. For even very modest fields at ω_1, large changes in the absolute value of the dispersion are obtained, which result in significant phase-shifts being imparted on the probe field by itself. Similarly, in the ultraslow group velocity experiments in a Doppler-free Rb scheme,[122] very high nonlinearities are evidenced by the highly efficient (near-unity) four-wave mixing that was observed. These authors also, therefore, highlight the strong connection between ultraslow group velocities and ultralarge nonlinearity.

A number of treatments have been carried out that demonstrate that the huge nonlinearities available in these schemes are large enough to mediate significant interaction between pairs of photons. There are important implications if a single photon can cause a measurable modification to another single photon (for example by a strong cross-phase modulation). For instance, applications are proposed for quantum nondemolition (QND) measurements and for quantum information processing where the strong mutual interactions can be utilized to generate entangled pairs of photons that form the basis of quantum logic gates. Discussions of this topic include an analysis of frequency mixing and nonlinear phase shifts at the few photon level,[147] techniques for generating squeezed light at very low input powers,[148] photon switching,[149] and photon blockade within an atom-cavity system.[150] These ideas are currently stimulating much further experimental and theoretical work.

23.15 FURTHER READING

E. Arimondo, "Coherent Population Trapping in Laser Spectroscopy," *Progress in Optics* **35**: (1996).

S.E. Harris, "Electromagnetically Induced Transparency" *Physics Today* 36 (June 1997).

O. Kocharovskaya, "Amplification and Lasing without Inversion," *Physics Reports* **219**:175 (1992).

M. Sargent III, M.O. Scully, and W.E. Lamb, Jr., *Laser Physics,* Addison-Wesley, Reading, Massachusetts, 1974.

M.O. Scully, "From Lasers and Masers to Phaseonium and Phasers," *Physics Reports* **219**:191 (1992).

B.W. Shore, "Counter Intuitive Physics," *Contemp. Physics* **36**:15 (1995).

B.W. Shore, "Theory of Coherent Atomic Excitation," John Wiley & Sons, New York, 1990.

M.O. Scully and M. Suhail Zubairy, *Quantum Optics,* Cambridge University Press, 1997.

23.16 REFERENCES

1. U. Fano, "Effects of Configuration Interaction on Intensities and Phase-Shifts," *Phys.Rev.* **124**:1866 (1961).
2. R.B. Madden and K. Codling, "Two-Electron Excitation States in Helium," *Astrophys. J.* **141**:364 (1965).
3. K. Maschke, P. Thomas, and E.O. Göbel, "Fano Interference in Type-II Semiconductor Quantum-Well Structures," *Phys.Rev.Lett.* **67**:2646 (1991).

4. S.E. Harris, "Electromagnetically Induced Transparency," *Physics Today* **50**:36 (1997).
5. S.E. Harris, J.E. Field, and A. Imamoglu, "Non-Linear Optical Processes Using Electromagnetically Induced Transparency," *Phys.Rev.Lett.* **64**:1107 (1990).
6. M.O. Scully, "From Lasers and Masers to Phaseonium and Phasers," *Physics Reports* **219**:191 (1992).
7. M.O. Scully, "Enhancement of the Index of Refraction via Quantum Coherence," *Phys.Rev.Lett.* **67**:1855 (1991).
8. B.W. Shore, *Theory of Coherent Atomic Excitation* (Volumes I and II), John Wiley & Sons, New York, 1990.
9. L.V. Hau, S.E. Harris, Z. Dutton, and C.H. Behroozi, "Light Speed Reduction to 17 Metres per Second in an Ultra-Cold Atomic Gas," *Nature* **397**:594 (1999).
10. O. Kocharovskaya and Y.I. Khanin, "Coherent Amplification of an Ultrashort Pulse in a Three Level Medium without Population Inversion," *JETP Lett.* **48**:630 (1988).
11. M.O. Scully, S.Y. Zhu, and A. Gavrielides, "Degenerate Quantum-Beat Laser: Lasing without Inversion and Inversion without Lasing," *Phys.Rev.Lett.* **62**:2813 (1989).
12. V.G. Arkhipkin and Y.I. Heller, "Radiation Amplification without Population Inversion at Transitions to Autoionising States," *Phy.Lett.* **98A**:12 (1983).
13. S.E. Harris, "Lasers without Inversion: Interference of a Lifetime Broadened Resonance," *Phys.Rev.Lett.* **62**:1033 (1989).
14. A. Imamoglu and S.E. Harris, "Lasers without Inversion: Interference of Dressed Lifetime-broadened states," *Opt.Lett.* **14**:1344 (1989).
15. E.E. Fill, M.O. Scully, and S.-Y. Zhu, "Lasing without Inversion via the Lambda Quantum-Beat Laser in the Collision Dominated Regime," *Opt.Commun.* **77**:36 (1990).
16. A.S. Zibrov, M.D. Lukin, D.E. Nikonov, L. Hollberg, M.O. Scully, V.L. Velichansky, and H.G. Robinson, "Experimental Observation of Laser Oscillation without Population Inversion via Quantum Interference in Rb," *Phys.Rev.Lett.* **75**:1499 (1995).
17. G.G. Padmabandu, G.R. Welch, I.N. Shubin, E.S. Fry, D.E. Nikonov, M.D. Lukin, and M.O. Scully, "Laser Oscillation without Population Inversion in a Sodium Atomic Beam," *Phys.Rev.Lett.* **76**:2053 (1996).
18. O. Kocharovskaya, "Amplification and Lasing without Inversion," *Physics Reports* **219**:175 (1992).
19. P. Mandel, "Lasing without Inversion: A Useful Concept?" *Contemp.Physics* **34**:235 (1993).
20. D.S. Lee and K.J. Malloy, "Analysis of Reduced Interband Absorption Mechanisms in Semiconductor Quantum Wells," *I.E.E.E. Journal of Quantum Electronics* **30**:85 (1994).
21. A. Imamoglu and R.J. Ram, "Semiconductor Lasers without Population Inversion," *Optics Letters* **19**:1744 (1994).
22. B.J. Dalton and P.L. Knight, *Laser Physics, Lecture Notes in Physics,* Vol. 182, J.D. Harvey and D.F. Walls (eds.), Springer-Verlag, Berlin, 1983.
23. H.I. Yoo and J.H. Eberly, "Dynamical Theory of an Atom with Two or Three Levels Interacting with Quantized Cavity Fields," *Physics Reports* **118**:239 (1985).
24. J.H. Eberly, "Transmission of Dressed Fields in Three-Level Media," *Quantum.Semiclass.Opt.* **7**:373 (1995).
25. E. Arimondo, "Coherent Population Trapping in Laser Spectroscopy," *Progress in Optics* **35**: ed. E.Wolf, Elsevier Science B.V (1996).
26. P.L. Knight, "Laser Induced Continuum Structure," *Comm.At.Mol.Phys.* **15**:193 (1984).
27. P.L. Knight, M.A. Lauder, and B.J. Dalton, "Laser Induced Continuum Structure," *Physics Reports* **190**:1 (1990).
28. S.H. Autler and C.H. Townes, "Stark Effect in Rapidly Varying Fields," *Phys.Rev.* **100**:703 (1955).
29. I.D. Abella, N.A. Kurnit, and S.R. Hartmann, "Photon Echoes," *Phys.Rev.* **141**:391 (1966).
30. B.R. Mollow, "Power Spectrum of Light Scattered by 2-Level Systems," *Phys.Rev.* **188**:1969 (1969).
31. B.R. Mollow, "Stimulated Emission and Absorption Near Resonance for Driven Systems," *Phys.Rev.A.* **5**:2217 (1972).
32. P.L. Knight and P.W. Miloni, "The Rabi Frequency in Optical Spectra," *Physics Reports* **66**:21 (1980).

33. L. Allen and J.H. Eberly, *Optical Resonance and 2-Level Atoms,* Dover, New York, 1987.
34. G. Alzetta, A. Gozzini, L. Moi, and G. Oriols, "An Experimental Method for the Observation of R.F. Transitions and Laser Beat Resonances in Orientated Na Vapour," *Nuovo Cimento B* **36**:5 (1976).
35. E. Arimondo and G. Orriols, "Nonabsorbing Atomic Coherences by Coherent Two-Photon Transitions in a Three-Level Optical Pumping," *Lett.Nuovo.Cimento* **17**:333 (1976).
36. G. Alzetta, L. Moi, and G. Orriols, "Nonabsorption Hyperfine Resonances in a Sodium Vapour Irradiated with a Multimode Dye Laser," *Nuovo.Comento B* **52**:209 (1979).
37. H.R. Gray, R.M. Whitley, and C.R. Stroud, "Coherent Trapping of Atomic Populations," *Optics.Letters* **3**:218 (1978).
38. J. Oreg, F.T. Hioe, and J.H. Eberly, "Adiabatic Following in Multilevel Systems," *Phys.Rev. A* **29**:690 (1984).
39. U. Gaubatz, P. Rudecki, S. Schieman, and K. Bergman, "Population Transfer Between Molecular Vibrational Levels by Stimulated Raman-Scattering with Partially Overlapping Laser Fields: A New Concept and Experimental Results," *J.Chem.Phys.* **92**:5363 (1990).
40. N. Dam, L. Oudejans, and J. Reuss, "Relaxation Rates of Ethylene Obtained from their Effect on Coherent Transients," *Chem.Phys.* **140**:217 (1990).
41. A. Aspect, E. Arimondo, R. Kaiser, N. Vansteenkiste, and C. Cohen-Tannoudji, "Laser Cooling Below the One-Photon Recoil Energy by Velocity-Selective Coherent Population Trapping," *Phys.Rev.Lett.* **61**:826 (1988).
42. F. Bardou, B. Saubamea, J. Lawall, K. Shimizu, O. Emile, C. Westbrook, A. Aspect, and C. Cohen-Tannoudji, "Sub-Recoil Laser Cooling with Pre-Cooled Atoms," *Comptes Rendus de Acad.Sci.Paris,* Serie II, **318**:877 (1994).
43. M.R. Doery, M.T. Widmer, M.J. Bellanca, W.F. Buell, T.H. Bergemann, H. Metcalf, and E.J.D. Vrenbregt, "Population Accumulation in Dark States and Sub-Recoil Laser Cooling," *Phys.Rev.A* **52**:2295 (1995).
44. R.M. Whitley and C.R. Stroud, Jr., "Double Optical Resonance," *Phys.Rev.A* **14**:1498 (1976).
45. P.M. Radmore and P.L. Knight, "Population Trapping and Dispersion in a Three-Level System," *J.Phys.B* **15**:561 (1982).
46. B.W. Shore, "Counter Intuitive Physics," *Contemp.Physics* **36**:15 (1995).
47. M.O. Scully and M. Suhail Zubairy, *Quantum Optics,* Cambridge University Press, Cambridge, 1997.
48. B. Lounis. and C. Cohen-Tannoudji, "Coherent Population Trapping and Fano Profiles" *J.Phys.II* **2**:579 (1992).
49. S.E. Harris and J.J. Macklin, "Lasers without Inversion: Single-Atom Transient Response" *Phys. Rev. A* **40**:4135 (1989).
50. J.L. Cohen and P.R. Berman, "Amplification without Inversion: Understanding Probability Amplitudes, Quantum Interferences and Feynman Rules in a Strongly Driven System," *Phys.Rev.A* **55**:3900 (1997).
51. D. ter Haar, "Theory and Application of the Density Matrix," *Rep.Prog.Phys.* **24**:304 (1961).
52. M. Sargent III, M.O. Scully, and W.E. Lamb, Jr., *Laser Physics* Addison-Wesley, Reading, Massachusetts, 1974.
53. L.R. Wilcox and W.E. Lamb, Jr., "Fine Structure of Short-Lived States of Hydrogen by a Microwave-Optical Method. II," *Phys.Rev.* **119**:1915 (1960).
54. H.R. Schlossberg and A. Javan, "Saturation Behaviour of a Doppler-Broadened Transition Involving Levels with Closely Spaced Structure," *Phys.Rev.* **150**:267 (1966).
55. T. Hänsch and P. Toschek, "Theory of Three-Level Gas Laser Amplifier," *Z.Physik* **236**:213 (1970).
56. C. Cohen-Tannoudji, B. Zambon, and E. Arimondo, "Quantum-Jump Approach to Dissipative Processes: Application to Amplification without Inversion," *J.Opt.Soc.Am.B* **10**:2107 (1993).
57. Y.-q. Li., and M. Xiao, "Transient Properties of an Electromagnetically Induced Transparency in Three-Level Atoms," *Opt.Lett.* **20**:1489 (1995).
58. S.E. Harris, "Electromagnetically Induced Transparency with Matched Pulses," *Phys.Rev.Lett.* **72**:552 (1993).

59. S.E. Harris, "Normal-Modes for Electromagnetically Induced Transparency," *Phys.Rev.Lett.* **72**:52 (1994).
60. J.H. Eberly, M.L. Pons, and H.R. Haq, "Dressed-Field Pulses in an Absorbing Medium," *Phys.Rev.Lett.* **72**:56 (1994).
61. S.E. Harris and Z.-F. Luo, "Preparation Energy for Electromagnetically Induced Transparency," *Phys.Rev.A* **52**:928 (1995).
62. J.E. Field, "Vacuum-Rabi-Splitting-Induced Transparency," *Phys.Rev.A* **47**:5064 (1993).
63. J.E. Field and A. Imamoglu, "Spontaneous Emission into an Electromagnetically Induced Transparency," *Phys.Rev.A* **48**:2486 (1993).
64. M. Fleischhauer, "Correlation of High-Frequency Phase Fluctuations in Electromagnetically Induced Transparency," *Phys.Rev.Lett.* **72**:989 (1994).
65. S.E. Harris., J.E. Field, and A. Kasapi, "Dispersive Properties of Electromagnetically Induced Transparency," *Phys.Rev.A* **46**:R29 (1992).
66. M.O. Scully and S.-Y. Zhu, "Ultra-Large Index of Refraction via Quantum Interference," *Opt.Commun.* **87:** 134 (1992).
67. M. Fleischhauer, C.H. Keitel, M.O. Scully, C. Su, "Lasing without Inversion and Enhancement of the Index of Refraction via Interference of Incoherent Pump Processes," *Opt.Commun.* **87**:109 (1992).
68. A.D. Wilson-Gordon and H. Friedman, "Enhanced Index of Refraction: A Comparison Between Two- and Three-Level Systems," *Opt.Commun.* **94**:238 (1992).
69. M. Fleischhauer, C.H. Keitel, M.O. Scully, C. Su, B.T. Ulrich, and S.-Y. Zhu, "Resonantly Enhanced Refractive Index without Absorption via Atomic Coherence," *Phys.Rev.A* **46**:1468 (1992).
70. U. Rathe, M. Fleischhauer, S.-Y. Zhu, T.W. Hänsch, and M.O. Scully, "Non-Linear Theory of Index Enhancement via Quantum Coherence and Interference," *Phys.Rev.A* **47**:4994 (1993).
71. A.S. Manka, J.P. Dowling, C.M. Bowden, and M. Fleischhauer, "Piezophotonic Switching Due to Local-Field Effects in a Coherently Prepared Medium of 3-Level Atoms," *Phys.Rev.Lett.* **73**:1789 (1994).
72. S.E. Harris, "Refractive-Index Control with Strong Fields," *Opt.Lett.* **19**:2018 (1994).
73. D.J. Fulton, R.R. Moseley, S. Shepherd, B.D. Sinclair, and M.H. Dunn, "Effects of Zeeman Splitting on Electromagnetically Induced Transparency," *Opt.Commun.* **116**:231 (1995).
74. G.Z. Zhang, M. Kasuragawa, K. Hakuta, R.I. Thompson, and B.P. Stoicheff, "Sum-Frequency Generation Using Strong-Field Coupling and Induced Transparency in Atomic Hydrogen," *Phys.Rev.A* **52**:1584 (1995).
75. R.R. Moseley, B.D. Sinclair, and M.H. Dunn, "Local Field Effects in the Three-Level Atom," *Opt.Comm.* **108**:247 (1994).
76. J.P. Dowling and C.M. Bowden, "Near Dipole-Dipole Effects in Lasing without Inversion: An Enhancement of Gain and Absorptionless Index of Refraction," *Phys.Rev.Lett.* **70**:1421 (1993).
77. G.S. Agarwal, "Exact Solution for the Influence of Laser Temporal Fluctuations on Resonance Fluorescence," *Phys.Rev.Lett.* **37**:1383 (1976).
78. S. Swain, "Theory of Atomic Processes in Strong Resonant Electromagnetic Fields," *Adv.At.Mol.Phys.* **16**:159 (1980).
79. B.J. Dalton and P.L. Knight, "The Effect of Laser Field Fluctuations on Coherent Population Trapping," *J.Phys.B* **15**:3997 (1982).
80. P.A. Lakshmi and S. Swain, "Effects of Laser Linewidths on Nonlinear Optical Processes Exploiting Electromagnetically Induced Transparency," *J.Mod.Opt.* **38**:2031 (1991).
81. J.C. Petch, C.H. Keitel, P.L. Knight, and J.P. Marangos, "Role of Electromagnetically Induced Transparency in Resonant Four-Wave Mixing Schemes," *Phys.Rev.A* **53**:543 (1996).
82. J.Y. Gea-Banacloche, Y.-Q. Li, S.-Z. Jin, and M. Xiao, "Electromagnetically Induced Transparency in Ladder-Type Inhomogeneously Broadened Media—Theory and Experiment," *Phys.Rev.A* **51**:576 (1995).
83. S. Shepherd, D.J. Fulton, and M.H. Dunn, "Wavelength Dependence of Coherently Induced Transparency in a Doppler-Broadened Cascade Medium," *Phys.Rev.A* **54**:5394 (1996).

84. M. Xiao, Y.-Q. Li, and J. Gea-Banacloche, "Measurements of Dispersive Properties of Electromagnetically Induced Transparency in Rubidium Atoms," *Phys.Rev.Lett.* **74**:666 (1995).
85. R.R. Moseley, S. Shepherd, D.J. Fulton, B.D. Sinclair, and M.H. Dunn, "Spatial Consequences of Electromagnetically Induced Transparency: Observation of Electromagnetically Induced Focusing," *Phys.Rev.Lett.* **74**:670 (1995).
86. M. Misunga, T. Mukai, K. Watanabe, and T. Mukai, "Dressed-Atom Spectroscopy of Cold Cs Atoms," *J.Opt.Soc.B* **13**:2696 (1996).
87. S.A. Hopkins, E. Usadi, H.X. Chen, and A.V. Durrant, "Electromagnetically Induced Transparency of Laser-Cooled Rubidium Atoms in Three-Level Λ Type Systems," *Optics.Commun.* **134**:185 (1997).
88. Y. Zhao, C. Wu, B.S. Ham, M.K. Kim, and E. Awad, "Microwave Induced Transparency in Ruby," *PRL* **79**:64 (1997).
89. B.S. Ham, P.R. Hemmer, and M.S. Shahiar, "Efficient Electromagnetically Induced Transparency in Rare-Earth Crystals," *Opt.Commum.* **144**:227 (1997).
90. B.S. Ham, S.M. Shahriar, and P.R. Hemmer, "Electromagnetically Induced Transparency over Spectral Hole-Burning Temperature in a Rare-Earth-Doped Solid," *JOSA B* **16**:801 (1999).
91. G.B. Serapiglia, E. Paspalakis, C. Sirtori, K.L. Vodopyanov, and C.C. Phillips, "Laser-Induced Quantum Coherence in a Semiconductor Quantum Well," *Phys.Rev.Lett.* **84**:1019 (2000).
92. K. Hakuta, M. Suzuki, M. Katsuragawa, and J.Z. Li, "Self-Induced Phase Matching in Parametric Anti-Stokes Stimulated Raman Scattering," *Phys.Rev.Lett.* **79**:209 (1997).
93. K.J. Boller, A. Imamoglu, and S.E. Harris, "Observation of Electromagnetically Induced Transparency," *Phys.Rev.Lett.* **66**:2593 (1991).
94. J.E. Field, K.H. Hahn, and S.E. Harris, "Observation of Electromagnetically Induced Transparency in Collisionally Broadened Lead Vapor," *Phys.Rev.Lett.* **67**:3062 (1991).
95. A. Kasapi, "Enhanced Isotope Discrimination Using Electromagnetically Induced Transparency," *Phys.Rev.Lett.* **77**:1035 (1996).
96. Hui Xia, A.J. Merriam, S.J. Sharpe, G.Y. Yin, and S.E. Harris, "Electromagnetically Induced Transparency with Spectator Momenta," *PRA* **59**:R3190 (1999).
97. Hui Xia, S.J. Sharpe, A.J. Merriam, and S.E. Harris, "Electromagnetically Induced Transparency in Atoms with Hyperfine Structure," *PRA* **56**:R3362 (1998).
98. Y.-Q. Li and M. Xiao, "Electromagnetically Induced Transparency in a Three-Level Λ System in Rubidium Atoms," *Phys.Rev.A* **51**:R2703 (1995).
99. Y.-Q. Li and M. Xiao, "Observation of Quantum Interference Between the Dressed States in an Electromagnetically Induced Transparency," *Phys.Rev.A* **51**:4959 (1995).
100. R.R. Moseley, S. Shepherd, D.J. Fulton, B.D. Sinclair, and M.H. Dunn, "Electromagnetically Induced Focusing," *Phys.Rev.A* **53**:408 (1996).
101. S. Wielandy and A. L. Gaeta, "Investigation of Electromagnetically Induced Transparency in the Strong Probe Regime," *Phys.Rev.A* **58**:2500 (1998).
102. A.V. Durrant, H.X. Chen, S.A. Hopkins, and J.A. Vaccaro, "Zeeman-Coherence-Induced Transparency and Gain Without Inversion in Laser-Cooled Rubidium," *Optics.Commun.* **151**:136 (1998).
103. W. Ketterle, K.B. Davis, M.A. Joffe, A. Martin, and D.E. Pritchard, "High Densities of Cold Atoms in a Dark Spontaneous-Force Optical Trap," *Phys.Rev.Lett.* **77**:2253 (1993).
104. T. van der Veldt, J.-F. Roch, P. Grelu, and P. Grangier, "Nonlinear Absorption and Dispersion of Cold Rb-87 Atoms," *Opt.Commun.* **137**:420 (1997).
105. H.X. Chen, A.V. Durran, J.P. Marangos, and J.A. Vaccaro, "Observation of Transient Electromagnetically Induced Transparency in a Rubidium Lambda System," *Phys.Rev.A* **58**:1545 (1998).
106. S. Scandolo and F. Bassani, "Non-Linear Sum Rules: The Three-Level and Anharmonic-Oscillator Modes," *Phys.Rev. B* **45**:13257 (1992).
107. F.S. Cataliotti, C. Fort, T.W. Hänsch, M. Ingusco, and M. Prevedelli, "Electromagnetically Induced Transparency in Cold Free Atoms: Test of a Sum Rule for Non-Linear Optics," *Phys.Rev.A* **56**:2221 (1997).

108. J. Gao, C. Guo, X. Guo, G. Jin, P. Wang, J. Zhao, H. Zhang, Y. Jiang, D. Wang, and D. Jiang, "Observation of Light Amplification without Population Inversion," *Optics.Commun.* **93**:323 (1992).
109. J. Gao, H.Z. Zhang, H.F. Cui, X.Z. Guo, Y. Jiang, Q.W. Wang, G.X. Jin, and J.S. Li, "Inversionless Amplification in Sodium," *Optics.Commun.* **110**:590 (1994).
110. J.A. Kleinfeld and A.D. Streater, "Observation of Gain Due to Coherence Effects in Potassium-Helium Mixture," *Phys.Rev.A* **49**:R4301 (1994).
111. E.S. Fry, X. Li, D. Nikonov, G.G. Padmabandu, M.O. Scully, A.V. Smith, F.K. Tittel, C. Wang, S.R. Wilkinson, and S.-Y. Zhu, "Atomic Coherence Effects within the Sodium D1 Line: Lasing Without Inversion via Population Trapping," *Phys.Rev.Lett.* **70**:3235 (1993).
112. A. Nottelman, C. Peters, and W. Lange, "Inversionless Amplification of Picosecond Pulses Due to Zeeman Coherence," *Phys.Rev.Lett.* **70**:1783 (1993).
113. W.E. van der Veer, R.J.J. van Dienst, A. Dönselmann, and H.B. van Linden van den Huevell, "Experimental Demonstration of Light Amplification without Population Inversion," *Phys.Rev.Lett.* **70**:3243 (1993).
114. C. Peters and W. Lang, "Laser Action Below Threshold Inversion Due to Coherent Population Trapping," *Applied.Phys.B* **62**:221 (1996).
115. A.S. Zibrov, M.D. Lukin, L. Hollberg, D.E. Nikonov, M.O. Scully, H.G. Robinson, and V.L. Velichansky, "Experimental Demonstration of Enhanced Index of Refraction via Quantum Coherence in Rb," *Phys.Rev.Lett.* **76**:3935 (1996).
116. M. Fleischhauer and M.O. Scully, "Quantum Sensitivity Limits of an Optical Magnetometer Based on Phase Coherence," *Phys.Rev.A* **49**:1973 (1994).
117. A. Kasapi, M. Jain, G.Y. Yin, and S.E. Harris, "Electromagnetically Induced Transparency: Propagation Dynamics," *Phys.Rev.Lett.* **74**:2447 (1995).
118. A. Kasapi, G.Y. Yin, M. Jain, and S.E. Harris, "Measurement of Lorentzian Linewidths by Pulse-Propagation Delay," *Phys.Rev.A* **53**:4547 (1996).
119. M. Jain, A.J. Merriam, A. Kasapi, G.Y. Yin, and S.E. Harris, "Elimination of Optical Self-Focusing by Population Trapping," *Phys.Rev.Lett.* **75**:4385 (1995).
120. M. Jain, H. Xia, G.Y. Yin, A.J. Merriam, and S.E. Harris, "Efficient Non-Linear Frequency Conversion with Maximal Atomic Coherence," *Phys.Rev.Lett.* **77**:4326 (1996).
121. O. Schmidt, R. Wynands, Z. Hussein, and D. Meschede, "Steep Dispersion and Group Velocity Dispersion Below c/3000 in Coherent Population Trapping," *Phys.Rev. A* **53**:R27 (1996).
122. M.M. Kash, V.A. Sautenkov, A.S. Zibrov, L. Hollberg, G.R. Welch, M.D. Lukin, Y. Rostovtsev, E.S. Fry, and M.O. Scully, "Ultraslow Group Velocity and Enhanced Non-Linear Optical Effects in a Coherently Driven Hot Atomic Gas," *PRL* **82**:5229 (1999).
123. D. Budker, D.F. Kimball, S.M. Rochester, and V.V. Yaschuk, "Nonlinear Magneto-Optics and Reduced Velocity of Light in Atomic Vapour with Slow Ground State Relaxation," *PRL* **83**:1767 (1999).
124. S.P. Tewari and G.S. Agarwal, "Control of Phase-Matching and Nonlinear Generation in Dense Media by Resonant Fields," *Phys.Rev.Lett.* **56**:1811 (1986).
125. G.S. Agarwal and S.P. Tewari, "Large Enhancements in Non-Linear Generation by External Electromagnetic Fields," *Phys.Rev.Lett.* **70**:1417 (1993).
126. M. Jain, G.Y. Yin, J.E. Field, and S.E. Harris, "Observation of Electromagnetically Induced Phase Matching," *Optics.Letters* **18**:998 (1993).
127. K. Hakuta, L. Marmet, and B.P. Stoicheff, "Electric-Field-Induced Second-Harmonic Generation with Reduced Absorption," *Phys.Rev.Lett.* **66**:596 (1991).
128. K. Hakuta, L. Marmet, and B.P. Stoicheff, "Nonlinear Optical Generation with Reduced Absorption Using Electric-Field Coupling in Atomic Hydrogen," *Phys.Rev.A* **45**:5152 (1992).
129. G.Z. Zhang, K. Hakuta, and B.P. Stoicheff, "Nonlinear Optical Generation Using Electromagnetically Induced Transparency in Hydrogen," *Phys.Rev.Lett.* **71**:3099 (1993).
130. R.S.D. Sihombing, M. Katsuragawa, G.Z. Zhang, and K. Hakuta, "Quantum Interference in Resonant Multi-Photon Ionisation Processes for Strongly Coupled Atomic Systems," *Phys.Rev.A.* **54**: 1551 (1996).

131. C. Dorman, I. Kucukkara, and J.P. Marangos, "Measurement of High Conversion Efficiency to 123.6nm Radiation in a Four-Wave Mixing Scheme Enhanced by Electromagnetically Induced transparency," Phys.Rev A **61**:013802-1 (2000).
132. L. Deng, W.R. Garret, M.G. Payne, and D.Z. Lee, "Observation of a Critical Concentration in Laser-Induced Transparency and Multi-Photon Excitation and Ionisation in Rubidium," *Optics.Letters* **21**:928 (1996).
133. Y.-Q. Li. and M. Xiao, "Enhancement of Non-Degenerate Four-Wave-Mixing Based on Electromagnetically Induced Transparency in Rubidium Atoms," *Optics.Letters* **21**:1064 (1996).
134. P.R. Hemmer, D.P. Katz, J. Donoghue, M. Cronin-Golomb, M.S. Shahriar, and P. Kumar, "Efficient Low-Intensity Optical Phase Conjugation Based on Coherent Population Trapping in Sodium," *Optics.Letters* **20**:982 (1995).
135. T.T. Grove, M.S. Shahriar, P.R. Hemmer, P. Kumar, V.S. Sudarshanam, and M. Cronin-Golomb, "Distortion-Free Gain and Noise Correlation in Sodium Vapor with Four-Wave Mixing and Coherent Population Trapping," *Optics.Letters* **22**:769 (1997).
136. S. Babin, U. Hinze, E. Tiemann, and B. Wellegehausen, "Continuous Resonant Four-Wave-Mixing in Double-Λ Level Configurations of Na_2," *Opt.Letters* **21**:1186 (1996).
137. A. Apolonskii, S. Balischev, U. Hinze, E. Tiemann, and B. Wellegehausen, "Continuous Frequency Up-Conversion in a Double-Λ Scheme in Na_2," *Appl.Phys B* **64**:435 (1997).
138. A.J. Merriam, S.J. Sharpe, H. Xia, D. Manuszak, G.Y. Yin, and S.E. Harris, "Efficient Gas-Phase Generation of Coherent Vacuum Ultra-Violet Radiation," *Optics.Letters* **24**:625 (1999).
139. S.E. Harris and M. Jain, "Optical Parametric Oscillators Pumped by Population-Trapped Atoms," *Optics.Letters* **22**:636 (1997).
140. S.E. Harris, G.Y. Yin, M. Jain, H. Xia, and A.J. Merriam, "Nonlinear Optics at Maximum Coherence," *Philos.Trans.R.Soc.London* (Ser A. Mathematical, Physical and Engineering Sciences) **355**:2291 (1997).
141. S.E. Harris and A.V. Sokolov, "Broadband Spectral Generation with Refractive Index Control," *Phys.Rev.A* **55**:R4019 (1997).
142. S.E. Harris and A.V. Sokolov, "Sub-Femtosecond Pulse Generation by Molecular Modulation," *PRL* **81**:2894 (1998).
143. F.E. Kien, J.Q. Liang, M. Katsuragawa, K. Ohtsuki, K. Hakuta, and A.V. Sokolov, "Subfemtosecond Pulse Generation with Molecular Coherence Control in Stimulated Raman Scattering," *Phys.Rev A* **60**:1562 (1999).
144. A. Lambrecht, J.M. Courty, S. Reynaud, and E. Giacobino, "Cold Atoms: A New Medium for Quantum Optics," *Apply.Phys.B* **60**:129 (1995).
145. D.N. Nikogosyan, *Properties of Optical and Laser-Related Materials: A Handbook,* John Wiley & Sons, New York, 1997.
146. H. Schmidt and A. Imamoglu, "Giant Kerr Nonlinearities Obtained by Electromagnetically Induced Transparency," *Optics.Letters* **21**:1936 (1996).
147. S.E. Harris and L.V. Hau, "Non-Linear Optics at Low Light Levels," *PRL* **82**:4611 (1999).
148. M.D. Lukin, A.B. Matsko, M. Fleischhauer, and M.O. Scully, "Quantum Noise and Correlations in Resonantly Enhanced Wave-Mixing Based on Atomic Coherence," *PRL* **82**:1847 (1999).
149. S.E. Harris and Y. Yamamoto, "Photon Switching by Quantum Interference," *PRL* **81**:3611 (1998).
150. A. Imamoglu, H. Schmidt, G. Woods, and M. Deutsch, "Strongly Interacting Photons in a Non-Linear Cavity," *PRL* **79**:1467 (1997).

CHAPTER 24
COHERENT OPTICAL TRANSIENTS

P. R. Berman and D. G. Steel
Physics Department
University of Michigan
Ann Arbor, Michigan

24.1 GLOSSARY

$\mathbf{E}(\mathbf{R}, t)$	electric field vector
$E(t)$	electric field amplitude
ω	field frequency
$\phi(t)$	field phase
ω_0	atomic transition frequency
$\overline{\omega}_0$	average atomic transition frequency
δ	atom-field detuning
δ_0	average atom-field detuning
$\Omega_0(t)$	Rabi frequency
$\mathbf{\Omega}(t)$	pseudofield vector
$\Omega(t)$	generalized Rabi frequency
$\mathbf{U}(t)$	Bloch vector
$\rho_{ij}(Z, t)$	density matrix element in a field interaction representation
$\rho_{ij}^T(\mathbf{R}, t)$	density matrix element in "normal" representation
(u, v, w)	elements of Bloch vector
γ	transverse relaxation rate
γ_2	excited-state decay rate or longitudinal relaxation rate
$\mathbf{P}(\mathbf{R}, t)$	polarization vector
$\mathbf{k}$	field propagation vector
$E_S(Z, t)$	complex signal electric field amplitude

This chapter is dedicated to Richard G. Brewer, a pioneer in coherent optical transients, a mentor and a friend.

Copyright 2001 by The McGraw-Hill Companies, Inc. Click Here for Terms of Use.

$P(Z, t)$	complex polarization field amplitude
$\mathcal{N}$	atomic density
L	sample length
μ	dipole moment matrix element
τ, τ_{ref}	pulse durations
θ	pulse area
Δ	difference between local and average transition frequency in a solid
$W_f(\Delta)$	distribution of frequencies in a solid
σ_w	width of $W_f(\Delta)$
$\mathbf{v}$	atomic velocity
u	most probable atomic speed
$W_0(\mathbf{v})$	atomic velocity distribution
$I(L, t)$	signal intensity exiting the sample
T_{21}, T	time interval between pulses
Γ_t	transit time decay rate
$\Gamma_{2,0}, \Gamma_{2,1}$	branching decay rates of the excited state
$\Omega_i^{(s)}(t)$	two-photon Rabi frequency
ω_k	recoil frequency
$\mathbf{P}$	center-of-mass momentum
$E_b(t_1, t_2)$	backscattered electric field amplitude
$J_N(x)$	Bessel function
ξ	one-half of the frequency chirp rate
ω_{RD}	frequency offset between reference and data pulses

24.2 INTRODUCTION

Optical spectroscopy is a traditional method for determining transition frequencies in atoms and molecules. One can classify optical spectroscopy into two broad categories, *continuous-wave* (CW) or stationary spectroscopy and *time-dependent* or transient spectroscopy. In CW spectroscopy, one measures absorption or emission line shapes as a function of the incident frequency of a probe field. The absorption or emission maximum determines the transition frequency, while the width of the line is a measure of relaxation processes affecting the atoms or molecules. It is necessary to model the atom-field interaction to obtain predictions for the line shapes, but, once this is done, it is possible to extract the relevant transition frequencies and relaxation rates from the line shapes. In transient spectroscopy, one can also determine relaxation rates and transition frequencies, but the methodology is quite different. Atomic state populations or coherences between atomic states are excited by pulsed optical fields. Following the excitation, the time-evolution of the atoms is monitored, from which transition frequencies and relaxation rates can be obtained. In certain cases the transient response is studied as a function of incident field frequency or intensity. Whether or not transient or CW spectroscopy offers distinct advantages depends on a number of factors, such as signal to noise and the reliability of lineshape formulas.[1]

In this chapter, we present basic concepts of coherent optical transient spectroscopy,[2–12] along with applications involving atomic vapors or condensed matter systems. Experimental techniques are discussed in Sec. 24.11. As in the case of CW spectroscopy, it will prove useful

to consider both linear and nonlinear interactions of the atoms with the fields. The examples chosen to illustrate the concepts are relatively simple, but it is important to note that sophisticated coherent transient techniques can now be used to probe complex structures, such as liquids and semiconductors. Although we consider ensembles of atoms interacting with the applied fields, current technology allows one to study the transient response of single atoms or molecules.[13]

24.3 OPTICAL BLOCH EQUATIONS

Many of the important features of coherent optical transients can be illustrated by considering the interaction of a radiation field with a two-level atom, with lower state $|1\rangle$ having energy $-\hbar\omega_0/2$ and upper state $|2\rangle$ having energy $\hbar\omega_0/2$. For the moment, the atom is assumed to be fixed at $\mathbf{R} = 0$ and all relaxation processes are neglected. The incident electric field is

$$\mathbf{E}(\mathbf{R} = 0, t) = \tfrac{1}{2}\boldsymbol{\varepsilon}\{E(t)\exp(-i[\omega t - \phi(t)]) + E(t)\exp(i[\omega t - \phi(t)])\} \tag{1}$$

where $E(t)$ is the field amplitude, $\boldsymbol{\varepsilon}$ is the field polarization, $\phi(t)$ is the field phase, and ω is the carrier frequency. The time dependence of $E(t)$ allows one to consider pulses having arbitrary shape while the time dependence of $\phi(t)$ allows one to consider arbitrary frequency *chirps*. It is convenient to expand the atomic state wave function in a field interaction representation as

$$|\psi(t)\rangle = c_1(t)\exp\left\{\frac{i[\omega t - \phi(t)]}{2}\right\}|1\rangle + c_2(t)\exp\left\{\frac{-i[\omega t - \phi(t)]}{2}\right\}|2\rangle \tag{2}$$

The atom-field interaction potential is

$$V(\mathbf{R}, t) = -\boldsymbol{\mu}\cdot\mathbf{E}(\mathbf{R}, t) \tag{3}$$

where $\boldsymbol{\mu}$ is a dipole moment operator. Substituting the state vector Eq. (2) into Schrödinger's equation and neglecting rapidly varying terms (rotating-wave approximation), one finds that the state amplitudes evolve according to

$$i\hbar\frac{d\mathbf{c}}{dt} = \tilde{\mathbf{H}}\mathbf{c} \qquad \tilde{\boldsymbol{H}} = \left(\frac{\hbar}{2}\right)\begin{pmatrix}-\delta(t) & \Omega_0(t)\\ \Omega_0(t) & \delta(t)\end{pmatrix} \tag{4}$$

where $\mathbf{c}$ is a vector having components (c_1, c_2),

$$\delta = \omega_0 - \omega \tag{5}$$

is an atom-field detuning,

$$\Omega_0(t) = -\frac{\mu E(t)}{2\hbar} = -\frac{\mu}{\hbar}\sqrt{\frac{S(t)}{2\varepsilon_0 c}} \tag{6}$$

is a Rabi frequency, $\mu = \langle 1|\boldsymbol{\mu}\cdot\boldsymbol{\varepsilon}|2\rangle = \langle 2|\boldsymbol{\mu}\cdot\boldsymbol{\varepsilon}|1\rangle$ is a dipole moment matrix element, ε_0 is the permittivity of free space, $\mathbf{S}(t)$ is the time-averaged Poynting vector of the field, and

$$\delta(t) = \delta + \frac{d\phi(t)}{dt} \tag{7}$$

is a generalized atom-field detuning. Equation (4) can be solved numerically for arbitrary pulse envelope and phase factors.

Expectation values of physical observables are conveniently expressed in terms of density matrix elements defined by

$$\rho_{ij} = c_i c_j^* \tag{8}$$

which obey equations of motion

$$\begin{aligned}
\dot{\rho}_{11} &= -i\Omega_0(t)\,(\rho_{21} - \rho_{12}) \\
\dot{\rho}_{22} &= i\Omega_0(t)\,(\rho_{21} - \rho_{12}) \\
\dot{\rho}_{12} &= -i\Omega_0(t)\,(\rho_{22} - \rho_{11}) + i\delta(t)\rho_{12} \\
\dot{\rho}_{21} &= i\Omega_0(t)\,(\rho_{22} - \rho_{11}) - i\delta(t)\rho_{21}
\end{aligned} \tag{9}$$

An alternative set of equations in terms of real variables can be obtained if one defines new parameters

$$\begin{aligned}
u &= \rho_{12} + \rho_{21} & \rho_{12} &= \frac{u + iv}{2} \\
v &= i(\rho_{21} - \rho_{12}) & \rho_{21} &= \frac{u - iv}{2} \\
w &= \rho_{22} - \rho_{11} & \rho_{22} &= \frac{m + w}{2} \\
m &= \rho_{11} + \rho_{22} & \rho_{11} &= \frac{m - w}{2}
\end{aligned} \tag{10}$$

which obey the equations of motion

$$\begin{aligned}
\dot{u} &= -\delta(t)v \\
\dot{v} &= \delta(t)u - \Omega_0(t)w \\
\dot{w} &= \Omega_0(t)v \\
\dot{m} &= 0
\end{aligned} \tag{11}$$

The last of these equations reflects the fact that $\rho_{11} + \rho_{22} = 1$, while the first three can be rewritten as

$$\dot{\mathbf{U}} = \boldsymbol{\Omega}(t) \times \mathbf{U} \tag{12}$$

where the *Bloch vector* $\mathbf{U}$ has components (u, v, w) and the *pseudofield vector* $\boldsymbol{\Omega}(t)$ has components $[\Omega_0, 0, \delta(t)]$. An important feature of a density matrix description is that relaxation can be incorporated easily into density matrix equations, but *not* into amplitude equations.

Equations (9) or (11) constitute the *optical Bloch equations* without decay.[8–10,14] The vector $\mathbf{U}$ has unit magnitude and precesses about the pseudofield vector with an instantaneous rate

$$\Omega(t) = \sqrt{[\Omega_0(t)]^2 + [\delta(t)]^2} \tag{13}$$

that is referred to as the *generalized Rabi frequency.* The tip of the Bloch vector traces out a path on the *Bloch sphere.* The component w is the population difference of the two atomic states, while u and v are related to the quadrature components of the atomic polarization (see following discussion).

It is possible to generalize Eqs. (9) and (11) to include relaxation. In the most general situation, each density matrix element can be coupled to all density matrix elements via relax-

ation. For optical transitions, however, it is often the case that the energy separation of levels 1 and 2 is sufficiently large to preclude any relaxational transfer of population from level 1 to level 2, although state $|2\rangle$ can decay to state $|1\rangle$ via spontaneous emission. For the present, we also assume that $\rho_{11} + \rho_{22} = 1$; there is no relaxation outside the two-level subspace. In this limit, relaxation can be included in Eq. (9) by modifying the equations as

$$\dot{\rho}_{11} = -i\Omega_0(t)\,(\rho_{21} - \rho_{12}) + \gamma_2\rho_{22} \tag{14a}$$

$$\dot{\rho}_{22} = i\Omega_0(t)\,(\rho_{21} - \rho_{12}) - \gamma_2\rho_{22} \tag{14b}$$

$$\dot{\rho}_{12} = -i\Omega_0(t)\,(\rho_{22} - \rho_{11}) - \gamma\rho_{12} + i\delta(t)\rho_{12} \tag{14c}$$

$$\dot{\rho}_{21} = i\Omega_0(t)\,(\rho_{22} - \rho_{11}) - \gamma\rho_{21} - i\delta(t)\rho_{21} \tag{14d}$$

where γ_2 is the spontaneous decay rate of level 2, γ is the real part of the decay rate of the coherence ρ_{12}, and the detuning

$$\delta(t) = \delta + \frac{d\phi(t)}{dt} - s \tag{15}$$

is modified to include the imaginary part s of the decay rate of the coherence ρ_{12}. The corresponding equations for the Bloch vector are

$$\begin{aligned} \dot{u} &= -\delta(t)v - \gamma u \\ \dot{v} &= \delta(t)u - \Omega_0(t)w - \gamma v \\ \dot{w} &= \Omega_0(t)v - \gamma_2(w + 1) \\ \dot{m} &= 0 \end{aligned} \tag{16}$$

With the addition of decay, the length of the Bloch vector is no longer conserved.

One can write

$$\gamma = \frac{\gamma_2}{2} + \mathrm{Re}\,(\Gamma_{12}) \qquad s = \mathrm{Im}\,(\Gamma_{12}) \tag{17}$$

where $\gamma_2/2$ is a radiative component and Γ_{12} is a complex decay parameter that could arise, for example, as a result of phase-interrupting collisions with a background gas. The quantity γ_2 is referred to as the *longitudinal relaxation rate.* Moreover, one usually refers to $T_1 = \gamma_2^{-1}$ as the *longitudinal relaxation time* and $T_2 = \gamma^{-1}$ as the *transverse relaxation time.* In the case of purely radiative broadening, $\gamma_2 = 2\gamma$ and $T_1 = T_2/2$.

The optical Bloch equations are easily generalized to include additional levels and additional fields. In particular, for an ensemble of three-level atoms interacting with two radiation fields, new classes of coherent optical transient effects can appear. Moreover, the sensitivity of the coherent transients to the polarization of the applied fields offers an additional degree of selectivity in the detection of the transient signals. Some examples of coherent transient phenomena in three-level and multilevel systems can be found in the references.[11,15–20] Chapter 23 ("Electromagnetically Induced Transparency") contains some interesting phenomena associated with such multilevel systems.

24.4 MAXWELL-BLOCH EQUATIONS

The optical Bloch equations must be coupled to Maxwell's equations to determine in a self-consistent way the modification of the atoms by the fields and the fields by the atoms. To

accomplish this task, we start with Maxwell's equations, setting $\mathbf{D} = \varepsilon_0\mathbf{E} + \mathbf{P}$. The wave equation derived from Maxwell's equations is

$$\nabla^2\mathbf{E} - \nabla(\nabla \cdot \mathbf{E}) = \frac{1}{c^2}\frac{\partial^2\mathbf{E}}{\partial t^2} + \frac{1}{\varepsilon_0 c^2}\frac{\partial^2\mathbf{P}}{\partial t^2} \tag{18}$$

As a result of atom-field interactions, it is assumed that a polarization is created in the medium of the form

$$\mathbf{P}(\mathbf{R}, t) = \tfrac{1}{2}\boldsymbol{\varepsilon}[P(\mathbf{R}, t)\exp i(kZ - \omega t) + P^*(\mathbf{R}, t)\exp -i(kZ - \omega t)] \tag{19}$$

which gives rise to a signal electric field of the form

$$\mathbf{E}_S(\mathbf{R}, t) = \tfrac{1}{2}\boldsymbol{\varepsilon}[E_S(\mathbf{R}, t)\exp i(kZ - \omega t) + E_S^*(\mathbf{R}, t)\exp -i(kZ - \omega t)] \tag{20}$$

The Z axis has been chosen in the direction of $\mathbf{k}$. It is assumed that the complex field amplitudes $P(\mathbf{R}, t)$ and $E_S(\mathbf{R}, t)$ vary slowly in space compared with $\exp(ikZ)$ and slowly in time compared with $\exp(i\omega t)$. To simplify matters further, transverse effects such as self-trapping, self-focusing, diffraction, and ring formation[21–25] are neglected. In other words, we take $P(\mathbf{R}, t)$ and $E_S(\mathbf{R}, t)$ to be functions of Z and t only, choose $\boldsymbol{\varepsilon} \cdot \mathbf{k} = 0$, and drop the $\nabla(\nabla \cdot \mathbf{E})$ term in the wave equation. When Eqs. (19) and (20) are substituted into the wave equation and terms of order $\partial^2 E_S(Z, t)/\partial t^2$, $\partial^2 E_S(Z, t)/\partial Z^2$, $\partial^2 P(Z, t)/\partial t^2$, and $\partial P(Z, t)/\partial t$ are neglected, one finds

$$2ik\left(\frac{\partial}{\partial Z} + \frac{\omega}{kc^2}\frac{\partial}{\partial t}\right)E_S(Z, t) - \left(k^2 - \frac{\omega^2}{c^2}\right)E_S(Z, t) = -\frac{\omega^2}{\varepsilon_0 c^2}P(Z, t) \tag{21}$$

It is important to note that the polarization field acts as the source of the signal field. Consequently, the signal field does *not* satisfy Maxwell's equations in vacuum, implying that there can be cases when $k \neq \omega/c$. For the moment, however, we assume that this *phase-matching* condition is met. Moreover, it is assumed that a quasi–steady state has been reached in which one can neglect the $\partial E_S(Z, t)/\partial t$ in Eq. (21). With these assumptions, Eq. (21) reduces to

$$\frac{\partial E_S(Z, t)}{\partial Z} = \frac{ik}{2\varepsilon_0}P(Z, t) \tag{22}$$

Additional equations would be needed if the applied fields giving rise to the polarization of the medium are themselves modified to any extent by the signal field.

The polarization $P(Z, t)$ is the link between Maxwell's equations and the optical Bloch equations. The polarization is defined as the average dipole moment per unit volume, or

$$\begin{aligned}\mathbf{P}(\mathbf{R}, t) &= \mathrm{Tr}\,(\rho^T\mu) = \frac{1}{V}\,\mathrm{Tr}\left[\sum_j \int d\mathbf{R}_j \rho^{T(j)}(\mathbf{R}_j, t)\,\mu\delta(\mathbf{R} - \mathbf{R}_j)\right] \\ &= \mathcal{N}\mu[\langle\rho_{12}^T(\mathbf{R}, t)\rangle + \langle\rho_{21}^T(\mathbf{R}, t)\rangle]\end{aligned} \tag{23}$$

where $\rho^{T(j)}(\mathbf{R}_j, t)$ and $\rho_{12}^T(\mathbf{R}, t)$ are single-particle density matrix elements, V is the sample volume, and $\mathcal{N}$ is the atomic density. The superscript T indicates that these are "true" density matrix elements rather than density matrix elements written in a field interaction. The relationship between the two is

$$\rho_{12}^T(\mathbf{R}, t) = \rho_{12}(Z, t)\exp[-i(kZ - \omega t)] \tag{24}$$

The angle brackets in Eq. (23) indicate that there may be additional averages that must be carried out. For example, in a vapor, there is a distribution of atomic velocities that must be

summed over, while in a solid, there may be an inhomogeneous distribution of atomic frequencies owing to local strains in the media. By combining Eqs. (19), (23), and (24), one arrives at

$$\frac{\partial E_S(Z,\,t)}{\partial Z} = \frac{ik\mathcal{N}\mu}{\varepsilon_0}\,\langle \rho_{21}(Z,\,t)\rangle = \frac{ik\mathcal{N}\mu}{2\varepsilon_0}\,\langle u(Z,\,t) - iv(Z,\,t)\rangle \tag{25}$$

which, together with Eqs. (14) or (16), constitutes the Maxwell-Bloch equations.

24.5 FREE POLARIZATION DECAY

As a first application of the Maxwell-Bloch equations, we consider free polarization decay (FPD),[26–30] which is the analog of free induction decay (FID) in nuclear magnetic resonance (NMR).[31,32] The basic idea behind FPD is very simple. An external field is applied to an ensemble of atoms and then removed. The field creates a phased array of atomic dipoles that radiate coherently in the direction of the incident applied field. The decay of the FPD signal provides information about the transverse relaxation times. We will discuss several possible scenarios for observing FPD. For the present, we assume that there is no inhomogeneous broadening of the sample (all atoms have the same frequency). Moreover, in this and all future examples, it is assumed that one can neglect any changes in the applied fields' amplitudes or phases as the fields propagate in the medium; the Rabi frequencies of the applied fields are functions of t only.

A short pulse is applied at $t = 0$, *short* meaning that

$$|\delta(t)|\tau,\ \gamma\tau,\ \gamma_2\tau \ll 1 \tag{26}$$

where τ is the pulse duration. The inequality Eq. (26) allows one to neglect any effects of detuning or relaxation during the pulse's action. Before the pulse arrives, the atom is in its ground state, implying that the components of the Bloch vector are $u = v = 0$, $w = -1$; that is, the Bloch vector points down (see Fig. 1*a*). *During* the pulse, the pseudofield vector can be approximated as $\mathbf{\Omega}(t) = [\Omega_0(t),\, 0,\, 0]$, owing to Eq. (26). The Bloch vector precesses in the wv plane and reaches a final value following the pulse given by

$$u(0^+) = 0 \qquad v(0^+) = \sin\theta \qquad w(0^+) = -\cos\theta \tag{27}$$

where

$$\theta = \int_{-\infty}^{\infty} \Omega_0\,(t)\,dt \tag{28}$$

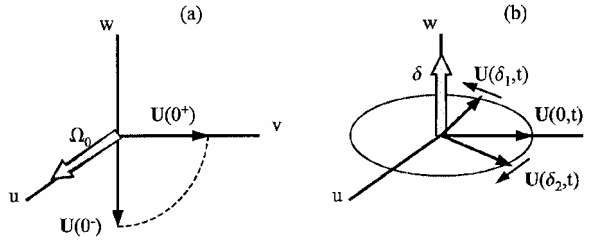

FIGURE 1 Evolution of the Bloch vector in free polarization decay. (*a*) A radiation pulse brings the Bloch vector from its initial position along the $-w$ axis to the uv plane. (*b*) With the field off, the Bloch vector precesses in the uv plane. In an inhomogeneously broadened sample, atoms having different detunings δ precess at different rates. The decay of the Bloch vector is not indicated in the figure.

is a *pulse area* and 0^+ is a time just after the pulse. *Following* the pulse, the pseudofield vector is $\mathbf{\Omega} = (0, 0, \delta)$, and the Bloch vector precesses about the w axis as it decays (see Fig. 1*b*). Explicitly, one finds

$$\begin{aligned} u(t) &= -\sin\theta \sin(\delta t) \exp(-\gamma t) \\ v(t) &= \sin\theta \cos(\delta t) \exp(-\gamma t) \\ w(t) &= -1 + (1 - \cos\theta) \exp(-\gamma_2 t) \end{aligned} \tag{29}$$

From this result, we can draw two conclusions. First, since the applied field is off when the atoms radiate, radiation is emitted at the natural frequency ω_0. This conclusion follows formally from Eqs. (29), (10), (23), and (24), which can be used to show that $P(Z, t)$ varies as $\exp(-i\delta t)$, and both $\mathbf{P}(\mathbf{R}, t)$ and $\mathbf{E}(\mathbf{R}, t)$ oscillate at frequency $\omega + \delta = \omega_0$. Second, one can use Eqs. (29) and (25) to obtain

$$\frac{\partial E_S(Z, t)}{\partial Z} = \frac{k\mathcal{N}\mu}{2\varepsilon_0} \sin\theta \exp[-(\gamma + i\delta)t] \tag{30}$$

If the sample under consideration is optically thin, the power exiting a sample of length L in the $\hat{\mathbf{Z}}$ direction is proportional to

$$I(L, t) = |E_S(L, t)|^2 = \left(\frac{k\mathcal{N}\mu L}{2\varepsilon_0} \sin\theta\right)^2 \exp(-2\gamma t) \tag{31}$$

The signal is maximal for a pulse area of $\pi/2$. A measure of the output power as a function of time following the excitation pulse enables one to obtain a value for the transverse relaxation rate. For a pencil-like sample, the neglect of cooperative effects such as superradiance is based on the assumption that $\mathcal{N}L/k^2 \ll 1$[25,33–35]

An alternative means for observing an FPD signal is to use an atomic beam that traverses a field interaction zone. The atom "sees" a radiation pulse in the atomic rest frame. If the atoms all have the same longitudinal velocity u_0, then the FPD signal measured at a distance L from the field interaction zone arises from atoms which were excited at time $t_e = t - L/u_0$. This implies that the phase factor $\exp[-(\gamma + i\delta)t]$ in Eq. (30) should be replaced by $\exp[-(\gamma + i\delta)(t - t_e)] = \exp[-(\gamma + i\delta)L/c]$. The emitted field is radiated at the incident field frequency ω rather than the atomic frequency ω_0. If the intensity is monitored as a function of L, one can obtain the transverse relaxation rate.

Often the atoms or molecules are characterized by an inhomogeneous distribution of frequencies. In a solid, this can occur as a result of different strains in the host medium. In a vapor, the velocity distribution of the atoms is equivalent to a distribution of atomic transition frequencies, when viewed in the laboratory frame. To discuss both solids and vapors in the same context, we define

$$\delta \equiv \delta(\omega_0, \mathbf{v}) = \omega_0 - \omega + \mathbf{k} \cdot \mathbf{v} = \delta_0 + \Delta + \mathbf{k} \cdot \mathbf{v} \tag{32}$$

where

$$\delta_0 = \overline{\omega}_0 - \omega \qquad \Delta = \omega_0 - \overline{\omega}_0 \tag{33}$$

and $\overline{\omega}_0$ is the average transition frequency. In a solid, $\mathbf{v} = 0$, but there is an inhomogeneous distribution of frequencies given by

$$W_f(\Delta) = \frac{1}{\sqrt{\pi}\sigma_w} \exp\left(-\frac{\Delta}{\sigma_w}\right)^2 \tag{34}$$

where σ_w characterizes the width of the inhomogeneous distribution. In a vapor, $\Delta = \sigma_w = 0$, but there is a Maxwellian velocity distribution

$$W_0(\mathbf{v}) = \frac{1}{(\pi u^2)^{3/2}} \exp\left[-(v/u)^2\right] \tag{35}$$

where u is the most probable atomic speed. The net effect is that Eq. (31) must be replaced by

$$\begin{aligned} I(L, t) &= \left(\frac{k\mathcal{N}\,\mu L}{\varepsilon_0}\right)^2 |\langle\rho_{21}(t)\rangle|^2 \\ &= \left(\frac{k\mathcal{N}\,\mu L}{2\varepsilon_0}\sin\theta\right)^2 \left|\int d\mathbf{v}\, W_0(\mathbf{v}) \int d\Delta W_f(\Delta) \exp\left(-[\gamma - i(\overline{\omega}_0 + \Delta + \mathbf{k}\cdot\mathbf{v})]t\right)\right|^2 \\ &= \left(\frac{k\mathcal{N}\,\mu L}{2\varepsilon_0}\sin\theta\right)^2 \exp(-2\gamma t) \exp\left[\frac{-(\sigma_\omega t)^2}{2}\right] \exp\left[\frac{-(kut)^2}{2}\right] \end{aligned} \tag{36}$$

If $\sigma_\omega \gg \gamma$ (solids) or $ku \gg \gamma$ (vapors), the signal decays mainly owing to inhomogeneous broadening. Bloch vectors corresponding to different frequencies precess about the w axis at different rates, implying that the optical dipoles created by the pulse lose their relative phase in a time of order $T_2^* = (2\sigma_\omega)^{-1}$ or $(2ku)^{-1}$ (see Fig. 1*b*). The FPD signal can be used to measure T_2^*, which can be viewed as an inhomogeneous, transverse relaxation time. At room temperature, ku/γ is typically on the order of 100. In a solid, σ_ω/γ can be orders of magnitude larger. An experimental FPD signal is shown in Fig. 2.

It is also possible to produce an FPD signal by preparing the atoms with a CW laser field and suddenly turning off the field. This method was used by Brewer and coworkers in a series of experiments on coherent optical transients in which Stark fields were used to tune molecules in a vapor into and out of resonance.[26] The CW field modifies the velocity distribution for the molecules. In the linear field regime, this again leads to an FPD signal that decays on a time scale of order $(ku)^{-1}$. It is fairly easy to obtain this result. To first order in the field, the steady-state solution of Eq. (14*d*), generalized to include the Doppler shift $\mathbf{k}\cdot\mathbf{v}$ and initial velocity distribution $W_0(\mathbf{v})$, is

$$\rho_{21}(\mathbf{v}) = -i\left(\frac{\Omega_0}{2}\right)[\gamma - i(\delta_0 + \mathbf{k}\cdot\mathbf{v})]^{-1} W_0(\mathbf{v}) \tag{37}$$

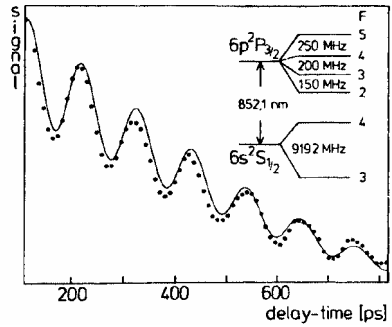

FIGURE 2 An FPD signal obtained on the D_2 transition in cesium. The excitation pulse has a duration of 20 ps. The decay time of the signal is determined by the inhomogeneous transverse relaxation rate $T_2^* = 1.4$ ns. Oscillations in the signal originate from the ground state hyperfine splitting. [*From H. Lehmitz and H. Harde, in* Methods of Laser Spectroscopy, *Y. Prior, A. Ben-Reuven, and M. Rosenbluh (eds.) (Plenum Press, New York, 1986), pp. 109–112. Reprinted with permission.*]

With this initial condition, it follows from Eq. (14*d*) that, for $t > 0$,

$$\langle \rho_{21}(\mathbf{v}, t)\rangle = \int d\mathbf{v}\, \frac{-i(\Omega_0/2)\exp\left[-\gamma t - i(\delta_0 + \mathbf{k}\cdot\mathbf{v})t\right]}{\gamma + i(\delta + \mathbf{k}\cdot\mathbf{v})}\, W_0(\mathbf{v})$$

$$= -i\frac{\sqrt{\pi}\Omega_0}{2ku}\exp\left[\left(\frac{\gamma + i\delta_0}{ku}\right)^2\right]\left[1 - \Phi\left(\frac{\gamma + i\delta_0}{ku} + \frac{kut}{2}\right)\right] \tag{38}$$

where Φ is the error function. For $kut > 1$ and $|\gamma + i\delta_0|/ku \ll 1$, $\langle \rho_{21}(\mathbf{v})\rangle \sim -i[\Omega_0/(k^2u^2t)]$ $\exp(-k^2u^2t^2/4)$.

When one considers *nonlinear* interactions with the field, the situation changes. The CW field excites only those atoms having $\mathbf{k}\cdot\mathbf{v} = -\delta \pm \gamma'$, where γ' is a power-broadened homogeneous width. These velocity-selected atoms are no longer subject to inhomogeneous broadening and give rise to a contribution to the FPD signal that decays with rate $T_2^{-1} = (\gamma + \gamma')$.[26] Thus, by using *nonlinear* atom-field interactions, one can extract *homogeneous* decay rates in situations where there is large inhomogeneous broadening. The price one pays is that only a small percentage of the atoms (those that have velocities for which the applied field is resonant) contribute to the signal. An example of an FPD signal of this type is shown in Fig. 3.

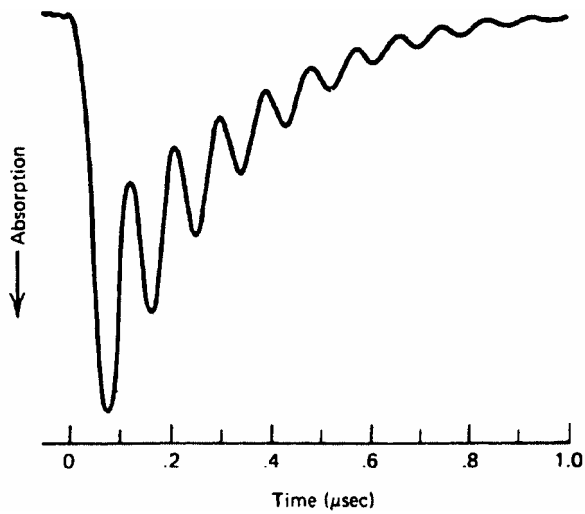

FIGURE 3 An FPD signal obtained in NH_2D at 10.6 μm using the method of Stark switching of a molecular transition frequency. Molecules that interact resonantly with a CW field are suddenly tuned out of resonance by the Stark switching. The oscillations result from the heterodyne detection method that is used, while the slowly varying increase in the signal is the result of optical nutation of molecules switched *into* resonance by the Stark pulse. The FPD signal manifests itself as a *reduction of the amplitude of the oscillation* with time. This amplitude decays with the (power-broadened) *homogeneous* decay rate T_2, owing to the fact that the nonlinear interaction with a CW field results in the excitation of only a small fraction of the Doppler profile of the molecules. [*From R. G. Brewer and R. L. Shoemaker,* Phys. Rev. A ***6:****2001 (1972). Reprinted with permission.*]

24.6 PHOTON ECHO

We have seen that it is possible to measure the transverse relaxation rate T_2 in an inhomogeneously broadened sample using FPD, but only a relatively small percentage of the atoms participate. The question arises as to whether other techniques would allow for full participation of the atoms. The *photon echo* is one such method.[8–10,36–38] The photon echo has very little to do with either photons or echoes, but the name has a nice ring to it. The photon echo, the optical analog of the spin echo,[39] was first observed in ruby by Kurnit et al.[36] A pulse having propagation vector $\mathbf{k}_1$ is applied at $t = 0$, a second pulse having propagation vector $\mathbf{k}_2 = \mathbf{k}_1$ is applied at $t = T_{21}$, and an echo is radiated at time $t = 2T_{21}$ in a direction $\mathbf{k} = \mathbf{k}_1$. There are many ways to explain echo formation, and some of these are indicated in the following discussion.

In the Bloch vector picture, a $\pi/2$ pulse excites the optical dipoles at $t = 0$, bringing the Bloch vector along the v axis (Fig. 4*a*). The Bloch vector then begins to precess in the uv plane

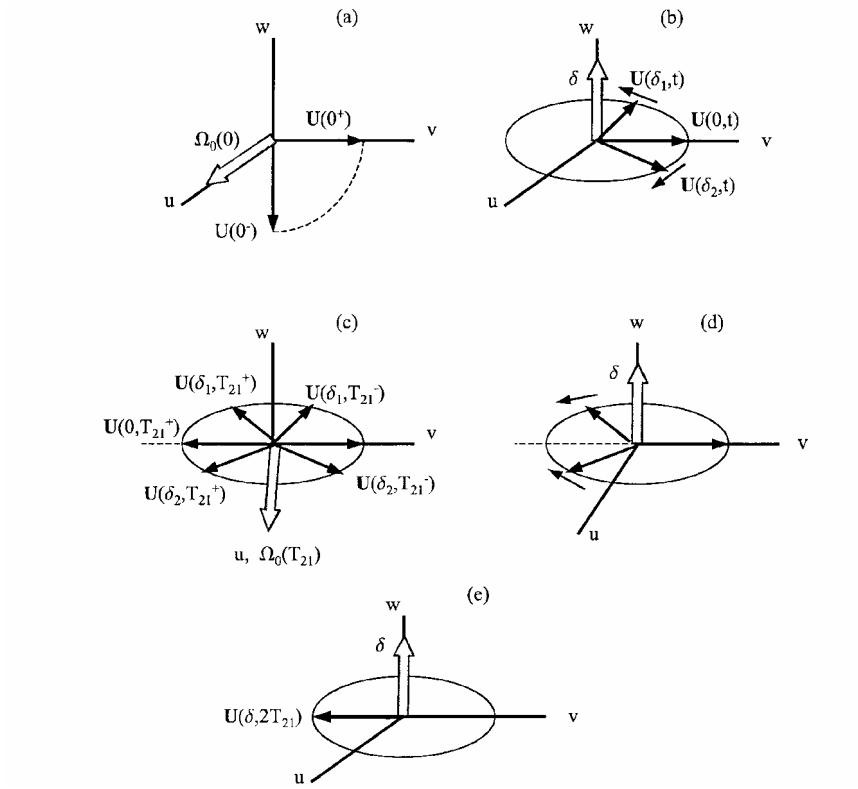

FIGURE 4 Bloch vector picture of echo formation. (*a*) An initial $\pi/2$ pulse brings the Bloch vector to the uv plane. (*b*) In a field-free region, the Bloch vector precesses in the uv plane; atoms with different detunings dephase relative to one another in a time equal to the inhomogeneous, transverse relaxation rate T_2^*. (*c*) At time T_{21}, a second pulse, this time a π pulse, reflects the Bloch vectors with respect to the uw plane. (*d*) In a field-free region, the Bloch vectors continue to precess. (*e*) At time $t = 2T_{21}$, all the vectors are aligned along the $-v$ axis (the optical dipoles have rephased), and an echo signal is emitted. The decay of the Bloch vector is not indicated in the figure.

at a rate equal to the atom-field detuning. In an inhomogeneously broadened medium, different atoms have different resonant frequencies. As a consequence, the Bloch vectors associated with different atoms precess at different rates and dephase relative to each other in a time T_2^* (Fig. 4*b*). The dipole coherence is not lost, however. If at time T_{21} a π pulse is applied, the net effect of the pulse is to cause a reflection about the *uw* plane (Fig. 4*c*). As the atoms continue to precess at different rates (Fig. 4*d*), the rates are such that the Bloch vectors for *all* the atoms will become aligned with the $-v$ axis at time $t = 2T_{21}$ and an *echo signal* is emitted (Fig. 4*e*). From time $t = 0$ to $t = 2T_{21}$ the dipoles decay with the homogeneous decay rate γ. By measuring the echo signal as a function of delay time T_{21} between the pulses, one can obtain the transverse relaxation time $T_2 = \gamma^{-1}$.

It is not necessary that the pulse areas be equal to $\pi/2$ and π, although these areas lead to a maximal signal. What *is* necessary is that the second pulse produce at least a partial reflection about the *uw* plane. This reflection takes the Bloch vector components $u + iv$ into $u - iv$, or, equivalently, takes density matrix element ρ_{12} into ρ_{21}. Since ρ_{12} and ρ_{21} are related to the real and imaginary parts of the average dipole moment operator, the second pulse must couple these real and imaginary parts. *Such coupling is impossible for a linear atom-field interaction.* Thus, by its very nature, the photon echo can occur only when nonlinear atom-field interactions are present.

An alternative way to picture echo formation is to use double-sided Feynman diagrams[40] that keep track of the relative phase of the different dipoles. Diagrams similar to those indicated in Fig. 5 were introduced by Hartmann and Friedberg in the context of a billiard ball echo model[41] and have been used extensively in theories of atom interferometry.[42–44] Each line represents a field amplitude. The abscissa is time, and the ordinate is the *phase* associated with the amplitude. In the absence of any interactions, it follows from Eq. (4) that the phase associated with the state $|1\rangle$ amplitude is $\delta t/2$ and that associated with the state $|2\rangle$ amplitude is $-\delta t/2$. In these diagrams, the phase of each amplitude is displaced by $-\delta t/2$ so that the state $|1\rangle$ amplitude evolves without any phase change and the state $|2\rangle$ amplitude evolves with a phase equal to $-\delta t$.

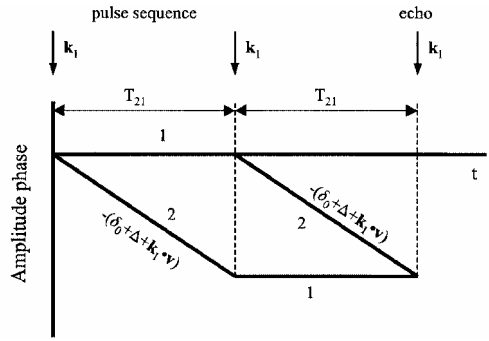

FIGURE 5 A phase diagram that can be used to analyze coherent transient phenomena. Each line corresponds to a state amplitude, and density matrix elements are obtained by multiplying a top line by the conjugate of a bottom line *at the same time.* The relative phase of a given density matrix element is given by the vertical separation of the two lines. The slopes of various line segments are shown on the graph. Lines corresponding to atoms having different atom-field detunings Δ (solid) or different velocities $\mathbf{v}$ (vapor) would have different slopes. The pulse sequence is shown at the top of the figure along with the temporal position and direction of the echo. This diagram corresponds to the two-pulse photon echo. Regardless of the atom-field detuning or atomic velocity, all lines cross at $t = 2T_{21}$, indicating that all the optical dipoles are in phase at this point.

We start with the atom in state $|1\rangle$ at $t = 0$. The atom-field interaction takes state $|1\rangle$ to $|2\rangle$ on absorption with a phase factor exp $(i\mathbf{k}_1 \cdot \mathbf{R})$ and $|2\rangle$ to $|1\rangle$ on emission with a phase factor exp $(-i\mathbf{k}_1 \cdot \mathbf{R})$. A vertical cut establishes the density matrix element of interest and the vertical distance between the two amplitudes is a measure of the *relative* phase of the amplitudes. For example, between $t = 0$ and $t = T_{21}$ in Fig. 5, the density matrix element ρ_{12} has been created with relative phase $(\delta_0 + \Delta + \mathbf{k}_1 \cdot \mathbf{v})t$ which grows with increasing t. One finds significant contributions to the dipole coherence at a given time *only* when the relative phase is the *same* for all the optical dipoles at that time. In a solid $\mathbf{v} = 0$, but $\Delta = \omega_0 - \overline{\omega}_0$ is different for different atoms owing to variations in ω_0; in a vapor $\Delta = 0$, but $\mathbf{k}_1 \cdot \mathbf{v}$ is different for different velocity subclasses of atoms. Thus, the slopes of the lines in Fig. 5 would differ for different atoms in both solids and vapors. On averaging over an inhomogeneous frequency distribution, the average dipole coherence would vanish, except at times near crossings of the state amplitudes, where the relative phase of all the dipoles is nearly equal to zero. Between $t = 0$ and $t = T_{21}$, this occurs only near $t = 0$, where an FPD signal is emitted. The application of a second pulse at $t = T_{21}$, however, converts ρ_{12} into ρ_{21} and begins a rephasing process for the dipoles. The state amplitudes in Fig. 5 intersect and the dipoles are rephased at $t = 2T_{21}$, *independent of the value of* $\mathbf{v}$ or Δ. The echo signal is radiated for times $t \approx 2T_{21}$.

Analytical calculations of the signal intensity can be carried out using Eqs. (14) and (16). One simply pieces together periods in which the pulses act with periods of free evolution. The results are rather complicated, in general. However, if $\sigma_w T_{21} \gg 1$ (solid) or $k_1 u T_{21} \gg 1$ (vapor), only terms in the density matrix sequence indicated schematically in Fig. 5 survive the average over the inhomogeneous frequency distribution in the vicinity of the echo at $t \approx 2T_{21}$. At these times, one finds a total averaged density matrix element

$$\langle \rho_{21}^T(\mathbf{R}, t)\rangle = \langle \rho_{21}(t)\rangle \exp\,(i[kZ - \omega t])$$

where

$$\mathbf{k} = -\mathbf{k}_1 + 2\mathbf{k}_1 = \mathbf{k}_1$$

$$\langle \rho_{21}(t)\rangle = \frac{i}{2} \sin\theta_1 \sin^2\left(\frac{\theta_2}{2}\right) \exp\,(-2\gamma T_{21}) \exp\,[-i\delta_0(t - 2T_{21})] \times \exp\left[\frac{-\sigma_\omega^2 (t - 2T_{21})^2}{4}\right] \exp\left[\frac{-k_1^2 u^2 (t - 2T_{21})^2}{4}\right] \quad (39)$$

and θ_i is the pulse area of pulse i. The corresponding echo intensity is

$$I(L, t) = \left(\frac{k\mathcal{N}\,\mu L}{\varepsilon_0}\right)^2 |\langle \rho_{21}(t)\rangle|^2 = \left[\frac{k\mathcal{N}\,\mu L}{2\varepsilon_0} \sin\theta_1 \sin^2\left(\frac{\theta_2}{2}\right)\right]^2 \times \exp\,(-4\gamma T_{21}) \exp\left[\frac{-\sigma_\omega^2 (t - 2T_{21})^2}{2}\right] \exp\left[\frac{-k_1^2 u^2 (t - 2T_{21})^2}{2}\right] \quad (40)$$

It is interesting to note that the echo intensity near $t = 2T_{21}$ mirrors the FPD intensity immediately following the first pulse.

For experimental reasons it is often convenient to use a different propagation vector for the second pulse. Let $\mathbf{k}_1$ and $\mathbf{k}_2$ be the propagation vectors of the first and second pulses, which have identical carrier frequencies ω. In this case, one must modify the definition (24) of the field interaction representation to account for the different $\mathbf{k}$ vectors. The final result for the total averaged density matrix element in the vicinity of the echo is

$$\langle \rho_{21}^T(\mathbf{R}, t)\rangle = \langle \rho_{21}(t)\rangle \exp\,(i[kZ - \omega t])$$

where

$$\mathbf{k} = 2\boldsymbol{k}_2 - \mathbf{k}_1$$

and

$$\langle \rho_{21}(t) \rangle = \frac{i}{2} \sin \theta_1 \sin^2 \left(\frac{\theta_2}{2} \right) \exp(-2\gamma T_{21}) \exp[-i\delta_0(t - 2T_{21})]$$

$$\exp\left[\frac{-\sigma_\omega^2 (t - 2T_{21})^2}{4} \right] \int d\mathbf{v}\, W_0(\mathbf{v}) \exp\{ i\mathbf{k}_1 \cdot \mathbf{v} T_{21} - \mathbf{k}_2 \cdot \mathbf{v}(t - T_{21}) \} \quad (41)$$

Recall that $\sigma_\omega = 0$ for a vapor and $W_0(\mathbf{v}) = \delta(\mathbf{v})$ for a solid. In these equations there are three things to note. First, the signal is emitted in a direction different from that of the applied fields, a desirable feature from an experimental point of view. Second, the phase matching condition $k = \omega/c$ is no longer satisfied since $k = |2\mathbf{k}_2 - \mathbf{k}_1|$ and $k_1 = k_2 = \omega/c$; however, if the fields are nearly collinear such that $(k^2 - \omega^2/c^2)L^2 \ll 1$, the effects of phase mismatch are negligible. Third, there is now a qualitative difference between the solid and vapor case. Owing to the fact that the detuning depends on the propagation vectors for the vapor, it is not possible to exactly rephase all the dipoles in the vapor when $\mathbf{k}_1 \neq \mathbf{k}_2$. If $|\mathbf{k}_2 - \mathbf{k}_1|/k_1 \ll 1$, however, nearly complete rephasing of the dipoles occurs for $t \approx 2T_{21}$. The photon echo signal observed by Kurnit et al.[36] is shown in Fig. 6.

As can be deduced from Fig. 5, the signal is sensitive only to off-diagonal density matrix elements in the entire time interval of interest. Thus, any disturbance of the off-diagonal density matrix elements or optical coherence will be reflected as a decrease in the echo intensity. As such, echo signals can serve as a probe of all contributions to transverse relaxation. Transverse relaxation generally falls into two broad categories which can lead to qualitatively different modifications of the coherent transient signals. First, there are *dephasing processes,* which produce an exponential damping of the coherences and contribute to γ. Second, there are *spectral diffusion* (solid)[45–48] or *velocity-changing collisions* (vapor),[47–49] which change the frequency associated with the optical coherences. Such terms enter the optical Bloch equations as *integral* terms, transforming the equations into differentio-integral equations. In a solid the change in frequency can be produced by fluctuating fields acting at each atomic site. Spectral diffusion of coherences in solids is difficult to detect, since phase-interrupting processes often dominate the signals. It has been measured in FPD using impurity ions in a crystalline host.[50] The situation in vapors is a bit more subtle. The phase-changing and velocity-changing aspects of collisions are entangled and cannot be separated, in general.[49] If the col-

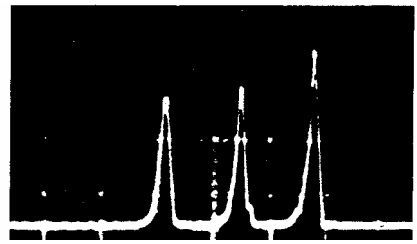

FIGURE 6 A photon echo signal from ruby. Time increases to the right with a scale of 100 ns/division. The pulse on the right is the echo signal, while the first two pulses are the (attenuated) input pulses. The echo appears at $t = 2T_{21}$, where T_{21} is the separation of the input pulses. [*From N. A. Kurnit, I. D. Abella, and S. R. Hartmann,* Phys. Rev. Lett. ***13:****567 (1964). Reprinted with permission.*]

lisional interaction is *state independent,* however, as it is for some molecular transitions, then collisions are purely velocity changing in nature, leading to an echo that decays exponentially as T_{21}^3 for early times and T_{21} for later times.[51] For electronic transitions, collisions are mainly phase changing in nature, but there is a velocity-changing contribution that persists in the forward diffractive-scattering cone. This diffractive scattering has been observed for Na–,[52] Li–,[53] and Yb–rare gas collisions[54] using photon echo techniques.

24.7 STIMULATED PHOTON ECHO

Up to this point, we have considered pulse sequences that are useful for measuring transverse relaxation times. Now we examine *stimulated photon echoes,*[8–10] which can be used to *simultaneously* measure both transverse and longitudinal relaxation times. Stimulated photon echoes have become an important diagnostic probe of relaxation in condensed-matter systems. The pulse sequence consists of three pulses, having areas θ_1, θ_2, θ_3 and propagation vectors $\mathbf{k}_1$, $\mathbf{k}_2$, $\mathbf{k}_3$, with $k_i = \omega/c$. In this section we take $\mathbf{k}_3 = \mathbf{k}_1$, and in the next section we will set $\mathbf{k}_3 = -\mathbf{k}_1$. The time interval between the first two pulses is T_{21}, and pulse 1 can precede or follow pulse 2. Pulse 3 occurs at time $t = T_{21} + T$ (Fig. 7). Signals can be generated in many different directions. For the sake of definiteness, we consider only the signal radiated in the $-\mathbf{k}_2 + \mathbf{k}_1 + \mathbf{k}_3$ direction. The phase diagram giving rise to this signal is shown in Fig. 7. For radiation to be emitted in the $-\mathbf{k}_2 + \mathbf{k}_1 + \mathbf{k}_3$ direction when $\mathbf{k}_3 = \mathbf{k}_1$, pulse 2 must precede pulse 1. (Of course, there are diagrams with pulse 1 preceding pulse 2, but these give rise to radiation in the $-\mathbf{k}_1 + \mathbf{k}_2 + \mathbf{k}_3$ direction.) It is assumed that T_{21} is greater than the inhomogeneous relaxation time T_2^*. The signal contains contributions from the optical coherence (off-diagonal density matrix elements) in the time intervals $(0, T_{21})$, $(T + T_{21}, t)$ and contributions from atomic state populations (diagonal density matrix elements) in the time interval T between the second and the third pulses. The echo appears when $t - (T_{21} + T) = T_{21}$.

The calculation of the echo signal is straightforward. Just before the second pulse, the density matrix $\rho_{12}(T_{21})$ varies as $\exp[-(\gamma - i\delta_2)T_{21}]$, where $\delta_i = \omega_0 - \omega + \mathbf{k}_i \cdot \mathbf{v}$. In the time interval T, the population difference $\omega = \rho_{22} - \rho_{11}$ decays at rate γ_2 and *oscillates* at frequency $\delta_2 - \delta_1 =$

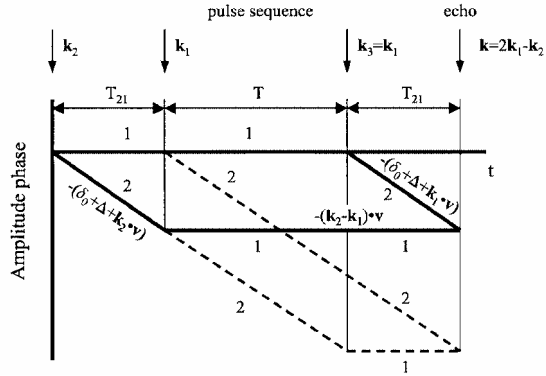

FIGURE 7 A phase diagram for the stimulated photon echo in which field 2 acts first and the echo is emitted in the $(-\mathbf{k}_2 + \mathbf{k}_1 + \mathbf{k}_3) = (2\mathbf{k}_1 - \mathbf{k}_2)$ direction. The solid lines involve the intermediate state population ρ_{11} while the dashed lines involve the intermediate state population ρ_{22}. All dipoles are in phase at $t = 2T_{21} + T$.

$(\mathbf{k}_2 - \mathbf{k}_1) \cdot \mathbf{v}$. In the final time interval, $\rho_{21}(t)$ varies as $\exp[-(\gamma + i\delta_3)(t - T - T_{21})]$, where $\delta_3 = \delta_1$ since $\mathbf{k}_3 = \mathbf{k}_1$. Combining the various field interaction and free propagation zones, one finds that the total averaged density matrix element in the vicinity of the echo $t \approx T + 2T_{21}$ is

$$\langle \rho_{21}^{T}(\mathbf{R}, t) \rangle = \langle \rho_{21}(t) \rangle \exp[i(kZ - \omega t)]$$

with

$$\mathbf{k} = -\mathbf{k}_2 + \mathbf{k}_1 + \mathbf{k}_3 = 2\mathbf{k}_1 - \mathbf{k}_2$$

and

$$\begin{aligned} \langle \rho_{21}(t) \rangle = \left(\frac{i}{2}\right) \sin\theta_1 \sin\theta_2 \sin\theta_3 \exp(-\gamma_2 T) \exp(-2\gamma T_{21}) \exp\{-i\delta_0[(t - T_{21} - T) - T_{21}]\} \\ \times \exp\left\{\frac{-\sigma_\omega^2[(t - T_{21} - T) - T_{21}]^2}{4}\right\} \int d\mathbf{v}\, W_0(\mathbf{v}) \\ \times \exp\{i[\mathbf{k}_2 \cdot \mathbf{v} T_{21} + (\mathbf{k}_2 - \mathbf{k}_1) \cdot \mathbf{v} T - (2\mathbf{k}_1 - \mathbf{k}_2) \cdot \mathbf{v}(t - T_{21} - T)]\} \end{aligned} \tag{42}$$

The optimal pulse sequence consists of three $\pi/2$ pulses. Phase matching can be achieved only for $|\mathbf{k}_1 - \mathbf{k}_2|L \ll 1$. In a solid, the integral in Eq. (42) is equal to unity, and the echo signal is maximal for $t = T + 2T_{21}$. In a vapor, the echo signal is degraded if $\mathbf{k}_1 \neq \mathbf{k}_2$; however, if $\mathbf{k}_1 \approx \mathbf{k}_2$, then, at $t = T + 2T_{21}$, the echo amplitude varies as

$$\exp(-\gamma_2 T) \exp(-2\gamma T_{21}) \exp\left[-\frac{|\mathbf{k}_1 - \mathbf{k}_2|^2 u^2 (T + 2T_{21})^2}{4}\right]$$

By varying the angle between $\mathbf{k}_1$ and $\mathbf{k}_2$, one can determine the Doppler width ku. By monitoring the echo signal as a function of T_{21} (T), one obtains information on the transverse (longitudinal) relaxation.

Relaxation other than spontaneous emission can occur for the populations in the time interval T. The inhomogeneous phase $\delta_1 T_{21}$, acquired in the time interval T_{21}, is canceled by the phase $\delta_3 T_{21}$, acquired in the interval T_{21} following the third pulse. If, between the second and third pulses, the frequency (solid) or velocity (vapor) has changed owing to spectral diffusion (solid)[45–48] or velocity-changing collisions (vapor),[47–49,55,56] the phase cancellation will not be complete. Thus, the echo signal as a function of T provides information on these relaxation processes. The rate of spectral diffusion or velocity-changing collisions must be of order or greater than γ_2 to be observable. One would have a longer time to observe such effects if it were the ground-state lifetime rather than the excited-state lifetime that was the relevant time scale, but, in a closed two-level system, such is not the case.

The situation changes if a three-level system, such as the one shown in Fig. 8, is used. The fields drive the 1–2 transition, but level 2 decays to both level 1 and level 0. The total population of the 1–2 state subsystem is no longer conserved, requiring an *additional* decay rate to account for relaxation. Let us suppose that all states decay with rate Γ_t as a result of their finite time in

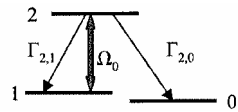

FIGURE 8 Open atomic-level scheme that can be used to observe transient signals limited only by some effective ground state lifetime. The field couples only states $|1\rangle$ and $|2\rangle$, but level 2 decays to both levels 1 and 0.

the laser beams. Moreover, let $\Gamma_{2,1}$ and $\Gamma_{2,0}$ be the decay rates of level 2 to levels 1 and 0, respectively, such that $\gamma_1 = \gamma_0 = \Gamma_t$ and $\gamma_2 = \Gamma_{2,1} + \Gamma_{2,0} + \Gamma_t$. For simplicity, let us also take $\mathbf{k}_1 \approx \mathbf{k}_2$. In the interval T, the decay dynamics resulting from spontaneous emission and transit time effects is

$$\dot{\rho}_{22} = -\gamma_2\rho_{22} = -(\Gamma_{2,1} + \Gamma_{2,0} + \Gamma_t)\rho_{22}$$

$$\dot{\rho}_{11} = -\Gamma_t\rho_{11} + \Gamma_{2,1}\rho_{22}$$

Assuming that $\gamma_2 T \gg 1$, one finds that at time $t = T_{21} + T$, $\rho_{22}(T_{21} + T) \sim 0$, and

$$\rho_{11}(T_{21} + T) \sim \frac{\Gamma_{2,0}}{\Gamma_{2,1} + \Gamma_{2,0}} \exp(-\Gamma_t T)$$

which then replaces the factor $\exp(-\gamma_2 T)$ in Eq. (42). If $\Gamma_{2,0} \neq 0$, there is a long-lived component in the ground-state population. One can exploit this feature of *open systems* to study spectral diffusion or velocity-changing collisions with very high sensitivity.[57,58] In Fig. 9, stimulated echo data is shown that was used to measure a cross section for collisions between ground-state Na and He atoms.[58] The echo occurs for time separations T much greater than the excited-state lifetime.

Open systems also offer interesting possibilities as storage devices. Since the effective ground-state lifetime can be as long as days in certain solids, one can write interferometric information into the sample by replacing one of the first two pulses by a signal pulse and reading it out at a later time with the third pulse.[59–62] In the case of vapors, it is also possible to replace some of the incident pulses by standing-wave fields.[63–71] In this manner, modulated ground-state populations with associated Doppler phases of order kuT can be created and rephased, providing sensitivity to velocity-changing collisions as small as a few centimeters per second.[72]

Before leaving this section, it is perhaps useful to make a slight digression on *homogeneously* broadened systems. A diagram of the type indicated in Fig. 10, *in which field 1 acts first,* also leads to a signal in the $\mathbf{k} = \mathbf{k}_1 - \mathbf{k}_2 + \mathbf{k}_3 = 2\mathbf{k}_1 - \mathbf{k}_2$ direction (with $\mathbf{k}_1 = \mathbf{k}_3$). We have not considered this contribution for inhomogeneously broadened systems since such a diagram leads to an overall phase of $\phi_d = -2(\delta_0 + \Delta + 2\mathbf{k}_1 \cdot \mathbf{v})T_{21}$ at time $t = T + 2T_{21}$. On averaging over either Δ or $\mathbf{v}$ in an inhomogeneously broadened sample, this contribution would vanish. In a homogeneously broadened sample, however, $\Delta = 0$ and $\mathbf{v} = 0$, giving an *identical* relative phase ϕ_d to all the atoms. For $t > T + T_{21}$, the corresponding density matrix element associated with this diagram is

$$\langle\rho_{21}(t)\rangle = \left(\frac{i}{2}\right) \sin\theta_1 \sin\theta_2 \sin\theta_3 \exp(-\gamma_2 T) \exp[-\gamma(t - T)] \exp[-i\delta_0(t - T)] \qquad (43)$$

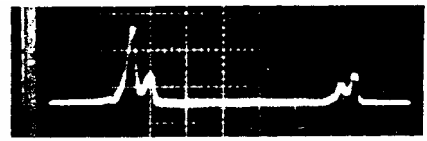

FIGURE 9 Stimulated photon echo observed on the D_1 transition in sodium. This is an "open" system for which a stimulated echo signal can be produced for separations T between the second and third pulses much larger than the excited-state lifetime. In this diagram T is 17 times the 16-ns lifetime of the excited state. The first three pulses are scattered light from the three input pulses and the fourth pulse is the echo. The echo appears at $t = T + 2T_{21}$, where T_{21} is the separation of the first two input pulses. [*From T. Mossberg, A. Flusberg, R. Kachru, and S. R. Hartmann,* Phys. Rev. Lett. ***42:****1665 (1979). Reprinted with permission.*]

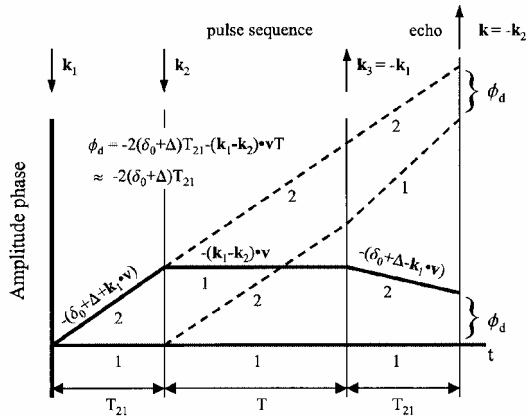

FIGURE 10 A phase diagram for the stimulated photon echo in which field 1 acts first. The direction of field 3 is opposite to that of field 1, and the echo is emitted in the $(\mathbf{k}_1 - \mathbf{k}_2 + \mathbf{k}_3) = -\mathbf{k}_2$ direction. We have taken $\mathbf{k}_2 \approx \mathbf{k}_1$. The solid lines involve the intermediate state population ρ_{11}, while the dashed lines involve the intermediate state population ρ_{22}. At time $t = 2T_{21} + T$ the relative phase is $\phi_d \approx -2(\delta_0 + \Delta)T_{21}$. For solids, the average over Δ washes out the signal. For vapors, $\Delta = 0$, the phase $\phi_d \approx -2\delta_0 T_{21}$ is the same for all the atoms, and an echo is emitted.

Equation (43) does not constitute an echo in the usual sense, since there is no dephasing-rephasing cycle. The signal appears promptly (it is actually an FPD signal) following the third pulse. If one measures the *time-integrated* intensity in the signal following the third pulse, however (as is often the case with ultrafast pulses in which time resolution of the echo is not possible), it is impossible to tell directly whether an echo has occurred or not. For such measurements, a signal emitted in the $\mathbf{k} = 2\mathbf{k}_1 - \mathbf{k}_2$ direction when pulse 1 acts first is a clear signature of a homogeneously broadened system, since such a signal vanishes for inhomogeneously broadened samples.

The time-integrated signal is proportional to

$$\int_{T+T_{21}}^{\infty} |\langle \rho_{21}(t) \rangle|^2 \, dt$$

When field 2 acts first, the time integrated, inhomogeneously broadened signal varies as exp $(-4\gamma T_{21})$, while the homogeneously broadened signal varies as exp $(-2\gamma T_{21})$. When field 1 acts first, the signal is vanishingly small {varying as exp $[-(\sigma_w^2 + k^2u^2)T_{21}^2/2]$} for inhomogeneously broadened samples, while the homogeneously broadened signal strength is essentially unchanged from that when pulse 2 acts first. This time-ordering asymmetry can be used to distinguish between homogeneously and inhomogeneously broadened samples.[73]

24.8 PHASE CONJUGATE GEOMETRY AND OPTICAL RAMSEY FRINGES

A qualitative difference between stimulated photon echo signals arises when $\mathbf{k}_3$ is in the $-\mathbf{k}_1$ direction rather than the $\mathbf{k}_1$ direction.[61,74,75] In this case, it is possible to generate a phase matched signal in the

$$\mathbf{k} = \mathbf{k}_1 - \mathbf{k}_2 + \mathbf{k}_3 = -\mathbf{k}_2$$

direction for *both* time orderings of fields 1 and 2. Moreover, in weak fields, the amplitude of the signal field is proportional to the conjugate of input field 2. As a consequence, the signal is referred to as a *phase conjugate* signal for this geometry.[76,77] To simplify matters, we will set $\mathbf{k}_1 \approx \mathbf{k}_2 = -\mathbf{k}$ and neglect terms of order $|\mathbf{k}_1 - \mathbf{k}_2|u(T + 2T_{21})$.

The appropriate phase diagrams are shown in Fig. 10 when field 1 acts before field 2 and Fig. 11 when field 2 acts before field 1. There is a qualitative difference between the phase diagrams of Figs. 10 and Fig. 7. At time $t = 2T_{21} + T$, the lines representing the state amplitudes *do not cross* in Fig. 10. Rather, they are separated by a phase difference of $\phi_d = -2(\delta_0 + \Delta)T_{21}$. The phase shift resulting from *Doppler shifts* cancels at $t = 2T_{21} + T$, but *not* the phase shift resulting from the atom-field detuning. The significance of these results will become apparent immediately. The averaged density matrix element in the vicinity of the echo is

$$\langle \rho_{21}(t) \rangle = \left(\frac{i}{2}\right) \sin\theta_1 \sin\theta_2 \sin\theta_3 \exp(-\gamma_2 T) \exp(-2\gamma T_{21}) \exp\{-i\delta_0[(t - T_{21} - T) + T_{21}]\}$$
$$\times \exp\left[\frac{-\sigma_\omega^2[(t - T_{21} - T) + T_{21}]^2}{4}\right] \exp\left[\frac{-k^2u^2[(t - T_{21} - T) - T_{21}]^2}{4}\right] \qquad (44)$$

In a solid, the signal vanishes near $t = 2T_{21} + T$, since $\sigma_\omega T_{21} \gg 1$.

In a vapor, an echo is formed at time $t = T + 2T_{21}$. At this time, the averaged density matrix element varies as $\exp(-2i\delta_0 T_{21})$, a factor which was absent for the nearly collinear geometry. This phase factor is the optical analog[78–80] of the phase factor that is responsible for the generation of Ramsey fringes.[81] One can measure the phase factor directly by heterodyning the signal field with a reference field, or by converting the off-diagonal density matrix element into a population by the addition of a *fourth* pulse in the $\mathbf{k}_3$ direction at time

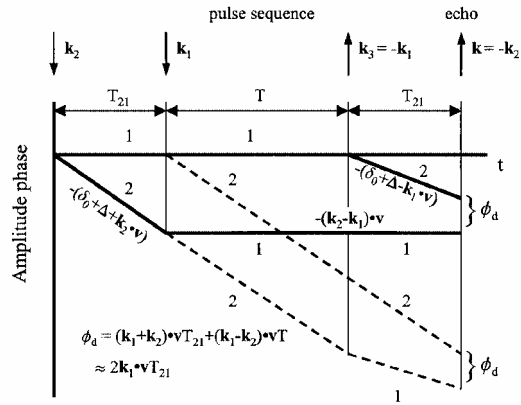

FIGURE 11 A phase diagram for the stimulated photon echo in which field 2 acts first and $\mathbf{k}_3 = -\mathbf{k}_1$. The echo is emitted in the $(-\mathbf{k}_2 + \mathbf{k}_1 + \mathbf{k}_3) = -\mathbf{k}_2$ direction, and we have taken $\mathbf{k}_2 \approx \mathbf{k}_1$. The solid lines involve the intermediate state population ρ_{11}, while the dashed lines involve the intermediate state population ρ_{22}. At time $t = 2T_{21} + T$ the relative phase is $\phi_d \approx 2\mathbf{k}_1 \cdot \mathbf{v}T_{21}$. For vapors, the average over the velocity distribution washes out the signal. For solids, $\mathbf{v} = 0$, the relative phase is zero for all the atoms, and an echo is emitted.

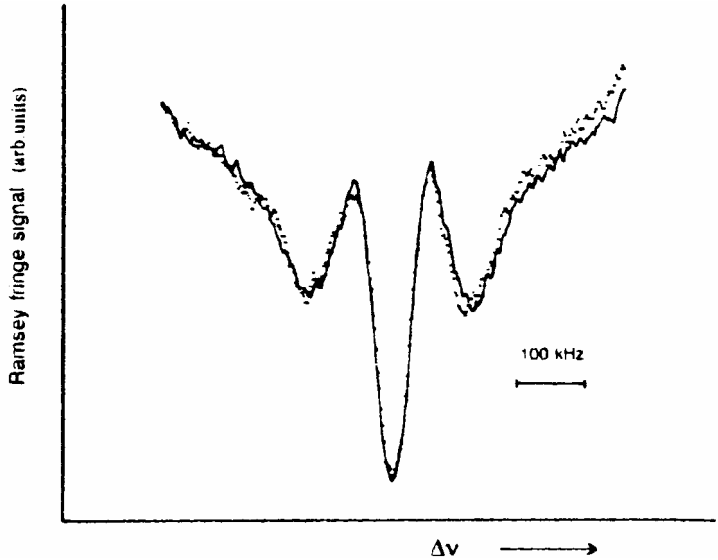

FIGURE 12 An optical Ramsey fringe signal on the 657-nm intercombination line in calcium. Four field zones were used. The most probable value of T_{21} was about 10^{-5} s for an effusive beam having a most probable longitudinal speed equal to 800 m/s, giving a central fringe width on the order of 60 kHz. The dashed and dotted lines represent runs with the directions of the laser field reversed, to investigate phase errors in the signals. [*From N. Ito, J. Ishikawa, and A. Morinaga, "Evaluation of the Optical Phase Shift in a Ca Ramsey Fringe Stabilized Optical Frequency Standard by Means of Laser Beam Reversal,"* Opt. Comm. ***109:****414 (1994). Copyright © 1994; reprinted with permission from Elsevier Science.*]

$t = T + 2T_{21}$.* In either case, the signal varies as $\cos(2\delta_0 T_{21})$. In itself, this dependence is useless for determining the optical frequency since one cannot identify the fringe corresponding to $\delta_0 = 0$. To accomplish this identification, there are two possibilities. If the experiment is carried out using an atomic beam rather than atoms in a cell, $T_{21} = L/u_0$ will be different for atoms having different u_0 (L = spatial separation of the first two pulses and u_0 is the longitudinal velocity of the atoms). When a distribution of u_0 is averaged over, the fringe having $\delta_0 = 0$ will have the maximum amplitude. Experiments of this type allow one to measure optical frequencies with accuracy of order T_{21}^{-1} (see Fig. 12). For experiments carried out using temporally separated pulses acting on atoms in a cell, it is necessary to take data as a function of δ_0 for several values of T_{21}, and then average the data over T_{21}; in this manner the central fringe can be identified. The optical Ramsey fringe geometry has been reinterpreted as an atom interferometer.[42,82] Atom interferometers are discussed in Sec. 24.9.

We now move to Fig. 11, in which field 2 acts before field 1. At time $t = 2T_{21} + T$, the lines representing the state amplitudes are separated by a phase difference of $\phi_d = -2\mathbf{k} \cdot \mathbf{v}T_{21}$. The phase shift resulting from the atom-field detuning cancels at $t = 2T_{21} + T$, but *not* the phase shift resulting from the Doppler effect. The corresponding density matrix element is

* In the case of atoms moving through spatially separated fields with different longitudinal velocities, one must first average Eq. (44) over *longitudinal* velocities before taking the absolute square to calculate the radiated field. As a result of this averaging, the radiated signal intensity is maximum for $\delta_0 = 0$. Consequently, for spatially separated fields, heterodyne detection or a fourth field is not necessary since the radiated field intensity as a function of δ_0 allows one to determine the line center.

$$\langle \rho_{21}(t) \rangle = i \sin\theta_1 \sin\theta_2 \sin\theta_3 \exp(-\gamma_2 T) \exp(-2\gamma T_{21}) \exp\{-i\delta_0[(t - T_{21} - T) - T_{21}]\}$$
$$\times \exp\left[\frac{-\sigma_\omega^2[(t - T_{21} - T) - T_{21}]^2}{4}\right] \exp\left[\frac{-k^2u^2[(t - T_{21} - T) + T_{21}]^2}{4}\right] \quad (45)$$

Near $t = T + 2T_{21}$, the signal vanishes for a vapor since $kuT_{21} \gg 1$, but gives rise to a phase conjugate signal in solids ($u = 0$). There are no Ramsey fringes in this geometry; optical Ramsey fringes cannot be generated in an inhomogeneously broadened solid.

When the first two fields are *identical,* there is no way to distinguish which field acts first, and Eqs. (44) and (45) must be added before taking the absolute square to determine the radiated electric field. There is no interference between the two terms, however, since one of the terms is approximately equal to zero in the vicinity of the echo for either the solid or the vapor.

24.9 TWO-PHOTON TRANSITIONS AND ATOM INTERFEROMETRY

In the previous section, we have already alluded to the fact that optical Ramsey fringes can serve as the basis of an atom interferometer.[44] There is some disagreement in the literature as to exactly what constitutes an atom interferometer. Ramsey fringes and optical Ramsey fringes were developed without any reference to quantization of the atoms' center-of-mass motion. As such, optical Ramsey fringes can be observed in situations where quantization of the center-of-mass motion is irrelevant. The interference observed in these interferometers is based on an *internal state* coherence of the atoms. Matter-wave effects (that is, effects related to quantization of the center-of-mass motion) may play a role under certain circumstances, but they are not critical to the basic operating principle associated with optical Ramsey fringes.

In this section, we consider a time-domain, matter-wave atom interferometer[83] which relies on the wave nature of the center-of-mass motion for its operation. Moreover, the interferometer illustrates some interesting features of coherent optical transients not found in NMR. We return to an ensemble of two-level atoms, which have been cooled in a magneto-optical trap. See Chap. 28 ("Laser Cooling and Trapping of Atoms") for a more detailed description of trapping of atoms. The atoms are subjected to two *standing-wave* optical pulses separated in time by T. The electric field amplitude of pulse i ($i = 1, 2$) is given by $\mathbf{E}_i(\mathbf{Z}, t) = \boldsymbol{\varepsilon} E_i(t) \cos(kZ) \cos(\omega t)$. Either off-resonant[83,84] or resonant[85] pulses can be used. For resonant pulses, grating echoes can be observed in situations where a classical description of the center-of-mass motion is valid.[66–68] We consider only off-resonant pulses in this discussion, for which echoes can occur only when quantized motion of the atoms is included. For an atom-field detuning $|\delta| \gg \Omega_0, \gamma, \gamma_2, ku$, it is possible to adiabatically eliminate the excited state amplitude and arrive at an effective hamiltonian for the ground state atoms given by

$$H = \frac{P^2}{2M} - \sum_{i=1,2} \hbar\Omega_i^{(s)}(t) \cos(2kZ)$$

where $\mathbf{P}$ is the center-of-mass momentum operator, M is the atomic mass, and

$$\Omega_i^{(s)}(t) = \frac{\mu^2 E(t)}{8\hbar^2\delta}$$

is a two-photon Rabi frequency. A spatially homogeneous term has been dropped from the hamiltonian.

The net effect of the field is to produce a spatially modulated, AC Stark or light shift of the ground state energy. Let us assume that the pulse duration τ is sufficiently short to ensure that $\tau^{-1} \gg \omega_{2k}, \gamma, \gamma_2, ku, \sqrt{\omega_{2k}\Omega_i^{(s)}(t)}$, where

$$\omega_{2k} = \frac{\hbar(2k)^2}{2M}$$

is a two-photon recoil frequency whose importance will become apparent. In this limit, any motion of the atoms during the pulses can be neglected. The net effect of pulse i is to produce a ground state amplitude that varies as exp $[i\theta_i^{(s)} \cos(2kZ)]$, where $\theta_i^{(s)} = \int \Omega_i^{(s)}(t)\, dt$ is a pulse area. In other words, the standing-wave field acts as a *phase grating* for the atoms. One can think of the two traveling-wave components of the standing-wave field exchanging momentum via the atoms. All even integral multiples of $2\hbar k$ can be exchanged by the fields, imparting impulsive momenta of $2n\hbar k$ (n is a positive or negative integer) to the atoms. The frequency change associated with this momentum change for an atom having momentum $\mathbf{P}$ is

$$\frac{E_{\mathbf{P},\,\mathbf{P}\pm 2n\hbar k\hat{Z}}}{\hbar} = \frac{\left(\dfrac{P^2}{2M} - \dfrac{|\mathbf{P}\pm 2n\hbar k\hat{Z}|^2}{2M}\right)}{\hbar} = \mp\frac{2nP_z k}{M} - \omega_{2nk}$$

and consists of two parts. The first part is independent of $\hbar$ and represents a classical Doppler shift, while the second part is proportional to $\hbar$ and represents a quantum matter-wave effect. The quantum contribution will become important for times of order ω_{2nk}^{-1}. In other words, following the first pulse, the atomic density will remain approximately constant for times $t < \omega^{-1}{}_{2nk}$ (the maximum value of n is the larger of $\theta_i^{(s)}$ and unity). For times larger than this, the quantum evolution of the center-of-mass motion can transform the phase grating into an amplitude grating which can be deposited on a substrate or probed with optical fields. In contrast to closed two-level systems, the signals can persist here for arbitrarily long times. The recoil associated with absorption and emission "opens" the system and allows for long-lived transients.[86]

The evolution of the system can be followed using phase diagrams in a manner similar to that used in Secs. 24.6 to 24.8. The situation is more complex, however, since a standing-wave field generates an infinity of different phase shifts $\mp 2nvkt$, where $v = P_z/M$. Details of the calculation can be found in the article by Cahn et al.[83] Here we sketch the general idea. The first pulse creates all even spatial harmonics of the fields, with weighting functions that are Bessel functions of the pulse area. The atomic density remains constant until a time $t \sim \omega_{2nk}^{-1}$. At this time one would expect to find a spatially modulated atomic density; however, if $ku \gg \omega_{2k}$ as is assumed, by the time the spatial modulation is established, the modulation is totally destroyed as a result of Doppler dephasing. As in the photon echo experiment, the Doppler dephasing can be reversed by the second pulse at time $t = T$. Since standing waves are used, there is an infinity of echo positions possible, corresponding to different dephasing-rephasing conditions for the various momentum components created by the fields.

Of the many echoes that can be produced, we consider only those echoes that are formed at times $t_N = (N + 1)T$, $N = 1, 2, \ldots$. Moreover, in an expansion of the atomic density in harmonics of the field, we keep only the second harmonic, since it can be probed by sending in a traveling-wave field and observing a *backscattered* signal. Phase matching is automatically guaranteed for the backscattered signal. For times $t = t_N + t_d$, with $t_d \gtrsim \frac{1}{2}ku \ll T$, the backscattered electric field amplitude varies as[83]

$$E_b(t_d, NT) = \exp\left[\frac{-(2k)^2u^2(t_d)^2}{4}\right] J_N[2\theta_1 \sin(\omega_{2k}t_d)]\, J_{N+1}[2\theta_2 \sin(N\omega_{2k}T + \omega_{2k}t_d)] \qquad (46)$$

where the Js are Bessel functions. The electric field can be measured using a heterodyne technique. The experimental data is shown as a function of t_d and T for $N = 1, 2$ in Figs. 13 and 14. One sees that the signal vanishes identically at the echo times, but not in the immediate vicinity of the echo points. The uniform atomic density at the echo point mirrors the uniform atomic density immediately after excitation by the first pulse. As a function of T, the signal is periodic with period $\pi/N\omega_{2k}$ for N odd and $2\pi/N\omega_{2k}$ for N even. By measuring the period, one can obtain values for $\hbar/M$. The interferometer can also be used to measure inertial effects such as the acceleration of the atoms owing to gravity. The advantage of this interferometer is that large interaction times are possible—one is limited only by the time it takes for the atoms to leave the atom-field interaction zone.

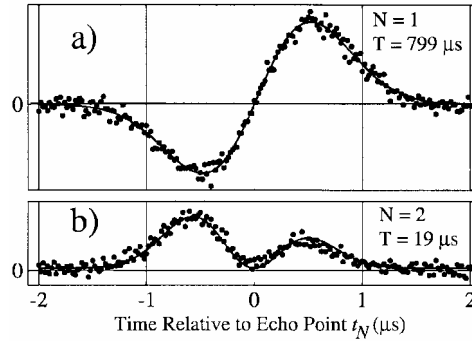

FIGURE 13 A time-domain atom interferometer. Two off-resonant, standing-wave optical pulses separated in time by T are applied to rubidium atoms in a magneto-optical trap and a probe field is applied near (*a*) $t = 2T$ or (*b*) $t = 3T$, giving rise to backscattered electric field signals. The electric field amplitude $E_b(t_d, NT)$ is recorded in the graphs as a function of t_d, the time from the echo position. The solid line is theory and the dots are experimental points. Note that the time delay between pulses is 799 μs in (*a*), indicating that these ground-state transients are limited only by some effective ground-state lifetime. [*From S. B. Cahn, A. Kumarakrishnan, U. Shim, T. Sleator, P. R. Berman, and B. Dubetsky,* Phys. Rev. Lett. ***79:****784 (1997). Reprinted with permission.*]

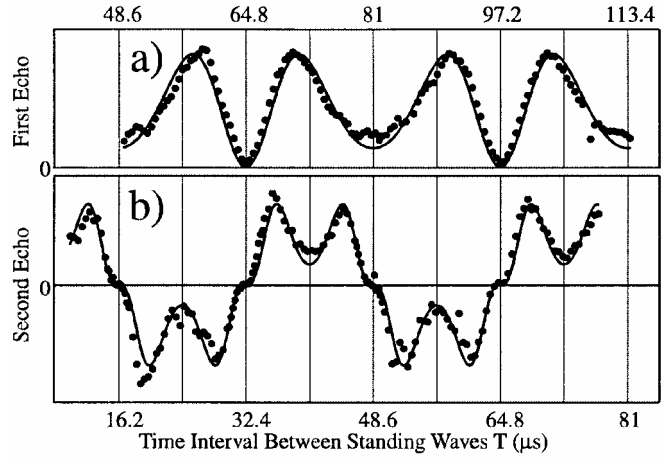

FIGURE 14 Same as in Fig. 13, but $E_b(t_d, NT)$ is now recorded as a function of T, the time separation of the pulses. The period of the signals is $\pi/\omega_{2k} \approx 32.39$ μs. [*From S. B. Cahn, A. Kumarakrishnan, U. Shim, T. Sleator, P. R. Berman, and B. Dubetsky,* Phys. Rev. Lett. ***79:****784 (1997). Reprinted with permission*].

24.10 CHIRPED PULSE EXCITATION

The discussion in this chapter has focused on transform-limited optical pulses, possessing smooth Fourier transforms centered about the carrier frequency. Alternative pulse shapes offer new and interesting possibilities. If one uses *stochastic* pulse envelope functions,[87–89] the correlation time τ_c associated with the pulse is much smaller than the pulse duration. In some sense, *each* pulse can be viewed as a sequence of pulses having duration of order τ_c. As a consequence, stimulated photon echoes using stochastic pulses can be used to measure relaxation times as short as τ_c rather than the pulse duration.

The idea of using a pulse whose effective coherence time is shorter than the pulse duration has been exploited by others[90–92] in schemes involving chirped pulses. It was shown both theoretically[90] and experimentally[91,92] that, by sweeping the pulse frequency, one can write and read data encoded in solids, using the equivalent of stimulated echoes, a process Mossberg[90] refers to as *swept-carrier time-domain optical memory.* Without going into the mathematical details of the calculations needed to arrive at expressions for the signals, we present the underlying physical concepts pertinent to this excitation scheme.

There are three pulses, as in a traditional stimulated photon echo, but the pulse characteristics differ markedly from those discussed in Sec. 24.7. The first pulse is a reference pulse having electric field

$$\mathbf{E}_1(\mathbf{R}, t) = \boldsymbol{\varepsilon} E_1(t) \cos(\mathbf{k}_1 \cdot \mathbf{R} - \bar{\omega}_0 t - \xi t^2)$$

where the amplitude $E_1(t)$ is a smooth function of t centered at $t = 0$ having temporal width τ_{ref} and $\phi(t) = -\xi t^2$ is the pulse phase. The central frequency of the pulse coincides with the optical frequency, but the frequency is chirped at rate 2ξ, giving an instantaneous frequency $\omega(t) = \omega - \dot{\phi} = \omega + 2\xi$ and an atom-field detuning $\delta(t) = \Delta - 2\xi t$. The frequency shifts $\pm\xi\tau_{\text{ref}}$ are assumed to be less than the inhomogeneous width σ_w. As the frequency is scanned, different atoms in the inhomogeneous distribution in the sample come into resonance with the field at different times. If $\sqrt{\xi} \gg \gamma, \tau_{\text{ref}}^{-1}$, for atoms having detuning $\Delta = \omega_0 - \omega$, the field comes into resonance at time $t_1 = \Delta/2\xi$ for a duration of order $\xi^{-1/2} \ll \tau_{\text{ref}}$. Thus, for each frequency group of atoms, the field acts as a *pulse having temporal width much less than the width of the pulse.* In calculating ρ_{12} resulting from this pulse one finds a phase factor of the form $\exp[i(-\mathbf{k}_1 \cdot \mathbf{R} + \Delta t_1 - \xi t_1^2)] = \exp[-i(\mathbf{k}_1 \cdot \mathbf{R} - \Delta^2/4\xi)]$.

The second or data pulse

$$\mathbf{E}_2(\mathbf{R}, t) = \boldsymbol{\varepsilon} E_2(t) \cos[\mathbf{k}_2 \cdot \mathbf{R} - (\bar{\omega}_0 - \omega_{\text{RD}})t - \xi t^2]$$

is similar to the first except that it is offset from the first by frequency ω_{RD}. Moreover, the field amplitude $E_2(t)$ is now assumed to consist of a sequence of input data, such as a number of individual pulses contained in the overall pulse envelope. If the Fourier spectrum of $E_2(t)$ contains frequency components ω_f, then the second pulse will come into resonance with atoms having detuning Δ at time $t_2 = (\Delta + \omega_{\text{RD}} - \omega_f)/2\xi$. To have pulse 2 act on the same atoms at a time greater than t_1, one must restrict the maximum value of ω_f to be less than ω_{RD}. We shall neglect ω_f in what follows. For each frequency group, the first two pulses act as a *sequence of short pulses,* separated in time by

$$T_{21} = \omega_{\text{RD}}/2\xi$$

As in the normal stimulated photon echo, the second pulse converts the density matrix element ρ_{12} created by the first pulse into population. One finds a population difference $(\rho_{22} - \rho_{11})$ that varies as $\exp[-i(\mathbf{k}_1 \cdot \mathbf{R} - \Delta^2/4\xi)] \exp(-\gamma T_{21}) \exp\{i[\mathbf{k}_2 \cdot \mathbf{R} - (\Delta + \omega_{\text{RD}})^2/4\xi]\} + \text{c c}$. Although the pulse durations are of order τ_{ref}, homogeneous decay occurs only on a time scale $T_{21} = \omega_{\text{RD}}/2\xi \ll \tau_{\text{ref}}$, which is the effective pulse separation for a given frequency group. The phase factor $\exp\{i[(\mathbf{k}_2 - \mathbf{k}_1) \cdot \mathbf{R} - \Delta T_{21}]\}$ associated with $(\rho_{22} - \rho_{11})$ is identical in form to that

found in the normal stimulated photon echo. It is not surprising then that a third pulse, identical to the first but propagating in the $\mathbf{k}_3$ direction and displaced in time from the first by $T > \tau_{ref}$ leads to a reconstruction of the data pulse propagating in the $(-\mathbf{k}_1 + \mathbf{k}_2 + \mathbf{k}_3)$ direction. In other words, on averaging over the inhomogeneous frequency distribution, one finds contributions to the signal only for those times that correspond to the time sequence of pulse 2, displaced by time T.

24.11 EXPERIMENTAL CONSIDERATIONS

Early coherent optical transient experiments were the optical analogs of NMR experiments. These experiments firmly established coherent transient spectroscopy as a viable technique in the optical domain. The relatively simple atomic and molecular vapors or rare-earth doped crystals that were used for these studies were chosen for practical reasons—their transition frequencies coincided with available laser frequencies and relaxation times (T_2 is typically on the order of 10 ns or longer) were longer than the lasers' pulse widths. The methodology is well described in numerous earlier reviews (see, for example, Levenson[9]). These relaxation time scales are relatively long by today's standards. Hence, the technology that was available based on photomultipliers, high-speed diodes, and fast oscilloscopes made it possible to observe the coherent transient phenomena that were created by fast laser-frequency or Stark switching. With high-speed detectors, photon echoes were readily observed with single-shot Q-switched lasers.

The continued advances in the development of ultrafast lasers have now reduced the pulse widths by nearly 6 orders of magnitude compared to the early Q-switched lasers. In addition, modern laser systems are characterized by high repetition rates (100 MHz if no amplification is used) compared to the relatively slow repetition rates of older laser systems (1 to 10 Hz). Ultrafast lasers have opened a host of possibilities for studying complex molecules, fluids, and solids, including semiconductors. This new capability was accompanied by new challenges, since standard detectors and electronics were not capable of time-resolving the emitted signals. In some cases, it was not even known whether the materials being investigated were homogeneously or inhomogeneously broadened. For these cases, it is important to check for the asymmetry predicted as a function of time delay in the stimulated photon echo, as described in Sec. 24.7. For the very shortest pulses (typically <100 fs), even the simplest laboratory operations of reflection from a mirror or transmission through a cryostat window or beam splitter become an issue. The transform-limited pulse bandwidth is so large that the linear dispersion in these systems leads to a chirp in the pulse, which can give rise to artifacts in the data if the chirp is not compensated at the sample by incorporation of grating or prism pairs in the system. High-repetition-rate systems also can give rise to thermal heating of the sample, leading to gratings which give signals that easily dominate the electronic signals of interest. Discrimination against these signals is critical. Sometimes, it is possible to perform the measurements of interest using orthogonally polarized fields, giving rise to a signal that is sensitive to spatially modulated magnetic-state coherence, but not thermal gratings. An alternative approach is to amplitude modulate one of the optical fields at a high frequency and use phase-sensitive detection. If the modulation frequency chosen is sufficiently high, then the modulation of the thermal grating is weak, and the electronic term dominates.

In the case of photon echo spectroscopy, determining the time origin $t = 0$ is important for accurate analysis of the signals. Although this does not pose any serious technical problems when dealing with nanosecond time-scale resolution, for femtosecond laser pulses, where distance scales can be as small as a few microns, the problem is not trivial. One solution, discussed in a recent review of photon echo spectroscopy,[73] is to measure the time-integrated signal as a function of pulse separation for the ordinary signal (in the $2\mathbf{k}_2 - \mathbf{k}_1$ direction for self-diffracted four-wave mixing) and the complimentary echo (in the $2\mathbf{k}_1 - \mathbf{k}_2$ direction). The intersection of the two superimposed mirror images allows one to determine the time origin. In some cases, it

may be necessary to time-resolve the emission either to confirm absolutely that the signal is indeed an echo or to determine the inhomogeneous broadening. The usual approach to achieve this goal is to mix some of the original laser beam with the signal beam in a second harmonic crystal and detect the upconverted signal. The signal is time resolved by measuring the upconverted signal as a function of delay between the signal and reference fields.[93,94]

An experimental configuration incorporating many of these features is shown in Fig. 15. Measurements of the dephasing rate are made by monitoring the signal amplitude as a function of time delay between fields E_1 and E_2, while measurements of the energy relaxation rate are made as a function of the time delay between fields E_2 and E_3. In the latter case, measurement of the relaxation rate as a function of the angle between fields E_1 and E_2 allows one to measure the grating (e.g., spatially modulated population) relaxation rate, due, for example, to diffusion.[95] Control of the fields' polarizations is essential in these experiments since the allowed electronic excitation depends critically on the selection rules. The modulator is used to amplitude modulate one of the optical fields to allow phase-sensitive detection. Because of scattering, it may also be necessary in some cases to modulate field E_1 at a different frequency and detect the sum or difference frequency in the lock-in amplifier. The forward three-pulse geometry is most prevalent in the literature; however, the more recently developed phase conjugate geometry shown in the figure is more desirable, owing to reduced incoherent scattering into the detector. In addition, this system is much easier to align, since the signal is exactly counterpropagating with respect to field E_2. Usually, the feedback into the oscillator for spectroscopy applications is small because of the presence of the attenuators. However, for high-intensity studies it may be necessary to add an optical isolator to eliminate feedback, or, as is more typical, simply arrange for a slight misalignment of fields E_1 and E_3. This results in a slight deviation of the signal field from the $-\mathbf{k}_2$ direction, but this poses no problem. It should also be noted that for ultrafast laser systems, the narrow pulses may experience group velocity dispersion (GVD) in propagating through various optical components and in reflection, requiring GVD compensation to avoid artifacts due to frequency chirps. In some cases, additional infor-

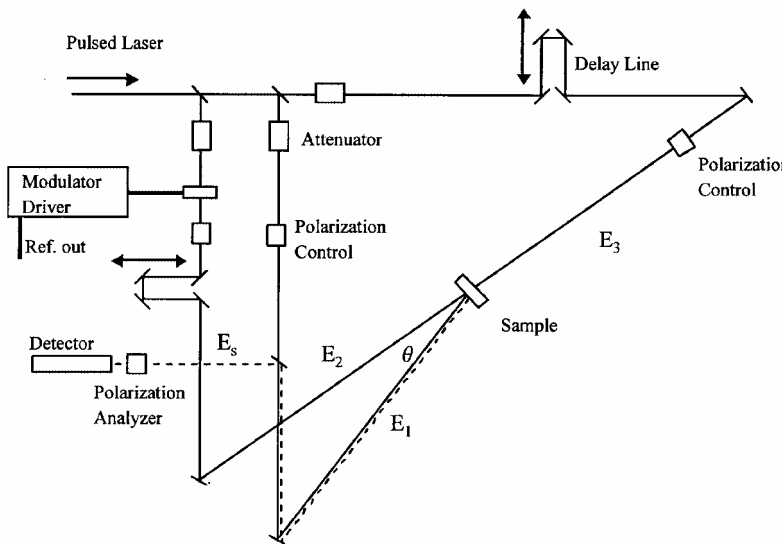

FIGURE 15 A typical experimental configuration, employing a high-repetition short-pulse laser system, that can be used for stimulated photon echo or transient four-wave mixing studies of an arbitrary sample.

mation can be obtained by time-resolving the optical phase[96] and/or polarization[97] of the signal, both of which may change during the time interval in which the signal is emitted.

Atoms undergoing collisions in a vapor and rare-earth-doped solids provided a convenient laboratory environment both to study coherent transients and to examine new physical phenomena associated with reservoir interactions. Moreover, such studies allowed one to gain theoretical and experimental insights upon which the new technology could build. It has now been possible to elevate the utility of these spectroscopic tools for application to more complex systems. In particular, coherent optical transients have yielded important data in both chemical physics[98,99] and condensed-matter physics.[100] In many cases, the theoretical framework described here, with appropriate refinements of the unperturbed hamiltonian and reservoir interactions, can adequately model these systems. For example, local field corrections and excitation-induced scattering can be accounted for by a relatively simple modification of the optical Bloch equations. As a result, additional phase diagrams, with time orderings different from those shown in Figs. 10 and 11, can contribute to echo signals.[101] However, in other cases, a major revision of the theoretical picture is needed to account for more complex many-body interactions.[102–104] An approach based on modified optical Bloch equation may not be appropriate in this limit.

24.12 CONCLUSION

Information on level structure and relaxation processes in vapors, solids, and liquids can be extracted from coherent optical transient signals. The most basic coherent optical transients have been reviewed in this chapter. Coherent optical transient spectroscopy is still an evolving field, as new techniques are being added to established ones. It is likely that one will see increased use of both temporal and spatial masks for coherent control of atomic state coherence. Although many of the coherent optical transients are direct analogs of similar effects in NMR, others are unique to the optical domain. The velocity selectivity associated with the Doppler effect offers unique possibilities. Velocity diffusion has been studied extensively using coherent optical transients, and coherent optical transients are being rediscovered as an important probe of cold atoms and Bose condensates.[105,106] Beyond the gas phase, developments in the area of coherent optical transient spectroscopy are moving very rapidly, as the power of this methodology is seen as a key that can help unlock the decay dynamics of complex molecules and semiconductor systems. One is also examining whether coherent optical transient methods similar to those employed in multidimensional NMR[107,108] can be used to probe electronic and molecular structure.

24.13 ACKNOWLEDGMENTS

This research is supported by the National Science Foundation under grant PHY-9800981, by the U.S. Army Research Office under grants DAAG55-97-0113 and DAAG55-98-1-0373, by the U.S. Air Force Office of Scientific Research under grant F49620-99-1-0045, and by the National Science Foundation through the Center of Ultrafast Optical Science at the University of Michigan under grant STC PHY-8920108.

24.14 REFERENCES

1. H. Metcalf and W. D. Phillips, "Time-Resolved Subnatural-Width Spectroscopy," *Opt. Lett.* **5:**540 (1980); W. D. Phillips and H. J. Metcalf, "Time Resolved Sub-Natural Width Spectroscopy," in *Precision Measurements and Fundamental Constants II,* B. N. Taylor and W. D. Phillips (eds.), U.S. National Bureau of Standards Special Publication 617 (1984).

2. R. G. Brewer, "Coherent Optical Spectroscopy," in *Frontiers in Laser Spectroscopy* (Les Houches, Session 27), R. Balian, S. Haroche, and S. Liberman (eds.) (North-Holland, Amsterdam, 1977), Vol. 1, pp. 341–396.
3. R. G. Brewer, "Coherent Optical Spectroscopy," in *Nonlinear Spectroscopy* (Proc. Int. School Phys., Enrico Fermi, Course 64), N. Bloembergen (ed.) (North-Holland, Amsterdam, 1977).
4. R. G. Brewer, "Coherent Optical Transients," *Physics Today* **30**(5):50 (1977).
5. R. L. Shoemaker, "Coherent Transient Infrared Spectroscopy," in *Laser and Coherence Spectroscopy,* J. I. Steinfeld (ed.) (Plenum Press, New York, 1978), pp. 197–371.
6. R. G. Brewer and E. L. Hahn, "Optical Memory," *Scientific American* **271**(6):50 (1984).
7. Special issue on coherent optical spectroscopy, *J. Opt. Soc. Amer.* **3**(4) (1986).
8. L. Allen and J. Eberly, *Optical Resonance and Two-Level Atoms* (Wiley, New York, 1975), Chaps. 2, 4, and 9.
9. M. D. Levenson and S. S. Kano, *Introduction to Nonlinear Laser Spectroscopy* (Academic Press, Boston, 1988), Chap. 6.
10. P. Meystre and M. Sargent III, *Elements of Quantum Optics* (Springer-Verlag, Berlin, 1991), Chap. 11.
11. T. W. Mossberg, R. Kachru, S. R. Hartmann, and A. M. Flusberg, "Echoes in Gaseous Media: A Generalized Theory of Rephasing Phenomena," *Phys. Rev. A* **20:**1976 (1979).
12. W. Zinth and W. Kaiser "Ultrafast Coherent Spectroscopy," in *Ultrashort Laser Pulses and Applications,* W. Kaiser (ed.), Vol. **60**, Springer Topics in Applied Physics series (Springer-Verlag, Berlin, 1988), pp. 235–277.
13. Special issue on single-molecule spectroscopy, *Science* **283:**1167–1694 (1999).
14. R. P. Feynman, F. L. Vernon, Jr., and R. W. Hellwarth, "Geometrical Representation of the Schrödinger Equation for Solving Maser Problems," *J. Appl. Phys.* **28:**49 (1957).
15. R. G. Brewer and E. L. Hahn, "Coherent Raman Beats," *Phys. Rev. A* **8:**464 (1973).
16. P. Hu, S. Geschwind, and T. M. Jedju, "Spin-Flip Raman Echo in *n*-Type CdS," *Phys. Rev. Lett.* **37:**1357 (1976).
17. T. Mossberg, A. Flusberg, R. Kachru, and S. R. Hartmann, "Tri-Level Echoes," *Phys. Rev. Lett.* **39:**1523 (1977).
18. M. Ducloy, J. R. R. Leite, and M. S. Feld, "Laser Saturation Spectroscopy in the Time-Delayed Mode: Theory of Optical Free Induction Decay in Coupled Doppler-Broadened Systems," *Phys. Rev. A* **17:**623 (1978).
19. N. Lu and P. R. Berman, "Photon Echoes Using Double-Resonance Optical Pulses," *J. Opt. Soc. Amer. B* **2:**1883 (1985).
20. I. V. Yevseyev, V. M. Yermachenko, and V. A. Reshtov, "The Stimulated Photon Echo as a New Method for Measuring Population, Orientation, and Alignment Relaxation Times," *J. Phys. B* **19:**185 (1986).
21. See, for example, R. Boyd, *Nonlinear Optics* (Academic Press, Boston, 1992), Chap. 6, and references therein.
22. See, for example, Y. R. Shen, *The Principles of Nonlinear Optics* (Wiley, New York, 1984), Chap. 17, and references therein.
23. See, for example, J. F. Valley, G. Khitrova, H. M. Gibbs, J. W. Grantham, and X. Jiajin, "CW Conical Emission: First Comparison and Agreement Between Theory and Experiment," *Phys. Rev. Lett* **64:**2362 (1990) and references therein.
24. See, for example, B. D. Paul, M. L. Dowell, A. Gallagher, and J. Cooper, "Observation of Conical Emission from a Single Self-Trapped Beam," *Phys. Rev. A* **59:**4784 (1999), and references therein.
25. A. I. Lvovsky and S. R. Hartmann, "Superradiant Self-Diffraction," *Phys. Rev. A* **59:**4052 (1999).
26. R. G. Brewer and R. L. Shoemaker, "Optical Free Induction Decay," *Phys. Rev. A* **6:**2001 (1972).
27. R. G. Brewer and A. Z. Genack, "Optical Coherent Transients by Laser Frequency Switching," *Phys. Rev. Lett.* **36:**959 (1976).
28. H. Lehmitz and H. Harde, "Measurement of First-Order Free-Induction Decay," in *Methods of Laser Spectroscopy,* Y. Prior, A. Ben-Reuven, and M. Rosenbluh (eds.) (Plenum Press, New York, 1986), pp. 109–112.

29. P. Dubé, M. D. Levenson, and J. L. Hall, "Free-Induction Decay in Molecular Iodine Measured with an Extended-Cavity Diode Laser," *Opt. Lett.* **22:**184 (1997).
30. R. M. Macfarlane and M. Zhu, "Observation of Coherent Transients by Use of Current Switching of a Semiconductor Diode Laser," *Opt. Lett.* **22:**248 (1997).
31. A. Abragam, *The Principles of Nuclear Magnetism* (Oxford University Press, New York, 1961).
32. C. P. Slichter, *Principles of Magnetic Resonance* (Harper & Row, New York, 1963).
33. R. H. Dicke, "Coherence in Spontaneous Radiation Processes," *Phys. Rev.* **93:**99 (1954).
34. See, for example, I. P. Herman, J. C. MacGillivray, N. Skribanowitz, and M. S. Feld, "Self-Induced Emission in Optically Pumped HF Gas: The Rise and Fall of the Superradiant State," in *Laser Spectroscopy,* R. G. Brewer and A. Mooradian (eds.) (Plenum Press, New York, 1974), pp. 379–412.
35. D. Polder, M. F. H. Schuurmans, and Q. H. F. Vrehen, "Superfluorescence: Quantum-Mechanical Derivation of Maxwell-Bloch Description with Fluctuating Field Source," *Phys. Rev. A* **19:**1192 (1979).
36. N. A. Kurnit, I. D. Abella, and S. R. Hartmann, "Observation of a Photon Echo," *Phys. Rev. Lett.* **13:**567 (1964).
37. R. G. Brewer and R. L. Shoemaker, "Photon Echo and Optical Nutation in Molecules," *Phys. Rev. Lett.* **27:**631 (1971).
38. L. S. Vasilenko and N. N. Rubtsova, "Photon Echo in Molecular Gases: I. Spatial, Temporal, Polarization, and Spectral Properties, II. Investigation of Collisional Relaxation," *Laser Phys.* **6:**821 (1996); **7:**903 (1997), and references therein.
39. E. L. Hahn, "Spin Echoes," *Phys. Rev.* **80:**580 (1950).
40. P. R. Berman, "Theory of Collision Effects on Line Shapes Using a Quantum-Mechanical Description of the Atomic Center-of-Mass Motion—Application to Lasers. I," *Phys. Rev. A* **2:**2435 (1970).
41. R. Beach, S. R. Hartmann, and R. Friedberg, "Billiard Ball Echo Model," *Phys. Rev. A* **25:**2658 (1982); R. Friedberg and S. R. Hartmann, "Billiard Balls and Matter-Wave Interferometry," *Phys. Rev. A* **48:**1446 (1993); "Echoes and Billiard Balls," *Laser Phys.* **3:**1128 (1993). See also T. W. Mossberg and S. R. Hartmann, "Diagrammatic Representation of Photon Echoes and Other Laser-Induced Ordering Processes in Gases," *Phys. Rev. A* **23:**1271 (1981).
42. C. J. Bordé, "Atomic Interferometry with Internal State Labeling," *Phys. Lett. A* **140:**10 (1989).
43. R. Friedberg and S. R. Hartmann, "Relaxation and Interferometry via Multiple Order Coherent Scattering in Atomic Vapors," *Laser Phys.* **5:**526 (1993).
44. P. R. Berman (ed.), *Atom Interferometry* (Academic Press, San Diego, 1997).
45. P. W. Anderson, B. I. Halperin, and C. M. Varma, "Anomalous Low Temperature Thermal Properties of Glasses and Spin Glasses," *Phil. Mag.* **25:**1 (1972).
46. W. M. Yen and P. M. Silzer (eds.), *Laser Spectroscopy of Solids,* Vol. **49**, Springer Topics in Applied Physics series (Springer-Verlag, Berlin, 1986).
47. P. R. Berman, "Validity Conditions for the Optical Bloch Equations," *J. Opt. Soc. Amer. B* **3:**564 (1986), and references therein.
48. P. R. Berman, "Markovian Relaxation Processes for Atoms in Vapors and in Solids: Calculation of Free-Induction Decay in the Weak External-Field Limit," *J. Opt. Soc. Amer. B* **3:**572 (1986), and references therein.
49. P. R. Berman, in *New Trends in Atomic Physics* (Les Houches, Session 38), G. Grynberg and R. Stora (eds.) (North-Holland, Amsterdam, 1984), Vol. 1, pp. 451–514.
50. R. G. Devoe and R. G. Brewer, "Experimental Test of the Optical Bloch Equations for Solids," *Phys. Rev. Lett.* **50:**1269 (1983).
51. P. R. Berman, J. M. Levy, and R. G. Brewer, "Coherent Optical Transient Study of Molecular Collisions: Theory and Observations," *Phys. Rev. A* **11:**1668 (1975).
52. T. W. Mossberg, R. Kachru, and S. R. Hartmann, "Observation of Collisional Velocity Changes Associated with Atoms in a Superposition of Dissimilar Electronic States," *Phys. Rev. Lett.* **44:**73 (1980).
53. R. Kachru, T. J. Chen, S. R. Hartmann, T. W. Mossberg, and P. R. Berman, "Measurement of a Total Atomic-Radiator-Perturber Scattering Cross Section," *Phys. Rev. Lett.* **47:**902 (1981).

54. R. A. Forber, L. Spinelli, J. E. Thomas, and M. S. Feld, "Observation of Quantum Diffractive Velocity-Changing Collisions by Use of Two-Level Heavy Optical Radiators," *Phys. Rev. Lett.* **50:**331 (1982).
55. J. C. Keller and J. L. LeGouët, "Stimulated Photon Echo for Collisional Study in Yb Vapor," *Phys. Rev. Lett.* **52:**2034 (1984).
56. A. G. Yodh, J. Golub, and T. W. Mossberg, "Collisional Relaxation of Excited State Zeeman Coherences in Atomic Ytterbium Vapor," *Phys. Rev. A* **32:**844 (1985).
57. R. Kachru, T. W. Mossberg, and S. R. Hartmann, "Stimulated Photon Echo Study of Na($3^2S_{1/2}$)-CO Velocity-Changing Collisions," *Opt. Comm.* **30:**57 (1979).
58. T. Mossberg, A. Flusberg, R. Kachru, and S. R. Hartmann, "Total Scattering Cross Section for Na on He Measured by Stimulated Photon Echoes," *Phys. Rev. Lett.* **42:**1665 (1979).
59. T. W. Mossberg, "Time-Domain Frequency-Selective Optical Storage Data," *Opt. Lett.* **7:**77 (1982).
60. N. W. Carlson, W. R. Babbitt, and T. W. Mossberg, "Storage and Phase Conjugation of Light Pulses Using Stimulated Photon Echoes," *Opt. Lett.* **8:**623 (1983).
61. M. K. Kim and R. Kachru, "Long Term Image Storage and Phase Conjugation by a Backward-Stimulated Echo in $Pr^{3+}LaF_3$," *J. Opt. Soc. Amer. B* **4:**305 (1987).
62. X. A. Shen and R. Kachru, "High Speed Recognition by Using Stimulated Echoes," *Opt. Lett.* **17:**520 (1992).
63. L. S. Vasilenko, N. M. Dyuba, and M. N. Skvortsov, "Coherent Emission in Time-Separated Fields," *Sov. J. Quant. Electron.* **8:**980 (1978).
64. Y. V. Baklonov, B. Y. Dubetsky, and V. P. Chebotaev, "Non-linear Ramsey Resonance in the Optical Region," *Appl. Phys.* **9:**171 (1976).
65. E. V. Baklonov, B. Y. Dubetsky and V. M. Semibalamut, "Theory of Stimulated Coherent Emission from Atoms in Spatially Separated Optical Fields," *Sov. Phys. JETP* **49:**244 (1979).
66. T. W. Mossberg, R. Kachru, E. Whittaker, and S. R. Hartmann, "Temporally Recurrent Spatial Ordering of Atomic Population in Gases: Grating Echoes," *Phys. Rev. Lett.* **43:**851 (1979).
67. J. L. LeGouët and P. R. Berman, "Photon Echoes in Standing Wave Fields: Time Separation of Spatial Harmonics," *Phys. Rev. A* **20:**1105 (1979).
68. R. Kachru, T. W. Mossberg, E. Whittaker, and S. R. Hartmann, "Optical Echoes Generated by Standing Wave Fields: Observations in Atomic Vapors," *Opt. Comm.* **31:**223 (1979).
69. M. V. Belyayev, V. P. Chebotaev, M. N. Skvortsov, and L. S. Vasilenko, "Resonant Coherent Transients in a Gas in the Standing Wave Field," *Appl. Phys. B* **26:**67 (1981).
70. L. S. Vasilenko, I. D. Matveyenko, and N. N. Rubtsova, "Study of Narrow Resonances of Coherent Radiation in Time Separated Fields in SF_6," *Opt. Comm.* **53:**371 (1985).
71. B. Dubetsky, P. R. Berman, and T. Sleator, "Grating Stimulated Echo," *Phys. Rev. A* **46:**2213 (1992).
72. P. R. Berman, "Collisional Decay and Revival of the Grating Stimulated Echo," *Phys. Rev. A* **49:**2922 (1994).
73. A. M. Weiner, S. De Silvestri, and E. P. Ippen, "Three-Pulse Scattering for Femtosecond Dephasing Studies: Theory and Experiments," *J. Opt Soc. Amer. B* **2:**624 (1985).
74. M. Fujita, H. Nakatsuka, H. Nakanishi, and M. Matsuoka, "Backward Echo in Two-Level Systems," *Phys. Rev. Lett.* **42:**974 (1979).
75. A. I. Alekseev and V. N. Beloborodov, "Forward and Backward Photon Echoes in Gases and Solids," *Opt. Spectrosc.* **57:**277 (1984).
76. R. A. Fisher (ed.), *Optical Phase Conjugation* (Academic Press, New York, 1983).
77. M. Gower and D. Proch (eds.), *Optical Phase Conjugation* (Springer-Verlag, Berlin, 1994).
78. J. C. Bergquist, S. A. Lee, and J. L. Hall, "Saturated Absorption with Spatially Separated Laser Fields: Observation of Optical 'Ramsey' Fringes," *Phys. Rev. Lett.* **38:**159 (1977), and references therein.
79. R. L. Barger, "Influence of Second-Order Doppler Effect on Optical Ramsey Fringe Profiles," *Opt. Lett.* **6:**145 (1981).

80. C. J. Bordé, C. Salomon, S. Avrillier, A. Van Lerberghe, C. Bréant, D. Bassi, and G. Scoles, "Optical Ramsey Fringes with Traveling Waves," *Phys. Rev. A* **30:**1836 (1984).
81. N. Ramsey, "A Molecular Beam Resonance Method with Separated Oscillating Fields," *Phys. Rev.* **78:**695 (1950).
82. B. Y. Dubetsky, A. P. Kazantsev, V. P. Chebotaev, and V. P. Yakolev, "Interference of Atoms in Separated Optical Fields," *Sov. Phys. JETP* **62:**685 (1985).
83. S. B. Cahn, A. Kumarakrishnan, U. Shim, T. Sleator, P. R. Berman, and B. Dubetsky, "Time-Domain de Broglie Wave Interferometry," *Phys. Rev. Lett.* **79:**784 (1997).
84. E. M. Rasel, M. K. Oberthaler, H. Batelaan, J. Schmiedmayer, and A. Zeilinger, "Atom Wave Interferometry with Diffraction Gratings of Light," *Phys. Rev. Lett.* **75:**2633 (1995).
85. B. Dubetsky and P. R. Berman, "Matter-Wave Interference Using Two-Level Atoms and Resonant Optical Fields," *Phys. Rev. A* **59:**2269 (1999).
86. J. Guo, P. R. Berman, D. Dubetsky, and G. Grynberg, "Recoil-Induced Resonances in Nonlinear Spectroscopy," *Phys. Rev. A* **46:**1426 (1992).
87. R. Beach and S. R. Hartmann, "Incoherent Photon Echoes," *Phys. Rev. Lett.* **53:**663 (1984).
88. M. Mitsunaga, "CW Photon Echo: Theory and Observations," *Phys. Rev. A* **42:**1617 (1990).
89. See, for example, B. Do, J. Cha, D. S. Elliott, and S. J. Smith, "Phase Conjugate Four Wave Mixing with Partially-Coherent Laser Fields," *Phys. Rev. A* **60:**508 (1999). This paper contains an extensive bibliography citing earlier work in this field.
90. T. W. Mossberg, "Swept-Carrier Time-Domain Optical Memory," *Opt. Lett.* **17:**535 (1992).
91. H. Lin, T. Wang, G. A. Wilson, and T. W. Mossberg, "Experimental Demonstration of Swept-Carrier Time-Domain Optical Memory," *Opt. Lett.* **20:**91 (1995).
92. K. D. Merkel and W. R. Babbitt, "Chirped-Pulse Programming of Optical Coherent Transient True-Time Delay," *Opt. Lett.* **23:**528 (1998).
93. L. Schultheis, M. D. Sturge, and J. Hegarty, "Photon Echoes from Two-Dimensional Excitons in GaAs-AlGaAs Quantum Wells," *Appl. Phys. Lett.* **47:**995 (1985).
94. M. D. Webb, S. T. Cundiff, and D. G. Steel, "Observation of Time-Resolved Picosecond Stimulated Photon Echoes and Free Polarization Decay in GaAs/AlGaAs Multiple Quantum Wells," *Phys. Rev. Lett.* **66:**934 (1991).
95. H. J. Eichler, P. Günter, and D. W. Pohl, *Laser-Induced Dynamic Gratings* (Springer-Verlag, Berlin, 1986).
96. J. Y. Bigot, M. A. Mycek, S. Weiss, R. G. Ulbrich, and D. S. Chemla, "Instantaneous Frequency Dynamics of Coherent Wave Mixing in Semiconductor Quantum-Wells," *Phys. Rev. Lett.* **70:**3307 (1993).
97. A. L. Smirl, "Coherent Exciton Dynamics: Time-Resolved Polarimetry," in *Semiconductor Quantum Optoelectronics: From Quantum Physics to Smart Devices,* A. Miller and D. M. Finlayson (eds.) (Institute of Physics, London, 1999).
98. C. J. Bardeen, W. Wang, and C. V. Shank, "Femtosecond Chirped Pulse Excitation of Vibrational Wave Packets in LD690 and Bacteriorhodopsin," *J. Phys. Chem. A* **102:**2759 (1998).
99. W. P. de Boeij, M. S. Pshenichnikov, and D. A. Wiersma, "Ultrafast Solvation Dynamics Explored by Femtosecond Photon Echo Spectroscopies," *Ann. Rev. Phys. Chem.* **49:**99 (1998).
100. J. Shah, *Ultrafast Processes in Semiconductors and Semiconductor Nanostructures,* Vol. 115 in Springer Solid-State Sciences series (Springer, Berlin, 1996).
101. See, for example, H. Wang, K. B. Ferrio, D. G. Steel, P. R. Berman, Y. Z. Hu, R. Binder, and S. W. Koch, "Transient Four-Wave Mixing Line Shapes: Effects of Excitation Induced Dephasing," *Phys. Rev. A* **49:**1551 (1994).
102. H. Haug and S. W Koch, *Quantum Theory of the Optical and Electronic Properties of Semiconductors* (World Scientific, Singapore, 1993).
103. C. Sieh, T. Meier, F. Jahnke, A. Knorr, S. W. Koch, P. Brick, M. Hübner, C. Ell, J. Prineas, G. Khitrova, and H. M. Gibbs, "Coulomb Memory Signatures in the Excitonic Optical Stark Effect," *Phys. Rev. Lett.* **82:**3112 (1999).

104. D. S. Chemla, "Ultrafast Transient Nonlinear Optical Processes in Semiconductors," *Semiconductors and Semimetals* **58:**175 (1999).

105. J. Stenger, S. Inouye, A. P. Chikkatur, D. M. Stamper-Kurn, D. E. Pritchard, and W. Ketterle, "Bragg Spectroscopy of a Bose-Einstein Condensate," *Phys. Rev. Lett.* **82:**4569 (1999).

106. Y. B. Ovchinnikov, J. H. Müller, M. R. Doery, E. J. D. Vredenbregt, K. Helmerson, S. L. Rolston, and W. D. Phillips, "Diffraction of a Released Bose-Einstein Condensate by a Pulsed Standing Light Wave," *Phys. Rev. Lett.* **83:**284 (1999).

107. S. Mukamel, A. Piryatinski, and V. Chernyak, "Two-Dimensional Raman Echoes: Femtosecond View of Molecular Structure and Vibrational Coherence" *Accts. Chem. Res.* **32:**145 (1999).

108. P. Hamm, M. Lim, W. F. DeGrado, and R. M. Hochstrasser, "The Two-Dimensional IR Nonlinear Spectroscopy of a Cyclic Penta-peptide in Relation to its Three-Dimensional Structure," *Proc. Natl. Acad. Sci. USA* **96:**2036 (1999).

CHAPTER 25

NONLINEAR OPTICAL PROCESSES FOR ULTRASHORT PULSE GENERATION

U. Siegner and U. Keller
Institute of Quantum Electronics
Physics Department
Swiss Federal Institute of Technology (ETH)
Zürich, Switzerland

25.1 GLOSSARY

A_A	laser beam cross section on the absorber
A_L	laser beam cross section in the laser gain material. If the cavity mode is not constant inside the gain medium, this area corresponds to an effective averaged value.
c	light velocity in vacuum
D_2	total group delay dispersion inside the laser cavity per cavity round-trip (i.e., second-order dispersion)
d	sample thickness
DR	differential reflectivity
DT	differential transmission
E_p	intracavity pulse energy
$E_{\mathrm{sat},A}$	saturation energy of the saturable absorber
$E_{\mathrm{sat},L}$	saturation energy of laser material
$F_{\mathrm{p},A}$	pulse fluence on the absorber

$$F_{p,A} = \frac{E_p}{A_A} = \int I_A(t)\mathrm{dt}$$

Copyright 2001 by The McGraw-Hill Companies, Inc. Click Here for Terms of Use.

$F_{\text{sat},A}$ saturation fluence of the absorber

$$F_{\text{sat},A} = \frac{E_{\text{sat},A}}{A_A}$$

$F_{\text{sat},L}$ saturation fluence of laser material

$$F_{\text{sat},L} = \frac{h\nu}{2\sigma_L} = \frac{\mathrm{E}_{\text{sat},L}}{A_L}$$

The factor of 2 is used in case of a linear resonator with a standing wave.

g saturated amplitude gain cross section

g_0 small signal amplitude gain coefficient

$I(t)$ time-dependent intensity

$I_A(t)$ time-dependent intensity on absorber

$I_L(t)$ time-dependent intensity inside the laser gain material

$I_{\text{sat},A}$ saturation intensity of the absorber

$$I_{\text{sat},A} = \frac{F_{\text{sat},A}}{\tau_A}$$

$I_{\text{sat},L}$ saturation intensity of laser material

$$I_{\text{sat},L} = \frac{F_{\text{sat},L}}{\tau_L}$$

k wave number in vacuum $k = \omega/c = 2\pi/\lambda$

k_n wave number in a dielectric with refractive index n: $k_n = kn$

$\mathbf{k}_1$ wave vector of the pump pulse in a pump-probe experiment or of the first pulse applied in a FWM experiment for positive time delay Δt

$\mathbf{k}_2$ wave vector of the probe pulse in a pump-probe experiment or of the second pulse applied in a FWM experiment for positive time delay Δt

L_L length of the laser gain medium

n_2 nonlinear refractive index

$P(t)$ time-dependent power: $E_p = \int P(t)dt$

$q(t)$ saturable amplitude loss coefficient (does not include any nonsaturable losses)

q_0 unsaturated amplitude loss coefficient, also corresponds to the maximal loss coefficient

α intensity absorption constant

$\Delta\alpha$ nonlinear change of the intensity absorption constant

ΔR maximum modulation depth of a saturable absorber integrated within a mirror structure (i.e., the maximum nonlinear intensity reflectivity change)

ΔR_{ns} nonsaturable loss of a saturable absorber integrated within a mirror structure

Δt time delay between the excitation pulses in a pump-probe or FWM experiment

ν	frequency
ν_0	center frequency
$\Delta\nu_g$	FWHM (full width half maximum) gain bandwidth
λ	wavelength in vacuum
λ_n	wavelength in a dielectric medium with a refractive index n
λ_0	center wavelength
σ_L	gain cross section: $F_{\text{sat, L}} = h\nu/\sigma_L$, where h is the Planck's constant
σ_A	absorber cross section: $F_{\text{sat, A}} = h\nu/\sigma_A$
τ_p	FWHM (full width half maximum) of pulse intensity
τ_A	recovery time of the saturable absorber
τ_L	upper state lifetime of laser medium

25.2 ABBREVIATIONS

A-FPSA	antiresonant Fabry-Perot saturable absorber
APM	additive pulse modelocking
As_{Ga}	arsenic antisite
As_{Ga}^{0}	neutral arsenic antisite
As_{Ga}^{+}	ionized arsenic antisite
CB	conduction band
CPM	colliding pulse modelocking
FWHM	full width half maximum
FWM	four-wave mixing
KLM	Kerr lens modelocking
LT	low temperature
MBE	molecular beam epitaxy
MOCVD	metal-organic chemical vapor deposition
SAM	self-amplitude modulation
SBR	saturable Bragg reflector
SESAM	semiconductor saturable absorber mirror
SPM	self-phase modulation
V_{Ga}	Ga vacancy
VB	valence band

25.3 INTRODUCTION

Since 1990 we have observed tremendous progress in ultrafast laser sources—a development that was triggered by the invention of the Ti:sapphire laser.[1] The strong interest in all-solid-state ultrafast laser technology was the driving force and formed the basis for many new inventions and discoveries. Solid-state lasers provide some of the best laser qualities in terms of high-quality spatial modes, high output power, energy storage and large pulse energy

when Q-switched, and large optical bandwidth necessary for ultrashort pulse generation. Today, the most important nonlinear optical processes that support short and ultrashort passive pulse generation are based on Kerr and/or semiconductor nonlinearities. Saturable absorbers based on either the Kerr effect or on semiconductors play a major role in ultrashort pulse generation. However, independent of the specific saturable absorber material or mechanism, we can define a few macroscopic saturable absorber parameters that will determine the pulse formation process. These parameters are defined in Sec. 25.4 and discussed in more detail for the specific cases of a slow and a fast saturable absorber. The material properties then can be modified over an even larger range if the absorber is integrated within a device structure. This will be discussed at the end of Sec. 25.4. Stable pulse generation can then be obtained when these macroscopic saturable absorber parameters are designed correctly. The crucial role of the optical Kerr effect in ultrashort pulse generation will be discussed in Sec. 25.5. Optimization of semiconductor saturable absorber parameters normally requires a better understanding of the underlying physics, that is, the microscopic properties (Sec. 25.6). Ultrafast nonlinear optical processes can be analyzed in various ways to extract the information about the material system involved in the process. Numerous studies with ultrafast laser pulses have been performed in atomic, molecular, and condensed matter systems. Thus, some of the most common experimental techniques in ultrafast spectroscopy will also be reviewed in Sec. 25.6. The results of such ultrafast spectroscopy measurements are then summarized for semiconductor materials because of their importance in ultrashort pulse generation.

Today ultrafast lasers demonstrate unsurpassed performances: pulse duration in the two-cycle regime,[2,3] compact and reliable picosecond and femtosecond all-solid-state lasers,[4,5] pulse repetition rates in the multi-10-GHz regime,[6,7] average powers well above 10 W,[8] and novel Q-switching performances that bridge the gap between modelocking and Q-switching both in terms of pulse durations and pulse repetition rates.[9]

Optical pulses in the two-cycle regime have been produced by a variety of methods: direct generation in a modelocked laser oscillator,[2,3] continuum generation together with parametric optical amplification,[10] and external pulse compression.[11,12] In Fig. 1, interferometric autocorrelation measurements of the two-cycle pulses are shown. Although this is a relatively crude characterization technique, it is the only common measurement that has been performed on these sources; thus it allows for a direct comparison. These pulse generation techniques rely essentially on three identical ingredients[13]: (1) an ultrabroadband amplifying process, (2) precise control of dispersion, and (3) the nonlinear optical Kerr effect.

Ultrafast all-solid-state lasers are based on diode-pumped solid-state lasers. Semiconductor saturable absorbers were the first intracavity saturable absorbers that reliably started and sustained passive modelocked diode-pumped solid-state lasers.[14,15] Any previous attempts to passively modelock such lasers with intracavity saturable absorbers resulted in Q-switching instabilities or Q-switched modelocking (see Fig. 2). The precise control of optical nonlinearities was necessary to resolve the Q-switching problem. Such a control can be achieved with epitaxially grown semiconductor saturable absorbers, which makes them very attractive for use as saturable absorbers in solid-state lasers. Semiconductor saturable absorbers provide a variety of bandgaps, ranging from the visible to the infrared, and can be easily integrated into different device structures (such as a mirror, for example), which allows for the control of the absorber parameters over an even larger range. This is actually required to obtain stable pulse generation with many solid-state lasers. The specific saturable absorber nonlinearities required for stable cw modelocking or Q-switching have recently been discussed in much more detail in Ref. 4 and will be briefly summarized in Sec. 25.4.

In this section we will put the emphasis on the nonlinearities used for ultrashort pulse generation. It is not our goal to provide a tutorial for pulse generation techniques such as passive modelocking or Q-switching. A more tutorial-type overview of the physics of ultrashort pulse generation was given in Refs. 5, 16, and 17. We would like to refer the interested readers to those chapters and the extensive references therein.

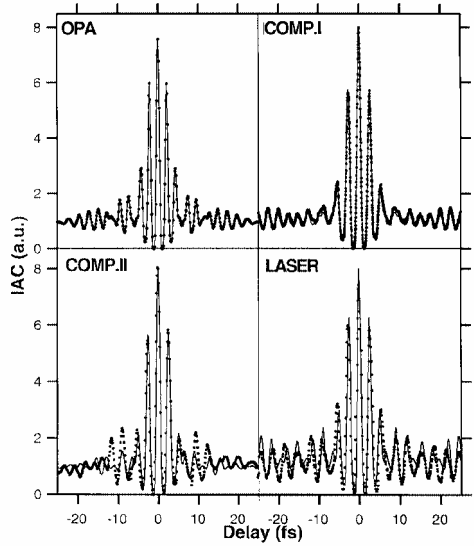

FIGURE 1 Interferometric autocorrelation measurements of different sources in the 5-fs range: OPA: optical parametric amplification.[10] Comp. I: compression of Ti:sapphire cavity-dumped pulses in silica fiber.[11] Comp. II: compression of amplified μJ pulses in a hollow fiber filled with Krypton.[12] Laser: pulses directly obtained from a Ti:sapphire laser without any external pulse compression.[2] Dots are measured data and lines correspond to fits that were used to estimate pulse duration from autocorrelation.

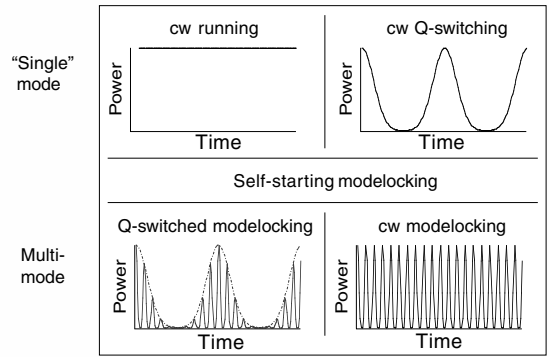

FIGURE 2 Different modes of operation of a laser with a saturable absorber. Continuous wave (cw) Q-switching typically occurs with much longer pulses and lower pulse repetition rates than cw modelocking.

25.4 SATURABLE ABSORBERS: MACROSCOPIC DESCRIPTION

Saturable Absorber: Self-Amplitude Modulation (SAM)

Saturable absorbers have been used to passively Q-switch and modelock many different lasers. Different saturable absorbers, such as organic dyes, colored filter glasses, dye-doped crystals, and semiconductors have been used. Independent of the specific saturable absorber material, we can define a few macroscopic absorber parameters that will determine the pulse generation process. The macroscopic properties of a saturable absorber are the modulation depth, the nonsaturable loss, the saturation fluence, the saturation intensity, and the impulse response or recovery times. These parameters determine the operation of a passively modelocked or Q-switched laser. In our notation we assume that the saturable absorber is integrated within a mirror structure. Thus we are interested in the nonlinear reflectivity change or the *differential reflectivity* DR(t) as a function of time or in the reflectivity $R(F_{p,A})$ as a function of the incident pulse energy fluence on the saturable absorber. If the saturable absorber is used in transmission, we simply characterize the absorber by nonlinear transmission measurements. Both the saturation fluence $F_{\text{sat},A}$ and the absorber recovery time τ_A are determined experimentally without any need to determine the microscopic properties of the nonlinearities. Thus, the saturation fluence of the absorber is not only dependent on material properties but also on the specific device structure the absorber is integrated in.

Standard pump-probe techniques determine the impulse response DR(t) and therefore τ_A (see Fig. 3). In the picosecond regime we normally only have to consider one recovery time, because much faster femtosecond nonlinearities in the saturable absorber result in a negligible modulation depth. This is shown in Fig. 3, where the impulse response DR(t) was measured for two different excitation pulse durations. For excitation with a picosecond pulse, the pump-probe trace clearly shows no significant modulation depth with a fast time constant. In the femtosecond pulse regime we normally have to consider more than one absorber recovery time. In this case the slow component normally helps to start the initial pulse formation process. The modulation depth of the fast component then determines the pulse duration at steady state. Further improvements of the saturable absorber normally require some better understanding of the underlying physics, which will be discussed in more detail in Sec. 25.6.

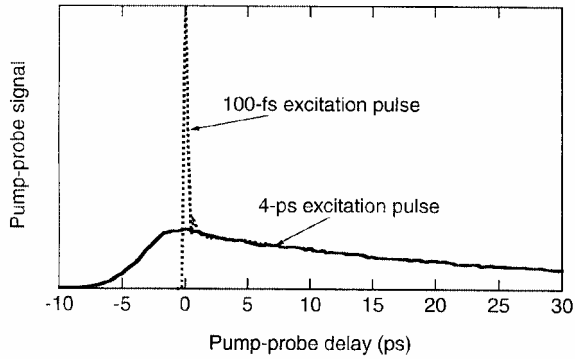

FIGURE 3 Standard pump-probe techniques determine the impulse response DR(t). (Here we assume that the saturable absorber is integrated within a mirror structure.) DR(t) for the same saturable absorber is different for different excitation pulse durations. For excitation with a picosecond pulse, the pump-probe trace clearly shows no significant modulation depth with a fast time constant.

The saturation fluence $F_{sat,A}$ is determined and defined by the measurement of the nonlinear change in reflectivity $R(F_{p,A})$ as a function of increased incident pulse fluence (see Fig. 4). The common traveling wave rate equations[18] in the slow absorber approximation normally give a very good fit and determine the saturation fluence $F_{sat,A}$, modulation depth ΔR, and nonsaturable losses ΔR_{ns} of the absorber. The modulation depth is typically small to prevent Q-switching instabilities in passively modelocked solid-state lasers.[19] Thus it is reasonable to make the following approximation:

$$\Delta R = 1 - e^{-2q_0} \approx 2q_0,\ q_0 \ll 1 \tag{1}$$

where q_0 is the unsaturated amplitude loss coefficient. Here, it is assumed that the nonsaturable losses are negligible.

The saturation of an absorber can be described with the following differential equation[18]:

$$\frac{dq(t)}{dt} = -\frac{q(t) - q_0}{\tau_A} - \frac{q(t)P(t)}{E_{sat,A}} \tag{2}$$

where $q(t)$ is the saturable amplitude loss coefficient that does not include any nonsaturable losses. At any time t the reflected (or transmitted) intensity $I_{out}(t)$ from the saturable absorber is given by

$$I_{out}(t) = R(t)I_{in}(t) = e^{-2q(t)}I_{in}(t) \tag{3}$$

Then the total net reflectivity is given by

$$R_{tot} = \frac{\int I_{out}(t)dt}{\int I_{in}(t)dt} = \frac{F_{out}}{F_{in}} = 1 - \frac{2}{F_{in}} \int q(t)I_{in}(t)dt \tag{4}$$

This determines the total absorber loss coefficient q_p, which results from the fact that part of the excitation pulse needs to be absorbed to saturate the absorber:

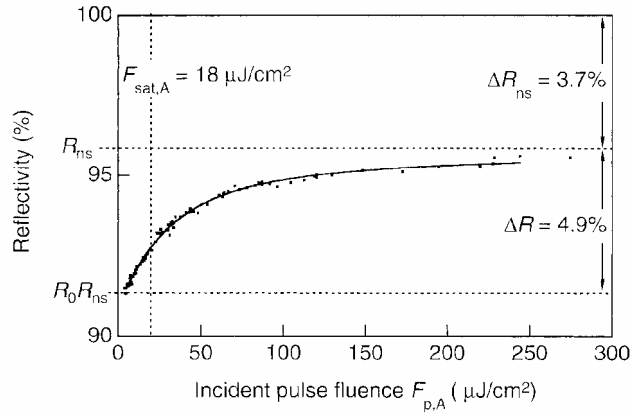

FIGURE 4 Nonlinear Reflectivity as function of the incident pulse fluence $R(F_{p,A})$. The measurement was made with a SESAM supporting 34-fs pulses in a Ti:sapphire laser. The measurements are fitted with common traveling wave rate equations[18] in the slow absorber approximation which normally give a very good fit and determine the saturation fluence $F_{sat,A}$, modulation depth ΔR, and nonsaturable losses ΔR_{ns} of the absorber.

$$R_{\text{tot}} = e^{-2q_p} \approx 1 - 2q_p \tag{5}$$

From Eqs. (4) and (5) it then follows that for $q_p \ll 1$

$$q_p = \frac{1}{F_{\text{in}}} \int q(t) I_{\text{in}}(t) dt = \int q(t) f(t) dt \tag{6}$$

where

$$f(t) \equiv \frac{I_{\text{in}}(t)}{F_{\text{in}}} = \frac{P_{\text{in}}(t)}{E_{p,\text{in}}}, \qquad \text{with} \quad \int f(t) dt = \frac{1}{F_{\text{in}}} \int I_{\text{in}}(t) dt = 1 \tag{7}$$

We then distinguish between two typical cases: a slow and a fast saturable absorber.

Slow Saturable Absorber

In the case of a slow saturable absorber, we assume that the excitation pulse duration is much shorter than the recovery time of the absorber (i.e., $\tau_p \ll \tau_A$). Thus, we can neglect the recovery of the absorber during pulse excitation, and Eq. (2) reduces to:

$$\frac{dq(t)}{dt} \approx -\frac{q(t)P(t)}{E_{\text{sat},A}} \tag{8}$$

This differential equation can be solved, and we obtain for the self-amplitude modulation (SAM):

$$q(t) = q_0 \exp\left[-\frac{E_{\text{p}}}{E_{\text{sat, A}}} \int_0^t f(t')dt'\right] \tag{9}$$

Equation (6) then determines the total absorber loss coefficient for a given incident pulse fluence $F_{p,A}$:

$$q_p(F_{p,A}) = \int q(t) f(t) dt = q_0 \frac{F_{\text{sat},A}}{F_{p,A}} (1 - e^{-F_{p,A}/F_{\text{sat},A}}) \tag{10}$$

It is not surprising that q_p does not depend on any specific pulse form, because $\tau_p \ll \tau_A$.

A slow saturable absorber has been successfully used to passively modelock dye and semiconductor lasers. In this case, dynamic gain saturation was supporting the pulse formation process (Fig. 5*a*), and much shorter pulses than the recovery time of the saturable absorber were obtained.[20,21] Dynamic gain saturation means that the gain experiences a fast pulse-induced saturation that then recovers again between consecutive pulses. Therefore, an ultrashort net-gain window can be formed by the combined saturation of absorber and gain for which the absorber has to saturate and recover faster than the gain, while the recovery time of the saturable absorber can be much longer than the pulse duration. Haus's master equation formalism can describe this passive modelocking technique very well.[22] This formalism is based on linearized differential operators that describe the temporal evolution of a pulse envelope inside the laser cavity. Generally, the linearized master equations of Haus describe modelocking very well, as long as they only have to deal with small nonlinearities and loss modulation. This is true for most lasers; otherwise a strong tendency for instabilities is observed. A review of Haus's modelocking formalism is presented in more recent articles and book chapters.[5,17,23] Assuming passive modelocking according to Fig. 5*a,* Haus predicts a modelocked pulse duration for a fully saturated absorber

$$\begin{aligned} \tau &\approx \frac{4}{\pi} \frac{1}{\Delta \nu_g} \\ \tau_{\text{p}} &\approx 1.76 \times \frac{4}{\pi} \frac{1}{\Delta \nu_g} \end{aligned} \tag{11}$$

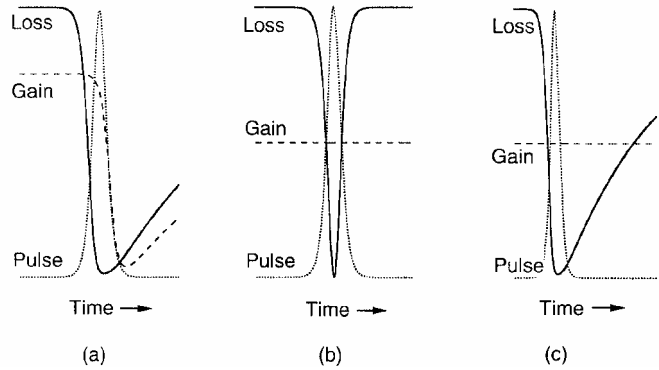

FIGURE 5 Passive modelocking mechanisms explained by three fundamental models: (*a*) slow saturable absorber modelocking with dynamic gain saturation, (*b*) fast saturable absorber modelocking, and (*c*) soliton modelocking.

with a predicted pulse form of

$$I(t) = I_0 \operatorname{sech}^2(t/\tau), \qquad \tau_p = 1.76 \cdot \tau \tag{12}$$

where τ_p is the FWHM pulse width of the pulse intensity. For dye lasers using Rhodamin 6G with a gain bandwidth $\Delta\nu_g \approx 4 \cdot 10^{13}$ Hz and DODCI as the saturable absorber with a absorber cross section $\sigma_A = 0.52 \cdot 10^{-16}$ cm^2, we would then predict a pulse duration τ_p of 56 fs at a center wavelength of 620 nm [Eqs. (11) and (12)]. Slightly shorter pulses of 27 fs duration were demonstrated.[24,25] The interplay of self-phase modulation and negative group velocity dispersion can result in pulses that are shorter than would be predicted by the SAM alone [Eq. (10)]. Martinez estimated the additional pulse shortening to be about a factor of 2.[26,27] This will be discussed in Sec. 25.5.

For solid-state lasers we cannot apply slow saturable absorber modelocking as shown in Fig. 5*a,* because no significant dynamic gain saturation is taking place, due to the small gain cross section and the long upper state lifetime of the laser. The gain cross section of ion-doped solid-state lasers is typically 10^{-19} cm^2 and smaller. This is at least 1000 times smaller than dye, semiconductor, or color center lasers. In addition, the upper-state lifetime of ion-doped solid-state lasers is typically in the μs to ms regime—much longer than the pulse repetition period that is typically in the ns regime. We therefore do not observe any significant dynamic gain saturation, and the gain is only saturated to a constant level by the average intracavity intensity (Fig. 5*b* and *c*).

Fast Saturable Absorber

In the case of a fast saturable absorber, the absorber recovery time is much faster than the pulse duration (i.e., $\tau_p \gg \tau_A$). Thus, we can assume that the absorption instantaneously follows the absorption of a certain power $P(t)$, and Eq. (2) reduces to

$$0 = -\frac{q(t) - q_0}{\tau_A} - \frac{q(t)P(t)}{E_{\text{sat},A}} \tag{13}$$

The saturation of the fast absorber then follows directly from Eq. (13):

$$q(t) = \frac{q_0}{1 + \dfrac{I_A(t)}{I_{\text{sat, }A}}} \tag{14}$$

where we used the fact that $P_{\text{sat, A}} = E_{\text{sat, }A}/\tau_A$ and $P(t)/P_{\text{sat, }A} = I_A(t)/I_{\text{sat, }A}$. In the linear regime we can make the following approximation in Eq. (14):

$$q(t) \approx q_0 - \gamma I_A(t), \text{ with } \quad \gamma \equiv \frac{q_0}{I_{\text{sat, }A}} \tag{15}$$

The total absorber loss coefficient q_p [Eqs. (10) to (12)] now depends on the pulse form, and for a sech^2-pulse shape we obtain for an incident pulse fluence $F_{p,A}$ and the linear approximation of $q(t)$ (Eq. 15):

$$q_p(F_{p,A}) = \frac{1}{F_{p,A}} \int q(t) I_A(t) dt = q_0 \left(1 - \frac{1}{3} \frac{F_{p,A}}{\tau I_{\text{sat, }A}}\right) \tag{16}$$

We only obtain an analytic solution for fast saturable absorber modelocking if we assume an ideal fast absorber that saturates linearly with pulse intensity over the full modulation depth [Eq. (15)]. For a maximum modulation depth, we then can assume that $q_0 = \gamma I_{0,A}$, where $I_{0,A}$ is the peak intensity on the saturable absorber. We then obtain with Eq. (16) a residual saturable absorber loss of $q_0/3$, which the pulse experiences to fully saturate the ideal fast saturable absorber.

A fast saturable absorber has been sucessfully used to passively modelock solid-state lasers (Fig. 5*b*). An analytical solution with Haus's master formalism[28] is only obtained if we assume an ideal fast saturable absorber that produces a decreased loss directly proportional to intensity of the incident laser pulse [Eq. (15)]. Then again a sech^2-pulse shape [Eq. (12)] with the following pulse duration is predicted

$$\tau_p = 1.76 \frac{4D_g}{\gamma F_{p,A}}, \text{ with } \quad D_g = \frac{g}{\pi^2 (\Delta \nu_g)^2} \tag{17}$$

where D_g is the gain dispersion. Unfortunately, fast saturable absorbers with femtosecond recovery times are often not sufficient for reliable self-starting of the modelocking process. In passive modelocking, pulse formation should start from normal noise fluctuations in a laser. One noise spike is strong enough to start saturating the absorber and thereby lowers the loss. This noise spike begins to grow in amplitude and becomes shorter until a stable pulse duration is obtained. Initially, these noise spike durations are on the order of the cavity round-trip time, introducing only very small loss modulations in a fast saturable absorber (see Fig. 3). A combination of a fast and a slow saturable absorber can help to solve this problem. Thus, semiconductor saturable absorbers are very interesting because they typically have a bitemporal impulse response which even can be modified.

For picosecond solid-state lasers, the self-amplitude modulation of a fast saturable absorber with a picosecond recovery time is sufficient for stable pulse generation. A picosecond recovery time can be achieved with low-temperature-grown semiconductor saturable absorbers where midgap defect states form very efficient traps for the photoexcited electrons in the conduction band. A more detailed description of the microscopic nonlinearities is given in Sec. 25.6. In the picosecond regime, we developed a very simple stability criteria for stable passive modelocking without Q-switching instabilities[19]:

$$E_p^2 > E_{p,c}^2 = E_{\text{sat, }L} E_{\text{sat, }A} \Delta R \tag{18}$$

The critical intracavity pulse energy $E_{p,c}$ is the minimum intracavity pulse energy that is required to obtain stable cw modelocking; that is, for $E_p > E_{p,c}$ we obtain stable cw modelocking and for $E_p < E_{p,c}$ we obtain Q-switched modelocking (see Fig. 2). For good stability of a mode-

locked laser against unwanted fluctuations of pulse energy, operation close to the stability limit is not recommended. Thus, a large modulation depth supports shorter pulses [Eqs. (1), (15), and (17)], but an upper limit is given by the onset of self-Q-switching instabilities [Eq. (18)].

Semiconductor Saturable Absorber Mirrors (SESAMs)

Semiconductor saturable absorbers were used as early as 1974 in CO_2 lasers and as early as 1980 for semiconductor diode lasers. A color center laser was the first solid-state laser that was cw modelocked with an intracavity semiconductor saturable absorber.[29] However, for both the diode and color center laser, dynamic gain saturation supported pulse formation, and a slow saturable absorber was sufficient for pulse generation (Fig. 5*a*). In addition, because of the much larger gain cross section and therefore smaller saturation energy $E_{sat,L}$ [Eq. (18)] (i.e., typically 1000 to 10,000 times smaller than ion-doped solid-state lasers), Q-switching instabilities were not a problem. Thus, semiconductor saturable absorber parameters (see Figs. 3 and 4) have to be chosen much more carefully for stable cw modelocking.

We typically integrate the semiconductor saturable absorber into a mirror structure that results in a device whose reflectivity increases as the incident optical intensity increases. This general class of device is called a *semiconductor saturable absorber mirror* (SESAM).[14,30] A detailed description and guidelines on how to design a SESAM for either passive modelocking or Q-switching for different laser parameters is given in Ref. 4. Such a SESAM device structure can be a simple Bragg mirror, where at least one quarter-wave-layer contains an absorber layer (saturable Bragg reflector -SBR).[31–33] A larger parameter range for the saturation fluence and modulation depth can be achieved if the saturable absorber is integrated inside a Fabry-Perot structure that is operated at antiresonance (A-FPSA).[14,34] The antiresonant Fabry-Perot structure is broadband and can be designed to have no significant bandwidth limitations even in the sub-10-fs pulse-width regime.[35] The top reflector of the A-FPSA provides an adjustable parameter that determines the intensity entering the semiconductor saturable absorber and therefore the saturation fluence of the saturable absorber device. A SiO_2/TiO_2 dielectric top reflector has an additional advantage in that the damage threshold for this SESAM design is significantly higher compared to a SESAM design with the same saturation fluence but based on semiconductor materials alone.

More recently, semiconductor-doped dielectric films have been demonstrated for saturable absorber applications.[36] Semiconductor-doped glasses have been used to modelock lasers as early as 1990.[37] However, the recently developed InAs-doped thin-film rf-sputtering technology offers similar advantages as SESAMs, which allows for the integration of the absorber into a device structure. At this point, however, the saturation fluence of ≈10 mJ/cm^2 is still rather high for stable solid-state laser modelocking [Eq. (18)]. In comparison, MBE or MOCVD-grown SESAMs have typically a saturation fluence of ≈10 μJ/cm^2, even though they can be modified from the μJ/cm^2 to the mJ/cm^2-range depending on the specific device structure.[4,30]

A more detailed discussion of microscopic semiconductor nonlinearities will be presented in Sec. 25.6. In principle, knowledge of the macroscopic absorber parameters is sufficient to understand pulse generation. However, further improvements of saturable absorbers will require a more detailed understanding of microscopic optical nonlinearities.

25.5 KERR EFFECT

Longitudinal and Transverse Kerr Effect

The extremely rapid response and broad bandwidth of the Kerr nonlinearity are very attractive for a modelocking process. For high intensities, polarization inside a dielectric medium does not proportionally follow the electric field anymore. This gives rise to an index change that is proportional to intensity. Off-resonance, this nonlinear optical effect is extremely fast,

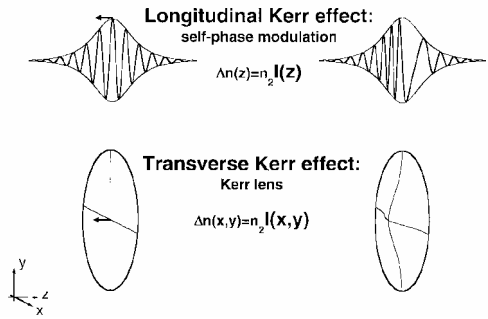

FIGURE 6 The Kerr effect produces a nonlinear intensity dependent refractive index change. The longitudinal Kerr effect (top) causes self-phase modulation (SPM). The transverse Kerr effect (bottom) causes a nonlinear focusing lens (Kerr lens).

with estimated response times in the few-femtosecond range. The transverse and longitudinal effects resulting from the intensity dependence are shown schematically in Fig. 6. The transverse Kerr effect retards the central and most intense part of a plane wavefront, thus acting as a focusing lens, referred to as the Kerr lens. Later we will indicate concepts that make use of the Kerr lens to produce short pulses. Along the axis of propagation, the longitudinal Kerr effect retards the center of an optical pulse, producing a red shift of the leading part of the pulse, and a blue shift in the trailing part. Consequently, the longitudinal Kerr effect has been named *self-phase modulation* (SPM).

Longitudinal Kerr Effect for External Pulse Compression

SPM generates extra bandwidth; in other words, it spectrally broadens the pulse. SPM alone does not modify the pulse width—but a much shorter pulse can be generated with the extra bandwidth and proper dispersion compensation.[38] To create a short pulse, the blue spectral components have to be advanced relative to the red ones, exactly counteracting the phase delays induced by the SPM (assuming $n_2 > 0$). To do so an effect opposite to the normal material dispersion is needed. This type of dispersion is called *anomalous* or *negative* dispersion. A careful balance between a nonlinear spectral broadening process and negative dispersion is needed for efficient compression of a pulse. Typically, self-phase modulation in a single-mode fiber is used to chirp the pulse, which is then compressed with a grating pair compressor.[39]

Ultimately, compression schemes are limited by uncompensated higher-order dispersion and higher-order nonlinearities. For pulses shorter than 100 fs, compression is typically limited to factors of less than 10. Compression of amplified CPM dye laser pulses with 50 fs duration produced the long-standing world record of 6 fs for short pulses.[40] Similar concepts have been recently used for external pulse compression of 13-fs pulses from a cavity dumped Ti:sapphire laser[11] and of 20-fs pulses from a Ti:sapphire laser amplifier[12] resulting, in both cases, in approximately 4.5-fs pulses (see Fig. 1). In the latter case, the use of a noble-gas-filled hollow fiber resulted in unsurpassed pulse energies of about 0.5 mJ, with 5.2 fs pulses and a peak power of 0.1 TW.[41]

Longitudinal Kerr Effect for Broadband Parametric Amplification

The extra bandwidth obtained with SPM can be extremely large, producing a white-light continuum[42] that can be used as a seed for broadband parametric amplification. Parametric pro-

cesses can provide amplification with even broader bandwidth than can typically be achieved in laser amplifiers. Noncollinear phase-matching at a crossing angle of 3.8° in Barium beta borate (BBO) provides more than 150 THz amplification bandwidth.[43] With this type of set-up, parametric amplification has been successfully demonstrated with pulse durations of less than 5 fs.[10]

Longitudinal Kerr Effect for Passive Modelocking: Soliton Modelocking

It was recognized early on that the longitudinal Kerr effect or SPM together with negative dispersion results in soliton formation and further reduces pulse duration by about a factor of 2 in dye lasers.[26,27] However, at that time an analytic solution for the pulse shortening effect was not presented. Using soliton perturbation theory, an analytic solution has been derived that describes how to make use of much more significant soliton pulse shortening in solid state-lasers.[44,45] This modelocking model, referred to as *soliton* modelocking, is fundamentally different from any previous models, because it treats soliton pulse shaping as the dominant pulse formation process and the saturable absorber as a perturbation to the soliton. This strongly relaxes the requirements of the saturable absorber as compared to pure saturable absorber modelocking. However, the saturable absorber is still required to start the modelocking process and to stabilize the soliton pulses against continuous wave breakthrough.

The soliton modelocking model was experimentally confirmed by the production of 300-fs-long soliton pulses with a saturable absorber response time of only 10 ps.[46] Pulses of 13 fs were achieved with a saturable absorber response time of about 60 fs.[45] Further improvements of extremely broadband saturable absorbers[35] with a higher modulation depth would be necessary to obtain even shorter pulses based on this modelocking mechanism.

In soliton modelocking the pulse duration is given by the soliton condition:

$$\tau_p = 1.76 \frac{|D_2|}{k n_2 L_L F_{p,L}} \tag{19}$$

where D_2 is the total group delay dispersion inside the laser cavity per cavity round-trip. Here we assume that the dominant SPM is produced in the laser material (i.e., n_2 is the nonlinear refractive index of the laser material, L_L is the length of the laser material and $F_{p,L}$ the pulse fluence inside the laser material). In other cases we have to add all other contributions as well. The pulse duration scales linearly with the negative intracavity dispersion. Reducing the intracavity dispersion results in shorter transform-limited pulses.[46] However, there is a limit. The soliton looses energy due to gain dispersion and losses in the cavity. This lost energy, called *continuum* in soliton perturbation theory,[47] is initially contained in a low-intensity background pulse, which experiences negligible SPM, but spreads in time due to group velocity dispersion. This continuum experiences a higher gain compared to the soliton pulse, because it only sees the gain at line center (while the soliton sees an effectively lower average gain due to its larger bandwidth). After a sufficient build-up time, the continuum would actually grow until it reaches lasing threshold, destabilizing the soliton. However, we can stabilize the soliton by introducing a "slow" saturable absorber into the cavity. This "slow" absorber has to be fast enough to add sufficient additional loss for the growing continuum that spreads in time so that it no longer reaches lasing threshold. For a given recovery time of the saturable absorber, the continuum pulse will not broaden fast enough when the negative dispersion becomes too small. Therefore there is a minimum pulse duration that can be achieved for a given set of absorber and laser parameters:

$$\tau_{p,\min} = 1.7627 \left(\frac{1}{\sqrt{6}\,\pi \Delta \nu_g} \right)^{3/4} \phi_s^{-1/8} \left(\frac{\tau_A g^{3/2}}{q_0} \right)^{1/4} \tag{20}$$

where ϕ_s is the phase shift of the soliton per cavity round trip (assuming that the dominant SPM occurs in the laser gain medium) and is given by:

$$\phi_s = \phi_s\,(z = 2L_L) = kn_2L_LI_{0,L} \tag{21}$$

Here we assume a fully saturated slow absorber with a linear approximation for the exponential decay of the slow saturable absorber, and a slow saturable absorber.

In the femtosecond regime, we observe a significant reduction of the tendency of Q-switching instabilities compared to pure saturable absorber modelocked picosecond lasers [Eq (18)]. This can be explained as follows: If the energy of an ultrashort pulse rises slightly due to relaxation oscillations, SPM and/or SAM broadens the pulse spectrum. A broader spectrum, however, reduces the effective gain due to the finite gain bandwidth, which provides some negative feedback, thus decreasing the critical pulse energy which is necessary for stable cw modelocking. The simple stability requirement of Eq. (18) then has to be modified as follows[19]:

$$E_{\text{sat},L}gK^2E_p^2 + E_p^2 > E_{\text{sat},L}E_{\text{sat},A}\Delta R \tag{22}$$

where K is given by

$$K \equiv \frac{0.315}{1.76}\,\frac{4\pi n_2L_L}{D_2A_L\lambda_0\Delta\nu_g} \tag{23}$$

Here we assume that the dominant SPM is produced in the laser medium. In other cases we have to add all other contributions as well.

Longitudinal Kerr Effect for Passive Modelocking with a Coupled Cavity: Soliton Laser, Additive Pulse Modelocking (APM)

The longitudinal Kerr effect can also be used to produce the same effect as a fast saturable absorber. To do this, the phase nonlinearity provided by the longitudinal Kerr effect has to be converted into an effective amplitude nonlinearity. The earliest modelocking schemes (based only on SPM) used a coupled cavity to convert SPM into SAM. In the soliton laser,[48] pulses compressed by SPM and anomalous dispersion in the coupled cavity are directly coupled back into the main laser cavity. This provides more gain for the center of the pulse. Pulses as short as 19 fs have been demonstrated with color center lasers.[49] Later, the SPM-to-SAM conversion with a coupled cavity was demonstrated for a case when the pulses inside the coupled cavity were broadened due to positive group velocity dispersion.[50] In this case, no compressed pulse was fed back into the main cavity. An effective SAM was obtained because SPM inside the coupled cavity generates a phase modulation on the pulse that adds constructively at the peak of the pulse in the main cavity and destructively in the wings, thus shortening the pulse duration inside the main cavity. This was also referred to as additive pulse modelocking (APM).[51] Although very powerful in principle, these coupled-cavity schemes have the severe disadvantage that the auxiliary cavity has to be stabilized interferometrically. An alternative method for converting the reactive Kerr nonlinearity into an effective saturable absorber has been developed: Kerr-lens modelocking (KLM).[52]

Transverse Kerr Effect for Passive Modelocking: Kerr Lens Modelocking (KLM)

The discovery of Kerr lens modelocking has been a breakthrough in ultrashort pulse generation.[52] Initially the modelocking mechanism was not understood and was somewhat of a mystery. But within a short time after the initial discovery it became clear that the transverse Kerr effect provides a fast saturable absorber. In KLM, the transverse Kerr effect produces a Kerr

lens (see Fig. 6) that focuses the high intensity part of the beam more strongly than the low intensity part. Thus, combined with an intracavity aperture the Kerr lens produces less loss for high intensity and forms an effective fast saturable absorber.[53–55] A similar modelocking effect can be obtained without a hard aperture when the Kerr lens produces an increased overlap of the laser mode with the pump profile in the gain medium.[56] The Kerr lens provides the strongest advantage for the pulsed operation when the cavity is operated close to the stability limit. Optimization guidelines for SAM produced by the Kerr lens in different cavities can be found in Ref. 57. Unfortunately, the transverse Kerr effect couples the modelocking process with the laser cavity mode. In contrast, the use of only the longitudinal Kerr effect in modelocking decouples the modelocking process from the laser mode. This allows optimum cavity design for scaling the laser to higher powers and to higher pulse repetition rates without being constrained by the Kerr lens.

KLM is well described by the fast absorber modelocking model discussed above[58] even though it is not so easy to determine the exact saturable absorber parameters such as the effective saturation fluence. However, the linearized model does not describe the pulse generation with Ti:sapphire lasers in the sub-10-fs regime very well. Pulse-shaping processes in these lasers are more complex.[59,60] Under the influence of the different linear and nonlinear pulse shaping mechanism, the pulse is significantly broadened and recompressed, giving rise to a "breathing" of the pulse width. The order of the pulse shaping elements in the laser cavity becomes relevant and the spectrum of the modelocked pulses becomes more complex. In this case, an analytical solution can no longer be obtained. As a rough approximation, the pulses still behave like solitons and consequently these lasers are also called solitary lasers.[59]

Longitudinal Kerr Effect for Passive Modelocking with Nonlinear Polarization Rotation

A Kerr effect–induced nonlinear polarization rotation in a weakly birefringent fiber has been used as a "pulse cleaner" to reduce the low-intensity pulse pedestals.[61,26] The same effect can also be used to form an effective fast saturable absorber.[63] Pulses as short as 38 fs have been generated with Nd-doped fiber lasers.

25.6 SEMICONDUCTOR ULTRAFAST NONLINEARITIES: MICROSCOPIC PROCESSES

The discussion of saturable absorbers in Sec. 25.4 has shown that semiconductors are well-suited absorber materials for ultrashort pulse generation. In contrast to saturable absorber mechanisms based on the Kerr effect (Sec. 25.5), ultrafast semiconductor nonlinearities can be studied outside the laser. Such studies give insight into the microscopic processes that determine the nonlinear optical properties of semiconductors on ultrashort time scales. This insight has substantially contributed to our understanding of the physics of semiconductors. Moreover, the information obtained from ultrafast semiconductor spectroscopy provides the basis for further improvement of ultrashort pulse generation with semiconductor saturable absorbers.

In this section, we will first give an overview of ultrafast semiconductor dynamics, which will be followed by a description of the most important experimental techniques for the study of ultrafast processes and nonlinearities. Then we summarize some of the results that have been obtained with these experimental techniques. This summary emphasizes aspects that are particularly relevant for saturable absorber applications, but goes beyond the saturable absorber issue if this is helpful to illustrate general concepts.

In ultrafast semiconductor spectroscopy, it is often convenient to distinguish between excitonic excitations (i.e., Coulomb-bound electron-hole pairs at the band edge[64]) and unbound electron-hole pairs in the continuum of the spectrum. Laser pulses with a temporal width well below 100 fs have a spectral bandwidth that is much larger than the spectral width of the exciton resonance and the exciton binding energy in most semiconductors. This is illustrated in Fig. 7 for the example of a 16 fs pulse and the absorption spectrum of a GaAs/AlGaAs quantum well[65] at room temperature. Therefore, saturable absorber applications with sub-100-fs pulses very often involve broadband continuum excitations. For this reason, we will focus on ultrafast continuum nonlinearities and dynamics. Exciton dynamics will be discussed only to outline some general concepts of ultrafast semiconductor spectroscopy. For a comprehensive, in-depth review of ultrafast semiconductor spectroscopy the interested reader is referred to Ref. 66.

Overview

Semiconductors are characterized by closely spaced electronic eigenstates in energy space. This electronic structure gives rise to strong interaction among optical excitations on ultrafast time scales and very complex dynamics. Despite the complexity of the dynamics, different time regimes can be distinguished in the evolution of optical excitations in semiconductors.[66,67] These different time regimes are schematically illustrated in Fig. 8, which shows the energy dispersion diagram of a 2-band bulk semiconductor. Optical excitation with an ultrafast laser pulse prepares the semiconductor in the coherent regime (time regime I in Fig. 8). In this regime, a well-defined phase relation exists between the optical excitations and the electric field of the laser pulse and among the optical excitations themselves. The coherence among the excitations in the semiconductor gives rise to a macroscopic polarization (dipole moment density). Since the macroscopic polarization enters as a source term in Maxwell's equations, it leads to an electric field which is experimentally accessible. The magnitude and decay of the polarization provide information on the properties of the semiconductor in the coherent regime. The irreversible decay of the polarization is due to scattering processes and is usually described by the so-called dephasing or transversal relaxation time. For a mathematical definition of this time constant the reader is referred to References 66, 68, 69, and 70. Some more details about dephasing and coherent dynamics in semiconductors will be given later.

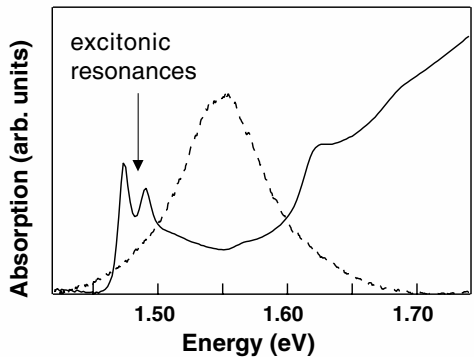

FIGURE 7 Room temperature linear absorption spectrum (solid) of a GaAs/AlGaAs semiconductor quantum well and power spectrum of a 16-fs laser pulse (dashed).

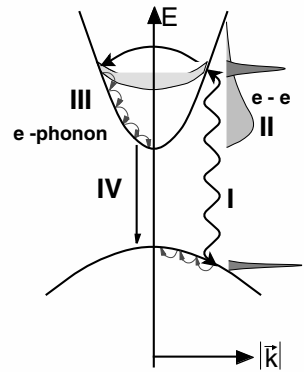

FIGURE 8 Schematic dispersion diagram of a two-band bulk semiconductor showing the time regimes I–IV after optical excitation; see text for more details. e-e: electron-electron scattering. e-phonon: electron-phonon scattering.

After the loss of coherence, ultrafast spectroscopy of semiconductors is solely concerned with the dynamics of the population (i.e., electron and hole distributions). In this incoherent regime, the time regimes II-IV can be distinguished, as described in the text that follows. The initial electron and hole distributions are nonthermal in most cases (i.e., they cannot be described by Fermi-Dirac statistics with a well-defined temperature). Scattering among charge carriers is mainly responsible for the redistribution of energy within the carrier distributions and for the formation of thermal distributions. This thermalization is shown as time regime II in Fig. 8, for the example of a thermalizing electron distribution where thermalization occurs through scattering among the electrons. For excitation of the continuum, thermalization usually occurs on a time scale of 100 fs under most experimental conditions. More details about the dynamics in the thermalization regime will be presented later.

In general, the carriers have a temperature different from the lattice temperature after thermalization has been completed. In Fig. 8 it is assumed that the carriers have a higher temperature than the lattice. For this case, Fig. 8 schematically shows the cooling of carriers by the emission of phonons (i.e., energy transfer to the lattice). Cooling defines the time regime III. Typical time constants are in the picosecond and tens of picosecond range.

Finally, the optically excited semiconductor returns to thermodynamic equilibrium by the recombination of electron-hole pairs. Recombination is shown as time regime IV in Fig. 8. In a perfect semiconductor crystal, recombination proceeds via the emission of photons or Auger processes at high carrier densities. These recombination processes take place on time scales of tens of picoseconds and longer. These slow recombination processes as well as the relatively slow carrier cooling will not be discussed in more detail in this chapter. An excellent review can be found in Ref. 66.

Another ultrafast process is encountered if large densities of deep-level traps are incorporated in a semiconductor. Trapping of carriers into deep levels can proceed on subpicosecond time scales (not shown in Fig. 8). Since carrier trapping is important in many saturable absorber applications, it is discussed at the end of this section.

We note that the different time regimes temporally overlap. For example, a scattering process may destroy the coherence and contribute to thermalization. Nevertheless, it is very useful to distinguish between the different time regimes because they are a convenient means for the description of the complex semiconductor dynamics. The schematic picture of the differ-

ent time regimes also demonstrates that two or more time constants are usually required to describe the temporal response of a semiconductor absorber. For example, we recall that thermalization typically takes place on the 100-fs time scale, while carrier trapping proceeds on times scales from a few hundreds of femtoseconds to picoseconds.

Experimental Techniques

In the following, we describe two very common experimental techniques for the study of ultrafast processes and nonlinearities. The discussion focuses on semiconductors. However, the experimental techniques have also been intensively used for the study of other condensed matter systems or molecules.

Transient Four-Wave-Mixing. Transient four-wave mixing (FWM) is an experimental technique for the study of the coherent regime. A schematic diagram of a transient FWM experiment is shown in Fig. 9. Two excitation pulses with wave vectors $\mathbf{k}_1$ and $\mathbf{k}_2$ excite the sample. In most FWM experiments the two pulses have the same spectrum (degenerate FWM). We assume here that the case of degenerate FWM is realized. An optical delay line is used to introduce a time delay Δt between the pulses where positive Δt refers to pulse $\mathbf{k}_1$ arriving before pulse $\mathbf{k}_2$ at the sample.

Pulse $\mathbf{k}_1$ generates a coherent polarization in direction $\mathbf{k}_1$ in the sample. If the time delay Δt is smaller than the dephasing time of the coherent polarization, in a second step, this polarization interacts with the electric field of pulse $\mathbf{k}_2$ to set up an interference grating. In a third step, pulse $\mathbf{k}_2$ is self-diffracted from this grating and an electric field is emitted in the phase-matching direction $2\mathbf{k}_2$-$\mathbf{k}_1$. The diffracted field constitutes the FWM signal. A more detailed analysis shows that the FWM signal is due to a nonlinear polarization in direction $2\mathbf{k}_2$-$\mathbf{k}_1$.[66,71]

The FWM emission can be analyzed in different ways. First, the time integral over the FWM intensity can be measured versus the time delay. Such measurements usually provide information about the dephasing time since the strength of the FWM emission is determined by the coherent polarization in direction $\mathbf{k}_1$ that is left when pulse $\mathbf{k}_2$ is applied.[66,71] Spectral information is obtained if the FWM emission is analyzed with a spectrometer at fixed time delays. If more than one resonance is excited, the FWM spectrum shows the magnitude of the optical nonlinearity of the different resonances. Moreover, for homogeneously broadened transitions, the dephasing time can be obtained from the spectral width of the FWM emission. For a fixed time delay, the decay of the FWM signal can be measured in real time by optical gating with a reference pulse. Usually, sum frequency generation in a nonlinear crystal is used for this purpose. This is essentially a cross correlation measurement between the FWM signal

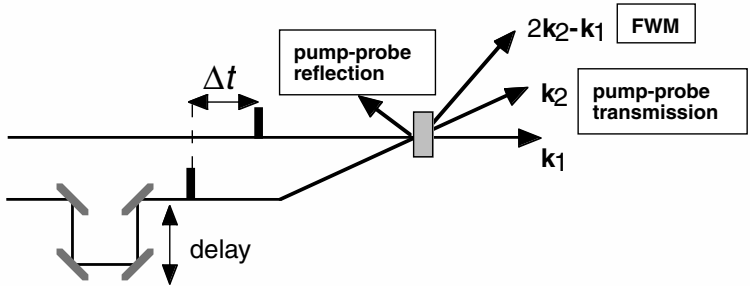

FIGURE 9 Schematic experimental setup for four-wave-mixing (FWM) and pump-probe spectroscopy.

pulse and the reference pulse, in which the time resolution is determined by the duration of the reference pulse. In such a correlation measurement, a slow photodetector can be used to detect the sum frequency signal. Real-time detection of FWM signals shows whether the excited optical transitions are homogeneously or inhomogeneously broadened. For homogeneous broadening, the FWM signal in direction $2\mathbf{k}_2$-$\mathbf{k}_1$ immediately sets in when pulse $\mathbf{k}_2$ is applied (for positive time delays). For inhomogeneous broadening, the FWM signal is emitted time-delayed with respect to pulse $\mathbf{k}_2$ as a so-called photon echo.[68] More details as well as a mathematical analysis of degenerate two-pulse FWM can be found in Refs. 66 and 71. Transient FWM with three pulses is treated in Ref. 72.

For excitation of interband transitions in semiconductors, occupation of valence and conduction band states contributes to the optical nonlinearity exploited in the FWM process. Occupation effects are a source of nonlinearity in many electronic systems, as shown by the analysis of simple two-level systems.[66,71] Other sources of nonlinearity will be briefly mentioned when we present some results of coherent semiconductor spectroscopy.

Pump-Probe Spectroscopy. Pump-probe spectroscopy is the most widely used technique for the study of ultrafast optical nonlinearities. As shown in Fig. 9, the sample is excited by the pump pulse $\mathbf{k}_1$. The nonlinear changes of the transmission or reflectivity of the sample are detected by the time-delayed probe pulse $\mathbf{k}_2$. The time delay is defined as positive if the pump pulse precedes the probe. Often, the pump pulse train is amplitude-modulated and a lock-in amplifier is used for detection of the nonlinear transmission or reflectivity changes at the modulation frequency. It is important to note that the pump-probe experiment is a correlation experiment, in which a slow photodetector can be used.

With this technique, nonlinear reflectivity changes are measured in saturable absorbers which are integrated within a mirror structure, as mentioned in Sec. 25.4. In studies of microscopic processes, very often the nonlinear changes of the probe transmission are measured, which is referred to as *differential transmission* (DT) spectroscopy. In the simplest arrangement, the DT signal is spectrally integrated over the spectrum of the probe pulse. If the probe pulse has a large bandwidth, the DT signal at various photon energies can be obtained from measurements of the spectrum of the transmitted probe pulse in the presence and absence of the pump. The difference between those spectra represents the DT spectrum. Spectral information can also be obtained if a tunable narrowband probe pulse is scanned over a spectral window.

The differential transmission signal contains information on the coherent and the incoherent regime. In the coherent regime, the DT signal is determined by the nonlinear polarization in the direction of the probe pulse. The DT signal in the coherent regime is analyzed in more detail in Refs. 73, 74, 75, and 76.

Coherent effects can be neglected on time scales much longer than the dephasing time of the polarization. The DT signal is then determined by the population (i.e., the electron and hole distributions) generated by the pump pulse. In the incoherent regime, one can roughly distinguish between two different sorts of effects that determine the DT signal of semiconductors: (1) occupation effects and (2) many-body Coulomb effects. Occupation effects are based on the fermionic nature of optical excitations and can be understood in the following way. A nonequilibrium carrier population in excited states reduces the optical transition rate into these states due to the reduced density of empty final states. This manifests itself by the reduction of the absorption at certain photon energies. Occupation effects are important in many electronic systems. Many-body effects are particularly important in semiconductors. They include the renormalization of the bandgap and screening of the Coulomb interaction. Details can be found in Refs. 77, 78, 79, and 80. Of course, the many-body effects are related to the occupation effects since they depend on the distribution of carriers.

If many-body effects can be neglected and if the optical matrix elements do not depend on the pump excitation, the nonlinear change $\Delta\alpha$ of the absorption constant α is directly proportional to the magnitude of the population (i.e., the electron and hole densities). In general, both refractive index changes and absorption changes $\Delta\alpha$ contribute to the differential trans-

mission signal.[81] A considerable simplification is obtained if refractive index changes can be neglected and if the relation $\Delta\alpha d \ll 1$ holds (d sample thickness). Then the DT signal is proportional to $\Delta\alpha$, and the decay of the DT signal can be identified with the decay of the electron and hole densities. We note that in studies of carrier trapping, pump-probe data are very often analyzed under the just-described assumptions.

Results

In this subsection, examples are given that show how ultrafast spectroscopy has contributed to the understanding of ultrafast processes and nonlinearities in semiconductors. We will highlight those aspects that are particularly relevant for broadband saturable absorbers. The material is organized according to the different time regimes which have been identified at the beginning of Sec. 25.6.

Coherent Regime: Excitonic Excitations. Studies of excitons in the coherent regime are an illustrative example for the issues addressed in coherent ultrafast spectroscopy of semiconductors. Therefore, we briefly discuss some aspects of coherent exciton dynamics even though excitonic excitations are less important for many ultrafast saturable absorber applications. This discussion will illustrate the main issues addressed in ultrafast semiconductor spectroscopy in the coherent regime: (1) dephasing times and underlying scattering mechanisms, (2) coupling and interference between optical excitations, and (3) the nature of the optical nonlinearity.

Four-wave-mixing has been intensively used to study the dephasing of excitons and the underlying scattering mechanisms. Varying the excitation intensity, the effects of exciton-exciton and exciton-electron scattering on the dephasing of excitons have been investigated in bulk semiconductors[82] and quantum wells.[83] Varying the temperature, dephasing of excitons due to interaction with lattice vibrations (phonons) has been studied in Ref. 84. Summarizing these results, exciton dephasing times can be in the picosecond range at moderate exciton and free-carrier densities and Helium temperatures. Increasing the temperature decreases the dephasing time due to enhanced phonon scattering. Likewise, enhanced carrier or exciton densities cause faster dephasing. A detailed analysis of exciton dephasing in three- and two-dimensional semiconductors is presented in Ref. 85. We note that exciton dephasing can also give insight into the structural properties of a semiconductor, such as interface roughness in quantum wells and alloy disorder in mixed crystals.[86,87]

More recent four-wave-mixing investigations of coherent exciton dynamics focus on quantum-mechanical coupling and interference between different exciton transitions. Beating phenomena between two exciton transitions have been observed in various systems[88–91] as well as beats involving the whole excitonic Rydberg series.[92] The study of beating phenomena allows for the extraction of level splittings and yields information on the quantum-mechanical coupling in multilevel systems (i.e., their internal structure[93,94]).

The nature of the optical nonlinearity in the coherent regime is another subject that has been intensively studied in four-wave-mixing experiments on excitons.[80,95–103] It has been shown that many-body Coulomb interaction substantially contributes to the coherent optical nonlinearity. With respect to the essence of this result we note that the polarization of a certain interband excitation gives rise to an electric field which has to be added to the external laser field in order to determine the coherent dynamics of other excitations. A rigorous theoretical treatment can be found in Refs. 78 and 80.

Coherent Regime: Continuum Excitations. Four-wave-mixing studies of continuum dephasing have been performed with broadband sub-10-fs pulses in three-dimensional bulk semiconductors[104] and quasi two-dimensional quantum wells.[105] These studies have shown that the decay of the coherent polarization of the semiconductor continuum is extremely fast. Decay times are only about 10 fs at high carrier densities, which are likely to be obtained in a

saturable absorber in a laser cavity. The ultrafast dephasing is mainly due to carrier-carrier scattering with a density dependence that reflects the dimensionality of the semiconductor.[105] More recent work[106] shows that at reduced carrier densities interaction with the lattice also needs to be considered in continuum dephasing experiments. The interaction with the lattice has been identified as electron-LO-phonon scattering,[106] which has a time constant of about 200 fs.[107–109]

The internal structure of the continuum has been experimentally investigated in Ref. 110. The observation of a photon echo has demonstrated that the semiconductor continuum can be treated as an ensemble of uncoupled excitations at higher carrier densities.[110] Interaction between continuum and exciton transitions in coherent nonlinear optics has been studied both for degenerate[111–113] and nondegenerate excitons and continua.[114–117] This work has demonstrated the importance of many-body coupling effects between different interband transitions at lower carrier densities.

We note that it is not yet clear how coherence in a semiconductor saturable absorber affects the formation of broadband ultrashort pulses in a laser cavity. Some theoretical predictions can be found in Refs. 118 and 119. Experimental results about this issue are missing so far. Given the ultrafast dephasing times in semiconductors under the conditions in a laser cavity, coherence effects are most likely to be important for the generation of sub-10-fs pulses.

Thermalization Regime. Here we will focus on the excitation of semiconductor continuum states. Studies of the thermalization of free electron and hole distributions are an instructive example for the usefulness of the differential transmission (DT) technique. In particular, measurements of differential transmission spectra have yielded considerable insight into the complex processes that determine the dynamics in the thermalization regime. For excitation well above the band gap, nonthermal carrier distributions can be observed in bulk semiconductors, such as GaAs[120] and quantum wells.[121] These nonthermal distributions manifest themselves as positive signal in the DT spectrum with a shape that is approximately given by the spectrum of the pump pulse. Often, this signature in the DT spectrum is referred to as a *spectral hole.* The decay of the spectral hole and the thermalization of the carrier distributions lead to a substantial change of the shape of the DT spectrum. Thermalization occurs on the 100-fs time scale in undoped semiconductors and is determined by carrier-carrier scattering in many experiments. The exact thermalization time strongly depends on the carrier density, the excess photon energy with respect to the band edge, and the type of carrier.[66,120–122] Thermalization of optically excited carriers in the presence of cold electron or hole plasmas has also been investigated by the differential transmission technique.[66,123] These experiments have been performed in modulation-doped quantum wells[65] and show that thermalization can occur in less than 10 fs.

Besides carrier-carrier scattering, intervalley scattering is another process which can affect carrier dynamics in the thermalization regime. Semiconductors such as GaAs possess several conduction band minima at different points of the Brillouin zone. If electrons are created near the center of the Brillouin zone with large enough excess energy, they can scatter to the side valleys. This process has been investigated in DT experiments, and intervalley scattering times in the sub-100-fs range have been deduced.[124,125]

Spectrally resolved DT measurements have also revealed interesting many-body effects. A closer inspection of DT spectra has shown that the spectral hole is redshifted with respect to the pump spectrum.[126] Moreover, at the high-energy edge of the pump spectrum a negative DT signal is observed. These signatures have been interpreted in terms of Fermi edge singularities at the upper and lower edge of the nonthermal electron distribution generated by the pump pulse.[126,127] The work on Fermi edge singularities is an instructive example for the interplay between occupation and many-body effects in differential transmission experiments in semiconductors.

Thermalization of carrier distributions and many-body effects also change the spectrally integrated DT signal or the impulse response of a semiconductor saturable absorber. In particular, thermalization contributes to the fast decay seen in the impulse response at early

times (cp. Fig. 3). It is important to note that this fast decay is the result of the complex redistribution of nonlinear transmission or reflectivity changes in frequency space. As a consequence, no general concept has evolved so far for the engineering of this fast decay.

The fast decay of a spectrally integrated DT curve in the thermalization regime also depends on the temporal structure of the pump and probe pulses themselves.[128,129] This point has been recently demonstrated in experiments in which a so-called frequency chirp was imposed on 20 fs pulses. In a frequency-chirped laser pulse the frequency varies over the temporal profile of the pulse. Such chirped pulses have been used in DT experiments on continuum transitions in bulk semiconductors. The results show that the fast decay of spectrally integrated DT curves can be enhanced by an appropriate frequency chirp.[128,129] The manipulation of ultrafast nonlinearities by the chirp of the pulses can be viewed as an example of a much more general concept known as *coherent control.*[130] In coherent control experiments, the temporal shape or spectral content of ultrafast laser pulses are adjusted[131] to reach preset goals. The chirp control experiments in Refs. 128 and 129 demonstrate that the detailed temporal and spectral structure of the laser pulses should be included in the optimization of semiconductor saturable absorbers. That probably also means that the position of the SESAM within the laser cavity may play a role in sub-10-fs pulse generation.

Carrier Trapping. Processes that remove electrons and holes from the bands of a semiconductor lead to a decay of the nonlinear transmission or to reflectivity changes resulting from the interband transitions. As discussed in Sec. 25.4, semiconductor saturable absorber applications in ultrashort pulse generation often require picosecond or subpicosecond absorber recovery times. The simplest way to obtain such short absorber recovery times would be to remove the optically excited carriers from the bands a few hundreds of femtoseconds after they have been created. Ultrafast depletion of the semiconductor band states is also important in all-optical switching devices[132,133] and optoelectronics.[134] However, intrinsic recombination processes are usually too slow to deplete the band states of a semiconductor on picosecond or subpicosecond time scales. Therefore, one generates defect states in the band gap which give rise to fast carrier trapping, thereby depleting the bands. The trapping time is determined by the density and the type of the traps. Higher trap densities give rise to faster trapping.

Standard methods for the controlled incorporation of defect and trap states are ion implantation[135] and low-temperature (LT) molecular beam epitaxy.[136] In ion-implanted semiconductors, the trap density and the type of defect are determined by the implantation dose. The growth temperature controls the defect density in LT semiconductors, where larger defect densities are incorporated at lower temperatures.[137] GaAs is the best-understood LT-grown III-V semiconductor. Low-temperature growth of GaAs is performed at temperatures of 200 to 300°C, as compared to about 600°C in standard molecular beam epitaxy. During LT growth of GaAs, excess arsenic is incorporated in the form of arsenic antisites (As on Ga lattice site: As_{Ga}) at densities as large as 10^{20} cm^{-3}.[137,138] In undoped LT GaAs, more than 90 percent of the antisites are neutral, while the rest is singly ionized due to presence of Ga vacancies (V_{Ga}) which are the native acceptors in the material (see Fig. 10*a*).[137,139] The ionized arsenic antisites have been identified as electron traps.[140] Annealing at higher temperatures (typically 600°C and higher) converts the arsenic antisite point defects into arsenic clusters, so-called As precipitates (see Fig. 10*b*).[141] A detailed review of the properties of LT GaAs can be found in Refs. 142 and 143.

The carrier trapping times in as-grown LT GaAs can be in the subpicosecond regime and show the expected decrease with decreasing growth temperature.[144,145] Subpicosecond recovery times of nonlinear transmission or reflectivity changes are also found in annealed LT GaAs, indicating that arsenic precipitates efficiently deplete the band states.[146,147] For more details about carrier trapping in LT semiconductors the reader is referred to Refs. 148 through 155.

Picosecond and subpicosecond carrier trapping times have also been found in semiconductors implanted with various ion species.[156–161] A decrease of the trapping time with increasing ion dose was observed at lower doses.[156,157,160] At higher ion doses, the trapping time can

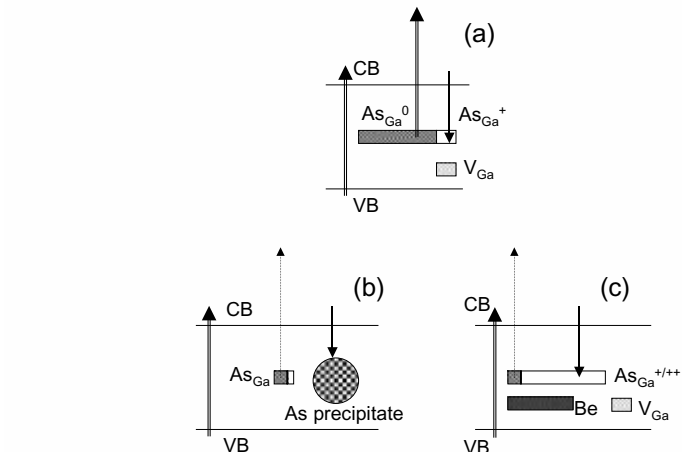

FIGURE 10 Electronic structure of undoped as-grown (*a*), undoped annealed (*b*), and Beryllium doped as-grown LT GaAs (*c*). The double arrows mark strong optical absorption transitions. Weak optical absorption transitions are indicated by dotted arrows. Trapping processes are shown by arrows that point downwards.

increase with the dose.[161] The correlation of trapping times with structural properties of ion implanted semiconductors has given more insight into this unexpected dose dependence of the trapping time.[162] This work indicates that not only the defect density but also the type of defect depends on the ion dose.[162] Both the density and the type of defect affect carrier trapping, leading to longer trapping times if less effective traps are generated at higher ion doses.[162]

Besides an ultrafast carrier trapping and absorber recovery time, other important saturable absorber parameters are the modulation depth and the nonsaturable losses which remain even at the highest pump energy fluences (see Sec. 25.4). Optimized materials combine an ultrafast recovery time with high modulation and small nonsaturable losses. This material optimization issue has been addressed in recent publications.[147,161,163] In these studies, the nonlinearity of continuum transitions was investigated in different modifications of GaAs. The preparation of the semiconductor layers ensured that the modulation depth and the nonsaturable losses were determined by nonlinear absorption changes.

It has been shown that standard as-grown LT GaAs with an ultrafast carrier trapping time suffers from a small absorption modulation and high nonsaturable absorption losses.[147,163] Note that large nonsaturable absorption decreases the modulation depth and causes large nonsaturable losses when the semiconductor absorber is integrated within a mirror structure. The high nonsaturable absorption mainly results from the strong defect absorption from the neutral As antisites to the conduction band (see Fig. 10*a*) whose saturation fluence has been shown to be extremely high.[147] Therefore, the goals of material optimization are (1) to reduce the nonsaturable absorption by the reduction of the density of neutral As antisites and (2) to maintain a fast trapping and absorber recovery time.

We have demonstrated two different ways to reach those goals. Annealing of LT GaAs strongly reduces the density of neutral As antisites and the nonsaturable absorption.[147] The simultaneous reduction of the density of useful ionized As antisite electron traps does not substantially increase the absorber recovery time due to the presence of the As precipitates (see Fig. 10*b*). Alternatively, doping with acceptors, such as Beryllium, can be used to reduce

the density of neutral As antisites.[164] The simultaneous increase of the ionized As antisite density results in ultrafast carrier trapping and absorber recovery times (see Fig. 10*c*).[163] Annealed LT GaAs and Be doped LT GaAs combine ultrafast recovery times with high modulation depth and small nonsaturable losses. These materials are well suited for saturable absorber devices in laser physics and for all-optical switching applications.

Studies of the modulation depth ΔR, the nonsaturable losses ΔR_{ns}, and the recovery time τ_A in ion implanted GaAs have shown that ΔR decreases and ΔR_{ns} increases with decreasing recovery time.[161] Nevertheless, if the ion species, ion dose, and annealing conditions are properly chosen, combinations of ΔR, ΔR_{ns}, and τ_A can be obtained which are appropriate for saturable absorber applications. Ion-implanted GaAs is an alternative to annealed or Be doped LT GaAs as a material for saturable absorber devices.[161]

25.7 REFERENCES

1. P. F. Moulton, "Spectroscopic and Laser Characteristics of Ti:Al_2O_3," *J. Opt. Soc. Am. B.* **3:**125–132 (1986).
2. D. H. Sutter, G. Steinmeyer, L. Gallmann, N. Matuschek, F. Morier-Genoud, U. Keller, V. Scheuer, G. Angelow, and T. Tschudi, "Semiconductor Saturable-Absorber Mirror-assisted Kerr-Lens Mode-Locked Ti:Sapphire Laser Producing Pulses in the Two-Cycle Regime," *Optics Lett.* **24:**631–633 (1999).
3. U. Morgner, F. X. Kärtner, S. H. Cho, Y. Chen, H. A. Haus, J. G. Fujimoto, E. P. Ippen, V. Scheuer, G. Angelow, and T. Tschudi, "Sub-Two-Cycle Pulses from a Kerr-Lens Mode-Locked Ti:Sapphire Laser: Addenda," *Optics Lett.* **24:**920 (1999).
4. U. Keller, "Semiconductor Nonlinearities for Solid-State Laser Modelocking and Q-Switching," in Chapter 4 in *Nonlinear Optics in Semiconductors,* E. Garmire and A. Kost, (eds.), Academic Press, Inc., Boston, 1999, vol. 59, pp. 211–286.
5. U. Keller, "Physics of Ultrashort Pulse Generation," in *Advances in Lasers and Applications,* D. M. Finlayson and B. D. Sinclair (eds.), Institute of Physics Publishing and Scottish Universities Summer Schools in Physics, ISBN: 0-7503-0631-9, 1999), vol. SUSSP-52, pp. 83–115.
6. L. Krainer, R. Paschotta, J. Aus der Au, C. Hönninger, U. Keller, M. Moser, D. Kopf, and K. J. Weingarten, "Passively Modelocked Nd:YVO4 Laser with Up to 13 GHz Repetition Rate," *Appl. Phys. B.* **69:**245–247 (1999).
7. L. Krainer, R. Paschotta, G. Spühler, M. Moser, and U. Keller, "29 GHz Modelocked Miniature Nd:YVO4 laser," *Electronics Lett.* **35:**1160–1161 (1999).
8. R. Paschotta, J. Aus der Au, G. J. Spühler, F. Morier-Genoud, R. Hövel, M. Moser, S. Erhard, M. Karszewski, A. Giesen, and U. Keller, "Diode-Pumped Passively Modelocked Lasers with High Average Power," *Appl. Phys. B.* **70:**S25–S32 (2000).
9. G. J. Spühler, R. Paschotta, R. Fluck, B. Braun, M. Moser, G. Zhang, E. Gini, and U. Keller, "Experimentally Confirmed Design Guidelines for Passively Q-Switched Microchip Lasers Using Semiconductor Saturable Absorbers," *J. Opt. Soc. Am. B.* **16:**376–388 (1999).
10. A. Shirakawa, I. Sakane, M. Takasaka, and T. Kobayashi, "Sub-5-fs Visible Pulse Generation by Pulse-Front-Matched Noncollinear Optical Parametric Amplification," *Appl. Phys. Lett.* **74:**2268–2270, 1999.
11. A. Baltuska, Z. Wei, M. S. Pshenichnikov, D. A. Wiersma, and R. Szipöcs, "All-Solid-State Cavity Dumped Sub-5-fs laser," *Appl. Phys. B.* **65:**175–188 (1997).
12. M. Nisoli, S. Stagira, S. D. Silvestri, O. Svelto, S. Sartania, Z. Cheng, M. Lenzner, C. Spielmann, and F. Krausz, "A Novel High-Energy Pulse Compression System: Generation of Multigigawatt Sub-5-fs Pulses," *Appl. Phys. B.* **65:**189–196 (1997).
13. G. Steinmeyer, D. H. Sutter, L. Gallmann, N. Matuschek, and U. Keller, "New Frontiers in Ultrashort Pulse Generation: Pushing the Limits in Linear and Nonlinear Optics," *Science,* **286:**1507–1512 (1999).

14. U. Keller, D. A. B. Miller, G. D. Boyd, T. H. Chiu, J. F. Ferguson, and M. T. Asom, "Solid-State Low-Loss Intracavity Saturable Absorber for Nd:YLF Lasers: An Antiresonant Semiconductor Fabry-Perot Saturable Absorber," *Opt. Lett.* **17:**505–507 (1992).
15. K. J. Weingarten, U. Keller, T. H. Chiu, and J. F. Ferguson, "Passively Mode-Locked Diode-Pumped Solid-State Lasers Using an Antiresonant Fabry-Perot Saturable Absorber," *Optics Lett.* **18:**640–642 (1993).
16. X. M. Zhao and J.-C. Diels, "Ultrashort Laser Sources," in *Handbook of Optics,* M. Bass, E. W. Stryland, D. R. Williams, and W. L. Wolfe, (eds.) McGraw-Hill, Inc., New York, 1995, vol. 1, pp. 14.1–14.29.
17. H. A. Haus, "Short Pulse Generation," in *Compact Sources of Ultrashort Pulses* I. I. N. Duling (ed.) Cambridge University Press, New York, 1995. pp. 1–56.
18. G. P. Agrawal and N. A. Olsson, "Self-Phase Modulation and Spectral Broadening of Optical Pulses in Semiconductor Laser Amplifiers," *IEEE J. Quantum Electron.* **25:**2297–2306 (1989).
19. C. Hönninger, R. Paschotta, F. Morier-Genoud, M. Moser, and U. Keller, "Q-Switching Stability Limits of Continuous-Wave Passive Mode Locking," *J. Opt. Soc. Am. B.* **16:**46–56 (1999).
20. G. H. C. New, "Modelocking of Quasi-Continuous Lasers," *Opt. Commun.* **6:**188–192 (1972).
21. G. H. C. New, "Pulse Evolution in Mode-Locked Quasi-Continuous Lasers," *IEEE J. Quantum Electron.* **10:**115–124 (1974).
22. H. A. Haus, "Theory of Mode Locking with a Slow Saturable Absorber," *IEEE J. Quantum Electron.* **11:**736–746 (1975).
23. E. P. Ippen, "Principles of Passive Mode Locking," *Appl. Phys. B.* **58:**159–170 (1994).
24. J. A. Valdmanis, R. L. Fork, and J. P. Gordon, "Generation of Optical Pulses as Short as 27 fs Directly from a Laser Balancing Self-Phase Modulation, Group-Velocity Dispersion, Saturable Absorption, and Saturable Gain," *Optics Lett.* **10:**131–133 (1985).
25. J. A. Valdmanis and R. L. Fork, "Design Considerations for a Femtosecond Pulse Laser Balancing Self Phase Modulation, Group Velocity Dispersion, Saturable Absorption, and Saturable Gain," *IEEE J. Quantum Electron.* **22:**112–118 (1986).
26. O. E. Martinez, R. L. Fork, and J. P. Gordon, "Theory of Passively Modelocked Lasers Including Self-Phase Modulation and Group-Velocity Dispersion," *Optics Lett.* **9:**156–158 (1984).
27. O. E. Martinez, R. L. Fork, and J. P. Gordon, "Theory of Passively Modelocked Lasers for the Case of a Nonlinear Complex Propagation Coefficient," *J. Opt. Soc. Am. B.* **2:**753 (1985).
28. H. A. Haus, "Theory of Modelocking with a Fast Saturable Absorber," *J. Appl. Phys.* **46:**3049–3058 (1975).
29. K. N. Islam, E. R. Sunderman, C. E. Soccolich, I. Bar-Joseph, N. Sauer, T. Y. Chang, and B. I. Miller, "Color Center Lasers Passively Mode Locked by Quantum Wells," *IEEE J. Quantum Electronics* **25:**2454–2463 (1989).
30. U. Keller, K. J. Weingarten, F. X. Kärtner, D. Kopf, B. Braun, I. D. Jung, R. Fluck, C. Hönninger, N. Matuschek, and J. Aus der Au, "Semiconductor Saturable Absorber Mirrors (SESAMs) for Femtosecond to Nanosecond Pulse Generation in Solid-State Lasers," *IEEE J. Sel. Top. Quantum Electron.* **2:**435–453 (1996).
31. B. G. Kim, E. Garmire, S. G. Hummel, and P. D. Dapkus, "Nonlinear Bragg Reflector Based on Saturable Absorption," *Appl. Phys. Lett.* **54:**1095–1097 (1989).
32. L. R. Brovelli, I. D. Jung, D. Kopf, M. Kamp, M. Moser, F. X. Kärtner, and U. Keller, "Self-Starting Soliton Modelocked Ti:sapphire Laser Using a Thin Semiconductor Saturable Absorber," *Electronics Lett.* **31:**287–289 (1995).
33. S. Tsuda, W. H. Knox, E. A. D. Souza, W. Y. Jan, and J. E. Cunningham, "Low-Loss Intracavity AlAs/AlGaAs Saturable Bragg Reflector for Femtosecond Mode Locking in Solid-State Lasers," *Optics Letters* **20:**1406–1408 (1995).
34. L. R. Brovelli, U. Keller, and T. H. Chiu, "Design and Operation of Antiresonant Fabry-Perot Saturable Semiconductor Absorbers for Mode-Locked Solid-State Lasers," *J. Opt. Soc. Am. B.* **12:**311–322 (1995).
35. I. D. Jung, F. X. Kärtner, N. Matuschek, D. H. Sutter, F. Morier-Genoud, Z. Shi, V. Scheuer, M. Tilsch, T. Tschudi, and U. Keller, "Semiconductor Saturable Absorber Mirrors Supporting Sub-10 fs Pulses," *Applied Physics B: Special Issue on Ultrashort Pulse Generation* **65:**137–150 (1997).

36. I. P. Bilinsky, J. G. Fujimoto, J. N. Walpole, and L. J. Missaggia, "InAs-Doped Silica Films for Saturable Absorber Applications," *Appl. Phys. Lett.* **74:**2411–2413 (1999).
37. N. Sarukura, Y. Ishida, T. Yanagawa, and H. Nakano, "All Solid-State cw Passively Modelocked Ti:Sapphire Laser Using a Colored Glass Filter," *Appl. Phys. Lett.* **57:**229–230 (1990).
38. L. F. Mollenauer, R. H. Stolen, and J. P. Gordon, "Experimental Observation of Picosecond Pulse Narrowing and Solitons in Optical Fibers," *Phys. Rev. Lett.* **45:**1095–1098 (1980).
39. W. J. Tomlinson, R. H. Stolen, and C. V. Shank, "Compression of Optical Pulses Chirped by Self-Phase Modulation in Fibers," *J. Opt. Soc. Am. B.* **1:**139–149 (1984).
40. R. L. Fork, C. H. B. Cruz, P. C. Becker, and C. V. Shank, "Compression of Optical Pulses to Six Femtoseconds by Using Cubic Phase Compensation," *Optics Lett.* **12:**483–485 (1987).
41. S. Sartania, Z. Cheng, M. Lenzner, G. Tempea, C. Spielmann, F. Krausz, and K. Ferencz, "Generation of 0.1-TW 5-fs Optical Pulses at a 1-kHz Repetition Rate," *Optics Lett.* **22:**1562–1564 (1997).
42. R. L. Fork, C. V. Shank, C. Hirlimann, R. Yen, and W. J. Tomlinson, "Femtosecond White-Light Continuum Pulses," *Optics Letters* **8:**1–3 (1983).
43. G. M. Gale, M. Cavallari, T. J. Driscoll, and F. Hache, "Sub-20 fs Tunable Pulses in the Visible from an 82 MHz Optical Parametric Oscillator," *Optics Lett.* **20:**1562–1564 (1995).
44. F. X. Kärtner and U. Keller, "Stabilization of Soliton-Like Pulses with a Slow Saturable Absorber," *Optics Lett.* **20:**16–18 (1995).
45. F. X. Kärtner, I. D. Jung, and U. Keller, "Soliton Modelocking with Saturable Absorbers," *Special Issue on Ultrafast Electronics, Photonics and Optoelectronics, IEEE J. Sel. Topics in Quantum Electronics (JSTQE)* **2:**540–556 (1996).
46. I. D. Jung, F. X. Kärtner, L. R. Brovelli, M. Kamp, and U. Keller, "Experimental Verification of Soliton Modelocking Using Only a Slow Saturable Absorber," *Optics Lett.* **20:**1892–1894 (1995).
47. D. J. Kaup, "Perturbation Theory for Solitons in Optical Fibers," *Phys. Rev. A.* **42:**5689–5694 (1990).
48. L. F. Mollenauer and R. H. Stolen, "The Soliton Laser," *Optics Lett.* **9:**13–15 (1984).
49. F. M. Mitschke and L. F. Mollenauer, "Ultrashort Pulses from the Soliton Laser," *Optics Lett.* **12:**407–409 (1987).
50. P. N. Kean, X. Zhu, D. W. Crust, R. S. Grant, N. Landford, and W. Sibbett, "Enhanced Modelocking of Color Center Lasers," *Optics Lett.* **14:**39–41 (1989).
51. E. P. Ippen, H. A. Haus, and L. Y. Liu, "Additive Pulse Modelocking," *J. Opt. Soc. Am. B.* **6:**1736–1745 (1989).
52. D. E. Spence, P. N. Kean, and W. Sibbett, "60-fsec Pulse Generation from a Self-Mode-Locked Ti:Sapphire Laser," *Optics Lett.* **16:**42–44 (1991).
53. U. Keller, G. W. 'tHooft, W. H. Knox, and J. E. Cunningham, "Femtosecond Pulses from a Continuously Self-Starting Passively Mode-Locked Ti:Sapphire Laser," *Optics Lett.* **16:**1022–1024 (1991).
54. F. Salin, J. Squier, and M. Piché, "Modelocking of Ti:Sapphire Lasers and Self-Focusing: A Gaussian Approximation," *Optics Lett.* **16:**1674–1676 (1991).
55. D. K. Negus, L. Spinelli, N. Goldblatt, and G. Feugnet, "Sub-100 Femtosecond Pulse Generation by Kerr Lens Modelocking in Ti:Sapphire," in *Advanced Solid-State Lasers,* G. Dubé and L. Chase (eds.) Optical Society of America, Washington, D.C., 1991, vol. 10, pp. 120–124.
56. M. Piché and F. Salin, "Self-Mode Locking of Solid-State Lasers without Apertures," *Optics Letters* **18:**1041–1043 (1993).
57. V. Magni, G. Cerullo, S. D. Silvestri, and A. Monguzzi, "Astigmatism in Gaussian-Beam Self-Focussing and in Resonators for Kerr-Lens Mode-Locking," *JOSA B.* **12:**476–485 (1995).
58. H. A. Haus, J. G. Fujimoto, and E. P. Ippen, "Analytic Theory of Additive Pulse and Kerr Lens Mode Locking," *IEEE J. Quantum Electron.* **28:**2086–2096 (1992).
59. T. Brabec, C. Spielmann, and F. Krausz, "Mode Locking in Solitary Lasers," *Optics Lett.* **16:**1961–1963 (1991).
60. F. Krausz, M. E. Fermann, T. Brabec, P. F. Curley, M. Hofer, M. H. Ober, C. Spielmann, E. Wintner, and A. J. Schmidt, "Femtosecond Solid-State Lasers," *IEEE J. Quantum Electron.* **28:**2097–2122 (1992).
61. J.-L. Tapié, and G. Mourou, "Shaping of Clean, Femtosecond Pulses at 1.053 μm for Chirped-Pulse Amplification," *Optics Letters* **17:**136–138 (1992).

62. Y. Beaudoin, C. Y. Chien, J. S. Coe, J. L. Tapié, and G. Mourou, "Ultrahigh-Contrast Ti:Sapphire/Nd:Glass Terawatt Laser System," *Optics Lett.* **17:**865–867 (1992).
63. M. Hofer, M. H. Ober, F. Haberl, and M. E. Fermann, "Characterization of Ultrashort Pulse Formation in Passively Mode-Locked Fiber Lasers," *IEEE J. Quantum Electron.* **28:**720–728 (1992).
64. R. J. Elliot, in *Polarons and Excitons,* C. G. Kuper and G. D. Whitefield (eds.), Plenum, New York, 1963.
65. C. Weisbuch and B. Vinter, *Quantum Semiconductor Structures: Fundamentals and Applications,* Academic, San Diego, 1991.
66. J. Shah, *Ultrafast Spectroscopy of Semiconductors and Semiconductor Nanostructures,* Springer-Verlag, Berlin, 1996.
67. E. O. Göbel, "Ultrafast Spectroscopy of Semiconductors," in *Advances in Solid State Physics,* U. Rössler (ed.) Friedrich Vieweg & Sohn, Braunschweig/Wiesbaden, 1990, vol. 30, pp. 269–294.
68. L. Allen and J. H. Eberly, *Optical Resonance and Two-Level Atoms,* Dover, New York, 1975.
69. Y. R. Shen, *The Principles of Nonlinear Optics,* John Wiley & Sons, New York, 1984.
70. K. Shimoda, *Introduction to Laser Physics* (Springer Series in Optical Science) Springer, Heidelberg, 1984.
71. T. Yajima, and Y. Taira, "Spatial Optical Parametric Coupling of Picosecond Light Pulses and Transverse Relaxation Effects in Resonant Media," *Journal of the Physical Society of Japan* **47:**1620–1626 (1979).
72. A. M. Weiner, S. De Silvestri, and E. P. Ippen, "Three-Pulse Scattering for Femtosecond Dephasing Studies: Theory and Experiment," *J. Opt. Soc. Am. B.* **2:**654–661 (1985).
73. C. H. Brito Cruz, J. P. Gordon, P. C. Becker, R. L. Fork, and C. V. Shank, "Dynamics of Spectral Hole Burning," *IEEE J. Quantum Electron.* **24:**261–266 (1988).
74. B. Fluegel, N. Peyghambarian, G. Olbright, M. Lindberg, S. W. Koch, M. Joffre, D. Hulin, A. Migus, and A. Antonetti, "Femtosecond Studies of Coherent Transients in Semiconductors," *Physical Review Letters* **59:**2588–2591 (1987).
75. M. Lindberg and S. W. Koch, "Transient Oscillations and Dynamics Stark Effect in Semiconductors," *Phys. Rev. B.* **38:**7607–7614 (1988).
76. J. P. Sokoloff, M. Joffre, B. Fluegel, D. Hulin, M. Lindberg, S. W. Koch, A. Migus, A. Antonetti, and N. Peyghambarian, "Transient Oscillations in the Vicinity of Excitons and in the Band of Semiconductors," *Phys. Rev. B.* **38:**7615–7621 (1988).
77. H. Haug and S. Schmitt-Rink, "Basic Mechanisms of the Optical Nonlinearities of Semiconductors Near the Band Edge," *J. Opt. Soc. Am. B.* **2:**1135–1142 (1985).
78. H. Haug and S. W. Koch, *Quantum Theory of the Optical and Electronic Properties of Semiconductors,* World Scientific, Singapore, 1993.
79. S. Schmitt-Rink, D. S. Chemla, and D. A. B. Miller, "Linear and Nonlinear Optical Properties of Semiconductor Quantum Wells," *Advances in Physics,* **38:**89–188 (1989).
80. D. S. Chemla, "Ultrafast Transient Nonlinear Optical Processes in Semiconductors," in *Semiconductors and Semimetals,* Academic Press, Boston, 1999, vol. 58, pp. 175–256.
81. S. Hunsche, H. Heesel, A. Ewertz, H. Kurz, and J. H. Collet, "Spectral-Hole Burning and Carrier Thermalization in GaAs at Room Temperature," *Phys. Rev. B.* **48:**17818–17826 (1993).
82. L. Schultheis, J. Kuhl, A. Honold, and C. W. Tu, "Ultrafast Phase Relaxation of Excitons via Exciton-Exciton and Exciton-Electron Collisions," *Physical Review Letters* **57:**1635–1638 (1986).
83. A. Honold, L. Schultheis, J. Kuhl, and C. W. Tu, "Collision Broadening of Two-Dimensional Excitons in a GaAs Single Quantum Well," *Physical Review B.* **40:**6442–6445 (1989).
84. L. Schultheis, A. Honold, J. Kuhl, K. Köhler, and C. W. Tu, "Optical Dephasing of Homogeneously Broadened Two-Dimensional Exciton Transitions in GaAs Quantum Wells," *Physical Review B.* **34:**9027–9030, 1986.
85. J. Kuhl, A. Honold, L. Schultheis, and C. W. Tu, "Optical Dephasing and Orientational Relaxation of Wannier Excitons and Free Carriers in GaAs and GaAs/AlGaAs Quantum Wells," in *Advances in Solid State Physics,* U. Rössler (ed.) Friedrich Vieweg & Sohn, Braunschweig/Wiesbaden, 1989, vol. 29, pp. 157–181.

86. U. Siegner, D. Weber, E. O. Göbel, D. Bennhardt, V. Heuckeroth, R. Saleh, S. D. Baranovskii, P. Thomas, H. Schwab, C. Klingshirn, J. M. Hvam, and V. G. Lyssenko, "Optical Dephasing in Semiconductor Mixed Crystals," *Physical Review B.* **46:**4564–4581 (1992).
87. S. T. Cundiff and D. G. Steel, "Coherent Transient Spectroscopy of Excitons in GaAs-AlGaAs Quantum Wells," *IEEE Journal of Quantum Electronics* **28:**2423 (1992).
88. E. O. Göbel, K. Leo, T. C. Damen, J. Shah, S. Schmitt-Rink, W. Schäfer, J. F. Müller, and K. Köhler, "Quantum Beats of Excitons in Quantum Wells," *Physical Review Letters* **64:**1801–1804 (1990).
89. K. Leo, T. C. Damen, J. Shah, E. O. Göbel, and K. Köhler, "Quantum Beats of Light and Heavy Hole Excitons in Quantum Wells," *Appl. Phys. Lett.* **57:**19–21 (1990).
90. B. F. Feuerbacher, J. Kuhl, R. Eccleston, and K. Ploog, "Quantum Beats Between the Light and Heavy Hole Excitons in a Quantum Well," *Solid State Communications* **74:**1279–1283 (1990).
91. K. Leo, T. C. Damen, J. Shah, and K. Köhler, "Quantum Beats of Free and Bound Excitons in $GaAs/Al_xGa_{1-x}As$ Quantum Wells," *Physical Review B.* **42:**11359 (1990).
92. J. Feldmann, T. Meier, G. V. Plessen, M. Koch, E. O. Göbel, P. Thomas, G. Bacher, C. Hartmann, H. Schweizer, W. Schäfer, and N. Nickel, "Coherent Dynamics of Excitonic Wave Packets," *Physical Review Letters* **70:**3027–3030 (1993).
93. M. Koch, J. Feldmann, G. V. Plessen, E. O. Göbel, P. Thomas, and K. Köhler, "Quantum Beats Versus Polarization Interference: An Experimental Distinction," *Physical Review Letters* **69:**3631–3634 (1992).
94. V. G. Lyssenko, J. Erland, I. Balslev, K.-H. Pantke, B. S. Razbirin, and J. M. Hvam, "Nature of Nonlinear Four-Wave-Mixing Beats in Semiconductors," *Physical Review B.* **48:**5720–5723 (1993).
95. K. Leo, M. Wegener, J. Shah, D. S. Chemla, E. O. Göbel, T. C. Damen, S. Schmitt-Rink, and W. Schäfer, "Effects of Coherent Polarization Interaction on Time-Resolved Degenerate Four-Wave Mixing," *Physical Review Letters,* **65:**1340–1343 (1990).
96. M. Wegener, D. S. Chemla, S. Schmitt-Rink, and W. Schäfer, "Line Shape of Time-Resolved Four-Wave Mixing," *Physical Review A.* **42:**5675–5683 (1990).
97. D. S. Kim, J. Shah, T. C. Damen, W. Schäfer, F. Jahnke, S. Schmitt-Rink, and K. Köhler, "Unusual Slow Temporal Evolution of Femtosecond Four-Wave-Mixing Signals in Intrinsic GaAs Quantum Wells: Direct Evidence for the Dominance of Interaction Effects," *Physical Review Letters* **69:**2725 (1992).
98. S. Weiss, M.-A. Mycek, J.-Y. Bigot, S. Schmitt-Rink, and D. S. Chemla, "Collective Effects in Excitonic Free Induction Decay: Do Semiconductors and Atoms Emit Coherent Light in Different Ways?" *Physical Review Letters* **69:**2685–2688 (1992).
99. H. Wang, K. Ferrio, D. G. Steel, Y. Z. Hu, R. Binder, and S. W. Koch, "Transient Nonlinear Optical Response from Excitation Induced Dephasing in GaAs," *Physical Review Letters* **71:**1261–1264 (1993).
100. P. Kner, S. Bar-Ad, M. V. Marquezini, D. S. Chemla, and W. Schäfer, "Magnetically Enhanced Exciton-Exciton Correlations in Semiconductors," *Physical Review Letters* **78:**1319–1322 (1997).
101. P. Kner, W. Schäfer, R. Lövenich, and D. S. Chemla, "Coherence of Four-Particle Correlations in Semiconductors," *Phys. Rev. Letters* **81:**5386–5389 (1998).
102. G. Bartels, A. Stahl, V. M. Axt, B. Haase, U. Neukirch, and J. Gutowski, "Identification of Higher-Order Electronic Coherences in Semiconductors by their Signature in Four-Wave-Mixing Signals," *Physical Review Letters* **81:**5880–5883 (1998).
103. P. Kner, S. Bar-Ad, M. V. Marquezini, D. S. Chemla, R. Lövenich, and W. Schäfer, "Effect of Magnetoexciton Correlations on the Coherent Emission of Semiconductors," *Phys. Rev. B.* **60:**4731 (1999).
104. P. C. Becker, H. L. Fragnito, C. H. Brito Cruz, R. L. Fork, J. E. Cunningham, J. E. Henry, and C. V. Shank, "Femtosecond Photon Echoes from Band-to-Band Transitions in GaAs," *Physical Review Letters* **61:**1647–1649 (1988).
105. J.-Y. Bigot, M. T. Portella, R. W. Schoenlein, J. E. Cunningham, and C. V. Shank, "Two-Dimensional Carrier-Carrier Screening in a Quantum Well," *Physical Review Letters* **67:**636–639 (1991).
106. S. Arlt, U. Siegner, J. Kunde, F. Morier-Genoud, and U. Keller, "Ultrafast Dephasing of Continuum Transitions in Bulk Semiconductors," *Physical Review B.* **59:**14860–14863 (1999).

107. J. A. Kash, J. C. Tsang, and J. M. Hvam, "Subpicosecond Time-Resolved Raman Spectroscopy of LO Phonons in GaAs," *Physical Review Letters* **54:**2151–2154 (1985).
108. G. Fasol, W. Hackenburg, H. P. Hughes, K. Ploog, E. Bauser, and H. Kano, "Continous-Wave Spectroscopy of Femtosecond Carrier Scattering in GaAs," *Physical Review B.* **41:**1461–1478 (1990).
109. J. H. Collet, "Screening and Exchange in the Theory of the Femtosecond Kinetics of the Electron-Hole Plasma," *Physical Review B.* **47:**10279–10291 (1993).
110. A. Lohner, K. Rick, P. Leisching, A. Leitenstorfer, T. Elsässer, T. Kuhn, F. Rossi, and W. Stolz, "Coherent Optical Polarization of Bulk GaAs Studied by Femtosecond Photon-Echo Spectroscopy," *Physical Review Letters* **71:**77–80 (1993).
111. U. Siegner, M.-A. Mycek, S. Glutsch, and D. S. Chemla, "Ultrafast Coherent Dynamics of Fano Resonances in Semiconductors," *Physical Review Letters* **74:**470–473 (1995).
112. U. Siegner, M.-A. Mycek, S. Glutsch, and D. S. Chemla, "Quantum Interference in the System of Lorentzian and Fano Magnetoexciton Resonances in GaAs," *Physical Review B.* **51:**4953–4961 (1995).
113. S. Arlt, U. Siegner, F. Morier-Genoud, and U. Keller, "Ultrafast Coherent Dynamics in Semiconductor Quantum Wells for Multi-Subband Excitation in Different Density Regimes," *Physical Review B.* **58:**13073–13080 (1998).
114. T. Rappen, U. Peter, M. Wegener, and W. Schäfer, "Coherent Dynamics of Continuum and Exciton States Studied by Spectrally Resolved fs Four-Wave Mixing," *Physical Review B.* **48:**4879–4882 (1993).
115. M. U. Wehner, D. Steinbach, and M. Wegener, "Ultrafast Coherent Transients Due to Exciton-Continuum Scattering in Bulk GaAs," *Physical Review B.* **54:**R5211–R5214 (1996).
116. D. Birkedal, V. G. Lyssenko, J. M. Hvam, and K. ElSayed, "Continuum Contribution to Excitonic Four-Wave Mixing Due to Interaction-Induced Nonlinearities," *Physical Review B.* **54:**R14250–R14253 (1996).
117. S. T. Cundiff, M. Koch, W. H. Knox, J. Shah, and W. Stolz, "Optical Coherence in Semiconductors: Strong Emission Mediated by Nondegenerate Interactions," *Physical Review Letters* **77:**1107–1110 (1996).
118. V. P. Kalosha, M. Müller, and J. Herrmann, "Coherent-Absorber Mode Locking of Solid-State Lasers," *Optics Letters* **23:**117–119 (1998).
119. V. P. Kalosha, M. Müller, and J. Herrmann, "Theory of Solid-State Laser Mode Locking by Coherent Semiconductor Quantum-Well Absorbers," *J. Opt. Soc. Am. B.* **16:**323 (1999).
120. J. L. Oudar, D. Hulin, A. Migus, A. Antonetti, and F. Alexandre, "Subpicosecond Spectral Hole Burning Due to Nonthermalized Photoexcited Carriers in GaAs," *Physical Review Letters* **55:**2074–2077 (1985).
121. W. H. Knox, C. Hirlimann, D. A. B. Miller, J. Shah, D. S. Chemla, and C. V. Shank, "Femtosecond Excitation of Nonthermal Carrier Populations in GaAs Quantum Wells," *Physical Review Letters* **56:**1191–1193 (1986).
122. R. W. Schoenlein, W. Z. Lin, E. P. Ippen, and J. G. Fujimoto, "Femtosecond Hot-Carrier Energy Relaxation in GaAs," *Appl. Phys. Lett.* **51:**1442–1444 (1987).
123. W. H. Knox, D. S. Chemla, G. Livescu, J. E. Cunningham, and J. E. Henry, "Femtosecond Carrier Thermalization in Dense Fermi Seas," *Physical Review Lett.* **61:**1290–1293 (1988).
124. J.-Y. Bigot, M. T. Portella, R. W. Schoenlein, J. E. Cunningham, and C. V. Shank, "Resonant Intervalley Scattering in GaAs," *Physical Review Letters* **65:**3429–3432 (1990).
125. P. C. Becker, H. L. Fragnito, C. H. Brito Cruz, J. Shah, R. L. Fork, J. E. Cunningham, J. E. Henry, and C. V. Shank, "Femtosecond Intervalley Scattering in GaAs," *Appl. Phys. Lett.* **53:**2089 (1988).
126. J.-P. Foing, D. Hulin, M. Joffre, M. K. Jackson, J.-L. Oudar, C. Tanguy, and M. Combescot, "Absorption Edge Singularities in Highly Excited Semiconductors," *Physical Review Letters* **68:**110–113, 1992.
127. C. Tanguy and M. Combescot, "X-Ray-Like Singularities for Nonequilibrium Fermi Sea," *Phys. Rev. Lett.* **68:**1935–1938 (1992).
128. J. Kunde, U. Siegner, S. Arlt, F. Morier-Genoud, and U. Keller, "Chirp-Controlled Ultrafast Optical Nonlinearities in Semiconductors," *Appl. Phys. Lett.* **73:**3025–3027 (1998).

129. J. Kunde, U. Siegner, S. Arlt, G. Steinmeyer, F. Morier-Genoud, and U. Keller, "Potential of Femtosecond Chirp Control of Ultrabroadband Semiconductor Continuum Nonlinearities," *J. Opt. Soc. Am. B.* **16:**2285–2294 (1999).
130. W. S. Warren, H. Rabitz and M. Dahleh, "Coherent Control of Quantum Dynamics: The Dream is Alive," *Science,* **259:**1581–1589 (1993).
131. A. M. Weiner, "Femtosecond Pulse Shaping Using Spatial Light Modulators," *Rev. Sci. Instruments,* **71:**1929–1960 (2000).
132. R. Takahashi, Y. Kawamura, and H. Iwamura, "Ultrafast 1.55 μm All-Optical Switching Using Low-Temperature-Grown Multiple Quantum Wells," *Appl. Phys. Lett.* **68:**153–155 (1996).
133. H. S. Loka and P. W. E. Smith, "Ultrafast All-Optical Switching in an Asymmetric Fabry-Perot Device Using Low-Temperature-Grown GaAs," *IEEE Phot. Tech. Lett.* **10:**1733–1735 (1998).
134. J. F. Whitaker, "Optoelectronic Applications of LTMBE III-V Materials," *Mater. Sci. Eng.* **B22:**61–67 (1993).
135. J. F. Ziegler, J. P. Biersack, and U. Littmark, *The Stopping and Range of Ions in Solids,* Pergamon, New York, 1989.
136. F. W. Smith, A. R. Calawa, C.-L. Chen, M. J. Manfra, and L. J. Mahoney, "New MBE Buffer Used to Eliminate Backgating in GaAs MESFETs," *IEEE Electron. Device Lett.* **9:**77–80 (1988).
137. X. Liu, A. Prasad, W. M. Chen, A. Kurpiewski, A. Stoschek, Z. Liliental-Weber, and E. R. Weber, "Mechanism Responsible for the Semi-Insulating Properties of Low-Temperature-Grown GaAs," *Appl. Phys. Lett.* **65:**3002–3004 (1994).
138. X. Liu, A. Prasad, J. Nishio, E. R. Weber, Z. Liliental-Weber, and W. Walukiewicz, "Native Point Defects in Low-Temperature Grown GaAs," *Appl. Phys. Lett.* **67:**279 (1995).
139. M. Luysberg, H. Sohn, A. Prasad, P. Specht, Z. Liliental-Weber, E. R. Weber, J. Gebauer, and R. Krause-Rehberg, "Effects of the Growth Temperature and As/Ga Flux Ratio on the Incorporation of Excess As into Low Temperature Grown GaAs," *J. Appl. Phys.* **83:**561–6, 1998.
140. Z. Liliental-Weber, J. Ager, D. Look, X. W. Lin, X. Liu, J. Nishio, K. Nichols, W. Schaff, W. Swider, K. Wang, J. Wasburn, E. R. Weber, and J. Whitaker, in *Proceedings of the Eighth Conference on Semi-insulating III–V Materials,* edited by M. Godlewski (World Scientific, Singapore, 1994), p. 305.
141. M. R. Melloch, N. Otsuka, J. M. Woodall, A. C. Warren, and J. L. Freeouf, "Formation of Arsenic Precipitates in GaAs Buffer Layers Grown by Molecular Beam Epitaxy at Low Substrate Temperatures," *Appl. Phys. Lett.* **57:**1531 (1990).
142. G. L. Witt, R. Calawa, U. Mishra, E. Weber (eds.), *Low Temperature (LT) GaAs and Related Materials,* Mat. Res. Soc. Symp. Proceedings, vol. 241 Pittsburgh, 1992.
143. G. L. Witt, "LTMBE GaAs: Present Status and Perspectives," *Mater. Sci. Eng.* **B22:**9 (1993).
144. S. Gupta, M. Y. Frankel, J. A. Valdmanis, J. F. Whitaker, G. A. Mourou, F. W. Smith, and A. R. Calawa, "Subpicosecond Carrier Lifetime in GaAs Grown by Molecular Beam Epitaxy at Low Temperatures," *Appl. Phys. Lett.* **59:**3276–3278 (1991).
145. S. Gupta, J. F. Whitaker, and G. A. Mourou, "Ultrafast Carrier Dynamics in III-V Semiconductors Grown by Molecular-Beam Epitaxy at Very Low Substrate Temperatures," *IEEE J. Quantum Electron.* **28:**2464–2472 (1992).
146. K. A. McIntosh, K. B. Nichols, S. Verghese, and E. R. Brown, "Investigation of Ultrashort Photocarrier Relaxation Times in Low-Temperature-Grown GaAs," *Appl. Phys. Lett.* **70:**354–356 (1997).
147. M. Haiml, U. Siegner, F. Morier-Genoud, U. Keller, M. Luysberg, R. C. Lutz, P. Specht, and E. R. Weber, "Optical Nonlinearity in Low-Temperature Grown GaAs: Microscopic Limitations and Optimization Strategies," *Appl. Phys. Lett.* **74:**3134 (1999).
148. E. S. Harmon, M. R. Melloch, J. M. Woodall, D. D. Nolte, N. Otsuka, and C. L. Chang, "Carrier Lifetime versus Anneal in Low Temperature Growth GaAs," *Appl. Phys. Lett.* **63:**2248–2250 (1993).
149. Y. Kostoulas, L. J. Waxer, I. A. Walmsley, G. W. Wicks, and P. M. Fauchet, "Femtosecond Carrier Dynamics in Low-Temperature-Grown Indium Phosphide," *Appl. Phys. Lett.* **66:**1821–1823 (1995).
150. Y. Kostoulas, K. B. Ucer, G. W. Wicks, and P. M. Fauchet, "Femtosecond Carrier Dynamics in Low-Temperature Grown $Ga_{0.51}In_{0.49}P$," *Appl. Phys. Lett.* **67:**3756–3758 (1995).
151. U. Siegner, R. Fluck, G. Zhang, and U. Keller, "Ultrafast High-Intensity Nonlinear Absorption Dynamics in Low-Temperature Grown Gallium Arsenide," *Appl. Phys. Lett.* **69:**2566–2568 (1996).

152. A. J. Lochtefeld, M. R. Melloch, J. C. P. Chang, and E. S. Harmon, "The Role of Point Defects and Arsenic Precipitates in Carrier Trapping and Recombination in Low-Temperature Grown GaAs," *Appl. Phys. Lett.* **69:**1465–1467 (1996).

153. G. Segschneider, T. Dekorsky, H. Kurz, R. Hey, and K. Ploog, "Energy Resolved Ultrafast Relaxation Dynamics Close to the Band Edge of Low-Temperature Grown GaAs," *Appl. Phys. Lett.* **71:**2779–2781 (1997).

154. T. S. Sosnowski, T. B. Norris, H. H. Wang, P. Grenier, and J. F. Whitaker, "High-Carrier-Density Electron Dynamics in Low-Temperature-Grown GaAs," *Appl. Phys. Lett.* **70:**3245–3247 (1997).

155. H. S. Loka, S. D. Benjamin, and P. W. E. Smith, "Optical Characterization of Low-Temperature-Grown GaAs for Ultrafast All-Optical Switching Devices," *IEEE J. Quantum Electron.* **34:**1426–1437 (1998).

156. M. B. Johnson, T. C. McGill, and N. G. Paulter, "Carrier Lifetimes in Ion-Damaged GaAs," *Appl. Phys. Lett.* **54:**2424–2426 (1989).

157. M. Lambsdorff, J. Kuhl, J. Rosenzweig, A. Axmann, and J. Schneider, "Subpicosecond Carrier Lifetimes in Radiation-Damaged GaAs," *Appl. Phys. Lett.* **58:**1881–1883 (1991).

158. A. Krotkus, S. Marcinkevicius, J. Jasinski, M. Kaminska, H. H. Tan, and C. Jagadish, "Picosecond Carrier Lifetime in GaAs Implanted with High Doses of As Ions: An Alternative Material to Low-Temperature GaAs for Optoelectronic Applications," *Appl. Phys. Lett.* **66:**3304–3306 (1995).

159. F. Ganikhanov, G.-R. Lin, W.-C. Chen, C.-S. Chang, and C.-L. Pan, "Subpicosecond Carrier Lifetimes in Arsenic-Implanted GaAs," *Appl. Phys. Lett.* **67:**3465–3467 (1995).

160. C. Jagadish, H. H. Tan, A. Krotkus, S. Marcinkevicius, K. P. Korona, and M. Kaminska, "Ultrafast Carrier Trapping in High Energy Ion Implanted Gallium Arsenide," *Appl. Phys. Lett.* **68:**2225–2227 (1996).

161. M. J. Lederer, B. Luther-Davies, H. H. Tan, C. Jagadish, M. Haiml, U. Siegner, and U. Keller, "Nonlinear Optical Absorption and Temporal Response of Arsenic- and Oxygen-Implanted GaAs," *Appl. Phys. Lett.* **74:**1993–1995 (1999).

162. H. H. Tan, C. Jagadish, M. J. Lederer, B. Luther-Davies, J. Zou, D. J. H. Cockayne, M. Haiml, U. Siegner, and U. Keller, "Role of Implantation-Induced Defects on the Response Time of Semiconductor Saturable Absorbers," *Appl. Phys. Lett.* **75:**1437–1439 (1999).

163. M. Haiml, U. Siegner, F. Morier-Genoud, U. Keller, M. Luysberg, P. Specht, and E. R. Weber, "Femtosecond Response Times and High Optical Nonlinearity in Beryllium Doped Low-Temperature Grown GaAs," *Appl. Phys. Lett.* **74:**1269–1271 (1999).

164. P. Specht, S. Jeong, H. Sohn, M. Luysberg, A. Prasad, J. Gebauer, R. Krause-Rehberg, and E. R. Weber, "Defect Control in As-rich GaAs," *Mater. Sci. Forum* 258–263, 951 (1997).

This page intentionally left blank.

CHAPTER 26
QUANTUM THEORY OF THE LASER

János A. Bergou[a,b]
Berthold-Georg Englert[a,c,d]
Melvin Lax[e]
Marlan O. Scully[a,c]
Herbert Walther[c,f]
M. Suhail Zubairy[a,g]

[a]*Institute for Quantum Studies and Department of Physics*
Texas A&M University
College Station, Texas

[b]*Department of Physics and Astronomy*
Hunter College of the City University of New York
New York, New York

[c]*Max-Planck-Institut für Quantenoptik*
Garching bei München, Germany

[d]*Abteilung Quantenphysik der Universität Ulm*
Ulm, Germany

[e]*Department of Physics*
City College of the City University of New York
New York, New York

[f]*Sektion Physik der Universität München*
Garching bei München, Germany

[g]*Department of Electronics*
Quaid-i-Azam University
Islamabad, Pakistan

Copyright 2001 by The McGraw-Hill Companies, Inc. Click Here for Terms of Use.

26.1 GLOSSARY

Section 26.3

$a_k, a_k^\dagger$	annihilation, creation operator for photons in the k-th mode
A	Einstein coefficient for spontaneous emission
$\mathbf{A}_k(\mathbf{r})$	kth electric mode function at position $\mathbf{r}$
B	Einstein coefficient for absorption and stimulated emission
$\mathbf{B}(\mathbf{r}, t)$	magnetic field at position $\mathbf{r}$ and time t
$\mathbf{B}_k(\mathbf{r})$	kth magnetic mode function at position $\mathbf{r}$
c	speed of light
$\mathbf{e}_k$	polarization unit vector of the kth mode
$\mathbf{E}_\perp(\mathbf{r}, t)$	transverse electric field at position $\mathbf{r}$ and time t
$h, \hbar$	*Planck's constant* $[\hbar = h/(2\pi)]$
$\mathbf{k}, k$	wave vector, its length
$(d\mathbf{k})$	three-dimensional volume element in $\mathbf{k}$ space
k_B	Boltzmann's constant
$\mathbf{n}_k$	propagation unit vector of the kth mode
N	photon number operator
N_e	number of excited-state atoms
N_g	number of ground-state atoms
$\mathbf{r}$	position vector
$(d\mathbf{r})$	three-dimensional volume element in $\mathbf{r}$ space
t, dt	time, time interval
T	temperature
$U_{1\mathrm{ph}}$	energy density for a one-photon state
dV	volume element
$\lvert\mathbf{vac}\rangle, \langle\mathbf{vac}\rvert$	ket and bra of the photon vacuum
$\overline{w^2}$	mean square energy fluctuations
W	spectral-spatial energy density of blackbody radiation
α_k	coherent state amplitudes
$\lvert\{\alpha\}_c\rangle$	ket of a coherent state
δ_{jk}	Kronecker's delta symbol
$\delta_\perp(\mathbf{r})$	transverse delta function at $\mathbf{r}$ (a dyadic)
ε_0	dielectric constant $[\varepsilon_0 = 1/(\mu_0 c^2) \simeq 8.854 \times 10^{-12}$ F/m]
μ_0	permeability constant $(4\pi \times 10^{-7}$ H/m)
$\nu, d\nu$	light frequency, frequency interval
ν_k	frequency of the kth mode
ϱ_ph	statistical operator of the photon field
ρ	probability amplitude for reflection
τ	probability amplitude for transmission
ψ_k, ψ_{jk}	probability amplitudes of the one-photon, two-photon states

$\|\{\psi\}_1\rangle$, $\|\{\psi\}_2\rangle$	kets for one-photon, two-photon states
∇	gradient vector differential operator

Section 26.4

A	destruction operator for the field
$\mathcal{A}$	laser gain coefficient
a, $a^\dagger$	photon ladder operators
$\mathcal{B}$	laser saturation parameter
b_k, $b_k^\dagger$	destruction and creation operators for the reservoir modes
$\mathcal{D}$	largest eigenvalue of the laser equation
$F(t)$	field noise operator
$F_\alpha(t)$, F_γ	noise operators associated with gain and loss, respectively
$F(1, x, y)$	hypergeometric function
g	radiant frequency stating the strength of atom-photon coupling
g_k	couping coefficient between reservoir and field
$G^{(1)}(t_0 + t, t_0)$	field correlation function
$\mathcal{H}$, $\mathcal{H}_0$, $\mathcal{H}_1$	total, free, and interaction hamiltonians for atom-field interaction
k	wave vector for the field
K	kick operator
$\mathcal{L}$	superoperator for cavity damping
$M(\tau)$	superoperator describing the effect of a single inverted atom on the field
$\bar{n}$, $\overline{n^2}$	mean and mean squared number of photons in a laser
n_m	maximum of the photon distribution of a laser
n_{th}	mean number of photons in a thermal reservoir
N_{ex}	number of atoms traversing the cavity during the lifetime of the cavity field
$N(t_i, t, \tau)$	notch function
p	transition dipole moment
$p(n)$	photon distribution function
$P(\tau)$	distribution function for the interaction times
q	a nonnegative integer
Q	Mandel Q function
r	atom injection rate inside a laser and micromaser
$S(\omega)$	spectrum of the laser field
T	temperature
t_m	measurement time
U	time evolution operator
$U_{\text{a f}}(\tau)$	atom-field time evolution operator
$\mathcal{V}$	interaction picture hamiltonian
$\alpha(t, t')$	gain function of a laser

Γ	atomic decay rate via spontaneous emission
$\gamma, \gamma_a, \gamma_b$	atomic decay rates
$\delta_{nn'}$	Kronecker delta function
ν_k	frequency of the reservoir mode
σ_+, σ_-	ladder operators for a two-level atom
σ_z	atomic inversion operator
ω_0	radiant frequency of an atomic transition
λ	eigenvalue
λ_j	eigenvalues of the laser equation
$\rho(t)$	reduced density operator for the field
ρ_{at}	total density operator for the atom-field system
$\rho_{nn'}$	matrix elements of the field density operator
$\rho_n^{(k)}$	off-diagonal density matrix element
κ	cavity loss rate
χ	square of the ratio of vacuum Rabi frequency and the atomic decay rate
$\theta(t)$	step function
$\phi(t)$	phase of the field

Section 26.5

a, b, c, d	parameters appearing in Table 1
$\underline{E}$	electric field strength
$\overline{E}$	mean field
$F(M), F_0$	free energy of a ferromagnet, its value for $M = 0$
g_k	undefined in Eqs. (126) and (127)
$G(E), G_0$	free energy of a laser, its value for $E = 0$
H	external magnetic field
H_{n0}	heating rate
K	one-fourth the spontaneous emission rate
K_{n0}	cooling rate
n_0	number of atoms in the Bose-Einstein condensate
$\langle n_0 \rangle$	mean number of atoms in the condensate
$\langle \dot{n}_0 \rangle$	time derivative of $\langle n_0 \rangle$
$\langle n_k \rangle_{n0}$	average number of atoms in the kth excited state, given n_0 atoms in the condensate
N	total number of Bose atoms
N', N''	normalization constants in Table 1
M	magnetization of a ferromagnet
$P(M)$	probability density for a ferromagnet
$P(E)$	probability density for a laser
$P(\alpha, \alpha^*)$	P representation for the field

S	injected signal
T_c	critical temperature
W_k	heat bath density of states
x, y	$x = \mathrm{Re}\,\alpha$, $y = \mathrm{Im}\,\alpha$
X	zero-field susceptibility of a ferromagnet
$Z(T, N)$	canonical partition function
α	eigenvalue of the coherent state $\lvert\alpha\rangle$
ε	scaled temperature (inversion) of a ferromagnet (laser) in Fig. 9
$\zeta(3)$	Riemann's zeta function $\zeta(3) = 1.2020569\ldots$
η	scaled thermodynamical variable (in Fig. 9)
$\langle\eta_k\rangle$	average occupation number of the kth heat bath oscillator
$\Theta(\,)$	Heaviside's unit step function
κ	undefined in Eq. (15)
ξ	laser analog of X
$\rho_{n0,\,n0}$	probability for having n_0 atoms in the condensate
$\dot{\rho}_{n0,\,n0}$	time derivative of $\rho_{n0,\,n0}$
σ	population inversion
σ_t	threshold inversion
$\Phi_\varepsilon(\eta)$	scaled thermodynamical potential (in Fig. 9)
Ω	trap frequency

Section 26.6

A	phase-shifted destruction operator for a free-electron laser (FEL)
c_b, c_c	probability amplitudes for atom to be in levels $\lvert b\rangle$ and $\lvert c\rangle$, respectively
$\mathcal{D}(\theta)$	phase diffusion function
$\mathscr{E}$	slowly varying field amplitude
g	coupling constant for the electron-field interaction in a FEL
j	parameter for the gain in an FEL
k	wavevector for the laser field in an FEL
$\mathscr{L}_{ij}$	linear gain ($i = j$) and cross-coupling ($i \neq j$) Liouville operators
m	mass of electron
$O(A, A^\dagger)$	arbitrary operator containing A, $A^\dagger$
p	electron momentum
$\overline{p}$	eigenvalue of electron momentum operator
P_b, P_c	probability of atom being in states $\lvert b\rangle$ and $\lvert c\rangle$, respectively
P_{emission}	probability of emission of radiation
$S(T)$	time-evolution operator for the electron-photon state
T	electron-photon interaction time
$\mathscr{T}$	time-ordering operator
z	electron coordinate

α_i	eigenvalue of the coherent state $\|\alpha_i\rangle$
α_{ij}	constants depending upon parameters of gain medium in a correlated emission laser (CEL)
β	normalized electron momentum
γ	relativistic factor for an electron
Δ	atom-field detuning in lasing without inversion (LWI)
ν_1, ν_2	frequencies of the two modes in a CEL
$\rho(t_i)$	atomic density operator at initial time t_i
$\rho_{ij}^{(0)}$	initial values of the ijth atomic matrix elements
ρ_i	classical amplitude of the ith mode
$\rho(a_1, a_1^\dagger; a_2, a_2^\dagger)$	reduced density operator for the two-mode field in a CEL
θ_i	phase of the ith field
ω_0	microwave frequency
$\omega_a, \omega_b, \omega_c$	frequencies associated with atomic levels
λ_s	wavelength of the field emitted in an FEL
λ_W	the period of the magnetic wiggler
κ	gain coefficient
$\kappa_{a\to b}, \kappa_{a\to c}$	constants depending upon the matrix elements between the relevant levels
ϕ	relative phase between atomic levels
Φ	total phase angle in two-mode CEL schemes
ψ	relative phase $\Phi + \theta_1 - \theta_2$

26.2 INTRODUCTION

Most lasers, and in particular all commercially sold ones, emit electromagnetic radiation whose properties can be accounted for quite well by a *semiclassical* description. In such a treatment, quantum aspects (level spacings, oscillator strengths, etc.) of the matter (atoms, molecules, electron-hole pairs, etc.) that constitute the gain medium are essential, but those of the electromagnetic field are disregarded. Quantum properties of the radiation are, however, of decisive importance for laser systems "at the limit" which reach fundamental bounds for the linewidth, for the regularity of photon statistics, or for other quantities of interest.

Recognition and understanding of these fundamental limitations are furnished by the quantum theory of the laser, whose foundations were laid in the 1960s. The two main approaches, the master-equation formalism and the Langevin method—equivalent in the physical contents and supplementing each other like spouses—can be roughly, and somewhat superficially, associated with the Schrödinger and the Heisenberg pictures of quantum mechanics. The master-equation method corresponds to the former, the Langevin approach to the latter. Both are reviewed in Sec. 26.4, but more room is given to the master-equation treatment. This bias originates in our intention to present a parallel exposition for both the standard laser theory and the theory of the micromaser, which in turn is traditionally and most conveniently treated by master equations.

The micromaser, in which the dynamic is dominated by the strong coupling of a single mode of the radiation field to a single atomic dipole transition, is the prototype of an open, driven quantum system. Accordingly, micromaser experiments are *the* test ground for the quantum theory of the laser; therefore, micromaser theory deserves the special attention that it receives in Sec. 26.4.

As a logical and historical preparation, we recall in Sec. 26.3, the theoretical and experimental facts that are evidence for quantum properties of electromagnetic radiation in general, and the reality of photons in particular. Some special issues are discussed in Secs. 26.5 and 26.6. In Sec. 26.5, we stress the analogy between the threshold behavior of a laser and the phase transition of a ferromagnet, and note the recent lessons about Bose-Einstein condensates taught by this analogy. Section 26.6 summarizes the most important features of some exotic lasers and masers, which exploit atomic coherences or the quantum properties of the atomic center-of-mass motion. Basics of the so-called free-electron laser are reported as well.

The quantum theory of the laser is a central topic in the field of quantum optics. An in-depth understanding of the various facets of quantum optics can be gained by studying the pertinent textbooks.[1–18]

26.3 SOME HISTORY OF THE PHOTON CONCEPT

Early History: Einstein's Light Quanta

Planck's formula of 1900[19] marks the beginning of quantum mechanics, and in particular of the quantum theory of light. It reads

$$W = \frac{8\pi\nu^2}{c^3} \frac{h\nu}{\exp\,(h\nu/k_B T) - 1} \tag{1}$$

and relates the spectral-spatial energy density W of blackbody radiation to the frequency ν of the radiation and the temperature T of the blackbody. Boltzmann's constant k_B and Planck's constant h are conversion factors that turn temperature and frequency into energy, and c is the speed of light. A volume dV contains electromagnetic energy of the amount $W\,d\nu\,dV$ in the frequency range $\nu \cdots \nu + d\nu$.

The first factor in Eq. (1) is the density of electromagnetic modes. It obtains as a consequence of the classical wave theory of light and owes its simplicity to an implicit short-wavelength approximation. For wavelengths of the order of magnitude set by the size of the cavity that contains the radiation, appropriate corrections have to be made that reflect the shape and size of the cavity. This is of great importance in the context of micromasers, but need not concern us presently.

The second factor in Eq. (1) is the mean energy associated with radiation of frequency ν. It is a consequence of the quantum nature of light. In the limits of very high frequencies or very low ones, it turns into the respective factors of Wien[20] and Rayleigh-Jeans[21,22]:

$$\begin{aligned} &\frac{h\nu}{\exp\,(h\nu/k_B T) - 1} && \text{(Planck)} \\ \rightarrow &\begin{cases} h\nu \exp -\dfrac{h\nu}{k_B T} & \text{for } \nu \gg \dfrac{k_B T}{h} \quad \text{(Wien)} \\ k_B T & \text{for } \nu \ll \dfrac{k_B T}{h} \quad \text{(Rayleigh-Jeans)} \end{cases} \end{aligned} \tag{2}$$

The relevant frequency scale is set by $k_B T/h$; at a temperature of $T = 288$ K it is about 6×10^{12} Hz, corresponding to a wavelength of 50 μm.

Ironically, Planck—whose stroke of genius was to interpolate between the two limiting forms of Eq. (2)—was not convinced of the quantum nature of electromagnetic radiation until much later. Legend has it that it was the discovery of Compton scattering in 1923 that did it.[23] We are, however, getting ahead of the story.

The true significance of Planck's formula, Eq. (1), started to emerge only after Einstein[24] had drawn the conclusions that led him to his famous *light-quantum hypothesis* of 1905, the *annus mirabilis.* In Pauli's words,

> He immediately applied [it] to the photoelectric effect and to Stokes' law for fluorescence, later also to the generation of secondary cathode rays by X-rays and to the prediction of the high frequency limit in the *Bremsstrahlung.*[25]

Quite a truckload, indeed.

The conflict with the well-established wave theory of light was, of course, recognized immediately, and so the introduction of light quanta also gave birth to the wave-particle duality. Upon its extension to massive objects by de Broglie in 1923 to 1924,[26,27] it was instrumental in Schrödinger's wave mechanics.[28]

Taylor's 1909 experiment,[29] in which feeble light produced interference fringes, although at most one light quantum was present in the interferometer at any time, addressed the issue of wave-particle duality from a different angle. Its findings are succinctly summarized in Dirac's dictum that "a photon interferes only with itself"[30]—a statement that became the innocent victim of misunderstanding and misquotation in the course of time.[31]

Another important step was taken the same year by Einstein.[32] By an ingenious application of thermodynamic ideas to Planck's formula, in particular consequences of Boltzmann's relation between entropy and statistics, he derived an expression for the mean-square energy fluctuations $\overline{w^2}$ of the radiation in a frequency interval $\nu \cdots \nu + d\nu$ and a volume dV:

$$\overline{w^2} = \left(\frac{c^3}{8\pi\nu^2} W + h\nu \right) W \, d\nu \, dV \tag{3}$$

where W is the spectral-spatial density of Eq. (1), so that $W \, d\nu \, dV$ is the mean energy in the frequency interval and volume under consideration. The first term is what one would get if classical electrodynamics accounted for all properties of radiation. There is no room for the second term in a wave theory of light; it is analogous to the fluctuations in the number of gas molecules occupying a given volume. This second term therefore supports Einstein's particle hypothesis of 1905,[24] in which electromagnetic energy is envisioned as being concentrated in localized lumps that are somehow distributed over the volume occupied by the electromagnetic wave.

Wave aspects (first term) and particle aspects (second term) enter Eq. (3) on equal footing. Since the thermodynamic considerations have no bias toward either one, one must conclude that Planck's formula, Eq. (1), is unbiased as well. Electromagnetic radiation is as much a particle phenomenon as it is a wave phenomenon.

Einstein left the center stage of quantum theory for some years, returning to it after completing his monumental work on general relativity. In 1913, Bohr's highly speculative postulates[33] had suddenly led to a preliminary understanding of many features of atomic spectra (the anomalous Zeeman effect was one big exception; it remained a bewildering puzzle for another decade). In the course, "quantum theory was liberated from the restriction to such particular systems as Planck's oscillators" (Pauli[25]).

Here was the challenge to rederive Planck's formula from Bohr's postulates, assuming that they hold for arbitrary atomic systems. Einstein's famous paper of 1917[34] accomplished just that, and more.

He considered radiation in thermal equilibrium with a dilute gas of atoms at temperature T. We shall here give a simplified treatment that contains the essential features without accounting for all details of lesser significance. Suppose that the energy spacing between two atomic levels e and g equals $h\nu$, so that the transition from the more energetic level e to the energetically lower level g (excited to ground state) is accompanied by the emission of a light quantum of frequency ν. According to Einstein, three processes are to be taken into account (see Fig. 1): spontaneous emission, absorption, and stimulated emission. The latter has no analog in Maxwell's electrodynamics.

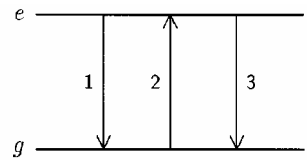

FIGURE 1 Transitions of three kinds happen between the excited level *e* and the ground level *g:* (1) spontaneous emission [see Eq. (4)], (2) absorption [see Eq. (5)], and (3) stimulated emission [see Eq. (6)].

Each of the three processes leads to a rate of change of the number of gas atoms in states *e* and *g.* Denoting these numbers by N_e and N_g we have the following contributions to their time derivatives. The *spontaneous emission* rate is proportional to the number of excited-state atoms:

Spontaneous emission
$$\frac{d}{dt}N_e = -\frac{d}{dt}N_g = -AN_e \tag{4}$$

where A is the first Einstein coefficient of the transition in question. The *absorption* rate is proportional to the number of ground-state atoms and to the energy density W of the radiation:

Absorption
$$\frac{d}{dt}N_e = -\frac{d}{dt}N_g = BWN_g \tag{5}$$

where B is the second Einstein coefficient. The *stimulated emission* rate is proportional to the number of excited state atoms and to the radiation energy density:

Stimulated emission
$$\frac{d}{dt}N_e = -\frac{d}{dt}N_g = BWN_e \tag{6}$$

where the same B coefficient appears as in the absorption rate.

The *detailed balance* between states *e* and *g* therefore requires:

Total
$$\frac{d}{dt}N_e = -\frac{d}{dt}N_g = -AN_e + BWN_g - BWN_e = 0 \tag{7}$$

under the circumstances of thermal equilibrium. Therefore, W can be expressed in terms of the ratios A/B and N_g/N_e:

$$W = \frac{A/B}{N_g/N_e - 1} = \frac{A/B}{\exp\,(h\nu/k_{\mathrm{B}}T) - 1} \tag{8}$$

where the second equality recognizes that Boltzmann's factor relates N_e to N_g. [The absence of additional weights here is the main simplification alluded to before; if taken into account, these weights would also require two closely related B coefficients in Eqs. (5) and (6).] In Eq. (8) we encounter the denominator of Planck's factor from Eq. (2), and Planck's formula, Eq. (1), is recovered in full if the relation

$$A = \frac{8\pi h\nu^3}{c^3}\,B \tag{9}$$

is imposed on Einstein's coefficients.

The main ingredients in this derivation of Eq. (1) are the postulate of the process of stimulated emission, with a strength proportional to the density of radiation energy, and the relation between the coefficients for spontaneous emission and stimulated emission, Eq. (9).

All of this is well remembered, but there was in fact more to the 1917 paper.[34] It also contains a treatment of the momentum exchange between atoms and light quanta, and Einstein succeeded in demonstrating that the Maxwell velocity distribution of the atoms is consistent with the recoil they suffer when absorbing and emitting quanta. Insights gained in his study of Brownian motion (another seminal paper of 1905[35]) were crucial for this success. When taken together, the considerations about energy balance and those concerning momentum balance are much more convincing than either one could have been alone.

The discovery of the Compton effect in 1923[23] finally convinced Bohr and other skeptics of the reality of the particlelike aspects possessed by light. But Bohr, who until then was decidedly opposed to Einstein's light-quantum hypothesis and the consequent wave-particle duality, did not give in without a last try. Together with Kramers and Slater,[36] he hypothesized that perhaps energy-momentum conservation does not hold for each individual scattering event, but only in a statistical sense for a large ensemble. Then one could account for Compton's data without conceding a particle nature to light in general, and X rays in particular. The refined measurements that were immediately carried out by Bothe and Geiger[37] showed, however, that this hypothesis is wrong: energy and momentum are conserved in each scattering event, not just statistically.

And then there was, also in 1924, Bose's seminal observation that it is possible to derive Planck's radiation law [Eq. (1)] from purely corpuscular arguments without invoking at all the wave properties of light resulting from Maxwell's field equations.[38,39] The main ingredient in Bose's argument was the indistinguishability of the particles in question and a new way of counting them—now universally known as *Bose-Einstein statistics*—which pays careful attention to what is implied by their being indistinguishable. In the case of light quanta, an additional feature is that their number is not conserved, because light is easily emitted and absorbed. Massive particles (atoms, molecules, etc.), by contrast, are conserved; therefore, as Einstein emphasized,[40–42] their indistinguishability has further consequences, of which the phenomenon of Bose-Einstein condensation (or should one rather say "Einstein condensation of a Bose gas"?) is the most striking one.

Quantum Electrodynamics

Theoretical studies of the quantum nature of light had a much more solid basis after Dirac's introduction of quantum electrodynamics (QED) in his seminal paper of 1927.[43] The basic ingredients of QED were all present in Dirac's formulation, although it is true that a consistent understanding of QED was not available until renormalized QED was developed 20 years later (see the papers reprinted in Ref. 44). In particular, the photon concept was clarified in the sense described in the following paragraphs.

The infinite number of degrees of freedom of the electromagnetic field—an operator field in QED—become manageable with the aid of a mode expansion. For the transverse part $\mathbf{E}_\perp(\mathbf{r}, t)$ of the electric field, for example, it reads

$$\mathbf{E}_\perp(\mathbf{r}, t) = \sum_k \sqrt{\frac{h\nu_k}{2\varepsilon_0}} \left[a_k(t)\mathbf{A}_k(\mathbf{r}) + a_k^\dagger(t)\mathbf{A}_k^*(\mathbf{r})\right] \tag{10}$$

The mode functions $\mathbf{A}_k(\mathbf{r})$ are complex vector functions of the position vector $\mathbf{r}$ that are eigenfunctions of the Laplace differential operator,

$$-\nabla^2 \mathbf{A}_k(\mathbf{r}) = \left(\frac{2\pi\nu_k}{c}\right)^2 \mathbf{A}_k(\mathbf{r}) \tag{11}$$

where the eigenvalue is determined by the frequency ν_k (>0) of the mode in question. The boundary conditions that the electric and magnetic field must obey at conducting surfaces imply respective boundary conditions on the $\mathbf{A}_k(\mathbf{r})$s.

The corresponding mode expansion for the magnetic field is given by

$$\mathbf{B}(\mathbf{r}, t) = \sum_k \sqrt{\frac{\mu_0 h\nu_k}{2}} \left[-ia_k(t)\mathbf{B}_k(\mathbf{r}) + ia_k^\dagger(t)\mathbf{B}_k^*(\mathbf{r}) \right] \tag{12}$$

where

$$\mathbf{B}_k(\mathbf{r}) = \frac{c}{2\pi\nu_k} \nabla \times \mathbf{A}_k(\mathbf{r}); \qquad \mathbf{A}_k(\mathbf{r}) = \frac{c}{2\pi\nu_k} \nabla \times \mathbf{B}_k(\mathbf{r}) \tag{13}$$

relates the two kinds of mode functions to each other.

Among others, the mode functions $\mathbf{A}_k(\mathbf{r})$ have the following important properties:

Transverse $$\nabla \cdot \mathbf{A}_k(\mathbf{r}) = 0 \tag{14a}$$

Orthonormal $$\int (d\boldsymbol{r})\, \mathbf{A}_j^*(\mathbf{r}) \cdot \mathbf{A}_k(\mathbf{r}) = \delta_{jk} \tag{14b}$$

Complete $$\sum_k \mathbf{A}_k(\mathbf{r})\mathbf{A}_k^*(\mathbf{r}') = \delta_\perp(\mathbf{r} - \mathbf{r}') \tag{14c}$$

The same statements hold for the $\mathbf{B}_k(\mathbf{r})$s as well. The property in Eq. (14*a*) states the radiation-gauge condition. The integration in Eq. (14*b*) covers the entire volume bounded by the conducting surfaces just mentioned; the eigenvalue equation Eq. (11) holds inside this volume, the so-called quantization volume. In the completeness relation in Eq. (14*c*), both positions $\mathbf{r}$ and $\mathbf{r}'$ are inside the quantization volume, and $\delta_\perp$ is the transverse delta function, a dyadic that is explicitly given by

$$\delta_\perp(\mathbf{r}) = \int \frac{(d\mathbf{k})}{(2\pi)^3} \exp(i\mathbf{k} \cdot \mathbf{r}) \left(\mathbf{1} - \frac{\mathbf{kk}}{k^2} \right) \tag{15}$$

where $\mathbf{1}$ is the unit dyadic and $k = \sqrt{\mathbf{k} \cdot \mathbf{k}}$ is the length of the wave vector $\mathbf{k}$ integrated over. The transverse character of $\delta_\perp(\mathbf{r})$ ensures the consistency of the properties in Eqs. (14*a*) and (14*c*).

The time dependence of $\mathbf{E}_\perp(\mathbf{r}, t)$ and $\mathbf{B}(\mathbf{r}, t)$ stems from the ladder operators $a_k(t)$ and $a_k^\dagger(t)$, which obey the bosonic equal-time commutation relations

$$[a_j, a_k] = 0 \quad [a_j, a_k^\dagger] = \delta_{jk} \quad [a_j^\dagger, a_k^\dagger] = 0 \tag{16}$$

The photon number operator

$$N = \sum_k a_k^\dagger a_k \tag{17}$$

has eigenvalues $N' = 0, 1, 2, \ldots$; its eigenstates with $N' = 1$ are the one-photon states, those with $N' = 2$ are the two-photon states, and so on. The unique eigenstate with $N' = 0$ is the photon vacuum. We denote its ket by $|\mathbf{vac}\rangle$. It is, of course, the joint eigenstate of all *annihilation operators* a_k with eigenvalue zero:

$$a_k|\mathbf{vac}\rangle = 0 \quad \text{for all } k \tag{18}$$

Application of the *creation operator* $a_k^\dagger$ to $|\mathbf{vac}\rangle$ yields a state with one photon in the kth mode:

$$a_k^\dagger|\mathbf{vac}\rangle = \{\text{state with 1 photon of the type } k\} \tag{19}$$

More generally, the ket of a pure one-photon state is of the form

$$|\{\psi\}_1\rangle = \sum_k \psi_k a_k^\dagger|\mathbf{vac}\rangle \qquad \text{with} \qquad \sum_k |\psi_k|^2 = 1 \tag{20}$$

where $|\psi_k|^2$ is the probability for finding the photon in the kth mode. Similarly, the kets of pure two-photon states have the structure

$$|\{\psi\}_2\rangle = \frac{1}{\sqrt{2}} \sum_{j,k} \psi_{jk} a_j^\dagger a_k^\dagger |\mathbf{vac}\rangle \qquad \text{with} \qquad \psi_{jk} = \psi_{kj} \text{ and } \sum_{j,k} |\psi_{jk}|^2 = 1 \tag{21}$$

and analogous expressions apply to pure states with 3, 4, 5, . . . photons.

Einstein's light quanta are one-photon states of a particular kind. In a manner of speaking, they are localized lumps of electromagnetic energy. In technical terms this means that the energy density

$$\begin{aligned} U_{1\text{ph}}(\mathbf{r}, t) &= \langle\{\psi\}_1| : [\mathbf{E}^2/(2\varepsilon_0) + \left(\frac{\mu_0}{2}\right)\mathbf{B}^2] : |\{\psi\}_1\rangle \\ &= \frac{h}{2} \sum_{j,k} \psi_j^* \psi_k \sqrt{\nu_j \nu_k} \left(\mathbf{A}_k^* \cdot \mathbf{A}_j + \mathbf{B}_k^* \cdot \mathbf{B}_j\right) \end{aligned} \tag{22}$$

is essentially nonzero in a relatively small spatial region only. The time dependence is carried by the probability amplitudes ψ_k, the spatial dependence by the mode functions $\mathbf{A}_k$ and $\mathbf{B}_k$. An arbitrarily sharp localization is not possible, but it is also not needed. The pair of colons : : symbolize the injunction to order the operator in between in the *normal* way: all creation operators $a_k^\dagger$ to the left of all annihilation operators a_k. This normal ordering is an elementary feature of renormalized QED.

At high frequencies, or when the quantization volume is unbounded, the eigenvalues of $-\nabla^2$ in Eq. (11) are so dense that the summations in Eqs. (10), (12), and (14*b*) are effectively integrations, and the Kronecker delta symbol in Eq. (14*b*) is a Dirac delta function. Under these circumstances, it is often natural to choose plane waves

$$\mathbf{A}_k(\mathbf{r}) \sim \mathbf{e}_k \exp\left(i \frac{2\pi\nu_k}{c} \mathbf{n}_k \cdot \mathbf{r}\right) \qquad \mathbf{B}_k(\mathbf{r}) \sim \mathbf{n}_k \times \mathbf{e}_k \exp\left(i \frac{2\pi\nu_k}{c} \mathbf{n}_k \cdot \mathbf{r}\right) \tag{23}$$

for the mode functions. The unit vector $\mathbf{e}_k$ that specifies the polarization is orthogonal to the unit vector $\mathbf{n}_k$ that specifies the direction of propagation.

With

$$\psi_k(t) \sim \exp(-i2\pi\nu_k t) \tag{24}$$

in Eq. (22), one then meets exponential factors of the form

$$\exp\left[i \frac{2\pi\nu_k}{c} (\mathbf{n}_k \cdot \mathbf{r} - ct)\right]$$

As a consequence, an einsteinian light quantum propagates without dispersion, which is the anticipated behavior.

The one-photon energy density in Eq. (22) illustrates the general feature that quantum-mechanical probabilities (the ψ_ks) with their interference properties appear together with the classical interference patterns of superposed mode functions [the $\mathbf{A}_k(\mathbf{r})$s and $\mathbf{B}_k(\mathbf{r})$s]. In other words, interference phenomena of two kinds are present in QED: (1) the classical interference of electromagnetic fields in the three-dimensional $\mathbf{r}$ space, and (2) the quantum interference of alternatives in the so-called Fock space; that is, the Hilbert space spanned by the photon vacuum $|\mathbf{vac}\rangle$, the one-photon states $|\{\psi\}_1\rangle$, the two-photon states $|\{\psi\}_2\rangle$, and all multiphoton states.

In the early days of QED, this coexistence of classical interferences and quantum interferences was a research topic, to which Fermi's paper of 1929 "Sulla teoria quantistica delle frange di interferenza" is a timeless contribution.[45] He demonstrated, at the example of Lippmann fringes, a very general property of single-photon interference patterns: the photon-

counting rates, as determined from quantum-mechanical probabilities, are proportional to the corresponding classical intensities.

Electromagnetic radiation is easily emitted and absorbed by antennas, processes that change the number of photons. Accordingly, the number of photons is not a conserved quantity, and therefore states of different photon numbers can be superposed. Particularly important are the *coherent states*

$$|\{\alpha\}_c\rangle = \exp\left(-\tfrac{1}{2}\sum_k |\alpha_k|^2 + \sum_k \alpha_k a_k^\dagger\right)|\mathbf{vac}\rangle \tag{25}$$

that are characterized by a set $\{\alpha\}_c$ of complex amplitudes α_k. As revealed in Glauber's 1963 papers,[46–48] they play a central role in the coherence theory of light.

Since the coherent states are common eigenstates of the annihilation operators

$$a_k|\{\alpha\}_c\rangle = |\{\alpha\}_c\rangle\alpha_k \tag{26}$$

the expectation values of the electric and magnetic field operators of Eqs. (10) and (12)

$$\begin{aligned}\langle\{\alpha(t)\}_c|\mathbf{E}_\perp(\mathbf{r},t)|\{\alpha(t)\}_c\rangle &= \sum_k \sqrt{\frac{h\nu_k}{(2\varepsilon_0)}}\,[\alpha_k(t)\mathbf{A}_k(\mathbf{r}) + \alpha_k^*(t)\mathbf{A}_k^*(\mathbf{r})]\\ \langle\{\alpha(t)\}_c|\mathbf{B}(\mathbf{r},t)|\{\alpha(t)\}_c\rangle &= \sum_k \sqrt{\frac{\mu_0 h\nu_k}{2}}\,[-i\alpha_k(t)\mathbf{B}_k(\mathbf{r}) + i\alpha_k^*(t)\mathbf{B}_k^*(\mathbf{r})]\end{aligned} \tag{27}$$

have the appearance of classical Maxwell fields. In more general terms, if the statistical operator ϱ_{ph} of the photonic degrees of freedom—in other words, the statistical operator of the radiation field—is a mixture of (projectors to) coherent states

$$\varrho_{\text{ph}} = \sum_{\{\alpha\}_c} |\{\alpha\}_c\rangle\, w(\{\alpha\}_c)\, \langle\{\alpha\}_c| \tag{28}$$

with

$$w(\{\alpha\}_c) \geq 0 \qquad \text{and} \qquad \sum_{\{\alpha\}_c} w(\{\alpha\}_c) = 1 \tag{29}$$

then the electromagnetic field described by ϱ_{ph} is very similar to a classical Maxwell field. Turned around, this says that whenever it is impossible to write a given ϱ_{ph} in the form of Eq. (28), then some statistical properties of the radiation are decidedly nonclassical.

During the 20-year period from Dirac's paper of 1927 to the Shelter Island conference in 1947, QED remained in a preliminary state that allowed various studies—the most important ones included the Weisskopf-Wigner treatment of spontaneous emission[49] and Weisskopf's discovery that the self-energy of the photon is logarithmically divergent[50]—although the not-yet-understood divergences were very troublesome. The measurement by Lamb and Retherford[51] of what is now universally known as the *Lamb shift,* first reported at the Shelter Island conference, was the crucial experimental fact that triggered the rapid development of renormalized QED by Schwinger, Feynman, and others.

Theoretical calculations of the Lamb shift rely heavily on the quantum properties of the electromagnetic field, and their marvelous agreement with the experimental data proves convincingly that these quantum properties are a physical reality. In other words, photons exist. The same remark applies to the theoretical and experimental values of the anomalous magnetic moment of the electron, one of the early triumphs of Schwinger's renormalized QED,[52] which finally explained an anomaly in the spectra of hydrogen and deuterium that Pasternack had observed in 1938[53] and a discrepancy in the measurements by Millman and Kusch[54] of nuclear magnetic moments.

Photon-Photon Correlations

Interferometers that exploit not the spatial intensity variations (or, equivalently, the photon-detection probabilities) but correlations between intensities at spatially separated positions became important tools in astronomy and spectroscopy after the discovery of the Hanbury-Brown–Twiss (HB&T) effect in 1954.[55–57] A textbook account of its classical theory is given in Sec. 4.3 of Ref. 58.

In more recent years, the availability of single-photon detectors made it possible to study the HB&T effect at the two-photon level. The essentials are depicted in Fig. 2. Two light quanta are incident on a half-transparent mirror from different directions, such that they arrive simultaneously. If their frequency contents are the same, it is fundamentally impossible to tell if an outgoing light quantum was reflected or transmitted. This indistinguishability of the two light quanta is of decisive importance in the situation where one is in each output channel. The two cases *both reflected* and *both transmitted* are then indistinguishable and, according to the laws of quantum mechanics, the corresponding probability amplitudes must be added.

Now, denoting the probability amplitudes for single-photon reflection and transmission by ρ and τ, respectively, the probability for one light quantum in each output port is given by

$$|\rho^2 + \tau^2|^2 = \left|\left(\frac{1}{\sqrt{2}}\right)^2 + \left(\frac{i}{\sqrt{2}}\right)^2\right|^2 = 0 \tag{30}$$

where we make use of $\rho = 1/\sqrt{2}$ and $\tau = i/\sqrt{2}$, which are the values appropriate for a symmetric half-transparent mirror. Thus, the situation of one light quantum in each output port does not occur. Behind the half-transparent mirror, one always finds both light quanta in the same output port.

If the light quanta arrived at very different times, rather than simultaneously, they would be distinguishable and one would have to add probabilities instead of probability amplitudes, so that

$$|\rho^2|^2 + |\tau^2|^2 = \tfrac{1}{2} \tag{31}$$

would replace Eq. (30). Clearly, there are intermediate stages at which the temporal separation is a fraction of the temporal coherence length and the two quanta are neither fully dis-

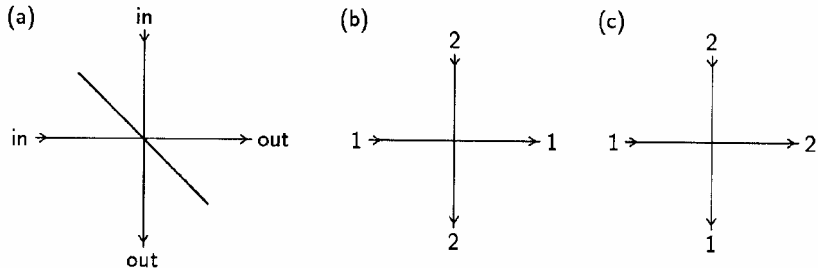

FIGURE 2 Essentials of the Hanbury-Brown–Twiss effect at the two-photon level. (*a*) Two light quanta are simultaneously incident at a symmetric half-transparent mirror. To obtain one quantum in each output port, the quanta must be either both transmitted (*b*) or both reflected (*c*). The probability amplitude for (*b*) is $(1/\sqrt{2})^2 = 1/2$, that for (*c*) is $(i/\sqrt{2})^2 = -1/2$. If the two cases are indistinguishable, the total amplitude is $1/2 - 1/2 = 0$.

tinguishable nor utterly indistinguishable. The probability for one light quantum in each output port is then a function of the separation, a function that vanishes when the separation does.

Experiments that test these considerations[59] employ correlated photon pairs produced by a process known as *parametric downconversion.* Roughly speaking, inside a crystal that has no inversion symmetry a high-frequency photon is absorbed and two lower-frequency photons are emitted, whereby the conservation of energy and momentum imposes geometrical restrictions on the possible propagation directions of the three photons involved. Downconversion sources with a high luminosity are available.[60,61]

The HB&T effect of Fig. 2 as well as closely related phenomena are crucial in many experiments in which entangled photons are a central ingredient. In particular, the recent realizations[62,63] of schemes for quantum teleportation[64] and the experiment[65] that demonstrated the practical feasibility of quantum-dense coding[66] are worth mentioning here.

None of these exciting developments could be understood without the quantum properties of radiation. Since the photon concept, in the sense of the discussion of Eqs. (10), (12), (19), (20), and so on is an immediate consequence of these quantum properties, the existence of photons is an established experimental fact beyond reasonable doubt.

26.4 QUANTUM THEORY OF THE LASER

The quantum theory of laser radiation is a problem in nonequilibrium statistical mechanics. There are several alternative, but ultimately equivalent, approaches to the characterization of the field inside the resonator. As is customary in the Scully-Lamb quantum theory, we describe the state of the laser field by a density operator.[67,68] In this section our main focus is on the review of the equation of motion, the so-called master equation, for this density operator as it emerges from an underlying physical model, with statistical considerations and some simplifying assumptions. The alternative procedure based on the quantum theory of noise sources introduced in Refs. 69 and 70 and summarized in Refs. 71 to 74 will also be briefly reviewed at the end of the section. For a recent, more detailed overview of the quantum Langevin point of view, we refer the reader to Ref. 75.

In general, a laser model should be based on the interaction of multimode fields with multilevel atoms as the active medium, and a detailed consideration of all possible processes among all the levels involved should be given. Decay channels and decay rates, in particular, play a crucial role in determining the threshold inversion and, thus, the necessary pumping rates. Of course, the pumping mechanisms themselves can be quite complicated. It is well established that a closed two-level model cannot exhibit inversion and, hence, lasing. In order to achieve inversion three- and four-level pumping schemes are employed routinely. On the other hand, to illustrate the essential quantum features a single mode field can serve as paradigm. The single-mode laser field inside the resonator interacts with one particular transition of the multilevel system—the lasing transition—and the role of the entire complicated level structure is to establish inversion on this transition—that is, to put more atoms in the upper level than there are in the lower one. If one is not interested in the details of how the inversion builds up, it is possible to adopt a much simpler approach than the consideration of a multilevel-multimode system. In order to understand the quantum features of the single-mode field it is sufficient to focus only on the two levels of the lasing transition and their interaction with the laser field. In this approach, the effect of pumping, decay, and so on in the multilevel structure is simply replaced by an initial condition; it is assumed that the atom is in its upper state immediately before the interaction with the laser mode begins. Since here we are primarily interested in the quantum signatures of the laser field and not in the largely classical aspects of cavity design, pumping mechanisms, and so on, we shall follow this simpler route from the beginning. The model that accounts for the resonant interaction of a two-level atom with a single quantized mode in a cavity was introduced by Jaynes and Cummings.[76]

We shall make an attempt to present the material in a tutorial way. We first derive an expression for the change of the field density operator due to the interaction with a single two-level atom, initially in its upper state, using the Jaynes-Cummings model. This expression will serve as the seed for both the laser and micromaser theories. We next briefly review how to account for cavity losses by using standard methods for modeling the linear dissipation loss of the cavity field due to mirror transmission. Then we show that with some additional assumptions the single-atom–single-mode approach can be used directly to derive what has become known as the Scully-Lamb master equation for the more traditional case of the laser and the micromaser. The additional assumptions include the Markov approximation or, equivalently, the existence of very different time scales for the atomic and field dynamics so that adiabatic elimination of the atoms and introduction of coarse-grained time evolution for the field become possible. The main difference between the laser and micromaser theories is that the interaction time of the active atoms with the field is governed by the lifetime of the atoms in the laser and by the transit time of the atoms through the cavity in the micromaser. In the laser case, the atoms decay out of the lasing levels into some far-removed other levels, and they are available for the lasing transition during their lifetime on the average. In the micromaser case, the transit time is approximately the same for all atoms in a monoenergetic pumping beam. Thus, the laser involves an extra averaging over the random interaction times. If we model the random interaction times by a Poisson distribution and average the change of the field density operator that is due to a single atom—the kick—over the distribution of the interaction times, we obtain the master equation of a laser from that of the micromaser. Historically, of course, the development was just the opposite: the master equation was derived in the context of the laser much earlier. However, it is instructive to see how the individual Rabi oscillations of single nondecaying atoms with a fixed interaction time, as in the micromaser, give rise to the saturating, nonoscillatory collective behavior of an ensemble of atoms, as in the laser, upon averaging over the interaction times. As applications of this fully quantized treatment we study the photon statistics, the linewidth, and spectral properties. Finally, we briefly discuss other approaches to the quantum theory of the laser.

Time Evolution of the Field in the Jaynes-Cummings Model

We shall consider the interaction of a single two-level atom with a single quantized mode of a resonator using the rotating-wave approximation (for a recent review of the Jaynes-Cummings model see Ref. 77). The arrangement is shown in Fig. 3.

The hamiltonian for this system is given by

$$\mathcal{H} = \mathcal{H}_0 + \mathcal{H}_1 \tag{32}$$

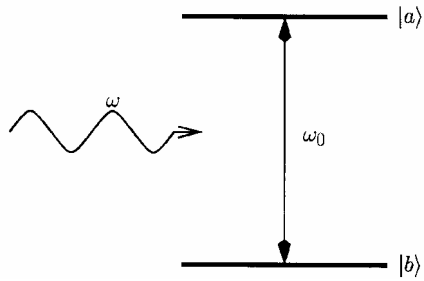

FIGURE 3 Scheme of a two-level atom interacting with a single mode quantized field. The text focuses on the resonant case, $\omega = \omega_0$.

where

$$\mathcal{H}_0 = \frac{1}{2}\hbar\omega_0\sigma_z + \hbar\omega_0 a^\dagger a \tag{33}$$

and

$$\mathcal{H}_1 = \hbar g(\sigma_+ a + a^\dagger \sigma_-) \tag{34}$$

Here a and $a^\dagger$ are the annihilation and creation operators for the mode. The upper level of the lasing transition is denoted by $|a\rangle$ and the lower level by $|b\rangle$. The atomic lowering and raising operators are expressed in terms of the state vectors as $\sigma_- = (\sigma_+)^\dagger = |b\rangle\langle a|$ and the population operator as $\sigma_z = |a\rangle\langle a| - |b\rangle\langle b|$. ω_0 is the frequency of the $|a\rangle - |b\rangle$ transition. For simplicity we assume perfect resonance with the mode. Finally, g is the coupling constant between the atom and the mode. In terms of atomic and field quantities it is given by $g = p\sqrt{\omega_0/2\hbar\varepsilon_0 v}$ where p is the transition dipole moment and v the quantization volume (the volume of the active medium, in our case). Again, for simplicity, p is assumed to be real.

In the interaction picture with respect to $\mathcal{H}_0$, the interaction hamiltonian becomes

$$\mathcal{V} = \exp\left(\frac{i\mathcal{H}_0 t}{\hbar}\right)\mathcal{H}_1 \exp\left(-\frac{i\mathcal{H}_0 t}{\hbar}\right) = \hbar g(\sigma_+ a + a^\dagger \sigma_-) \equiv \mathcal{H}_1 \tag{35}$$

since $\mathcal{H}_0$ and $\mathcal{H}_1$ commute.

In the two-dimensional Hilbert space spanned by the state vectors $|a\rangle$ and $|b\rangle$ the interaction hamiltonian can be written as

$$\mathcal{H}_1 = \hbar g \begin{pmatrix} 0 & a \\ a^\dagger & 0 \end{pmatrix} \tag{36}$$

The time evolution operator for the coupled atom-field system satisfies the equation of motion in this picture

$$\frac{i\hbar dU}{dt} = \mathcal{V}U \tag{37}$$

and since $\mathcal{H}_1$ is time independent the solution is formally

$$U(\tau) = \exp\left(-\frac{i}{h}\mathcal{V}\tau\right) \tag{38}$$

Using the properties of the σ_- and σ_+ matrices, it is easy to show that $U(\tau)$ can be written in the preceding 2×2 matrix representation as

$$U(\tau) = \begin{pmatrix} \cos\left(g\tau\sqrt{aa^\dagger}\right) & -i\dfrac{\sin\left(g\tau\sqrt{aa^\dagger}\right)}{\sqrt{aa^\dagger}}a \\ -ia^\dagger\dfrac{\sin\left(g\tau\sqrt{aa^\dagger}\right)}{\sqrt{aa^\dagger}} & \cos\left(g\tau\sqrt{a^\dagger a}\right) \end{pmatrix} \tag{39}$$

Let us now assume that initially, at t_0, the atom is in its upper state given by the atomic density operator $\varrho_{at}(t_0) = |a\rangle\langle a|$ and the field is in an arbitrary state which, in general, can be described by the density operator $\varrho(t_0)$, so that the joint atom-field system is characterized by the initial density operator $\varrho_{af}(t_0) = \varrho_{at}(t_0) \otimes \varrho(t_0)$. After the interaction, $\varrho_{af}(t_0 + \tau) = U(\tau)\varrho_{af}(t_0)U(\tau)^{-1}$. Our main interest here is in the evolution of the field density operator. This we obtain if we trace the atom-field density operator over the atomic states, yielding

$$\begin{aligned}\varrho(t_0+\tau) &= \mathrm{Tr}_{\mathrm{atom}}\,[\varrho_{\mathrm{af}}(t+\tau)] \\ &= \cos\,(g\tau\sqrt{aa^\dagger})\varrho(t_0)\cos\,(g\tau\sqrt{aa^\dagger}) + a^\dagger\,\frac{\sin\,(g\tau\sqrt{aa^\dagger})}{\sqrt{aa^\dagger}}\,\varrho(t_0)\,\frac{\sin\,(g\tau\sqrt{aa^\dagger})}{\sqrt{aa^\dagger}}a \\ &\equiv M(\tau)\varrho(t_0)\end{aligned} \tag{40}$$

Here in the last step we just introduced the superoperator *M,* which describes the effect of a single inverted atom on the field and is a key ingredient of laser and micromaser theory. The matrix elements in photon number representation take the form

$$(M(\tau)\varrho)_{nn'} = A_{nn'}\,(\tau)\,\varrho_{nn'} + B_{n-1\,n'-1}\,(\tau)\,\varrho_{n-1\,n'-1} \tag{41}$$

where the coefficients are given by

$$A_{nn'}(\tau) = \cos\,(g\tau\sqrt{n+1})\cos\,(g\tau\sqrt{n'+1}) \tag{42}$$

$$B_{nn'}(\tau) = \sin\,(g\tau\sqrt{n+1})\sin\,(g\tau\sqrt{n'+1}) \tag{43}$$

For later purposes, we also introduce the change in the state of the field due to the interaction with a single inverted atom as

$$\varrho(t_0+\tau) - \varrho(t_0) = M(\tau)\varrho(t_0) - \varrho(t_0) = (M-1)\varrho(t_0) \equiv K\varrho(t_0) \tag{44}$$

The operator *K,* sometimes called the *kick operator,* contains all the information we will need to build the quantum theory of the single-mode laser and micromaser. In matrix representation, $[K(\tau)\varrho]_{nn'} = [A_{nn'}(\tau) - \tilde{\delta}_{nn'}]\varrho_{nn'} + B_{n-1\,n'-1}(\tau)\varrho_{n-1\,n'-1}$.

For more elaborate systems (multimode lasers driven by multilevel atoms, for example) one cannot give M in such a simple analytical form, but the principle remains always the same. One should find the superoperator M or, equivalently, the kick operator $K = M - 1$ which gives the action of a single (possibly multilevel) atom on the (possibly multimode) field from the general expression $\varrho(t_0+\tau) = \mathrm{Tr}_{\mathrm{atom}}\,[U_{\mathrm{af}}(\tau)\varrho_{\mathrm{at}}(t_0) \otimes \varrho(t_0)U_{\mathrm{af}}(\tau)^{-1}] \equiv M(\tau)\varrho(t_0)$. In order to determine the full time-evolution operator $U_{\mathrm{af}}(\tau)$ of the coupled atom-field system, however, one usually needs to resort to approximation methods, such as perturbation theory, in the more complicated multilevel-multimode cases.

Derivation of the Scully-Lamb Master Equation

In 1954, Gordon, Zeiger, and Townes showed that coherent electromagnetic radiation can be generated in the radio frequency range by the maser (acronym for *microwave amplification by stimulated emission of radiation*).[78] The first maser action was observed in a beam of ammonia.[79] The maser principle was extended to the optical domain by Schawlow and Townes,[80] and also by Prokhorov and Basov,[81] thus obtaining a laser (acronym for *light amplification by stimulated emission of radiation*). A laser consists of a large ensemble of inverted atoms interacting resonantly with the electromagnetic field inside a cavity. The cavity selects only a specific set of modes corresponding to a discrete set of eigenfrequencies. The active atoms—that is, the ones that are pumped to the upper level of the laser transition—are in resonance with one of the eigenfrequencies of the cavity in the case of the single-mode laser and with a finite set of frequencies in the case of the multimode laser. As discussed in the introduction to this section, for the discussion of the essential quantum features of the radiation field of a laser it is sufficient to confine our treatment to the single-mode case, and that is what we will do for the remainder of this section. A resonant electromagnetic field gives rise to stimulated emission, and the atoms thereby transfer their energy to the radiation field. The emitted radiation is still at resonance. If the upper level is sufficiently populated, this radiation gives rise to further transitions in other atoms. In this way, all the excitation energy of the atoms is transferred to the single mode of the radiation field.

The first pulsed laser operation was demonstrated by Maiman in ruby.[82] The first continuous wave (CW) laser, a He-Ne gas laser, was built by Javan.[83] Since then a large variety of systems have been demonstrated to exhibit lasing action. Coherent radiation has been generated this way over a frequency domain ranging from infrared to soft X rays. These include dye lasers, chemical lasers, solid-state lasers, and semiconductor lasers.

Many of the laser properties can be understood on the basis of a semiclassical theory. In such a theory the radiation field is treated classically, but the active medium is given a full quantum-mechanical treatment. Such a theory can readily explain threshold and saturation, transient dynamics, and general dependence on the external parameters (pumping and losses). It is not our aim here to give an account of the semiclassical theory; therefore we just refer the reader to the ever instructive and wonderfully written seminal paper by Lamb[84] and a more extended version in Ref. 67. Although quantum effects play only a minor role in usual practical laser applications because of the large mean photon numbers, they are essential for the understanding of the properties of micromasers, in which excited two-level atoms interact one after the other with a single mode of the radiation field.[85] Nevertheless, the quantum properties of the laser field are of fundamental interest as well. They have been thoroughly investigated theoretically with respect to the photon statistics and the spectrum of the laser. In particular, the quantum limitation of the laser linewidth caused by the inevitably noisy contribution of spontaneous emission has attracted much attention. It gives rise to the so-called Schawlow-Townes linewidth, which is inversely proportional to the laser intensity (see Ref. 80). Because of the importance of stable coherent signals for various high-precision measurements, the problem of the intrinsic quantum-limited linewidth has gained renewed interest recently, and the investigations have been extended to cover bad-cavity lasers and several more exotic systems. In this review, however, we shall restrict ourselves to good-cavity lasers in which the cavity damping time is long compared to all other relevant time scales, and present a fully quantized theory of the most fundamental features.

Cavity Losses. To account for the decay of the cavity field through the output mirror of the cavity, we simply borrow the corresponding result from reservoir theory. Its usage has become fairly standard in laser physics and quantum optics (see, for example, Refs. 67 and 68), and here we just quote the general expression without actually deriving it.

$$\left(\frac{d\varrho}{dt}\right)_{\text{loss}} = \mathcal{L}\varrho \equiv -\frac{\kappa}{2}n_{\text{th}}(aa^\dagger\varrho + \varrho aa^\dagger - 2a^\dagger\varrho a) - \frac{\kappa}{2}(n_{\text{th}}+1)(a^\dagger a\varrho + \varrho a^\dagger a - 2a\varrho a^\dagger) \quad (45)$$

This equation refers to a loss reservoir which is in thermal equilibrium at temperature T, with n_{th} being the mean number of thermal photons $n_{\text{th}} = [\exp(\hbar\omega_0/kT) - 1]^{-1}$, and κ is the cavity damping rate. For the laser case, it is sufficient to take the limiting case of a zero temperature reservoir since $\hbar\omega_0 \gg kT$ and n_{th} is exponentially small. We obtain this limit by substituting $n_{\text{th}} = 0$ into Eq. (45). For the description of most micromaser experiments, however, we need the finite temperature version, since even at very low temperatures the thermal photon number is comparable to the total number of photons in the cavity.

The Laser Master Equation. After introducing the loss part of the master equation, we now turn our attention to the part that stems from the interaction with the gain reservoir. The gain reservoir is modeled by an ensemble of initially excited two-level atoms allowed to interact with the single-mode cavity field. A central role in our subsequent discussions will be played by the so-called kick operator, $K = M - 1$, describing the change of the field density operator due to the interaction with a single atom. This quantity was introduced in Eq. (44). While in the micromaser case the effect of each of the atoms can be represented by the same kick operator, since in a monoenergetic pumping beam each atom has the same interaction time with the cavity field, this is no longer the case for a laser. In a typical CW gas laser, such as the He-Ne laser, atoms are excited to the upper level of the lasing transition at random times and, more important, they can also interact with the field for a random length of time. The interaction time thus becomes a random variable. Since at any given time the number of atoms is

large (about 10^6 to 10^7 active atoms in the lasing volume of a CW He-Ne laser), it is a legitimate approach to describe their effect on the field by an average kick operator. We can arrive at the interaction-time-averaged master equation quickly if we take the average of Eq. (44) with respect to the interaction time τ

$$(M-1)\varrho(t) = \int_0^\infty d\tau\, P(\tau)(M(\tau)-1)\varrho(t) \tag{46}$$

where the distribution function for the interaction time $P(\tau)$ is defined as

$$P(\tau) = \gamma e^{-\gamma\tau} \tag{47}$$

This distribution function corresponds to the exponential decay law. Individual atoms can decay from the lasing levels at completely random times, but for an ensemble of atoms the probability of finding an initially excited atom still in the lasing levels in the time interval $(\tau, \tau + d\tau)$ is given by Eq. (47). With increasing τ it is increasingly likely that the atoms have decayed outside the lasing transition. Also note that our model corresponds to an open system: the atoms decay to other nonlasing levels both from the upper state $|a\rangle$ and the lower state $|b\rangle$, and, in addition, we assume that decay rate γ is the same for both levels, as indicated in Fig. 4.

Obviously, these restrictions can be relaxed and, indeed, there are various more general models available. For example, the upper level $|a\rangle$ can have two decay channels. It can decay to the lower level $|b\rangle$ and to levels outside the lasing transition. Or, in some of the most efficient lasing schemes, the lower level decays much faster than the upper one, $\gamma_b \gg \gamma_a$. In these schemes virtually no population builds up in the lower level; hence, saturation of the lasing transition occurs at much higher intensities than in lasers with equal decay rates for both levels. These generalizations, however, are easily accounted for (see Ref. 67) and it is not our concern here to provide the most general treatment possible. Instead, we want to focus on the essential quantum features of the laser field and employ the simple two-level model with equal decay rates for both.

The formal averaging in Eq. (46) can be performed most easily if we transform to a particular representation of the density matrix. For our purposes, the photon number representation suffices, although other options are readily available and some of them will be summarized briefly at the end of this section. Taking the n, n' elements of Eq. (46) and using Eqs. (42) and (43), the averaging yields

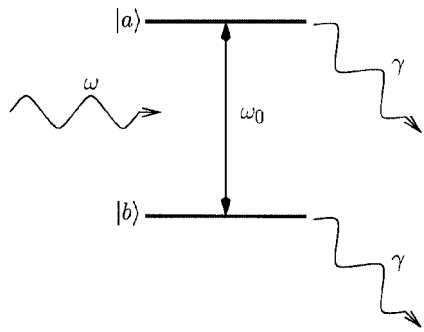

FIGURE 4 Scheme of a two-level atom, with atomic decay permitted, interacting with a single-mode quantized field.

$$[(M-1)\varrho]_{nn'} = -\frac{\chi(n+1+n'+1)+\chi^2(n-n')^2}{1+2\chi(n+1+n'+1)+\chi^2(n-n')^2}\,\varrho_{nn'} + \frac{2\chi\sqrt{nn'}}{1+2\chi(n+n')+\chi^2(n-n')^2}\,\varrho_{n-1\,n'-1} \tag{48}$$

where the notation $\chi = g^2/\gamma^2$ is introduced. Finally, taking into account cavity losses $(\mathscr{L}\varrho)_{nn'}$ from Eq. (45), with $n_{\text{th}} = 0$, we obtain the following master equation for our quantum-mechanical laser model:

$$\dot{\varrho}_{nn'} = -\frac{\mathscr{N}'_{nn'}\mathscr{A}}{1+\mathscr{N}_{nn'}\mathscr{B}/\mathscr{A}}\,\varrho_{nn'} + \frac{\sqrt{nn'}\mathscr{A}}{1+\mathscr{N}_{n-1\,n'-1}\mathscr{B}/\mathscr{A}}\,\varrho_{n-1\,n'-1} - \frac{\kappa}{2}(n+n')\varrho_{nn'} + \kappa\sqrt{(n+1)(n'+1)}\,\varrho_{n+1\,n'+1} \tag{49}$$

Here we introduced the original notations of the Scully-Lamb theory—the linear gain coefficient:

$$\mathscr{A} = 2r\chi \tag{50}$$

the self-saturation coefficient:

$$\mathscr{B} = 4\chi\mathscr{A} \tag{51}$$

and the dimensionless factors:

$$\mathscr{N}' = \frac{1}{2}(n+1+n'+1) + \frac{(n-n')^2\mathscr{B}}{8\mathscr{A}} \tag{52}$$

and

$$\mathscr{N} = \frac{1}{2}(n+1+n'+1) + \frac{(n-n')^2\mathscr{B}}{16\mathscr{A}} \tag{53}$$

Equation (49) is the Scully-Lamb master equation, which is the central equation of the quantum theory of the laser. Along with the notations introduced in Eqs. (50) to (53), it constitutes the main result of this section and serves as the starting point for our treatment of the quantum features of the laser. Among the specific problems we shall consider are the photon statistics, which is the physical information contained in the diagonal elements, and the spectrum, which is the physical information contained in the off-diagonal elements of the field density matrix.

The Micromaser Master Equation. The development of the single-atom maser or micromaser plays a particularly important role in cavity quantum electrodynamics because it realizes one of the most fundamental models, the Jaynes-Cummings hamiltonian. The experimental situation[86] is very close to the idealized case of a single two-level atom interacting with a single-mode quantized field, as previously discussed, and allows a detailed study of fundamental quantum effects in the atom-field interaction.

In the micromaser, a stream of two-level atoms is injected into a superconducting microwave cavity of very high quality Q. The injection rate r is low enough to ensure that at most only one atom is present inside the cavity at any given time and that most of the time the cavity is empty. The decay time of the high-Q cavity field is very long compared to both the

interaction time τ, which is set by the transit time of atoms through the cavity, and the inverse of the single-photon Rabi frequency g^{-1}. In typical experimental situations, however, $g\tau \simeq 1$. Therefore, a field is built up in the cavity provided the interval between atomic injections does not significantly exceed the cavity decay time. Sustained oscillation is possible with less than one atom on the average in the cavity.

In addition to the progress in constructing superconducting cavities, advances in the selective preparation of highly excited hydrogenlike atomic states, called *Rydberg states,* have made possible the realization of the micromaser. In Rydberg atoms the probability of induced transitions between adjacent states is very large, and the atoms may undergo several Rabi cycles—that is, several periodic energy exchanges between the atom and the cavity field may take place in the high-Q cavity. The lifetime of Rydberg states for spontaneous emission decay is also very long, and atomic decay can be neglected during the transit time in the cavity.

Here we set out to derive a master equation for the micromaser. For this, we consider a single-mode resonator into which two-level atoms are injected in their upper states. Due to the different time scales, the effect of cavity damping can be neglected during the interaction. Then the effect of a single atom on the field density operator, injected at t_i and interacting with the field for a time τ, is given by Eq. (44) with t_0 replaced by t_i. If several atoms are injected during a time interval Δt which is still short on the time scale governed by the cavity decay time κ^{-1} but long on the time scale of the interaction time τ, then the cumulative effect on the field is simply the sum of changes

$$\Delta\varrho = \sum_{t \le t_i \le t + \Delta t} (M(\tau) - 1)\varrho(t_i) = r \int_t^{t + \Delta t} (M(\tau) - 1)\varrho(t_i) dt_i \tag{54}$$

where in the last step we turned the sum into an integral by using the injection rate r as the number of excited-state atoms entering the cavity per unit time.

At this point we introduce some of the most important approximations of laser physics, or reservoir theory in general—the so-called Markov or adiabatic approximation and coarse time graining. These approximations are based on the existence of three very different time scales in the problem. First, the interaction time τ for individual atoms is of the order of the inverse single-photon Rabi frequency g^{-1}, and is the shortest of all. In fact, on the time scale set by the other relevant parameters, it appears as a delta-function-like kick to the state of the field with the kick operator K of Eq. (44). The second time scale is set by r^{-1}, the average time separation between atomic injections. It is supposed to be long compared to τ but short compared to the cavity-damping time κ^{-1}. Thus, we have the following hierarchy of timescales: $\tau \ll r^{-1} \ll \kappa^{-1}$. When we turned the sum in Eq. (54) into an integral we already tacitly assumed that there is a time scale on which the injection appears to be quasicontinuous. We now see that it is the time scale set by κ^{-1}. This is the time scale that governs the time evolution of the cavity field. In the evaluation of the integral in Eq. (54) we assume that Δt is an intermediate time interval such that $r^{-1} < \Delta t < \kappa^{-1}$. Then during this interval the state of the field does not change appreciably, and we can replace $\varrho(t_i)$ on the right-hand side of Eq. (54) by $\varrho(t)$. This is the essential step in transforming the integral equation into a differential equation, and it constitutes what is called the *Markov approximation.* It is also called the *adiabatic approximation* since the field changes very slowly (adiabatically) on the time scale set by the atoms. As a result, $\varrho(t)$ can now be taken out of the integral, and the integration in Eq. (54) yields $\Delta\varrho = r\Delta t(M - 1)\varrho(t)$. Dividing both sides by Δt, we obtain

$$\frac{\Delta\varrho}{\Delta t} = r(M(\tau) - 1)\varrho \tag{55}$$

The left-hand side is not a true derivative; it only appears to be one on the time scale of the cavity decay time. However, if we are interested in the large-scale dynamics of the field, we can still regard it as a good approximation to a time derivative. It is called the *coarse-grained derivative* and the Eq. (55) now properly describes the time rate of change of the field due to the interaction with an ensemble of active atoms, the gain reservoir.

Equation (55) gives the time rate of change of the field density operator due to the gain reservoir $(d\varrho/dt)_{\text{gain}}$. To this, we add the time rate of change of the density operator due to the cavity losses by hand. For the parameters of the Garching micromaser experiment, $T = 0.5$ K and $\omega_0/2\pi = 21.5$ GHz, yielding $n_{\text{th}} = 0.15$. The thermal background cannot be neglected since, as we shall see, the steady-state field contains but a few photons. The complete master equation for the micromaser, including both gain and loss, is then simply the sum of Eqs. (55) and (45):

$$\frac{d\varrho}{dt} = \left(\frac{d\varrho}{dt}\right)_{\text{gain}} + \left(\frac{d\varrho}{dt}\right)_{\text{loss}} = r(M(\tau) - 1)\varrho + \mathcal{L}\varrho \tag{56}$$

For later purposes, we also give the master equation in matrix representation:

$$\begin{aligned}\frac{d\varrho_{nn'}}{dt} = {} & r\,[(A_{nn'}(\tau) - 1)\varrho_{nn'} + B_{n-1\,n'-1}(\tau)\varrho_{n-1\,n'-1}] \\ & - \frac{\kappa}{2} n_{\text{th}}[(n + n' + 2)\varrho_{nn'} - 2\sqrt{nn'}\varrho_{n-1\,n'-1}] \\ & - \frac{\kappa}{2}(n_{\text{th}} + 1)[(n + n')\varrho_{nn'} - 2\sqrt{(n+1)(n'+1)}\varrho_{n+1\,n'+1}]\end{aligned} \tag{57}$$

Here $A_{nn'}(\tau)$ and $B_{nn'}(\tau)$ are given by Eqs. (42) and (43). Equation (57) is identical to the one obtained by more standard methods[87] and employed widely in the context of micromasers. It forms the basis for most studies (with a few notable exceptions, as discussed at the end of this section) on the quantum statistical properties of the micromaser and, naturally, it will be our starting point as well.

Physics on the Main Diagonal: Photon Statistics

To begin to bring to light the physical consequences of the laser and maser master equations, we shall first focus on the diagonal elements of the field density matrix ϱ_{nn}, which give us the photon-number distribution since $\varrho_{nn} = p(n)$ is the probability of finding n photons in the cavity mode. The case of the laser is sufficiently different from that of the micromaser that we shall deal with them separately.

Laser Photon Statistics. Taking the diagonal $n = n'$ elements in Eq. (49) and regrouping the terms, we obtain the following equation for the photon-number probabilities:

$$\dot{p}(n) = -\frac{(n+1)\mathcal{A}}{1 + (n+1)\mathcal{B}/\mathcal{A}}\,p(n) + \kappa(n+1)p(n+1) + \frac{n\mathcal{A}}{1 + n\mathcal{B}/\mathcal{A}}\,p(n-1) - \kappa n p(n) \tag{58}$$

Here the overdot stands for the time derivative. Note that diagonal elements are coupled only to diagonal elements. This holds quite generally; Eq. (49) describes coupling along the same diagonal only. For example, elements on the first side diagonal are coupled to other elements on the first side diagonal, and so on, and in general only elements with the same difference $n - n'$ are coupled. The quantity $k = n - n'$ corresponds to elements on the kth side diagonal. Elements on different diagonals are not coupled, which greatly simplifies the solution of laser-related problems.

Before we begin the solution of Eq. (58), we want to give a simple intuitive physical picture of the processes it describes in terms of a probability flow diagram, shown in Fig. 5.

The left-hand side is the rate of change of the probability of finding n photons in the cavity. The right-hand side contains the physical processes that contribute to the change. Each process is represented by an arrow in the diagram. The processes are proportional to the probability of

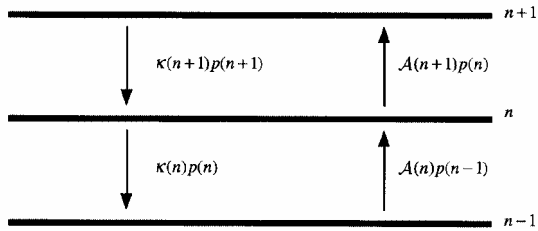

FIGURE 5 Probability flow diagram for the laser.

the state they are starting from and this will be the starting point of the arrow. The tip of the arrow points to the state the process is leading to. There are two kinds of elementary processes: emission of a photon into the cavity mode (upward arrows) and loss of a photon from the cavity through the output mirror (downward arrows). Furthermore, the processes that start from a given state and end in a different one will decrease the probability of the state they are starting from and increase the probability of the state they are ending at. For example, the first term on the right-hand side describes emission of a photon into the cavity mode provided there are n photons already present before the emission event takes place. Since there will be $n+1$ photons after the emission, this process decreases the probability of finding n photons, hence the minus sign. The total emission rate $\mathcal{A}(n+1)$ has a contribution from stimulated emission, the $\mathcal{A}n$ term, and another one from spontaneous emission, the $\mathcal{A}$ term. The third term on the right-hand side corresponds similarly to emission, conditioned on the presence of $n-1$ photons in the cavity initially. After the emission, there will be n photons, hence the plus sign. The second term describes the loss of a photon through the cavity mirror, provided there are n photons initially. After the escape of a photon, there will be $n-1$ photons; therefore this term decreases $p(n)$. Finally, the last term corresponds similarly to a loss process, with initially $n+1$ photons in the cavity. After the escape of a photon there will be n photons left, so this term increases the probability $p(n)$ of finding n photons in the cavity.

After this brief discussion of the meaning of the individual terms, we now turn our attention to the solution of the equation. Although it is possible to obtain a rather general time-dependent solution to Eq. (58), our main interest here is in the steady-state properties of the field. To obtain the steady-state photon statistics, we replace the time derivative with zero. Note that the right-hand side of the equation is of the form $F(n+1)-F(n)$, where

$$F(n) = \kappa n p(n) - \frac{n\mathcal{A}}{1+n\mathcal{B}/\mathcal{A}}\, p(n-1) \tag{59}$$

simply meaning that in steady-state $F(n+1) = F(n)$. In other words, $F(n)$ is independent of n and is, therefore, a constant c. Furthermore, the equation $F(n) = c$ has normalizable solution only for $c = 0$. From Eq. (59) we then immediately obtain

$$p(n) = \frac{\mathcal{A}/\kappa}{1+n\mathcal{B}/\mathcal{A}}\, p(n-1) \tag{60}$$

which is a very simple two-term recurrence relation to determine the photon-number distribution. Before we present the solution, a remark is called for here. The fact that $F(n) = 0$ and $F(n+1) = 0$ hold separately is called the *condition of detailed balance.* As a consequence, we do not need to deal with all four processes affecting $p(n)$. It is sufficient to balance the processes connecting a pair of adjacent levels in Fig. 5, and instead of solving the general three-term recurrence relation resulting from the steady-state version of Eq. (58), it is enough to solve the much simpler two-term recursion, Eq. (60).

It is instructive to investigate the photon statistics in some limiting cases before discussing the general solution. Below threshold the linear approximation holds. Since only very small n states are populated appreciably, the denominator on the right-hand side of Eq. (60) can be replaced by unity in view of $n\mathcal{B}/\mathcal{A} \ll 1$. Then

$$p(n) = p(0)\left(\frac{\mathcal{A}}{\kappa}\right)^n \tag{61}$$

The normalization condition $\sum_{n=0}^{\infty} p(n) = 1$ determines the constant $p(0)$, yielding $p(0) = (1 - \mathcal{A}/\kappa)$. Finally,

$$p(n) = \left(1 - \frac{\mathcal{A}}{\kappa}\right)\left(\frac{\mathcal{A}}{\kappa}\right)^n \tag{62}$$

Clearly, the condition of existence for this type of solution is $\mathcal{A} < \kappa$. Therefore, $\mathcal{A} = \kappa$ is the threshold condition for the laser. At threshold, the photon statistics change qualitatively and very rapidly in a narrow region of the pumping parameter. It should also be noted that below threshold the distribution function Eq. (62) is essentially of thermal character. If we introduce an effective temperature T defined by

$$\exp\left(-\frac{\hbar\omega_0}{kT}\right) = \frac{\mathcal{A}}{\kappa} \tag{63}$$

we can cast Eq. (62) to the form

$$p(n) = \left[1 - \exp\left(-\frac{\hbar\omega_0}{kT}\right)\right]\exp\left(-\frac{n\hbar\omega_0}{kT}\right) \tag{64}$$

This is just the photon-number distribution of a single mode in thermal equilibrium with a thermal reservoir at temperature T. The inclusion of a finite temperature-loss reservoir to represent cavity losses will not alter this conclusion about the region below threshold.

There is no really good analytical approximation for the region around threshold, although the lowest-order expansion of the denominator in Eq. (60) yields some insight. The solution with this condition is given by

$$p(n) = p(0)\left(\frac{\mathcal{A}}{\kappa}\right)^n \prod_{k=0}^{n}\left(1 - \frac{k\mathcal{B}}{\mathcal{A}}\right) \tag{65}$$

This equation clearly breaks down for $n > \mathcal{A}/\mathcal{B} = n_{\max}$, where $p(n)$ becomes negative. The resulting distribution is quite broad, exhibiting a long plateau and a rapid cutoff at $n_{\max}$. The broad plateau means that many values of n are approximately equally likely; therefore, the intensity fluctuations are large around threshold. The most likely value of $n = n_{\text{opt}}$ can be obtained from the condition $p(n_{\text{opt}} - 1) = p(n_{\text{opt}})$ since $p(n)$ is increasing before $n = n_{\text{opt}}$ and decreasing afterwards. This condition yields $n_{\text{opt}} = (\mathcal{A} - \kappa)/\mathcal{B}$, which is smaller by the factor $\kappa/\mathcal{A}$ than the value obtained from the full nonlinear equation [cf. Eq. (70) following].

The third region of special interest is the one far above threshold. In this region, $\mathcal{A}/\kappa \gg 1$ and the n values contributing the most to the distribution function are the ones for which $n \gg \mathcal{A}/\mathcal{B}$. We can then neglect 1 in the denominator of Eq. (60), yielding

$$p(n) = \exp\left(-\overline{n}\,\frac{\overline{n}^n}{n!}\right) \tag{66}$$

with $\overline{n} = \mathcal{A}^2/(\kappa\mathcal{B})$. Thus, the photon statistics far above threshold are poissonian, the same as for a coherent state. This, however, does not mean that far above threshold the laser is in a

coherent state. As we shall see later, the off-diagonal elements of the density matrix remain different from those of a coherent state for all regimes of operation.

After developing an intuitive understanding of the three characteristically different regimes of operation, we give the general solution of Eq. (60), valid in all three regimes:

$$p(n) = p(0) \prod_{k=1}^{n} \frac{(\mathcal{A}/\kappa)}{(1 + k\mathcal{B}/\mathcal{A})} \tag{67}$$

The normalization constant $p(0)$ may be expressed in terms of the confluent hypergeometric function

$$\begin{aligned} p(0) &= \left[\sum_{n=0}^{\infty} \frac{\left(\frac{\mathcal{A}}{\mathcal{B}}\right)! \left(\frac{\mathcal{A}^2}{\mathcal{B}\kappa}\right)^n}{\left(n + \frac{\mathcal{A}}{\mathcal{B}}\right)!} \right]^{-1} \\ &= \left[F\left(1; \frac{\mathcal{A}}{\mathcal{B}} + 1; \frac{\mathcal{A}^2}{\mathcal{B}\kappa}\right) \right]^{-1} \end{aligned} \tag{68}$$

In Fig. 6, the photon-number distribution is displayed for various regimes of operation.

It is interesting to note that $p(n)$ is a product of n factors of the form $(\mathcal{A}/\kappa)/(1 + k\mathcal{B}/\mathcal{A})$. This is an increasing function of k as long as the factors are larger than 1 and decreasing afterwards. The maximum of the distribution function can be found from the condition

$$\frac{(\mathcal{A}/\kappa)}{(1 + n_m\mathcal{B}/\mathcal{A})} = 1 \tag{69}$$

or

$$n_m = \frac{\mathcal{A}}{\mathcal{B}} \frac{\mathcal{A} - \kappa}{\kappa} \tag{70}$$

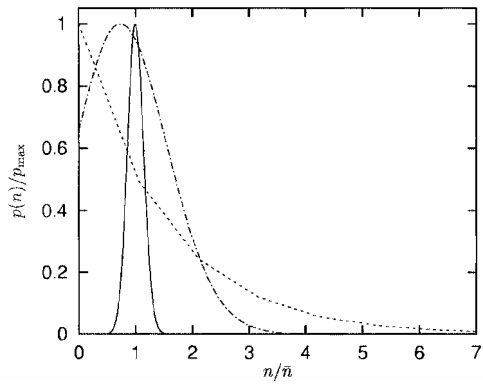

FIGURE 6 Photon statistics of the laser for various regimes of operation. Dotted line: laser 50 percent below threshold ($\mathcal{A}/\kappa = ½$), distribution thermal in character, Mandel $Q_M = 1$. Dot-dashed line: laser 10 percent above threshold, ($\mathcal{A}/\kappa = 1.1$), distribution is broad, $Q_M = 5$. Solid line: laser 100 percent above threshold ($\mathcal{A}/\kappa = 2$), distribution super-Poissonian, $Q_M = 1$. Since in the various regimes the actual photon numbers and $p(n)$ values differ by several orders of magnitude, in order to comparatively display the statistics in one figure, we plot $p(n)/p_{max}$ versus $n/\bar{n}$. This way the maximum of each curve is 1 and unity on the horizontal axis corresponds to the average photon number. $\mathcal{A}/\mathcal{B} = 50$ is used for all plots, for illustrative purposes only. For more realistic values, the above-threshold distributions are much narrower on this scale.

Clearly, for $\mathcal{A} < \kappa$ the maximum is at $n = 0$ and the distribution is monotonically decreasing, which is characteristic of a thermal distribution. This is in agreement with the previous findings for the below-threshold region. Around $\mathcal{A} \simeq \kappa$ the distribution quickly changes its character. The factor $\mathcal{A}/\mathcal{B}$ governs the magnitude of the photon number while $(\mathcal{A} - \kappa)/\kappa$ is a measure of how far away from threshold the laser is operating. Typical values for CW gas lasers (the He-Ne laser, for example) are $\mathcal{A}/\mathcal{B} \simeq 10^6$ and $\kappa \simeq 10^6$ Hz. Around threshold, $\mathcal{A} \simeq \kappa$ and the factors appearing in $p(n)$, given by Eq. (69), are effectively unity for a broad range of n. For example, for $\mathcal{A}/\kappa = 1.001$ (i.e., one-tenth of a percent above threshold), the factors are slightly above 1 for $1 < n < 1000$. So, in the threshold region, the distribution very quickly changes from a thermal one, dominated by the vacuum state, to a broad distribution with large intensity fluctuations. Farther above threshold the distribution becomes more and more peaked around n_m and becomes essentially poissonian for $\mathcal{A}/\kappa > 2$.

It is easy to obtain the mean photon number $\overline{n}$ from Eq. (67):

$$\overline{n} = \sum_{n=0}^{\infty} np(n) = \frac{\mathcal{A}}{\mathcal{B}} \frac{\mathcal{A} - \kappa}{\kappa} + \frac{\mathcal{A}}{\mathcal{B}} p(0) \tag{71}$$

Above threshold, $p(0) \ll 1$ and the last term becomes quickly negligible. Then $\overline{n}$ coincides with n_m, the maximum of the distribution. We can obtain $\overline{n^2}$ similarly. The result is

$$\overline{n^2} = \overline{n}^2 + \frac{\mathcal{A}^2}{\mathcal{B}\kappa} \tag{72}$$

Using Eq. (71), the variance can be expressed as

$$\sigma^2 = \overline{n^2} - \overline{n}^2 = \overline{n} \frac{\mathcal{A}}{\mathcal{A} - \kappa} \tag{73}$$

From here we see that the variance always exceeds that of a poissonian distribution ($\sigma^2 > \overline{n}$), but it approaches one far above threshold. A good characterization of the photon-number distribution is given by the Mandel Q_M parameter:

$$Q_M = \frac{\overline{n^2} - \overline{n}^2}{\overline{n}} - 1 \tag{74}$$

For our case, it is given by

$$Q_M = \frac{\kappa}{\mathcal{A} - \kappa} \tag{75}$$

Since $Q_M > 0$ above threshold, the field is superpoissonian. Very far above threshold, when $\mathcal{A} \gg \kappa$, Q_M approaches zero, which is characteristic of a poissonian distribution, again in agreement with our discussion of the far-above-threshold region.

Micromaser Photon Statistics. As a first application of the micromaser master equation, Eq. (56), we shall study the steady-state photon statistics arising from it. To this end we take the diagonal $n = n'$ elements, and after regrouping the terms we obtain:

$$\begin{aligned}\dot{p}(n) = &-N_{\text{ex}} \sin^2(g\tau\sqrt{n+1})p(n) + (n_{\text{th}} + 1)(n+1)p(n+1) - n_{\text{th}}(n+1)p(n) \\ &+ N_{\text{ex}} \sin^2(g\tau\sqrt{n})p(n-1) - (n_{\text{th}} + 1)np(n) + n_{\text{th}}np(n-1)\end{aligned} \tag{76}$$

Here the overdot stands for derivative with respect to the scaled time, $t' = \kappa t$. $N_{\text{ex}} = r/\kappa$ is the number of atoms traversing the cavity during the lifetime of the cavity field, and the diagonal matrix elements of the density operator $p(n) = \varrho_{nn}$ are the probabilities of finding n photons

in the cavity. The various processes in the right-hand side of this equation are again visualized in Fig. 5. They have the structure $F(n+1) - F(n)$ where $F(n+1)$ corresponds to the processes connecting $p(n+1)$ to $p(n)$. In the steady state the left-hand side is zero and $F(n+1) = F(n)$, yielding $F(n) =$ constant. The only normalizable solution to the photon statistics arises when this constant is zero, $F(n) = 0$. Once again, this is the condition of detailed balance because the probability flows between adjacent levels are separately balanced. More explicitly, this leads to the following recurrence relation for the photon-number probabilities:

$$p(n) = \frac{N_{\text{ex}} \sin^2 (g\tau\sqrt{n})/n + n_{\text{th}}}{n_{\text{th}} + 1} p(n-1) \tag{77}$$

The solution to this simple recurrence relation is straightforward:

$$p(n) = p(0) \prod_{i=1}^{n} \frac{N_{\text{ex}} \sin^2 (g\tau\sqrt{i})/i + n_{\text{th}}}{n_{\text{th}} + 1} \tag{78}$$

where $p(0)$ is determined from the normalization condition $\sum_{n=0}^{\infty} p(n) = 1$. The photon-number distribution $p(n)$ versus n can be multipeaked in certain parameter regimes. This can be easily understood on the basis of Fig. 5. The gain processes (upward arrows) balance the loss (downward arrows). Since the gain is an oscillatory function of n, several individual peaks [with the property $p(n+1) = p(n)$] will develop for those values of n where the gain perfectly balances the loss. The resulting mean photon number (first moment of the distribution) and photon-number fluctuations (second moment Q_M) versus the scaled interaction parameter $\theta = g\tau\sqrt{N_{\text{ex}}}$ are displayed in Fig. 7.

The mean photon number is an oscillatory function of the scaled interaction time. The oscillations correspond to subsequent Rabi cycles the atoms are undergoing in the cavity as function of the interaction time. The first threshold occurs at $\theta = 1$; the higher ones occur where θ is approximately an integer multiple of 2π. Around the thresholds the micromaser field is superpoissonian; in the parameter region between the thresholds it is subpoissonian, which is a signature of its nonclassicality.

Physics off the Main Diagonal: Spectrum and Linewidth

In the subsection on laser photon statistics we have shown that the laser has poissonian photon statistics far above threshold, just as a coherent state would. However, it is erroneous to conclude from this that the laser field is in a coherent state far above threshold. Only the intensity of the laser becomes stabilized due to a delicate balance of the nonlinear gain and loss. Any deviation from the steady-state intensity induces a change that tries to restore the steady-state value; as a result, the intensity is locked to this value. The phase of the field, on the other hand, evolves freely and is not locked to any particular value. In fact, it performs a random walk due to the separate spontaneous emission events. Each such event contributes a small random phase change to the instantaneous phase of the field. The mean of these changes averages to zero, but the mean of the square of these changes remains finite. As a result, the phase undergoes a diffusionlike process and will become uniformly distributed over the 2π interval. Any information contained in the instantaneous phase will be erased in this process. The time scale for the decay of the phase information is given by the rate of the phase diffusion. In the following, we shall determine this characteristic time scale, the so-called phase diffusion constant for the laser and micromaser.

Spectral Properties of the Laser Field. The decay of the phase information can be directly read out from the temporal behavior of the two-time correlation function of the field amplitude:

$$g^{(1)}(t_0 + t, t_0) = \frac{\langle a^\dagger(t_0 + t) a(t_0) \rangle}{\langle a^\dagger(t_0) a(t_0) \rangle} \tag{79}$$

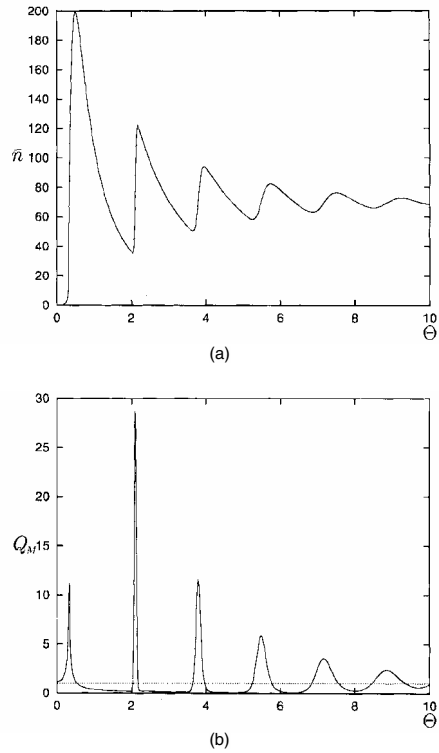

FIGURE 7 (*a*) Mean photon number and (*b*) Mandel Q_M parameter versus interaction parameter for the micromaser, for $N_{ex} = 200$.

With increasing time difference between their amplitudes, the fields become less and less correlated since spontaneous emission randomizes their phases. At steady state, the two-time correlation function [Eq. (79)] depends only on the time difference t and is independent of the choice of the initial time t_0.

A quantum regression "theorem,"[88] based on a system-reservoir factorization of the density matrix, was developed to permit the time evolution of the two-time correlation function at steady state to be calculated from the time evolution of the single-time correlation function for a Markov process. The unusual success of this procedure (see Ref. 89 for a comparison between experiment and theory for the phase linewidth, the intensity linewidth, the photocount distribution, and the spectral moments) requires additional explanation. This was supplied in a proof that regression is valid when the system is markovian.[90] In the quantum case, the system is only approximately markovian. But this assumption has already been made in all cases for which solutions have been found. Therefore, it is sufficient for us to study the time evolution of the amplitude itself:

$$\langle a^\dagger(t)\rangle = \sum_{n=0}^{\infty} \sqrt{n+1}\, \varrho_{nn+1} \tag{80}$$

At this point it is useful to define a column vector with the components $\varrho_n^{(k)} \equiv \varrho_{nn+k}$. This way, we simply arrange the elements of the kth diagonal in the form of a vector. For example, elements on the first side diagonal correspond to $k = 1$, and so on. Let us note that the equation of motion for the off-diagonal matrix elements of the density operator can now be written in a simple matrix form

$$\dot{\varrho}_n^{(k)} = A_{nn'} \varrho_{n'}^{(k)} \tag{81}$$

where summation is implied over repeated indexes and the matrix elements $A_{nn'}$ can be read out from Eq. (49). They are given by

$$\begin{aligned} A_{nn'} = &-\left[\frac{\mathcal{N}'_{nn+k}\mathcal{A}}{1 + \mathcal{N}_{nn+k}\mathcal{B}/\mathcal{A}} + \kappa\left(n + \frac{k}{2}\right) \right] \delta_{nn'} + \frac{\sqrt{n(n+k)}\mathcal{A}}{1 + \mathcal{N}_{n-1\,n+k-1}\mathcal{B}/\mathcal{A}}\, \delta_{nn'+1} \\ &+ \kappa\sqrt{(n+1)(n+k+1)}\delta_{nn'-1} \end{aligned} \tag{82}$$

Clearly, $A_{nn'}$ is a tridiagonal matrix. Due to its linearity, we can look for the solution of Eq. (81) by the simple exponential Ansatz, $\varrho_n^{(k)}(t) = e^{-\lambda t}\, \varrho_n^{(k)}(0)$. With this substitution, Eq. (81) can be written in the form of an eigenvalue equation to determine λ,

$$\lambda \varrho_n^{(k)} = -\sum_{n-1}^{n+1} A_{nn'} \varrho_{n'}^{(k)} \tag{83}$$

We restrict the following treatment to $k = 1$ because that is what we need for the calculation of the $g^{(1)}$ correlation function. Higher-order correlation functions, $g^{(k)}$ with $k > 1$, are related to $\varrho_n^{(k)}$ with $k > 1$. From the structure of the $-A$ matrix, one can show that all eigenvalues are positive. There is a smallest eigenvalue, which we denote by D. This eigenvalue will dominate the longtime behavior of the field amplitude, as can easily be seen from the following considerations. Let us denote the set of eigenvalues by $\{D, \lambda_j\}$ with $j = 1, 2, 3, \ldots$. Then $\varrho_n^{(1)}(t)$ can be written as

$$\varrho_n^{(1)}(t) = \varrho_{n0}^{(1)}(0)\, \exp\,(Dt) + \sum_{j=1}^{\infty} \varrho_{nj}^{(1)}(0)\, \exp\,(-\lambda_j t) \tag{84}$$

From this we see that, indeed, the longtime behavior of the off-diagonal elements will be governed by the first term, since the other terms decay faster according to our assumption of D being the smallest positive eigenvalue. Therefore, our task is reduced to the determination of D. In order to obtain an analytical insight, we can proceed as follows. First, let us note that in the longtime limit all elements of the vector $\varrho_n^{(1)}(t)$ decay the same way—they are proportional to $\exp(-Dt)$. Therefore, the sum of the elements also decays with the same rate, D, in this limit. It is quite easy to obtain an equation of motion for the sum of the elements. Starting from Eq. (81) and using Eq. (82) for the case $k = 1$, we immediately obtain

$$\dot{\varrho}^{(1)} = -\sum_{n=0}^{\infty} \left[\frac{n + 3/2 - \sqrt{(n+1)(n+2)}}{1 + (n+3/2)\mathcal{B}/\mathcal{A}} \mathcal{A} + \kappa\left(n + 1/2 - \sqrt{n(n+1)}\right) \right] \varrho_n^{(1)} \tag{85}$$

Here we introduced the notation $\sum_{n=0}^{\infty} \varrho_n^{(1)} = \varrho^{(1)}$ and used the fact that $\mathcal{N}'_{nn+1} = n + 3/2 + \mathcal{B}/(8\mathcal{A}) \approx n + 3/2$ and $\mathcal{N}_{nn+1} = n + 3/2 + \mathcal{B}/(16\mathcal{A}) \approx n + 3/2$ since $\mathcal{B}/\mathcal{A} \approx 10^{-6}$ and can therefore safely be neglected next to 3/2. In the longtime limit the time derivative on the left-hand side can simply be replaced by $-D$ due to Eq. (84). It is also plausible to assume that in the same limit those values of n will contribute the most that lie in the vicinity of $\bar{n}$. Then we can expand the coefficients around the steady-state value of the photon number. This is certainly a good approximation in some region above threshold. The key point is that after the expansion the coefficients of $\varrho_n^{(1)}$ on the right-hand side become independent of the summation index n and

can be factored out from the sum. Then, after the summation, the quantity $\varrho^{(1)}$ also appears on the right-hand side of the equation:

$$D\varrho^{(1)} = \frac{\mathscr{A} + \kappa}{8\bar{n}}\varrho^{(1)} \tag{86}$$

From this we can simply read out the decay rate:

$$D = \frac{\mathscr{A} + \kappa}{8\bar{n}} \tag{87}$$

This quantity, called the *phase diffusion coefficient,* plays a crucial role in determining the transient behavior of the laser as well as its spectral properties. It exhibits the characteristic line narrowing for high intensity, first found by Schawlow and Townes.[80] The mean amplitude, Eq. (80), can now be written as

$$\langle a^\dagger(t)\rangle = e^{-Dt}\langle a^\dagger(0)\rangle \tag{88}$$

The decay of any initial coherent component of the laser field is governed by the phase diffusion constant, due to the randomization of the initial phase information. The randomization is due to two separate processes, as can be read out from the analytical expression, Eq. (87) of the phase diffusion constant. The part proportional to the spontaneous emission rate $\mathscr{A}$ is due to the random addition of photons to the field via spontaneous emission; the part proportional to the cavity decay rate is due to leaking of vacuum fluctuations into the cavity through the output mirrors. Both processes randomize the phase of the initial field; as a result, the phase performs a random walk with a diffusion rate given by Eq. (87). Ultimately, of course, vacuum fluctuations are also responsible for spontaneous emission.

The phase diffusion constant also determines the linewidth of the spectrum of the laser field. Using the quantum regression theorem, we immediately find that the (nonnormalized) steady-state field correlation function is given by

$$g^{(1)}(t_0 + t,\, t_0) = \langle a^\dagger(t_0 + t)a(t_0)\rangle = \bar{n}\exp\,(i\omega_0 t - Dt) \tag{89}$$

where ω_0 denotes the operating frequency of the laser, as before. The power spectrum is given by the Fourier transform of the field correlation function:

$$S(\omega) = \frac{1}{\pi}\,\mathrm{Re}\int_0^\infty g^{(1)}(t_0 + t,\, t_0)\, e^{-i\omega t}\, dt = \frac{\bar{n}}{\pi}\,\frac{D}{(\omega - \omega_0)^2 + D^2} \tag{90}$$

This is a lorentzian spectrum centered around the operating frequency, $\omega = \omega_0$. The full width at half-maximum (FWHM) is given by $2D$. Figure 8 depicts the normalized spectrum $S(\omega)/S(\omega_0)$ versus the detuning $\Delta = (\omega - \omega_0)/D$.

It should be emphasized that our method of obtaining the preceding analytical approximations is justified only if the mean photon number is large, the photon-number distribution consists of a single large peak, and cross-coupling between intensity and phase, arising from the nonlinearity of the gain very far above threshold, is negligible. These conditions are met for a laser in some region above threshold. Near the threshold, however, the intensity fluctuations cannot be neglected. From numerical studies[91] it was concluded that their contribution to the linewidth is approximately equal to the phase diffusion constant, and the linewidth in this region is about twice what is predicted by Eq. (90); i.e., it is $4D$; and far above threshold (for $\mathscr{A}/\kappa > 2$), the linewidth is smaller than the prediction of Eq. (90). These numerical findings are confirmed by a recent analytical approach to the problem.[92] One of the earliest quantum calculations of the laser linewidth[69] was based on the quantum theory of noise sources.[70] The laser linewidth above threshold was established to be due mostly to phase noise,[69] and it was explained that the factor of 2, too large, was obtained by many previous authors because

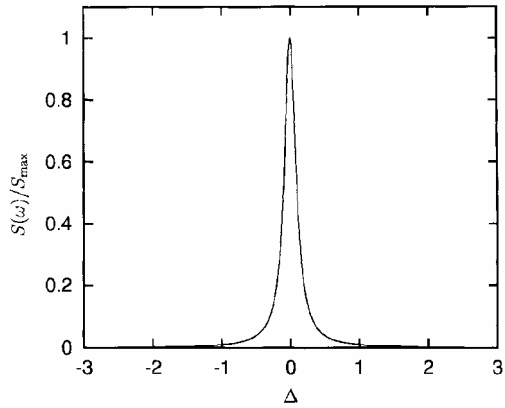

FIGURE 8 Laser spectrum $S(\omega)/S_{max}$ versus detuning $\Delta = (\omega - \omega_0)/\kappa$, for a laser 100 percent above threshold (note that detuning is in units of bare-cavity linewidth). For our parameters the spectral width D is about 1 percent of the bare-cavity linewidth, an example of the Schawlow-Townes narrowing.

they had permitted amplitude fluctuations, which were valid near threshold but not far above. These ideas were confirmed by analytic calculations below and above threshold[93] and by a numerical solution of the associated Fokker-Planck equation.[94,95] Moreover, the effects of laser detuning on the linewidth were determined without assuming that the light field decays much slower than the atomic decay rates. It was found that the effective linewidth was a harmonic mean between the field and electronic decay rates, as shown in Eq. (35) of Ref. 69.

The calculations of the phase linewidth done in this section are equivalent to the quasilinear approximation employed in the Langevin noise source procedure in Ref. 93 and shown in Ref. 94 to be valid for dimensionless pump rates $p > 10$. Below threshold, $p < -10$, the components of the electromagnetic field can be treated as uncoupled gaussian variables, leading to the Schawlow-Townes formula. Only the region in the immediate vicinity of threshold requires careful analysis. In that region, it is shown in footnote 10 in Ref. 93 that the coefficients in the Fokker-Planck equation can be expanded in powers of n, retaining only the first nonlinear term. The result then reduces to the rotating-wave Van der Pol oscillator. One advantage of this reduction is that the equation can be scaled in time and in amplitude, leaving the dimensionless pump parameter p as the only remaining parameter. This greatly reduces any subsequent numerical calculations. The ability to retain only one nonlinear term is based only on the requirement that we are dealing with a good oscillator—that is, one whose signal-to-noise ratio is large. Equivalent approximations can be introduced in the density matrix treatment, as well.

The assumption made here that the phase linewidth comes predominantly from the smallest decay eigenvalue was established in Ref. 94, where the actual line shape is shown to be a sum of lorentzians, and the percentage from each lorentzian is calculated. The intensity fluctuations are also expressed as a sum of lorentzians but several modes contribute, not just the lowest. The percentage in each is given in Ref. 94. Part of the reason for this is that the modes approach degeneracy in pairs as one moves above threshold. The lifting of such a degeneracy was shown in Ref. 96 to be associated with a phase transition. Since our system is finite, the phase change occurs gradually and can be observed. The view of lasing as a phase transition will be explored in more detail in Sec. 26.5.

Spectral Properties of the Micromaser Field. If we take the n, $n+1$ matrix elements of Eq. (57), then, following the methods of the previous subsection, it is straightforward to derive the diffusion constant. In particular, elements of the first side diagonal can again be arranged in the form of a column vector, and this vector again satisfies an equation of motion similar to Eq. (81), with an appropriate redefinition of the tridiagonal matrix appearing in the equation:

$$\begin{aligned} A_{nn'} = &- \{r[1 - \cos(g\tau\sqrt{n+1})\cos(g\tau\sqrt{n+2})] + \kappa(2n_{\text{th}}(n+1) + n + 1/2)\}\delta_{nn'} \\ &+ \left(r\sin(g\tau\sqrt{n})\sin(g\tau\sqrt{N+1}) + \kappa n_{\text{th}}\sqrt{n(n+1)}\right)\delta_{nn'+1} \\ &+ \kappa(n_{\text{th}}+1)\sqrt{(n+1)(n+2)}\,\delta_{nn'-1} \end{aligned} \tag{91}$$

The exponential Ansatz for the decay of the column vector again turns the equation of motion into an eigenvalue equation for the matrix A and the longtime behavior will again be governed by the smallest eigenvalue, which we denote by D. Summing over all elements of the resulting eigenvalue equation and replacing the coefficients on the right-hand side by their longtime value—that is, expanding the coefficients around $n = \bar{n}$—will finally yield

$$D = 2r\sin^2\left(\frac{g\tau}{4\sqrt{\bar{n}}}\right) + \kappa\frac{(2n_{\text{th}}+1)}{8\bar{n}} \tag{92}$$

for the phase diffusion constant of the micromaser. Here $\bar{n}$ is the mean photon number of the (single-peaked) distribution. This expression was first derived by Scully et al.[97] It leads to a lorentzian spectrum similar to Eq. (90) but with D appropriately replaced by that of the micromaser. It should be noted, however, that the analytical formula has a more restricted validity than in the case of the laser. Namely, in the case of the micromaser, the photon-number distribution can be multipeaked, and the simple expansion around the $\bar{n}$ value corresponding to a single dominating peak may not hold. For this more general case several numerical approaches have been developed (see Ref. 98). When Eq. (92) is valid it coincides with the results of the numerical calculations.

For small values of the argument in the sine function, Eq. (92) can be cast to a form which is formally identical to the usual laser phase diffusion constant[99] [cf. Eq. (87)]:

$$\begin{aligned} D &= r\frac{g^2\tau^2}{8\bar{n}} + \kappa\frac{2n_{\text{th}}+1}{8\bar{n}} \\ &= \frac{\mathcal{A} + \kappa(2n_{\text{th}}+1)}{8\bar{n}} \end{aligned} \tag{93}$$

Here we introduced the small signal gain $\mathcal{A} \equiv rg^2\tau^2$, in analogy to the laser gain. However, for other values of the argument the first term in Eq. (92) may dominate, and the phase diffusion constant can exceed the bare-cavity linewidth, which is a unique quantum feature of the micromaser and makes it distinctly different from the classical Schawlow-Townes-type behavior.

Without going into the specifics, we just mention a few other aspects of the quantum theory of the micromaser. As we have just seen a steady state is reached due to the equilibrium between the gain and loss processes. In some cases, however, a steady state can be reached even in a lossless cavity. This happens if the probability flow in Fig. 5 due to the gain process is interrupted for some value of the interaction parameter. The upward flow is interrupted when

$$g\tau\sqrt{n_q+1} = q\pi \tag{94}$$

and the downward flow is interrupted when

$$g\tau\sqrt{n_q} = q\pi \tag{95}$$

with $q = 1, 2, \ldots$ in both cases. They are called the *upward* and *downward trapping states,* respectively.[100] In such cases the state of the field is a number state. The signature of the number state is a large maximum in the linewidth at the corresponding interaction parameter. It can easily be understood qualitatively: since the state of the field is a number state, it cannot have any phase information. Therefore, the phase randomizes on a very rapid time scale; in other words, the phase correlations decay very rapidly, and a large phase diffusion constant ensues. Further, if the atoms are injected in a coherent superposition of their upper and lower levels in the cavity then, under certain conditions, the so-called tangent and cotangent states of the field may develop.[101] Finally, it should be mentioned that the master equations Eqs. (49) and (56) hold only for the case when the time interval between consecutive atomic injections is completely random. Other arrival times statistics, including the case of regular injections, have been investigated by a number of authors.[102] A closely related area of recent theoretical studies pertains to the detection of the statistical properties of the (experimentally inaccessible) intracavity field via monitoring the statistics of the outgoing atoms for poissonian[103] as well as nonpoissonian[104] pumping. For regular (subpoissonian) pumping, transient oscillations in field correlation function and a corresponding multipeaked spectrum were predicted.[105]

Most of the predictions of this theory have been confirmed by experiments. For example, trapping states have been observed in recent experiments by the Garching group.[106] Without providing an exhaustive list, we just refer the reader to recent progress in the experimental department.[107]

Other Approaches

So far we have considered laser theory based on a density-operator approach. An equivalent approach to a laser theory can be formulated using a Heisenberg-Langevin approach. In this approach explicit equations of motion are derived for the field operator.

The quantum-noise operator formalism was presented in essentially its final form by Lax at the 1965 meeting on the Physics of Quantum Electronics.[69] There, it was applied to the laser, calculating, the laser linewidth in its most general form. For the general theory, see the 1966 Brandeis lecture notes of Lax.[71]

In the present formulation, our goals are more specific—namely, the Heisenberg-picture quantum theory of the laser. To that end, we will here give a quantum-noise treatment along the lines of that followed in the previous subsection—namely, a single laser mode damped at a rate κ by a (dissipative) reservoir and driven by atoms injected into the laser cavity at random times t_j.

First we discuss the simple example of damping of the field by a reservoir and derive the quantum Langevin equation for the field operator. We then discuss the gain noise in a laser and derive the laser linewidth.

Damping of Field by Reservoir. We consider the damping of a single-mode field of frequency ν interacting with a reservoir consisting of simple harmonic oscillators. The system describes, for example, the damping of a single-mode field inside a cavity with lossy mirrors. The reservoir in this case consists of a large number of phononlike modes in the mirror.

The field is described by the creation and destruction operators $a^\dagger$ and a, whereas the harmonic oscillators of frequency $\nu_k = ck$ are described by the operators $b_k^\dagger$ and b_k. The field-reservoir system evolves in time under the influence of the total hamiltonian:

$$\mathcal{H} = \hbar\omega_0(a^\dagger a + \tfrac{1}{2}) + \hbar \sum_k \nu_k(b_k^\dagger b_k + \tfrac{1}{2}) + \hbar \sum_k g_k(ab_k^\dagger + b_k a^\dagger) \tag{96}$$

Here g_k are the coupling constants and we have made the rotating-wave approximation. We are interested in the evolution of the field operator a. The Heisenberg equations of motion for the field and reservoir are:

$$\dot{a}(t) = -i\omega_0\, a(t) - i \sum_k g_k b_k(t) \tag{97}$$

$$\dot{b}_k(t) = -i\nu_k\, b_k(t) - i g_k a(t) \tag{98}$$

The equation for b_k can be formally solved, and the resulting expression is substituted in Eq. (97). In the Weisskopf-Wigner approximation, the annihilation operator in the interaction picture $a = a(t) \exp [i\omega_0(t - t_0)]$ satisfies a Langevin equation

$$\dot{a} = -\frac{\kappa}{2} a + F(t) \tag{99}$$

where

$$F(t) = -i \sum_k g_k b_k(0) \exp [-i(\nu_k - \omega_0)(t - t_0)] \tag{100}$$

is a noise operator. Equation (99) clearly indicates that the damping of the field (represented by the term $-\kappa a/2$) is accompanied by noise.

For the damping of the single-mode field inside a cavity via transmission losses, the damping constant κ is related to the quality factor Q of the cavity via $\kappa = \omega_0/Q$.

Atomic (Gain) Noise and Laser Linewidth. As discussed earlier, the natural linewidth of the laser arises due to spontaneous emission by the atoms. In the density-operator approach, a fully nonlinear treatment was followed. Here, we present a simple linear analysis to calculate the laser linewidth in the Heisenberg-Langevin approach. We assume that the atoms are long lived, and that they interact with the cavity field for a time τ. This treatment allows us to include the memory effects inside a laser, and is one of the simplest examples of a nonmarkovian process.[108,109]

We start with the hamiltonian describing the atom-field interaction:

$$\mathcal{H} = \mathcal{H}_F + \mathcal{H}_{\text{atom}} + \hbar\, g \sum_i \{\sigma^i a^\dagger N(t_i, t, \tau) + Hc\} \tag{101}$$

where $\mathcal{H}_F$ and $\mathcal{H}_{\text{atom}}$ describe the field and atoms, respectively; g is the atom-field coupling constant; and σ_i is the lowering operator for the ith atom; Hc is the injunction to add the Hermitian conjugate. The operators a and $a^\dagger$ represent the annihilation and creation operators, and $N(t_i, t, \tau)$ is a notch function which has the value

$$N(t_i, t, \tau) = \begin{cases} 1 & \text{for } t_i \le t < \tau \\ 0 & \text{otherwise} \end{cases} \tag{102}$$

Using this hamiltonian, we write the equations for the atom-field operators in the interaction picture as

$$\begin{aligned} \dot{a} &= -ig \sum_i \sigma^i N(t_i, t, \tau) - \tfrac{1}{2}\kappa a(t) + F_\kappa(t) \\ \dot{\sigma}^i &= igN(t_i, t, \tau)\sigma_z^i a(t) \end{aligned} \tag{103}$$

where the effects of cavity damping are determined by the cavity decay rate κ and the associated Langevin noise source F_κ. Integrating the equation for the atom operator and substituting it into that for the field operator, we obtain

$$\dot{a}(t) = \int_{-\infty}^{t} dt'\, \alpha(t, t') a(t') - \tfrac{1}{2}\gamma a + F_\alpha(t) + F_\kappa(t) \tag{104}$$

where

$$\alpha(t, t') = g^2 \sum_i N(t_i, t, \tau)N(t_i, t', \tau)\sigma_z^i(t') \tag{105}$$

$$F\alpha(t) = -ig \sum_i N(t_i, t, \tau)\sigma^i(t_i) \tag{106}$$

Here, the noise operator Eq. (106) may be seen to have the moments

$$\langle F_\alpha(t)\rangle = 0 \tag{107}$$

$$\langle F_\alpha^\dagger(t)F_\alpha(t')\rangle = g^2 \sum_{ij} N(t_i, t, \tau)N(t_i, t', \tau)\langle\sigma^{\dagger i}(t_i)\sigma^j(t_j)\rangle \tag{108}$$

Because we are injecting our lasing atoms in the upper state, the atomic average is given by $\langle\sigma^{\dagger i}(t_i)\sigma^j(t_j)\rangle = \delta_{ij}$. After replacing the sum upon i in Eq. (108) by an integration over injection times t_i, we find

$$\langle F_\alpha^\dagger(t)F_\alpha(t')\rangle = rg^2 \{ N(t' - \tau, t, \tau)[t - (t' - \tau)] - N(t', t, \tau)[t - (t' + \tau)]\} \tag{109}$$

where r is the atomic injection rate. The phase variance can then be calculated through the noise operator product:

$$\langle\phi^2(t)\rangle = -\frac{1}{2\pi}\int_0^t dt' \int_0^t dt'' \langle F^\dagger(t')F(t'')\rangle \exp\{i[\phi(t') - \phi(t'')]\} \tag{110}$$

On insertion of Eq. (109) into Eq. (110), the expression for the generalized maser phase diffusion noise $\langle\phi^2(t)\rangle$ is found to be

$$\langle\phi^2(t)\rangle = \left(\frac{\mathcal{A}}{2\bar{n}}\right)\left[\left(\frac{t^2}{\tau} - \frac{t^3}{3\tau^2}\right)\theta(\tau - t) + \left(t - \frac{\tau}{3}\right)\theta(t - \tau)\right] \tag{111}$$

Here $\mathcal{A} = rg^2\tau^2$ is the small-signal gain of the maser [cf. Eq. (93), with $n_{\text{th}} = 0$ and using that in steady state $\mathcal{A} = \kappa$]. In the case involving atoms which are injected at random times t_i but which decay via spontaneous emission to far-removed ground states at a rate γ, a similar but more complicated analysis can be carried out. The result in this case is given by

$$\langle\phi^2(t)\rangle = \left(\frac{\mathcal{A}}{2\bar{n}}\right)[t + \gamma^{-1}(e^{-\gamma t} - 1)] \tag{112}$$

Here $\mathcal{A} = 2rg^2/\gamma^2$ is the small-signal gain of the laser [cf. Eq. (50)]. In both of the preceding cases, we find that for times $t = t_m$ small compared to the atomic lifetime, the phase diffusion is quadratic in the measurement time t_m; that is, we now have a phase error which goes as

$$\Delta\phi^2 = \left(\frac{\mathcal{A}t_m}{2n}\right)\left(\frac{\gamma t_m}{2}\right) \tag{113}$$

Therefore, we see that the quantum noise due to spontaneous emission is reduced from the Schawlow-Townes linewidth $2D = \mathcal{A}/2\bar{n}$ by the factor $\gamma t_m/2$, which can be a significant reduction for short measurement times. For times long compared to the atomic lifetime, however, the Schawlow-Townes result is obtained from both Eqs. (111) and (112) as expected.

26.5 THE LASER PHASE-TRANSITION ANALOGY

Considerations involving the analogies between phase transitions in ferromagnets, superfluids, and superconductors have emphasized the similarities between these systems near their critical temperatures.[110]

A natural comparison can be made between second-order phase transitions, such as the order-disorder transitions of ferromagnetic and ferroelectric materials or the vapor-liquid transition of a pure fluid, and the laser threshold. As we have discussed in Sec. 26.4, the state of a laser changes abruptly upon passing through the threshold point. This point is characterized by a threshold population inversion.

The physical basis for this similarity becomes evident when it is recalled that the usual treatments of laser behavior are self-consistent theories. In the laser analysis we assume that each atom evolves in a radiation field due to all the other atoms, and then calculate the field produced by many such evolving atoms in a self-consistent fashion. In this way the laser problem is similar to that of a ferromagnet, in which each spin sees a mean magnetic field due to all the other spins and aligns itself accordingly, thus contributing to the average magnetic field.

Following this point of view, we can discuss the laser theory using the language of second-order phase transitions.

The density matrix of the laser field obeys Eq. (49). The time dependence of the expectation value $\overline{E}$ of the electric field operator $E = (a + a^\dagger)$ is there given by the following equation:

$$\dot{\overline{E}} = \frac{1}{2}(\mathscr{A} - \kappa)\overline{E} - \frac{\mathscr{B}}{2}\overline{E^3} \tag{114}$$

Here we have assumed that the laser is operating close to threshold ($\mathscr{B}\overline{n}/\mathscr{A} \ll 1$) so that we retain only the terms proportional to $\mathscr{B}$. In addition, we assume $\overline{E} \gg 1$. We can then replace $\overline{E^3}$ by $\overline{E}^3$ and Eq. (114) becomes the well-known result of Lamb's semiclassical theory. The steady-state properties of the laser oscillator are described by the following equation of state:

$$(\mathscr{A} - \kappa)\overline{E} - \mathscr{B}\overline{E}^3 = 0 \tag{115}$$

The threshold condition is given by $\mathscr{A} = \kappa$ as before. Upon putting $\mathscr{A} = a\sigma$, $\mathscr{B} = b\sigma$, and $\kappa = a\sigma_t$ where σ_t is the threshold population inversion, the steady-state solution of Eq. (115) is

$$\begin{aligned} &\overline{E} = 0 && \text{if} \quad \sigma - \sigma_t < 0 \quad \text{(below threshold)} \\ &\overline{E} = \left[\frac{a}{b}\left(\frac{\sigma - \sigma_t}{\sigma}\right)^{1/2}\right] && \text{if} \quad \sigma - \sigma_t > 0 \quad \text{(above threshold)} \end{aligned} \tag{116}$$

Equation (116) is formally identical to the equation for a ferromagnet in the Weiss mean-field theory. The electric field E corresponds to the static magnetization M, which is the order parameter in the ferromagnetic transition. The quadratic polarization $P = (\mathscr{A}\overline{E} - \mathscr{B}\overline{E}^3)/2$ in Eq. (115) corresponds to the magnetic field H generated by a magnetization M, and the term $\kappa\overline{E}/2$ corresponds to a local magnetic field which is assumed proportional to M in the mean-field theory. Furthermore, the steady-state points depend on $\sigma - \sigma_t$ in the same way that M in the ferromagnetic case depends on $T - T_c$, where T_c is the critical temperature. Therefore, σ and σ_T correspond to T and T_c, respectively. The similarity between these two systems is summarized in Table 1 and illustrated in Fig. 9.

We recall that the probability density $P(M)$ for a ferromagnetic system with magnetization M near a phase transition is given by, in thermal equilibrium,

$$P(M) = N'' \exp\left(-\frac{F(M)}{k_B T}\right) \tag{117}$$

where

TABLE 1 Summary of Comparison Between the Laser and a Ferromagnetic System Treated in a Mean-Field Approximation

Parameter	Ferromagnet	Laser
Order parameter	Magnetization M	Electric field strength E
Reservoir variable	Temperature T	Population inversion σ Threshold inversion σ_t
Coexistence curve*	$M = \Theta(T_c - T)\left[\frac{c}{d}\ \frac{T - T_c}{T}\right]^{1/2}$	$E = \Theta(\sigma - \sigma_t)\left[\frac{a}{b}\ \frac{\sigma - \sigma_t}{\sigma}\right]^{1/2}$
Symmetry breaking mechanism	External field H	Injected signal S
Critical isotherm†	$M = \left[\frac{H}{dT_c}\right]^{1/2}$	$E = \left[\frac{2S}{b\sigma_t}\right]^{1/2}$
Zero field susceptibility*	$X \equiv \left(\frac{\partial M}{\partial H}\right)\Big\vert_{H=0}$	$\xi \equiv \left(\frac{\partial E}{\partial S}\right)\Big\vert_{S=0}$
	$= \Theta(T_c - T)[2c(T_c - T)]^{-1}$	$= \Theta(\sigma_t - \sigma)\left[\frac{a(\sigma_t - \sigma)}{2}\right]^{-1}$
	$+\Theta(T - T_c)[c(T - T_c)]^{-1}$	$+\Theta(\sigma - \sigma_t)[a(\sigma - \sigma_t)]^{-1}$
Thermodynamic potential	$F(M) = \frac{1}{2}c(T - T_c)M^2$	$G(E) = -\frac{a}{4}(\sigma - \sigma_t)E^2$
	$+\frac{1}{4}dT\,M^4$	$+\frac{1}{8}b\sigma\,E^4$
	$-HM + F_0$	$-SE + G_0$
Statistical distribution	$P(M) = N'' \exp\left(-\frac{F(M)}{k_B T}\right)$	$P(E) = N' \exp\left(-\frac{G(E)}{k_B \sigma}\right)$

* $\Theta()$ is Heaviside's unit step function.
† Value of order parameter at critical point.

$$F(M) = \tfrac{1}{2}\,c(T - T_c)M^2 + \tfrac{1}{4}\,dT\,M^4 \tag{118}$$

is the free energy. In the corresponding laser analysis, the probability density for the electromagnetic field $P(E)$ is derived in the form

$$P(E) = N' \exp\left(-\frac{G(E)}{k_B \sigma}\right) \tag{119}$$

For this purpose we transform the laser equation for the density matrix for the field [Eq. (49)] into an equivalent equation in terms of the $P(\alpha, \alpha^*)$ representation defined by

$$\rho = \int d^2\alpha P(\alpha, \alpha^*)|\alpha\rangle\langle\alpha|, \tag{120}$$

where $|\alpha\rangle$ is an eigenstate of the annihilation operator a with eigenvalue α. The P representation allows us to evaluate any normally ordered correlation function of the field operators using the methods of classical statistical mechanics. The quantity $P(\alpha, \alpha^*)$ represents the probability density for finding the electric field corresponding to α.

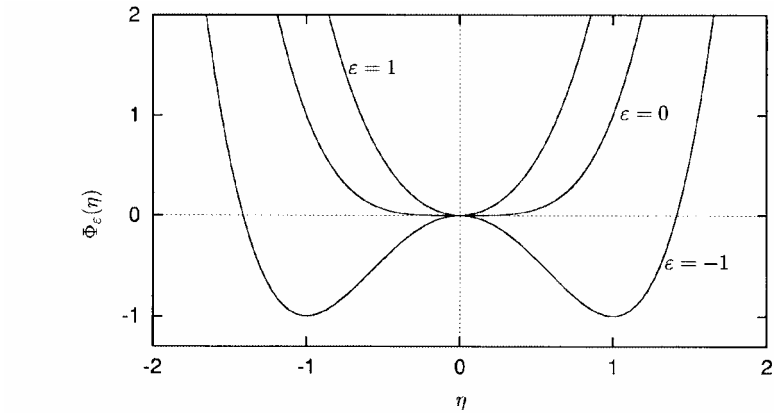

FIGURE 9 Scaled thermodynamical potentials. The $H = 0$ version of $F(M)$ and the $S = 0$ version of $G(E)$ can be expressed in terms of $\Phi_\varepsilon(\eta) = 2\varepsilon\eta^2 + \eta^4$ because

$$\Phi_\varepsilon(\eta) = \begin{cases} \dfrac{[F(M) - F_0]}{\dfrac{c^2 T_c}{4d}} & \text{with} \quad M = (c/d)^{1/2}(T/T_c)^{1/4}\eta \\ & \text{and} \quad \varepsilon = (T - T_c)/(TT_c)^{1/2} \\ \dfrac{[G(E) - G_0]}{\dfrac{a^2\sigma_t}{8b}} & \text{with} \quad E = (a/b)^{1/2}(\sigma_t/\sigma)^{1/4}\eta \\ & \text{and} \quad \varepsilon = (\sigma_t - \sigma)/(\sigma\sigma_t)^{1/2} \end{cases}$$

are equivalent to the respective entries in Table 1. The plot shows $\Phi_\varepsilon(\eta)$ for $\varepsilon = 1$ (ferromagnet above T_c, laser below threshold), $\varepsilon = 0$ (ferromagnet at T_c, laser at threshold), and $\varepsilon = -1$ (ferromagnet below T_c, laser above threshold).

Near threshold, $P(\alpha, \alpha^*)$ obeys the following Fokker-Planck equation:

$$\begin{aligned} \frac{\partial P}{\partial t} = &-\frac{\partial}{\partial \alpha}\left[\frac{1}{2}(\mathcal{A} - \kappa)\alpha P - \frac{1}{2}\mathcal{B}|\alpha|^2\alpha P\right] \\ &-\frac{\partial}{\partial \alpha^*}\left[\frac{1}{2}(\mathcal{A} - \kappa)\alpha^* P - \frac{1}{2}\mathcal{B}|\alpha|^2\alpha^* P\right] + \mathcal{A}\frac{\partial^2 P}{\partial\alpha\partial\alpha^*} \end{aligned} \tag{121}$$

The steady-state solution of this equation is given by

$$P(\alpha, \alpha^*) = \mathcal{N} \exp\left[\frac{(\mathcal{A} - \kappa)|\alpha|^2 - \mathcal{B}|\alpha|^4/2}{2\mathcal{A}}\right] \tag{122}$$

where $\mathcal{N}$ is a normalization constant. The P representation can be rewritten in terms of the variables $x = \text{Re}\,\alpha$ and $y = \text{Im}\,\alpha$ as

$$P(x, y) = \mathcal{N} \exp\left[-\frac{G(x, y)}{K\sigma}\right] \tag{123}$$

with

$$G(x, y) = -\tfrac{1}{4}\, a(\sigma - \sigma_t)(x^2 + y^2) + \tfrac{1}{8}\, b\sigma(x^2 + y^2)^2 \tag{124}$$

Here $K = a/4$ is one-fourth of the gain of one atom, $a(\sigma - \sigma_t) = \mathcal{A} - \kappa$, and $b\sigma = \mathcal{B}$.

We can see that the steady-state situation of the laser corresponds to the minimum value of G, i.e., $\partial G/\partial x = \partial G/\partial y = 0$. These solutions are $x = y = 0$ and $|\alpha|^2 = (x^2 + y^2) = a(\sigma - \sigma_t)/b\sigma$. Thus, for $(\sigma - \sigma_t) < 0$, the only allowed solution is $x = y = 0$. However, for $(\sigma - \sigma_t) > 0$, $x = y = 0$ is an unstable solution as the second derivative of G with respect to x and y is positive. This is seen clearly in Fig. 9, where we have plotted G versus $x = E$ for $y = 0$.

We thus see that G behaves in essentially the same way as the free energy of a thermodynamic system.

It should be emphasized that in the thermodynamic treatment of the ferromagnetic order-disorder transition, there are three variables required: (1) magnetization M, (2) external magnetic field H, and (3) temperature T. In order to have a complete analogy, it is important to realize that in addition to the electric-field-magnetization, population inversion-temperature correspondences, there must exist a further correspondence between the external magnetic field and a corresponding symmetry-breaking mechanism in the laser analysis. As shown in Ref. 111 and illustrated in Fig. 10, this symmetry breaking mechanism in the laser problem corresponds to an injected classical signal S. This leads to a skewed effective free energy.

An example of how the analogy can provide us with deeper insight is contained in the fact that we are able to *guess* correctly the $P(E)$ for a laser influenced by an injected signal, by analogy with the corresponding magnetic problem in the broken symmetry mode of operation.

More recently we have been turning the tables and using the quantum laser theory to learn about Bose-Einstein condensation (BEC). Recent experiments on BEC in laser-cooled gases,[112–114] and in He^4 in porous gel,[115] have stimulated a wealth of theoretical work[116–118] on the equilibrium and nonequilibrium properties of confined quantum degenerate gases.[119–124] Presently the partition function, critical temperature, and other such quantities are of interest for N bosons in a box below T_c. But the canonical ensemble is difficult to use in practice, because the state sums must be restricted to N particles. Indeed, the canonical partition function for a Bose gas of N particles at temperature T has not been so widely studied as one might have thought. To quote Herzog and Olshanii,

> To our knowledge there is no simple analytic expression for the canonical partition function in [the case of N bosons in a three-dimensional trap].[121]

Furthermore, there are questions of principle concerning the critical temperature and the validity of using phase-transition concepts in a mesoscopic sample having a small number of particles ($N \simeq 10^3$). In fact, Uhlenbeck pointed out to Einstein many years ago that BEC rigorously occurs only in the limit of infinite particle number.[125] Indeed, for a finite number of atoms there is no sharp "critical point" or critical temperature T_c. But the same can be said for the laser threshold. There is a *gradual* transition from disorder to order in both cases. However, as discussed later, even when fluctuations are present, T_c for a Bose gas and the laser threshold inversion are well defined.

Motivated by the preceding, we extend the laser-phase transition analogy to include BEC. We present a new approach to the problem of N bosons in thermal equilibrium below T_c. We emphasize that the present work provides another example[126] in which steady-state (detailed

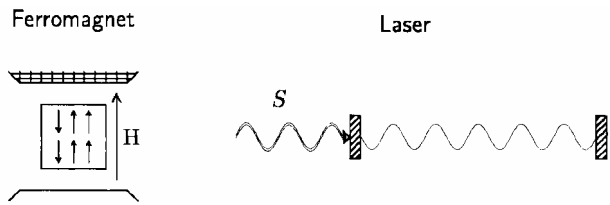

FIGURE 10 Figure depicting the broken symmetry mode of operation for both a ferromagnet and a laser.

balance) solutions to nonequilibrium equations of motion provide a supplementary approach to conventional statistical mechanics (e.g., partition-function calculations). The present approach lends itself to different approximations; yielding, among other things, a simple (approximate) analytic expression for the ground-state density matrix for N trapped bosons and the partition function for same.

Thus, we seek a nonequilibrium equation of motion for the ground state of an ideal Bose gas in a three-dimensional harmonic trap coupled to the thermal reservoir, as shown elsewhere.[127]

$$\dot{\rho}_{n_0,n_0} = -K_{n_0}(n_0+1)\rho_{n_0,n_0} + K_{n_0-1}n_0\rho_{n_0-1,n_0-1} - H_{n_0}n_0\rho_{n_0,n_0} + H_{n_0+1}(n_0+1)\rho_{n_0+1,n_0+1} \tag{125}$$

The cooling and heating coefficients K_{n_0} and H_{n_0} are given by

$$K_{n_0} = \sum_k 2\pi W_k g_k^2 \langle \eta_k + 1\rangle \langle n_k\rangle_{n_0} \tag{126}$$

and

$$H_{n_0} = \sum_k 2\pi W_k g_k^2 \langle \eta_k\rangle \langle n_k + 1\rangle_{n_0} \tag{127}$$

where W_k is the heat-bath density of states, $\langle \eta_k\rangle$ is the average occupation number of the kth heat-bath oscillator, and $\langle n_k\rangle_{n_0}$ is the average number of atoms in the kth excited state, given n_0 atoms in the condensate. Here the coefficient K_{n_0} denotes the cooling rate from the excited states to the ground state, and similarly H_{n_0} stands for the heating rate for the ground state.

The heating term is approximately

$$H_{n_0} \simeq \kappa \sum_k \langle \eta(\varepsilon_k)\rangle = \kappa \sum_{\ell,m,n} \left[\exp\left(\frac{\hbar\Omega}{k_B T}\right)(\ell+n+m) - 1\right]^{-1} \tag{128}$$

In the weak trap limit, this yields

$$H_{n_0} \simeq \kappa\left(\frac{k_B T}{\hbar\Omega}\right)^3 \zeta(3) \tag{129}$$

where $\zeta(3)$ is the Riemann zeta function and Ω is the trap frequency. Likewise, the cooling term in Eq. (125) is governed by the total number of excited state bosons,

$$K_{n_0} \simeq \kappa \sum_k \langle n_k\rangle_{n_0} = \kappa(N - n_0) \tag{130}$$

By writing the equation of motion for $\langle n_0\rangle$ from Eq. (125), using H_{n_0} in the weak trap limit, and Eq. (130) for K_{n_0}, we find

$$\langle \dot{n}_0\rangle = \kappa\left[(N+1)\langle n_0\rangle - \langle (n_0+1)^2\rangle - \zeta(3)\left(\frac{k_B T}{\hbar\Omega}\right)^3 \langle n_0\rangle\right] + \kappa(N+1) \tag{131}$$

Noting that near T_c, $\langle n_0\rangle \ll N$, we may neglect $\langle (n_0+1)^2\rangle$ compared to $N\langle n_0\rangle$, and neglecting the spontaneous emission term $\kappa(N+1)$, Eq. (131) becomes

$$\langle \dot{n}_0\rangle = \kappa\left[N - \zeta(3)\left(\frac{k_B T}{\hbar\Omega}\right)^3\right]\langle n_0\rangle \tag{132}$$

We now define the critical temperature (in analogy with the laser threshold) such that cooling (gain) equals heating (loss) and $\langle \dot{n}_0\rangle = 0$ at $T = T_c$; this yields

$$T_c = \left(\frac{\hbar\Omega}{k_B}\right)\left[\frac{N}{\zeta(3)}\right]^{1/3} \tag{133}$$

Thus, by defining the critical temperature as that temperature at which the rate of removal of atoms from the ground state equals the rate of addition, we arrive at the usual definition for the critical temperature, even for mesoscopic systems.

26.6 EXOTIC MASERS AND LASERS

Lasing Without Inversion

For a long time, it was considered that population inversion was necessary for laser action to take place. Recently, it has been shown both theoretically[128–130] and experimentally[131–134] that it is also possible to achieve lasing without inversion (LWI). In LWI, the essential idea is the cancellation of absorption by atomic coherence and interference.

Consider a system of three-level atoms interacting with a laser field in a cavity. The simple model we will focus on is that of Fig. 11. The atoms have one upper level $|a\rangle$ and two lower levels $|b\rangle$ and $|c\rangle$, with energies $\hbar\omega_a$, $\hbar\omega_b$, and $\hbar\omega_c$, respectively. The cavity field of frequency ν can be detuned from the atomic transition, as shown in the figure. The transitions $|a\rangle \rightarrow |b\rangle$ and $|a\rangle \rightarrow |c\rangle$ are now induced by one classical light field of frequency ν. The transition $|b\rangle \rightarrow |c\rangle$ is dipole forbidden. The atoms are pumped at a rate r_a in a coherent superposition of states

$$\rho(t_i) = \rho_{aa}^{(0)}|a\rangle\langle a| + \rho_{bb}^{(0)}|b\rangle\langle b| + \rho_{cc}^{(0)}|c\rangle\langle c| + \rho_{bc}^{(0)}|b\rangle\langle c| + \rho_{cb}^{(0)}|c\rangle\langle b|. \tag{134}$$

Here $\rho_{\alpha\alpha}^{(0)}$ ($\alpha = a, b, c$) are the level populations and $\rho_{\alpha\alpha'}^{(0)}$ ($\alpha \neq \alpha'$) are the atomic coherences. We give a simple argument to show how cancellation of absorption can lead to lasing without inversion in this scheme.

As the levels $|b\rangle$ and $|c\rangle$ are independent, the probability of emission is given by

$$\begin{aligned} P_{\text{emission}} &= P_b + P_c \\ &= (|\kappa_{a\rightarrow b}|^2\mathscr{E}^2 + |\kappa_{a\rightarrow c}|^2\mathscr{E}^2)\rho_{aa}^{(0)} \end{aligned} \tag{135}$$

where $\kappa_{a\rightarrow b}$ and $\kappa_{a\rightarrow c}$ are constants which depend on the matrix element between the relevant levels and the coupling of the atom with the field. On the other hand, the absorption probability is given by

$$\begin{aligned} P_{\text{absorption}} &= \kappa|c_b + c_c|^2\mathscr{E}^2 \\ &= \kappa(\rho_{bb}^{(0)} + \rho_{cc}^{(0)} + \rho_{bc}^{(0)} + \rho_{cb}^{(0)})\mathscr{E}^2 \end{aligned} \tag{136}$$

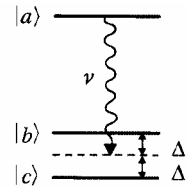

FIGURE 11 Level diagram for lasing without inversion.

where c_a and c_b are the probability amplitudes for the states $|b\rangle$ and $|c\rangle$. Therefore, the rate of growth of the laser field amplitude, under appropriate conditions, becomes

$$\dot{\mathscr{E}} = \frac{\mathscr{A}}{2}(\rho_{aa}^{(0)} - \rho_{bb}^{(0)} - \rho_{cc}^{(0)} - \rho_{bc}^{(0)} - \rho_{cb}^{(0)})\mathscr{E} \tag{137}$$

Here $\mathscr{A}$ is a constant. Thus, if the terms $\rho_{bc}^{(0)}$ and $\rho_{cb}^{(0)}$ cancel $\rho_{bb}^{(0)}$ and $\rho_{cc}^{(0)}$, we have

$$\dot{\mathscr{E}} = \frac{\mathscr{A}}{2}\rho_{aa}^{(0)}\mathscr{E} \tag{138}$$

and we can have lasing even if only a small fraction of atoms is in the excited state $|a\rangle$, that is, even if $\rho_{aa} < (\rho_{bb} + \rho_{cc})$.

Physically, the lack of absorption in the three-level system considered here is a manifestation of quantum coherence phenomena. When an atom makes a transition from the upper level to the two lower levels, the total transition probability is the sum of $|a\rangle \rightarrow |b\rangle$ and $|a\rangle \rightarrow |c\rangle$ probabilities. However, the transition probability from the two lower levels to the single upper level is obtained by squaring the sum of the two probability amplitudes. When there is coherence between the two lower levels, this can lead to interference terms yielding a null in the transition probability corresponding to photon absorption.

Correlated (Spontaneous) Emission Laser

As discussed earlier, the fundamental source of noise in a laser is spontaneous emission. A simple pictorial model for the origin of the laser linewidth envisions it as being due to the random phase diffusion process arising from the addition of spontaneously emitted photons with random phases to the laser field. Here we show that the quantum noise leading to the laser linewidth can be suppressed below the standard Schawlow-Townes limit by preparing the atomic systems in a coherent superposition of states as in the Hanle-effect and quantum-beat experiments. In such coherently prepared atoms, the spontaneous emission is said to be *correlated.* Lasers operating via such a phase-coherent atomic ensemble are known as *correlated emission lasers* (CELs).[135]

An interesting aspect of the CEL is that it is possible to eliminate the spontaneous emission quantum noise in the relative linewidths by correlating the two spontaneous emission noise events.

A number of schemes exist in which quantum noise quenching below the standard limit can be achieved. In two-mode schemes a correlation between the spontaneous emission events in two different modes of the radiation field is established via atomic coherence so that the relative phase between them does not diffuse or fluctuate. In a Hanle laser[136] and a quantum-beat laser[137] this is achieved by pumping the atoms coherently such that every spontaneously emitting atom contributes equally to the two modes of the radiation, leading to a reduction and even vanishing of the noise in the phase difference. In a two-photon CEL, a cascade transition involving three-level atoms is coupled to only one mode of the radiation field.[138] A well-defined coherence between the upper and lower levels $|a\rangle$ and $|c\rangle$ leads to a correlation between the light emitted by an $|a\rangle \rightarrow |b\rangle$ and a subsequent $|b\rangle \rightarrow |c\rangle$ transition.

The quantum theory of quantum-beat or Hanle-effect lasers may be conveniently cast in terms of the equation of motion for the density matrix describing the laser radiation field $\rho(a_1, a_1^\dagger; a_2, a_2^\dagger)$; that is,

$$\dot{\rho} = \sum_{ij} \mathscr{L}_{ij}\rho \tag{139}$$

where the linear gain and cross-coupling Liouville operators are given by

$$\mathcal{L}_{ii}\rho = -\tfrac{1}{2}[\alpha_{ii}\rho a_i a_i^\dagger + \alpha_{ii}^* a_i a_i^\dagger \rho - (\alpha_{ii} + \alpha_{ii}^*) a_i^\dagger \rho a_i] \tag{140}$$

$$\mathcal{L}_{12}\rho = -\tfrac{1}{2}[\alpha_{12}\rho a_2 a_1^\dagger + \alpha_{21}^* a_2 a_1^\dagger \rho - (\alpha_{12} + \alpha_{21}^*) a_1^\dagger \rho a_2] e^{i\Phi} \tag{141}$$

$$\mathcal{L}_{21}\rho = -\tfrac{1}{2}[\alpha_{21}\rho a_1 a_2^\dagger + \alpha_i^* a_1 a_2^\dagger \rho - (\alpha_i + \alpha_i^*) a_2^\dagger \rho a_1] e^{i\Phi} \tag{142}$$

Here α_{ij} are constants that depend on the parameters of the gain medium such as detunings, Rabi frequency of the driving field, and so on. When the coherent mixing of levels $|a\rangle$ and $|b\rangle$ is produced via a microwave signal having frequency ω_0, the phase angle ϕ is given by $\Phi(t) = (\nu_1 - \nu_2 - \omega_0)t - \phi$, where ϕ is the (microwave determined) atomic-phase difference $\phi_a - \phi_b$. In the case of polarization-induced coherent mixing, the phase angle is $\Phi(t) = (\nu_1 - \nu_2)t - \phi$, where ϕ is again the relative phase between levels $|a\rangle$ and $|b\rangle$ but determined this time by the state of elliptic polarization of the pump light used to excite the atoms.

The Liouville equation (31) for the reduced-density operator for the field can be converted into an equivalent Fokker-Planck equation by introducing coherent state representation for a_1 and a_2 and the P representation $P(\alpha, \alpha^*)$ for ρ. If we define the coherent states as

$$a_i|\alpha_1, \alpha_2|\rangle = \alpha_i|\alpha_1, \alpha_2|\rangle; \; i = 1, 2 \tag{143}$$

where α is an arbitrary complex number, and we represent α_i as

$$\alpha_i = \rho_i \exp(i\theta_i); \; i = 1, 2 \tag{144}$$

then the Fokker-Planck equation in terms of ρ_i, θ_i will contain a term which describes diffusion of relative phase $\theta = \theta_1 - \theta_2$ as

$$\dot{P} = \frac{\partial^2}{\partial\theta^2}[\mathcal{D}(\theta)P] \tag{145}$$

with

$$\mathcal{D} = \frac{1}{16}\left\{\left(\frac{\alpha_{11}}{\rho_1^2} + \frac{\alpha_{22}}{\rho_2^2}\right) - \frac{(\alpha_{12} + \alpha_{21}^*)e^{-i\psi}}{\rho_1\rho_2}\right\} \tag{146}$$

and $\psi = \Phi + \theta_1 - \theta_2$ with θ_i being the phase of the ith field. The diffusion constant $\mathcal{D}$ for the relative phase vanish for $\psi = 0$, $\rho_1 = \rho_2$, and $\alpha_{11} = \alpha_{22} = \alpha_{12} = \alpha_{21}^*$, thus leading to CEL action.

Free-Electron Laser

A coherent emission of radiation in a free-electron laser (FEL) is due to the bunching of a relativistic electron beam propagating along a periodic magnetic structure. The electrons experience a Lorentz force and thus follow oscillating orbits and radiate. This spontaneous emission coupled with the periodic magnetic structure give rise to a periodic ponderomotive potential. The electrons bunch together and radiate coherently.[139] The spontaneous emission pattern of a relativistic electron of energy $E = \gamma mc^2$ with $\gamma \gg 1$ is mostly in the forward direction. For a magnetic wiggler of period λ_W, the spectrum in the forward direction is symmetric about the wavelength $\lambda_s \cong \lambda_W/2\gamma^2$. Thus, a change of the periodicity of the wiggler λ_W can be used to tune the coherent light emitted by the FEL over a very wide range.

Many interesting features of FEL can be understood classically. However, the quantum-statistical properties of radiation emitted by FEL exhibit many interesting features such as squeezing and subpoissonian statistics.[140–142]

Here we describe a free-electron amplifier in the small-signal noncollective regime. Such an FEL can be described by the one-electron nonrelativistic Bambini-Renieri hamiltonian which refers to a moving frame, where the laser and the wiggler frequencies coincide with $\omega = ck/2$.[143] In this frame, resonance occurs when the electron is at rest; therefore, the electron can be treated nonrelativistically. The hamiltonian is given by

$$\mathcal{H} = \frac{p^2}{2m} + \hbar\omega A^\dagger A + i\hbar g(A - A^\dagger) \tag{147}$$

with $A = a \exp(ikz)$. Here a is the annihilation operator of the laser field, p and z are the electron's momentum and coordinate with $[z, p] = i\hbar$, $[A, A^\dagger] = 1$, $[p, A] = \hbar kA$, m is the effective mass of the electron, and

$$g = \left(\frac{e^2 B}{mk}\right)\left(\frac{2}{V\varepsilon_0\hbar\omega}\right)^{1/2} \tag{148}$$

with V the quantization volume and B the magnetic-field strength of the wiggler field in the moving frame. In Eq. (147) we have already taken the classical limit of the wiggler field. By transforming to the interaction picture we obtain

$$\mathcal{H}_I = ig\hbar\left\{\exp\left[-\frac{it(\hbar k^2 + 2kp)}{2m}\right]A^\dagger - Hc\right\} \tag{149}$$

We now consider an initial state made up by an electron with momentum p and the field vacuum, i.e., $|\text{in}\rangle = |\bar{p}, 0\rangle$

$$p|\bar{p}, 0\rangle = \bar{p}|\bar{p}, 0\rangle \tag{150}$$

$$A|\bar{p}, 0\rangle = 0 \tag{151}$$

$$A^\dagger|\bar{p}, 0\rangle = |\bar{p} - \hbar k, 1\rangle \tag{152}$$

The final-state expectation value of any operator $O(A, A^\dagger)$ is then

$$\langle\text{out}|O|\text{out}\rangle = \langle\bar{p}, 0|S^\dagger(T)OS(T)|\bar{p}, 0\rangle \tag{153}$$

where

$$S(T) = T\exp\left[-\frac{i}{\hbar}\int_{-T/2}^{T/2} dt\, H_I(t)\right] \tag{154}$$

is the time-evolution operator for the electron-photon state.

The evaluation of Eq. (153) is straightforward in the small-signal limit along the lines given in Ref. 141, and we obtain

$$(\Delta A_1)^2 = \frac{1}{4} - \frac{\hbar k^2}{2m} j\frac{\partial j}{\partial\beta} \tag{155a}$$

$$(\Delta A_1)^2 = \frac{1}{4} + \frac{\hbar k^2}{2m} j\frac{\partial j}{\partial\beta} \tag{155b}$$

$$(\Delta A_1)(\Delta A_2) = \tfrac{1}{4} \tag{155c}$$

$$\Delta n^2 - \langle n\rangle = -\frac{2\hbar k^2}{m} j^3\frac{\partial j}{\partial\beta} \tag{155d}$$

where

$$j = \left(\frac{2g}{\beta}\right) \sin\left(\frac{\beta T}{2}\right) \tag{156}$$

$$\beta = \frac{k\bar{p}}{m} \tag{157}$$

In our notation, the gain of the free-electron laser is proportional to $-j\partial j/\partial\beta$. Hence, Eqs. (155*a*) and (155*b*) show that, depending on the sign of the gain, either A_1 or A_2 is squeezed while, because of Eq. (155*c*), minimum uncertainty is maintained. Here, we have defined squeezing with respect to the operator A instead of the annihilation operator a of the radiation field. This must be so because we employ electron-photon states, and the annihilation of a photon always comes up to increasing the momentum of the electron by $\hbar k$. Finally, Eq. (155*d*) shows that we have subpoissonian, poissonian, or superpoissonian statistics if the electron momentum is below resonance ($\beta < 0$), at resonance ($\beta = 0$), or below resonance ($\beta > 0$), respectively.

Exploiting the Quantized Center-of-Mass Motion of Atoms

In the treatment of the interaction of a two-level atom with photons of a single, dynamically privileged mode by the Jaynes-Cummings model, as discussed in Sec. 26.4, the center-of-mass motion of the atom is regarded as classical. This is a well-justified approximation, since the atom's kinetic energy of typically ~10^{-2} eV is many orders of magnitude larger than the interaction energy of typically ~10^{-11} eV if the atom belongs to a thermal beam. For ultracold atoms, however, matters can be quite different, and the quantum properties of the center-of-mass motion must be taken into account.

Early studies showed that very slow atoms can be reflected at the entry port of a resonator[144] or trapped inside.[145] The reflection probability is considerable even if the photon lifetime is not short as compared with the relatively long interaction time.[146]

Whereas Refs. 144 to 146 deal mainly with the mechanical effects on the center-of-mass motion of the atom, the modifications in the maser action are addressed in Refs. 147 to 150. For thermal atoms, the emission probability displays the usual Rabi oscillations (see Sec. 26.4) as a function of the interaction *time.* For very slow atoms, however, the emission probability is a function of the interaction *length* and exhibits resonances such as the ones observed in the intensity transmitted by a Fabry-Perot resonator. The resonances occur when the resonator length is an integer multiple of half the de Broglie wavelength of the atom inside the cavity.

A detailed calculation[147] shows that the emission probability is 50 percent at a resonance, irrespective of the number of photons that are present initially. Owing to this unusual emission probability, a beam of ultracold atoms can produce unusual photon distributions, such as a shifted thermal distribution. In the trilogy (Refs. 148 to 150) this *microwave amplification by z-motion-induced emission of radiation* (mazer) is studied in great detail.

In order to see the mazer resonances for atoms with a certain velocity spread, the interaction length has to be small. Therefore, micromaser cavities of the usual cylindrical shape, for which the smallest cavity length is given by half the wavelength of the microwaves, cannot be used for this purpose. But cavities of the reentrant type (familiar as components of klystrons) allow for an interaction length that is much smaller than the wavelength. With such a device, an experiment with realistic parameters seems possible.[149] As a potential application, we mention that a working mazer could be used as a velocity filter for atoms.[151]

26.7 ACKNOWLEDGMENTS

The authors gratefully acknowledge the generous support of the Office of Naval Research over the many years spent on completing the works reviewed here. It is also a pleasure to

acknowledge the Max-Planck-Institute for Quantum Optics (Garching, Germany) for providing the excellent working atmosphere and the intellectual stimulus for the most interesting works in this field.

26.8 REFERENCES

1. J. R. Klauder and E. C. G. Sudarshan, *Fundamentals of Quantum Optics* (W. A. Benjamin, New York, 1970).
2. R. Loudon, *The Quantum Theory of Light* (Oxford University Press, New York, 1973).
3. W. H. Louisell, *Quantum Statistical Properties of Radiation* (John Wiley, New York, 1973).
4. H. M. Nussenzveig, *Introduction to Quantum Optics* (Gordon and Breach, New York, 1974).
5. M. Sargent III, M. O. Scully, and W. E. Lamb, Jr., *Laser Physics* (Addison-Wesley, Reading, Mass., 1974).
6. L. Allen and J. H. Eberly, *Optical Resonance and Two-Level Atoms* (John Wiley, New York, 1975).
7. H. Haken, *Light*, Vols. I and II (North-Holland, Amsterdam, 1981).
8. P. L. Knight and L. Allen, *Concepts of Quantum Optics* (Pergamon Press, Oxford, 1983).
9. P. Meystre and M. Sargent III, *Elements of Quantum Optics* (Springer-Verlag, Berlin, 1990).
10. C. W. Gardiner, *Quantum Noise* (Springer-Verlag, Berlin, 1991).
11. C. Cohen-Tannoudji, J. Dupont-Roc, and G. Grynberg, *Atom-Photon Interactions* (John Wiley, New York, 1992).
12. H. Carmichael, *An Open Systems Approach to Quantum Optics* (Springer-Verlag, Berlin, 1993).
13. W. Vogel and D.-G. Welsch, *Lectures on Quantum Optics* (Akademie Verlag, Berlin, 1994).
14. J. Peřina, Z. Hradil, and B. Jurčo, *Quantum Optics and Fundamentals of Physics* (Kluwer, Dordrecht, Netherlands, 1994).
15. D. F. Walls and G. J. Milburn, *Quantum Optics* (Springer-Verlag, Berlin, 1994).
16. L. Mandel and E. Wolf, *Optical Coherence and Quantum Optics* (Cambridge University Press, London, 1995).
17. E. R. Pike and S. Sarkar, *Quantum Theory of Radiation* (Cambridge University Press, London, 1995).
18. M. O. Scully and M S. Zubairy, *Quantum Optics* (Cambridge University Press, London, 1997).
19. M. Planck, *Verh. Phys. Ges.* **2**:202, 237 (1900).
20. W. Wien, *Ann. Physik* **58**:662 (1896).
21. Lord Rayleigh, *Phil. Mag.* **49**:539 (1900).
22. J. H. Jeans, *Phil. Mag.* **10**:91 (1905).
23. A. H. Compton, *Phys. Rev.* **21**:483 (1923).
24. A. Einstein, *Ann. Physik* **17**:132 (1905).
25. W. Pauli, "Einstein's Contributions to Quantum Theory," in *Albert Einstein: Philosopher-Scientist,* P. A. Schilpp (ed.) (Library of Living Philosophers, Evanston, Ill., 1949).
26. L. de Broglie, *C. R. Acad. Sci. Paris* **177**:517 (1923).
27. L. de Broglie, *Thèse* (Masson et Cie., Paris, 1924).
28. E. Schrödinger, *Ann. Physik* **79**:361 (1926).
29. G. I. Taylor, *Proc. Camb. Phil. Soc.* **15**:114 (1909).
30. P. A. M. Dirac, *The Principles of Quantum Mechanics,* 4th ed. (Oxford University Press, Oxford, 1958).
31. R. J. Glauber, *Am. J. Phys.* **63**:12 (1995).
32. A. Einstein, *Phys. Z.* **10**:185 (1909).
33. N. Bohr, *Phil. Mag.* **26**:1, 476, 857 (1913).
34. A. Einstein, *Phys. Z.* **18**:121 (1917).

35. A. Einstein, *Ann. Physik* **17**:549 (1905)
36. N. Bohr, H. A. Kramers, and J. C. Slater, *Phil. Mag.* **47**:785 (1924).
37. W. Bothe and H. Geiger, *Z. Phys.* **26**:44 (1924).
38. S. N. Bose, *Z. Phys.* **26**:178 (1924).
39. S. N. Bose, *Z. Phys.* **27**:384 (1924).
40. A. Einstein, "Quantentheorie des einatomigen Gases," in *Sitzungsber. Preuss. Akad. Wiss., Phys.-math. Kl.,* 1924, p. 261.
41. A. Einstein, "Quantentheorie des einatomigen Gases. 2. Abhandlung," in *Sitzungsber. Preuss. Akad. Wiss., Phys.-math. Kl.,* 1925, p. 3.
42. A. Einstein, "Quantentheorie des idealen Gases," in *Sitzungsber. Preuss. Akad. Wiss., Phys.-math. Kl.,* 1925, p. 18.
43. P. A. M. Dirac, *Proc. Roy. Soc. London* **A114**:710 (1927).
44. J. Schwinger (ed.), *Quantum Electrodynamics* (Dover, New York, 1958).
45. E. Fermi, *Rend. Lincei* **10**:72 (1929).
46. R. J. Glauber, *Phys. Rev.* **130**:2529 (1963).
47. R. J. Glauber, *Phys. Rev.* **131**:2766 (1963).
48. R. J. Glauber, *Phys. Rev. Lett.* **10**:84 (1963).
49. V. F. Weisskopf and E. P. Wigner, *Z. Phys.* **63**:47 (1930).
50. V. F. Weisskopf, *Phys. Rev.* **56**:72 (1939).
51. W. E. Lamb, Jr., and R. C. Retherford, *Phys. Rev.* **72**:241 (1947).
52. J. Schwinger, *Phys. Rev.* **73**:416 (1948).
53. S. Pasternack, *Phys. Rev.* **54**:1113 (1938).
54. S. Millman and P. Kusch, *Phys. Rev.* **57**:438 (1940).
55. H. Hanbury-Brown and R. Q. Twiss, *Phil. Mag.* **45**:663 (1954).
56. H. Hanbury-Brown and R. Q. Twiss, *Nature* (London) **178**:1046 (1956).
57. H. Hanbury-Brown and R. Q. Twiss, *Proc. Roy. Soc.* **A242**:300 (1957).
58. R. G. Newton, *Scattering Theory of Waves and Particles* (McGraw-Hill, New York, 1966).
59. C. K. Hong, Z. Y. Ou, and L. Mandel, *Phys. Rev. Lett.* **59**:2044 (1987).
60. P. G. Kwiat, K. Mattle, H. Weinfurter, and A. Zeilinger, *Phys. Rev. Lett.* **75**:4337 (1995).
61. P. G. Kwiat, E. Waks, A. G. White, I. Appelbaum, and P. H. Eberhard, *Phys. Rev. A* **60**:773 (1999).
62. D. Bouwmeester, J.-W. Pan, K. Mattle, M. Eibl, H. Weinfurter, and A. Zeilinger, *Nature* (*London*) **390**:575 (1997).
63. D. Boschi, S. Branca, F. De Martini, L. Hardy, and S. Popescu, *Phys. Rev. Lett.* **80**:1121 (1998)
64. C. H. Bennett, G. Brassard, C. Crepeau, R. Josza, A. Peres, and W. Wootters, *Phys. Rev. Lett.* **70**:1895 (1993).
65. K. Mattle, H. Weinfurter, P. G. Kwiat, and A. Zeilinger, *Phys. Rev. Lett.* **76**:4656 (1996).
66. C. H. Bennett and S. J. Wiesner, *Phys. Rev. Lett.* **69**:2881 (1992).
67. M. Sargent, M. O. Scully, and W. E. Lamb, *Laser Physics* (Addison-Wesley, Reading, Mass., 1974).
68. M. O. Scully and M. S. Zubairy, *Quantum Optics* (Cambridge University Press, Cambridge, 1997).
69. M. Lax, "Phase Noise in a Homogeneously Broadened Maser," in *Physics of Quantum Electronics,* P. L. Kelley, B. Lax, and P. E. Tannenwald (eds.) (McGraw-Hill, New York, 1966).
70. M. Lax, *Phys. Rev.* **145**:110 (1966).
71. M. Lax, "Fluctuations and Coherence Phenomena in Classical and Quantum Physics," in *1966 Brandeis Summer Lecture Series on Statistical Physics,* Vol. 2, M. Chretien, E. P. Gross, and S. Dreser (eds.) (Gordon and Breach, New York, 1968; Mir, Moscow, 1975).
72. W. H. Louisell, *Quantum Statistical Properties of Radiation* (John Wiley, New York, 1973).
73. H. Haken, "Laser Theory," in *Encyclopedia of Physics,* Vol. 35/c, S. Flügge (ed.) (Springer, Berlin, 1970).

74. H. Risken, *The Fokker Planck Equation* (Springer, Heidelberg, 1984).
75. M. Lax, "The Theory of Laser Noise," keynote address, 1990 Conference on Laser Science and Optics Applications, *Proceedings SPIE* **1376**:2 (1991).
76. E. T. Jaynes and F. W. Cummings, *Proc. IEEE* **51**:89 (1963).
77. B. W. Shore and P. L. Knight, *J. Mod. Opt.* **40**:1195 (1993).
78. J. P. Gordon, H. J. Zeiger, and C. H. Townes, *Phys. Rev.* **95**:282L (1955).
79. J. P. Gordon, H. J. Zeiger, and C. H. Townes, *Phys. Rev.* **99**:1264 (1955).
80. A. L. Schawlow and C. H. Townes, *Phys. Rev. A* **112**:1940 (1958).
81. N. G. Basov and A. M. Prokhorov, *Dokl. Ak. Nauk* **101**:47 (1955).
82. T. H. Maiman, *Nature* (London) **187**:493 (1960).
83. A. Javan, W. R. Bennett, and D. R. Herriott, *Phys. Rev. Lett.* **6**:106 (1961).
84. W. E. Lamb, *Phys. Rev.* **134**:A1429 (1964).
85. For recent reviews, see, e.g., B.-G. Englert, M. Löffler, O. Benson, B. Varcoe, M. Weidinger, and H. Walther, *Fortschr. Phys.* **46**:897 (1998); G. Raithel, C. Wagner, H. Walther, L. M. Narducci, and M. O. Scully, in *Advances in Molecular and Optical Physics,* P. Berman (ed.) (Academic, New York, 1994), Suppl. 2.
86. D. Meschede, H. Walther, and G. Müller, *Phys. Rev. Lett.* **54**:551 (1985).
87. P. Filipowicz, J. Javanainen, and P. Meystre, *Phys. Rev. A* **34**:3077 (1986).
88. M. Lax, *Phys. Rev.* **129**:2342 (1963).
89. M. Lax and M. Zwanziger, *Phys. Rev. A* **7**:750 (1973).
90. M. Lax, *Phys. Rev.* **172**:350 (1968).
91. N. Lu, *Phys. Rev. A* **47**:4322 (1993).
92. U. Herzog, and J. Bergou *Phys. Rev. A* **62** (2000). In press.
93. M. Lax, *Phys. Rev.* **160**:290 (1967).
94. R. D. Hempstead and M. Lax, *Phys. Rev.* **161**:350 (1967).
95. H. Risken and H. D. Vollmer, *Z. Physik* **191**:301 (1967).
96. M. Kac, in *1966 Brandeis Summer Lecture Series on Statistical Physics,* Vol. 1, M. Chretien, E. P. Gross, and S. Dreser (eds.) (Gordon and Breach, New York, 1968).
97. M. O. Scully, H. Walther, G. S. Agarwal, T. Quang, and W. Schleich, *Phys. Rev. A* **44**:5992 (1991).
98. N. Lu, *Phys. Rev. Lett.* **70**:912 (1993); N. Lu, *Phys. Rev. A* **47**:1347 (1993); T. Quang, G. S. Agarwal, J. Bergou, M. O. Scully, H. Walther, K. Vogel, and W. P. Schleich, *Phys. Rev. A* **48**:803 (1993); K. Vogel, W. P. Schleich, M. O. Scully, and H. Walther, *Phys. Rev. A* **48**:813 (1993); R. McGowan and W. Schieve, *Phys. Rev. A* **55**:3813 (1997).
99. S. Qamar and M. S. Zubairy, *Phys. Rev. A* **44**:7804 (1991).
100. P. Filipowicz, J. Javanainen, and P. Meystre, *J. Opt. Soc. Am. B* **3**:154 (1986).
101. J. J. Slosser, P. Meystre, and S. L. Braunstein, *Phys. Rev. Lett.* **63**:934 (1989).
102. J. Bergou, L. Davidovich, M. Orszag, C. Benkert, M. Hillery, and M. O. Scully, *Phys. Rev. A* **40**:7121 (1989); J. D. Cresser, *Phys. Rev. A* **46**:5913 (1992); U. Herzog, *Phys. Rev. A* **52**:602 (1995).
103. H.-J. Briegel, B.-G. Englert, N. Sterpi, and H. Walther, *Phys. Rev. A* **49**:2962 (1994); U. Herzog, *Phys. Rev. A* **50**:783 (1994); J. D. Cresser and S. M. Pickless, *Phys. Rev. A* **50**:R925 (1994); U. Herzog, *Appl. Phys. B* **60**:S21 (1995).
104. H.-J. Briegel, B.-G. Englert, Ch. Ginzel, and A. Schenzle, *Phys. Rev. A* **49**:5019 (1994).
105. H.-J. Briegel, B.-G. Englert, *Phys. Rev. A* **52**:2361 (1995); J. Bergou, *Quantum and Semiclass. Optics* **7**:327 (1995); U. Herzog and J. Bergou, *Phys. Rev. A* **54**:5334 (1996); ibid. **55**:1385 (1997).
106. M. Weidinger, B. T. H. Varcoe, R. Heerlein, and H. Walther, *Phys. Rev. Lett.* **82**:3795 (1999).
107. H. Walther, *Phys. Rep.* **219**:263 (1992).
108. M. O. Scully, G. Süssmann, and C. Benkert, *Phys. Rev. Lett.* **60**:1014 (1988).
109. M. O. Scully, M. S. Zubairy, and K. Wódkiewicz, *Opt. Commun.* **65**:440 (1988).

110. H. E. Stanley, *Introduction to Phase Transitions and Critical Phenomema,* (Oxford University Press, Oxford, 1971).
111. V. DeGiorgio and M. O. Scully, *Phys. Rev. A* **2**:1170 (1970).
112. M. Anderson, J. Ensher, M. Matthews, C. Wieman, and E. Cornell, *Science* **269**:198 (1995).
113. C. Bradley, C. Sackett, J. Tollett, and R. Hulet, *Phys. Rev. Lett.* **75**:1687 (1995).
114. K. Davis, M. Mewes, M. Andrews, N. van Druten, D. Durfee, D. Kurn, and W. Ketterle, *Phys. Rev. Lett.* **75**:3969 (1995).
115. M. H. W. Chen, K. I. Blum, S. Q. Murphy, G. K. S. Wong, and J. D. Reppy, *Phys. Rev. Lett.* **61**:1950 (1998).
116. K. Huang, *Statistical Mechanics* (John Wiley, New York, 1987).
117. R. Arnowitt and M. Girardeau, *Phys. Rev.* **113**:745 (1959).
118. G. Baym and C. Pethick, *Phys. Rev. Lett.* **76**:6 (1996).
119. H. Politzer, *Phys. Rev. A* **54**:5048 (1996).
120. S. Grossmann and M. Holthaus, *Phys. Rev. E* **54**:3495 (1996).
121. C. Herzog and M. Olshanii, *Phys. Rev. A* **55**:3254 (1997).
122. P. Navez, D. Bitouk, M. Gajda, Z. Idziaszek, and K. Rzążewski, *Phys. Rev. Lett.* **79**:1789 (1997).
123. M. Wilkens and C. Weiss, *J. Mod. Opt.* **44**:1801 (1997).
124. S. Grossmann and M. Holthaus, *Phys. Rev. Lett.* **79**:3557 (1997).
125. H. Woolf (ed.), *Some Strangeness in the Proportion: A Centennial Symposium to Celebrate the Achievements of Albert Einstein* (Addison-Wesley, Reading, Mass., 1980), p. 524.
126. J. Goldstein, M. O. Scully, and P. Lee, *Phys. Lett.* **A35**:317 (1971).
127. M. O. Scully, *Phys. Rev. Lett.* **82**:3927 (1999).
128. O. Kocharovskaya and Ya I. Khanin, *JETP Lett.* **48**:630 (1988).
129. S. E. Harris, *Phys. Rev. Lett.* **62**:1033 (1989).
130. M. O. Scully, S.-Y. Zhu, and A. Gavrieleides, *Phys. Rev. Lett.* **62**:2813 (1989).
131. A. Nottelmann, C. Peters, and W. Lange, *Phys. Rev. Lett.* **70**:1783 (1993).
132. E. S. Fry, X. Li, D. Nikonov, G. G. Padmabandu, M. O. Scully, A. V. Smith, F. K. Tittel, C. Wang, S. R. Wilkinson, and S.-Y. Zhu, *Phys. Rev. Lett.* **70**:3235 (1993).
133. W. E. van der Veer, R. J. J. van Diest, A. Dönszelmann, and H. B. van Linden van den Heuvell, *Phys. Rev. Lett.* **70**:3243 (1993).
134. A. S. Zibrov, M. D. Lukin, D. E. Nikonov, L. W. Hollberg, M. O. Scully, V. L. Velichansky, and H. G. Robinson, *Phys. Rev. Lett.* **75**:1499 (1995).
135. M. O. Scully, *Phys. Rev. Lett.* **55**:2802 (1985).
136. J. Bergou, M. Orszag, and M. O. Scully, *Phys. Rev. A* **38**:768 (1988).
137. M. O. Scully and M. S. Zubairy, *Phys. Rev. A* **35**:752 (1987).
138. M. O. Scully, K. Wodkiewicz, M. S. Zubairy, J. Bergou, N. Lu, and J. Meyer ter Vehn, *Phys. Rev. Lett.* **60**:1832 (1988).
139. J. M. J. Madey, *J. Appl. Phys.* **42**:1906 (1971).
140. W. Becker, M. O. Scully, and M. S. Zubairy, *Phys. Rev. Lett.* **48**:475 (1985).
141. W. Becker and M. S. Zubairy, *Phys. Rev. A* **25**:2200 (1982).
142. R. Bonifacio, *Opt. Commun.* **32**:440 (1980).
143. A. Bambini and A. Renieri, *Opt. Commun.* **29**:244 (1978).
144. B.-G. Englert, J. Schwinger, A. O. Barut, and M. O. Scully, *Europhys. Lett.* **14**:25 (1991).
145. S. Haroche, M. Brune, and J.-M. Raimond, *Europhys. Lett.* **14**:19 (1991).
146. M. Battocletti and B.-G. Englert, *J. Phys. II France* **4**:1939 (1994).
147. M. O. Scully, G. M. Meyer, and H. Walther, *Phys. Rev. Lett.* **76**:4144 (1996).
148. G. M. Meyer, M. O. Scully, and H. Walther, *Phys. Rev. A* **56**:4142 (1997).
149. M. Löffler, G. M. Meyer, M. Schröder, M. O. Scully, and H. Walther, *Phys. Rev. A* **56**:4153 (1997).
150. M. Schröder, K. Vogel, W. P. Schleich, M. O. Scully, and H. Walther, *Phys. Rev. A* **56**:4164 (1997).
151. M. Löffler, G. M. Meyer, and H. Walther, *Europhys. Lett.* **41**:593 (1998).

CHAPTER 27
LASER STABILIZATION

John L. Hall, Matthew S. Taubman, and Jun Ye
JILA
University of Colorado
and National Institute of Standards and Technology
Boulder, Colorado

27.1 INTRODUCTION AND OVERVIEW

For laser applications in which measurement precision is a key feature, frequency-stabilized lasers are preferred, if not essential. This observation was true in the gas laser days when the 10^{-6} fractional Doppler width set the uncertainty scale. Now we have diode-pumped solid state lasers with fractional tuning range approaching 10^{-2} or more, and laser diode systems with several percent tuning. Such tuning is useful to find the exact frequency for our locking resonance, but then stabilization will be essential. Locking to cavities and atomic references can provide excellent stability, even using a widely tunable laser source. Indeed, laser frequency stability between independent systems has been demonstrated at 5×10^{-14} in 1 s averaging time, and more than a decade better at 300 s. This incredible performance enhancement is possible because of a feedback from measurement of the laser's frequency error from our setpoint, this signal being fed into a filter/amplifier system and finally to an actuator on the laser itself which changes its frequency in response. While such feedback in response to performance may be the most important principle in evolution, in machines and lasers feedback enables the design of lighter, less costly systems. The accuracy is obtained, not by great bulk and stiffness, but rather by error correction, comparing the actual output against the ideal. This continuous correction will also detect and suppress the system's nonlinearity and noise. The performance limitation ultimately is set by imprecision of the measurement, but there is a lot of care required to get into that domain: we must have a very powerful correction effort to completely hide the original sins.

This chapter is our attempt to lead the worker newly interested in frequency control of lasers on a guided tour of stabilized lasers, ideally providing enough insight for recruiting yet another colleague into this wonderful arena. As nonlinear optics becomes just part of our everyday tools, the buildup cavities that enhance the nonlinear couplings are taking on a more critical role: This is the reason that we focus on the taming of PZT-based systems. We then cover locking with other transducers, and present some details about their construction and use. We consider the frequency discriminator, which is a key element for these control systems. The chapter concludes with description of the design and performance of several full practical systems.

Copyright 2001 by The McGraw-Hill Companies, Inc. Click Here for Terms of Use.

Quantifying Frequency Stability

In thinking about the stability of our lasers, one may first wonder whether time or frequency domain pictures will be more powerful and instructive. Experience shows that time-domain perturbations of our lasers are usually associated with unwelcome sounds—doors slamming, telephone bells, loud voices. Eventually these time-localized troubles can be eliminated. But what remains is likely the sum of zillions of smaller perturbations—none too conspicuous, but too many in number to attack individually. This perspective leads to a frequency-domain discussion where we can add the Fourier amplitudes caused by the many little sources. Eventually we are led to idealize our case to a continuum of spectrally described perturbations. This physical outlook is one reason we will mainly be specifying our performance measures in the frequency domain.

Another important issue concerns the nifty properties of Mr. Fourier's description: In the frequency domain, cascaded elements are represented by the multiplication of their individual transfer functions. If we had chosen instead the time domain, we would need to work with convolutions, nonlocal in time. Today's result in time is the sum of all previous temporal events that have the proper delay to impact us now. So it seems clear that frequency domain is good for analysis. What about describing the results?

Frequency versus Time: Drift—The Allan Variance Method. At the other end of our laser stabilization project, describing the results, it is convenient to measure and record the frequency as a function of time. We can measure the frequency averaged over a one-second gating time, for example, and stream 100 points to a file. This would be a good way to see the variations around a mean for the 1 s time intervals. This measurement could be repeated using a succession of gate times, 3 s, 10 s, 30 s, 100 s . . . Surely it will be attractive to make this measurement just once and numerically combine the data to simulate the longer gate times. Thinking this way brings us a new freedom; we can process this data to recover more than just the mean and the standard deviation. Of course, we can expect to eventually see some drift, particularly over long times. When we look at the drift and slowly varying laser frequency, one wishes for a method to allow us to focus on the random noise effects that are still visible, even with the extended gate times. This is where the resonance physics is, while the drift is mainly due to technical problems. Dave Allan introduced the use of first differences, which has come to be called the Allan Variance method.[1] If we take the difference between adjacent samples of the measured frequency, we focus on the random processes that are averaged down to small, but not insignificant values within each gate time τ. These first differences (normalized by $1/\sqrt{2}$ to account for random noise in each entry) form a new data set which is first-order insensitive to long-term processes such as drift that dominate the directly recorded data.

Essentially the Allan Variance calculation presents us with a display of the laser's fractional frequency variation, σ_y, as a function of the time over which we are interested. At medium times, say τ of a few seconds, most laser stabilization systems will still be affected by the random measurement noise arising from shot noise and perhaps laser technical noise. At longer times the increased signal averaging implies a smaller residual fluctuation due to random processes. It is easy to show that the dependence of σ_y versus τ can be expected to be $1/\tau^{1/2}$, in the domain controlled by random (white) frequency noise. The Allan deviation also has a great utility in compressing our statement of laser stability: we might say, for example, "the (in-)stability is 2×10^{-12} at 1 s, with the $1/\tau^{1/2}$ dependence which shows that only random noise is important out to a time of 300 s."

Allan Deviation Definition. With a counter linked to a computer, it is easy to gather a file of frequency values f_i measured in successive equal gate time intervals, t_g. Usually there is also some dead time, say t_d, while the counter-to-computer data transfers occur via the GPIB connection. This leads to a sample-to-sample time interval of $t_s = t_g + t_d$. Allan's variance is one-half of the average squared difference between adjacent samples, and the usually quoted quantity, the Allan Deviation, is the square root of this averaged variance,

$$\sigma_y(\tau) = \left[\frac{1}{2(N-1)} \sum_{n=1}^{N-1} (f_{n+1} - f_n)^2 \right]^{1/2} \tag{1}$$

The dependence of σ_y upon the measuring time τ contains information essential for diagnosis of the system performance. These values for several times can be efficiently calculated from the (large) data set of frequencies observed for a fixed minimum gate time by adding together adjacent measurements to represent what would have been measured over a longer gate time. (This procedure neglects the effects of the small dead-time t_d, which are negligible for the white frequency noise $1/\sqrt{\tau}$ of usual interest.) Fewer samples will be available when the synthetic gate time becomes very long, so the uncertainty of this noise measurement increases strongly. Usually one insists on 3 or 4 samples to reduce wild variations, and so the largest synthetic gate time τ_{max} will be the total measurement time/3. For a serious publication we might prefer 5 or 10 such synthetic measurements for the last point on the graph.

The Allan deviation has one curiosity in the presence of a distinct sinusoidal modulation of the laser's frequency: When the gate time is one-half the sinusoid's period, adjacent samples will show the maximum deviation between adjacent measurements, leading to a localized peak in σ_y versus τ. Interestingly, there will be "ghosts" or aliases of this when the gate time/modulation period ratio is ¼, ⅛, and so forth. For longer gate times compared with the modulation, some fractional cycle memories can be expected also. So a clean slope of –½ for a log-log plot of σ_y versus τ makes it clear that there is no big coherent FM process present.

Historically, Allan's Variance has been valuable in locating time scales at which new physical processes must be taken into account. For example, at long times it is usual for a laser or other stable oscillator to reach a level of unchanging σ_y versus τ. We speak of this as a "flicker" floor. It arises from the interplay of two opposite trends, of which the first is the decreasing random noise with increasing τ (decreasing σ_y versus τ). At longer times one sees an increasing σ_y versus τ, due to drifts in the many system parameters (e.g., electronic offsets, temperature), which make our lasers lock at points increasingly offset from the ideal one. If we wait long enough, ever larger changes become likely. So for several octaves of time, the combination of one decreasing and one increasing contribution leads to a flat curve. Eventually significant drift can occur even within one measurement time, and this will be mapped as a domain of rising σ_y increasing as the +1 power of τ.

It is useful to note that the frequency/time connection of the Allan Variance transformation involves very strong data compression and consequently cannot at all be inverted to recover the original data stream in the way we know from the Fourier transform pair. However in the other direction, we can obtain the Allan Deviation from the Phase Spectral Density.[2]

Noise as Spectral Density. As noted earlier, when the number of individual contributions to the noise becomes too large to enumerate, it is convenient to move to a spectral density form of representation. Two natural quantities to use would be the frequency deviations occurring at some rate and the narrow bandwidth within which they occur. To work with a quantity which is positive definite and has additive properties, it is convenient to discuss the squared frequency deviations $<(f^2_N)>$ which occur in a noise bandwidth B around the Fourier frequency f. This Frequency Noise Power Spectral Density, $S_f \equiv <(f^2_N)>/B$, will have dimensions of Hz^2 (deviation^2)/Hz (bandwidth). The summation of these deviations over some finite frequency interval can be done simply by integrating S_f between the limits of interest.

Connecting Allan Deviation and Spectral Density Measures. Sometimes one can estimate that the system has a certain spectrum of frequency variations described by S_f (f), and the question arises of what Allan Deviation this would represent. We prefer to use the Allan presentation only for experimental data. However Ref. 2 indicates the weighted transform from S_f to Allan Variance.

Connecting Linewidth and Spectral Density Measures. A small surprise is that an oscillator's linewidth generally will not be given by the summation of these frequency deviations!

Why? The answer turns on the interesting properties of Frequency Modulated (FM) signals. What counts in distributing power is the Phase Modulation Index, β, which is the ratio of the peak frequency excursion compared with the modulation rate. Speaking of pure tone modulation for a moment, we can write the phase-modulated field as

$$E(t) = \sin(\Omega t + \beta \sin(\omega t))$$
$$= J_0(\beta) \exp(i\Omega t) + \sum_{n=1}^{\infty} J_n(\beta) \exp(i(\Omega + n\omega)t) + \sum_{n=1}^{\infty} J_n(\beta)(-1)^n \exp(i(\Omega - n\omega)t) \quad (2)$$

where Ω is the "carrier" frequency, and $\omega = 2\pi f$ and its harmonics are the modulation frequencies. The frequency offset of one of these "sidebands," say the n-th one, is n times the actual frequency of the process' frequency f. The strength of the variation at such an n-th harmonic decreases rapidly for $n > \beta$ according to the Bessel function $J_n(\beta)$. We can distinguish two limiting cases.

Large excursions, slow frequency rate. This is the usual laboratory regime with solid state or HeNe and other gas lasers. The perturbing process is driven by laboratory vibrations that are mainly at low frequencies. The extent of the frequency modulation they produce depends on our mechanical design, basically how efficient or inefficient an "antenna" have we constructed to pick up unwanted vibrations. Clearly a very stiff, lightweight structure will have its mechanical resonances at quite high frequencies. In such case both laser mirrors will track with nearly the same excursion, leading to small differential motion (i.e., low pickup of the vibrations in the laser's frequency). Heavy articulated structures, particularly mirror mounts with soft springs, have resonances in the low audio band and lead to big FM noise problems. A typical laser construction might use a stiff plate, say 2 inches thick, of Al or honeycomb-connected steel plates. The mirror mounts would be clamped to the plate, and provide a laser beam height of 2 inches above the plate. Neglecting air pressure variations, such a laser will have vibration-induced excursions $(\langle f^2_N \rangle)^{1/2}$ of << 100 kHz. An older concept used low expansion rods of say 15 mm diameter Invar, with heavy Invar plates on the ends, and kinematic but heavy mirror mounts. This system may have a vibration-induced linewidth $(\langle f^2_N \rangle)^{1/2}$ in the MHz range. Only when the "rods" become several inches in diameter is the axial and transverse stiffness adequate to suppress the acceleration induced forces. With such massive laser designs we have frequency excursions of 10's to thousands of kHz, driven by vibrations in a bandwidth B < 1 kiloHertz. In this case $(\langle f^2_N \rangle)^{1/2} >> B$, and the resulting line shape is Gaussian. The linewidth is given by Ref. 3, $\Delta f_{FWHM} = [8 \ln(2) (\langle f^2_N \rangle)]^{1/2} \cong 2.355 (\langle f^2_N \rangle)^{1/2}$.

The broadband fast, small excursion limit. This is the domain in which we can usually end up if we can achieve adequate servo gain to reduce the vibration-induced FM. Since the drive frequency is low, it is often feasible to obtain a gain above 100, particularly if we use a speedy transducer such as an acousto-optic modulator (AOM) or an electro-optic modulator (EOM). In general we will find a noise floor fixed, if by nothing else than the broadband shot noise which forms a minimum noise level in the measurement process. Here we can expect small frequency excursions at a rapid rate, $(\langle f^2_N \rangle)^{1/2} << B$, leading to a small phase modulation index. If we approximate that the Frequency Noise Power Spectral Density $S_f = (\langle f^2_N \rangle)/B$ is flat, with the value S_f Hz^2 (deviation^2)/Hz (bandwidth), then the linewidth in this domain is Lorentzian,[3] with the $\Delta f_{FWHM} = \pi S_f = \pi(\langle f^2_N \rangle)/B$.

This summary of frequency-domain measures is necessarily brief, and the interested reader may find additional discussion useful.[3,4,5] A number of powerful consequences and insights flow from reworking the above discussions in terms of a Phase Noise Power Spectral Density, $S_\phi = S_f/f^2$. The Frequency and Time Division of the National Institute of Standards and Technology (NIST) publishes collections of useful tutorial and overview articles from time to time. The currently available volume[2] covers these topics in more detail. Vendors of rf-domain spectrum analyzers also have useful application notes.[6]

27.2 SERVO PRINCIPLES AND ISSUES[7,8]

Bode Representation of a Servo System

We will describe our systems by transfer functions, output/input, as a function of Fourier frequency ω. We begin purely in the domain of electronics. The amplifier gain is G(ω). The electrical feedback is represented as H(ω). Both will have voltage as their physical domain, but are actually dimensionless in that they are output/input ratios. Considering that we will have to represent phase of these AC signals, both G(ω) and H(ω) will generally be complex. It will be fundamental to view these functions with their dependence on frequency, for both the amplitude and phase response.

Imagine a closed loop system with this amplifier as the forward gain G(ω) between input V_i and output V_o. Some fraction of the output is tapped off and sent back to be compared with the actual input. For more generality we will let H(ω) represent this feedback transfer ratio. The actual input, minus this sampled output will be our input to our servo amplifier $G(\omega)$. After a line of algebra we find the new gain of the closed loop—in the presence of feedback—is

$$A_{cl} = \frac{V_0}{V_i} = \frac{G(\omega)}{1 + G(\omega)H(\omega)} \tag{3}$$

A particularly instructive plot can be made for the product G(ω)H(ω), called the *open loop gain,* which appears in the denominator. In this so-called Bode plot, the gain and phase are separately plotted. Also, from inspection of Eq. (3) we can learn one of the key advantages that feedback brings us: if the feedback factor GH were >>1, the active gain *G* would basically cancel out and we would be left with $A_{cl} \sim 1/H$. We imagine this feedback channel will be passive, formed from nearly ideal nondistorting components. The noise, exact value of the gain, and distortion introduced by it are seen to be nearly unimportant, according to the large magnitude of 1 + GH. Gentle amplifier overload will lead to overtone production, but could alternatively be represented by a decrease of G with signal. Since the output doesn't depend sensitively upon G anyway, we are sure these distortion products and internally-generated noise will be suppressed by the feedback. We can identify the denominator 1 + GH as the noise and distortion reduction factor.

What is the cost of this reduced dependence on the active components G(ω) and their defects? Basically it is that the gain is reduced and we must supply a larger input signal to obtain our desired output. For a music system one can then worry about the distortion in the preamplifier system. However, we want to make quiescent lasers, without the slightest hint of noise. So it is nice that the amplification of internal noise is reduced.

To be concrete, the circuit of Fig. 1 represents a common building block in our servo design, and represents a simple case of feedback. We show it as a current summing input node; the subtraction at the input happens here because the sign of the gain is negative. With the nearly ideal high-gain operational amplifiers now available, G>>1 and we can closely approximate the closed loop gain by $1/H(\omega)$, yielding a flat gain above and a rising gain below some corner frequency $\omega_0 = 1/\tau_0$, with $\tau_0 = R_f C$. Remember $1/H(\omega)$ is the closed-loop gain between V_o and V_i. To find the exact relationship between the signal V_s and V_o, we notice the related voltage divider effect gives $V_i = (1 - H(\omega))V_s$, which leads to

$$\frac{V_o}{V_s} = -\frac{R_f}{R_i}\,\frac{(1 + j\omega/\omega_0)}{j\omega/\omega_0} = -\frac{R_f}{R_i}\,\frac{(1 + j\omega\tau_0)}{j\omega\tau_0} \tag{4}$$

The negative sign arises from the fact that the forward gain is negative. When the corner frequency ω_0 is chosen to be sufficiently high, we may have to consider the bandwidth issue of the OpAmp: G(ω) could start to roll off and no longer satisfy the approximation of G>>1. A

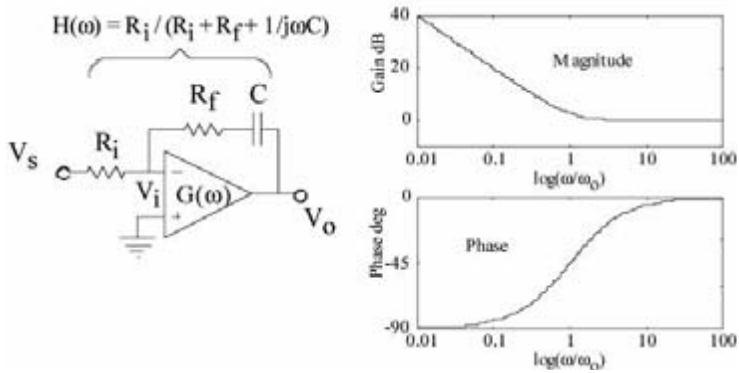

FIGURE 1 Phase and amplitude response of a Proportional-Integral (PI) Amplifier Circuit. The PI function is implemented using an inverting OpAmp.

more complex network is needed to compensate for the gain roll-off, and that is exactly the topic of feedback we wish to cover next.

Phase and Amplitude Responses versus Frequency

We can plot[9] the gain magnitude and phase of this elementary feedback example in Fig. 1, where we can see the flat gain at high frequencies and the rising response below ω_0. Our laser servo designs will need to echo this shape, since the drift of the laser will be greater and greater at low frequencies, or as we wait longer. This will require larger and larger gains at low frequencies (long times) to keep the laser frequency nearby our planned lock point. The phase in Fig. 1 shows the lag approaching 90° at the lowest frequencies. (An overall minus sign is put into the subtractor unit, as our circuit shows an adder.) The time domain behavior of this feedback system is a prompt inverted output, augmented later by the integration's contribution.

As a first step toward modeling our realistic system, Fig. 2 shows the laser included in our control loop. The servo system's job is to keep the laser output at the value defined by the reference or setpoint input. Some new issues will arise at the high frequency end with the physical laser, as its PiezoElectric Transducer (PZT) will have time delay, finite bandwidth, and probably some resonances.

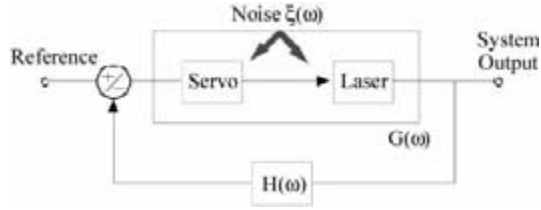

FIGURE 2 Schematic model of laser system, with frequency noise included as part of a servo control loop.

One way we should expand the model is to include the laser's operation as a frequency transducer, converting our control voltage to a frequency change. Probably the laser will have some unwanted frequency noises, and in Fig. 3 we can indicate their unwanted contributions arriving in the optical frequency discriminator, which functions like a summing junction. The emitted laser field encounters an optical frequency discriminator and the laser frequency is compared with the objective standard, which we will discuss shortly. In our diagram we show this laser frequency discriminator's role as an optical frequency-to-voltage converter element. More exactly, laser frequency *differences* from the discriminator's reference setpoint are converted to a voltage output. Laser amplitude noises (due to the intrinsic property of the laser itself or external beam propagation) and vibration effects on the discriminator will appear as undesired additive noises also.

The first simple idea is that the feedback loop can be closed when the servo information, carried as a voltage signal in our amplifier chain, is converted to a displacement (in m) by the PZT, then into laser frequency changes by the laser's standing-wave boundary condition. As the length changes, the "accordian" in which the waves are captive is expanded or compressed, and along with it the wavelength and frequency of the laser's light.

A second truth becomes clear as well: There is freedom in designating the division into the forward gain part and the feedback path part. Actually, we probably would like the laser to be tightly locked onto the control cavity/discriminator, and then we will tune the whole system by changing the set-point which is the discriminator's center frequency. This leads us to view the optical frequency discriminator as the summing junction, with the amplifier and PZT transducer as the forward gain part. The output is taken as an optical frequency, which would be directly compared to the set-point frequency of the discriminator. So the feedback path H = 1.

We should consider some magnitudes. Let K_{PZT} represent the tuning action of the PZT transducer, expressed as displacement (m)/Volt. A typical value for this would be $K_{PZT} = 0.5$ nm/Volt. The laser tunes a frequency interval c/2L for a length change by λ/2, so the PZT-generated tuning will be ~600 Volts/order at 633 nm.

$$K_V = K_{PZT} \frac{2}{\lambda} \frac{c}{2L} \tag{5}$$

So we obtain a tuning sensitivity $K_V \sim 800$ kHz/Volt tuning for a foot-long laser, assuming a disk-type PZT geometry. See the section on PZT design that follows.

Measurement Noise as a Performance Limit—It Isn't. Usually our desire for laser stability exceeds the range of the possible by many orders, and we soon wonder about the ultimate limitations. Surely the ultimate limit would be due to measurement noise. However, we rarely encounter the shot-noise limited case, since the shot noise limited S/N of a 100 μW locking signal is $\sim 6 \times 10^6$ in a 1 Hz bandwidth (see subsequent section on cavity frequency discrimina-

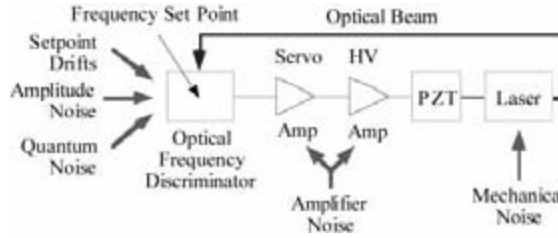

FIGURE 3 Detailed model of frequency-controlled laser, showing noise entry points into the Frequency Discriminator, Servo Amplifiers, and the Laser.

tors). Rather we are here dealing with the laser noise remaining because our servo gain is inadequate to reduce the laser's intrinsic noise below the shot noise limit, the clear criterion of gain sufficiency. So our design task is to push up the gain as much as possible to reduce the noise, limited by the issue of *stability* of the thus-formed servo system.

Servo Stability: Larger Gain at Lower Frequencies, Decreasing to Unity Gain and Below . . .

Our need for high gain is most apparent in the low-frequency domain ~1 kHz and below. Vibrations abound in the dozens to hundreds of Hz domain. Drifts can increase almost without limit as we wait longer or consider lower Fourier frequencies. Luckily, we are allowed to have more gain at low frequencies without any costs in stability. At high frequencies, it is clear we will not help reduce our noise if our correction is applied too late and so no longer has an appropriate phase. One important way we can characterize the closed-loop behavior of our servo is by a time delay t_{delay}. Here we need to know the delay time before any servo response appears; a different (longer) time characterizes the full scale or 1/e response. The latter depends on the system gain, while the ultimate high-speed response possible is controlled by the delay until the first action appears. A good criterion is that the useful unity gain frequency can be as high as $f_\tau = \frac{1}{2}\pi\, t_{delay}$, corresponding to 1 rad extra phase-shift due to the delay. Below this ultimate limit we need to increase the gain—increase it a lot—to effectively suppress the laser's increased noise at low frequencies. This brings us to address the closed-loop stability issue.

Closed-Loop Stability Issues

One can usefully trace the damping of a transient input as it repetitively passes the amplifier and transducer, and is reintroduced into the loop by the feedback. Evidently stability demands that the transient is weaker on each pass. The settling dynamics will be more beautiful if the second-pass version of the perturbation is reduced in magnitude and is within, say, ±90° of the original phase. Ringing and long decay times result when the return phasor approaches –1 times the input signal vector, as then we are describing a sampled sinewave oscillation. These time domain pictures are clear and intuitive, but require treatment in terms of convolutions, so here we will continue our discussion from the frequency-domain perspective that leads to more transparent algebraic forms. We can build up an arbitrary input and response from a summation of sinusoidal inputs. This leads to an output as the sum of corresponding sinusoidal outputs, each including a phase shift.

In our earlier simple laser servo example, no obvious limitation of the available closed-loop gain was visible. The trouble is, we left out two fundamental laboratory parasites: *time delay,* as just noted, and *mechanical resonances.* We will usually encounter the mechanical resonance problem in any servo based on a PZT transducer. For design details, see "Practical Issues" (Section 3). A reasonable unit could have its first longitudinal resonance at about 25 kHz, with a Q ~ 10. In servo terms, the actual mechanical PZT unit gives an added 2-pole roll-off above the resonance frequency and a corresponding asymptotic phase lag of 180°. Including this reality in our model adds another transfer function $R_{PZT} = \omega_0^2/(\omega_0^2 + 2\omega\ \eta\ \omega_0 + \omega^2)$, where ω_0 is 2π times the resonance frequency, and $\eta = \frac{1}{2}Q$ is the damping factor of the resonance. This response is shown in Fig. 4.

We now talk of stabilizing this system. The first appealing option is to try a pure integrator. The problem then is that we are limited in gain by the peak height of the resonance, which must remain entirely below unity gain to avoid instability. In Fig. 5 case (*a*) we see that the unity gain frequency is limited to a value of 1.5 kHz. Some margin is left to avoid excessive ringing near the resonant frequency, but it is still visible in the time domain. One technique that helps this case is a roll-off filter between the unity gain and PZT resonance frequencies.

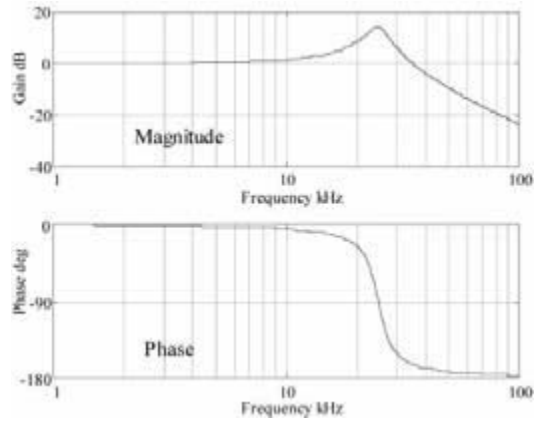

FIGURE 4 The amplitude and phase response of a tubular PZT transducer and an 8mm-diameter by 5mm-thick mirror. The resonance is at 25 kHz with a Q of 10. (This mechanical design is discussed in Section 3.)

Figure 5 shows the "open loop" gain function GH of the feedback equation, and the corresponding phase response. We already noted the dangerous normalized response of −1 where the denominator of Eq. (3) vanishes. In the time domain iterative picture, the signal changes sign on successive passes and leads to instability/oscillation. We need to deal with care as we approach near this point in order to obtain maximum servo gain: It is useful to consider two stability margins. The *phase stability margin* is the phase of the open loop function when the gain is unity. It needs to be at least 30°. The *gain margin* is the closed loop gain when the phase is 180°. In Fig. 5 case (*a*) we see that the phase is not shifted very much until we

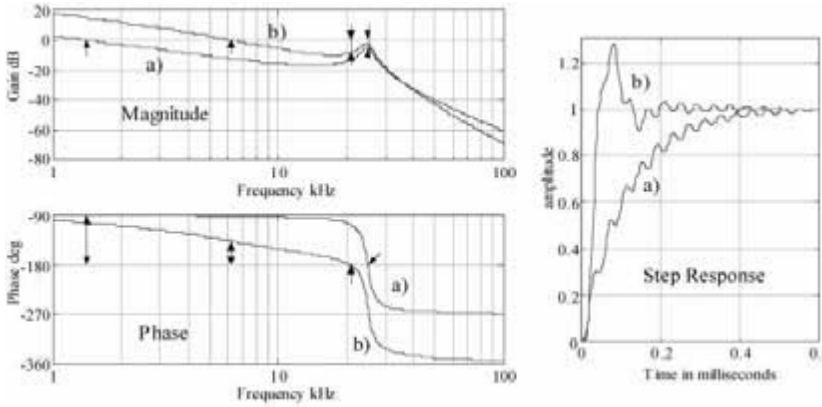

FIGURE 5 (*a*) Integrator gain function alone. Gain must be limited so that gain is <1 even at the resonance. (*b*) Single-pole low pass at 6 kHz inserted. Now unity gain can increase to 6 kHz and time response is ~ threefold faster. Small arrows in the graph indicate the phase margin at the unity gain frequency (gain = 0 dB) and gain margin at a phase shift of −180°.

really "sense" the amplitude increase from the resonance. So this resonance may tend to fix an apparently solid barrier to further servo improvement. But as shown in Fig. 5 case (*b*), just a low pass filter to push down the PZT resonance is very helpful.

In fact, there are many ways of improving the low frequency gain of this system. They include imposing yet another high frequency roll-off (or multi-pole low pass filter) just before the resonance, thus pushing its height down and allowing the open loop transfer function to come up; adding lag compensators before the resonance to push the low frequency gain up while keeping the high frequency response relatively unchanged; adding lead compensators just above the resonance to advance the phase and increase the unity gain point; or placing a notch at the resonant frequency to "cut it out" of the open loop transfer function. The last two options in this list are quite promising and are discussed in more detail later.

Proportional Integral Derivative (PID) Controller versus Notch Filters. Like many "absolute" barriers, it is readily possible to shoot ahead and operate with a larger closed loop bandwidth than that represented by the first PZT resonance. The issue is that we must control the lagging phase that the resonance introduces. A good solution is a *differentiator* stage, or a phase lead compensator, which could also be called a high frequency boost gain step circuit. In Fig. 6 case (*a*) we show the Bode plot of our PZT-implemented laser frequency servo, based on a PID (proportional integral differentiator) controller design. Just a few moments of design pays a huge benefit, as the unity gain frequency has now been pushed to 40 kHz, almost a factor of 2 *above* the PZT's mechanical resonance. For this PID controller example, unity gain occurs at a sevenfold increased frequency compared with Fig. 5 case (*b*). Thus at the lower frequencies we would hope to have increased the servo gain by a useful factor of 7× or 17 dB. However, comparison of Fig. 5 (*b*) and Fig. 6 (*a*) shows that the low frequency gain is hardly changed, even though we greatly increased the servo bandwidth.

How *do* we go forward? We could in principle continue to increase the gain and unity gain frequency, but this is not really practical, since we will again be limited by additional structure

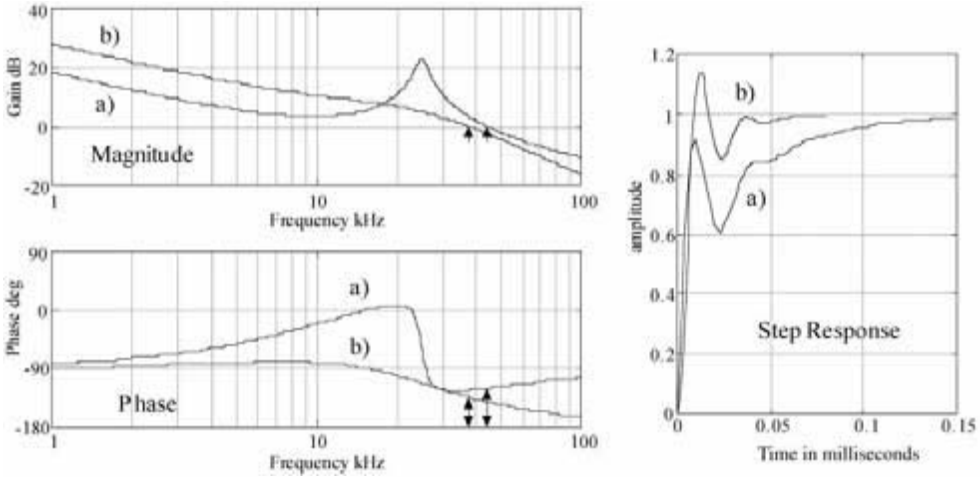

FIGURE 6 Two methods of working through and beyond a resonance. (*a*) PID controller where the Derivative term advances the phase near the resonance. (*b*) Adding a notch is a better approach, where the notch function approximates the inverse of the resonance peak. Transient response settles much more quickly. Again, we use the small arrows in the graph to indicate the phase margin at the unity gain frequency.

resonances that exist beyond the first resonance. Also, the derivatives needed to tame these resonances cost low frequency gain, and it is hard to win. To make progress, we use a notch as an alternative technique to suppress the resonance. Now a D term is not needed, and we can conserve the gain at low frequencies. The notch filter, combined with a proportional-integral (PI) stage, gives unity gain at higher frequencies, and increases gain for low ones. See Fig. 6 case (*b*). Then Fig. 7 compares adding another PI stage to the two cases of Fig. 6, PID in (*a*) and notch plus PI in (*b*). The time domain approach, shown in Fig. 7, shows that case (*b*) settles rather nicely. AND the gain has increased more than 20 dB at frequencies of 1 kHz and below. So this is very encouraging.

While we have come to the cascaded-integrators approach cautiously in this discussion, in fact at least 2 integrators would always be used in practice. Workers with serious gain requirements, for example the LIGO and VIRGO gravitational wave detector groups, may use the equivalent of 4 cascaded integrators! Such a design is "conditionally stable" only, meaning that the gain cannot be smoothly reduced or increased. Such aggressive stabilizer designs have their place, but not for a first design!

"Rule of Thumb" PID Design for System with a Transducer Resonance. Optimizing servo performance is an elegant art, turned into science by specification of our "cost function" for the system performance shortcomings. In the case that we wish to minimize the time-integrated magnitude of the residuals following a disturbance, one comes to the case studied by Ziegler and Nichols for the PID controller used in a system with a combined roll-off and time delay.[8] Such a case occurs also in thermal controllers. With only the P term, one first looks for the frequency f_{osc} where the system first oscillates when the gain is increased. The PD corner is then set 1.27× higher than this f_{osc}, the P gain is set at 0.6 of the oscillation gain, and the PI corner is set at 0.318 times the oscillation frequency. This "rule of thumb" design of the phase compensation produces a transient response which settles reasonably well, so as to minimize the Time-Integrated Error. For phase-locking lasers, a cost function with more emphasis on long-lasting errors leads to another kind of "optimum" tuning, but with qualitatively similar results.

When a notch is used to suppress the resonance, there is no longer an anomalous gain at the resonant frequency and one is returned to the same case as in its absence. A reasonable

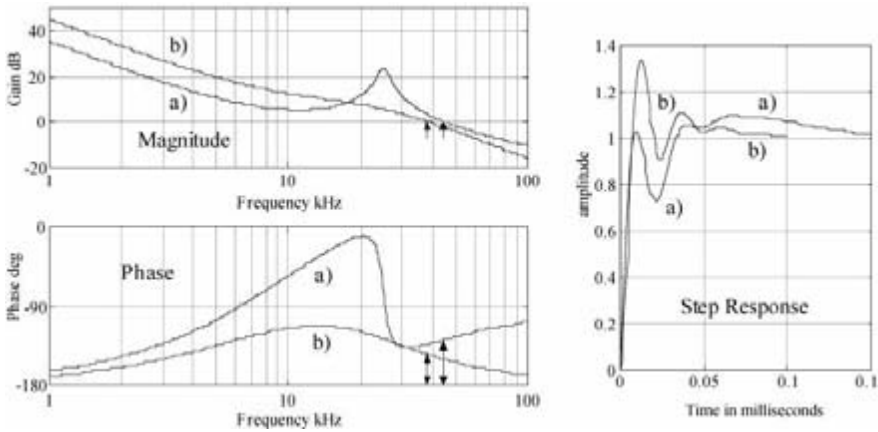

FIGURE 7 Adding an additional PI stage to (*a*) the PID and (*b*) the PI-plus-notch stabilizers of Fig. 6. Note that low frequency gain is strongly increased.

servo approach to using two PI stages is to design with only one, achieving the desired unity gain frequency. The second PI is then added to have its corner frequency at this same point or up to 10-fold lower in frequency, depending on whether we wish the most smooth settling or need the highest feasible low frequency gain. Figures 6(*b*) and 7 show the Bode plot of such designs, along with the system's closed-loop transient response. An elegant strategy is to use adaptive clamping to softly turn on the extra stage when the error is small enough, thus dynamically increasing the order of the controller when it will not compromise the dynamics of recovery.

27.3 PRACTICAL ISSUES

Here we offer a number of important tidbits that are useful background material for a successful application of the grand schemes previously discussed.

Frequency Discriminators for Laser Locking

Frequency-Locking Tools and Issues. So far we have devoted our main effort to addressing the issues of the feedback scheme. Of equal importance is the subject of frequency reference system. After all, a good servo eliminates intrinsic noises of the plant (laser), and replaces them with the measurement noise associated with the reference system. Indeed, development of prudent strategies in high-precision spectroscopy and the progress of laser stabilization have been intimately connected to each other through the years,[10] with the vigorous pursuit of resolution and sensitivity resulting in amazing achievements in both fields.

To stabilize a laser, one often employs some kind of resonance information to derive a frequency/phase-dependent discrimination signal. The resonance can be of material origin, such as modes of an optical interferometer; or of natural origin, such as atomic or molecular transitions. If the desired quantity of a stabilized laser, an optical frequency standard, is its long-term stability or *reproducibility,* the use of a natural resonance is preferred. Reproducibility is a measure of the degree to which a standard repeats itself from unit to unit and upon different occasions of operation. The ultimate reproducibility is limited to the accuracy of our knowledge of the involved transitions of free atoms or molecules. The term *free* means the resonance under study has a minimum dependence on the laboratory conditions, such as the particle's moving frame (velocity), electromagnetic fields, collisions, and other perturbations. To realize these goals, modern spectroscopy has entered the realm of quantum limited measurement sensitivities and exquisite control of internal and external degrees of freedom of atomic motions.

A careful selection of a high-quality resonance can lead to superior system performance and high working efficiency. For example, the combined product of the transition quality factor Q and the potential signal-to-noise ratio (S/N) is a major deciding factor, since this quantity controls the time scale within which a certain measurement precision (fractional frequency) can be obtained. This importance is even more obvious when one considers that the waiting time for a systematic study is proportional to the inverse square of ($Q \times S/N$). A narrower transition linewidth of course also helps to reduce the susceptibility to systematic errors. The resonance line shape is another important aspect to explore. By studying the line shape we will find out whether we have come to a complete understanding of the involved transition and whether there are other unresolved small lines nearby ready to spoil our stabilization system.

Sometimes it may be not sufficient (or necessary) to use the natural resonance alone for stabilization work. The saturation aspect of the atomic transition limits the attainable S/N. To stabilize a noisy laser we need to use, for example, an optical resonator, which can provide a high contrast and basically unlimited S/N of the resonance information. Careful study of the

design and control of the material properties can bring the stability of material reference to a satisfactory level. A more detailed discussion on this topic follows.

Ideally, a resonance line shape is even symmetric with respect to the center frequency of the resonance, and deviations from this ideal case will lead to frequency offsets. However, for the purpose of feedback, the resonance information needs to be converted to an odd symmetric discriminator shape: We need to know in which direction the laser is running away from the resonance. A straightforward realization of an error signal using direct absorption technique is to have the laser tuned to the side of resonance.[11] The slope of the line is used to convert the laser frequency noise to amplitude information for the servo loop. This technique is essentially a DC approach and can suffer a huge loss in S/N due to the low frequency amplitude noise of the laser. A differential measurement technique using dual beams is a requirement if one wishes to establish a somewhat stable operation. With a dual beam approach, the information about the laser noise can be measured twice, and therefore it is possible to completely eliminate the technical noise and approach the fundamental limit of shot noise using clever designs of optoelectronic receivers. Conventional dual-beam detection systems use delicate optical balancing schemes,[12] which are often limited by the noise and drift of beam intensities, residual interference fringes, drift in amplifiers, and spatial inhomogenity in the detectors. Electronic auto cancellation of the photo detector currents has provided near-shot-noise-limited performance.[13] Although this process of input normalization helps to increase S/N of the resonance, the limitation on the locking dynamic range remains as a problem. The servo loop simply gets lost when the laser is tuned to the tail or over the top of the resonance. Further, it is found that transient response errors basically limit the servo bandwidth to be within the cavity linewidth.[14] Another effective remedy to the DC measurement of resonances is the use of zero-background detection techniques, for example, polarization spectroscopy.[15,16] In polarization spectroscopy the resonance information is encoded in the differential phase shifts between two orthogonally polarized light beams. Homodyne detection between the two beams can reveal an extremely small level of absorption-induced polarization changes of light, significantly improving the detection sensitivity. However, any practical polarizer has a finite extinction ratio (ε) which limits the attainable sensitivity. Polarization spectroscopy reduces the technical noise level by a factor of $\sqrt{\varepsilon}$, with $\varepsilon \sim 10^{-7}$ for a good polarizer. Polarization techniques do also suffer the problem of long-term drifts associated with polarizing optics.

Modulation techniques are of course often used to extract weak signals from a noisy background. Usually noises of technical origins tend to be more prominent in the low frequency range. Small resonance information can then be encoded into a high frequency region where both the source and the detector possess relatively small noise amplitudes. Various modulation schemes allow one to compare on-resonant and off-resonant cases in quick succession. Subsequent demodulations (lock-in detection) then simultaneously obtain and subtract these two cases, hence generating a signal channel with no output unless there is a resonance. Lorentzian signal recovery with the frequency modulation method has been well-documented.[17] The associated lock-in detection can provide the first, second, and third derivative type of output signals. The accuracy of the modulation waveform can be tested and various electronic filters can be employed to minimize nonlinear mixing among different harmonic channels, and so excellent accuracy is possible. In fact, the well-established 633 nm HeNe laser system[18] is stabilized on molecular iodine transitions using this frequency dither technique and third harmonic (derivative) signal recovery. Demodulation at the third or higher order harmonics helps to reduce the influence of other broad background features.[19] The shortcoming of the existence of dither on the output beam can be readily cured with an externally implemented "undithering" device based on an AOM.[20] However, in this type of modulation spectroscopy the modulation frequency is often chosen to be relatively low to avoid distortions on the spectral profile by the auxiliary resonances associated with modulation-induced spectral sidebands. An equivalent statement is that the line is distorted because it cannot reach an equilibrium steady state in the face of the rapidly-tuning excitation. This low-frequency operation (either intensity chopping or derivative line shape recovery) usually is still partly contaminated by

the technical noise, and the achievable signal-to-noise ratio (S/N) is thereby limited. To recover the optimum signal size, large modulation amplitudes (comparable to the resonance width) are also employed, leading to a broadened spectral linewidth. Therefore the intrinsic line shape is modified by this signal recovery process and the direct experimental resolution is compromised.

A different modulation technique was later proposed and developed in the microwave magnetic resonance spectroscopy and similarly in the optical domain.[21–24] The probing field is phase-modulated at a frequency much larger than the resonance linewidth under study. When received by a square-law photodiode, the pure FM signal will generate no photo-current at the modulation frequency unless a resonance feature is present to upset the FM balance. Subsequent heterodyne and rf phase-sensitive detection yield the desired signal. The high sensitivity associated with the FM spectroscopy is mainly due to its high modulation frequency, usually chosen to lie in a spectral region where the amplitude noise level of the laser source approaches the quantum (shot noise) limit. The redistribution of some of the carrier power to its FM sidebands causes only a slight penalty in the recovered signal size. Another advantage of FM spectroscopy is the absence of linewidth broadening associated with low-frequency modulation processes. The wide-spread FM spectra allows each individual component to interact with the spectral features of interest and thereby preserves the ultrahigh resolution capability of contemporary narrow-linewidth lasers.

Since its invention, FM spectroscopy has established itself as one of the most powerful spectroscopic techniques available for high sensitivity, high resolution, and high-speed detection. The high bandwidth associated with the radio frequency (rf) modulation enables rapid signal recovery, leading to a high Nyquist sampling rate necessary for a high bandwidth servo loop. The technique has become very popular in nonlinear laser spectroscopy,[23] including optical heterodyne saturation spectroscopy,[24] two-photon spectroscopy,[25] Raman spectroscopy,[26] and heterodyne four-wave mixing.[27] Recent developments with tunable diode lasers have made the FM technique simpler and more accessible. The field of FM-based laser diode detection of trace gas and remote sensing is rapidly growing. In terms of laser frequency stabilization, the rf sideband-based Pound-Drever-Hall locking technique[28] has become a uniformly adopted fast stabilization scheme in the laser community. The error signal in a high-speed operating regime is shown to correspond to the instantaneous phase fluctuations of the laser, with the atom or optical cavity serving the purpose of holding the phase reference. Therefore a properly designed servo loop avoids the response time of the optical phase/frequency storage apparatus and is limited only by the response of frequency correcting transducers.

In practice some systematic effects exist to limit the ultimate FM sensitivity and the resulting accuracy and stability. Spurious noise sources include residual amplitude modulation (RAM), excess laser noise, and étalon fringes in the optical system.[29] A number of techniques have been developed to overcome these problems. In many cases FM sidebands are generated with electro-optic modulators. A careful EOM design should minimize the stress on the crystal and the interference between the two end surfaces (using angled incidence or antireflection coatings). Temperature control of the EOM crystal is also important and has been shown to suppress the long-term variation of RAM.[30] The RAM can also be reduced in a faster loop using an amplitude stabilizer[31] or a tuning filter cavity.[32] The étalon fringe effect can be minimized by various optical or electronic means.[33] An additional low-frequency modulation (two-tone FM)[34] can be used to reduce drifts and interference of the demodulated baseline.

In closing this section we note that a laser is not always stabilized to a resonance but is sometimes referenced to another optical oscillator.[35] Of course the working principle does not change; one still compares the frequency/phase of the laser with that of reference. The technique for acquiring the error information is more straightforward however, often with a direct heterodyne detection of the two superposed waveforms on a *fast photo detector.* The meaning of the fast photo detector can be quite broad, sometime referring to a whole table-top system that provides THz-wide frequency gap measurement capabilities.[36,37,38] Since it is the phase information that is detected and corrected, an optical phase-locked loop usually provides a

tight phase coherence between two laser sources. This is attractive in many measurement applications where the relative change of optical phase is monitored to achieve a high degree of precision. Other applications include phase-tracked master-slave laser systems, where independent efforts can be made to optimize laser power, tunability, and intrinsic noise.

The Optical Cavity-Based Frequency Discriminator. It is difficult to have both sensitive frequency discrimination and short time delay, unless one uses the reflection mode of operation; these issues have been discussed carefully elsewhere.[28] With ordinary commercial mirrors, we can have a cavity linewidth of 1 MHz, with a contrast C above 50 percent. We can suppose using 200 μW optical power for the rf sideband optical frequency discriminator, leading to a DC photo current i_0 of ~100 μA and a signal current of ~25 μA. The shot noise of the DC current is $i_n = \sqrt{2ei_0}$ in a 1 Hz bandwidth, leading to a S/N of ~4×10^6. The frequency noise-equivalent would then be 250 milliHertz/√Hz. If we manage to design enough useful gain in the controller to suppress the laser's intrinsic noise below this level, the laser output frequency spectrum would be characterized by this power spectral density. Under these circumstances the output spectrum would be Lorentzian, of width $\Delta\nu_{FWHM} = \pi\ S_f = \pi(0.25\ \text{Hz})^2/\text{Hz} \sim 0.8$ Hz. One comes to impressive predictions in this business! But usually the results are less impressive.

What goes wrong? From measurements of the servo error, we can see that the electronic lock is very tight indeed. However, the main problem is that vibrations affect the optical reference cavity's length and hence its frequency. For example, measurements show that the Quiet Room floor at the JILA building has a horizontal seismic noise spectrum which can be approximated by 4×10^{-9} m rms/√Hz from below 1 Hz to about 20 Hz, breaking there to an f^{-2} roll-off. Below 1 Hz the displacement noise climbs as f^{-3}. Accelerations associated with these motions lead to forces on the reference cavity that will lead to mechanical distortion and hence frequency shifts. In the axial direction, holding the cavity in the midplane seems wise as the net length change would tend be cancelled: one half is under compression, the other half is under tension at a particular moment in the AC vibration cycle. We denote this cancellation by symmetry as ε, with $0 \le \varepsilon \le 1$. The asymmetry value observed for our pendulum mountings is $\varepsilon = 0.05$. Simple approximate analysis leads to a dynamic modulation of the cavity length l by the acceleration a, as

$$\frac{\Delta l}{l}\Big|_{\text{axial}} = \frac{a l \varepsilon \rho}{2Y} \tag{6}$$

where Y ~ 70 GPa is the Young's modulus for the ULE or Zerodur spacer. The density ρ is about 2.5×10^3 kG/m^3. For $\varepsilon = 1$, l = 10 cm and a = 1 g, we expect $\Delta l/l = -\Delta f/f \sim 7.5$ MHz/g, supposing λ = 633 nm and not yet counting the nearly symmetric mounting. Inclusion of this factor makes our horizontal sensitivity 375 kHz/g. Vertically accelerating the interferometer produces length changes through the distortion coupling between the lateral and lengthwise dimension, the effect of "extrusion of the toothpaste," with a displacement reduction by the Poisson ratio σ = 0.17. Also the vertical height is really the spacer's diameter ϕ, which is about fivefold less than the length.

$$\frac{\Delta l}{l}\Big|_{\text{vertical}} = \frac{a \phi \sigma \rho}{2Y} \tag{7}$$

We come to a vertical sensitivity of 250 kHz/g. Integrating the acceleration produced by the midband vibration spectrum just quoted leads to a broadband noise of a few Hz in both H and V planes. Left out, however, is the 1 milli-"g" vibration near 30 Hz due to AC motors in JILA (Pepsi refrigerators!). So we should have a vibration-induced linewidth of something like ½ kHz, which correlates well with experience. Active antivibration measures suppress this linewidth below 10 Hz, while improved passive mountings at NIST have recently led to sub-Hertz cavity-locked laser linewidths.[39]

Quantum Resonance Absorption.[40] Establishing a long-term stable optical frequency standard requires a natural reference of atomic or molecular origin. Historically the use of atomic/molecular transitions was limited to those that had accidental overlap with some fixed laser wavelengths. With the advent of tunable lasers, research on quantum absorbers has flourished. A stabilized laser can achieve a fractional frequency stability $\delta\nu/\nu = 1/Q \cdot 1/(S/N) \cdot 1/\sqrt{\tau}$, where Q is the quality factor of the transition involved, S/N is the recovered signal-to-noise ratio of the resonance information, and τ is the averaging time. Clearly one wishes to explore the limits on both resolution and sensitivity of the detected signal. The nonlinear nature of a quantum absorber, while on one hand limiting the attainable S/N, permits sub-Doppler resolutions. With sensitive techniques such as FM-based signal modulation and recovery, one is able to split a MHz scale linewidth by a factor of 10^4 to 10^5, at an averaging time of 1 s or so. Sub-Hertz long-term stability can be achieved with carefully designed optical systems where residual effects on baseline stability are minimized. However, a pressing question is: How accurate is our knowledge of the center of the resonance? Collisions, electromagnetic fringe fields, probe field wave-front curvature, and probe power can all bring undesired linewidth broadening and center shifts. Distortion in the modulation process and other physical interactions can produce asymmetry in the recovered signal line shape. These issues will have to be addressed carefully before one can be comfortable talking about accuracy. A more fundamental issue related to time dilation of the reference system (second-order Doppler effect) can be solved in a controlled fashion: one simply knows the sample velocity accurately (for example, by velocity selective Raman process), or the velocity is brought down to a negligible level using cooling and trapping techniques.

The simultaneous use of quantum absorbers and an optical cavity offers an attractive laser stabilization system. On one hand, a laser prestabilized by a cavity offers a long phase coherence time, reducing the need of frequent interrogations of the quantum absorber. In other words, information of the atomic transition can be recovered with an enhanced S/N, and the long averaging time translates into a finer examination of the true line center. On the other hand, the quantum absorber's resonance basically eliminates inevitable drifts associated with material standards. The frequency offset between the cavity mode and atomic resonance can be bridged by an AOM. In this case the cavity can be made of totally passive elements: mirrors are optically contacted to a spacer made of ultralow expansion material such as ULE or Zerodur. In case that the cavity needs to be made somewhat tunable, an intracavity Brewster plate driven by Galvo or a mirror mounted on PZT are often employed. Of course these mechanical parts bring additional thermal and vibrational sensitivities to the cavity, along with nonlinearity and hysteresis. Temperature tuning of a resonator is potentially less noisy but slow. Other tuning techniques also exist, for example, through the use of magnetic force or pressure (change of intracavity refractive index or change of cavity dimension by external pressure). A powerful, often-used technique called frequency-offset-locking brings the precision rf tuning capability to the optical world.[14]

Transducers

Transducer Design Using a PZT Disk. We will usually encounter the mechanical resonance problem in any servo based on a PZT transducer: Small mirrors clearly are nice as they can have higher resonance frequencies. A mirror, say 7.75 mm $\Phi \times 4$ mm high, might be waxed onto a PZT disk 10 mm diameter $\times$ 0.5 mm thick. The PZT, in turn, is epoxied onto a serious backing plate. This needs to be massive and stiff, since the PZT element will produce a differential force between the mirror and the backing plate. At short times there will be a "reduced mass" kind of splitting of the motion between the mirror and the support plate. At lower frequencies, one hates to get a lot of energy coupled into the mirror mount since it will have a wealth of resonances in the sub-kHz range. For this size mirror, the backing plate might be stainless steel, 1 inch diameter by ~¾ inch wedged thickness, and with the PZT deliberately decentered to break down high Q modes. The piston mode will be at ~75 kHz.

Transducer Design Using Tubular PZT. Often it is convenient to use a tubular form of PZT, with the electric field radially applied across a thin wall of thickness t. This gives length expansion also, transverse to the field using a weaker d_{31} coefficient, but wins a big geometric factor in that the transverse field is generating a length response along the entire tube height h. The PZT tube could be ½″ Φ × ½″ high, with a wall thickness t = 1.25 mm. This geometry leads to a ~sevenfold sensitivity win, when $d_{31} \approx 0.7\, d_{33}$ is included. Typical dimensions for the mirror might be 12.5 mm diameter × 7 mm high. The PZT tube also is epoxied onto a serious backing plate. For the high-voltage isolation of the PZT electrodes at the tube ends, a thin sheet (say <0.5 mm) of stiff ceramic, alumina for example, will suffice. An alternative way to provide the electrical isolation of the ends involves removing the silver electrodes for several mm at the end. A new technique uses a diamond-charged tubular core drill mounted into a collet in a lathe. The active tool face projects out only 2 mm so that hand-held PZT grinding leads to clean electrode removal, inside and out. This end of the PZT tube is attached to the backing mass with strong epoxy. The mirror is attached to the open PZT tube end with melted wax. This is vastly better than epoxy in that it does not warp the optic, and the small energy dissipation occurs at the best place to damp the Q of the PZT assembly. If done well, this unit will have its first longitudinal resonance at about 25 kHz, with a Q ~ 10. As already noted, in servo terms, the actual mechanical PZT unit gives an added 2-pole roll-off above the resonance frequency and a corresponding asymptotic phase lag of 180°. So it is useful to design for high resonant frequency and low Q.

Comparing disk and tubular designs, the disk approach can have a threefold higher resonance frequency, while the tubular design is ~sevenfold more sensitive. Perhaps more important is the tube's reduced stiffness, moving the PZT/mirror resonance down into the 20 kHz domain. This brings us to the subject of spectral shaping of the amplifier gain and limitations of servo performance due to electronic issues.

Amplifier Strategies for PZT Driver. We enjoy the tubular PZT for its large response per volt and its relatively high resonance frequencies. But it poses a problem in having a large capacitance, for example of 10 nf in the just described design. Even with the high sensitivity of 70 V/order, achieving a tight lock requires high frequency corrections and can lead to a problem in supplying the necessary AC current, supposing that we ask the HV amplifier alone to do the job. An apparent answer is to use a pair of amplifiers, one fast and the other HV, separately driving the two sides of the PZT. This alone doesn't solve the problem, as the big high-frequency AC current is only returned via the HV amplifier. The answer is to use a crossover network on the HV amplifier side. A capacitor to ground, of perhaps three- or fivefold larger value than the PZT will adequately dump the fast currents coming through the PZT's capacitance. A resistor to this PZT/shunt capacitor junction can go to the HV amplifier. Now this HV amp has indeed more capacitance to drive, but is only needed to be active below a few hundred Hz where the current demand becomes reasonable. An alternative topology sums the two inputs on one side of the PZT.

Other Useful Transducers—Slow but Powerful. Commercial multiple wafer designs utilize 100 or more thin PZT sheets mechanically in series and electrically in parallel to produce huge excursions such as 10 μm for 100 V. Of course the capacitance is ~0.1 μF, and the stability leaves something to be desired. These are useful for applications that can tolerate some hysteresis and drift, such as grating angle tuning in a diode laser. When a large dynamic range is needed to accommodate wide tuning range or to correct for extensive laser frequency drifts at low frequencies, a galvo-driven Brewster plate can be used inside the optical cavity. Typically a Brewster plate inflicts an insertion loss less than 0.2 percent if its angular tuning range is limited within ±4 degrees. Walk-off of the optical beam by the tuning plate can be compensated with a double-passing arrangement or by using dual plates. In the JILA-designed Ti:Sapphire laser, we use the combination of PZT and Brewster plate for the long-term frequency stabilization. The correction signal applied to the laser PZT is integrated and then fed to the Brewster plate to prevent saturation of the PZT channel. At higher frequencies we use much faster transducers, such as AOM and EOM, which are discussed in the text that follows.

Temperature control of course offers the most universal means to control long-term drifts. Unfortunately, the time constant associated with thermal diffusion is usually slow, and therefore the loop bandwidth of thermal control is mostly limited to Hz scale. However, thoughtful designs can sometimes push this limit to a much higher value. For example, a Kapton thin-film heater tape wrapped around the HeNe plasma tube has produced a thermal control unity gain bandwidth in excess of 100 Hz.[41] The transducer response is reasonably modeled as an integrator above 0.3 Hz, and excessive phase shifts associated with the thermal diffusion do not become a serious issue until ~200 Hz. This transfer function of the transducer can be easily compensated with an electronic PI filter to produce the desired servo loop response. Radiant heating of a glass tube by incandescent lamps has achieved a time delay <30 ms and has also been used successfully for frequency control of HeNe lasers.[42] If a bipolar thermal control is needed, Peltier-based solid state heat pumps (thermoelectric coolers) are available and can achieve temperature differences up to 70 °C, or can transfer heat at a rate of 125 W, given a proper configuration of heat sinking. Parallel use of these Peltier devices result in a greater amount of heat transfer while cascaded configuration achieves a larger temperature difference.

Combining various servo transducers in a single feedback loop requires thorough understanding of each actuator, their gains and phase shifts, and the overall loop filter function one intends to construct. Clearly, to have an attractive servo response in the time domain, the frequency transfer functions of various gain elements need to cross over each other smoothly. A slow actuator may have some resonance features in some low-frequency domain, hence the servo action needs to be relegated to a faster transducer at frequency ranges beyond those resonances. The roll-off of the slow transducer gain at high frequencies needs to be steep enough so that the overall loop gain can be raised without exciting the associated resonance. On the other hand, the high-frequency channel typically does not have as large a dynamic range as the slow ones. So one has to pay attention not to overload the fast channel. Again, a steep filter slope is needed to rapidly relinquish the gain of the fast channel toward the low-frequency range. However, we stress here that the phase difference between the two channels at the crossover point needs to be maintained at less than 90°. In the end, predetermined gains and phase shifts will be assigned to each transducer so that the combined filter function resembles a smooth single channel design. Some of these issues will be addressed briefly in the following section on example designs.

Servo Design in the Face of Time Delay: Additional Transducers Are Useful. As one wishes for higher servo gain, with stability, it means a higher closed-loop bandwidth must be employed. Eventually the gain is sufficiently large that the intrinsic laser noise, divided by this gain, has become less than the measurement noise involved in obtaining the servo error signal. This should be sufficient gain. However it may not be usable in a closed-loop scenario, due to excessive time delay. If we have a time delay of t_{delay} around the loop from an injection to the first receipt of correction information, a consideration of the input and response as vectors will make it clear that no real servo noise suppression can occur unless the phase of the response at least approximates that required to subtract from the injected error input to reduce its magnitude on the next cycle through the system. A radian of phase error would correspond to a unity-gain frequency of $\frac{1}{2}\pi t_{delay}$, and we find this to be basically the upper useful limit of servo bandwidth. One finds that to correct a diode laser or dye laser to leave residual phase errors of 0.1 rad, it takes about 2 MHz servo bandwidth. This means a loop delay time, at the absolute maximum, of $t_{delay} = \frac{1}{2}\pi\, 2\text{MHz} = 80$ ns. Since several amplifier stages will be in this rf and servo-domain control amplifier chain, the individual bandwidths need to be substantially beyond the 12 MHz naively implied by the delay spec. In particular rf modulation frequencies need to be unexpectedly large, 20 MHz at least, and octave rf bandwidths need to be utilized, considering that the modulation content can only be one half the bandwidth. Suppression of even-order signals before rf phase detection is done with narrow resonant rf notches.

Of course a PZT transducer will not be rated in the ns regime of time delay. Rather, one can employ an AOM driven by a fast-acting voltage-controlled oscillator to provide a fre-

quency shift. Unfortunately the minimum acoustic time delay from the ultrasonic transducer to the optical interaction seems always to be 400 ns, and more if we are dealing with a very intense laser beam and wish to avoid damage to the delicate AO transducer. The AOM approach works well with diode-pumped solid state lasers, where the bandwidth of major perturbations might be only 20 kHz. By double-passing the AOM the intrinsic angular deflection is suppressed. Usually the AOM prefers linear polarization. To aid separation of the return beam on the input side, a spatial offset can be provided with a collimating lens and roof prism, or with a cat's-eye retroreflector. Amplitude modulation or leveling can also be provided with the AOM's dependence on rf drive, but it is difficult to produce a beam still at the shot noise level after the AOM.

The final solution is an *EOM phase modulator.* In the external beam, this device will produce a phase shift per volt, rather than a frequency shift. So we will need to integrate the control input to generate a rate of change signal to provide to the EOM, in order to have a frequency relationship with the control input.[43] Evidently this will bring the dual problems of voltage saturation when the output becomes too large, and a related problem, the difficulty of combining fast low-delay response with high voltage capability. The standard answer to this dilemma was indicated in our PZT section, namely, one applies fast signals and high-voltage signals independently, taking advantage of the fact that the needed control effort at high frequencies tends to cover only a small range. So fast low-voltage amplifier devices are completely adequate, particularly if one multipasses the crystal several times. A full discussion of the crossover issues and driver circuits will be prepared for another publication.

Representative/Example Designs

Diode-Pumped Solid State Laser. Diode-pumped solid state lasers are viewed as the most promising coherent light sources in diverse applications, such as communications, remote detection, and high-precision spectroscopy. Nd:YAG laser is among the first developed diode-pumped solid state lasers and has enjoyed continuous improvements in its energy efficiency, size, lifetime, and intrinsic noise levels. The laser's free-running linewidth of ~10 kHz makes it a straightforward task to stabilize the laser via an optical cavity or an optical phase locked loop. In our initial attempt to stabilize the laser on a high finesse (F ~ 100,000, linewidth ~3 kHz) cavity, we employ an external AOM along with the laser internal PZT, which is bonded directly on the laser crystal. The frequency discrimination signal between the laser and cavity is obtained with 4 MHz FM sidebands detected in cavity reflection. The PZT corrects any slow but potentially large laser frequency noise. Using the PZT alone allows the laser to be locked on cavity. However, the loop tends to oscillate around 15 kHz, and the residual noise level is more than 100 times higher than that obtained with the help of an external AOM. The AOM is able to extend the servo bandwidth to ~150 kHz, limited by the propagation time delay of the acoustic wave inside the AOM crystal. The crossover frequency between the PZT and AOM is about 10 kHz. Such a system has allowed us to achieve a residual frequency noise spectral density of 20 mHz/$\sqrt{\text{Hz}}$. The laser's linewidth relative to cavity is thus a mere 1.3 mHz,[44] even though the noise spectral density is still 100 times higher than the shot noise. This same strategy of servo loop design has also been used to achieve a microradian level phase locking between two Nd:YAG lasers.[45]

It is also attractive to stabilize the laser directly on atomic/molecular transitions, given the low magnitude of the laser's intrinsic frequency noise. Of course the limited S/N of the recovered resonance information will not allow us to build speedy loops to clean off the laser's fast frequency/phase noise. Rather we will use the laser PZT alone to guide the laser for a long-term stability. An example here is the 1.064 μm radiation from the Nd:YAG, which is easily frequency doubled to 532 nm where strong absorption features of iodine molecules exist.[46,47] The doubling is furnished with a noncritical phase-matched KN_bO_3 crystal located inside a buildup cavity. 160 mW of green light output is obtained from an input power of 250 mW of

IR. Only mW levels of the green light are needed to probe the iodine-saturated absorption signal. Low vapor pressure (~0.5 Pa) of the iodine cell is used to minimize the collision-induced pressure shift and to reduce the influence on baseline by the linear Doppler absorption background. The signal size decreases as the pressure is reduced. However, this effect is partly offset due to the reduced resonance linewidth (less pressure broadening) which helps to increase the slope of the frequency locking error signal. A lower pressure also helps to reduce power-related center frequency shifts since a lower power is needed for saturation. With our 1.2-m long cells, we have achieved a S/N of 120 in a 10 kHz bandwidth, using the modulation transfer spectroscopy.[48] (Modulation transfer is similar to FM except that we impose the frequency sideband on the saturating beam and rely on the nonlinear medium to transfer the modulation information to the probe beam which is then detected.) Normalized to 1-s averaging time, this S/N translates to the possibility of a residual frequency noise level of 10 Hz when the laser is locked on the molecular resonance, given the transition linewidth of 300 kHz. We have built two such iodine-stabilized systems, and the heterodyne beat between the two lasers permits systematic studies on each system and checks the reproducibility of the locking scheme.[49] With a 1-s counter gate time, we have recorded the beat frequency between the two lasers. The standard deviation of the beat frequency noise is ~20 Hz, corresponding to ~14 Hz rms noise per IR laser, basically a S/N limited performance. The beat record can be used to calculate the Allan standard deviation: starting at 5×10^{-14} at 1-s, decreasing with a slope of $1/\sqrt{\tau}$ up to 100-s. (τ is the averaging time.) After 100-s the deviations reach the flicker noise floor of $\sim 5 \times 10^{-15}$. At present, the accuracy of the system is limited by inadequate optical isolation in the spectrometer and the imperfect frequency modulation process (residual amplitude noise, RAM) used to recover the signal. This subject is under intense active study worldwide.

External Cavity Diode Lasers. Diode lasers are compact, reliable, and coherent light sources for many different applications.[50] The linewidth of a free-running diode laser is limited by the fundamental spontaneous emission events, enhanced by the amplitude-phase coupling inside the gain medium. With a low noise current driver, a typical mW scale AlGaAs diode laser has a linewidth of several MHz. To reduce this fast frequency noise, one typically employs an external cavity formed between one of the diode laser facets and a grating (or an external mirror that retroreflects the first-order grating diffraction).[51,52,53] This optical feedback mechanism suppresses the spontaneous emission noise, replaced by much slower fluctuations of mechanical origin. The linewidth of the grating-stabilized external cavity diode laser (ECDL) is usually between 100 kHz and 1 MHz, determined by the quality factor of the optical feedback. The ECDL also offers much better tuning characteristics compared against a solitary diode. To do such tuning, the external grating (or the mirror that feeds the grating-dispersed light back to the laser) is controlled by a PZT for scanning. Synchronous tuning of the grating dispersion and the external cavity mode can be achieved with a careful selection of the grating rotation axis position. Similarly, this PZT controlled grating can be used to stabilize the frequency of an ECDL. However, owing to the low bandwidth limited by the mechanical resonance of PZT, a tight frequency servo is possible only through fast transducers such as the laser current or intracavity phase modulators.

This hybrid electro-optic feedback system is attractive, and ECDLs have been demonstrated to show Hz level stability under a servo bandwidth of the order of 1 MHz. For a solitary diode, feedback bandwidth of tens of MHz would have been needed in order to bring the frequency noise down to the same level. However, considering that the optical feedback has a strong impact on the laser frequency noise spectrum, one finds the frequency response of the compound laser system is clearly dependent upon the optical alignment. Therefore for each particular ECDL system, we need to measure the frequency response function of the laser under the optimally aligned condition. We are dealing with a multichannel feedback system (for example, PZT plus current), so that designing smooth crossovers between different transducers requires knowledge of the transfer functions of each transducer. Normally the current-induced FM of a solitary diode has a flat response up to 100 kHz, and then starts to

roll off in the region between 100 kHz and 1 MHz, initially with a single-pole character. This is mainly due to the time response of the current-induced thermal change of the refractive index inside the diode. (At a faster time scale, the carrier density variation will dominate the laser frequency response.) Design of a fast feedback loop needs to take this intrinsic diode response into account. Fortunately the time delay associated with the current response is low, typically below 10 ns.

In our example system, the frequency discrimination signal of the ECDL is obtained from a 100 kHz linewidth cavity with a sampling frequency of 25 MHz. The error signal is divided into three paths: PZT, current modulation through the driver, and direct current feedback to the diode head. The composite loop filter function is shown in Fig. 8. The crossover between the slow current channel and the PZT usually occurs around 1 kHz, in order to avoid mechanical resonance of the PZT at a few kHz. In our system, the frequency response of the PZT/grating is 10 GHz/V. To furnish this in-loop gain of ~1000 at 1 kHz, we need to supply an electronic gain of 0.1, given that the error signal has a slope of 1 V/1 MHz. Towards the lower frequency range the PZT gain increases by 40 dB/decade (double integrators) to suppress the catastrophically rising laser frequency noise. It is obvious from Fig. 8 that the intermediate current channel tends to become unstable at a few hundred kHz, due to the excessive phase shift there. The fast current loop, bypassing the current driver to minimize additional time delay and phase shift, has a phase lead compensator to push the unity gain bandwidth to 2

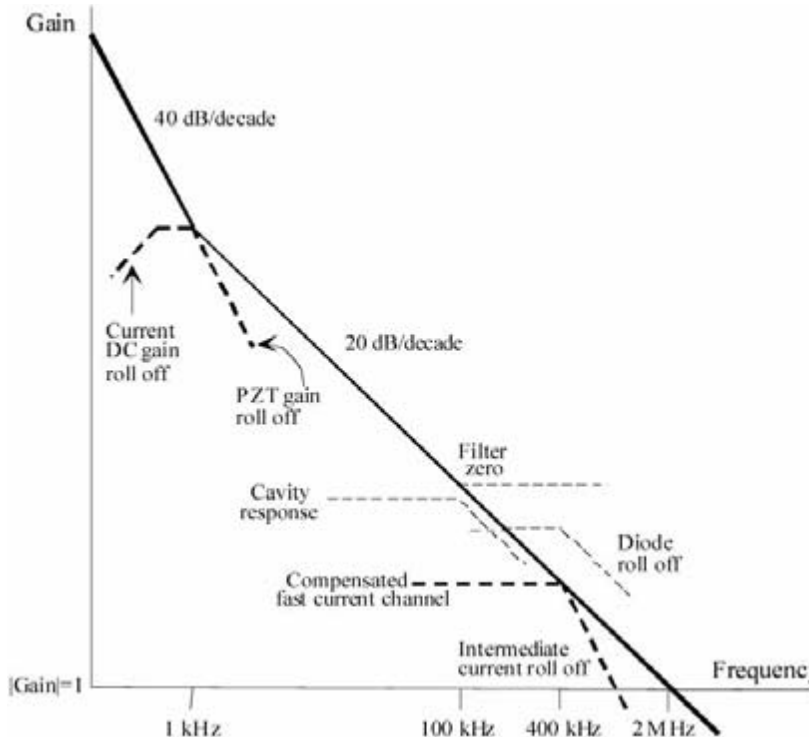

FIGURE 8 The combined loop filter function for ECDL frequency stabilization.

MHz. With this system we can lock the ECDL robustly on the optical cavity, with a residual noise spectral density of 2 Hz/$\sqrt{\text{Hz}}$, leading to a relative linewidth of 12 Hz. The achieved noise level is about 100 times higher than the fundamental measurement limit set by shot noise. We note in passing that when an ECDL gradually goes out of alignment, the previously adjusted gain of the current loop will tend to make the servo oscillate so a new alignment is needed. The laser FM sideband used to generate the locking signal is produced directly by current modulation. An electronic filter network is employed to superimpose the slow servo, fast servo, and modulation inputs to the diode. Exercise caution when accessing the diode head, as a few extra mA current increase can lead to drastic output power increase and melted laser facets, all in 1 μs!

27.4 SUMMARY AND OUTLOOK

The technology of laser frequency stabilization has been refined and simplified over the years and has become an indispensable research tool in any modern laboratory involving optics. Research on laser stabilization has been and still is pushing the limits of measurement science. Indeed, a number of currently active research projects on fundamental physical principles benefit a great deal from stable optical sources and will need a continued progress of the laser stabilization front.[54] Using extremely stable phase coherent optical sources, we will be entering an exciting era when picometer resolution can be achieved over a million kilometer distance in the space[55] or a few Hertz linewidth of an ultraviolet resonance can be probed with a high S/N.[56] One has to be optimistic looking at the stabilization results of all different kinds of lasers. To list just a few examples of cw tunable lasers, we notice milliHertz linewidth stabilization (relative to a cavity) for diode-pumped solid state lasers; dozen milliHertz linewidth for Ti:Sapphire lasers; and sub-Hertz linewidths for diode and dye lasers. Long-term stability of lasers referenced to atoms and molecules have reached mid 10^{-15} level in a short averaging time of ~300 s. Phase locking between different laser systems can be achieved, even for diode lasers that have fast frequency noise. Recent developments in ultrawide bandwidth optical frequency combs based on femtosecond laser technologies have brought a revolutionary step in the field of optical frequency metrology, [57,58] promising further rapid advances in this field. A network of ultrastable frequency marks across the entire visible spectrum has just been realized.[59]

Quantum noise is the usual limit of the measurement process and therefore will be the limit of the stabilization process as well. Effort to circumvent the quantum noise altogether forms an active research field itself.[60] We, however, have not reached this quantum limit just yet. For instance, we have already stated that the Nd:YAG laser should be able to reach microHertz stability if the shot noise is the true limit. What have we done wrong? A main part of the deficiency is due to the inadequacy of the measurement process, namely the lack of accuracy. This is because the signal recovery effort—modulation and demodulation process—is contaminated by spurious optical interference effects and RAM associated with the modulation frequency. Every optical surface along the beam path can be a potential time bomb to damage the modulation performance. In cases that some low contrast interference effects are not totally avoidable, we would need to have the whole system controlled in terms of the surrounding pressure and temperature. The degree to which we can exert control of course dictates the ultimate performance.

27.5 CONCLUSIONS AND RECOMMENDATIONS

It becomes clear that there are many interlinking considerations involved in the design of laser stabilization systems, and it is difficult to present a full description in an article such as this. Still it is hoped that the reader will see some avenues to employ feedback control meth-

ods to the laser systems of her current interest. We are optimistic that some of this technology may become commercially available in the future, thus simplifying the user's task.

27.6 ACKNOWLEDGMENTS

The work discussed here has profited from interactions with many colleagues, postdoctoral researchers, and graduate students over many years. In particular we must thank Leo Hollberg and Miao Zhu for their earlier contributions. One of us (JLH) is particularly grateful to his wife Lindy for patience beyond the call of duty during these many years of laser research. The work at JILA has been supported over the years by the Office of Naval Research, the National Science Foundation, the Air Force Office of Scientific Research, and the National Institute of Standards and Technology, as part of its frontier research into basic standards and their applications.

27.7 REFERENCES

1. D. W. Allan, *Proc. IEEE* **54**:221 (1966).
2. "Characterization of Clocks and Oscillators," D. B. Sullivan, D. W. Allan, D. A. Howe, and F. L. Walls (eds.) NIST Technical Note 1337, U.S. Government Printing Office, Washington DC, 1990.
3. D. S. Elliot, R. Roy and S. J. Smith, *Phys. Rev.* **A 26**:12 (1982).
4. J. L. Hall and M. Zhu, in *Proc. of the International School of Phys.* 'Enrico Fermi', Course CXVIII, *Laser Manipulation of Atoms and Ions,* 671, E. Arimondo, W. D. Phillips and F. Strumia (eds.), North Holland, 671 (1992).
5. M. Zhu and J. L. Hall, *J. Opt. Soc. Am.* **B 10**:802 (1993).
6. For similar issues in the microwave/rf field, see the application note "Time keeping and Frequency Calibration," Hewlett Packard Company, Palo Alto, CA.
7. For general references on feedback systems, please refer to Richard C. Dorf, *Modern Control Systems,* 3rd edition, Addison-Wesley, Reading, MA, 1980.
8. Gene F. Franklin, J. David Powell, and A. Emami-Naeini, *Feedback Control of Dynamic Systems,* 3rd edition, Addison-Wesley, Reading, MA, 1994.
9. The simulations presented here are performed with the following software: Matlab Control Systems Toolbox: User's Guide; Matlab Simulink: User's Guide; The Math Works Inc., Nattick MA (1996).
10. See, e.g., J. L. Hall, in *Frequency-Stabilized Lasers and Their Applications,* Y. C. Chung (ed.), *Proc. SPIE* **1837**:2 (1993).
11. R. L. Barger, M. S. Sorem, and J. L. Hall, *Appl. Phys. Lett.* **22**:573 (1973).
12. G. D. Houser and E. Garmire, *Appl. Opt.* **33**:1059 (1994).
13. K. L. Haller and P. C. D. Hobbs, in *Optical Methods for Ultrasensitive Detection and Analysis: Techniques and Applications,* B. L. Fearey (ed.), *Proc. SPIE* **1435**:298 (1991).
14. J. Helmcke, S. A. Lee, and J. L. Hall, *Appl. Opt.* **21**:1686 (1982).
15. C. E. Wieman and T. W. Hänsch, *Phys. Rev. Lett.* **36**:1170 (1976).
16. T. W. Hänsch and B. Couillaud, *Opt. Comm.* **35**:441 (1980).
17. H. Wahlquist, *J. Chem. Phys.* **35**:1708 (1961).
18. T. J. Quinn, *Metrologia* **30**:524 (1994).
19. J. Hu, E. Ikonen, and K. Riski, *Opt. Comm.* **120**:65 (1995).
20. M. S. Taubman and J. L. Hall, *Opt. Lett.* (in press 2000).
21. B. Smaller, *Phys. Rev.* **83**:812–820 (1951); and R. V. Pound, *Rev. Sci. Instrum.* **17**:490 (1946).
22. G. C. Bjorklund, *Opt. Lett.* **5**:15 (1980).
23. G. C. Bjorklund and M. D. Levenson, *Phys. Rev.* **A 24**:166–169 (1981).

24. J. L. Hall, L. Hollberg, T. Baer, and H. G. Robinson, *Appl. Phys. Lett.* **39**:680–682 (1981).
25. W. Zapka, M. D. Levenson, F. M. Schellenberg, A. C. Tam, and G. C. Bjorklund, *Opt. Lett.* **8**:27 (1983).
26. G. J. Rosasco and W. S. Hurst, *J. Opt. Soc. Am.* **B 2**:1485–1496 (1985).
27. J. H. Shirley, *Opt. Lett.* **7**:537 (1982).
28. R. W. P. Drever, J. L. Hall, F. V. Kowalski, J. Hough, G. M. Ford, A. J. Munley, and H. Ward, *Appl. Phys.* **B 31**:97 (1983).
29. P. Werle, *Appl. Phys.* **B 60**:499 (1995).
30. J. L. Hall, J. Ye, L.-S. Ma, K. Vogel, and T. Dinneen, in *Laser Spectroscopy XIII,* Z.-J. Wang, Z.-M. Zhang, and Y.-Z. Wang (eds.), World Scientific, Singapore, 1998 pp. 75–80.
31. N. C. Wong and J. L. Hall, *J. Opt. Soc. Am.* **B 2**:1527 (1985).
32. M. S. Taubman and J. L. Hall (work in progress 2000).
33. D. R. Hjelme, S. Neegård, and E. Vartdal, *Opt. Lett.* **20**:1731 (1995).
34. G. R. Janik, C. B. Carlisle, and T. F. Gallagher, *J. Opt. Soc. Am.* **B 3**:1070 (1986).
35. J. L. Hall, L.-S. Ma, and G. Kramer, *IEEE J. Quan. Electro.* **QE-23**:427 (1987).
36. M. Kourogi, K. Nakagawa, and M. Ohtsu, *IEEE J. Quan. Electron.* **QE-29**:2693 (1993).
37. Th. Udem, J. Reichert, R. Holzwarth, and T. W. Hänsch, *Opt. Lett.* **24**:881 (1999).
38. S. A. Diddams, L.-S. Ma, J. Ye, and J. L. Hall, *Opt. Lett.* **24**:1747 (1999).
39. B. C. Young, F. C. Cruz, W. M. Itano, and J. C. Bergquist, *Phys. Rev. Lett.* **82**:3799 (1999).
40. Interested readers are referred to the following book for more detailed discussions: *The Quantum Physics of Atomic Frequency Standards,* volumes I and II, Jacques Vanier and Claude Audoin, Adam Hilger, Institute of Physics Publishing Ltd, Bristol, UK (1989).
41. T. M. Niebauer, J. E. Faller, H. M. Godwin, J. L. Hall and R. L. Barger, *Appl. Opt.* **27**:1285 (1988).
42. Jun Ishikawa, private communications (1996).
43. J. L. Hall and T. W. Hänsch, *Opt. Lett.* **9**:502 (1984).
44. J. Ye, L.-S. Ma, and J. L. Hall, *J. Opt. Soc. Am.* **B 15**:6 (1998).
45. J. Ye and J. L. Hall, *Opt. Lett.* **24**:1838 (1999).
46. A. Arie and R. L. Byer, *J. Opt. Soc. Am.* **B 10**:1990 (1993).
47. M. L. Eickhoff and J. L. Hall, *IEEE Trans. Instrum. & Meas.* **44**:155 (1995); and P. Jungner, M. Eickhoff, S. Swartz, J. Ye, J. L. Hall and S. Waltman, *IEEE Trans. Instrum. & Meas.* **44**:151 (1995).
48. J. Ye, L. Robertsson, S. Picard, L.-S. Ma, and John L. Hall, *IEEE Trans. Instrum. & Meas.* **48**:544 (1999).
49. J. L. Hall, L.-S. Ma, M. Taubman, B. Tiemann, F.-L. Hong, O. Pfister, and J. Ye, *IEEE Trans. Instrum. & Meas.* **48**:583, (1999).
50. C. E. Wieman and L. Hollberg, *Rev. Sci. Instrum.* **62**:1 (1991).
51. M. G. Littman and H. J. Metcalf, *Appl. Opt.* **17**:2224 (1978).
52. B. Dahmani, L. Hollberg, and R. Drullinger, *Opt. Lett.* **12**:876 (1987).
53. K. MacAdam, A. Steinbach, and C. E. Wieman, *Am. J. Phys.* **60**:1098 (1992).
54. P. Fritschel, G. González, B. Lantz, P. Saha, and M. Zucker, *Phys. Rev. Lett.* **80**:3181 (1998).
55. K. Danzmann, *Class. Quantum Grav.* **14**:1399 (1997).
56. J. C. Bergquist, W. M. Itano, and D. J. Wineland, in *Frontiers in Laser Spectroscopy,* 359 (1994); J. C. Bergquist, private communications (1999).
57. T. Udem, J. Reichert, R. Holzwarth, and T. W. Hänsch, *Phys. Rev. Lett.* **82**:3568 (1999).
58. S. A. Diddams, D. J. Jones, J. Ye, S. T. Cundiff, J. L. Hall, J. K. Ranka, R. S. Windeler, T. Udem, R. Holzwarth, and T. W. Hänsch, *Phys. Rev. Lett.* **84**:5012 (2000).
59. J. Ye, J. L. Hall, and S. A. Diddams, *Opt. Lett.* in press, 2000.
60. V. B. Braginsky and F. Y. Khalili, *Quantum Measurement,* Cambridge University Press, Cambridge, UK, 1992.

CHAPTER 28
LASER COOLING AND TRAPPING OF ATOMS

H. J. Metcalf
Department of Physics, State University of New York
Stony Brook, New York

P. van der Straten
Debye Institute, Department of Atomic and Interface Physics
Utrecht University
Utrecht, The Netherlands

28.1 INTRODUCTION

This chapter begins with some of the general ideas about laser cooling. One of the characteristics of optical control of atomic motion is that the speed of atoms can be considerably reduced. Since the spread of velocities of a sample of atoms is directly related to its temperature, the field has been dubbed *laser cooling,* and this name has persisted throughout the years.

In Sec. 28.2 we introduce the general idea of optical forces and how they can act on atoms. We show how such forces can be velocity dependent, and thus nonconservative, which makes it possible to use optical forces for cooling. The section concludes with the discussion of a few special temperatures. Section 28.3 presents a quantum mechanical description of the origin of the force resulting from the atomic response to both stimulated and spontaneous emission processes. This is quite different from the familiar quantum mechanical calculations using state vectors to describe the state of the system, since spontaneous emission causes the state of the system to evolve from a pure state into a mixed state. Since spontaneous emission is an essential ingredient for the dissipative nature of the optical forces, the density matrix is introduced to describe it. The evolution of the density matrix is given by the optical Bloch equations (OBE), and the optical force is calculated from them. It is through the OBE that the dissipative aspects of laser cooling are introduced to the otherwise conservative quantum mechanics. The velocity dependence is treated as an extension of the force on an atom at rest.

In Sec. 28.4 the first modern laser cooling experiments are described. Atoms in beams were slowed down from thermal velocity to a few m/s, and the dominant problem was the change in Doppler shift arising from such a large change in velocity. Some typical values of parameters are discussed and tabulated. Section 28.5 introduces true cooling by optical forces to the μK regime. Such experiments require at least two laser beams, and are called *optical molasses* because the resulting viscous force can slow atoms to extremely slow velocities, and hence compress the width of the velocity distribution. The limits of such laser cooling are dis-

Copyright 2001 by The McGraw-Hill Companies, Inc. Click Here for Terms of Use.

cussed, as well as the extension from experiments in 1D to 3D. Here the velocity dependence of the force is built into the description via the Doppler shift instead of being added in as an extension of the treatment. In 1988 some experiments reported temperatures below the limit calculated for optical molasses, and Sec. 28.6 presents the new description of laser cooling that emerged from this surprise. For the first time, the force resulting from spontaneous emission in combination with the multiple level structure of real atoms were embodied in the discussion. Here the new limits of laser cooling are presented.

The discussion up to this point has been on atomic velocities, and thus can be described in terms of a velocity space. Laser cooling thus collects atoms near the origin of velocity space. It is also possible to collect atoms into a small region of ordinary configuration space, and such trapping is discussed in Sec. 28.7. Neutral atom traps can employ magnetic fields, optical fields, and both working together. However, such traps are always very shallow, and so only atoms that have been cooled to the few mK domain can be captured. The combination of laser cooling and atom trapping has produced astounding new tools for atomic physicists, and Sec. 28.8 describes some of the applications and uses of these wonderful new capabilities.

28.2 GENERAL PROPERTIES CONCERNING LASER COOLING

These experiments almost always involve atomic absorption of nearly resonant light. The energy of the light $\hbar\omega$ raises the internal energy of the atom, and the angular momentum $\hbar$ changes the internal angular momentum ℓ of the electron, as described by the well-known selection rule $\Delta\ell = \pm 1$. By contrast, the linear momentum of the light $p = E/c = h/\lambda$ ($\vec{p} = \hbar\vec{k}$) cannot be absorbed by internal atomic degrees of freedom, and therefore must change the motion of the atoms in the laboratory frame. The force resulting from this momentum exchange between the light field and the atoms can be used in many ways to control atomic motion, and is the subject of this chapter.

Absorption of light populates the atomic excited state, and the return to the ground state can be either by spontaneous or by stimulated emission. The nature of the optical force that arises from these two different processes is quite different, and will be described separately. Such atomic transitions (*i.e.,* the motion of the atomic electrons) must be described quantum mechanically in the well-known form of the Schrödinger equation. By contrast, the center-of-mass motion of the atoms can usually be described classically, but there are many cases where even this is not possible so it must also involve quantum mechanics.

In the simplest possible case, the absorption of well-directed light from a laser beam, the momentum exchange between the light field and the atoms results in a force

$$\vec{F} = d\vec{p}/dt = \hbar\vec{k}\gamma_p \tag{1}$$

where γ_p is the excitation rate of the atoms. The absorption leaves the atoms in their excited state, and if the light intensity is low enough so that they are much more likely to return to the ground state by spontaneous emission than by stimulated emission, the resulting fluorescent light carries off momentum $\hbar k$ in a random direction. The momentum exchange from the fluorescence averages zero, so the net total force is given by Eq. (1).

The scattering rate γ_p depends on the laser detuning from atomic resonance $\delta = \omega_\ell - \omega_a$, where ω_ℓ is the laser frequency and ω_a is the atomic resonance frequency. This detuning is measured in the atomic reference frame, and it is necessary that the Doppler-shifted laser frequency in the moving atoms' reference frame be used to calculate the absorption and scattering rate. Then γ_p is given by the Lorentzian

$$\gamma_p = \frac{s_0\gamma/2}{1 + s_0 + [2(\delta + \omega_D)/\gamma]^2} \tag{2}$$

where $\gamma \equiv 1/\tau$ is the angular frequency corresponding to the decay rate of the excited state. Here $s_0 = I/I_s$ is the ratio of the light intensity I to the saturation intensity $I_s \equiv \pi hc/3\lambda^3\tau$, which is a few mW/cm^2 for typical atomic transitions (λ is the optical wavelength). The Doppler shift seen by the moving atoms is $\omega_D = -\vec{k} \cdot \vec{v}$ (note that $\vec{k}$ opposite to $\vec{v}$ produces a positive Doppler shift). The force is thus velocity-dependent, and the experimenter's task is to exploit this dependence to the desired goal, for example, optical friction for laser cooling.

The spontaneous emission events produce unpredictable changes in atomic momenta so the discussion of atomic motion must also include a "random walk" component. This can be described as a diffusion of the atomic momenta in momentum space, similar to Brownian motion in real space. The evolution of the momentum in such circumstances is described by the Fokker-Planck equation, and it can be used for a more formal treatment of the laser cooling process. Solutions of the Fokker-Planck equation in limiting cases can ultimately be used to relate the velocity distribution of the atoms with their temperature.

The idea of "temperature" in laser cooling requires some careful discussion and disclaimers. In thermodynamics, temperature is carefully defined as a parameter of the state of a closed system in thermal equilibrium with its surroundings. This, of course, requires that there be thermal contact (*i.e.,* heat exchange) with the environment. In laser cooling this is clearly not the case because a sample of atoms is always absorbing and scattering light. Furthermore, there is essentially no heat exchange (the light cannot be considered as heat even though it is indeed a form of energy). Thus the system may very well be in a steady-state situation, but certainly not in thermal equilibrium, so that the assignment of a thermodynamic "temperature" is completely inappropriate.

Nevertheless, it is convenient to use the label of temperature to describe an atomic sample whose average kinetic energy $\langle E_k \rangle$ in one dimension has been reduced by the laser light, and this is written simply as $k_B T/2 = \langle E_k \rangle$, where k_B is Boltzmann's constant. It must be remembered that this temperature assignment is absolutely inadequate for atomic samples that do not have a Maxwell-Boltzmann velocity distribution, whether or not they are in thermal equilibrium: there are infinitely many velocity distributions that have the same value of $\langle E_k \rangle$ but are so different from one another that characterizing them by the same "temperature" is a severe error.

With these ideas in mind, it is useful to define a few rather special values of temperatures associated with laser cooling. The highest of these temperatures corresponds to the energy associated with atoms whose speed and concomitant Doppler shift puts them just at the boundary of absorption of light. This velocity is $v_c \equiv \gamma/k \sim$ few m/s, and the corresponding temperature is $k_B T_c \equiv M\gamma^2/k^2$, and is typically several mK. (Here M is the atomic mass.)

The next characteristic temperature corresponds to the energy associated with the natural width of atomic transitions, and is called the *Doppler temperature.* It is given by $k_B T_D \equiv \hbar\gamma/2$. Because it corresponds to the limit of certain laser cooling processes, it is often called the *Doppler limit,* and is typically several hundred μK. Associated with this temperature is the one-dimensional velocity $v_D = \sqrt{k_B T_D/M} \sim 30$ cm/s.

The last of these three characteristic temperatures corresponds to the energy associated with a single photon recoil. In the absorption or emission process of a single photon, the atoms obtain a recoil velocity $v_r \equiv \hbar k/M$. The corresponding energy change can be related to a temperature, the *recoil limit,* defined as $k_B T_r \equiv \hbar^2 k^2/M$, and is generally regarded as the lower limit for optical cooling processes (although there are a few clever schemes that cool below it). It is typically a few μK, and corresponds to speeds of $v_r \sim 1$ cm/s.

These three temperatures are related to one another through a single dimensionless parameter $\varepsilon \equiv \omega_r/\gamma$ that is ubiquitous in describing laser cooling. It is the ratio of the recoil frequency $\omega_r \equiv \hbar k^2/2M$ to the natural width γ, and as such embodies most of the important information that characterize laser cooling on a particular atomic transition. Typically $\varepsilon \sim 10^{-3} - 10^{-2}$, and clearly $T_r = 4\varepsilon T_D = 4\varepsilon^2 T_c$.

In laser cooling and related aspects of optical control of atomic motion, the forces arise because of the exchange of momentum between the atoms and the laser field. Since the energy and momentum exchange is necessarily in discrete quanta rather than continuous, the

interaction is characterized by finite momentum *kicks*. This is often described in terms of *steps* in a fictitious space whose axes are momentum rather than position. These steps in momentum space are of size $\hbar k$ and thus are generally small compared to the magnitude of the atomic momenta at thermal velocities $\bar{v}$. This is easily seen by comparing $\hbar k$ with $M\bar{v}$,

$$\frac{\hbar k}{M\bar{v}} = \sqrt{\frac{T_r}{T}} \ll 1 \tag{3}$$

Thus the scattering of a single photon has a negligibly small effect on the motion of thermal atoms, but repeated cycles of absorption and emission can cause a large change of the atomic momenta and velocities.

28.3 THEORETICAL DESCRIPTION

Force on a Two-Level Atom

We begin the calculation of the optical force on atoms by considering the simplest schemes, namely, a single-frequency light field interacting with a two-level atom confined to one dimension. It is based on the interaction of two-level atoms with a laser field as discussed in many textbooks.[1]

The philosophy of the correspondence principle requires a smooth transition between quantum and classical mechanics. Thus the force F on an atom is defined as the expectation value of the quantum mechanical force operator $\mathcal{F}$, as defined by $F = \langle \mathcal{F} \rangle = \mathrm{d}\langle p \rangle / \mathrm{d}t$. The time evolution of the expectation value of a time-independent quantum mechanical operator $\mathcal{A}$ is given by

$$\frac{\mathrm{d}}{\mathrm{d}t}\langle \mathcal{A} \rangle = \frac{i}{\hbar}\langle [\mathcal{H}, \mathcal{A}] \rangle \tag{4}$$

The commutator of $\mathcal{H}$ and p is given by $[\mathcal{H}, p] = i\hbar(\partial\mathcal{H}/\partial z)$, where the operator p has been replaced by $-i\hbar(\partial/\partial z)$. The force on an atom is then given by

$$F = -\left\langle \frac{\partial \mathcal{H}}{\partial z} \right\rangle \tag{5}$$

This relation is a specific example of the Ehrenfest theorem and forms the quantum mechanical analog of the classical expression that the force is the negative gradient of the potential.

Discussion of the force on atoms caused by light fields begins with that part of the Hamiltonian that describes the electric dipole interaction between the atom and the light field. The electric field of the light is written as $\vec{\mathcal{E}}(\vec{r}, t) = E_0\hat{\varepsilon}\cos(kz - \omega t)$ and the interaction Hamiltonian is $\mathcal{H}' = e\vec{\mathcal{E}}(\vec{r}, t) \cdot \vec{r}$ where $\vec{r}$ is the electron coordinate. It has only off-diagonal matrix elements given by $\mathcal{H}'_{eg} = -eE_0\hat{\varepsilon} \cdot \langle e|\vec{r}|g\rangle$ where e and g represent the excited and ground states respectively. The force depends on the atomic state as determined by its interaction with the light, and is calculated from the expectation value $\langle \mathcal{A} \rangle = \mathrm{Tr}(\rho\mathcal{A})$ as in Eq. (4), where ρ is the density matrix found by solving the optical Bloch equations (OBE).[1] Then

$$F = \hbar\left(\frac{\partial\Omega}{\partial z}\rho^*_{eg} + \frac{\partial\Omega^*}{\partial z}\rho_{eg}\right) \tag{6}$$

where the Rabi frequency is defined as $\hbar\Omega \equiv \mathcal{H}'_{eg}$. Note that the force depends on the state of the atom, and in particular, on the optical coherence between the ground and excited states, ρ_{eg}.

Although it may seem a bit artificial, it is instructive to split $\partial\Omega/\partial z$ into its real and imaginary parts (the matrix element that defines Ω can certainly be complex):

$$\frac{\partial\Omega}{\partial z} = (q_r + iq_i)\Omega \tag{7}$$

Here $q_r + iq_i$ is the logarithmic derivative of Ω. In general, for a field $E(z) = E_0(z)\exp(i\phi(z)) + \text{c.c.}$, the real part of the logarithmic derivative corresponds to a gradient of the amplitude $E_0(z)$ and the imaginary part to a gradient of the phase $\phi(z)$. Then the expression for the force becomes

$$F = \hbar q_r(\Omega\rho_{eg}^* + \Omega^*\rho_{eg}) + i\hbar q_i(\Omega\rho_{eg}^* - \Omega^*\rho_{eg}) \tag{8}$$

Equation (8) is a very general result that can be used to find the force for any particular situation as long as the OBE for ρ_{eg} can be solved. In spite of the chosen complex expression for Ω, it is important to note that the force itself is real, and that first term of the force is proportional to the real part of $\Omega\rho_{eg}^*$, whereas the second term is proportional to the imaginary part.

A Two-Level Atom at Rest

There are two important special optical arrangements to consider. The first one is a traveling wave whose electric field is $E(z) = (E_0/2)\,(e^{i(kz-\omega t)} + \text{c.c.})$. In calculating the Rabi frequency from this, the rotating wave approximation (RWA) causes the positive frequency component of $E(z)$ to drop out. Then the gradient of the Rabi frequency becomes proportional to the gradient of the surviving negative frequency component, so that $q_r = 0$ and $q_i = k$. For such a traveling wave the amplitude is constant but the phase is not, and this leads to the nonzero value of q_i.

This is in direct contrast to the case of a standing wave, composed of two counterpropagating traveling waves so its amplitude is twice as large, for which the electric field is given by $E(z) = E_0 \cos(kz)\,(e^{-i\omega t} + \text{c.c.})$, so that $q_r = -k \tan(kz)$ and $q_i = 0$. Again, only the negative frequency part survives the RWA, but the gradient does not depend on it. Thus a standing wave has an amplitude gradient, but not a phase gradient.

The steady-state solutions of the OBE for a two-level atom at rest provide simple expressions for ρ.[1] Substituting the solution for ρ_{eg} into Eq. (8) gives

$$F = \frac{\hbar s}{1+s}\left(-\delta q_r + \frac{1}{2}\gamma q_i\right) \tag{9}$$

where $s \equiv s_0/[1 + (2\delta/\gamma)^2]$ is the off-resonance saturation parameter. Note that the first term is proportional to the detuning δ, whereas the second term is proportional to the decay rate γ. For zero detuning, the force for a traveling wave becomes $F = (\hbar k\gamma/2)[s_0/(s_0 + 1)]$, a very satisfying result because it is simply the momentum per photon $\hbar k$, times the scattering rate γ_p at resonance of Eq. (2).

It is instructive to identify the origin of both terms in Eq. (9). Absorption of light leads to the transfer of momentum from the optical field to the atoms. If the atoms decay by spontaneous emission, the recoil associated with the spontaneous fluorescence is in a random direction, so its average over many emission events results in zero net effect on the atomic momentum. Thus the force from absorption followed by spontaneous emission can be written as $F_{\text{sp}} = \hbar k\gamma\rho_{ee}$, where $\hbar k$ is the momentum transfer for each photon, γ is the rate for the process, and ρ_{ee} is the probability for the atoms to be in the excited state. Using Eq. (2), the force resulting from absorption followed by spontaneous emission becomes

$$F_{\text{sp}} = \frac{\hbar k s_0 \gamma/2}{1 + s_0 + (2\delta/\gamma)^2} \tag{10}$$

which saturates at large intensity as a result of the term s_0 in the denominator. Increasing the rate of absorption by increasing the intensity does not increase the force without limit, since

that would only increase the rate of stimulated emission, where the transfer of momentum is opposite in direction compared to the absorption. Thus the force saturates to a maximum value of $\hbar k\gamma/2$, because ρ_{ee} has a maximum value of ½.

Examination of Eq. (10) shows that it clearly corresponds to the second term of Eq. (8). This term is called the *light pressure force, radiation pressure force, scattering force,* or *dissipative force,* since it relies on the scattering of light out of the laser beam. It vanishes for an atom at rest in a standing wave where $q_i = 0$, and this can be understood because atoms can absorb light from either of the two counterpropagating beams that make up the standing wave, and the average momentum transfer then vanishes. This force is dissipative because the reverse of spontaneous emission is not possible, and therefore the action of the force cannot be reversed. It plays a very important role in the slowing and cooling of atoms.

By contrast, the first term in Eq. (8) derives from the light shifts of the ground and excited states that depend on the strength of the optical electric field. A standing wave is composed of two counterpropagating laser beams, and their interference produces an amplitude gradient that is not present in a traveling wave. The force is proportional to the gradient of the light shift, and the ground-state light shift $\Delta E_g = \hbar\Omega^2/4\delta$ can be used to find the force on ground-state atoms in low intensity light:

$$F_{\text{dip}} = -\frac{\partial(\Delta E_g)}{\partial z} = \frac{\hbar\Omega}{2\delta}\frac{\partial\Omega}{\partial z} \tag{11}$$

For an amplitude-gradient light field such as a standing wave, $\partial\Omega/\partial z = q_r\Omega$, and this force corresponds to the first term in Eq. (8) in the limit of low saturation ($s \ll 1$).

For the case of a standing wave Eq. (9) becomes

$$F_{\text{dip}} = \frac{2\hbar k\delta s_0 \sin 2kz}{1 + 4s_0\cos^2 kz + (2\delta/\gamma)^2} \tag{12}$$

where s_0 is the saturation parameter of each of the two beams that form the standing wave. For $\delta < 0$ the force drives the atoms to positions where the intensity has a maximum, whereas for $\delta > 0$ the atoms are attracted to the intensity minima. The force is conservative and therefore cannot be used for cooling. This is called the *dipole force, reactive force, gradient force,* or *redistribution force.* It has the same origin as the force of an inhomogeneous DC electric field on a classical dipole, but relies on the redistribution of photons from one laser beam to the other.

It needs to be emphasized that the forces of Eqs. (10) and (12) are two fundamentally different kinds of forces. For an atom at rest, the scattering force vanishes for a standing wave, whereas the dipole force vanishes for a traveling wave. The scattering force is dissipative, and can be used to cool, whereas the dipole force is conservative, and can be used to trap. Dipole forces can be made large by using high-intensity light because they do not saturate. However, since the forces are conservative, they cannot be used to cool a sample of atoms. Nevertheless, they can be combined with the dissipative scattering force to enhance cooling in several different ways. By contrast, scattering forces are always limited by the rate of spontaneous emission γ and cannot be made arbitrarily strong, but they are dissipative and are required for cooling.

Atoms in Motion

Laser cooling requires dissipative or velocity-dependent forces that cannot be conservative. The procedure followed here is to treat the velocity of the atoms as a small perturbation, and make first-order corrections to the solutions of the OBE obtained for atoms at rest.[2] It begins by adding drift terms in the expressions for the relevant quantities. Thus the Rabi frequency satisfies

$$\frac{d\Omega}{dt} = \frac{\partial\Omega}{\partial t} + v\frac{\partial\Omega}{\partial z} = \frac{\partial\Omega}{\partial t} + v(q_r + iq_i)\Omega \tag{13}$$

where Eq. (7) has been used to separate the gradient of Ω into real and imaginary parts. Differentiating the steady state density matrix elements found by solving the OBE[1] leads to

$$\frac{dw}{dt} = \frac{\partial w}{\partial t} + v\frac{\partial w}{\partial z} = \frac{\partial w}{\partial t} - \frac{2vq_r s}{(1+s)^2} \tag{14}$$

since $s_0 = 2|\Omega|^2/\gamma^2$ and Ω depends on z. Here $w \equiv \rho_{gg} - \rho_{ee}$. Similarly,

$$\frac{d\rho_{eg}}{dt} = \frac{\partial \rho_{eg}}{\partial t} + v\frac{\partial \rho_{eg}}{\partial z} = \frac{\partial \rho_{eg}}{\partial t} - \frac{iv\Omega}{2(\gamma/2 - i\delta)(1+s)}\left[q_r\left(\frac{1-s}{1+s}\right) + iq_i\right] \tag{15}$$

Since neither w nor ρ_{eg} is explicitly time-dependent, both $\partial w/\partial t$ and $\partial \rho_{eg}/\partial t$ vanish. The Eqs. (14) and (15) are still difficult to solve analytically for a general optical field, and the results are not very instructive. However, the solution for the two special cases of the standing and traveling waves provide considerable insight.

For a traveling wave $q_r = 0$, and the velocity-dependent force can be found by combining Eqs. (14) and (15) with the OBE to eliminate the time derivatives. The resulting coupled equations can be separated and substituted into Eq. (8) for the force to find, after considerable algebra,

$$F = \hbar q_i \frac{s\gamma/2}{1+s}\left(1 + \frac{2\delta v q_i}{(1+s)(\delta^2 + \gamma^2/4)}\right) \equiv F_0 - \beta v \tag{16}$$

The first term is the velocity-independent force F_0 for an atom at rest given by Eq. (9). The second term is velocity-dependent and can lead to compression of the velocity distribution. For a traveling wave $q_i = k$ and thus the damping coefficient β is given by

$$\beta = -\hbar k^2 \frac{4s_0(\delta/\gamma)}{(1 + s_0 + (2\delta/\gamma)^2)^2} \tag{17}$$

Such a force can compress the velocity distribution of an atomic sample for negative values of δ (*i.e.,* for red detuned light). For small detuning and low intensity the damping coefficient β is linear in both parameters. However, for detunings much larger than γ and intensities much larger than I_s, β saturates and even decreases as a result of the dominance of δ in the denominator of Eq. (17). This behavior can be seen in Fig. 1, where the damping coefficient β has been plotted as a function of detuning for different saturation parameters. The decrease of β for large detunings and intensities is caused by saturation of the transition, in which case the absorption rate becomes only weakly dependent on the velocity. The maximum value of β is obtained for $\delta = -\gamma/2$ and $s_0 = 2$, and is given by $\beta_{max} = \hbar k^2/4$. The damping rate Γ is given by $\Gamma \equiv \beta/M$, and its maximum value is $\Gamma_{max} = \omega_r/2$, where ω_r is the recoil frequency. For the alkalis this rate is of the order of 10^4–10^5 s^{-1}, indicating that atomic velocity distributions can be compressed in about 10–100 μs. Furthermore, F_0 in Eq. (16) is always present and so the atoms are *not* damped toward any constant velocity.

For a standing wave $q_i = 0$, and just as above, the velocity-dependent force can be found by combining Eqs. (14) and (15) with the OBE to eliminate the time derivatives. The resulting coupled equations can again be separated and substituted into Eq. (8) for the force to find

$$F = -\hbar q_r \frac{s\delta}{1+s}\left(1 - vq_r \frac{(1-s)\gamma^2 - 2s^2(\delta^2 + \gamma^2/4)}{(\delta^2 + \gamma^2/4)(1+s)^2\gamma}\right) \tag{18}$$

where $q_r = -k \tan(kz)$. In the limit of $s \ll 1$, this force is

$$F = \hbar k \frac{s_0\delta\gamma^2}{2(\delta^2 + \gamma^2/4)}\left(\sin 2kz + kv\frac{\gamma}{(\delta^2 + \gamma^2/4)}(1 - \cos 2kz)\right) \tag{19}$$

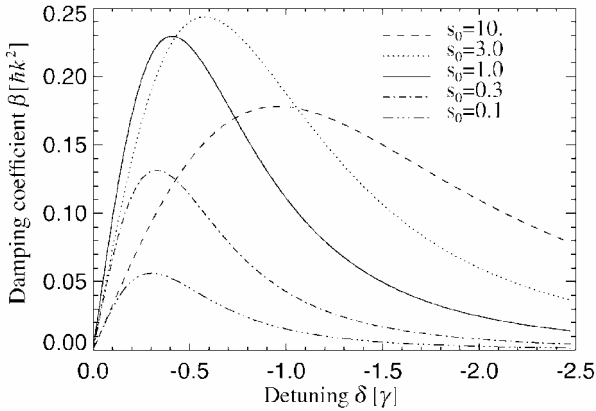

FIGURE 1 The damping coefficient β for an atom in a traveling wave as a function of the detuning for different values of the saturation parameter s_0. The damping coefficient is maximum for intermediate detunings and intensities.

Here s_0 is the saturation parameter of each of the two beams that compose the standing wave. The first term is the velocity-independent part of Eq. (9) and is sinusoidal in space, with a period of λ/2. Thus its spatial average vanishes. The force remaining after such averaging is $F_{av} = -\beta v$, where the damping coefficient β is given by

$$\beta = -\hbar k^2 \frac{8s_0(\delta/\gamma)}{(1 + (2\delta/\gamma)^2)^2} \tag{20}$$

In contrast to the traveling-wave case, this is a true damping force because there is no F_0, so atoms are slowed toward $v = 0$ independent of their initial velocities. Note that this expression for β is valid only for $s \ll 1$ because it depends on spontaneous emission to return atoms to their ground state.

There is an appealing description of the mechanism for this kind of cooling in a standing wave. With light detuned below resonance, atoms traveling toward one laser beam see it Doppler shifted upward, closer to resonance. Since such atoms are traveling away from the other laser beam, they see its light Doppler shifted further downward, hence further out of resonance. Atoms therefore scatter more light from the beam counterpropagating to their velocity so their velocity is reduced. This damping mechanism is called *optical molasses,* and is one of the most important tools of laser cooling.

Needless to say, such a pure damping force would reduce the atomic velocities, and hence the absolute temperature, to zero. Since this violates thermodynamics, there must be something left out of the description. It is the discreteness of the momentum changes in each case, $\Delta p = \hbar k$, that results in a minimum velocity change. The consequences of this discreteness can be described as a diffusion of the atomic momenta in momentum space by finite steps as discussed earlier.

The Fokker-Planck Equation

The random walk in momentum space associated with spontaneous emission is similar to Brownian motion in coordinate space. There is an analogous momentum diffusion constant

D, and so the atomic motion in momentum space can be described by the Fokker-Planck equation

$$\frac{\partial W(p,t)}{\partial t} = -\frac{\partial [F(p,t)W(p,t)]}{\partial p} + \frac{\partial^2 [D(p,t)W(p,t)]}{\partial p^2} \tag{21}$$

where $W(p, t)$ is the momentum distribution of the atoms. For the special case when both the force and the diffusion are independent of time, the formal stationary solution is

$$\overline{W}(p) = \frac{C}{D(p)} \exp\left(\int_0^p \frac{F(p')}{D(p')} \mathrm{d}p'\right) \tag{22}$$

where C is an integration constant. Once the force and diffusion are known, the stationary solution of the Fokker-Planck equation emerges easily.

In the simplest and most common case in laser cooling the force is proportional to the velocity and the diffusion is independent of velocity:

$$F(v) = -\beta v \text{ and } D(v) = D_0 \tag{23}$$

Then the stationary solution of Eq. (21) for $\overline{W}(v)$ is

$$\overline{W}(p) \propto e^{-\beta p^2/2MD_0} \tag{24}$$

This is indeed a Maxwell-Boltzmann distribution. For low intensity where spontaneous emission dominates, $D_0 = s\gamma(\hbar k)^2/2$, so the steady state temperature is given by $k_B T = D_0/\beta = \hbar\gamma/2$ for $\delta = -\gamma/2$, its optimum value.[1] This is called the *Doppler temperature* because the velocity dependence of the cooling mechanism derives from the Doppler shift. The fact that the conditions of Eq. (23) for the force and diffusion are often approximately correct explains why the notion of temperature often appears as a description of a laser-cooled sample.

One of the most important properties of laser cooling is its ability to change the phase space density of an atomic sample. Changing the phase space density provides a most important distinction between light optics and atom optics. The Hamiltonian description of geometrical optics leads to the brightness theorem, that can be found in many optics books. Thus bundles of light rays obey a similar phase space density conservation. But there is a fundamental difference between light and atom optics. In the first case, the "forces" that determine the behavior of bundles of rays are "conservative" and phase space density is conserved. For instance, a lens can be used to focus a light beam to a small spot; however, at the same time the divergence of the beam must be increased, thus conserving phase space density. By contrast, in atom optics dissipative forces that are velocity-dependent can be used, and thus phase space density is no longer conserved. Optical elements corresponding to such forces cannot exist for light, but in addition to the atom optic elements of lenses, collimators, and others, phase space compressors can also be built. Such compression is essential in a large number of cases, such as atomic beam brightening for collision studies or cooling for the achievement of Bose-Einstein condensation.

28.4 SLOWING ATOMIC BEAMS

Among the earliest laser cooling experiments was deceleration of atoms in a beam.[3] The authors exploited the Doppler shift to make the momentum exchange (hence the force) velocity-dependent. It worked by directing a laser beam opposite to an atomic beam so the atoms could absorb light, and hence momentum $\hbar k$, very many times along their paths through the apparatus as shown in Fig. 2.[3,4] Of course, excited-state atoms cannot absorb light efficiently from the laser that excited them, so between absorptions they must return to the ground state by spontaneous decay, accompanied by emission of fluorescent light. The spatial

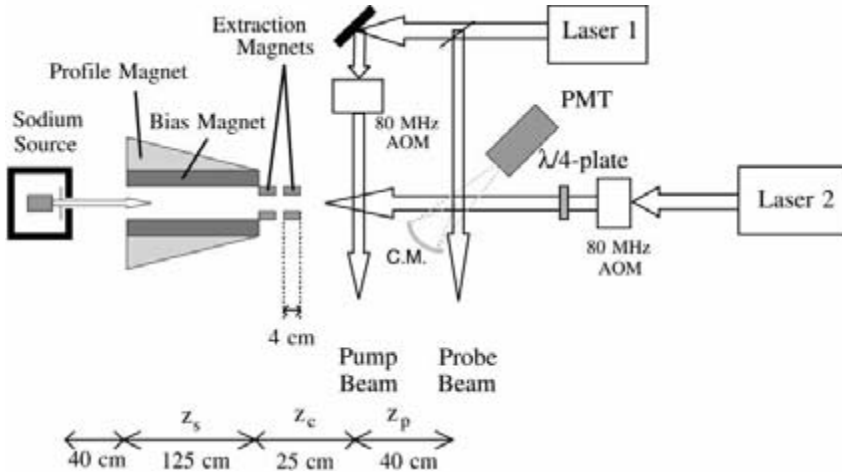

FIGURE 2 Schematic diagram of the apparatus for beam slowing. The tapered magnetic field is produced by layers of varying length on the solenoid, and the bias field is produced by full-length windings. The TOF aspect is implemented with Laser 1 whose beams optically pump the atoms between the hfs states.

symmetry of the emitted fluorescence results in an average of zero net momentum transfer from many such fluorescence events. Thus the net force on the atoms is in the direction of the laser beam, and the maximum deceleration is limited by the spontaneous emission rate γ.

The maximum attainable deceleration is obtained for very high light intensities, and is limited because the atom must then divide its time equally between ground and excited states. High-intensity light can produce faster absorption, but it also causes equally fast stimulated emission; the combination produces neither deceleration nor cooling because the momentum transfer to the atom in emission is then in the opposite direction to what it was in absorption. The force is limited to $F = \hbar k \gamma_p$, and so the deceleration therefore saturates at a value $\vec{a}_{\max} = \hbar \vec{k} \gamma / 2M$ [see Eq. (2)]. Since the maximum deceleration $\vec{a}_{\max}$ is fixed by atomic parameters, it is straightforward to calculate the minimum stopping length $L_{\min}$ and time $t_{\min}$ for the rms velocity of atoms $\bar{v} = 2\sqrt{k_B T/M}$ at the chosen temperature. The result is $L_{\min} = \bar{v}^2/2a_{\max}$ and $t_{\min} = \bar{v}/a_{\max}$. In Table 1 are some of the parameters for slowing a few atomic species of interest from the peak of the thermal velocity distribution.

Maximizing the scattering rate γ_p requires $\delta = -\omega_D$ in Eq. (2). If δ is chosen for a particular atomic velocity in the beam, then as the atoms slow down, their changing Doppler shift will take them out of resonance. They will eventually cease deceleration after their Doppler shift has been decreased by a few times the power-broadened width $\gamma' = \gamma\sqrt{1 + s_0}$, corresponding to Δv of a few times γ'/k. Although this Δv of a few m/s is considerably larger than the typical atomic recoil velocity $\hbar k/M$ of a few cm/s, it is still only a small fraction of the atoms' average thermal velocity $\bar{v}$, so that significant further cooling or deceleration cannot be accomplished.

In order to achieve deceleration that changes the atomic speeds by hundreds of m/s, it is necessary to maintain $(\delta + \omega_D) \ll \gamma$ by compensating such large changes of the Doppler shift. This can be done by changing ω_D, or δ via either ω_ℓ or ω_a. The two most common methods for maintaining this resonance are sweeping the laser frequency ω_ℓ along with the changing ω_D of the decelerating atoms,[5–7] or by spatially varying the atomic resonance frequency with an inhomogeneous DC magnetic field to keep the decelerating atoms in resonance with the fixed frequency laser.[1,3,8]

The use of a spatially varying magnetic field to tune the atomic levels along the beam path was the first method to succeed in slowing atoms.[3] It works as long as the Zeeman shifts of

TABLE 1 Parameters of Interest for Slowing Various Atoms

Atom	T_{oven} (K)	$\bar{v}$ (m/s)	L_{min} (m)	t_{min} (ms)
H	1000	5000	0.012	0.005
He*	4	158	0.03	0.34
He*	650	2013	4.4	4.4
Li	1017	2051	1.15	1.12
Na	712	876	0.42	0.96
K	617	626	0.77	2.45
Rb	568	402	0.75	3.72
Cs	544	319	0.93	5.82

The stopping length L_{min} and time t_{min} are minimum values. The oven temperature T_{oven} that determines the peak velocity is chosen to give a vapor pressure of 1 Torr. Special cases are H at 1000 K and He in the metastable triplet state, for which two rows are shown: one for a 4 K source and another for the typical discharge temperature.

the ground and excited states are different so that the resonant frequency is shifted. The field can be tailored to provide the appropriate Doppler shift along the moving atom's path. For uniform deceleration $a \equiv \eta a_{max}$ from initial velocity v_0, the appropriate field profile is $B(z) = B_0\sqrt{1 - z/z_0}$, where $z_0 \equiv Mv_0^2/\eta\hbar k\gamma$ is the length of the magnet, $B_0 = \hbar k v_0/\mu'$, $\mu' \equiv (g_e M_e - g_g M_g)\mu_B$, subscripts g and e refer to ground and excited states, $g_{g,e}$ is the Landé g-factor, μ_B is the Bohr magneton, and $M_{g,e}$ is the magnetic quantum number. The design parameter $\eta < 1$ determines the length of the magnet z_0. A solenoid that can produce such a spatially varying field has layers of decreasing lengths as shown schematically in Fig. 2. The technical problem of extracting the beam of slow atoms from the end of the solenoid can be simplified by reversing the field gradient and choosing a transition whose frequency decreases with increasing field.[9]

For alkali atoms such as Na, a time-of-flight (TOF) method can be used to measure the velocity distribution of atoms in the beam. It employs two additional beams labeled *pump* and *probe* from laser 1 as shown in Fig. 2. Because these beams cross the atomic beam at 90°, $\omega_D = -\vec{k} \cdot \vec{v} = 0$ and they excite atoms at all velocities. The pump beam is tuned to excite and empty a selected ground hyperfine state (hfs), and it transfers more than 98 percent of the population as the atoms pass through its 0.5 mm width. To measure the velocity distribution of atoms in the selected hfs, this pump laser beam is interrupted for a period $\Delta t = 10 - 50$ μs with an acoustic optical modulator (AOM). A pulse of atoms in the selected hfs passes the pump region and travels to the probe beam. The time dependence of the fluorescence induced by the probe laser, tuned to excite the selected hfs, gives the time of arrival, and this signal is readily converted to a velocity distribution. Figure 3 shows the measured velocity distribution of the atoms slowed by laser 2.

28.5 OPTICAL MOLASSES

Doppler Cooling

In Sec. 28.3 there was a discussion of the radiative force on atoms moving in a standing wave (counterpropagating laser beams). The slowing force is proportional to velocity for small enough velocities, resulting in viscous damping[10,11] that gives this technique the name *optical molasses* (OM). By using three intersecting orthogonal pairs of oppositely directed beams, the movement of atoms in the intersection region can be severely restricted in all three

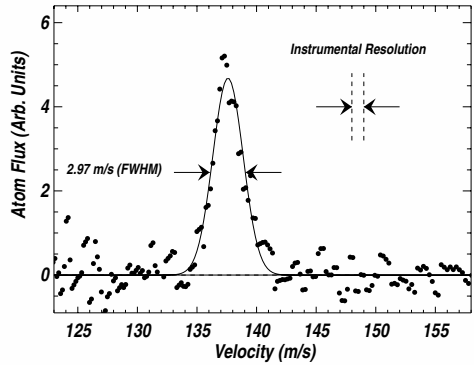

FIGURE 3 The velocity distribution measured with the time-of-flight (TOF) method. The experimental width of approximately $\frac{1}{6}$ (γ/k) is shown by the dashed vertical lines between the arrows. The Gaussian fit through the data yields a FWHM of 2.97 m/s (figure from Ref. 78).

dimensions, and many atoms can thereby be collected and cooled in a small volume. OM has been demonstrated at several laboratories,[12] often with the use of low-cost diode lasers.[13]

It is straightforward to estimate the force on atoms in OM from Eq. (10). The discussion here is limited to the case where the light intensity is low enough so that stimulated emission is not important. In this low intensity case the forces from the two light beams are simply added to give $\vec{F}_{\rm OM} = \vec{F}_+ + \vec{F}_-$, where

$$\vec{F}_\pm = \pm\frac{\hbar\vec{k}\gamma}{2}\,\frac{s_0}{1 + s_0 + [2(\delta \mp |\omega_D|)/\gamma]^2} \tag{25}$$

Then the sum of the two forces is

$$\vec{F}_{\rm OM} \cong \frac{8\hbar k^2 \delta s_0 \vec{v}}{\gamma(1 + s_0 + (2\delta/\gamma)^2)^2} \equiv -\beta\vec{v} \tag{26}$$

where terms of order $(kv/\gamma)^4$ and higher have been neglected [see Eq. (20)].

These forces are plotted in Fig. 4. For $\delta < 0$, this force opposes the velocity and therefore viscously damps the atomic motion. $\vec{F}_{\rm OM}$ has maxima near $v \approx \pm\gamma'/2k$ and decreases rapidly for larger velocities.

If there were no other influence on the atomic motion, all atoms would quickly decelerate to $v = 0$, and the sample would reach $T = 0$, a clearly unphysical result. There is also some heating caused by the light beams that must be considered, and it derives from the discrete size of the momentum steps the atoms undergo with each emission or absorption as previously discussed for Brownian motion (see Sec. 28.3). Since the atomic momentum changes by $\hbar k$, their kinetic energy changes on the average by at least the recoil energy $E_r = \hbar^2k^2/2M = \hbar\omega_r$. This means that the average frequency of each absorption is $\omega_{\rm abs} = \omega_a + \omega_r$ and the average frequency of each emission is $\omega_{\rm emit} = \omega_a - \omega_r$. Thus the light field loses an average energy of $\hbar(\omega_{\rm abs} - \omega_{\rm emit}) = 2\hbar\omega_r$ for each scattering. This loss occurs at a rate $2\gamma_p$ (two beams), and the energy is converted to atomic kinetic energy because the atoms recoil from each event. The atomic sample is thereby heated because these recoils are in random directions.

The competition between this heating with the damping force of Eq. (26) results in a nonzero kinetic energy in steady state where the rates of heating and cooling are equal. Equating the cooling rate, $\vec{F}\cdot\vec{v}$, to the heating rate, $4\hbar\omega_r\gamma_p$, the steady-state kinetic energy is

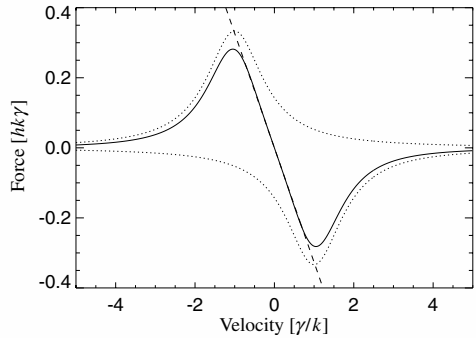

FIGURE 4 Velocity dependence of the optical damping forces for one-dimensional optical molasses. The two dotted traces show the force from each beam, and the solid curve is their sum. The straight line shows how this force mimics a pure damping force over a restricted velocity range. These are calculated for $s_0 = 2$ and $\delta = -\gamma$ so there is some power broadening evident.

$(\hbar\gamma/8)(2|\delta|/\gamma + \gamma/2|\delta|)$. This result is dependent on $|\delta|$, and it has a minimum at $2|\delta|/\gamma = 1$, whence $\delta = -\gamma/2$. The temperature found from the kinetic energy is then $T_D = \hbar\gamma/2k_B$, where T_D is called the *Doppler temperature* or the *Doppler cooling limit.* For ordinary atomic transitions, T_D is typically below 1 mK.

Another instructive way to determine T_D is to note that the average momentum transfer of many spontaneous emissions is zero, but the rms scatter of these about zero is finite. One can imagine these decays as causing a random walk in momentum space with step size $\hbar k$ and step frequency $2\gamma_p$, where the factor of 2 arises because of the two beams. The random walk results in diffusion in momentum space with diffusion coefficient $D_0 \equiv 2(\Delta p)^2/\Delta t = 4\gamma_p(\hbar k)^2$ as discussed in Sec. 28.3. Then Brownian motion theory gives the steady-state temperature in terms of the damping coefficient β to be $k_B T = D_0/\beta$. This turns out to be $\hbar\gamma/2$ as above for the case $s_0 \ll 1$ when $\delta = -\gamma/2$. This remarkable result predicts that the final temperature of atoms in OM is independent of the optical wavelength, atomic mass, and laser intensity (as long as it is not too large).

Atomic Beam Collimation—One-Dimensional Optical Molasses

When an atomic beam crosses a one-dimensional OM as shown in Fig. 5, the transverse motion of the atoms is quickly damped while the longitudinal component is essentially unchanged. This transverse cooling of an atomic beam is an example of a method that can actually increase its brightness (atoms/sec-sr-cm^2) because such active collimation uses dissipative forces to compress the phase space volume occupied by the atoms. By contrast, the usual realm of beam focusing or collimation techniques for light beams and most particle beams is restricted to selection by apertures or conservative forces that preserve the phase space density of atoms in the beam.

This velocity compression at low intensity in one dimension can be simply estimated for two-level atoms in 1D to be about $v_c/v_D = \sqrt{\gamma/\omega_r} = \sqrt{1/\varepsilon}$. For Rb, $v_D = 12$ cm/s, $v_c = \gamma/k \simeq$ 4.6 m/s, $\omega_r \simeq 2\pi \times 3.8$ kHz, and $1/\varepsilon \simeq 1600$. Including two transverse directions along with the longitudinal slowing and cooling just discussed, the decrease in phase space volume from the momentum contribution alone for laser cooling of a Rb atomic beam can exceed 10^6.

Clearly optical techniques can create atomic beams enormously more times intense than ordinary thermal beams, and also many orders of magnitude brighter. Furthermore, this number could be increased by several orders of magnitude if the transverse cooling could pro-

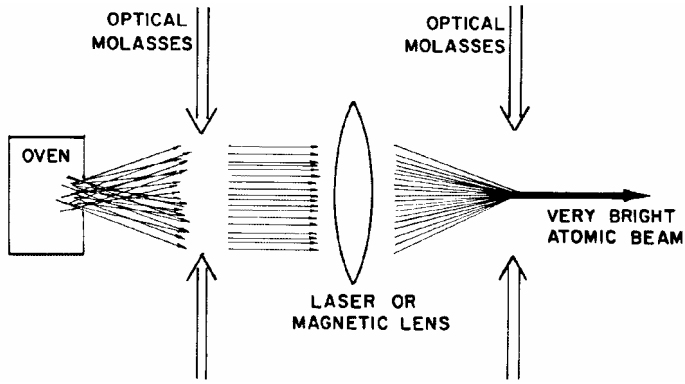

FIGURE 5 Scheme for optical brightening of an atomic beam. First the transverse velocity components of the atoms are damped out by an optical molasses, then the atoms are focused to a spot, and finally the atoms are recollimated in a second optical molasses (figure from Ref. 79).

duce temperatures below the Doppler temperature. For atoms cooled to the recoil temperature $T_r = \hbar\omega_r/k_B$ where $\Delta p = \hbar k$ and $\Delta x = \lambda/\pi$, the brightness increase could be 10^{17}.

Experiments in Three-Dimensional Optical Molasses

Optical molasses experiments can also work in three dimensions at the intersection of three mutually orthogonal pairs of opposing laser beams (see Fig. 6). Even though atoms can be collected and cooled in the intersection region, it is important to stress again that this is *not* a

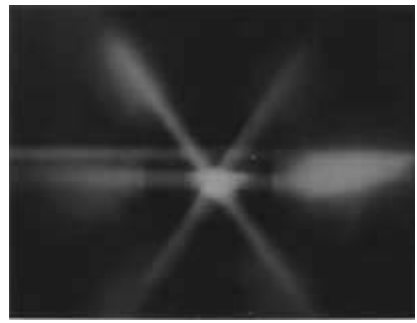

FIGURE 6 Photograph of optical molasses in Na taken under ordinary snapshot conditions in the lab at NIST. The upper horizontal streak is from the slowing laser while the three beams that cross at the center are on mutually orthogonal axes viewed from the (111) direction. Atoms in the optical molasses glow brightly at the center (figure from Ref. 19).

trap. That is, atoms that wander away from the center experience no force directing them back. They are allowed to diffuse freely and even escape, as long as there is enough time for their very slow diffusive movement to allow them to reach the edge of the region of the intersection of the laser beams. Because the atomic velocities are randomized during the damping time $M/\beta = 2/\omega_r$, atoms execute a random walk with a step size of $2v_D/\omega_r = \lambda/\pi\sqrt{2\varepsilon} \cong$ few μm. To diffuse a distance of 1 cm requires about 10^7 steps or about 30 s.[14,15]

Three-dimensional OM was first observed in 1985.[11] Preliminary measurements of the average kinetic energy of the atoms were done by blinking off the laser beams for a fixed interval. Comparison of the brightness of the fluorescence before and after the turnoff was used to calculate the fraction of atoms that left the region while it was in the dark. The dependence of this fraction on the duration of the dark interval was used to estimate the velocity distribution and hence the temperature. The result was not inconsistent with the two-level atom theory previously described.

A few months later a more sensitive ballistic technique was devised at the National Institute of Standards and Technology (NIST) that showed the astounding result that the temperature of the atoms in OM was very much lower than T_D.[16] These experiments also found that OM was less sensitive to perturbations and more tolerant of alignment errors than was predicted by the 1D, two-level atom theory. For example, if the intensities of the two counterpropagating laser beams forming an OM were unequal, then the force on atoms at rest would not vanish, but the force on atoms with some nonzero drift velocity *would* vanish. This drift velocity can be easily calculated by using Eq. (25) with unequal intensities s_{0+} and s_{0-}, and following the derivation of Eq. (26). Thus atoms would drift out of an OM, and the calculated rate would be much faster than observed by deliberately unbalancing the beams in the experiments.[12]

It was an enormous surprise to observe that the ballistically measured temperature of the Na atoms was as much as 10 times *lower* than $T_D = 240\ \mu K$,[16] the temperature minimum calculated from the theory. This breaching of the Doppler limit forced the development of an entirely new picture of OM that accounts for the fact that in three dimensions, a two-level picture of atomic structure is inadequate. The multilevel structure of atomic states, and optical pumping among these sublevels, must be considered in the description of 3D OM, as discussed in the text that follows.

28.6 COOLING BELOW THE DOPPLER LIMIT

Introduction

In response to the surprising measurements of temperatures below T_D, two groups developed a model of laser cooling that could explain the lower temperatures.[17,18] The key feature of this model that distinguishes it from the earlier picture was the inclusion of the multiplicity of sublevels that make up an atomic state (*e.g.,* Zeeman and hfs). The dynamics of optically pumping atoms among these sublevels provides the new mechanism for producing the ultra-low temperatures.[19]

The dominant feature of these models is the nonadiabatic response of moving atoms to the light field. Atoms at rest in a steady state have ground-state orientations caused by optical pumping processes that distribute the populations over the different ground-state sublevels. In the presence of polarization gradients, these orientations reflect the local light field. In the low-light-intensity regime, the orientation of stationary atoms is completely determined by the ground-state distribution: The optical coherences and the exited-state population follow the ground-state distribution adiabatically.

For atoms moving in a light field that varies in space, optical pumping acts to adjust the atomic orientation to the changing conditions of the light field. In a weak pumping process, the orientation of moving atoms always lags behind the orientation that would exist for sta-

tionary atoms. It is this phenomenon of nonadiabatic following that is the essential feature of the new cooling process.

Production of spatially dependent optical pumping processes can be achieved in several different ways. As an example, consider two counterpropagating laser beams that have orthogonal polarizations (as will be discussed shortly). The superposition of the two beams results in a light field having a polarization that varies on the wavelength scale along the direction of the laser beams. Laser cooling by such a light field is called *polarization gradient cooling.* In a three-dimensional optical molasses, the transverse wave character of light requires that the light field always has polarization gradients.

Linear ⊥ Linear Polarization Gradient Cooling

One of the most instructive models for discussion of sub-Doppler laser cooling was introduced in Ref. 17 and very well described in Ref. 19. If the polarizations of two counterpropagating laser beams are identical, the two beams interfere and produce a standing wave. When the two beams have orthogonal linear polarizations (same frequency ω_ℓ) with their $\hat{\varepsilon}$ vectors perpendicular (*e.g.,* $\hat{x}$ and $\hat{y}$), the configuration is called *lin* ⊥ *lin* or *lin-perp-lin.* Then the total field is the sum of the two counterpropagating beams given by

$$\begin{aligned}\vec{E} &= E_0\,\hat{x}\cos(\omega_\ell t - kz) + E_0\,\hat{y}\cos(\omega_\ell t + kz)\\ &= E_0[(\hat{x}+\hat{y})\cos\omega_\ell t\cos kz + (\hat{x}-\hat{y})\sin\omega_\ell t\sin kz]\end{aligned} \tag{27}$$

At the origin, where $z = 0$, this becomes

$$\vec{E} = E_0(\hat{x}+\hat{y})\cos\omega_\ell t \tag{28}$$

which corresponds to linearly polarized light at an angle $+\pi/4$ to the x-axis. The amplitude of this field is $\sqrt{2}E_0$. Similarly, for $z = \lambda/4$, where $kz = \pi/2$, the field is also linearly polarized but at an angle $-\pi/4$ to the x-axis.

Between these two points, at $z = \lambda/8$, where $kz = \pi/4$, the total field is

$$\vec{E} = E_0\,[\hat{x}\sin(\omega_\ell t + \pi/4) - \hat{y}\cos(\omega_\ell t + \pi/4)] \tag{29}$$

Since the $\hat{x}$ and $\hat{y}$ components have sine and cosine temporal dependence, they are $\pi/2$ out of phase, and so Eq. (29) represents circularly polarized light rotating about the z-axis in the negative sense. Similarly, at $z = 3\lambda/8$ where $kz = 3\pi/4$, the polarization is circular but in the positive sense. Thus in this lin ⊥ lin scheme the polarization cycles from linear to circular to orthogonal linear to opposite circular in the space of only half a wavelength of light, as shown in Fig. 7. It truly has a very strong polarization gradient.

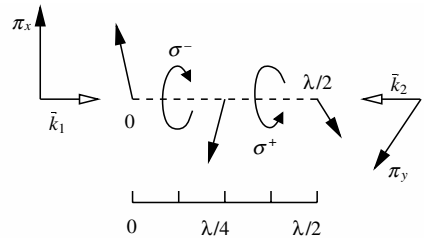

FIGURE 7 Polarization gradient field for the lin ⊥ lin configuration.

Since the coupling of the different states of multilevel atoms to the light field depends on its polarization, atoms moving in a polarization gradient will be coupled differently at different positions, and this will have important consequences for laser cooling. For the $J_g = ½ \rightarrow J_e = ⅔$ transition (the simplest transition that shows sub-Doppler cooling), the optical pumping process in purely σ^+ light drives the ground-state population to the $M_g = +½$ sublevel. This optical pumping occurs because absorption always produces $\Delta M = +1$ transitions, whereas the subsequent spontaneous emission produces $\Delta M = \pm 1, 0$. Thus the average $\Delta M \geq 0$ for each scattering event. For σ^--light the population is pumped toward the $M_g = -½$ sublevel. Thus atoms traveling through only a half wavelength in the light field need to readjust their population completely from $M_g = +½$ to $M_g = -½$ and back again.

The interaction between nearly resonant light and atoms not only drives transitions between atomic energy levels, but also shifts their energies. This light shift of the atomic energy levels plays a crucial role in this scheme of sub-Doppler cooling, and the changing polarization has a strong influence on the light shifts. In the low-intensity limit of two laser beams, each of intensity $s_0 I_s$, the light shifts ΔE_g of the ground magnetic substates are given by[1]

$$\Delta E_g = \frac{\hbar \delta s_0 C_{ge}^2}{1 + (2\delta/\gamma)^2} \tag{30}$$

where C_{ge} is the Clebsch-Gordan coefficient that describes the coupling between the atom and the light field.

In the present case of orthogonal linear polarizations and $J = ½ \rightarrow ⅔$, the light shift for the magnetic substate $M_g = ½$ is three times larger than that of the $M_g = -½$ substate when the light field is completely σ^+. On the other hand, when an atom moves to a place where the light field is σ^-, the shift of $M_g = -½$ is three times larger. So in this case the optical pumping previously discussed causes there to be a larger population in the state with the larger light shift. This is generally true for any transition J_g to $J_e = J_g + 1$. A schematic diagram showing the populations and light shifts for this particular case of negative detuning is shown in Fig. 8.

Origin of the Damping Force

To discuss the origin of the cooling process in this polarization gradient scheme, consider atoms with a velocity v at a position where the light is σ^+-polarized, as shown at the lower left of Fig. 8. The light optically pumps such atoms to the strongly negative light-shifted $M_g = +½$ state. In moving through the light field, atoms must increase their potential energy (climb a hill) because the polarization of the light is changing and the state $M_g = ½$ becomes less strongly coupled to the light field. After traveling a distance $\lambda/4$, atoms arrive at a position where the light field is σ^--polarized, and are optically pumped to $M_g = -½$, which is now lower than the $M_g = ½$ state. Again the moving atoms are at the bottom of a hill and start to climb. In climbing the hills, the kinetic energy is converted to potential energy, and in the optical pumping process, the potential energy is radiated away because the spontaneous emission is at a higher frequency than the absorption (see Fig. 8). Thus atoms seem to be always climbing hills and losing energy in the process. This process brings to mind a Greek myth, and is thus called *Sisyphus laser cooling.*

The cooling process just described is effective over a limited range of atomic velocities. The force is maximum for atoms that undergo one optical pumping process while traveling over a distance $\lambda/4$. Slower atoms will not reach the hilltop before the pumping process occurs, and faster atoms will already be descending the hill before being pumped toward the other sublevel. In both cases the energy loss is smaller and therefore the cooling process less efficient. Nevertheless, the damping constant β for this process is much larger than for Doppler cooling, and therefore the final steady-state temperature is lower.[17,19]

In the experiments of Ref. 20, the temperature was measured in a 3D molasses under various configurations of the polarization. Temperatures were measured by a ballistic technique, where the flight time of the released atoms was measured as they fell through a probe a few

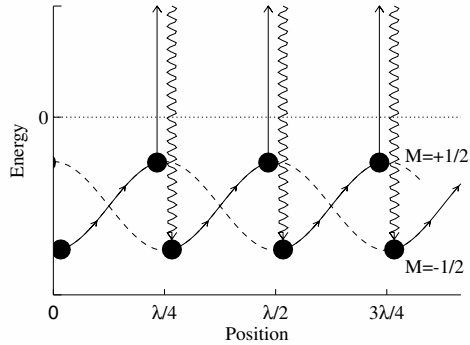

FIGURE 8 The spatial dependence of the light shifts of the ground-state sublevels of the $J = ½ \Leftrightarrow ½$ transition for the case of the lin ⊥ lin polarization configuration. The arrows show the path followed by atoms being cooled in this arrangement. Atoms starting at $z = 0$ in the $M_g = +½$ sublevel must climb the potential hill as they approach the $z = \lambda/4$ point where the light becomes σ^- polarized, and there they are optically pumped to the $M_g = -½$ sublevel. Then they must begin climbing another hill toward the $z = \lambda/2$ point where the light is σ^+ polarized and they are optically pumped back to the $M_g = +½$ sublevel. The process repeats until the atomic kinetic energy is too small to climb the next hill. Each optical pumping event results in absorption of light at a lower frequency than emission, thus dissipating energy to the radiation field.

cm below the molasses region. Results of their measurements are shown in Fig. 9*a,* where the measured temperature is plotted for different detunings as a function of the intensity. For each detuning, the data lie on a straight line through the origin. The lowest temperature obtained is 3 μK, which is a factor 40 below the Doppler temperature and a factor 15 above the recoil temperature of Cs. If the temperature is plotted as a function of the light shift (see Fig. 9*b*), all the data are on a single universal straight line.

The Limits of Laser Cooling

The lower limit to Doppler laser cooling of two-level atoms arises from the competition with heating. This cooling limit is described as a random walk in momentum space whose steps are of size $\hbar k$ and whose rate is the scattering rate, $\gamma_p = s_0\gamma/2$ for zero detuning and $s_0 \ll 1$. As long as the force can be accurately described as a damping force, then the Fokker-Planck equation is applicable, and the outcome is a lower limit to the temperature of laser cooling given by the Doppler temperature $k_B T_D \equiv \hbar\gamma/2$.

The extension of this kind of thinking to the sub-Doppler processes described in Sec. 28.5 must be done with some care, because a naive application of the consequences of the Fokker-Planck equation would lead to an arbitrarily low final temperature. In the derivation of the Fokker-Planck equation it is explicitly assumed that each scattering event changes the atomic momentum p by an amount that is a small fraction of p as embodied in Eq. (3), and this clearly fails when the velocity is reduced to the region of $v_r \equiv \hbar k/M$.

This limitation of the minimum steady-state value of the average kinetic energy to a few times $2E_r \equiv k_B T_r = Mv_r^2$ is intuitively comforting for two reasons. First, one might expect that

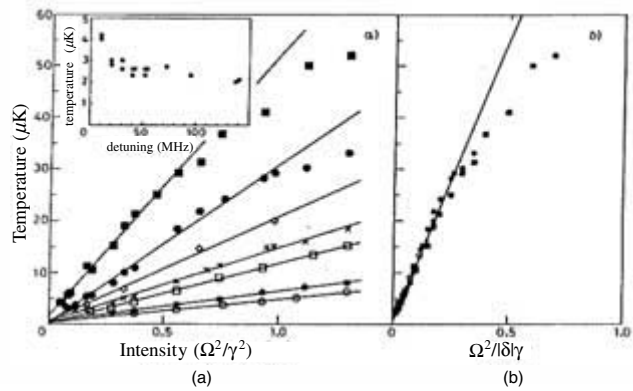

FIGURE 9 Temperature as a function of laser intensity and detuning for Cs atoms in an optical molasses from Ref. 20. (*a*) Temperature as a function of the detuning for various intensities. (*b*) Temperature as a function of the light shift. All the data points are on a universal straight line.

the last spontaneous emission in a cooling process would leave atoms with a residual momentum of the order of $\hbar k$, since there is no control over its direction. Thus the randomness associated with this would put a lower limit on such cooling of $v_{\min} \sim v_r$. Second, the polarization gradient cooling mechanism just described requires that atoms be localizable within the scale of $\sim\lambda/2\pi$ in order to be subject to only a single polarization in the spatially inhomogeneous light field. The uncertainty principle then requires that these atoms have a momentum spread of at least $\hbar k$.

The recoil limit discussed here has been surpassed by evaporative cooling of trapped atoms[21] and two different optical cooling methods, neither of which can be based in simple notions. One of these uses optical pumping into a velocity-selective dark state and is described in Ref. 1. The other one uses carefully chosen, counterpropagating laser pulses to induce velocity-selective Raman transitions, and is called *Raman cooling.*[22]

28.7 TRAPPING OF NEUTRAL ATOMS

Introduction

Although ion trapping, laser cooling of trapped ions, and trapped ion spectroscopy were known for many years,[23] it was only in 1985 that neutral atoms were first trapped.[24] Confinement of neutral atoms depends on the interaction between an inhomogeneous electromagnetic field and an atomic multipole moment. Unperturbed atoms do not have electric dipole moments because of their inversion symmetry, and therefore electric (*e.g.,* optical) traps require induced dipole moments. This is often done with nearly resonant optical fields, thus producing the optical traps that will be discussed shortly. On the other hand, many atoms have ground- or metastable-state magnetic dipole moments that may be used for trapping them magnetically.

In order to confine any object, it is necessary to exchange kinetic for potential energy in the trapping field, and in neutral atom traps the potential energy must be stored as internal atomic energy. There are two immediate and extremely important consequences of this requirement. First, the atomic energy levels will necessarily shift as the atoms move in the trap, and these shifts will affect the precision of spectroscopic measurements, perhaps

severely. Second, practical traps for ground-state neutral atoms are necessarily very shallow compared with thermal energy because the energy level shifts that result from convenient size fields are typically considerably smaller than $k_B T$ for $T = 1$ K. Neutral atom trapping therefore depends on substantial cooling of a thermal atomic sample, and is often connected with the cooling process.

The small depth of neutral atom traps also dictates stringent vacuum requirements, because an atom cannot remain trapped after a collision with a thermal energy background gas molecule. Since these atoms are vulnerable targets for thermal energy background gas, the mean free time between collisions *must* exceed the desired trapping time. The cross section for destructive collisions is quite large because even a gentle collision (*i.e.,* large impact parameter) can impart enough energy to eject an atom from a trap. At pressure P sufficiently low to be of practical interest, the trapping time is ~$(10^{-8}/P)$ s, where P is in Torr.

Magnetic Traps

An atom with a magnetic moment $\vec{\mu}$ can be confined by an inhomogeneous magnetic field because of an interaction between the moment and the field. This produces a force given by $\vec{F} = \vec{\nabla}(\vec{\mu} \cdot \vec{B})$. Several different magnetic traps with varying geometries that exploit this force have been studied in some detail, and their general features have been presented.[25] The simplest magnetic trap is a quadrupole comprised of two identical coils carrying opposite currents (see Fig. 10) that has a single center where the field is zero. When the coils are separated by 1.25 times their radius, such a trap has equal depth in the radial (x-y plane) and longitudinal (z-axis) directions.[25] Its experimental simplicity makes it most attractive, both because of ease of construction and of optical access to the interior. Such a trap was used in the first neutral atom trapping experiments at NIST.

The magnitude of the field is zero at the center of this trap, and increases in all directions as $B = A\sqrt{\rho^2 + 4z^2}$, where $\rho^2 \equiv x^2 + y^2$, and the field gradient A is constant. The field gradient is fixed along any line through the origin, but has different values in different polar directions. Therefore the force that confines the atoms in the trap is neither harmonic nor central, and angular momentum is not conserved. There are several motivations for studying the motion of atoms in a magnetic trap. Knowing their positions may be important for trapped atom spectroscopy. Moreover, simply studying the motion for its own sake has turned out to be an interesting problem because the distorted conical potential of the quadrupole trap does not have analytic solutions, and its bound states are not well known. For the two-coil quadrupole magnetic trap of Fig. 10, stable circular orbits can be found classically.[1] The fastest trappable atoms

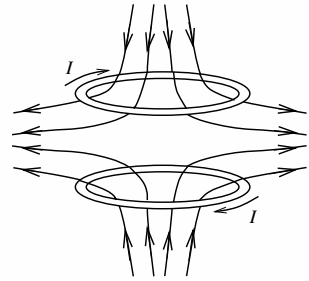

FIGURE 10 Schematic diagram of the coil configuration used in the quadrupole trap and the resultant magnetic field lines. Because the currents in the two coils are in opposite directions, there is a $|\vec{B}| = 0$ point at the center.

in circular orbits have $v_{max} \sim 1$ m/s so the orbital frequency becomes $\omega_T/2\pi \sim 20$ Hz. Because of the anharmonicity of the potential, the orbital frequencies depend on the orbit size, but in general, atoms in lower energy orbits have higher frequencies.

Because of the dependence of the trapping force on the angle between the field and the atomic moment the orientation of the magnetic moment with respect to the field must be preserved as the atoms move about in the trap. This requires velocities low enough to ensure that the interaction between the atomic moment $\vec{\mu}$ and the field $\vec{B}$ is adiabatic, especially when the atom's path passes through a region where the field magnitude is small. This is especially critical at the low temperatures of the Bose condensation experiments. Therefore energy considerations that focus only on the trap depth are not sufficient to determine the stability of a neutral atom trap: orbit and/or quantum state calculations and their consequences must also be considered.

The condition for adiabatic motion can be written as $\omega_z \gg |dB/dt|/B$, where $\omega_z = \mu B/\hbar$ is the Larmor precession rate in the field. The orbital frequency for circular motion is $\omega_T = v/\rho$, and since $v/\rho = |dB/dt|/B$ for a uniform field gradient, the adiabaticity condition is $\omega_z \gg \omega_T$. For the two-coil quadrupole trap, the adiabaticity condition can be easily calculated.[1] A practical trap ($A \sim 1$ T/m) requires $\rho \gg 1$ μm as well as $v \gg 1$ cm/s. Note that violation of these conditions results in the onset of quantum dynamics for the motion (deBroglie wavelength ≈ orbit size). Since the nonadiabatic region of the trap is so small (less than 10^{-18} m^3 compared with typical sizes of ~2 cm corresponding to 10^{-5} m^3), nearly all the orbits of most atoms are restricted to regions where they are adiabatic.

Modern techniques of laser and evaporative cooling have the capability to cool atoms to energies where their deBroglie wavelengths are on the micron scale. Such cold atoms may be readily confined to micron-size regions in magnetic traps with easily achievable field gradients, and in such cases, the notion of classical orbits is inappropriate. The motional dynamics must be described in terms of quantum mechanical variables and suitable wave functions. Furthermore, the distribution of atoms confined in various quantum states of motion in quadrupole as well as other magnetic traps is critical for interpreting the measurements on Bose condensates.

Studying the behavior of extremely slow (cold) atoms in the two-coil quadrupole trap begins with a heuristic quantization of the orbital angular momentum using $Mr^2\omega_T = n\hbar$ for circular orbits.[1] For velocities of optically cooled atoms of a few cm/s, $n \sim 10$–100. By contrast, evaporative cooling[21] can produce velocities ~1 mm/s resulting in $n \sim 1$. It is readily found that $\omega_z = n\omega_T$, so that the adiabatic condition is satisfied only for $n \gg 1$. The separation of the rapid precession from the slower orbital motion is reminiscent of the Born-Oppenheimer approximation for molecules, and three-dimensional quantum calculations have also been described.[1]

Optical Traps

Optical trapping of neutral atoms by electrical interaction must proceed by inducing a dipole moment. For dipole optical traps, the oscillating electric field of a laser induces an oscillating atomic electric dipole moment that interacts with the laser field. If the laser field is spatially inhomogeneous, the interaction and associated energy level shift of the atoms varies in space and therefore produces a potential. When the laser frequency is tuned below atomic resonance ($\delta < 0$), the sign of the interaction is such that atoms are attracted to the maximum of laser field intensity, whereas if $\delta > 0$, the attraction is to the minimum of field intensity.

The simplest imaginable trap (see Fig. 11) consists of a single, strongly focused Gaussian laser beam[26,27] whose intensity at the focus varies transversely with r as $I(r) = I_0 e^{-r^2/w_0^2}$, where w_0 is the beam waist size. Such a trap has a well-studied and important macroscopic classical analog in a phenomenon called *optical tweezers.*[28–30] With the laser light tuned below resonance ($\delta < 0$), the ground-state light shift is everywhere negative, but is largest at the center of the Gaussian beam waist. Ground-state atoms therefore experience a force attracting them toward this center given by the gradient of the light shift. In the longitudinal direction there is

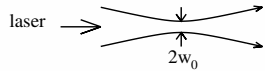

FIGURE 11 A single focused laser beam produces the simplest type of optical trap.

also an attractive force that depends on the details of the focusing. Thus this trap produces an attractive force on atoms in three dimensions.

The first optical trap was demonstrated in Na with light detuned below the D-lines.[27] With 220 mW of dye laser light tuned about 650 GHz below the Na transition and focused to a ~10 μm waist, the trap depth was about $15\hbar\gamma$ corresponding to 7 mK. Single-beam dipole force traps can be made with the light detuned by a significant fraction of its frequency from the atomic transition. Such a far-off-resonance trap (FORT) has been developed for Rb atoms using light detuned by nearly 10 percent to the red of the D_1 transition at $\lambda = 795$ nm.[31] Between 0.5 and 1 W of power was focused to a spot about 10 μm in size, resulting in a trap 6 mK deep where the light scattering rate was only a few hundred/s. The trap lifetime was more than half a second.

The dipole force for blue light repels atoms from the high intensity region, and offers the advantage that trapped atoms will be confined where the perturbations of the light field are minimized.[1] On the other hand, it is not as easy to produce hollow light beams compared with Gaussian beams, and special optical techniques need to be employed.

In a standing wave the light intensity varies from zero at a node to a maximum at an antinode in a distance of $\lambda/4$. Since the light shift, and thus the optical potential, vary on this same scale, it is possible to confine atoms in wavelength-size regions of space. Of course, such tiny traps are usually very shallow, so loading them requires cooling to the μK regime. The momentum of such cold atoms is then so small that their deBroglie wavelengths are comparable to the optical wavelength, and hence to the trap size. In fact, the deBroglie wavelength equals the size of the optical traps ($\lambda/2$) when the momentum is $2\hbar k$, corresponding to a kinetic energy of a few μK. Thus the atomic motion in the trapping volume is not classical, but must be described quantum mechanically. Even atoms whose energy exceeds the trap depth must be described as quantum mechanical particles moving in a periodic potential that display energy band structure.[32]

Atoms trapped in wavelength-sized spaces occupy vibrational levels similar to those of molecules. The optical spectrum can show Raman-like sidebands that result from transitions among the quantized vibrational levels[33,34] as shown in Fig. 19. These quantum states of atomic motion can also be observed by spontaneous or stimulated emission.[33,35] Considerably more detail about atoms in such optical lattices is to be found in Ref. 34.

Magneto-Optical Traps

The most widely used trap for neutral atoms is a hybrid, employing both optical and magnetic fields. The resultant *magneto-optical trap* (MOT) was first demonstrated in 1987.[36] The operation of a MOT depends on both inhomogeneous magnetic fields and radiative selection rules to exploit both optical pumping and the strong radiative force.[1,36] The radiative interaction provides cooling that helps in loading the trap, and enables very easy operation. The MOT is a very robust trap that does not depend on precise balancing of the counterpropagating laser beams or on a very high degree of polarization. The magnetic field gradients are modest and can readily be achieved with simple, air-cooled coils. The trap is easy to construct because it can be operated with a room-temperature cell where alkali atoms are captured from the vapor. Furthermore, low-cost diode lasers can be used to produce the light appropriate for all the alkalis except Na, so the MOT has become one of the least expensive ways to produce atomic samples with temperatures below 1 mK. For these and other reasons

it has become the workhorse of cold atom physics, and has also appeared in dozens of undergraduate laboratories.

Trapping in a MOT works by optical pumping of slowly moving atoms in a linearly inhomogeneous magnetic field $B = B(z) \equiv Az$, such as that formed by a magnetic quadrupole field. Atomic transitions with the simple scheme of $J_g = 0 \rightarrow J_e = 1$ have three Zeeman components in a magnetic field, excited by each of three polarizations, whose frequencies tune with field (and therefore with position) as shown in Fig. 12 for one dimension. Two counterpropagating laser beams of opposite circular polarization, each detuned below the zero field atomic resonance by δ, are incident as shown.

Because of the Zeeman shift, the excited state $M_e = +1$ is shifted up for $B > 0$, whereas the state with $M_e = -1$ is shifted down. At position z' in Fig. 12 the magnetic field therefore tunes the $\Delta M = -1$ transition closer to resonance and the $\Delta M = +1$ transition further out of resonance. If the polarization of the laser beam incident from the right is chosen to be σ^- and correspondingly σ^+ for the other beam, then more light is scattered from the σ^- beam than from the σ^+ beam. Thus the atoms are driven toward the center of the trap, where the magnetic field is zero. On the other side of the center of the trap, the roles of the $M_e = \pm 1$ states are reversed, and now more light is scattered from the σ^+ beam, again driving the atoms towards the center.

The situation is analogous to the velocity damping in an optical molasses from the Doppler effect as previously discussed, but here the effect operates in position space, whereas for molasses it operates in velocity space. Since the laser light is detuned below the atomic resonance in both cases, compression and cooling of the atoms is obtained simultaneously in a MOT.

For a description of the motion of the atoms in a MOT, consider the radiative force in the low intensity limit [see Eq. (10)]. The total force on the atoms is given by $\vec{F} = \vec{F}_+ + \vec{F}_-$, where

$$\vec{F}_\pm = \pm \frac{\hbar \vec{k} \gamma}{2} \frac{s_0}{1 + s_0 + (2\delta_\pm/\gamma)^2} \tag{31}$$

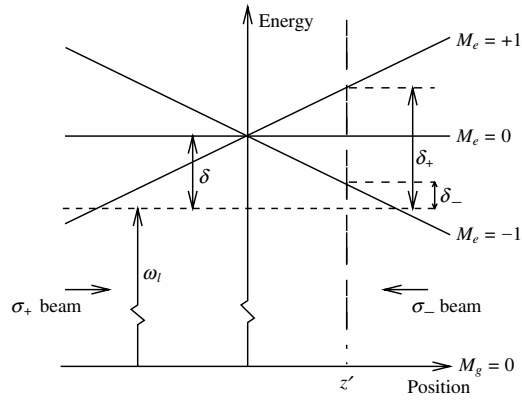

FIGURE 12 Arrangement for a magneto-optical trap (MOT) in 1D. The horizontal dashed line represents the laser frequency seen by an atom at rest in the center of the trap. Because of the Zeeman shifts of the atomic transition frequencies in the inhomogeneous magnetic field, atoms at $z = z'$ are closer to resonance with the σ^- laser beam than with the σ^+ beam, and are therefore driven toward the center of the trap.

and the detuning $\delta_\pm$ for each laser beam is given by

$$\delta_\pm = \delta \mp \vec{k} \cdot \vec{v} \pm \mu' B/\hbar \tag{32}$$

Here $\mu' \equiv (g_e M_e - g_g M_g)\mu_B$ is the effective magnetic moment for the transition used. Note that the Doppler shift $\omega_D \equiv -\vec{k} \cdot \vec{v}$ and the Zeeman shift $\omega_Z = \mu' B/\hbar$ both have opposite signs for opposite beams.

When both the Doppler and Zeeman shifts are small compared to the detuning δ, the denominator of the force can be expanded and the result becomes $\vec{F} = -\beta\vec{v} - \kappa\vec{r}$, where β is the damping coefficient. The spring constant κ arises from the similar dependence of $\vec{F}$ on the Doppler and Zeeman shifts, and is given by $\kappa = \mu' A\beta/\hbar k$. This force leads to damped harmonic motion of the atoms, where the damping rate is given by $\Gamma_{\text{MOT}} = \beta/M$ and the oscillation frequency $\omega_{\text{MOT}} = \sqrt{\kappa/M}$. For magnetic field gradients $A \approx 10$ G/cm, the oscillation frequency is typically a few kHz, and this is much smaller than the damping rate that is typically a few hundred kHz. Thus the motion is overdamped, with a characteristic restoring time to the center of the trap of $2\Gamma_{\text{MOT}}/\omega_{\text{MOT}}^2 \sim$ several ms for typical values of the detuning and intensity of the lasers.

Since the MOT constants β and κ are proportional, the size of the atomic cloud can easily be deduced from the temperature of the sample. The equipartition of the energy of the system over the degrees of freedom requires that the velocity spread and the position spread are related by $k_B T = m v_{\text{rms}}^2 = \kappa z_{\text{rms}}^2$. For a temperature in the range of the Doppler temperature, the size of the MOT should be of the order of a few tenths of a mm, which is generally the case in experiments.

So far the discussion has been limited to the motion of atoms in one dimension. However, the MOT scheme can easily be extended to 3D by using six instead of two laser beams (see Fig. 13). Furthermore, even though very few atomic species have transitions as simple as $J_g = 0 \rightarrow J_e = 1$, the scheme works for any $J_g \rightarrow J_e = J_g + 1$ transition. Atoms that scatter mainly from the σ^+ laser beam will be optically pumped toward the $M_g = +J_g$ substate, which forms a closed system with the $M_e = +J_e$ substate.

The atomic density in a MOT cannot increase without limit as more atoms are added. The density is limited to ~10^{11}/cm^3 because the fluorescent light emitted by some trapped atoms is absorbed by others, and this diffusion of radiation presents a repulsive force between the atoms.[37,38] Another limitation lies in the collisions between the atoms, and the collision rate for excited atoms is much larger than for ground-state atoms. Adding atoms to a MOT thus increases the density up to some point, but adding more atoms then expands the volume of the trapped sample.

28.8 APPLICATIONS

Introduction

The techniques of laser cooling and trapping as described in the previous sections have been used to manipulate the positions and velocities of atoms with unprecedented variety and precision.[1] These techniques are currently used in the laboratories to design new, highly sensitive experiments that move experimental atomic physics research to completely new regimes. In this section only of few of these topics will be discussed. One of the most straightforward of these is the use of laser cooling to increase the brightness of atomic beams, which can subsequently be used for different types of experiments. Since laser cooling produces atoms at very low temperatures, the interaction between these atoms also takes place at such very low energies. The study of these interactions, called *ultracold collisions,* has been a very fruitful area of research in the last decade.

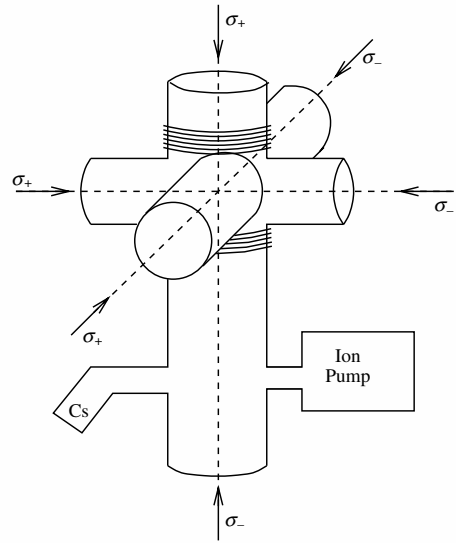

FIGURE 13 The schematic diagram of a MOT shows the coils and the directions of polarization of the six light beams. It has an axial symmetry and various rotational symmetries, so some exchanges would still result in a trap that works, but not all configurations are possible. Atoms are trapped from the background vapor of Cs that arises from a piece of solid Cs in one of the arms of the setup.

The atom-laser interaction not only produces a viscous environment for cooling the atoms down to very low velocities, but also provides a trapping field for the atoms. In the case of interfering laser beams, the size of such traps can be of the order of a wavelength, thus providing microscopic atomic traps with a periodic structure. These optical lattices described later in this section provide a versatile playground to study the effects of a periodic potential on the motion of atoms and thus simulate the physics of condensed matter. Another topic of considerable interest that will be discussed exists only because laser cooling has paved the way to the observation of Bose-Einstein condensation. This was predicted theoretically more than 80 years ago, but was observed in a dilute gas for the first time in 1996. Finally, the physics of dark states is also discussed in this section. These show a rich variety of effects caused by the coupling of internal and external coordinates of atoms.

Atomic Beam Brightening

In considering the utility of atomic beams for the purposes of lithography, collision studies, or a host of other applications, maximizing the beam intensity may not be the best option. Laser cooling can be used for increasing the phase space density, and this notion applies to both atomic traps and atomic beams. In the case of atomic beams, other quantities than phase space density have been defined as well, but these are not always consistently used. The geometrical solid angle occupied by atoms in a beam is $\Delta\Omega = (\Delta v_\perp/\overline{v})^2$, where $\overline{v}$ is some measure of the longitudinal velocity of atoms in the beam and $\Delta v_\perp$ is a measure of the width of the transverse velocity distribution of the atoms. The total current or flux of the beam is Φ, and

the flux density or intensity is $\Phi/\pi(\Delta x)^2$ where Δx is a measure of the beam's radius. Then the beam brightness or radiance R is given by $R = \Phi/\pi(\Delta x_\perp)^2\Delta\Omega$. Optical beams are often characterized by their frequency spread, and, because of the deBroglie relation $\lambda = h/p$, the appropriate analogy for atomic beams is the longitudinal velocity spread. Thus the spectral brightness or brilliance B, is given by $B = R\bar{v}/\Delta v_z$. Note that both R and B have the same dimensions as flux density, and this is often a source of confusion. Finally, B is simply related to the 6D phase space density. Recently a summary of these beam properties has been presented in the context of phase space (see Fig. 14).

One of the first beam-brightening experiments was performed by Nellesen et al.[39,40] where a thermal beam of Na was slowed with the chirp technique.[1] Then the slow atoms were deflected out of the main atomic beam and transversely cooled. In a later experiment[41] this beam was fed into a two-dimensional MOT where the atoms were cooled and compressed in the transverse direction by an optical molasses of σ^+–σ^- polarized light. Another approach was used by Riis et al. who directed a slowed atomic beam into a hairpin-shaped coil that they called an *atomic funnel.*[42] The wires of this coil generated a two-dimensional quadrupole field that was used as a two-dimensional MOT as described before.

These approaches yield intense beams when the number of atoms in the uncooled beam is already high. However, if the density in the beam is initially low, for example in the case of metastable noble gases or radioactive isotopes, one has to capture more atoms from the source in order to obtain an intense beam. Aspect et al.[43] have used a quasi-standing wave of converging laser beams whose incidence angle varied from 87° to 90° to the atomic beam direction, so that a larger solid angle of the source could be captured. In this case they used a few mW of laser light over a distance of 75 mm. One of the most sophisticated approaches to this problem has been developed for metastable Ne by Hoogerland et al.[44] They used a three-stage process to provide a large solid angle capture range and produce a high brightness beam.

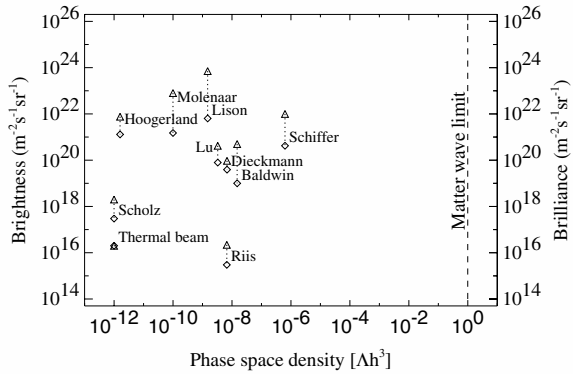

FIGURE 14 Plot of brightness (diamonds) and brilliance (triangles) versus phase space density for various atomic beams cited in the literature. The lower-left point is for a normal thermal beam, and the progression toward the top and right has been steady since the advent of laser cooling. The experimental results are from Riis et al.,[42] Scholz et al.,[80] Hoogerland et al.,[44] Lu et al.,[81] Baldwin et al.,[82] Molenaar et al.,[78] Schiffer et al.,[83] Lison et al.,[84] and Dieckmann et al.[85] The quantum boundary for Bose-Einstein condensation, where the phase space density is unity, is shown by the dashed line on the right (figure adapted from Ref. 84).

Applications to Atomic Clocks

Perhaps one of the most important practical applications of laser cooling is the improvement of atomic clocks. The limitation to both the accuracy and precision of such clocks is imposed by the thermal motion of the atoms, so a sample of laser-cooled atoms could provide a substantial improvement in clocks and in spectroscopic resolution.

The first experiments intended to provide slower atoms for better precision or clocks were attempts at an atomic fountain by Zacharias in the 1950s.[1,45] This failed because collisions depleted the slow atom population, but the advent of laser cooling enabled an atomic fountain because the slow atoms far outnumber the faster ones. The first rf spectroscopy experiments in such a fountain using laser-cooled atoms were reported in 1989 and 1991,[46,47] and soon after that some other laboratories also reported successes.

Some of the early best results were reported by Gibble and Chu.[48,49] They used a MOT with laser beams 6 cm in diameter to capture Cs atoms from a vapor at room temperature. These atoms were launched upward at 2.5 m/s by varying the frequencies of the MOT lasers to form a moving optical molasses as described in Sec. 28.5, and subsequently cooled to below 3 μK. The atoms were optically pumped into one hfs sublevel, then passed through a 9.2 GHz microwave cavity on their way up and again later on their way down. The number of atoms that were driven to change their hfs state by the microwaves was measured versus microwave frequency, and the signal showed the familiar Ramsey oscillations. See Chapter 24, "Coherent Optical Transients," for a discussion of Ramsey fringes. The width of the central feature was 1.4 Hz and the S/N was over 50. Thus the ultimate precision was 1.5 mHz corresponding to $\delta\nu/\nu \cong 10^{-12}/\tau^{1/2}$ where τ is the number of seconds for averaging.

The ultimate limitation to the accuracy of this experiment as an atomic clock was collisions between Cs atoms in the beam. Because of the extremely low relative velocities of the atoms, the cross sections are very large (see the next subsection) and there is a measurable frequency shift.[50] By varying the density of Cs atoms in the fountain, the authors found frequency shifts of the order of a few mHz for atomic density of $10^9/\text{cm}^3$, depending on the magnetic sublevels connected by the microwaves. Extrapolation of the data to zero density provided a frequency determination of $\delta\nu/\nu \cong 4 \times 10^{-14}$. More recently the frequency shift has been used to determine a scattering length of $-400a_0$[51] so that the expected frequency shift is 10^4 times larger than other limitations to the clock at an atomic density of $n = 10^9/\text{cm}^3$. Thus the authors suggest possible improvements to atomic timekeeping of a factor of 1000 in the near future. Even more promising are cold atom clocks in orbit (microgravity) where the interaction time can be very much longer than 1 s.[52]

Ultra-cold Collisions

Laser-cooling techniques were developed in the early 1980s for a variety of reasons, such as high-resolution spectroscopy.[1] During the development of the techniques to cool and trap atoms, it became apparent that collisions between cold atoms in optical traps was one of the limiting factors in the achievement of high-density samples. Trap loss experiments revealed that the main loss mechanisms were caused by laser-induced collisions. Further cooling and compression could only be achieved by techniques not exploiting laser light, such as evaporative cooling in magnetic traps. Elastic collisions between atoms in the ground state are essential in that case for the rethermalization of the sample, whereas inelastic collisions lead to destruction of the sample. Knowledge about collision physics at these low energies is therefore essential for the development of high-density samples of atoms using either laser or evaporative cooling techniques.

Ground-state collisions play an important role in evaporative cooling. Such elastic collisions are necessary to obtain a thermalization of the gas after the trap depth has been lowered, and a large elastic cross section is essential to obtain a rapid thermalization. Inelastic

collisions, on the other hand, can release enough energy to accelerate the atoms to energies too high to remain trapped. Ground-state collisions for evaporative cooling can be described by one parameter, the scattering length *a.* At temperatures below T_D, these collisions are in the s-wave scattering regime where only the phase shift δ_0 of the lowest partial wave $\ell = 0$ is important. Moreover, for sufficiently low energies, such collisions are governed by the Wigner threshold laws where the phase shift δ_0 is inversely proportional to the wavevector k of the particle motion. Taking the limit for low energy gives the proportionality constant, defined as the scattering length $a = -\lim_{k \to 0}(\delta_0/k)$. The scattering length not only plays an important role in ultracold collisions, but also in the formation of Bose-Einstein condensates. In the Wigner threshold regime the cross section approaches a constant, $\sigma = 8\pi a^2$.[53]

Although ground-state collisions are important for evaporative cooling and BEC, they do *not* provide a very versatile research field from a collision physics point of view. The situation is completely different for the excited-state collisions. For typical temperatures in optical traps, the velocity of the atoms is sufficiently low that atoms excited at long range by laser light decay before the collision takes place. Laser excitation for low-energy collisions has to take place during the collision. By tuning the laser frequency, the collision dynamics can be altered and information on the states formed in the molecular system can be obtained. This is the basis of the new technique of photo-associative spectroscopy, which for the first time has identified purely long-range states in diatomic molecules.[1,54]

For atoms colliding in laser light closely tuned to the S-P transition, the potential is a C_3/R^3 dipole-dipole interaction when one of the atoms is excited. Absorption takes place at the Condon point R_C given by $\hbar\delta = -C_3/R_C^3$ or $R_C = (C_3/\hbar|\delta|)^{1/3}$. Note that the light has to be tuned below resonance, which is mostly the case for laser cooling. The Condon point for laser light detuned a few γ below resonance is typical 1000–2000 a_0.

Once the molecular complex becomes excited, it can evolve to smaller internuclear distances before emission takes place. Two particular cases are important for trap loss: (1) the emission of the molecular complex takes place at much smaller internuclear distance, and the energy gained between absorption and emission of the photon is converted into kinetic energy, or (2) the complex undergoes a transition to another state and the potential energy difference between the two states is converted into kinetic energy. In both cases the energy gain can be sufficient to eject one or both atoms out of the trap. In the case of the alkalis, the second reaction can take place because of the different fine-structure states and the reaction is denoted as a fine-structure changing collision. The first reaction is referred to as *radiative escape.*

Trap loss collisions in MOTs have been studied to great extent, but results of these studies have to be considered with care. In most cases, trap loss is studied by changing either the frequency or the intensity of the trapping laser, which also changes the conditions of the trap. The collision rate is not only changed because of a change in the collision cross section, but also because of changes in both the density and temperature of the atoms in the trap. Since these parameters cannot be determined with high accuracy in a high-density trap, where effects like radiation trapping can play an important role, obtaining accurate results this way is very difficult.

The first description of such processes was given by Gallagher and Pritchard.[55] In their semiclassical model (the GP-model), the laser light is assumed to be weak enough that the excitation rate can be described by a quasi-static excitation probability. Atoms in the excited state are accelerated toward one another by the C_3/R^3 potential. In order to calculate the survival of the atoms in the excited state, the elapsed time between excitation and arrival is calculated. The total number of collisions is then given by the number of atoms at a certain distance, the fraction of atoms in the excited state, and the survival rate, integrated over all distances. For small detunings, corresponding to large internuclear distances, the excitation rate is appreciable over a very large range of internuclear distances. However the excitation occurs at large internuclear distances so the survival rate of the excited atoms is small. For large detunings the excitation is located in a small region at small internuclear distances, so the total excitation rate is small, but the survival rate is large. As a result of this competition, the collision rate peaks at intermediate detunings.

Another description of optical collisions is given by Julienne and Vigue.[56] Their description of optical collisions (JV model) is quantum mechanical for the collision process, where they make a partial wave expansion of the incoming wavefunction. The authors describe the excitation process in the same way as it was done in the GP model. Thus the excitation is localized around the Condon point with a probability given by the quasi-static Lorentz formula.

In still another approach, a completely semiclassical description of optical collisions has been given by Mastwijk et al.[57] These authors start from the GP model, but make several important modifications. First, the Lorentz formula is replaced by the Landau-Zener formula. Second, the authors consider the motion of the atoms in the collision plane. At the Condon point, where the excitation takes place, the trajectory of the atom in the excited state is calculated by integration of the equation of motion. The results for their model are shown in Fig. 15, and are compared with experiment and the JV model. The agreement between the theory and experiment is rather good. For the JV model two curves are shown. The first curve shows the situation for the original JV model. The second curve shows the result of a modified JV model, where the quasi-static excitation rate is replaced by the Landau-Zener formula. The large discrepancies between the results for these two models indicates that it is important to use the correct model for the excitation. The agreement between the modified JV model and the semiclassical model is good, indicating that the dynamics of optical collisions can be described correctly quantum mechanically or semiclassically. Since the number of partial waves in the case of He* is in the order of 10, this is to be expected.

The previous description of optical collisions applies to the situation that the quasi-molecule can be excited for each frequency of the laser light. However, the quasi-molecule has well-defined vibrational and rotational states and the excitation frequency has to match the transition frequency between the ground and excited rovibrational states. Far from the dissociation limit, the rovibrational states are well-resolved and many resonances are observed. This has been the basis of the method of photo-associative spectroscopy (PAS) for alkali-metal atoms, where detailed information on molecular states of alkali dimers have been obtained recently. Here *photo-association* refers to the process where a photon is absorbed to transfer the system from the ground to the excited state where the two atoms are bound by their mutual attraction.

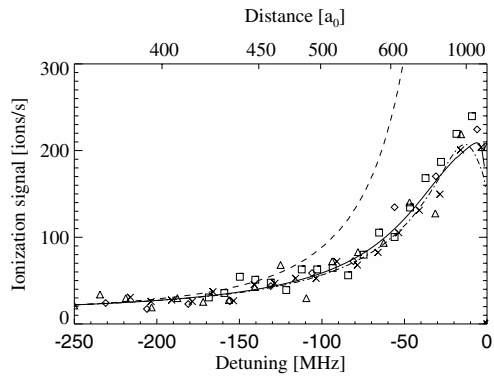

FIGURE 15 The frequency dependence for the associative ionization rate of cold He* collisions. The experimental results (symbols) are compared with the semiclassical model (solid line), JV-model (dashed line), and modified JV-model (dashed-dotted line). The axis on top of the plot shows the Condon point, where the excitation takes place.

The process of PAS is depicted graphically in Fig. 16. When two atoms collide in the ground state, they can be excited at a certain internuclear distance to the excited molecular state and the two atoms may remain bound after the excitation and form a molecule. This transient molecule lives as long as the system remains excited. The number of rotational states that can contribute to the spectrum is small for low temperature. The resolution is limited only by the linewidth of the transition, which is comparable to the natural linewidth of the atomic transition. With PAS, molecular states can be detected with a resolution of ≈10 MHz, which is many orders of magnitude better than traditional molecular spectroscopy. The formation of the molecules is probed by absorption of a second photon of the same color, which can ionize the molecule.

PAS has also been discussed in the literature as a technique to produce cold molecules. The methods discussed employ a double resonance technique, where the first color is used to create a well-defined rovibrational state of the molecule and a second color causes stimulated emission of the system to a well-defined vibrational level in the ground state. Although such a technique has not yet been shown to work experimentally, cold molecules have been produced in PAS recently using a simpler method.[58] The 0_g^- state in Cs_2 has a double-well structure, where the top of the barrier is accidentally close to the asymptotic limit. Thus atoms created in the outer well by PAS can tunnel through the barrier to the inner well, where there is a large overlap of the wavefunction with the vibrational levels in the ground state. These molecules are then stabilized against spontaneous decay and can be observed. The temperature of the cold molecules has been detected and is close to the temperature of the atoms. This technique and similar techniques will be very important for the production and study of cold molecules.

Optical Lattices

In 1968 V. S. Letokhov[59] suggested that it is possible to confine atoms in the wavelength-size regions of a standing wave by means of the dipole force that arises from the light shift. This

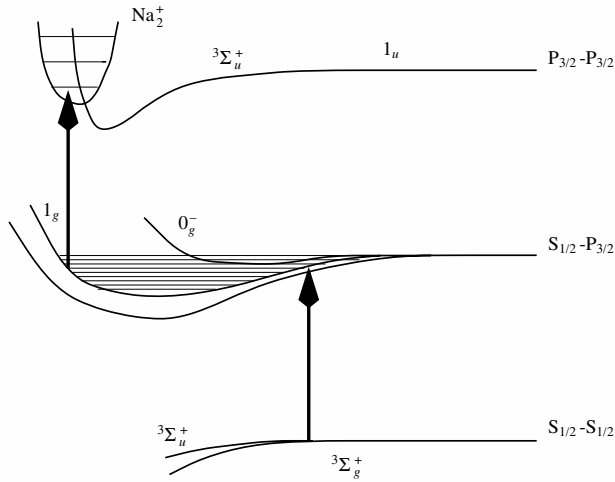

FIGURE 16 Photoassociation spectroscopy of Na. By tuning the laser below atomic resonance, molecular systems can be excited to the first excited state in which they are bound. By absorption of a second photon the system can be ionized, providing a high detection efficiency.

was first accomplished in 1987 in one dimension with an atomic beam traversing an intense standing wave.[60] Since then, the study of atoms confined in wavelength-size potential wells has become an important topic in optical control of atomic motion because it opens up configurations previously accessible only in condensed matter physics using crystals.

The basic ideas of the quantum mechanical motion of particles in a periodic potential were laid out in the 1930s with the Kronig-Penney model and Bloch's theorem, and optical lattices offer important opportunities for their study. For example, these lattices can be made essentially free of defects with only moderate care in spatially filtering the laser beams to assure a single transverse mode structure. Furthermore, the shape of the potential is exactly known, and doesn't depend on the effect of the crystal field or the ionic energy level scheme. Finally, the laser parameters can be varied to modify the depth of the potential wells without changing the lattice vectors, and the lattice vectors can be changed independently by redirecting the laser beams. The simplest optical lattice to consider is a one-dimensional pair of counterpropagating beams of the same polarization, as was used in the first experiment.[60]

Because of the transverse nature of light, any mixture of beams with different $\vec{k}$-vectors necessarily produces a spatially periodic, inhomogeneous light field. The importance of the "egg-crate" array of potential wells arises because the associated atomic light shifts can easily be comparable to the very low average atomic kinetic energy of laser-cooled atoms. A typical example projected against two dimensions is shown in Fig. 17.

The name *optical lattice* is used rather than *optical crystal* because the filling fraction of the lattice sites is typically only a few percent (as of 1999). The limit arises because the loading of atoms into the lattice is typically done from a sample of trapped and cooled atoms, such as a MOT for atom collection, followed by an optical molasses for laser cooling. The atomic density in such experiments is limited to a few times $10^{11}/\text{cm}^3$ by collisions and multiple light scattering. Since the density of lattice sites of size $\lambda/2$ is a few times $10^{13}/\text{cm}^3$, the filling fraction is necessarily small.

At first thought it would seem that a rectangular 2D or 3D optical lattice could be readily constructed from two or three mutually perpendicular standing waves.[61,62] However, a subwavelength movement of a mirror caused by a small vibration could change the relative phase of the standing waves. In 1993 a very clever scheme was described.[63] It was realized that an n-dimensional lattice could be created by only $n + 1$ traveling waves rather than $2n$. Instead of producing optical wells in 2D with four beams (two standing waves), these authors used only three. The $\vec{k}$-vectors of the coplanar beams were separated by $2\pi/3$, and they were all linearly polarized in their common plane (not parallel to one another). The same immunity to vibrations was established for a 3D optical lattice by using only four beams arranged in a quasi-

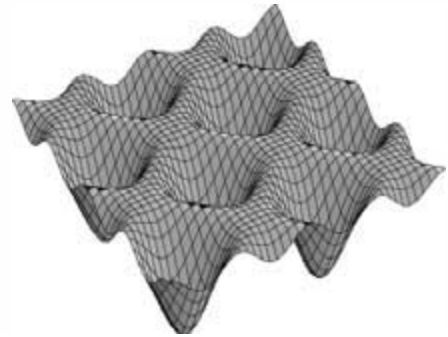

FIGURE 17 The "egg-crate" potential of an optical lattice shown in two dimensions. The potential wells are separated by $\lambda/2$.

tetrahedral configuration. The three linearly polarized beams of the 2D arrangement just described were directed out of the plane toward a common vertex, and a fourth circularly polarized beam was added. All four beams were polarized in the same plane.[63] The authors showed that such a configuration produced the desired potential wells in 3D.

The NIST group studied atoms loaded into an optical lattice using Bragg diffraction of laser light from the spatially ordered array.[64] They cut off the laser beams that formed the lattice, and before the atoms had time to move away from their positions, they pulsed on a probe laser beam at the Bragg angle appropriate for one of the sets of lattice planes. The Bragg diffraction not only enhanced the reflection of the probe beam by a factor of 10^5, but by varying the time between the shut-off of the lattice and turn-on of the probe, they could measure the "temperature" of the atoms in the lattice. The reduction of the amplitude of the Bragg scattered beam with time provided some measure of the diffusion of the atoms away from the lattice sites, much like the Debye-Waller factor in X-ray diffraction.

Laser cooling has brought the study of the motion of atoms into an entirely new domain where the quantum mechanical nature of their center-of-mass motion must be considered.[1] Such exotic behavior for the motion of whole atoms, as opposed to electrons in the atoms, has not been considered before the advent of laser cooling simply because it is too far out of the range of ordinary experiments. A series of experiments in the early 1990s provided dramatic evidence for these new quantum states of motion of neutral atoms, and led to the debut of de Broglie wave atom optics.

The limits of laser cooling discussed in Sec. 28.6 suggest that atomic momenta can be reduced to a "few" times $\hbar k$. This means that their de Broglie wavelengths are equal to the optical wavelengths divided by a "few." If the depth of the optical potential wells is high enough to contain such very slow atoms, then their motion in potential wells of size $\lambda/2$ must

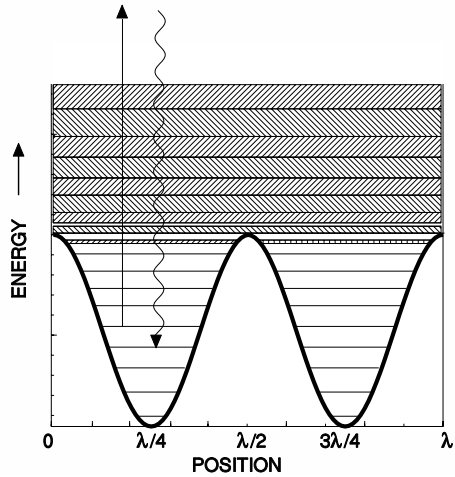

FIGURE 18 Energy levels of atoms moving in the periodic potential of the light shift in a standing wave. There are discrete bound states deep in the wells that broaden at higher energy, and become bands separated by forbidden energies above the tops of the wells. Under conditions appropriate to laser cooling, optical pumping among these states favors populating the lowest ones as indicated schematically by the arrows.

be described quantum mechanically, since they are confined to a space of size comparable to their de Broglie wavelengths. Thus they do not oscillate in the sinusoidal wells as classical localizable particles, but instead occupy discrete, quantum-mechanical bound states, as shown in the lower part of Fig. 18.

The group at NIST also developed a new method that superposed a weak probe beam of light directly from the laser upon some of the fluorescent light from the atoms in a 3D optical molasses, and directed the light from these combined sources onto on a fast photodetector.[65] The resulting beat signal carried information about the Doppler shifts of the atoms in the optical lattices.[34] These Doppler shifts were expected to be in the sub-MHz range for atoms with the previously measured 50 μK temperatures. The observed features confirmed the quantum nature of the motion of atoms in the wavelength-size potential wells (see Fig. 19).[16]

In the 1930s Bloch realized that applying a uniform force to a particle in a periodic potential would not accelerate it beyond a certain speed, but instead would result in Bragg reflection when its de Broglie wavelength became equal to the lattice period. Thus an electric field applied to a conductor could not accelerate electrons to a speed faster than that corresponding to the edge of a Brillouin zone, and that at longer times the particles would execute oscillatory motion. Ever since then, experimentalists have tried to observe these Bloch oscillations in increasingly pure and/or defect-free crystals.

Atoms moving in optical lattices are ideally suited for such an experiment, as was beautifully demonstrated in 1996.[66] The authors loaded a one-dimensional lattice with atoms from a 3D molasses, further narrowed the velocity distribution, and then instead of applying a constant force, simply changed the frequency of one of the beams of the 1D lattice with respect to the other in a controlled way, thereby creating an accelerating lattice. Seen from the atomic reference frame, this was the equivalent of a constant force trying to accelerate them. After a variable time t_a the 1D lattice beams were shut off and the measured atomic velocity distribution showed beautiful Bloch oscillations as a function of t_a. The centroid of the very narrow velocity distribution was seen to shift in velocity space at a constant rate until it reached $v_r = \hbar k/M$, and then it vanished and reappeared at $-v_r$ as shown in Fig. 20. The shape of the "dispersion curve" allowed measurement of the "effective mass" of the atoms bound in the lattice.

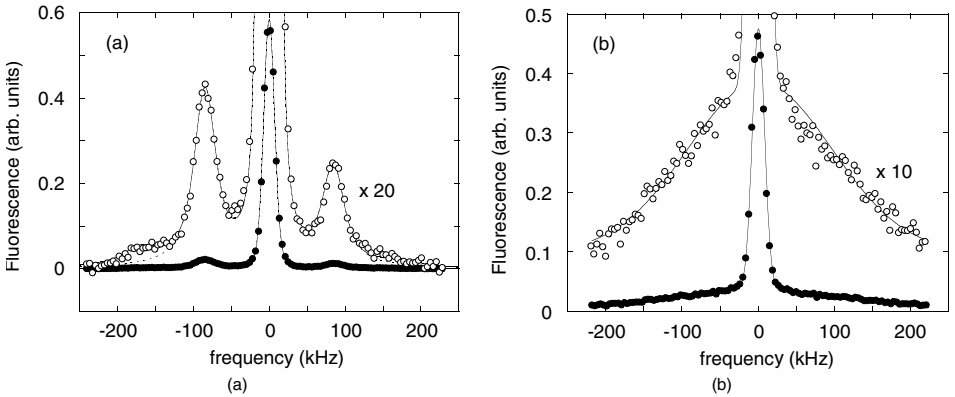

FIGURE 19 (*a*) Fluorescence spectrum in a 1D lin ⊥ lin optical molasses. Atoms are first captured and cooled in an MOT, then the MOT light beams are switched off leaving a pair of lin ⊥ lin beams. Then the measurements are made with $\delta = -4\gamma$ at low intensity. (*b*) Same as (*a*) except the 1D molasses is σ^+–σ^- which has no spatially dependent light shift and hence no vibrational motion (figure from Ref. 34).

Bose-Einstein Condensation

In 1924 S. Bose found the correct way to evaluate the distribution of identical entities, such as Planck's radiation quanta, that allowed him to calculate the Planck spectrum using the methods of statistical mechanics. Within a year Einstein had seized upon this idea, and generalized it to identical particles with discrete energies. This distribution is

$$N(E) = \frac{1}{e^{\beta(E-\mu)} - 1} \tag{33}$$

where $\beta \equiv 1/k_B T$ and μ is the chemical potential that vanishes for photons: Eq. (33) with $\mu = 0$ is exactly the Planck distribution. Einstein observed that this distribution has the peculiar property that for sufficiently low average energy (*i.e.,* low temperature), the total energy could be minimized by having a discontinuity in the distribution for the population of the lowest allowed state.

The condition for this Bose-Einstein condensation (BEC) in a gas can be expressed in terms of the de Broglie wavelength λ_{dB} associated with the thermal motion of the atoms as $n\lambda_{dB}^3 \geq 2.612\ldots$, where n is the spatial density of the atoms. In essence, this means that the atomic wave functions must overlap one another.

The most familiar elementary textbook description of BEC focuses on noninteracting particles. However, particles *do* interact, and the lowest order approximation that is widely used to account for the interaction takes the form of a mean-field repulsive force. It is inserted into the Hamiltonian for the motion of each atom in the trap (*n.b.,* not for the internal structure of the atom) as a term V_{int} proportional to the local density of atoms. Since this local density is itself $|\Psi|^2$, it makes the Schrödinger equation for the atomic motion nonlinear, and the result bears the name *Gross-Pitaevski equation.* For N atoms in the condensate it is written

$$\left[-\frac{\hbar^2}{2M}\nabla_{\vec{R}}^2 + V_{\text{trap}}(\vec{R}) + NV_{\text{int}}|\Psi(\vec{R})|^2\right]\Psi(\vec{R}) = E_N\Psi(\vec{R}) \tag{34}$$

where $\vec{R}$ is the coordinate of the atom in the trap, $V_{\text{trap}}(\vec{R})$ is the potential associated with the trap that confines the atoms in the BEC, and $V_{\text{int}} \equiv 4\pi\hbar^2 a/M$ is the coefficient associated with strength of the mean field interaction between the atoms. Here a is the scattering length, and M is the atomic mass.

For $a > 0$ the interaction is repulsive so that a BEC would tend to disperse. This is manifest for a BEC confined in a harmonic trap by having its wavefunction somewhat more spread out

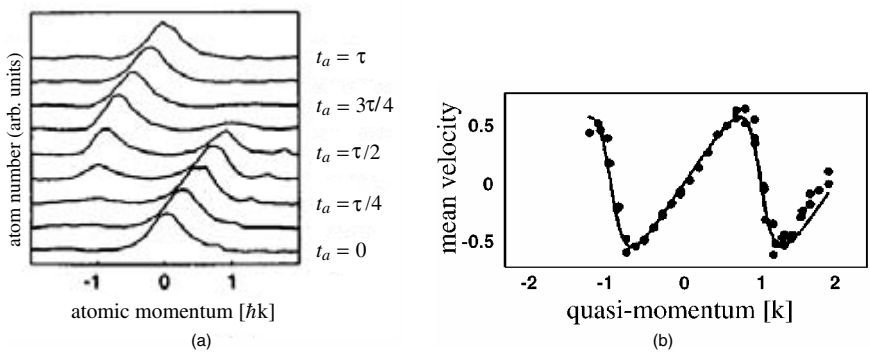

FIGURE 20 Plot of the measured velocity distribution versus time in the accelerated 1D lattice. The atoms accelerate only to the edge of the Brillouin zone where the velocity is $+v_r$, and then the velocity distribution appears at $-v_r$ (figure from Ref. 66).

and flatter than a Gaussian. By contrast, for $a < 0$ the interaction is attractive and the BEC eventually collapses. However, it has been shown that there is metastability for a sufficiently small number of particles with $a < 0$ in a harmonic trap, and that a BEC can be observed in vapors of atoms with such negative scattering length as ^{7}Li.[67–69] This was initially somewhat controversial.

Solutions to this highly nonlinear Eq. (34), and the ramifications of those solutions, form a major part of the theoretical research into BEC. Note that the condensate atoms all have exactly the same wave function, which means that adding atoms to the condensate does not increase its volume, just like the increase of atoms to the liquid phase of a liquid-gas mixture makes only an infinitesimal volume increase of the sample. The consequences of this predicted condensation are indeed profound. For example, in a harmonic trap, the lowest state's wavefunction is a Gaussian. With so many atoms having *exactly* the same wave function they form a new state of matter, unlike anything in the familiar experience.

Achieving the conditions required for BEC in a low-density atomic vapor requires a long and difficult series of cooling steps. First, note that an atomic sample cooled to the recoil limit T_r would need to have a density of a few times 10^{13} atoms/cm^3 in order to satisfy BEC. However, atoms cannot be optically cooled at this density because the resulting vapor would have an absorption length for on-resonance radiation approximately equal to the optical wavelength. Furthermore, collisions between ground- and excited-state atoms have such a large cross section that at this density the optical cooling would be extremely ineffective. In fact, the practical upper limit to the atomic density for laser cooling in a 3D optical molasses (see Sec. 28.6) or MOT (see Sec. 28.7) corresponds to $n \sim 10^{10}$ atoms/cm^3. Thus it is clear that the final stage of cooling toward a BEC must be done in the dark. The process typically begins with a MOT for efficient capture of atoms from a slowed beam or from the low-velocity tail of a Maxwell-Boltzmann distribution of atoms at room temperature. Then a polarization gradient optical molasses stage is initiated that cools the atomic sample from the mK temperatures of the MOT to a few times T_r. For the final cooling stage, the cold atoms are confined in the dark in a purely magnetic trap and a forced evaporative cooling process is used to cool.[1]

The observation of BEC in trapped alkali atoms in 1995 has been the largest impetus to research in this exciting field. As of this writing (1999), the only atoms that have been condensed are Rb,[70] Na,[71] Li,[72] and H.[73] The case of Cs is special because, although BEC is certainly possible, the presence of a near-zero energy resonance severely hampers its evaporative cooling rate.

The first observations of BEC were in Rb,[70] Li,[72] and Na,[71] and the observation was done using ballistic techniques. The results from one of the first experiments are shown in Fig. 21. The three panels show the spatial distribution of atoms some time after release from the trap. From the ballistic parameters, the size of the BEC sample as well as its shape and the velocity distribution of its atoms could be inferred. For temperatures too high for BEC, the velocity distribution is Gaussian but asymmetrical. For temperatures below the transition to BEC, the distribution is also not symmetrical, but now shows the distinct peak of a disproportionate number of very slow atoms corresponding to the ground state of the trap from which they were released. As the temperature is lowered further, the number of atoms in the narrow feature increases very rapidly, a sure signature that this is truly a BEC and not just very efficient cooling.

The study of this "new form" of matter has spawned innumerable subtopics and has attracted enormous interest. Both theorists and experimentalists are addressing the questions of its behavior in terms of rigidity, acoustics, coherence, and a host of other properties. Extraction of a coherent beam of atoms from a BEC has been labeled an "atom laser" and will surely open the way for new developments in atom optics.[1]

Dark States

The BEC discussed in the previous subsection is an example of the importance of quantum effects on atomic motion. It occurs when the atomic de Broglie wavelength λ_{dB} and the inter-

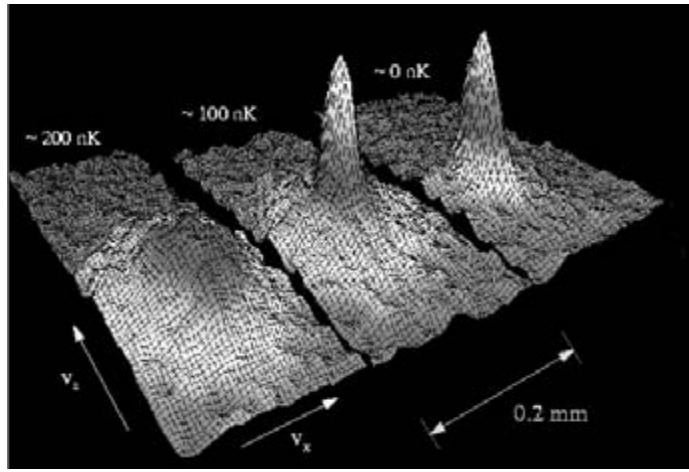

FIGURE 21 Three panels showing the spatial distribution of atoms after release from the magnetostatic trap following various degrees of evaporative cooling. In the first one, the atoms were cooled to just before the condition for BEC was met, in the second one, to just after this condition, and in the third one to the lowest accessible temperature consistent with leaving some atoms still in the trap (figure taken from the JILA Web page).

atomic distances are comparable. Other fascinating quantum effects occur when atoms are in the light and λ_{dB} is comparable to the optical wavelength. Some topics connected with optical lattices have already been discussed, and the *dark states* described here are another important example. These are atomic states that cannot be excited by the light field.

The quantum description of atomic motion requires that the energy of such motion be included in the Hamiltonian. The total Hamiltonian for atoms moving in a light field would then be given by

$$\mathcal{H} = \mathcal{H}_{\text{atom}} + \mathcal{H}_{\text{rad}} + \mathcal{H}_{\text{int}} + \mathcal{H}_{\text{kin}} \tag{35}$$

where $\mathcal{H}_{\text{atom}}$ describes the motion of the atomic electrons and gives the internal atomic energy levels, $\mathcal{H}_{\text{rad}}$ is the energy of the radiation field and is of no concern here because the field is not quantized, $\mathcal{H}_{\text{int}}$ describes the excitation of atoms by the light field and the concomitant light shifts, and $\mathcal{H}_{\text{kin}}$ is the kinetic energy E_k of the motion of the atoms' center of mass. This Hamiltonian has eigenstates of not only the internal energy levels and the atom-laser interaction that connects them, but also of the kinetic energy operator $\mathcal{H}_{\text{kin}} \equiv \mathcal{P}^2/2M$. These eigenstates will therefore be labeled by quantum numbers of the atomic states as well as the center of mass momentum p. For example, an atom in the ground state, $|g; p\rangle$, has energy $E_g + p^2/2M$ which can take on a continuous range of values.

To see how the quantization of the motion of a two-level atom in a monochromatic field allows the existence of a velocity-selective dark state, consider the states of a two-level atom with single internal ground and excited levels, $|g; p\rangle$ and $|e; p'\rangle$. Two ground eigenstates $|g; p\rangle$ and $|g; p''\rangle$ are generally not coupled to one another by an optical field except in certain cases. For example, in oppositely propagating light beams (1D) there can be absorption-stimulated emission cycles that connect $|g; p\rangle$ to itself or to $|g; p \pm 2\rangle$ (in this section, momentum is measured in units of $\hbar k$). The initial and final E_k of the atom differ by $\pm 2(p \pm 1)/M$ so energy conservation requires $p = \mp 1$ and is therefore velocity-selective (the energy of the light field is unchanged by the interaction since all the photons in the field have energy $\hbar\omega_\ell$).

The coupling of these two degenerate states by the light field produces off-diagonal matrix elements of the total Hamiltonian $\mathcal{H}$ of Eq. (35), and subsequent diagonalization of it results in the new ground eigenstates of $\mathcal{H}$ given by (see Fig. 22) $|\pm\rangle \equiv (|g;-1\rangle \pm |g;+1\rangle)/\sqrt{2}$. The excitation rate of these eigenstates $|\pm\rangle$ to $|e;0\rangle$ is proportional to the square of the electric dipole matrix element $\vec{\mu}$ given by

$$|\langle e;0|\vec{\mu}|\pm\rangle|^2 = |\langle e;0|\vec{\mu}|g;-1\rangle \pm \langle e;0|\vec{\mu}|g;+1\rangle|^2/2 \tag{36}$$

This vanishes for $|-\rangle$ because the two terms on the right-hand side of Eq. (36) are equal since $\vec{\mu}$ does not operate on the external momentum of the atom (dotted line of Fig. 22). Excitation of $|\pm\rangle$ to $|e;\pm2\rangle$ is much weaker since it's off resonance because its energy is higher by $4\hbar\omega_r = 2\hbar^2k^2/M$, so that the required frequency is higher than to $|e;0\rangle$. The resultant detuning is $4\omega_r = 8\varepsilon(\gamma/2)$, and for $\varepsilon \sim 0.5$, this is large enough so that the excitation rate is small, making $|-\rangle$ quite dark. Excitation to any state other than $|e;\pm2\rangle$ or $|e;0\rangle$ is forbidden by momentum conservation. Atoms are therefore optically pumped into the dark state $|-\rangle$ where they stay trapped, and since their momentum components are fixed, the result is velocity-selective coherent population trapping (VSCPT).

A useful view of this dark state can be obtained by considering that its components $|g;\pm1\rangle$ have well-defined momenta, and are therefore completely delocalized. Thus they can be viewed as waves traveling in opposite directions but having the same frequency, and therefore they form a standing de Broglie wave. The fixed spatial phase of this standing wave relative to the optical standing wave formed by the counterpropagating light beams results in the vanishing of the spatial integral of the dipole transition matrix element so that the state cannot be excited. This view can also help to explain the consequences of p not exactly equal ±1, where the de Broglie wave would be slowly drifting in space. It is common to label the average of the momenta of the coupled states as the *family momentum,* $\mathcal{P}$, and to say that these states form a *closed family,* having family momentum $\mathcal{P} = 0$.[74,75]

In the usual case of laser cooling, atoms are subject to both a damping force *and* to random impulses arising from the discrete photon momenta $\hbar k$ of the absorbed and emitted light. These can be combined to make a force versus velocity curve as shown in Fig. 23*a.* Atoms with $\mathcal{P} \neq 0$ are always subject to the light field that optically pumps them into the dark state and thus produces random impulses as shown in Fig. 23*b.* There is no damping force in the most commonly studied case of a real atom, the $J = 1 \rightarrow 1$ transition in He*, because the Doppler and polarization gradient cooling cancel one another as a result of a numerical "accident" for this particular case.

Figures 23*a* and *b* should be compared to show the velocity dependence of the sum of the damping and random forces for the two cases of ordinary laser cooling and VSCPT. Note that for

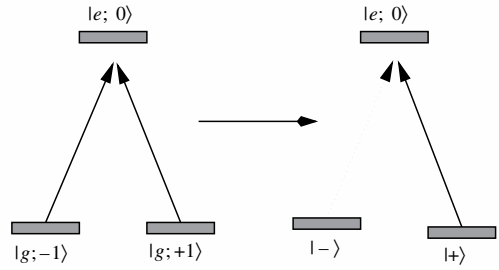

FIGURE 22 Schematic diagram of the transformation of the eigenfunctions from the internal atomic states $|g;p\rangle$ to the eigenstates $|\pm\rangle$. The coupling between the two states $|g;p\rangle$ and $|g;p''\rangle$ by Raman transitions mixes them, and since they are degenerate, the eigenstates of $\mathcal{H}$ are the nondegenerate states $|\pm\rangle$.

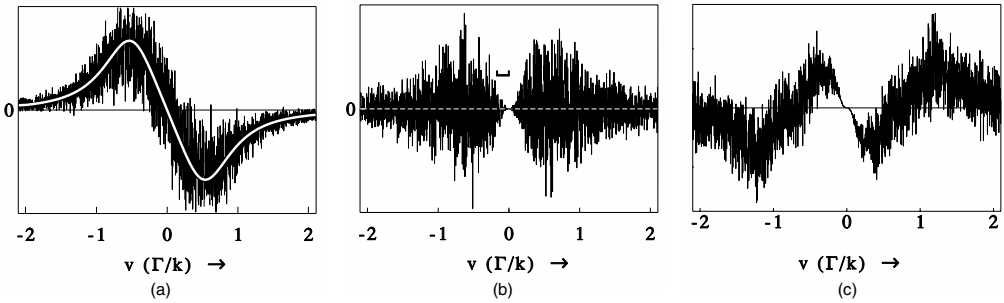

FIGURE 23 Calculated force versus velocity curves for different laser configurations showing both the average force and a typical set of simulated fluctuations. Part (*a*) shows the usual Doppler cooling scheme that produces an atomic sample in steady state whose energy width is $\hbar\gamma/2$. Part (*b*) shows VSCPT as originally studied in Ref. 74 with no damping force. Note that the fluctuations vanish for $\mathcal{P} = 0$ because the atoms are in the dark state. Part (*c*) shows the presence of both a damping force and VSCPT. The fluctuations vanish for $\mathcal{P} = 0$, and both damping *and* fluctuations are present at $\mathcal{P} \neq 0$.

VSCPT the momentum diffusion vanishes when the atoms are in the dark state at $\mathcal{P} = 0$, so they can collect there. In the best of both worlds, a damping force would be combined with VSCPT as shown in Fig. 23*c*. Such a force was predicted in Ref. 76 and was first observed in 1996.[77]

28.8 REFERENCES

1. H. J. Metcalf and P. van der Straten, *Laser Cooling and Trapping,* Springer-Verlag, New York, 1999.
2. J. Gordon and A. Ashkin, "Motion of Atoms in a Radiation Trap," *Phys. Rev. A* **21**:1606 (1980).
3. W. Phillips and H. Metcalf, "Laser Deceleration of an Atomic Beam," *Phys. Rev. Lett.* **48**:596 (1982).
4. J. Prodan, W. Phillips, and H. Metcalf. "Laser Production of a Very Slow Monoenergetic Atomic Beam," *Phys. Rev. Lett.* **49**:1149 (1982).
5. J. Prodan and W. Phillips, "Chirping the Light Fantastic—Recent NBS Atom Cooling Experiments," *Prog. Quant. Elect.* **8**:231 (1984).
6. W. Ertmer, R. Blatt, J. L. Hall, and M. Zhu, "Laser Manipulation of Atomic Beam Velocities: Demonstration of Stopped Atoms and Velocity Reversal," *Phys. Rev. Lett.* **54**:996 (1985).
7. R. Watts and C. Wieman, "Manipulating Atomic Velocities Using Diode Lasers," *Opt. Lett.* **11**:291 (1986).
8. V. Bagnato, G. Lafyatis, A. Martin, E. Raab, R. Ahmad-Bitar, and D. Pritchard, "Continuous Stopping and Trapping of Neutral Atoms," *Phys. Rev. Lett.* **58**:2194 (1987).
9. T. E. Barrett, S. W. Dapore-Schwartz, M. D. Ray, and G. P. Lafyatis, "Slowing Atoms with (σ^-)-Polarized Light," *Phys. Rev. Lett.* **67**:3483–3487 (1991).
10. J. Dalibard and W. Phillips, "Stability and Damping of Radiation Pressure Traps," *Bull. Am. Phys. Soc.* **30**:748 (1985).
11. S. Chu, L. Hollberg, J. Bjorkholm, A. Cable, and A. Ashkin, "Three-Dimensional Viscous Confinement and Cooling of Atoms by Resonance Radiation Pressure," *Phys. Rev. Lett.* **55**:48 (1985).
12. P. D. Lett, R. N. Watts, C. E. Tanner, S. L. Rolston, W. D. Phillips, and C. I. Westbrook, "Optical Molasses," *J. Opt. Soc. Am. B* **6**:2084–2107 (1989).
13. D. Sesko, C. Fan, and C. Wieman. "Production of a Cold Atomic Vapor Using Diode-Laser Cooling," *J. Opt. Soc. Am. B* **5**:1225 (1988).
14. P. Gould, P. Lett, and W. D. Phillips, "New Measurement with Optical Molasses," in *Laser Spectroscopy VIII,* W. Persson and S. Svanberg, (eds.) Springer, Berlin, 1987.

15. T. Hodapp, C. Gerz, C. Westbrook, C. Furtlehner, and W. Phillips, "Diffusion in Optical Molasses," *Bull. Am. Phys. Soc.* **37**:1139 (1992).
16. P. Lett, R. Watts, C. Westbrook, W. Phillips, P. Gould, and H. Metcalf, "Observation of Atoms Laser Cooled Below the Doppler Limit," *Phys. Rev. Lett.* **61**:169 (1988).
17. J. Dalibard and C. Cohen-Tannoudji, "Laser Cooling Below the Doppler Limit by Polarization Gradients—Simple Theoretical-Models," *J. Opt. Soc. Am. B* **6**:2023–2045 (1989).
18. P. J. Ungar, D. S. Weiss, S. Chu, and E. Riis, "Optical Molasses and Multilevel Atoms—Theory," *J. Opt. Soc. Am. B* **6**:2058–2071 (1989).
19. C. Cohen-Tannoudji and W. D. Phillips, "New Mechanisms for Laser Cooling," *Phys. Today* **43**: October, 33–40 (1990).
20. C. Salomon, J. Dalibard, W. D. Phillips, A. Clairon, and S. Guellati, "Laser Cooling of Cesium Atoms Below 3 μK," *Europhys. Lett.* **12**:683–688 (1990).
21. W. Ketterle and N. J. van Druten, "Evaporative Cooling of Trapped Atoms," *Adv. Atom. Mol. Opt. Phys.* **37**:181 (1996).
22. M. Kasevich and S. Chu, "Laser Cooling Below a Photon Recoil with 3-Level Atoms," *Phys. Rev. Lett.* **69**:1741–1744 (1992).
23. D. Wineland, W. Itano, J. Bergquist, and J. Bollinger, "Trapped Ions and Laser Cooling," Technical Report 1086, N.I.S.T. (1985).
24. A. Migdall, J. Prodan, W. Phillips, T. Bergeman, and H. Metcalf, "First Observation of Magnetically Trapped Neutral Atoms," *Phys. Rev. Lett.* **54**:2596 (1985).
25. T. Bergeman, G. Erez, and H. Metcalf, "Magnetostatic Trapping Fields for Neutral Atoms," *Phys. Rev. A* **35**:1535 (1987).
26. A. Ashkin, "Acceleration and Trapping of Particles by Radiation Pressure," *Phys. Rev. Lett.* **24**:156 (1970).
27. S. Chu, J. Bjorkholm, A. Ashkin, and A. Cable, "Experimental Observation of Optically Trapped Atoms," *Phys. Rev. Lett.* **57**:314 (1986).
28. A. Ashkin, "Application of Laser Radiation Pressure," *Science* **210**:1081–1088 (1980).
29. A. Ashkin and J. M. Dziedzic, "Observation of Radiation-Pressure Trapping of Particles by Alternating Light Beams," *Phys. Rev. Lett.* **54**:1245 (1985).
30. A. Ashkin and J. M. Dziedzic, "Optical Trapping and Manipulation of Viruses and Bacteria," *Science* **235**:1517 (1987).
31. J. D. Miller, R. A. Cline, and D. J. Heinzen, "Far-Off-Resonance Optical Trapping of Atoms," *Phys. Rev. A* **47,** R4567–R4570 (1993).
32. Y. Castin and J. Dalibard, "Quantization of Atomic Motion in Optical Molasses," *Europhys. Lett.* **14**:761–766 (1991).
33. P. Verkerk, B. Lounis, C. Salomon, C. Cohen-Tannoudji, J. Y. Courtois, and G. Grynberg, "Dynamics and Spatial Order of Cold Cesium Atoms in a Periodic Optical-Potential," *Phys. Rev. Lett.* **68**:3861–3864 (1992).
34. P. S. Jessen, C. Gerz, P. D. Lett, W. D. Phillips, S. L. Rolston, R. J. C. Spreeuw, and C. I. Westbrook, "Observation of Quantized Motion of Rb Atoms in an Optical-Field," *Phys. Rev. Lett.* **69**:49–52 (1992).
35. B. Lounis, P. Verkerk, J. Y. Courtois, C. Salomon, and G. Grynberg, "Quantized Atomic Motion in 1D Cesium Molasses with Magnetic-Field," *Europhys. Lett.* **21**:13–17 (1993).
36. E. Raab, M. Prentiss, A. Cable, S. Chu, and D. Pritchard, "Trapping of Neutral-Sodium Atoms with Radiation Pressure," *Phys. Rev. Lett.* **59**:2631 (1987).
37. T. Walker, D. Sesko, and C. Wieman, "Collective Behavior of Optically Trapped Neutral Atoms," *Phys. Rev. Lett.* **64**:408–411 (1990).
38. D. W. Sesko, T. G. Walker, and C. E. Wieman, "Behavior of Neutral Atoms in a Spontaneous Force Trap," *J. Opt. Soc. Am. B* **8**:946–958 (1991).
39. J. Nellessen, J. H. Muller, K. Sengstock, and W. Ertmer, "Laser Preparation of a Monoenergetic Sodium Beam," *Europhys. Lett.* **9**:133–138 (1989).

40. J. Nellessen, J. H. Muller, K. Sengstock, and W. Ertmer, "Large-Angle Beam Deflection of a Laser-Cooled Sodium Beam," *J. Opt. Soc. Am. B* **6**:2149–2154 (1989).
41. J. Nellessen, J. Werner, and W. Ertmer, "Magnetooptical Compression of a Monoenergetic Sodium Atomic-Beam," *Opt. Commun.* **78**:300–308 (1990).
42. E. Riis, D. S. Weiss, K. A. Moler, and S. Chu, "Atom Funnel for the Production of a Slow, High-Density Atomic-Beam," *Phys. Rev. Lett.* **64**:1658–1661 (1990).
43. A. Aspect, N. Vansteenkiste, R. Kaiser, H. Haberland, and M. Karrais, "Preparation of a Pure Intense Beam of Metastable Helium by Laser Cooling," *Chem. Phys.* **145**:307–315 (1990).
44. M. D. Hoogerland, J. P. J. Driessen, E. J. D. Vredenbregt, H. J. L. Megens, M. P. Schuwer, H. C. W. Beijerinck, and K. A. H. van Leeuwen, "Bright Thermal Atomic-Beams by Laser Cooling—A 1400-Fold Gain in-Beam Flux," *App. Phys. B* **62,** 323–327 (1996).
45. R. A. Nauman and H. Henry Stroke, "Apparatus Upended: A Short History of the Fountain A-Clock," *Phys. Today* 89 (May 1996).
46. M. A. Kasevich, E. Riis, S. Chu, and R. G. Devoe, "RF Spectroscopy in an Atomic Fountain," *Phys. Rev. Lett.* **63**:612–616 (1989).
47. A. Clairon, C. Salomon, S. Guellati, and W. D. Phillips, "Ramsey Resonance in a Zacharias Fountain," *Europhys. Lett.* **16**:165–170 (1991).
48. K. Gibble and S. Chu, "Future Slow-Atom Frequency Standards," *Metrologia* **29**:201–212 (1992).
49. K. Gibble and S. Chu, "Laser-Cooled Cs Frequency Standard and a Measurement of the Frequency-Shift Due to Ultracold Collisions," *Phys. Rev. Lett.* **70**:1771–1774 (1993).
50. K. Gibble and B. Verhaar, "Eliminating Cold-Collision Frequency Shifts," *Phys. Rev. A* **52**:3370 (1995).
51. R. Legere and K. Gibble, "Quantum Scattering in a Juggling Atomic Fountain," *Phys. Rev. Lett.* **81**:5780 (1998).
52. Ph. Laurent, P. Lemonde, E. Simon, G. Santorelli, A. Clairon, N. Dimarcq, P. Petit, C. Audoin, and C. Salomon, "A Cold Atom Clock in the Absence of Gravity," *Eur. Phys. J. D* **3**:201 (1998).
53. P. S. Julienne and F. H. Mies, "Collisions of Ultracold Trapped Atoms," *J. Opt. Soc. Am.* **B6**:2257–2269 (1989).
54. P. D. Lett, P. S. Julienne, and W. D. Phillips, "Photoassociative Spectroscopy of Laser-Cooled Atoms," *Annual Rev. Phys. Chem.* **46**:423 (1995).
55. A. Gallagher and D. E. Pritchard, "Exoergic Collisions of Cold Na*-Na," *Phys. Rev. Lett.* **63**:957–960 (1989).
56. P. S. Julienne and J. Vigue, "Cold Collisions of Ground-State and Excited-State Alkali-Metal Atoms," *Phys. Rev. A* **44**:4464–4485 (1991).
57. H. Mastwijk, J. Thomsen, P. van der Straten, and A. Niehaus, "Optical Collisions of Cold, Metastable Helium Atoms," *Phys. Rev. Lett.* **80**:5516–5519 (1998).
58. A. Fioretti, D. Comparat, A. Crubellier, O. Dulieu, F. Masnou-Seeuws, and P. Pillet, "Formation of Cold Cs_2 Molecules through Photoassociation," *Phys. Rev. Lett.* **80**:4402–4405 (1998).
59. V. S. Lethokov, "Narrowing of the Doppler Width in a Standing Light Wave," *JETP Lett.* **7**:272 (1968).
60. C. Salomon, J. Dalibard, A. Aspect, H. Metcalf, and C. Cohen-Tannoudji, "Channeling Atoms in a Laser Standing Wave," *Phys. Rev. Lett.* **59**:1659 (1987).
61. K. I. Petsas, A. B. Coates, and G. Grynberg, "Crystallography of Optical Lattices," *Phys. Rev. A* **50**:5173–5189 (1994).
62. P. S. Jessen and I. H. Deutsch, "Optical Lattices," *Adv. Atom. Mol. Opt. Phys.* **37**:95–138 (1996).
63. G. Grynberg, B. Lounis, P. Verkerk, J. Y. Courtois, and C. Salomon, "Quantized Motion of Cold Cesium Atoms in 2-Dimensional and 3-Dimensional Optical Potentials," *Phys. Rev. Lett.* **70**:2249–2252 (1993).
64. G. Birkl, M. Gatzke, I. H. Deutsch, S. L. Rolston, and W. D. Phillips, "Bragg Scattering from Atoms in Optical Lattices," *Phys. Rev. Lett.* **75**:2823–2826 (1995).
65. C. I. Westbrook, R. N. Watts, C. E. Tanner, S. L. Rolston, W. D. Phillips, P. D. Lett, and P. L. Gould, "Localization of Atoms in a 3-Dimensional Standing Wave," *Phys. Rev. Lett.* **65**:33–36 (1990).
66. M. Dahan, E. Peik, J. Reichel, Y. Castin, and C. Salomon, "Bloch Oscillations of Atoms in an Optical Potential," *Phys. Rev. Lett.* **76**:4508 (1996).

67. H. T. C. Stoof, "Atomic Bose-Gas with a Negative Scattering Length," *Phys. Rev. A* **49**:3824–3830 (1994).
68. T. Bergeman, "Hartree-Fock Calculations of Bose-Einstein Condensation of ^{7}Li Atoms in a Harmonic Trap for $T > 0$," *Phys. Rev. A* **55**:3658 (1997).
69. T. Bergeman, "Erratum: Hartree-Fock Calculations of Bose-Einstein Condensation of ^{7}Li Atoms in a Harmonic Trap for $T > 0$," *Phys. Rev. A* **56**:3310 (1997).
70. M. H. Anderson, J. R. Ensher, M. R. Matthews, C. E. Wieman, and E. A. Cornell, "Observation of Bose-Einstein Condensation in a Dilute Atomic Vapor," *Science* **269**:198–201 (1995).
71. K. Davis, M-O. Mewes, M. Andrews, M. van Druten, D. Durfee, D. Kurn, and W. Ketterle, "Bose-Einstein Condensation in a Gas of Sodium Atoms," *Phys. Rev. Lett.* **75**:3969 (1995).
72. C. C. Bradley, C. A. Sackett, J. J. Tollett, and R. G. Hulet, "Evidence of Bose-Einstein Condensation in an Atomic Gas with Attractive Interactions," *Phys. Rev. Lett.* **75**:1687–1690 (1995).
73. D. Fried, T. Killian, L. Willmann, D. Landhuis, S. Moss, D. Kleppner, and T. Greytak, "Bose-Einstein Condensation of Atomic Hydrogen," *Phys. Rev. Lett.* **81**:3811 (1998).
74. A. Aspect, E. Arimondo, R. Kaiser, N. Vansteenkiste, and C. Cohen-Tannoudji, "Laser Cooling below the One-Photon Recoil Energy by Velocity-Selective Coherent Population Trapping," *Phys. Rev. Lett.* **61**:826 (1988).
75. A. Aspect, C. Cohen-Tannoudji, E. Arimondo, N. Vansteenkiste, and R. Kaiser, "Laser Cooling Below the One-Photon Recoil Energy by Velocity-Selective Coherent Population Trapping—Theoretical-Analysis," *J. Opt. Soc. Am. B* **6**:2112–2124 (1989).
76. M. S. Shahriar, P. R. Hemmer, M. G. Prentiss, P. Marte, J. Mervis, D. P. Katz, N. P. Bigelow, and T. Cai, "Continuous Polarization-Gradient Precooling-Assisted Velocity-Selective Coherent Population Trapping," *Phys. Rev. A* **48**:R4035–R4038 (1993).
77. M. Widmer, M. J. Bellanca, W. Buell, H. Metcalf, M. Doery, and E. Vredenbregt, "Measurement of Force-Assisted Population Accumulation in Dark States," *Opt. Lett.* **21**:606–608 (1996).
78. P. A. Molenaar, P. van der Straten, H. G. M. Heideman, and H. Metcalf, "Diagnostic-Technique for Zeeman-Compensated Atomic-Beam Slowing—Technique and Results. *Phys. Rev. A* **55**:605–614 (1997).
79. B. Sheehy, S. Q. Shang, P. van der Straten, and H. Metcalf, "Collimation of a Rubidium Beam Below the Doppler Limit," *Chem. Phys.* **145**:317–325 (1990).
80. A. Scholz, M. Christ, D. Doll, J. Ludwig, and W. Ertmer, "Magneto-optical Preparation of a Slow, Cold and Bright Ne* Atomic-Beam," *Opt. Commun.* **111**:155–162 (1994).
81. Z. T. Lu, K. L. Corwin, M. J. Renn, M. H. Anderson, E. A. Cornell, and C. E. Wieman, "Low-Velocity Intense Source of Atoms from a Magnetooptical Trap," *Phys. Rev. Lett.* **77**:3331–3334 (1996).
82. K. G. H. Baldwin, private communication.
83. M. Schiffer, M. Christ, G. Wokurka, and W. Ertmer, "Temperatures Near the Recoil Limit in an Atomic Funnel," *Opt. Commun.* **134**:423–430 (1997).
84. F. Lison, P. Schuh, D. Haubrich, and D. Meschede, "High Brilliance Zeeman Slowed Cesium Atomic Beam," *Phys. Rev.* **A61:** 013405 (2000).
85. K. Dieckmann, R. J. C. Spreeuw, M. Weidemüller, and J. T. M. Walraven, "Two-Dimensional Magneto-Optical Trap as a Source of Slow Atoms," *Phys. Rev. A* **58**:3891 (1998).

INDEX

Index notes: This index is cumulative; it incorporates Vols. I through IV. The *f* after a page number refers to a figure, the *n* to a note, and the *t* to a table.

Abbe condenser, **II.**17.2
Abbe illumination, **III.**2.23–**III.**2.24, **III.**2.24*f*
  lens arrays in, **III.**2.35, **III.**2.36*f*
Abbe number, **II.**18.40, **II.**33.27
Abbe prism, **II.**4.7*f*–**II.**4.8*f*
Abbe sine condition, **I.**1.34–**I.**1.35, **II.**7.3, **II.**18.38, **II.**18.40
ABC (K correlation) model, **I.**7.9, **I.**7.11
Abelès' condition, **I.**5.16, **II.**3.40
Abelès' method, **I.**5.9
Aberration:
  chromatic (*see* Chromatic aberration)
  coefficients, **I.**34.12
  correcting, **III.**10.6–**III.**10.12, **III.**27.1
  and étendue preservation, **III.**2.19
  fifth-order, **I.**34.11
  higher-order, **II.**18.41, **III.**10.1, **III.**10.3–**III.**10.5, **III.**10.7, **III.**10.9
  lateral (*see* Aberration curves, transverse)
  low-order, **III.**10.1, **III.**10.4
  monochromatic (*see* Monochromatic aberration)
  oblique spherical, **II.**18.41
  ocular, **III.**8.3, **III.**9.7, **III.**10.1, **III.**10.8
  in point images, **I.**1.92–**I.**1.93
  ray, **I.**1.95, **I.**1.95*f,* **I.**1.96
  in reflection gratings, **III.**21.8–**III.**21.9
  Seidel, **I.**1.98, **I.**34.10
  spherical (*see* Spherical aberration)
  in spherical lenses, **III.**2.8–**III.**2.9
  third-order, **I.**1.98, **I.**34.12, **II.**18.42
  wavefront (*see* Wavefront aberration)
  and Zernike polynomials, **III.**1.12, **III.**10.4
  and zone plates, **III.**23.3
Aberration curves, **I.**33.1–**I.**33.6
  field plots, **I.**33.2, **I.**33.4–**I.**33.5
  H-tan *U* curves, **I.**33.5
  third-order, **II.**7.3*f*
  transverse, **I.**33.2
Aberration variation, **I.**1.100
Absolute accuracy, **II.**24.22–**II.**24.23
Absolute detectors, **II.**24.29
Absolute instrument, **I.**1.33
Absolute measurements, **II.**24.22–**II.**24.23
Absolute presbyopia, **III.**11.3
Absolute sources, **II.**24.25
Absorbance, **I.**43.10
Absorbing substrate (AS) chips, **I.**12.7
Absorptance, **I.**43.10, **II.**25.4, **II.**25.8, **II.**35.41
  measurement of, **II.**25.11
  vs. temperature, for molybdenum, **II.**35.53*f*
  vs. wavelength
    for aluminum, **II.**35.42*f*
    for copper, **II.**35.42*f*
    for gold, **II.**35.43*f*
    for iron, **II.**35.43*f*
    for molybdenum, **II.**35.44*f*
    for nickel, **II.**35.44*f*
    for platinum, **II.**35.45*f*
    for silicon carbide, **II.**35.45*f*–**II.**35.46*f*
    for silver, **II.**35.47*f*
    for tungsten, **II.**35.47*f*
Absorptance-emittance relations, **II.**25.9*t*
Absorption, **II.**25.4, **II.**36.37
  bio-optical models for, **I.**43.27, **I.**43.29–**I.**43.30
  chlorophyll-specific curve of, **I.**43.30
  coefficient, **I.**16.8, **I.**16.9*f,* **I.**43.11
  in crystals, **I.**9.30*f,* **I.**9.32
  damage, **I.**42.18
  defect, **II.**36.37–**II.**36.38
  EL2, **II.**36.39, **II.**36.39*f*
  and fiber attenuation, **IV.**1.10, **IV.**1.44, **IV.**2.2
  impurity, **II.**36.37
  index, **I.**5.4
  interband, **I.**9.28
    in semiconductors, **I.**9.24
  laser amplifiers and, **I.**11.9
  linear, **IV.**17.20, **IV.**17.22–**IV.**17.24

Copyright 2001 by The McGraw-Hill Companies, Inc. Click Here for Terms of Use.

Absorption (*Cont.*):
measurement of, **II.**28.20
microwave, in germanium, **II.**36.50*f*
multiphonon, **II.**33.18–**II.**33.19, **II.**33.19*f*
multiphoton, **I.**9.31
OH vibrational impurity, **II.**33.20*n*
in optical molasses, **IV.**28.12
polarized, **II.**20.16, **II.**20.16*f,* **II.**20.17
processes, **I.**11.8*f*
in quantum theory, **I.**9.24, **IV.**26.8–**IV.**26.9, **IV.**26.9*f,* **IV.**27.16, **IV.**28.2, **IV.**28.5
and quantum well lasers, **IV.**4.29, **IV.**4.30*f*
radiative processes and, **I.**11.7–**I.**11.8
Smith and Baker values of, **I.**43.22–**I.**43.23
in spectroscopic systems, **II.**36.65–**II.**36.67
temperature dependence of, **II.**35.41, **II.**35.46
in the transparent region, **II.**33.19
(*See also* Nonlinear absorption (NLA); Two-photon absorption (2PA); *specific topic*)
Absorption coefficient, **II.**20.3, **II.**35.4, **II.**36.9
effects of polarization on, **II.**20.19
spectral, **I.**43.28*f*
Absorption edge, **II.**36.26, **II.**36.26*f*–**II.**36.27*f*
fundamental, **II.**36.23–**II.**36.24, **II.**36.24*f,* **II.**36.25, **II.**36.25*f*
infrared room-temperature equation constants, ultraviolet and, **II.**33.82*t*–**II.**33.83*t*
parameters for, **II.**33.83*t*–**II.**33.84*t*
Absorption/luminescence spectra, **II.**20.9–**II.**20.10, **II.**20.10*f,* **II.**20.17
polarized, **II.**20.17, **II.**20.19
Absorption saturation, **IV.**17.22–**IV.**17.23, **IV.**17.23*f,* **IV.**17.24
Absorption spectra, **II.**28.13, **II.**36.30*f*–**II.**36.31*f*
of Cr^{3+}, **II.**28.20, **II.**28.20*f,* **II.**28.21–**II.**28.22
of photopigments, **I.**25.7
of semiconductors, **II.**36.12, **II.**36.12*f*
ultraviolet, of rare earth ions, **II.**28.12*f*
Accelerators, as neutron beam source, **III.**36.12
Acceptance, in étendue, **I.**1.25
Acceptance bandwidth, in parametric generation, **IV.**22.62
Accommodation response, ocular, **I.**24.27–**I.**24.28, **I.**24.29*f,* **I.**24.31*f*
accuracy of, **I.**24.30
and age, **I.**24.33, **I.**24.33*f,* **I.**24.34, **III.**12.30–**III.**12.31, **III.**13.4, **III.**13.9, **III.**13.9*f,* **III.**16.5
application to instrumentation and, **I.**24.32
and computer work, **III.**16.5
and convergence, **III.**12.24, **III.**12.29, **III.**12.32
definition of, **III.**12.1
differential, **III.**12.19
Accommodation response, ocular (*Cont.*):
dynamics of, **I.**24.29, **I.**24.29*f,* **I.**24.30
as extraretinal information, **III.**12.3
and head-mounted display systems, **III.**12.31–**III.**12.32, **III.**18.10–**III.**18.13
in human eye, **III.**11.2, **III.**11.6, **III.**11.18, **III.**12.25
miosis, **I.**24.28
and pupil diameter, **III.**15.9
stability of, **I.**24.30
tonic level of, **I.**24.32
vergence input and, **I.**24.32
Accommodative convergence/accommodation (AC/A) ratio, **III.**12.24
Accommodative hysteresis, **III.**16.5
Accommodative vergence, **III.**12.24–**III.**12.25
Accordion solutions, **IV.**18.29
Accuracy, **II.**29.2
Accurate traceability, **II.**24.22
Achromatic doublet lenses, **II.**1.23, **II.**1.23*f,* **II.**1.24, **II.**1.24*f,* **II.**1.25, **II.**1.25*t,* **II.**1.26
spherical aberration in, **II.**1.24
Achromaticity, in coupling, **IV.**8.3–**IV.**8.4, **IV.**8.4*f*
Achromatic layout, **I.**32.13–**I.**32.14
Achromatic rhombs, **II.**3.56, **II.**3.56*t*
Achromatism, **I.**32.14–**I.**32.15, **I.**32.15*f*
Achromats, athermal optical glass, **I.**39.13–**I.**39.14, **I.**39.14*t*
AC loss, **IV.**6.7
Acoustic attenuation, **II.**12.15, **II.**12.25
Acoustic beam height, **II.**12.22
decreasing, **II.**12.25
Acoustic beam steering, **II.**12.22, **II.**12.24*f,* **II.**12.25
Acoustic filters, **II.**39.27
Acousto-optic bandshapes, **II.**12.12*f*–**II.**12.13*f*
Acousto-optic deflectors, **II.**12.15, **II.**12.19–**II.**12.21, **II.**12.21*f,* **II.**12.26*f*
high-resolution cell, **II.**12.34–**II.**12.35
laser scanning, **II.**12.36–**II.**12.37
multichannel cells, **II.**12.36
optically-rotated, **II.**12.35
time aperture of, **II.**12.25
wide bandwidth cell, **II.**12.35
Acousto-optic devices, **I.**30.11, **I.**30.13
figures of merit for, **II.**12.19*t*
Acousto-optic diffraction, **II.**12.2, **II.**12.5, **II.**12.7*f,* **II.**12.8, **II.**12.20, **II.**12.26
in an anisotropic medium, **II.**12.7
birefringent, **II.**12.30
in birefringent crystals, **II.**12.22
plane wave analysis and, **II.**12.4
suppression of multiple, **II.**12.25
Acousto-optic figures of merit, **II.**12.14–**II.**12.15

Acousto-optic interaction:
of finite geometry, **II.**12.11–**II.**12.12
frequency characteristics of, **II.**12.10
momentum mismatch in, **II.**12.11*f*
Acousto-optic materials, **II.**12.14, **II.**12.18*t*–**II.**12.19*t*
diffraction efficiency and, **II.**12.21
properties of, **II.**12.16
Acousto-optic modulation bandwidth, **II.**12.28, **II.**12.28*f,* **II.**12.29
Acousto-optic modulators (AOM), **I.**28.14, **II.**12.15, **II.**12.26, **II.**12.27*f,* **II.**12.29, **II.**12.37–**II.**12.38, **II.**12.38*t,* **II.**12.39, **IV.**12.31, **IV.**27.4, **IV.**27.16–**IV.**27.19, **IV.**28.11, **IV.**12.31
Acousto-optic receiver, **II.**12.45, **II.**12.46*f,* **II.**12.47
Acousto-optic scanners (*see* Scanners, acousto-optic)
Acousto-optic signal processor, **II.**12.43–**II.**12.44, **II.**12.44*f*
Acousto-optic tunable filter (AOTF), **II.**12.29–**II.**12.30, **II.**12.31*f*–**II.**12.32*f,* **IV.**13.23
angle of deflection in, **II.**12.33–**II.**12.34
angular aperture in, **II.**12.33
drive power of, **II.**12.40–**II.**12.41
fiber optic communication in, **II.**12.43
infrared, **II.**12.34
multispectral imaging in, **II.**12.42–**II.**12.43
out-of-band rejection in, **II.**12.41
performance of, **II.**12.40*t*
rapid-scan spectrometers, **II.**12.42
resolution in, **II.**12.33
sidelobe suppression in, **II.**12.41
spectral resolution in, **II.**12.41
spectral tuning range in, **II.**12.39–**II.**12.40
transmission and drive power in, **II.**12.34
Actinic effects, **II.**24.7
Actinometry, **II.**24.7, **II.**24.12–**II.**24.13
Action spectra:
for cataract, **III.**15.5
in photochemical injuries, **III.**15.3, **III.**15.4*f*
photometric units for, **III.**7.18
Activated-phosphor light sources, **I.**10.46
Active pixel sensor (APS), **III.**4.2, **III.**4.8, **III.**4.8*f,* **III.**4.9
Active scanning, **II.**19.5, **II.**19.9
Acuity chart, in vision testing, **III.**11.5
Acutance, **I.**20.19–**I.**20.21
of color photographic film, **III.**6.2, **III.**6.5
Adams, Ansel, **III.**6.25
Adaptive optics (AO):
applications of, **III.**1.4, **III.**10.3, **III.**10.12–**III.**10.14
and atmospheric turbulence, **III.**1.5, **III.**1.6*f,* **III.**1.8–**III.**1.23
definition of, **III.**10.1
Adaptive optics (AO) (*Cont.*):
and higher-order wavefront sensing, **III.**1.25–**III.**1.28, **III.**1.37–**III.**1.38
in imaging systems, **III.**1.5–**III.**1.8
laser beacons in, **III.**1.28–**III.**1.35
real-time processors for, **III.**1.35–**III.**1.37
retinal microscopy with, **III.**10.9
system design for, **III.**1.40–**III.**1.48
tracking hardware for, **III.**1.23–**III.**1.25
and vision correction, **III.**10.3, **III.**10.7–**III.**10.12, **III.**10.12*f*
wavefront correction in, **III.**1.38–**III.**1.40
Adaptive optics camera, **III.**10.6*f,* **III.**10.7
Add-drop multiplexer (ADM), **IV.**13.12, **IV.**13.13*f,* **IV.**13.15, **IV.**13.25, **IV.**13.25*f*
Addition, analog, **I.**30.4
Additive pulse mode locking (AMPL), **I.**14.15, **I.**14.15*f,* **I.**14.16, **IV.**25.14
Adiabatic approximation, **IV.**26.22
Adjustment tasks, **I.**29.2, **I.**29.4
ADONIS AO system, **III.**1.36
Advanced Photo System (APS), **III.**6.22, **III.**6.26–**III.**6.28
Advanced Satellite for Cosmology and Astrophysics (ASCA), **III.**28.1, **III.**28.6
Advanced television (ATS), **III.**4.21
Advanced X-ray Astrophysical Facility (AXAF), **II.**11.4, **II.**11.10, **II.**11.11*f*
budget error allocation, **II.**11.11–**II.**11.12
Aeroglaze, **II.**37.19–**II.**37.20, **II.**37.33*f*
BRDF of, **II.**37.49*f*–**II.**37.51*f*
hemispherical reflectance of, **II.**37.48*f*
infrared diffuse reflectivity of, **II.**37.49*f*
Z series, **II.**37.34–**II.**37.35
Affine transformation, **I.**1.62
Afocal attachments, **I.**32.8, **I.**32.9*f*–**I.**32.10*f*
Afocal lenses (*see* Lenses, afocal)
Afocal optical systems, **I.**32.7, **I.**32.7*f*
Age-related macular degeneration (AMD), **III.**13.1, **III.**13.3, **III.**13.10, **III.**13.20
Aging:
of global population, **III.**13.2–**III.**13.3, **III.**13.3*f,* **III.**13.4, **III.**13.25
of human vision system, **III.**13.5–**III.**13.19
and ocular diseases, **III.**13.19–**III.**13.22
Ahrens prisms, **II.**3.7, **II.**3.21
AHU pelloid, **III.**6.5
Air, refractive index of, **III.**1.8
Aircraft flight path, **I.**30.9*f*
Airy diffraction, **II.**17.8
Airy disk, **II.**17.6–**II.**17.9, **II.**17.40, **II.**17.42
in diffractive contact lenses, **III.**11.13
size of, as optical resolution measure, **III.**4.15–**III.**4.16

Airy-disk-type distribution, **I.**3.29–**I.**3.30
Airy-Drude formula, **II.**27.7
Airy equation, **I.**5.8
Airy pattern, **II.**17.7*f*–**II.**17.8*f*
  in circular apertures, **II.**11.9
Akhieser loss, **II.**12.15
Akzo paints, **II.**37.35
Akzo 463-3-8 (*see* Bostic 463-3-8)
Algebra, matrix, **I.**26.44
Aliasing, **III.**4.17–**III.**4.19
  definition of, **III.**10.1
  and frame grabbers, **III.**4.20
  by human photoreceptors, **III.**10.11
  of laser frequency, **IV.**27.3
  and walkoff, **IV.**3.7
Alkali halides, F-center in, **II.**28.13
Allan deviation, **IV.**27.2–**IV.**27.3
Allan Variance method, **IV.**27.2–**IV.**27.3
Allelotropia, **III.**12.6
All-Optical Network (AON) Consortium, **IV.**13.16
All-optical switching, **IV.**12.36–**IV.**12.38, **IV.**12.38*f,* **IV.**17.14, **IV.**17.33, **IV.**21.1–**IV.**21.2
  device geometries for, **IV.**21.5, **IV.**21.5*f,* **IV.**21.6
  materials for, **IV.**21.2–**IV.**21.3, **IV.**25.24
  operation of, **IV.**21.3–**IV.**21.7, **IV.**25.22
Altenhof objectives, **II.**18.36, **II.**18.36*f*
Aluminum:
  BRDF in, **II.**37.54*f*
  extinction coefficient for, **II.**35.13*t*
    vs. photon energy, **II.**35.21*f*–**II.**35.22*f*
  flame-sprayed, **II.**37.60
  index of refraction in, **II.**35.13*t*
    vs. photon energy, **II.**35.22*f*
  penetration depth, vs. wavelength, **II.**35.52*f*
  reflectance of, **II.**35.29*t*–**II.**35.30*t*
    vs. wavelength, **II.**35.42*f,* **II.**35.49*f,* **II.**35.51*f*
  scatter profiles in, **II.**37.55*f*
  specific heat of, **II.**35.70*f*
  thermal conductivity of, **II.**35.62*f*–**II.**35.63*f*
Amblyopia, **I.**25.37
American Conference of Governmental Industrial Hygienists (ACGIH), **III.**15.6, **III.**15.9–**III.**15.10, **III.**15.14
American National Standards Institute (ANSI), **III.**7.3, **III.**15.10, **III.**15.13, **III.**18.4
American Optometric Association, **III.**16.1
American Society for Testing and Materials (ASTM), **III.**14.12
Ames 24E, **II.**37.28–**II.**37.29
  BRDF of, **II.**37.32*f*
Ametrope, **III.**12.1
Ametropia, **III.**11.2, **III.**12.18, **III.**12.26
Amici lenses, **II.**1.11, **II.**1.11*f*
Amici prism, **II.**4.11, **II.**4.12*f,* **II.**5.6*f*
Amici-type objective, **II.**17.1, **II.**17.3*f*
Amorphous substances, structural characteristics of, **II.**33.6
Ampere, **III.**7.2
Amplification without inversion, **IV.**23.10, **IV.**23.17–**IV.**23.18
Amplified spontaneous emission (ASE), **IV.**2.12, **IV.**3.11
  in Raman generators, **IV.**18.4
  with rare-earth doped amplifiers, **IV.**5.2–**IV.**5.3, **IV.**5.5–**IV.**5.6
Amplifiers, **I.**18.11
  chirped pulse, **I.**14.22
  differential, **I.**18.12
  in digital systems, **IV.**2.9
  fiber, **II.**6.29
  fiber Raman, **IV.**3.5, **IV.**5.2
  high bandwidth, **I.**18.11
  high input impedance, **I.**18.11
  high-repetition-rate, **I.**14.22
  laser, **I.**11.3, **I.**11.9–**I.**11.10, **I.**13.47, **I.**14.21, **IV.**2.12
  limiting, **IV.**12.40
  lock-in, **I.**18.14, **I.**18.16
  low offset drift, **I.**18.11
  low-repetition-rate, **I.**14.22
  moderate input impedance, **I.**18.11
  noise generated by, **IV.**7.6
  optical (*see* Optical amplifier)
  photorefractive, **II.**39.5
  in point-to-point communications links, **IV.**1.27–**IV.**1.28, **IV.**1.28*f*–**IV.**1.29*f*
  properties of, **I.**11.3
  regenerative, **I.**14.22
    Ti:sapphire, **I.**14.22*f*
  transconductance, **I.**18.12–**I.**18.13
  transformer inputs, **I.**18.11
  variable-gain, **IV.**12.40
  voltage, **I.**18.11–**I.**18.12
Amplitude division, **I.**2.14, **II.**22.6
  in neutron interferometry, **III.**36.10–**III.**36.11
Amplitude scattering matrix, **I.**6.11
Amplitude-shift-keyed transmission (ASK), **II.**6.28, **II.**10.34–**II.**10.36, **IV.**1.36–**IV.**1.37, **IV.**1.37*t,* **IV.**1.38
Amplitude zone plate, **III.**23.4, **III.**23.4*f,* **III.**23.5, **III.**23.5*f*
Analog communications systems:
  communication rate in, **IV.**2.7
  optical fiber for, **IV.**2.14–**IV.**2.15
  signal-dependent noise in, **IV.**2.9
  signal-to-noise ratio in, **IV.**6.2
Analog fiber-optic links, distortions in, **IV.**6.5–**IV.**6.7

Analog optical signal and image processing, **I.**30.3–**I.**30.24
Analog signal:
  noise on, **IV.**12.10
  reconstructed, **IV.**12.5–**IV.**12.6, **IV.**12.7*f*
  sampling of, **IV.**12.4–**IV.**12.6, **IV.**12.6*f,* **IV.**12.9*f*
  transmission of, **IV.**12.6, **IV.**12.7*f*
Analog-to-digital (A-to-D) conversion, **IV.**12.11
Analog-to-digital converter (ADC), **IV.**12.4
Analyzer, **II.**22.6
  left circular, **II.**22.13–**II.**22.14
  vs. polarizer, **II.**22.13
Anamorphoser, **II.**2.16, **II.**2.16*f*
  keplerian, **II.**2.19
Anastigmatic, **II.**18.40
Angle measurements, **II.**29.12
Angle tuning, in optical parametric generation, **IV.**22.62
Angular correlation function, **I.**4.6, **I.**4.7*f*
Angular dilution, **III.**2.6
Angular frequency, **III.**10.1
Angular spectrum representation, **I.**4.15, **I.**4.15*f*
Aniseikonia, **III.**11.15, **III.**12.1, **III.**12.18–**III.**12.19, **III.**12.21, **III.**12.26–**III.**12.27, **III.**13.19, **III.**18.1
Anisometropia, **III.**11.14, **III.**12.18–**III.**12.21, **III.**12.23, **III.**12.26–**III.**12.27, **III.**12.29–**III.**12.31
Anisophoria, **III.**11.15, **III.**12.21, **III.**12.26–**III.**12.27
Anisoplanatism, **III.**1.21
  centroid, **III.**1.17
  focus, **III.**1.29–**III.**1.30, **III.**1.30*f*–**III.**1.32*f,* **III.**1.42, **III.**1.44
Anisotropic diffraction, **II.**12.8–**II.**12.9, **II.**12.9*f*
Anisotropy, **IV.**9.3
Annealed proton exchange (APE) process, **II.**6.15
Anode current, **II.**20.7
Anomalous diffraction, **I.**6.12
  approximation, **I.**6.6, **I.**6.7*f*
Anomalous dispersion, **II.**33.15, **IV.**1.11, **IV.**25.12–**IV.**25.14
  in optical fibers, **II.**10.9
  range of, **II.**35.5
Anomalous scatter, **II.**35.28
Antenna remoting, **II.**6.30, **II.**6.31*f,* **II.**6.32
Anterior chamber phakic lens implants (ACPLIs), **III.**11.17
Antiblooming, **I.**22.9–**I.**22.10, **I.**22.10*f,* **I.**22.11, **I.**22.32
Antihalation undercoat (AHU), in color photographic film, **III.**6.5
Antireflection coatings, **I.**2.24–**I.**2.25, **I.**42.23
  of absorbing media, **I.**42.30
  achromatic, **I.**42.33
Antireflection coatings (*Cont.*):
  additive/subtractive method, **I.**42.28
  of amplifying media, **I.**42.30
  broadband, **I.**42.28*f,* **I.**42.31*f*
  high-efficiency, **I.**42.27*f*
  from homogeneous layers, **I.**42.21–**I.**42.22, **I.**42.22*f,* **I.**42.23
  infrared materials, transmissions of, **I.**42.25, **I.**42.29*f*
  inhomogeneous, **I.**42.25–**I.**42.27, **I.**42.29*f*–**I.**42.30*f,* **I.**42.31
  at nonnormal angles of incidence, **I.**42.32, **I.**42.32*f,* **I.**42.33, **I.**42.33*f,* **I.**42.34, **I.**42.34*f*
  of opaque metals, **I.**42.31*f*
  performance of, **I.**42.26*f*
    effects of surface reflections on, **I.**42.19–**I.**42.20, **I.**42.20*f,* **I.**42.21
  refractive index of, **I.**42.22–**I.**42.23, **I.**42.23*f*
  single-surface transmittance of, **I.**42.32*f*
  structured, **I.**42.25
  of thin-film surfaces, **I.**42.32
  types of, **I.**42.20–**I.**42.21, **I.**42.21*f,* **I.**42.24*t*–**I.**42.25*t,* **I.**42.27*f*
  ultraviolet, **I.**42.28*f*
Antiresonance Fabry-Perot saturable absorber (A-FPSA), **IV.**25.11
Anti-Stokes four-wave mixing, **IV.**18.2, **IV.**18.2*f,* **IV.**18.3, **IV.**18.5*f,* **IV.**18.7, **IV.**18.33
Anti-Stokes Raman laser, **IV.**18.33
Anti-Stokes scattering, **IV.**3.5, **IV.**17.5*t,* **IV.**17.7, **IV.**17.7*f,* **IV.**18.2, **IV.**18.32–**IV.**18.33, **IV.**18.33*f,* **IV.**18.34–**IV.**18.35, **IV.**18.35*f*
  phase matching in, **IV.**18.7
  spontaneous versus stimulated, **IV.**18.3–**IV.**18.4
Anti-Stokes shifted Brillouin scattering, **IV.**17.17, **IV.**17.20, **IV.**18.44
Anti-Stokes shifted Raman scattering, **IV.**17.17, **IV.**17.17*f,* **IV.**17.18, **IV.**18.1–**IV.**18.2, **IV.**18.2*f,* **IV.**18.3, **IV.**18.3*t*
APART, **I.**38.12, **I.**38.27, **II.**37.21
  Mini-, **I.**38.28
APD excess noise, **IV.**2.7
Aperiodic gratings, **IV.**9.7
Aperture:
  in biological eye, **III.**9.3–**III.**9.4, **III.**9.8, **III.**9.13, **III.**13.7, **III.**15.9
  change of, **I.**1.81*f*
  with clipped Lambertian distribution, **III.**2.4
  division of, **II.**22.5
  full, paraxial invariant for, **I.**1.84
  and image size, **III.**1.22
  nonideal, **II.**24.39, **II.**24.39*f*
  numerical (*see* Numerical aperture (NA))
  optical transfer function for, **III.**1.21

Aperture (*Cont.*):
rectangular, **I.**3.17, **I.**3.17*f,* **I.**3.24*f*
and telecentric distribution, **III.**2.18
telescope, in adaptive optics, **III.**1.7, **III.**1.15, **III.**1.17
Aperture flash mode, **III.**2.8
Aperture stop, **I.**1.81, **I.**38.6–**I.**38.7, **II.**1.8, **II.**18.5, **II.**18.40, **II.**24.20
Aphakic correction, **III.**11.13–**III.**11.14, **III.**12.19, **III.**12.27, **III.**13.1, **III.**13.23
Aplanatic, definition of, **II.**18.40
Aplanatic lenses, **II.**1.6, **II.**1.10
spherical, **III.**2.8–**III.**2.9, **III.**2.9*f*
Apochromatic objective, **II.**17.1, **II.**17.3*f,* **II.**17.12–**II.**17.13
Apodization, **III.**9.1, **III.**9.7, **IV.**9.7, **IV.**9.8*f*
Apodization data, **III.**2.7
Apophyllite, **II.**3.53
Apostilb, **III.**7.8
Apo-vertex surfaces, for conic reflectors, **III.**2.11
Aqueous humor, **III.**13.7, **III.**13.21–**III.**13.22
Architecture dilation, in WDM network, **IV.**13.26
Archives de la République (Paris), **III.**7.2
Area-solid-angle-product, **I.**1.25
Argon arc lamps, **I.**10.11
Arperture, **I.**34.4
Array functions, **II.**12.25
Arrays, **I.**19.7
coherent vs. incoherent, **I.**6.3
color filter, **III.**4.18
ferroelectric bolometer, **I.**19.11, **I.**19.12*f*
high-power laser, **I.**13.31
lens, **III.**2.33–**III.**2.38
melted-resin, **II.**7.27–**II.**7.28, **II.**7.28*f*
microlens, **II.**7.2
mode selection, **I.**13.31
MOS, **I.**22.13
noise equivalent temperature difference (NETD), **I.**19.8–**I.**19.9
photodiode (PDAs), **I.**21.2
pyroelectric hybrid, **I.**19.11, **I.**19.12*f*
resistive bolometer, **I.**19.10, **I.**19.11*f*
solid-state, **III.**4.3–**III.**4.6, **III.**4.9–**III.**4.13, **III.**4.20–**III.**4.21
theoretical limits of, **I.**19.9, **I.**19.10*f*
thermoelectric, **I.**19.12, **I.**19.13*f*
(*See also specific type*)
Arrhenius relationship, **I.**16.14
Artificial neural networks, **III.**1.38
ASAP, **I.**38.28, **II.**37.21
ASK envelope detection, **IV.**1.38, **IV.**1.38*f*
Aspheric lenses, **III.**2.9, **III.**2.10*f*
Aspheric surfaces, **I.**40.6–**I.**40.7, **II.**18.3, **II.**34.9–**II.**34.10
centration tolerance of, **II.**7.11
cutting, **I.**41.8
Assembly specifications, for optical systems, **I.**35.1
Associative memories, **II.**39.30
Astigmatic dial, **III.**11.5, **III.**11.6*f*
Astigmatic difference, **I.**1.48
Astigmatic imaging, of a point, **I.**1.47*f*
Astigmatic keratotomy (AK), **III.**11.16
Astigmatism, **I.**33.3, **I.**33.3*f,* **II.**18.40–**II.**18.41, **III.**10.4, **III.**11.3
contact lenses for, **III.**11.10, **III.**11.12
of cornea, **III.**11.4
correction of, **III.**10.2, **III.**10.9, **III.**10.11, **III.**11.3, **III.**11.6, **III.**11.17, **III.**12.17–**III.**12.18, **III.**12.27, **III.**13.24
determining, **III.**11.5–**III.**11.6
in gain-guided laser output, **IV.**4.14
and head-mounted display image quality, **III.**18.6, **III.**18.10
in micro-optics, **II.**7.3
ASTRO-E mission, **III.**28.6
Astronomy:
adaptive optics applications for, **III.**1.4
Schwarzschild objective applications for, **III.**27.1
X-ray applications for, **III.**19.6, **III.**28.1–**III.**28.12, **III.**30.4, **III.**37.3
Zernike polynomial use in, **III.**10.4
Asymmetric concentrators, **III.**2.18
Asynchronous transfer mode (ATM), **IV.**16.6–**IV.**16.7
and LED response time, **IV.**4.44
Athermalization, **I.**32.15–**I.**32.16, **I.**32.16*f*
by image processing, **I.**39.13
intrinsic, **I.**39.7, **I.**39.8*f*
mechanical, **I.**39.7
active, **I.**39.1*f,* **I.**39.8–**I.**39.10, **I.**39.12
active/passive, **I.**39.12, **I.**39.12*f*
passive, **I.**39.7–**I.**39.9, **I.**39.9*f*–**I.**39.11*f*
optical, **I.**39.13
diffractive optics in, **I.**39.16
in optical polymers, **II.**34.10
of separated components, **I.**39.16
Athermal solutions, three-material, **I.**39.14–**I.**39.15, **I.**39.15*t*
ATM Forum, **IV.**16.6
Atmosphere:
aerosols and particulates in, **I.**44.5–**I.**44.6, **I.**44.6*f,* **I.**44.8*f*–**I.**44.9*f,* **I.**44.38, **I.**44.40*f*
interaction with light in, **I.**44.10
molecular absorption of, **I.**44.11–**I.**44.14
molecular gas concentration of, **I.**44.4, **I.**44.5*t*

Atmosphere (*Cont.*):
ozone in, **I.**44.8*f*
pressure of, **I.**44.4
radiance measurement, of Earth's, **II.**25.14
standard, **I.**44.4
temperature, **I.**44.4
vs. altitude in, **I.**44.7*f*
transmission spectrum of, **I.**44.2*f,* **I.**44.3
water vapor in, **I.**44.8*f*
Atmospheric optics, **I.**44.2–**I.**44.3
Atmospheric tilt, **III.**1.15–**III.**1.17, **III.**1.44
Atmospheric transmission software, **I.**44.3, **I.**44.21
Atmospheric turbulence:
in adaptive optics, **III.**1.5, **III.**1.6*f,* **III.**1.8–**III.**1.23, **III.**10.3
ensemble averaging of, **III.**1.36
light source for sensing, **III.**1.28–**III.**1.29
optical strength of (C_n^2), **III.**1.9–**III.**1.11*f,* **III.**1.41
Zernike modes of, **III.**1.12–**III.**1.15, **III.**10.4
Atomic beam:
brightness of, **IV.**28.24–**IV.**28.25, **IV.**28.25*f*
collimation of, **IV.**28.13–**IV.**28.14, **IV.**28.14*f*
slowing in, **IV.**28.9–**IV.**29.10, **IV.**29.10*f,* **IV.**29.11, **IV.**29.11*t*
Atomic clock, **IV.**28.27
Atomic coherence, **IV.**23.3–**IV.**23.5
dephasing of, **IV.**23.12–**IV.**23.13
maximal, and nonlinear optics, **IV.**23.26, **IV.**23.26*f,* **IV.**23.27
Atomic emission lines, analysis of, **II.**28.5
Atomic energy levels, spectroscopic measurements of, **II.**28.2
Atomic force microscopy (AFM), **III.**26.5
Atomic fountain, **IV.**28.27
Atomic funnel, **IV.**28.26
Atomic motions (*see* Lattice vibrations)
Atomic movement:
and laser cooling, **IV.**28.32, **IV.**28.32*f,* **IV.**28.33
in magneto-optical trapping, **IV.**28.23–**IV.**28.24
in momentum space, **IV.**28.9
nonadiabatic following in, **IV.**28.15–**IV.**28.16
optical control of, **IV.**28.1–**IV.**28.4, **IV.**28.31
in optical molasses, **IV.**28.12–**IV.**28.13
in optical trapping, **IV.**28.22
quantum effects on, **IV.**28.35–**IV.**28.36
Atomic noise, **IV.**26.35–**IV.**26.36
Atomic oxygen environment, **II.**37.14
and black surfaces, **II.**37.18–**II.**37.19
Atomic photoabsorption of X-rays in matter, **III.**A.1, **III.**A.2*f*
Atomic radiative decay, **IV.**20.6
Atomic scattering of X-rays in matter, **III.**A.1, **III.**A.2*f*
Atomic spectra, **II.**28.14
Atomic systems, three-level, **IV.**23.4–**IV.**23.6, **IV.**23.6*f,* **IV.**24.5
and lasing without inversion, **IV.**26.42, **IV.**26.42*f,* **IV.**26.43
and stimulated photon echo, **IV.**24.16, **IV.**24.16*f,* **IV.**24.17
Atomic transitions, **IV.**28.2
and Doppler temperature, **IV.**28.3, **IV.**28.13
and magneto-optical trapping, **IV.**28.23
in photo-associative spectroscopy, **IV.**28.30
and polarization gradient cooling, **IV.**28.17
Atom interaction with radiation field, **IV.**24.3, **IV.**24.12
longitudinal velocity in, **IV.**24.20*n*
Atom interferometer, **IV.**24.20–**IV.**24.22, **IV.**24.23*f*
Atom laser, **IV.**28.35
Atoms:
dark states of, **IV.**28.35–**IV.**28.38
lithium (Li), term diagram of, **I.**8.16*f*
lithium (Li) and sodium (Na), comparison between, **I.**8.15
multielectron, **I.**8.12–**I.**8.13
spin orbital in, **I.**8.12
multiple-level structure of, **IV.**28.2, **IV.**28.15
1-electron, spectroscopy of, **I.**8.10–**I.**8.12
photo-association of, **IV.**28.29
sodium (Na), term diagram of, **I.**8.17*f*
thallium (Tl), term diagram of, **I.**8.15, **I.**8.18*f*
Atoms, two-level:
eigenstates for, **IV.**28.36–**IV.**28.37, **IV.**28.37*f*
laser cooling limit for, **IV.**28.18
in laser theory, **IV.**26.15–**IV.**26.16, **IV.**26.16*f,* **IV.**26.17–**IV.**26.20, **IV.**26.20*f,* **IV.**26.21
in micromaser theory, **IV.**26.21–**IV.**26.22
optical force on, **IV.**28.4–**IV.**28.5
in quantum mechanics, **IV.**26.8–**IV.**26.9, **IV.**26.9*f*
at rest, **IV.**28.5–**IV.**28.6
Atom trapping, **IV.**28.2, **IV.**28.19–**IV.**28.20
applications for, **IV.**28.25
and Bose-Einstein condensation, **IV.**28.34–**IV.**28.35, **IV.**28.36*f*
magnetic, **IV.**28.20, **IV.**28.20*f,* **IV.**28.21
magneto-optical, **IV.**28.22–**IV.**28.23, **IV.**28.23*f,* **IV.**28.24, **IV.**28.25*f,* **IV.**28.26–**IV.**28.28, **IV.**28.35
optical, **IV.**28.21–**IV.**28.22, **IV.**28.22*f*
and optical lattices, **IV.**28.31
AT&T digital hierarchy, **IV.**12.21, **IV.**12.22*f*
Attenuation:
in infrared fiber, **IV.**14.2, **IV.**14.2*f*
limiting, **IV.**1.44, **IV.**6.2
measurement of, **IV.**1.14–**IV.**1.16, **IV.**1.16*f*
and multimode fiber, **IV.**1.9

Attenuation (*Cont.*):
in typical fiber, **IV.**1.10, **IV.**1.10*f,* **IV.**2.2–**IV.**2.3, **IV.**2.3*f,* **IV.**13.2, **IV.**13.2*f*
and wavelength, **IV.**6.7–**IV.**6.8
Attenuation coefficients, **I.**43.13, **II.**35.46
for photons, **II.**35.53*t*
Attenuators:
design of, **IV.**10.8, **IV.**10.9*f*
in fiber-optic network, **IV.**10.2
tapered fiber, **IV.**8.1, **IV.**8.5, **IV.**8.5*f*
(*see also* Filters)
Audiotape, **I.**31.1
Auger energies, **III.**A.3*t*–**III.**A.6*t,* **III.**A.8*f*
Auger recombination, **I.**13.18, **I.**13.18*f,* **I.**13.19
Autler-Townes splitting, **IV.**23.4, **IV.**23.10, **IV.**23.23
Autocollimator, **II.**29.14, **II.**29.14*f,* **II.**29.15, **II.**29.15*f,* **II.**29.17, **II.**29.19–**II.**29.20, **II.**29.21*f,* **II.**29.23, **II.**29.23*f*
Autoexposure, **II.**15.10–**II.**15.12
Automatic fault detection, in SONET, **IV.**13.13
Automatic gain control (AGC), **IV.**12.40
Avalanche multiplication, **I.**16.10
Avalanche photodetector (APD), **IV.**1.29–**IV.**1.30, **IV.**1.30*f,* **IV.**2.1, **IV.**2.7, **IV.**2.9, **IV.**4.2, **IV.**4.66, **IV.**4.76–**IV.**4.77
dark current for, **IV.**4.77
gain in, **IV.**4.76
noise in, **IV.**4.77
in OTDM system, **IV.**12.39
separate absorber and multiplication, **IV.**4.76–**IV.**4.77
speed of, **IV.**4.77
Avalanche photodiodes (APDs) (*see* Photodiodes, avalanche)
Aviator Night Vision Imaging Systems (ANVIS), **III.**18.3
Axial ametropia, **III.**12.18
Axial aniseikonia, **III.**12.18
Axial color, **I.**33.2–**I.**33.3, **II.**18.9, **II.**18.41
Axial distances, directed, gaussian, **I.**1.50*t*
Axial gradient lenses, **II.**9.3–**II.**9.4, **II.**9.4*f*
Axial myopia, **III.**12.18, **III.**12.26
Axial object, switching, **I.**1.46
Axial points, gaussian, **I.**1.50*t*
Axial preload, **I.**37.2, **I.**37.4
acceleration forces and, **I.**37.10
temperature and:
assembly, **I.**37.8–**I.**37.9
elevated, **I.**37.9
highest survival, **I.**37.10
torque required to produce, **I.**37.10
Axial rays, **I.**1.39
Axial resolution, **II.**17.9, **II.**17.12
Axial stigmatism, **II.**18.38, **II.**18.41
Axial stress:
and radial stress, combined, **I.**37.11
reduced temperatures and, **I.**37.10
Azomethine dyes:
excited state properties of, **III.**6.12–**III.**6.13, **III.**6.13*f*
photochemistry of, **III.**6.11–**III.**6.12
in photographic materials, **III.**6.10, **III.**6.11*f*

Babcock, Horace, **III.**1.4, **III.**10.3
Babinet compensator, **II.**3.57–**II.**3.58, **II.**3.58*f,* **II.**3.59–**II.**3.60, **II.**13.21
Babinet principle, **I.**3.9–**I.**3.11, **I.**3.13
Back-conversion, in stimulated Raman scattering, **IV.**3.5
Background temperature, **I.**15.8
Backscattering, of coherent light, **III.**3.13–**III.**3.15
Backward Raman amplifier, **IV.**18.4, **IV.**18.5*f,* **IV.**18.42
Backward trace, in nonimaging optics, **III.**2.8
Baffles, **I.**38.11–**I.**38.12, **II.**37.1, **II.**37.14, **II.**37.16
black, **II.**37.18
BRDF of, **II.**37.21, **II.**37.62*f*
for extreme environments, **II.**37.20–**II.**37.21
in precision photometry, **III.**2.25
reflectance in, **II.**37.59*f*
secondary, **I.**38.3, **I.**38.3*f*–**I.**38.4*f,* **I.**38.7*f*
increasing diameter of, **I.**38.5*f*
shields, extended, **I.**38.10*f*
Baker-Nunn objectives, **II.**18.24, **II.**18.24*f*
Baker relay, **II.**2.18
Baker super-Schmidt objectives, **II.**18.23, **II.**18.23*f*
Ball Black, **II.**37.8*f*–**II.**37.9*f,* **II.**37.17, **II.**37.42–**II.**37.43
Balmer a spectrum, **I.**8.10, **I.**8.10*f,* **I.**8.11
Balmer a transition, **I.**8.10, **I.**8.10*f,* **I.**8.11–**I.**8.12
Balmer b spectrum, **I.**8.12
Balmer b transition, **I.**8.12
Bandgap, **IV.**20.2–**IV.**20.3
in photonic crystals with 2D periodicity, **IV.**20.9
3D, **IV.**20.3–**IV.**20.5
(*See also* Photonic bandgap (PBG) materials)
Band limiting, optical, **III.**4.18
Bandpass filters, **I.**42.73–**I.**42.75, **I.**42.76*f*–**I.**42.77*f,* **IV.**12.13–**IV.**12.14, **IV.**12.14*f,* **IV.**12.15
with evaporated spacers, **I.**42.86
induced-transmission, **I.**42.85, **I.**42.85*f*
narrow- and medium-, **I.**42.77–**I.**42.78
polarization splitting in, little or no, **I.**42.90, **I.**42.91*f*
rejection region in, **I.**42.76
square-top multicavity, **I.**42.80–**I.**42.81, **I.**42.81*f*–**I.**42.85*f*
stability of, **I.**42.92

Bandpass filters (*Cont.*):
temperature dependence of, **I.**42.92
very narrow, **I.**42.85
wide-, **I.**42.87
wide-angle, **I.**42.91, **I.**42.91*f*
for X-ray regions, **I.**42.92, **I.**42.93*f*–**I.**42.94*f*
for XUV regions, **I.**42.92, **I.**42.93*f*–**I.**42.94*f*
Bandpass interference filters, angular properties of, **I.**42.89–**I.**42.90, **I.**42.90*f*
Band spectra, molecular, **I.**8.21, **I.**8.23–**I.**8.24, **I.**8.24*f,* **I.**8.25
Band splitter, tapered fiber, **IV.**8.6, **IV.**8.6*f*
Band structure, **I.**9.24, **I.**9.27, **IV.**20.3
energy, **I.**9.25
Bandwidth, **IV.**12.1
acceptance, in parametric generation, **IV.**22.63
in ATM, **IV.**16.6
for broadcast applications, **III.**4.3
control loop, in AO system, **III.**1.36
for digital transmission, **IV.**12.10
and dispersion, **IV.**2.3
for erbium-doped fiber amplifier, **IV.**13.21, **IV.**13.22*f*
of fiber Bragg grating, **IV.**9.4–**IV.**9.5, **IV.**15.8
and higher-order phase fluctuations, **III.**1.20–**III.**1.21
for human eye, **III.**10.10
measurement of, for optical fiber, **IV.**1.16
in multiplexing, **IV.**12.4, **IV.**12.16
and nonlinear transmission, **IV.**3.1
of optical amplifier, **IV.**11.2, **IV.**11.4
for optical fiber, **IV.**1.16, **IV.**2.3, **IV.**13.2
in packet switching, **IV.**13.17
for point-to-point system, **IV.**1.26
and self-phase modulation, **IV.**25.12
servo, **III.**1.18, **III.**1.24, **III.**1.40, **IV.**27.10, **IV.**27.18, **IV.**27.20
as throughput limitation, **IV.**2.13–**IV.**2.14
tracking, **III.**1.17–**III.**1.19, **III.**1.20*f,* **III.**1.24
for video compatible cameras, **III.**4.15
Bandwidth normalization, **III.**7.15–**III.**7.16, **III.**7.16*t,* **III.**7.18, **III.**7.18*f*
Banning beam splitter, **II.**3.45
Barium titanate ($BaTiO_3$), **II.**39.15, **II.**39.16*f,* **II.**39.17
limitation of, **II.**39.16
Barrel distortion, **II.**1.30, **II.**2.12
Barrier, reservoir, and quantum well electron transfer (BRAQWET), **IV.**4.2, **IV.**4.63, **IV.**4.65
Baryta, in color photographic papers, **III.**6.5
Base rays (*see* Rays, central)
Beacons:
artificial (synthetic), **III.**1.29–**III.**1.35
brightness of, **III.**1.40–**III.**1.41, **III.**1.46–**III.**1.47
Beacons (*Cont.*):
TIR Fresnel lenses used in, **III.**2.10
(*See also* Laser guide star (LGS) sensing; Natural guide star (NGS))
Beam:
gaussian, **IV.**22.9, **IV.**22.10*t*
(*See also* Atomic beam)
Beam amplification, photorefractive, **II.**39.7
Beam attenuation, **I.**43.42, **I.**43.42*f,* **I.**43.43
chlorophyll concentration and, **I.**43.43–**I.**43.44, **I.**43.44*f*
depth dependence of, **I.**43.43*f*
spectral, **I.**43.11
Beam compression, **II.**19.33
illustration of invariance in, **II.**19.34*f*
Beam coupler, mutually incoherent, **II.**39.9, **II.**39.9*f*
Beam coupling, photorefractive, **II.**39.5
Beam deflection, lens arrays used in, **III.**2.33
Beam diffraction:
convergent, **III.**37.3–**III.**37.4
focused, **III.**35.12–**III.**35.13, **III.**35.13*f,* **III.**35.14, **III.**35.14*f*
Beam expansion/compression, **II.**19.33*n*
Beam fanning, **II.**39.29
Beam forming, **III.**2.23, **III.**2.34, **III.**2.35*f,* **III.**2.40
Beam modulation distance measurements, **II.**29.5, **II.**29.7, **II.**29.9
Beam propagation method (BPM), **II.**6.8, **IV.**8.4
Beam scanning, **II.**17.40
Beam separators, **I.**28.10
Beam shaping, **I.**31.9–**I.**31.10, **II.**8.12, **II.**8.13*f*
Beam-shearing interference contrast system, **II.**17.32
Beam smearing, **III.**2.34–**III.**2.35, **III.**2.40
Beam spatial profiles, nonlinearity and, **II.**39.10
Beam splitters (BS), **I.**28.9–**I.**28.10, **I.**31.23, **I.**42.61
achromatic, **I.**42.62–**I.**42.63, **I.**42.66, **I.**42.66*f*
bandpass filters, **I.**42.66
color-selective, **I.**42.66, **I.**42.67*f*
cube as, **IV.**10.5, **IV.**10.6*f,* **IV.**10.9, **IV.**10.9*f*
nonpolarizing, **I.**42.63, **I.**42.65, **I.**42.65*f,* **I.**42.66
pellicle, **I.**42.62
performance of, **I.**42.63*f*–**I.**42.64*f*
plate as, **IV.**10.6, **IV.**10.7*f,* **IV.**10.9
polarized (PBS), **I.**31.10*f,* **I.**31.23, **I.**31.24*f*
polarizing, **I.**42.68–**I.**42.69, **I.**42.71–**I.**42.73, **I.**42.73*f*–**I.**42.74*f,* **IV.**10.7, **IV.**10.8*f*
types of, **I.**42.61*f*
using, **I.**42.62*f*
for the X-ray region, **I.**42.63
Beam transformer, **III.**2.18, **III.**2.19*f*
Beat length, **II.**10.12, **IV.**1.14
Becke lines, **II.**17.22, **II.**17.25

Becker's tables, **II.**6.55, **II.**6.55*t*
Beer-Lambert law, **I.**25.5, **I.**44.10, **I.**44.21
Beer's law, **I.**9.7, **I.**11.10
Bend-and-polish technique, **I.**40.7
Bending, component, axial forces and, **I.**37.11, **I.**37.11*f,* **I.**37.12
Benes switch, **II.**6.32, **II.**6.33*f*
Bent crystals, **III.**22.4–**III.**22.6
  in microfocus X-ray fluorescence, **III.**35.22, **III.**35.22*f*–**III.**35.23*f*
  in microscopes for laser-generated plasmas, **III.**35.4
  with polycapillary optics, **III.**37.3
  in X-ray diffraction, **III.**35.8–**III.**35.9, **III.**35.9*t,* **III.**35.11*t,* **III.**335.10*t*
Berning's method of effective indexes, **I.**5.9–**I.**5.10
Beryllium:
  black surfaces and, **II.**37.45–**II.**37.46
  extinction coefficient for, **II.**35.13*t*
    vs. wavelength, **II.**35.22*f*
  index of refraction in, **II.**35.13*t*
    vs. wavelength, **II.**35.22*f*
  reflectance of, **II.**35.30*t*–**II.**35.31*t*
    vs. wavelength, **II.**35.50*f*–**II.**35.51*f*
  specific heat of, **II.**35.72*f*
  surface, sputtered, **II.**37.9*f*
  thermal conductivity of, **II.**35.62*f*–**II.**35.63*f*
Bessel functions, **I.**6.13, **I.**6.15–**I.**6.16, **II.**10.7*f*
  for step-index fiber, **IV.**1.9*f*
Beta-cloth, BRDF of, **II.**37.62*f*
Bevel gauge, **II.**29.13*f*
Bias, in electroabsorption modulators, **IV.**4.62
Bidirectional reflectance distribution function (BRDF), **I.**7.2–**I.**7.4, **I.**38.24, **I.**38.26*f,* **I.**44.18, **II.**25.5, **II.**25.14, **II.**26.2–**II.**26.3, **II.**26.3*f,* **II.**26.4, **II.**37.7, **II.**37.15, **II.**37.22, **III.**14.10
  of Aeroglaze, **II.**37.49*f*–**II.**37.51*f*
  of aluminum, **II.**37.27*f*–**II.**37.29*f,* **II.**37.54*f*
  of baffle materials, **II.**37.62*f*
  of beta-cloth, **II.**37.62*f*
  of black baffles, **II.**37.21
  of black chrome, **II.**37.60*f*
  of black cobalt, **II.**37.60*f*
  of Black Kapton, **II.**37.61*f*
  of black nickel, **II.**37.25*f*
  in black surfaces, **II.**37.58*f*
    profiles of, **II.**37.44*f*–**II.**37.47*f*
  of Black Tedlar, **II.**37.61*f*
  of Boron Black, **II.**37.59*f*
  of Cardinal black paint, **II.**37.53*f*
  characteristics of, **I.**38.24
  cosine-corrected, **II.**26.4
  of Cu black, **II.**37.26*f*
  of glossy surfaces, **II.**37.52*f*
Bidirectional reflectance distribution function (BRDF) (*Cont.*):
  of gold iridite, **II.**37.25*f*
  of Infrablack, **II.**37.56*f*–**II.**37.57*f*
  limitations of, **I.**38.25*f*
  of Martin Black, **II.**37.55*f*–**II.**37.56*f*
  Mueller (MBRDF), **II.**22.27
  of NSB69–82, **II.**37.26*f*
  of roughened aluminum, **II.**37.24*f*
  scatterometer, **II.**26.5*f*
  of SolarChem, **II.**37.54*f*
Bidirectional scattering distribution function (BSDF), **I.**7.4–**I.**7.9, **I.**7.11, **II.**26.12
  inverse-power-law form of, **I.**7.9
  noise equivalent (NESBDF), **II.**26.4, **II.**26.6, **II.**26.11*t*
    reduction of, **II.**26.10–**II.**26.11
  speckle effects in, **II.**26.12
Bidirectional transmittance distribution function (BTDF), **II.**25.4, **II.**26.4
Bifocal intraocular lenses, **III.**13.23
Bifocal intraocular lens implants, **III.**11.14
Bifocal jump, **III.**12.15–**III.**12.16, **III.**12.16*f*
Bifocal lenses, designing, **II.**8.13*f*
Bifocal spectacles, **III.**11.2, **III.**11.6–**II.**11.8, **III.**11.8*f,* **III.**12.15–**III.**12.16, **III.**12.27, **III.**12.29–**III.**12.31, **III.**13.22–**III.**13.23, **III.**16.6
Big bang, **I.**4.25
Billet's split lens, **I.**2.17, **I.**2.17*f*
Bimorph mirrors, **III.**1.38, **III.**1.39*f*
Binary digits:
  optical representation of, **IV.**12.12, **IV.**12.12*f*
  signal as, **IV.**12.11
  transmission of, **IV.**12.12–**IV.**12.14
Binary optics:
  advantages of, **II.**8.2
  analytical models of, **II.**8.3
  diffraction efficiency in, **II.**8.9, **II.**8.9*f,* **II.**8.10, **II.**8.10*t*
  element, representation of, **II.**8.3
  fabrication of, **II.**8.14–**II.**8.15, **II.**8.15*f*–**II.**8.16*f,* **II.**8.16*t*
    errors in, **II.**8.17
  micromachining techniques in, **II.**8.17
  in micro-optics, **II.**8.7, **II.**8.7*f,* **II.**8.8
  singlet, aberration of, **II.**8.5
  vector diffraction theory and, **II.**8.14, **II.**8.14*f*
  wavefront quality in, **II.**8.9
Binary units, **II.**13.27*f*
  digital light deflection and, **II.**13.26
Binocular disparity, **I.**25.42, **III.**12.1, **III.**12.4, **III.**12.6, **III.**12.8–**III.**12.12, **III.**12.20, **III.**12.23–**III.**12.24, **III.**12.28

Binocular fusion, **III.**12.1, **III.**12.12–**III.**12.13, **III.**12.19–**III.**12.20, **III.**16.5
Binocular parallax, **III.**12.1, **III.**12.22–**III.**12.24
Binocular rivalry, **III.**12.1, **III.**12.13, **III.**12.19–**III.**12.20, **III.**12.34
Binoculars, **II.**2.10
  imaging in, **II.**2.13, **II.**2.13*f*
Binocular vision, **III.**12.6–**III.**12.7
  and computer work, **III.**16.5–**III.**16.6
  as optical design consideration, **III.**12.3
  and phoria, **III.**12.22
  single and clear, **III.**12.25
Biological tissue, light propagation through, **III.**3.12
Biotar lenses, **II.**1.28, **II.**1.29*f*
Bi-phase coding, **IV.**12.12, **IV.**12.12*f*
  power spectrum for, **IV.**12.13*f,* **IV.**12.14
Birefringence, **II.**22.6
  in optical fiber, **IV.**1.14
Birefringent diffraction, **II.**12.10–**II.**12.12
Birefringent materials, **I.**5.13, **II.**3.47*t,* **II.**3.53*f,* **II.**3.53*n,* **II.**3.54*f*
Bit error rate (BER), **IV.**1.26
  and clocking, **IV.**6.16
  for datacom systems, **IV.**6.1
  for digital transmission, **IV.**6.2
  and mode partition noise, **IV.**6.12
  and radiation-induced loss, **IV.**6.18
  and received optical power, **IV.**6.2–**IV.**6.3, **IV.**6.3*f,* **IV.**6.4, **IV.**6.4*f*
  with VGA versus limiting amplifier, **IV.**12.40
Bit interleaving, **IV.**12.20*f*
Bit rate:
  distance limits on, **IV.**2.10
  increasing, **IV.**2.11, **IV.**2.16
  in optical TDMA, **IV.**12.18
  per user, in passive optical network, **IV.**2.13
  for SONET channel, **IV.**12.22
Bits, **IV.**12.4
Bit-timing synchronization, **IV.**12.20
$Bi_{12}GeO_{20}$ (BGO), **II.**39.18, **II.**39.18*t*
$Bi_{12}SiO_{20}$ (BSO), **II.**39.18, **II.**39.18*t*
$Bi_{12}TiO_{20}$ (BTO), **II.**39.18, **II.**39.18*t,* **II.**39.19, **II.**39.19*f*
Blackbody:
  D-star, **I.**15.8
  EOI, **I.**10.12*f,* **I.**10.14*f*
  goldpoint, **I.**10.6–**I.**10.7
  Mikron, **I.**10.13*f*
  responsivity, **I.**15.8
  variable temperature, **I.**10.7*f*
Blackbody cavity dimensions, **I.**10.6*f*
Blackbody cavity theory, **I.**10.4
Blackbody detectivity, **I.**15.8
Blackbody noise equivalent power, **I.**15.8
Blackbody radiation:
  distribution temperature of, **III.**14.7
  infrared fibers to measure, **IV.**14.4, **IV.**14.13
  and luminance, **III.**2.3, **III.**7.13, **III.**7.13*f*
  and luminous intensity, **III.**14.3
  peak wavelength of, **III.**14.12
  in Planck's formula, **IV.**26.7
  and spectral irradiance, **III.**7.14, **III.**7.15*f,* **III.**7.16
  and spectral radiance, **III.**4.11
  and X-ray production, **III.**19.6
Blackbody radiator, **II.**24.25
Blackbody simulator, **I.**10.4, **I.**10.6*f,* **I.**10.11, **II.**24.25–**II.**24.28
Black chrome, **II.**37.47–**II.**37.48
  BRDF of, **II.**37.60*f*
Black cobalt, **II.**37.47
  BRDF of, **II.**37.60*f*
Black felt paper:
  reflectance of, **II.**37.36*f*
  transmittance of, **II.**37.40*f*
Black glass, **II.**37.60
Black Kapton, **II.**37.60
  BRDF of, **II.**37.61*f*
Black-light lamps, **I.**10.35, **I.**10.36*t,* **I.**10.37
Black paint, electrically conductive, **II.**37.48
Black surfaces, optical, **II.**37.1, **II.**37.6*t*–**II.**37.7*t,* **II.**37.15*t*
  anodized, **II.**37.5*t,* **II.**37.37
  BRDF profiles of, **II.**37.44*f*–**II.**37.47*f*
  characterization of, **II.**37.21
  coatings, types of, **II.**37.29–**II.**37.30
  contamination of, **II.**37.16
  creation of, **II.**37.15, **II.**37.17–**II.**37.18
  CVD surfaces, **II.**37.53
  as design elements, **II.**37.16
  designer blacks, **II.**37.16
  electrodeposited surfaces, **II.**37.47–**II.**37.48
  electroless nickel, etching of, **II.**37.41–**II.**37.43
  environmental resistance of, **II.**37.15, **II.**37.18
  far-infrared, **II.**37.23–**II.**37.24, **II.**37.27
  hemispherical reflectivity of, **II.**37.22*t*
  high-resistivity coatings, **II.**37.53
  ion beam-sputtered surfaces, **II.**37.46
  lambertian, **II.**37.16
  multiple-layer approach, **II.**37.27
  painted, **II.**37.2*t*–**II.**37.4*t*
  paints for, **II.**37.30–**II.**37.31
  plasma-sprayed surfaces, **II.**37.43, **II.**37.45–**II.**37.46
  properties of, **II.**37.16
  selection process for, **II.**37.12, **II.**37.12*f,* **II.**37.13, **II.**37.13*f,* **II.**37.14

Black surfaces, optical (*Cont.*):
silicon carbide, **II.**37.53
specular reflectance spectra of, **II.**37.30*f*
sputtered surfaces, **II.**37.53
substrates, **II.**37.29–**II.**37.30
surface contamination of, **II.**37.18
Teflon overcoat, **II.**37.27–**II.**37.28
for ultraviolet applications, **II.**37.23
(*See also specific type*)
Black Tedlar, BRDF of, **II.**37.61*f*
Black velvet:
reflectance of, **II.**37.38*f*
transmittance of, **II.**37.41*f*
Blazed gratings, **IV.**9.7
Blindness:
from age-related macular degeneration, **III.**13.20
and cataracts, **III.**13.19
from diabetic retinopathy, **III.**13.21
from glaucoma, **III.**13.22
incidence of, **III.**13.25
temporary, from snow, **III.**15.4–**III.**15.5
Blink rate, and computer work, **III.**16.4
BLIP, in focal plane arrays (FPA), **I.**23.26
Blip detector, **I.**15.8
Bloch equations, optical, **IV.**24.3–**IV.**24.5, **IV.**24.27, **IV.**28.1, **IV.**28.4, **IV.**28.6
Bloch oscillations, in optical lattices, **IV.**28.33
Bloch's law, **I.**25.30
Bloch solution, **I.**9.26
Bloch sphere, **IV.**24.4
Bloch's theorem, **IV.**28.31
Bloch vector, **IV.**24.4, **IV.**24.7, **IV.**24.7*f,* **IV.**24.8
in photon echo, **IV.**24.11, **IV.**24.11*f,* **IV.**24.12
Blocking filter, **II.**23.20
Blooming, **I.**22.6, **I.**22.9, **I.**27.6, **I.**27.20
Blue-light hazard:
action spectrum curve for, **III.**15.3, **III.**15.4*f,* **III.**15.10–**III.**15.11
retinal damage from, **III.**15.4, **III.**15.7
Bohr, Niels, **IV.**26.8, **IV.**26.10
Bohr magnetron, **II.**36.41
Bohr theory, **I.**8.5
Bolometers, **I.**15.5, **I.**19.1, **I.**19.4
capacitive, **I.**23.10
carbon, **I.**19.5
cooled, **I.**15.4
electrical circuit, **I.**15.23*f*
electron (*see* Bolometers, InSb)
ferroelectric arrays, **I.**19.11, **I.**19.12*f*
Ge, **I.**15.30*f*–**I.**15.31*f*
Ge(Ga), **I.**15.27–**I.**15.28
InSb, **I.**15.26–**I.**15.27, **I.**15.29*f*–**I.**15.30*f*
metal, **I.**19.4
perfect, **I.**15.15*f*
Bolometers (*Cont.*):
resistive, **I.**23.10
resistive arrays, **I.**19.10, **I.**19.11*f*
semiconductor, **I.**19.5
superconducting, **I.**19.5
thermistor, **I.**15.22
Border effect, **I.**20.13
Borescope, **II.**1.10
Bormann transmission, **III.**25.2, **III.**25.3*f*
Born approximation, **I.**7.3–**I.**7.5, **I.**7.11
definition of, **III.**9.1
in neutron optics, **III.**36.4
and single scattering, **III.**3.4
in vision optics, **III.**9.15
Born-Oppenheimer approximation, **I.**8.22–**I.**8.23, **I.**8.25–**I.**8.26
Boron Black, **II.**37.43, **II.**37.45
BRDF of, **II.**37.59*f*
Boron Carbide, **II.**37.45
Boron neutron capture therapy (BNCT), **III.**35.34
Bose, S., **IV.**28.34
Bose-Einstein condensation (BEC), **IV.**26.40–**IV.**26.42, **IV.**28.9, **IV.**28.25, **IV.**28.28, **IV.**28.34–**IV.**28.35, **IV.**28.36*f*
Bose-Einstein distribution, **II.**33.19
Bose-Einstein statistics, **IV.**26.10
Bostic 463-3-8, **II.**37.52*f*
Bound electronic Kerr effect, **IV.**17.5*t,* **IV.**17.12, **IV.**17.14–**IV.**17.15
Bound modes, **II.**6.4
Bowman's membrane, **III.**13.5
Boys points, **I.**28.11
Brace half-shade plate, **II.**3.60
Bragg, Sir Lawrence, **IV.**20.5
Bragg, William, **III.**35.6, **III.**35.15
Bragg acousto-optic deflector, **II.**19.46*f*
Bragg-Brentano geometry, **III.**35.11*f*–**III.**35.12*f*
Bragg cells, **II.**12.15, **II.**12.35
acousto-optic, **II.**12.35*t*
birefringent phased-array, **II.**12.25
frequency-dispersion characteristics of, **II.**12.43–**II.**12.44
high-resolution, **II.**12.34–**II.**12.35
intermodulation products (IMPs) in, **II.**12.47–**II.**12.48
multichannel (MCBC), **II.**12.36
peak diffraction efficiency of, **II.**12.20
wideband, **II.**12.35, **II.**12.47
Bragg cell spectrum analyzer, **I.**30.12, **I.**30.12*f*
Bragg construction, in X-ray diffraction, **III.**35.6, **III.**35.6*f*
Bragg diffraction, **I.**30.11, **I.**30.11*f,* **II.**12.5–**II.**12.6, **II.**12.8
in optical lattice, **IV.**28.32

Bragg-Fresnel optics, **III.**23.7–**III.**23.8, **III.**23.8*f*
Bragg index grating, **II.**10.38, **II.**10.41, **IV.**12.27
(*See also* Fiber Bragg grating (FBG))
Bragg-matched volume hologram, **II.**39.2
Bragg mirror:
reflectivity of:
in DBR lasers, **IV.**4.34–**IV.**4.35
in VCSELs, **IV.**4.46–**IV.**4.47, **IV.**4.50
in saturable Bragg reflector, **IV.**25.11
Bragg planes, **III.**22.1–**III.**22.2, **III.**22.2*t,* **III.**22.5
Bragg reflection, **III.**22.1–**III.**22.4, **III.**23.7, **III.**24.2, **III.**25.2–**III.**25.3, **III.**25.3*f,* **III.**25.4, **III.**25.6, **III.**27.4, **III.**36.11
and optical lattices, **IV.**28.33
Bragg reflectors, **II.**6.8, **II.**6.28
Bragg's law, **III.**19.8–**III.**19.9, **III.**19.9*f,* **III.**22.1, **III.**25.7, **III.**33.3
Bragg wavelength, **IV.**9.1, **IV.**9.3, **IV.**15.6, **IV.**15.8
Brashear-Hastings prism, **II.**4.25*f*
Bravais biplate, **II.**3.60
Breadboard documentation system, **II.**23.20
Bremsstrahlung radiation:
and capillary optics, **III.**30.13, **III.**30.13*f*
in energy-dispersive X-ray fluorescence, **III.**35.18
intensity increase for, **III.**31.10
and laser-generated plasma, **III.**33.2
in microfocus X-ray fluorescence, **III.**35.22
in wavelength-dispersive X-ray fluorescence, **III.**35.17
and X-ray production, **III.**19.6, **III.**31.6–**III.**31.7, **III.**31.7*f*
Brewster angles, **I.**5.10, **I.**5.14, **I.**5.14*f,* **I.**5.15, **I.**5.20, **I.**5.21*f,* **I.**5.22
pseudo, **I.**5.11
reflection polarizers, **I.**5.16
second, **I.**5.12
transmittance and extinction ration near, **I.**5.19*f*
Brewster plate, in transducer design, **IV.**27.17
Bridgeman technique, of substrate growth, **I.**12.22
Bright field microscopy, **II.**17.22–**II.**17.24
Brightness, heterochromatic, **II.**24.44
Brightness matching, **I.**26.42–**I.**26.43
Brillouin amplifiers, **IV.**11.3–**IV.**11.4
Brillouin-enhanced four-wave mixing (BEFWM), **IV.**18.54–**IV.**18.55, **IV.**18.55*f*
Brillouin linewidth, **IV.**3.8–**IV.**3.9
Brillouin scattering, **I.**9.18–**I.**9.19, **II.**20.30, **II.**33.12*f,* **II.**33.29–**II.**33.30, **II.**36.77–**II.**36.78, **IV.**18.44–**IV.**18.45
vs. Raman scattering, **IV.**18.1, **IV.**18.45, **IV.**18.49
stimulated (*see* Stimulated Brillouin scattering (SBS))
Brillouin zone, **I.**9.26, **I.**9.26*f,* **I.**9.31, **II.**36.15, **II.**36.50, **II.**36.80, **IV.**20.3–**IV.**20.5
Broad-area twin-ridge structure (BTRS) lasers, **I.**13.21, **I.**13.23*f*
Broadband:
optical radiation damage from, **III.**15.2
in photometric to radiometric conversion, **III.**7.14
Broadband radiation:
and transient Raman effects, **IV.**18.29–**IV.**18.30, **IV.**18.30*f,* **IV.**18.31–**IV.**18.32
Broadband visible region phosphors, **II.**28.12
Broadband WDM, and dispersion flattening, **IV.**1.18
Broadband X-ray (BBXRT) telescope, **II.**11.5, **II.**11.12–**II.**11.13, **II.**11.13*f*
mission, **III.**28.6
Broadening:
Doppler, **I.**11.6, **I.**11.7*f,* **I.**11.10
homogeneous, **I.**8.9, **I.**11.6–**I.**11.7, **I.**11.7*f,* **I.**11.9
line, **I.**11.5
types of, **I.**11.6–**I.**11.7
Brooks, F. P., **I.**34.25
Brownian motion, **II.**17.25
Bruch's membrane, **III.**9.1, **III.**13.20
Bruning interferometers, **II.**29.10*f*
Buffer:
in SONET transmission, **IV.**12.23
in time-division multiple access, **IV.**12.16, **IV.**12.18
Bulk modulus, **II.**35.8
Bunsen-Roscoe law of photochemistry, **III.**15.1, **III.**15.3, **III.**15.7
Burch interferometers, **II.**30.7
Buried-channel charge coupled device (BCCD), **I.**22.15, **I.**23.14, **I.**23.16
Buried heterostructure (BH) lasers, **I.**13.9–**I.**13.10, **IV.**4.6, **IV.**4.14
Buried V-groove-substrate inner stripe (BVSIS) lasers, **I.**13.21
Bus configuration, for Ethernet LANs, **IV.**16.7
Butt-coupling, **II.**6.18–**II.**6.19
Byte interleaving, **IV.**12.20*f,* **IV.**12.23, **IV.**16.5

Cable television (CATV), **I.**16.12
fiber analog transmission for, **IV.**2.14–**IV.**2.15
modulation for, **IV.**4.2, **IV.**4.50
CAD programs, **I.**34.2
Caged compounds, **II.**17.48
Calcite, **II.**3.3*f*
absorption coefficients for, **II.**3.5*t*–**II.**3.6*t*
characteristics of, **II.**3.2
double refraction in, **II.**3.2
refractive indices for, **II.**3.5*t*–**II.**3.6*t,* **II.**33.70*t*

Calcium molybdate, refractive index for, **II.**33.70*t*
Calibration transfer devices, **II.**24.34–**II.**24.35
Call setup, in time-division multiple access, **IV.**12.18
Calorimeter, **II.**25.16, **II.**25.17*f*
Camcorders, solid-state camera applications for, **III.**4.3
Camera lenses:
  back focal length (BFL) in, **II.**16.2
  classification system of, **II.**16.20
  design limitations of, **II.**16.1–**II.**16.2
  fish-eye, **II.**16.5
  inverted telephoto, **II.**16.5
  microprism focusing in, **II.**16.1
  performance data for, **II.**16.24*t,* **II.**16.25
  point-and-shoot, 35-mm F/3.2 for, **II.**16.6*t*
  polychromatic optical transfer function of, **II.**16.20
  70–210-mm F/2.8–4 at f=70, **II.**16.18*t*
  70–210-mm F/2.8–4 at f=210, **II.**16.19*t*
  spatial frequency of, **II.**16.20
  telephoto, **II.**16.5, **II.**16.15
  35-mm SLR
    15-mm F/2.8 for, **II.**16.13*t*
    17-mm F/2.8 for, **II.**16.14*t*
    20-mm F/1.4 for, **II.**16.9*t*
    24-mm F/2 for, **II.**16.10*t*
    28-mm F/1.4 aspheric for, **II.**16.11*t*
    28-mm F/2.8 for, **II.**16.8*t*
    35-mm F/1.2 aspheric for, **II.**16.12*t*
    35-mm F/2.8 for, **II.**16.7*t*
    55-mm F/1.2 for, **II.**16.3*t*
    90-mm F/2.5 for, **II.**16.4*t*
    200-mm F/2.8 for, **II.**16.16*t*
    300-mm F/2 for, **II.**16.17*t*
  35-mm SLR normal, **II.**16.2
  28–150-mm F/4.1–5.7 at f=28, **II.**16.21*t*
  28–150-mm F/4.1–5.7 at f=50, **II.**16.22*t*
  28–150-mm F/4.1–5.7 at f=150, **II.**16.23*t*
  wide-angle, **II.**16.2, **II.**16.5
    highly complex extreme, **II.**16.5
  zoom, **II.**15.11, **II.**16.15, **II.**16.20
Cameras:
  adaptive optics for, **III.**10.6*f,* **III.**10.7
  aerial, **II.**1.21, **II.**1.24
  astronomical, **III.**4.3
  autoexposure, **II.**15.10–**II.**15.12
  autofocus systems in
    active, **II.**15.12, **II.**15.12*f,* **II.**15.13
    passive, **II.**15.13
  automation in, **II.**15.10
  clandestine, **II.**1.22
  color separation in, **I.**22.35*f,* **I.**26.34
  color versus black-and-white, **III.**4.3, **III.**4.20
Cameras (*Cont.*):
  day/night, **I.**21.30
  digital, **III.**6.23
  endoscopic, **II.**1.22, **II.**1.22*f*
  exposure bracketing in, **II.**15.12
  flash units for, **II.**15.16–**II.**15.17
  high-speed, **II.**1.23
    microchannel plates in, **II.**1.23*f*
  II SSA, **I.**21.2–**I.**21.6, **I.**21.6*f,* **I.**21.7, **I.**21.11, **I.**21.19–**I.**21.21
    active imaging and, **I.**21.31
    digital, **I.**21.26–**I.**21.27
    electron-bombarded (EBSSAs), **I.**21.24, **I.**21.24*f,* **I.**21.25, **I.**21.25*f,* **I.**21.26
    fiber-optic-coupled, **I.**21.21, **I.**21.21*f*
    lens-coupled, **I.**21.23, **I.**21.23*f,* **I.**21.24
    modulation transfer function (MTF) of, **I.**21.28
    mosaic, **I.**21.30
    optical multichannel analyzers (OMAs), **I.**21.28, **I.**21.29*t*
  large format, **II.**15.19
  low-light-level (LLL), **I.**21.20*f,* **III.**4.3
  major features of, **II.**15.20*f*
  multilayer coated mirrors for EUV in, **III.**24.3, **III.**24.6, **III.**24.8*f*
  output analysis for, **III.**4.20–**III.**4.21
  panoramic, **II.**1.26–**II.**1.27, **II.**1.27*f*
  periphery, **II.**1.23
  point-and-shoot, **II.**15.12
  retinal, **III.**8.3
  scientific, **III.**4.3, **III.**4.21
  sewer, **II.**1.24
  single-use, **III.**6.26–**III.**6.27
  size of, **III.**4.17
  SLR, **II.**15.8–**II.**15.9
    autofocus (AFSLRs), **II.**15.13–**II.**15.14, **II.**15.14*f,* **II.**15.15
    beam splitter, **II.**15.9, **II.**15.9*f*
    eye tracking, **II.**15.15, **II.**15.15*f,* **II.**15.16, **II.**15.16*f*
    microprism focusing in, **II.**16.1
  special, **II.**1.21
  stereo, **II.**1.24, **II.**1.25*f*
  streak, **II.**1.24, **II.**1.26*f*
  television
    low-light-levels (LLL), **I.**21.2–**I.**21.4
    self-scanned array (SSA), **I.**21.2
  thermal imaging, **II.**1.25–**II.**1.26
  35-mm, **II.**15.18–**II.**15.19, **II.**15.19*f*
  time lag in, **II.**15.9, **II.**15.10*f*
  underwater, **II.**1.26
  video, **II.**15.7–**II.**15.8
  vidicon, **I.**21.22

Cameras (*Cont.*):
view, **II.**1.21, **II.**15.19
(*See also* Charge-coupled device (CCD) cameras; Film; Final image; Solid-state camera)
Camouflage, perception of, **III.**12.8
Canada balsam, **II.**3.21
Canada-France-Hawaii telescope, **III.**1.24
Candela, **II.**29.2, **III.**7.2, **III.**7.5–**III.**7.7, **III.**7.12, **III.**14.1–**III.**14.3, **III.**14.4*t,* **III.**14.5
Candlepower, **II.**24.48, **III.**14.3
Canon EOS A2E, **II.**15.15, **II.**15.15*f,* **II.**15.16, **II.**15.16*f,* **II.**15.17 (*See under* Cameras, SLR)
Capacitor, MOS, **I.**22.4*f,* **I.**22.7–**I.**22.8, **I.**22.8*n,* **I.**22.11*f*
(*See also* Metal oxide semiconductor (MOS))
Capillary optics:
condensing, **III.**29.2–**III.**29.3, **III.**29.3*f,* **III.**29.4–**III.**29.6
imaging, **III.**29.3, **III.**29.3*f,* **III.**29.4
multiple (polycapillary), **III.**30.1, **III.**30.4–**III.**30.15, **III.**31.11, **III.**35.4–**III.**35.5, **III.**35.8–**III.**35.15, **III.**35.19–**III.**35.21, **III.**36.15
with neutron beams, **III.**36.15
progress in, **III.**37.3
single, **III.**29.1–**III.**29.6, **III.**31.11, **III.**35.4, **III.**35.8–**III.**35.9
Capillary puller, **III.**29.4, **III.**29.5*f*
Carbon arc lamps, **I.**10.19, **I.**10.22*f*–**I.**10.23*f,* **I.**10.24*t,* **I.**10.25, **I.**10.25*t,* **I.**10.26*f*
Carbon-black suspension (CBS), optical limiting in, **IV.**19.11, **IV.**19.11*f,* **IV.**19.12
Carbon dioxide (CO_2) lasers, **I.**11.17, **I.**11.17*f,* **I.**11.33
Carbon disulfide molecule, and reorientational Kerr effect, **IV.**17.15, **IV.**17.15*f,* **IV.**17.16
Cardboarding effect, in visual perception, **III.**12.15
Cardinal Black, **II.**37.36
BRDF of, **II.**37.53*f*
Cardinal points (*see* Gauss points)
Carey Lea silver (CLS), in color photographic film, **III.**6.4
Carlisle objectives, **II.**18.9
Carlson, Chester, **III.**5.1
Carl Zeiss Jena infinity-corrected objectives, **II.**17.17, **II.**17.20*f*
Carl Zeiss prism, **II.**4.16, **II.**4.16*f*
Carrier populations, changing, **II.**6.10–**II.**6.11
Carrier sense multiple access with collision detection (CSMA/CD), **IV.**16.7
Carrier-to-noise ratio (CNR), **I.**31.26
in digital vs. analog systems, **IV.**2.15*f,* **IV.**12.14
Carrier transit time, in photodetectors, **I.**17.6
Carrier trapping, **IV.**25.22–**IV.**25.23, **IV.**25.23*f,* **IV.**25.24
Cascaded limiter, **IV.**19.6
Cascaded third-order nonlinearities, **IV.**17.22–**IV.**17.25, **IV.**17.25*f,* **IV.**17.26
Cassegrain design, typical, **I.**38.3*f*
Cassegrain-Mersenne telescope, afocal, **II.**18.10, **II.**18.10*f*
Cassegrain objectives, **II.**18.7, **II.**18.7*f,* **II.**18.8
dual-focal, **II.**18.10*f*
with field corrector, **II.**18.9, **II.**18.9*f*
Schmidt-meniscus, **II.**18.23, **II.**18.23*f*
with Schwarzschild relay, **II.**18.36, **II.**18.36*f*
spherical primary, **II.**18.10, **II.**18.10*f*
three-mirror, **II.**18.32, **II.**18.32*f,* **II.**18.33, **II.**18.33*f*
Cassegrain telescope, **III.**27.1, **III.**28.1
Catadioptric, definition of, **II.**18.41
Catadioptric lenses, **II.**2.21
Herschelian, **II.**18.30, **II.**18.30*f*
Catadioptric systems, **I.**1.10, **I.**1.36
Cat-a-lac Black, **II.**37.36
glossy, specular reflection for, **II.**37.51*f*
Cataracts:
and aging, **III.**13.8, **III.**13.19
correction of, with lenses, **III.**11.3
definition of, **III.**13.1
incidence of, **III.**13.3, **III.**13.8, **III.**13.19
infrared, **III.**15.8, **III.**15.11
surgical correction of, **III.**11.13–**III.**11.14, **III.**13.4, **III.**13.9, **III.**13.19
and ultraviolet radiation, **III.**11.10, **III.**11.13–**III.**11.14, **III.**13.8, **III.**13.19, **III.**15.1, **III.**15.4–**III.**15.6, **III.**15.7*f*
Cathodeluminescence (CL), **II.**36.72
Cathode ray tube (CRT), **I.**28.17, **II.**15.7, **II.**19.26
bandwidth, **I.**27.7
characteristics of light from, **I.**27.15
characterization characteristics, **I.**27.35–**I.**27.36
color
calibration of, **I.**27.21–**I.**27.22
design of, **I.**27.3
viewing environments for, **I.**27.19–**I.**27.20
colorimetric standards in, **I.**27.15
electronics and controls, **I.**27.7
emission spectra of, **I.**27.6*f*
frames and fields in, **I.**27.10, **I.**27.10*f,* **I.**27.11
gamma correction exponent in, **I.**27.7*f*
horizontal scanning in, **I.**27.11, **I.**27.11*f,* **I.**27.12
image display setup, **I.**27.20
input signal, **I.**27.11
light from, **I.**27.17*f*
characteristics of, **I.**27.16
linearization, **I.**27.35

Cathode ray tube (CRT) (*Cont.*):
monochrome, **I.**27.4, **I.**27.4*f*
amplification in, **I.**27.8–**I.**27.9, **I.**27.9*f*
operation, **I.**27.9
operational characteristics of, **I.**27.14
output, stability of, **I.**27.16–**I.**27.17
raster generation in, **I.**27.9–**I.**27.10
shadowmask, **I.**27.5, **I.**27.5*f*
problems in, **I.**27.6
spatial uniformity in, **I.**27.18, **I.**27.18*f,* **I.**27.19, **I.**27.19*f*
synchronization standards in, **I.**27.14
vertical scanning in, **I.**27.12, **I.**27.12*f,* **I.**27.13
Cauchy formula, **II.**33.26
Causality, mathematical expression of, **IV.**17.11, **IV.**17.13
Caustics, **I.**1.96
Cavities:
emissivities of, **I.**10.5, **I.**10.5*f*
of lasers, **I.**11.3
temperature gradients in, **I.**10.6
Cavity dumping, **I.**11.29
Cavity resonators, **I.**3.24
CD, linear velocity of, **I.**31.6*n*
CD-ROM, **I.**31.2
Cellulose acetate, **I.**20.4–**I.**20.5
Celor lenses, **II.**1.31*f*
Center for X-Ray Optics, **III.**21.3
Center-of-mass motion, of atom, **IV.**26.46, **IV.**28.2, **IV.**28.32
Center of rotation, **III.**12.1
Center of symmetry, in optical fiber, **IV.**1.6, **IV.**1.43
Central Commission for International Telephone and Telegraphy (CCITT) (*see* International Telecommunications Union (ITU))
Central field potential, **I.**8.14
Central limit theorem, **I.**4.9
Centroid anisoplanatism, **III.**1.17
CEPT digital hierarchy, **IV.**12.22*f*
CEPT1 30-channel system, **IV.**12.21
CGH-Maksutov test, **II.**31.9, **II.**31.10*f*
Cgs gaussian system, **II.**38.23–**II.**38.24
Chalcogenide fiber, **II.**10.45–**II.**10.46, **IV.**1.47–**IV.**1.48, **IV.**14.2*t*–**IV.**14.3*t,* **IV.**14.7, **IV.**14.7*f,* **IV.**14.8, **IV.**21.3
Chandra X-ray Observatory, **III.**28.1, **III.**28.3*f,* **III.**28.6, **III.**28.10
Channel add/drop, **IV.**13.14
Channel capacity, of fiber communications systems, **IV.**5.1
Channel electron multipliers (CEMs), **III.**34.6
Channeling radiation, **III.**33.1, **III.**33.3
Channel power, in WDM networks, equalization of, **IV.**13.21–**IV.**13.23, **IV.**13.23*f,* **IV.**13.24, **IV.**13.24*f*
Channel spacing, unequal, **IV.**3.10
Channel substrate planar (CSP) lasers, **I.**13.21, **I.**13.23*f,* **I.**13.39*f*
Chaos, **II.**28.5
Characteristic temperatures, of crystalline materials, **II.**33.34
Characteristic X-ray radiation, **III.**31.6–**III.**31.7, **III.**31.7*f,* **III.**31.10, **III.**33.2, **III.**35.15
Charge-coupled device (CCD), **I.**16.11–**I.**16.12, **I.**21.2, **I.**21.6*f,* **I.**21.7, **I.**22.8*n,* **I.**22.16*f,* **II.**15.7, **III.**4.2, **III.**35.32
array architecture of, **III.**4.3–**III.**4.6
backside-illuminated, **I.**22.8
buried-channel (BCCD), **I.**22.15, **I.**23.14, **I.**23.16
characteristics of, **I.**22.18–**I.**22.19, **I.**22.19*f,* **I.**22.20, **I.**22.20*f*
correlated double sampling (CDS) and, **I.**22.21
intensified (*see* Intensified charge-coupled device (ICCD))
operation of, **I.**22.13–**I.**22.14, **I.**22.14*f,* **I.**22.15
output of, **I.**22.15–**I.**22.16
performance of, **I.**22.34
readout, **I.**22.22
resolution from, **II.**15.8
silicon, **I.**23.14
surface channel (SCCD), **I.**23.16
transfer inefficiency in, **I.**22.20–**I.**22.21
types of, **I.**22.16–**I.**22.17, **I.**22.17*f,* **I.**22.18
(*See also* Image sensors)
Charge-coupled device (CCD) cameras, **I.**21.20*f,* **III.**2.7, **III.**4.2–**III.**4.3, **III.**4.17
Charged particle accelerators, **II.**24.29
Charge injection device (CID), **III.**4.2, **III.**4.6–**III.**4.8
advantages of, **III.**4.8
functional array layout for, **III.**4.7*f*
in medical X-ray imaging, **III.**35.32
pixel architecture for, **III.**4.6*f*
pixel operation for, **III.**4.7*f*
signal-to-noise ratio for, **III.**4.7
Charge-injection devices (CIDs), **I.**21.2, **I.**23.16
Charge-sensing elements, antiblooming in, **I.**22.9–**I.**22.10, **I.**22.10*f,* **I.**22.11
Charge spectrograph, **III.**5.8, **III.**5.9*f*
Charge sweep device (CDS), **I.**23.14
Chemglaze (*see* Aeroglaze)
Chemical beam epitaxy (CBE), **I.**13.7, **II.**6.16–**II.**6.17
Chemically assisted reactive ion beam etching (CAIBE), **II.**6.18

Chemical vapor deposition (CVD), **II.**7.14, **II.**10.43, **IV.**1.44–**IV.**1.45, **IV.**1.47
plasma-assisted, **II.**6.17
Chief ray, **I.**1.82*f,* **II.**18.41
Chirp:
parametric enhancement and pulse compression, **I.**14.14
in semiconductor lasers, **I.**13.39
Chirped gratings, **IV.**9.7
Chirped pulse excitation, **IV.**24.24–**IV.**24.25
Chromatic aberration, **I.**1.100, **I.**24.17, **I.**26.39, **I.**34.10, **I.**34.12
in human eye, **III.**11.5, **III.**12.33, **III.**13.10, **III.**13.12
and retinal microscopy, **III.**10.9
and Stiles-Crawford effect, **III.**9.7
correction, in binary optics, **II.**8.6, **II.**8.6*f*
in eyes, **I.**24.18, **I.**24.18*f,* **I.**24.19
longitudinal (LCA), **I.**24.17–**I.**24.18, **I.**24.18*f*
off-axis, **I.**33.3
transverse (TCA), **I.**24.18–**I.**24.19
Chromatic dispersion, **IV.**6.9–**IV.**6.11
in optical fiber, **IV.**13.4–**IV.**13.5, **IV.**13.5*f,* **IV.**13.6, **IV.**13.6*f*
Chromaticity diagrams, **I.**26.23–**I.**26.24
CIE 1931 xy, **I.**26.23*f,* **I.**26.24
Chromatic smearing, **III.**18.6, **III.**18.8*f*
Chromium:
extinction coefficient for, **II.**35.14*t*–**II.**35.15*t*
vs. wavelength, **II.**35.23*f*
index of refraction in, **II.**35.14*t*–**II.**35.15*t*
vs. wavelength, **II.**35.23*f*
reflectance of, **II.**35.32*t*–**II.**35.33*t*
Chromogenic color film, **I.**20.15
CIELAB color space, **III.**8.4
CIELAB coordinates, **I.**26.37
CIELUV coordinates, **I.**26.37
CIE standard photometric observer for photopic vision, **III.**14.2
CIE 1931 color-matching functions, **I.**26.13, **I.**26.14*t*
CIF, **II.**8.15
Cilia, **III.**9.1
Ciliary-type photoreceptors, in vertebrates, **III.**9.3
Circle polynomials, **I.**1.98
Circuit switching, **IV.**13.16
Circular absorption dichroism, **III.**25.5, **III.**25.5*f,* **III.**25.6
Circular aperture, diffraction image of, **II.**17.10*f*
Circular dichroism, **II.**20.19
magnetic, **II.**20.20
Circularly polarized light, **I.**5.24–**I.**5.25, **I.**5.26*n,* **I.**5.28
Circularly polarized radiation, **II.**20.21
Circular phase plate, **III.**25.6, **III.**25.7*f*
Circular polarization, **III.**25.5–**III.**25.8
analyzers for, **III.**25.6–**III.**25.7, **III.**25.7*f,* **III.**25.8
and bending magnets, **III.**32.6–**III.**32.7, **III.**32.7*f,* **III.**32.8, **III.**32.8*f*
Circulator (*see* Optical circulator)
Cladding, of optical fiber, **IV.**1.6–**IV.**1.7, **IV.**1.11
fabrication of, **IV.**1.44, **IV.**1.47–**IV.**1.48
and radiative loss, **IV.**2.2
Cladding layers, **I.**13.4–**I.**13.5
Cladding mode coupling device, **IV.**8.1
Cladding modes, **II.**10.6, **IV.**1.7, **IV.**1.7*f*
Clausius-Mosotti relationship, **II.**33.28
Clausius-Mosotti theory, **I.**6.18
Clear lens exchange (CLE), **III.**11.17
Cliff effect, **IV.**6.5
Clipped Lambertian distribution, **III.**2.4, **III.**2.6
Clock:
atomic, **IV.**28.27
and bit error rate, **IV.**6.4
and jitter, **IV.**6.15–**IV.**6.16
Clock recovery:
optical, **IV.**12.34–**IV.**12.35, **IV.**12.35*f,* **IV.**12.36, **IV.**12.38–**IV.**12.39
for return-to-zero data stream, **IV.**12.13, **IV.**12.14*f*
Clock signal:
in demultiplexing, **IV.**12.9, **IV.**12.12
and line filtering, **IV.**12.15
Closed-circuit television (CCTV):
camera output standard for, **III.**4.20
Closed-loop stability, in laser servo system, **IV.**27.8–**IV.**27.12
Cluster hopping, **IV.**22.25, **IV.**22.25*f,* **IV.**22.26, **IV.**22.30
CMT-Acutance index, **I.**20.21
Coatings, optical (*see* Black surfaces, optical; Multilayer reflective coatings; Optical coatings)
Coaxial combination of lenses, **I.**1.68–**I.**1.69, **I.**1.69*f,* **I.**1.70, **I.**1.70*f*
Cochlea, **III.**9.1
as light guide, **III.**9.24–**III.**9.26
organ of Corti in, **III.**9.2
Coddington's equations, **I.**1.48
Code mark inversion (CMI), **IV.**12.12, **IV.**12.12*f*
Coding, quantum-dense, **IV.**26.15
Cohen's "Matrix R," **I.**26.33
Coherence:
area, **I.**4.3
atomic, **IV.**23.12–**IV.**23.13, **IV.**23.3–**IV.**23.5, **IV.**23.26, **IV.**23.26*f,* **VI.**23.27
complex degree of, **I.**4.4

Coherence (*Cont.*):
degree of, **I.**2.38
in electromagnetically induced transparency, **IV.**23.3–**IV.**23.5, **IV.**23.8–**IV.**23.9
maximal atomic, and nonlinear optics, **IV.**23.26, **IV.**23.26*f,* **IV.**23.27
measurements of, **I.**4.3–**I.**4.4
in optical fiber, **IV.**1.14
in semiconductor saturable absorber, **IV.**25.20–**IV.**25.21
spatial, **I.**2.39, **I.**4.3
spectral, complex degree of, **I.**4.5, **I.**4.14, **I.**4.18
temporal, **I.**2.42
transverse, **III.**35.3
volume, **I.**4.3
Coherence collapse, **IV.**4.25–**IV.**4.28
Coherence function:
definitions of, **I.**4.4–**I.**4.9
higher-order, **I.**4.9
mutual, **I.**2.37, **I.**2.37*f,* **I.**2.38, **I.**4.4, **I.**4.7
temporal, **I.**2.37
Coherence length, **IV.**22.11
Coherence theory, **I.**2.37, **I.**4.21*f*
classical, **I.**4.1
quantum, **I.**4.2
sources, of light (*see* Light, sources of)
Coherence time, **I.**4.3
Coherency matrix, **II.**22.8
Coherent adiabatic population transfer, **IV.**23.3–**IV.**23.5, **IV.**23.7, **IV.**23.20
Coherent anti-Stokes Raman scattering (CARS), **II.**36.58–**II.**36.59, **IV.**17.5*t,* **IV.**17.19–**IV.**17.20, **IV.**18.3*t,* **IV.**18.4, **IV.**18.5*f,* **IV.**18.35, **IV.**18.43, **IV.**18.43*t*
energy level diagram for, **IV.**17.7, **IV.**17.7*f*
Coherent control, **IV.**25.22
Coherent coupling, **I.**24.26
Coherent crosstalk, in WDM network, **IV.**13.25–**IV.**13.25*f*, **IV.**13.26, **IV.**13.26*f*
Coherent demodulation, **II.**10.36, **IV.**1.38–**IV.**1.39
Coherent image amplification, **II.**39.27–**II.**39.28
Coherent interference:
and crystals, **III.**22.2
and mixing rod applications, **III.**2.33
and synchrotron radiation, **III.**32.1
and X rays, **III.**19.7–**III.**19.8
Coherent mode function, **I.**4.21–**I.**4.22
Coherent optical communications, **II.**10.32–**II.**10.33, **II.**10.33*f,* **IV.**1.34–**IV.**1.35, **IV.**1.35*f,* **IV.**1.36–**IV.**1.38
demodulation in, **II.**10.36, **II.**10.36*f*
fiber requirements in, **II.**10.37
heterodyne/homodyne detection in, **II.**10.33, **II.**10.33*f,* **II.**10.34
Coherent optical communications (*Cont.*):
modulation formats, **II.**10.34–**II.**10.35
receiver sensitivity in, **II.**10.34, **II.**10.35*t*
repeater spacing in, **IV.**2.11
source requirements in, **II.**10.35
stimulated Brillouin scattering in, **IV.**1.40
Coherent optical transients, Bloch equations for, **IV.**24.3–**IV.**24.5
Coherent population trapping (CPT), **IV.**23.3–**IV.**23.5, **IV.**23.5*f,* **IV.**23.20
classical versus quantum approach to, **IV.**23.9–**IV.**23.10
in lambda three-level atomic scheme, **IV.**23.6–**IV.**23.7
and nonlinear frequency conversion, **IV.**23.26–**IV.**23.27
Coherent radiation, **III.**2.2, **III.**19.6, **III.**32.2, **III.**32.19
producing, **IV.**18.42–**IV.**18.43, **IV.**26.19
Coherent receivers, **IV.**2.11
Coherent scattering, **III.**3.3, **III.**3.5–**III.**3.7, **III.**20.8, **III.**36.4, **III.**A.1
Coherent spectroscopy, Raman interactions in, **IV.**18.43, **IV.**18.43*t,* **IV.**18.44*f*
Coherent states, of photons, **IV.**26.13
Coherent Stokes Raman scattering (CSRS), **IV.**17.5*t,* **IV.**17.19–**IV.**17.20, **IV.**18.43*t*
Coherent Stokes Raman spectroscopy (CSRS), **II.**36.58–**II.**36.59
Coherent transient spectroscopy, **IV.**24.25–**IV.**24.27
Coherent wave, **II.**19.10*n*
Coherent X-ray metrology, **III.**26.5
Cold cathode lamps, **I.**10.35, **I.**10.40
Cold molecules, production of, **IV.**28.30
Coleoptile, in plant structure, **III.**9.1, **III.**9.27, **III.**9.27*f*
Collected volatile condensable materials (CVCM), **II.**37.19
Collimation, **I.**31.9–**I.**31.10
of atomic beam, **IV.**28.13–**IV.**28.14, **IV.**28.14*f*
limitations to, **III.**35.7, **III.**35.7*f,* **III.**35.8
methods for, **III.**35.9–**III.**35.11
in multicapillary X-ray optics, **III.**30.6*f,* **III.**30.8–**III.**30.11, **III.**30.11*f*–**III.**30.12*f,* **III.**30.15
of neutrons, **III.**36.13–**III.**36.14
parallel beams in, **III.**35.11, **III.**35.11*f,* **III.**35.12, **III.**35.12*f*
and synchrotron radiation, **III.**32.1
Collinear transformation, **I.**1.61–**I.**1.63, **I.**1.68
matrix representation of, **I.**1.64
properties of, **I.**1.67
Collineation, **I.**1.60–**I.**1.63

Collisional broadening, **I.**11.6
Color:
  axial, **I.**33.2, **I.**33.2*f,* **I.**33.3
  computational constancy, **I.**26.34–**I.**26.35
  context effects, **I.**26.41
  lateral, **I.**33.4, **II.**18.41
  sensitivity regulation in, **I.**26.42
  use of, **I.**8.4
Color-anomolous observers, **I.**26.39
Color appearance, **I.**26.41–**I.**26.42
Color center, **II.**28.13
  lasers, **I.**11.36
Color constancy, **I.**26.42
  in imaging, **III.**17.6
Color coordinate systems, **I.**26.12
  CIELUV and CIELAB spaces, **I.**26.37–**I.**26.38
  CIE uniform color spaces, **I.**26.36, **I.**26.36*f*
  cone modulation space, **I.**26.15
  cone sensitivities in, **I.**26.14
    Smith-Porkorny estimates of, **I.**26.17*t,* **I.**26.18*f*
    Stockman-McLeod-Johnson estimates of, **I.**26.18*t*
  DLK color space, **I.**26.15–**I.**26.16
  opponent and modulation spaces in, **I.**26.14–**I.**26.15
  stimulus spaces in, **I.**26.12
  transformations between color spaces, **I.**26.17, **I.**26.19, **I.**26.19*t,* **I.**26.20–**I.**26.21
  transformations between visual systems, **I.**26.34
Color copying, xerographic, **III.**5.2, **III.**5.5, **III.**5.11–**III.**5.13
  full color, **III.**5.11–**III.**5.12, **III.**5.12*f*
  highlight color, **III.**5.13, **III.**5.13*f*
Color data, visualizing, **I.**26.22
  chromaticity diagrams, **I.**26.23
  three-dimensional approaches to, **I.**26.22, **I.**26.22*f,* **I.**26.23
  wavelength, functions of, **I.**26.24
Color-deficient observers, **I.**26.39
Color differences, measurement of small, **I.**26.35–**I.**26.36, **I.**26.36*f*
Color discrimination, **I.**26.35
Color filter array (CFA), **III.**4.18
Color imaging, **I.**22.34
Colorimeters, **I.**26.24
Colorimetry, **I.**27.22, **III.**14.12
  color-matching experiments in, **I.**26.7, **I.**26.7*f*
  empirical foundations of, **I.**26.7
  goal of, **I.**26.1
  linear models, of stimulus representation, **I.**26.6
    basis vectors in, **I.**26.6
    matrix representation of, **I.**26.5, **I.**26.6*f*
    use of, **I.**26.5
  measurements, **I.**26.24
Colorimetry (*Cont.*):
  reference sources for, **I.**26.2
  spectral functions in, **I.**26.3
  stimulus representation in, **I.**26.3
  surfaces in, **I.**26.25
  updated recommendations in, **III.**8.4
  vector representation of spectral functions in, **I.**26.3, **I.**26.4*f*
  visible spectrum, sampling of, **I.**26.6
Color-matching, **I.**26.8–**I.**26.9
  CIE 1931 functions, **I.**26.13, **I.**26.14*t,* **I.**26.16*t*
  cone coordinates in, **I.**26.11
  consistency in, **I.**26.9
  critical properties of, **I.**26.8
  effects of errors in, **I.**26.40, **I.**26.40*f*
  experiments, **I.**26.7, **I.**26.7*f,* **I.**26.8, **I.**26.38
  functions, **I.**26.11, **I.**26.13*f*
  Judd-Vos modified functions, **I.**26.13, **I.**26.15*t*
  mechanisms of, **I.**26.10
  1964 10° functions, **I.**26.13–**I.**26.14
  tristimulus coordinates and, **I.**26.8–**I.**26.9
Color negative photographic film, **III.**6.10, **III.**6.18, **III.**6.23, **III.**6.26–**III.**6.28, **III.**6.28*t,* **III.**6.29, **III.**6.29*t*
Color-normal observers, differences among, **I.**26.38
Color perception, **III.**4.18–**III.**4.19, **III.**6.16, **III.**6.17*f,* **III.**9.19–**III.**9.20
  aesthetic concerns in, **III.**17.10–**III.**17.11
  and aging, **III.**13.13–**III.**13.15
  and cataracts, **III.**11.13
  and electronic imaging, **III.**17.5–**III.**17.6, **III.**17.9
Color photography:
  emulsions for, **III.**6.6–**III.**6.10
  film for, **III.**6.2–**III.**6.5
  image dyes in, **III.**6.10–**III.**6.13
  papers for, **III.**6.5–**III.**6.6
  spectral sensitizers in, **III.**6.14–**III.**6.19
Color record, in photographic film, **III.**6.4
Color reproduction, subtractive, **I.**20.14–**I.**20.15
Color reversal film, **III.**6.23–**III.**6.24, **III.**6.24*t,* **III.**6.25
Colors, out-of-gamut, **I.**27.25, **I.**27.28
Color sequential imaging, **I.**22.35
Color space (*see* Color coordinate systems)
Color stimuli, metameric, **I.**26.8
Color temperature, **II.**24.48
  measurement of, **III.**14.4*t,* **III.**14.7
Coma, **III.**10.4, **III.**10.7
  with conic reflectors, **III.**2.11
  defined, **II.**18.41
  with spherical lenses, **III.**2.8
Combinations of properties, **II.**33.38

Comité International des Poids et Mesures (CIPM), **III.**14.2
Commando cloth:
  reflectance of, **II.**37.37*f*
  transmittance of, **II.**37.42*f*
Commercial lighting, lens arrays used in, **III.**2.33
Commission Internationale de l'Éclairage (CIE) (*see* International Commission on Illumination (CIE))
Communications links:
  length limit for, **IV.**1.11
  point-to-point, **IV.**1.24–**IV.**1.31
Commutator, **IV.**12.1, **IV.**12.6, **IV.**12.8, **IV.**12.8*f*
Compact audio disk (CD), **I.**31.1, **II.**9.7
  plastic lenses in, **II.**7.7
Compact-source arc lamps, **I.**10.31, **I.**10.31*f*–**I.**10.32*f*
Compander, **IV.**12.11
Compensator:
  Dall, **II.**30.22*f*
  holographic, **II.**30.23
  Offner, **II.**30.23, **II.**30.23*f*
  reflective, **II.**30.22
  refractive, **II.**30.22
  (*See also* Retardation plates, variable)
Complementary metal-oxide semiconductor (CMOS), **III.**4.2, **III.**4.8–**III.**4.9
Component power, minimizing, **I.**32.12–**I.**32.13, **I.**32.13*f*
Component specifications, for optical systems, **I.**35.1
Composite second-order (CSO) distortion, **IV.**2.15
Composite triple-beat (CTB) distortion, **IV.**2.15
Compound elliptical concentrator (CEC), **III.**2.15, **III.**2.15*f,* **III**.2.17
Compound elliptic reflector, **III.**2.38
Compound hyperbolic concentrator (CHC), **III.**2.15–**III.**2.16, **III.**2.16*f,* **III.**2.17
Compound hyperbolic reflector, **III.**2.38
Compound parabolic concentrator (CPC), **III.**2.1, **III.**2.14, **III.**2.14*f*–**III.**2.15*f,* **III.**2.20, **III.**2.28
Compound refractive lens (CRL), **III.**20.4, **III.**20.4*f,* **III.**20.5, **III.**20.5*f,* **III.**20.6–**III.**20.8
Compression:
  in electronic imaging, **III.**7.7, **III.**17.3–**III.**17.4
  of signal, **IV.**12.11
Compression delay, in time-division multiple access, **IV.**12.18
Compressive strain:
  and electrorefraction, **IV.**4.65
  on quantum wells, **IV.**4.33–**IV.**4.34
Compton scattering, **III.**20.7–**III.**20.8, **III.**30.15, **III.**35.20, **III.**35.21*f,* **III.**35.27, **III.**35.30, **IV.**26.7, **IV.**26.10
Computed radiography, **III.**35.27, **III.**35.30–**III.**35.32, **III.**35.32*f*
Computer-aided drafting (CAD), spline surfaces used in, **III.**2.7
Computer-Augmented Virtual Environment (CAVE), **III.**12.32–**III.**12.33
Computer-generated holograms (CGH), **II.**31.5*f*–**II.**31.6*f*
  interferometers using, **II.**31.6, **II.**31.6*f,* **II.**31.7
  null lens test, **II.**31.8, **II.**31.9*f*
  plotting, **II.**31.3–**II.**31.6
  types of, **II.**31.2
Computer-numerical control (CNC) lathe turning, **II.**34.13
Computers:
  screen reflections on, **III.**16.2–**III.**16.3
  spectacle lenses for working at, **III.**11.8–**III.**11.9
  and vision problems, **III.**16.1–**III.**16.6
Computer Vision Syndrome (CVS), **III.**16.1
Computing environment, **I.**34.23
Concatenation, of SONET frames, **IV.**16.6
Concentrated arc lamps, **I.**10.39
Concentration:
  calculating, **III.**2.6
  definition of, **III.**2.1
  methods for, **III.**2.13–**III.**2.23
  2D versus 3D geometries for, **III.**2.20–**III.**2.22
Concomitant vision, **III.**12.1
Condensed matter systems:
  atomic motion control in, **IV.**28.31
  relaxation in, **IV.**24.15
  study of, **IV.**28.5
  and ultrashort laser pulses, **IV.**25.4
Condensers, **I.**32.10, **I.**32.10*f,* **I.**32.11, **I.**32.11*f*
Condensing capillary optics, **III.**29.2–**III.**29.3, **III.**29.3*f,* **III.**29.4–**III.**29.6
Condition of detailed balance, in laser photon statistics, **IV.**26.24
Condon point, in ultracold collisions, **IV.**28.28–**IV.**28.29, **IV.**28.29*f*
Conduction band, **I.**12.4, **I.**16.3
Conductive magnetic brush (CMB), **III.**5.7
Cone concentrator, **III.**2.14, **III.**2.17
Cone polymorphism, **I.**26.39
Cones, **I.**25.5, **I.**25.7*f,* **I.**25.9*f,* **III.**6.16, **III.**7.8–**III.**7.9, **III.**7.12, **III.**10.3*f*
  and aging, **III.**13.13–**III.**13.14, **III.**13.14*f,* **III.**13.15
  alignment of, **III.**9.8
  directional sensitivity of, **III.**9.4
  Henle's fibers in, **III.**9.1
  idealized model of, **III.**9.22*f*
  pedicle in, **III.**9.2, **III.**9.20
  physiology of, **III.**9.3, **III.**9.9*f,* **III.**9.12, **III.**9.21–**III.**9.22

Conférence Générale des Poids et Mesures (CGPM), **III.**14.2
Confidence interval (CI), **II.**24.24
Configurational coordinate model, **I.**8.26
Configurational relaxation, **II.**28.15, **II.**28.16*f*–**II.**28.17*f*
  measurement of, **II.**28.17
  temperature dependence and, **II.**28.18, **II.**28.18*f*
Configuration factor, **II.**24.16
Confocal parabolas (*see under* Lenses, afocal)
Conical foil imaging mirrors, **II.**11.12, **II.**11.12*t,* **II.**11.13
Conical foil X-ray telescopes, high energy X-ray astrophysics with, **II.**11.26
Conic constant, **II.**18.41
Conic lenses, **III.**2.9, **III.**2.10*f*
Conic parameter, **I.**1.38
Conic reflectors, **III.**2.11, **III.**2.12*f*
Conics, of rotation, **I.**3.38
Conic surfaces, **II.**18.2–**II.**18.3, **II.**18.3*f*
Conjugate equations, **I.**1.53–**I.**1.54
  focal lenses and, **I.**1.53*f*
Conjugate eye movements, **III.**12.1, **III.**12.7–**III.**12.8, **III.**12.21–**III.**12.22
Conjugate imaging system, **II.**19.5*f*
Conjugate lines, **I.**1.64
Conjugate planes, **I.**1.63
Conjugate points, **I.**1.33
Conjunctiva, **III.**15.1, **III.**15.7
Connector loss, **IV.**6.8, **IV.**6.8*t,* **IV.**6.17
  measurement of, **IV.**1.15–**IV.**1.16
Connectors, reflection from, **IV.**1.25, **IV.**6.14
Conoscopic observation, **II.**17.39–**II.**17.40, **II.**17.40*f*
Conservation of momentum, **I.**9.28
  linear photon, **II.**38.12–**II.**38.13, **II.**38.13*f,* **II.**38.14, **II.**38.14*f*
Constricted double-heterostructure large optical cavity (CDH-LOC) lasers, **I.**13.23*f*
Consultative Committee on Photometry and Radiometry (CCPR), **III.**7.2
Contacting, wafer processing and, **I.**12.25–**I.**12.26
Contact lenses, **III.**10.2, **III.**10.11–**III.**10.12, **III.**11.3, **III.**11.10
  and cataracts, **III.**11.13–**III.**11.14
  and computer work, **III.**16.4
  and eye movement, **III.**12.29
  implantable, **III.**13.24
  and presbyopia, **III.**11.12–**III.**11.13, **III.**12.19
  rigid, **III.**11.11–**III.**11.12
  scleral, **III.**11.13
  soft, **III.**11.10–**III.**11.11, **III.**11.11*f*
  and unequal magnification, **III.**12.26–**III.**12.27
Continuous object, **II.**32.2
Continuous phase multiplexer, **II.**8.11
Continuous polishers (CP), **I.**40.6
Continuous-wave (CW) dye laser, **III.**1.34, **III.**1.34*f,* **III.**1.35, **III.**1.35*f*
Continuous-wave (CW) optical spectroscopy, **IV.**24.2
Continuous-wave optical parametric oscillator (CW OPO), **IV.**22.15, **IV.**22.29–**IV.**22.30, **IV.**22.55
  (*See also specific types*)
Continuum excitations, **IV.**25.20–**IV.**25.21
Contour generation, **II.**23.7
Contrast, **I.**29.4
Contrast, image:
  and cataracts, **III.**11.13
  in medical X-ray applications, **III.**35.26, **III.**35.26*f,* **III.**35.27, **III.**35.28*f,* **III.**35.29–**III.**35.30, **III.**35.30*f*
Contrast constancy, **I.**25.35
Contrast discrimination, **I.**25.33, **I.**25.33*f,* **I.**25.34
Contrast estimation, **I.**25.35
Contrast generation, in microscopes, **II.**17.22, **II.**17.24*f*
Contrast masking, **I.**25.33–**I.**25.34, **I.**25.34*f,* **III.**17.3–**III.**17.4
Contrast ratio, in modulators, **IV.**4.58–**IV.**4.60
Contrast sensitivity, **III.**10.1, **III.**12.20, **III.**13.8, **III.**13.15–**III.**13.16, **III.**13.23
Contrast sensitivity function (CSF), **I.**25.21–**I.**25.22, **I.**25.22*f*–**I.**25.23*f,* **I.**25.26, **I.**25.27*f,* **III.**13.15–**III.**13.16, **III.**13.17*f,* **III.**17.3
  chromatic, **I.**25.31, **I.**25.33
  falloff, high-frequency, **I.**25.29–**I.**25.30
  isochromatic, **I.**25.32*f*
  low-frequency falloff in, **I.**25.28
  spatio-temporal, **I.**25.30
  temporal, **I.**25.31*f*
Contrast transfer functions (CTF), **II.**32.8
  and modulation transfer function (MTF), **II.**32.9*f*
Control pulse, in all-optical switching, **IV.**21.4–**IV.**21.7
Control signal switching, **IV.**21.2
Convention of the Meter, **III.**7.2
Convergence, **III.**12.1, **III.**12.22, **III.**12.25
  in CRTs, **I.**27.13–**I.**27.14
  errors of, **III.**12.13, **III.**12.20, **III.**12.27
  as extraretinal information, **III.**12.3
Convergence accommodation, **III.**12.24, **III.**12.29, **III.**12.32
Convergence-accommodation/convergence (CA/C) ratio, **III.**12.24
Convergent beam diffraction, **III.**37.3–**III.**37.4
Converging reflector, **II.**2.39*f,* **III.**2.38, **III.**2.40

Conversion efficiency, second-harmonic, **II.**38.14–**II.**38.16
Converter, analog-to-digital, **II.**6.23
Cook objectives, three-mirror, **II.**18.34, **II.**18.34*f*
Cooling:
  for atom trapping, **IV.**28.20–**IV.**28.22
  evaporative, **IV.**28.27–**IV.**28.28, **IV.**28.35, **IV.**28.36*f*
  optical, **IV.**28.1, **IV.**28.3, **IV.**28.6, **IV.**28.35 (*See also* Laser cooling)
  sub-Doppler, **IV.**28.15–**IV.**28.19
Cooper pairs, **III.**34.9
Copepod, **III.**9.1
Copilia, vision system of, **III.**9.4
Copper:
  electrical resistance of, **II.**35.58*f*
  extinction coefficient for, **II.**35.13*t*–**II.**35.14*t* vs. wavelength, **II.**35.23*f*
  index of refraction in, **II.**35.13*t*–**II.**35.14*t* vs. wavelength, **II.**35.23*f*
  reflectance of, **II.**35.31*t*–**II.**35.32*t* vs. wavelength, **II.**35.42*f*
  specific heat of, **II.**35.70*f*
  thermal conductivity of, **II.**35.64*f*–**II.**35.65*f*
Copper distributed data interface (CDDI), **IV.**16.4
Copper vapor lasers, **I.**11.14, **I.**11.14*f,* **I.**11.16, **I.**11.32, **I.**14.21
Core, of optical fiber, **IV.**1.6–**IV.**1.8
  fabrication of, **IV.**1.44, **IV.**1.47–**IV.**1.48
Cornea:
  in aberration correction, **III.**10.6–**III.**10.7, **III.**10.12
  and aging, **III.**13.5–**III.**13.7
  and contact lenses, **III.**11.10
  corrective surgery on, **III.**13.24–**III.**13.25
  distortion of (*see* Kerataconus)
  implants in, **III.**11.17
  inflammation of, **III.**15.1
  radiation damage to, **III.**15.1, **III.**15.4–**III.**15.6, **III.**15.13
  as refractive element, **III.**11.2, **III.**11.4, **III.**13.6
  unequal powers of, **III.**12.26
Corneal endothelium, **III.**13.6
Corneal irradiance, **III.**15.8
Cornell Black, **II.**37.28
Cornell High Energy Synchrotron Source (CHESS), **III.**29.4, **III.**29.5*f*
Corning Glass Works (Corning, Inc.), **II.**7.6–**II.**7.7, **II.**7.9*f,* **IV.**1.5, **IV.**1.44
Corning lenslet, **II.**7.19*f*
Cornu equation, **II.**33.26
Coroneo effect, **III.**15.1, **III.**15.6, **III.**15.6*f,* **III.**15.7
Corotron, **III.**5.2, **III.**5.3*f*
Corpuscular theory, of rays, **I.**1.9
Correlated double sampling (CDS), **I.**22.21, **III.**4.11
Correlated emission laser (CEL), **IV.**26.43–**IV.**26.44
Correlation fringes, **II.**23.11
Correlation length, **I.**7.10
Correlation of properties, **II.**33.37–**II.**33.38
Corresponding retinal points, **III.**12.1
Cosine condition, **I.**1.33, **I.**1.33*f*
Cosine law of emission, **II.**24.9
Cosine law of irradiation, **II.**24.9
Cosine-to-the-fourth approximation, **I.**1.88
Couder objectives, **II.**18.13, **II.**18.13*f*
Coulomb attraction, **I.**9.32
Coulomb energy, Dirac form of, **I.**8.6
Coulomb explosion, **II.**28.7–**II.**28.8
Coulomb repulsion, **II.**28.7
Couple-cleaved cavity (C^3) laser, **IV.**12.27
Coupled cavity lasers, **I.**13.40, **I.**13.40*f,* **I.**13.41
Coupled-dipole method, **I.**6.12, **I.**6.17–**I.**6.18
Coupled mode theory, **II.**6.24
Coupled plasma-phonon behavior, **II.**36.37
Coupled-wave equations, in optical parametric generation, **IV.**22.4, **IV.**22.8–**IV.**22.9
Coupled-wave theory, time-dependent, **II.**39.10
Couplers, fiber-optic, **IV.**8.1–**IV.**8.3
  directional, **IV.**10.2–**IV.**10.3, **IV.**10.3*f*
  fabrication technologies for, **IV.**8.1
  half-beat-length, **IV.**21.5
  nonlinear directional, **IV.**21.5, **IV.**21.5*f,* **IV.**21.6
  polarization-maintaining, **IV.**8.6–**IV.**8.7, **IV.**8.7*f*
  propagation through, **IV.**8.3
  tapered, **IV.**8.1–**IV.**8.2, **IV.**8.2*f,* **IV.**8.3–**IV.**8.4
  in wavelength-division multiplexing, **IV.**8.1, **IV.**8.4
Coupling:
  achromaticity in, **IV.**8.3–**IV.**8.4, **IV.**8.4*f*
  detector-fiber, **IV.**4.71
  and EDFAs, **IV.**2.12
  with fiber pigtail, **IV.**4.9, **IV.**4.14, **IV.**4.50
  in-plane, in photonic crystals, **IV.**20.10–**IV.**20.11
  laser-fiber, **IV.**1.7, **IV.**2.6, **IV.**4.26, **IV.**4.45
  laser-modulator, **IV.**4.50, **IV.**4.57, **IV.**4.60–**IV.**4.61
  LED-fiber, **IV.**2.5, **IV.**4.40–**IV.**4.41, **IV.**4.41*f,* **IV.**4.42
  out-of-plane, in photonic crystals, **IV.**20.11–**IV.**20.13
  in passive optical networks, **IV.**2.13
  in stimulated Raman scattering, **IV.**3.4–**IV.**3.5, **IV.**3.7
  technology of, **IV.**8.1
Coupling coefficient, in distributed Bragg reflector lasers, **IV.**4.34

Coupling field, in electromagnetically induced transparency, **IV.**23.7
Coupling loss, **IV.**10.1–**IV.**10.2
with optical amplifier, **IV.**11.3–**IV.**11.4
Covariance mapping, **II.**28.7
Creep strength, **II.**35.9
Critical fusion frequency (CFF), **III.**13.16–**III.**13.18
Critical illumination, **III.**2.24
Critical objects, **I.**38.2
illuminated, **I.**38.5
imaged, **I.**38.4–**I.**38.5
real-space, **I.**38.3
Critical points, **II.**36.33
Cronar, **I.**20.4
Crossed converging reflector, **II.**2.39*f,* **III.**2.38
Crossed diverging reflector, **II.**2.39*f,* **III.**2.38
Cross-gain modulation (XGM), **IV.**11.10, **IV.**11.10*f,* **IV.**11.11
Cross-phase modulation (XPM), **IV.**3.2–**IV.**3.3, **IV.**3.11, **IV.**13.7, **IV.**13.7*f*
and disperson-managed soliton transmission, **IV.**7.14, **IV.**7.14*f,* **IV.**7.15
for wavelength conversion, **IV.**11.10, **IV.**11.10*f*
Cross-spectral density function, **I.**4.5–**I.**4.6, **I.**4.15, **I.**4.15*f,* **I.**4.16, **I.**4.16*f*–**I.**4.17*f*
Crosstalk, **II.**6.36
in cross-phase modulation, **IV.**3.3–**IV.**3.4
from nonlinear transmissions, **IV.**3.1
optical, **III.**9.4
with optical amplifier, **IV.**11.3
and stimulated Raman scattering, **IV.**3.7
in tapered fiber switch/attenuator, **IV.**8.5
and waveguide intersections, **IV.**20.17
in wavelength-division multiplexing, **IV.**1.34, **IV.**11.2
in WDM networks, **IV.**13.24, **IV.**13.24*f,* **IV.**13.25, **IV.**13.25*f,* **IV.**13.26, **IV.**13.26*f*
Crown-in-front lens design, **II.**1.24
Cryogenic X-ray detectors, **III.**34.8–**III.**34.9
Crystal growth:
epitaxial (*see* Epitaxial growth, crystal)
evaluating, **II.**6.16
Crystalline fiber, **IV.**14.1, **IV.**14.2*t*–**IV.**14.3*t,* **IV.**14.8–**IV.**14.10
Crystalline lens:
and aging, **III.**13.2, **III.**13.8–**III.**13.9, **III.**15.6
and cataracts, **III.**11.13–**III.**11.14, **III.**13.19, **III.**15.4, **III.**15.6
in clear lens exchange, **III.**11.17
laser damage to, **III.**15.13
and myopia, **III.**11.17
optical density of, **III.**13.5, **III.**13.8
radiation exposure limit for, **III.**11.10
Crystalline lens (*Cont.*):
as refractive element, **III.**11.2
sclerosing of, **III.**11.3
Crystalline materials:
characteristic temperatures of, **II.**33.34
engineering moduli values of, **II.**33.33
Crystalline solids, **II.**33.5
Crystallographic systems, **II.**33.6*n*
Crystallography:
capillary optics in, **III.**29.4, **III.**30.11–**III.**30.12
protein, **III.**30.11–**III.**30.12, **III.**35.7, **III.**35.14–**III.**35.15
Crystalographic point groups, **I.**9.9*t*
Crystals:
absorption edge of, **I.**9.30*f*
anisotropic, **I.**9.8, **I.**9.11, **I.**9.13, **II.**13.4, **II.**13.4*f*
bent (*see* Bent crystals)
biaxial, **I.**9.10–**I.**9.11, **II.**13.4–**II.**13.6
centrosymmetric, **II.**13.10
and channeling radiation, **II.**33.3
characterization of, **II.**33.30
and circular polarization, **III.**25.6–**III.**25.7, **III.**25.7*f,* **III.**25.8
classes and symmetries of, **II.**33.9*t*
composition of, **II.**33.30–**II.**33.31, **II.**33.40*t*–**II.**33.43*t*
cubic, room temperature elastic constants of, **II.**33.45*t*
damage limitations of, **IV.**17.16
density of, **II.**33.31, **II.**33.40*t*–**II.**33.43*t*
elastic properties of, **II.**33.31–**II.**33.32
ferroelectric (*see* Ferroelectric liquid crystals)
hardness of, **II.**33.33
hexagonal, room temperature elastic constants of, **II.**33.47*t*
ice, **I.**44.39, **I.**44.42*f*
impermeability tensor in, **II.**13.6, **II.**13.10–**II.**13.11
index ellipsoid in, **II.**13.5, **II.**13.5*f*–**II.**13.6*f*
linear electro-optic coefficients, **II.**13.8*t*
and linear polarization, **III.**25.2–**III.**25.4
liquid (*see* Liquid crystals)
lyotropic (*see* Liquid crystals, lyotropic)
mechanical properties of, **II.**33.39, **II.**33.48*t*–**II.**33.50*t*
in microfocus X-ray fluorescence systems, **III.**35.22, **III.**35.22*f*–**III.**35.23*f*
molecular weight of, **II.**33.31
monoclinic, **II.**33.21
mosaic, **II.**22.2
nematic (*see* Nematic liquid crystals)
in neutron interferometry, **II.**36.11, **III.**36.12
noncentrosymmetric, **II.**13.6–**II.**13.7, **II.**13.10

Crystals (*Cont.*):
nonlinear optical, **II.**38.11, **II.**38.22, **IV.**22.2
commonly-used, **II.**38.20–**II.**38.21
properties of, **II.**38.21*t*–**II.**38.23*t*
optical axis in, **II.**3.2*n*
optical modes of, **II.**33.79*t*–**II.**33.80*t*
with cesium chloride structure, **II.**33.72*t*
with chalcopyrite structure, **II.**33.78*t*–**II.**33.79*t*
with corundum structure, **II.**33.74*t*
with cubic perovskite structure, **II.**33.78*t*
with diamond structure, **II.**33.72*t*
with fluorite structure, **II.**33.74*t*
with a-quartz structure, **II.**33.76*t*
with rutile structure, **II.**33.76*t*
with scheelite structure, **II.**33.77*t*
with sodium chloride structure, **II.**33.73*t*
with spinel structure, **II.**33.77*t*
with tetragonal perovskite structure, **II.**33.7*t*
with trigonal selenium structure, **II.**33.75*t*
with wurzite structure, **II.**33.75*t*
with zincblende structure, **II.**33.73*t*
organic, **II.**39.23–**II.**39.24
orthorhombic, **II.**33.21
room temperature elastic constants of, **II.**33.48*t*
and parametric radiation, **II.**33.3
photonic, **IV.**20.2–**IV.**20.18
piezoelectric, **I.**9.19
polymer-dispersed (*see* Polymer-dispersed liquid crystals (PDLC))
properties of
combinations of, **II.**33.38
correlation of, **II.**33.37–**II.**33.38
tables, **II.**33.38–**II.**33.39
quadratic electro-optic coefficients, **II.**13.9*t*
quadratic electro-optic effect, **II.**13.10
refractive indices in, **I.**9.10*f*
room-temperature dispersion formulas for, **II.**33.61*t*–**II.**33.67*t*
Sellmeier formula and, **I.**9.15
strength of, **II.**33.33
structure of, **II.**33.40*t*–**II.**33.43*t*
summary optical properties of, **II.**33.56*t*–**II.**33.59*t*
symmetries in, **I.**9.11
tetragonal, room temperature elastic constants of, **II.**33.46*t*
thermal properties of, **II.**33.51*t*–**II.**33.54*t*
thermotropic (*see* Thermotropic liquid crystals)
triclinic, **II.**33.21
uniaxial, **I.**9.8
refractive indices of, **II.**3.46*t*
unit cell parameters of, **II.**33.31
Crystals (*Cont.*):
unperturbed principal refractive indices in, **II.**13.11, **II.**13.12*f*
in wavelength-dispersive X-ray fluorescence systems, **III.**35.16
for X-ray diffraction, **III.**19.8, **III.**22.1–**III.**22.6, **III.**35.6–**III.**35.7
CR-39 (*see* Poly-diallylglycol)
Cubic oxides, **II.**39.18–**II.**39.19
Curie temperature:
of ferroelectric materials, **II.**33.34
phase transition, **II.**33.34
Current (*see specific type*)
Current-confined constricted double-heterostructure large optical cavity (CC-CDH-LOC) lasers, **I.**13.21
Curvature, measurement of, **II.**29.20–**II.**29.23
confocal cavity arrangements, **II.**29.24, **II.**29.24*f*
optical methods, **II.**29.23–**II.**29.25
Cut angle, in prisms, **II.**3.13*n*
Cut-back method of attenuation measurement, **IV.**1.14–**IV.**1.16
Cutoff wavelength, **I.**15.8
Cyanine dyes, **III.**6.14, **III.**6.14*f*
Cyano-biphenyls, **II.**14.7
Cycling instability, **II.**35.12
Cyclopean eye, **III.**12.1, **III.**12.6–**III.**12.8
Cyclopegia, **III.**11.5, **III.**18.11
Cyclotron resonance, **II.**36.13, **II.**36.49–**II.**36.52, **II.**36.52*f*
experiments, **I.**5.25
Cyclovergence, **III.**12.1, **III.**12.23, **III.**12.27, **III.**12.36
Cylinders, **I.**6.16
Cylindrical waves (*see* Wavefronts, cylindrical)
Czerny-Turner monochromator, **II.**20.6

Dall-Kirkham objectives, **II.**18.9, **II.**18.9*f*
Damage thresholds:
for nonlinear materials, **IV.**22.2, **IV.**22.53–**IV.**22.54, **IV.**22.64–**IV.**22.65
in optical limiting, **IV.**19.3–**IV.**19.4, **IV.**19.6, **IV.**19.10
Dammann approach, **II.**8.12
Damped least-squares method (DLS), **I.**34.18–**I.**34.20
Dark current, **I.**15.8, **I.**22.12–**I.**22.13, **I.**22.13*n*, **II.**20.7–**II.**20.8, **III.**4.12
diffusion current in, **I.**16.7
generation-recombination current in, **I.**16.8
of germanium, **IV.**4.69
in photodetectors, **IV.**4.3–**IV.**4.75, **IV.**4.72*t*, **IV.**4.77
in photosensing elements, **I.**22.11

Dark current (*Cont.*):
in point-to-point communications links, **IV.**1.27–**IV.**1.28
sources of, **I.**22.11
tunneling current in, **I.**16.8
Dark field microscopy, **II.**17.25
Dark focus, **I.**24.31, **I.**24.32*f,* **I.**24.33
Dark states, **IV.**28.25, **IV.**28.35–**IV.**28.38
Database, lens (*see* Lenses, database)
Datacom devices, **IV.**4.1
Datacom systems, **IV.**6.1–**IV.**6.2
bit error rate in, **IV.**6.1
timing delays in, **IV.**12.16
Data rate:
for ATM, **IV.**16.6
for FDDI, **IV.**16.3
with optical amplifier, **IV.**5.1
for SONET, **IV.**16.6
DaVinci stereopsis, **III.**12.4
Daylight, CIE basis vectors for, **I.**26.26*t,* **I.**26.27*f*
DC loss, **IV.**6.7
de Broglie wave:
in dark state, **IV.**28.37
de Broglie wave atom optics, **IV.**28.32–**IV.**28.33
de Broglie wavelength:
and Bose-Einstein condensation, **IV.**28.34
of electrons, **I.**9.4, **I.**13.11
and optical lattices, **IV.**28.32–**IV.**28.33
in optical trapping, **IV.**28.22
de Broglie waves, **III.**36.3
Debye temperature, **II.**33.35
Decaytime, radiative, **I.**8.9
Decemet's membrane, **III.**13.5
Decision tasks, **I.**29.2
Decommutator, **IV.**12.1, **IV.**12.8, **IV.**12.8*f*
Default topology, for Fibre Channel, **IV.**16.4
Defect absorption, **II.**36.37–**II.**36.39
Defocus, **I.**1.90, **I.**1.90*f,* **I.**1.98, **III.**9.7, **III.**10.4, **III.**12.24
correction of, **III.**10.2, **III.**10.9, **III.**10.11
and head-mounted display image quality, **III.**18.6, **III.**18.9, **III.**18.11*t*–**III.**18.12*t*
thermal (*see* Thermal defocus)
Defocusing:
and Doppler broadening, **IV.**23.13
electromagnetically induced, **IV.**23.19
Deformable mirror, **III.**10.1
actuator requirements for, **III.**1.15*f*–**III.**1.16*f*
in adaptive optics, **III.**1.7*f,* **III.**1.8, **III.**1.11, **III.**8.3, **III.**10.8
and higher-order wavefront sensing, **III.**1.25–**III.**1.27, **III.**1.38
in retinal camera, **III.**10.6*f,* **III.**10.7
Degenerate four-wave mixing (DFWM), **IV.**17.30–**IV.**17.31, **IV.**18.50, **IV.**25.18
DeLange's temporal contrast sensitivity functions measurements, **I.**25.29
Delta-beta reversal modulator, **IV.**4.57
Delta gun CRTs, **I.**27.5
Delta modulation, **I.**28.16
Demodulation:
coherent, **II.**10.36, **IV.**1.38–**IV.**1.39
incoherent, **IV.**1.38, **IV.**1.38*f*
of lasers, **IV.**27.22
in spectroscopy, **IV.**27.13
Demultiplexers, **IV.**10.4, **IV.**10.4*f,* **IV.**10.5, **IV.**10.10, **IV.**10.10*f*–**IV.**10.11*f*
IO, **II.**6.36
nonlinear loop mirror as, **IV.**21.6, **IV.**21.6*f*
prism as, **IV.**10.5, **IV.**10.6*f*
time, **IV.**12.8*f*
Demultiplexing, **IV.**1.31, **IV.**2.11, **IV.**12.1, **IV.**12.4, **IV.**12.8
all-optical switch for, **IV.**12.36–**IV.**12.38
synchronization of, **IV.**12.9
Dense wavelength-division multiplexing (DWDM), **IV.**2.16, **IV.**5.1, **IV.**8.6
Densitometer, **I.**20.7
Density:
analytical, **I.**20.15
equivalent neutral (END), **I.**20.15–**I.**20.16
integral, **I.**20.15
matrix, **I.**5.28
spectral dye curves, in film, **I.**20.16*f*
of states, **I.**9.28–**I.**9.29, **I.**9.29*f*
Density matrix, **IV.**17.21–**IV.**17.22, **IV.**18.6, **IV.**24.4–**IV.**24.5
for coherent population trapping, **IV.**23.5
in photon echo formation, **IV.**24.12*f,* **IV.**24.13–**IV.**24.14
for spontaneous emission, **IV.**28.1
in stimulated photon echo, **IV.**24.15–**IV.**24.16
for three-level atomic systems, **IV.**23.8–**IV.**23.9
Dephasing processes, **IV.**24.14, **IV.**25.16
continuum, **IV.**25.20–**IV.**25.21
of excitons, **IV.**25.20
Depletion, in photodiodes, **I.**16.6
Depletion layer, **III.**34.5
Depletion layer generation current, **I.**22.11–**I.**22.12, **I.**22.12*n*
Depolarization, **II.**22.6, **II.**22.23, **II.**22.25, **II.**22.30–**II.**22.31
Depth magnitude, **III.**12.12
Depth of field, diffraction-limited, **II.**17.12
Depth of focus, **III.**12.12–**III.**12.13, **III.**13.8
ocular, **I.**24.26–**I.**24.27, **I.**24.28*f*

Depth perception, **III.**12.2–**III.**12.3, **III.**12.8, **III.**12.11, **III.**12.11*f,* **III.**12.14–**III.**12.15, **III.**12.20
and aging, **III.**13.18
stereoscopic, **III.**12.2
DeSoto Black, **II.**37.36
Detected beam, **II.**19.35*n*
Detection acuity, **III.**10.1
Detection tasks, **I.**29.2
Detective quantum efficiency (DQE), **I.**15.8, **I.**20.24–**I.**20.25
Detective time constant, **I.**15.8
Detectivity, spectral, **I.**15.10
Detector arrays, **II.**5.13, **IV.**2.11
Detector nonlinearity, **II.**24.37–**II.**24.38
Detectors, **I.**28.22–**I.**28.23, **I.**28.24*t*
absolute (*see* Absolute detectors)
array, **II.**36.65
in coherent optical communications, **IV.**1.34–**IV.**1.36
fast photo, **IV.**27.14
metal-semiconductor-metal (MSM), **II.**10.27
motion, **III.**2.33
neutron, **III.**36.15–**III.**36.16
in optical fiber system, **IV.**2.1, **IV.**2.7, **IV.**4.1–**IV.**4.2, **IV.**4.66
photoelectric, **II.**3.60
photovoltaic, **II.**36.64
in point-to-point communications links, **IV.**1.24, **IV.**1.27–**IV.**1.28, **IV.**1.28*f,* **IV.**1.29, **IV.**1.29*f*
pyroelectric, **I.**19.2, **I.**19.6–**I.**19.7, **I.**19.7*f*
semiconductor, **III.**34.5–**III.**34.6
solid-state, **II.**36.64
superconducting tunneling junction, **III.**34.9
thermal, **I.**15.4, **I.**15.14, **I.**19.2, **I.**19.4*f,* **I.**19.7
general properties of, **I.**19.8*t*
ideal, **I.**19.3, **I.**19.3*f*
thermistor (*see* Thermistors)
in wave-division multiplexing, **IV.**1.32
X-ray (*see* X-ray detectors)
(*See also specific type*)
Detuning:
and damping coefficient in traveling wave, **IV.**28.8, **IV.**28.9*f*
of laser, **IV.**28.2
in magneto-optical trapping, **IV.**28.23–**IV.**28.24
negative, **IV.**28.17–**IV.**28.18*f*
in optical molasses, **IV.**28.19*f*
Detuning parameter, in distributed Bragg reflector lasers, **IV.**4.34
Deuterium arc lamps, **I.**10.11, **I.**10.45, **I.**10.49*f*
Deuterium lamp standards, **I.**10.10
Developer, film, local exhaustion of, **I.**20.13
Development inhibitor-releasing (DIR) chemicals, **III.**6.3
Device independent color, **III.**17.5
DeVries-Rose law, **I.**25.27
Diabetes:
adaptive optics applications for, **III.**10.13
and cataracts, **III.**11.13, **III.**13.19
types of, **III.**13.20
Diabetic retinopathy, **III.**13.1, **III.**13.3, **III.**13.20–**III.**13.21
Dialyte lenses, **II.**1.25, **II.**1.25*t,* **II.**1.26, **II.**1.31*f*
Diamagnification, **I.**1.26
Diamond tools, **I.**41.7–**I.**41.8
Diamond turning, **I.**40.7, **I.**41.9*f*
advantages of, **I.**41.1–**I.**41.3
basic steps in, **I.**41.7–**I.**41.8
cutting speeds for, **I.**41.8
limits of, **I.**41.12
machines for, **I.**41.5, **I.**41.6*f*
materials, **I.**41.3–**I.**41.4, **I.**41.4*t*
and optical requirements, conflicts between, **I.**41.2
of plastics, **I.**41.5
process, **I.**41.2
surface finish, **I.**41.8–**I.**41.10, **I.**41.12*f*
tool wear, **I.**41.3
and traditional optical fabrication, compared, **I.**41.5
Diapoints, **I.**1.26
Diattenuation, **II.**22.6, **II.**22.23, **II.**22.25, **II.**22.28–**II.**22.29
Diattenuator, **II.**22.6
Dichroic, **II.**3.26*n*
Dichroic materials, **I.**5.13
Dichroism, **II.**20.17, **II.**20.19–**II.**20.20, **II.**22.6
Dichromated gelatin, **II.**23.14
Dicke narrowing, **IV.**18.9, **IV.**18.10*f*
Die fab, wafer processing and, **I.**12.26
Dielectric compound parabolic concentrator (DCPC), **III.**2.16, **III.**2.17*f*
Dielectric constant, **I.**9.22*f,* **I.**9.23, **II.**33.15–**II.**33.16
infrared, **II.**33.14
and lattice vibrations, **II.**33.17
and multiple scattering, **III.**3.8
relative permittivity of, **II.**33.10
static, **II.**33.14
Dielectric function:
for beryllium, vs. photon energy, **II.**35.28*f*
models of, **II.**36.14
optical constants and, **II.**36.9
Dielectric materials:
in 3D bandgaps, **IV.**20.4–**IV.**20.5
wave propagation in, **IV.**20.2

Dielectric optical waveguides, **IV.**1.6, **IV.**1.8, **IV.**2.2
Dielectric q_1/q_2 concentrator, **III.**2.20, **III.**2.20*f*
Dielectric tensor, **II.**33.20
  inverse, **II.**33.22
Dielectric total internal reflecting concentrator (DTIRC), **III.**2.17
Dielectric waveguide, mode of, **III.**9.2
Difference-frequency generation (DFG), **IV.**11.10, **IV.**22.3
Differential interference contrast (DIC) microscopy, **II.**17.26, **II.**17.32–**II.**17.34, **II.**17.35*f*
Differential phase-shift keying (DPSK), **II.**10.36, **IV.**1.38
Differential quantum efficiency, in lasers, **IV.**4.11
Differential transmission (DT) spectroscopy, **IV.**25.19–**IV.**25.22
Diffraction, **I.**6.4
  angular spectrum formulation of, **I.**3.21
  Bragg, in optical lattice, **IV.**28.32
  closed surface, **I.**3.20*f*
  complementary screens, **I.**3.11*f*
  dynamical, **III.**22.2–**III.**22.4
  effect on photographic acutance, **III.**6.2
  focused beam, **III.**35.12–**III.**35.13, **III.**35.13*f,* **III.**35.14, **III.**35.14*f*
  Fraunhofer, **I.**3.22, **I.**3.24*f,* **I.**3.26*f*
  Fresnel, **I.**3.22
  and human vision, **III.**10.2, **III.**10.4–**III.**10.5, **III.**10.9
  and intensity gain, **III.**35.8–**III.**35.11
  kinematical, **III.**22.2–**III.**22.4, **III.**35.6, **III.**35.6*f,* **III.**35.7
  of laser-emitted light, **IV.**4.4*f,* **IV.**4.13–**IV.**4.14
  mathematical theory of, **I.**3.19
  of neutron beams, **III.**36.3, **III.**36.9–**III.**36.10, **III.**37.3–**III.**37.4
  off-axis amplitude, **I.**3.8*f*
  on-axis irradiance, **I.**3.9, **I.**3.9*f*–**I.**3.10*f*
  parallel beams in, **III.**35.11–**III.**35.12
  and resolution, in optics, **III.**35.4
  straightedge, irradiance in, **I.**3.16*f*
  unobstructed zones, **I.**3.7
  of X rays, **III.**19.5, **III.**19.7–**III.**19.8, **III.**19.8*f,* **III.**19.9, **III.**19.9*f,* **III.**22.1–**III.**22.6, **III.**35.6
  and zone plates, **III.**23.3–**III.**23.4
  (*See also specific type*)
Diffraction analysis, **III.**30.4, **III.**35.6–**III.**35.8
Diffraction gratings, **I.**3.27, **II.**20.6*f*–**II.**20.7*f,* **II.**30.18, **II.**36.63
  in monochromators, **II.**20.6
  rotating, **II.**29.28
  (*See also* Polarizers, grating)
Diffraction-limited imaging, **III.**1.4
Diffraction-limited lenses, **I.**35.3, **II.**1.39, **II.**1.39*f,* **II.**1.40, **II.**1.40*f,* **II.**1.41
Diffraction-limited optic, **I.**39.5, **I.**39.6*f*
Diffraction patterns, **I.**3.26*f,* **I.**3.28*f*
  from circular apertures, **I.**3.10*f,* **I.**3.25*f*
  from rectangular apertures, **I.**3.24*f*
Diffraction spectrometry, **III.**35.16
Diffraction vector, **I.**3.27, **I.**3.29*f*
Diffractive elements, **I.**1.29
Diffractive optics, **II.**23.14
Diffuse attenuation, **I.**43.44, **I.**43.46*t*
  chlorophyll concentrations and, **I.**43.48*f*
  coefficient, spectral, **I.**43.13
  depth of euphotic zone, **I.**43.49*t*
  in pure sea water, **I.**43.45*t,* **I.**43.47*t*
Diffuse Infrared Background Explorer, **II.**37.33*f*–**II.**37.35*f*
Diffusers, **I.**28.10, **I.**28.10*f,* **II.**8.12, **II.**8.13*f*
  perfect, **III.**14.9–**III.**14.10
  in precision photometry, **III.**2.25
Diffuse scattering, **III.**36.4
Diffusion:
  floating, **I.**22.15, **I.**22.16*f*
  phenomena, **I.**20.13
  wafer processing and, **I.**12.25
Diffusion current, **I.**22.11–**I.**22.12, **I.**22.12*n*
  in dark current, **I.**16.7
  in photodetectors, **I.**17.9, **I.**17.9*f*
Digital communications systems:
  bit rate/distance limitations in, **IV.**2.10–**IV.**2.11
  communication rate in, **IV.**2.7
  signal-dependent noise in, **IV.**2.9
  as standard, **IV.**12.4
Digital electronic imaging, **III.**6.29
Digital image:
  processing, in microscopy, **II.**17.45, **II.**17.46*f*
  representations, **I.**26.29
Digital Libraries, **III.**17.7–**III.**17.8, **III.**17.11
Digital light deflectors, **II.**13.26
Digital signal, quantization of, **IV.**12.10
Digital Video Broadcasters (DVB) Measurements Group, **IV.**6.4
Dilution, **III.**2.6
  avoiding, **III.**2.13
  in faceted optics, **III.**2.40
Dimensional instability, **II.**35.11–**II.**35.12
Diode laser array collimators, **III.**2.33
Diode laser arrays, for wavelength-division multiplexing, **IV.**1.34
Diode-pumped solid state laser, **IV.**27.19–**IV.**27.20, **IV.**27.22
Diopter, **III.**11.2, **III.**18.1
Dioptric systems, **I.**1.10

Dipole active modes, infrared, **I.**9.16–**I.**9.17, **I.**9.17*f*
Dipole approximation, discrete, **I.**6.17–**I.**6.18
Dipole (bending) magnets:
brightness of, **III.**32.9–**III.**32.10
and circular polarization, **III.**32.6–**III.**32.7, **III.**32.7*f,* **III.**32.8, **III.**32.8*f*
power of, **III.**32.8–**III.**32.9, **III.**32.9*f*
as synchrotron radiation source, **III.**32.1, **III.**32.3–**III.**32.6, **III.**32.6*f*
Dipole force, **IV.**28.6
Dipole optical trap, **IV.**28.21–**IV.**28.22
Dipole transitions:
circularly polarized, **II.**20.19*f*
electric, **II.**20.15
symmetry in, **II.**20.16
Dirac delta function, **I.**4.13
Directional coupler, **II.**6.26, **IV.**4.57, **IV.**10.2–**IV.**10.3, **IV.**10.3*f,* **IV.**10.9, **IV.**10.9*f*
passive, and Y-branch IO splitter, **II.**6.20, **II.**6.21*f*
Directionality, **IV.**10.2
Direct modulation, **IV.**12.30, **IV.**12.31*f*
Direct ophthalmoscopy, **III.**11.4
Direct readout (DRO) FET arrays, **I.**23.16
Direct transitions, **II.**36.24
Dirichlet boundary condition, **I.**7.2
Disability glare, **III.**13.11, **III.**13.19
Discharged area development (DAD), **III.**5.5
Discomfort glare, **III.**13.11
Disconjugate eye movements, **III.**12.2, **III.**12.7, **III.**12.21
Discrete cosine transform (DCT), **III.**17.4
Discrete dipole approximation, **I.**6.17–**I.**6.18
Discrete signals, incoherent processing of, **I.**30.19–**I.**30.20
Discrimination tasks, **I.**25.16, **I.**29.2
Disks:
access time of, **I.**31.6
angular velocity of, **I.**31.6
magneto-optical, **I.**31.2–**I.**31.4, **I.**31.5*f,* **II.**36.47*f*
organization of data on, **I.**31.7
rotation speed of, **I.**31.6
seek time of, **I.**31.6
Dispersion, **II.**33.25, **IV.**2.3–**IV.**2.5
anomalous (negative), **IV.**25.12–**IV.**25.14
in coherent detection system, **IV.**1.39
evaluation of, **IV.**1.13
and fiber amplifiers, **IV.**5.1
group velocity, **IV.**24.26, **IV.**25.9, **IV.**25.13–**IV.**25.14
and Kramers-Kronig relations, **IV.**17.11
measurement of, **IV.**1.16–**IV.**1.18
and mode partition noise, **IV.**2.9–**IV.**2.10
in optical link power budget, **IV.**6.9–**IV.**6.11
Dispersion (*Cont.*):
polarization, **IV.**1.14
and soliton transmission, **IV.**7.1–**IV.**7.2, **IV.**7.4, **IV.**7.4*f,* **IV.**7.12–**IV.**7.14, **IV.**7.17
and system performance, **IV.**1.25
types of, **IV.**1.9–**IV.**1.12
Dispersion-compensating fiber (DCF), **IV.**6.10, **IV.**13.9, **IV.**13.9*f*
Dispersion compensation, **IV.**2.12, **IV.**13.8–**IV.**13.9, **IV.**13.9*f,* **IV.**13.10–**IV.**13.11, **IV.**13.11*f*
tunable, **IV.**13.11– **IV.**13.12, **IV.**13.12*f*
Dispersion-flattened fiber, **IV.**6.10, **IV.**7.12
Dispersion length, **IV.**7.2
Dispersion-managed (DM) soliton transmission, **IV.**7.12–**IV.**7.13, **IV.**7.13*f,* **IV.**7.14–**IV.**7.15
wavelength-division multiplexed, **IV.**7.15–**IV.**7.17
Dispersion-optimized fiber, **IV.**6.10
Dispersion principle, **II.**33.27
Dispersion relations, **I.**9.13–**I.**9.15, **I.**9.17–**I.**9.18, **I.**9.22*f*
Lorentz model for, **I.**9.14
Dispersion shifting, **IV.**1.18, **IV.**1.19*f,* **IV.**2.1, **IV.**2.4, **IV.**2.10, **IV.**6.10, **IV.**13.3, **IV.**13.6, **IV.**13.8, **IV.**13.10, **IV.**13.10*f*
Dispersion-tapered fiber, **IV.**7.11–**IV.**7.12
Dispersity, in color photographic materials, **III.**6.9–**III.**6.10
Displacement-controlled process, **I.**41.5
Dissipative force, **IV.**28.6
Distance, measurement of, **II.**29.5
Distance meter, wave modulation, **II.**29.8*f*
Distortion, **I.**1.99, **II.**18.41
Distributed Bragg reflector (DBR) lasers, **I.**13.41, **I.**13.43, **II.**6.26, **II.**6.28, **IV.**4.1, **IV.**4.8, **IV.**4.15, **IV.**4.34–**IV.**4.35, **IV.**4.35*f,* **IV.**4.36, **IV.**12.27
Distributed feedback (DFB), **IV.**4.36
Distributed feedback (DFB) lasers, **I.**11.30, **I.**13.39, **I.**13.41, **I.**13.43, **I.**14.19–**I.**14.20, **II.**6.26, **IV.**4.1, **IV.**4.8, **IV.**4.15, **IV.**4.25*f,* **IV.**4.36, **IV.**4.36*f,* **IV.**4.37–**IV.**4.39, **IV.**12.27–**IV.**12.28, **IV.**12.28*f,* **IV.**20.2, **IV.**20.6
with electroabsorption modulator, **IV.**4.49*f,* **IV.**4.57
inversion grating in, **I.**14.20*f*
to limit coherent crosstalk in WDM network, **IV.**13.26
Distributed-index lenses, **II.**7.3
Distribution temperature, **II.**24.48
Divergence:
in collimating optics, **III.**35.7
global, and lithographic feature, **III.**35.5, **III.**35.5*f*
ocular, **III.**12.2, **III.**12.22
Diverging reflector, **II.**2.39*f,* **III.**2.38, **III.**2.40

D-log H curve, **I.**1.47, **I.**20.9, **I.**20.9*f,* **I.**20.10–**I.**20.11, **I.**20.13, **I.**20.18, **I.**20.20
Doerner's expression, **I.**20.24
Doming, **I.**27.6
Donor-acceptor pair (DAP) transition, **II.**36.72–**II.**36.73, **II.**36.76
Dopant:
  chemistry of, **IV.**1.46–**IV.**1.47
  for optical fibers, **IV.**1.44, **IV.**6.18
  in pin photodiodes, **IV.**4.68
  rare-earth, **IV.**5.1
  for saturable absorbers, **IV.**25.11
Doppler broadening, **I.**11.6, **I.**11.7*f,* **I.**11.10
  inhomogeneous, **IV.**23.13, **IV.**23.15–**IV.**23.17, **IV.**23.21, **IV.**23.24
Doppler limit, **IV.**28.3
  cooling below, **IV.**28.15–**IV.**28.19
  in optical molasses, **IV.**28.13, **IV.**28.15
Doppler shift, **I.**2.14, **IV.**24.22, **IV.**24.27, **IV.**27.16, **IV.**28.2
  in atomic beam slowing, **IV.**28.10–**IV.**28.11
  and cooling in standing wave, **IV.**28.8
  in magneto-optical trapping, **IV.**28.24
  in optical lattice, **IV.**28.33
Doppler temperature, **IV.**28.3, **IV.**28.9, **IV.**28.13, **IV.**28.18
Double-channel planar-buried heterostructure (DC-PBH) lasers, **I.**13.26, **I.**13.26*f,* **I.**13.27, **I.**13.37*f*
Double-Gauss lenses, **II.**1.28
  unsymmetrical, **II.**1.29*f,* **II.**1.33*f*–**II.**1.35*f*
Double heterostructure (DH) lasers, **I.**13.5, **I.**13.7, **I.**13.15, **IV.**4.1
  design issues for, **IV.**4.3–**IV.**4.9
  temperature sensitivity in, **IV.**4.13
  threshold carrier density in, **I.**13.13*f,* **I.**13.14, **I.**13.14*f*
Double phase conjugate mirror, **II.**39.7, **II.**39.8*f,* **II.**39.9, **II.**39.28
Double refraction, **III.**25.5, **III.**25.5*f,* **III.**25.6
  in parametric generation, **IV.**22.9–**IV.**22.10, **IV.**22.10*t,* **IV.**22.63–**IV.**22.64
Doubly resonant oscillator (DRO), **II.**38.19, **IV.**22.14–**IV.**22.15
  conversion efficiency in, **IV.**22.17–**IV.**22.21, **IV.**22.21*t,* **IV.**22.38
  devices using, **IV.**22.29–**IV.**22.32
  dual-cavity, **IV.**22.28, **IV.**22.30–**IV.**22.31, **IV.**22.31*f*
  frequency diagram for, **IV.**22.22*f,* **IV.**22.23
  parameters for, **IV.**22.29*t*
  steady-state threshold in, **IV.**22.16–**IV.**22.17, **IV.**22.21*t*
  tuning of, **IV.**22.24, **IV.**22.24*f,* **IV.**22.25, **IV.**22.25*f,* **IV.**22.26, **IV.**22.26*f,* **IV.**22.27, **IV.**22.27*f,* **IV.**22.28, **IV.**22.28*f,* **IV.**22.30
Doubly telecentric distribution, in nonimaging optics systems, **III.**2.18, **III.**2.19*f*
Dove prism, **II.**4.9, **II.**4.9*f*
  double, **II.**4.10, **II.**4.10*f*
Downchirp, **I.**14.6–**I.**14.7
Downwelling average cosine, spectral, **I.**43.12
Dragon system (spherical-grating monochromator), **III.**21.5
Drain current, and shot noise, **IV.**1.27, **IV.**1.28*f*
Drawn preform cylindrical lenses, **II.**7.27
Drude approximation, **II.**36.35
Drude model, **I.**9.19, **I.**9.22*f,* **I.**9.23, **II.**6.10, **II.**35.5–**II.**35.6, **II.**38.6–**II.**38.7, **IV.**17.20, **IV.**17.22
Drusen, **III.**13.20
Dry eye condition, **III.**13.6, **III.**16.4
D-star (*D**), **I.**15.3, **I.**15.11, **I.**15.13*f,* **I.**16.13
  double, **I.**15.10
  explicit values of, **I.**15.14*t*
  as a function of wavelength, **I.**15.16*f*
  in infrared detectors, **I.**23.25
  maximized, **I.**15.9
  of a photodiode, **I.**15.17
  photon-noise-limited, **I.**15.15*f*
  for silicon detectors, **I.**15.18
  spectral, **I.**15.10
Dual-cavity doubly resonant oscillator, **IV.**22.28
Ductility, **II.**35.9
Duplexer, **IV.**10.5, **IV.**10.5*f,* **IV.**10.10
  prism as, **IV.**10.5
Dupont photopolymer, **II.**23.24
Dyes, photographic:
  color image, **III.**6.10–**III.**6.14
  spectral sensitizing, **III.**6.14–**III.**6.19
Dynamic gain saturation, **I.**14.16, **IV.**25.8–**IV.**25.9, **IV.**25.9*f,* **IV.**25.11
Dynamic range:
  for amplifiers, **IV.**5.3
  for analog link, **IV.**6.7
  and optical limiters, **IV.**19.3
  of solid-state array, **III.**4.11
  of solid-state camera, **III.**4.14–**III.**4.15
Dynamic retardation (*see* Modulation, polarization)
Dynamic scattering, **III.**3.7–**III.**3.8
Dynode biasing, in photomultiplier tubes, **I.**18.9–**I.**18.10
Dyson lenses, **II.**2.21, **II.**2.21*f*

Eagle gratings, **II.**5.8, **II.**5.11*f*
Eberhard effects, **I.**20.13
  on photographic materials, **III.**6.3
Ebert-Fastie gratings, **II.**5.8, **II.**5.10
Eccentric field, **II.**2.22
Eccentric gaze, **III.**12.9–**III.**12.12
Eccentricity (*see* Conics, of rotation)

Echelette grating (*see* Polarizers, grating)
Eclipse burn, **III.**15.4, **III.**15.7
Edge-defined film-fed growth (EFG), **IV.**14.9–**IV.**14.10, **IV.**14.10*f*
Edge effect, **I.**20.13, **I.**20.14*f*
Edge-emitting lasers, **IV.**4.1
  connection of, **IV.**4.9
  geometry of, **IV.**4.3, **IV.**4.4*f*
  optical confinement for, **IV.**4.4–**IV.**4.5, **IV.**4.5*f,* **IV.**4.6–**IV.**4.7
  packaging of, **IV.**4.8, **IV.**4.8*f*
  as telecommunications source, **IV.**4.3
Edge-emitting LEDs (E-LEDs), **IV.**4.1, **IV.**4.39–**IV.**4.40, **IV.**4.42
Edge rays:
  in concentrator design, **III.**2.23, **III.**2.39–**III.**2.40
  in projection systems, **III.**2.24
Edging, of lenses, **I.**40.4–**I.**40.5
Effective group refractive index, for lasers, **IV.**4.15
Effective medium theory (EMT), **I.**6.18, **II.**27.5
e-folding distance, **I.**6.14
Egocenter, in visual perception, **III.**12.2, **III.**12.7–**III.**12.8
Ehrenfest theorem, **IV.**28.4
Eigenpolarization, **II.**13.13, **II.**13.17, **II.**22.6–**II.**22.7
Eikonal equations, **I.**1.13–**I.**1.14
Eikonals, **I.**1.15–**I.**1.16
Einstein, Albert, **IV.**26.8, **IV.**28.34
Einstein Observatory, **III.**28.1, **III.**28.6
Einstein relationship, **I.**11.4
Eisenburg and Pearson two-mirror objectives, **II.**18.27, **II.**18.27*f*
Elastic moduli:
  in polycrystalline materials, **II.**35.73*t*
  properties of, **II.**35.58
Elastic stiffness, **II.**35.58
  in crystal metals, **II.**35.73*t*
Elasto-optic coefficients, **II.**33.25
  of materials, **II.**12.16*t*–**II.**12.18*t*
Elasto-optic effect, **II.**12.2–**II.**12.3
  indirect, **II.**12.4
Electrical power measurement, accuracy of, **II.**24.31
Electric field vector, **I.**2.3
Electroabsorption, **IV.**4.57, **IV.**4.60
  in quantum wells, **IV.**4.57, **IV.**4.63
Electroabsorption (EA) modulator, **IV.**4.57–**IV.**4.63, **IV.**12.31, **IV.**12.33–**IV.**12.34, **IV.**12.34*f*
  with DFB laser, **IV.**4.57, **IV.**4.59*f*
  integration of, **IV.**4.60–**IV.**4.61
  intensity modulation by, **IV.**4.58–**IV.**4.60
Electroabsorption (EA) modulator (*Cont.*):
  performance of, **IV.**4.61–**IV.**4.63
  waveguide in, **IV.**4.57–**IV.**4.58
Electrodeless discharge lamps, **I.**10.37
Electrodeposited surfaces, **II.**37.47–**II.**37.48
Electroless nickel, etching of, **II.**37.41–**II.**37.43
Electroluminescence (EL), **II.**36.72, **IV.**4.39
Electromagnetically induced transparency (EIT), **IV.**23.2–**IV.**23.4
  applications for, **IV.**23.3
  atomic and laser parameters for, **IV.**23.12*t*
  coherence dephasing in, **IV.**23.12–**IV.**23.13
  dressed susceptibilities in, **IV.**23.10, **IV.**23.11*f*
  gain without inversion in, **IV.**23.17–**IV.**23.18
  and Kerr-type nonlinearity, **IV.**23.27–**IV.**23.28
  in lambda three-level atomic scheme, **IV.**23.8*f,* **IV.**23.16*f*
  with laser pulses, **IV.**23.14, **IV.**23.14*f,* **IV.**23.15
  lasing without inversion in, **IV.**23.3, **IV.**23.10, **IV.**23.18
  in nonlinear frequency mixing, **IV.**23.22–**IV**.23.23, **IV.**23.23*f,* **IV.**23.25*f,* **IV.**23.34–**IV.**23.25
  optical response in, **IV.**23.5
  phenomena associated with, **IV.**23.9–**IV.**23.13
  physical basis of, **IV.**23.5–**IV.**23.9
  and pulse propagation, **IV.**23.9, **IV.**23.19–**IV.**23.22, **IV.**23.22*f,* **IV.**23.28
  refractive index in, **IV.**23.18–**IV.**23.20, **IV.**23.27
  steady-state, with cw lasers, **IV.**23.15–**IV.**23.17
Electromagnetic radiation, **I.**11.4
  dynamics of, **IV.**26.10–**IV.**26.13
  as laser emission, **IV.**26.6
  and semiconductors, **II.**36.8
  spectrum of, **I.**11.3, **I.**11.3*f*
  as wave/particle phenomenon, **IV.**26.8
Electromagnetic spectrum, **II.**36.5*f*
Electromagnetic theory, **I.**5.2
Electromigration, **II.**7.14
Electron beam impact X-ray sources, **III.**31.5, **III.**31.5*f*
  anode material for, **III.**31.10
  brightness of, **III.**31.7–**III.**31.8, **III.**31.8*f,* **III.**31.9, **III.**31.9*f,* **III.**31.11
  focussed beam in, **III.**31.10–**III.**31.11
  optics for, **III.**31.11
  parallel beam in, **III.**31.10
  processes of, **III.**31.5–**III.**31.7, **III.**31*f*
  voltage for, **III.**31.10
Electron beam lithography, **III.**23.6–**III.**23.7
Electron-beam recorders, **II.**31.5, **II.**31.8*f*
Electron binding energies, emission lines, and Auger electron energies, **III.**A.3*t*–**III.**A.5*t*
Electron-bombarded (EBSSAs) (*see under* Cameras, II SSA)

Electron-hole drops, **II.**36.31*t,* **II.**36.73
Electron-hole pairs:
in cascaded linear processes, **IV.**17.22
in electroabsorption, **IV.**4.62
in photorefraction, **IV.**17.24
in *pin* photodiodes, **IV.**4.67–**IV.**4.69
in semiconductor excitation, **IV.**25.16–**IV.**25.17
Electronic imaging:
aesthetic/emotional features in, **III.**17.9–**III.**17.11
color in, **III.**17.5–**III.**17.6
complex features in, **III.**17.6–**III.**17.9
content versus pixel representation, **III.**17.9
digital watermarks used in, **III.**17.5
early models in, **III.**17.2–**III.**17.6
image tube intensified (*see* Image tube intensifier (II))
progress in, **III.**17.1, **III.**17.11–**III.**17.12
Electronic time-division multiplexing (ETDM), **IV.**13.3, **IV.**13.4*f*
Electronic transitions, **II.**33.12, **II.**33.15, **II.**33.16*f*
Electron lenses, **I.**21.8, **I.**21.8*f*–**I.**21.9*f*
Electron multipliers, **III.**34.6
Electron-phonon coupling, **II.**28.10
Electrons:
lifetime of, **I.**8.9
wavefunctions of, **I.**8.14
Electro-optic effect, **II.**13.6–**II.**13.7, **II.**13.10, **II.**33.29, **IV.**4.52–**IV.**4.54, **IV.**19.10
linear, **II.**13.7, **II.**39.2–**II.**39.3
in lithium niobate, **IV.**4.50–**IV.**4.52, **IV.**4.55
in semiconductors, **IV.**4.64
Electro-optic modulator (EOM), **IV.**12.31–**IV.**12.32, **IV.**12.32*f,* **IV.**12.33, **IV.**12.33*f,* **IV.**21.1, **IV.**27.4, **IV.**27.14, **IV.**27.17, **IV.**27.19
Electro-optic scanners (*see* Scanners, electro-optic)
Electro-optic waveguides, **II.**39.35
Electroreflectance, **II.**36.70
Electrorefraction, **IV.**4.2
in semiconductors, **IV.**4.64–**IV.**4.65
Electrorefractive photorefractive (ERPR) effect, **II.**39.21
Electrostriction, **IV.**17.20
Ellipsoid, **III.**9.1
in idealized photoreceptor, **III.**9.8, **III.**9.11, **III.**9.15
Ellipsoidal gratings, **III.**21.3, **III.**21.6*t*
Ellipsometer, **II.**27.2, **II.**27.10*f*
PCSA null, **II.**27.20
photometric, **II.**27.13
polarizer-compensator-sample-analyzer, **II.**27.21
rotating-analyzer (RAE), **II.**27.13
Ellipsometer (*Cont.*):
rotating-detector (RODE), **II.**27.14, **II.**27.14*f*
spectroscopic, **II.**36.66, **II.**36.68
(*See also* Photopolarimeter)
Ellipsometric problems, **I.**5.26
Ellipsometry, **II.**22.7, **II.**22.26, **II.**27.2, **II.**27.2*f,* **II.**27.4*f,* **II.**27.5, **II.**36.71–**II.**36.72
applications of, **II.**27.22
azimuth-measured, **II.**27.17, **II.**27.20
conventions in, **II.**27.3
generalized (GE), **II.**27.20
gradient index (GRIN) film in, **II.**27.9
interferometric, **II.**27.19
Jones-matrix generalized, **II.**27.19–**II.**27.20
microscopically inhomogeneous thin film, **II.**27.10
modeling in, **II.**27.4
Mueller-matrix generalized, **II.**27.20–**II.**27.22
multilayer film in, **II.**27.7–**II.**27.8, **II.**27.8*f,* **II.**27.9, **II.**27.9*f*
multiple-angle-of-incidence (MAIE), **II.**27.3
normal-incidence rotating-sample (NIRSE), **II.**27.19, **II.**27.19*f*
null, **II.**27.11, **II.**27.13
perpendicular-incidence (PIE), **II.**27.18
photometric, **II.**27.13
return-path (RPE), **II.**27.17, **II.**27.18*f*
three-phase model, **II.**27.6–**II.**27.7
transmission, **II.**27.10
two-phase model, **II.**27.5–**II.**27.6, **II.**27.6*f*
using four-detector photopolarimeters, **II.**27.15
variable-angle spectroscopic (VASE), **II.**27.3
Emission:
laser amplifiers and, **I.**11.9
processes, **I.**11.8*f*
radiative processes and, **I.**11.7–**I.**11.8
stimulated cross section, **I.**11.9
Emission-line broadening, **I.**11.6
Emission linewidth, **I.**11.6–**I.**11.7, **I.**11.9
Doppler, **I.**11.10
of radiating species, **I.**11.5
Emission spectra:
absorption and, of rare earth ions, **II.**28.9*f*
of CRT (cathode ray tube), **I.**27.6*f*
triplet state, **II.**28.13
Emissivities, of cavities, **I.**10.5, **I.**10.5*f*
Emittance, **II.**25.3, **II.**25.7, **II.**35.46, **III.**2.3
hemispheric, calorimetric measurement of, **II.**25.17*f*
measurement of, **II.**25.16–**II.**25.17
of metals, **II.**35.54*t*–**II.**35.56*t*
vs. temperature, of silicon carbide, **II.**35.55*t*
total, **II.**35.48
vs. wavelength, of silicon carbide, **II.**35.54*t*

Emmetropia, **III.**11.2, **III.**11.2*f,* **III.**12.2, **III.**13.5, **III.**18.11, **III.**18.13
Emmetropization, **III.**11.17–**III.**11.18
Empty field myopia, **I.**24.31, **I.**24.33
Emulsions, photographic, **III.**6.8
(*See also* Silver halide crystals)
Encoding, of signal, **IV.**12.11
Endoscopes, **II.**9.2, **II.**9.6
Energy, as radiometric unit, **III.**7.5
Energy band, **I.**9.31
magnetic field effects on, **II.**36.41, **II.**36.43
Energy band gap, **I.**9.27, **I.**9.32
Energy flow, **I.**9.7–**I.**9.8
Energy-momentum conservation, **IV.**26.10
English units, versus SI units, **III.**14.7–**III.**14.8, **III.**14.8*t*
Enhanced refraction, **IV.**23.19
Enterprise System Connection (ESCON) standard, **IV.**16.1–**IV.**16.2
Entrance pupil, **II.**1.8, **II.**18.41, **II.**24.20, **III.**12.2
Entrance window, **II.**1.8, **II.**24.20
Epicotyl, in plant structure, **III.**9.26, **III.**9.27*f*
Epi-illumination, **II.**17.38–**II.**17.39, **II.**17.39*f,* **II.**17.41
Epileptic seizure, visual stimulation of, **III.**8.4
Epitaxial growth, **I.**12.9, **IV.**4.2
crystal, III-V, **II.**6.16–**II.**6.17
(*See also specific type*)
techniques, **I.**12.23
(*See also specific type*)
Equations, for rays, **I.**1.22–**I.**1.23
Equilibrium mode distribution, **IV.**1.15, **IV.**1.15*f*
Equipartition energy, **IV.**7.6
Equivalent neutral density (END), **I.**20.15–**I.**20.16
Equivalent noise input (ENI), **I.**15.8
Equivalent particles, in coherent light scattering, **III.**3.7, **III.**3.7*f*
Erbium-doped fiber amplifiers (EDFAs), **IV.**2.12, **IV.**5.1, **IV.**11.4, **IV.**13.2
energy levels in, **IV.**5.3–**IV.**5.4, **IV.**5.4*f,* **IV.**5.5
fluoride-based, **IV.**13.19
gain flattening in, **IV.**5.6, **IV.**13.19
gain formation in, **IV.**5.5
gain transients of, **IV.**13.20, **IV.**13.20*f*
in long distance transmissions, **IV.**13.3
noise in, **IV.**5.5–**IV.**5.6
nonuniform gain of, **IV.**13.18, **IV.**13.18*f*–**IV.**13.19*f*
in OTDM system, **IV.**12.39
and phase noise, **IV.**3.11
pump wavelength for, **IV.**5.5
Q factor for, **IV.**13.20, **IV.**13.21*f*
in reconfigurable network, **IV.**13.15
ultrawideband, **IV.**13.21, **IV.**13.22*f*
in WDM networks, **IV.**13.1, **IV.**13.17–**IV.**13.21
Erbium/ytterbium doped fiber amplifier (EYDFA), **IV.**5.7
Erickson-Leslie equation, **II.**14.17
Error budget tree, **II.**11.8, **II.**11.8*f*
for optical polymers, **II.**34.11
Errors:
in BSDF, **II.**26.14
types of, **II.**24.23–**II.**24.25
Error sources, type B:
detector nonlinearity, **II.**24.37–**II.**24.38
nonideal aperture, **II.**24.39, **II.**24.39*f*
nonuniformity, **II.**24.39
offset subtraction, **II.**24.36
polarization effects, **II.**24.37
scattered radiation, **II.**24.36
size of source effect, **II.**24.36–**II.**24.37
spectral errors, **II.**24.39–**II.**24.40
temperature dependence, **II.**24.40
time-dependent error, **II.**24.38–**II.**24.39
Erythema, **III.**15.1
ESCON duplex fiber-optic connector, **IV.**16.2, **IV.**16.2*f*
ESCON extended distance feature (XDF), **IV.**16.2
Esophoria, **III.**12.28, **III.**12.32, **III.**16.5
Estar, **I.**20.4
Estimation tasks, **I.**25.16
sequential, **I.**29.10
Étalon fringes, **IV.**27.14
Etching:
for coupler fabrication, **IV.**8.1
III-V, **II.**6.17
chemically assisted reactive ion beam (CAIBE), **II.**6.18
dry, **II.**6.18
reactive ion (RIE), **II.**6.18
wet, **II.**6.17
laser-assisted chemical (*see* Laser-assisted chemical etching (LACE))
reactive ion (RIE), **II.**8.17
Étendue, **II.**3.8, **II.**24.16
calculating, **III.**2.4–**III.**2.5, **III.**2.5*f*
and concentration, **III.**2.6
conservation of, **I.**1.24–**I.**1.25, **III.**2.4, **III.**2.4*f,* **III.**2.13–**III.**2.14, **III.**2.19, **III.**2.32
definition of, **III.**2.3
loss, **III.**2.6, **III.**2.10
total lens, **I.**1.88
Ethernet, **IV.**16.7
Euler angles, **II.**13.33
Euler equations, **I.**1.23
Evanescent wave spectroscopy (EWS), **IV.**14.14
Evaporative cooling, **IV.**28.27–**IV.**28.28, **IV.**28.35, **IV.**28.36*f*

Event-driven programs, **I.**34.8
Ewald construction, in X-ray diffraction, **III.**35.6, **III.**35.6*f,* **III.**35.7
Ewald sphere, **III.**25.7, **III.**25.8*f*
Excess loss, **IV.**10.2
Excess noise, **I.**15.8
Excess noise factor, **IV.**1.29, **IV.**1.30*f,* **IV.**2.9
Excimer lasers, **I.**11.13, **I.**11.16, **I.**11.33, **I.**11.33*f*
Excitation spectrum, single-particle, **II.**36.84*f*
Excited-probe techniques, for nonlinear characteristics, **IV.**17.29, **IV.**17.29*f,* **IV.**17.30
Excited state absorption (ESA), **IV.**17.21, **IV.**19.5
Excited-state collisions, **IV.**28.28–**IV.**28.29, **IV.**28.35
Excited-state ESR transitions, **II.**20.22
Excitonic excitations, in ultrafast spectroscopy of semiconductors, **IV.**25.20
Exciton resonance, **IV.**4.57, **IV.**4.64–**IV.**4.65
Excitons, **I.**9.32, **I.**12.6–**I.**12.7, **II.**33.16, **II.**36.27, **II.**36.29, **II.**36.29*f*–**II.**36.30*f,* **II.**36.31, **II.**36.72–**II.**36.73
  bound, **II.**36.30, **II.**36.48
  types of, **II.**36.28*t*
  Wannier, **II.**36.28
Exhaustive characterization methods (ECM), of CRTs, **I.**27.21
  interpolation algorithms, **I.**27.23–**I.**27.24
  inverses, **I.**27.24
  out-of-gamut colors, **I.**27.25
  sampling densities, **I.**27.22
Exitance, **II.**24.9, **III.**2.3
Exit pupil, **II.**18.41, **II.**24.20
  for head-mounted display, **III.**18.6–**III.**18.9, **III.**18.9*f,* **III.**18.10
Exit window, **II.**1.8, **II.**24.20
Exophoria, **III.**12.28, **III.**16.5
EXOSAT, **III.**28.1, **III.**28.6
Expander, **IV.**12.11
Experimental conditions, **I.**29.2
  advice for, **I.**29.11
Exposure, photographic, **I.**20.6
Exposure limits (ELs), for optical radiation, **III.**15.9–**III.**15.12
Exposure time:
  for color photographic papers, **III.**6.5
  and granularity, **III.**6.19–**III.**6.20
  to optical radiation, **III.**15.3
Extended boundary condition method (EBCM), **I.**6.17
Extended Gordon-Haus effect, **IV.**7.11
Extended objects, **I.**1.30
Extended X-ray absorption fine structure (EXAFS), **III.**34.4, **III.**35.3, **III.**35.17
External cavity diode laser (ECDL), **IV.**27.20–**IV.**27.21, **IV.**27.21*f,* **IV.**27.22
External limiting membrane (ELM), **III.**9.8, **III.**9.10*f,* **III.**9.12
External lithium niobate modulators, **IV.**4.2
External modulation, **IV.**12.30–**IV.**12.31, **IV.**12.31*f*
External slope efficiency, in lasers, **IV.**4.11–**IV.**4.12
Extinction coefficient, for metals, **II.**35.12, **II.**35.13*t*–**II.**35.27*t*
Extinction paradox, **I.**6.9
Extinction ratio, **I.**5.12–**I.**5.15, **I.**5.19*n,* **I.**5.21, **I.**5.21*f*
  in optical link power budget, **IV.**6.14
  variation of, **I.**5.20*f*
Extinction reflectors, **III.**2.11
Extracapsular cataract extraction (ECCE), **III.**11.13
Extraretinal cues, **III.**12.2–**III.**12.3
Extreme ultraviolet (EUV) astronomy, **II.**11.25
Extreme ultraviolet (EUV) imaging, **II.**11.2, **II.**11.4
  normal-incidence, **II.**11.6
Extreme ultraviolet (EUV) light, **III.**19.6
  and multilayer reflective coatings, **III.**24.1–**III.**24.3, **III.**24.6, **III.**24.8*f*
  projection lithography using, **III.**35.4
  and Schwarzschild objective applications, **III.**27.1, **III.**27.4, **III.**35.4
Extreme Ultraviolet Explorer (EUVE), **II.**37.23
  imaging, **II.**11.5
Extremum principal, **I.**1.13
Extrinsic Fabry-Perot interferometric (EFPI) sensors, **IV.**15.2–**IV.**15.4
  configuration of, **IV.**15.2*f*
  transfer function curve for, **IV.**15.3*f*
Extrinsic semiconductor operation, **I.**15.8
Eye, human:
  aberrations of, **III.**8.3, **III.**10.2–**III.**10.8, **III.**11.5
  aging of, **III.**13.2–**III.**13.5
  centering, **I.**28.8
  coordination/alignment of, **III.**12.21–**III.**12.29, **III.**16.5–**III.**16.6
  damage thresholds for, **IV.**19.3, **IV.**19.3*f*
  depth of focus in, **III.**12.12–**III.**12.13
  lens of, **III.**13.2
    (*See also* Crystalline lens)
  line-of-sight for, **III.**18.3, **III.**18.3*f*
  movement of, **III.**12.2–**III.**12.3, **III.**12.8, **III.**12.20–**III.**12.21, **III.**12.23, **III.**12.29–**III.**12.30, **III.**17.7–**III.**17.8
  physiology of, **III.**10.3*f*
  position of rest for, **III.**16.5
  radiation damage to, **III.**15.2–**III.**15.8, **III.**15.10, **III.**15.12–**III.**15.15
    sources of, **III.**15.13*f*
  refractive errors in, **III.**11.1–**III.**11.5

Eye, human (*Cont.*):
spectral responsivity of, **II.**24.45, **III.**14.1–**III.**14.3
testing of, **III.**11.4–**III.**11.5
(*See also* Human visual system (HVS); Visual system)
Eye degradation, of receivers, **IV.**2.9–**IV.**2.10
Eye focus, **III.**18.10–**III.**18.13
Eyeglasses (*see* Lenses; Spectacles)
Eye loupe, **II.**1.9
Eye margin, with VGA versus limiting amplifier, **IV.**12.40
Eye relief (ER), **II.**2.8, **II.**2.8*f,* **II.**2.9, **II.**2.11*f*
Eye space, **II.**2.4, **II.**2.6
Eyewidth, **IV.**6.4, **IV.**6.16
EZ-scan, **IV.**17.31, **IV.**17.33

Fabry-Perot elation filters, **IV.**7.8
Fabry-Perot (FP) amplifiers, **IV.**11.4
Fabry-Perot (FP) cavity, **I.**2.35*f,* **I.**2.36, **I.**2.42, **I.**11.21*f*
Fabry-Perot (FP) interference filters (*see* Filters, Fabry-Perot (FP) interference)
Fabry-Perot interferometer, **I.**2.34, **I.**2.34*f,* **I.**2.35, **I.**11.21, **I.**42.17
Fabry-Perot laser, **IV.**2.9, **IV.**4.14
as optical system transmitter, **IV.**2.9, **IV.**4.14, **IV.**12.26, **IV.**12.26*f,* **IV.**12.27
Faceted reflectors, **III.**2.2, **III.**2.40–**III.**2.42
Facet intensity, reducing, **I.**13.19
Facet structure, of Fresnel lenses, **III.**2.10, **III.**2.11*f*
Family momentum, **IV.**28.37
Fano interference, **IV.**23.2, **IV.**23.7–**IV.**23.8, **IV.**23.8*f*
Fans, ray, **I.**1.39–**I.**1.40
Faraday cage, for xerographic toner charge measurement, **III.**5.8–**III.**5.8*f*
Faraday rotation, **II.**36.45
free-carrier, **II.**36.52
interband, **II.**36.47*f*
Faraday rotator, **IV.**10.7, **IV.**10.7*f,* **IV.**10.9
Faraday shutters, **II.**1.23
Far-off resonance trap (FORT), **IV.**28.22
Far-sightedness (*see* Hypermetropia; Hyperopia)
Far Ultraviolet Spectroscopic Explorer (FUSE) program, **II.**11.4, **II.**11.25, **II.**11.26*f*
FASCODE, **I.**44.14, **I.**44.21–**I.**44.23, **I.**44.26
FASCOD2, **I.**44.24
Fastie gratings, **II.**5.12*f*
Fast photo detector, in laser stabilization, **IV.**27.14
Fatigue, of fiber, **IV.**1.20
Fatigue strength, **II.**35.9
FDDI duplex fiber-optic connector, **IV.**16.3, **IV.**16.3*f*
FDDI-II, **IV.**16.4
Feedback:
distributed, **IV.**4.36
in laser servo system, **IV.**27.5–**IV.**27.7, **IV.**27.18
regimes of, **IV.**4.25–**IV.**4.26, **IV.**4.26*f,* **IV.**4.27–**IV.**4.28, **IV.**4.29*f*
and resonance line shape, **IV.**27.13
Feedback parameter, **IV.**4.26, **IV.**4.28
Femtosecond quantum beats, **II.**38.5
Fermat's principal, **I.**1.13
Fermi edge singularities, **IV.**25.21
Fermi pseudopotential, **III.**36.4
Fermi's Golden Rule, **I.**8.7, **I.**9.25, **I.**9.28
Fermi wave vector, **II.**36.81
Ferrimagnetism, **I.**31.26–**I.**31.27
Ferroelectric liquid crystals, **II.**14.19
deformed helix ferroelectric (DHF) effect in, **II.**14.21, **II.**14.21*f*
soft-mode (SMFLCs), **II.**14.22, **II.**14.22*f,* **II.**14.23
surface-stabilized (SSFMCs), **II.**14.19–**II.**14.20, **II.**14.20*f,* **II.**14.21–**II.**14.23
Ferroelectric materials, Curie temperatures of, **II.**33.34
Ferroelectric oxides, **II.**39.14
Feussner prisms, **II.**3.7, **II.**3.24, **II.**3.24*f,* **II.**3.25
Feynman diagrams, for photon echo formation, **IV.**24.12, **IV.**24.12*f*
Fiber Bragg grating (FBG), **IV.**1.43, **IV.**9.1–**IV.**9.2, **IV.**20.2
applications for, **IV.**9.8–**IV.**9.9
bandwidth of, **IV.**9.4–**IV.**9.5, **IV.**15.8
chirped, for dispersion compensation, **IV.**13.10–**IV.**13.11, **IV.**13.11*f,* **IV.**13.12, **IV.**13.12*f*
fabrication of, **IV.**9.5, **IV.**9.5*f,* **IV.**9.6, **IV.**9.6*f,* **IV.**9.7–**IV.**9.8
mode coupling in, **IV.**15.6, **IV.**15.6*f*
reflectivity of, **IV.**9.3–**IV.**9.4, **IV.**9.4*f*
spectral response of, **IV.**9.7–**IV.**9.8*f*
Fiber Bragg grating sensors, **IV.**15.5–**IV.**15.9
fabrication of, **IV.**15.6–**IV.**15.7, **IV.**15.7*f*
limitations of, **IV.**15.8–**IV.**15.9
operation of, **IV.**15.5–**IV.**15.6
Fiber distributed data interface (FDDI), **I.**12.36, **IV.**4.44, **IV.16.**2–**IV.**16.4
Fiber-fiber coupling, **IV.**1.7
Fiber gyro circuits, **II.**6.15
Fiber-interferometer rotation sensor, **II.**21.17
Fiber-optic amplifiers, **IV.**11.3–**IV.**11.4
Fiber-optic communications, **I.**12.13, **I.**12.16*f*
Fiber-optic component, **IV.**10.1–**IV.**10.2, **IV.**10.2*f*
Fiber-optic-coupled II SSAs (*see under* Cameras, II SSA)

Fiber-optic couplers, lens arrays used in, **III.**2.33
Fiber optic gyroscopes (FOG), **II.**6.20, **II.**6.32–**II.**6.33, **II.**6.33*f,* **II.**10.37
APE $LiNbO_3$, **II.**6.34*t*
applications of, **II.**6.34
Fiber optic links, analog, **II.**6.29, **II.**6.30*f*
Fiber optics (*see* Optical fiber)
Fiber pigtail:
for edge-emitting lasers, **IV.**4.9, **IV.**4.14
with LEDs, **IV.**4.41
and noise in lasers, **IV.**4.25
Fiber Raman amplifier, **IV.**3.5, **IV.**5.2
Fiber ring laser, **IV.**5.1
Fiber strain, assessment of, **IV.**1.18–**IV.**1.20, **IV.**1.20*f,* **IV.**1.21, **IV.**1.21*f*
Fiber-to-fiber couplers, mixing rods in, **III.**2.33
Fiber transmission line, subcomponent insertion into, **IV.**10.8, **IV.**10.8*f*
Fibre Channel Arbitrated Loop (FC-AL), **IV.**16.4
Fibre Channel (FC), **IV.**16.2, **IV.**16.4–**IV.**16.5
physical layer, **IV.**16.5*t*
Field:
depth of, **I.**1.92, **II.**1.38
full, paraxial invariant for, **I.**1.84
Field amplitude, **I.**4.2–**I.**4.3
Field angle, **I.**1.82
Field curvature, **I.**1.99, **I.**33.4, **I.**33.4*f,* **I.**33.5, **I.**33.5*f,* **II.**18.41
tangential, **II.**1.18, **II.**1.28
Field effective transistor (FET), **IV.**1.27, **IV.**1.28*f*
Field flattener, **II.**1.29
Field-induced director axis reorientation, **II.**14.11
Field-induced nematic-cholesteric phase change, **II.**14.11
Field lenses, **I.**1.89, **I.**1.89*f,* **I.**32.8, **II.**1.10
Field of view (FOV), **I.**1.80–**I.**1.81, **I.**15.9, **I.**34.4
in Cassegrain telescopes, **III.**27.1
in head-mounted displays, **III.**18.2, **III.**18.5–**III.**18.10, **III.**18.10*t*
of human vision system, **III.**12.34, **III.**13.18
plots, **II.**18.38–**II.**18.39, **II.**18.39*f*–**II.**18.40*f*
in scanning systems, **III.**27.1
Field patch trace, **III.**2.8
Field sag plots, **I.**34.14
Field stop, **I.**38.8, **I.**38.9*f,* **II.**1.8, **II.**18.5, **II.**18.41, **II.**24.20
Figure of merit (FOM):
for limiting systems, **IV.**19.2–**IV.**19.3, **IV.**19.6–**IV.**19.7
in parametric generation, **IV.**22.62
Fill factor, **I.**22.2*n*
Film:
black-and-white, **III.**6.25–**III.**6.26, **III.**6.26*t*
choice of, **II.**15.5
Film (*Cont.*):
color negative, **III.**6.10, **III.**6.18, **III.**6.23, **III.**6.26–**III.**6.29, **III.**6.29*t,* **6.**28*t*
gradient index (GRIN), **II.**27.9
infrared, **III.**6.22
Kodachrome, **III.**6.24, **III.**6.24*t*
legacy, **III.**6.24, **III.**6.24*t,* **6.**25, **6.**25*t,* **6.**26
microscopically inhomogeneous thin, **II.**27.10
motion picture, **III.**6.5, **III.**6.11, **III.**12.6
multilayer, **II.**27.7–**II.**27.8
photographic (*see* Photographic film)
size of, **II.**15.6
slide, **III.**6.10, **III.**6.23
transparency, **III.**6.10, **III.**6.23
tungsten, **III.**6.24*t*
(*See also* Photographic film, color)
Filter bank, **II.**29.29
Filters:
achromatic all-dielectric, **I.**42.69*f*
acousto-optic tunable, **IV.**13.23
bandpass (*see* Bandpass filters)
broadband, **I.**42.88*f*
metal dielectric, **I.**42.59*f*
circular variable square-top, **I.**42.89*f*
cut-off, **I.**42.54–**I.**42.55, **I.**42.55*f,* **I.**42.57*f*
absorption in, **I.**42.60, **I.**42.60*f*
angle-of-incidence effects in, **I.**42.56
experimental results in, **I.**42.56
metal-dielectric reflection, **I.**42.59, **I.**42.59*f*
reflectance maxima, suppressed, **I.**42.55*f*
rejection region, transmission in, **I.**42.56
slope of, **I.**42.56
transmission region, width of, **I.**42.54–**I.**42.55, **I.**42.55*f,* **I.**42.58*f*
dichroic polarizing, **II.**17.27
dielectric layered, **IV.**10.6
Fabry-Perot elation, **IV.**7.8
Fabry-Perot (FP) interference, **I.**42.77
with all-dielectric reflectors, **I.**42.79–**I.**42.80
frustrated-internal-reflection, **I.**42.80
with metal-dielectric reflectors, **I.**42.80
with metallic reflecting coatings, **I.**42.78–**I.**42.79, **I.**42.79*f*
for the soft X-ray region, **I.**42.94
with solid spacers, **I.**42.86
heat-control, **I.**42.54
holographic edge, **I.**42.52
infrared-suppressing, **I.**42.58
interference, **I.**42.101, **IV.**20.2
black absorbers, **I.**42.100, **I.**42.100*f*
cut-off, **I.**42.101*f*
with multiple peaks, **I.**42.88
narrow-bandpass, **I.**42.101*f*

Filters, interference (*Cont.*):
neutral attenuators, **I.**42.100, **I.**42.101*f*
thin metal film in, **I.**42.98, **I.**42.100*f*
inverse, **I.**30.19
coherent optical realization of, **I.**30.18
for image enhancement, **I.**30.17
Mach-Zehnder, **IV.**8.6, **IV.**8.6*f*
matched, **I.**30.15
deficiencies of, **I.**30.16
minus, **I.**42.49–**I.**42.50, **I.**42.50*f*–**I.**42.51*f*
narrowband reflection, **I.**42.45–**I.**42.46, **I.**42.46*f*
narrowband rejection, **I.**42.52
narrow-line spectral, **IV.**19.1
neutral density, **I.**28.13, **I.**28.15*t,* **I.**42.67, **I.**42.67*f,* **I.**42.68, **I.**42.68*f*
novelty, **II.**39.29–**II.**39.30, **II.**39.33*f*
optical (*see* Optical filters)
PBG waveguides in, **IV.**20.18
phase-dispersion, **I.**42.87
rejection, **I.**42.49, **I.**42.49*f,* **I.**42.50, **I.**42.50*f*–**I.**42.51*f*
rugate, **I.**42.50–**I.**42.51, **I.**42.51*f,* **I.**42.52, **I.**42.52*f*
solar-cell cover, **I.**42.54
tapered fiber, **IV.**8.1
temperature effects of, **I.**42.59
tunable, **I.**42.87, **I.**42.87*f*
types of, **I.**28.13
Vander Lugt, **I.**30.15, **I.**30.15*f,* **I.**30.16
wavelength selection, **I.**28.12
wedge, **I.**42.89
Wiener, **I.**30.17–**I.**30.18, **I.**31.19
coherent optical realization of, **I.**30.18
Final image, **II.**15.6
display of, **II.**15.6–**II.**15.7
flow chart, **II.**15.4*f*
properties of, **II.**15.4–**II.**15.5
resolution of, **II.**15.5, **II.**15.5*f,* **II.**15.6
in transfer functions, **II.**32.2
Finish specifications, **I.**7.11
Finite conjugate lenses, **II.**2.12
Finite-difference time-domain (FDTD) method, **I.**6.18, **IV.**20.3–**IV.**20.4, **IV.**20.15
Finite linewidth (phase noise), of lasers, **IV.**2.6
Finite-well potential, **II.**28.13
First differences, in laser frequencies, **IV.**27.2
First-order layout, **I.**32.4
First-order optics, **I.**1.32, **I.**1.42
Fish-eye lenses, **II.**1.37*f*
Fixation, **III.**12.2, **III.**12.21, **III.**12.24
Fixation, ocular, **I.**24.34
Fixed-pattern noise (FPN):
for solid-state array, **III.**4.12
for solid-state camera, **III.**4.13
Fizeau interferometers (*see* Interferometers, Fizeau)
Flame brushing, **IV.**9.2
Flame hydrolysis (FHD), **II.**6.13
Flash, **II.**34.12
Flash-lamp-pumped lasers, **I.**11.18, **I.**11.19*f*
Flicker, sensitivity to, **III.**13.16–**III.**13.18
Flicker floor, **IV.**27.3, **IV.**27.20
Flicker noise, **I.**15.9
Flint-in-front designs, of lenses, **II.**1.24
Floating payload, in SONET, **IV.**12.22–**IV.**12.24, **IV.**16.5
Floquil™ Black for lens edges, **II.**37.36–**II.**37.37
Fluence, **III.**9.1
Fluids, light propagation through, **III.**3.12
Fluorescence, **IV.**28.2
from atomic beam slowing, **IV.**28.9–**IV.**29.11
by chlorophyll, **I.**43.52
laser-induced, **I.**44.21
parametric, **II.**38.17, **IV.**22.8
spontaneous, **IV.**28.5
from 3D optical molasses, **IV.**28.15, **IV.**28.33, **IV.**28.33*f*
Fluorescence, X-ray (XRF), **III.**35.15–**III.**35.16
energy-dispersive, **III.**35.17–**III.**35.23
wavelength-dispersive, **III.**35.16–**III.**35.17, **III.**35.17*f*
Fluorescence line narrowing (FLN), **I.**8.21, **II.**20.29, **II.**20.29*f,* **II.**28.14–**II.**28.15, **II.**28.15*f,* **II.**28.16
Fluoride fibers, **II.**10.46, **IV.**1.48
Flux:
distribution of, **III.**2.18, **III.**2.19*f*
in integrating cavities, **III.**2.26–**III.**2.28
Lambertian source of, **III.**2.4
in lightpipe, **III.**2.28–**III.**2.31
luminous (*see* Lumens)
radiant (*see* Watts)
in radiation transfer, **III.**2.1, **III.**2.13
uniformity criteria for, **III.**2.2
for X-ray optics, **III.**35.3
Flux density:
maximizing, **III.**2.1–**III.**2.2
radiometric, **I.**21.4–**I.**21.5, **III.**7.5
Flux models, for multiple scattering, **III.**3.12–**III.**3.13
Fly-by-light (FBL), **I.**13.4
Flycutting, **I.**41.7
Flying-spot scanning, **II.**19.5
FM spectroscopy, **IV.**27.14
F-number, **II.**1.9, **II.**24.21
problems with, **I.**1.86
Focal length, **II.**1.7
Focal length measurements, **II.**29.20, **II.**29.25

Focal lenses (*see* Lenses, focal)
Focal plane arrays (FPA), **I.**23.7*f*
  BLIP in, **I.**23.26
  buffered direct injection, **I.**23.23
  capacitive transimpedance amplifier (CTIA), **I.**23.24–**I.**23.25
  charge sweep device (CDS), **I.**23.14
  chopper-stabilized direct injection, **I.**23.23
  clock generation and, **I.**23.17
  current performance of, **I.**23.30–**I.**23.31, **I.**23.32*t*
  detector interface, **I.**23.19
  direct-charge-injection silicon, **I.**23.14, **I.**23.21–**I.**23.22, **I.**23.22*f*
  direct detector integration, **I.**23.19
  direct readout architectures in, **I.**23.17
  D-star (*D**) in, **I.**23.25
  electronically scanned staring, **I.**23.18
  future trends, **I.**23.33, **I.**23.33*f*
  gate modulation, **I.**23.23–**I.**23.24
  hybrid, **I.**23.15–**I.**23.16, **I.**23.21*f*
  input circuit, **I.**23.19
  LWIR, **I.**23.33
  microbolometer, **I.**23.14–**I.**23.15
  minimum resolvable temperature (MRT), **I.**23.29, **I.**23.29*f*
  MIS photogate, **I.**23.11, **I.**23.13
  monolithic, **I.**23.10–**I.**23.11, **I.**23.12*f,* **I.**23.15
  MWIR, **I.**23.31
  NE DT in, **I.**23.26–**I.**23.27, **I.**23.27*f,* **I.**23.28
  nonsilicon readouts in, **I.**23.16
  output circuits and, **I.**23.19
  performance, **I.**23.20*t*
  scanning, **I.**23.7, **I.**23.15
  sharing, **I.**23.4
    infrared, **I.**23.5
  silicon, **I.**23.13
  staring, **I.**23.7, **I.**23.15, **I.**23.32*t*
  SWIR, **I.**23.31
  thermal expansion match, **I.**23.15
  time delay integration (TDI), scanning, **I.**23.18, **I.**23.18*f,* **I.**23.19
  types of, **I.**23.7
  vertically integrated photodiode (VIP), **I.**23.11
  x-*y* addressing and, **I.**23.17
Focal-plane-to-focal-plane geometry, **I.**30.5
Focal ratio, **II.**18.41
Focimeters, **II.**29.26, **II.**29.26*f,* **II.**29.27
Focus:
  automatic, **I.**31.13–**I.**31.14
  depth of, **I.**1.92, **I.**35.7–**I.**35.8, **I.**35.8*f,* **II.**1.37, **II.**1.38*f,* **II.**1.39
  electromagnetically induced, **IV.**23.19
  of lasers, **I.**31.10–**I.**31.12
Focus anisoplanatism, **III.**1.29–**III.**1.30, **III.**1.30*f*–**III.**1.32*f,* **III.**1.42, **III.**1.44
Focused beam diffraction, **III.**35.12–**III.**35.13, **III.**35.13*f,* **III.**35.14, **III.**35.14*f*
Focused beams:
  and parametric generation, **IV.**22.9–**IV.**22.10, **IV.**22.10*t*
  and stimulated Raman scattering, **IV.**18.40–**IV.**18.42
Focus error signal (FES), **I.**31.13, **I.**31.14*f*
Focus of expansion, **III.**12.2
Fokker-Planck equation:
  for laser cooling process, **IV.**28.3, **IV.**28.8–**IV.**28.9, **IV.**28.18
  in laser theory, **IV.**26.32, **IV.**26.39, **IV.**26.44
Footcandle, **II.**24.47, **III.**7.8, **III.**14.8*t*
Foot-lambert, **II.**24.47, **III.**7.8, **III.**14.8, **III.**14.8*t*
Forbidden energy gap, **II.**36.38, **II.**36.41, **II.**36.61
Force-controlled process, **I.**41.5
Form deprivation myopia, **III.**11.17–**III.**11.18
Foster prisms, **II.**3.7, **II.**3.21, **II.**3.23
Foucault knife-edge measurement, **I.**24.20
Foucault prisms, **II.**3.19
Foucault test, **II.**29.23, **II.**30.1–**II.**30.2, **II.**30.2*f,* **II.**30.3, **II.**30.3*f*
Fourier-transform interferometers, **II.**36.63*f*
Fourier transforms:
  analog optical, **I.**30.5, **I.**30.5*f,* **I.**30.6
  other geometries, **I.**30.6–**I.**30.7, **I.**30.7*f*
Fourier transform spectrometers, **I.**42.16
Four-photon mixing (FPM), **IV.**11.10
Four-powered-mirror lenses, **II.**2.20, **II.**2.20*f*
Four-wave mixing (FWM), **II.**39.7, **IV.**1.42, **IV.**1.42*f,* **IV.**1.43, **IV.**3.1–**IV.**3.2, **IV.**3.9–**IV.**3.12, **IV.**13.8, **IV.**13.8*f*
  anti-Stokes, **IV.**18.2, **IV.**18.2*f,* **IV.**18.3, **IV.**18.5*f,* **IV.**18.7, **IV.**18.33
  Brillouin-enhanced, **IV.**18.54–**IV.**18.55, **IV.**18.55*f*
  degenerate, **IV.**17.28–**IV.**17.29, **IV.**18.50, **IV.**25.18
  to determine nonlinear characteristics, **IV.**17.30, **IV.**17.30*f,* **IV.**17.31
  and electromagnetically induced transparency, **IV.**23.22–**IV.**23.23, **IV.**23.23*f,* **IV.**23.24–**IV.**23.25, **IV.**23.25*f*
  and exciton dephasing, **IV.**25.20
  frequency diagrams for, **IV.**3.9*f,* **IV.**3.11*f*
  heterodyne, **IV.**27.14
  and multiple Stokes generation, **IV.**18.39
  in soliton systems, **IV.**7.11, **IV.**7.15
  transient, **IV.**25.18, **IV.**25.18*f,* **IV.**25.19
Fovea, **III.**9.20–**III.**9.21
  cross section of, **III.**10.3*f*
  damage to, **III.**15.12
  for detailed vision, **III.**12.3

Fovea (*Cont.*):
fixation of, **III.**12.2
and macular pigment, **III.**13.10
and moving target, **III.**12.20
and visual direction, **III.**12.8
Foveation, **III.**12.21
Fractional encircled energy, **II.**11.6, **II.**11.21, **II.**11.29*f*
Fracture toughness, **II.**35.9
of selected materials, **II.**33.34, **II.**33.34*t*
Frame:
CEPT1, **IV.**12.21
for Ethernet, **IV.**16.7
in FDDI, **IV.**16.3
for Fibre Channel, **IV.**16.4
for gigabit Ethernet, **IV.**16.7
in SDH, **IV.**12.22
in SONET, **IV.**12.22, **IV.**16.6
in synchronization, **IV.**12.9
in time-division multiple access, **IV.**12.17, **IV.**12.17*f,* **IV.**12.18
in time-division multiplexing, **IV.**12.18–**IV.**12.19, **IV.**12.20*f,* **IV.**12.21
T1, **IV.**12.21
Frame grabbers, **III.**4.20–**III.**4.21
Frame scanning, **II.**19.4
Frame transfer devices, array architecture for, **III.**4.3–**III.**4.6
Frankford arsenal prism, **II.**4.18*f*–**II.**4.24*f*
Franklin, Benjamin, **III.**13.22
Frank-Ritter prisms, **II.**3.7, **II.**3.15
Franz-Keldysh effect, **II.**6.11, **II.**6.11*f,* **II.**39.22, **IV.**4.57, **IV.**4.62
Franz-Keldysh oscillations, **II.**36.70
Fraunhofer diffraction, **I.**3.22, **I.**3.22*f,* **I.**3.23, **I.**3.23*f,* **I.**3.26*f,* **I.**3.27, **I.**3.27*f,* **I.**3.30, **I.**3.30*f,* **II.**5.3, **II.**17.6–**II.**17.7
for neutron beams, **III.**36.9
patterns, **I.**3.24, **I.**3.24*f,* **I.**3.27
Fraunhofer theory, **I.**6.12
Free-carrier effects, **II.**33.12, **II.**33.17–**II.**33.18, **II.**33.18*f,* **II.**36.49
Faraday rotation and, **II.**36.52
Free carriers, **II.**36.35
Free-electron laser (FEL), **I.**11.38, **I.**11.38*f,* **I.**11.39, **III.**33.1, **III.**33.4, **IV.**26.44–**IV.**26.46
Free electron properties, Drude model for, **I.**9.19
Free induction decay (FID), **IV.**24.7
Free polarization decay (FPD), **IV.**24.7–**IV.**24.9, **IV.**24.9*f,* **IV.**24.10, **IV.**24.10*f*
Free spectral range, **I.**42.76
Free-to-bound transition, **II.**36.75
Free viewing, **I.**28.2, **I.**28.2*f*
Frequency acquisition, **IV.**12.15
Frequency chirp, **IV.**12.1, **IV.**12.30
avoiding, **IV.**4.50
in communications system design, **IV.**1.27
and edge-emitting lasers, **IV.**4.1
in electroabsorption modulators, **IV.**4.62
and four-way mixing, **IV.**3.12
of lasers, **IV.**2.6, **IV.**4.20–**IV.**4.21, **IV.**4.21*f,* **IV.**4.22, **IV.**25.22
and LEDs, **IV.**4.45
modulation-induced, **IV.**1.25, **IV.**1.26*f*
from self-phase modulation, **IV.**3.3
in semiconductor amplifier, **IV.**11.6
and solitons, **IV.**7.2
and stimulated echoes, **IV.**24.24
Frequency discriminators, **IV.**27.7, **IV.**27.7*f,* **IV.**27.12–**IV.**27.15
Frequency-division multiplexing (FDM), **IV.**12.9
channel capacity in, **IV.**1.42
in multichannel video transmission, **IV.**2.14–**IV.**2.15
Frequency-domain analysis, **II.**12.12, **II.**12.14, **IV.**1.18
Frequency doubling, **IV.**1.43
Frequency footprint, **I.**7.10
Frequency generation, **IV.**17.7
Frequency guiding filters:
sliding, **IV.**7.8–**IV.**7.9
in soliton transmission, **IV.**7.2, **IV.**7.7–**IV.**7.8
Frequency justification, **IV.**12.19, **IV.**12.21, **IV.**12.23–**IV.**12.24
Frequency locking, **IV.**27.12–**IV.**27.15
Frequency meters, **II.**29.29
Frequency mixing, **IV.**17.5*t,* **IV.**17.7
(*See also* Four-wave mixing (FWM); Three-wave mixing)
Frequency modes, **IV.**4.14–**IV.**4.15
Frequency modulation, **IV.**27.4, **IV.**27.13
Frequency multiplexing, **II.**39.35
Frequency-offset locking, for laser stability, **IV.**27.16
Frequency-of-seeing data, interpolation of, **I.**29.10*n*
Frequency-selective feedback lasers, **I.**13.40, **I.**13.40*f,* **I.**13.41
Frequency shifter, **IV.**4.54, **IV.**21.7
Frequency shift keying (FSK), **II.**10.35–**II.**10.36, **IV.**1.37, **IV.**1.37*t,* **IV.**1.38
laser modulation and, **I.**13.39
Frequency stabilization, in lasers, **IV.**27.1–**IV.**27.2, **IV.**27.22
for diode-pumped solid state laser, **IV.**27.19–**IV.**27.20
discriminators for, **IV.**27.12–**IV.**27.16
for external cavity diode laser, **IV.**27.20–**IV.**27.21, **IV.**27.21*f,* **IV.**27.22

Frequency stabilization, in lasers (*Cont.*):
limits on, **IV.**27.7–**IV.**27.8
quantum absorbers in, **IV.**27.16
servo system for, **IV.**27.6, **IV.**27.6*f,* **IV.**27.7, **IV.**27.7*f,* **IV.**27.8–**IV.**27.9, **IV.**27.9*f,* **IV.**27.10, **IV.**27.10*f,* **IV.**27.11, **IV.**27.11*f,* **IV.**27.12
transducers in, **IV.**27.16–**IV.**27.19
Frequency tracking, **IV.**12.15
Frequency tuning:
in doubly resonant oscillator, **IV.**22.21–**IV.**22.28
of lasers, **IV.**27.1
of laser servo system, **IV.**27.7
Fresnel, A. J., **III.**2.10
Fresnel diffraction, **I.**3.22
for neutron beams, **III.**36.9–**III.**36.10
patterns, **I.**3.18, **I.**3.18*f*
Fresnel equations, **I.**5.4, **I.**5.9
Fresnel formulas, **I.**6.4, **II.**33.22–**II.**33.23
Fresnel-Kirchhoff diffraction formula, **I.**3.19–**I.**3.21, **I.**3.27
Fresnel lenses, **II.**7.23, **II.**7.23*f,* **III.**2.10–**III.**2.11
in Bragg-Fresnel optics, **III.**23.7
facet structure of, **III.**2.10, **III.**2.11*f*
Fresnel number, **I.**3.23–**I.**3.24
Fresnel reflection:
in Bragg gratings, **IV.**9.3
in double heterostructure lasers, **IV.**4.7
and modulator insertion loss, **IV.**4.56
Fresnel rhomb, **II.**3.48, **II.**3.52, **III.**25.5, **III.**25.5*f,* **III.**25.6
Fresnel Risley prism, **II.**4.27*f*
Fresnel's biprism, **I.**2.16, **I.**2.16*f*
Fresnel's law, **III.**36.5
Fresnel-Soret zone plates, **III.**23.3
Fresnel zone, **I.**3.13, **I.**3.14*f*–**I.**3.15*f*
Fresnel zone construction, **I.**3.5, **I.**3.5*f,* **I.**3.6, **I.**3.7*f,* **I.**3.12, **I.**3.23
Fresnel zone plates, **II.**7.18, **III.**23.3, **III.**32.19
aberration characteristics of, **II.**7.23
diffraction efficiency of, **II.**7.25
Fried, David L., **III.**1.8
Fried's coherence diameter, **III.**1.4, **III.**1.12, **III.**1.15
Fringe analysis, by computer, **II.**30.12
Fringe carrier techniques, **II.**23.7
Fringe effect, **I.**20.13
Fringe localization, **I.**2.14
Fringes:
coherence length of, **I.**2.19
of equal inclination, **I.**2.22*f,* **I.**2.25, **I.**2.27
high-visibility fringes of, **I.**2.21
plane-parallel plate, **I.**2.21
of equal thickness, **I.**2.22–**I.**2.23, **I.**2.23*f,* **I.**2.24, **I.**2.28
Fringe visibility, **I.**2.7–**I.**2.8, **I.**2.21, **I.**2.36
vs. OPD, **I.**2.43*f*
Fronto-parallel plane, in visual perception, **III.**12.2, **III.**12.9
FSK dual-filter detection, **IV.**1.38, **IV.**1.38*f*
Full-aperture tilt, **III.**1.23. **III.**1.29
Full-duplex transmission, circulator for, **IV.**10.4
Full-frame array architecture, **III.**4.3–**III.**4.4, **III.**4.4*f*
Full involute, **III.**2.12, **III.**2.12*f,* **III.**2.40
Full width at half minimum (FWHM), **I.**8.9
gaussian spectral profile of, **I.**8.9
of the point spread function (PSF), **II.**11.6
Functional specifications, for optical systems, **I.**35.1
Fusing, in xerographic process, **III.**5.10–**III.**5.11
Fusional vergence, **III.**12.24–**III.**12.25
Fusion tapering, for coupler fabrication, **IV.**8.1

Gabor objectives, **II.**18.22, **II.**18.22*f*
Gabor zone plate, **III.**23.5–**III.**23.6
Gain:
for avalanche photodiode, **IV.**4.76
Brillouin, in fibers, **IV.**1.40
for Brillouin amplifiers, **IV.**11.4
for erbium-doped fiber amplifier, **IV.**5.5–**IV.**5.6, **IV.**13.18, **IV.**13.18*f*–**IV.**13.19*f*
for erbium/ytterbium doped fiber amplifier, **IV.**5.7
in laser servo system, **IV.**27.5–**IV.**27.6, **IV.**27.8–**IV.**27.9, **IV.**27.9*f,* **IV.**27.10–**IV.**27.11, **IV.**27.11*f,* **IV.**27.12, **IV.**27.18
modal, **IV.**4.9, **IV.**4.33, **IV.**4.33*f*
open loop, **IV.**27.5, **IV.**27.9, **IV.**27.9*f*
optical, **III.**30.9–**III.**30.11, **III.**31.10–**III.**31.11
for optical amplifiers, **IV.**11.2
in parametric devices, **IV.**22.13
in parametric generation, **IV.**22.8–**IV.**22.10, **IV.**22.10*t,* **IV.**22.11, **IV.**22.61
for praseodymium-doped fiber amplifier, **IV.**5.6–**IV.**5.7
for quantum wells, **IV.**4.4, **IV.**4.29–**IV.**4.30
Raman, in fibers, **IV.**1.40, **IV.**3.5, **IV.**3.6*f,* **IV.**3.7
for semiconductor amplifiers, **IV.**11.4–**IV.**11.5, **IV.**11.5*f*
for semiconductor lasers, **IV.**4.9
in stimulated Brillouin scattering, **IV.**18.47–**IV.**18.49
stimulated emission, **IV.**4.4
in stimulated Raman scattering, **IV.**18.8–**IV.**18.9, **IV.**18.16, **IV.**18.21, **IV.**18.42
for strained layer lasers, **IV.**4.33
Gain coefficient, **I.**11.10
Gain efficiency, of rare-earth doped amplifier, **IV.**5.5

Gain flattening:
in EDFAs, **IV.**5.6, **IV.**13.19
Mach-Zehnder devices for, **IV.**8.6
Gain-guided lasers, **I.**13.8, **IV.**4.6, **IV.**4.14
Gain margin, in laser servo system, **IV.**27.9, **IV.**27.9*f*
Gain medium, **I.**11.10
of lasers, **I.**11.3–**I.**11.4
Gain reservoir, in quantum laser theory, **IV.**26.19, **IV.**26.22–**IV.**26.23
Gain saturation, **I.**11.10–**I.**11.11, **I.**11.12*f,* **IV.**4.18, **IV.**4.20, **IV.**4.23
dynamic, **IV.**25.8–**IV.**25.9, **IV.**25.9*f,* **IV.**25.11
in optical amplifiers, **IV.**11.3, **IV.**11.5
in rare-earth doped amplifiers, **IV.**5.2–**IV.**5.3
Galilean lenses, **II.**2.7, **II.**2.14, **II.**2.14*f*
Galvanometer, **II.**19.44, **II.**19.45*f*
Gamma correction, **I.**27.7
Gamma radiation, **III.**35.33, **III.**36.9, **III.**36.12
Ganglion cells, **III.**9.8*f,* **III.**10.1, **III.**13.21–**III.**13.22
Gap modes (GM), **II.**36.19
Gas mantle, **I.**10.15
Nerst glower, globar and, compared, **I.**10.16, **I.**10.17*f*
Gas phase media, and electromagnetically induced transparency, **IV.**23.3
Gaussian analysis of lenses, **II.**2.2
Gaussian assumption, and noise effects, **IV.**1.30, **IV.**2.9*n*
Gaussian beams, in parametric generation, **IV.**22.9, **IV.**22.10*t*
Gaussian image point, for reflection gratings, **III.**21.7–**III.**21.8
Gaussian mode, **I.**11.27
of lasers, **I.**11.23, **I.**11.24*f*
Gaussian notation and definitions, **I.**1.50*t*
Gaussian optics, **I.**1.32, **I.**1.48
Gaussian statistical concepts, **II.**24.23–**II.**24.24
Gaussian statistics, and effects of atmospheric turbulence, **III.**1.11
Gauss points, **I.**1.48
Gauss-Seidel Iterative Method, **I.**44.21
Gaze control, **III.**12.29–**III.**12.30
Gaze eccentricity, **III.**12.9–**III.**12.12
Gaze holding, **I.**24.34
Gaze shifting, **I.**24.34
Gédamine, **II.**3.10
Geiger counters, **III.**34.5
Gelbstoff, **I.**43.14
Gemini North 8-m telescope, **III.**1.22, **III.**1.23*f*
General Conference on Weights and Measures (CIPM), **III.**7.2
Generalized fiber-interferometer sensor, **II.**21.17, **II.**21.19
Generalized permittivity, **II.**33.10
Generalized van der Waals theory, **II.**14.8
Generating, of optical surfaces, **I.**40.4, **I.**40.5*f*
Generation noise, **I.**15.9
Generation-recombination (GR):
current, in dark current, **I.**16.8
noise, **I.**15.9
Geometrical configuration factor, of surfaces (GCF), **II.**37.14–**II.**37.15
Geometrical optical transfer function (GOTF), **I.**34.17
Geometric models, in nonimaging optics system design, **III.**2.7
Geometric optics, **I.**6.12
(*See also* Ray optics)
Geometric vector flux, for concentrators, **III.**2.22
Geometric wavefronts, of rays, **I.**1.13–**I.**1.14
Geometry-controlled lasers, **I.**13.40, **I.**13.40*f*
Germanate fiber, **IV.**14.2*t,* **IV.**14.6, **IV.**14.6*f*
Germania-silia fibers, frequency-doubling in, **II.**10.41
Germicidal lamps, **I.**10.35
Gerschberg-Saxton-type algorithms, **II.**39.32
Gestalt organizational principles, **III.**17.9
Ghost reflections, **II.**18.7
Gigabit Ethernet, **IV.**16.7–**IV.**16.8
Gigabit interface converter (GBIC), **IV.**16.7
Gigabit networks, **IV.**12.13
Gilvin, **I.**43.14
Glancing angle, **III.**22.1, **III.**26.4
Glan-Foucault prisms, **II.**3.7, **II.**3.9, **II.**3.9*n,* **II.**3.11, **II.**3.13, **II.**3.26
Glan prisms, **II.**3.7, **II.**3.9, **II.**3.9*n*
defects in, **II.**3.15–**II.**3.16
testing of, **II.**3.16–**II.**3.17
Glan-Taylor prisms, **II.**3.11, **II.**3.13–**II.**3.14
Glan-Thompson prisms, **II.**3.7, **II.**3.9, **II.**3.9*n,* **II.**3.10–**II.**3.11, **II.**3.21, **II.**3.29–**II.**3.30
beam-splitting, **II.**3.24
field angles for, **II.**3.11
transmittance curves in, **II.**3.12*f*
Glare sensitivity:
and age, **III.**13.11
and cataracts, **III.**11.13
and computer work, **III.**16.2
Glare stop (*see* Lyot stop)
Glass, **II.**33.5–**II.**33.6
characterization of, **II.**33.30
composition of, **II.**33.30–**II.**33.31
definition of, **II.**33.34
density of, **II.**33.31
elastic properties of, **II.**33.31–**II.**33.32
hardness of, **II.**33.33
molecular weight of, **II.**33.31

Glass (*Cont.*):
nonoxide, **II.**33.6
optical
mechanical properties of, **II.**33.50*t*–**II.**33.51*t*
physical properties of, **II.**33.43*t*–**II.**33.44*t*
summary optical properties of, **II.**33.60*t*
thermal properties of, **II.**33.54*t*–**II.**33.55*t*
properties of, **II.**33.7*n*
combinations of, **II.**33.38
correlation of, **II.**33.37–**II.**33.38
tables, **II.**33.38–**II.**33.39
room-temperature dispersion formulas for, **II.**33.67*t*–**II.**33.69*t*
specialty
mechanical properties of, **II.**33.50*t*–**II.**33.51*t*
physical properties of, **II.**33.44*t*
summary optical properties of, **II.**33.60*t*
thermal properties of, **II.**33.54*t*–**II.**33.55*t*
strength of, **II.**33.33
transmission range of, **II.**33.6
unit cell parameters of, **II.**33.31
varieties of, **II.**18.2*t*
Glass-ceramics, **II.**33.35
Glass fiber, **IV.**14.1, **IV.**14.2*t*–**IV.**14.3*t,* **IV.**14.4–**IV.**14.8, **IV.**17.14, **IV.**21.3
Glass-forming compounds, **II.**33.6
Glass optics, molded, **II.**7.6, **II.**7.6*f*
Corning process of, **II.**7.6–**II.**7.7, **II.**7.9*f*
Kodak process of, **II.**7.7
tolerances for, **II.**7.7, **II.**7.8*t*
Glaucoma, **III.**13.21–**III.**13.22
adaptive optics applications for, **III.**10.12
definition of, **III.**13.1
incidence of, **III.**13.3, **III.**13.21–**III.**13.22
Glazebrook prisms, **II.**3.7, **II.**3.10
Global divergence:
in collimating optics, **III.**35.7
effect of, on lithographic feature, **III.**35.5, **III.**35.5*f*
Globar, **I.**10.13, **I.**10.15*f*
Nerst glower, gas mantle and, compared, **I.**10.16, **I.**10.17*f*
spectral characteristics of, **I.**10.15, **I.**10.16*f*
Glow modulator tubes, **I.**10.40, **I.**10.46*f*–**I.**10.47*f,* **I.**10.48*t*
Goebel mirrors, **III.**35.9
Goerz prism, **II.**4.17*f*
Golay cells, **I.**19.2, **I.**19.6
Gold:
extinction coefficient for, **II.**35.15*t*
vs. wavelength, **II.**35.24*f*
index of refraction in, **II.**35.15*t*
vs. wavelength, **II.**35.24*f*
reflectance of, **II.**35.33*t*–**II.**35.34*t*
Gold (*Cont.*):
reflectance vs. wavelength for, **II.**35.43*f*
specific heat of, **II.**35.70*f*
thermal conductivity of, **II.**35.64*f*–**II.**35.65*f*
Gold black, **II.**37.58
Goniometers, **II.**25.14, **II.**29.13
Goniometric classification of materials, **II.**25.5*t*
Goniophotometer, **III.**7.7
Goniophotometry, **II.**24.46–**II.**24.47
Goos-Hanchen shift, **II.**6.4
Gordon-Haus effect, **IV.**1.31, **IV.**7.7–**IV.**7.8, **IV.**7.11, **IV.**7.13
Gordon-Haus limit, **II.**10.29
Gouffé, method of, **I.**10.4
Graded index (GRIN) lens, **II.**7.3, **II.**9.1, **II.**9.7*f,* **IV.**4.9, **IV.**4.14, **IV.**4.29, **IV.**10.8, **IV.**10.8*f,* **IV.**10.9
axial lenses, **II.**9.3–**II.**9.4, **II.**9.4*f*
in ellipsometry, **II.**27.9
materials in, **II.**9.8–**II.**9.9
mathematical representations of, **II.**9.2–**II.**9.3
radial gradients in, **II.**9.5, **II.**9.5*f,* **II.**9.6
with curved surfaces, **II.**9.7
Graded index separate confinement heterostructure (GRINSCH) laser, **I.**13.15, **I.**13.15*f,* **IV.**4.5, **IV.**4.5*f,* **IV.**4.6, **IV.**4.30–**IV.**4.31, **IV.**4.31*f*
for VCSELs, **IV.**4.47
Gradient force, **IV.**28.6
Gradient-freeze technique:
of substrate growth, **I.**12.22
Gradient-index fibers, **IV.**1.7, **IV.**1.7*f,* **IV.**1.11
dispersion in, **IV.**2.3–**IV.**2.4
index profile for, **IV.**1.19*f*
Grain boundaries, **II.**33.7
Grains, photographic, **I.**20.4–**I.**20.5, **I.**20.19
sensitometry, variation of, **I.**20.11, **I.**20.11*f*
Gram-Schmidt orthogonalization procedure, **II.**30.14
Granularity, **I.**20.19
photographic
and film speed, **III.**6.19–**III.**6.20
in medical X-ray imaging, **III.**35.32
power spectrum of, **I.**20.23
rms-, **I.**20.21–**I.**20.22, **I.**20.24
and sharpness, together, **I.**20.24
Graphic arts imager, **II.**19.11*n*
Graphite surface, textured, **II.**37.11*f*
Grasshopper monochromator, **III.**21.5
Grassman's laws, **I.**26.9–**I.**26.10, **I.**26.42
implications of, **I.**26.10
Grating, **II.**5.5, **II.**5.7
beam-splitter, **II.**8.11*t*
binary optics, **II.**8.11–**II.**8.12

Grating (*Cont.*):
Bragg index, **IV.**12.27
chirped (aperiodic), **IV.**9.7, **IV.**13.10–**IV.**13.12
corrugated-waveguide, **II.**6.8
diffraction, **II.**5.3–**II.**5.4
drifting, temporal frequency of, **I.**25.39*n*
eagle, **II.**5.8, **II.5**.11*f*
Ebert-Fastie, **II.**5.8, **II.**5.10
fabrication of, **II.**6.18
Fastie, **II.**5.12*f*
holographic (*see* Holographic gratings)
Littrow, **II.**5.10
long-period, **IV.**13.19, **IV.**13.19*f,* **IV.**15.9–**IV.**15.14
multifocal lenses in, **II.**8.12
in multiplexer/demultiplexer, **IV.**10.6, **IV.**10.7*f*
Paschen-Runge, **II.**5.7
Pfund, **II.**5.10
Rowland, mounting of, **II.**5.10*f*
short-period, **IV.**15.6
tilted (blazed), **IV.**9.7
Wadsworth, **II.**5.8, **II.**5.12*f*
(*See also* Fiber Bragg grating (FBG); Reflection gratings)
Grating combiners, in WDM, **IV.**1.32, **IV.**1.33*f*
Grating-diffraction efficiency, **II.**23.15
Grating formation, **II.**39.1
Grating functions, **II.**12.25
Gravity reflectometer, **III.**36.6
Gray code, **I.**31.18
Gray gel, in color photographic film, **III.**6.5
Grayscale tones, **III.**6.25
Gray world assumption, **I.**26.35
Grazing incidence, **II.**37.14, **II.**37.22
Grazing incidence optics, **III.**28.1–**III.**28.12
collecting area in, **III.**28.5–**III.**28.6, **III.**28.6*f*
divergence in, **III.**35.7
for free-electron lasers, **III.**33.4
with high angular resolution, **III.**28.10–**III.**28.12
with pinch plasmas, **III.**33.3
Green flash, **I.**44.40, **I.**44.43
Green's function, **I.**3.19–**I.**3.21, **I.**6.17–**I.**6.18
Greenwood frequency, **III.**1.21, **III.**1.24
Gregorian-Mersenne telescope, afocal, **II.**18.13*f*
Gregorian objectives, **II.**18.10–**II.**18.11, **II.**18.11*f*
aplanatic, **II.**18.12, **II.**18.12*f,* **II.**18.13
Grey's orthonormalization method, **I.**34.20
Grinding, optical, **I.**40.4
Gross-Pitaevski equation, **IV.**28.34
Ground-state collisions, **IV.**28.27–**IV.**28.28, **IV.**28.30, **IV.**28.35
Ground states, **I.**11.4
Group dispersion:
and cross-phase modulation, **IV.**3.4
Group dispersion (*Cont.*):
and four-way mixing, **IV.**3.12
and self-phase modulation, **IV.**3.3
Group velocity dispersion (GVD):
in slow saturable absorber, **IV.**25.9
in ultrafast laser systems, **IV.**24.26, **IV.**25.13–**IV.**25.14
Group velocity walkoff, in parametric generation, **IV.**22.64
Grüneisen relationship, **II.**12.15, **II.**33.36
GSDII, **II.**8.15
G-tilt, **III.**1.17–**III.**1.18
Guard ring, **I.**15.9
GUERAP (General Unwanted Energy Rejection Analysis Program), **I.**38.27, **II.**37.21
Guest-host system, **II.**14.10–**II.**14.11
Guided-wave components:
beam propagation method (BPM) of, **II.**6.8
coupled-mode theory of, **II.**6.8
phase evolution of, **II.**6.7
Guided-wave devices, **II.**6.20, **II.**6.22
Guide stars:
laser, **III.**1.22, **III.**1.23*f,* **III.**1.25, **III.**1.28–**III.**1.35
natural, **III.**1.22, **III.**1.23*f,* **III.**1.29, **III.**1.33
sodium, **III.**1.29
and tracking, **III.**1.22–**III.**1.24
Guide tubes, for neutron beams, **III.**36.8–**III.**36.9, **III.**36.12, **III.**36.14–**III.**36.15
Gurney-Mott mechanism, **I.**20.5
Gyroscopes, fiber optic (*see* Fiber optic gyroscopes (FOG))

H-aggregate spectral sensitizers, **III.**6.14
Haidinger fringes, **I.**2.22, **I.**2.27
formation of, **I.**2.23*f*
Halation, in color photography, **III.**6.5
Half-beat-length coupler, **IV.**21.5
Half-shade devices, **II.**3.60
Halftoning, **III.**17.3, **III.**17.5
Hamiltonian optics, **I.**1.15, **I.**1.97
Hamilton's equations, **I.**1.23
Hanbury-Brown-Twiss (HB&T) effect, **IV.**26.14, **IV.**26.14*f,* **IV.**26.15
Handshaking, in optical network switching, **IV.**13.16
Hanle laser, **IV.**26.43
Haplopia, **III.**12.2
Hard disks, **I.**31.1
achievable densities on, **I.**31.1*n*
Hardness, **II.**35.9
Harmonic distortions:
in analog fiber-optic links, **IV.**6.5
Harmonic generation, intracavity, **I.**14.12
Harmonic oscillators, **I.**8.23
interionic potential and, **I.**8.26*f*

Harmonic trap, **IV.**28.34–**IV.**28.35
Harrick's polarizers, **II.**3.37
Harting-Dove prism, **II.**4.9, **II.**4.9*f*
Hartmann formula, **II.**33.26
Hartmann sensors, **III.**2.33
Hartmann-Shack wavefront sensor (HSWS), **III.**1.25–**III.**1.28
  in adaptive optics system design example, **III.**1.42
  definition of, **III.**10.1
  Fried geometry for, **III.**1.27*f*
  geometry of, **III.**1.25*f*
  least-squares reconstructor matrix for, **III.**1.28*f*
  to measure ocular aberration, **III.**8.3, **III.**10.5, **III.**10.6*f*
Hartmann test, **II.**30.1, **II.**30.4, **II.**30.5*f,* **II.**30.6, **II.**30.6*f*
Hartnack-Prazmowski prisms, **II.**3.7, **II.**3.19
Hartree-Fock variational approach, **I.**8.14
H-atom spectroscopy, **I.**8.11
Haus's formalism, for mode-locking, **IV.**25.8, **IV.**25.10
Head-mounted display (HMD) systems, **III.**12.31–**III.**12.36, **III.**18.1
  design considerations in, **III.**18.2–**III.**18.6
  image quality in, **III.**18.7–**III.**18.10
  and misaccommodation, **III.**18.10–**III.**18.13
Heat capacity, **II.**33.35
Heavy metal fluoride glass (HMFG), **IV.**14.1, **IV.**14.4–**IV.**14.6
  attenuation in, **IV.**14.5, **IV.**14.5*f*
  fabrication of, **IV.**14.4–**IV.**14.5
  properties of, **IV.**14.4*t*
  reliability of, **IV.**14.6
Heisenberg-Langevin approach to quantum laser theory, **IV.**26.34–**IV.**26.36
Heisenberg's matrix mechanics, **I.**8.5
Heisenberg's Uncertainty Principle, **IV.**17.7–**IV.**17.8, **IV.**17.21
Helium:
  Doppler effect on, **II.**28.3
  energy levels of, **II.**28.3
  inhomogeneous broadening in, **II.**28.3, **II.**28.4*f*
Helium-cadmium lasers, **I.**11.16–**I.**11.17, **I.**11.17*f,* **I.**11.32
Helium-neon lasers, **I.**11.12, **I.**11.16, **I.**11.17*f,* **I.**11.32
Helmholtz, Hermann von, **III.**10.4, **III.**10.9
Helmholtz equation, **I.**4.10, **III.**1.10
Helmholtz invariant, **I.**1.84
Helmholtz reciprocity principle, **II.**25.13, **III.**9.1–**III.**9.2, **III.**9.25, **III.**9.29
Hemispherical reflectivity, of black surfaces, **II.**37.22*t*
Henle's fibers, **III.**9.1, **III.**9.20
Hering's law, **III.**12.21, **III.**12.26–**III.**12.27
Herschel condition, **I.**1.34–**I.**1.35, **II.**18.38, **II.**18.41
Herschelian objectives, **II.**18.7
Heterodyne detection, **IV.**1.35, **IV.**1.35*f,* **IV.**1.36, **IV.**1.37*t,* **IV.**1.39, **IV.**2.11
Heterodyne/homodyne detection, **II.**10.33, **II.**10.33*f,* **II.**10.34
Heterogeneous media, **I.**1.10
Heterojunctions, **I.**12.18
Heterophoria, **III.**12.2, **III.**12.27
Heterostructure:
  for fiber-optics, **IV.**4.2–**IV.**4.3
  polarization in, **IV.**4.15
  in semiconductor production, **IV.**4.2
Heterostructure lasers, **I.**13.7
  double, **I.**13.5*f*
Heterostructures, LED, **I.**12.12*f,* **I.**12.13, **I.**12.13*f,* **I.**12.19
Hewlett-Packard interferometers, **II.**29.11*f*
Hexagonal silicon carbide, reflectance vs. wavelength, **II.**35.45*f*–**II.**35.46*f*
Higgins-Jones acutance, **I.**20.21
High-definition television (HDTV), **II.**15.7, **III.**4.21
  in Advanced Photo System, **III.**6.27
  image quality in, **III.**17.10, **III.**18.6
High-dry objectives, **II.**17.15, **II.**17.16*f*
High-energy sources, **I.**10.48
Higher-order aberrations, **II.**18.41
Higher-order anti-Stokes scattering (HORASS), **II.**36.59
Higher-order Stokes-effect scattering (HORSES), **II.**36.59
High-gain fiber amplifiers, **I.**13.4
High Resolution Doppler Imager (HRDI), **I.**44.36, **I.**44.37*f*
High-resolution optical filters, **IV.**2.11
High-voltage power supply, for microchannel plates (MCP), **I.**21.10, **I.**21.10*f*
Hilbert space formulation, **I.**4.2
Hill gratings, **IV.**9.5
HITRAN, **I.**44.21–**I.**44.23, **I.**44.23*f,* **I.**44.23*t,* **I.**44.26, **I.**44.26*f*
Hobby-Eberly telescope, **III.**1.4
Hold over time, **IV.**12.15
Hole accumulation diode (HAD), **I.**22.8
Hole burning (*see* Optical hole burning (OHB))
Hollow-cathode lamps, **I.**10.36*t,* **I.**10.37, **I.**10.37*t*–**I.**10.40*t,* **I.**10.41*f*
Hollow waveguide, **IV.**14.1, **IV.**14.2*t*–**IV.**14.3*t,* **IV.**14.11–**IV.**14.13
  applications for, **IV.**14.11

Hollow waveguide (*Cont.*):
glass (HGW), **IV.**14.11–**IV.**14.12, **IV.**14.12*f,* **IV.**14.13, **IV.**14.13*f*
metal/plastic, **IV.**14.11
Holocamera systems, **II.**23.8
Holograms, **II.**39.30
accuracy limitations of, **II.**31.7–**II.**31.8
binary detour-phase, **II.**31.2, **II.**31.4*f*
binary synthesis, **II.**31.2–**II.**31.3
Bragg-matched volume, **II.**39.2
computer-generated (CGH) (*see* Computer-generated holograms (CGH))
Fourier transform, **II.**39.25
laser transmission, **II.**23.3*f*
Lee, **II.**31.2–**II.**31.3
null, **II.**7.6
photorefractive, **II.**39.1–**II.**39.2
storage of, **II.**39.34–**II.**39.35
programming for, **I.**34.8–**I.**34.9
recording and construction process, **II.**23.4
types of, **II.**23.5
Holographic gratings, **II.**23.14–**II.**23.15
Holographic inspection, **II.**23.17–**II.**23.18, **II.**23.18*f*–**II.**23.19*f,* **II.**23.20
disadvantages of, **II.**23.20–**II.**23.21, **II.**23.21*f*
Holographic interferometry, **II.**23.5–**II.**23.7, **II.**23.9*f,* **II.**23.10–**II.**23.11, **II.**23.17
time-average, **II.**23.6, **II.**23.8*f*
vibration analysis in, **II.**23.8–**II.**23.9
Holographic lithography, **II.**23.22–**II.**23.24, **II.**23.25*f*
Holographic memory storage, **II.**23.25–**II.**23.26
Holographic moiré, **II.**23.7
Holographic optical elements (HOEs), **I.**31.30, **I.**31.30*f,* **II.**23.12–**II.**23.16, **II.**23.16*f,* **II.**23.17, **II.**39.28
computer-generated, **II.**23.14
Holographic sundial, **II.**23.17
Holography, **II.**23.2–**II.**23.3
electronic, **II.**23.9
electro-optic (EOH), **II.**23.12, **II.**23.14*f*
in grating formation, **IV.**1.43
pattern recognition in, **II.**39.25–**II.**39.27
photorefractive, **II.**39.25
real-time, **II.**39.25, **II.**39.26*f*
in spectroscopic gratings, **III.**21.3, **III.**21.5–**III.**21.6
and zone plates, **III.**23.6
Homodyne detection, **IV.**1.35, **IV.**1.35*f,* **IV.**1.36, **IV.**1.37*t,* **IV.**1.38–**IV.**1.39, **IV.**2.11
Homogeneous broadening, **I.**8.9, **I.**11.6–**I.**11.7, **I.**11.7*f,* **I.**11.9, **IV.**12.1, **IV.**24.17–**IV.**24.18, **IV.**24.18*f,* **IV.**25.19
Homogeneous media, **I.**1.10, **I.**1.27–**I.**1.28
Homogeneous polarization element, **II.**22.7
Homogeneous reflectors, **III.**2.40
Homojunctions, LED, **I.**12.9–**I.**12.11
Hooke's law, **II.**33.32
Hoop forces, **I.**37.2
Hopkin's formula, **I.**4.14
Horizontal linear polarizer, **II.**22.14
Horopter, **III.**12.2, **III.**12.8–**III.**12.11
theoretical, **III.**12.8, **III.**12.9*f*
Hottel strings, **III.**2.4–**III.**2.5, **III.**2.15
Houghton-Cassegrain objectives, **II.**18.24*f,* **II.**18.25, **II.**18.25*f*
HRCam tracking system, **III.**1.24
Hubble telescope, **II.**30.23
Hufnagel-Valley model, **III.**1.9–**III.**1.10
Hughes Airborne Optical Adjunct coating, **II.**37.41
Human visual system (HVS):
adaptive optics applications for, **III.**7.12*f,* **III.**10.3, **III.**10.7–**III.**7.12
aging of, **III.**13.5–**III.**13.19
color perception in, **III.**4.18–**III.**4.19, **III.**6.16, **III.**6.17*f,* **III.**9.19–**III.**9.20, **III.**13.13–**III.**13.15, **III.**17.5
and computer work, **III.**16.1–**III.**16.6
current research on, **III.**8.4
and electronic imaging, **III.**17.1–**III.**17.6, **III.**17.11–**III.**17.12
evolution of, **III.**17.6
field of view of, **III.**12.34, **III.**13.18
imperfections in, **III.**10.2
(*See also* Aberration, ocular)
in photometry, **III.**7.6, **III.**7.8–**III.**7.9, **III.**7.12
physiology of, **III.**9.3
range of light response of, **III.**5.17*f,* **III.**6.16
scanpaths in, **III.**17.7
(*See also* Eye, human; Visual system)
Humidity, and fiber strain, **IV.**1.21
Hund's rule, **I.**8.15
Huygens-Fresnel construction, **I.**3.4–**I.**3.5, **I.**3.19
Hybrid reflectors, **III.**2.40
Hyde maxim, **I.**34.24
Hydrogen arc lamps, **I.**10.45, **I.**10.48*f*
Hydrogenatic atoms:
energy-level spectrum for, **I.**8.5
structure splittings in, **I.**8.11*f*
Hydrogen ion, in astrophysics, **II.**28.3
Hydrogen loading, **IV.**9.2
Hydrologic optics (*see* Water)
Hyperacuity, **I.**25.36, **III.**13.19, **III.**13.23
Hyperfocal distance, range of focus and, **I.**1.92
Hyperhemispheric lenses, **III.**2.9
Hypermetropia, **III.**13.5, **III.**13.9

Hyperopia, **III.**11.2, **III.**11.2*f,* **III.**11.3, **III.**11.6, **III.**12.2, **III.**12.31, **III.**13.24, **III.**15.9, **III.**16.5, **III.**18.10–**III.**18.11
Hyper-Raman scattering, **IV.**18.2, **IV.**18.2*f,* **IV.**18.3, **IV.**18.3*t*
Hypocotyl, in plant structure, **III.**9.27, **III.**9.27*f,* **III.**19.2
Hysteresis instability, **II.**35.11–**II.**35.12
Hysteresis loops, **I.**31.28, **I.**31.29*f,* **II.**14.11
  coercivity and, **I.**31.27

IBM Black, **II.**37.56
Iceland spar, **II.**3.2
Ideal-observer theory, **I.**25.17–**I.**25.19, **I.**25.19*f,* **I.**25.20, **I.**25.20*f,* **I.**25.25, **I.**29.6–**I.**29.7
  photon noise limited observer, **I.**25.20*n*
Ideal polarizer, **II.**22.7
Identification tasks, **I.**25.16
Idler, in optical parametric generation, **IV.**22.2–**IV.**22.4, **IV.**22.5*f,* **IV.**22.7–**IV.**22.8, **IV.**22.62
II SSAs (*see* Cameras, II SSA)
Illuminance, **II.**24.12, **II.**24.44
  luminance relationship with, **III.**14.9, **III.**14.9*f*
  photometric measure of, **III.**14.1, **III.**14.4*t,* **III.**14.5, **III.**14.5*f*
  of photosensitive devices, **III.**7.17–**III.**7.18
  retinal (*see* Retinal illuminance)
  unit conversions in, **III.**7.8*t*
Illuminance meters, **II.**24.47
Illuminants, **I.**26.26*t*
  CIE, **I.**26.31*t*
  in colorimetry, **I.**26.25
  linear model representations for, **I.**26.25–**I.**26.26
  reflection model of, **I.**26.25
Illumination:
  Abbe, **III.**2.23–**III.**2.24, **III.**2.24*f,* **III.**2.35, **III.**2.36*f*
  for biological photoreceptors, **III.**9.12–**III.**9.13
  bright field, **II.**17.24
  CPC use in, **III.**2.15
  critical, **II.**17.37
  definition of, **III.**2.1
  Köhler, **I.**28.6, **II.**17.37, **II.**17.40, **III.**2.23–**III.**2.24, **III.**2.24*f,* **III.**2.35, **III.**2.36*f*
  measurement of, **I.**28.18
  multiple surface concentrators in, **III.**2.17
  oblique, **II.**17.24
  and pupil diameter, **III.**13.7
  ranges, **I.**21.3*f*
  stroboscopic, **II.**23.6
  types of, **I.**21.3
  uniformity in, **III.**2.23–2.42
Illumination Engineering Society of North America (IESNA), **III.**14.12, **III.**16.2
Illumination subsystem, **III.**2.23
Image:
  inverted, **II.**4.2
  medial, **II.**18.41
  reverted, **II.**4.2
  types of, **I.**1.29
  virtual, **II.**18.42
Image analysis, **III.**17.7
Image coding, **III.**17.7, **III.**17.9
Image compression, **III.**17.3–**III.**17.4, **III.**17.7
Image contrast:
  and cataracts, **III.**11.13
  in medical X-ray applications, **III.**35.26, **III.**35.26*f,* **III.**35.27, **III.**35.28*f,* **III.**35.29–**III.**35.30, **III.**35.30*f*
Image creation:
  in biological eyes, **III.**9.4, **III.**9.7, **III.**10.2, **III.**10.4, **III.**13.7, **III.**13.10–**III.**13.12, **III.**17.7
    (*See also* Photoreceptors, biological)
  color photographic, **III.**6.1–**III.**6.2, **III.**17.10
  digital, **III.**6.29
  granularity in, **III.**6.19–**III.**6.20
  multiple, from cataracts, **III.**13.19
  in xerographic systems, **III.**5.2–**III.**5.5
Image development:
  and color photographic paper, **III.**6.5
  xerographic, **III.**5.5–**III.**5.10
Image distance, **II.**2.3
Image dyes, photographic, **III.**6.10–**III.**6.13
  in Kodachrome film, **III.**6.24
Image formation, **I.**1.29, **I.**25.3–**I.**25.4
Image height, **I.**1.31
Image intensifier (*see* Image tube intensifier (II))
Image intensifier self-scanned array (II SSA) (*see* Cameras, II SSA; Image tube intensifier (II))
Image irradiance, **I.**1.29
  for Lambertian objects, **I.**1.87
Image lag, **I.**22.7
Image plane, **I.**1.31
Image point, **I.**1.30
Image quality:
  in head-mounted displays, **III.**18.6
  metrics for, **III.**17.3–**III.**17.4
  subjective elements in, **III.**17.10
Image receptor, in xerographic process, **III.**5.1
Image relation, in scanning, **II.**19.17
Image rendering, models for, **III.**17.4
Imagery, afocal, **II.**2.6, **II.**2.6*f*
Image sensors:
  area image, **I.**22.26, **I.**22.26*t,* **I.**22.27
  color, **I.**22.35–**I.**22.37, **I.**22.37*f*
  elements for, **I.**22.2
  frame transfer CCD, **I.**22.27–**I.**22.29, **I.**22.29*f*

Image sensors (*Cont.*):
interline transfer CCD, **I.**22.29–**I.**22.30, **I.**22.31*f,* **I.**22.32, **I.**22.33*f,* **I.**22.34
linear image, **I.**22.23, **I.**22.23*f,* **I.**22.24, **I.**22.24*f,* **I.**22.25, **I.**22.25*f,* **I.**22.26
MOS area, **I.**22.27, **I.**22.28*f*
multilinear arrays, **I.**22.26
solid-state, **I.**22.22
staggered linear arrays, **I.**22.26
time-delay and integrate (TDI), **I.**22.26
types of, **I.**22.2
Image sharpness, **I.**20.20
Image space, **I.**1.30
mapping objects to, **I.**1.30
numerical aperture, **I.**1.85
Image structure, in photographic films, **I.**20.18
Image tube intensifier (II), **I.**21.2, **I.**21.7–**I.**21.9, **I.**21.22*f*–**I.**21.23*f*
comparison of, **I.**21.22*t*
families of, **I.**21.8
Geb-2, **I.**21.19, **I.**21.20*f*
resolution curves, **I.**21.19*f*
scanned arrays, **I.**21.20, **I.**21.20*f*
(*See also* Cameras, II SSA)
Imaging:
astigmatic, of a point, **I.**1.47*f*
conditions, quantum limited (QLI), **I.**21.3–**I.**21.5
conoscopic, **II.**17.39–**II.**17.40, **II.**17.40*f*
electronic (*see* Electronic imaging)
ideal, **I.**1.32
isoplanic, **I.**1.34
maxwellian, **I.**1.32
medical, **III.**19.5, **III.**19.10, **III.**34.7, **III.**35.24–**III.**35.26
multilayer reflective coatings used in, **III.**24.6–**III.**24.7
optical transfer function in, **III.**1.21–**III.**1.22
orthoscopic, **II.**17.39
paraxial, **I.**1.42
ratio, **II.**17.46
and Schwarzschild objective, **III.**27.1
single-plane, **I.**1.32
stigmatic, **I.**1.33, **I.**1.35
three-dimensional, **II.**17.47
time-gated, **IV.**18.43–**IV.**18.44, **IV.**18.45*f*
X rays in, **III.**19.5, **III.**19.10, **III.**20.3, **III.**20.8, **III.**35.24–**III.**35.33
(*See also specific imaging techniques*)
Imaging capillary optics, **III.**29.3–**III.**29.4
Imaging-forming rays, **I.**1.81
Imaging science, **III.**17.1
Imaging systems:
adaptive optics applications for, **III.**1.5–**III.**1.8
feature detection in, **III.**17.8
Imaging systems (*Cont.*):
f-number in, **IV.**19.3
Fresnel lenses used in, **III.**2.10
vs. nonimaging systems, **III.**2.8
sampling in, **III.**4.17–**III.**4.20
solid-state camera applications for, **III.**4.3
(*See also specific systems*)
Imaging wavelength, **III.**1.40–**III.**1.43, **III.**1.45*f,* **III.**1.46–**III.**1.47, **III.**1.47*f*
Impact ionization coefficient, in avalanche process, **IV.**4.76
Implants, for vision correction, **III.**11.14, **III.**11.17
(*See also specific types of implants*)
Impulse response, **II.**32.2
Impurity gettering, **I.**22.5*n*
Impurity magnetoabsorption, **II.**36.52–**II.**36.53, **II.**36.53*f*
Incoherent demodulation, **II.**10.36, **IV.**1.38, **IV.**1.38*f*
Incoherent radiation, **III.**2.2, **III.**2.42, **III.**15.2, **III.**19.6
Incoherent scattering, **III.**3.3–**III.**3.5
Incoherent X-ray metrology, **III.**26.5
Index confinement, **IV.**20.6–**IV.**20.9, **IV.**20.14
Index ellipsoid, **II.**13.5, **II.**13.5*f*–**II.**13.6*f,* **II.**33.21, **II.**33.21*f*
Index-guided lasers, **I.**13.9, **I.**13.30, **IV.**4.14
Index of refraction, **I.**1.10, **I.**5.4, **I.**5.5*f,* **I.**5.7*f,* **I.**9.23, **II.**33.8, **II.**35.4
of air, formula for, **III.**1.8
in all-optical switching, **IV.**21.1, **IV.**21.3, **IV.**21.7
in biological photoreceptor, **III.**9.12, **III.**9.22, **III.**9.24
changes in, **II.**24.14
cornea/lens ratio of, **III.**13.6
dispersion formulas for, **II.**33.25
distributed (*see* Graded index (GRIN) lens)
and electromagnetically induced transparency, **IV.**23.18–**IV.**23.20
of fiber-optic materials, **III.**9.4
for infrared fiber, **IV.**14.2–**IV.**14.3
and laser irradiance, **IV.**17.22
for lasers, **IV.**4.6, **IV.**4.15, **IV.**4.20
and magnification, **III.**12.26
in metals, **II.**35.12, **II.**35.13*t*–**II.**35.20*t*
in neutron optics, **III.**36.5, **III.**36.7–**III.**36.8
in nonlinear fiber optics, **IV.**1.42, **IV.**3.2–**IV.**3.3, **IV.**17.8–**IV.**17.10, **IV.**19.7
for optical fiber, **IV.**1.6–**IV.**1.7, **IV.**1.44–**IV.**1.45, **IV.**2.2, **IV.**13.6
of optical systems, **I.**34.7
phase velocity, **II.**13.13, **II.**13.13*f,* **II.**13.14, **II.**13.14*f,* **II.**13.15
for photoreceptors, **III.**9.5

Index of refraction (*Cont.*):
and photosensitivity, **IV.**9.2–**IV.**9.3
reflections in, **I.**5.8
and semiconductor modulators, **IV.**4.2
symmetries, **I.**1.24
in 3D bandgap materials, **IV.**20.4–**IV.**20.5
uniformity of, through optical elements, **II.**33.7
of X rays, **III.**19.6–**III.**19.7, **III.**20.3
of Yttria, **II.**33.13*f*
Index of refraction gradients (*see* Graded index (GRIN) lens)
Indirect modulation, **IV.**12.30
Indirect transitions, **II.**36.25–**II.**36.26
Induced wave shift, **II.**13.18
Inertial guidance, **II.**6.34–**II.**6.35
Infectious developers, **I.**20.5
Infrablack, **II.**37.27–**II.**37.28, **II.**37.40
BRDF of, **II.**37.32*f,* **II.**37.56*f*–**II.**37.57*f*
Infrared absorption, **II.**36.21*f*
Infrared allowed processes:
in diamond structure, **II.**36.17*t*
in zincblende structure, **II.**36.18*t*
Infrared cataract, **III.**15.8, **III.**15.11
Infrared emitters, **I.**12.9
Infrared fiber fabrication, **IV.**1.47–**IV.**1.48
Infrared Handbook, The, **I.**10.27
Infrared heterodyne detection, **I.**15.87
Infrared (IR) fibers, **IV.**14.1–**IV.**14.4
applications for, **IV.**14.3, **IV.**14.3*t,* **IV.**14.4, **IV.**14.11, **IV.**14.13–**IV.**14.14
categories of, **IV.**14.1, **IV.**14.2*t*
crystalline, **IV.**14.8–**IV.**14.10
glass, **IV.**14.4–**IV.**14.8
hollow waveguides, **IV.**14.11–**IV.**14.14
loss spectra for, **IV.**14.2, **IV.**14.2*f*
properties of, **IV.**14.2–**IV.**14.3, **IV.**14.3*t*
Infrared (IR) light:
and cataracts, **III.**13.8, **III.**13.19
exposure limits for, **III.**15.9–**III.**15.11
eye damage from, **III.**15.2, **III.**15.4, **III.**15.5*f*
in photometry, **III.**7.18
in radiometry, **III.**7.5, **III.**14.1
and Schwarzschild objective applications, **III.**27.1
Infrared sensors, **I.**23.4
spectral bands for, **I.**23.5
Infrared spectrum, of sapphire, **II.**33.15*f*
Inhomogeneous broadening, **I.**11.6, **II.**20.23, **II.**28.14
and degenerate two-pulse FWM, **IV.**25.19
in electromagnetically induced transparency, **IV.**23.13, **IV.**23.15–**IV.**23.17, **IV.**23.21, **IV.**23.24
elimination of, **II.**20.24
Inhomogeneous broadening (*Cont.*):
and free polarization decay, **IV.**24.10, **IV.**24.10*f*
and stimulated photon echo, **IV.**24.17–**IV.**24.18
Inhomogeneous media:
in nonimaging systems, **III.**2.23
and surface scattering, **III.**3.3
Inhomogeneous polarization element, **II.**22.7
Inhomogeneous reflectors, **III.**2.40
Inhomogeneous systems, and volume scattering, **III.**3.3
Injection, **IV.**4.39
Injection-locked lasers, **I.**13.40, **I.**13.40*f,* **I.**13.41
Injection locking, **II.**39.28
Injection seeding, **I.**14.18
In-line gun CRTs, **I.**27.5
In-plane coupling, in photonic crystals, **IV.**20.10–**IV.**20.11
Input saturation power, for rare-earth doped amplifier, **IV.**5.3
Insertion devices:
as synchrotron radiation source, **III.**32.1–**III.**32.2, **III.**32.6, **III.**32.10, **III.**32.10*f,* **III.**32.11–**III.**32.18
(*See also* Undulators; Wigglers)
Insertion loss:
definition of, **IV.**10.2
in modulators, **IV.**4.56, **IV.**4.58–**IV.**4.60
with splitter, **IV.**10.2
in wavelength-division multiplexing, **IV.**1.32–**IV.**1.33
Installation loss, for optical link power budget, **IV.**6.7–**IV.**6.9
Instant pictures, **II.**15.8
Instrument calibration, **II.**26.13–**II.**26.14
Instrument myopia, **I.**24.32
Instrument signature, **II.**26.4, **II.**26.10–**II.**26.11
Insulating magnetic brush (IMB), **III.**5.7
Insystems Wafer Inspection System, **II.**23.20, **II.**23.23*f*
Integral color filter arrays (CFA), **I.**22.36, **I.**22.36*f*
Integrated circuit photomasks, **II.**23.17, **II.**23.19*f*
Integrated optic circuit (IOC), **II.**6.2
lithium niobate, **II.**6.37
research and development in, **II.**6.37
Integrated optics (IO):
advantages of, **II.**6.2
on silicon substrates, **II.**6.13–**II.**6.14
Integrating bucket, **II.**30.19–**II.**30.20, **II.**30.20*f*
Integrating cavities, in nonimaging optics, **III.**2.25–**III.**2.28
Integrating spheres, **I.**28.10, **III.**14.10–**III.**14.11, **III.**14.11*f*
Monte Carlo techniques used to evaluate, **III.**2.7

Integrating spheres (*Cont.*):
as nonimaging optics uniformity control, **III.**2.2, **III.**2.25, **III.**2.25*f,* **III.**2.26, **III.**2.26*f*
Intelligent Physical Protocol Enhanced Physical Project, **IV.**16.4
Intensified charge-coupled device (ICCD), **III.**4.3
Intensity, **I.**4.7, **II.**24.8–**II.**24.9, **III.**7.5, **III.**14.1
autocorrelation, in ultrashort lasers, **I.**14.23
interferometry, **I.**4.24
luminous (*see* Candela)
mutual, **I.**4.11
scaling, of light, **I.**26.3–**I.**26.4, **I.**26.4*f*–**I.**26.5*f*
Intensity distribution:
gaussian, for lightpipe, **III.**2.29, **III.**2.30*f*
for integrating spheres, **III.**2.25, **III.**2.26*f*
Intensity gain, in X-ray diffraction, **III.**35.8–**III.**35.9, **III.**35.9*t,* **III.**35.10, **III.**35.10*t,* **III.**35.11, **III.**35.11*t*
Intensity modulation:
with direct detection, **IV.**1.34
by electroabsorption, **IV.**4.58–**IV.**4.60
semiconductors for, **IV.**4.2
Interband absorption, **I.**9.28, **I.**9.30
fundamental edge, **II.**36.23–**II.**36.24, **II.**36.24*f,* **II.**36.25, **II.**36.25*f*
Interband Faraday rotation, **II.**36.47*f*
Interband magneto-optical effects, **II.**36.43–**II.**36.44
Interband transitions, **I.**9.24, **I.**9.31–**I.**9.32, **II.**36.34, **II.**36.34*f*–**II.**36.35*f*
Interconnected switchable network (fabric), for Fibre Channel, **IV.**16.4
Interference, **I.**2.3
by amplitude division, **I.**2.19–**I.**2.20
extended source, **I.**2.20–**I.**2.21
plane-parallel plate, **I.**2.20–**I.**2.21
atomic, **IV.**23.3–**IV.**23.4
in coherent population trapping, **IV.**23.7
constructive, **IV.**23.2, **IV.**23.23–**IV.**23.24, **IV.**23.27
destructive, **IV.**23.2, **IV.**23.10, **IV.**23.23–**IV.**23.24, **IV.**23.27
effects, **I.**2.6
in electromagnetically induced transparency, **IV.**23.7–**IV.**23.8, **IV.**23.8*f,* **IV.**23.9
Fano, **IV.**23.2, **IV.**23.7–**IV.**23.8, **IV.**23.8*f*
patterns of three wavelengths, **I.**2.18*f*
quantum electrodynamics, **IV.**26.12
temporal beats, **I.**2.13
Interference filters, **IV.**20.2
Interference fringes, **I.**2.6, **I.**2.6*f,* **I.**2.7, **I.**2.7*f*
generation of, **I.**28.20
Interference gratings, **II.**23.14
Interference pattern, from a linear source, **I.**2.40*f*
Interferogram:
binary synthesis (*see* Holograms, binary synthesis)
density of fringes in, **II.**30.13
evaluation of, **II.**30.12, **II.**30.12*f*
fixed, **II.**30.12
Fourier analysis of, **II.**30.12, **II.**30.14–**II.**30.15
interpolation of, **II.**30.13–**II.**30.14
laterally-sheared, **II.**30.10*f*
Interferometeric wave meters, **II.**21.19
Interferometers, **I.**28.25
atom, **IV.**24.20–**IV.**24.22, **IV.**24.23*f*
Bruning, **II.**29.10*f*
Burch, **II.**30.7
computer-generated holograms (CGH), **II.**31.6, **II.**31.6*f,* **II.**31.7
distance-measuring, **II.**29.8–**II.**29.9, **II.**29.9*f,* **II.**29.10–**II.**29.12
double-passed two-beam, **II.**21.8, **II.**21.9*f*
Fabry-Perot, **I.**42.17, **II.**21.6–**II.**21.7, **II.**21.7*f,* **II.**21.13, **II.**21.20, **II.**21.24
feedback, **II.**21.18*f*
fiber, **II.**21.17, **II.**21.18*f,* **II.**21.19
Fizeau, **I.**2.25, **I.**2.26*f,* **I.**2.34, **II.**21.2, **II.**21.2*f,* **II.**21.14, **II.**21.20–**II.**21.21, **II.**21.22*f,* **II.**30.7, **II.**30.8*f*
Fourier-transform, **II.**36.63*f*
frequency-modulation, **II.**21.11, **II.**21.11*f,* **II.**21.12
fringe-counting, **II.**21.10, **II.**21.10*f*
grating, **II.**21.5, **II.**21.5*f*
gravitational-wave, **II.**21.23–**II.**21.25, **II.**21.25*f*
and the HB&T effect, **IV.**26.14
heterodyne, **I.**2.13, **II.**21.12–**II.**21.13, **II.**21.13*f,* **II.**29.28, **II.**30.21
heterodyne stellar, **II.**21.23
Hewlett-Packard, **II.**29.11*f*
increasing the sensitivity of, **II.**30.8
infrared heterodyne stellar, **II.**21.24*f*
intensity, **II.**21.23
Jamin, **II.**21.8
laser-Doppler, **II.**21.15–**II.**21.16, **II.**21.16*f*
laser-feedback, **II.**21.16, **II.**21.16*f,* **II.**21.17
Mach-Zehnder, **I.**28.26, **I.**28.26*f,* **II.**6.10, **II.**6.12, **II.**6.14–**II.**6.15, **II.**6.29, **II.**10.15, **II.**12.48, **II.**13.23, **II.**13.23*f,* **II.**21.3, **II.**21.3*f,* **II.**21.4–**II.**21.5, **II.**21.21*f,* **II.**23.5, **IV.**1.17, **IV.**4.64, **IV.**9.8, **IV.**12.32, **IV.**12.32*f,* **IV.**12.36
in all-optical switching, **IV.**12.36–**IV.**12.38, **IV.**12.38*f,* **IV.**21.2, **IV.**21.2*f,* **IV.**21.3–**IV.**21.5
as modulator, **IV.**4.66
and measurements, **II.**29.17
Michelson, **II.**21.2–**II.**21.3, **II.**21.3*f,* **II.**21.5, **II.**21.22, **II.**21.22*f,* **II.**21.23, **II.**23.5, **II.**29.8, **II.**36.63, **IV.**9.8, **IV.**9.8*f*

Interferometers (*Cont.*):
Minkowitz, **II.**29.10*f*
Mirau, **II.**21.14*f*
multimode, **IV.**4.66
multiple-pass, **II.**30.9
multiple-reflection, **II.**30.8
Murty, **II.**30.8, **II.**30.11*f*
Newton, **II.**30.7
Nomarski, **II.**21.4, **II.**21.5*f*
nonreacting, **II.**29.9–**II.**29.10
phase conjugate, **II.**21.21, **II.**21.22*f,* **II.**39.31*f*–**II.**39.32*f*
phase-locked, **II.**21.14–**II.**21.15, **II.**21.15*f*
phase-shifting, **II.**21.13
point diffraction, **II.**30.7
polarization, **II.**21.4, **II.**30.21
reflectors for, **I.**42.41
Sagnac, **II.**6.32–**II.**6.33, **II.**21.4, **II.**21.4*f,* **II.**21.17, **IV.**12.38
second-harmonic, **II.**21.21, **II.**21.21*f*
shearing, **II.**21.6, **II.**21.6*f,* **II.**30.7–**II.**30.8, **II.**30.11*f*
stellar, **II.**21.22
three-beam, **II.**21.8, **II.**21.9*f*
Twyman-Green, **I.**2.28, **II.**21.3, **II.**21.14, **II.**23.5, **II.**30.7, **II.**30.7*f,* **II.**30.9*f,* **II.**30.16, **II.**30.16*f*
types of, **II.**21.2
unbalanced nonlinear (UNI), **IV.**12.38
Zernicke's three-beam, **II.**21.8, **II.**21.8*f*
(*See also specific type*)
Interferometric correlation, in ultrashort lasers, **I.**14.23
Interferometric measurement, **IV.**1.17, **IV.**1.17*f,* **IV.**17.29
Interferometric modulators, **IV.**4.51, **IV.**4.51*f,* **IV.**4.54–**IV.**4.56
Interferometric Spectra Analyzer (ISA), **II.**12.48
Interferometric tests, **II.**30.6
Interferometry:
direct, **II.**30.15
fringe linearization, **II.**23.7
holographic (*see* Holographic interferometry)
infrared, **II.**30.23
neutron, **III.**36.4, **III.**36.10–**III.**36.11, **III.**36.11*f,* **III.**36.12
phase conjugate, **II.**39.30
phase-shifting, **II.**30.16–**II.**30.17, **II.**30.17*f,* **II.**30.18, **II.**30.18*f,* **II.**30.19–**II.**30.21
two steps plus one method, **II.**30.20
sinusoidal phase-modulating, **II.**21.15
speckle-pattern, **II.**23.9–**II.**23.11, **II.**23.12*f*–**II.**23.13*f*
electronic (ESPI), **II.**23.10–**II.**23.11
sub-Nyquist, **II.**30.25
Interferometry (*Cont.*):
two-wavelength, **II.**21.11, **II.**30.23–**II.**30.24
X-ray, **III.**28.10–**III.**28.12, **III.**36.11
Interimage effect, **I.**20.13
Interlayer interimage effects (IIE), of photographic film, **III.**6.3, **III.**6.17, **III.**6.19
Interleaving, **IV.**12.4, **IV.**12.6, **IV.**12.8, **IV.**12.9*f,* **IV.**12.19, **IV.**12.20*f,* **IV.**12.23
Interline transfer array architecture, **III.**4.3–**III.**4.6
Intermediate frequency, **IV.**1.35–**IV.**1.36
Intermodal dispersion, **IV.**1.10–**IV.**1.11, **IV.**2.3–**IV.**2.5
Intermodulation distortion (IMD), **IV.**2.15, **IV.**6.5, **IV.**6.6, **IV.**6.6*f,* **IV.**6.7
Intermodulation products (IMPs), **II.**12.48–**II.**12.49
in Bragg cells, **II.**12.47–**II.**12.48
Internal quantum efficiency, in lasers, **IV.**4.10
Internal self-action, **IV.**19.8, **IV.**19.11
Internal writing technique, for fiber grating fabrication, **IV.**9.5
International Bureau of Weights and Measures (BIPM), **III.**7.2
International candle, **III.**14.3
International Commission on Illumination (CIE), **III.**7.3, **III.**14.2, **III.**14.12, **III.**15.3, **III.**15.10
International Commission on Non-Ionizing Radiation Protection (ICNIRP), **III.**15.6, **III.**15.10–**III.**15.11, **III.**15.14
International Electrotechnical Commission, **III.**15.10
International Standards Organization (ISO), **I.**35.11, **III.**7.2–**III.**7.3
International System of Units (*see* SI units (Système International d'Unités))
International Telecommunications Union (ITU), jitter definition from, **IV.**6.16
International Union of Pure and Applied Physics (IUPAP), **III.**7.2–**III.**7.3
Internet, traffic on, **IV.**12.3
Internuclear separation, **I.**8.21, **I.**8.22*f,* **I.**8.23
Interphotoreceptor matrix (IPM), **III.**9.8
Interpupillary distance (IPD), **III.**12.15, **III.**12.22
Interstitial matrix, in biological photoreceptors, **III.**9.2, **III.**9.5
Interstitial oxygen, **II.**36.21*f,* **II.**36.23*f*
Intersymbol interference, **II.**10.23, **IV.**1.25, **IV.**6.9, **IV.**6.12, **IV.**13.5
Intraband, **II.**36.49
in germanium, **II.**36.51*f*
Intracapsular cataract extraction (ICCE), **III.**11.13
Intracavity doubly resonant oscillator (ICDRO), **IV.**22.15, **IV.**22.42

Intracavity optical parametric oscillator (ICOPO), **IV.**22.42–**IV.**22.50
conversion efficiency of, **IV.**22.43–**IV.**22.48
layout of, **IV.**22.43, **IV.**22.43*f*
operating characteristics of, **IV.**22.48, **IV.**22.49*f*
operating regimes of, **IV.**22.43, **IV.**22.44*f*
tuning of, **IV.**22.48, **IV.**22.50*f*
Intracavity pulse energy, **I.**14.4, **I.**14.5*f*
Intracavity singly resonant oscillator (ICSRO), **IV.**22.15, **IV.**22.42
Intramodal dispersion, **IV.**2.3–**IV.**2.5, **IV.**2.5*f*
Intraocular aniso-magnification, **III.**12.17–**III.**12.20
Intraocular lens (IOL), **III.**13.1, **III.**13.23–**III.**13.24, **III.**13.24*f*
bifocal, **III.**13.23
implant of, **III.**11.14–**III.**11.15, **III.**13.9, **III.**13.19
phakic, **III.**13.24
Intraocular pressure (IOP), **III.**13.21–**III.**13.22
Intraocular scattered light, **I.**24.19
Intraocular suppression, **III.**12.13, **III.**12.19
Intrastromal corneal rings (ICRs), **III.**11.17
Intrinsic Fabry-Perot interferometric (IFPI) sensors, **IV.**15.4, **IV.**15.4*f,* **IV.**15.5
Intrinsic jitter, **IV.**6.17
Intrinsic resolution, **II.**11.13
Intrinsic semiconductor operation, **I.**15.9
Inverse Raman effect, **IV.**3.5
Inverse square law, **II.**24.15–**II.**24.16, **III.**14.9
Inversion layers, in photogates, **I.**16.12
Inverted channel substrate planar (ICSP) lasers, **I.**13.23*f,* **I.**13.24
Involute reflectors, **III.**2.12, **III.**2.12*f,* **III.**2.40
Ion-assisted deposition, **I.**42.15
Ion beam-sputtered surfaces, **II.**37.46
Ion-beam sputtering, **I.**42.15
Ionic bonding, **I.**8.19
Ion implantation, **IV.**25.22–**IV.**25.24
Ionization chambers, **III.**34.3–**III.**34.4
Ionization X-ray detectors, **III.**34.3–**III.**34.6
Ionizing excitations, **II.**36.32
Ion plating, **I.**42.15
Ion trapping, **IV.**28.19
Ion writing systems, **III.**5.4–**III.**5.5
Iris, **III.**13.7, **III.**13.11, **III.**15.9
Iron:
extinction coefficient for, **II.**35.16*t*
vs. wavelength, **II.**35.24*f*
index of refraction in, **II.**35.16*t*
vs. wavelength, **II.**35.24*f*
reflectance of, **II.**35.34*t*–**II.**35.35*t*
vs. wavelength, **II.**35.43*f*
specific heat of, **II.**35.71*f*
thermal conductivity of, **II.**35.65*f*–**II.**35.66*f*
Irradiance, **I.**3.4, **II.**24.8–**II.**24.9
versus exitance/emittance, **III.**2.3
for laser-generated plasmas, **III.**33.1
net, **I.**43.9
off-axis, **II.**24.17–**II.**24.18
on-axis, **I.**3.9–**I.**3.11
plane, **I.**43.9
as radiometric unit, **III.**7.5, **III.**14.1, **III.**14.4*t,* **III.**14.5, **III.**14.5*f*
retinal exposure to, **III.**15.1, **III.**15.8
scalar, **I.**43.8–**I.**43.9
spectral, **I.**10.10, **I.**10.10*f,* **I.**43.13
in straightedge diffraction, **I.**3.16–**I.**3.17
Irradiance distribution, **II.**24.8
Irradiance ratio, **I.**43.13
Irradiance reflectance, **I.**43.48, **I.**43.49*f*
in natural waters, **I.**43.49*f*
IR radiometic standards, **I.**10.9
Irregular aberrations, **III.**10.4, **III.**10.7
Irregular refraction, **III.**11.3
Isodiscrimination contours, **I.**26.36*f*
Isoelectric dopants, **I.**12.17–**I.**12.18
Isolation, **IV.**10.2
Isolator, **IV.**10.3, **IV.**10.9, **IV.**10.10*f*
Isoluminance, **I.**25.31, **I.**25.32*f*
Isoplanatic angle, **III.**1.21
Isoplanatic patch, **I.**29.4*n*
Isoplanic imaging, **I.**1.34
Isotope broadening, **I.**11.6–**I.**11.7
Isotropic, definition of, **III.**7.4
Isotropic diffraction, **II.**12.10, **II.**12.21–**II.**12.22
Isotropic intensity, **III.**2.3
Isotropic luminance, **III.**2.3
Isotropic media, **I.**1.10

Jackson Cross cylinder, **III.**11.5
Jacobi method, **II.**13.10–**II.**13.11, **II.**13.13
J-aggregate spectral sensitizers, **III.**6.14–**III.**6.15
Jahn-Teller effect, **II.**28.9, **II.**28.26
Jamin interferometers, **II.**21.8
Jaynes-Cummings model, **IV.**26.15–**IV.**26.16, **IV.**26.16*f,* **IV.**26.17–**IV.**26.18, **IV.**26.21
Jellet-Cornu prisms, **II.**3.60
Jerlov water types, **I.**43.29, **I.**43.44–**I.**43.45, **I.**43.45*t,* **I.**43.46, **I.**43.46*f*
Jitter:
accumulation in repeaters, **IV.**6.17
effect on Strehl ratio, **III.**1.18*f*
intrinsic, **IV.**6.17
maximum tolerable input (MTIJ), **IV.**6.17
in optical link power budget, **IV.**6.15–**IV.**6.17
in soliton transmission systems, **IV.**7.6–**IV.**7.8, **IV.**7.11, **IV.**7.13–**IV.**7.17

Jitter (*Cont.*):
from synchronously pumped parametric oscillators, **IV.**22.55
in telescope mount, **III.**1.24
Jitter transfer function (JTF), **IV.**6.17
Johnson noise, **I.**15.9, **I.**18.4, **IV.**1.27–**IV.**1.28, **IV.**1.28*f*
in photodetectors, **IV.**4.74–**IV.**4.75
Jones calculus, **I.**5.26–**I.**5.28
Jones matrix, **I.**5.28, **I.**6.11, **I.**7.2, **II.**22.8, **II.**22.31–**II.**22.32
Jones unit, **I.**15.9, **I.**15.11
Josephson pairs, **III.**34.9
Joules, **III.**7.5, **III.**14.6
Judd-Vos modified function, **I.**26.13, **III.**7.12
Judgment tasks, **I.**29.2, **I.**29.6–**I.**29.7, **I.**29.9
Just noticeable distortion (JND), **III.**17.4

Kane momentum matrix, **I.**9.27
Kane's theory, **II.**36.25
Kao, Charles, **IV.**1.5
K-correlation (ABC) model, **I.**7.9, **I.**7.11
Keck telescopes, **III.**1.4
Kelvin, **III.**7.2, **III.**14.7
Kennedy scanner, **II.**19.15, **II.**19.17
Keplerian lenses, **II.**2.7–**II.**2.8, **II.**2.11*f,* **II.**2.12
Kerataconus, **III.**10.12, **III.**11.3, **III.**11.10
Keratocytes, **III.**13.5
Keratometer mire, **III.**11.4
Keratometry, **III.**11.4
Keratomileusis, **III.**10.11, **III.**11.16–**III.**11.17
Kerr cell, **II.**1.23, **II.**20.9
Kerr effect, **IV.**7.2, **IV.**12.1, **IV.**12.32, **IV.**17.11–**IV.**17.12, **IV.**22.3
in all-optical switching, **IV.**12.36–**IV.**12.37
bound electronic optical, **IV.**17.5*t,* **IV.**17.12, **IV.**17.14–**IV.**17.15
and electromagnetically induced transparency, **IV.**23.22, **IV.**23.27–**IV.**23.28
longitudinal, **IV.**25.11–**IV.**25.12, **IV.**25.12*f,* **IV.**25.13–**IV.**25.15
molecular orientational, **IV.**17.5*t,* **IV.**17.15–**IV.**17.16
and phase conjugation, **IV.**17.30
polar magneto-optical, **I.**31.22, **I.**31.22*f*
Raman-induced, **IV.**17.5*t,* **IV.**17.14, **IV.**17.19
transverse, **IV.**25.11–**IV.**25.12, **IV.**25.12*f,* **IV.**25.14–**IV.**25.15
and ultrashort pulse generation, **IV.**25.4
Kerr-lensing, **IV.**17.25, **IV.**25.12, **IV.**25.12*f*
Kerr lens mode-locking (KLM), **IV.**25.14–**IV.**25.15
Kilogram, **III.**7.2
Kinematograms, random-dot, **I.**25.40
Kirchhoff's law, **II.**24.27, **II.**25.8, **II.**25.16
Kirchhoff theory, **I.**3.20
Kirkpatrick-Baez optics, **III.**28.7, **III.**28.8*f,* **III.**28.9, **III.**28.9*f,* **III.**28.10, **III.**35.15
Kirkpatrick-Baez telescope, **II.**11.3*f*
Knapp's Law, **III.**11.15, **III.**12.18, **III.**12.26
Knife-edge test, **II.**30.1–**II.**30.2
Knoop hardness number, **II.**33.33, **II.**33.33*f*
Kodachrome film, **III.**6.24, **III.**6.24*t*
Kodak Cobra Flash, **II.**15.17, **II.**15.18*f*
Kodak glass, **II.**7.7
Köhler illumination, **I.**28.6, **I.**32.11*f,* **II.**17.5, **II.**17.37, **II.**17.40, **III.**2.23–**III.**2.24, **III.**2.24*f*
lens arrays in, **III.**2.35, **III.**2.36*f*
Kolmogorov, Andrey Nikolayevich, **III.**1.8
Kolmogorov spatial power spectral density, **III.**1.9
Korsch, three-mirror objectives, **II.**18.34, **II.**18.34*f*
four-reflection, **II.**18.35, **II.**18.35*f*
and two-mirror, **II.**18.38, **II.**18.38*f*
Kramers-Kronig (K-K) relations, **I.**9.15–**I.**9.16, **II.**6.10–**II.**6.11, **II.**33.11, **II.**33.14, **II.**33.27, **II.**36.4, **II.**36.10–**II.**36.11
to calculate electrorefraction, **IV.**4.64
in nonlinear optics, **IV.**17.3, **IV.**17.10–**IV.**17.13, **IV.**19.7
Kramers system, **II.**20.19, **II.**20.19*f,* **II.**20.20
Krinecker delta function, **I.**4.21
Kronig-Penney model, **IV.**28.31
Krypton lasers, **I.**11.16
Kubelka-Munk theory of radiative transfer, **III.**3.12–**III.**3.13, **III.**3.13*f*

LADAR (laser detection and ranging), **I.**21.29–**I.**21.31
Ladder (cascade) three-level atomic scheme, **IV.**23.6, **IV.**23.6*f,* **IV.**23.15
transparency in, **IV.**23.12, **IV.**23.16, **IV.**23.16*f,* **IV.**23.17
Lagrange invariant, **I.**1.84
and étendue conservation, **III.**2.4
generalized, **I.**1.25
Lambda (Λ) three-level atomic scheme, **IV.**23.6, **IV.**23.6*f*
electromagnetically induced transparency in, **IV.**23.6–**IV.**23.8, **IV.**23.8*f,* **IV.**23.9, **IV.**23.15–**IV.**23.16, **IV.**23.16*f*
Lambert, **III.**7.8
Lambertian, definition of, **III.**7.4–**III.**7.5
Lambertian approximation, **II.**24.16
Lambertian black surfaces, **II.**37.16
Lambertian objects, image irradiance for, **I.**1.87
Lambertian radiator, **III.**2.3
Lambertian source, **II.**24.16
spherical, **II.**24.18
Lambertian surface, **III.**14.9–**III.**14.10

Lambert's cosine law, **III.**14.9, **III.**14.9*f*
Lambert's law, **I.**4.13, **I.**4.20
Lamb-Retherford radio-frequency experiment, **I.**8.12
Lamb shift, **I.**8.6, **I.**8.11–**I.**8.12, **IV.**26.13
Lamipol structures, **II.**3.61
Lamps:
  argon arc, **I.**10.11
  black-light, **I.**10.35, **I.**10.36*t,* **I.**10.37
  carbon arc, **I.**10.19, **I.**10.22*f*–**I.**10.23*f,* **I.**10.24*t,* **I.**10.25, **I.**10.25*t,* **I.**10.26*f*
  cold cathode, **I.**10.35, **I.**10.40
  compact-source arc, **I.**10.31, **I.**10.31*f*–**I.**10.32*f*
  concentrated arc, **I.**10.39
  deuterium arc, **I.**10.11, **I.**10.45, **I.**10.49*f*
  electrodeless discharge, **I.**10.37
  germicidal, **I.**10.35
  glow modulator tubes, **I.**10.40, **I.**10.46*f*–**I.**10.47*f,* **I.**10.48*t*
  hollow-cathode, **I.**10.36*t,* **I.**10.37, **I.**10.37*t*–**I.**10.40*t,* **I.**10.41*f*
  hydrogen arc, **I.**10.45, **I.**10.48*f*
  Lucalox, **I.**10.29, **I.**10.30*f*
  mercury arc, **I.**10.25, **I.**10.27, **I.**10.27*f*–**I.**10.30*f,* **I.**10.33*f*
  mercury-xenon, **I.**10.32, **I.**10.33*f*–**I.**10.34*f*
  multivapor arc, **I.**10.28, **I.**10.29*f*
  Pen-Ray low pressure, **I.**10.35*f*
  photomicrographic, **I.**10.39
  Plueker spectrum tubes, **I.**10.38, **I.**10.44*f,* **I.**10.44*t*
  quartz envelope, **I.**10.19
  safety standards for, **III.**15.15
  for scientific purposes, **I.**10.20*f*–**I.**10.21*f*
  short-arc, **I.**10.34
  spectral, **I.**10.38, **I.**10.42*f*–**I.**10.43*f,* **I.**10.43*t*
  spectral irradiance, **I.**10.10
  spectral radiance filament, **I.**10.9
  Sterilamps, **I.**10.35
  tungsten arc (photomicrographic), **I.**10.39, **I.**10.45*f*
  tungsten-filament, **I.**10.17, **I.**10.18*f,* **I.**10.19, **II.**20.6
  Uviarc, **I.**10.27, **I.**10.27*f*
  xenon, **I.**10.34
  zirconium arc, **I.**10.39, **I.**10.44*f*
  (*See also specific type*)
Lamp standards, **I.**10.8
Landau levels, **II.**36.41, **II.**36.43, **II.**36.43*f*–**II.**36.44*f,* **II.**36.48, **II.**36.51
Landé interval, **I.**8.19–**I.**8.20
Landolt fringe, **II.**3.19
Landolt ring target, **I.**25.36
Lands, in optical disks, **I.**31.4
Landscape lenses, **II.**1.17, **II.**1.17*f*–**II.**1.18*f,* **II.**1.19*t*–**II.**1.20*t*
Langevin method, in laser theory, **IV.**26.6, **IV.**26.15, **IV.**26.34–**IV.**26.36
Laporte selection rule, **I.**8.13
Lapping, abrasive, **I.**40.4
Large Binocular Telescope (LBT), **III.**1.8
Larmor precession, in neutron optics, **III.**36.13
Laser absorption saturation spectroscopy, **I.**8.12
Laser amplifiers, **I.**11.9–**I.**11.10, **I.**13.47, **IV.**2.12
Laser-assisted chemical etching (LACE), **II.**7.27, **II.**7.29, **II.**7.29*f*
Laser beam expanders, athermal, **I.**39.14
Laser beams, interaction with molecules, **II.**28.6
Laser cavities, **IV.**20.6, **IV.**26.18, **IV.**26.31
  configurations of, **I.**11.26*f*
  losses in, **IV.**20.19
  mode-locking, **I.**11.29–**I.**11.30
  net gain development in, **I.**14.8*f*
  optimum output coupling from, **I.**11.15–**I.**11.16
  Q-switching, **I.**11.28–**I.**11.29
  resonators, unstable, **I.**11.27–**I.**11.28, **I.**11.28*f*
  stability of, **I.**11.25
Laser cooling, **IV.**28.1
  applications for, **IV.**28.24–**IV.**28.38
  properties of, **IV.**28.2–**IV.**28.4, **IV.**28.35, **IV.**28.37, **IV.**28.38*f*
  sub-Doppler, **IV.**28.15–**IV.**28.19
  theory in, **IV.**28.4–**IV.**28.9
  of trapped ions, **IV.**28.19
  (*See also* Atomic beam, collimation of; Atomic beam, slowing in; Atom trapping; Optical molasses (OM))
Laser diode collimators, **II.**7.5
Laser diodes (LD), **IV.**4.3, **IV.**12.26
  high-power (*see* Lasers, high-power)
Laser dressed states, **IV.**23.3, **IV.**23.8*f*
Laser-fiber coupling, **IV.**1.7
Laser field:
  in cooling process, **IV.**28.3–**IV.**28.4
  interaction with three-level atom, **IV.**23.6
  in Langevin approach, **IV.**26.34–**IV.**26.35
  in optical trapping, **IV.**28.21
  in quantum mechanics, **IV.**26.15, **IV.**26.18–**IV.**26.20
Laser frequency discriminator, **IV.**27.7, **IV.**27.7*f*
Laser-generated plasmas (LGPs), **II.**11.2, **III.**19.6, **III.**33.1–**III.**33.2
  applications for, **III.**35.4–**III.**35.5
  characteristics of, **III.**33.2*t*
Laser guide star (LGS) sensing, **III.**1.22, **III.**1.23*f,* **III.**1.25, **III.**1.28–**III.**1.35
  in adaptive optics system design, **III.**1.42, **III.**1.44

Laser guide star (LGS) sensing (*Cont.*):
expected performance of, **III.**1.30
mesospheric sodium, **III.**1.33–**III.**1.35, **III.**1.35*f*
versus natural guide star, **III.**1.29
Rayleigh, **III.**1.30–**III.**1.33, **III.**1.33*f*
Laser-heated pedestal growth (LHPG), **IV.**14.9–**IV.**14.10, **IV.**14.10*f*
Laser-induced continuum structure (LICS), **IV.**23.8
Laser-induced damage threshold (LIDT), **I.**42.17–**I.**42.18
Laser-induced phase change, **II.**14.11–**II.**14.12
Laser in-situ keratomileusis (LASIK), **III.**11.16–**III.**11.17, **III.**13.2, **III.**13.25
Laser lines, in scanning, **II.**19.27
Laser modes, **I.**4.24
lateral, stabilizing, **I.**13.19–**I.**13.20
longitudinal, **I.**11.20–**I.**11.22
stable, **I.**11.26, **I.**11.27*f*
transverse, **I.**11.22–**I.**11.23, **I.**11.23*f,* **I.**11.24, **I.**11.24*f,* **I.**11.25, **I.**11.27
Laser noise, **I.**31.12
Laser photocoagulation, for diabetic retinopathy, **III.**13.21
Laser power:
combining, **II.**39.28
modulation (LPM), recording by, **I.**31.19
Laser printer, **II.**19.11*n*
Laser pump source, in parametric generation, **IV.**22.61
Laser radar, **II.**29.5
Lasers:
AlGaAs, **I.**13.35*f*
pattern effect for, **I.**13.35*f*
amplifier parameters for, **I.**11.8*t*
anti-Stokes Raman, **IV.**18.33
argon, **I.**11.16
argon ion, **I.**11.16, **I.**11.16*f,* **I.**11.32
array-mode stability in, **I.**13.30–**I.**13.31
atom, **IV.**28.35
in atom trapping, **IV.**28.21–**IV.**28.22, **IV.**28.22*f,* **IV.**28.23
broad-area twin-ridge structure (BTRS), **I.**13.23*f*
broad bandwidth, **I.**11.36
buried heterostructure, **I.**13.9–**I.**13.10
buried TRS (BTRS), **I.**13.21
buried V-groove-substrate inner stripe (BVSIS), **I.**13.21
carbon dioxide (CO_2), **I.**11.17, **I.**11.17*f,* **I.**11.33
channel substrate planar (CSP), **I.**13.21, **I.**13.23*f,* **I.**13.39*f*
in collision physics, **IV.**28.28
color center, **I.**11.36
Lasers (*Cont.*):
components of, **I.**11.3
constricted double-heterostructure large optical cavity (CDH-LOC), **I.**13.23*f*
continuous-wave, **IV.**26.19
continuous-wave (CW) dye, **III.**1.34, **III.**1.34*f,* **III.**1.35
copper vapor, **I.**11.14, **I.**11.14*f,* **I.**11.16, **I.**11.32, **I.**14.21
correlated emission, **IV.**26.43–**IV.**26.44
couple-cleaved cavity (C^3), **IV.**12.27
coupled cavity, **I.**13.40*f,* **I.**13.41
mode-locked, **I.**14.16
current-confined constricted double-heterostructure large optical cavity (CC-CDH-LOC), **I.**13.21
for datacom applications, **IV.**4.2
defined, **I.**11.2
diffraction of emissions from, **IV.**4.13–**IV.**4.14
diode
direct-modulation capability of, **I.**31.8
multiple-track read-write, **I.**31.29
optical output power of, **I.**31.8*f*–**I.**31.9*f*
diode-pumped solid state, **IV.**27.19–**IV.**27.20, **IV.**27.22
distributed Bragg reflector (DBR), **I.**13.41, **I.**13.43, **II.**6.26, **II.**6.28, **IV.**4.1, **IV.**4.8, **IV.**4.15, **IV.**4.34–**IV.**4.35, **IV.**4.35*f,* **IV.**4.36, **IV.**12.27
distributed feedback (DFB), **I.**11.30, **I.**13.39, **I.**13.41, **I.**13.43, **I.**14.19–**I.**14.20, **II.**6.17, **II.**6.26, **IV.**4.1, **IV.**4.8, **IV.**4.15, **IV.**4.25*f,* **IV.**4.36, **IV.**4.36*f,* **IV.**4.37–**IV.**4.39, **IV.**12.27–**IV.**12.28, **IV.**12.28*f*
double-channel planar-buried heterostructure (DC-PBH), **I.**13.26, **I.**13.26*f,* **I.**13.27, **I.**13.37*f*
double heterostructure (DH), **I.**13.5, **I.**13.7, **I.**13.13*f,* **I.**13.14, **I.**13.14*f,* **I.**13.15, **IV.**4.1, **IV.**4.3–**IV.**4.9
edge-emitting (*see* Edge-emitting lasers)
in electromagnetically induced transparency, **IV.**23.13–**IV.**23.17
excimer, **I.**11.13, **I.**11.16, **I.**11.33, **I.**11.33*f*
external cavity diode, **IV.**27.20–**IV.**27.21, **IV.**27.21*f,* **IV.**27.22
eye damage from, **III.**15.1–**III.**15.2, **III.**15.4, **III.**15.12–**III.**15.14
eye protection for, **III.**15.14–**III.**15.15
Fabry-Perot, **IV.**2.9, **IV.**4.14, **IV.**12.26, **IV.**12.26*f,* **IV.**12.27
ferromagnetic system comparison with, **IV.**26.37–**IV.**26.38, **IV.**26.38*t,* **IV.**26.39, **IV.**26.39*f,* **IV.**26.40, **IV.**26.40*f*

Lasers (*Cont.*):
fiber ring, **IV.**5.1
flash-lamp-pumped, **I.**11.18, **I.**11.19*f*
focusing of, **I.**31.10–**I.**31.12
free electron, **I.**11.38, **I.**11.38*f,* **I.**11.39, **II.**11.2, **III.**33.1, **III.**33.4, **IV.**26.44–**IV.**26.46
frequency chirp in, **IV.**2.6, **IV.**4.20–**IV.**4.21, **IV.**4.21*f,* **IV.**4.22, **IV.**25.22
frequency-selective feedback, **I.**13.40*f,* **I.**13.41
frequency shift keying (FSK), **I.**13.39
frequency stability in, **IV.**27.1–**IV.**27.16, **IV.**27.22
gain-guided, **I.**13.8
gain saturation in, **IV.**4.18, **IV.**4.20, **IV.**4.23
gaseous, **I.**11.32–**I.**11.34
geometry-controlled, **I.**13.40*f*
glass, **I.**14.11
Hanle, **IV.**26.43
helium-cadmium, **I.**11.7, **I.**11.16–**I.**11.17, **I.**11.17*f,* **I.**11.32
helium-neon (He-Ne), **I.**11.12, **I.**11.16, **I.**11.17*f,* **I.**11.32, **I.**14.15, **II.**21.10
heterostructure (*see* Heterostructure lasers; Semiconductor lasers)
high-power, **I.**13.19–**I.**13.20, **I.**13.20*f,* **I.**13.21, **I.**13.25
arrays, **I.**13.29*f,* **I.**13.32*t*
geometries for, **I.**13.23*f*
mode-stabilized, characteristics of, **I.**13.22*t,* **I.**13.27*t*
nonabsorbing mirror technology in, **I.**13.25
output power vs. current, **I.**13.24*f*
phase-locked arrays, **I.**13.30*t*
thermal properties of, **I.**13.28, **I.**13.29*f*
two-dimensional, **I.**13.31, **I.**13.33*f*
index-guided, **I.**13.9, **I.**13.30
injection-locked, **I.**13.40*f,* **I.**13.41
InP-based, **I.**13.8
intracavity pulse energy of, **I.**14.4, **I.**14.5*f*
inverted channel substrate planar (ISCP), **I.**13.23*f,* **I.**13.24
ion bombardment stripe, **I.**13.8
krypton, **I.**11.16
Langevin approach to, **IV.**26.34–**IV.**26.36
lead salt, **I.**13.8
lead vapor, **I.**11.14*f*
L-I curve for, **IV.**4.10–**IV.**4.12, **IV.**4.12*f*
liquid, **I.**11.34
locking of, with frequency discriminators, **IV.**27.12–**IV.**27.16
for long-distance communications, **I.**13.8
LPE-based, **I.**13.26*f*
master equation for, **IV.**26.19–**IV.**26.21
metalorganic chemical vapor deposition (MOCVD), **I.**13.29*f,* **I.**13.31
Lasers (*Cont.*):
miniature dye, **I.**14.19
mixing rod applications for, **III.**2.33
mode-locked, **I.**14.2–**I.**14.3, **I.**14.7, **I.**14.9, **I.**14.9*f,* **II.**10.40
by regenerative feedback, **I.**14.21
for soliton generation, **IV.**1.42
(*See also* Mode-locking)
modulation response in, **IV.**4.19, **IV.**4.19*f,* **IV.**4.20
molecular nitrogen, **I.**11.16
multilongitudinal mode Fabry-Perot, **IV.**2.6
multimode, **IV.**4.12, **IV.**4.15, **IV.**4.23, **IV.**26.18
multiquantum well (MQWs), **I.**13.16, **I.**13.27, **I.**13.38
multiquantum well (MQWs)-distributed Bragg reflector (DBR), **II.**6.35
Nd:Glass, **I.**11.35
Nd:YAG, **I.**11.14, **I.**11.15*f,* **I.**11.35, **I.**14.22*f*
mode locking of, **I.**14.21
noise in, **IV.**4.22–**IV.**4.28, **IV.**26.35–**IV.**26.36, **IV.**26.43, **IV.**27.3–**IV.**27.4, **IV.**27.13–**IV.**27.14, **IV.**27.22
for optical data storage, **I.**13.8
as optical fiber system transmitter, **IV.**2.1, **IV.**2.5–**IV.**2.6, **IV.**12.24–**IV.**12.27
and optical lattices, **IV.**28.31–**IV.**28.32
organic dye, **I.**11.14, **I.**11.18–**I.**11.19, **I.**11.19*f,* **I.**11.34, **I.**11.34*f*
oxide stripe, **I.**13.8
and parametric device development, **IV.**22.1–**IV.**22.2
phase diffusion constant for, **IV.**26.28–**IV.**26.32
photon statistics for, **IV.**26.23–**IV.**26.26, **IV.**26.26*f,* **IV.**26.27
in point-to-point communications links, **IV.**1.24–**IV.**1.25
power and energy measurement of, **II.**24.35
probability flow diagram for, **IV.**26.24*f*
protection from (*see* Optical limiting)
proton-bombardment-defined, **I.**13.45
proton stripe, **I.**13.38*f*
pulsed, **I.**11.13, **IV.**26.19
pulsed-dye, **III.**1.34, **III.**1.34*f,* **III.**1.35
pumping and, **I.**11.10, **I.**11.13, **I.**11.19*f*–**I.**11.20*f*
quantum mechanics for, **IV.**26.6–**IV.**26.7, **IV.**26.15–**IV.**26.21
quantum well, **I.**11.37–**I.**11.38, **I.**13.7, **I.**13.10–**I.**13.11, **I.**13.11*f,* **I.**13.12, **I.**13.13*f*–**I.**13.14*f,* **I.**13.15, **I.**13.18, **I.**13.24, **I.**13.38, **IV.**4.1, **IV.**4.3–**IV.**4.4, **IV.**4.28–**IV.**4.31
long-wavelength, **I.**13.18–**I.**13.19
ridge waveguide, **I.**13.21
strained, **I.**13.16–**I.**13.17, **I.**13.28, **I.**13.28*t*

Lasers (*Cont.*):
quantum wire, **I.**13.19
as a radiometric characterization tool, **II.**24.35–**II.**24.36
reflectors for, **I.**42.41
relaxation oscillations in, **IV.**4.16–**IV.**4.17, **IV.**4.17*f,* **IV.**4.18–**IV.**4.19
resonance frequency of, **IV.**2.6
ridge waveguide, **I.**13.10, **I.**13.21
ring, **I.**11.31–**I.**11.32
ruby, **I.**11.14, **I.**11.14*f,* **I.**11.35, **I.**14.14
safety standards for, **III.**15.13–**III.**15.14
saturable absorbers in, **IV.**25.4–**IV.**25.11
semiconductor (*see* Semiconductor lasers)
servo system for, **IV.**27.6, **IV.**27.6*f,* **IV.**27.7, **IV.**27.7*f,* **IV.**27.8–**IV.**27.12
short cavity, **I.**14.20
single-frequency, **I.**13.40*f*
single-longitudinal-mode, **I.**13.41–**I.**13.42, **IV.**2.6, **IV.**12.27
single-mode, **IV.**4.12, **IV.**4.14, **IV.**12.27, **IV.**26.18
solid-state, **I.**11.13–**I.**11.14, **I.**11.18, **I.**11.19*f,* **I.**11.30, **I.**11.35
mode-locked, **I.**14.13
solid-state sum-frequency, **III.**1.34, **III.**1.34*f*
solitary, **IV.**25.15
soliton, **I.**14.6–**I.**14.7, **I.**14.18–**I.**14.19
spectral characteristics of emissions from, **IV.**4.14–**IV.**4.15
strained layer, **IV.**4.1, **IV.**4.31–**IV.**4.34
surface-emitting, **I.**13.42–**I.**13.43, **I.**13.44*f,* **I.**13.45
for surgical vision correction, **III.**11.11, **III.**11.16–**III.**11.17
synchronously pumped, **I.**14.9*f*
temperature dependence of, **IV.**4.12–**IV.**4.13
temporal coherence properties of, **I.**2.42
threshold for, **IV.**4.9–**IV.**4.10
Ti:Al_2O_3, **I.**11.36, **I.**11.36*f*
Ti:sapphire, **I.**14.9–**I.**14.10, **I.**14.14, **I.**14.18, **II.**39.21
transverse junction stripe, **I.**13.10
tunable, **IV.**2.6, **IV.**2.11, **IV.**18.43, **IV.**19.1, **IV.**27.14
tunable dye, **II.**20.6
turn-on delay for, **IV.**4.16, **IV.**4.17*f,* **IV.**4.18
twin-channel substrate mesa, **I.**13.23*f,* **I.**13.24
twin-channel (TCL), **I.**13.31
twin-ridge structure (TRS), **I.**13.21
types of, **I.**28.21*t*–**I.**28.22*t*
ultrafast, **IV.**24.25–**IV.**24.26, **IV.**25.3–**IV.**25.4, **IV.**25.16, **IV.**25.16*f,* **IV.**25.22
ultrashort (*see* Ultrashort lasers)
vertical cavity, **I.**13.44, **I.**13.45*f,* **I.**13.46*t*
surface-emitting, **IV.**2.6*n,* **IV.**4.2, **IV.**4.45–**IV.**4.50
wavelength division multiplexing (WDM), **I.**13.45
X-ray, **I.**11.33–**I.**11.34, **III.**33.1, **III.**33.4
(*See also specific type*)
Laser scanning, **II.**12.26*f,* **III.**5.4
Laser speckle, as multiple scattering effect, **III.**3.14
Laser stripe structure, **I.**13.8
Laser threshold, **IV.**4.9–**IV.**4.10, **IV.**26.27, **IV.**26.40
operation above, **I.**11.13
Lasing transition, **IV.**26.15, **IV.**26.18, **IV.**26.20
Lasing without inversion (LWI), **IV.**23.3, **IV.**23.10, **IV.**23.18, **IV.**26.42, **IV.**26.42*f,* **IV.**26.43
Latency, **IV.**12.16
Latent image (LI):
in color photography, **III.**6.8, **III.**6.8*n,* **III.**6.9, **III.**6.9*f*
and high-energy radiation, **III.**6.20–**III.**6.21
Latent-image speck, **I.**20.5
Lateral aniseikonia, **III.**12.18
Lateral color, **II.**18.41
Lateral geniculate nucleus (LGN), **I.**25.13–**I.**25.14, **I.**25.14*f,* **III.**10.1, **III.**10.3*f*
Lattice:
optical, **IV.**28.22, **IV.**28.25, **IV.**28.30–**IV.**28.31, **IV.**28.31*f,* **IV.**28.32–**IV.**28.33
semiconductor
multiphonon absorption, **II.**36.16–**II.**36.17, **II.**36.17*t,* **II.**36.18, **II.**36.18*f,* **II.**36.18*t*
and phonons, **II.**36.14–**II.**36.16
vibrational optical effects, **II.**36.18–**II.**36.23
Lattice absorption coefficient, **II.**36.19*f*
Lattice filters, tapered fiber fabrication of, **IV.**8.6
Lattice geometries, in photonic crystals, **IV.**20.4–**IV.**20.5
Lattice interactions adiabatic approximation, **I.**9.16
Lattice matching, **IV.**4.2
Lattice properties, **II.**36.6–**II.**36.7
Lattice vibrations, **II.**33.12–**II.**33.13, **II.**33.15, **II.**36.8, **II.**36.67, **II.**36.78
and dielectric constant, **II.**33.17
model parameters, **II.**33.81*t*
Laue, Max von, **III.**19.5, **III.**35.6
Laue diffraction, **III.**37.3–**III.**37.4
Laue equations, **III.**22.1
Laurent half shade, **II.**3.60
Layer Adding Method, **I.**44.21
Lead fluoride, refractive index for, **II.**33.71*t*
Lead molybdate, refractive index for, **II.**33.70*t*

Lead salt lasers, **I.**13.8
Lead vapor lasers, **I.**11.14*f*
Leakage current, **I.**22.12
Leaky-mode elements, in lasers, **I.**13.31
Leaky rays, **IV.**1.8, **IV.**1.8*f*
Least-squares method, **I.**34.18
Legacy film, **III.**6.24, **III.**6.24*t,* **III.**6.25–**III.**6.26, **III.**6.26*t*
Legal traceability, **II.**24.22
Legendre transformation, **I.**1.15, **I.**1.17–**I.**1.18
Legrende functions, **I.**6.15
Leica Summitar lenses, **II.**1.29, **II.**1.29*f,* **II.**1.33*f*–**II.**1.35*f*
Leman prism, **II.**4.13*f*
Length, measurement of, **II.**29.3
Lens arrays:
  as nonimaging optics uniformity control, **III.**2.2, **III.**2.33–**III.**2.38
  single, **III.**2.34–**III.**2.35, **III.**2.35*f*
  tandem, **III.**2.33–**III.**2.34, **III.**2.34*f,* **III.**2.35, **III.**2.36*f*–**III.**2.38*f*
Lenses:
  aberration curves in, **I.**33.1
  achromatic doublets, **II.**1.23, **II.**1.23*f,* **II.**1.24, **II.**1.24*f,* **II.**1.25, **II.**1.25*t,* **II.**1.26
    spherical aberration in, **II.**1.24
  afocal, **I.**1.49, **I.**1.57*f,* **I.**1.58, **I.**1.58*f,* **I.**1.59–**I.**1.60, **I.**1.60*f,* **I.**1.63, **II.**2.4
    catadioptric, **II.**2.21
    coaxial combination of, **I.**1.69*f,* **I.**1.70, **I.**1.70*f*
    finite conjugate, **II.**2.12
    vs. focal lenses, **I.**1.58
    four-powered-mirror, **II.**2.20, **II.**2.20*f*
    galilean, **II.**2.7, **II.**2.14, **II.**2.14*f*
    gaussian analysis of, **II.**2.2
    gaussian parameters of, **I.**1.59
    imaging geometry of, **II.**2.5, **II.**2.5*f*
    keplerian, **II.**2.7–**II.**2.8, **II.**2.11*f,* **II.**2.12
    optical invariant and, **II.**2.7
    relay train designs and, **II.**2.17, **II.**2.17*f*
    for scanners, **II.**2.12, **II.**2.12*f*
    three-powered-mirror, **II.**2.20, **II.**2.20*f*
    two-powered-mirror, **II.**2.19, **II.**2.19*f,* **II.**2.20
    unit power conjugate, **II.**2.21, **II.**2.21*f,* **II.**2.22
  alignment of, **I.**28.11
  Amici, **II.**1.11, **II.**1.11*f*
  antireflective (AR) coatings for, **III.**11.10
  aplanatic, **II.**1.6, **II.**1.10
  aspheric, **III.**2.9–**III.**2.10, **III.**2.10*f*
  for astigmatism, **III.**11.3, **III.**12.27
  axial gradient, **II.**9.3–**II.**9.4, **II.**9.4*f*
  axial preload in (*see* Axial preload)
  axis, **I.**1.35
  bicentric grinding of, **III.**11.15
Lenses (*Cont.*):
  bifocal, designing, **II.**8.13*f*
  bifocal intraocular, **III.**13.23
    implants, **III.**11.14
  Biotar, **II.**1.28, **II.**1.29*f*
  Bragg-Fresnel, **III.**23.7–**III.**23.8, **III.**23.8*f*
  camera (*see* Camera lenses)
  Celor, **II.**1.31*f*
  coaxial combinations of, **I.**1.68–**I.**1.70
  combined with concentrators, **III.**2.17
  for computer users, **III.**11.8–**III.**11.9
  contact (*see* Contact lenses)
  corrective, **III.**11.7–**III.**11.10
    (*See also* Spectacles)
  crown-in-front designs of, **II.**1.24
  custom, for higher-order aberrations, **III.**10.3
  database, **I.**34.3–**I.**34.4
  design process, **I.**34.3*f*
  diagrams of, **I.**1.51*f*–**I.**1.52*f*
  dialyte, **II.**1.25, **II.**1.25*t,* **II.**1.26, **II.**1.31*f*
  diffraction-limited, **I.**35.3, **II.**1.39, **II.**1.39*f,* **II.**1.40, **II.**1.40*f,* **II.**1.41
  dioptric power of, **III.**11.2
  distributed-index, **II.**7.3
  Double-Gauss, **II.**1.28
    unsymmetrical, **II.**1.29*f,* **II.**1.33*f*–**II.**1.35*f*
  drawn preform cylindrical, **II.**7.27
  Dyson, **II.**2.21, **II.**2.21*f*
  edging of, **I.**40.4–**I.**40.5
  electron, **I.**21.8, **I.**21.8*f*–**I.**21.9*f*
  entry process, **I.**34.3
  field, **I.**1.89, **I.**1.89*f,* **I.**32.8, **II.**1.10
  field flattener, **II.**1.29
  fish-eye, **II.**1.37*f*
  flint-in-front designs of, **II.**1.24
  focal, **I.**1.49, **I.**1.51*f*–**I.**1.52*f,* **II.**2.2–**II.**2.3, **II.**2.3*f*
    vs. afocal lenses, **I.**1.58
    axial separations in, **I.**1.56
    coaxial combination of, **I.**1.68, **I.**1.68*f,* **I.**1.69
    conjugate equations for, **I.**1.53–**I.**1.54
    distance between object and image in, **I.**1.55–**I.**1.56
    distortion-free, **II.**2.4
    images of distant objects and, **I.**1.55
    magnification in, **I.**1.54, **I.**1.56–**I.**1.57
    mechanical distances in, **I.**1.57
    nodal points of, **I.**1.52, **I.**1.52*f,* **I.**1.53
    principal focal lengths of, **I.**1.52
    principal focal points of, **I.**1.49
    principal planes of, **I.**1.49
    principal surfaces of, **II.**2.4
    reduced coordinates in, **I.**1.57
  focal length of, **II.**1.7
  to focus laser emission, **IV.**4.14

Lenses (*Cont.*):
Fresnel (hologram), **II.**7.23, **II.**7.23*f,* **III.**2.10–**III.**2.11
graded index (GRIN), **II.**7.3, **IV.**4.9, **IV.**4.14, **IV.**4.29, **IV.**10.8, **IV.**10.8*f,* **IV.**10.9
housings, **II.**34.17
clamshell, **II.**34.17*f*
collet, **II.**34.17*f*
hyperhemispheric, **III.**2.9
image quality of, **I.**35.5
imaging by
of spherical object, **II.**1.6*f*
of tilted object, **II.**1.7*f*
immersion, **II.**1.10
intraocular (*see* Intraocular lens (IOL))
landscape, **II.**1.17, **II.**1.17*f*–**II.**1.18*f,* **II.**1.19*t*–**II.**1.20*t*
Leica Summitar, **II.**1.29, **II.**1.29*f,* **II.**1.33*f*–**II.**1.35*f*
linear spot size in, **II.**1.36, **II.**1.38*f*
low-distortion telecentric projection, **I.**37.17
Luneberg, **I.**1.24, **III.**2.23
(*See also* Microlenses, distributed-index planar)
magnification by, **III.**12.17
materials for, **III.**11.7
micro-Fresnel (MFL), **II.**7.18, **II.**7.20*f*–**II.**7.21*f,* **II.**7.22, **II.**7.22*f*
aberration characteristics of, **II.**7.23, **II.**7.28*f*
advantages of, **II.**7.21
diffraction efficiency of, **II.**7.24, **II.**7.26*f*
fabrication technologies for, **II.**7.24, **II.**7.24*f*–**II.**7.26*f,* **II.**7.27, **II.**7.27*f*
thermal variations in, **II.**7.23
micro-optic (*see* Micro-optics)
microscope (*see* Microscope lenses; specific type)
molded glass aspheric, **I.**31.13*f*
mounting individual, **I.**37.2
adhesive rings for, **I.**37.5*f,* **I.**37.7*f*
burnished into cells, **I.**37.4, **I.**37.5*f*
conical interfaces for, **I.**37.6*f*
designs, low-cost, **I.**37.3–**I.**37.4
elastomeric designs for, **I.**37.13, **I.**37.13*f*
flat bevels, contact against, **I.**37.8, **I.**37.8*f*
sharp corner interfaces for, **I.**37.5*f*
spherical interfaces for, **I.**37.7, **I.**37.7*f*
threaded retaining rings for, **I.**37.4, **I.**37.7–**I.**37.8
toroidal interfaces for, **I.**37.6*f,* **I.**37.7
(*See also* Mirrors, mountings for; Prisms, mountings for)
mounting multicomponent
drop-in techniques for, **I.**37.14, **I.**37.14*f*–**I.**37.15*f*

Lenses, mounting multicomponent (*Cont.*):
machine-at-assembly techniques for, **I.**37.14–**I.**37.15, **I.**37.16*f*–**I.**37.17*f*
stacked-cell assembly techniques for, **I.**37.15, **I.**37.17, **I.**37.18*f*–**I.**37.19*f*
multi-element design of, **I.**31.11*f*
multifocal, in binary optics, **II.**8.12
negative, **II.**34.15
in neutron optics, **III.**36.6
noncoaxial combinations of, **I.**1.70
object-image relationship of, **II.**1.7
parabolic compound refractive, **III.**20.4, **III.**20.4*f,* **III.**20.8
performance of, **II.**1.30, **II.**1.36
periscopic, **II.**1.27, **II.**1.27*f,* **II.**1.28
Petzval, **II.**1.29, **II.**1.29*f,* **II.**1.36*f,* **II.**2.9, **II.**2.9*f*
photochromic, **III.**2.9
Planar, **II.**1.28
plastic, **I.**37.19–**I.**37.20, **I.**37.20*f,* **II.**7.7, **II.**7.8*f,* **II.**7.10
index of refraction for, **II.**7.7
shapes of, **II.**7.11*f*
tolerances for, **II.**7.7, **II.**7.10*t*
Polaroid, **III.**11.10
polychromatic, modulation transfer function (MTF) in, **II.**1.41
positive-powered, **II.**34.15
power of, **I.**1.49
prescriptions for, **III.**11.3, **III.**11.5, **III.**11.10, **III.**11.12, **III.**11.14–**III.**11.15
radial gradient, **II.**9.5, **II.**9.5*f,* **II.**9.6
Rapid Rectilinear, **II.**1.28, **II.**1.31*f*
refractive, thickness of, **II.**8.8*f*
relay, **II.**1.10
retrofocus, **I.**1.57
rotationally symmetric, **I.**1.65–**I.**1.67, **I.**1.67*f,* **I.**1.68
Schupmann, **II.**1.26
setup, in optical design, **I.**34.7
shape of, ease of manufacture and, **II.**7.11, **II.**7.11*f*
simple
imaging by, **II.**1.5*f*
thermal focus shift of, **I.**39.2
single element, **II.**1.11–**II.**1.12, **II.**1.12*f,* **II.**1.13–**II.**1.16, **II.**1.16*f*–**II.**1.17*f*
performance of, **II.**1.36–**II.**1.37
spherical, **III.**2.8–**III.**2.9
in nonimaging optics systems, **III.**2.8
spherical aberration in, **II.**1.11
stresses in
bending and, **I.**37.11–**I.**37.12
operating conditions and, **I.**37.12, **I.**37.12*f*
surface location, **I.**34.5

Lenses (*Cont.*):
surface profile, **I.**34.5
symmetrical, **II.**1.27–**II.**1.28
double astigmat, **II.**1.32*f*
telecentric, **I.**1.91, **I.**1.91*f,* **II.**2.11–**II.**2.12
telephoto, **I.**1.57, **II.**1.29–**II.**1.30
reverse, **II.**1.30, **II.**1.35*f*
Tessar, **II.**1.26*f,* **II.**1.27, **II.**1.33*f*
thin, power of, **III.**11.2
tinted, **III.**11.9, **III.**11.9*f,* **III.**11.9*t*
triplet, **II.**1.26, **II.**1.26*f,* **II.**1.27, **II.**1.32*f*
two-lens systems, **II.**1.20, **II.**1.20*f,* **II.**1.21, **II.**1.21*f,* **II.**1.22, **II.**1.22*f*
and vergence, **III.**12.22, **III.**12.25–**III.**12.27
X-ray, **III.**20.3–**III.**20.8
zoom, **II.**15.11
(*See also* Camera lenses, zoom)
(*See also* Contact lenses; Crystalline lens; Intraocular lens (IOL); Microlenses; Monolithic lenslet modules (MLMs); Objectives)
Lens law, **II.**1.7
Lenticular absorption, **I.**24.10, **I.**24.20
Leslie viscosity, **II.**14.10
Levels, **II.**29.16, **II.**29.16*f*
autoset, **II.**29.17*f*
L-I curve:
for lasers, **IV.**4.11–**IV.**4.12, **IV.**4.12*f*
for VCSELs, **IV.**4.49
LIDAR (light detection and ranging), **I.**16.12, **I.**44.38
Doppler, **I.**44.36, **I.**44.39*f*
Light:
atmospheric, **I.**44.10
circularly polarized, **I.**5.24–**I.**5.25, **I.**5.26*n,* **I.**5.28
classical wave versus quantum theory of, **IV.**26.7–**IV.**26.8, **IV.**28.4
in colorimetry, **I.**26.3
common sources of, **I.**28.20, **I.**28.20*t*
corpuscular theory of, **I.**8.5
from CRTs, **I.**27.15–**I.**27.16, **I.**27.17*f*
direction of propagation of, **I.**5.25
exposure to, **I.**28.19
finding metameters of, **I.**26.32–**I.**26.33
Mie scattering of, **I.**38.18, **I.**38.19*t*
partially polarized, **II.**22.7
from particulate-contaminated surfaces, **I.**38.18–**I.**38.19, **I.**38.20*f*–**I.**38.21*f,* **I.**38.22
perfectly coherent, **I.**4.13
polarized, **II.**22.7
propagation of, **I.**4.13–**I.**4.14
atmospheric turbulence effect on, **III.**1.8
in biological photoreceptor cells, **III.**9.3–**III.**9.4, **III.**9.12–**III.**9.15
Light (*Cont.*):
reflected, computing, **I.**26.25
scattering (*see* Scattering, of light)
sources of
Lambertian, **I.**4.13
nonradiating, **I.**4.19
perfectly coherent, **I.**4.10–**I.**4.11
perfectly incoherent, **I.**4.13, **I.**4.19–**I.**4.20
planar secondary, **I.**4.10
quasi-homogeneous, **I.**4.12–**I.**4.13, **I.**4.15, **I.**4.18
quasi-monochromatic, **I.**4.11–**I.**4.12
Schell model, **I.**4.12
thermal, **I.**4.13
spectrum of, **I.**4.20, **I.**4.24
limitations, **I.**4.20
normalized, **I.**4.6
stray
evaluation of
build-and-test approach, **I.**38.29, **I.**38.30*f*
computer analysis of, **I.**38.30–**I.**38.31
methods of evaluation, **I.**38.28
software analysis of, **I.**38.25–**I.**38.26
suppression of, **I.**38.1, **I.**38.11, **I.**38.11*f,* **II.**18.5, **II.**18.5*f*
varying sources of, **I.**28.14
(*See also* Radiation)
Light beams, polarization properties of, **II.**22.9–**II.**22.10
Light-emitting diodes (LEDs), **I.**12.1, **IV.**4.39–**IV.**4.41
$Al_xGa_{1-x}As$ system, **I.**12.18, **I.**12.18*t*
AlGaAs, output degradation of, **I.**12.30, **I.**12.30*f*
AlInGap system, **I.**12.19–**I.**12.20, **I.**12.20*f*
alphanumeric displays, **I.**12.34
blue, **I.**12.21
circuitry in, **IV.**4.45
dark-line defects in, **I.**12.30
in datacom systems, **IV.**4.1, **IV.**4.40
device structures, **I.**12.8
edge-emitting, **IV.**4.1, **IV.**4.39–**IV.**4.40, **IV.**4.42
extraction efficiency, **I.**12.8*t,* **I.**12.12*f*–**I.**12.13*f*
failure rate of, **I.**12.28*f*
for fiber-optic communications, **I.**12.16*f*
fiber-optics and, **I.**12.36
field quality of, **I.**28.11
GaAlAs, **I.**12.14*f*–**I.**12.15*f*
GaAs, **I.**12.10*f,* **I.**12.12*f*
GaAsP, **I.**12.11*f*
light output degradation of, **I.**12.29, **I.**12.29*f*
$GaAs_{1-x}P_x$ system, **I.**12.15
performance summary of, **I.**12.17*t*
hyperhemispheric lenses in, **III.**2.9
infrared, **I.**12.9*f*–**I.**12.10*f*

Light-emitting diodes (LEDs) (*Cont.*):
light degradation in, **I.**12.29–**I.**12.31
light generation in, **I.**12.3
to limit coherent crosstalk in WDM network, **IV.**13.26
Monte Carlo techniques used to evaluate, **III.**2.7
and multimode fiber, **IV.**1.9
numeric displays
monolithic, **I.**12.33–**I.**12.34
stretched-segment, **I.**12.33, **I.**12.33*f*–**I.**12.34*f*
operating characteristics of, **IV.**4.43–**IV.**4.45, **IV.**20.11
as optical fiber system transmitter, **IV.**2.1, **IV.**2.5–**IV.**2.6, **IV.**4.39, **IV.**12.25
optocouplers, **I.**12.35, **I.**12.35*f,* **I.**12.36
output optical power of, **IV.**4.43, **IV.**4.43*f*
in photometric to radiometric conversion, **III.**7.14, **III.**7.14*f*
plastic encapsulation of, **I.**12.8, **I.**12.27–**I.**12.28
plastic indicator lamps, **I.**12.31, **I.**12.31*f,* **I.**12.32, **I.**12.32*f*
quality of, **I.**12.27
radiative recombination in, **I.**12.3
reliability of, **I.**12.27–**I.**12.28
response times of, **IV.**4.44
reverse breakdown in, **I.**12.31
safety standards for, **III.**5.15
sensors
reflective, **I.**12.37
scattering, **I.**12.38
transmissive, **I.**12.37
structure of, **IV.**4.39, **IV.**4.40*f*
substrate criteria for, **I.**12.21
substrate doping in, **I.**12.22
surface-emitting, **IV.**4.39–**IV.**4.40, **IV.**4.40*f,* **IV.**4.41–**IV.**4.42
three-dimensional carrier confinement, **I.**12.16*f*
TIR Fresnel lenses in, **III.**2.11
wafer processing, **I.**12.24
water vapor and, **I.**12.27
in xerographic image creation, **III.**5.4
Light field, spectrum of, **I.**4.24
Light-gathering power, **I.**1.25
Light grasp, **I.**1.25
Light holes (LHs), and strained quantum wells, **IV.**4.32, **IV.**4.32*f,* **IV.**4.33
Lighting:
commercial, **III.**2.33
and Computer Vision Syndrome, **III.**16.1–**III.**16.2
Light intensity:
control of, **I.**28.12
distribution of, **I.**31.16*f*
scaling of, **I.**26.3–**I.**26.4, **I.**26.4*f*–**I.**26.5*f*
Light-material interaction, **II.**35.4
Lightpipes:
bent, **III.**2.20
as concentration method, **III.**2.13–**III.**2.14
for illumination uniformity (*see* Mixing rods)
and nonsequential surfaces, **III.**2.7
tapered, **III.**2.32, **III.**2.32*f,* **III.**2.33
Light piping, in photographic emulsions, **III.**6.7, **III.**6.7*f*
Light pressure force, **IV.**28.6
Light-quantum hypothesis, **IV.**26.8
Light scattering, **II.**20.30
polarization, **II.**22.27
(*See also* Scattering, of light)
Light-specimen interaction, **II.**36.60*f*
Light waves, **I.**3.2
Limiting amplifier, **IV.**12.40
Linear absorption, **I.**44.10, **IV.**17.20, **IV.**17.22–**IV.**17.24
Linear arrays, **III.**4.3
Linear birefringence, **III.**25.5, **III.**25.5*f,* **III.**25.6
Linear-chain model calculations, **II.**36.21*f*
Linear diattenuation, **II.**22.29
Linear dichroism, **II.**20.19, **III.**25.3
Linear electro-optic effect, **II.**6.22
Linear equations, **I.**26.46
simultaneous, **I.**26.47
Linearity, system, **II.**26.13
Linear optical materials:
harmonic oscillator model of, **II.**38.6, **II.**38.6*f*
macroscopic polarization in, **II.**38.4
Linear optical properties, of semiconductors, **II.**36.12
Linear polarization, **I.**2.4, **I.**5.12
analyzers for, **III.**25.4, **III.**25.4*f*
sensitivity, **II.**22.29
of X rays, **III.**25.2–**III.**25.3, **III.**25.3*f*
Linear polarizer, **II.**22.7
Linear resonance, **IV.**17.9
Linear spot size, in lenses, **II.**1.36, **II.**1.38*f*
Linear-systems analysis, **II.**32.1
Line filtering, **IV.**12.13, **IV.**12.14*f,* **IV.**12.15–**IV.**12.16
Linewidth:
Brillouin, **IV.**3.8–**IV.**3.9
broadening of, **I.**11.5, **IV.**12.30
of diode laser, **IV.**27.19–**IV.**27.20, **IV.**27.22
in doubly resonant oscillator, **IV.**22.26, **IV.**22.26*f*
of laser, **IV.**4.24–**IV.**4.25, **IV.**4.25*f,* **IV.**26.19, **IV.**26.31–**IV.**26.32, **IV.**26.32*f,* **IV.**26.35, **IV.**27.3–**IV.**27.4, **IV.**27.12, **IV.**27.15
of micromaser, **IV.**26.33–**IV.**26.34
Raman, **IV.**18.9, **IV.**18.10*f*

Linewidth enhancement factor, **IV.**4.20–**IV.**4.22, **IV.**4.25–**IV.**4.28
Liouville's theorem, **I.**1.45, **III.**31.7–**III.**31.8, **III.**31.10, **III.**35.7, **III.**36.15
Lippich half shade, **II.**3.60
Lippich prism, **II.**3.7, **II.**3.9*n,* **II.**3.11, **II.**3.13, **II.**3.13*n*
Lippman-Bragg holographic mirrors, **I.**42.52
Liquid crystal displays (LCDs), **I.**28.17, **II.**15.7
  aspheric lenses in, **III.**2.9
  backlit, **III.**2.42
  color
    geometry of, **I.**27.40
    pixel colorimetry, **I.**27.40–**I.**27.41
    quality of, **I.**27.36, **I.**27.39
    standards, **I.**27.42
  CPC use in, **III.**2.15
  monochrome, **I.**27.38
    components of, **I.**27.37, **I.**27.37*f*
  Monte Carlo techniques used to evaluate, **III.**2.7
  output variations, **I.**27.42–**I.**27.43
  pixel structure of, **I.**27.38, **I.**27.38*f*–**I.**27.40*f*
  and Polaroid lenses, **III.**11.1
Liquid crystals:
  dynamic scattering in, **II.**14.10
  field-induced director axis reorientation on, **II.**14.11
  field-induced nematic-cholesteric phase change in, **II.**14.11
  guest-host system in, **II.**14.10–**II.**14.11
  laser-induced phase change in, **II.**14.11–**II.**14.12
  light scattering in, **II.**14.12
  lyotropic, **II.**14.2
  modulating light in, **II.**14.10
  polymer-dispersed (*see* Polymer-dispersed liquid crystals (PDLC))
Liquid crystal spatial light modulators (LC-SLMs), **III.**8.3, **III.**10.8
Liquid Encapsulated Czochralski (LEC) technique, **I.**12.22
Liquid immersion development:
  in xerographic systems, **III.**5.10*f*
Liquid phase epitaxy (LPE), **I.**12.23, **I.**13.7, **I.**13.29*f,* **II.**6.16
Lister-type objective, **II.**17.1, **II.**17.3*f*
Lithium-drifted silicon detectors, **III.**34.5
Lithium niobate ($LiNbO_3$), **II.**6.25, **II.**6.37–**II.**6.38, **II.**39.14–**II.**39.15, **II.**39.34
  electro-optic effect in, **IV.**4.50–**IV.**4.52, **IV.**4.55
  in integrated optics (IO), **II.**6.14–**II.**6.16, **II.**6.16*f*
  optical damage and, **IV.**4.56–**IV.**4.57
  phase modulator for, **IV.**4.53, **IV.**4.53*f,* **IV.**4.54
  photorefractivity of, **IV.**4.56–**IV.**4.57
  velocity match in, **II.**6.23
Lithium niobate ($LiNbO_3$) modulators, **II.**6.19, **II.**6.23, **II.**13.18, **IV.**4.50–**IV.**4.57
  external, **IV.**4.2
  high-speed operation of, **IV.**4.55–**IV.**4.56
  insertion loss in, **IV.**4.56
  photorefractivity in, **IV.**4.56–**IV.**4.57
  polarization in, **IV.**4.55–**IV.**4.56
  propagation loss in, **IV.**4.56
Lithium tantalate ($LiTaO_3$), **II.**6.14, **II.**39.14
Lithography:
  electron beam, **II.**6.18, **III.**23.6–**III.**23.7
  EUV projection, **III.**35.5
  and global divergence, **III.**35.5. III.35.5*f*
  Schwarzschild objective applications in, **III.**27.1
  soft X-ray projection, **II.**11.6
  X-ray, **III.**19.10, **III.**30.3–**III.**30.4, **III.**33.2, **III.**35.5
Littrow gratings, **II.**5.10
Lloyd's mirror, **I.**2.18
Load resistor, for photodetector, **IV.**4.72
Lobster-eye optics, **III.**30.3
Local area network (LAN), **I.**13.4, **IV.**2.13
  amplification in, **IV.**11.2
  Ethernet standard for, **IV.**16.7
  FDDI as backbone in, **IV.**16.2
  optical fiber applications for, **IV.**1.24
  splitter used in, **IV.**10.2
Local characterization methods (LCM), of CRTs, **I.**27.21
  individual colors, **I.**27.25
  inverses, **I.**27.27–**I.**27.28
  one-dimensional color spaces, **I.**27.26
  out-of-gamut colors, **I.**27.28
  regions of color, **I.**27.26
Local gain, for lasers, **IV.**4.9
Local subscriber loop, optical fiber applications for, **IV.**1.24
Local vibrational modes (LVM), **II.**36.19–**II.**36.20, **II.**36.22, **II.**36.22*f*
  eigenvectors for, **II.**36.21*f*
  in semiconductors, **II.**36.22*t*
Locking range, **IV.**12.15
Long distance telecommunications:
  and chromatic dispersion, **IV.**13.6
  erbium-doped fiber amplifiers in, **IV.**13.3
  evolution of, **IV.**2.16
  optical amplifiers in, **IV.**2.12
  and rare-earth doped fibers, **IV.**1.47
  and single-mode fiber, **IV.**1.9, **IV.**1.11
  solitons in, **IV.**2.12, **IV.**7.5
Long Duration Exposure Facility (LDEF), **II.**37.19
Longitudinal chromatic aberration, **III.**9.7

Longitudinal Kerr effect, **IV.**25.11–**IV.**25.12
and external pulse compression, **IV.**25.12
and parametric amplification, **IV.**25.12–**IV.**25.13
and passive mode-locking, **IV.**25.13–**IV.**25.15
and self-phase modulation, **IV.**25.12, **IV.**25.12*f*
Longitudinal propagation velocity, of optical fiber, **IV.**1.10
Longitudinal relaxation rate, **IV.**24.5
Longitudinal relaxation time, **IV.**24.5, **IV.**24.15–**IV.**24.16
Long-period grating (LPG), for EDFA gain equalization, **IV.**13.19, **IV.**13.19*f*
Long-period grating (LPG) sensor, **IV.**15.9–**IV.**15.14
fabrication of, **IV.**15.10, **IV.**15.10*f*
operation of, **IV.**15.9–**IV.**15.10, **IV.**15.10*f*
strain sensitivity of, **IV.**15.11, **IV.**15.11*t,* **IV.**15.12, **IV.**15.12*f*–**IV.**15.13*f*
temperature sensitivity of, **IV.**15.12–**IV.**15.14, **IV.**15.14*t*
transmission spectrum of, **IV.**15.10, **IV.**15.11*f*
Long-trace profiler (LTP), **III.**26.5
Lorentzian signal recovery, **IV.**27.13
Lorentz micrograph, **I.**31.18*f,* **I.**31.19
Lorentz model, **I.**9.19, **I.**9.23, **II.**35.4–**II.**35.5
Lorentz theory, **II.**35.4–**II.**35.5
Loss (*see specific types*)
Loss discrimination, in optical fiber, **IV.**1.14
Loss minimum, and zero dispersion, **IV.**1.18
Lossy modes, **II.**10.13
Low-distortion telecentric projection lenses, **I.**37.17
Low-frequency fluctuations (LFFs), **IV.**4.28
LOWTRAN, **I.**44.21–**I.**44.24, **I.**44.24*f,* **I.**44.25, **I.**44.25*f,* **I.**44.26
LPE-based lasers, **I.**13.26*f*
Lucalox lamps, **I.**10.29, **I.**10.30*f*
Lumens:
conversion to watts, **III.**7.7
as photometric unit, **III.**7.7, **III.**14.1, **III.**14.4, **III.**14.4*t,* **III.**14.7
Luminance, **I.**25.31*n,* **II.**24.12, **II.**24.44
and computer work, **III.**16.2, **III.**16.2*f*
definition of, **III.**2.3, **III.**7.7
illuminance relationship with, **III.**14.9, **III.**14.9*f*
and integrating cavities, **III.**2.26–**III.**2.28
maximizing, **III.**2.12–**III.**2.13
photometric measure of, **III.**14.1, **III.**14.4*t,* **III.**14.5, **III.**14.6*f*
of point source, **III.**2.7
of spatially uniform sources, **III.**2.24
and spectral responsivity of human eye, **III.**14.3
and troland value, **III.**14.8
unit conversions in, **III.**7.9*t*
Luminance coefficient, **III.**14.10
Luminance factor, **III.**14.10
Luminescence, **IV.**4.39
electric dipole operators for, **II.**20.17
parametric, **II.**38.17
(*See also* Cathodeluminescence (CL); Electroluminescence (EL); Photoluminescence (PL); Thermoluminescence (TL))
Luminescence decay, **II.**36.74*f*
Luminescence spectroscopy, **II.**36.72
Luminescence spectrum, **II.**36.61, **II.**36.77*f*
of Cr^{3+}, **II.**28.20–**II.**28.21, **II.**28.21*f,* **II.**28.22, **II.**28.24*f*
of multiquantum wells (MQWs), **II.**28.23*f*
Luminosity, **I.**1.25
Luminous energy, **III.**14.4*t,* **III.**14.6
Luminous exitance, **III.**14.4*t,* **III.**14.6, **III.**14.6*f*
Luminous exposure, **III.**14.4*t,* **III.**14.6
Luminous flux, **II.**24.12, **II.**24.43
standards, **I.**10.9
total, **II.**24.46
(*See also* Lumens)
Luminous intensity, **II.**24.12, **II.**24.44, **III.**14.4, **III.**14.4*t,* **III.**14.5, **III.**14.5*f*
of Lambertian surface, **III.**14.9
standards, **I.**10.8
(*See also* Candela)
Luminous power, measuring, **I.**28.18
Lumped-electrode devices, **II.**6.15
Luneberg lens, **I.**1.24, **III.**2.23
(*See also* Microlenses, distributed-index planar)
Lux, **III.**7.7, **III.**14.4*t,* **III.**14.5
Lyddane-Sachs-Teller (LST) relationship, **I.**9.18, **II.**33.14, **II.**36.15
Lyot stop, **I.**38.8–**I.**38.9, **II.**18.5, **II.**18.41

Mach bands, **I.**25.38
Machine vision systems, **III.**4.3
Mach-Zehnder devices, tapered fiber technology for, **IV.**8.6, **IV.**8.6*f*
Mach-Zehnder filter, for EDFA gain equalization, **IV.**13.19
Mach-Zehnder interferometers (*see* Interferometers, Mach-Zehnder)
Mach-Zehnder modulators (*see* Modulators, Mach-Zehnder (MZ))
MacNeille polarizers, **I.**42.71, **I.**42.72*f*–**I.**42.73*f,* **I.**42.75*f*
Macrofocal reflectors, **III.**2.11
Macropsia, **III.**12.32
Macula lutea, **III.**15.1, **III.**15.12
Macular degeneration:
adaptive optics applications for, **III.**10.12–**III.**10.13
age-related, **III.**13.1, **III.**13.3, **III.**13.10, **III.**13.20

Macular pigment (MP), **III.**13.10, **III.**13.10*f*
Magnetic anisotropy, perpendicular, **I.**31.27
Magnetic atom trapping, **IV.**28.20, **IV.**28.20*f,* **IV.**28.21, **IV.**28.27
Magnetic circular dichroism (MCD), **III.**32.7
Magnetic circular polarization (MCP), **II.**20.21
Magnetic coercivity, high, **I.**31.18, **I.**31.18*n,* **I.**31.19
Magnetic field modulation (MFM), **I.**31.20, **I.**31.20*f,* **I.**31.21
Magnetic fields, in germanium, **II.**36.50*f*
Magnetic resonance imaging (MRI), **III.**35.25
Magnetic tape, **I.**31.1
Magneto-optical disks, **I.**31.2–**I.**31.4, **I.**31.5*f,* **II.**36.47*f*
Magneto-optical effects:
  excitonic, **II.**36.47–**II.**36.48
  interband, **II.**36.43–**II.**36.44
  Kerr, polar, **I.**31.22
Magneto-optical phenomena, **II.**36.42*t*
  in semiconductors, **II.**36.40–**II.**36.41
Magneto-optical readout, **I.**31.22
  differential detection system in, **I.**31.23, **I.**31.24*f*
  sources of noise in, **I.**31.25, **I.**31.25*f*
Magneto-optical recording, materials of, **I.**31.26
Magneto-optical systems, direct overwrite, **I.**31.31, **I.**31.31*f*
Magneto-optical trap (MOT), **IV.**28.22–**IV.**28.23, **IV.**28.23*f,* **IV.**28.24, **IV.**28.25*f,* **IV.**28.26–**IV.**28.28, **IV.**28.35
Magnetopolaron, **II.**36.51
Magnetoreflection, **II.**36.44–**II.**36.45, **II.**36.45*f*
  stress-modulated, **II.**36.46*f*
Magnets, dipole (bending), **III.**32.1, **III.**32.3–**III.**32.10
Magnification, **I.**1.31, **I.**1.46
  afocal, **II.**2.5
  airgap, **III.**35.30, **III.**35.31*f*–**III.**35.32*f*
  angular, **I.**1.56–**I.**1.57
    invariance in, **II.**2.5–**II.**2.6
  axial, **I.**1.31
  and bifocal jump, **III.**12.15–**III.**12.16
  in focal lenses, **I.**1.54, **I.**1.56–**I.**1.57
  lateral, **I.**1.31, **II.**1.5–**II.**1.7
  linear, **II.**2.3
  longitudinal, **I.**1.31, **I.**1.56, **II.**1.6–**II.**1.7
  and motion parallax, **III.**12.15
  nonuniform, from prism, **III.**12.10, **III.**12.10*f*
  and perspective distortion, **III.**12.13–**III.**12.14
  polycapillary optics for, **III.**30.15
  in reflection gratings, **III.**21.9
  relationship between, **I.**1.57
  scan, **II.**19.5
  secondary, **II.**18.42
  and stereopsis, **III.**12.14–**III.**12.15
  transverse, **I.**1.31, **I.**1.54
Magnification (*Cont.*):
  unequal binocular, **III.**12.17–**III.**12.20
  and vergence, **III.**12.25–**III.**12.27
  visual, **I.**1.31
  in X-ray microscopy, **III.**20.7
Magnification anamorphoser, adjustable, **II.**2.16
Magnification ellipse, **III.**12.17*f*
Magnifiers, **I.**32.8
  aplanatic hemispherical, **II.**1.11*f*
  aplanatic hyperhemispherical, **II.**1.11*f*
Magnifying glass, **II.**1.9
Magnifying power (MP), **II.**1.9
  definition of, **I.**32.8
Magnitude estimation, **I.**29.9
Maier and Meier theory, **II.**14.6
Maksutov-Cassegrain objectives, solid, **II.**18.21, **II.**18.21*f*
Maksutov objectives, **II.**18.21, **II.**18.21*f*
Malus, E. L., **I.**5.2, **I.**5.5*n*
Malus-Dupin principal, **I.**1.14
Mammography, **III.**35.25–**III.**35.27, **III.**35.31
Manchester coding, **IV.**12.12, **IV.**12.12*f*
  (*See also* Bi-phase coding)
Mandelbaum's phenomenon, **III.**18.11–**III.**18.13
Mandrel wrap, **II.**10.13*f*
Mangin-Cassegrain objectives, with correctors, **II.**18.26, **II.**18.26*f*
Mangin objectives, **II.**18.6–**II.**18.7, **II.**18.7*f*
Manly Rowe fraction, **IV.**18.16
Many-body effects, **IV.**25.19–**IV.**25.21
Marechal criterion, **I.**24.16
Marginal rays, **I.**1.82*f,* **II.**18.41
Markov approximation, **I.**44.31, **IV.**26.16, **IV.**26.22
Marple-Hess prism, **II.**3.14
Martin Black, **II.**37.8*f,* **II.**37.14, **II.**37.16–**II.**37.17, **II.**37.19, **II.**37.23, **II.**37.38–**II.**37.39
  BRDF of, **II.**37.32*f,* **II.**37.55*f*–**II.**37.56*f*
  enhanced, **II.**37.39
  post-treated, **II.**37.39
Maser, **IV.**26.18
Mask layout, **II.**8.14–**II.**8.15, **II.**8.15*f,* **II.**8.16, **II.**8.16*f,* **II.**8.17
Mass transport, **II.**7.27, **II.**7.29, **II.**7.29*f*–**II.**7.30*f*
Master-equation formulation, in laser theory, **IV.**26.6, **IV.**26.15–**IV.**26.23
Master oscillator power amplifier (MOPA) laser amplifier, **I.**13.43, **II.**6.27, **II.**6.27*f*
Matching, of stimuli, **I.**29.6
Material dispersion, **IV.**1.11, **IV.**1.18, **IV.**2.4
  in optical fibers, **II.**10.9
Materials, properties of, **II.**33.7, **II.**33.8*t*
MathCad, **III.**1.41
Mathematica, **III.**1.41
Matrices, **I.**26.44–**I.**26.45
Matrix algebra, **I.**26.44

Matrix multiplication, in wavefront reconstruction, **III.**1.35
Matrix transposition, **I.**26.44
Matrix-vector multiplier:
optical systolic, **I.**30.22
parallel, **I.**30.21, **I.**30.21*f*
serial incoherent, **I.**30.20, **I.**30.20*f,* **I.**30.21
Matter, condensed, optical properties of, **I.**9.4
MAXIMUM microscope, **III.**27.4
Maximum spectral luminous efficacy (of radiation) for photopic vision, **III.**14.2
Maximum tolerable input jitter (MTIJ), **IV.**6.17
Maxwell-Bloch equations, for coherent optical transients, **IV.**24.5–**IV.**24.7
Maxwell-Boltzmann velocity distribution, **II.**20.23–**II.**20.24
for atomic samples, **IV.**28.3, **IV.**28.9, **IV.**28.35
Maxwell fisheye, **I.**1.24, **III.**2.23
Maxwell-Garnett mixing formula, **III.**3.8
Maxwell-Helmholtz-Drude dispersion formula, **II.**33.14, **II.**33.25
Maxwellian perfection, **I.**1.32, **I.**1.60
Maxwellian view system, **I.**28.4, **I.**28.5*f,* **I.**28.17–**I.**28.18, **III.**15.1, **III.**15.9
advantages of, **I.**28.7
construction of complex, **I.**28.23
disadvantages of, **I.**28.8
focus of, **I.**28.4
retinal illuminance in, **I.**28.6
size of, **I.**28.5
two-channel apparatus, **I.**28.23, **I.**28.25*f*
Maxwell's electromagnetic theory, **I.**8.5
Maxwell's equations, **I.**3.2, **I.**5.2–**I.**5.4, **I.**6.4, **I.**6.17, **I.**7.3, **I.**9.5–**I.**9.6, **II.**36.4, **II.**36.54–**II.**36.55
nonlinear wave, in optical parametric generation, **IV.**22.3–**IV.**22.4
for photonic bandgap materials, **IV.**20.3–**IV.**20.4
in quantum theory, **IV.**26.10
and wave propagation, **III.**1.10, **III.**9.2
Maxwell's principle, **III.**6.17
Maxwell velocity distribution, **IV.**26.10
Mazer, **IV.**26.46
McCarthy objectives, **II.**18.35, **II.**18.35*f*
Mean-field approximation, **I.**6.18
Mean field theory, in thermotropic liquid crystals, **II.**14.
Measurement:
angle, **II.**29.12
in prisms, **II.**29.17–**II.**29.20
of curvature, **II.**29.20–**II.**29.23
distance, **II.**29.5
beam modulation, **II.**29.5, **II.**29.7, **II.**29.9
interferometric, **II.**29.8–**II.**29.12
focal length, **II.**29.20, **II.**29.25, **II.**29.27
interferometric, **II.**29.17
Measurement (*Cont.*):
length, **II.**29.3
simultaneous, **II.**30.20
straightness, **II.**29.12
time-of-flight method of, **II.**29.5
transverse aberration, **II.**29.27
velocity, **II.**29.27–**II.**29.29
Measurement bandwidths, **I.**7.10
Mechanical cycling, **II.**35.11
Mechanical resonances, in laser servo system, **IV.**27.8, **IV.**27.9*f,* **IV.**27.16, **IV.**27.20
Mechanical scanning, **II.**19.4
Mechanics:
Heisenberg's matrix, **I.**8.5
quantum, **I.**8.5
wave, **I.**8.5
Media interface connector (MIC), for FDDI, **IV.**16.3, **IV.**16.3*f*
Medial image, **II.**18.41
Medical X-ray imaging, **III.**19.5, **III.**19.10, **III.**35.24–**III.**35.33, **III.**37.3
contrast in, **III.**35.26, **III.**35.26*f,* **III.**35.27, **III.**35.28*f,* **III.**35.29–**III.**35.30, **III.**35.30*f*
resolution in, **III.**35.27, **III.**35.30–**III.**35.31, **III.**35.31*f,* **III.**35.32
scatter in, **III.**35.27, **III.**35.29, **III.**35.29*t,* **III.**35.30*f*–**III.**35.31*f*
Melt data sheet, **II.**33.31
Mercury arc lamps, **I.**10.25, **I.**10.27, **I.**10.27*f*–**I.**10.30*f,* **I.**10.33*f*
Mercury-xenon lamps, **I.**10.32, **I.**10.33*f*–**I.**10.34*f*
Meridional curves, off-axis, **I.**33.5, **I.**33.6*f*
Meridional plane, **I.**1.36
Meridional rays, **I.**1.25, **I.**1.39, **I.**1.41, **III.**2.13–**III.**2.14, **IV.**1.8, **IV.**1.8*f*
errors in, **I.**33.6
Mersenne objectives, afocal, **II.**18.11
Mersenne telescope, **II.**2.19
Mesh network topology, **IV.**13.14, **IV.**13.14*f*
Mesocotyl, **III.**9.2
Mesopic vision, **II.**24.41, **III.**7.9, **III.**7.13, **III.**14.3
Mesospheric sodium laser beacon, **III.**1.33–**III.**1.35, **III.**1.35*f*
Metal-insulator semiconductor (MIS) capacitor, **III.**4.2
Metalorganic chemical vapor deposition (MOCVD) lasers, **I.**13.24, **I.**13.29*f,* **I.**13.31
Metalorganic molecular beam epitaxy (MOMBE), **I.**13.7, **II.**6.16
Metalorganic vapor phase epitaxy (MOCVD), **I.**12.23–**I.**12.24, **I.**13.7
Metalorganic vapor phase epitaxy (MOVPE), **II.**6.16–**II.**6.17, **II.**6.19
Metal oxide semiconductor (MOS), **III.**4.2
readout, **I.**22.21–**I.**22.22

Metals:
absorption of light energy by, **II.**35.6
composition of, **II.**35.57*t*
crystal, elastic stiffness in, **II.**35.73*t*
elastic properties of, **II.**35.69
emittance of, **II.**35.54*t*–**II.**35.56*t*
extinction coefficient in, **II.**35.12, **II.**35.13*t*–**II.**35.20*t*
field propagating in, **II.**35.6
fracture properties of, **II.**35.74*t*
index of refraction in, **II.**35.12, **II.**35.13*t*–**II.**35.20*t*
linear thermal expansion of, **II.**35.60*t*–**II.**35.61*t*
mechanical properties of, **II.**35.8–**II.**35.9
optical properties of, **II.**35.3–**II.**35.5
physical properties of, **II.**35.7, **II.**35.57*t*
reflectance of, **II.**35.29*t*–**II.**35.41*t*
specific heat, temperature dependence of, **II.**35.68*t*–**II.**35.69*t*
strength of, **II.**35.9, **II.**35.69, **II.**35.74*t*
thermal properties of, **II.**35.7–**II.**35.8, **II.**35.56, **II.**35.59*t*
Metal-semiconductor-metal (MSM) detectors, **IV.**4.2, **IV.**4.66, **IV.**4.77–**IV.**4.78
Metameric black, **I.**26.33
Metamerism, **I.**26.8
light and, **I.**26.32
surface and illuminant, **I.**26.33
tristimulus coordinates and, **I.**26.31–**I.**26.32
Metamorphopsia, **III.**13.20
Meteorological optics, phenomena in, **I.**44.39–**I.**44.40
Meter, **II.**29.2
as SI base unit, **III.**7.2
Meter angle (MA), **III.**12.22
Meter-candle, **III.**7.8
Method of moments, **I.**6.18
Metrogon, **II.**1.35*f*
Metrology:
definition of, **II.**29.1
fundamental units of, **II.**29.2*t*
and mirror performance, **III.**26.5
Metropolitan area network (MAN), **IV.**2.13
MH2200, **II.**37.34
Michelson contrast, **I.**29.4
Michelson interferometer, **I.**2.26, **I.**2.27*f,* **I.**2.28, **I.**2.28*f,* **I.**2.41, **I.**2.41*f,* **II.**21.2–**II.**21.3, **II.**21.3*f,* **II.**21.5, **II.**21.22, **II.**21.22*f,* **II.**21.23, **II.**23.5, **II.**29.8, **II.**36.63, **IV.**9.8, **IV.**9.8*f*–**IV.**9.9*f*
Microanalysis:
with polycapillary optics, **III.**30.14
X-ray, **III.**20.5, **III.**20.8
Microaneurysm:
adaptive optics to detect, **III.**10.1, **III.**10.13
in diabetic retinopathy, **III.**13.21
Microbeam irradiation, **II.**17.47
Microbolometers, **I.**23.14–**I.**23.15
Microcalorimeter, **III.**34.8
Microcavities, in photonic crystals:
creating, **IV.**20.6–**IV.**20.7, **IV.**20.7*f*
and crosstalk, **IV.**20.17
quality factor of, **IV.**20.7–**IV.**20.8, **IV.**20.8*f*
Microchannel plates (MCPs), **I.**21.9, **I.**21.9*f*–**I.**21.10*f,* **I.**21.11–**I.**21.12, **I.**21.12*t,* **I.**21.13*f,* **III.**34.6
electron multipliers, **I.**21.7
gain in, **I.**21.14*t*
II, proximity-focused, **I.**21.17–**I.**21.18, **I.**21.18*t*
Microchannel plate tubes (MCPT), **I.**15.31, **I.**15.32*f*
Microcreep strength, **II.**35.9
Microdensitometers, **I.**20.16–**I.**20.17, **I.**20.17*f,* **I.**20.22*f*
Microdiffraction, **III.**26.6, **III.**35.14
Microelectromechanical membrane systems (MEMS):
in head-mounted displays, **III.**18.2
in wavefront correction, **III.**10.8
Microfluorescence, **III.**26.6, **III.**30.14, **III.**35.14
Microfocusing, **III.**20.5–**III.**20.6, **III.**20.6*f,* **III.**20.7, **III.**26.6, **III.**35.15
Microfocus X-ray fluorescence (MXRF):
crystal diffraction in, **III.**35.22, **III.**35.22*f*–**III.**35.23*f*
monocapillary, **III.**35.18
polycapillary, **III.**35.19, **III.**35.19*f,* **III.**35.20, **III.**35.20*f*–**III.**35.21*f*
ultra-high resolution in, **III.**35.22–**III.**35.23
Micro-Fresnel (MFL) lenses, **II.**7.18, **II.**7.20*f*–**II.**7.21*f,* **II.**7.22, **II.**7.22*f*
aberration characteristics of, **II.**7.23, **II.**7.28*f*
advantages of, **II.**7.21
diffraction efficiency of, **II.**7.24, **II.**7.26*f*
fabrication technologies for, **II.**7.24, **II.**7.24*f*–**II.**7.26*f,* **II.**7.27, **II.**7.27*f*
thermal variations in, **II.**7.23
Microlenses:
Corning, **II.**7.19*f*
cylindrical, **II.**7.31
distributed-index planar, **II.**7.13, **II.**7.13*f*–**II.**7.15*f*
aberrations in, **II.**7.14*f,* **II.**7.15, **II.**7.17*f*
characteristics of, **II.**7.17*t*
diffusion times for, **II.**7.14*t*
fabrication techniques for, **II.**7.13–**II.**7.14
index distribution in, **II.**7.14, **II.**7.16*f*
ion exchange in, **II.**7.13
elliptical cylindrical, **II.**7.30*f*
molded, **II.**7.5
SMILE, **II.**7.14, **II.**7.17–**II.**7.18, **II.**7.18*f*–**II.**7.20*f*

Micromanipulator, **II.**17.48
Micromaser, **IV.**26.6, **IV.**26.16, **IV.**26.18–**IV.**26.19
  master equation for, **IV.**26.21–**IV.**26.23
  phase diffusion constant for, **IV.**26.33–**IV.**26.34
  photon statistics for, **IV.**26.27–**IV.**26.28, **IV.**26.29*f*
Micro-optic lenses (*see* Micro-optics)
Micro-optics:
  binary optics and, **II.**8.7, **II.**8.7*f,* **II.**8.8
  design considerations of, **II.**7.2–**II.**7.5
  properties of materials in, **II.**7.9*t*
  uses of, **II.**7.2
Micro-optic technologies:
  for coupling functions, **IV.**8.1
  for networking, **IV.**10.1–**IV.**10.11
Micropsia, **III.**12.32
Microroughness (MR), **III.**26.4–**III.**26.5, **III.**28.5
Microscope lenses:
  aberrations in, **II.**17.19–**II.**17.20, **II.**17.20*f*
  classification of, **II.**17.12
  color-coded rings on, **II.**17.15*t*
  coverslip correction of, **II.**17.13, **II.**17.15*f*
  design of, **II.**17.12, **II.**17.18–**II.**17.19
  distortion in, **II.**17.18
  field size of, **II.**17.17–**II.**17.18
  high-dry objectives, **II.**17.15, **II.**17.16*f*
  infinity-focused, **II.**17.16–**II.**17.17, **II.**17.17*f*
  nonhomogeneous immersion, **II.**17.15
  nonimmersion, **II.**17.13
  oil immersion, **II.**17.13
    aplanatic condition of, **II.**17.19*f*
  types, **II.**17.14*t*
    and corrections, **II.**17.13*t*
  water immersion, **II.**17.13–**II.**17.14
  working distance and, **II.**17.17, **II.**17.17*t*
Microscopes, **I.**32.8, **I.**32.8*f*
  aperture function in, **II.**17.38
  aperture scanning, **II.**17.43
  beam-scanning, **II.**17.41
  beam-shearing, **II.**17.28
  bright field, **II.**17.22–**II.**17.24
  compound, **II.**1.9
  confocal, **II.**17.40–**II.**17.41, **II.**17.41*f,* **II.**17.42–**II.**17.43, **II.**17.47
    Kino-type real-time, **II.**17.42*f*
  conjugate planes in, **II.**17.5
  contrast generation in, **II.**17.22, **II.**17.24*f*
  dark field, **II.**17.25
  depth in specimen space in, **II.**17.12
  depth of field in, **II.**17.9, **II.**17.12
  depth of focus in, **II.**17.9–**II.**17.10
  differential interference contrast (DIC), **II.**17.26, **II.**17.32–**II.**17.34, **II.**17.35*f*
  dimensions of, **II.**17.48*f,* **II.**17.49, **II.**17.49*t*
  dissecting, **II.**17.47
Microscopes (*Cont.*):
  electron, **II.**17.3
  epi-illumination in, **II.**17.38, **II.**17.39*f,* **II.**17.41
  fluorescence, **II.**17.34–**II.**17.37, **II.**17.46
  high-resolution compound, early, **II.**17.2
  history of, **II.**17.1
  interference, **II.**17.28, **II.**17.31, **II.**17.31*f,* **II.**17.32, **II.**17.34*f*
  Jamin-Lebedeff, **II.**17.33*f*
  laser-scanning epi-illuminating confocal, **II.**17.42
  light, **II.**17.3, **II.**17.44
    specimen manipulation in, **II.**17.47
  Mach-Zehnder, **II.**17.28, **II.**17.31, **II.**17.31*f,* **II.**17.32
  Mirau, **II.**17.31–**II.**17.32, **II.**17.34*f*
  modulation contrast, **II.**17.26, **II.**17.27*f*
  Nomarski, **I.**41.11, **I.**41.11*f*
  objective
    definition of numerical aperture, **II.**17.2*f*
    oil-contacted achromatic, **II.**17.3*f*
  oculars in (*see* Oculars)
  phase contrast, **II.**17.2, **II.**17.44
  polarizing, **II.**17.27, **II.**17.29*f*–**II.**17.30*f,* **II.**17.32
    birefringence in, **II.**17.28
  proximity-scanning, **II.**17.43
  ray paths in, **II.**17.4, **II.**17.4*f,* **II.**17.5, **II.**17.5*f,* **II.**17.6, **II.**17.6*f*
  Schwarzschild soft X-ray, **II.**11.28, **II.**11.28*f,* **II.**11.29
  single sideband enhancement (SSBEE), **II.**17.26
  total frustrated reflection, **II.**17.25
  transilluminating, **II.**17.5, **II.**17.37, **II.**17.38*f*
  traveling, **II.**29.24, **II.**29.24*f,* **II.**29.25
  video, digital enhanced, **II.**17.43
Microscopy:
  atomic force, **III.**26.5
  retinal, **III.**10.2, **III.**10.9
  scanning electron, **III.**35.16, **III.**35.18
  Schwarzschild objective applications for, **III.**27.1, **III.**27.2*f,* **III.**27.4, **III.**27.4*f,* **III.**27.5
  X-ray applications for, **III.**19.6, **III.**19.10, **III.**20.8*f*–**III.**20.9*f,* **III.**32.19, **III.**33.2, **III.**35.4
Microspectroscopy, **III.**27.1
Microstrain, **II.**35.9
Microwave links, fiber analog transmission for, **IV.**2.14–**IV.**2.15
Microyield strength, **II.**35.9
Midsagittal plane, **III.**12.2
Mie, Gustav, **I.**6.12
Mie calculations, **I.**6.13–**I.**6.14
Mie scattering, **I.**38.18, **I.**43.33, **I.**44.10
  aerosols, particulates and clouds, **I.**44.15–**I.**44.16, **I.**44.16*f*–**I.**44.19*f*

Mie theory, **I.**6.12, **I.**6.17, **III.**6.4, **III.**6.6
Miller algorithm, **I.**6.16
Miller's rule, **II.**38.9
Millilambert, **III.**7.8
Milliphot, **III.**7.8
Mini-APART, **I.**38.28
Miniature dye lasers, **I.**14.19
Minimum acceptable power (MAP), for receiver, **IV.**1.27
Minimum resolvable contrast (MRC), **III.**4.3
Minimum resolvable temperature (MRT), in focal plane arrays (FPA), **I.**23.29, **I.**23.29*f*
Minkowitz interferometers, **II.**29.10*f*
Minority-carrier injection, **I.**12.2
Minox camera, **II.**1.22
Mirage, **I.**44.40, **I.**44.42*f*–**I.**44.43*f*
  ray path of, **II.**9.2*f*
Mirau interferometers, **II.**21.14*f*
Mirrored tiling, in lightpipes, **III.**2.30, **III.**2.30*f*–**III.**2.31*f*
Mirror-image effect, **I.**5.6, **I.**5.11
Mirrors:
  bimorph, **III.**1.38, **III.**1.39*f*
  bird-wing, **II.**39.9, **II.**39.9*f*
  Bragg, **IV.**4.34–**IV.**4.35, **IV.**4.46–**IV.**4.47, **IV.**4.50
  bridge, **II.**39.9, **II.**39.9*f*
  cat, **II.**39.9, **II.**39.9*f*
  cold, **I.**42.58, **I.**42.58*f*
  combined with concentrators, **III.**2.18
  conic, **II.**18.2, **II.**18.3*f*
  conical foil imaging (*see* Conical foil imaging mirrors)
  deformable, **III.**1.7*f,* **III.**1.8, **III.**1.11, **III.**10.1, **III.**10.8
  design of, **II.**35.9–**II.**35.11, **II.**35.11*t*
  and electron impact sources, **III.**31.11
  in Fabry-Perot semiconductor lasers, **IV.**12.26
  focal spot size of, **III.**35.4
  Fresnel's, **I.**2.16*f*
  frogs' legs, **II.**39.9, **II.**39.9*f*
  graded reflectivity, **I.**42.52, **I.**42.53*f*
  heat load on, **III.**26.5–**III.**26.6
  high-reflectivity, **III.**24.5–**III.**24.6, **III.**24.7*f*
  hot, **I.**42.58
  Lippman-Bragg holographic, **I.**42.52
  magnetic, **III.**36.7
  for microfocusing, **III.**26.6
  mountings for
    bonded, **I.**37.22, **I.**37.23*f*
    flexure, **I.**37.23, **I.**37.24*f,* **I.**37.25
    mechanically clamped, **I.**37.21, **I.**37.21*f*–**I.**37.22*f*
  multilayer coatings for, **III.**24.1–**III.**24.3, **III.**24.5–**III.**24.6, **III.**35.4
Mirrors (*Cont.*):
  nested, for X-ray focusing, **III.**28.6–**III.**28.7, **III.**28.8*f,* **III.**35.8–**III.**35.9, **III.**35.9*t*–**III.**35.11*t*
  parabaloidal, in lithographic applications, **III.**35.5
  Pfund, **II.**5.8*f*
  in piezoelectric transducers, **IV.**27.16–**IV.**27.17
  in Raman oscillators, **IV.**18.4
  in Schwarzschild objective, **III.**27.1, **III.**27.2*f*–**III.**27.3*f*
  segmented, **III.**1.38–**III.**1.39, **III.**1.39*f,* **III.**10.2, **III.**10.8
  self-pumped phase conjugate (*see* Self-pumped phase conjugate mirrors (SPPCMs))
  single-sheeted, **III.**1.17–**III.**1.18, **III.**10.2
  stacked-actuator continuous-facesheet, **III.**1.38–**III.**1.40
  steering, **III.**1.17–**III.**1.18
  surface quality of, **III.**26.4–**III.**26.5, **III.**28.4–**III.**28.5
  in synchrotron X-ray optics, **III.**26.3–**III.**26.6
  telescope secondary, **I.**37.25
  threshold conditions, **I.**11.11–**I.**11.12, **I.**11.12*f*
  TIR used for, in nonimaging devices, **III.**2.17
  X-ray, **III.**20.6, **III.**35.9
  XUV, **I.**42.53
  Zerodur, **I.**37.25
MIT Media Lab, **III.**17.11
Mixing rods:
  applications of, **III.**2.33
  as nonimaging optics uniformity control, **III.**2.2, **III.**2.28–**3.**2.33
  shape of, **III.**2.28–**III.**2.31
  (*See also* Lightpipes)
MKS system, rationalized, **II.**38.23–**II.**38.24
Mobile radios, multichannel AM transmission for, **IV.**12.15
Modal bandwidth concatenation length scaling factor, **IV.**6.9
Modal dispersion, **IV.**6.9
Modal gain:
  for lasers, **IV.**4.9
  for strained layer lasers, **IV.**4.33, **4.**33*f*
Modal noise, **IV.**2.10
  in optical link power budget, **IV.**6.17–**IV.**6.18
  in VCSELs, **IV.**4.49
Mode converter, TE-TM, **II.**6.25, **II.**6.25*f*
Mode coupling, **IV.**8.4
  in Fiber Bragg grating, **IV.**15.6, **IV.**15.6*f*
  in long-period grating, **IV.**15.9, **IV.**15.10*f*
Mode hopping:
  in doubly resonant oscillators, **IV.**22.24, **IV.**22.24*f,* **IV.**22.25–**IV.**22.26, **IV.**22.30, **IV.**22.32

Mode hopping (*Cont.*):
in multimode lasers, **IV.**4.15, **IV.**4.23, **IV.**4.25, **IV.**4.27
in optical link power budget, **IV.**6.11, **IV.**6.13
in pump-enhanced oscillators, **IV.**22.41
in VCSELs, **IV.**4.48
Model-dependent characterization methods (MDCM), of CRTs, **I.**27.21, **I.**27.28
conditions for use, **I.**27.32
gun independence, **I.**27.29
inverse transformations, **I.**27.34
out-of-gamut colors, **I.**27.35
parameters, measurement of, **I.**27.32–**I.**27.34
phosphor constancy, **I.**27.30–**I.**27.31
phosphor output models, **I.**27.31
Mode-locking, **I.**14.20, **IV.**12.28–**IV.**12.29, **IV.**12.29*f,* **IV.**12.30
acousto-optic, **I.**14.18
additive pulse (APM), **I.**14.15, **I.**14.18, **IV.**25.14
continuous wave, **IV.**25.5*f,* **IV.**25.10–**IV.**25.11, **IV.**25.14
double, **I.**14.9–**I.**14.10, **I.**14.10*f*
hybrid, **I.**14.9, **I.**14.11, **I.**14.18
injection seeding, **I.**14.18
with interactivity second harmonic, **I.**14.12, **I.**14.12*f*
intracavity parametric, **I.**14.12–**I.**14.13
Kerr lens, **I.**14.17–**I.**14.18, **IV.**17.27
of lasers, **IV.**25.4, **IV.**25.5*f,* **IV.**25.6, **IV.**25.8–**IV.**25.9, **IV.**25.9*f,* **IV.**25.10
and longitudinal Kerr effect, **IV.**25.13–**IV.**25.15
moving mirror, **I.**14.18
passive, **I.**11.22, **I.**11.29–**I.**11.30, **I.**11.31*f,* **I.**14.2–**I.**14.3, **I.**14.7, **I.**14.11–**I.**14.12, **I.**14.16, **I.**14.18, **IV.**25.6, **IV.**25.8–**IV.**25.9, **IV.**25.9*f,* **IV.**25.10–**IV.**25.11
absorption saturation in, **I.**14.5–**I.**14.6
high-power oscillators and, **I.**14.4
methods of, **I.**14.4
pulse-shaped elements, **I.**14.7
phase modulation and dispersion in, **I.**14.6
pulse shaping in, **I.**14.4–**I.**14.5
regenerative, **IV.**12.40
by regenerative feedback, **I.**14.21
self, **I.**14.14, **I.**14.18
self-defocusing in, **I.**14.6
self-starting, **I.**14.16–**I.**14.17
in semiconductor lasers, **I.**14.7
in solid-state lasers, **I.**14.13
synchronously pumped, **I.**14.7–**I.**14.9, **I.**14.18
Mode partition noise, **IV.**2.9–**IV.**2.10, **IV.**6.2, **IV.**12.1
in edge-emitting lasers, **IV.**4.1
in multimode lasers, **IV.**4.23, **IV.**4.24*f*
Mode partition noise (*Cont.*):
in optical link power budget, **IV.**6.11–**IV.**6.12, **IV.**6.12*f,* **IV.**6.13–**IV.**6.14
Mode stripping, **II.**10.13, **IV.**1.15
Modified chemical vapor deposition (MCVD), **II.**10.43, **II.**10.43*f,* **IV.**1.45, **IV.**1.45*f*
Modified involute, with gap, **III.**2.12, **III.**2.12*f*
MODTRAN, **I.**44.21–**I.**44.23, **I.**44.26
Modulation, **I.**15.9, **IV.**21.1
all-optical, **IV.**21.2, **IV.**21.7
amplitude, **II.**13.21, **II.**13.30
analog, **II.**13.15
in coherent optical communications, **IV.**1.36–**IV.**1.37, **IV.**1.37*f*
color spaces, **I.**26.15
cross-phase, **IV.**3.3–**IV.**3.4
degree of, **II.**13.32
delta, **I.**28.16
depth-of-amplitude, **II.**13.21
depth-of-phase, **II.**13.18
efficiency, **II.**13.32
frequency, **II.**13.23
index
amplitude, **II.**13.21, **II.**13.29
phase, **II.**13.18, **II.**13.29–**II.**13.30
laser, **IV.**2.6, **IV.**27.12–**IV.**27.14, **IV.**27.22
frequency shift keying (FSK) and, **I.**13.39
mode locking and, **I.**14.6
in semiconductors (*see* Semiconductor lasers, modulation in)
of LEDs, **IV.**2.6, **IV.**4.41
linear, **II.**13.21
OTDM networks, **IV.**12.30–**IV.**12.31
percent, **II.**13.31–**II.**13.32
phase, in ruby lasers, **I.**14.14
piezoelectrically induced diffraction, **I.**14.20
in point-to-point communications links, **IV.**1.24–**IV.**1.25
polarization, **II.**13.18–**II.**13.19, **II.**13.19*f,* **II.**13.21
vertical linear, **II.**13.20*f*
pulse-width, **I.**28.16
self-phase, **IV.**3.1, **IV.**3.3
techniques, **II.**36.69*t*
voltage, **II.**13.18
Modulation error ratio (MER), **IV.**6.4–**IV.**6.5
Modulation instability, **IV.**3.3, **IV.**3.11
Modulation response:
in lasers, **IV.**4.19, **IV.**4.19*f,* **IV.**4.20
in LEDs, **IV.**4.45
Modulation transfer function (MTF), **I.**35.2, **I.**35.4–**I.**35.5, **I.**35.5*f,* **II.**1.40, **II.**11.28, **II.**19.6*f,* **II.**32.3, **II.**32.9
and aging, **III.**13.11–**III.**13.12, **III.**13.12*f*
calculations, **II.**32.4

Modulation transfer function (MTF) (*Cont.*):
and chromatic smear, **III.**18.6, **III.**18.8*f*
comparison of, **I.**24.24, **I.**24.24*f*
in computed radiography, **III.**35.30–**III.**35.32, **III.**35.32*f*
and contrast transfer functions (CTF), **II.**32.9*f*
diffraction-limited, **II.**32.4, **II.**32.5*f,* **II.**32.6, **II.**32.8
effect of defocus on, **II.**32.5, **II.**32.5*f*
field angle and, **I.**24.25*f*
geometrical-aberration, **II.**32.8
and human visual aberrations, **III.**10.4, **III.**10.5*f*
and image resolution, **III.**18.6, **III.**18.7*f*
measurements, **II.**32.7
in microscopes, **II.**17.23*f*–**II.**17.24*f*
in ocular systems, **I.**24.14, **I.**24.14*f,* **I.**24.20, **I.**24.21*f,* **I.**24.22, **I.**24.22*f*
in photographic emulsions, **III.**6.6
in polychromatic lenses, **II.**1.41
and sampling, **III.**4.18, **III.**4.18*f*–**III.**4.19*f*
in scanner apertures, **II.**19.10
for Schwarzschild objective, **III.**27.1, **III.**27.2*f,* **III.**27.3
of solid-state camera, **III.**4.15
in xerographic image development, **III.**5.7
Modulation transfer spectroscopy, **IV.**27.20
Modulators, **IV.**4.1–**IV.**4.2
acousto-optic (*see* Acousto-optic modulators (AOM))
balanced bridge, **II.**6.23
bandwidth in, **II.**13.30–**II.**13.31
bulk, **II.**13.15–**II.**13.16
cut-off, **II.**6.25
Debye-Sears, **II.**20.9
delta-beta reversal, **IV.**4.57
directional coupler, **II.**6.23
electroabsorption, **IV.**4.57–**IV.**4.63
electro-optic, **II.**3.57, **II.**6.20, **II.**13.15, **IV.**4.64, **IV.**12.31–**IV.**12.32, **IV.**12.32*f,* **IV.**12.33, **IV.**12.33*f,* **IV.**21.1, **IV.**27.4, **IV.**27.14, **IV.**27.17, **IV.**27.19
design considerations in, **II.**13.28
frequency response in, **II.**13.28
signal voltage in, **II.**13.28
electrorefractive semiconductor, **IV.**4.64–**IV.**4.65
extinction ratio in, **II.**13.31
frequency, **II.**13.24, **II.**13.24*f*
deviation, maximum, **II.**13.31
half-way drive, **II.**6.31
integrated optical, **II.**6.30
integrated semiconductor laser/electroabsorption, **II.**6.26*f*
Modulators (*Cont.*):
intensity, **II.**13.21, **II.**13.22*f*
interferometric, **II.**6.29–**II.**6.30, **II.**6.31*f*
lithium niobate (*see* Lithium niobate ($LiNbO_3$) modulators)
longitudinal, **II.**13.15–**II.**13.16, **II.**13.16*f,* **II.**13.17, **II.**13.17*f,* **II.**13.19–**II.**13.20
lumped-electrode, **II.**6.30
Mach-Zehnder (MZ), **II.**6.23–**II.**6.24, **II.**6.24*f,* **II.**6.25–**II.**6.26, **II.**6.29–**II.**6.30, **II.**10.35
optical insertion loss in, **II.**13.32
package traveling-wave, **II.**6.30
parameters of, **II.**6.30
performance criteria in, **II.**13.30
phase-change, **IV.**4.2
piezo-optic, **II.**3.57
polarization, **II.**13.26
polymer, **II.**6.23
push-pull, **II.**13.23
scophony light, **II.**12.29
semiconductor, **II.**6.23
semiconductor interferometric, **IV.**4.66
sinusoidal transfer characteristics in, **II.**6.23
spatial light, **I.**30.8
transverse, **II.**13.15–**II.**13.16, **II.**13.16*f,* **II.**13.18
traveling, **II.**6.23
wave, **II.**13.29, **II.**13.29*f,* **II.**13.30
Mohs scale, **II.**33.33, **II.**33.33*f*
Moiré test, **II.**30.25
Molded glass aspheric lenses, **I.**31.13*f*
Mole, as SI base unit, **III.**7.2
Molecular absorption, **I.**44.11–**I.**44.12
Molecular beam epitaxy (MBE), **I.**12.23–**I.**12.24, **I.**13.7, **II.**6.16, **II.**36.8, **IV.**25.22
defined, **I.**13.7
Molecular nitrogen lasers, **I.**11.16
Molecular orientational Kerr effect, **IV.**17.5*t,* **IV.**17.15–**IV.**17.16
Molecules, vibrational and rotational spectra of, **I.**8.21–**I.**8.24
Molybdenum:
absorptance vs. temperature in, **II.**35.53*f*
extinction coefficient for, **II.**35.16*t*–**II.**35.17*t* vs. wavelength, **II.**35.25*f*
index of refraction in, **II.**35.16*t*–**II.**35.17*t* vs. wavelength, **II.**35.25*f*
reflectance of, **II.**35.35*t*–**II.**35.37*t* vs. wavelength, **II.**35.44*f*
specific heat of, **II.**35.71*f*
thermal conductivity of, **II.**35.65*f*–**II.**35.66*f*
Moments method, in bandwidth normalization, **III.**7.16
Monin-Obukhov similarity theory, **I.**44.30
Monitors (*see* Cathode ray tube (CRT))

Monocapillary X-ray optics:
applications for, **III.**29.4–**III.**29.6, **III.**35.4, **III.**35.8–**III.**35.9, **III.**35.18
condensing, **III.**29.2–**III.**29.3, **III.**29.3*f,* **III.**29.4–**III.**29.6
design of, **III.**29.1, **III.**29.2*f,* **III.**29.3, **III.**29.3*f,* **III.**29.4
and electron impact sources, **III.**31.11
fabrication of, **III.**29.4
imaging, **III.**29.3, **III.**29.3*f,* **III.**29.4
materials for, **III.**29.1, **III.**29.2*t*
Monocentric system, **II.**18.41
Monochromatic aberration:
in binary optics, **II.**8.7
ocular, **I.**24.15–**I.**24.16, **I.**24.16*f,* **I.**24.17, **I.**24.17*f*
Monochromatic diffraction theory, **I.**4.11
Monochromators:
Bragg case, **III.**22.1, **III.**22.2*f,* **III.**22.4–**III.**22.6
crystal, **III.**22.1–**III.**22.5, **III.**22.5*f,* **III.**22.6, **III.**22.6*f*
Czerny-Turner, **II.**20.6
double-pass, **II.**5.9*f*
grating, **II.**20.7, **II.**24.37
Laue case, **III.**22.1, **III.**22.2*f,* **III.**22.4–**III.**22.6
in medical X-ray imaging, **III.**35.33
Perkin-Elmer Model 99 double-pass, **II.**5.4, **II.**5.9*f*
prism-based, **II.**36.63
prism-grating double, **II.**5.13
refraction-grating, **III.**21.5
Seya-Namioka vacuum-ultraviolet, **II.**3.40
and synchrotron beam mirrors, **III.**26.3–**III.**26.4
and throughput-limited applications, **III.**32.1
in X-ray diffraction analysis, **III.**35.8
Monocular visual cues, **III.**12.4–**III.**12.6, **III.**12.13
Monolithic lenslet modules (MLMs), **II.**7.12, **II.**7.12*f*
Monovision:
for presbyopia correction, **III.**13.23
in virtual reality environments, **III.**12.33–**III.**12.34
Monte Carlo techniques, **I.**44.21
for lightpipe, **III.**2.29
in nonimaging optics, **III.**2.7
in optical link power budget modeling, **IV.**6.5
for photographic emulsions, **III.**6.6
for ray tracing, **II.**11.12, **III.**2.7–**III.**2.8
in stray light evaluation, **III.**2.7
Mordant, in color photographic film, **III.**6.4
Morse interatomic potential, **II.**33.19
Mosaic crystals, **III.**22.2
Moseley's law, **III.**31.7
MOSFET and CCD (MOS/CCD) arrays, **I.**23.16
Motion detection, **I.**25.38–**I.**25.39, **I.**25.39*f,* **I.**25.40–**I.**25.42, **III.**2.33
Motion parallax, **III.**12.2–**III.**12.3, **III.**12.5*f,* **III.**12.6, **III.**12.15, **III.**12.30, **III.**12.32
Motion perspective, **III.**12.5*f,* **III.**12.7*f*
Motion picture film, **III.**6.5, **III.**6.11, **III.**12.6
Mott-Wannier exiton model, **II.**36.27–**II.**36.29
Moving Electron Beam Exposure System (MEBES), **II.**8.16–**II.**8.17
Mueller calculus, **I.**5.26–**I.**5.28, **II.**22.8
Mueller matrix, **I.**6.11, **II.**22.8, **II.**22.10, **II.**22.11*t*–**II.**22.12*t,* **II.**22.14
coordinate system for, **II.**22.12–**II.**22.13
inhomogeneity of, **II.**22.33
interpretation of, **II.**22.28
nondepolarizing, **II.**22.31–**II.**22.32
physically realizable, **II.**22.30
for polarization component characterization, **II.**22.25
sample-measuring polarimeters for, **II.**22.16–**II.**22.17
Multichannel communications, four-wave mixing in, **IV.**1.42–**IV.**1.43
Multichannel dispersion compensator, **IV.**9.8–**IV.**9.9, **IV.**9.8*f*
Multichannel plate (MCP) X-ray optics, **III.**30.1–**III.**30.2, **III.**30.2*f,* **III.**30.3, **III.**30.3*f*–**III.**30.4*f*
Multichannel video transmission, **IV.**2.14–**IV.**2.15
Multifilter radiometry, **III.**7.16
Multifocal lenses, in binary optics, **II.**8.12
Multilayer reflective coatings:
and absorption, **III.**24.1–**III.**24.2, **III.**24.5, **III.**24.6*t*
applications for, **III.**24.3, **III.**24.5–**III.**24.6, **III.**35.4, **III.**35.8–**III.**35.9
design of, **III.**24.2, **III.**24.5
performance of, **III.**24.2–**III.**24.11, **III.**35.9*t*–**III.**35.11*t*
with pinch plasmas, **III.**33.3
production of, **III.**24.5
programs for (URLs), **III.**24.5
properties of, **III.**24.3, **III.**24.3*f,* **III.**24.4–**III.**24.5, **III.**24.7–**III.**24.8
with Schwarzschild objective, **III.**27.4
Multilayer structures:
signal-to-noise ratio enhancement, **I.**31.23
thermal optimization of media in, **I.**31.21, **I.**31.21*f*
Multilongitudinal mode Fabry-Perot laser, **IV.**2.6
Multimode fibers, **IV.**1.9, **IV.**2.1–**IV.**2.2
attenuation measurement for, **IV.**1.15, **IV.**1.15*f*
bandwidth measurement for, **IV.**1.17, **IV.**2.3–**IV.**2.4

Multimode fibers (*Cont.*):
for datacom systems, **IV.**4.1
dispersion in, **IV.**1.9–**IV.**1.11, **IV.**2.3–**IV.**2.4, **IV.**6.9
effective area of, **IV.**3.7
and gain-guided lasers, **IV.**4.14
noise in, **IV.**2.10, **IV.**6.17
normalized variables for, **IV.**1.12
transmission loss for, **IV.**6.7
Multimode interferometer (MMI), **IV.**4.66
Multimode lasers:
for low-cost communications systems, **IV.**4.12
mode hopping in, **IV.**4.15
mode partition noise in, **IV.**4.23
operation of, **IV.**26.18
Multiparticle coherent emission, **III.**32.2, **III.**32.19
Multipass fiber strain measurement, **IV.**1.20, **IV.**1.21*f*
Multipath interference, in optical link power budget, **IV.**6.14
Multiphase reflectors, **III.**2.40
Multiphonon absorption, **II.**36.19*f,* **II.**36.20*t*
in semiconductors, **II.**36.16–**II.**36.17, **II.**36.17*t,* **II.**36.18, **II.**36.18*f,* **II.**36.18*t*
Multiphoton absorption, **I.**9.31
Multiple-beam Bragg diffraction (MBD), **III.**25.7–**III.**25.8, **III.**25.8*f*
Multiple beam interference, **I.**2.34
diffraction grating, **I.**2.29, **I.**2.29*f*–**I.**2.30*f,* **I.**2.34
plane-parallel plate, **I.**2.31, **I.**2.31*f,* **I.**2.32, **I.**2.33*f*
Multiple Mirror Telescope (MMT), **III.**1.8
Multiple quantum wells (MQWs), **IV.**4.30, **IV.**4.31*f,* **IV.**12.33
Multiple scattering, **III.**3.3
diffusion approach to, **III.**3.11–**III.**3.12
effects in, **III.**3.13–**III.**3.16
equations for, **III.**3.9–**III.**3.10
radiative transfer in, **III.**3.10–**III.**3.13
and wave attenuation, **III.**3.8–**III.**3.9
Multiple Stokes scattering, **IV.**18.2*f,* **IV.**18.3, **IV.**18.3*t,* **IV.**18.39, **IV.**18.41*f*
Multiple surface concentrators, **III.**2.17–**III.**2.18
Multiple-wafer transducers, **IV.**27.17
Multiplexed fiber-interferometer sensor, **II.**21.19
Multiplexer, **IV.**10.4, **IV.**10.4*f,* **IV.**10.5, **IV.**10.10, **IV.**10.10*f*–**IV.**10.11*f*
add-drop, **IV.**13.12, **IV.**13.13*f,* **IV.**13.15, **IV.**13.25, **IV.**13.25*f*
prism as, **IV.**10.5, **IV.**10.6*f*
time, **IV.**12.8*f*
Multiplexing, **IV.**1.31, **IV.**12.1, **IV.**12.4, **IV.**13.2 (*See also specific type*)
Multiplication, analog, **I.**30.5
Multiplier phototube, **I.**15.9
Multipop photography, **III.**6.23
Multiquantum well (MQWs), **II.**28.13, **II.**39.21–**II.**39.22, **II.**39.22*f,* **II.**39.23
lasers, **I.**13.16, **I.**13.27, **I.**13.38
photorefractive, **II.**39.22, **II.**39.23*f*
Multispeed chopper, **I.**10.12
Multi-TeraHertz bandwidth transmission channel, **II.**10.14
Multivapor arc lamps, **I.**10.28, **I.**10.29*f*
Multiwavelength Optical Network (MONET), **IV.**13.16
Murty interferometers, **II.**30.8, **II.**30.11*f*
Mutually incoherent beam coupler, **II.**39.9, **II.**39.9*f*
Mutually pumped phase conjugator (MPPC) (*see* Double phase conjugate mirror)
Mux noise, **III.**4.11
Mylar, **I.**20.4–**I.**20.5
Myoid, **III.**9.2
in idealized photoreceptor, **III.**9.8, **III.**9.10*f,* **III.**9.15
photomechanical responses by, **III.**9.11–**III.**9.12
Myopia, **I.**24.31–**I.**24.33, **III.**11.2, **III.**11.2*f,* **III.**11.6, **III.**12.2, **III.**12.31, **III.**13.5
axial, **III.**12.18, **III.**12.26
and computer work, **III.**16.5
current research on, **III.**11.17–**III.**11.18
and head-mounted display systems, **III.**12.32
and image stabilization, **III.**12.30
and pupil size, **III.**15.9
surgical correction of, **III.**11.16–**III.**11.17, **III.**13.24
Mythical Man-Month, The (Brooks), **I.**34.25

Nakamura biplate, **II.**3.60
Naperian absorption coefficient, **III.**9.8
Narrow beams, **I.**1.47
Narrow pencils, **I.**1.47
National Institute of Standards and Technology (NIST), **III.**7.3, **III.**14.12
Frequency and Time Division, **IV.**27.4
neutral atom trapping experiments at, **IV.**28.20
optical molasses experiments at, **IV.**28.15
National Synchrotron Light Source (NSLS), **III.**33.2
In-Vacuum UNdulator (IVUN), **III.**32.14*f*–**III.**32.16*f*
Natural broadening, **I.**11.6
Natural guide star (NGS), **III.**1.5–**III.**1.7, **III.**1.22, **III.**1.23*f,* **III.**1.29, **III.**1.33
Natural stop shift, **II.**7.3
Navigation:
virtual reality applications for, **III.**17.10
and visual perception, **III.**12.6

NBS Black, **II.**37.17, **II.**37.41–**II.**37.42
diffuse scatter in, **II.**37.57*f*
total integrated scatter in, **II.**37.57*f*
Nd:Glass lasers, **I.**11.35
Nd:YAG lasers, **I.**11.14, **I.**11.15*f,* **I.**11.35, **I.**14.22*f*
mode locking of, **I.**14.21
Nearsightedness (*see* Myopia)
Near triad, **III.**12.24
NE DT, **I.**23.28*f*
in focal plane arrays (FPA), **I.**23.26–**I.**23.27, **I.**23.27*f*
spatial noise in, **I.**23.28
Negative dispersion, **IV.**25.12–**IV.**25.14
Negative feedback, in lasers, **I.**14.11
Negative lenses, **II.**34.15
NEI, **I.**15.9
Nelsonian illumination, **III.**2.24
Nematic liquid crystals:
director's distribution of, **II.**14.15–**II.**14.16, **II.**14.16*f*
dynamic response in, **II.**14.17
homeotropic alignment of, **II.**14.13
optical transmission of, **II.**14.14–**II.**14.15, **II.**14.15*f*
parallel alignment of, **II.**14.12–**II.**14.13
reorientational effects in, field induced, **II.**14.12
total free energy of, **II.**14.15
twist alignment of, **II.**14.13–**II.**14.14, **II.**14.14*f*
Neodymium-doped fiber amplifier (PDFA), **IV.**11.3
Neoprene:
reflectance of, **II.**37.39*f*
transmittance of, **II.**37.43*f*
Nerst glower, **I.**10.12, **I.**10.15*f*
globar, gas mantle and, compared, **I.**10.16, **I.**10.17*f*
spectral characteristics of, **I.**10.13
Nerve fiber, in human eye, **III.**10.1, **III.**10.3*f*
Nested mirrors, for X-ray focusing, **III.**28.6–**III.**28.7, **III.**28.8*f,* **III.**35.8–**III.**35.9, **III.**35.9*t*–**III.**35.11*t*
Networks:
of dielectric materials, **IV.**20.4–**IV.**20.5
neural (*see* Neural networks)
passive optical, **IV.**2.13
reconfigurable, **IV.**13.14–**IV.**13.15, **IV.**13.15*f,* **IV.**13.16
topologies for, **IV.**13.13–**IV.**13.14, **IV.**13.14*f*
(*See also specific types*)
Neumann boundary condition, **I.**7.2
Neumann's principle, **II.**33.7
Neural networks:
artificial, **III.**1.38
in electronic imaging technology, **III.**17.7
and spline surfaces, **III.**2.7
Neural networks, **II.**39.30–**II.**39.31
Neural pathways, retinal, **I.**25.10, **I.**25.11*f*
Neurons:
cortical, **I.**25.15
receptive-field properties of, **I.**25.12*n,* **I.**25.14–**I.**25.15
V1 (*see* Visual cortex, primary (V1))
Neutron detectors, **III.**36.15–**III.**36.16
Neutron diffraction, **III.**36.3
Neutron gravity spectrometer, **III.**36.6*f*
Neutron optical filter, **III.**36.14, **III.**36.14*f*
Neutron optics:
applications for, **III.**36.3–**III.**36.4
attenuation in, **III.**36.7
development of, **III.**19.5, **III.**36.3–**III.**36.5, **III.**37.3–**III.**37.4
diffraction in, **III.**36.3, **III.**36.9–**III.**36.10
guides in, **III.**36.8–**III.**36.9, **III.**36.12, **III.**36.14–**III.**36.15
interference in, **III.**36.10–**III.**36.11, **III.**36.11*f,* **III.**36.12
Larmor precession in, **III.**36.13
polycapillary application to, **III.**36.15
refraction in, **III.**36.5–**III.**36.6
sources in, **III.**36.12–**III.**36.13
Neutrons:
collimation of, **III.**36.13–**III.**36.14
polarization of, **III.**36.6–**III.**36.7, **III.**36.13
prism deflection of, **III.**36.6
properties of, **III.**36.3
ultracold, **III.**36.9–**III.**36.10
Neutron scattering, **III.**3.6, **III.**36.3–**III.**36.5, **III.**36.7–**III.**36.8, **III.**36.8*f,* **III.**36.12
Neutron therapy, **III.**35.34
New oxide materials, index of refraction for, **II.**33.71*t*
Newtonian objectives, **II.**18.7
Newtonian view system, **I.**28.2, **I.**28.2*f,* **I.**28.6
limits to, **I.**28.4
Newton imaging equation, **II.**1.8
Newton interferometer, **I.**2.25, **II.**30.7
Newton's equations, **I.**1.53–**I.**1.56, **I.**1.76
Newton's rings, **I.**2.11–**I.**2.12, **I.**2.20, **I.**2.22, **I.**2.25
Nextel Black Velvet, **II.**37.32–**II.**37.33
hemispheric reflectivity of, **II.**37.44*f*
Nextel Brand Suede Coating Series 3101–C10, **II.**37.33
Nextel 2010, **II.**37.33
Nickel:
extinction coefficient for, **II.**35.17*t*–**II.**35.18*t*
vs. wavelength, **II.**35.25*f*
index of refraction in, **II.**35.17*t*–**II.**35.18*t*
vs. wavelength, **II.**35.25*f*
reflectance, **II.**35.37*t*–**II.**35.38*t,* **II.**35.52*f*
vs. wavelength, **II.**35.44*f,* **II.**35.52*f*

Nickel (*Cont.*):
specific heat of, **II.**35.71*f*
thermal conductivity of, **II.**35.65*f*–**II.**35.66*f*
Nicol prisms, **II.**3.7, **II.**3.17, **II.**3.17*f*–**II.**3.18*f*
square-ended, **II.**3.19
trimmed, **II.**3.18
Night myopia, **I.**24.32
Night-vision devices, **I.**21.9, **I.**21.19
1964 10° color-matching functions, **I.**26.13–**I.**26.14
Nipi modulator, **IV.**4.65
Nippon Sheet Glass, **II.**9.2, **II.**9.6–**II.**9.7
Nitrous oxide, Fourier-transform infrared spectrum of, **II.**28.5, **II.**28.6*f*
Nits, **II.**24.47, **III.**7.7
Nodal slide bench, **II.**29.25–**II.**29.26, **II.**29.26*f*
Noise, **I.**18.3*f*
atomic, **IV.**26.35–**IV.**26.36
in erbium-doped fiber amplifiers, **IV.**5.5–**IV.**5.6
as a function of frequency, **I.**15.18
Johnson, **I.**15.9, **I.**18.4
laser, **I.**31.12, **IV.**4.22–**IV.**4.28, **IV.**26.35–**IV.**26.36, **IV.**26.43, **IV.**27.3–**IV.**27.4, **IV.**27.13–**IV.**27.14, **IV.**27.22
in laser servo system, **IV.**27.5, **IV.**27.7–**IV.**27.8
low-frequency, **I.**18.4
in optical amplifier, **IV.**11.3, **IV.**11.6–**IV.**11.7
and optical link power budget, **IV.**6.5, **IV.**6.14–**IV.**6.15
parametric, **IV.**22.8
in photodetectors, **IV.**4.73–**IV.**4.74, **IV.**4.77
in point-to-point communications links, **IV.**1.24, **IV.**1.26–**IV.**1.28, **IV.**1.28*f,* **IV.**1.28*t,* **IV.**1.29–**IV.**1.30
and quantization, **IV.**12.10
and receiver sensitivity, **IV.**2.7–**IV.**2.9
and solid-state arrays, **III.**4.11–**III.**4.13
and solid-state cameras, **III.**4.13–**III.**4.15
with solitons, **IV.**1.31
sources of, **I.**18.3, **I.**18.5*f*–**I.**18.6*f*
in magneto-optical readouts, **I.**31.25, **I.**31.25*f*
nonessential, **I.**18.5
visual, and photoreceptor waveguiding, **III.**9.4
(*See also specific types*)
Noise-equivalent electrons, **III.**4.11
Noise equivalent exposure (NEE), **III.**4.10–**III.**4.11
Noise equivalent power (NEP), **IV.**4.75
spectral, **I.**15.10
Noise equivalent quanta (NEQ), **I.**20.25
Noise equivalent temperature difference (NETD), in thermal arrays, **I.**19.8–**I.**19.9
Noise figure, of rare-earth doped amplifier, **IV.**5.6
Noise floor, **III.**4.11
Noise spectrum, **I.**15.9
Noll, R. J., **III.**1.12–**III.**1.13
Nomarski interferometers, **II.**21.4, **II.**21.5*f*
Nomarski microscope, **I.**41.10, **I.**41.11*f*
Nonchromogenic color film, **I.**20.15
Nonconcomitant vision, **III.**12.2
Noncritical phase matching (NPM), **II.**12.30, **II.**12.32*f*
Nondegenerate four-wave mixing (NDFWM), **IV.**23.25
Non-diffraction-limited optic, **I.**39.6
Nonimaging optics, **III.**2.1
computer simulation of, **III.**2.6–**III.**2.8
concentration methods used in, **III.**2.12–**III.**2.23
flux uniformity control in, **III.**2.2
system components of, **III.**2.8–**III.**2.12
terms used in, **III.**2.2–**III.**2.6
Nonlinear absorption (NLA), **IV.**17.9–**IV.**17.11, **IV.**17.14–**IV.**17.15, **IV.**17.15*f,* **IV.**17.21, **IV.**17.28
for optical limiting, **IV.**19.4*f,* **IV.**19.5, **IV.**19.5*f,* **IV.**19.6, **IV.**19.6*f,* **IV.**19.7
in organic molecules, **IV.**19.10
Z-scan to measure, **IV.**17.31–**IV.**17.33
Nonlinear directional coupler (NLDC), **IV.**21.5, **IV.**21.5*f,* **IV.**21.6
Nonlinear distortion, **IV.**18.49–**IV.**18.50
compensation for, **IV.**3.12
in fiber analog systems, **IV.**2.15
Nonlinear frequency mixing, **IV.**3.1–**IV.**3.2, **IV.**23.22–**IV.**23.23, **IV.**23.23*f,* **IV.**23.24–**IV.**23.25, **IV.**23.25*f*
Nonlinearities, optical, **IV.**3.1–**IV.**3.2, **IV.**13.3–**IV.**13.4, **IV.**13.6
and all-optical switching, **IV.**21.1
as coherent radiation source, **IV.**22.1–**IV.**22.2
cross-phase modulation, **IV.**3.3–**IV.**3.4, **IV.**13.7, **IV.**13.7*f*
and electromagnetically induced transparency, **IV.**23.2–**IV.**23.3, **IV.**23.27–**IV.**23.28
in femtosecond SPPOs, **IV.**22.58
four-wave mixing, **IV.**1.42–**IV.**1.43, **IV.**3.9–**IV.**3.12, **IV.**13.8, **IV.**13.8*f,* **IV.**25.18, **IV.**25.18*f,* **IV.**25.19
and free polarization decay, **IV.**24.10
frequency dependence of, **IV.**17.4–**IV.**17.5, **IV.**17.5*t*
in gas phase media, **IV.**23.3
and impairments, **IV.**2.16
at maximal atomic coherence, **IV.**23.26–**IV.**23.27, **IV.**23.36*f*
in optical limiting, **IV.**19.1–**IV.**19.9
photorefractive, **IV.**1.43
pulse compression, **IV.**1.41–**IV.**1.42
in saturable absorbers, **IV.**25.6

Nonlinearities, optical (*Cont.*):
self-phase modulation, **IV.**3.3, **IV.**13.7, **IV.**13.7*f*
in semiconductors, **IV.**19.10
and soliton propagation, **IV.**1.40–**IV.**1.42, **IV.**7.1, **IV.**7.4, **IV.**7.4*f,* **IV.**7.12–**IV.**7.13, **IV.**7.17
stimulated Brillouin scattering, **IV.**1.39–**IV.**1.40, **IV.**3.7–**IV.**3.9
stimulated Raman scattering, **IV.**1.39–**IV.**1.40, **IV.**3.4–**IV.**3.7
tensor nature of, **IV.**17.5
third-order (*see* Third-order optical nonlinearities)
and ultrashort pulse generation, **IV.**25.4, **IV.**25.15
(*See also specific types*)
Nonlinearity, microscopic origin of, **II.**38.11
Nonlinear laser spectroscopy, **IV.**27.14
Nonlinear loop mirror (NOLM), **IV.**12.38
in all-optical switching, **IV.**21.5, **IV.**21.5*f,* **IV.**21.6, **IV.**21.6*f*
Nonlinear materials:
for optical parametric generation, **IV.**22.62–**IV.**22.65
quasi-phase-matched (QPM), **IV.**22.2, **IV.**22.33, **IV.**22.35, **IV.**22.54, **IV.**22.59–**IV.**22.60
Nonlinear optical effects, **II.**38.5
Nonlinear optical media, anharmonic oscillator model of, **II.**38.8*f*
Nonlinear optical parametric wavelength conversion, **IV.**11.10, **IV.**22.1–**IV.**22.2
Nonlinear optical phenomena, **II.**36.55*t*–**II.**36.56*t*
Nonlinear optical processes, second-order, phase-matching in, **II.**38.12–**II.**38.13, **II.**38.13*f,* **II.**38.14, **II.**38.14*f*
Nonlinear optical properties, **II.**36.54–**II.**36.55
Raman scattering and, **II.**36.57–**II.**36.58
second-order, **II.**36.56
third-harmonic generation, **II.**36.57
third-order, **II.**36.55
Nonlinear optical susceptibility:
quantum theory of, **II.**38.10–**II.**38.11
second-order, anharmonic oscillator model of, **II.**38.7
tensor, second-order, **II.**38.11–**II.**38.12
Nonlinear polarization, **IV.**3.2, **IV.**3.5, **IV.**3.8, **IV.**3.10, **IV.**17.4, **IV.**17.9, **IV.**17.24, **IV.**17.26–**IV.**17.27, **IV.**17.31
Nonlinear refraction (NLR), **IV.**17.9–**IV.**17.11, **IV.**17.13–**IV.**17.14, **IV.**17.28
for optical limiting, **IV.**19.4*f,* **19.**7–**IV.**19.8
Z-scan to measure, **IV.**17.31–**IV.**17.33
Nonlinear scattering, for optical limiting, **IV.**19.4*f,* **IV.**19.8–**IV.**19.9
Nonlinear Schrödinger equation (NSE), **II.**10.39, **II.**10.39*f,* **IV.**1.41, **IV.**1.41*t,* **IV.**3.4, **IV.**7.2, **IV.**17.28, **IV.**28.34
Nonlinear switching devices, **IV.**5.1
Nonlinear wave equation, **IV.**3.2
Nonpolarizing element, **II.**22.7
Non-return-to-zero (NRZ) format, **IV.**12.12, **IV.**12.12*f,* **IV.**12.37*f*
clock recovery for, **IV.**12.15*f,* **IV.**12.16, **IV.**12.36
power spectrum for, **IV.**12.13*f*
Nonsequential ray tracing, **III.**2.6–**III.**2.7
Non-Uniform Rational B Splines (NURBS), **III.**2.7
Non-zero dispersion-shifted fibers (NZ-DSF), **IV.**13.10, **IV.**13.10*f*
Normal dispersion, range of, **II.**35.5
Normalization, **III.**7.15–**III.**7.18
Normalized Detector Irradiance (NDI), **I.**38.23
Normalized water-leaving radiance, **I.**43.49
chlorophyll concentration and, **I.**43.50, **I.**43.50*f,* **I.**43.51
North American digital hierarchy, **IV.**2.16
NTSC standard, for color broadcast camera output, **III.**4.20
Nuclear fission, **III.**36.12
Nuclear magnetic resonance (NMR), **IV.**24.7, **IV.**24.27
Nuclear reactors, thermal, **III.**36.12
Nulling, of stimuli, **I.**29.5
Null Ronchi screens, **II.**7.6
Null space, **I.**26.47
Numerical aperture (NA), **I.**1.85, **II.**1.9, **II.**24.21
of cochlear hair cells, **III.**9.25
equation for, **III.**9.2
in fiber optics, **III.**2.1
for laser light, **IV.**4.14
for optical fiber, **IV.**1.7, **IV.**1.7*f,* **IV.**1.8, **IV.**2.2
of X-ray lenses, **III.**20.3, **III.**20.8
Nutting's law, **I.**20.6–**I.**20.7
Nyquist frequency:
and imaging system sampling, **III.**4.17–**III.**4.19
Nyquist noise, **I.**15.9
in photodetectors, **IV.**4.75

OARDAS, **I.**38.28
Object and image plane, **I.**1.46*f*
Object distance, **II.**2.3
Object height, **I.**1.30
Objective amplitude of accommodation, **I.**24.30
Objective optics:
double-pass, **II.**19.33*f*
flat-field, **II.**19.31–**II.**19.32, **II.**19.32*f*
on-axis, **II.**19.30–**II.**19.31, **II.**19.32*f*

Objectives:
Altenhof, **II.**18.36, **II.**18.36*f*
Baker-Nunn, **II.**18.24, **II.**18.24*f*
Baker super-Schmidt, **II.**18.23, **II.**18.23*f*
Carlisle, **II.**18.9
Cassegrain, **II.**18.7, **II.**18.7*f,* **II.**18.8
dual-focal, **II.**18.10*f*
with field corrector, **II.**18.9, **II.**18.9*f*
Schmidt-meniscus, **II.**18.23, **II.**18.23*f*
with Schwarzschild relay, **II.**18.36, **II.**18.36*f*
spherical primary, **II.**18.10, **II.**18.10*f*
three-mirror, **II.**18.32, **II.**18.32*f,* **II.**18.33, **II.**18.33*f*
Cassegrain-Mersenne telescope, afocal, **II.**18.10, **II.**18.10*f*
catadioptric, **II.**18.6
Herschelian, **II.**18.30, **II.**18.30*f*
Cook, three-mirror, **II.**18.34, **II.**18.34*f*
Couder, **II.**18.13, **II.**18.13*f*
Dall-Kirkham, **II.**18.9, **II.**18.9*f*
Eisenburg and Pearson two-mirror, **II.**18.27, **II.**18.27*f*
Gabor, **II.**18.22, **II.**18.22*f*
Gregorian, **II.**18.10–**II.**18.11, **II.**18.11*f*
aplanatic, **II.**18.12, **II.**18.12*f,* **II.**18.13
Gregorian-Mersenne telescope, afocal, **II.**18.13, **II.**18.13*f*
Herschelian, **II.**18.7
Houghton-Cassegrain, **II.**18.24*f,* **II.**18.25, **II.**18.25*f*
Korsch, three-mirror, **II.**18.34, **II.**18.34*f*
four-reflection, **II.**18.35, **II.**18.35*f*
and two-mirror, **II.**18.38, **II.**18.38*f*
Maksutov, **II.**18.21, **II.**18.21*f*
Maksutov-Cassegrain, solid, **II.**18.21, **II.**18.21*f*
Mangin, **II.**18.6–**II.**18.7, **II.**18.7*f*
Mangin-Cassegrain with correctors, **II.**18.26, **II.**18.26*f*
McCarthy, **II.**18.35, **II.**18.35*f*
Mersenne, afocal, **II.**18.11
Newtonian, **II.**18.7
parabolic, **II.**18.6, **II.**18.6*f,* **II.**18.7
Paul-Gregorian, off-axis, eccentric-pupil, **II.**18.31, **II.**18.31*f,* **II.**18.32
Paul three-mirror, **II.**18.31, **II.**18.31*f*
alternative, **II.**18.31, **II.**18.31*f*
Pfund, **II.**18.7
reflective, **II.**18.6
Ritchey-Chretien, **II.**18.8, **II.**18.8*f*
Schiefspiegler, **II.**18.29, **II.**18.29*f*
Schmidt, **II.**18.15, **II.**18.15*f*
field-flattened, **II.**18.16, **II.**18.16*f*
reflective, **II.**18.17, **II.**18.17*f*
Shafer relayed virtual, **II.**18.19, **II.**18.19*f,* **II.**18.20, **II.**18.20*f*
Objectives, Schmidt (*Cont.*):
solid, **II.**18.17, **II.**18.17*f*
Schmidt-Cassegrain, **II.**18.18, **II.**18.18*f*
reflective, **II.**18.19, **II.**18.19*f*
Schupmann, **II.**18.7
Schwarzschild
anastigmatic, flat-image, **II.**18.15, **II.**18.15*f*
aplanatic, **II.**18.13, **II.**18.13*f,* **II.**18.14, **II.**18.14*f*
SEAL, **II.**18.30, **II.**18.30*f*
Shafer
five-mirror, **II.**18.37, **II.**18.37*f*
four-mirror, **II.**18.37, **II.**18.37*f*
two-mirror, **II.**18.27, **II.**18.27*f*
Shenker, **II.**18.25, **II.**18.25*f,* **II.**18.26
spherical primary, with Schmidt principal, **II.**18.20, **II.**18.20*f*
terminology used for, **II.**18.6–**II.**18.7
three-lens prime focus corrector, **II.**18.11, **II.**18.11*f*
three-mirror
afocal telescope, **II.**18.32, **II.**18.32*f*
spherical mirror, **II.**18.33, **II.**18.33*f,* **II.**18.34
Trischiefspiegler, **II.**18.29
two-mirror, three-reflection, **II.**18.28, **II.**18.28*f*
Wetherell and Womble, three-mirror, **II.**18.34*f,* **II.**18.35
wide-field, with Maksutov correction, **II.**18.22, **II.**18.22*f*
Wright, **II.**18.16, **II.**18.16*f,* **II.**18.17
Yolo, **II.**18.28*f,* **II.**18.29
(*See also* Lenses; Objective optics)
Object plane, **I.**1.31
Object point, **I.**1.30
Object relief (OR), **II.**2.11, **II.**2.11*f*
Object space, **I.**1.30
numerical aperture, **I.**1.85
Oblique spherical aberration, **II.**18.41
Obscurations, **II.**18.4, **II.**18.4*f,* **II.**18.5
Occupation effects, in nonlinearity, **IV.**25.19
Oceanic optics, **I.**43.4
(*See also* Sea water)
Ocular ametropia, **I.**24.8
Ocular media:
optical density of, **III.**13.5, **III.**13.6*f,* **III.**13.7, **III.**13.11, **III.**13.16
radiant energy penetration of, **III.**15.3
Ocular radiometry, **I.**24.11–**I.**24.12
Ocular refraction (*see* Refractive error)
Oculars, **II.**17.20
design standards for, **II.**17.21
focal length in, **II.**17.21
Ramsden-type, **II.**17.21
zoom, **II.**17.21
Ocular safety, **I.**28.19
Ocular transmittance, **I.**24.9

Off-Axis Rejection (OAR), **I.**38.23–**I.**38.24
Offner compensator, **II.**30.23, **II.**30.23*f*
Omnidirectional reflectors, **IV.**20.2
100Base-FX, **IV.**16.7
100Base-T, **IV.**16.7
One-mode components analysis, **I.**26.28
110 format color film, **III.**6.27
1000Base-FX, **IV.**16.7
$1 \times N$ power splitters, **IV.**8.1, **IV.**8.4, **IV.**8.5*f*
Opaque strip observation, in diffraction, **I.**3.18–**I.**3.19, **I.**3.19*f*
Open aperture Z-scan, **IV.**17.33
Open fiber control (OFC), **IV.**16.5
Open loop gain, **IV.**27.5, **IV.**27.9, **IV.**27.9*f*
Open systems, stimulated photon echo in, **IV.**24.17, **IV.**24.17*f*
Ophthalmoheliosis, **III.**15.1, **III.**15.6, **III.**15.6*f,* **III.**15.7
Ophthalmology:
  and aging, **III.**13.4
  and higher-order aberrations, **III.**10.5
  optical power in, **III.**11.2
Ophthalmoscope, **III.**10.2, **III.**10.9, **III.**10.10*f,* **III.**11.4–**III.**11.5
Ophthalmoscopic methods, **I.**24.22–**I.**24.24
  off-axis image quality and, **I.**24.24–**I.**24.25
Opponent color spaces, **I.**26.15
Opponent process model, **I.**26.43, **I.**26.43*f,* **I.**26.44
Optical absorption transitions, **I.**44.11, **I.**44.11*f*
Optical amplifier, **IV.**2.1, **IV.**2.11–**IV.**2.12, **IV.**5.1–**IV.**5.7
  applications of, **IV.**11.2, **IV.**11.3*f*
  fiber, **IV.**11.3–**IV.**11.4
  in OTDM system, **IV.**12.39
  properties of, **IV.**11.2–**IV.**11.3
  semiconductor, **IV.**11.4–**IV.**11.7
Optical anisophoria, **III.**11.15
Optical axis, **I.**1.35, **II.**18.41
  atomic displacement and, **I.**9.18
Optical birefringence, **II.**12.15–**II.**12.16
Optical bistability, **IV.**17.31, **IV.**22.3
Optical Bloch equations, **IV.**24.3–**IV.**24.5, **IV.**24.27, **IV.**28.1, **IV.**28.4, **IV.**28.6
Optical carrier signal, **IV.**12.22, **IV.**16.6
Optical cavities, of lasers, **I.**11.20
Optical cavity-based frequency discriminators, **IV.**27.15
Optical circulator, **IV.**9.8–**IV.**9.9, **IV.**9.9*f,* **IV.**10.3–**IV.**10.4, **IV.**10.4*f,* **IV.**10.9
Optical coatings:
  absorption in, **I.**42.16
  antireflection (*see* Antireflection coatings)
  laser damage in, **I.**42.17
  laser-induced damage threshold (LIDT) in, **I.**42.17–**I.**42.18
Optical coatings (*Cont.*):
  multilayer:
    optical properties of, **I.**42.18
    for three spectral regions, **I.**42.95–**I.**42.96, **I.**42.96*f*–**I.**42.97*f*
    for two spectral regions, **I.**42.94–**I.**42.95, **I.**42.95*f*
    (*See also* Periodic multilayers; Reflectors, multilayer)
  optical constants in, **I.**42.17
  in polymers, **II.**34.19–**II.**34.20
  reflection in, **I.**42.16
  special-purpose, **I.**42.107–**I.**42.108, **I.**42.108*f*
  textured metallic, **II.**37.14
  transmission in, **I.**42.16
  (*See also* Black surfaces, optical)
Optical code-division multiplexing (OCDM), **IV.**2.16
Optical coefficients, nonlinear, **II.**33.29, **II.**33.29*t*
Optical collisions, **IV.**28.28–**IV.**28.30
Optical confinement (*see* Optical trapping)
Optical constants, **I.**5.2, **I.**6.14, **I.**9.6–**I.**9.7, **I.**42.17
  and dielectric function, **II.**36.9
Optical cooling, **IV.**28.1, **IV.**28.3, **IV.**28.6, **IV.**28.35
Optical crossconnects (OCCs), **IV.**13.14–**IV.**13.15, **IV.**13.15*f*
Optical damage, to lithium niobate ($LiNbO_3$), **IV.**4.56–**IV.**4.57
Optical data storage, **I.**31.1–**I.**31.2, **I.**31.3*f*–**I.**31.5*f,* **II.**6.36
Optical density (OD), **I.**43.10, **IV.**19.2
  measurements, projection, **I.**20.7*f*
  nonneutral, **I.**20.8
  in photography, **I.**20.6, **I.**20.7*f*
  reflection, **I.**20.8–**I.**20.9
  transmission, **I.**20.7–**I.**20.8
Optical design:
  lens setup in, **I.**34.7
  project, typical, **I.**34.2, **I.**34.3*f*
Optical design software:
  for adaptive optics systems, **III.**1.41
  boundary conditions in, **I.**34.20
  buying, **I.**34.23
  cost of, **I.**34.25
  error functions in, **I.**34.21
  features of, **I.**34.24
  global optimization of, **I.**34.23
  hardware for, **I.**34.23–**I.**34.24
  multiconfiguration optimization in, **I.**34.22
  optimization of, **I.**34.18
  primary function of, **I.**34.2
  programming considerations in, **I.**34.8
  simulation in, **I.**34.22
  support for, **I.**34.25
  tolerance calculation in, **I.**36.11

Optical design software (*Cont.*):
tolerancing in, **I.**34.22
user interface of, **I.**34.24
(*See also* Software)
Optical elements, holographic (*see* Holographic optical elements (HOEs))
Optical extent, **I.**1.25
Optical fabrication:
basic steps in, **I.**40.3–**I.**40.5
methods, **I.**41.3*t*
peak-to-valley accuracy in, **I.**40.3
rough shaping in, **I.**40.3–**I.**40.4
Optical feedback, **I.**11.3
Optical fiber, **I.**28.10
anomalous dispersion in, **II.**10.9
applications for, **IV.**1.9, **IV.**1.11, **IV.**1.21–**IV.**1.24
a-profile of, **IV.**1.6–**IV.**1.7, **IV.**1.11
attenuation in, **II.**10.8, **II.**10.8*f,* **II.**10.14, **II.**10.14*f,* **IV.**1.9–**IV.**1.10, **IV.**1.10*f,* **IV.**1.14–**IV.**1.16, **IV.**2.2–**IV.**2.3, **IV.**2.3*f,* **IV.**13.2, **IV.**13.2*f*
mandrel wrap for, **II.**10.13*f*
attenuation measurement in, **II.**10.12–**II.**10.13
bandwidth of, **II.**10.14–**II.**10.15, **IV.**1.16, **IV.**2.3, **IV.**13.2
in biological photoreceptors, **III.**9.3–**III.**9.4, **III.**9.15
chalcogenide fibers, **II.**10.45–**II.**10.46
chemistry of, **II.**10.42
chromatic dispersion of, **IV.**13.4–**IV.**13.5, **IV.**13.5*f,* **IV.**13.6, **IV.**13.6*f*
communication, **II.**12.43
core size of, **IV.**1.7–**IV.**1.8
coupling of, **IV.**1.7–**IV.**1.8, **IV.**1.14, **IV.**2.5
design of, **II.**10.4*f,* **IV.**1.6, **IV.**1.6*f,* **IV.**1.7, **IV.**1.7*f,* **IV.**2.2
detector/amplifier configurations for, **II.**10.27*f*
development of, **IV.**1.5, **IV.**2.1
dispersion-flattened, **II.**10.16, **II.**10.17*f*
dispersion in, **IV.**1.9–**IV.**1.13, **IV.**1.16
effects of, **II.**10.23
evaluation of, **II.**10.11, **II.**10.11*f,* **II.**10.15, **II.**10.15*f,* **II.**10.16
intermodal, **II.**10.8
material, **II.**10.9
profile, **II.**10.9
dispersion-shifted, **IV.**1.18, **IV.**1.19*f*
dopant chemistry in, **II.**10.44–**II.**10.45
external acceptance angles in, **II.**10.5*f*
fabrication of, **II.**10.42–**II.**10.43, **II.**10.44*f,* **II.**10.45, **IV.**1.44–**IV.**1.48
fiber-fiber coupling, **II.**10.5
fiber requirements in, **II.**10.37
fluoride fibers, **II.**10.46
flux budget in, **I.**12.36
Optical fiber (*Cont.*):
four-wave mixing in, **II.**10.40, **II.**10.40*f,* **II.**10.41
gradient index fibers, **II.**10.5, **II.**10.9
history of, **II.**10.3
human hair cells as, **III.**9.26
infrared, **II.**10.45, **IV.**14.1–**IV.**14.14
intermodal dispersion in, **II.**10.8
laser-fiber coupling, **II.**10.6
LEDs and, **I.**12.36
medical applications for, **IV.**1.6, **IV.**14.1
metrology applications for, **IV.**1.6
minimizing fiber size in, **III.**2.1–**III.**2.2
modes supported by, **IV.**1.6, **IV.**1.9, **IV.**2.2
modulation-induced frequency chirp and, **II.**10.23–**II.**10.24, **II.**10.24*f*
multimode fibers in, **II.**10.7, **II.**10.9, **II.**10.13*f,* **II.**22.23, **III.**9.24–**III.**9.25
nonlinear properties of, **II.**10.37, **IV.**1.39–**IV.**1.43, **IV.**3.1–**IV.**3.12, **IV.**13.4, **IV.**13.6–**IV.**13.8
normalized variables for, **II.**10.9–**II.**10.10, **II.**10.10*t,* **IV.**1.11–**IV.**1.12, **IV.**1.12*t*
numerical aperture of, **IV.**1.7, **IV.**1.7*f,* **IV.**1.8, **IV.**2.2
photorefractive nonlinearities in, **II.**10.41
photosensitivity of, **IV.**9.1–**IV.**9.3
plant tissue as, **III.**9.26–**III.**9.29
point-to-point links in, **II.**10.20–**II.**10.23, **II.**10.23*f*
polarization, **IV.**1.13–**IV.**1.14
characteristics of, **II.**10.11–**II.**10.12
profile dispersion in, **II.**10.9
ray path in, **II.**10.5, **II.**10.5*f,* **II.**10.6, **II.**10.6*f*
receiver noise in, **II.**10.26*t*
refractive index of, **IV.**1.6–**IV.**1.7, **IV.**1.11, **IV.**1.13, **IV.**2.2, **IV.**13.6
relative noise intensity (RIN) in, **II.**10.20–**II.**10.21, **II.**10.23*f*
reliability of, **II.**10.16–**II.**10.19, **II.**10.19*f,* **II.**10.21*f,* **IV.**1.18–**IV.**1.21
Weibull distribution and, **II.**10.18, **II.**10.20*t,* **II.**10.21*f*–**II.**10.22*f*
signal-to-noise ratio in, **II.**10.24–**II.**10.25, **II.**10.26*f,* **II.**10.28
soliton propagation in, **II.**10.9
source diameter in, **I.**12.36
specialty, for dispersion management, **IV.**13.9–**IV.**13.10
speed in, **I.**12.36
step-index fibers, **II.**10.5, **II.**10.9
of circular symmetry, **II.**10.7, **II.**10.7*f*
stimulated scattering processes in, **II.**10.37
in telecommunications, **II.**10.7, **II.**10.19
system design of, **II.**10.24–**II.**10.28

Optical fiber (*Cont.*):
ultrashort pulse transmission in, **II.**10.29
waveguide dispersion in, **II.**10.9
Optical fiber communication system:
amplification in, **IV.**11.1
(*See also* Amplifiers)
analog, **IV.**2.14–**IV.**2.15
applications for, **IV.**2.16, **IV.**6.1–**IV.**6.2
characteristics of, **IV.**6.2–**IV.**6.7
components of, **IV.**2.1–**IV.**2.10, **IV.**4.1
evolution of, **IV.**2.1, **IV.**13.1, **IV.**13.3, **IV.**13.4*f*
limitations in, **IV.**2.10–**IV.**2.11
networks in, **IV.**2.13
Optical fiber sensors, **IV.**15.1–**IV.**15.2
extrinsic Fabry-Perot interferometric, **IV.**15.2, **IV.**15.2*f,* **IV.**15.3, **IV.**15.3*f,* **IV.**15.4
intrinsic Fabry-Perot interferometric, **IV.**15.4, **IV.**15.4*f,* **IV.**15.5
Optical films (*see* Optical coatings)
Optical filters:
defined, **I.**42.4
performance, ways of describing, **I.**42.5, **I.**42.5*f,* **I.**42.6
in series, reflection of, **I.**42.8–**I.**42.9, **I.**42.9*f*
spectral transmittance of, **I.**42.6–**I.**42.7, **I.**42.7*f,* **I.**42.8
tunable, **IV.**13.15
Optical finish measurements, **I.**7.10
Optical force:
effect of, on atoms, **IV.**28.4–**IV.**28.5
types of, **IV.**28.6
velocity dependence of, **IV.**28.1–**IV.**28.2, **IV.**28.6
Optical glasses, **II.**34.7*f*
Optical heterodyne saturation spectroscopy, **IV.**27.14
Optical hole burning (OHB), **I.**8.21, **II.**28.14–**II.**28.16, **IV.**4.15, **IV.**4.48–**IV.**4.49
spectroscopy, **II.**20.24, **II.**20.24*f,* **II.**20.25–**II.**20.26, **II.**20.26*f*
Optical image enhancement, coherent:
inverse filter, **I.**30.17
Wiener filter, **I.**30.17–**I.**30.18
Optical image transformer, **III.**2.21–**III.**2.22, **III.**2.22*f*
Optical indicatrix, **II.**33.20–**II.**33.21, **II.**33.21*f*
Optical injection locking, for clock recovery, **IV.**12.35, **IV.**12.35*f,* **IV.**12.36
Optical interactions, **I.**44.21
Optical Kerr effect (OKE), **IV.**17.5*t,* **IV.**17.12–**IV.**17.16, **IV.**17.30, **IV.**22.3
in ultrashort pulse generation, **IV.**25.4
Optical lattice, **IV.**28.22, **IV.**28.25, **IV.**28.30–**IV.**28.31, **IV.**28.31*f,* **IV.**28.32–**IV.**28.33
Optical limiter, **II.**39.29, **IV.**19.1
applications for, **IV.**19.1
figure of merit for, **IV.**19.2–**IV.**19.3, **IV.**19.6–**IV.**19.7
responses of, **IV.**19.2, **IV.**19.2*f*
self-protecting, **IV.**19.10
Optical limiting, **IV.**19.1
active versus passive systems for, **IV.**19.1–**IV.**19.2
in carbon-black suspensions, **IV.**19.11, **IV.**19.11*f,* **IV.**19.12
and damage thresholds, **IV.**19.3–**IV.**19.4, **IV.**19.6, **IV.**19.10
liquid crystals in, **IV.**19.13, **IV.**19.13*f*
nonlinear absorption in, **IV.**19.4, **IV.**19.4*f,* **IV.**19.5, **IV.**19.5*f,* **IV.**19.6, **IV.**19.6*f,* **IV.**19.7
nonlinear refraction in, **IV.**19.4*f,* **IV.**19.7–**IV.**19.8
nonlinear scattering in, **IV.**19.4*f,* **IV.**19.8–**IV.**19.9
optically induced phase change in, **IV.**19.4*f,* **IV.**19.9
in organics, **IV.**19.10–**IV.**19.11
photorefractivity in, **IV.**19.4*f,* **IV.**19.9, **IV.**19.12, **IV.**19.12*f*
in semiconductors, **IV.**19.10, **IV.**19.10*f*
Optical link power budget, **IV.**6.2–**IV.**6.5
assembly loss in, **IV.**6.9–**IV.**6.18
installation loss in, **IV.**6.7–**IV.**6.9
Optically detected magnetic resonance (ODMR), **II.**20.21, **II.**20.23, **II.**20.23*f,* **II.**28.24–**II.**28.25, **II.**28.25*f,* **II.**28.26
Optically induced phase change, **IV.**19.4*f,* **IV.**19.9
Optical matrix vector multiplication, **II.**39.29*f*
Optical measurements, **I.**18.2*f*
Optical metrology, **II.**22.27
Optical mixing, **IV.**2.11
Optical mode conditioner, **IV.**16.8
Optical molasses (OM), **IV.**28.1, **IV.**28.8, **IV.**28.11–**IV.**28.13, **IV.**28.23, **IV.**28.35
atomic beam collimation in, **IV.**28.13–**IV.**28.14, **IV.**28.14*f*
in atomic clock experiments, **IV.**28.27
and optical lattices, **IV.**28.31, **IV.**28.33, **IV.**28.33*f*
temperature in, **IV.**28.19*f*
three-dimensional experiments in, **IV.**28.13, **IV.**28.13*f,* **IV.**28.14
velocity dependence in, **IV.**28.12, **IV.**28.13*f*
Optical multichannel analyzers (OMAs) (*see under* Cameras, II SSA)
Optical Networks Technology Consortium (ONTC), **IV.**13.16
Optical nutation, **II.**38.5
Optical parameters (*see* Optical constants)
Optical parametric amplifier (OPA), **I.**14.13, **IV.**2.12, **IV.**2.16, **IV.**22.14, **IV.**22.61

Optical parametric generation, **IV.**22.1–**IV.**22.2
gain factor in, **IV.**22.8–**IV.**22.10, **IV.**22.10*t,* **IV.**22.11, **IV.**22.62
phase matching in, **IV.**22.10–**IV.**22.11, **IV.**22.11*f,* **IV.**22.12, **IV.**22.61–**IV.**22.62
physical principles of, **IV.**22.2–**IV.**22.8
tuning in, **IV.**22.62
Optical parametric generator (OPG), **IV.**22.14, **IV.**22.61
Optical parametric oscillator (OPO), **IV.**22.2, **IV.**22.7, **IV.**22.13–IV.15, **IV.**23.27
cavity configurations for, **IV.**22.14, **IV.**22.14*f*
design of, **IV.**22.61–**IV.**22.65
doubly resonant, **IV.**22.14–**IV.**22.32
intracavity, **IV.**22.42–**IV.**22.50
pulsed, **IV.**22.50–**IV.**22.54
pump-enhanced, **IV.**22.35–**IV.**22.42
singly resonant, **IV.**22.14–**IV.**22.16, **IV.**22.32–**IV.**22.35, **IV.**22.50
synchronously pumped, **IV.**22.55–**IV.**22.60
Optical parametric oscillator (OPO), **I.**14.13, **II.**38.18–**II.**38.19, **II.**38.19*f,* **II.**38.20
Optical path, **I.**31.7
length, **I.**1.33
absolute, **I.**1.95
Optical path difference (OPD), **I.**2.7, **I.**33.1–**I.**33.2, **I.**33.6, **I.**34.14
of rays, **I.**34.13, **I.**34.13*f*
Optical phenomena, **I.**44.2
Optical polymers, **II.**34.7*f*
aberration control in, **II.**34.8
abrasive forming of, **II.**34.13
additives to, **II.**34.5
antiabrasion coatings in, **II.**34.20
antireflection coatings in, **II.**34.19
antistatic coatings in, **II.**34.20
aspheric surfaces in, **II.**34.9–**II.**34.10
athermalization in, **II.**34.10
casting of, **II.**34.12–**II.**34.13
compression molding of, **II.**34.14
computer-numerical control (CNC) lathe turning of, **II.**34.13
conductivity of, **II.**34.4
configurations of, **II.**34.16*f*
density of, **II.**34.2
design strategy for, **II.**34.8
dimensional variations in, **II.**34.11
documentation of, **II.**34.5
error budget tree in, **II.**34.11
figure variations in, **II.**34.11–**II.**34.12
geometry considerations in, **II.**34.15
hardness of, **II.**34.3
homogeneity of, **II.**34.8
injection moding of, **II.**34.14–**II.**34.15
Optical polymers (*Cont.*):
material selection in, **II.**34.9
mechanical assembly of, **II.**34.16–**II.**34.18
multiple cavities and, **II.**34.11
null correctors in, **II.**34.18–**II.**34.19
outgassing from, **II.**34.4
physical properties of, **II.**34.4*t*
processing considerations in, **II.**34.10
radiation resistance of, **II.**34.5
reflective coating in, **II.**34.19
refractive index of, **II.**34.6–**II.**34.7, **II.**34.7*t,* **II.**34.8
rigidity of, **II.**34.3
service temperature of, **II.**34.3–**II.**34.4
shrinkage on, **II.**34.16
single-point turning, **II.**34.13–**II.**34.14
specifications for, **II.**34.12
spectral transmission in, **II.**34.6
vendor selection of, **II.**34.15
verification of, **II.**34.18
water absorption of, **II.**34.5
Optical power:
conversion to, in lasers, **IV.**4.10–**IV.**4.12
definition of, **III.**14.4
and electroabsorption modulators, **IV.**4.62
flow of, **IV.**10.3
of LEDs, **IV.**4.43, **IV.**4.43*f*
of lenses, **III.**11.2
and mode-locking, **IV.**12.30
penalties on, **IV.**6.9–**IV.**6.18
Optical preamplifiers, **IV.**2.11
Optical processing, coherent, **I.**30.8, **I.**30.10
Optical processing arrangement, **I.**3.23*f*
Optical properties, **II.**33.8
intrinsic, **II.**33.12
Optical pumping:
in laser cooling, **IV.**28.15–**IV.**28.18, **IV.**28.18*f,* **IV.**28.19
in magneto-optical trap, **IV.**28.22
(*See also* Pumping)
Optical radar, **II.**29.5
Optical radiation:
exposure limits for, **III.**15.9–**III.**15.12
measurement of (*see* Radiometry)
photochemical versus thermal damage from, **III.**15.2–**III.**15.3
sources of damage from, **III.**15.13*f*
Optical resonator, for laser stabilization, **IV.**27.12
Optical/retinal inhomogeneity, **I.**25.26
Optical second-harmonic generation, **II.**38.4
Optical signal, properties of, **IV.**21.2
Optical sine theorem, **II.**1.6
Optical sources, nonlinear, **I.**14.12
Optical spectroscopy, **I.**8.5, **I.**8.14, **IV.**24.2–**IV.**24.3

Optical spectrum analyzer, fabrication of, **IV.**9.7
Optical storage loop, **IV.**5.1
Optical switches, **IV.**12.15
Optical systems, **II.**24.20*f*
aplanatic, **II.**24.21
building, **I.**28.8
coherent vs. incoherent, **I.**30.4
combining lights in, **I.**28.9, **I.**28.9*f*
data, types of, **I.**34.4–**I.**34.7
designing, **I.**18.2
limitations on, **I.**1.32
metals in (*see under* Metals)
optical and thermal data for, **I.**39.3*t*–**I.**39.4*t*
radar data processing, **I.**30.9–**I.**30.10, **I.**30.10*f*
signal analysis in, **I.**18.3
specifications, **I.**35.1–**I.**35.2
coating specifications, **I.**35.10
depth of focus, **I.**35.7–**I.**35.8, **I.**35.8*f*
environmental, **I.**35.10
gaussian parameters, **I.**35.4, **I.**35.6*t*
image, **I.**35.2
image irradiance, **I.**35.7
international standards, use of, **I.**35.10
ISO standards, use of, **I.**35.11
material specifications, **I.**35.9
mechanical dimensions, **I.**35.9
mechanical vs. optical, **I.**35.2
optical parameters, **I.**35.9
preparation of, **I.**35.4
presentation of, **I.**35.10–**I.**35.11
system vs. components, **I.**35.2
vs. tolerances, **I.**36.1
wavefront, **I.**35.3
writing, problems with, **I.**35.12
stray radiation in, **I.**38.2
surface data in, **I.**34.5–**I.**34.6
techniques for calibrating, **I.**28.18*f*
thermal effects in
homogeneous, **I.**39.2
thin-film (*see* Optical filters; Thin-film coatings)
tolerances in, **I.**36.4*f,* **I.**36.4*t*
assembly, **I.**36.8
basis for, **I.**36.2
boresight, **I.**36.8
budgeting of, **I.**36.2–**I.**36.3
combination of, **I.**36.6, **I.**36.6*t,* **I.**36.7*f*
compensation in, **I.**36.7
determination of, **I.**36.1–**I.**36.2
direct calculation of, **I.**36.10
distortion, **I.**36.8
individual, computation of, **I.**36.4–**I.**36.5, **I.**36.5*f,* **I.**36.5*t*
judgment factors in, **I.**36.1
lens-design programs and, **I.**36.11
Optical systems, tolerances in (*Cont.*):
material properties and, **I.**36.9
measurement practice, **I.**36.9
optical vs. mechanical, **I.**36.2
overloosening in, **I.**36.12
overtightening in, **I.**36.11
parameter error quality definitions for, **I.**36.4
problems in, **I.**36.11
procedures for, **I.**36.9–**I.**36.10
shop practice, **I.**36.8
spreadsheet calculation of, **I.**36.10
verification of, **I.**36.3
wavefront, **I.**36.3
(*See also specific types*)
Optical tank circuit, for clock recovery, **IV.**12.34–**IV.**12.35, **IV.**12.35*f*
Optical TDMA (OTDMA), **IV.**12.17–**IV.**12.18, **IV.**12.19*f*
Optical theorem, **I.**6.6, **I.**6.9
Optical time-division multiplexing (OTDM), **IV.**2.16, **IV.**12.17, **IV.**12.24, **IV.**13.3, **IV.**13.4*f*
components in, **IV.**12.38–**IV.**12.39, **IV.**12.39*f,* **IV.**12.40, **IV.**12.41*f*
devices for, **IV.**12.24
performance of, **IV.**12.40–**IV.**12.41
transmission in, **IV.**12.30
Optical time domain reflectometry (OTDR), **II.**10.14*f,* **IV.**1.16, **IV.**1.16*f*
Optical-to-acoustic divergence ratio, **II.**12.27–**II.**12.28, **II.**12.28*f*
Optical transfer function (OTF), **I.**20.19–**I.**20.20, **I.**20.20*f,* **I.**25.23–**I.**25.24, **II.**11.6–**II.**11.7, **II.**32.3–**II.**32.4, **II.**32.9, **III.**1.21–**III.**1.23
geometrical-aberration, **II.**32.6
measurements, **II.**32.7–**II.**32.8
Optical transitions (*see* Transitions, optical)
Optical trapping, **IV.**4.4–**IV.**4.5, **IV.**4.5*f,* **IV.**4.6, **IV.**4.13–**IV.**4.14, **IV.**28.19, **IV.**28.21–**IV.**28.22, **IV.**28.22*f,* **IV.**28.27
lateral, **IV.**4.6–**IV.**4.7
in quantum well lasers, **IV.**4.29–**IV.**4.30
Optical tube length, **II.**1.10
Optical turbulence:
atmospheric, **I.**44.26
beam spread, **I.**44.31–**I.**44.32, **I.**44.32*f,* **I.**44.33
beam wander, **I.**44.30–**I.**44.31
characteristics of, **I.**44.26–**I.**44.28, **I.**44.28*f,* **I.**44.29–**I.**44.30, **I.**44.30*f*
heterodyne detection in, **I.**44.33
Hufnagle model of, **I.**44.29
imaging in, **I.**44.33
scintillation in, **I.**44.34–**I.**44.35, **I.**44.35*f*
Optical tweezers, **II.**17.48, **IV.**28.21

Optical wavelength converter, **IV.**11.7–**IV.**11.9
Optic axis, **I.**9.8
Optic flow, **III.**12.2, **III.**12.5–**III.**12.6, **III.**12.15
Optic flow field, **I.**25.41, **I.**25.41*f*
Optics:
  atmospheric (*see* Atmospheric optics)
  binary (*see* Binary optics)
  capillary (*see* Capillary optics)
  crystalline, **I.**40.6
    (*See also* Crystals)
  diamond-turned (*see* Diamond turning)
  diffractive, **I.**31.30
  first-order, **I.**1.32, **I.**1.42
  gaussian, **I.**1.32
  geometrical, **I.**34.17
  glass (*see* Glass optics, molded)
  gradient index (GRIN) (*see* Graded index (GRIN) lens)
  hydrologic (*see* Water)
  inhomogeneous (*see* Graded index (GRIN) lens)
  lobster-eye, **III.**30.3
  meteorological (*see* Meteorological optics)
  objective (*see* Objective optics)
  oceanic (*see* Oceanic optics)
  parabasal, **I.**1.47
  paraxial, **I.**1.32
  physical, **I.**34.17
  plano, **I.**40.6
  polymeric, **II.**34.1
  purchasing, **I.**40.7–**I.**40.8
Optocouplers, **I.**12.35, **I.**12.35*f,* **I.**12.36
Optoelectrics, applications for, **II.**36.85*t*
Optoelectronic integrated circuit (OEIC), **II.**6.2, **II.**6.17, **II.**6.38, **II.**6.38*f*
  chips, photodiodes and, **I.**16.16
Optoelectronic wavelength conversion, **IV.**11.9–**IV.**11.10
Optokinetic nystagmus, **I.**24.36
Optokinetic (OKN) reflex, **III.**12.21
Optometer, **III.**18.11
Orbital states, parity of, **I.**8.23
Organic detritus, absorption by, **I.**43.26, **I.**43.28*f*
Organic dye lasers, **I.**11.14, **I.**11.18–**I.**11.19, **I.**11.19*f,* **I.**11.34, **I.**11.34*f*
Organic polymers, **II.**39.24–**II.**39.25
Organ of Corti, **III.**9.2, **III.**9.24–**III.**9.26
Organometallic vapor phase deposition (OMPVE), **I.**13.7
Orientation, visual, **III.**12.4
Orlando Black, **II.**37.11*f,* **II.**37.48
  total integrated scatter in, **II.**37.61*f*
Orthogonal reference beams, **II.**39.35
Orthokeratology, **III.**11.12
Orthonormal basis vectors, **I.**6.10
Orthonormalization, **I.**34.20
Orthoscopic observation, **II.**17.39
Orthotomic systems, of rays, **I.**1.11, **I.**1.14
Oscillator models:
  anharmonic, **II.**38.7–**II.**38.8, **II.**38.8*f,* **II.**38.9, **II.**38.11
  harmonic, **II.**38.6–**II.**38.7
  with photorefractive gain, **II.**39.7
Oscillator strength, **I.**9.15
Oseen-Frank equation, **II.**14.16
Osipov-Terentjev theory, **II.**14.10
OSI reference model, and FDDI, **IV.**16.2
Outer product processor, **I.**30.22, **I.**30.22*f*
Outgassing, in space, **II.**37.14
  and black surfaces, **II.**37.18–**II.**37.19
  collected volatile condensable materials (CVCM) and, **II.**37.19
  total mass loss (TML) and, **II.**37.19
  water vapor regained (WVR) and, **II.**37.20
Out-of-plane coupling, in photonic crystals, **IV.**20.11–**IV.**20.13
Outside process, for optical fiber fabrication, **IV.**1.45–**IV.**1.46, **IV.**1.46*f*
Outside vapor deposition (OVD), **II.**10.44, **IV.**1.46
Overhead projectors, lenses in, **III.**2.9
Overscan, in CRTs, **I.**27.13
Oxide stripe lasers, **I.**13.8
Ozone, pressure of, **I.**44.4

Packet, **IV.**13.2, **IV.**13.16*f,* **IV.**13.17
  in ATM, **IV.**16.6
  in FDDI, **IV.**16.3–**IV.**16.4
Packet-switched data networks:
  timed-division multiple access in, **IV.**12.16
Packet switching, **IV.**13.16, **IV.**13.16*f,* **IV.**13.17
PADE (Program for the Analysis of Diffracted Energy), **I.**38.27
PAL standard, for color broadcast camera output, **III.**4.20
Panoramic vision, **III.**12.3
Panum's fusional area (PFA), **III.**12.12–**III.**12.13, **III.**12.23
Parabasal optics, **I.**1.47
Parabolic compound refractive lens, **III.**20.4, **III.**20.4*f,* **III.**20.8
Parabolic objectives, **II.**18.6, **II.**18.6*f,* **II.**18.7
Parallax stereogram, **II.**1.24
Parallel beams:
  in collimating optics, **III.**35.11, **III.**35.11*f,* **III.**35.12, **III.**35.12*f*
  in medical X-ray applications, **III.**35.33
Parallel multiplexing, **IV.**12.24, **IV.**12.25*f*

Parametric amplification, **IV.**17.5*t,* **IV.**22.1, **IV.**22.3, **IV.**22.8–**IV.**22.10, **IV.**22.10*t*
broadband, and longitudinal Kerr effect, **IV.**25.12–**IV.**25.13
third-order, **IV.**17.7, **IV.**17.24
Parametric devices, **IV.**22.1–**IV.**22.2, **IV.**22.12–**IV.**22.13, **IV.**22.61
applications for, **IV.**22.65
nanosecond, **IV.**22.53–**IV.**22.54
Parametric downconversion, **IV.**26.15
Parametric fluorescence, **IV.**22.8
Parametric generation (*see* Optical parametric generation)
Parametric noise, **IV.**22.8
Parametric process, **II.**38.16–**II.**38.17
spontaneous, **II.**38.17, **II.**38.17*f,* **II.**38.18
stimulated, **II.**38.18
Parametric radiation (PXR), **III.**33.1, **III.**33.3–**III.**33.4
Paraxial analysis, **I.**34.9, **I.**34.9*f,* **I.**34.10
Paraxial invariant, **I.**1.46
two-ray, **I.**1.45
Paraxial limit, **I.**1.42
Paraxial matrix methods, **I.**1.70
afocal lenses, **I.**1.76
angle instead of reduced angle, **I.**1.79
arbitrary lenses, **I.**1.77
characteristic functions, **I.**1.80
conjugate matrix and, **I.**1.74
decomposition, **I.**1.78
derivative matrices, **I.**1.79
determinant, **I.**1.73
dimensions, **I.**1.73
experimental determination of elements in, **I.**1.78
focal plane-to-focal plane, **I.**1.75
input and output planes, **I.**1.74
input-out combinations, **I.**1.79
inverse systems, **I.**1.77
matrix elements and, **I.**1.72–**I.**1.73
nodal plane–to–nodal plane, **I.**1.74
for nonrotationally symmetric systems, **I.**1.80
operation on two rays, **I.**1.73–**I.**1.74
possible zeros, **I.**1.73
power matrix and, **I.**1.72
principal focal planes, **I.**1.76
principal plane–to–principal plane, **I.**1.74
reversing lenses, **I.**1.77
skew rays, **I.**1.80
symmetrical lenses, **I.**1.77
transfer matrix and, **I.**1.71
translation from conjugate positions, **I.**1.75
translation from focal planes, **I.**1.75
translation from principal planes, **I.**1.75–**I.**1.76
two-ray specification, **I.**1.78
Paraxial optics, **I.**1.32, **I.**1.42
linearity in, **I.**1.45, **I.**1.71
Paraxial rays, **I.**1.39, **I.**1.41
Parenthetic augmentation, **II.**19.13
Parson's Black, **II.**37.37
Partial involute, **III.**2.12, **III.**2.12*f,* **III.**2.40
Partially polarized light, **II.**22.7
Particle accelerators, **II.**24.29
Particle generation by surfaces, **II.**37.14, **II.**37.18, **II.**37.20
Particle-induced X-ray emission (PIXE), **III.**35.18
Particles:
atmospheric, **I.**6.2
chiral, **I.**6.2
isotropic homogeneous sphere, **I.**6.12
light scattering by, **I.**6.2–**I.**6.3, **I.**6.5–**I.**6.6, **I.**6.9
nonspherical, scattering by, **I.**6.17
in periodic potential, **IV.**28.31
Particle-wave duality, **IV.**26.8, **IV.**26.10
Paschen-Runge gratings, **II.**5.7, **II.**5.11*f*
Passband, **IV.**12.1
in sampling theorem, **IV.**12.5
transmission in, **I.**42.54
Passivation, wafer processing, **I.**12.25
Passive antiguide region (PAR), in VCSEL, **IV.**4.46*f,* **IV.**4.48
Passive mode-locking:
and longitudinal Kerr effect, **IV.**25.13–**IV.**25.15
by saturable absorbers, **IV.**25.6–**IV.**25.9, **IV.**25.9*f,* **IV.**25.10–**IV.**25.11
Passive optical networks, **IV.**12.13
Path reconfiguration, **IV.**13.14
Pattern discrimination, **I.**25.37–**I.**25.38
Pattern noise, **I.**22.13
for solid-state array, **III.**4.12
for solid-state camera, **III.**4.13
Pattern recognition, optical matched filtering for, **I.**30.15
Patterns:
generating complex, **I.**28.16, **I.**28.17*f*
interference, modulation of, **I.**28.27
Paul-Gregorian objectives, off-axis, eccentric-pupil, **II.**18.31, **II.**18.31*f,* **II.**18.32
Pauli Exclusion Principle, **I.**8.14
Paul three-mirror objectives, **II.**18.31, **II.**18.31*f*
alternative, **II.**18.31, **II.**18.31*f*
Peak-to-peak radial distance, **I.**31.15
Pechan prism, **II.**4.11*f*
Pellin-Broca prism, **II.**5.6*f*
Penetration depth vs. wavelength, for aluminum, **II.**35.52*f*
Pen-Ray low pressure lamps, **I.**10.35*f*
Pentaprism, **II.**4.13, **II.**4.14*f,* **II.**29.5

Perception:
of color (*see* Color perception)
definition of, **III.**12.2
of depth, **III.**12.2–**III.**12.3, **III.**12.8, **III.**12.11, **III.**12.11*f,* **III.**12.14–**III.**12.15, **III.**12.20, **III.**13.18
of direction, **III.**12.7–**III.**12.8, **III.**12.15
of distance, **III.**12.13–**III.**12.14, **III.**12.24, **III.**12.30–**III.**12.33, **III.**13.18–**III.**13.19
of image features, **III.**17.8
of motion, **III.**12.6, **III.**12.7*f*
of space, **III.**12.3–**III.**12.4, **III.**12.13–**III.**12.21, **III.**12.31
Percept rivalry suppression, **III.**12.13
Perceptual attention, **III.**17.7
Perceptual Subband Image Coder (PIC), **III.**17.4
Percus-Yevick approximation, **III.**3.5
Perfect diffuser, **III.**14.9–**III.**14.10
Perfect Diffuse Reflector (PDR), **II.**37.31*f*
Ames, **II.**37.10*f*
Performance requirements, **I.**7.11
Perimetry, **III.**13.18
Periodic multilayers:
of absorbing materials, **I.**42.40–**I.**42.41
all-dielectric, **I.**42.36
angular sensitivity of, **I.**42.40
high-reflectance zone, width of, **I.**42.38, **I.**42.39*f*
nonabsorbing $[AB]^N$ and $[AB]^NA$ types, **I.**42.34, **I.**42.34*f,* **I.**42.35, **I.**42.35*f,* **I.**42.36, **I.**42.36*f*
maximum reflectance of, **I.**42.36
phase change on reflection, **I.**42.36–**I.**42.37
$[xH\bullet(1-x)L]^N\bullet$xH type, **I.**42.38, **I.**42.40*f*
$[(0.5A)B(0.5A)]^N$ type, **I.**42.37, **I.**42.37*f,* **I.**42.38, **I.**42.38*f*
Periodic potential, and particle motion, **IV.**28.31–**IV.**28.32, **IV.**28.32*f,* **IV.**28.33
Periscopes, **I.**32.10*f,* **II.**2.18, **II.**2.18*f,* **II.**2.19
Periscopic lenses, **II.**1.27, **II.**1.27*f,* **II.**1.28
Perkin-Elmer Model 99 double-pass monochromator, **II.**5.4, **II.**5.9*f*
Perspective:
definition of, **III.**12.2
distortion of, **III.**12.4, **III.**12.13–**III.**12.14
linear, **III.**12.4, **III.**12.13
motion, **III.**12.5*f*
Perturbation theory, **I.**7.3, **IV.**8.4
time-dependent, **I.**8.6
Petzold scattering, **I.**43.33–**I.**43.34
Petzval curvature, **I.**1.99
Petzval lenses, **II.**1.29, **II.**1.29*f,* **II.**1.36*f,* **II.**2.9, **II.**2.9*f*
Petzval sum, **II.**17.18–**II.**17.19, **II.**18.42
Pfund gratings, **II.**5.10
Pfund mirrors, **II.**5.8*f*
Pfund objectives, **II.**18.7
Pfund spectrograph, **II.**5.13*f*
Phacoemulsification, **III.**11.13
Phakic intraocular lens, **III.**13.24
Phakic vision, **III.**13.2
Phase change:
field-induced nematic-cholesteric, **II.**14.11
laser-induced, **II.**14.11–**II.**14.12
Phase-change modulators, **IV.**4.2
Phase-changing collisions, **IV.**24.14–**IV.**24.15
Phase coating, **I.**42.96, **I.**42.98, **I.**42.99*f*
Phase conjugate geometry, **IV.**24.18, **IV.**24.18*f,* **IV.**24.19, **IV.**24.26
Phase conjugate resonators, **II.**39.32, **II.**39.34*f*
Phase conjugation:
Brillouin scattering for, **IV.**18.5*4f,* **IV.**18.45, **IV.**18.49–**IV.**18.50, **IV.**18.50*f,* **IV.**18.54
and DFWM, **IV.**17.28, **IV.**18.50
and optical parametric generation, **IV.**22.3
Phase contrast, **II.**17.25, **II.**17.26*f*
Phase diffusion constant:
for laser, **IV.**26.28–**IV.**26.32
for micromaser, **IV.**26.33–**IV.**26.34
Phase discrimination, **I.**25.38
Phase diversity, **III.**1.38
Phase diversity reception, **IV.**1.38
Phase fluctuations, higher-order, **III.**1.20–**III.**1.21
Phase function, **I.**6.9
Phase-interruption broadening, **I.**11.6
Phase-locked loop (PLL), **II.**29.29, **IV.**12.15, **IV.**12.15*f,* **IV.**12.16
Phase locking, **II.**30.21, **II.**30.21*f*
in lasers, **I.**13.31
Phase mask technique, for fiber grating fabrication, **IV.**9.5–**IV.**9.6, **IV.**9.6*f,* **IV.**15.7, **IV.**15.7*f,* **IV.**15.8
Phase matching, **II.**6.12, **II.**6.25*f,* **II.**12.7, **II.**12.13–**II.**12.14, **II.**38.14–**II.**38.16
acoustically-rotated (AR), **II.**12.22
anisotropic diffraction and, **II.**12.8–**II.**12.9, **II.**12.9*f*
birefringent, **II.**12.22
in doubly resonant oscillator, **IV.**22.22–**IV.**22.23
electromagnetically induced, **IV.**23.24
in four-wave mixing, **IV.**1.43, **IV.**3.11
for frequency doubling, **IV.**1.43
isotropic diffractions and, **II.**12.7
noncritical (NPM), **II.**12.30
and nonlinear mixing, **IV.**3.1–**IV.**3.2, **IV.**17.3, **IV.**17.18
optically-rotated (OR), **II.**12.22

Phase matching (*Cont.*):
in optical parametric conversion, **IV.**22.7, **IV.**22.10–**IV.**22.11, **IV.**22.11*f,* **IV.**22.12, **IV.**22.61–**IV.**22.62
in second-order nonlinear optical processes, **II.**38.12–**II.**38.13, **II.**38.13*f,* **II.**38.14, **II.**38.14*f*
and stimulated Raman scattering, **IV.**18.7, **IV.**18.34–**IV.**18.35, **IV.**18.35*f*
tangential (TPM), **II.**12.11, **II.**12.23*f,* **II.**12.25
Phase modulation, **II.**6.10, **II.**6.15, **II.**6.23, **II.**13.17, **IV.**12.30, **IV.**12.32, **IV.**13.26
in ruby lasers, **I.**14.14
self-, **II.**6.12, **II.**10.39
Phase modulation index, **IV.**27.4
Phase modulator:
electro-optic semiconductors as, **IV.**4.64
for lithium niobate, **IV.**4.53, **IV.**4.53*f,* **IV.**4.54
Phase noise:
of edge-emitting lasers, **IV.**4.1
with erbium-doped fiber amplifiers, **IV.**3.11
of lasers, **IV.**2.6, **IV.**4.1, **IV.**4.24–**IV.**4.25, **IV.**4.27, **IV.**26.31
Phase plate, **II.**6.3, **II.**17.25, **III.**25.6, **III.**25.7*f*
Phase retardation:
and circular polarization, **III.**25.6
and multilayer reflective coatings, **III.**24.8
Phase-sensitive detection, **II.**20.9
Phase-shift keying (PSK), **II.**10.35, **IV.**1.37, **IV.**1.37*t,* **IV.**1.38, **IV.**2.11
Phase-shift measurement, **IV.**1.18
Phasesonium, **IV.**23.3
Phase space, **III.**2.3
Phase space density:
in atomic beam brightening, **IV.**25.26, **IV.**25.26*f,* **IV.**28.25
laser cooling effect on, **IV.**28.9
Phase stability, in laser operation, **IV.**4.27
Phase stability margin, in laser servo system, **IV.**27.9
Phase stepping, **II.**30.18–**II.**30.19, **II.**30.19*f*
Phase structure function, **III.**1.12
Phase tomography, **III.**26.5
Phase transfer function (PTF), **II.**32.3
linearity of, **II.**32.4
Phase transition, laser analogy to, **IV.**26.37–**IV.**26.42
Phase zone plates, **III.**23.5–**III.**23.6, **III.**23.6*f*
Phonon broadening, **I.**11.6
Phonon dispersion, **II.**36.16*f*
Phonon energy, **II.**36.61
Phoria, **III.**12.2, **III.**12.21–**III.**12.23, **III.**12.25, **III.**12.28–**III.**12.29, **III.**12.34, **III.**16.5
Phoropter, **III.**11.5
Phosphor constancy, **I.**27.30–**I.**27.31
Phosphors, **III.**34.6–**III.**34.7
Phosphor screens, **I.**21.14–**I.**21.15, **I.**21.15*f,* **I.**21.15*t,* **I.**21.16*f,* **III.**35.32
spectral response characteristics of, **I.**21.16
Phot, **III.**7.8
Photoabsorption, atomic, **III.**A.1, **III.**A.2*f*
Photo-association, **IV.**28.29
Photo-associative spectroscopy (PAS), **IV.**28.28–**IV.**28.30, **IV.**28.30*f*
Photobleaching, **II.**6.19, **IV.**6.18
Photocapacitor, **I.**22.2, **I.**22.6*f*
Photocathode assemblies/input window, **I.**21.11, **I.**21.11*f*–**I.**21.12*f*
Photocathode dark current, **I.**15.39*f*
Photocathode efficiency, **I.**15.33*f*–**I.**15.34*f,* **I.**15.38
Photocathodes, **III.**34.6
internally processed (IP), **I.**21.25
processing, **I.**21.11
Photocathode transfer, **I.**21.25
Photocathode/window combinations, **I.**15.33*f,* **I.**15.35*f*
Photo cell, **I.**15.9
segmented, **II.**15.11
Photochemical injury, **III.**15.2–**III.**15.7
Photocoagulation, **III.**15.3–**III.**15.4
Photoconductive gain, **I.**15.9
Photoconductive mode of operation, in detectors, **I.**15.6*n*
Photoconductivity, far-infrared, **II.**36.40, **II.**36.40*f*
Photoconductors, **I.**16.5*f*–**I.**16.6*f,* **I.**17.25*f,* **I.**22.2, **II.**36.64
amorphous silicon, **I.**22.4*f,* **I.**22.6*f,* **I.**22.9
frequency response of, **I.**17.23, **I.**17.24*f*
gain in, **I.**16.5–**I.**16.6
high speed, **I.**17.22–**I.**17.23, **I.**17.23*f,* **I.**17.24–**I.**17.25
types of, **I.**16.4–**I.**16.5
in xerographic process, **III.**5.3
(*See also* Photodetectors)
Photocopolymerization, **II.**9.9
Photocurrent, and shot noise, **IV.**1.27
Photodetectors, **I.**15.9, **I.**16.4, **II.**29.28
absorbing material in, **I.**17.4, **I.**17.6
amplifiers, **I.**18.3
applications for, **I.**16.12–**I.**16.13
avalanche, **I.**17.4, **I.**17.21, **I.**17.21*f,* **I.**17.22, **IV.**1.29, **IV.**1.30*f,* **IV.**1.40, **IV.**2.1, **IV.**2.7, **IV.**2.9, **IV.**4.66, **IV.**4.76–**IV.**4.77, **IV.**12.39
high speed, **I.**17.19, **I.**17.19*f*
blue-enhanced, **I.**15.57–**I.**15.58, **I.**15.58*f*–**I.**15.59*f*
cadmium selenide (CdSe), **I.**15.43–**I.**15.44, **I.**15.44*f*–**I.**15.49*f*

Photodetectors (*Cont.*):
cadmium sulfide (CdS), **I.**15.43–**I.**15.44, **I.**15.44*f*–**I.**15.49*f*
cadmium sulfide selenide (CdSSe), **I.**15.48*f,* **I.**15.50*f*
cadmium telluride (CdTe), **I.**15.50, **I.**15.50*f*
carrier transit time in, **I.**17.6–**I.**17.7, **I.**17.7*f,* **I.**17.8
carrier trapping in, **I.**17.10, **I.**17.10*f*
characteristics of, **IV.**4.72*t*
contact type and configuration of, **I.**17.4
dark current in, **IV.**4.71–**IV.**4.75
defined, **I.**16.2
diffusion current in, **I.**17.9, **I.**17.9*f*
extended wavelength, **I.**16.10–**I.**16.11, **I.**16.11*t*
extrinsic, **I.**15.6
future, **I.**16.16
gallium nitride (GaN), **I.**15.43, **I.**15.43*f*
germanium avalanche (Ge APD), **I.**15.71, **I.**15.72*f*
germanium (Ge), **I.**15.66–**I.**15.68, **I.**15.69*f,* **I.**15.70, **I.**15.70*f*–**I.**15.71*f,* **I.**15.83*f*–**I.**15.85*f*
copper-doped (Ge:Cu), **I.**15.95, **I.**15.95*f*–**I.**15.97*f*
gallium-doped (Ge:Ga), **I.**15.98
gold-doped (Ge:Au), **I.**15.82–**I.**15.83, **I.**15.83*f,* **I.**15.84, **I.**15.84*f*
mercury-doped (Ge:Hg), **I.**15.91, **I.**15.92*f*–**I.**15.93*f*
zinc-doped (Ge:Zn), **I.**15.96, **I.**15.97*f*–**I.**15.98*f*
high-speed, **I.**17.3
impedance in, **I.**17.11*f*
indium antimonide (InSb), **I.**15.81, **I.**15.81*f,* **I.**15.82, **I.**15.82*f,* **I.**23.9
indium arsenide (InAs photovoltaic), **I.**15.75–**I.**15.76, **I.**15.77*f*–**I.**15.78*f*
indium gallium arsenide avalanche (InGaAs APD), **I.**15.64–**I.**15.65, **I.**15.65*f,* **I.**15.66, **I.**15.66*f,* **I.**15.67, **I.**15.67*f*–**I.**15.69*f*
indium gallium arsenide (InGaAs), **I.**15.62–**I.**15.63, **I.**15.63*f*–**I.**15.64*f*
infrared, **I.**23.7, **I.**23.9–**I.**23.10
interpreting specifications for, **III.**7.17–**III.**7.18
intrinsic, **I.**15.6
lead selenide (PbSe), **I.**15.75*f,* **I.**15.77–**I.**15.78, **I.**15.78*f,* **I.**15.79, **I.**15.79*f*–**I.**15.80*f*
lead sulfide (PbS), **I.**15.71–**I.**15.73, **I.**15.73*f,* **I.**15.73*t,* **I.**15.74, **I.**15.74*f*–**I.**15.77*f*
lead tin telluride (PbSnTe), **I.**15.90, **I.**15.91*f*
life test (accelerated aging), **I.**16.14
lifetime of, **I.**17.6
light history effects of, **I.**15.50*f*
materials in, **I.**16.3*t*

Photodetectors (*Cont.*):
mercury cadmium telluride (HgCdTe), **I.**15.85, **I.**15.85*f,* **I.**15.86–**I.**15.87, **I.**15.87*f*–**I.**15.90*f,* **I.**23.7, **I.**23.9
photoconductive, **I.**15.88
photovoltaic, **I.**15.89–**I.**15.90
mercury cadmium zinc telluride (HgCdZnTe), **I.**15.86
mercury manganese telluride (HgMnTe), **I.**15.85
mercury zinc telluride (HgZnTe), **I.**15.85
metal-insulator-semiconductor (*see* Photogates)
noise in, **IV.**4.74–**IV.**4.75
nonimaging, **I.**18.2*f*
in optical communications systems, **IV.**2.1, **IV.**2.7
orientation of light in, **I.**17.4
output current of, **IV.**2.11
packaging of, **I.**17.10–**I.**17.11
performance of, **I.**15.11, **I.**15.19
photoconductive, **I.**15.6, **I.**15.16
mode of operation, **I.**15.6*n*
photoelectromagnetic, **I.**15.7
photoemissive, **I.**15.5, **I.**15.30
photographic, **I.**15.7, **I.**15.98–**I.**15.99, **I.**15.99*f*
photoionization, **I.**15.8
as photometric measuring device, **III.**14.2
photon, **I.**15.5, **I.**23.8*f*
background-limited, **I.**15.12–**I.**15.13
strong-signal, **I.**15.12
photon flux limited, **I.**15.17
photon-noise-limited, **I.**15.11, **I.**15.13*f*–**I.**15.15*f*
photovoltaic, **I.**15.6–**I.**15.7, **I.**15.17, **I.**17.3
p-i-n, **IV.**1.29, **IV.**2.1, **IV.**2.7–**IV.**2.8, **IV.**4.2, **IV.**4.66–**IV.**4.75
absorption spectra for, **IV.**4.69, **IV.**4.70*f*
geometry for, **IV.**4.67, **IV.**4.67*f,* **IV.**4.68–**IV.**4.69
materials for, **IV.**4.66
sensitivity of, **IV.**4.69, **IV.**4.72*t*
spectral response of, **IV.**4.69, **IV.**4.71*f*
speed of, **IV.**4.70–**IV.**4.72
positive-negative (p-n), **IV.**4.68, **IV.**4.72
pyroelectric, **I.**15.5, **I.**15.24–**I.**15.25, **I.**15.25*f,* **I.**15.28*f*
quantum, **I.**15.5, **I.**17.6
efficiency, **I.**15.16, **I.**23.9*f*
quantum well infrared (QWIP), **I.**16.17, **I.**16.18*f,* **I.**23.10
RC time constant in, **I.**17.8, **I.**17.8*f*
readout structures, **I.**23.11*f*
reliability of, **I.**16.13
resonant, **IV.**4.69
response speed of, **I.**15.16, **I.**15.18, **I.**15.19*f*

Photodetectors (*Cont.*):
silicon, **I.**15.18, **I.**15.51, **I.**15.51*f,* **I.**15.57*f,* **III.**4.2
boron-doped (Si:B), **I.**15.94
gallium-doped (Si:Ga), **I.**15.92, **I.**15.94, **I.**15.94*f*
silicon avalanche (APDs), **I.**15.59, **I.**15.59*f*–**I.**15.62*f,* **I.**15.65*f*
silicon junction pin, **I.**15.51, **I.**15.52*f,* **I.**15.54*f,* **I.**15.56–**I.**15.57, **I.**15.57*f*–**I.**15.58*f*
silicon junction pn, **I.**15.51, **I.**15.51*f,* **I.**15.52–**I.**15.53, **I.**15.53*f*–**I.**15.56*f*
spectral response of, **I.**15.15–**I.**15.16
speed limitations in, **I.**17.6
stability of, **I.**15.18
structures, **I.**17.3
testing of, **I.**16.14*t*
thermal, **I.**23.8*f*
triglycine sulfate (TGS), **I.**15.24*f*–**I.**15.27*f*
types of, **I.**16.3, **I.**16.4*f,* **I.**17.3, **I.**17.5*f*
uniformity of, **I.**15.18
UV-enhanced, **I.**15.57–**I.**15.58, **I.**15.58*f*–**I.**15.59*f*
(*See also* Photodiodes)
Photodiodes, **II.**24.33
avalanche, **I.**16.9–**I.**16.10, **I.**16.10*f*
in optical fibers, **II.**10.27, **II.**10.28*f*
separated absorption, grading, multiplication (SAGM APD), **I.**17.20, **I.**17.22*f*
(*See also* Photodetectors, avalanche)
depletion in, **I.**16.6–**I.**16.7
in frame transfer devices, **III.**4.2, **III.**4.4
hole-accumulated, **I.**22.4*f*
hole accumulation diode (HAD), **I.**22.8
indium gallium arsenide (InGaAs), **I.**16.14, **I.**16.15*f*
junction, **I.**22.2–**I.**22.3, **I.**22.4*f,* **I.**22.5–**I.**22.6, **I.**22.6*f*
mean-time-to-failure (MTTF) in, **I.**16.14–**I.**16.15
mesa vs. planar, **I.**16.15, **I.**16.15*f,* **I.**16.16
on optoelectronic integrated circuit (OEIC) chips, **I.**16.16
p-i-n, **I.**16.6–**I.**16.7, **I.**16.7*f,* **I.**16.16, **I.**17.22*f,* **IV.**1.29, **IV.**2.1, **IV.**2.7–**IV.**2.8
double heterostructure, **I.**17.14
lateral, **I.**16.16, **I.**16.16*f,* **I.**16.17
in optical fibers, **II.**10.27
resonant, **I.**17.16, **I.**17.16*f*–**I.**17.17*f*
Schottky, **I.**17.17–**I.**17.18, **I.**17.18*f,* **I.**17.19
vertically illuminated, **I.**17.11, **I.**17.12*f,* **I.**17.13, **I.**17.13*f*
waveguide, **I.**17.14–**I.**17.15, **I.**17.15*f,* **I.**17.16
pinned, **I.**22.2, **I.**22.8–**I.**22.9
quantum well infrared, **I.**16.16
silicon, **II.**24.33
solid-state, **II.**24.33
(*See also* Photodetectors)
Photoelastic coefficient, **II.**33.28
Photoelectric effect, **I.**8.5
Photoemitters:
quantum efficiency of, **I.**15.38*f*
spectral sensitivity of, **I.**15.33*f*
Photo energy, **II.**36.49*f*
Photoexcitation, above-band-gap, **II.**36.61
Photo gain, in photoconductors, **I.**16.5
Photogates, **I.**16.11, **I.**16.11*f,* **I.**16.12
in frame transfer devices, **III.**4.2, **III.**4.4
Photogenerated carriers, **I.**22.5*n*
Photographic emulsions, **III.**6.8
X-ray sensitivity of, **III.**6.20
(*See also* Silver halide crystals)
Photographic film:
black-and-white, **III.**6.25–**III.**6.26, **III.**6.26*t*
stability of, **III.**6.25
as X-ray detector, **III.**34.7–**III.**34.8
classes of, **I.**20.15
color, **III.**6.2–**III.**6.5
acutance of, **III.**6.2, **III.**6.5
Eberhard effects on, **III.**6.3
formats for, **III.**6.22–**III.**6.23, **III.**6.26
multilayer factors in, **III.**6.3*f*
negative, **III.**6.10, **III.**6.18, **III.**6.23, **III.**6.26–**III.**6.28, **III.**6.28*t,* **III.**6.29, **III.**6.29*t*
optical effects on, **III.**6.2
professional vs. amateur, **III.**6.21–**III.**6.24
spectral sensitivity of, **III.**6.16–**III.**6.19
speed of, **III.**6.19–**III.**6.21, **III.**6.26
structure of, **III.**6.3–**III.**6.5
X-ray sensitivity of, **III.**6.20–**III.**6.21
(*See also* Film, Kodachrome)
detective quantum efficiency in, **I.**20.24
dye density in, **I.**20.16*f*
image structure in, **I.**20.18
information capacity of, **I.**20.26
manufacturers of, **I.**20.27
performance data for, **I.**20.19*t*
performance parameters for, **I.**20.9–**I.**20.10, **I.**20.11*f*
Polaroid Instant Color, **I.**20.15
resolving power in, **I.**20.26
signal-to-noise ratio in, **I.**20.24
35-mm, **I.**21.22*f,* **III.**6.21, **III.**6.26–**III.**6.27, **III.**6.28*t*
Photographic image dyes, **III.**6.10–**III.**6.14
Photographic layers, silver halide (*see* Silver halide photographic layers)
Photographic papers:
black-and-white, **III.**6.25
color, **III.**6.5–**III.**6.6, **III.**6.10
Photographic plate, **I.**3.4

Photographic systems, tone reproduction in, **I.**20.17–**I.**20.18, **I.**20.18*f*
Photography, **II.**23.2
  color, **I.**20.14, **I.**20.14*f*
  speckle-pattern, **II.**23.10
Photoionization detector, **II.**24.32
Photokeratitis, **III.**15.1, **III.**15.4–**III.**15.6
Photolabile pigments, **III.**9.3, **III.**9.8, **III.**9.11–**III.**9.12
Photolithography, **II.**2.21, **II.**8.17
Photoluminescence (PL), **II.**36.72, **II.**36.75*f,* **II.**36.76
  decay time, **II.**20.12, **II.**20.13*f*
  excitation spectroscopy (PLE), **II.**36.76
  measurement of, **II.**28.20, **II.**36.74
  measurements, **II.**20.21
  spectrum
    of F-centers in KBr, **I.**8.30*f*
    low-temperature, **I.**8.20*f*
    in O_2, **I.**8.28*f*
    in tri-positive Cr ions, **I.**8.29*f*
Photomasks (*see* Mask layout)
Photometer, **II.**24.47
Photometric calibrations, **II.**24.46
Photometric radiation transfer calculations, **II.**24.44
Photometry, **I.**26.42–**I.**26.43, **I.**27.22, **II.**24.7, **II.**24.11, **II.**24.13, **III.**7.6, **III.**14.1
  applications of, **III.**14.12
  definition of, **II.**24.40
  heterochromatic flicker, **II.**24.44
  integrated cavities used in, **III.**2.25
  physical, **III.**7.6, **III.**14.2
  purpose of, **III.**14.1–**III.**14.2
  vs. radiometry, **III.**2.2, **III.**7.6*t,* **III.**14.1
  scope of, **II.**24.41
  standards in, **I.**10.8, **III.**7.2–**III.**7.3, **III.**14.3
  Stiles-Crawford effect in, **III.**9.7
  terminology used in, **III.**2.2*t,* **III.**7.3
  unit conversions in, **III.**7.8*t*–**III.**7.9*t,* **III.**7.13–**III.**7.15
  units of measurement in, **III.**7.6–**III.**7.12
Photomicrographic lamp, **I.**10.45*f*
Photomultiplier, **I.**15.9
  for photon counting, **I.**15.42*f*
Photomultiplier tubes (PMT), **I.**15.30–**I.**15.31, **I.**15.32*f,* **I.**18.7, **I.**18.7*f,* **II.**36.64
  bandwidth in, **I.**18.8
  base design, **I.**18.9
  cathode shielding in, **I.**18.10
  dark counts in, **I.**18.8–**I.**18.9
  dynode biasing in, **I.**18.9–**I.**18.10
  gain in, **I.**18.7
  gallium phosphide dynodes and, **I.**15.40
Photomultiplier tubes (PMT) (*Cont.*):
  linearity of, **I.**15.40
  magnetic shielding in, **I.**18.10
  oscilloscope presentation of, **I.**15.41*f*
  photon counting and, **I.**15.40
  pulse height in, **I.**18.8
  quantum efficiency of, **I.**18.7
  range of D^* for, **I.**15.36*f*–**I.**15.37*f*
  recommended circuit for, **I.**15.41*f*
  response time of, **I.**15.39
  secondary electrons and, **I.**15.42*f*
  snubbing in, **I.**18.10
  solar radiation and, **I.**15.36
Photon absorption:
  in nonlinear interactions, **IV.**17.6–**IV.**17.9
  in Raman scattering, **IV.**17.16–**IV.**17.17
  (*See also* Two-photon absorption (2PA))
Photon bunching, **I.**4.2
Photon contrast, spectral bands and, **I.**23.6*f*
Photon correlation spectroscopy (PCS), **III.**3.8
Photon counting, **I.**15.9, **I.**18.7*f,* **I.**18.16, **I.**21.26–**I.**21.27
  in signal analysis, **I.**18.15
Photon detectors, **I.**23.8*f*
Photon dose, **II.**24.6
  and Einstein, **II.**24.13
Photon echo, **II.**38.5, **IV.**23.4, **IV.**24.11, **IV.**24.11*f,* **IV.**24.12, **IV.**24.12*f,* **IV.**24.13–**IV.**24.14, **IV.**24.14*f,* **IV.**24.15, **IV.**25.19
  stimulated, **IV.**24.15, **IV.**24.15*f,* **IV.**24.16–**IV.**24.17, **IV.**24.17*f,* **IV.**24.18, **IV.**24.18*f*
  stimulated, with stochastic pulse, **IV.**24.24–**IV.**24.25
Photon echo spectroscopy, **IV.**24.25–**IV.**24.26, **IV.**24.26*f*
Photon energy:
  for beryllium, **II.**35.28*f*
  of *K*- and *L*-shell emission lines, **III.**A.6*t*–**III.**A.7*t*
Photon flux, **II.**24.6–**II.**24.7
  irradiance, **II.**24.46
Photonic bandgap (PBG) materials, **IV.**20.2
  applications for, **IV.**20.18
  Maxwell's equations for, **IV.**20.3–**IV.**20.4
  and waveguides, **IV.**20.13–**IV.**20.17
  (*See also* Photonic crystals)
Photonic crystals, **IV.**20.3–**IV.**20.5, **IV.**20.5*f,* **IV.**20.6
  line defects in, **IV.**20.13–**IV.**20.14, **IV.**20.14*f,* **IV.**20.15, **IV.**20.15*f,* **IV.**20.16, **IV.**20.16*f,* **IV.**20.17, **IV.**20.17*f*
  microcavities in, **IV.**20.6–**IV.**20.7, **IV.**20.7*f,* **IV.**20.8, **IV.**20.8*f,* **IV.**20.17
  point defects in, **IV.**20.9–**IV.**20.10, **IV.**20.10*f,* **IV.**20.11–**IV.**20.13

Photonic excitation, **I.**16.3, **I.**16.3*f*
Photonic integrated circuits (PICs), **I.**17.6, **II.**6.2, **II.**6.26, **II.**6.26*f,* **II.**6.27, **II.**6.27*f*
balanced heterodyne, **II.**6.27, **II.**6.27*f*
cross-talk in, **II.**6.35–**II.**6.36
reliability of, **II.**6.28
wavelength division multiplexing (WDM), **II.**6.35, **II.**6.35*f*
(*See also specific types*)
Photon lifetime, **IV.**12.1
Photon-photon correlations, in quantum mechanics, **IV.**26.14–**IV.**26.15
Photons, **I.**16.2
attenuation coefficients for, **II.**35.53*t*
concept of, **IV.**26.8
generation of, **IV.**17.6–**IV.**17.9
radiometric measurements using, **III.**7.6
states of, **IV.**26.11–**IV.**26.13
in synchrotron X-ray optics, **III.**26.3
as X-ray emissions, **III.**19.6
Photon statistics:
laser, **IV.**26.23–**IV.**26.24, **IV.**26.24*f,* **IV.**26.25–**IV.**26.26, **IV.**26.26*f,* **IV.**26.27
micromaser, **IV.**26.27–**IV.**26.28, **IV.**26.29*f*
Photon survival, probability of, **I.**43.12
Photon transfer:
in solid-state arrays, **III.**4.12, **III.**4.13*f*
in solid-state cameras, **III.**4.13
Photopic action spectrum curve, **III.**15.3, **III.**15.4*f*
Photopic vision, **II.**24.41–**II.**24.42, **III.**7.8–**III.**7.9, **III.**7.9*f,* **III.**7.10, **III.**7.10*f,* **III.**7.11, **III.**7.11*f,* **III.**7.12–**III.**7.13, **III.**13.13, **III.**14.2–**III.**14.3
luminous efficiency functions, **II.**24.42*t*
Photopigments, **I.**25.8
absorption spectra of, **I.**25.7
Photopolarimeter:
division-of-amplitude (DOAP), **II.**27.15, **II.**27.15*f,* **II.**27.16, **II.**27.16*f,* **II.**27.17, **II.**27.20
division-of-wavefront (DOWP), **II.**27.15, **II.**27.15*f*
dual rotating-retarder Mueller matrix, **II.**27.21*f*
four-detector, **I.**5.27, **II.**27.15–**II.**27.16, **II.**27.20, **II.**27.22*f*
Mueller matrix, Fourier amplitudes and, **II.**27.21*t*
rotating-compensator fixed-analyzer (RCFA), **II.**27.14, **II.**27.20
rotating-element (REP), **II.**27.14, **II.**27.14*f*
(*See also* Ellipsometer)
Photoreceptor optics, **III.**9.3
Photoreceptors, **I.**25.6*f,* **I.**25.9*f*
biological
and aging, **III.**13.13
alignment of, **III.**9.6–**III.**9.7, **III.**9.7*f*
Photoreceptors, biological (*Cont.*):
ciliary vs. rhabdomeric, **III.**9.3
definition of, **III.**10.2
ellipsoid in, **III.**9.1
idealized model of, **III.**9.8, **III.**9.8*f,* **III.**9.9, **III.**9.9*f*–**III.**9.10*f,* **III.**9.11, **III.**9.11*f,* **III.**9.12
index of refraction for, **III.**9.5
light incidence on, **III.**9.4, **III.**9.5*f,* **III.**9.18–**III.**9.21, **III.**13.11
location of, in human eye, **III.**10.3*f*
in macular degeneration, **III.**10.13
microscopic view of, **III.**10.9, **III.**10.11*f*
myoid in, **III.**9.2
orientation of, **III.**9.6, **III.**9.8, **III.**9.20, **III.**9.29
single, optical model of, **III.**9.15–**III.**9.18
spacing of, **III.**9.2, **III.**10.10–**III.**10.11, **III.**10.13, **III.**10.13*f*
transfer function of, **III.**9.25*f*
waveguiding in, **III.**9.3–**III.**9.5, **III.**9.12–**III.**9.24
(*See also* Cones; Rods)
density distribution of, **I.**25.5
image sampling by, **I.**25.5
lengths of, **I.**25.8
response properties of, **I.**25.9
types of, **I.**25.5
xerographic, **III.**5.1
belt, **III.**5.4
charging of, **III.**5.2, **III.**5.2*f*
discharge of, **III.**5.3. III.5.3*f,* **III.**5.4
in magnetic brush development, **III.**5.6, **III.**5.6*f,* **III.**5.7
(*See also* Cones; Rods)
Photoreflectance (PR), **II.**36.70, **II.**36.71*f*
Photorefractive beam amplification, **II.**39.7
Photorefractive beam coupling, **II.**39.5, **II.**39.30
Photorefractive damage, **IV.**22.64
Photorefractive effect, **II.**39.1
band-edge, **II.**39.21
electrorefractive photorefractive (ERPR), **II.**39.21
grating formation and, **II.**39.1
Photorefractive gain, in two-beam coupling, **II.**39.27
Photorefractive holograms, **II.**39.1–**II.**39.2
storage of, **II.**39.34–**II.**39.35
Photorefractive holography, **II.**39.25
Photorefractive keratectomy (PRK), **III.**11.16, **III.**13.2, **III.**13.25
Photorefractive materials:
beam depletion in, **II.**39.29
comparison of, **II.**39.13, **II.**39.13*t,* **II.**39.14
figures of merit for, **II.**39.11–**II.**39.13
performance, **II.**39.11–**II.**39.13

Photorefractive mechanism, **II.**39.2*f*
Photorefractive semiconductors, **II.**39.20*t,* **II.**39.21
Photorefractive waveguides, **II.**39.35
Photorefractivity:
  of lithium niobate, **IV.**4.56–**IV.**4.57
  as nonlinearity, **IV.**17.24
  in optical limiting, **IV.**19.4*f,* **IV.**19.9, **IV.**19.12, **IV.**19.12*f*
Photoresist, **II.**23.15
Photoresponse nonuniformity (PRNU):
  for solid-state array, **III.**4.12
  for solid-state camera, **III.**4.13
Photoretinitis, **III.**15.1, **III.**15.7–**III.**15.8, **III.**15.10
Photosensing elements, dark current in, **I.**22.11, **I.**22.11*f*
Photosensitivity, **IV.**9.1–**IV.**9.3, **IV.**15.5
Photosynthesis, **I.**43.9
Photosynthetically available radiation (PAR), **I.**43.9
Phototransistors, **I.**17.4
Phototropism, **III.**9.2
Phototubes, gallium arsenide, **II.**20.6, **II.**20.8
Physical constants, fundamental, **II.**33.10*t*
Physical-optics theory, **I.**7.3
Physical photometry, **III.**7.6, **III.**14.2
Phytoplankton cells:
  absorption by, **I.**43.24, **I.**43.25*f,* **I.**43.26
    chlorophyll-specific, **I.**43.26*f,* **I.**43.27*t*
    features of, **I.**43.25
  refractive indices of, **I.**43.19–**I.**43.20
Pickups, **I.**34.7
Picosecond quantum beats, **II.**38.5
Picosecond relaxation, **II.**20.14
Pidgeon and Brown model, **II.**36.43
Piezoelectric transducer (PZT):
  designs for, **IV.**27.16–**IV.**27.19
  in laser servo system, **IV.**27.6, **IV.**27.8, **IV.**27.9*f,* **IV.**27.10, **IV.**27.16–**IV.**27.21
Piezo-optic coefficient, **II.**33.25
Pigment self-screening, **I.**26.40
Pikhtin-Yas'kov formula, **II.**33.27
Pinch plasmas, **III.**33.3
Pinhole optics, **III.**31.5, **III.**31.11
Piston error, **I.**1.95, **I.**1.99
Pixel density:
  for computer monitors, **III.**16.3
  for head-mounted displays, **III.**18.6
Pixels, in image quality, **III.**17.6
Pixel sensors, **III.**4.2, **III.**4.8, **III.**4.8*f,* **III.**4.9
Plan Apochromat oil-immersion lens, **II.**17.18–**II.**17.19
Planar buried heterostructure (PBH) lasers, **IV.**4.6
Planar lenses, **II.**1.28
Planar lightwave circuit multiplexer (PLC MUX), **IV.**12.41
Planck, Max, **IV.**26.7
Planckian radiation, **III.**14.7, **III.**14.11–**III.**14.12
Planckian radiator, **II.**24.25
Planck's constant, **I.**8.5
Planck's formula, **IV.**26.7–**IV.**26.8, **IV.**26.10
Planck's law, **I.**10.8, **I.**44.16–**I.**44.17, **II.**24.7, **II.**24.25–**II.**24.26, **III.**14.11
Plane angle, **III.**7.3–**III.**7.4, **III.**7.4*f*
Plane-grating monochromator (PGM), **III.**21.5
Plane mirror, reflection by, **I.**1.28
Plane of polarization, **I.**5.5*n*
Plane of vibration, **I.**5.5*n*
Plane waves, **I.**2.4–**I.**2.5, **I.**2.9–**I.**2.10, **I.**2.10*f,* **I.**3.3*f,* **I.**3.4
  decomposition, **I.**3.21
Plano optics, **I.**40.6
Plant tissue, as fiber optic, **III.**9.26–**III.**9.29
Plasma-assisted chemical etching (PACE), **II.**11.5
Plasma-assisted chemical vapor deposition (PCVD), **II.**10.43, **IV.**1.45
Plasma radiation sources:
  characteristics of, **III.**33.2*t*
  laser-generated, **III.**33.1
  pinch, **III.**33.3
Plasmas:
  energy balance of, **II.**28.5
  optical generation of, **IV.**17.22
Plasmons, **I.**9.24, **II.**36.35–**II.**36.36, **II.**36.36*f*
Plastic lenses, **I.**37.19–**I.**37.20, **I.**37.20*f,* **II.**7.7, **II.**7.8*f,* **II.**7.10
  index of refraction for, **II.**7.7
  shapes of, **II.**7.11*f*
  tolerances for, **II.**7.7, **II.**7.10*t*
Platinum:
  extinction coefficient for, **II.**35.18*t*
    vs. wavelength, **II.**35.26*f*
  index of refraction in, **II.**35.18*t*
    vs. wavelength, **II.**35.26*f*
  reflectance of, **II.**35.38*t*–**II.**35.39*t*
    vs. wavelength, **II.**35.45*f*
Pleisosynchronous network, **IV.**16.6
Plotter distortion, **II.**31.5, **II.**31.7
Plueker spectrum tubes, **I.**10.38, **I.**10.44*f,* **I.**10.44*t*
P-n junction, **IV.**12.1–**IV.**12.2
  in semiconductor laser, **IV.**12.26
Pn photodetector, **IV.**4.68, **IV.**4.72
Pockels cells, **II.**20.9
Pockels effect, **II.**6.10, **II.**6.19, **II.**6.22, **II.**13.6, **II.**33.29, **IV.**12.2, **IV.**12.32–**IV.**12.33, **IV.**12.33*f,* **IV.**17.24, **IV.**22.3
Pockels' theory, **II.**12.3, **II.**12.5

Poincaré sphere, **I.**5.26–**I.**5.27
  references for, **I.**5.26
Point-angle characteristic function, of rays, **I.**1.17
Point-by-point technique, for fiber grating fabrication, **IV.**9.7–**IV.**9.8
Point characteristic function, of rays, **I.**1.15
Point eikonal, **I.**1.15
Pointer processing, **IV.**12.22–**IV.**12.23
Point images, aberrations of, **I.**1.92–**I.**1.93
Point source irradiance transmittance (PSIT), **I.**38.24
Point source normalized irradiance transmittance (PSNIT), **I.**38.23
Point source power transmittance (PSPT), **I.**38.24
Point sources, in nonimaging optics system design, **III.**2.7
Point source transmittance (PST) plot, **I.**38.6, **I.**38.6*f,* **I.**38.7, **I.**38.8*f,* **I.**38.21, **I.**38.21*f*
Point spread function (PSF), **II.**11.6, **III.**10.5, **III.**10.7*f,* **III.**13.10–**III.**13.11
Point-to-point approximation, **II.**24.15–**II.**24.16
Point-to-point links, **IV.**1.24–**IV.**1.31
  components of, **IV.**1.24, **IV.**1.24*f*
  evolution of, **IV.**2.1
  Fibre Channel as, **IV.**16.4
  modulation in, **IV.**1.24–**IV.**1.25
  pulse distortion in, **IV.**1.25, **IV.**1.26*f*
  signal-to-noise ratio in, **IV.**1.26
  in SONET systems, **IV.**2.16
  system design for, **IV.**1.26–**IV.**1.31
  in time-division multiplexing, **IV.**12.6, **IV.**12.8*f*
  for wavelength-division multiplexing, **IV.**13.12–**IV.**13.13, **IV.**13.13*f*
Poisson's ratio, **II.**33.32–**II.**33.33, **II.**35.58
  in polycrystalline materials, **II.**35.73*t*
Polacoat, **II.**3.27, **II.**3.30
  extinction ratio in, **II.**3.30*n*
Polanret system, **II.**17.25–**II.**17.26
Polarimeter, **II.**22.7
  complete/incomplete, **II.**22.4
  division of amplitude and, **II.**22.6
  division of aperture and, **II.**22.5
  dual rotating, **II.**22.19, **II.**22.19*f*
    polarizer, **II.**22.20, **II.**22.20*f,* **II.**22.21*t,* **II.**22.22
  light-measuring, **II.**22.3–**II.**22.4, **II.**22.14–**II.**22.16
    classes of, **II.**22.5
  sample-measuring, **II.**22.4–**II.**22.5, **II.**22.16*f*
    incomplete, **II.**22.20
    for Mueller matrix elements, **II.**22.16–**II.**22.17
  time-sequential, **II.**22.5
Polarimetric data reduction equation, **II.**22.17–**II.**22.19
Polarimetric measurement equation, **II.**22.17–**II.**22.19
Polarimetry, **II.**22.26–**II.**22.27
Polariton, **II.**36.32
Polarizance, **II.**22.29
Polarization, **II.**22.7
  in all-optical switching, **IV.**21.6
  circular, **III.**25.4–**III.**25.8, **III.**32.6–**III.**32.8, **IV.**28.16
  with coherent optical transients, **IV.**24.6–**IV.**24.10
  in coherent transmissions, **IV.**1.39
  degrees of, **I.**5.12, **I.**5.12*n,* **I.**5.13
  dependent loss, **II.**22.29
  and electroabsorption modulators, **IV.**4.62
  and electrorefraction, **IV.**4.65
  in fiber-optic sensor applications, **IV.**8.6–**IV.**8.7, **IV.**8.7*f*
  induced, **II.**36.54
  of insertion devices, **III.**32.18
  of laser emissions, **IV.**4.15
  linear, **III.**25.2–**III.**25.4
  in lithium niobate modulators, **IV.**4.55–**IV.**4.56
  magnetic circular (MCP), **II.**20.21
  matrix methods for computing, **I.**5.25–**I.**5.26
  and multilayer reflective coatings, **III.**24.7–**III.**24.8, **III.**24.9*f*
  of neutrons, **III.**36.6–**III.**36.7, **III.**36.13
  nonlinear, **IV.**3.2, **IV.**3.5, **IV.**3.8, **IV.**3.10, **IV.**17.4, **IV.**17.9, **IV.**17.24, **IV.**17.26–**IV.**17.27, **IV.**17.31
  nonnormal-incidence reflection, **I.**5.12–**I.**5.13
  nonnormal-incidence transmission, **I.**5.16, **I.**5.19
  optical, **I.**5.2
  optical amplifier sensitivity to, **IV.**11.3–**IV.**11.4
  of optical fiber, **II.**10.11–**II.**10.12, **IV.**1.13–**IV.**1.14
  plane of, **I.**5.5*n*
  power series expansion, **II.**36.54
  in Raman effect, **IV.**18.4–**IV.**18.6, **IV.**18.42, **IV.**18.42*t*
  reflected state of, **I.**31.22*n*
  reflection amplitudes, **I.**9.12*f*
  rotation of, **I.**9.11
  in semiconductors, **II.**36.32, **IV.**25.16
  sensitivity, **II.**22.28–**II.**22.29
  state of (SOP), **IV.**10.7
  transitions in, **II.**20.15
  transmittances and degree of, **I.**5.17*t*–**I.**5.18*t*
  underwater, **I.**43.51–**I.**43.52
  of VCSEL emissions, **IV.**4.49–**IV.**4.50
  of X rays, **III.**25.1–**III.**25.8
Polarization analyzer, **II.**22.4–**II.**22.5, **II.**22.16
Polarization anisotropy measurements, **II.**20.7

Polarization attenuators, **I.**5.13
Polarization controller, **II.**6.25
Polarization coupling, **II.**22.7
Polarization dispersion, **IV.**1.14
Polarization effects, **I.**4.23
  type B errors and, **II.**24.37
Polarization element, **II.**22.7
  common defects of, **II.**22.23–**II.**22.24
  homogeneous, **II.**22.32–**II.**22.33
  inhomogeneous, **II.**22.32–**II.**22.33, **II.**22.33*f*
  nonideal, **II.**22.22
  polarization properties of, **II.**22.23–**II.**22.25
Polarization generator, **II.**22.4–**II.**22.5
Polarization gradient cooling, **IV.**28.16, **IV.**28.16*f,* **IV.**28.17–**IV.**28.18, **IV.**28.18*f*
Polarization metrology, **II.**22.27–**II.**22.28
Polarization modulation, **II.**22.5
Polarization multiplexing, **IV.**8.1
Polarization ratios, **I.**9.14*f*
Polarization scans, **II.**26.12
Polarization scrambling, **IV.**13.26
Polarization spectroscopy, **IV.**27.13
Polarization state, **I.**2.3
Polarized beam splitters (PBS), **I.**31.10*f,* **I.**31.23, **I.**31.24*f*
Polarized light, **II.**22.7
Polarized radiation, vs. angle of incidence, **II.**35.48*f*
Polarizer-compensator-sample-analyzer (PCSA), **II.**27.11, **II.**27.11*f*–**II.**27.12*f*
Polarizers, **I.**5.13, **II.**22.7, **II.**22.24, **IV.**10.7, **IV.**10.8*f,* **IV.**10.9
  vs. analyzers, **II.**22.13
  basic relations for, **I.**5.12
  beam-splitting, **II.**3.44–**II.**3.45
  Beilby-layer, **II.**3.30
  Brewster angle, **II.**3.36–**II.**3.37, **II.**3.40, **II.**3.41*t,* **II.**3.42, **II.**3.42*t,* **II.**3.43*f*
    types of, **II.**3.37*t*
  dichroic, **II.**3.26–**II.**3.27, **II.**3.28*f*
    coatings for, **II.**3.30
  embedded, **I.**42.71
  grating, **II.**3.32, **II.**3.35
    diffraction, **II.**3.35
    echelette, **II.**3.35
  Harrick's, **II.**3.37
  horizontal linear, **II.**22.14
  for integrated circuits, **II.**3.61
  interference, **I.**42.68, **II.**3.42–**II.**3.44
  iodine-polyvinyl alcohol, **II.**3.29
  left circular, **II.**22.13–**II.**22.14
  MacNeille, **I.**42.71, **I.**42.72*f*–**I.**42.73*f,* **I.**42.75*f*
  measuring polarization of, **II.**3.35–**II.**3.36, **II.**3.38*t*–**II.**3.39*t*
Polarizers (*Cont.*):
  miniature, **II.**3.61
  multicomponent, **I.**42.70*f*–**I.**42.71*f*
    reflection equivalent of, **I.**42.69
    X-ray, **I.**42.70
  non-normal-incidence, **II.**3.42–**II.**3.44
  optical fiber, **II.**3.61
  pile-of-plates, **II.**3.36, **II.**3.42
  plastic laminated HR, **II.**3.29*f*
  plate, **I.**42.71
  polyvinyl alcohol, **II.**3.30
  pyrolitic-graphite, **II.**3.31, **II.**3.31*f*
  reflection, **II.**3.36–**II.**3.37, **II.**3.38*t*–**II.**3.39*t,* **II.**3.44
  sheet, **II.**3.27–**II.**3.30
  sodium nitrate, **II.**3.27
  thin-film, **II.**20.7
  wire grid, **II.**3.32, **II.**3.32*n,* **II.**3.33, **II.**3.33*f,* **II.**3.34–**II.**3.35
    types of, **II.**3.34*t*
Polarizing angle, **I.**5.10
Polaroid, **II.**3.27–**II.**3.30, **II.**15.8
  Instant Color Film, **I.**20.15
Polaroid lenses, **III.**11.10
Poling, **IV.**1.43
Polishing, **I.**40.4–**I.**40.5
Pollution monitoring, **I.**16.12
Polycapillary X-ray optics:
  angle of acceptance in, **III.**35.27
  angle of incidence in, **III.**30.5, **III.**30.5*f*
  applications for, **III.**30.4, **III.**30.15, **III.**35.4–**III.**35.5, **III.**35.8–**III.**35.9, **III.**35.15, **III.**35.19–**III.**35.21
  collimation in, **III.**30.6*f,* **III.**30.8–**III.**30.11, **III.**30.11*f*–**III.**30.12*f,* **III.**30.15
  composition of, **III.**30.5, **III.**30.6*f*–**III.**30.7*f,* **III.**30.8*t*
  and electron impact sources, **III.**31.11
  energy filtering in, **III.**30.13, **III.**30.13*f*
  in focused beam diffraction, **III.**35.13, **III.**35.14*f*
  focusing with, **III.**30.13–**III.**30.14, **III.**30.14*f,* **III.**30.15
  function of, **III.**30.4–**III.**30.7
  with neutron beams, **III.**36.15
  radiation damage in, **III.**30.14
  transmission data for, **III.**30.5–**III.**30.7, **III.**30.7*f*–**III.**30.10*f,* **III.**35.9*t*–**III.**35.11*t*
Polycarbonate, **II.**7.8*f,* **II.**7.10, **II.**34.6, **II.**34.7*f*
Polychromatic lenses, **II.**1.41
Polychromatic radiation:
  calculations, **II.**24.11
  definitions, **II.**24.10–**II.**24.11
Polycrystalline metals:
  elastic moduli in, **II.**35.73*t*
  electrical resistivity of, **II.**35.59*t*

Polycrystalline metals (*Cont.*):
Poisson's ratio in, **II.**35.73*t*
thermal conductivities of, **II.**35.58
Polycrystalline optical materials, **II.**33.6–**II.**33.7
Polycrystalline (PC) fiber, **IV.**14.2*t*–**IV.**14.3*t*, **IV.**14.8–**IV.**14.9, **IV.**14.9*f*
Poly-diallylglycol, **II.**34.6, **II.**34.13
Polyethylene terephthalate, **I.**20.4
Polymer-dispersed liquid crystals (PDLC), **II.**14.2, **II.**14.17–**II.**14.18, **II.**14.18*f*, **II.**14.19, **II.**14.19*f*
dynamic response of, **II.**14.18
light transmission in, **II.**14.18*f*
light-valve, photoactivated, **II.**14.19, **II.**14.19*f*
physical mechanism of, **II.**14.18
Polymer films, organic, **II.**39.24–**II.**39.25
Polymeric optics, **II.**34.1
Polymers:
optical (*see* Optical polymers)
organic, **II.**6.19–**II.**6.20
Polymethylmethacrylate, **II.**34.6, **II.**34.7*f*
Polystyrene, **II.**7.8*f*, **II.**7.10
Population inversions, **I.**11.9, **I.**11.13
thermal equilibrium and, **I.**11.13
Porro prism, **II.**4.3, **II.**4.5*f*
Abbé modification of, **II.**4.6*f*
Porro prisms, mounting, **I.**37.22*f*
Positive-intrinsic-negative (p-i-n) photodetectors (*see* Photodetectors, p-i-n)
Positive-powered lenses, **II.**34.15
Postamplifier, in OTDM system, **IV.**12.39–**IV.**12.40
Posterior chamber phakic lens implants (PCPLIs), **III.**11.17
Potassium niobate ($KNbO_3$), **II.**39.17
Pound-Drever-Hall locking technique, **IV.**27.14
Powder cloud development, in xerographic systems, **III.**5.9–**III.**5.10, **III.**5.10*f*
Power:
and dispersion, **IV.**1.25
measurement of, **II.**26.13
in nonlinear transmissions, **IV.**3.1
optical, **III.**11.2
as radiometric unit, **III.**7.5
as throughput limitation, **IV.**2.13–**IV.**2.14
(*See also* Optical power)
Power amplifier, **IV.**5.3
Power conversion efficiency (PCE), in amplifiers, **IV.**5.3
Power enhancement effect, in dispersion-managed soliton transmission, **IV.**7.12–**IV.**7.13
Power penalty, **IV.**2.10
Power/pixel, **I.**1.88
Power spectra, for digital coding formats, **IV.**12.12, **IV.**12.13*f*
Power spectra analyzer (PSA), **II.**12.44, **II.**12.45*f*
Power spectral density (PSD), **I.**7.4–**I.**7.8, **I.**7.10–**I.**7.11, **III.**26.4, **III.**28.5
Power splitter (*see* Splitter)
Poynting vectors, **I.**1.9, **I.**3.4, **I.**5.8, **I.**6.5, **I.**9.7
Praseodymium-doped fiber amplifier (PDFA), **IV.**5.6–**IV.**5.7, **IV.**11.3
Preamplifiers:
Brillouin, **IV.**11.4
noise in, **IV.**27.5
optical, **IV.**2.11, **IV.**11.2
in OTDM system, **IV.**12.38–**IV.**12.39, **IV.**12.39*f*
Precision, **II.**29.2
Predictable quantum efficiency (PQE) devices, **II.**24.32
light-trapping, **II.**24.33
Pre-form free drawing, in fiber fabrication, **IV.**1.47
Prentice's rule, **III.**12.15, **III.**12.19, **III.**12.28
Presbyopia, **III.**11.3, **III.**11.6–**III.**11.9, **III.**13.2, **III.**13.9
absolute vs. functional, **III.**12.30
and computer work, **III.**16.5–**III.**16.6
and contact lenses, **III.**11.12–**III.**11.13, **III.**12.19, **III.**13.23
incidence of, **III.**13.4
and prismatic dissociation, **III.**11.15
spectacles for, **III.**13.22–**III.**13.23
Primaries, in spectral sensitivity, **III.**6.17
Primary position of gaze, **III.**12.2
Principal transmittances, **I.**5.12–**I.**5.13
Principal values, **II.**33.7
Principle dispersion, **II.**33.27
Prism adaptation, **III.**12.22–**III.**12.23
Prismatic displacement, **III.**12.13, **III.**12.15, **III.**12.19, **III.**12.28–**III.**12.29
Prism diopter, **III.**18.1
Prism effectivity, **III.**12.28–**III.**12.29
Prisms:
air-spaced, **II.**3.7, **II.**3.14
amount of flux through, **II.**3.7
angle measurements in, **II.**29.17–**II.**29.20
axis of, **II.**3.8*n*
axis wander in, **II.**3.17
beam-splitter, polarizing, **II.**3.7, **II.**3.19, **II.**3.20*f*
and bifocal jump, **III.**12.15
calcite polarizing, **II.**17.27
cemented, **II.**3.7
in compound parabolic concentrators, **III.**2.20
correction of, **III.**10.2
deviation and, **II.**4.2
direct-vision, **II.**4.2
dispersive, **II.**5.1
displacement and, **II.**4.2

Prisms (*Cont.*):
extinction ratio of, **II.**3.10
and eye alignment, **III.**12.28–**III.**12.29
in Fresnel lenses, **III.**2.10
general deviation, **II.**4.28*f*–**II.**4.29*f*
Glan-Thompson, **II.**20.7
Halle, **II.**3.18–**II.**3.19
Jellett-Cornu, **II.**3.60
length-to-aperture (L/A) ratio in, **II.**3.8, **II.**3.8*f*
Lippich conventional polarizing, **II.**3.7, **II.**3.13–**II.**3.15
Marple-Hess, **II.**3.13–**II.**3.15
measurements in, **II.**29.19*f*
micro-optic functions of, **IV.**10.5, **IV.**10.6*f*
milling, **II.**29.19*f*
mountings for
bonded, **I.**37.22
flexure, **I.**37.25*f*
mechanically clamped, **I.**37.22, **I.**37.22*f*
Porro, **I.**37.22*f*
neutron deflection by, **III.**36.6
Nomarski, **II.**17.33–**II.**17.34
and nonsequential surfaces, **III.**2.7
nonuniform magnification by, **III.**12.10, **III.**12.10*f,* **III.**12.17
and perceived direction, **III.**12.6
polarizing, **II.**3.2, **II.**3.26
field angle for, **II.**3.8, **II.**3.8*f,* **II.**3.9
noncalcite, **II.**3.25
types of, **II.**3.6–**II.**3.7, **II.**3.7*f*
properties of, **II.**4.2, **II.**4.3*t*
pyramidal error in, **II.**29.17, **II.**29.18*f*
right-angle, **II.**4.3, **II.**4.4*f*
Steeg and Reuter, **II.**3.18
transmission curve in, **II.**3.10, **II.**3.11*f*
vergence responses to, **III.**12.20, **III.**12.25–**III.**12.27
Wollaston, **II.**17.33–**II.**17.34, **II.**17.36*f*
(*See also* Polarizers; *specific types*)
Probe beam, in atomic beam slowing, **IV.**28.10*f,* **IV.**28.11
Profile dispersion, **IV.**1.11
in optical fibers, **II.**10.9
Profile measurements, **I.**7.8–**I.**7.10
Progressive addition lenses (PALs), **III.**11.2, **III.**11.8, **III.**11.8*f,* **III.**11.9, **III.**16.6
Progressive scan architecture, **III.**4.3
Projected area, **III.**7.3, **III.**7.3*t*
Projected solid angle (PSA):
in radiation transfer, **III.**2.5, **III.**2.6*f*
symbol for, **III.**7.3–**III.**7.4
Projection systems:
aspheric lenses in, **III.**2.9
examples of, **III.**2.23
Projection systems (*Cont.*):
flux density in, **III.**2.2
liquid crystal display (LCD), **III.**2.7
mixing rods in, **III.**2.33
uniformity in, **III.**2.23–**III.**2.25
Projective transformation (*see* Collineation)
Propagation constant, **IV.**1.10–**IV.**1.12, **IV.**2.4, **IV.**8.3
Propagation delay:
in communications system design, **IV.**1.27
measuring, **IV.**1.18
in multimode fiber, **IV.**2.3
Propagation loss:
in cross-phase modulation, **IV.**3.4
in lithium niobate modulator, **IV.**4.56
Properties of materials, definitions of, **II.**33.8*t*
Proportional counters, **III.**34.4–**III.**34.5
Proportional integral differentiator (PID), in laser servo system, **IV.**27.10, **IV.**27.10*f,* **IV.**27.11, **IV.**27.11*f*
Proportional-integral (PI) amplifier circuit, **IV.**27.6*f*
Protection switching, in SONET ring architecture, **IV.**13.13
Protein crystallography, **III.**30.11–**III.**30.12, **III.**35.7, **III.**35.14–**III.**35.15
Proton-bombardment-defined lasers, **I.**13.45
Proton stripe lasers, **I.**13.38*f*
Provostaye-Desains formula, **I.**5.22
Proximal vergence, **III.**12.24
Proximity-focused electronic lens, **I.**21.9, **I.**21.9*f*
Pseudofield vector, for coherent optical transients, **IV.**24.4, **IV.**24.7
Pseudogap, **IV.**20.2
Pseudointerlacing (field integration), **III.**4.5, **III.**4.6*f,* **III.**4.19, **III.**4.20*f*
Pseudophakic, **III.**11.14, **III.**13.2, **III.**13.9, **III.**13.23
Psychophysical measurement, **I.**29.1*n*
Psychophysical methods, defined, **I.**29.1
Psychophysical research, **I.**29.2–**I.**29.3
magnitude production in, **I.**29.6
matching in, **I.**29.6
nulling in, **I.**29.5
Psychophysics, **III.**10.2–**III.**10.3, **III.**10.7
Pterygium, **III.**13.6, **III.**15.1, **III.**15.6–**III.**15.7
Public switched telephone network, **IV.**13.16
Pulse, chirped, **IV.**24.24–**IV.**24.25
Pulse amplitude modulation (PAM), **IV.**12.6, **IV.**12.7*f,* **IV.**12.8
Pulse code modulation (PCM), **IV.**12.6, **IV.**12.10–**IV.**12.11
24-channel format, **IV.**12.21, **IV.**12.21*f*
Pulse compression, **II.**10.38, **II.**10.39*f,* **II.**10.40, **IV.**1.41, **IV.**1.41*f,* **IV.**1.42, **IV.**18.42, **IV.**18.45, **IV.**25.12

Pulsed-dye laser, **III.**1.34, **III.**1.34*f,* **III.**1.35, **III.**1.35*f*
Pulse distortion, **IV.**1.25, **IV.**1.26*f*
Pulsed lasers, **I.**11.13
Pulsed optical parametric oscillators, **IV.**22.50–**IV.**22.61
  femtosecond, **IV.**22.55–**IV.**22.61
  nanosecond, **IV.**22.51–**IV.**22.54
  picosecond, **IV.**22.55–**IV.**22.57
Pulse generation:
  in two-cycle regime, **IV.**25.4, **IV.**25.5*f*
  ultrashort, **IV.**25.4
Pulse length modulation (PLM), **IV.**12.6, **IV.**12.7*f*
Pulse modulation, **IV.**12.4
Pulse position modulation (PPM), **IV.**12.6, **IV.**12.7*f*
Pulse propagation, **II.**10.38
  and electromagnetically induced transparency, **IV.**23.9, **IV.**23.19–**IV.**23.22, **IV.**23.22*f,* **IV.**23.28
  self-phase modulation effects on, **IV.**3.3, **IV.**13.7, **IV.**13.7*f*
Pulse shaping, **I.**14.7
  and Kerr lens mode-locking, **IV.**25.15
  and nonlinear transmissions, **IV.**3.1, **IV.**3.3
Pulse sources, ultrashort, **I.**14.18
Pulse-width modulation (PWM), **I.**28.16
Pump beam, in atomic beam slowing, **IV.**28.10*f,* **IV.**28.11
Pump-enhanced optical parametric oscillator, **IV.**22.15, **IV.**22.35–**IV.**22.42
  conversion efficiency in, **IV.**22.38–**IV.**22.39
  dual-cavity, **IV.**22.39, **IV.**22.42*f*
  layout of, **IV.**22.36*f*
  parameters for, **IV.**22.40*t*
  tuning of, **IV.**22.41–**IV.**22.42
Pump-enhanced singly resonant oscillator (PESRO), **IV.**22.15
Pumping, **I.**11.16, **I.**11.18
  lasers and, **I.**11.10, **I.**11.13, **I.**11.18–**I.**11.19, **I.**11.19*f*–**I.**11.20*f*
  in optical parametric generation, **IV.**22.3–**IV.**22.4, **IV.**22.5*f*–**IV.**22.6*f,* **IV.**22.7–**IV.**22.8, **IV.**22.61–**IV.**22.62
  photon, **I.**11.16
  in Raman scattering, **IV.**18.1
  in semiconductor lasers, **I.**13.4
  synchronous, **I.**11.30
Pumping efficiency, of optical amplifier, **IV.**11.3–**IV.**11.4
Pump laser frequency, **IV.**17.16, **IV.**17.29–**IV.**17.30
Pump-probe spectroscopy, **IV.**25.18*f,* **IV.**25.19–**IV.**25.20
Pump tuning, **IV.**22.62
  in doubly resonant oscillator, **IV.**22.28
  in pump-enhanced oscillator, **IV.**22.41–**IV.**22.42
  in singly resonant oscillator, **IV.**22.35
Punch through, in color photography, **III.**6.4
Pupil directions, **I.**1.84, **I.**1.84*f,* **I.**1.85, **I.**1.94
  numerical aperture and, **I.**1.85
Pupils, of human eyes:
  and aging, **III.**13.7–**III.**13.8, **III.**15.9
  diameter of, **I.**24.11, **III.**13.7, **III.**13.7*f,* **III.**13.8, **III.**13.18, **III.**14.8
    retinal line spread functions for, **I.**24.23*f*
  distance between, **III.**12.15, **III.**12.22
  paraxial description of, **I.**1.83
  red reflex in, **III.**11.4
  size of, **III.**10.4, **III.**10.9–**III.**10.10
Purcell-Pennypacker method, **I.**6.17
Pure diattenuator, **II.**22.7
Pure retarder, **II.**22.7
Pursuit eye movements, **III.**12.21
Pushbroom scanning, **II.**19.4, **II.**19.17–**II.**19.18
Push processing, for photographic film, **III.**6.23
Pyknostereopsis, **III.**18.5
Pyrazolotriazole magenta dyes, **III.**6.12
Pyroelectric detectors (*see* Photodetectors, pyroelectric)
Pyrolytic graphite, **II.**3.27
PZT disk, **IV.**27.16

Q-switching, **I.**11.28–**I.**11.29, **I.**11.30*f,* **IV.**25.4. **IV.**25.5*f,* **IV.**25.6–**IV.**25.7, **IV.**25.10
Quantization:
  of digital signal, **IV.**12.10, **IV.**12.10*f*
  and signal distortion, **IV.**12.11
Quantized elastic waves, propagation of, **II.**20.30
Quantum, of light, **IV.**26.8, **IV.**26.10, **IV.**26.12
  in Hanbury-Brown-Twiss effect, **IV.**26.14
Quantum-beat laser, **IV.**26.43
Quantum-confined Stark effect (QCSE), **II.**6.11, **IV.**4.57, **IV.**4.58*f,* **IV.**4.65, **IV.**12.2, **IV.**12.33
Quantum-dense coding, **IV.**26.15
Quantum detection efficiency (QDE), **III.**34.7
Quantum efficiency, **I.**15.9, **I.**16.8, **I.**22.2*n*
  of LEDs, **IV.**4.40
  of photodiodes, **IV.**4.69
  of rare-earth doped amplifiers, **IV.**5.6–**IV.**5.7
  of silicon, **IV.**2.7
  of spectral sensitizers, **III.**6.14
Quantum electrodynamic (QED) shifts, **I.**8.6, **I.**8.11
Quantum electrodynamics (QED), **IV.**26.10–**IV.**26.13
Quantum jump experiments, **II.**28.5

Quantum mechanics:
and atomic transitions, **IV.**28.2
beginnings of, **IV.**26.7–**IV.**26.10
in laser theory, **IV.**26.6–**IV.**26.7, **IV.**26.15–**IV.**26.21
in optical collisions, **IV.**28.29
in optical trapping, **IV.**28.22
photon-photon correlations in, **IV.**26.14–**IV.**26.15
Schrödinger vs. Heisenberg pictures of, **IV.**26.6, **IV.**26.34
Quantum resonance absorption, **IV.**27.16
Quantum sensitivity:
in color photographic emulsions, **III.**6.10
Quantum teleportation, **IV.**26.15
Quantum well, **IV.**12.2
electroabsorption in, **IV.**4.57, **IV.**4.63
in electroabsorption modulator, **IV.**12.33–**IV.**12.34
in electro-optic semiconductor modulators, **IV.**4.64
and electrorefraction, **IV.**4.65
in LEDs, **IV.**4.40
in VCSELs, **IV.**4.46, **IV.**4.49–**IV.**4.50
Quantum well (QW) lasers, **I.**11.37–**I.**11.38, **I.**13.7, **I.**13.10–**I.**13.11, **I.**13.11*f,* **I.**13.12, **I.**13.14*f,* **I.**13.15, **I.**13.24, **I.**13.28, **I.**13.38, **IV.**4.1, **IV.**4.3–**IV.**4.4, **IV.**4.28–**IV.**4.31
absorption spectrum for, **IV.**4.29, **IV.**4.30*f*
band diagrams for, **IV.**4.29, **IV.**4.31*f*
long wavelength, **I.**13.18–**I.**13.19
ridge waveguide, **I.**13.21
strained, **I.**13.16–**I.**13.18, **I.**13.28*t*
threshold carrier density in, **I.**13.13*f,* **I.**13.17*f*
Quantum wire lasers, **I.**13.19
Quarter-wavelength-shifted grating, **IV.**4.38, **IV.**4.38*f,* **IV.**12.28, **IV.**12.28*f,* **IV.**20.6
Quarter-wave plates, **I.**5.22, **I.**5.24, **I.**5.24*f,* **I.**5.25, **III.**25.6
Quartz envelope lamps, **I.**10.19
Quasi-phase-matched (QPM) nonlinear materials, **IV.**22.2, **IV.**22.33, **IV.**22.35, **IV.**22.54, **IV.**22.59–**IV.**22.60
Quasi-phase matching, in optical parametric generation, **IV.**22.11–**IV.**22.12, **IV.**22.34–**IV.**22.35
Quaternary, **IV.**4.2–**IV.**4.3

Rabi effect, optical, **II.**38.5
Rabi frequency:
in electromagnetically induced transparency, **IV.**23.6, **IV.**23.12*t,* **IV.**23.13
generalized, **IV.**24.4, **IV.**24.7
in micromaser, **IV.**26.22
and optical force on atoms, **IV.**28.4, **IV.**28.6
two-photon, **IV.**24.21
Racah parameters, **I.**8.14
Radar polarimetry, **II.**22.28
Radial clearance, growth of, **I.**37.11
Radial distance, peak-to-peak, **I.**31.15
Radial gradients (*see* Graded index (GRIN) lens, radial gradients in)
Radial keratotomy (RK), **III.**11.16, **III.**13.24
Radial stress:
and axial stress, combined, **I.**37.11
reduced temperatures and, **I.**37.10
Radial symmetry, **II.**19.5
Radian, **III.**7.3
Radiance, **II.**24.8–**II.**24.10, **II.**24.10*f*
of lasers, **III.**15.12, **III.**15.12*f*
as radiometric unit, **III.**7.6, **III.**14.1, **III.**14.4*t,* **III.**14.5, **III.**14.6*f*
spectral, **I.**43.6, **I.**43.8
calibrations, **I.**10.9*f*
filament lamps, **I.**10.9
thermal, molecular emission and, **I.**44.16–**I.**44.17, **I.**44.20*f*
Radiance coefficient, **III.**14.10
Radiance conservation theorem, **II.**24.13–**II.**24.14
Radiance factor, **III.**14.10
Radiance function, **I.**4.8
Radiance temperature, **III.**14.4*t,* **III.**14.7
Radiant emittance, **I.**4.8, **II.**25.3
Radiant energy, **II.**24.8, **III.**14.4*t,* **III.**14.6
Radiant exitance, **III.**7.5, **III.**14.4*t,* **III.**14.6, **III.**14.6*f,* **III.**14.12
Radiant exposure, **II.**14.6, **III.**14.4*t,* **III.**15.3
Radiant flux, **II.**24.14*f*
to photon flux conversion, **II.**24.12–**II.**24.13
through a Lambertian reflecting sphere, **II.**24.18–**II.**24.19
(*See also* Watts)
Radiant incidance, **III.**7.5
Radiant intensity, **I.**4.8, **III.**7.5, **III.**14.4, **III.**14.4*t,* **III.**14.5, **III.**14.5*f*
Radiant power, **II.**24.8
Radiant power transfer, **II.**24.13, **II.**24.13*t*
Radiating species:
emission linewidth of, **I.**11.5
line broadening of, **I.**11.5
Radiation:
artificial sources of, **I.**10.3
baseline standard of, **I.**10.6
blackbody, **IV.**14.4, **IV.**26.7
Bremsstrahlung, **III.**19.6, **III.**30.13, **III.**30.13*f,* **III.**31.5–**III.**31.6, **III.**31.7*f,* **III.**31.10
broadband, and transient Raman effects, **IV.**18.29–**IV.**18.30, **IV.**18.30*f,* **IV.**18.31–**IV.**18.32
channeling, **III.**33.1, **III.**33.3

Radiation (*Cont.*):
coherent, **III.**2.2, **III.**19.6, **III.**32.2, **III.**32.19, **IV.**18.42–**IV.**18.43, **IV.**26.19
commercial sources of, **I.**10.11
electromagnetic, interaction of matter with, **II.**36.4
field, **I.**4.16–**I.**4.17
high-energy, **III.**6.20–**III.**6.21
incoherent, **III.**2.2, **III.**2.42, **III.**15.2, **III.**19.6
infrared, **II.**24.7
ionizing, effect on fiber links, **IV.**6.18
laboratory sources of
argon arc lamps, **I.**10.11
deuterium arc lamps, **I.**10.11
deuterium lamp standards, **I.**10.10
IR radiometic standards, **I.**10.9
lamp standards, **I.**10.8
luminous flux standards, **I.**10.9
luminous intensity standards, **I.**10.8
photometric standards, **I.**10.8
radiometric sources in the far ultraviolet, **I.**10.10
source calibrations in the ultraviolet, **I.**10.10–**I.**10.11
spectral irradiance calibrations, **I.**10.10*f*
spectral irradiance lamps, **I.**10.10
spectral radiance calibrations, **I.**10.9*f*
spectral radiance filament lamps, **I.**10.9
tungsten lamp standards, **I.**10.10
linearly polarized, **III.**25.5
and matter, interaction of, **II.**28.4
optical
damage from, **III.**15.2–**III.**15.8
measurement of (*see* Radiometry)
parametric, **III.**33.1, **III.**33.3
photosynthetically available (PAR), **I.**43.9
Planckian, **III.**14.7, **III.**14.11–**III.**14.12
scattered, analysis of, **I.**38.24
shot noise, **I.**15.3
solar, **III.**13.8, **III.**15.1–**III.**15.2, **III.**15.4, **III.**15.6
stray paths, **I.**38.23
synchrotron (*see* Synchrotron radiation)
in therapeutic applications, **III.**35.33–**III.**35.34
transfer, basic equation of, **I.**38.22–**I.**38.23
transition, **III.**33.1, **III.**33.3
tungsten, **III.**7.16
wavelength, **I.**7.7
working standards of, **I.**10.8
(*See also* Blackbody radiation; Light)
Radiation-induced darkening, **IV.**6.18
Radiation-induced loss, **IV.**6.18
Radiation modes, **II.**6.4
Radiation pressure force, **IV.**28.6
Radiation scattering (*see* Scattering)
Radiation transfer:
through absorbing media, **II.**24.15
approximations, **II.**24.15
from blackbody source, **III.**2.3, **III.**7.13*f,* **III.**7.14, **III.**7.15*f,* **III.**713
between a circular source and detector, **II.**24.17
conic reflectors used in, **III.**2.11
constraints on, **III.**2.12–**III.**2.13
high-energy, and photographic image creation, **III.**6.20–**III.**6.21
and multiple scattering, **III.**3.10–**III.**3.13
through nonimaging optics, **III.**2.1
process, **I.**44.10
in retinal waveguiding, **III.**9.3
theory, **I.**43.4
Radiative decay, measurement of, **II.**28.20
Radiative escape, in ultracold collisions, **IV.**28.28
Radiative lifetime, **I.**11.5
of transitions, **II.**20.12–**II.**20.13
Radiative loss, and fiber attenuation, **IV.**2.2
Radiative processes, **I.**11.7
Radiative quantum efficiency:
in praseodymium-doped fiber amplifier systems, **IV.**5.6
Radiative recombination, **I.**12.3, **I.**12.4*f,* **I.**12.6
secondary, **I.**12.7
Radio astronomy, **I.**4.24
Radiography:
computed, **III.**35.27, **III.**35.30–**III.**35.32, **III.**35.32*f*
neutron, **III.**36.7
Radiometers, electrical substitution, **II.**24.29–**II.**24.30
sources of error in, **II.**24.31
Radiometric measurements, **II.**24.8
Radiometric sources in the far ultraviolet, **I.**10.10
Radiometric-to-photometric conversion, **II.**24.46
Radiometry, **I.**21.4, **II.**24.6–**II.**24.7, **II.**24.13
applications of, **III.**14.12
definition of, **III.**7.5, **III.**14.1
nomenclature in, **II.**24.6
vs. photometry, **III.**2.2, **III.**7.6*t,* **III.**14.1
standards bodies in, **III.**7.2–**III.**7.3
terminology used in, **III.**2.2*t,* **III.**7.3
unit conversion to photometric, **III.**7.12–**III.**7.13
units of measure in, **III.**7.5–**III.**7.6
Rainbows, **I.**44.39, **I.**44.41*f*
Raman amplification, **IV.**11.3–**IV.**11.4, **IV.**18.4, **IV.**18.5*f,* **IV.**18.24, **IV.**18.24*f,* **IV.**18.25, **IV.**18.25*t,* **IV.**18.28*f*
Raman cooling, **IV.**28.19
Raman effect:
electronic, **IV.**17.12
inverse, **II.**36.59

Raman effect (*Cont.*):
quantum mechanics of, **IV.**18.6
source of, **IV.**18.4–**IV.**18.5
Raman gain:
for fused silica, **IV.**3.5, **IV.**3.6*f*
and stimulated Raman scattering, **IV.**3.7
Raman generator, **IV.**18.4, **IV.**18.5*f*
Raman-induced Kerr-effect spectroscopy (RIKES), **II.**36.58–**II.**36.59, **IV.**17.5*t,* **IV.**17.14, **IV.**17.19
Raman modes, **II.**33.13, **II.**33.15
Raman-Nath diffraction, **I.**30.11, **I.**30.11*f*
Raman-Nath equations, **II.**12.4–**II.**12.5
Raman oscillator, **IV.**18.4, **IV.**18.5*f*
Raman scattering, **I.**9.18–**I.**9.19, **I.**43.51*f,* **I.**43.52, **I.**44.11, **II.**20.31, **II.**20.31*f,* **II.**28.17–**II.**28.18, **II.**33.29–**II.**33.30, **II.**36.57–**II.**36.58, **II.**36.77–**II.**36.82, **IV.**18.1–**IV.**18.2
anti-Stokes, **IV.**17.5*t,* **IV.**17.7, **IV.**17.7*f,* **IV.**17.17, **IV.**17.17*f,* **IV.**17.18–**IV.**17.20, **IV.**18.2, **IV.**18.2*f,* **IV.**18.32–**IV.**18.33, **IV.**18.33*f,* **IV.**18.34–**IV.**18.35, **IV.**18.35*f*
vs. Brillouin scattering, **IV.**18.1, **IV.**18.45, **IV.**18.49
electronic, **IV.**17.12, **IV.**17.14
interaction types in, **IV.**18.2, **IV.**18.2*f,* **IV.**18.3
laser-induced, **I.**44.21
regimes of, **IV.**18.3–**IV.**18.4
resonant vs. nonresonant, **IV.**17.17
stimulated (SRS), **II.**10.37–**II.**10.38, **II.**10.40
Stokes, **IV.**17.5*t,* **IV.**17.17, **IV.**17.17*f,* **IV.**17.18–**IV.**17.20, **IV.**18.2, **IV.**18.2*f*
in time domain measurement, **IV.**1.18
(*See also* Coherent anti-Stokes Raman scattering (CARS); Stimulated Raman scattering (SRS))
Raman spectroscopy, **IV.**27.14
Raman spectrum, **II.**36.80–**II.**36.81, **II.**36.81*f,* **II.**36.83*f*
Raman tensors, **I.**9.20*t*–**I.**9.21*t*
Ramsden disk, **II.**17.21
Ramsey fringe, **IV.**24.19–**IV.**24.20, **IV.**24.20*f,* **IV.**24.21, **IV.**28.27
Range compensator, **II.**29.5, **II.**29.6*f*–**II.**29.7*f*
Range error, **II.**29.4
Range finder, **II.**29.4*f*
Range gating, **I.**21.29–**I.**21.31
Rapid Rectilinear lenses, **II.**1.28, **II.**1.31*f*
Rare-earth doped fiber amplifiers, **IV.**1.44, **IV.**5.1–**IV.**5.7, **IV.**11.3
configuration of, **IV.**5.2, **IV.**5.2*f,* **IV.**5.3
operating regimes for, **IV.**5.3
Rare-earth elements, as fiber dopants, **IV.**1.44, **IV.**1.47
Rare-earth ions:
absorption and emission spectra of, **II.**28.9*f*
and transition-metal ion spectra, **II.**28.8
tri-positive, **I.**8.15, **I.**8.19, **I.**8.19*t,* **I.**8.20–**I.**8.21
trivalent, in ionic crystals, **II.**28.8
ultraviolet absorption spectrum of, **II.**28.12*f*
Rare-earth transition metals (RE-TM), in magneto-optical recording, **I.**31.26–**I.**31.27, **I.**31.28*f*
Raster:
controls that affect, **I.**27.13
and CRT input signal, **I.**27.11
generation, **I.**27.9
scanning, **I.**28.22
Raster output scanning (ROS), **III.**5.4
Rating scale tasks, **I.**29.7–**I.**29.8
Ratio imaging, **II.**17.46
Ray aberrations, **I.**1.95, **I.**1.95*f,* **I.**1.96
in reflection gratings, **III.**21.8
Ray densities, **I.**1.96
Ray equations, cartesian coordinates for, **I.**1.22
Ray error curves, transverse, **I.**33.5
Ray fans, **I.**1.39
Ray intercept curves, **I.**33.2, **I.**33.2*f,* **I.**33.4, **I.**33.4*f,* **I.**34.14
(*See also* Aberration curves, transverse)
Rayleigh-Gans approximation, **I.**6.10, **I.**6.10*f,* **I.**6.18
Rayleigh-Rice vector perturbation theory, **I.**7.5
Rayleigh scattering, **I.**43.31–**I.**43.33, **I.**44.10, **I.**44.14–**I.**44.15, **II.**20.30, **II.**33.12, **II.**33.29–**II.**33.30, **IV.**17.16
and erbium-doped fiber amplifiers, **IV.**5.5–**IV.**5.6
and fiber attenuation, **IV.**1.10, **IV.**1.44, **IV.**2.2
and fluoride fibers, **IV.**1.48
and laser beacons, **III.**1.30–**III.**1.33, **III.**1.33*f*
in polycapillary microfocus X-ray fluorescence, **III.**35.20, **III.**35.21*f*
stimulated, **IV.**17.20
wing, **IV.**17.15
in X-ray diffraction, **III.**35.6
Rayleigh-Sommerfeld diffraction formula, **I.**3.20
Rayleigh theory, **I.**6.12
Ray optics:
predictions of, **I.**1.10
(*See also* Geometric optics)
Ray paths, **I.**1.11
invariance of, **I.**1.24
Rays:
additional, in first-order layout, **I.**32.12, **I.**32.12*f*
angle characteristic function of, **I.**1.16–**I.**1.17, **I.**1.17*f*
angle-point characteristic function of, **I.**1.18

Rays (*Cont.*):
arbitrary, expansions about, **I.**1.18
attributes of, **I.**1.10
axial, **I.**1.39
axis, expansions about, **I.**1.18–**I.**1.19
base, **I.**1.47
behavior of, **I.**1.10
and biological waveguiding, **III.**9.12–**III.**9.14, **III.**9.14*f*
central, **I.**1.47
characteristic functions of, **I.**1.15, **I.**1.19–**I.**1.20
examples of, **I.**1.19–**I.**1.20
chief, **I.**1.82, **I.**1.82*f,* **II.**1.8
collimated, **II.**2.1
corpuscular theory of, **I.**1.9
curved path, **I.**1.20
definition of, **I.**1.9
differential equations for, **I.**1.22–**I.**1.23
geometry, **I.**1.21–**I.**1.22
direction cosines of, **I.**1.11–**I.**1.12
edge, **III.**2.23
exact, **I.**34.4
extraordinary
angle of refraction for, **II.**3.6
principal index for, **II.**3.4
refraction of, **II.**3.2
fields of, **I.**1.14
finite, **I.**1.39
geometric path length of, **I.**1.12
geometric wavefronts of, **I.**1.13–**I.**1.14
groups of, **I.**1.11
in heterogeneous media, **I.**1.20
image-forming, **I.**1.81
intersection points of, **I.**1.40, **I.**1.40*f*
invariance properties of, **I.**1.11
iterated, **I.**34.13
lagrangian, **I.**34.12
leaky, **II.**10.6
in a lens, classification of, **I.**1.39
marginal, **I.**1.82, **I.**1.82*f,* **II.**1.8, **II.**18.41
meridional, **I.**1.25, **I.**1.39, **I.**1.41, **II.**10.6, **III.**2.13–**III.**2.14
nonsequential tracing of, **III.**2.7
normal congruence of, **I.**1.11
in optical fiber
classification of, **IV.**1.8, **IV.**1.8*f*
propagation of, **IV.**1.6–**IV.**1.7, **IV.**1.7*f*
optical path difference (OPD) of, **I.**34.13, **I.**34.13*f*
optical path length of, **I.**1.12–**I.**1.13
ordinary, **I.**34.12
orthotomic systems of, **I.**1.11, **I.**1.14
paraxial, **I.**1.39, **I.**1.41, **II.**1.5
point characteristic function of, **I.**1.13
Rays (*Cont.*):
principal, **II.**1.8
real, **I.**1.39
vs. virtual, **I.**1.11
reference, **I.**34.13
reversibility of, **I.**1.10
skew, **I.**1.25–**I.**1.26, **I.**1.39, **II.**10.6, **III.**2.7, **III.**2.13–**III.**2.14, **III.**2.20–**III.**2.21, **III.**2.21*f*
two meridional paraxial, **I.**1.11
variational integrals for, **I.**1.22
wave theory of, **I.**1.9
Ray tracing, **I.**1.39, **I.**32.4, **I.**32.4*f,* **I.**32.5, **I.**34.2, **I.**34.12, **I.**38.26
backward, **III.**2.8
in binary optics, **II.**8.4
computer models for, **III.**26.4, **III.**29.2
field patch, **III.**2.8
by the grating equation, **II.**8.4
and head-mounted display design, **III.**18.6–**III.**18.7
Monte Carlo techniques for, **II.**11.12, **III.**2.7–**III.**2.8
nonsequential, **III.**2.6–**III.**2.7
by the Sweatt model, **II.**8.4
Ray transfer, **I.**1.40
Reactive force, **IV.**28.6
Readout noise, **III.**4.11
Receiver:
extinction ratio of, **IV.**6.14
in OTDM system, **IV.**12.38–**IV.**12.39, **IV.**12.39*f,* **IV.**12.40
in point-to-point communications system, **IV.**1.27–**IV.**1.28, **IV.**1.28f, **IV.**1.28*t,* **IV.**1.29, **IV.**1.29*f,* **IV.**1.30
sensitivity of, **IV.**1.36, **IV.**1.37*t,* **IV.**2.1, **IV.**2.7–**IV.**2.11, **IV.**6.3
types of, **IV.**2.1
Receiver operating characteristic (ROC), **I.**29.7, **I.**29.8*f*
Receiver thermal noise, **IV.**2.7
Reciprocity failure, in silver halide photographic layers, **I.**20.12–**I.**20.13
Reciprocity theorem, **I.**4.18–**I.**4.19
Recoil limit, in optical cooling, **IV.**28.3, **IV.**28.19
Recording process, thermomagnetic, **I.**31.18, **I.**31.18*f*
Red eye, **II.**15.17–**II.**15.18, **III.**11.4
Redistribution force, **IV.**28.6
Red shift, noncosmological, **I.**4.24–**I.**4.25
Red Spot Paint and Varnish, **II.**37.32
Reference burst, in time-division multiple access frame, **IV.**12.17, **IV.**12.17*f,* **IV.**12.18

Reflectance, **II.**25.3–**II.**25.4, **II.**25.8, **II.**35.28, **III.**14.10
of black felt paper, **II.**37.36*f*
of black velvet, **II.**37.38*f*
of commando cloth, **II.**37.37*f*
conical, **II.**25.7
diffuse, standards of, **II.**25.14–**II.**25.15, **II.**25.15*t*
directional, **II.**25.7
geometrical definitions of, **II.**25.7
incident irradiance and unit volume, **I.**6.8*f*
irradiance, **I.**43.48
measurement of, **II.**25.11–**II.**25.12, **II.**25.12*f,* **II.**25.13, **II.**25.13*f,* **II.**25.14–**II.**25.16
in metals, **II.**35.6
of neoprene, **II.**37.39*f*
of nickel, **II.**35.52*f*
nomenclature for, **II.**25.6*t*
of polarized light, **I.**5.14*f*
for polarized radiation vs. angle of incidence, **II.**35.48*f*
in Spire Corp. baffles, **II.**37.59*f*
vs. wavelength
for aluminum, **II.**35.42*f,* **II.**35.49*f,* **II.**35.51*f*
for beryllium, **II.**35.50*f*–**II.**35.51*f*
for copper, **II.**35.42*f*
for gold, **II.**35.43*f*
for iron, **II.**35.43*f*
for molybdenum, **II.**35.44*f*
for nickel, **II.**35.44*f,* **II.**35.52*f*
for platinum, **II.**35.45*f*
for silicon, **II.**35.51*f*
for silicon carbide, **II.**35.45*f*–**II.**35.46*f,* **II.**35.51*f*
for silver, **II.**35.47*f*
for tungsten, **II.**35.47*f*
(*See also* Reflection)
Reflectance factor, nomenclature for, **II.**25.6*t*
Reflectance functions, Cohen's basis vectors for, **I.**26.27*t,* **I.**26.28*f*
Reflection:
from computer screen, **III.**16.2–**III.**16.3
by crystals, **III.**22.2–**III.**22.3, **III.**22.3*f,* **III.**22.4–**III.**22.6
distributed, in lasers, **IV.**4.34
in double heterostructure lasers, **IV.**4.7–**IV.**4.8
effect on photographic acutance, **III.**6.2
in extrinsic Fabry-Perot interferometric sensor, **IV.**15.3
Fresnel, **IV.**22.21–**IV.**22.28, **IV.**27.1, **IV.**27.7
and multilayer coatings, **III.**24.1–**III.**24.11
in neutron optics, **III.**36.5, **III.**36.9
in optical communications systems, **IV.**1.25
from optical networks, **IV.**1.16
of sunlight, **III.**13.5, **III.**15.4
total internal (TIR), **III.**2.13
Reflection (*Cont.*):
of X rays, **III.**19.5, **III.**19.9–**III.**19.10, **III.**26.3, **III.**28.5
(*See also* Reflectance)
Reflection birefringence, **III.**25.5
Reflection coefficients, **II.**36.9–**II.**36.10
Reflection gratings:
dispersion properties of, **III.**21.9
efficiency of, **III.**21.10, **III.**22.1
equation for, **III.**21.4–**III.**21.5
groove pattern in, **III.**21.3, **III.**21.5–**III.**21.6
holography in, **III.**21.3
imaging properties of, **III.**21.5–**III.**21.8
notation for, **III.**21.4, **III.**21.4*f,* **III.**21.6*f*
resolution properties of, **III.**21.9–**III.**21.10
shape of, **III.**21.3, **III.**21.5
zone plates as, **III.**23.1
(*See also* Grating)
Reflection-induced noise, **IV.**2.9, **IV.**6.15
Reflection in spectroscopic systems, **II.**36.65–**II.**36.67
Reflection optics, **III.**19.10
Reflection phase change, **I.**5.10, **I.**5.11*f*
Reflection spectrum restrahlen, **II.**36.15*f*
Reflection zone plate, **III.**23.7, **III.**23.8*f*
Reflective apertures, **I.**28.10
Reflective grating:
fiber Bragg, **IV.**9.1–**IV.**9.9
in multiplexer/demultiplexer, **IV.**10.6, **IV.**10.7*f*
Reflective objectives, **II.**18.6
Reflective systems, **I.**1.10, **I.**1.36
Reflectivity, **I.**9.19, **I.**9.23, **II.**25.3
of Aeroglaze, **II.**37.48*f*–**II.**37.49*f*
of Bragg grating, **IV.**9.3–**IV.**9.4, **IV.**9.4*f*
differential, of saturable absorber, **IV.**25.6–**IV.**25.7, **IV.**25.7*f*
far-infrared, **II.**36.37*f*
hemispheric, of Nextel Black Velvet, **II.**37.44*f*
omnidirectional, **IV.**20.2
in semiconductor saturable absorber mirror, **IV.**25.11
surface, **I.**44.18, **I.**44.20*f*
Reflectometer:
rotating light pipe, **II.**36.66, **II.**36.66*f*
"VW," **II.**25.11*f*
Reflectors:
conic, **III.**2.11, **III.**2.12*f*
faceted, **III.**2.2, **III.**2.40–**III.**2.42
heat, **I.**42.58
ideal, **III.**7.8
involute, **III.**2.12, **III.**2.12*f*
in Köhler illumination, **III.**2.24
in lens array combination, **III.**2.35–**III.**2.38, **III.**2.37*f*–**III.**2.38*f*

Reflectors (*Cont.*):
macrofocal, **III.**2.11
metallic, **I.**42.101–**I.**42.102, **I.**42.102*f,* **I.**42.103, **I.**42.103*f*
metallic-dielectric:
protective coatings in, **I.**42.104, **I.**42.104*f*–**I.**42.105*f*
reflection, enhancement of, **I.**42.104–**I.**42.105, **I.**42.105*f*
selective, **I.**42.106, **I.**42.106*f*
multilayer:
absorption in, **I.**42.43, **I.**42.43*f*
all-dielectric, **I.**42.41*f*
all-dielectric broadband, **I.**42.46–**I.**42.47, **I.**42.47*f*–**I.**42.49*f*
broadband, phase change from, **I.**42.49
experimental results in, **I.**42.41
far-infrared, **I.**42.52, **I.**42.53*f*
imperfections in, **I.**42.42–**I.**42.43, **I.**42.43*f,* **I.**42.44, **I.**42.44*f,* **I.**42.45, **I.**42.45*f*
measured reflectances and transmittances of, **I.**42.41, **I.**42.41*f*–**I.**42.42*f*
narrowband reflection coatings in, **I.**42.45–**I.**42.46, **I.**42.46*f*
resonant, **I.**42.46, **I.**42.47*f*
for soft X-ray regions, **I.**42.53, **I.**42.54*f*
for XUV regions, **I.**42.53, **I.**42.54*f*
(*See also specific types*)
multiple-reflection, **I.**42.106, **I.**42.106*f,* **I.**42.107, **I.**42.107*f*–**I.**42.108*f*
phase-retarding, **I.**42.98, **I.**42.99*f*
tailoring of, **III.**2.38–**III.**2.40
Refraction:
double, **III.**25.5, **III.**25.5*f,* **III.**25.6
and electromagnetically induced transparency, **IV.**23.2
enhanced, **IV.**23.19
index of (*see* Index of refraction)
of X rays, **III.**19.5–**III.**19.7, **III.**19.8*f,* **III.**20.3–**III.**20.8
Refractive ametropia, **III.**12.26
Refractive aspheric surfaces, **III.**2.9
Refractive error, **III.**11.1–**III.**11.2
assessing, **III.**11.4–**III.**11.6
axial, **III.**12.26
and cataracts, **III.**13.19
and computer work, **III.**16.4–**III.**16.5
correcting, **III.**11.6–**III.**11.15, **III.**12.18
and head-mounted display systems, **III.**12.32, **III.**18.10–**III.**18.11
surgical correction of, **III.**11.15–**III.**11.17
types of, **III.**11.2–**III.**11.3
and visual deprivation, **III.**11.17–**III.**11.18
Refractive index (*see* Index of refraction)
Refractive index grating, **II.**39.2, **II.**39.2*f*
Refractive lenses, thickness of, **II.**8.8*f*
Refractive surgery, **III.**10.11, **III.**13.24–**III.**13.25
Refractive systems, **I.**1.10
Regenerative feedback, in mode locking, **I.**14.21
Regenerative mode locking, **IV.**12.40
Regenerators, **IV.**13.17, **IV.**13.18*f*
Registration, in color copying, **III.**5.12
Rejection region, **I.**42.76
Relative intensity noise (RIN), **IV.**1.24–**IV.**1.25, **IV.**1.25*f,* **IV.**1.26, **IV.**2.7, **IV.**2.9, **IV.**6.2
of lasers, **IV.**4.1, **IV.**4.22–**IV.**4.23, **IV.**4.23*f*
in optical link power budget, **IV.**6.14–**IV.**6.15
of VCSELs, **IV.**4.49
Relative measurements, **II.**24.23
Relative ray height, **I.**33.2*f*
Relaxation oscillations, **I.**11.13, **I.**13.34*f,* **I.**13.35–**I.**13.36
Relaxation oscillations, in lasers, **IV.**4.16–**IV.**4.17, **IV.**4.17*f,* **IV.**4.18–**IV.**4.19, **IV.**4.28
Relay lenses, **II.**1.10
Relay trains, **II.**2.16–**II.**2.17, **II.**2.17*f,* **II.**2.18
Reliability assessment, of optical fiber, **IV.**1.18–**IV.**1.21
Remote processing (RP), **I.**21.11
Remote sensing, **I.**43.48, **I.**43.51, **I.**44.21, **II.**19.3, **II.**19.3*t,* **II.**19.7, **II.**19.34, **II.**19.35*n,* **II.**22.26–**II.**22.27
along-track in, **II.**19.7*n*
atmospheric optical, **I.**44.36
chlorophyll concentrations and, **I.**43.49
cross-track in, **II.**19.7*n*
image consequences in, **II.**19.16
scanners for, **II.**19.15, **II.**19.15*f*
(*See also specific topics*)
Repeaters:
in datacom versus telecom systems, **IV.**6.2
fiber amplifiers as, **IV.**5.1
jitter accumulation in, **IV.**6.17
Repeater spacing, increasing, **IV.**2.11, **IV.**2.16
Replicated foil optics, **III.**28.6–**III.**28.7, **III.**28.7*f*
Reset noise, **III.**4.11
Residual amplitude modulation (RAM), **IV.**27.14, **IV.**27.20, **IV.**27.22
Resins (*see specific types*)
Resolution:
in computer monitors, **III.**16.3
and crystal diffraction, **III.**22.4–**III.**22.5, **III.**22.5*f*
diffraction effects on, **III.**35.4
in electronic imaging, **III.**17.7, **III.**17.10
with grazing incidence optics, **III.**28.10–**III.**28.12
in head-mounted display image, **III.**18.6, **III.**18.7*f,* **III.**18.10

Resolution (*Cont.*):
and laser-generated plasmas, **III.**33.2, **III.**35.4
in medical X-ray imaging, **III.**35.27, **III.**35.30–**III.**35.31, **III.**35.31*f,* **III.**35.32
in neutron optics, **III.**36.5
in polycapillary X-ray optics, **III.**30.8, **III.**30.11
in reflection gratings, **III.**21.9–**III.**21.10
of Schwarzschild objective, **III.**27.3, **III.**27.5, **III.**35.4
in solid-state camera, **III.**4.15–**III.**4.17
in wavelength-dispersive X-ray fluorescence systems, **III.**35.16
with Wolter-I optics, **III.**28.2, **III.**28.3*f,* **III.**28.4, **III.**28.4*f*
in X-ray diffraction analysis, **III.**35.8
in X-ray microscopy, **III.**20.8, **III.**35.4
with zone plates, **III.**35.4
Resonance, mechanical, in laser servo system, **IV.**27.8, **IV.**27.9*f,* **IV.**27.16, **IV.**27.20
Resonance enhancement, **II.**36.82
Resonance excitation, **II.**36.79
Resonance frequency, for lasers, **IV.**2.6, **IV.**27.12–**IV.**27.16
Resonant modes (RM), **II.**36.19
in photonic crystal, **IV.**20.6–**IV.**20.7, **IV.**20.7*f,* **IV.**20.8, **IV.**20.10, **IV.**20.12–**IV.**20.13
Resonant photodiode, **IV.**4.69
Resonant Raman scattering, **IV.**17.17
Resonators:
cavity, **I.**3.24
configurations, **I.**11.25
of lasers, **I.**11.20
phase conjugate, **II.**39.32, **II.**39.34*f*
ring, **II.**39.34
ring, unidirectional, **II.**39.7
stable laser, **I.**11.25, **I.**11.25*f*
unstable, **I.**11.27–**I.**11.28, **I.**11.28*f*
Response time, **I.**15.10
Responsive quantum efficiency (*see* Quantum efficiency)
Responsivity, **I.**16.8
of solid-state arrays, **III.**4.9–**III.**4.10
spectral, **I.**15.10
Restrahlen reflection spectrum, **II.**36.15*f*
Restricted exit angle concentrators, **III.**2.18–**III.**2.20
Retardance, **II.**22.7–**II.**22.8, **II.**22.23, **II.**22.25
Retardation plates, **I.**5.22–**I.**5.23, **I.**5.23*f,* **I.**5.24, **I.**5.24*f,* **II.**3.46, **II.**3.48, **II.**22.8
achromatic, **II.**3.48, **II.**3.52–**II.**3.53, **II.**3.54*f,* **II.**3.55–**II.**3.56
composite, **II.**3.57
compound, **II.**3.55
Retardation plates (*Cont.*):
crystalline-quartz, **II.**3.49
angle of incidence and, **II.**3.52
"first-order," **II.**3.49–**II.**3.50
multiple order, **II.**3.51
single order, **II.**3.50
temperature changes and, **II.**3.51
mica, **II.**3.48–**II.**3.49
variable, **II.**3.57
Retarder, **II.**22.8, **II.**22.24
Retina:
in binocular vision, **III.**12.8, **III.**12.18
damage to, **III.**9.21, **III.**15.1, **III.**15.3–**III.**15.4, **III.**15.7–**III.**15.8, **IV.**19.1, **IV.**19.3
detached, **III.**13.1, **III.**13.21
detecting pathology in, **III.**10.12
directional sensitivity of, **III.**9.5, **III.**13.19
examining, **III.**11.4, **III.**15.1
focus of light on, **III.**11.2, **III.**15.9
laser damage to, **III.**15.12–**III.**15.13, **III.**15.13*f*
in macular degeneration, **III.**13.20
macular pigment in, **III.**13.10, **III.**15.1, **III.**15.12
microscopic structure of, **III.**10.9, **III.**10.11*f,* **III.**10.13
peripheral, **III.**12.3
photoreceptors in, **III.**8.3 (*See also* Photoreceptors, biological)
physiology of, **III.**9.3, **III.**9.12, **III.**10.3*f*
radiation exposure limits for, **III.**15.10–**III.**15.11
schematic of, **III.**9.8*f*
tilting of, **III.**11.3
in vertebrates, **III.**9.4
visual information from, **III.**12.3–**III.**12.12, **III.**12.20, **III.**12.29
Retinal anatomy, **I.**25.10–**I.**25.11
Retinal blur, **III.**10.4, **III.**11.18, **III.**13.7–**III.**13.8
Retinal camera, **III.**8.3, **III.**10.6*f,* **III.**10.9
Retinal disparity, **III.**12.2, **III.**12.14–**III.**12.15, **III.**12.23
Retinal illuminance, **I.**24.9, **I.**24.11–**I.**24.12, **I.**28.3, **I.**28.18, **II.**24.44–**II.**24.46
calibration of, **I.**28.17
maximum permissible, **I.**28.19, **I.**28.19*f*
in maxwellian view systems, **I.**28.6–**I.**28.7
photopic, **I.**25.4
Retinal image, **I.**28.18*f*
quality of, **I.**24.19, **I.**25.3–**I.**25.4
aberration data, calculation from, **I.**24.20
psychophysical comparison method, **I.**24.20–**I.**24.22
size, **III.**15.9, **III.**15.9*f,* **III.**15.12
spatial frequency content of, **I.**28.7–**I.**28.8
with visual instruments, **I.**24.25–**I.**24.26
Retinal inhomogeneity, **I.**26.39

Retinal irradiance, **III.**15.8–**III.**15.9
Retinal microscopy, **III.**10.2, **III.**10.9
Retinal neurons, **I.**25.6*f*
Retinal physiology, **I.**25.12, **I.**25.12*f,* **I.**25.12*n,* **I.**25.13
Retinal planes, and source planes, **I.**28.8–**I.**28.9
Retinal processing, **I.**25.10
Retinal reflectance, **I.**24.10*f*
Retinal thermal hazard function, **III.**15.4*f,* **III.**15.10–**III.**15.11
Retina pigment epithelium (RPE), **III.**9.12, **III.**13.20
Retinoscopy, **III.**11.4–**III.**11.5
Retrofocus lenses, **I.**1.57
Retroreflectors, **II.**4.28, **II.**4.28*f,* **II.**29.9
  afocal, **II.**2.21*f*
  cat's eye, **II.**29.5
  in observer's pupils, **II.**29.20*f*
Return-to-zero (RZ) format, **IV.**12.12, **IV.**12.12*f,* **IV.**12.37*f*
  clock recovery for, **IV.**12.13, **IV.**12.14*f,* **IV.**12.16, **IV.**12.36
  data stream for, **IV.**12.12–**IV.**12.13, **IV.**12.13*f*
  and mode-locking, **IV.**12.28
  power spectrum for, **IV.**12.13, **IV.**12.13*f*
Reverse-saturable absorption (RSA), **IV.**19.5, **IV.**19.6*f,* **IV.**19.8–**IV.**19.9, **IV.**19.11
Reversion prism, **II.**4.14*f*
Reversion theorem, **III.**9.1
Revolution:
  paraxial optics systems of, **I.**1.41
  sphere of, **I.**1.38–**I.**1.39
  surfaces of, **I.**1.37*f*
RF channelization, **II.**12.44
RF spectrum analysis, **II.**12.45
Rhabdomeric-type photoreceptors (invertebrates), **III.**9.3
Rhomboidal prism, **II.**4.25*f*
Riccati-Bessel functions, **I.**6.13
Ridge waveguide (RWG) lasers, **I.**13.10, **IV.**4.6–**IV.**4.7, **IV.**4.7*f,* **IV.**4.14, **IV.**4.58
Right circularly polarized (RCP) radiation, **II.**20.15
Ring field system, **II.**18.28, **II.**18.28*f*
Ring lasers, **I.**11.31–**I.**11.32
Ring network topology, **IV.**13.13–**IV.**13.14, **IV.**13.14*f*
Ring resonators, **II.**39.34
  unidirectional, **II.**39.7
Riser angle, in Fresnel lens facet structure, **III.**2.10, **III.**2.11*f*
Risley mirrors, **II.**4.27*f*
Risley prism, **II.**4.25, **II.**4.26*f*
Ritchey-Chretien imaging system, **III.**2.18
Ritchey-Chretien telescope, **II.**18.8, **II.**18.8*f*
Rms contrast, **I.**29.4
Rms noise, **I.**15.10
Rochon prisms, **II.**3.7, **II.**3.19, **II.**3.21, **II.**3.23, **II.**3.25–**II.**3.26
  defects in, **II.**3.22
  glass-calcite, **II.**3.22
Rock salt prism, Littrow-type, **II.**5.7
Rod intrusion, **I.**26.39
Rods, **I.**25.5, **I.**25.7*f,* **I.**25.9*f*
  and aging, **III.**13.13
  alignment of, **III.**9.8
  directional sensitivity of, **III.**9.4
  electrodynamic properties of, **III.**9.17
  in human eye, **III.**6.16, **III.**7.9, **III.**10.3*f*
  physiology of, **III.**9.3, **III.**9.9*f*
  spherule in, **III.**9.2
Roentgen, Wilhelm Conrad, **III.**19.5, **III.**34.7, **III.**35.26
Roentgen satellite (ROSAT) (*see* ROSAT (Röntgensatellit))
Ronchi patterns, **II.**30.5*f*
Ronchi test, **II.**30.1, **II.**30.3–**II.**30.4, **II.**30.4*f*
ROSAT (Röntgensatellit), **II.**11.4, **III.**28.1, **III.**28.6
Rose limit, **I.**21.5
Rotating wave approximation (RWA), **IV.**28.5
Rotation, conics of, **I.**1.38
Rotationally symmetric lenses, **I.**1.30, **I.**1.65–**I.**1.67, **I.**1.67*f,* **I.**1.68, **I.**1.71
Rotationally symmetric systems, **II.**2.3
  aberration symmetries for, **I.**1.97
  paraxial forms for, **I.**1.19
  wavefront aberrations for, **I.**1.97
Rotational-vibrational spectra of molecules, **II.**20.29
Rotational viscosity, in thermotropic liquid crystals, **II.**14.9–**II.**14.10
Roto-optic effect, **II.**12.4
Routing:
  in networks, **IV.**2.13
  nonlinear directional coupler for, **IV.**21.6
  nonlinear loop mirror for, **IV.**21.6
Rowland gratings, **II.**5.10*f,* **III.**21.3, **III.**21.5, **III.**21.8
RR concentrators, **III.**2.18
Ruby, absorption and luminescence spectra of, **II.**28.10*f,* **II.**28.11
Ruby lasers, **I.**11.14, **I.**11.14*f,* **I.**11.35, **I.**14.14
Rupture, modulus of, **II.**35.9
RX concentrators, **III.**2.18, **III.**2.18*f*
RXI concentrators, **III.**2.18, **III.**2.18*f*
Rydberg constant, **I.**8.5
Rydberg states, **IV.**26.22

Rytov's series of exponential approximations, **III.**3.4
Rytov transformation, **III.**1.11

Saccade, **III.**12.21, **III.**12.27, **III.**15.8, **III.**17.7
Saccadic suppression, **I.**24.35, **I.**24.35*f*
Saggital fans, **I.**1.40
Sagnac interferometers (*see* Interferometers, Sagnac)
Sagnac loop, **IV.**9.8
Sample-and-hold circuit, **IV.**12.4
Sampled-servo format, of tracks, **I.**31.18
Sampling, **III.**4.17–**III.**4.20, **IV.**12.2, **IV.**12.4
  insufficient (*see* Aliasing)
  and quantization, **IV.**12.11
Sampling theorem, **IV.**12.4–**IV.**12.6, **IV.**12.6*f*
S- and *t*-trace formulae, **I.**1.48
Satellite spheres, in precision photometry, **III.**2.25
Saturable absorbers, **I.**14.10, **I.**14.12, **IV.**25.4
  artificial, **I.**14.7
  fast, **IV.**25.9–**IV.**25.10, **IV.**25.14–**IV.**25.15
  in lasers, **IV.**25.4, **IV.**25.5*f,* **IV.**25.6
  parameters for, **IV.**25.6, **IV.**25.6*f,* **IV.**25.7, **IV.**25.7*f,* **IV.**25.8
  in pump-probe spectroscopy, **IV.**25.19
  semiconductor, **IV.**25.11, **IV.**25.20–**IV.**25.24
  slow, **IV.**25.8–**IV.**25.9, **IV.**25.9*f,* **IV.**25.13–**IV.**25.14
  and soliton mode-locking, **IV.**25.13
Saturable Bragg reflector (SBR), **IV.**25.11
Saturated absorption, **II.**20.24
Saturated output power, for rare-earth doped amplifiers, **IV.**5.3
Saturation current, in photodetectors, **IV.**4.72
Saturation equivalent exposure (SEE), **III.**4.11
Saturation output power, for rare-earth doped amplifier, **IV.**5.3
Savart plate, **II.**3.60
Scalar diffraction theory, analytical models of, **II.**8.10–**II.**8.11
Scalar field, **I.**4.3
Scalars, gaussian, **I.**1.50*t*
Scalar wave equation, **IV.**1.8, **IV.**8.2
Scaling, wavelength, **I.**7.7, **I.**7.9
Scaling law, **I.**4.22–**I.**4.23
Scan-error reduction, **II.**19.51*f*
  anamorphic, **II.**19.51–**II.**19.52
  double-reflection, **II.**19.52, **II.**19.52*f,* **II.**19.53, **II.**19.53*f,* **II.**19.54
  passive methods of, **II.**19.51
Scan magnification, **II.**19.5
Scanner lenses, **II.**2.12, **II.**2.12*f*
Scanner-lens relationships, **II.**19.38, **II.**19.38*f,* **II.**19.39
Scanners, **II.**13.25, **II.**23.16*f*
  acousto-optic, **II.**19.47–**II.**19.48
  afocal lenses for, **II.**2.12, **II.**2.12*f*
  analog, **II.**13.25, **II.**13.25*f,* **II.**13.26, **II.**13.26*f*
  angular, **II.**19.5
  carousel, **II.**19.23, **II.**19.23*f*
  circular, **II.**19.17, **II.**19.19*f*
  classification of, **II.**19.5
  common module, **II.**19.25*f*
  compound-mirror-optics, **II.**19.15
  convergent-beam, **II.**19.20*f*
  design considerations for, **II.**19.37
  devices, **II.**19.34
  digital, **II.**13.27*f*
  early single-mirror, **II.**19.15
  electro-optic, **II.**19.48–**II.**19.49, **II.**19.49*f*–**II.**19.50*f*
    drive power in, **II.**19.50
  flat-field, **II.**19.44
  frame, **II.**19.4
  galvanometer, **II.**19.44, **II.**19.45*f*
  holographic, **II.**19.39–**II.**19.41, **II.**19.41*f,* **II.**23.15
    operations in the Bragg regime, **II.**19.41–**II.**19.42, **II.**19.42*f,* **II.**19.43, **II.**19.43*f,* **II.**19.44, **II.**19.44*f*
  image-space, **II.**19.19–**II.**19.20, **II.**19.21*f,* **II.**19.23
    convergent-beam, **II.**19.21
  Kennedy, **II.**19.15, **II.**19.17
  mechanical, **II.**19.4
  monogon, **II.**19.35–**II.**19.36
  object-space, **II.**19.19–**II.**19.20, **II.**19.20*f*–**II.**19.22*f*
  one-dimensional, **II.**19.21
  parallel-beam, **II.**19.20*f,* **II.**19.24, **II.**19.26
  performance characteristics of, **II.**19.38
  polygon, **II.**19.35
  prismatic polygon, **II.**19.8*t,* **II.**19.35*f,* **II.**19.36, **II.**19.36*f,* **II.**19.37
  pushbroom, **II.**19.4, **II.**19.17–**II.**19.18
  pyramidal, **II.**19.8*t*
  real-time, **II.**19.25*f*–**II.**19.26*f*
  reflective polygon, **II.**19.20
  refractive prism, **II.**19.22*f*
  remote sensing, **II.**19.15*f*
  resonant, **II.**19.45, **II.**19.45*f,* **II.**19.46–**II.**19.47
  rotating prism, **II.**19.15, **II.**19.17
  rotating reflective, **II.**19.23*f*
  rotating wedge, **II.**19.17, **II.**19.17*f*–**II.**19.18*f*
  soupbowl, **II.**19.23, **II.**19.23*f*
  split-aperture, **II.**19.16*f*
  system classifications in, **II.**19.3
  two-dimensional, **II.**19.19, **II.**19.20*f*
  vibrational, **II.**19.44, **II.**19.45*f*
    suspension system in, **II.**19.46–**II.**19.47

Scanners (*Cont.*):
wide-field-of-view line, **II.**19.15–**II.**19.16, **II.**19.16*f*
windshield wiper, **II.**19.23, **II.**19.24*f*
Scanning:
active, **II.**19.5
airborne light-, geometry for, **II.**19.7*f*
angular, **II.**19.29
aperture shape factors in, **II.**19.10–**II.**19.11, **II.**19.11*t*
coherent source in, **II.**19.27
data rates in, **II.**19.7
duty cycle of, **II.**19.14
flying-spot, **II.**19.5, **II.**19.26
incoherent source in, **II.**19.26–**II.**19.27
input/output, **II.**19.4*f,* **II.**19.7*n,* **II.**19.9
aperture shape factor in, **II.**19.10*t*
for input/output imaging, **II.**19.26
monogon postobjective, **II.**19.30*f*
multiplexed, **II.**19.24
objective, **II.**19.29, **II.**19.29*n*
overillumination in, **II.**19.14, **II.**19.35
passive, **II.**19.22
polygon preobjective, **II.**19.30*f*
power density in, **II.**19.26
power transfer in, **II.**19.26, **II.**19.28*f*
resolution in, **II.**19.9, **II.**19.11, **II.**19.11*n,* **II.**19.12*f*–**II.**19.13*f*
augmentation of, **II.**19.12–**II.**19.14
conservation of, **II.**19.34
transverse translational, **II.**19.29
underillumination in, **II.**19.14–**II.**19.15, **II.**19.35
(*See also* Objective optics)
Scanning arrays, **I.**23.7, **I.**23.15
Scanning electron microscopes (SEMs), **III.**35.16, **III.**35.18
Scanning image, **II.**19.36–**II.**19.37
Scanning methods, **II.**19.4
Scanning microscope, **III.**27.5
Scanning systems:
for digital film, **III.**6.27
as Schwarzschild objective application, **III.**27.1
xerographic process in, **III.**5.4
Scan overlap, **II.**19.17
Scanpaths, in human vision, **III.**17.7
Scan velocity, **II.**32.6
Scatter, **II.**33.29
anomalous, **II.**35.28
beam-splitter, **II.**26.12
Doppler-shifted, **II.**26.2
near specular, **II.**26.9*f*
measurement of, **II.**26.9–**II.**26.10
point sources of, **II.**26.1–**II.**26.2
stoichiometric, **II.**33.30
Scatter (*Cont.*):
total integrated (TIS) (*see* Total integrated scatter (TIS))
Scatterance, spectral, **I.**43.10–**I.**43.11
Scattered radiation, **II.**24.36
Scattering, **II.**36.84*f*
anisotropic, **II.**39.7
anti-Stokes, **IV.**3.5, **IV.**17.5*t,* **IV.**17.7, **IV.**17.7*f,* **IV.**18.32–**IV.**18.35
applications of, **III.**3.2
in biological photoreceptors, **III.**9.11–**III.**9.12, **III.**13.10–**III.**13.12
bio-optical models for, **I.**43.41*f*
in black surfaces, use of, **II.**37.17
Brillouin (*see* Brillouin scattering)
coherent, **III.**3.5–**III.**3.7, **III.**20.8, **III.**36.4
Compton, **III.**20.7–**III.**20.8, **III.**30.15, **III.**35.27, **III.**35.30, **IV.**26.7, **IV.**26.10
from crystals, **III.**22.2
by cylinders, **I.**6.16
defect, **I.**7.6
diffraction-dominated, **I.**43.33
diffuse, **III.**36.4
dynamic, **II.**14.10, **III.**3.7–**III.**3.8
effect in color photography, **III.**6.2, **III.**6.6–**III.**6.7
effects in X-ray telescopes, **II.**11.4, **II.**11.16, **II.**11.16*f*–**II.**11.17*f,* **II.**11.22–**II.**11.23, **II.**11.23*f*
and fiber attenuation, **IV.**1.10, **IV.**2.2
forward, **I.**43.33, **I.**43.34*f*
Gordon-Morel model of, **I.**43.42
Haltrin-Kattawar model of, **I.**43.42
incoherent, **III.**3.5–**III.**3.7
inelastic, **I.**43.51, **I.**43.51*f,* **II.**36.77–**II.**36.79, **II.**36.80*f*
integral equation for, **III.**3.4
Kopelevich model of, **I.**43.38–**I.**43.39, **I.**43.42
in laser cooling, **IV.**28.2–**IV.**28.3
of light, **I.**6.2–**I.**6.6, **I.**6.7*f,* **I.**6.10*f*
differential scattering cross section, **I.**6.9
vibration ellipses of, **I.**6.11*f*
and linear polarization, **III.**25.2
material, **I.**7.6
Mie, **I.**6.12, **I.**43.33, **I.**44.10, **I.**44.15–**I.**44.16, **I.**44.16*f*–**I.**44.19*f*
molecular, **I.**6.12
multiple, **I.**44.18, **III.**3.8–**III.**3.16
neutron, **II.**36.12, **III.**3.6, **III.**36.7–**III.**36.8, **III.**36.8*f*
nonlinear, in optical limiting, **IV.**19.4*f,* **IV.**19.8–**IV.**19.9
by nonspherical particles, **I.**6.17
in optical molasses, **IV.**28.12

Scattering (*Cont.*):
by particles, **I.**43.33–**I.**43.35, **III.**3.2, **III.**3.5–**III.**3.7
from particular defects, **I.**7.7
Petzold, **I.**43.33–**I.**43.34
and photographic latent image creation, **III.**6.20
plane, **I.**6.10
properties of, **III.**3.2
Raman, **I.**9.18–**I.**9.19, **I.**43.51*f,* **I.**43.52, **I.**44.11, **I.**44.21
Rayleigh, **I.**43.31–**I.**43.33, **I.**44.10, **I.**44.14–**I.**44.15
Rayleigh wing, **IV.**17.15
by regular particles, **I.**6.15
schematic representation of, **III.**3.4*f*
shift-invariant, **II.**11.17
single, **III.**3.4–**III.**3.8
small-angle, **I.**7.3
by spheres vs. cylinders, **I.**6.16
stimulated photorefractive (SPS), **II.**39.10
stimulated versus spontaneous, **IV.**17.19
stimulation of, in fibers, **IV.**1.39–**IV.**1.40, **IV.**3.2, **IV.**3.4–**IV.**3.9, **IV.**17.16–**IV.**17.20
surface (*see* Surface scattering)
surface transfer function and, **II.**11.17
theory of, **III.**3.3–**III.**3.4
topographic, **I.**7.5
in ultracold collisions, **IV.**28.28
in water, **I.**43.30–**I.**43.32, **I.**43.32*t,* **I.**43.35, **I.**43.36*t*
wave (*see* Surface scattering)
wavelength dependence of, **I.**43.35, **I.**43.37, **I.**43.39–**I.**43.40, **I.**43.40*f*
X-ray, **III.**3.6, **III.**19.7, **III.**20.8, **III.**26.4, **III.**35.27, **III.**35.29*t,* **III.**35.30, **III.**35.30*f*–**III.**35.31*f,* **III.**A.1, **III.**A.2*f*
(*See also* Brillouin scattering; Optical fiber, stimulated scattering processes in; Raman scattering; Rayleigh scattering; *specific types*)
Scattering centers, **III.**3.2–**III.**3.3
in coherent scattering, **III.**3.6–**III.**3.7
in dynamic scattering, **III.**3.8
in incoherent scattering, **III.**3.4–**III.**3.5
in multiple scattering, **III.**3.8, **III.**3.10
Scattering force, **IV.**28.6
Scattering functions:
and surface power spectral density (PSD) function, **II.**11.22
volume, **I.**43.33, **I.**43.35*f,* **I.**43.39*t*
wavelength dependence of, **I.**43.38*f,* **I.**43.38*t*
Scattering rate:
in atomic beam slowing, **IV.**28.10
in laser cooling, **IV.**28.2–**IV.**28.3
Scatterometers, **I.**42.17, **II.**26.5–**II.**26.7, **II.**26.7*f,* **II.**26.8–**II.**26.9
bidirectional scattering distribution function (BSDF), **II.**26.6
BRDF, **II.**26.5*f*
large-radius, **II.**26.10
measurement issues in, **II.**26.11–**II.**26.12
Schawlow-Townes formula, **IV.**26.31–**IV.**26.32, **IV.**26.35
Scheimpflug condition, **I.**1.67, **II.**1.7*f,* **II.**2.4, **II.**15.19, **II.**15.20*f*
Scheimpflug rule, **II.**2.4, **II.**2.8
Schell model source, **I.**4.12
Schiefspiegler objectives, **II.**18.29, **II.**18.29*f*
Schmidt-Cassegrain objectives, **II.**18.18, **II.**18.18*f*
reflective, **II.**18.19, **II.**18.19*f*
Schmidt corrector system, **III.**2.9, **III.**2.17
Schmidt objectives, **II.**18.15, **II.**18.15*f*
field-flattened, **II.**18.16, **II.**18.16*f*
reflective, **II.**18.17, **II.**18.17*f*
Shafer relayed virtual, **II.**18.19, **II.**18.19*f,* **II.**18.20, **II.**18.20*f*
solid, **II.**18.17, **II.**18.17*f*
Schmidt prism, **II.**4.12, **II.**4.12*f*
Schottky barrier, **I.**23.11
detector (SBD), **I.**23.7, **I.**23.13, **I.**23.31
IT-CCD-FPA, **I.**23.13
in optical fibers, **II.**10.27
photodiodes, on focal plane arrays (FPA), **I.**23.13
Schottky photodiodes, **IV.**1.29, **IV.**4.66, **IV.**4.68
Schrödinger equation, **I.**9.25, **IV.**20.3, **IV.**28.2
for neutron waves, **III.**36.4
nonlinear, **IV.**1.41, **IV.**1.41*t,* **IV.**3.4, **IV.**7.2, **IV.**17.28, **IV.**28.34
Schupmann lenses, **II.**1.26, **II.**18.7
Schwarzschild soft X-ray microscope, **II.**11.28, **II.**11.28*f,* **II.**11.29
Schwarzschild objectives, **III.**27.1–**III.**27.5, **III.**35.4
anastigmatic, flat-image, **II.**18.15, **II.**18.15*f*
aplanatic, **II.**18.13, **II.**18.13*f,* **II.**18.14, **II.**18.14*f*
Schwinger formula, **III.**32.17
Scintillating fibers, **III.**2.7
Scintillation, **I.**44.26, **III.**1.11, **IV.**6.18
Scintillation X-ray detectors, **III.**34.6–**III.**34.7
Scophony system, **III.**5.4
Scorotron, **III.**5.2, **III.**5.3*f*
Scotopic vision, **II.**24.41–**II.**24.42, **III.**7.9, **III.**7.9*f*–**III.**7.10*f,* **III.**7.11, **III.**7.11*f,* **III.**7.12–**III.**7.13, **III.**13.7, **III.**13.13, **III.**14.3
luminous efficiency functions, **II.**24.42*t,* **II.**24.43
Scully-Lamb master equation, **IV.**26.16, **IV.**26.18–**IV.**26.23
SEAL objectives, **II.**18.30, **II.**18.30*f*

Sea water:
absorption coefficient of, **I.**43.22, **I.**43.23*t*
index of refraction in, **I.**43.18–**I.**43.19, **I.**43.19*f,* **I.**43.21*t*
inherent optical properties of, **I.**43.35
inorganic particles in, **I.**43.15
organic particles in, **I.**43.14–**I.**43.15
particulate matter in, **I.**43.14–**I.**43.16, **I.**43.16*f*
pure, **I.**43.14
spectral absorption coefficient for, **I.**43.29*t*
SECAM standard, for color broadcast camera output, **III.**4.20
Second:
definition of, **II.**29.2
as SI base unit, **III.**7.2
Secondary magnification, **II.**18.42
Secondary spectrum, **II.**18.42
Second-harmonic generation (SHG), **II.**33.29, **IV.**3.2, **IV.**17.16, **IV.**17.24–**IV.**17.25, **IV.**22.1, **IV.**22.3, **IV.**23.24
Sectors, in optical disks, **I.**31.4
Segmented mirror, **III.**1.38–**III.**1.39, **III.**1.39*f,* **III.**10.2
in vision correction, **III.**10.7–**III.**10.8
Segmented piston correctors, for wavefront aberrations, **III.**10.8
Seidel aberrations, **I.**1.98, **III.**27.1
Selenium films, extinction ratios for, **II.**3.43*f*
Self-action effects, **IV.**17.27–**IV.**17.28
internal, **IV.**19.8, **IV.**19.11
Self-amplitude modulation, of saturable absorbers, **IV.**25.6–**IV.**25.8, **IV.**25.10, **IV.**25.14
Self-defocusing, **I.**14.7, **IV.**19.7–**IV.**19.8
in mode locking, **I.**14.6
Self-focusing, **I.**14.7, **IV.**17.27, **IV.**17.32, **IV.**19.7–**IV.**19.8
Self-induced transparency, **II.**38.5
Self-motion, perception of, **III.**12.6
Self-phase modulation (SPM), **IV.**1.41, **IV.**3.1, **IV.**3.3, **IV.**13.7, **IV.**13.7*f*
in dispersion-managed soliton transmission, **IV.**7.13
and longitudinal Kerr effect, **IV.**25.12, **IV.**25.12*f,* **IV.**25.13–**IV.**25.14
in slow saturable absorber, **IV.**25.9
and transform-limited pulse, **IV.**7.2–**IV.**7.3, **IV.**7.3*f,* **IV.**7.4
Self-protecting optical limiters, **IV.**19.10
Self-pumped phase conjugate mirrors (SPPCMs), **II.**39.7, **II.**39.8*f*
Self-scanned array (SSA), **I.**21.22*f*–**I.**21.23*f*
television cameras, **I.**21.2
Self-steepening, **IV.**3.4
Self-switching, **IV.**21.2, **IV.**21.4
Sellmeier formula, **I.**9.15, **II.**33.17, **II.**33.25–**II.**33.27
for material dispersion curves, **IV.**1.13
Selwyn's law, **I.**20.21, **I.**20.23–**I.**20.24
Semiconductor detectors, **III.**34.5–**III.**34.6, **III.**35.17–**III.**35.18
Semiconductor laser amplifier loop optical mirror (SLALOM), **IV.**12.38
Semiconductor laser amplifiers (SLAs), **IV.**2.12, **IV.**11.4–**IV.**11.7
design of, **IV.**11.4, **IV.**11.6*f*
gain spectrum for, **IV.**11.5*f*
Semiconductor lasers, **I.**11.37, **I.**11.37*f,* **I.**11.38, **IV.**4.1, **IV.**4.7
applications for, **I.**13.3–**I.**13.4
arrays, **I.**13.28, **I.**13.29*f*
band structure of, **I.**13.17*f*
basic operation of, **I.**13.4, **I.**13.4*f*
blue, **I.**13.8
double heterostructure, **I.**13.5*f*
gallium arsenide (GaAs), **I.**31.7
life cycle of, **IV.**4.9
light-vs.-current relationship in, **I.**13.6*f*
mode locking in, **I.**14.7
modulation in, **I.**13.32–**I.**13.33, **I.**13.34*f,* **I.**13.35, **I.**13.35*f,* **I.**13.36, **I.**13.36*f,* **I.**13.37–**I.**13.38, **I.**13.38*f,* **I.**13.39
noise in, **IV.**4.24–**IV.**4.25, **IV.**4.28
operation of, **IV.**4.9
as optical system transmitters, **IV.**12.24–**IV.**12.27
packaging for, **IV.**4.8, **IV.**4.8*f*
parasitic elements affecting, **I.**13.36, **I.**13.37*f*
phase-locked, **I.**13.30
pumping in, **I.**13.4
resonant cavity of, **I.**13.5–**I.**13.6
resonant optical feedback, **I.**13.41*f*
spectral properties of, **I.**13.39–**I.**13.41
threshold current of, **I.**13.7
transparency in, **I.**13.6
turn-on delay for, **IV.**4.16, **IV.**4.17*f*
Semiconductor modulators, **IV.**4.2
Semiconductor optical amplifier (SOA), **IV.**21.6–**IV.**21.7, **IV.**21.7*f*
Semiconductor optical wavelength converter, **IV.**11.10–**IV.**11.11
Semiconductors:
in all-optical switching, **IV.**21.3
band structure of, **I.**12.3, **I.**12.3*f*–**I.**12.4*f,* **I.**12.5, **I.**12.5*f*
compound, **II.**39.20–**II.**39.21
photorefractive, **II.**39.20*t*
and continuum excitation, **IV.**25.20–**IV.**25.21
diamond and zinc blende, **I.**9.27

Semiconductors (*Cont.*):
direct vs. indirect, **I.**12.4
electro-optic, **II.**39.21
and exciton excitation, **IV.**25.20
indirect, **I.**12.6, **I.**12.6*f*
light extraction in, **I.**12.7
linear optical properties of, **II.**36.12
local vibrational modes (LVM) in, **II.**36.22*t*
magneto-optical phenomena of, **II.**36.40–**II.**36.41
materials for, **II.**36.85*t*
materials parameters, **II.**36.86*t*–**II.**36.91*t*
metal oxide (MOS), **I.**16.11
nondegenerate, **II.**36.48
nonlinear optical properties of, **II.**36.54, **II.**36.55*t,* **II.**36.56, **II.**36.56*t,* **II.**36.57–**II.**36.59
optical limiting in, **IV.**19.10, **IV.**19.10*f*
optical properties of, **II.**36.3–**II.**36.4, **II.**36.6–**II.**36.7
measurement of, **II.**36.59, **II.**36.60*f,* **II.**36.61
optical responses for, by wavelength, **II.**36.13*t*
optoelectronic technologies of, **II.**36.7
photoexcitation and relaxation in, **II.**36.73*f*
substrates, properties of, **I.**12.21*t*
in thermalization regime, **IV.**25.21–**IV.**25.22
transmission spectra in, **II.**36.67–**II.**36.68, **II.**36.68*f*
and ultrashort pulse generation, **IV.**25.4, **IV.**25.15–**IV.**25.16, **IV.**25.16*f,* **IV.**25.17, **IV.**25.17*f,* **IV.**25.18
wafer processing, **I.**12.24
Semiconductor saturable absorber mirror (SESAM), **IV.**25.11, **IV.**25.22
Sénarmont compensator, **II.**3.57
Sénarmont polariscope, **I.**5.28
Sénarmont prisms, **II.**3.7, **II.**3.19, **II.**3.21, **II.**3.23
Sensitivity, **I.**15.10
Sensors (*see specific types*)
Separate confinement heterostructure (SCH), **IV.**4.5, **IV.**4.5*f*
Serial byte connection (SBCON), standard for, **IV.**16.1
Serial multiplexing, **IV.**12.24, **IV.**12.25*f*
Serrodyne signal, **II.**6.33
Servo bandwidth, **IV.**27.10, **IV.**27.18, **IV.**27.20
Servo lag, in adaptive optics system design, **III.**1.43
Servo system:
Bode representation of, **IV.**27.5
and closed-loop stability, **IV.**27.8–**IV.**27.12
for doubly resonant oscillators, **IV.**22.27–**IV.**22.28, **IV.**22.31–**IV.**22.32
for laser, **IV.**27.6, **IV.**27.6*f,* **IV.**27.7, **IV.**27.7*f,* **IV.**27.8
phase and amplitude response in, **IV.**27.6*f*
Seya-Namioka vacuum-ultraviolet monochromator, **II.**3.40
Shack-Hartmann analyzer, **III.**26.5
Shack-Hartmann wavefront sensor (*see* Hartmann-Shack wavefront sensor (HSWS))
SHADOW, for X-ray optics modeling, **III.**19.10, **III.**26.4
Shafer objectives, **II.**18.27, **II.**18.27*f,* **II.**18.37, **II.**18.37*f*
Shallow gradient index (SRGRIN) optics, **II.**9.7–**II.**9.8
Shape error (SHE), and mirror surface quality, **III.**26.4–**III.**26.5
Sharpness, and granularity, **I.**20.24
Shear, **III.**12.2, **III.**12.6, **III.**12.27
Shearing interferometers, **III.**1.37
Shear modulus, **II.**35.8
Shenker objectives, **II.**18.25, **II.**18.25*f,* **II.**18.26
Short-arc lamps, **I.**10.34
Short-cavity lasers, **I.**14.20
Short-period grating (SPG), **IV.**15.6
Shot noise, **I.**15.10, **I.**18.3, **I.**22.13, **III.**4.12
bandwidth and, **I.**18.4
integration time and, **I.**18.3
in lasers, **IV.**4.22, **IV.**27.7–**IV.**27.8
in photodiodes, **IV.**4.74
in point-to-point communications links, **IV.**1.27, **IV.**1.28*f,* **IV.**1.29–**IV.**1.30
and receiver sensitivity, **IV.**2.7, **IV.**2.9
Shutters, **I.**28.12
types of, **I.**28.14*t*
Signal:
digital, **IV.**12.10
frequency modulated (FM), **IV.**27.4
in imaging system sampling, **III.**4.17–**III.**4.20
optical, properties of, **IV.**21.2
in optical parametric generation, **IV.**22.2–**IV.**22.4, **IV.**22.5*f,* **IV.**22.7–**IV.**22.8, **IV.**22.62
in solid-state arrays, **III.**4.9–**III.**4.11
in solid-state cameras, **III.**4.14
Signal analysis:
best technique in, **I.**18.15
boxcar averaging in, **I.**18.14
gated integration and, **I.**18.13–**I.**18.14, **I.**18.14*f*
lock-in amplifiers and, **I.**18.14, **I.**18.14*f,* **I.**18.15
modulated sources, **I.**18.13
in optical systems, **I.**18.3
photon counting and, **I.**18.15
transient photon counting and, **I.**18.15
unmodulated sources, **I.**18.13
Signal-dependent noise, **IV.**2.9–**IV.**2.10
Signal processing, Fabry-Perot amplifiers for, **IV.**11.4
Signal recovery:
Lorentzian, **IV.**27.13
problems in, **IV.**27.22

Signal representation, analytical, **I.**4.2
Signal-to-noise ratio (SNR), **I.**21.4
  for charge injection device, **III.**4.7
  in fiber-optic systems, **IV.**4.74, **IV.**6.2
  in fiber-optic telecommunications, **II.**10.24–**II.**10.25
  in frame transfer devices, **III.**4.8
  for lasers, **IV.**4.1, **IV.**4.22–**IV.**4.23, **IV.**27.12–**IV.**27.14
  in medical X-ray imaging, **III.**35.30, **III.**35.31*f*
  and noise equivalent exposure, **III.**4.10
  in point-to-point communications links, **IV.**1.26, **IV.**1.30
  for quantized digital signals, **IV.**12.11
  and receiver sensitivity, **IV.**2.7
  for solid-state camera, **III.**4.14
  and video compression, **III.**17.4
  in X-ray diffraction analysis, **III.**35.8
Silicon:
  doped polycrystalline, **I.**22.3, **I.**22.3*f*
  hydrogenated amorphous, **I.**22.3, **I.**22.3*f*
  reflectance vs. wavelength, **II.**35.51*f*
  single-crystal, **I.**22.3, **I.**22.3*f*
  specific heat of, **II.**35.72*f*
  thermal conductivity of, **II.**35.67*f*–**II.**35.68*f*
Silicon carbide:
  in black surfaces, **II.**37.53
  emittance vs. temperature for, **II.**35.55*t*
  emittance vs. wavelength for, **II.**35.54*t*
  extinction coefficient for, **II.**35.20*t*
    vs. wavelength, **II.**35.26*f*
  index of refraction in, **II.**35.20*t*
    vs. wavelength, **II.**35.26*f*
  reflectance vs. wavelength, **II.**35.51*f*
  thermal conductivity of, **II.**35.67*f*–**II.**35.68*f*
Silicon photodetectors, **III.**4.2
Sillenites (*see* Cubic oxides)
Silver:
  extinction coefficient for, **II.**35.18*t*–**II.**35.19*t*
    vs. wavelength, **II.**35.27*f*
  index of refraction in, **II.**35.18*t*–**II.**35.19*t*
    vs. wavelength, **II.**35.27*f*
  reflectance of, **II.**35.39*t*–**II.**35.40*t*
  reflectance vs. wavelength for, **II.**35.47*f*
  specific heat of, **II.**35.70*f*
  thermal conductivity of, **II.**35.64*f*–**II.**35.65*f*
Silver halide crystals, **III.**6.1
  blue sensitivity of, **III.**6.4
  in film X-ray detector, **III.**34.7
  light scatter by, **III.**6.6–**III.**6.7
  and photographic speed, **III.**6.20
  photophysics of, **III.**6.8–**III.**6.10
  and spectral sensitizers, **III.**6.14
  and ultraviolet light, **III.**6.4
Silver halide film, **II.**23.7–**II.**23.8
Silver halide photographic layers:
  development effects in, **I.**20.13
  emulsion in, **I.**20.4
  exposure of, **I.**20.6
  grains in, **I.**20.4
  optical density of, **I.**20.6
  processing, **I.**20.5
  reciprocity failure in, **I.**20.12–**I.**20.13
  spectral sensitivity in, **I.**20.11–**I.**20.12, **I.**20.12*f*
  structure of, **I.**20.4
Simple lenses:
  imaging by, **II.**1.5*f*
  thermal focus shift of, **I.**39.2
Simulated annealing, **I.**34.20
Simulator sickness, **III.**12.33
Simultaneous measurement, **II.**30.20
Simultaneous multiple surfaces (SMS) concentrators, **III.**2.18, **III.**2.18*f*
Sine plate, **II.**29.13*f*
Single-channel video transmission, **IV.**2.14
Single-component development, in xerographic systems, **III.**5.9, **III.**5.9*f*
Single-crystal (SC) fiber, **IV.**14.2*t*–**IV.**14.3*t,* **IV.**14.8–**IV.**14.10, **IV.**14.10*f*
Single element lenses, **II.**1.11–**II.**1.12, **II.**1.12*f,* **II.**1.13–**II.**1.16, **II.**1.16*f*–**II.**1.17*f*
  performance of, **II.**1.36–**II.**1.37
Single-hop network, **IV.**13.14
Single lens reflex cameras (*see* Cameras, SLR)
Single-longitudinal-mode lasers (SLM), **I.**13.41–**I.**13.42, **IV.**2.6
Single-mode fiber (SMF), **IV.**1.9, **IV.**2.1–**IV.**2.2
  for coherent communications links, **IV.**1.39
  cut-back method applied to, **IV.**1.15
  and dispersion, **IV.**1.11, **IV.**1.13*f,* **IV.**1.17, **IV.**2.4, **IV.**2.4*n,* **IV.**6.11, **IV.**6.11*f*
  effect area of, **IV.**3.7
  electric field of, **IV.**13.4
  and gain-guided lasers, **IV.**4.14
  long-distance applications for, **IV.**1.9, **IV.**1.11
  noise in, **IV.**6.17
  nonlinearities in, **IV.**3.1
  normalized variables for, **IV.**1.11–**IV.**1.12
  polarization modes in, **IV.**8.6
  in telecom systems, **IV.**4.3
  transmission loss for, **IV.**6.7
Single-mode lasers, **IV.**12.27
  for high-cost communications systems, **IV.**4.12
  index-guided, **IV.**4.14
  operation of, **IV.**26.18
Single-mode SC duplex fiber-optic connector, **IV.**16.5, **IV.**16.5*f*
Single quantum well (SQW), **IV.**4.29, **IV.**4.31*f*
Single scattering, **III.**3.4–**III.**3.8
  coherent, **III.**3.5–**III.**3.7

Single scattering (*Cont.*):
dynamic, **III.**3.7–**III.**3.8
incoherent, **III.**3.4–**III.**3.5
Single-scattering albedo, spectral, **I.**43.12
Single-sheeted mirror, **III.**10.1
Single transverse mode, for VCSELs, **IV.**4.48
Single-use cameras, **III.**6.26–**III.**6.27
Singly-resonant optical parametric oscillator (SRO), **II.**38.19–**II.**38.20
Singly resonant oscillator (SRO), **IV.**22.14–**IV.**22.15, **IV.**22.50
cavity geometries for, **IV.**22.33–**IV.**22.34, **IV.**22.34*f*
conversion efficiency in, **IV.**22.20–**IV.**22.21, **IV.**22.21*t,* **IV.**22.38
devices using, **IV.**22.32–**IV.**22.35
parameters for, **IV.**22.33*t*
pulsed, **IV.**22.50–**IV.**22.51
pump-enhanced, **IV.**22.15
steady-state threshold in, **IV.**22.15–**IV.**22.16, **IV.**22.21*t*
tuning of, **IV.**22.34–**IV.**22.35
Singular value decomposition (SVD), **I.**26.47–**I.**26.48, **I.**26.48*f,* **III.**1.27
Sinusoidal grating patches, **I.**29.4, **I.**29.5*f*
Sinusoids, in vision science, **III.**10.4
Sisyphus laser cooling, **IV.**28.17
SI units (Système International d'Unités), **II.**24.22, **II.**29.2, **III.**7.2, **III.**14.3
base units in, **III.**7.2, **III.**14.4–**III.**14.7, **III.**14.4*t*
vs. English units, **III.**14.7–**III.**14.8, **III.**14.8*t*
Size of source effect, **II.**24.36–**II.**24.37
Skew (eye) movement, **III.**12.2, **III.**12.23
Skew invariant, **I.**1.25, **I.**1.61
Skew rays, **I.**1.25–**I.**1.26, **I.**1.39, **III.**2.7, **III.**2.13, **III.**21.4, **IV.**1.8, **IV.**1.8*f*
in concentrator geometries, **III.**2.20–**III.**2.21, **III.**2.21*f*
Skin depth, **II.**35.6
Skot, **III.**7.8
Slater parameters, **I.**8.14–**I.**8.15, **I.**8.19
Slater wavefunctions, **I.**8.14
Slide film, **III.**6.10, **III.**6.23
Sliding frequency-guiding filters, **IV.**7.8–**IV.**7.9
Slit width, effect of, **I.**2.15
Slope error (SLE), and mirror surface quality, **III.**26.4–**III.**26.5, **III.**28.5
Slowly varying envelope approximation (SVEA), **IV.**3.2, **IV.**3.4
Smakula's formula, **II.**20.4
Smart pixels, and VCSELs, **IV.**4.45
Smear, **I.**22.32
Smirnov, M. S., **III.**10.2–**III.**10.3
Smith and Baker absorption values, **I.**43.22, **I.**43.23*t*
Smith invariant, **I.**1.84
Smoothing, **I.**42.54
Snell's law, **I.**1.11, **I.**1.24, **I.**1.27, **I.**5.4, **I.**9.11, **I.**9.23, **I.**12.7, **II.**3.2, **II.**3.4, **II.**3.22, **III.**9.2, **III.**9.13–**III.**9.14, **III.**19.7, **III.**19.10, **III.**36.5
Snow blindness, **III.**15.4–**III.**15.5
SOAR, **I.**38.28
Society of Photooptical Instrumentation Engineers (SPIE), **III.**2.13
Sodium (laser) guide star, **III.**1.29, **III.**1.33–**III.**1.35
Sodium nitrate, **II.**3.25
Softening temperature, **II.**33.34
Software:
atmospheric transmission (*see* Atmospheric transmission software)
for nonimaging optics systems, **III.**2.8
optical design (*see* Optical design software)
for X-ray optics modeling, **III.**19.10, **III.**26.4
Solar cell covers, **I.**42.58*f,* **I.**42.59
SolarChem, **II.**37.37
BRDF of, **II.**37.54*f*
Solar collection:
CPC use in, **III.**2.15
and étendue, **III.**2.4
requirements of, **III.**2.1
Solar radiation:
and cataracts, **III.**13.8
exposure to, **III.**13.5, **III.**15.1–**III.**15.2, **III.**15.4
and ozone depletion, **III.**15.6
Solar retinitis, **III.**15.1, **III.**15.7
Solar simulators:
mixing rods in, **III.**2.33
Soleil compensator, **II.**3.57, **II.**3.59, **II.**3.59*f,* **II.**3.60
Solid angle, **II.**24.10, **II.**24.10*f,* **III.**7.3–**III.**7.4, **III.**7.4*f,* **III.**14.5, **III.**14.5*f*
for biological photoreceptor waveguiding, **III.**9.4, **III.**9.5*f*
in radiation transfer, **III.**2.5, **III.**2.6*f*
Solids:
mechanical properties of, **I.**9.4
optical properties of, **I.**9.24
propagation of light in, **I.**9.4
Solid-state array:
architecture for, **III.**4.3–**III.**4.9, **III.**4.20
performance of, **III.**4.9–**III.**4.13
in solid-state camera, **III.**4.2
versatility of, **III.**4.21
Solid-state camera, **III.**4.1–**III.**4.21
imaging system applications of, **III.**4.3
output analysis for, **III.**4.20–**III.**4.21

Solid-state camera (*Cont.*):
performance of, **III.**4.13–**III.**4.15
resolution of, **III.**4.15–**III.**4.17
Solid-state ion chambers, **III.**34.5
Solid-state lasers, **I.**11.13–**I.**11.14, **I.**11.18, **I.**11.19*f,* **I.**14.13
Solid-state sum-frequency laser, **III.**1.34, **III.**1.34*f,* **III.**1.35, **III.**1.35*f*
Solid-state theory, photography application of, **III.**6.8
Solitary lasers, **IV.**25.15
Soliton lasers, **I.**14.6–**I.**14.7, **I.**14.18–**I.**14.19
Soliton mode locking, **IV.**25.9*f,* **IV.**25.13–**IV.**25.14
Soliton perturbation theory, **IV.**25.13
Solitons, **II.**10.30, **II.**10.40
applications for, **IV.**12.42
frequency of, controlling, **IV.**7.7–**IV.**7.8
generation of, **IV.**3.1, **IV.**3.3, **IV.**17.25–**IV.**17.26, **IV.**25.13
in long-distance transmissions, **IV.**2.12, **IV.**7.5
nature of, **IV.**7.2–**IV.**7.4
propagation of, **IV.**1.40–**IV.**1.41, **IV.**1.41*f,* **IV.**1.41*t,* **IV.**1.42, **IV.**17.14
in optical fibers, **II.**10.9, **II.**10.38
properties of, **IV.**7.4–**IV.**7.5
purpose of, **IV.**7.1–**IV.**7.2
and self-switching, **IV.**21.4
in stimulated Raman scattering, **IV.**18.26–**IV.**18.29, **IV.**18.29*f*
transmission and amplification of, **II.**10.29
in ultrashort pulse transmissions, **IV.**1.31–**IV.**1.32
Soliton transmission systems, **IV.**7.5–**IV.**7.7
dispersion-managed (DM), **IV.**7.12–**IV.**7.13, **IV.**7.13*f,* **IV.**7.14–**IV.**7.15
frequency-guiding filters in, **IV.**7.7–**IV.**7.9
wavelength-division multiplexing, **IV.**7.9–**IV.**7.12
Solves, **I.**34.4
specifications of, **I.**34.6
SONET rings, **IV.**2.16, **IV.**13.13
SOR 3.5-m telescope AO system, **III.**1.36
Source calibrations in the ultraviolet, **I.**10.10–**I.**10.11
Source diameter, wavelength in, **I.**12.36
Source irradiance, **III.**15.8
Source modeling, for nonimaging optics, **III.**2.7–**III.**2.8
Sources:
in optical communication systems, **IV.**4.1
in photosensitivity, **IV.**9.2
Space curves, differential geometry of, **I.**1.20–**I.**1.21
Space Eikonometer, **III.**11.15
Space-integrating compressive receiver, **II.**12.45–**II.**12.46
Space-integrating correlator, **I.**30.13
Space Interferometry Mission, **III.**28.12
Space perception, **III.**12.3–**III.**12.4
distortion by monocular magnification, **III.**12.13–**III.**12.17
distortion by unequal binocular magnification, **III.**12.17–**III.**12.20
and prism, **III.**12.20–**III.**12.21
Space switching, **II.**6.32
Spar cutting, **II.**3.13
Spatial contrast sensitivity, **I.**25.24–**I.**25.25
Spatial contrast sensitivity function, **III.**17.3
Spatial dilution, **III.**2.6
Spatial filters, **I.**25.25, **I.**28.22, **I.**30.8, **I.**30.8*f*
Spatial frequency, **II.**32.2
Spatial hole burning, **I.**11.31, **IV.**4.15, **IV.**4.48–**IV.**4.49, **IV.**12.2, **IV.**12.26
Spatial mode:
in lasers, **IV.**4.15
in VCSELs, **IV.**4.59
Spatial multiplexing, **II.**39.35
Spatial sinusoid, **I.**25.21, **I.**25.27*f*
Spatial walkoff, in parametric generation, **IV.**22.63–**IV.**22.64
Specific heat, **II.**35.8
of aluminum, **II.**35.70*f*
of beryllium, **II.**35.72*f*
of copper, **II.**35.70*f*
of gold, **II.**35.70*f*
of iron, **II.**35.71*f*
of molybdenum, **II.**35.71*f*
of nickel, **II.**35.71*f*
of silicon, **II.**35.72*f*
of silver, **II.**35.70*f*
of stainless steel, **II.**35.71*f*
temperature dependence of, in metals, **II.**35.68*t*–**II.**35.69*t*
Speckle, **I.**4.23–**I.**4.24
Speckle effects:
in BSDF, **II.**26.12
with mixing rods, **III.**2.33
in monochromatic beam, **III.**26.5
in multiple scattering, **III.**3.15–**III.**3.16
on synchrotron beam lines, **III.**35.4
Speckle fields, generation of, **I.**28.22
Speckle spectroscopy, **III.**26.5
Spectacles, for vision correction, **III.**10.2, **III.**10.11
for aniseikonia, **III.**12.18
for anisometropia, **III.**12.23
for cataracts, **III.**11.13
and eye movement, **III.**12.29–**III.**12.30

Spectacles, for vision correction (*Cont.*):
lenses for, **III.**11.2, **III.**11.6–**III.**11.10
optic axes of, **III.**18.4
vertex error from, **III.**11.1
(*See also* Bifocal spectacles)
Spectra:
atomic, **II.**28.14
homogeneous lineshape of, **II.**28.14
Spectral bands, for infrared imaging, **I.**23.5–**I.**23.6, **I.**23.6*f*
Spectral data:
linear models and, **I.**26.28–**I.**26.29
singular value decomposition (SVD) and, **I.**26.28
Spectral density, in lasers, **IV.**27.3–**IV.**27.4
Spectral diffusion, **IV.**24.14, **IV.**24.16–**IV.**24.17
Spectral errors, **II.**24.39–**II.**24.40
Spectral filter, narrow-line, as optical limiter, **IV.**19.1
Spectral hole, **IV.**25.21
Spectral hole burning, **IV.**4.15
Spectral inversion, **IV.**3.11, **IV.**3.11*f,* **IV.**3.12
Spectral luminous efficiency function for photopic vision, **III.**7.8–**III.**7.9, **III.**7.9*f,* **III.**7.16, **III.**7.16*t,* **III.**7.17*f,* **III.**14.2
Spectral luminous efficiency function for scotopic vision, **III.**7.9, **III.**7.9*f*–**III.**7.10*f*
Spectral mode:
in lasers, **IV.**4.15
in VCSELs, **IV.**4.49
Spectral representation, **I.**4.24
Spectral sensitizing dyes, **III.**6.14–**III.**6.19
Spectrograph, **III.**21.4
off-axis, double-pass, **II.**5.13*f*
Pfund, **II.**5.13*f*
Spectroheliograms, **II.**11.6
Spectrometers, **II.**25.10, **III.**34.4, **III.**35.16
dispersion, **II.**36.63
double-beam, **II.**20.4, **II.**20.5*f*
Fourier transform, **I.**42.16, **II.**36.63, **II.**36.63*f,* **II.**36.64–**II.**36.65, **II.**36.74
grating, **II.**20.6
luminescence, **II.**20.5–**II.**20.6
using phase-sensitive detection, **II.**20.8, **II.**20.8*f,* **II.**20.9
luminescence excitation, **II.**20.11, **II.**20.11*f,* **II.**20.12, **II.**20.12*f*
mirror, **II.**5.8*f*
modulation, **II.**36.67, **II.**36.67*f,* **II.**36.68, **II.**36.70
neutron gravity, **III.**36.6*f*
optical absorption, **II.**20.2–**II.**20.3
absorption coefficient in, **II.**20.3
optically detected magnetic resonance (ODMR), **II.**20.22*f*
Spectrometers (*Cont.*):
Perkins-Elmer Model 112, **II.**5.9*f*
phase sensitive detection, **II.**20.13
polarization, **II.**20.15, **II.**20.15*f*
polarized absorption, **II.**20.26
prism, **II.**5.1, **II.**5.3*f*
Bunsen-Kirchoff, **II.**5.5*f*
Perkin-Elmer Model, **II.**5.4
rapid-scan, **II.**12.42
unicam prism-grating, **II.**5.15*f*
(*See also* Spectroscopy)
Spectrophotometer, **I.**42.16, **II.**25.9
double-beam, **II.**20.4, **II.**20.5*f*
(*See also* Spectrometers)
Spectropolarimetry, **II.**22.8
for chemical applications, **II.**22.26
Spectroradiometers, **II.**5.1, **II.**5.2*f*
prism/grating, **II.**5.14*t*
Spectroradiometry, **III.**7.16, **III.**14.1
Spectroradiometry, **I.**27.22
Spectroscopic phenomena, quantum basis of, **I.**8.4
Spectroscopic systems:
broadband, **II.**36.62
components of, **II.**36.61–**II.**36.62, **II.**36.62*f*
laser, **II.**36.62–**II.**36.63
reflection in, **II.**36.65
transmission/absorption in, **II.**36.65–**II.**36.67
Spectroscopic techniques, nonlinear, **II.**36.61
Spectroscopic transition, rates of, **I.**8.6–**I.**8.7
Spectroscopy:
adaptive optics for, **III.**1.14–**III.**1.15
atomic, **II.**28.5
and atom trapping, **IV.**28.19–**IV.**28.20
coherent, Raman interactions in, **IV.**18.43, **IV.**18.43*t,* **IV.**18.44*f*
coherent anti-Stokes Raman, **II.**36.58
coherent Stokes Raman (CSRS), **II.**36.58
coherent transient, **IV.**24.25–**IV.**24.27
of condensed matter, **II.**28.8
differential transmission, **IV.**25.19–**IV.**25.22
Doppler-free saturation, **II.**20.25*f*
electric-field-modulated reflection, **II.**36.70
electromagnetically induced transparency in, **IV.**23.3
evanescent wave, **IV.**14.14
excitation, **II.**28.22
excitation photoluminescence (PLE), **II.**36.76
FM, **IV.**27.14
Fourier transform, **II.**28.5
gas-phase, **I.**8.9
H-atom, **I.**8.11
high-resolution time-domain, **IV.**22.55
Lamb dip, **II.**28.5, **II.**28.7*f*
laser absorption saturation, **I.**8.12

Spectroscopy (*Cont.*):
laser cooling in, **IV.**28.27
and laser stabilization, **IV.**27.12–**IV.**27.16
laser Stark, **II.**20.27, **II.**20.27*f,* **II.**20.28, **II.**20.28*f,* **II.**20.29
linear dichroism, **III.**25.2
luminescence, **II.**36.72
modulation transfer, **IV.**27.20
molecular, **II.**28.6
gas-phase, **II.**28.5
neutron, **III.**36.13
of 1-electron atoms, **I.**8.10–**I.**8.12
optical, **I.**8.14, **II.**36.6, **IV.**24.2–**IV.**24.3
optical hole-burning (OHB), **II.**20.24, **II.**20.24*f,* **II.**20.25–**II.**20.26, **II.**20.26*f*
optical transfer function in, **III.**1.22–**III.**1.23
photo-associative, **IV.**28.28–**IV.**28.30, **IV.**28.30*f*
photon correlation, **III.**3.8
photon echo, **IV.**24.25–**IV.**24.26, **IV.**24.26*f*
polarization, **II.**28.23–**II.**28.24, **IV.**27.13
pump probe, **IV.**25.19–**IV.**25.20
Raman, **II.**28.18–**II.**28.19, **II.**28.19*f,* **II.**36.57–**II.**36.58, **II.**36.59*f,* **II.**36.61
Raman-induced Kerr-effect (RIKES), **II.**36.58
reflection gratings in, **III.**21.3
saturated absorption, **II.**20.25
solid state, **I.**8.25, **II.**28.14
polarization effects in, **II.**28.23
speckle, **III.**26.5
Stark, **II.**28.14
time-of-flight (TOF), **II.**28.7–**II.**28.8
transition-metal ion, **II.**28.11
trapped ion, **IV.**28.19
ultrafast, **IV.**25.4, **IV.**25.15–**IV.**25.17, **IV.**25.20–**IV.**25.24
ultraviolet photoemission (UPS), **II.**36.33
X-ray photoemission (XPS), **II.**36.33
Zeeman, **II.**28.24–**II.**28.26
(*See also* Spectrometers)
Spectrum:
of light, **I.**4.20, **I.**4.24
limitations, **I.**4.20
normalized, **I.**4.6
secondary, **II.**18.42
Spectrum analyzer, **II.**29.28
Specular reflection, **I.**6.4–**I.**6.5
Spheres, coated, **I.**6.15–**I.**6.16
Spherical aberration, **I.**1.98, **II.**18.42, **III.**10.4, **III.**10.7, **III.**18.10
in achromatic doublets, **II.**1.24
in landscape lenses, **II.**1.18, **II.**1.19*f*
left-hand solution for, **II.**1.24
in lenses, **II.**1.11
reciprocal object distance and, **II.**1.13*f*–**II.**1.14*f*
Spherical aberration (*Cont.*):
right-hand solution for, **II.**1.24
shape factor and, **II.**1.14*f*
in single lenses, **II.**1.11–**II.**1.12, **II.**1.14*f*
zonal, **II.**18.42
Spherical-grating monochromator (SGM), **III.**21.5, **III.**21.8
Spherical lenses, in nonimaging optics systems, **III.**2.8–**III.**2.9
Spherical Micro Integrated Lenses (SMILE) (*see* Microlenses, SMILE)
Spherical primary objectives, with Schmidt principal, **II.**18.20, **II.**18.20*f*
Spherical surfaces, **I.**1.37
refraction and reflection by, **I.**1.41
tracing rays in, **I.**1.39
Spherical waves, **I.**2.4–**I.**2.5, **I.**2.9–**I.**2.10, **I.**2.10*f,* **I.**2.12*f*–**I.**2.13*f,* **I.**3.3*f,* **I.**3.4
Spherochromatism, **I.**33.3
Sphero-cylindrical lens, **III.**11.3, **III.**11.3*f,* **III.**11.5
Spherometers, **II.**29.21, **II.**29.21*f,* **II.**29.23
automatic, **II.**29.22
bar, **II.**29.22, **II.**29.23*t*
mechanical, **II.**29.22
precision, **II.**29.22*t*
Spire Corp. baffles:
reflectance in, **II.**37.59*f*
Splay, **II.**34.12
Splice:
of fiber amplifiers, **IV.**11.4
loss from, **IV.**6.8*t,* **IV.**6.14, **IV.**6.17
types of, **IV.**6.9
Spline surfaces, **III.**2.7
Split-off band, and strained quantum wells, **IV.**4.33
Splitter, **IV.**10.2, **IV.**10.3*f*
design of, **IV.**10.9, **IV.**10.9*f*
polarization, **IV.**8.7*f*
tapered fiber, **IV.**8.1, **IV.**8.6
Spontaneous decay rate, **I.**8.9
Spontaneous emission, **IV.**12.2, **IV.**28.1–**IV.**28.2
from amplifiers, **IV.**7.6
from free-electron lasers, **IV.**26.44
in laser cooling, **IV.**28.2–**IV.**28.3, **IV.**28.17, **IV.**28.19
from lasers, **IV.**4.10–**IV.**4.11, **IV.**4.18, **IV.**4.20, **IV.**4.22, **IV.**26.31, **IV.**26.35, **IV.**26.43
from LEDs, **IV.**4.39–**IV.**4.41, **IV.**12.26
in optical molasses, **IV.**28.12–**IV.**28.13
parametric, **IV.**22.8
and photonic crystal microcavities, **IV.**20.8, **IV.**20.11–**IV.**20.12
in quantum theory, **IV.**26.8–**IV.**26.9, **IV.**26.9*f,* **IV.**26.10, **IV.**26.13, **IV.**28.5

Spontaneous Raman scattering, **IV.**18.3, **IV.**18.22
Spot-diagram analysis, **I.**34.15–**I.**34.17
Spurious-free dynamic range (SFDR), **IV.**6.7
Sputtering, magnetron, **I.**42.15
Square root law, **I.**25.27
Squeezed light states, **I.**4.2
Squirm, **II.**3.17
Stable mode, **I.**11.26
Stacked-actuator mirrors, **III.**1.38–**III.**1.40
Stadia, **II.**29.3
  range meter, **II.**29.3*f*
Stage scanning, **II.**17.40
Stainless steel, specific heat of, **II.**35.71*f*
Standard deviation, **II.**24.24
Standard rate equation model, **II.**39.3–**II.**39.4
Standards:
  cathode ray tube (CRT)
    colorimetric, **I.**27.15
    synchronization, **I.**27.14
  color, for liquid crystal displays (LCDs), **I.**27.42
  deuterium lamp, **I.**10.10
  international specifications, **I.**35.10
  IR radiometric, **I.**10.9
  ISO specifications, **I.**35.11
  on jitter, **IV.**6.16
  lamp, **I.**10.8
  for lamp safety, **III.**15.15
  for laser safety, **III.**15.13–**III.**15.14
  luminous flux, **I.**10.9
  luminous intensity, **I.**10.8
  oculars, design for, **II.**17.21
  for optical communications, **IV.**16.1–**IV.**16.8
  photometric, **I.**10.8
  radiation, **I.**10.8
  in radiometry/photometry, **III.**7.2–**III.**7.3, **III.**14.3
  reflectance, **II.**25.14–**II.**25.15, **II.**25.15*t*
  for solid-state camera output, **III.**4.20–**III.**4.21
  for spectacle prescriptions, **III.**11.10
  tungsten-filament lamps, **I.**10.10
  tungsten lamp, **I.**10.10
  types of, **II.**29.2
  for UV radiation exposure, **III.**15.6
  (*See also specific standards*)
Standing wave:
  de Broglie, **IV.**28.37
  light intensity in, **IV.**28.22
  optical force from, **IV.**28.6–**IV.**28.8, **IV.**28.11
  and optical lattices, **IV.**28.30–**IV.**28.32, **IV.**28.32*f*
  production of, **IV.**28.16
Stanford/MSFC Multispectral Solar Telescope Array, **II.**11.6
Star architecture, in power-limited transmission medium, **IV.**2.13
Star concentrator, **III.**2.21
Staring arrays, **I.**23.7, **I.**23.15
Stark effect, **II.**28.23, **II.**39.22, **IV.**4.2, **IV.**4.57, **IV.**4.58*f,* **IV.**17.5*t,* **IV.**17.12, **IV.**17.14–**IV.**17.15, **IV.**17.25, **IV.**23.20
Star network topology, **IV.**13.13–**IV.**13.14, **IV.**13.14*f*
  in FDDI, **IV.**16.3
Static state director's distribution, in LC cells, **II.**14.15–**II.**14.16, **II.**14.16*f*
Statistical radiometry, **I.**4.24
Steering mirrors, **III.**1.17–**III.**1.18
Stefan-Boltzmann's law, **III.**14.12
Step-index fibers, **IV.**1.7, **IV.**1.9, **IV.**1.11
  Bessel functions for, **IV.**1.9*f*
  core diameter-wavelength relation for, **IV.**1.12
  dispersion in, **IV.**2.3–**IV.**2.4
  index profile for, **IV.**1.19*f*
Steradian, **III.**7.3, **III.**14.5
Stereoacuity, **I.**25.43, **II.**2.13
Stereopsis, **I.**24.37, **I.**25.42–**I.**25.43
  and aging, **III.**13.18
  calculation of, **III.**12.12
  DaVinci, **III.**12.4
  definition of, **III.**12.2
  in head-mounted display systems, **III.**12.31–**III.**12.32
  and intraocular blur, **III.**12.19–**III.**12.20
  and magnification, **III.**12.10*f,* **III.**12.14–**III.**12.15
Stereoscopic acuity, **I.**24.38–**I.**24.39, **I.**24.39*f*
Stereoscopic instruments, **I.**24.39
Sterilamps, **I.**10.35
Steward Observatory group, **III.**1.7
Stigmatic imaging, **I.**1.33, **I.**1.35
Stilb, **III.**7.8
Stiles-Crawford effect, **I.**24.12, **I.**24.12*f,* **I.**24.13, **I.**24.20, **I.**25.8, **III.**9.2, **III.**9.6*f*
  first kind (SCE I), **III.**9.3, **III.**9.5–**III.**9.7, **III.**9.13, **III.**9.21–**III.**9.22, **III.**9.29
  second kind (SCE II), **III.**9.5, **III.**9.22
Stimulated Brillouin scattering (SBS), **II.**10.37–**II.**10.38, **II.**39.9, **IV.**1.39–**IV.**1.40, **IV.**3.1, **IV.**3.7–**IV.**3.9, **IV.**17.16–**IV.**17.17, **IV.**17.20
  backward, **IV.**18.48
  beam geometry for, **IV.**3.8*f*
  equations for, **IV.**18.45–**IV.**18.49
  frequency shift in, **IV.**18.46–**IV.**18.48
  gain in, **IV.**18.47–**IV.**18.49
  k vector diagrams for, **IV.**18.46*f*–**IV.**18.47*f*
  linewidth in, **IV.**18.48
  noise buildup in, **IV.**18.49
  parameters for various materials, **IV.**18.51*t*–**IV.**18.53*t*

Stimulated Brillouin scattering (SBS) (*Cont.*):
for phase conjugation, **IV.**18.45, **IV.**18.49–**IV.**18.50, **IV.**18.50*f,* **IV.**18.54, **IV.**18.54*f*
Stimulated emission, **IV.**12.2, **IV.**28.2
from atomic beam slowing, **IV.**28.10
from lasers, **IV.**4.11, **IV.**4.45, **IV.**12.26, **IV.**26.18
in quantum theory, **IV.**26.8–**IV.**26.9, **IV.**26.9*f,* **IV.**26.10
Stimulated photon echo, **IV.**24.15, **IV.**24.15*f,* **IV.**24.16–**IV.**24.17, **IV.**24.17*f,* **IV.**24.18, **IV.**24.18*f*
Stimulated photorefractive scattering (SPS), **II.**39.10
Stimulated Raman Adiabatic Passage (STIRAP), **IV.**23.4
Stimulated Raman scattering (SRS), **IV.**1.39–**IV.**1.40, **IV.**1.42, **IV.**3.1, **IV.**3.4–**IV.**3.7, **IV.**17.5*t,* **IV.**17.19, **IV.**17.19*f,* **IV.**17.20, **IV.**18.4
applications for, **IV.**18.42–**IV.**18.44
backward, **IV.**18.42
beam geometry for, **IV.**3.5, **IV.**3.5*f*
broadband effects in, **IV.**18.29–**IV.**18.30, **IV.**18.30*f,* **IV.**18.31–**IV.**18.32
equations for, **IV.**18.6–**IV.**18.7, **IV.**18.20*t,* **IV.**18.22
and focused beams, **IV.**18.40–**IV.**18.42
frequency shifts in, **IV.**18.11*t*–**IV.**18.15*t,* **IV.**23.27
gain in, **IV.**18.8–**IV.**18.9, **IV.**18.16*t*–**IV.**18.18*t,* **IV.**18.42
gain narrowing in, **IV.**18.16, **IV.**18.21
geometries for, **IV.**18.4, **IV.**18.5*f*
linewidth in, **IV.**18.9, **IV.**18.10*f,* **IV.**18.16*t*–**IV.**18.18*t,* **IV.**18.32
multiple Stokes generation in, **IV.**18.39, **IV.**18.41*f*
for phase conjugation, **IV.**18.49
phase pulling in, **IV.**18.25–**IV.**18.26, **IV.**18.28*f*
photon interactions in, **IV.**18.21–**IV.**18.22
polarization dependence in, **IV.**18.42, **IV.**18.42*t*
pulsed transient effects in, **IV.**18.23–**IV.**18.24, **IV.**18.24*f,* **IV.**18.25, **IV.**18.25*t,* **IV.**18.26*f*
pump depletion in, **IV.**18.9–**IV.**18.10, **IV.**18.15–**IV.**18.16, **IV.**18.21*f,* **IV.**18.23, **IV.**18.31
soliton solutions in, **IV.**18.26–**IV.**18.29, **IV.**18.29*f*
Stokes/anti-Stokes, **IV.**18.2, **IV.**18.2*f,* **IV.**18.4, **IV.**18.33–**IV.**18.35
(*See also* Anti-Stokes scattering)
Stokes noise in, **IV.**18.35–**IV.**18.39, **IV**18.40*f*
temperature dependence in, **IV.**18.19*t*–**IV.**18.20*t*
Stimulated Rayleigh scattering, **IV.**17.20
Stimulated Rayleigh-wing scattering, **IV.**17.5*t*
Stimuli, constant, **I.**29.10
Stimulus sequencing, **I.**29.10
Stochastic errors, **II.**29.2
Stokes-Poincaré parameters, **III.**25.8
Stokes scattering matrix, **I.**7.2
Stokes shift, **II.**28.17
Stokes-shifted Brillouin scattering, **IV.**3.7–**IV.**3.9, **IV.**17.20, **IV.**18.44, **17.**17
Stokes-shifted Raman scattering, **IV.**3.4–**IV.**3.7, **IV.**17.17, **IV.**17.17*f,* **IV.**17.18, **IV.**18.1–**IV.**18.2, **IV.**18.2*f,* **IV.**18.3, **IV.**18.3*t*
Stokes sideband, **I.**8.27*f,* **I.**8.29
Stokes vectors, **I.**5.26–**I.**5.27, **II.**22.4, **II.**22.8–**II.**22.9, **II.**22.11*t*–**II.**22.12*t,* **II.**22.16, **II.**22.28
definition of, **II.**22.8–**II.**22.9
measurement, **II.**22.16
Stokes wave, **II.**39.9
Stop placement, **I.**38.6
Stop shift, **I.**1.100
Storage media, alternative, **I.**31.31
Storage rings, as synchrotron radiation sources, **III.**32.2–**III.**32.3, **III.**32.3*f,* **III.**32.10
Strabismus, **III.**12.2, **III.**16.5
Straightness measurements, **II.**29.12
Strain, **IV.**4.2, **IV.**4.15, **IV.**4.29
Strained layers, in LEDs, **IV.**4.40
Strained layer (SL) lasers, **IV.**4.1, **IV.**4.31–**IV.**4.34
band diagrams for, **IV.**4.32*f*
Strained-layer superlattices (SLSs), **II.**28.13, **II.**28.13*f*
Stratified-medium model (SMM), **II.**27.4
STRAY, **I.**38.28
Stray light, **III.**13.11
Monte Carlo techniques used to evaluate, **III.**2.7
Strehl ratio, **I.**7.11, **II.**11.6
in adaptive optics system design, **III.**1.40–**III.**1.42, **III.**1.44–**III.**1.48
atmospheric tilt effect on, **III.**1.15–**III.**1.17, **III.**1.23
definition of, **III.**10.2
from focus anisoplanatism, **III.**1.30, **III.**1.31*f*–**III.**1.32*f*
and human eye aberrations, **III.**10.7*f,* **III.**10.8
jitter effect on, **III.**1.18*f*
for least-squares adaptive estimator, **III.**1.37*f*
in spectroscopy, **III.**1.14–**III.**1.15, **III.**1.22
and tracking bandwidth, **III.**1.20*f,* **III.** 1. 24*f*
Stress-optical measurements, **I.**5.26
String method (edge rays), in concentrator design, **III.**2.23
Stripe geometry, in lasers, **IV.**4.6
Stripe lasers:
GaAs/AlGaAs, **I.**13.9*f*
ion bombardment, **I.**13.8

Strip loading, **IV.**4.7
Strip mirror integrator (SMI), **III.**2.41
Stroma, **III.**13.5–**III.**13.6
Strontium barium niobate (SBN), **II.**39.17
Strontium titanate, refractive index for, **II.**33.72*t*
Structure functions, **III.**1.9
Strut design, **I.**38.22, **I.**38.22*f*
Stylus writing, **III.**5.5
Subaperture:
  in adaptive optics system design, **III.**1.40–**III.**1.46
  in Shack-Hartmann sensor, **III.**1.25–**III.**1.27
Subjective amplitude of accommodation, **I.**24.30
Sub-picosecond relaxation, **II.**20.14, **II.**20.14*f*
Substrate growth:
  Bridgeman technique, **I.**12.22
  gradient-freeze technique, **I.**12.22
  Liquid Encapsulated Czochralski (LEC) technique, **I.**12.22
Substrate materials:
  mechanical properties of, **II.**33.50*t*–**II.**33.51*t*
  physical properties of, **II.**33.44*t*
  thermal properties of, **II.**33.54*t*–**II.**33.55*t*
Substrates, **I.**12.21
  doping, in LEDs, **I.**12.22
  growth techniques for, **I.**12.22
Sum-and-difference-frequency processes, **II.**38.14–**II.**38.16
Sum frequency generation (SFG), **IV.**17.4, **IV.**17.5*t,* **IV.**17.7, **IV.**17.16, **IV.**17.25, **IV.**22.3, **IV.**25.18
Sum rule relationships, **II.**33.11, **II.**36.11
Sum rules, for electronic interactions, **I.**9.15–**I.**9.16
Superconducting tunneling junction (STJ) detectors, **III.**34.9
Supermirrors, **III.**24.6, **III.**35.9, **III.**36.9, **III.**36.13
Superposition:
  coherent, of atomic states, **IV.**23.6–**IV.**23.7
  as nonimaging optics uniformity control, **III.**2.2, **III.**2.33, **III.**2.34*f*–**III.**2.35*f,* **III.**2.40–**III.**2.41
  in X-ray diffraction, **III.**35.6
Supersensitizers, in color photography, **III.**6.15–**III.**6.16, **III.**6.16*f*
Surface acoustic wave (SAW), **II.**12.2, **II.**12.47
Surface acoustic wave (SAW) devices, **II.**6.14
Surface current, **I.**22.11–**I.**22.12, **I.**22.12*n*
Surface-emitting lasers (SEL), **I.**13.42–**I.**13.43, **I.**13.44*f,* **I.**13.45
  distributed grating, **I.**13.43
  with a 45° mirror, **I.**13.42
Surface-emitting LEDs (S-LEDs), **IV.**4.39–**IV.**4.40, **IV.**4.40*f,* **IV.**4.41–**IV.**4.42
Surface location, **I.**34.5
Surface power spectral density (PSD) function, **II.**11.2, **II.**11.22, **II.**11.24, **II.**11.24*f*–**II.**11.25*f*
Surface profile, **I.**34.5–**I.**34.6
Surfaces:
  color coordinates of, **I.**26.30
  in colorimetry, **I.**26.25
  description of, **I.**1.36
  fractal errors in, **I.**7.12
  illuminates, simulation of, **I.**26.30
  nonsequential, **I.**34.7
  of revolution, **I.**1.37*f*
  spherical, **I.**1.37, **I.**1.39, **I.**1.41
Surface scattering, **I.**7.1–**I.**7.2
  scalar treatment for, **II.**11.25
Surface transfer function, of scattering surfaces, **II.**11.18, **II.**11.18*f*
Sweatt model, of ray tracing, **II.**8.4
Sweep-out, **I.**15.18
Swept-carrier time-domain optical memory, **IV.**24.24
Swept-frequency methods, **IV.**1.17
Switch, **IV.**10.5, **IV.**10.5*f,* **IV.**10.11, **IV.**10.11*f*
  acousto-optic tunable wavelength, **II.**6.25
  all-optical, **IV.**12.36–**IV.**12.38, **IV.**12.38*f,* **IV.**13.15
  Benes, **II.**6.32, **II.**6.33*f*
  crossbar, **II.**6.32
  directional coupler, **II.**6.23–**II.**6.24, **II.**6.24*f*
  integrated optical, **II.**6.32
  tapered fiber, **IV.**8.1, **IV.**8.5, **IV.**8.5*f*
Switching:
  circuit, **IV.**13.16, **IV.**13.16*f*
  control signal, **IV.**21.2
  in networks, **IV.**2.13
  packet, **IV.**13.16, **IV.**13.16*f,* **IV.**13.17
  protection, in SONET rings, **IV.**13.13
  self-, **IV.**21.2, **IV.**21.4
  in time-division multiplexing, **IV.**12.8, **IV.**12.8*f*
  (*See also* All-optical switching)
Symmetrical lenses, **II.**1.27–**II.**1.28
  double astigmat, **II.**1.32*f*
Symmetry properties, of materials, **II.**33.7
Synchronization:
  in demultiplexing, **IV.**12.9
  in time-division multiple access, **IV.**12.16–**IV.**12.18
  in time-division multiplexing, **IV.**12.19–**IV.**12.20
Synchronous digital hierarchy (SDH), **IV.**2.16, **IV.**12.20–**IV.**12.21
Synchronously pumped parametric oscillator (SPPO), **IV.**22.55–**IV.**22.60
  femtosecond, **IV.**22.57–**IV.**22.60, **IV.**22.60*f*
  picosecond, **IV.**22.55–**IV.**22.57, **IV.**22.58*f*
Synchronous optical network (SONET), **IV.**2.16, **IV.**12.20–**IV.**12.23, **IV.**12.23*f,* **IV.**16.6
  and FDDI, **IV.**16.4

Synchronous payload envelope (SPE), **IV.**12.22–**IV.**12.23
Synchronous pumping, in ultra-short-pulse OPOs, **IV.**22.55
Synchronous transmission signal (STS), **IV.**12.22–**IV.**12.23, **IV.**16.6
Synchrotron radiation, **II.**24.28–**II.**24.29
  from bending magnets, **III.**3.6*f,* **III.**32.3–**III.**3.6, **III.**32.7–**III.**32.9, **III.**32.9f, **III.**32.10
  function of, **III.**32.2, **III.**32.3*f*
  from insertion devices, **III.**32.10–**III.**32.18
  and ionization chambers, **III.**34.4
  and linearly polarized X rays, **III.**25.2–**III.**25.3
  output from, **III.**32.4, **III.**32.5*f*
  sources of, **III.**32.1–**III.**32.2, **III.**32.19
  speckle effects with, **III.**35.4
Synchrotron sources, **II.**11.2
Synchrotron X-ray optics, **III.**19.6, **III.**19.10, **III.**22.4, **III.**26.3–**III.**26.6, **III.**35.3, **III.**37.3
  vs. point source/optic combination, **III.**35.5
  polycapillary application for, **III.**30.14, **III.**30.15*t*
  in protein crystallography, **III.**35.14
  and Schwarzschild objective, **III.**27.4
Synthetic aperture radar, **I.**30.8–**I.**30.9, **I.**30.9*f*
Systematic error, **II.**29.2
System calibration, **II.**26.13–**II.**26.14
System combinations, gaussian properties of, **I.**1.68
Systems of revolution:
  angle of incidence in, **I.**1.43
  axial object and, **I.**1.46
  description of, **I.**1.35
  image locations in, **I.**1.44, **I.**1.46, **I.**1.46*f*
  magnification in, **I.**1.46
  paraxial limit in, **I.**1.42
  paraxial optics of, **I.**1.41, **I.**1.45
  paraxial ray tracing in, **I.**1.44
  principal focal lengths in, **I.**1.44
  reflection in, **I.**1.43
  refraction in, **I.**1.43
  surface power in, **I.**1.43
  three-ray rule in, **I.**1.46
  transfer in, **I.**1.42
  two-ray paraxial invariant, **I.**1.45

Tailoring, as nonimaging optics uniformity control, **III.**2.2, **III.**2.24, **III.**2.38–**III.**2.40
Talystep roughness, **I.**7.11
Tanabe-Sugano diagrams, **II.**28.10, **II.**28.10*f,* **II.**28.11, **II.**28.20
Tandem limiter, **IV.**19.6–**IV.**19.7
Tangential fans, **I.**1.39
Tangential phase matching (TPM), **II.**12.11
Tapered fibers, **IV.**8.1–**IV.**8.8
  bending in, **IV.**8.5, **IV.**8.5*f*
Tapered single-mode fiber-optic power splitter, **IV.**8.1
Tapped bus, in power-limited transmission medium, **IV.**2.13
Target brightness, **III.**1.46, **III.**1.46*f,* **III.**1.47, **III.**1.47*f*
Target detection, **III.**4.3, **III.**17.5
Tatarskii, V. I., **III.**1.8–**III.**1.9, **III.**1.11
Taylor expansions, **I.**1.45
T carriers, **IV.**12.23–**IV.**12.24
Tear production, **III.**13.6
Technical specifications, for optical systems, **I.**35.2
Technology mirror assemble (TMA), **II.**11.4
Teflon, in optical black surfaces, **II.**37.27–**II.**37.28
Telecentric distribution, in nonimaging optics systems, **III.**2.18
Telecentricity, **I.**1.91, **I.**1.91*f,* **II.**19.31–**II.**19.32, **II.**19.32*f*
Telecentric lenses, **I.**1.91, **I.**1.91*f,* **II.**2.11–**II.**2.12
Telecentric stop, **II.**1.8
Telecom devices, **IV.**4.1
Telecommunications:
  edge-emitting lasers as source for, **IV.**4.3
  long distance, **IV.**1.9, **IV.**1.11, **IV.**1.47
  optical fiber applications for, **IV.**1.21
  optimal laser source for, **IV.**4.3
Telecom systems, **IV.**6.1–**IV.**6.2
Telephoto lenses, **I.**1.57, **II.**1.29–**II.**1.30
  reverse, **II.**1.30, **II.**1.35*f*
Telepresence, **III.**12.31
Telescopes, **I.**4.24
  adaptive optics used in, **III.**1.4, **III.**1.6*f,* **III.**1.41–**III.**1.48
  aperture in, **III.**1.7, **III.**1.15, **III.**1.17
  astronomical (*see* Telescopes, keplerian)
  broadband X-ray (BBXRT), **II.**11.5, **II.**11.12–**II.**11.13, **II.**11.13*f*
  Canada-France-Hawaii, **III.**1.24
  Cassegrain, **II.**2.20, **II.**11.4, **II.**32.4, **III.**27.1, **III.**28.1
  Cassegrain-Mersenne, afocal, **II.**18.10*f*
  dual-field-of-view infrared, **I.**39.12
  galilean, **II.**2.14
    field of view in, **II.**2.14–**II.**2.15
  Gemini North 8-m, **III.**1.22, **III.**1.23*f*
  grazing incidence, **II.**11.14
  Gregorian-Mersenne, afocal, **II.**18.13*f*
  Hobby-Eberly, **III.**1.4
  Hubble, **II.**30.23
  inverse galilean, **II.**2.14–**II.**2.15, **II.**2.15*f,* **II.**2.16
    field of view in, **II.**2.16
  keplerian, **II.**2.7, **II.**2.7*f,* **II.**2.8–**II.**2.11

Telescopes (*Cont.*):
Kirkpatrick-Baez, **II.**11.3*f*
large binocular, **III.**1.8
Mersenne, **II.**2.19
micro-optic, **II.**8.8*f*
Multiple Mirror, **III.**1.8
Ritchey-Chretien, **II.**18.8*f*
ROSAT (Röntgensatellit), **II.**11.4–**II.**11.5
Stanford/MSFC Multispectral Solar Telescope Array, **II.**11.6
subaperture in, **III.**1.42–**III.**1.46
terrestrial, **II.**2.10, **II.**2.10*f*
theodolite, **II.**29.15
three-mirror afocal, **II.**18.32, **II.**18.32*f*
unit magnification galilean, **II.**29.5, **II.**29.7*f*
and wavefront tilt, **III.**1.23, **III.**1.25
Wolter, **II.**11.3*f*–**II.**11.4*f,* **II.**11.5–**II.**11.6
diffraction-limited performance of, **II.**11.10
ghost images in, **II.**11.14, **II.**11.14*f,* **II.**11.15, **II.**11.15*f,* **II.**11.16
XPECT, **II.**11.5, **II.**11.15, **II.**11.26
error budget in, **II.**11.27*f*
X ray, **III.**19.10, **III.**28.1
conical foil, **II.**11.26
grazing incidence, **II.**11.4, **II.**11.13
scattering effects in, **II.**11.16, **II.**11.16*f*–**II.**11.17*f*
solar, **II.**11.27, **II.**11.27*f*
(*See also* Astronomy)
Telescopic lens (*see* Lenses, afocal)
Telestereoscope, **III.**12.15
Television:
aliasing on, **III.**4.18
closed-circuit, **III.**4.20
compression scheme for, **III.**17.7
digital, **III.**4.21
high-definition, **III.**4.21, **III.**6.27, **III.**17.10, **III.**18.6
solid-state camera applications for, **III.**4.3
Temperature:
vs. absorptance, for molybdenum, **II.**35.53*f*
and frequency drift control, **IV.**27.18
and laser cooling, **IV.**28.3, **IV.**28.9
laser sensitivity to, **IV.**4.12–**IV.**4.13
tuning of, in optical parametric generation, **IV.**22.62
Temperature change, homogeneous tolerable, **I.**39.5–**I.**39.6
Temperature noise, **I.**15.10
Templates, **II.**29.21
Temporal despeckling, **I.**28.22
Temporal instability, **II.**35.11
Temporal sensitivity:
and aging, **III.**13.16–**III.**13.18
10Base-T, **IV.**16.7
Tensile strain, on quantum wells, **IV.**4.33–**IV.**4.34
Tensile strength, of optical fiber, **IV.**1.18–**IV.**1.19
Tensor characteristics, **II.**33.7, **II.**33.8*t*
Tensor-to-matrix conversions, **II.**33.32*t*
Terahertz optical asymmetric demultiplexer (TOAD), **IV.**12.38
Ternary layers, **IV.**4.2
Tessar lenses, **II.**1.26*f,* **II.**1.27, **II.**1.33*f*
Test plates, **II.**29.21
Tests (*see specific types*)
Texture:
imaging of, **III.**17.6
in visual perception, **III.**12.4–**III.**12.5, **III.**12.13–**III.**12.14, **III.**12.14*f*
Theodolites, **II.**2.10, **II.**29.3, **II.**29.15
accessories for, **II.**29.16
Therapy:
neutron, **III.**35.34
X-ray radiation, **III.**35.33–**III.**35.34
Thermal blooming, **IV.**17.24
Thermal circuit theory, **I.**19.2
Thermal conductivity, **II.**33.36–**II.**33.37, **II.**33.37*f,* **II.**35.8
Thermal cycling, **II.**35.11
Thermal defocus, **I.**39.4, **I.**39.16
compound optical construction and, **I.**39.4, **I.**39.5*f*
Thermal detectors (*see* Detectors, thermal; Photodetectors, thermal)
Thermal distortion, **II.**35.11
Thermal expansion, **II.**33.36, **II.**35.7–**II.**35.8
Thermal expansion match arrays, **I.**23.15
Thermal gradients:
effect of, **I.**39.6–**I.**39.7
transient longitudinal, **I.**39.16
Thermal injury, from optical radiation, **III.**15.2–**III.**15.5, **III.**15.7–**III.**15.8
Thermal instability, **II.**35.11
Thermalization, of semiconductors, **IV.**25.21–**IV.**25.22
Thermal noise, **I.**15.10
in photodetectors, **IV.**4.74–**IV.**4.75
Thermal runaway, **IV.**4.13
Thermistor bolometer, **I.**15.22–**I.**15.23
Thermistors, **I.**15.5, **I.**15.23*f*
D^* of, **I.**15.22*f*
spectral response of, **I.**15.22*f*
Thermocouples, **I.**15.4, **I.**15.19, **I.**19.1–**I.**19.2, **I.**19.5
frequency spectra, **I.**15.20*f*
spectral response curves in, **I.**15.20*f*
unwanted, **I.**18.6
Thermodynamic equilibrium, **I.**11.2–**I.**11.3
Thermoluminescence (TL), **II.**36.72

Thermo-optic coefficient, **II.**33.25, **II.**33.28, **II.**33.28*f*
Thermo-optic effect, as nonlinearity, **IV.**17.22
Thermopiles, **I.**15.4, **I.**15.10, **I.**15.20–**I.**15.21, **I.**19.2, **I.**19.6
  spectral absorption of, **I.**15.21*f*
  spectral reflectance of, **I.**15.21*f*
Thermoplastic recording material, **II.**23.8–**II.**23.9
Thermoplastic resins, **II.**34.2
Thermoset resins, **II.**34.2
Thermotropic liquid crystals, **II.**14.3*f*–**II.**14.4*f*
  dielectric constants in, **II.**14.6–**II.**14.7, **II.**14.7*f*
  elastic constants in, **II.**14.8, **II.**14.8*f*–**II.**14.9*f*
  electronic structures in, **II.**14.3*f*
  molecular vibrational absorptions in, **II.**14.5, **II.**14.5*f*–**II.**14.6*f*
  optical properties of, **II.**14.2
  phenyl rings in, **II.**14.3*f,* **II.**14.4
  refractive index dispersions in, **II.**14.4
  viscosities of, **II.**14.9–**II.**14.10
θ_1/θ_2 concentrator, **III.**2.19, **III.**2.19*f,* **III.**2.20
Thin-film coatings:
  contamination assessment techniques for, **II.**37.18
  design of, **I.**42.9
    analytical synthesis methods of, **I.**42.15
    graphical vector methods in, **I.**42.9
    numerical methods in, **I.**42.10
  manufacturing considerations of, **I.**42.14–**I.**42.16
  materials, **I.**42.14
  multilayer systems
    analysis, matrix theory for, **I.**42.10–**I.**42.12
    analysis of, **I.**42.15
    properties of, **I.**42.12, **I.**42.12*f,* **I.**42.13, **I.**42.13*f*
  optical interference of light in, **II.**37.17
  thermal conductivities of, **I.**42.17
  (*See also* Optical coatings)
Thin-film oxides, **II.**6.13–**II.**6.14
Thin films, **I.**2.24–**I.**2.25, **I.**2.28
Third-harmonic generation (THG), **IV.**17.4, **IV.**17.5*t,* **IV.**17.9, **IV.**17.13, **IV.**17.16
  energy level diagram for, **IV.**17.7, **IV.**17.7*f*
  production of, **IV.**17.24–**IV.**17.25, **IV.**22.3
Third-order aberrations, **I.**1.98, **II.**18.42
Third-order optical nonlinearities, **IV.**17.3–**IV.**17.5
  in all-optical switching, **IV.**21.2–**IV.**21.3
  cascaded processes as, **IV.**17.22–**IV.**17.26
  determining characteristics of, **IV.**17.28–**IV.**17.33
  energy level diagrams for, **IV.**17.6–**IV.**17.7, **IV.**17.7*f*
  frequency terms for, **IV.**17.5*t*
  Kramers-Kronig dispersion relation in, **IV.**17.3, **IV.**17.10–**IV.**17.113
Third-order optical nonlinearities (*Cont.*):
  nonlinear absorption, **IV.**17.9–**IV.**17.11, **IV.**17.14–**IV.**17.15, **IV.**17.15*f,* **IV.**17.21, **IV.**17.28, **IV.**17.31–**IV.**17.33
  nonlinear refraction, **IV.**17.9–**IV.**17.11, **IV.**17.13–**IV.**17.14, **IV.**17.28, **IV.**17.31–**IV.**17.33
  and optical Kerr effect, **IV.**17.13–**IV.**17.16
  quantum mechanics of, **IV.**17.6–**IV.**17.9, **IV.**17.20
  self-focusing as, **IV.**17.27
  soliton formation as, **IV.**17.27–**IV.**17.28
  stimulated scattering as, **IV.**17.16–**IV.**17.20
  thermo-optic effect as, **IV.**17.24
  time-ordering sequences of, **IV.**17.6*f*
  two-photon absorption as, **IV.**17.5*t,* **IV.**17.7*f,* **IV.**17.12, **IV.**17.14–**IV.**17.15, **IV.**17.21, **IV.**17.33, **IV.**19.5–**IV.**19.7
Third-order parametric amplification, **IV.**17.7
35-mm color film (*see* Photographic film, 35-mm)
Three-chip color imaging, **I.**22.36
Three-dimensional diffraction pattern, **II.**17.9, **II.**17.11*f*
Three-dimensional imaging, **II.**17.47
Three-lens prime focus corrector objectives, **II.**18.11, **II.**18.11*f*
Three-mirror objectives, **II.**18.32, **II.**18.32*f,* **II.**18.33, **II.**18.33*f,* **II.**18.34
3M Nextel Black Velvet, **II.**37.31
Three-powered-mirror lenses, **II.**2.20, **II.**2.20*f*
Three-ray rule, **I.**1.46
Three-wave mixing, **IV.**3.2, **IV.**23.24
Threshold, **I.**29.3, **I.**29.3*f,* **I.**29.4
  adjustment settings, **I.**29.5
  carrier density, in lasers, **I.**13.13, **I.**13.13*f*–**I.**13.14*f,* **I.**13.17*f*
  estimation. stages to, **I.**29.10
  voltage, in photogates, **I.**16.12
Thresholding, **II.**39.32–**II.**39.34
Threshold-limit values (TLVs), **III.**15.9–**III.**15.10
Throughput, **I.**1.25
  in passive optical network, **IV.**2.13
Tilt:
  atmospheric, **III.**1.15–**III.**1.17, **III.**1.44
  as human eye aberration, **III.**10.2, **III.**10.4
  in visual perception, **III.**12.2, **III.**12.4, **III.**12.14, **III.**12.14*f*
Tilted gratings, **IV.**9.7
Tilted plane processor, **I.**30.10, **I.**30.10*f*
Tilt sensing, **III.**1.23
Time constant, **I.**15.11
Time delay, in laser servo system, **IV.**27.8, **IV.**27.11, **IV.**27.15, **IV.**27.18–**IV.**27.19
Time delay and integration (TDI), **III.**4.3

Time-dependent error, **II.**24.38–**II.**24.39
Time-dependent (transient) optical spectroscopy, **IV.**24.2–**IV.**24.3
  Bloch equations for, **IV.**24.3–**IV.**24.5
Time-division multiple access (TDMA), **IV.**12.3, **IV.**12.16–**IV.**12.17, **IV.**12.17*f,* **IV.**12.18
Time-division multiplexing (TDM), **II.**10.29, **IV.**1.31, **IV.**12.16–**IV.**12.24, **IV.**13.2
  analog, **IV.**12.4, **IV.**12.6, **IV.**12.9
  applications for, **IV.**12.18
  for FDDI-II, **IV.**16.4
  frames in, **IV.**12.18–**IV.**12.19, **IV.**12.20*f,* **IV.**12.21
  to increase bit rate, **IV.**2.11
  in networks, **IV.**12.3
  for SONET, **IV.**12.22–**IV.**12.23, **IV.**12.23*f,* **IV.**12.24
  synchronization in, **IV.**12.19–**IV.**12.20
  system components in, **IV.**12.38–**IV.**12.40
  30-channel, **IV.**12.21
  timing information in, **IV.**12.9
  timing recovery in, **IV.**12.15
  24-channel, **IV.**12.21, **IV.**12.21*f*
Time domain, **I.**6.18
Time domain measurement, **II.**10.14, **II.**10.16, **II.**10.18*f,* **IV.**1.16–**IV.**1.18
  of fiber strain, **IV.**1.20*f*
Time-gated imaging, Raman amplification in, **IV.**18.43–**IV.**18.45, **IV.**18.46*f*
Time-integrating architecture, **II.**12.45–**II.**12.47
Time-integrating correlator, **I.**30.13–**I.**30.14, **I.**30.14*f*
Time-multiplexed switching (TMS), **II.**6.32
Time-of-flight Laue diffraction techniques, **III.**37.3–**III.**37.4
Time-of-flight measurement, **II.**29.5
Time slot, **IV.**12.9
  and intersymbol interference, **IV.**13.5
  in time-division multiple access, **IV.**12.16–**IV.**12.18
  in time-division multiplexing, **IV.**12.18–**IV.**12.19, **IV.**12.20*f,* **IV.**13.2
Timing recovery, **IV.**12.14–**IV.**12.16
  in time-division multiple access, **IV.**12.17
Timing signal, **IV.**12.14
Tiodize V-E17 surface, **II.**37.40–**II.**37.41
T-matrix method, **I.**6.12, **I.**6.17
TN cells (*see* Nematic liquid crystals, twist alignment of)
Token, in FDDI, **IV.**16.3
Token passing ring, FDDI as, **IV.**16.2
Toner, xerographic, **III.**5.1
  charge measurement for, **III.**5.8, **III.**5.8*f*
  in fusing process, **III.**5.10–**III.**5.11
  removal of, **III.**5.11
  in two-component magnetic brush development, **III.**5.5–**III.**5.7
Tone reproduction, in photographic film, **I.**20.17–**I.**20.18
T1 signal, **IV.**12.21
Tonic level of accommodation, **I.**24.32
Toroidal-grating monochromator (TGM), **III.**21.5, **III.**21.8
Toroidal gratings, **III.**21.3, **III.**21.7*t*
Toroidal mirror, **III.**26.4, **III.**26.6
Torsion, in visual perception, **III.**12.2, **III.**12.4, **III.**12.23, **III.**12.27
Total flux, into a hemisphere, **II.**24.16–**II.**24.17
Total frustrated reflection microscopy, **II.**17.25
Total integrated scatter (TIS), **I.**7.10–**I.**7.11, **II.**26.2, **II.**26.4–**II.**26.5, **II.**26.7, **II.**26.9, **II.**37.21
  with a Coblentz Sphere, **II.**26.8*f*
  with a diffuse integrating sphere, **II.**26.8*f*
Total internal reflection (TIR), **III.**2.13, **III.**2.17
  of prism, **IV.**10.5, **IV.**10.6*f*
Total internal reflection (TIR) facets, in Fresnel lenses, **III.**2.10–**III.**2.11
Total mass loss (TML), **II.**37.19
Total power law, **II.**33.24, **II.**33.24*f*
Trabecular meshwork, **III.**13.21–**III.**13.22
Track-error signal (TES), **I.**31.15
Tracking:
  as adaptive optics system design parameter, **III.**1.40–**III.**1.41, **III.**1.44
  automatic, **I.**31.15
  bandwidth for, **III.**1.17–**III.**1.19, **III.**1.20*f,* **III.**1.24
  continuous/composite format, **I.**31.15, **I.**31.15*f*
  on grooves, **I.**31.15–**I.**31.16, **I.**31.16*f*
  hardware for, **III.**1.23–**III.**1.25
  sampled, **I.**31.17, **I.**31.17*f*
Track-pitch, **I.**31.3
Tracks, **I.**31.3, **I.**31.5
  defining, **I.**31.4
  seek operation
    counting during, **I.**31.17–**I.**31.18
Track-servo marks, **I.**31.17
Transatlantic fiber cable link, **IV.**1.18
Transconductance amplifiers, **I.**18.12–**I.**18.13
Transducer:
  designs for, **IV.**27.16–**IV.**27.18
  piezoelectric (PZT), **IV.**27.6, **IV.**27.8, **IV.**27.9*f,* **IV.**27.10, **IV.**27.16–**IV.**27.21
Transducer array, beam-steered, **II.**12.22
Transfer functions, **II.**32.1–**II.**32.2
  analysis, **II.**32.2
Transfer matrix method, to solve Maxwell's equations, **IV.**20.3–**IV.**20.4
Transformation:
  affine, **I.**1.62
  afocal, **I.**1.65

Transformation (*Cont.*):
collinear (*see* Collinear transformation)
matrix representation of, **I.**1.64–**I.**1.65
projective (*see* Collineation)
Transform-limited pulse, **IV.**7.2–**IV.**7.3, **IV.**7.3*f,* **IV.**7.4
Transient four-wave mixing, **IV.**25.18, **IV.**25.18*f,* **IV.**25.19
Transillumination, **II.**17.37–**II.**17.38
Transition-edge sensor (TES), **III.**34.8
Transition-edge sensor (TES) microcalorimeters, **III.**35.22–**III.**35.23, **III.**35.23f, **III.**35.24*f*–**III.**35.25*f*
Transition frequencies, in molecular physics, **II.**28.5
Transition-metal ions, **II.**28.9
and rare-earth ions, **II.**28.8
spectroscopy, **II.**28.11
Transition radiation, **III.**33.1, **III.**33.3
Transitions:
direct, **II.**36.24
electric dipole, **I.**8.13
electronic, **II.**36.38–**II.**36.39
forbidden, **I.**9.30–**I.**9.32
high-energy, **II.**36.32, **II.**36.33*f*
homogeneous width of, **I.**8.10
indirect, **II.**36.25–**II.**36.26
interband, **II.**36.34*f*–**II.**36.35*f*
(*See also* Interband transitions)
multiphonon, **II.**36.48
natural linewidth of, **I.**11.5
optical, **I.**8.8–**I.**8.9
distribution frequencies in, **I.**8.9
radiative, **I.**8.8
spectroscopic, **I.**8.6–**I.**8.7
two-photon absorption, **I.**8.12
zero-phonon, **I.**8.28
Transmission, in spectroscopic systems, **II.**36.65–**II.**36.67
Transmission coefficients, **II.**36.9
Transmission loss, **IV.**6.7
Transmission reflection, **II.**25.2*f*
Transmission spectra, in semiconductors, **II.**36.67
Transmission zone plate, **III.**23.7, **III.**23.8*f*
Transmittance, **II.**25.3–**II.**25.4, **II.**25.8, **II.**25.10
of black felt paper, **II.**37.40*f*
of black velvet, **II.**37.41*f*
of commando cloth, **II.**37.42*f*
measurement of, **II.**25.8–**II.**25.10, **II.**25.10*f,* **II.**25.11
in metals, **II.**35.6
of neoprene, **II.**37.43*f*
Transmitter arrays, **IV.**2.11
Transmitters:
analog, **II.**6.29
CATV, **II.**6.32
digital, **II.**6.28–**II.**6.29
extinction ratio of, **IV.**6.14
in optical fiber communications system, **IV.**2.1, **IV.**2.5–**IV.**2.6
semiconductor laser as, **IV.**12.24–**IV.**12.25
spectral, **I.**43.10
Transparency, **III.**2.24
Transparency film, **III.**6.10, **III.**6.23
Transparent fiber systems, **IV.**5.2
Transparent head-mounted display, **III.**18.4–**III.**18.5, **III.**18.10
Transparent substrate (TS) chip, **I.**12.7
Transverse chromatic aberration (TCA), **III.**9.7
Transverse coherence, **III.**35.3
Transverse electric (TE) waveguide mode, **IV.**4.15
Transverse electromagnetic (TEM) modes, **I.**11.23–**I.**11.24
transverse laser modes, **I.**11.23–**I.**11.24, **I.**11.24*f*
Transverse holographic technique, for fiber grating fabrication, **IV.**9.5, **IV.**9.5*f*
Transverse junction stripe (TJS) lasers, **I.**13.10
Transverse Kerr effect, **IV.**25.11–**IV.**25.12, **IV.**25.12*f,* **IV.**25.14–**IV.**25.15
Transverse laser modes, **I.**11.22–**I.**11.23, **I.**11.25–**I.**11.27
TEM (transverse electromagnetic), **I.**11.23–**I.**11.24, **I.**11.24*f*
Transverse magnetic (TM) waveguide mode, **IV.**4.15
Transverse ray plots, **I.**33.2
Transverse relaxation, and echo signals, **IV.**24.14
Transverse relaxation rate, **IV.**24.8, **IV.**24.11*f*
Transverse relaxation time, **IV.**24.5, **IV.**24.7, **IV.**24.9, **IV.**24.12, **IV.**24.15, **IV.**25.16
Transverse spatial coherence, **III.**32.19
Trap loss, **IV.**28.28
Trapped ion spectroscopy, **IV.**28.19
Trapped needle system, in autoexposure cameras, **II.**15.11
Trapping, of neutral atoms (*see* Atom trapping)
Trapping states, for micromaser, **IV.**26.34
Traveling wave:
in dark state, **IV.**28.37
optical force for, **IV.**28.5–**IV.**28.8, **IV.**28.8*f*
Traveling wave (TW) amplifiers, **IV.**11.4
Tribo, in xerographic toner charge measurement, **III.**5.8
Tributary signal, **IV.**12.18, **IV.**12.20
Trichromatic color-matching, **I.**26.8
Trifocal spectacles, **III.**11.7–**III.**11.8, **III.**13.23
Trigger detection, **II.**20.22

Tri-Level color copying, **III.**5.13, **III.**5.13*f*
Trinitron CRTs, **I.**27.5
Triplet lenses, **II.**1.26, **II.**1.26*f,* **II.**1.27, **II.**1.32*f*
Triply resonant oscillator (TRO), **IV.**22.15
Trischiefspiegler objectives, **II.**18.29
Troland, **I.**28.3, **II.**24.45–**II.**24.46, **III.**14.8
TRU-color diffuse black, **II.**37.41
Trumpet (concentrator), **III.**2.16, **III.**2.16*f*
Tunable lasers, **IV.**2.6, **IV.**2.11, **IV.**18.43, **IV.**27.14
  optical protection from, **IV.**19.1
Tungsten:
  extinction coefficient for, **II.**35.19*t*–**II.**35.20*t*
    vs. wavelength, **II.**35.27*f*
  index of refraction in, **II.**35.19*t*–**II.**35.20*t*
    vs. wavelength, **II.**35.27*f*
  reflectance of, **II.**35.40*t*–**II.**35.41*t*
  reflectance vs. wavelength for, **II.**35.47*f*
Tungsten arc (photomicrographic) lamps, **I.**10.39, **I.**10.45*f*
Tungsten-filament lamps, **I.**10.17, **I.**10.18*f,* **I.**10.19
  standards, **I.**10.10
Tungsten film, **III.**6.24*t*
Tungsten hexafluoride, **II.**37.56
Tungsten radiation, **III.**7.16
Tunneling current, in dark current, **I.**16.8
Twin-channel substrate mesa lasers, **I.**13.23*f,* **I.**13.24
Twin-channel (TCL) lasers, **I.**13.31
Twin-ridge structure (TRS) lasers, **I.**13.21
Two-alternative forced choice task (2afc), **I.**29.9
Two-beam coupling, **IV.**19.10, **IV.**19.12
  amplification, **II.**39.28
  photorefractive gain in, **II.**39.27
  photorefractive loss in, **II.**39.28–**II.**39.29
  wave interactions in, **II.**39.4, **II.**39.4*f,* **II.**39.5–**II.**39.6
Two-component magnetic brush development, **III.**5.5–**III.**5.7
Two-component systems, **I.**32.5
  with finite conjugates, **I.**32.6*f*
  with infinitely distant objects, **I.**32.6*f*
Two-dimensional images, optical processing of, **I.**30.14
Two-lens systems, **II.**1.20, **II.**1.20*f,* **II.**1.21, **II.**1.21*f,* **II.**1.22, **II.**1.22*f*
Two-mirror, three-reflection objectives, **II.**18.28, **II.**18.28*f*
Two-parameter tuning, **IV.**22.28, **IV.**22.31
Two-photon absorption (2PA), **IV.**17.5*t,* **IV.**17.12, **IV.**17.14–**IV.**17.15, **IV.**17.21, **IV.**17.33
  energy level diagram for, **IV.**17.7*f*
  and optical limiting, **IV.**19.5–**IV.**19.6, **IV.**19.6*f,* **IV.**19.7
  in semiconductors, **IV.**19.10
Two-photon spectroscopy, **IV.**27.14
Two-photon transitions, **IV.**24.21–**IV.**24.22, **IV.**24.23*f*
Two plane waves, interference of, **I.**2.8, **I.**2.8*f,* **I.**2.9, **I.**2.9*f*
Two-powered-mirror lenses, **II.**2.19, **II.**2.19*f,* **II.**2.20
Two steps plus one method, **II.**30.20
Twyman-Green interferometers (*see* Interferometers, Twyman-Green)

Ultimate strength, **II.**35.9
Ultracold collisions, **IV.**28.24, **IV.**28.27–**IV.**28.29, **IV.**28.29*f,* **IV.**28.30
Ultrafast lasers, **IV.**25.3–**IV.**25.4, **IV.**25.16, **IV.**25.16*f,* **IV.**25.22
Ultrashort lasers:
  intensity correlation in, **I.**14.22–**I.**14.23
  interferometric correlation in, **I.**14.23
  phase reconstruction in, **I.**14.25
  pulse amplitude in, **I.**14.25
  (*See also specific types*)
Ultrashort pulse generation, **IV.**25.4, **IV.**25.13–**IV.**25.15
  experimental study techniques for, **IV.**25.18–**IV.**25.24
  semiconductors in, **IV.**25.15–**IV.**25.16, **IV.**25.16f, **IV.**25.17, **IV.**25.17*f,* **IV.**25.18
  (*See also* Saturable absorbers)
Ultrashort pulse transmission, **IV.**1.31–**IV.**1.32
Ultrasound imaging, **III.**35.25
Ultraviolet photoemission spectroscopy (UPS), **II.**36.33
Ultraviolet radiation, regions of, **II.**36.4
Ultraviolet (UV) light:
  and cataracts, **III.**11.13–**III.**11.14, **III.**13.8, **III.**13.19, **III.**15.1, **III.**15.4–**III.**15.6
  and color photographic film, **III.**6.4
  and color photographic paper, **III.**6.5
  exposure limits for, **III.**15.9–**III.**15.10
  extreme, **III.**19.6
  eye damage from, **III.**13.6, **III.**15.2, **III.**15.4–**III.**15.7, **III.**15.10
  in fiber grating fabrication, **IV.**9.5–**IV.**9.7
  ocular effect of, **III.**13.5–**III.**13.7, **III.**13.9
  and photographic image dyes, **III.**6.10
  in photometry, **III.**7.18
  in photosensitivity, **IV.**9.2–**IV.**9.3
  in radiometry, **III.**7.5, **III.**14.1
  and Schwarzschild objective applications, **III.**27.1
  skin damage from, **III.**15.1, **III.**15.10
  and spectacle lenses, **III.**11.9–**III.**11.10
Unbalanced nonlinear interferometer (UNI), **IV.**12.38

Uncertainty principle, **I.**8.9
Uncrossed converging reflector, **II.**2.39*f,* **III.**2.38–**III.**2.39
Uncrossed diverging reflector, **II.**2.39*f,* **III.**2.38
Underscan, in CRTs, **I.**27.13
Undersea communications:
  amplified soliton transmission for, **IV.**1.31
  couplers for, **IV.**8.4
  optical amplifiers in, **IV.**2.12
Undulators, **III.**26.4, **III.**32.1–**III.**32.2, **III.**32.6, **III.**32.13, **III.**32.13*f,* **III.**32.14–**III.**32.17
  free-electron laser as, **III.**33.4
  NSLS In-Vacuum UNdulator (IVUN), **III.**32.14*f*–**III.**32.16*f*
  polarization of, **III.**32.18
  power of, **III.**32.17–**III.**32.18
Unfolded diagrams, reflection, **I.**1.36, **I.**1.36*f*
Uniformity, in illumination, **III.**2.2
  faceted reflectors for, **III.**2.40–**III.**2.42
  and integrating cavities, **III.**2.25–**III.**2.28
  lens arrays for, **III.**2.33–**III.**2.38
  mixing rods for, **III.**2.28–**III.**2.33
  for projection system, **III.**2.23–**III.**2.25
  tailoring for, **III.**2.38–**III.**2.40
Unit conversions:
  illuminance, **III.**7.8*t*
  luminance, **III.**7.9*t*
  photometric to radiometric, **III.**7.13–**III.**7.15
  radiometric to photometric, **III.**7.12–**III.**7.13
Unit power relays, **II.**2.21
Upchirp, **I.**14.6
  Kerr-effect-induced, **I.**14.7
Upper Atmospheric Research Satellite (UARS), **I.**44.36, **I.**44.37*f*
Upwelling average cosine, spectral, **I.**43.12
Urbach tail model, **II.**33.17, **II.**33.39
  parameters, **II.**33.81*t*–**II.**33.82*t*
U.S. Air Force Airborne Laser program, **III.**1.4
U.S. Federal Product Performance Standard, **III.**15.14
UV hazard action spectrum curve, **III.**15.3, **III.**15.4*f*
Uviarc lamps, **I.**10.27, **I.**10.27*f*

Valence band, **II.**36.6–**II.**36.7
  photoemission from, **II.**36.32*f*
  theory of covalency, **I.**8.21–**I.**8.22
Van Cittert-Zernike theorem, **I.**2.39, **I.**2.39*f,* **I.**2.40, **I.**4.14, **I.**4.18–**I.**4.20
Vander Lugt filters (*see* Filters, Vander Lugt)
Vanes, **I.**38.11–**I.**38.12, **I.**38.12*f*–**I.**38.13*f,* **II.**37.1, **II.**37.14
  angle consideration in, **I.**38.14, **I.**38.14*f,* **I.**38.15, **I.**38.15*f,* **I.**38.16, **I.**38.16*f*
Vanes (*Cont.*):
  bevel placement on, **I.**38.14, **I.**38.14*f*
  depth consideration in, **I.**38.16–**I.**38.17, **I.**38.17*f,* **I.**38.18
  designing, **I.**38.13
  specular, **I.**38.18, **I.**38.19*f*
Van Hove singularities, **II.**36.33
Vanishing point, **III.**12.4, **III.**12.4*f*
Vantage point, **III.**12.3
Vapor axial deposition (VAD), **II.**10.44, **IV.**1.46
Vapor phase epitaxy (VPE), **I.**12.23–**I.**12.24, **II.**6.16–**II.**6.17
Variable-gain amplifier (VGA), **IV.**12.40
Varifocal systems, **I.**32.11
Vector diffraction, **I.**3.27, **I.**3.29*f*
  theory, **II.**8.14, **II.**8.14*f*
Vector electromagnetic field, **I.**4.23
Vector matching, **IV.**17.5
Vectors, **I.**26.44–**I.**26.45
  linear combinations of, **I.**26.46
Vector scattering amplitude, **I.**6.6
Vee (V) three-level atomic scheme, **IV.**23.6, **IV.**23.6*f*
Velocimetry:
  Doppler, **II.**29.27
  laser Doppler, **II.**29.28, **II.**29.28*f,* **II.**29.29
  particle image (PIV), **II.**29.27
Velocity-changing collisions, **IV.**24.14–**IV.**24.17
Velocity dependence:
  in laser cooling/VSCPT, **IV.**28.37, **IV.**28.38*f*
  of optical forces, **IV.**28.1–**IV.**28.2, **IV.**28.6–**IV.**8.8
  in optical molasses, **IV.**28.12, **IV.**28.13*f*
Velocity distribution:
  in atomic beam slowing, **IV.**28.10–**IV.**28.11, **IV.**28.12*f,* **IV.**28.25–**IV.**28.26
  of atomic sample, **IV.**28.3, **IV.**28.7
  for Bose-Einstein condensation, **IV.**28.35
  in optical lattices, **IV.**28.33, **IV.**28.34*f*
Velocity-selective coherent population trapping (VSCPT), **IV.**23.5, **IV.**28.37–**IV.**28.38, **IV.**28.38*f*
Verdet constant, **IV.**10.7
Vergence, **I.**24.35–**I.**24.36
  in binocular vision, **III.**12.8, **III.**12.20–**III.**12.25
  lens effects on, **III.**12.25–**III.**12.27
  prism, **III.**12.29
VeriMask, **II.**23.20
Version, in binocular vision, **III.**12.8, **III.**12.21–**III.**12.22
Vertex plane, **I.**1.37
Vertical cavity lasers, **I.**13.44, **I.**13.45*f*
  performance characteristics of, **I.**13.46*t*

Vertical cavity surface-emitting laser (VCSEL), **IV.**2.6*n,* **IV.**4.2, **IV.**4.45–**IV.**4.50
electrical injection of, **IV.**4.47–**IV.**4.48, **IV.**4.48*f*
geometry of, **IV.**4.45, **IV.**4.46*f*
L-I curve for, **IV.**4.49
long-wavelength, **IV.**4.50
mirror reflectivity of, **IV.**4.46–**IV.**4.47, **IV.**4.50
quantum wells in, **IV.**4.46
spatial characteristics of emissions from, **IV.**4.48–**IV.**4.49
spectral characteristics of emissions from, **IV.**4.49–**IV.**4.50
Vestibular organs, **III.**12.29
Vestibulo-ocular reflex (VOR), **III.**12.21, **III.**12.29–**III.**12.30, **III.**12.33
Vestibulo-ocular responses, **I.**24.34
Vibrational optical effects, in semiconductors, **II.**36.18–**II.**36.23
Vibrational sideband, **I.**8.28, **II.**28.16, **II.**28.17*f*
Vibrational symmetries, infrared and Raman-active, **I.**9.20*t*–**I.**9.21*t*
Video back, **II.**15.7
Video coding standards, **III.**17.4
Video enhancement, in microscopy, **II.**17.44, **II.**17.44*f,* **II.**17.45, **II.**17.45*f,* **II.**17.46, **II.**17.46*f*
Video monitors (*see* Cathode ray tube (CRT))
Video Quality Experts Group (VQEG)s, **III.**17.4
Video transmission, analog, on fiber, **IV.**2.14–**IV.**2.15
Vidicon cameras, **I.**21.22
Vieth-Müller circle, **III.**12.8–**III.**12.9, **III.**12.9*f,* **III.**12.10
Vignetting, **I.**1.89, **I.**1.89*f,* **II.**1.8, **II.**18.42, **II.**24.20–**II.**24.21
Virtual image, **II.**18.42
Virtual reality environments:
distance perception in, **III.**12.32–**III.**12.33
imaging in, **III.**17.1, **III.**17.10
visual-vestibular information from, **III.**12.33–**III.**12.34
Virtual transitions, in nonlinear interactions, **IV.**17.8, **IV.**17.21
Virtual tributaries, in SONET, **IV.**16.6
Visible spectrum:
exposure limits for, **III.**15.9–**III.**15.11
eye damage from, **III.**15.2, **III.**15.4, **III.**15.5*f*
multilayer reflective coatings for, **III.**24.1–**III.**24.2
in radiometry, **III.**7.5, **III.**14.1
Visible spectrum sampling, **I.**26.6
Visual acuity, **I.**25.35–**I.**25.36, **III.**10.2
through accommodation, **III.**12.3
and aging, **III.**13.11, **III.**13.15–**III.**13.16, **III.**13.16*f,* **III.**13.23
Visual acuity (*Cont.*):
assessment of, **I.**25.36*f*
binocular stereoscopic discrimination, **I.**25.42–**I.**25.44
and cataracts, **III.**10.13, **III.**13.19
and corneal desiccation, **III.**13.6
disparity discrimination thresholds, **I.**25.44*f*
and head-mounted displays, **III.**18.3, **III.**18.11
measurement of, **III.**10.3, **III.**11.5, **III.**13.15
motion detection and, **I.**25.38–**I.**25.39, **I.**25.39*f,* **I.**25.40–**I.**25.42
pattern discrimination and, **I.**25.37–**I.**25.38
postsurgical, **III.**10.15–**III.**11.17
of retina, **III.**15.12
retinal eccentricities in, **I.**25.36, **I.**25.37*f*
Visual angles, **I.**25.3
Visual cortex, primary (V1), **I.**25.13, **I.**25.14*f,* **I.**25.15
direction selectivity of, **I.**25.15*n*
Visual differences predictor, **III.**17.3–**III.**17.4
Visual field, **III.**12.3
and aging, **III.**13.18
and binocular vision, **III.**12.3, **III.**12.8
peripheral, **III.**12.29, **III.**13.22
Visualization, **III.**17.7–**III.**17.9
Visual photometry, **III.**7.6
Visual plane, **III.**12.3
Visual processing, central, **I.**25.13
anatomy of, **I.**25.13
physiology of, **I.**25.14
Visual stimulus:
commonly used, **I.**29.4
size of, **I.**28.1
Visual system, **I.**24.6
aberration-free, **I.**24.13–**I.**24.14, **I.**24.14*f,* **I.**24.15, **I.**24.15*f*
adaptation and inhibition in, **I.**25.26–**I.**25.28
chromatic aberrations in, **I.**24.17–**I.**24.18, **I.**24.18*f,* **I.**24.19
contrast detection in, **I.**25.21, **I.**25.27
chromatic, **I.**25.31
temporal, **I.**25.28–**I.**25.29, **I.**25.29*f*
contrast discrimination in, **I.**25.33–**I.**25.34
contrast estimation in, **I.**25.35
contrast masking in, **I.**25.33–**I.**25.34
controlling luminance intensity in, **I.**28.12–**I.**28.13
depth-of-focus in, **I.**24.26–**I.**24.27, **I.**24.28*f*
diffraction-limited (*see* Visual system, aberration-free)
information-processing model of, **I.**25.16*f*
intraocular scattered light and, **I.**24.19
light, varying source of, **I.**28.14
line-spread function (LSF) in, **I.**24.14

Visual system (*Cont.*):
mean oblique astigmatism of, **I.**24.17*f*
modulation transfer function (MTF) in, **I.**24.14, **I.**24.14*f,* **I.**24.24, **I.**24.24*f*
monochromatic ocular aberration in, **I.**24.15–**I.**24.16, **I.**24.16*f,* **I.**24.17, **I.**24.17*f*
movements in, **I.**24.34–**I.**24.35, **I.**25.22–**I.**25.23
ocular ametropia in, **I.**24.8
ophthalmoscopic methods, **I.**24.22–**I.**24.24
optical/retinal inhomogeneity in, **I.**25.26
paraxial models of, **I.**24.6*t,* **I.**24.7, **I.**24.7*f,* **I.**24.8
phase transfer function (PTF) in, **I.**24.14
pupil diameter in, **I.**24.11
receptors in, **I.**25.24–**I.**25.25
reduced, **I.**24.7
refractive errors in, **I.**24.8–**I.**24.9, **I.**24.9*f*
schematic, **I.**24.5*f,* **I.**24.7
spatial channels in, **I.**25.25–**I.**25.26
spectral sensitivity of, **I.**28.3
stability of fixation in, **I.**24.36–**I.**24.37, **I.**24.37*f*
stereoscopic acuity in, **I.**24.38, **I.**24.38*f*
stereoscopic instruments and, **I.**24.39
tasks in, **I.**25.16, **I.**25.16*n,* **I.**25.17
transmittance in, **I.**24.10, **I.**24.10*f*
vestibulo-ocular responses in, **I.**24.34
wide-angle models of, **I.**24.8
(*See also* Eye, human; Human visual system (HVS); *specific topics*)
Vitreous humor, **III.**13.7
Voice communication, timing delays in, **IV.**12.16
Voigt effect, **II.**36.46
Voigt profile, **I.**44.13
Voltage amplifiers, **I.**18.11–**I.**18.12
Voltage-controlled oscillator (VCO), **IV.**12.15, **IV.**12.15*f,* **IV.**12.16
Volume scattering, **III.**3.2, **III.**3.5
Volume scattering function, spectral, **I.**43.11–**I.**43.12
Von Kármán spectrum, **III.**1.9
V-parameter:
for cochlear hair cells, **III.**9.25
for waveguides, **III.**9.2, **III.**9.15–**III.**9.16, **III.**9.16*f,* **III.**9.17, **III.**9.17*f,* **III.**9.19

Wadsworth constant-deviation, prism-mirror arrangement, **II.**5.5*f*
Wadsworth gratings, **II.**5.8, **II.**5.12*f*
Wafer processing:
laser scribing of, **I.**12.26
of semiconductors, **I.**12.24
testing and, **I.**12.26
Walkoff:
group velocity, **IV.**22.64
spatial, **IV.**22.63–**IV.**22.64
and stimulated Raman scattering, **IV.**3.7
Wander, **IV.**6.16
Wannier excitons, **II.**36.28
Wannier Stark localization (WSL), **IV.**4.63
Water, **I.**43.3–**I.**43.4, **I.**43.17
apparent optical properties (AOP), **I.**43.4, **I.**43.6*t,* **I.**43.12–**I.**43.13
electromagnetic properties of, **I.**43.17–**I.**43.18
environmental conditions in, **I.**43.7*f*
fundamental quantities in, **I.**43.5*t*
geometry used in, **I.**43.10*f*
homogeneous waters in, **I.**43.13
index of refraction in, **I.**43.20*t*–**I.**43.21*t*
inherent optical properties (IOP), **I.**43.4, **I.**43.5*t,* **I.**43.7*f,* **I.**43.10–**I.**43.12, **I.**43.37*t*
Jerlov types (*see* Jerlov water types)
optical constants of, **I.**43.17–**I.**43.18, **I.**43.18*f*
optical properties of, **I.**43.3
pure, absorption coefficients of, **I.**43.19*t*
radiometric quantities in, **I.**43.5*t,* **I.**43.6, **I.**43.7*f*
scattering in, **I.**43.30–**I.**43.32
sea (*see* Sea water)
spectral absorption coefficient for, **I.**43.20, **I.**43.29
Water vapor regained (WVR), **II.**37.20
Watts, **I.**21.4
conversion to lumens, **III.**7.12
vs. lumens, **III.**7.7
as radiometric unit, **III.**7.5, **III.**14.1, **III.**14.4, **III.**14.4*t,* **III.**14.7
Wave attenuation, **III.**3.8–**III.**3.9
Waveband materials, optical and thermal data for, **I.**39.3*t*–**I.**39.4*t*
Wave equations, **I.**9.6–**I.**9.7
Wavefront aberration, **I.**1.94, **I.**1.94*f,* **I.**1.95, **I.**1.97
and adaptive optics, **III.**1.5–**III.**1.7, **III.**1.12–**III.**1.15, **III.**10.3
and anisoplanatism, **III.**1.21
and atmospheric tilt, **III.**1.15–**III.**1.17, **III.**1.23
correctors for, **III.**1.38–**III.**1.40, **III.**10.8
definition of, **III.**10.2
in eyes, **I.**24.16, **I.**24.16*f*
fringe patterns in, **I.**2.12
of human eye, **III.**10.4–**III.**10.5, **III.**10.6*f,* **III.**10.8, **III.**10.8*f*
and ray aberrations, **I.**1.95
rotational symmetric systems and, **I.**1.94, **I.**1.94*f,* **I.**1.97
Wavefront deviations, **II.**7.4*f*–**II.**7.5*f*
Wavefront division, **I.**2.14
interference by, **I.**2.14, **I.**2.16*f*
in neutron interferometry, **III.**36.10
Wavefront error, **I.**35.3
in adaptive optics system design, **III.**1.42–**III.**1.43

Wavefront error (*Cont.*):
for a lens, **I.**35.5
root-mean-square, **I.**35.4
tolerancing method, in optical systems, **I.**36.3
Wavefront multiplexers, grating designs and, **II.**8.11, **II.**8.11*t,* **II.**8.12
Wavefronts, **I.**2.5, **I.**3.4
aspherical
hologram for testing, **II.**30.24*f*
measuring, **II.**30.22
cylindrical, **I.**3.13, **I.**3.14*f*–**I.**3.15*f*
examples of, **I.**2.5*f*
gradient (slope) of, **III.**1.25–**III.**1.26
propagation in atmospheric turbulence, **III.**1.10–**III.**1.11
Wavefront sensing, **III.**1.25–**III.**1.28
in adaptive optics retina camera, **III.**10.6*f*
as adaptive optics system design parameter, **III.**1.40–**III.**1.43
data latency in, **III.**1.36*f*
higher-order, **III.**1.25–**III.**1.28, **III.**1.37–**III.**1.38
laser beacons for, **III.**1.28–**III.**1.35
Wavefunctions:
antisymmetric, **I.**8.14
of electrons, **I.**8.14
Slater, **I.**8.14
Waveguide confinement factor, **IV.**4.4
Waveguide dispersion, **IV.**1.11, **IV.**1.18, **IV.**2.4–**IV.**2.5
Waveguide modulator, **IV.**4.57–**IV.**4.60
Waveguides, **II.**6.3, **IV.**1.6, **IV.**1.8, **IV.**2.2, **IV.**3.1–**IV.**3.2
active index-changing mechanisms in, **II.**6.9
bends, **II.**6.20
biological
hair cells as, **III.**9.24–**III.**9.26
modal patterns, **III.**9.16–**III.**9.24
analysis of, **III.**9.22–**III.**9.23, **III.**9.23*f*–**III.**9.24*f*
changes in, by species, **III.**9.20*f*
human, **III.**9.18*f*
schematics of, **III.**9.16*f*
transmitted energy as function of *V* parameter for, **III.**9.17*f*
models for, **III.**9.7–**III.**9.15, **III.**9.22
mode of, **III.**9.2, **III.**9.12–**III.**9.13, **III.**9.15–**III.**9.19, **III.**9.22
plant cells as, **III.**9.26–**III.**9.29
for retina, **III.**9.3–**III.**9.5
single-receptor model for, **III.**9.15–**III.**9.18
sources of, **III.**9.2
V-parameter for, **III.**9.2, **III.**9.15–**III.**9.17, **III.**9.17*f,* **III.**9.19, **III.**91.6*f*
carrier effects in, **II.**6.10
Waveguides (*Cont.*):
channel, **II.**6.4, **II.**6.4*f*
coupling phenomenon, **II.**6.7–**II.**6.8
dielectric, **II.**6.3, **II.**10.4
diffused, **II.**6.5
dispersion, in optical fibers, **II.**10.9
effective index method in, **II.**6.5
fabrication techniques for, **II.**6.4
frequency doubling in, **II.**6.12
index of refraction in, **II.**6.8–**II.**6.9
ion-exchanged glass, **II.**6.12–**II.**6.13
leaky, **II.**6.3
linear electro-optic effect in, **II.**6.9–**II.**6.10
and line defects in photonic crystals, **IV.**20.13–**IV.**20.14, **IV.**20.14*f,* **IV.**20.15, **IV.**20.15*f,* **IV.**20.16, **IV.**20.16*f,* **IV.**20.17, **IV.**20.17*f*
mode matching in, **II.**6.21, **II.**6.22*f*
multilayer slab, **II.**6.5, **II.**6.5*f,* **II.**6.6
nonlinear effects in, **II.**6.12
and optical confinement, **IV.**4.4–**IV.**4.5, **IV.**4.5*f,* **IV.**4.6, **IV.**4.29
photorefractive, **II.**39.35
planar, **IV.**8.1
and point defects in photonic crystals, **IV.**20.9–**IV.**20.10, **IV.**20.10*f,* **IV.**20.11–**IV.**20.13
stripe, **II.**6.4, **II.**6.4*f*
symmetric slab, **II.**6.3, **II.**6.3*f,* **II.**6.4, **II.**6.7, **II.**6.7*f*
thermal effects in, **II.**6.11
for wavelength-division multiplexing, **IV.**1.32–**IV.**1.33
Wave interactions:
anisotropic scattering, **II.**39.7
four-wave mixing, **II.**39.6, **II.**39.6*f,* **II.**39.7
two-beam coupling, **II.**39.4, **II.**39.4*f,* **II.**39.5–**II.**39.6
Wavelength, **I.**34.4
and attenuation, **IV.**6.7–**IV.**6.8
controlling, **I.**28.12, **I.**28.13*t*
de Broglie, in optical trapping, **IV.**28.22
for lasers in telecom applications, **IV.**4.2
in network architectures, **IV.**13.14
and ocular radiation damage, **III.**15.2–**III.**15.8
for optical amplifier, **IV.**11.3
in optical fiber applications, **IV.**1.22–**IV.**1.23, **IV.**2.3
optical responses for semiconductors, **II.**36.13*t*
vs. penetration depth, for aluminum, **II.**35.52*f*
for photodetectors, **IV.**4.72*t*
for point-to-point system, **IV.**1.26
scaling, **I.**7.7, **I.**7.9
selection filters, **I.**28.12

Wavelength (*Cont.*):
splitting, with tapered fiber technology, **IV.**8.6, **IV.**8.6*f*
switch, acousto-optic tunable, **II.**6.25
of thermal neutron beam, **III.**36.3
of X rays, **III.**19.6
Wavelength conversion, **IV.**11.7–**IV.**11.9
Wavelength-dispersive X-ray fluorescence (WDXRF), **III.**35.16–**III.**35.17, **III.**35.17*f*
Wavelength division multiplexing (WDM), **II.**6.34–**II.**6.35, **II.**6.35*f,* **II.**6.36, **II.**10.30, **II.**10.30*f*–**II.**10.31*f,* **II.**10.32, **II.**10.32*f,* **II.**12.43, **IV.**1.32–**IV.**1.34, **IV.**1.33*f*–**IV.**1.34*f,* **IV.**12.9, **IV.**32.*f*
applications for, **IV.**13.1–**IV.**13.2
broadband, and dispersion flattening, **IV.**1.18
channel capacity in, **IV.**1.42, **IV.**13.3, **IV.**13.3*f,* **IV.**13.12
couplers for, **IV.**8.1, **IV.**8.4
dispersion compensation in, **IV.**13.8–**IV.**13.12
fabrication of, **II.**10.31
four-wave mixing in, **IV.**3.11, **IV.**13.8
frequency-guiding filters in, **IV.**7.8–**IV.**7.9
to increase bit rate, **IV.**2.11
laser, **I.**13.45
and soliton transmission, **IV.**7.2, **IV.**7.9–**IV.**7.12, **IV.**7.15–**IV.**7.17
traveling wave amplifiers for, **IV.**11.4
and tunable lasers, **IV.**2.6, **IV.**2.11
Wavelength-routed network, **IV.**13.13, **IV.**13.13*f*
Wavelength routers, **IV.**13.14
Wavelength scans, **II.**26.12
Wavelength-tunable lasers, **IV.**13.14
Wave mechanics, **I.**8.5
Wave meters:
dynamic, **II.**21.19, **II.**21.19*f,* **II.**21.20
interferometric, **II.**21.19
static, **II.**21.20, **II.**21.20*f*
Wave modulation distance meter, **II.**29.8*f*
Wave-particle duality, **IV.**26.8, **IV.**26.10
Waveplate, **II.**22.8
Waves, examples of, **I.**2.5*f*
(*See also specific wave types*)
Wave theory, of rays, **I.**1.9
WDM networks, **IV.**11.7
architecture for, **IV.**13.12–**IV.**13.17
channel power equalization in, **IV.**13.21–**IV.**13.23, **IV.**13.23*f,* **IV.**13.24, **IV.**13.24*f*
crosstalk in, **IV.**13.24, **IV.**13.24*f,* **IV.**13.25, **IV.**13.25*f,* **IV.**13.26, **IV.**13.26*f*
erbium-doped fiber amplifiers for, **IV.**13.1, **IV.**13.17–**IV.**13.21
for large throughput, **IV.**12.13
WDM networks (*Cont.*):
regeneration vs. optical amplification in, **IV.**13.17, **IV.**13.18*f*
WDM ring network, blocking probability in, **IV.**13.13–**IV.**13.14, **IV.**13.15*f*
WDM-TDM optical networking, **IV.**12.42
Weber contrast, **I.**29.4
Weber's law, **I.**25.27, **I.**25.29, **I.**25.33
Web inspection cameras, **III.**4.21
Weibull exponent, **IV.**1.20, **IV.**1.21*t,* **IV.**1.22*f*–**IV.**1.23*f*
Weisskopf-Wigner approximation, **IV.**26.35
Welder's flash, **III.**15.4
Weld-line phenomenon, **II.**34.15
Well capacity, in photogates, **I.**16.12
Welsbach mantle, **I.**10.15
Wernicke prism, **II.**5.6*f*
Wetherell and Womble objectives, three-mirror, **II.**18.34*f,* **II.**18.35
Weyl's plane-wave decomposition, **I.**3.21
Wide area network (WAN), **IV.**2.13
Wide-field objectives, with Maksutov correction, **II.**18.22, **II.**18.22*f*
Wiener filters (*see* Filters, Wiener)
Wiener-Khintchine theorem, **I.**4.5, **I.**4.22
Wiener spectrum, **I.**20.23–**I.**20.24
Wien's displacement law, **III.**14.11–**III.**14.12
Wigglers, **III.**26.4, **III.**32.1, **III.**32.6, **III.**32.11–**III.**32.12, **III.**32.12*f*
polarization of, **III.**32.18
power of, **III.**32.17
Wigner threshold laws, for ground-state collisions, **IV.**28.28
Williamson construction, for lightpipes, **III.**2.13, **III.**2.13*f,* **III.**2.29*f*
Window materials, far-infrared, **I.**15.4*n*
Windshear detection, **I.**16.12
Wind velocity profiles, **III.**1.19*f*
Winner-take-all, **II.**39.33*f,* **II.**39.34
Wolf shift, **I.**4.22
Wollaston, W. H., **II.**1.17
Wollaston prisms, **II.**3.7, **II.**3.19, **II.**3.21, **II.**3.23, **II.**3.25, **II.**4.15, **II.**4.15*f*
Wolter telescopes (*see* Telescopes, Wolter)
Wolter X-ray optics, **III.**28.1–**III.**28.7
applications for, **III.**35.4
collecting area with, **III.**28.1, **III.**28.3*f,* **III.**28.5–**III.**28.6, **III.**28.6*f*
fabrication of, **III.**28.6–**III.**28.7
geometry of, **III.**28.1–**III.**28.2, **III.**28.2*f*
mirror surface in, **III.**28.4–**III.**28.5
resolution in, **III.**28.2, **III.**28.3*f,* **III.**28.4, **III.**28.4*f*
Work function, of photodetectors, **I.**16.2
World Health Organization (WHO), **III.**15.10

WORM (write-once-read-only) technology, **I.**31.2–**I.**31.3
Wright objectives, **II.**18.16, **II.**18.16*f,* **II.**18.17

Xenon lamps, **I.**10.34
Xerographic process:
  cleaning/erasing image in, **III.**5.11
  color images in, **III.**5.2, **III.**5.5, **III.**5.11–**III.**5.13
  exposure systems in, **III.**5.4
  features of, **III.**5.2
  fusing in, **III.**5.10–**III.**5.11
  ghost images in, **III.**5.4, **III.**5.11
  image creation in, **III.**5.2–**III.**5.5
  image development in, **III.**5.5–**III.**5.10
  image transfer in, **III.**5.10
  invention of, **III.**5.1
  quality control in, **III.**5.11
  schematic of, **III.**5.1*f*
X-ray absorption near-edge structure (XANES), **III.**34.4, **III.**35.3, **III.**35.17
X-ray detectors:
  criteria for, **III.**34.3, **III.**34.8*t*–**III.**34.9*t*
  cryogenic, **III.**34.8, **III.**36.9
  film, **III.**34.7, **III.**36.8
  ionization, **III.**34.3–**III.**34.6
  phosphor screen for, **III.**35.32
  scintillation, **III.**34.6, **III.**36.7
  semiconductor, **III.**35.18
X-ray diffraction:
  bent crystals in, **III.**35.8–**III.**35.9, **III.**35.9*t,* **III.**35.11*t,* **III.**335.10*t*
  Bragg construction in, **III.**35.6, **III.**35.6*f*
  crystals for, **III.**19.8, **III.**22.1–**III.**22.6, **III.**35.6–**III.**35.7
  in Ewald construction, **III.**35.6, **III.**35.6*f,* **III.**35.7
  intensity gain in, **III.**35.8–**III.**35.9, **III.**35.9*t,* **III.**35.10, **III.**35.10*t,* **III.**35.11, **III.**35.11*t*
  superposition in, **III.**35.6
X-ray diffraction analysis, **III.**35.8
X-ray fluorescence (XRF), **III.**30.4, **III.**35.15–**III.**35.16
  bent crystals in, **III.**35.22, **III.**35.22*f*–**III.**35.23*f*
  Bremsstrahlung radiation in, **III.**35.17–**III.**35.18, **III.**35.22
  crystals in, **III.**35.16, **III.**35.22, **III.**35.22*f*–**III.**35.23*f*
  energy-dispersive, **III.**35.17–**III.**35.23
  microfocus (MXRF)
    crystal diffraction in, **III.**35.22, **III.**35.22*f*–**III.**35.23*f*
    monocapillary, **III.**35.18
    polycapillary, **III.**35.19, **III.**35.19*f,* **III.**35.20, **III.**35.20*f*–**III.**35.21*f*
    ultra-high resolution in, **III.**35.22–**III.**35.23
X-ray fluorescence (XRF) (*Cont.*):
  Rayleigh scattering in, **III.**35.20, **III.**35.21*f*
  wavelength-dispersive (WDXRF), **III.**35.16–**III.**35.17, **III.**35.17*f*
    resolution in, **III.**35.16
X-ray imaging, medical, **III.**19.5, **III.**19.10, **III.**35.24–**III.**35.33, **III.**37.3
  contrast in, **III.**35.26, **III.**35.26*f,* **III.**35.27, **III.**35.28*f,* **III.**35.29–**III.**35.30, **III.**35.30*f*
  in monochromators, **III.**35.33
  resolution in, **III.**35.27, **III.**35.30–**III.**35.31, **III.**35.31*f,* **III.**35.32
  scatter in, **III.**35.27, **III.**35.29, **III.**35.29*t,* **III.**35.30*f*–**III.**35.31*f*
X-ray imaging systems:
  annular apertures, obscured, **II.**11.9, **II.**11.9*f,* **II.**11.10
  design and analysis pitfalls in, **II.**11.7
  development of, **II.**11.2
  grazing incidence, **II.**11.3, **II.**11.8
    effects of, **II.**11.19, **II.**11.19*f*
  quality criteria in, **II.**11.6, **II.**11.7*f*
  residual surface roughness in, **II.**11.20, **II.**11.20*f*
  short-wavelength considerations in, **II.**11.21, **II.**11.21*f*
  solar physics, **II.**11.27
X-ray interferometer, **III.**28.10, **III.**28.10*f,* **III.**28.11, **III.**28.11*f,* **III.**28.12, **III.**36.11
X-ray interferometry, **III.**28.10–**III.**28.12, **III.**36.11
X-ray lasers, **I.**11.33–**I.**11.34, **III.**33.1, **III.**33.4
  characteristics of, **III.**33.1, **III.**33.2*t*
  optics for, **III.**33.4
X-ray lenses, **III.**20.3–**III.**20.8
  numerical aperture (NA) of, **III.**20.3, **III.**20.8
X-ray lithography, **III.**19.10, **III.**30.3–**III.**30.4, **III.**33.2, **III.**35.5
X-ray metrology, **III.**26.5, **III.**28.11
X-ray microanalysis, **III.**20.5, **III.**20.8
X-ray microlithography, **II.**11.2
X-ray microscopy, **III.**19.6, **III.**19.10, **III.**20.7–**III.**20.8, **III.**20.9*f,* **III.**32.19, **III.**33.2, **III.**35.4
  resolution in, **III.**20.8, **III.**35.4
X-ray Multimirror Mission (XMM), **III.**28.1–**III.**28.2, **III.**28.3*f,* **III.**28.6
X-ray optics:
  modeling, software for, **III.**19.10, **III.**26.4
  monocapillary:
    applications for, **III.**29.4–**III.**29.6, **III.**35.4, **III.**35.8–**III.**35.9, **III.**35.18
    condensing, **III.**29.2–**III.**29.3, **III.**29.3*f,* **III.**29.4–**III.**29.6

X-ray optics, monocapillary (*Cont.*):
design of, **III.**29.1, **III.**29.2*f,* **III.**29.3, **III.**29.3*f,* **III.**29.4
and electron impact sources, **III.**31.11
fabrication of, **III.**29.4
imaging, **III.**29.3, **III.**29.3*f,* **III.**29.4
materials for, **III.**29.1, **III.**29.2*t*
multicapillary, collimation in, **III.**30.6*f,* **III.**30.8–**III.**30.11, **III.**30.11*f*–**III.**30.12*f,* **III.**30.15
polycapillary:
angle of acceptance in, **III.**35.27
angle of incidence in, **III.**30.5, **III.**30.5*f*
applications for, **III.**30.4, **III.**30.15, **III.**35.4–**III.**35.5, **III.**35.8–**III.**35.9, **III.**35.15, **III.**35.19–**III.**35.21
collimation in, **III.**30.6*f,* **III.**30.8–**III.**30.11, **III.**30.11*f*–**III.**30.12*f,* **III.**30.15
composition of, **III.**30.5, **III.**30.6*f*–**III.**30.7*f,* **III.**30.8*t*
and electron impact sources, **III.**31.11
energy filtering in, **III.**30.13, **III.**30.13*f*
in focused-beam diffraction, **III.**35.13, **III.**35.14*f*
focusing with, **III.**30.13–**III.**30.14, **III.**30.14*f,* **III.**30.15
function of, **III.**30.4–**III.**30.7
with neutron beams, **III.**36.15
radiation damage in, **III.**30.14
resolution in, **III.**30.8, **III.**30.11
synchrotron, photons in, **III.**26.3
transmission data for, **III.**30.5–**III.**30.7, **III.**30.7*f*–**III.**30.10*f,* **III.**35.9*t*–**III.**35.11*t*
SHADOW, **III.**19.10, **III.**26.4
synchrotron, **III.**19.6, **III.**19.10, **III.**22.4, **III.**26.3–**III.**26.6, **III.**35.3, **III.**37.3
vs. point source/optic combination, **III.**35.5
polycapillary application for, **III.**30.14, **III.**30.15*t*
in protein crystallography, **III.**35.14
and Schwarzschild objective, **III.**27.4
Wolter, **III.**28.1–**III.**28.7
applications for, **III.**35.4
collecting area with, **III.**28.1, **III.**28.3*f,* **III.**28.5–**III.**28.6, **III.**28.6*f*
fabrication of, **III.**28.6–**III.**28.7
geometry of, **III.**28.1–**III.**28.2, **III.**28.2*f*
mirror surface in, **III.**28.4–**III.**28.5
resolution in, **III.**28.2, **III.**28.3*f,* **III.**28.4, **III.**28.4*f*
X-Ray Optics, Center for, **III.**21.3
X-ray photoemission spectroscopy (XPS), **II.**36.33
X-ray production:
and blackbody radiation, **III.**19.6
and Bremsstrahlung radiation, **III.**19.6, **III.**31.6–**III.**31.7, **III.**31.7*f*
X-ray radiation:
characteristic, **III.**31.6–**III.**31.7, **III.**31.7*f,* **III.**31.10, **III.**33.2, **III.**35.15
X-ray radiation therapy, **III.**35.33–**III.**35.34
X rays:
absorption for, **III.**19.7, **III.**20.3
applications for, **III.**19.5, **III.**19.10, **III.**20.5, **III.**20.7, **III.**35.3, **III.**35.14, **III.**35.24–**III.**35.33, **III.**37.3
in astronomical optics, **III.**28.1–**III.**28.12
astronomy, applications for, **III.**19.6, **III.**28.1–**III.**28.12, **III.**30.4, **III.**37.3
atomic photoabsorption of, **III.**A.1, **III.**A.2*f*
atomic scattering of, **III.**A.1, **III.**A.2*f*
characteristic, **III.**31.6–**III.**31.7, **III.**31.7*f,* **III.**31.10, **III.**35.15
collimating, **III.**35.7–**III.**35.8
cosmic sources of, **III.**28.1, **III.**28.10
crystalline dispersion for, **III.**22.1–**III.**22.6
diffraction of, **III.**19.5, **III.**19.7–**III.**19.8, **III.**19.8*f,* **III.**19.9, **III.**19.9*f,* **III.**35.6–**III.**35.8
discovery of, **III.**19.5, **III.**34.7
electron impact sources of, **III.**31.5–**III.**31.11
fluorescence (XRF), **III.**35.15–**III.**35.23
incidence angle for, **III.**22.1
interaction in matter, **III.**A.1–**III.**A.2, **III.**A.3*t*–**III.**A.8*t*
microfocusing of, **III.**26.6
monocapillary optics for, **III.**29.1–**III.**29.6, **III.**31.11
multichannel plate optics for, **III.**30.1–**III.**30.3, **III.**30.3*f*–**III.**30.4*f*
and multilayer reflective coatings, **III.**24.1–**III.**24.2
novel sources of, **III.**33.1–33.4
optics of, progress in, **III.**19.5
and polarization, **III.**25.1–**III.**25.8, **III.**32.6–**III.**32.8
polycapillary optics for, **III.**30.1, **III.**30.4–**III.**30.15, **III.**31.11
production of, **III.**19.6
property changes for, **III.**19.7
for radiation therapy, **III.**35.33–**III.**35.34
reflection of, **III.**19.5, **III.**19.9–**III.**19.10
refraction of, **III.**19.5–**III.**19.7, **III.**19.8*f,* **III.**20.3–**III.**20.8
scattering of, **III.**3.6, **III.**19.7, **III.**20.8, **III.**26.4, **III.**35.27, **III.**35.29*t,* **III.**35.30, **III.**35.30*f*–**III.**35.31*f,* **III.**A.1, **III.**A.2*f*
simulations for, **III.**19.10
soft, **II.**11.5–**II.**11.6
spectral range for, **III.**19.5–**III.**19.6
synchrotron optics for, **III.**26.3–**III.**26.6
zone plate use with, **III.**23.1–**III.**23.7, **III.**35.4

X-ray scattering, **III.**3.6, **III.**19.7, **III.**20.8, **III.**26.4, **III.**35.27, **III.**35.29*t,* **III.**35.30, **III.**35.30*f*–**III.**35.31*f,* **III.**A.1, **III.**A.2*f*
X-ray sources:
electron beam impact, **III.**31.5, **III.**31.5*f*
anode material for, **III.**31.10
brightness of, **III.**31.7–**III.**31.8, **III.**31.8*f,* **III.**31.9, **III.**31.9*f,* **III.**31.11
focussed beam in, **III.**31.10–**III.**31.11
optics for, **III.**31.11
parallel beam in, **III.**31.10
processes of, **III.**31.5–**III.**31.7, **III.**31.*f*
voltage for, **III.**31.10
X-ray synchrotron sources, **II.**11.29, **II.**11.29*f*
X-ray telescopes, **III.**19.10, **III.**28.1
X-y addressed switch-FET (SWIFET), **I.**23.16

Y-branch interferometric modulator, **IV.**4.51, **IV.**4.51*f,* **IV.**4.54–**IV.**4.56
Yellow matter, **I.**43.14, **I.**43.22, **I.**43.30
absorption by, **I.**43.23, **I.**43.24*t*
concentrations, variability in, **I.**43.24
Yield strength, **II.**35.9
Yolo objectives, **II.**18.28*f,* **II.**18.29
Young, Thomas, **III.**10.2, **III.**10.7
Young's astigmatic formulae, **I.**1.48
Young's double-slit experiment, **I.**2.14–**I.**2.15, **I.**2.15*f,* **I.**2.17, **I.**2.17*f*
Young's modulus, **II.**33.32–**II.**33.33, **II.**35.8
Young-Thollon prism, **II.**5.7*f*

Zeeman effect, **II.**20.19–**II.**20.20, **II.**28.23, **II.**36.48
Zeeman pattern, **II.**20.17, **II.**20.18*f*
Zeeman shift, in magneto-optical trapping, **IV.**28.23–**IV.**28.24
Zeeman splitting, **IV.**23.4, **IV.**23.18, **IV.**26.8
Zeiss Infinity Color-Corrected Systems Plan Apo objective, **II.**17.19
Zenger prism, **II.**5.6*f*
Zernicke's three-beam interferometers, **II.**21.8, **II.**21.8*f*
Zernike formula, **II.**33.26
Zernike polynomials, **I.**1.98
definition of, **III.**10.2
and optical aberrations, **III.**1.12–**III.**1.15, **III.**10.4
Zernike test, **II.**30.10
Zero-phonon lines, **I.**8.27*f,* **I.**8.28–**I.**8.30, **II.**28.14, **II.**28.15*f,* **II.**28.16, **II.**28.17*f*
Zero-phonon transition, **I.**8.28
Zirconium arc lamps, **I.**10.39, **I.**10.44*f*
ZO-MOD BLACK, **II.**37.58
Zonal spherical aberration, **II.**18.42
Zone of clear and single binocular vision (ZCSBV), **III.**12.25, **III.**12.25*f*
Zone plates, **I.**3.11, **I.**3.12*f,* **I.**3.13
amplitude, **III.**23.4, **III.**23.4*f,* **III.**23.5, **III.**23.5*f*
Bragg-Fresnel optics for, **III.**23.7–**III.**23.8, **III.**23.8*f*
focusing properties of, **III.**23.1–**III.**23.2
Fresnel, **II.**7.18, **III.**23.3, **III.**32.19
aberration characteristics of, **II.**7.23
diffraction efficiency of, **II.**7.25
geometry of, **III.**23.2–**III.**23.4
with laser-generated plasmas, **III.**33.2
manufacture of, **III.**23.6–**III.**23.7
phase, **III.**23.5–**III.**23.6, **III.**23.6*f*
resolution with, **III.**35.4
shapes of, **III.**23.1, **III.**23.1*f*
terminology for, **III.**23.2*n*
Zoom lenses, **II.**15.11, **II.**16.15, **II.**16.20
Zoom systems, **I.**32.11
Z-scan, to determine nonlinear characteristics, **IV.**17.31–**IV.**17.32, **IV.**17.32*f,* **IV.**17.33
Z-tilt, **III.**1.17

ABOUT THE EDITORS

Michael Bass is Professor of Optics, Physics, and Electrical and Computer Engineering in the School of Optics/Center for Research and Education in Optics and Lasers at the University of Central Florida. He received his B.S. in physics from Carnegie-Mellon, and his M.S. and Ph.D. in physics from the University of Michigan.

Jay M. Enoch is Professor of the Graduate School and Dean Emeritus, School of Optometry, University of California at Berkeley. He also serves as a professor in the Department of Ophthalmology at the University of California at San Francisco. He received his B.S. in optics and optometry from Columbia University and his Ph.D. in physiological optics from Ohio State University.

Eric W. Van Stryland is Professor of Optics, Physics, and Electrical and Computer Engineering in the School of Optics/Center for Research and Education in Optics and Lasers at the University of Central Florida. He received his Ph.D. from the University of Arizona.

William L. Wolfe is a Professor Emeritus at the Optical Sciences Center at the University of Arizona. He received his B.S. in physics from Bucknell University, and his M.S. in physics and M.S.E. in electrical engineering from the University of Michigan.

The **Optical Society of America** is dedicated to advancing study, teaching, research, and engineering in optics.

Copyright 2001 by The McGraw-Hill Companies, Inc. Click Here for Terms of Use.